SERBIATRIB '13

Serbian Tribology Society

Faculty of Engineering
University of Kragujevac

SERBIATRIB '13

13th International Conference on Tribology

15 – 17 May 2013, Kragujevac, Serbia

PROCEEDINGS

SERBIATRIB '13

SERBIATRIB '13

Serbian Tribology Society

University of Kragujevac,
Faculty of Engineering

SERBIATRIB ‘13

13th International Conference on Tribology

15 – 17 May 2013, Kragujevac, Serbia

PROCEEDINGS

EDITORS: Miroslav Babić, Slobodan Mitrović

SERBIATRIB ‘13

13th International Conference on Tribology – SERBIATRIB '13 PROCEEDINGS

ISBN: 978-86-86663-98-6

Editors:	Miroslav Babić, Ph.D. University of Kragujevac, Faculty of Engineering Slobodan Mitrović, Ph.D. University of Kragujevac, Faculty of Engineering
Publisher:	Serbian Tribology Society Sestre Janjić 6, 34000 Kragujevac, Serbia University of Kragujevac, Faculty of Engineering Sestre Janjić 6, 34000 Kragujevac, Serbia
For the Publisher:	Miroslav Babić, Ph.D., Faculty of Engineering Branko Ivković, Ph.D., Serbian Tribology Society
Technical editor:	Slobodan Mitrović, Ph.D. University of Kragujevac, Faculty of Engineering Dragan Džunić, research assistent University of Kragujevac, Faculty of Engineering Marko Pantić, research assistent University of Kragujevac, Faculty of Engineering
Printed by:	KOPIRNICA MAŠINAC, 34000 Kragujevac, Serbia
Circulation:	100 copies

The publication of this Proceedings was financially supported by the Ministry of Education, Science and Technological Development of the Republic of Serbia.

Supported by

Ministry of Education, Science and Technological Development of the Republic of Serbia

International Scientific Committee

Aleksandar Marinković	University of Belgrade (Serbia)
Aleksandar Rac	Serbian Tribology Society (Serbia)
Aleksandar Vencl	University of Belgrade (Serbia)
Andrei Tudor	University Politehnica of Bucharest (Romania)
Bharat Bhushan	The Ohio State University (USA)
Bogdan Sovilj	University of Novi Sad (Serbia)
Branko Ivković	Serbian Tribology Society (Serbia)
Damir Kakaš	University of Novi Sad (Serbia)
Dušan Stamenković	University of Niš (Serbia)
Emilia Assenova	Technical University of Sofia (Bulgaria)
Friedrich Franek	Vienna University of Technology (Austria)
Geetha Manivasagam	VIT University (India)
Hakan Kaleli	Yildiz Technical University (Turkey)
Konstantinos-Dionysios Bouzakis	Aristotle University of Thessaloniki (Greece)
Lorena Deleanu	University Dunarea de Jos (Romania)
Mara Kandeva	Technical University of Sofia (Bulgaria)
Marion Merklein	Friedrich Alexander Universität Erlangen Nürnberg (Germany)
Mehmet Baki Karamis	Erciyes University (Turkey)
Miroslav Babić	University of Kragujevac (Serbia)
Niculae Napoleon Antonescu	Petroleum-Gas University of Ploiesti (Romania)
Nikolai Myshkin	V.A. Belyi Metal-Polymer Research Institute of National Academy of Sciences of Belarus (Belarus)
Nyagol Manolov	Technical University of Sofia (Bulgaria)
Slobodan Mitrović	University of Kragujevac (Serbia)
Slobodan Tanasijević	University of Kragujevac (Serbia)

Organising Committee

Honorary President:

Branko Ivković	Serbian Tribology Society (Serbia)

Presidents:

Miroslav Babić	University of Kragujevac (Serbia)
Slobodan Mitrović	University of Kragujevac (Serbia)

Members:

Blaža Stojanović	University of Kragujevac (Serbia)
Fatima Zivić	University of Kragujevac (Serbia)
Marko Pantić	University of Kragujevac (Serbia)
Dragan Dzunić	University of Kragujevac (Serbia)

Preface

The International Conference on Tribology – SERBIATRIB, is traditionally organized by the Serbian Tribology Society every two years, since 1989. The previous conferences were held in Kragujevac (1989, 1991, 1993, 1999, 2005, 2007 and 2011), Herceg Novi (1995), Kopaonik (1997), Belgrade (2001, 2003 and 2009). This year the 13th International Conference on Tribology – SERBIATRIB '13 also takes place on May 15-17, 2013 in Kragujevac.

This Conference is organized by the Serbian Tribology Society (STS) and the University of Kragujevac, Faculty of Engineering. Organizing Scientific Conferences, STS plays a significant role in helping engineers and researchers to introduce in the fundamentals of tribology and to present their experience, solutions and research results.

The scope of the 13th International Conference on Tribology – SERBIATRIB '13 embraces the state of art and future trends in tribology research and application. The following two aspects of tribology practice require special attention. Firstly, the requirement for higher productivity of machinery means that machines must operate under higher loads and at higher speeds and temperatures, and that is why finding the right solutions for tribological processes is extremely important. Secondly, the good tribology knowledge can greatly contribute to the saving of material and energy.

The Conference program generally includes the following topics: fundamentals of friction and wear; tribological properties of solid materials; surface engineering and coating tribology; lubricants and lubrication; tribotesting and tribosystem monitoring; tribology in machine elements; tribology in manufacturing processes; tribology in transportation engineering; design and calculation of tribocontacts; sealing tribology; biotribology; nano and microtribology and other topics related to tribology.

All together 76 papers of authors from 18 countries (Taiwan, Russia, Belarus, Ukraine, Germany, Poland, India, Pakistan, Nigeria, Slovenia, Croatia, Bosnia and Herzegovina, Italy, Romania, Bulgaria, Greece, Turkey and Serbia) are published in the Proceedings. Approximately 37 papers were submitted by the foreign authors and app. 39 papers by the Serbian authors. All papers are classified into five chapters:

- Plenary lectures (4)
- Tribological properties of materials and coatings (29)
- Tribology in machine elements (23)
- Tribometry (13)
- Trenje, habanje i podmazivanje (7) – papers written in Serbian language

It was a great pleasure for us to organize this Conference and we hope that the Conference, bringing together specialists, research scientists and industrial technologists, and Proceedings will stimulate new ideas and concepts, promoting further advances in the field of tribology. The

Editors would like to thank the Scientific and the Organizing Committee and all those who have helped in making the Conference better. We would like to thank especially prof. Miroslav Babić and prof. Branko Ivković for the helpful suggestions and support.

The Conference is financially supported by the Ministry of Education, Science and Technological Development, Republic of Serbia.

We wish to all participants a pleasant stay in Kragujevac and we are looking forward to seeing you all together at the 14th International Conference on Tribology – SERBIATRIB '15.

Kragujevac, May 2013 Editors

Contents

Plenary Lectures

Tribological Properties of Materials and Coating

Tribology of Machine Elements

Tribometry

Trenje, habanje i podmazivanje

Plenary Lectures

13th International Conference on Tribology – SERBIATRIB ’13

15 – 17 May 2013, Kragujevac, Serbia

Serbian Tribology Society

SERBIATRIB '13

13th International Conference on Tribology

Faculty of Engineering in Kragujevac

Kragujevac, Serbia, 15 – 17 May 2013

THE GREEN AUTOMOBILE – DEFINITION AND REALIZATION –

Wilfried J. Bartz[1]

[1]T+S Tribology and Lubrication Engineering, Technische Akademie Esslingen e. V., Ostfildern, Germany

Abstract: *The green automobile has to be green from the cradle to the grave. This means that the life cycle assessment should be the required approach which means the environmental impact of raw material generation, of production, during use and of disposal and recycling have to be taken into account.*
The overall aim is the reduction of energy as well as health and safety of the mankind. Nowadays the resources of energy carriers are consumed faster than expected.
The impacts mentioned above can be characterized by emissions, primary energy demand, consumption of resources and waste generation. Often these environmental impacts are evaluated as CO2-emissions, contribution to the greenhouse effect and summer smog and as primary energy demand during life cycle of all energy consumers.
Mostly these impacts are simplified to the contribution of lubricants by higher efficiency in powertrains, by longer lubricants lifetimes, by energy reductions during the production of automobiles and during their use. The last mentioned aspects mainly mean the reduced fuel consumption by reducing the friction between all moving parts.
Some of the aspects mentioned above are explained and evaluated in this presentation. As an result an overall energy reduction is possible.

THE ECO-LABEL AND THE CONFLICT BETWEEN BIODEGRADABILITY AND ENVIRONMENTALLY ACCEPTABILITY OF LUBRICANTS

Wilfried J. Bartz[1]

[1]T+S Tribology and Lubrication Engineering, Technische Akademie Esslingen e. V., Ostfildern, Germany

Abstract: *Often the environmentally acceptability is equated with the fast biodegradability. But for the degradation process oxygen is necessary. If large amounts of lubricants will be introduced into the environment, for instance as an accident, so much oxygen has to be taken from the surrounding, that other organisms will suffer.*
Nevertheless the regulations to define environmentally acceptable lubricants, which are listed in the framework to receive the European Eco-Label do not consider this aspect. The criteria for the Eco-Label include environmentally and human health hazards, aquatic toxicity requirements, biodegradability , exclusion of specific substances, the imperative use of renewable raw materials and of course the technical performance.
Details of these criteria will be explained in the presentation.

Serbian Tribology Society

SERBIATRIB '13

13th International Conference on Tribology

Faculty of Engineering in Kragujevac

Kragujevac, Serbia, 15 – 17 May 2013

ROUGHNESS AND TEXTURE CONCEPTS IN TRIBOLOGY

N.K. Myhkin[1], A.Ya. Grigoriev[1]
[1]Metal-Polymer Research Institute, Belarus, nkmyshkin@mail.ru

Abstract: *Current knowledge on scale and spatial organization of engineering surfaces is presented. Main methods of surface roughness analysis are discussed. A review of theoretical and practical problems in tribology involving concept of rough surface is presented. Critical analysis of rough surface description in the evolution from 2D to 3D set of parameters is carried out. Advantages and disadvantages of traditional and modern approaches of surface analysis based on concepts of roughness and texture are discussed.*

Keywords: *surface roughness, roughness parameters, texture, wear surface, debris.*

1. INTRODUCTION

Surface asperities influence practically all the aspects of solids contact. There are a lot of theoretical and experimental data on mutual dependence of roughness and such phenomena as adhesion, contact stiffness, abrasion and many others which occur during friction and wear [1-3]. It is commonly accepted that understanding of friction phenomena is directly connected to analysis of surface structure and its transformation due to wear. So, at present any friction and wear model is involving surface roughness parameters.

Traditional concept of rough surface based mainly on profile parameters is not fully satisfied modern trends in tribology. Development of 3D parameters did not change the situation significantly. Only recently, a new view of surface spatial organization was introduced. The concept is known as texture and it reflects the appearance of distinctive surface pattern. The current paper presents a review of the problems of rough surfaces analysis in their evolution from statistical height and step parameters of profiles to dimensionless and scale invariant representation of surface texture.

2. ROUGHNESS ORIGIN

The deviation of a real surface from the ideally smooth are associated with the action of various factors, which can be divided onto structural, technological, and operational ones [4-6]. Their features define scale and textural properties which form surface geometric irregularities and as a result different types of roughness.

Structural roughness is inherently connected with discrete nature of solids. Having small but finite sizes, the atoms and molecules of solids are located within a certain distance from each other. If assume that the boundary of solids corresponds to some constant potential of atomic interaction with the surrounding phase, it is evident that its relief has a periodic nature. Surface image with atomic resolution presented on Figure 1a confirms that.

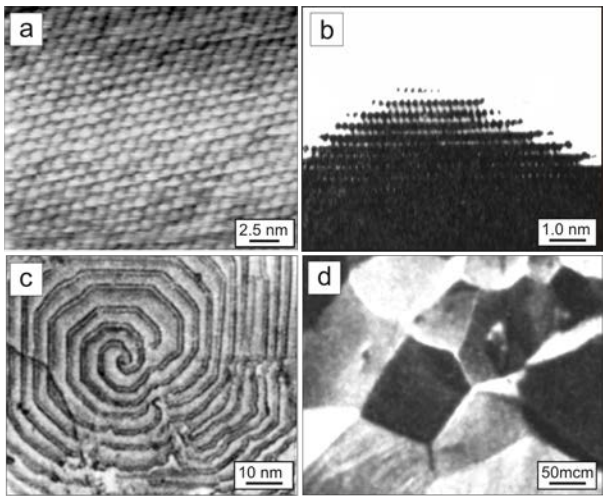

Figure 1. a – AFM image of pyrolytic graphite surface (amplitude of surface deviation 0.43 nm); b – deformation of gold surface structure under effect of surface forces [7] (TEM); c – surface of spiral dislocation; d – surface of steel fracture.

The relief characteristics at this level are closely related to surface forces and here significant quantum-mechanical effects occurs such as thermal oscillations of atoms with amplitudes up to 10% percent of interatomic distances and spontaneous changes in their position. Moreover various atomic stacking faults in the surface layer produce compensating deformations of the layer material (Figure 1 b). However, from a practical point of view, these properties are not significant, at least for the present level of tribological problems.

Strict periodicity of atomic roughness is characteristic only for ideal crystals. Real solids are imperfect. The imperfections of atomic structure known as dislocations form next level of physical roughness (Figure 1 c).

Crystalline structure of solids can form last level of structural roughness. Unlike to previous types of irregularities which characterized by sub-nanometer heights, the size of corresponded asperities is comparable to the size of crystallites and can reach up to hundreds of microns. Usually this type of relief is observed on the fracture surfaces of metals (Figure 1 d).

Technological roughness is a result of mechanical, thermal or any other types of material processing. These surface deviations consist of periodical and random components. Formation of periodical components results from the processes of copying of tool cutting edges and roughness is affected by technology (Figure 2). The appearance of the random components is associated with material destruction during chip formation and its adhesion to cutting edges (build-up), work hardening and fatigue failure of surface layers, etc.

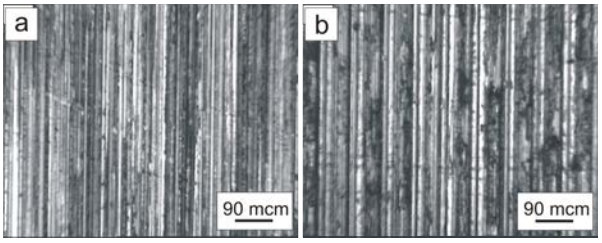

Figure 2. Machined surfaces (Ra 1.6): a – cylindrical grinding ; b – turning

Errors in mounting of the parts during machining, the presence of elastic deformations and vibration in the machine-tool system, cutting tool wear, and so on, leads to waviness and deviations of form (hour-glassing, faceting, barrelling, etc.) of the real surface or the profile from the corresponding parameters specified on the basis of design. These deviations can be periodic or stochastic.

Operation roughness. Main reasons of surface degradation of machine parts during operation are wear and corrosion. Nowadays it is generally accepted that mechanisms of wear and corrosion corresponded to certain morphological types of formed surfaces and fracture fragments (wear particles or oxides). It is a basis of modern methods of tribomonitoring and triboanalysis [8,9].

The theoretical background of the methods is provided by phenomenological models of friction contact damage. While using these models the actual wear mechanism is established basing on classification of friction surface morphology (Figure 3).

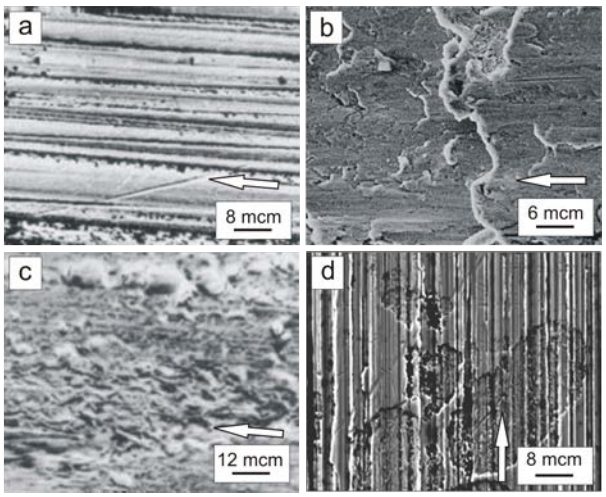

Figure 3. Surface damage at friction: a – abrasion wear; b – plastic deformation; c – ploughing and adhesive fracture; d – fatigue wear

Thus, the delamination of thin material layers and the formation of exfoliation and spalling regions are related to fatigue wear at cyclic elastic contact. It is followed by the separation of material debris which points to plastic deformation of the surface layer at excessive loading and lubricant film tearing. The appearance linear relief of asperities with sharp edges indicates abrasive wear. Defects shaped as deep tear-outs, delaminated thin films point to adhesive and cohesive interaction of the contact surfaces. Thus, analysis of wear debris and friction surfaces allows for evaluation of the operating conditions of tribosystem, condition of lubricant, and provides the opportunity to predict failure of the tribosystem and take measures to prevent it [10].

3. SCALE STRUCTURE OF ROUGH LAYER

As it can be seen the heights of the surface asperities lie in a wide range. On lower side they are limited by the dimensions of the atomic and supermolecular formations, on the upper one by maximal heights which are proportional to the length of the examined profile [11].

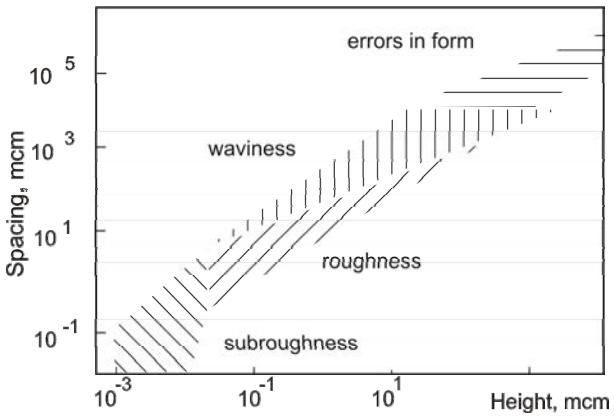

Figure 4. Diagram of the height and spacing parameters of surface asperities

It is evident that in this case there are no limitations on the existence of asperities in various dimensional ranges (both spacing-wise and height-wise). However, in spite of the fact that there is no universally substantiated criterion for distinguishing asperities on the basis of scale, at the present time there exists the concept of the surface as an ensemble of asperities of four dimensional levels: macrodeviations, waviness, roughness, and subroughness [12].

4. SURFACE MEASUREMENT

In studying the topography the need arises for the solution of three basic problems: description of the surface, development of representative surface evaluation systems and technical realization of the measurement processes. In spite of the fact that these problems are interdependent, the last problem is of special importance, since our theoretical concepts, and therefore our understanding of how any particular phenomena may take place on the surface, are based on the quantitative estimates. Therefore it is evident that roughness measurements are of primary importance in studying the topography. Nowadays a great number of experimental methods of surface measurement are used. Stylus methods remain the most widespread; they yield results forming the basis for current standards. Optical methods involving electromagnetic radiation such as light section, shadow projection, interference techniques etc. have became widely applied. Atomic-force microscopy has found a wide spread in surface metrology now. Figure 5 represents some capabilities of different methods of roughness measurement and their vertical and lateral resolution. As can be seen there is no method for measuring full range of asperities deviations.

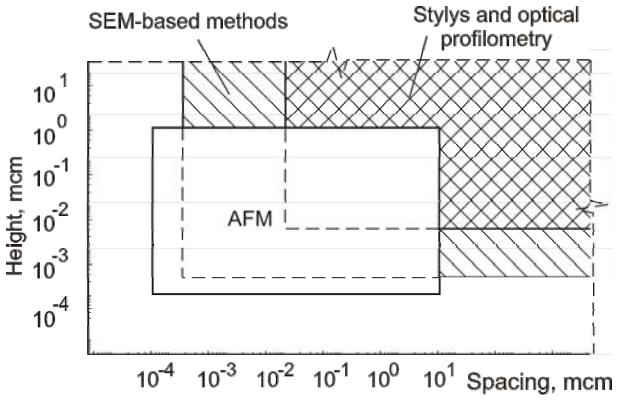

Figure 5. Resolution of various methods of roughness measurement

The foregoing concepts form the basis of the representation of a surface in such disciplines as mechanical engineering, machine design, technology, tribology, heattransfer, and so on. On the whole in this representation the surface is examined as the realization of a random field, the characteristics of which are evaluated on the basis of two-dimensional profilogram samples [12]. In this case the system of topography estimates is based on analysis of the histogram characteristics of the asperities in some range of their values.

A characteristic feature of this approach is the fact that the mutual influence and interrelationship of the asperities are generally ignored (except for the fact that the surfaces may be classified as isotropic or anisotropic), i.e., the spatial organization of the asperities is not taken into account. We can illustrate the ambiguity arising in the surface representations in this case. Figure 6 a, b shows photographs (obtained on a scanning electron microscope (SEM)) of surfaces having different spatial structure. Table 1 present the results of a comprehensive study of their microgeometry.

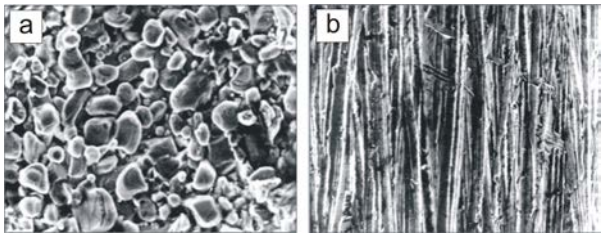

Figure 6. Two types of surface textures

Table 1. Roughness parameters of surfaces on Figure 6.

Roghness parameter	Sample on Figure 5	
	a	b
Ra	3.2±0.5	2.3±0.3
Rz	19.3±4.2	15.9±2.0
Rmax	15.0±3.7	12.2±1.4
S	56.7±18.6	43.2±7.6
Sm	165.9 ±4.4	117.7±8.7

It can be seen that in spite of the significant difference between the studied objects practically all the quantitative estimates coincide in the limits of the measurement errors. It is impossible to determine criteria on the basis of which we can judge the difference between these surfaces.

The principal reasons why it is not possible to evaluate the topographic properties of surfaces solely with the aid of histogram estimates were discussed in [14, 15]. Specifically, it was shown that on the basis of these characteristics we cannot construct a satisfactory prognostic model, since in the final analysis it is valid only in the limits of those values that were used for its construction. The use of this model may lead to unexpected results. For example, according to the authors of [15], by superposing the parameters we can achieve a good description of practically any phenomenon, including those not relating to the examined object. Considering that the modern instruments yield about fifty different characteristics (including 3D) that may be subsequently used, the drawbacks of this approach become still more evident [6]

For more correct representation of the surface it is necessary to have the possibility of characterizing it as an object, having a definite topology. In tribology this approach is formalized by concept of texture [16, 17].

5. CONCEPT OF TEXTURE

Surface texture is rather difficult to define. Most authors agree that this notion reflects the features of the surface relief caused by the two-level model of spatial relations of irregularities heights [18, 19]. The mode of these relations at the local level governs the shape of irregularities and at the global level, the position of irregularities relatively to each other. To some extent, the concept of texture unites the ideas of treatment direction and irregularity direction according to the USSR Standards GOST 2789–73 and 9378–93. The texture is outlined qualitatively by several adjectives characterizing the shape and mutual position of irregularities, such as stepwise linear, facet random, spherical, spherical radial, etc.

There are numerous approaches to the description of texture; however, all of them are reduced to one of the following: comparative and parametrical approach, usage of invariant presentations, and parameterization of visual content.

Comparative methods are based on expert visual evaluation of the similarity of the object under investigation and the reference. The features of man's vision allow him to notice and identify minute distinctions in roughness, texture, color, and shape of objects. The simplicity of comparative methods and the fact that they provide sufficient accuracy for most applications encouraged their widespread use. Thus, for qualitative evaluation of roughness, sample reference surfaces are used according to GOST 9378–93 (Figure 2).

Comparative methods are very simple and in most cases a set of references and an optical microscope are sufficient to realize them. Their disadvantages are the subjective and qualitative nature of the estimates obtained. To overcome them, the opinions and agreement of multiple experts are used [20].

Parametric methods use different statistics of surface asperity heights and spacing, brightness, and color characteristics of their images.

In order to evaluate texture properties, roughness parameters are most often used, e.g., according to GOST 25142–82. Since 2007, the ISO 25178 standard has been used to describe 3D surface properties. However, they are mainly similar to standard profile estimates and hence inherit all their shortcomings [6, 15].

The advantages of the parametric approach are in the simple interpretation of the respective estimates, while their weak descriptive ability can be considered a shortcoming. Nevertheless, when a great number of similar characteristics are used, the approach is capable to solve the problems with accuracy sufficient for most practical applications.

The essence of *invariant representation* is the application of normalized description methods, i.e., the representation of analysis objects in a form independent of their scale and coordinate origin.

The simplest procedure of invariant representation is based on the Fourier transform of surface heights [21]. With respective normalization, the coefficients of the amplitude spectrum (Fourier descriptors) do not depend on the scale and position and can be considered as a complete (single-valued and reversible) system of features. More complicated methods use fractal compression of images and wavelet transforms [22, 23].

Features are not defined in the given approach at all. It is believed that all elements of normalized representations are features. It is of no significance that they can be numerous and do not have visual interpretation. It is assumed that they are analyzed and classified by computer methods; therefore, the size of the feature vector is not important. The approach is unsuitable for research because of the absence of any visual and geometric interpretation.

Parameterization of visual content is based on the assumption that representative description of texture is the only possible by means of estimates reflecting the visual content of the objects under investigation.

Realization of the approach is based on the introduction of a structural element, i.e., the minimal visually perceived region of the object under analysis. It is believed that the features of dislocation of structural elements relative to each other govern local morphological properties at small distances, and global ones at large distances. Differences in the choice of structural element type and description of their mutual position are responsible for the variety of the methods for realizing the given approach.

One of the methods is based on the use of co-occurrence matrices (COM) [16, 17]. The use of COM is motivated by the known assumption that the second order probabilities of features derived from the images reflect their visual content [24].

In order to describe the texture by the given method, a surface region is chosen as a structural element whose position is characterized by the direction of gradient G_i and distance P_i from the coordinate center (Figure 7 a). The mutual position of two structural elements is specified by the distance between them ρ and the difference invariant description based on COM (Figure 7 b), the number of pairs of structural elements is counted with certain ρ and *g* being present at the surface area under analysis. Both height-coded and half-tone images can be used taken by various microscopy methods arranged as upside lightening.

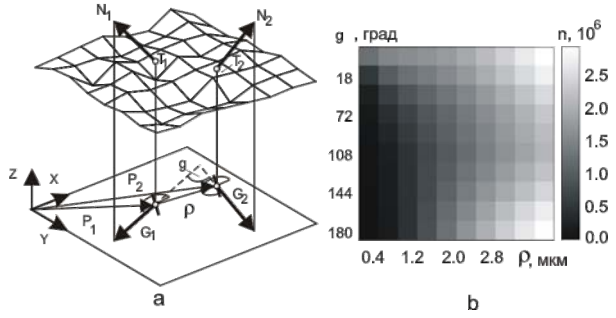

Figure 7. Parameterization of visual contents of texture: a – scheme of determination of structure element; b – matrix of co-occurrence of texture elements

With respective normalization, COM does not depend on scale and object position in the field of view. As with invariant presentations, each of the COM elements can be considered as a feature. However, since COM elements define the areas of the surface, and then the possibility arises of non-parametric comparison of objects with visualization of their similarity or dissimilarity [25, 26]. The technique involves marking the areas whose COM elements have either close or essentially different values on the images of the compared objects. In the former case, this allows for visualizing the similarity of the objects, and in the latter their distinction. Figure 8 shows the results of the solutions of this problem.

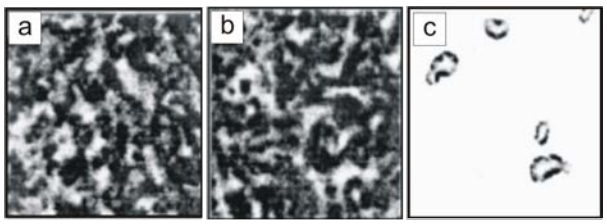

Figure 8. The visual matching of surface texture differences: a, b – surface of two types of hard drive magnetic media; d – difference of the surface a from b (presence of "kidney-like" structures)

The advantage of the approach consists in its general nature, allowing us to unite the features of texture of objects. This makes analysis of their morphology and classification much easier. However, its realization is rather complicated.

Prospects in development of texture analysis and applications look very promising. The analytical and computational tools in texture analysis are progressing quickly [27]. The progress in technology results in a possibility to use a variety of methods for making regular textures and micro-textures e.g. by laser [28] or patterning with rigid asperities [29]. These technological advances can bring a lot of fruitful applications in many areas of tribology.

6. CONCLUSIONS

Surface 3D organization can be described by definition of texture. Experience of image recognition theory can provide methods for rough surface texture description and visualization of texture similarity/dissimilarity. The description of a surface texture by special type of COM is in a good agreement with the texture distinctions obtained by expert visual perception. Texture analysis can be efficiently applied for solving practical tribological problems in micro/nanoscale.

REFERENCES

[1] N.K. Myshkin, C.K. Kim, M.I Petrokovets: *Introduction to Tribology*, Cheong Moon Gak, 1997.

[2] *Micro/Nano Tribology*, Ed. By B. Bhushan, CRC Press, 1998.

[3] G. W. Stachowiak: *Engineering Tribology. Butterworth-Heinemann*, 2005.

[4] I.V. Dunin-Barkovskii and A.N. Kartashova: *Measurement and Analysis of Surface Roughness, Waviness, and Noncircularity* [in Russian], Moscow, 1978.

[5] T.R. Thomas: *Rough Surfaces*, Imperial College Press, London, 1999.

[6] D. Whitehouse: *Surface and Their Meausrement*, Kogan Page Science, 2004.

[7] M. Pruton: *Surface Physics*, Clarendon: Oxford, 1985.

[8] B.J. Roylance, R. Dwyer-Joyce: *Wear debris and associated wear phenomena – fundamental re-*

search and practice, Proc. Inst. Mech. Eng. Part JJ Eng. Tribology, No. 214, pp. 79-105, 2000.
[9] N.K. Myshkin, A.Ya. Grigoriev: *Morphology: Texture, Shape and Color of Friction Surfaces and Wear Debris*, Journal of Friction and Wear, Vol. 29, No. 3, pp. 192-199, 2008.
[10] D.W. Anderson: *Wear particle atlas*, Report NAEC-92-163.
[11] R.S. Sayles, T.R. Thomas: *Surface Topography as a Non-Stationary Random Process*, Nature 271 (5644), pp. 431–434, 1978.
[12] N.B. Demkin and E.V. Ryzhov: *Surface Quality and Contact of Machine Parts* [in Russian], Moscow, 1981.
[13] A.P. Khusu, Yu.R. Vitenberg, and V.A. Pal'mov: *Surface Roughness (Theoretical-Probabilistic Approach)* [in Russian], Moscow, 1975.
[14] A.Ya. Grigoriev, N.K. Myshkin, O.V. Kholodilov: *Surface Microgeometry Analysis Methods*, Soviet Journal of Friction and Wear, Vol. 10, No. 1, pp. 138-155, 1989.
[15] M. Zecchino: *Characterization surface quality: why average roughness is not enough*, AP. Notes of Iveco Instrument, December, pp. 24–30, 2003.
[16] A.Ya. Grigoriev, S.A. Chizhik, N.K. Myshkin: *Texture classification of engineering surfaces with nanoscale roughnes*, Int. J. of Machine Tools and Manufacture, Vol. 38, No. 5–6, pp. 719–724, 1998.
[17] N. K. Myshkin, A. Ya. Grigoriev: *Spatial characterization of engineering surface*, in Proc. of 3rd International Conference on Surface Engineering, Chengdu, China, pp. 54–61, 2002
[18] R.M. Haralick: *Statistical and structural approaches to texture*, Proceedings IEEE, Vol. 67, No. 5, pp. 786–804, 1979.
[19] M. Sonka, V. Hlavac, R. Boyle: *Image processing, analysis and machine*, Boston: PWS publishing, 1999.
[20] A.Ya. Grigoriev, R. Chang, E.S. Yoon, H. Kong: *Classification of Wear Particles by Semantic Features*, Journal of Friction and Wear, Vol. 20, No. 2 pp. 42-48, 1999.
[21] Z. Peng, T.B. Kirk: *Two-Dimensional Fast Fourier Transform and Power Spectrum for Wear Particle Analysis*, Tribology Int, Vol. 30, No. 8, pp. 583-590, 1997.
[22] T.B. Kirk, G.W. Stachowiak, A.W. Batchelor: *Fractal Parameters and Computer Image Analysis Applied to Wear Particles Isolated by Ferrography*, Wear, Vol. 145, pp. 347-365, 1991.
[23] S.-H. Lee, H. Zahouani, R. Caterini, T.G. Mathia: *Morphological characterization of engineered surfaces by wavelet transform*, in Proc. of 7th Int. Conf. on Metrology and Properties of Eng. Surfaces, Goteborg, pp. 182-190, 1997.
[24] H. Tamura, S. Mori, T. Yamawaki: *Texture features corresponding to visual perception*, IEEE Trans. SMC-8, Vol. 8, pp. 460–473, 1978.
[25] N.K. Myshkin, A.Ya. Grigoriev, S.A. Chizhik, K.Y. Choi, M.I.: *Surface Roughness and Texture Analysis in Microscale*, Wear, Vol. 254, pp. 1001-1009, 2003.
[26] P. Podsiadlo, G.W. Stachowiak: *Development of advanced quantitative analysis methods for wear particle characterization and classification to aid tribological diagnosis*, Tribology International, Vol. 38, pp. 887-892, 2005.
[27] P.Podsiadlo, G.W.Stachowiak: *Directional Multiscale Analysis and Optimization for Surface Textures*, Tribology Letters, Vol. 49, pp. 179-191, 2013.
[28] I. Etsion, *State of the Art in Laser Surface Texturing*, ASME J. Tribology, Vol. 127, pp. 248-253, 2005.
[29] D.T. Nguen et al.: *Friction of Rubber with Srfaces Patterned with Rigid Spherical Asperities*, Tribology Letters, Vol. 49, pp. 135-144, 2013.

Serbian Tribology Society

SERBIATRIB '13

13th International Conference on Tribology

Faculty of Engineering in Kragujevac

Kragujevac, Serbia, 15 – 17 May 2013

RECENT DEVELOPMENTS IN COATINGS' CHARACTERIZATRION FOR FACILITATING THE COATED TOOL LIFE PREDICTION

K.-D. Bouzakis[1,2], G. Skordaris[1,2], E. Bouzakis[1,2], N. Michailidis[2,3]

[1]Laboratory for Machine Tools and Manufacturing Engineering, Mechanical Engineering Department, Aristoteles University of Thessaloniki, Greece

[2]Fraunhofer Project Center Coatings in Manufacturing, in Centre for Research and Technology Hellas in Thessaloniki and in Fraunhofer Institute for Production Technology in Aachen, Germany

[3]Physical Metallurgy Laboratory, Mechanical Engineering Department, Aristoteles University of Thessaloniki, Greece

Abstract: *Coated tools constitute the majority of the tools applied in material removal processes. The paper introduces analytical-experimental methodologies for predicting film properties and cutting performance of coated tools. In a first stage, procedures for calculating stress-strain curves and fatigue critical loads of coatings by nanoindentations and impact tests respectively, at various temperatures determined, are presented. In a further stage, methodologies for the assessment of the film adhesion by inclined impact tests and of the film brittleness by nano-impacts are described. Moreover, the effect of the cutting edge impact duration in milling on the tool performance is demonstrated and explained via impact tests at various force signal times. Finally, the potential of micro-blasting on PVD coatings at appropriate conditions to improve the coated tool life is exhibited. In this context, a tool life increase is associated with the appropriate selection of micro-blasting conditions. The relevant results are evaluated by Finite Elements Method (FEM) supported procedures. The described procedures allow the prediction of coated tool cutting performance and the effective adaption of the cutting conditions to the film properties, thus restricting the related experimental cost.*

Tribological Properties of Materials and Coatings

13th International Conference on Tribology – SERBIATRIB '13

15 – 17 May 2013, Kragujevac, Serbia

Serbian Tribology Society

SERBIATRIB '13

13th International Conference on Tribology

Faculty of Engineering in Kragujevac

Kragujevac, Serbia, 15 – 17 May 2013

PREDICTION OF COATED TOOLS PERFORMANCE IN MILLING BASED ON THE FILM FATIGUE AT DIFFERENT STRAIN RATES

K.D. Bouzakis[1,2,a], R. Paraskevopoulou [1,b], G. Katirtzoglou [1,2,c], S. Makrimallakis [1,2,d], E. Bouzakis[1,2,e], P. Charalampous[1,f]

[1]Laboratory for Machine Tools and Manufacturing Engineering, Aristoteles University of Thessaloniki, Thessaloniki, Greece
[2]Fraunhofer Project Center Coatings in Manufacturing, in Centre for Research and Technology Hellas in Thessaloniki, Greece and in Fraunhofer Institute for Production Technology in Aachen, Germany
[a]bouzakis@eng.auth.gr, [b]paraskeu@auth.gr, [c]gkatirz@auth.gr, [d]makrimallakis_s@eng.auth.gr, [e]E.Bouzakis@certh.gr, [f]paschalischaralampous@gmail.com

Abstract: *The knowledge of coated tool wear mechanisms in milling is pivotal for explaining the film failure and selecting the appropriate cutting strategy and conditions. In this paper, tool wear experiments were carried out in milling of four different steels using coated cemented carbide inserts. The variable stress, strain and strain rate fields developed in the tool during cutting affect the film-substrate deformations and in this way the resulting coating's loads and its fatigue failure. For investigating the influence of cyclic impact loads magnitude and duration on the films' fatigue of coated speciments, an impact tester was employed which facilitates the modulation of the force signal. The attained tool life up to the films' fatigue failure was assosiated to a critical force for the film fatigue endurance and to the cutting edge entry impact duration. These factors converge sufficiently to the tool life in all examined milling kinematics and workpiece material cases.*

Keywords: *milling, tool wear, entry impact duration*

1. INTRODUCTION

Milling operations are often associated with complicated cutting edge-workpiece contact and intensive tool impact loads. These facts render the prediction of the tool wear development a difficult to be achieved task [1, 2]. Recent investigations with coated cemented carbide inserts revealed that the milling up or down kinematic, as well as the cutting parameters, significantly affect the stress field developed in the cutting edge during the material removal and consequently the cutting performance [3, 4].

The present paper introduces a method for calculating the coated tool wear evolution in milling. In such cutting procedures, repetitive impact loads with variable duration and magnitudes are exerted on the coated cutting edge, caused by the interrupted material removal. Hence, it was necessary to quantify the effect of the cutting edge entry impact duration on the coated tool fatigue failure at various cutting loads. This was enabled by a developed impact tester, facilitating the applied impact force modulation [5].

2. EXPERIMENTAL DETAILS

In the conducted investigations, peripheral and face milling experiments were conducted by a 3-axis numerically controlled milling center applying milling cutters of 17, 35, 57 and 90 mm effective diameters. The geometry of the cutters and the employed cutting inserts is exhibited in Figure 1. The cemented carbide inserts are coated by a TiAlN PVD film of ca. 3 μm thickness.

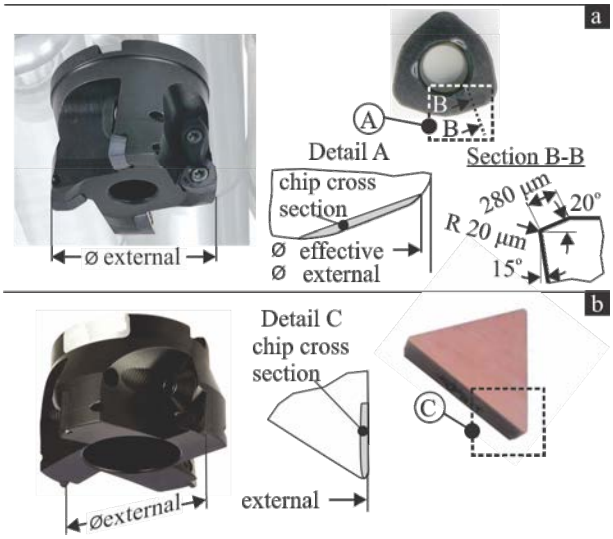

Figure 1. The employed milling cutters

The chamfer of ca. 280 µm and edge radius 20 µm respectively (see Figure 1) contribute to cutting edge stabilization especially at elevated dynamic loads. This may lead to an effective avoidance of cutting edge micro breakages, especially when the chip formation is not stable, as for example at the cutting edge entry into the workpiece material during up milling [3].

The specifications of the applied workpiece material are displayed in Figure 2. Four different steels were used; the hardened steel IMPAX, the stainless steel 304 L and the hardened steels NIMAX and 42CrMo4.

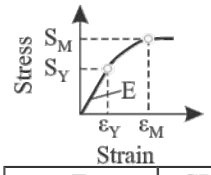

		IMPAX (AISI P20 modified)	AISI 304 L
E	GPa	205	205
S_Y/ε_Y	GPa/-	0.9/0.00439	0.24/0.00117
S_M/ε_M	GPa/-	1.2/0.13	0.58/0.55
C/Si/Mn/Cr/Ni /S/Mo/P	%	0.37/0.3/1.4/2.0/ 2.0/0.01/0.2/-	0.03/1/2/18/8 /0.03/-/0.045
Thermal conductivity	W/(m K)	21	17
Specific heat	J/(kg K)	460	500
Hardness	HB	290-330	88 (max)

		NIMAX	EN 42CrMo4 QT
E	GPa	205	210
S_Y/ε_Y	GPa/-	0.785/-	0.75/-
S_M/ε_M	GPa/-	1.265/-	1.1/-
C/Si/Mn/Cr/Ni /S/Mo/P	%	0.1/0.3/2.5/3/1 /-/0.3/-	0.42/0.25/0.8/1.05/- /0.02/0.2/-
Thermal conductivity	W/(m K)	28	41.7
Specific heat	J/(kg K)	460	480
Hardness	HB	360-400	280

Figure 2. The employed workpiece material properties

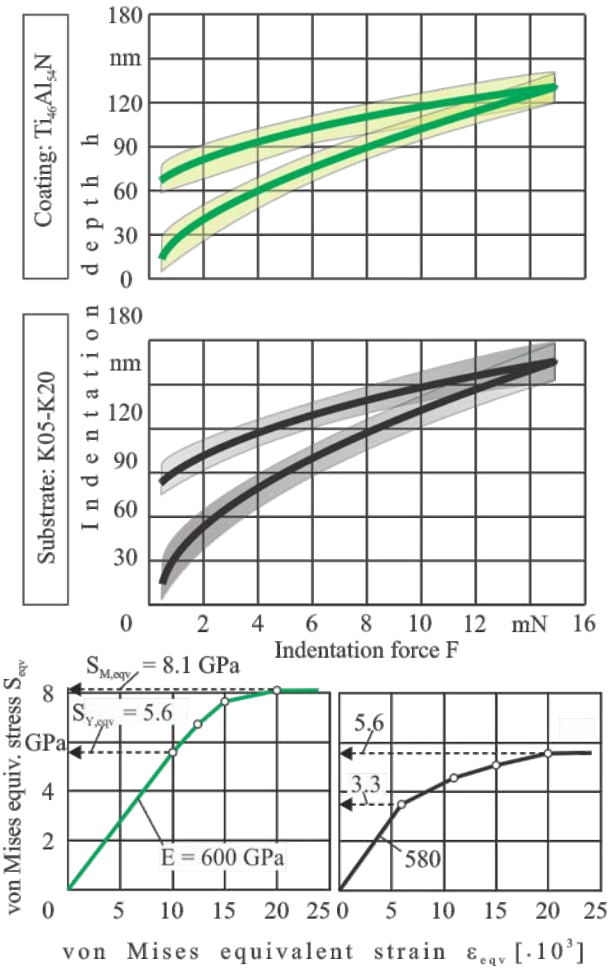

Figure 3. The employed coatings and substrate properties

The mechanical properties of the applied coating and substrate materials were detected by nanoindentations and a FEM-based algorithm, facilitating the determination of related stress-strain curves [6]. The elastoplastic film material laws are demonstrated in Figure 3.

For rendering possible the modulation of the impact force characteristics such as of frequency, impact duration and force signal pattern, an impact tester has been employed, in which a piezoelectric actuator is applied for the force generation [5]. By this device, the fatigue behaviour of thin hard coatings at different impact force patterns amplitudes and durations can be investigated.

3. IMPACT FORCE AMPLITUDE AND DURATION EFFECT ON COATINGS' FATIGUE FAILURE

For detecting the effect of the cutting edge entry impact duration on the film fatigue failure, impact tests at forces of various durations and amplitudes were carried out on the used coated inserts (see Figure 4a).

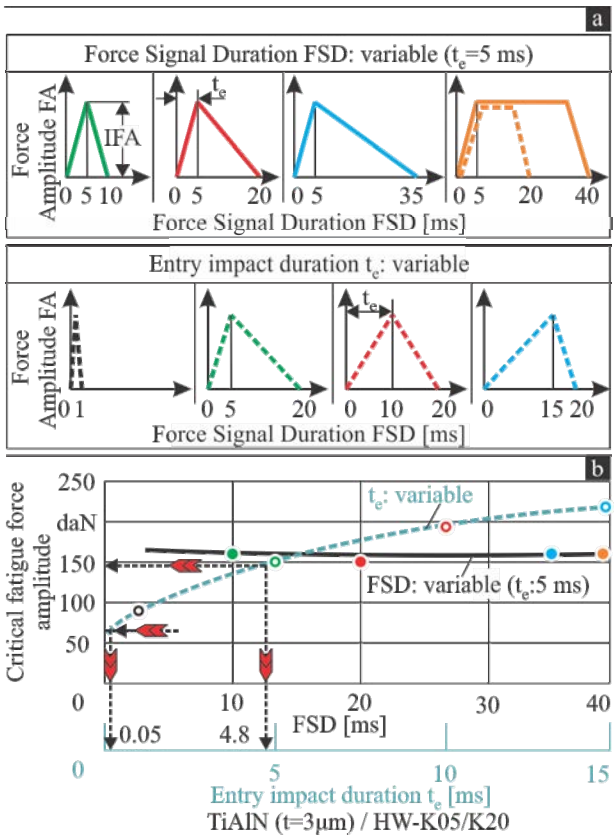

Figure 4. a) Triangular and trapezoidal impact force signals b) Effect of impact signal and entry impact durations on the critical force amplitude

All applied triangular force signals with durations (FSD) of 10 ms, 20 ms and 35 ms and the trapezoidal ones of 20 ms and 40 ms, which are presented at the upper Figure 4a part, had a constant signal growth time t_e of 5 ms (entry impact duration t_e). In contrast, the displayed force signals at the bottom of Figure 4a possess different entry impact durations t_e from about 0.5 ms up to 15 ms. These force signals are created by the piezoelectric actuator and measured by the piezoelectric force transducer.

The effect of the force pattern on the critical force amplitude, which induces coating fatigue failure after one million impacts, is monitored in Figure 4b. According to these results, the critical fatigue force amplitude remains practically invariable versus the force signal duration at constant t_e. On the other hand, t_e affects significantly the film fatigue behaviour, as it is exhibited in the same diagram. An increase of the impact entry duration t_e from 0.05 ms up to 15 ms results in a significant critical fatigue impact force amplitude augmentation from about 60 daN up to 220 daN respectively. The cutting load signal, i.e. the stress course versus the cutting length, when a chamfered cutting edge is used, resembles to a triangular force signal at entry impact duration of 3.6 ms [3]. Moreover, the stress course on a cutting edge without chamfer and smaller radius, versus the cutting length corresponds to a trapezoidal force pattern at significantly lower entry impact duration of 0.036 ms.

Considering these facts and the results exhibited in Figure 4b, the chamfered coated cutting edges can withstand to fatigue failure approximately a two and half times higher entry impact force amplitude. In this way, at the same stress level, the film failure of a chamfered cutting edge may appear in up milling after a longer cutting time compared to an insert without chamfer. The temperature developed close to the transient region of the cutting edge between flank and rake amounts to about 200 ^{o}C at a cutting speed of 200 m/min and chip tool contact time up to roughly 15 ms [4]. Thus, in this cutting edge region, the crystalline structure of the investigated TiAlN film remains stable, no diffusion or oxidation takes place and the film fatigue, which can be investigated by the impact test, is the prevailing factor.

4. FLANK WEAR DEVELOPMENT VERSUS THE CUTTING EDGE ENTRY IMPACT DURATION

The contact conditions at the tool entry into the material in milling are pivotal for the tool wear [1, 2, 4, 7, 8]. The impact load on the cutting edge at the tool entrance into the workpiece material depends on the milling kinematic (up or down, peripheral or face), since these factors affect the developed chip geometry and thus the stress fields of the coating versus the tool rotation. The entry impact duration corresponds to the cutting time, up to the development of the maximum equivalent stress in the coating.

For describing the effect of the entry impact duration on the tool wear in milling with coated tools, the accumulated tool life is introduced. The latter parameter refers to a flank wear land width VB of 0.15 mm. This parameter can be calculated considering the undeformed chip length l_{cu}, the cutting speed v and the attained number of cuts $NC_{0.15}$ up to the same VB according to the equation shown in the upper part of Figure 5a. In Figure 5a and 5b characteristic examples concerning the effect of the entry impact duration on the tool life are exhibited. These examples refer to peripheral and face milling of different undeformed chip lengths. Further examples in milling at various conditions, kinematics and materials are presented in [3, 9, 10, 11]. As it can be observed in Figure 5a, at an undeformed chip length of roughly 80 mm, a similar tool wear evolution in up and down, face or peripheral milling develops, leading to almost the same accumulative tool life.

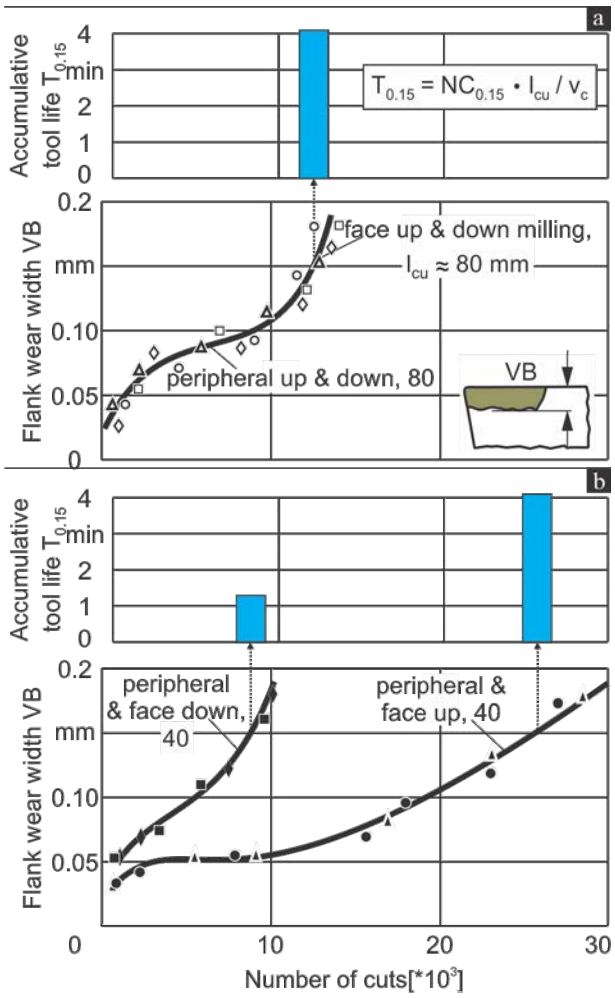

Figure 5. Flank wear land width versus number of cuts in various cases of face and peripheral milling

Moreover, as it is demonstrated in Figure 5b, when up milling is applied, the flank wear development is less intense compared to down peripheral or face milling at a chip length of about 40 mm. The attained accumulative tool life in up milling is approximately three times higher compared to those ones in down milling. This behaviour can be explained, based on the developed cutting edge entry impact duration in the previously described cases.

To highlight this effect, in Figure 6, the obtained accumulative tool life in the investigated peripheral and face milling cases is displayed versus the cutting edge entry impact duration t_e. The curve in this chart describes the effect of the cutting entry impact duration on the accumulated tool life. The relevant results were obtained in milling, at various tool geometries, cutting kinematics and conditions [3, 9, 10, 11].

In down milling, face or peripheral, at undeformed chip lengths l_{cu} of ca. 40 mm, the cutting edge entry impact durations t_e amount to approximately 0.1 ms leading to the accumulative tool life diminishing.

Furthermore, in up milling at an undeformed chip length l_{cu} of ca. 40 mm, due to the smoother chip thickness growth at chip formation start, the cutting edge entry impact duration t_e is approximately 2.2 ms and the accumulative tool life increases significantly compared to the corresponding one in down milling.

In contrary, in down and up milling, face or peripheral, at undeformed chip lengths l_{cu} of about 80 mm, the entry impact duration varies from 3.1 to 5.4 ms and the accumulative life remains almost on the same level.

Considering Figure 6, it can be concluded that entry impact duration larger than 2 ms lead practically to almost the same accumulative tool life. Furthermore, it is obvious, that short entry impact durations correspond to comparably lower coating fatigue critical forces (see Figure 4) and diminishes the coated tool life. Longer entry durations improve the film fatigue behaviour, thus enhancing the coated tool life.

The accumulated tool life in milling of the employed hardened steel IMPAX versus the entry impact duration at various cutting speeds is displayed in Figure 7. The accumulated tool life in milling of the employed hardened steel IMPAX versus the entry impact duration, displayed in Figure 7, can be described by the equations, displayed in Figure 7b, for the cutting speeds of 100, 200 and 300 m/min.

Similar experiments were conducted for all employed hardened steels. Figure 8 illustrates the accumulated tool life in milling of NIMAX, AISI 304 L and the 42CrMo4 versus the entry impact duration at various cutting speeds. The obtained accumulated tool life of NIMAX is substantially lower than the corresponding of IMPAX at the same cutting speed and almost equal to 1/3 of that.

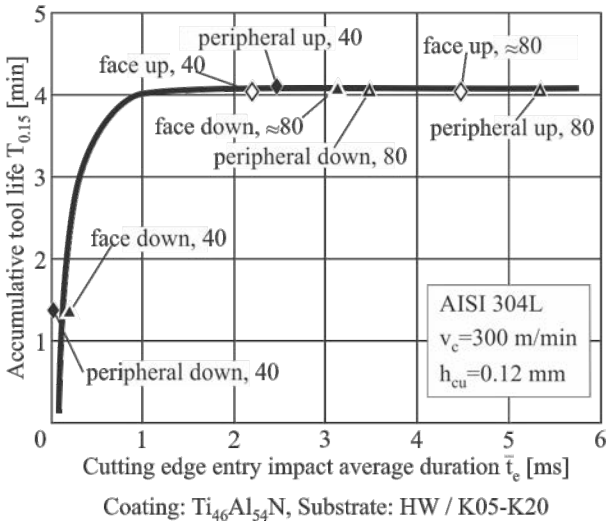

Figure 6. Accumulated tool life in milling versus the entry impact duration

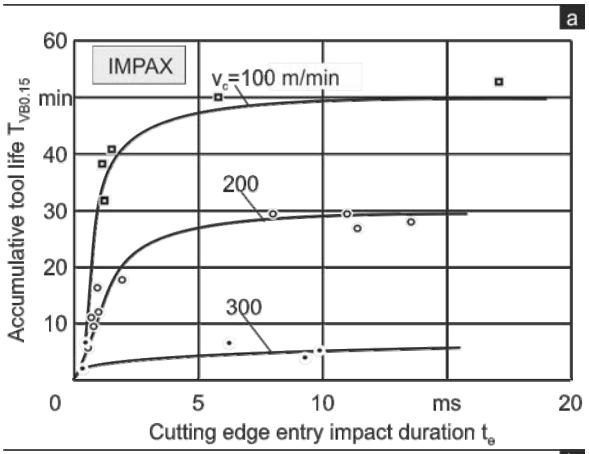

b

v_c=100 m/min	$T_{VB0.15} = -\frac{2000}{e^{(0.8t_e + 3.7)}} + 50$
200	$T_{VB0.15} = -\frac{800}{e^{(0.3t_e + 3.3)}} + 30$
300	$T_{VB0.15} = -\frac{80}{e^{(0.15t_e + 2.9)}} + 6$

Figure 7. Accumulated tool life in milling of the employed hardened steel IMPAX versus the entry impact duration at various cutting speeds

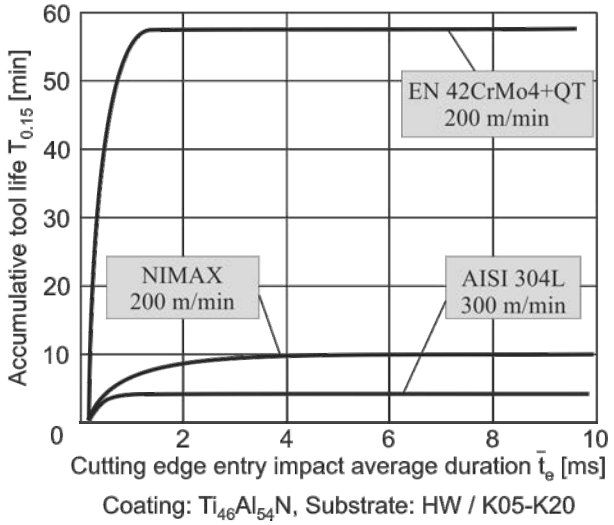

Figure 8. Accumulated tool life in milling of the employed hardened steels versus the entry impact duration at various cutting speeds

This is due to comparatively higher hardness of NIMAX. Moreover, it is obvious that due to reasons described in [11, 12, 13, 14] stainless steel is difficult to cut.

5. THE DEVELOPED MODEL FOR DESCRIBING THE WEAR EVOLUTION ON COATED TOOLS IN MILLING BASED ON CUTTING EDGE ENTRY IMPACT DURATION

The general form of the equations, shown in Figure 7, describing the accumulated tool life as a function of the cutting speed and the entry impact duration is:

$$T_{0.15}(v,t_e) = -\frac{C_3}{e^{(C_1 \times t_e + C_2)}} + C_4 \qquad (1)$$

The parameters C_1, C_2, C_3 and C_4 depend on the cutting tool and workpiece material data. Moreover, these parameters are functions of the cutting speed and the entry impact duration.

Considering the entry impact duration, using equation (1), the cutting tool life $T_{0.15}$ up to a flank wear land width VB equal to 0.15 mm can be estimated. Moreover, the number of cuts $NC_{0.15}$ corresponding to a flank wear land width VB equal to 0.15 mm can be calculated based on the undeformed chip length and the cutting speed using the relation (2).

$$T_{0.15} = NC_{0.15} * l_{cu} / v \qquad (2)$$

Bearing in mind that a number of cuts equal to zero corresponds to a tool wear VB also equal to zero and the number of cuts $NC_{0.15}$ is associated to VB equal to 0.15 mm, the evolution of the tool wear during milling can be calculated as described in [9].

6. COMPUTATION OF THE TOOL WEAR IN MILLING AT CHANGEABLE CUTTING CONDITIONS

During milling a workpiece, the values of parameters influencing the tool wear development such as chip length, chip thickness, entry impact duration etc. may vary in the successive tool paths. Considering these circumstances, for computing the tool wear developed during milling, the methodology explained in Figure 9, is applied [15, 16].

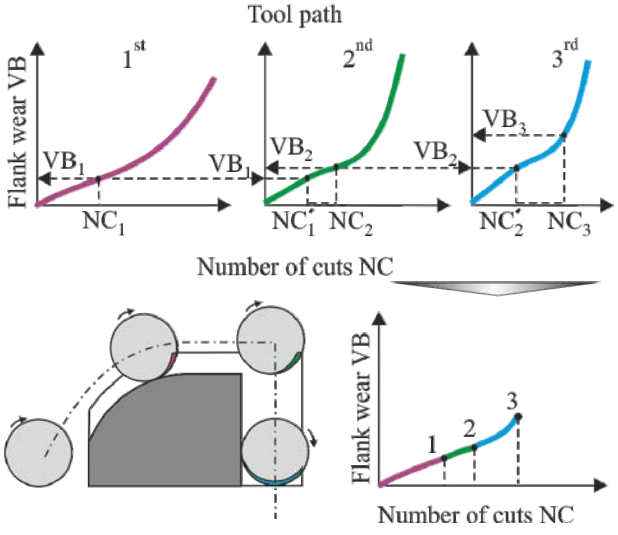

Figure 9. Determination of tool wear evolution in milling at various cutting conditions

Based on the cutting data of every tool path, the number of cuts NC_i and furthermore the tool wear VB_i at the end of a tool path (i) can be calculated, as demonstrated in this figure. The flank wear VB_{i-1} developed in the previous tool path (i-1), is related to a number of cuts NC_{i-1} considering the cutting data of the actual tool path. The number of cuts NC_i data of the actual tool path is added to the NC_{i-1} and thus the flank wear VB_i at the tool path (i) can be determined. By this method the flank wear development can be effectively predicted in all successive cutting tool paths.

7. AN APPLICATION EXAMPLE OF THE DEVELOPED METHODOLOGY

The analytical method for estimating the tool wear is applied in the case of a test part presented in Figure 10. Considering the initial and final workpiece's geometry, the tool paths required to remove the raw material volume were defined using the commercial "OPUS-CAM" system [17].

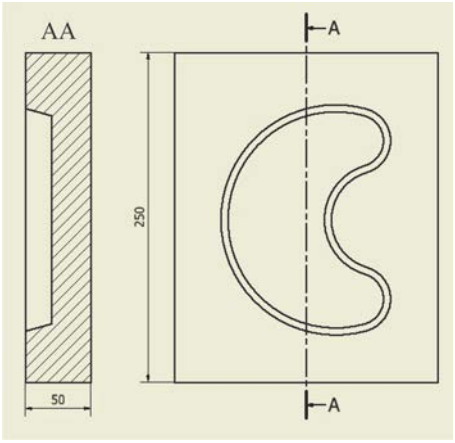

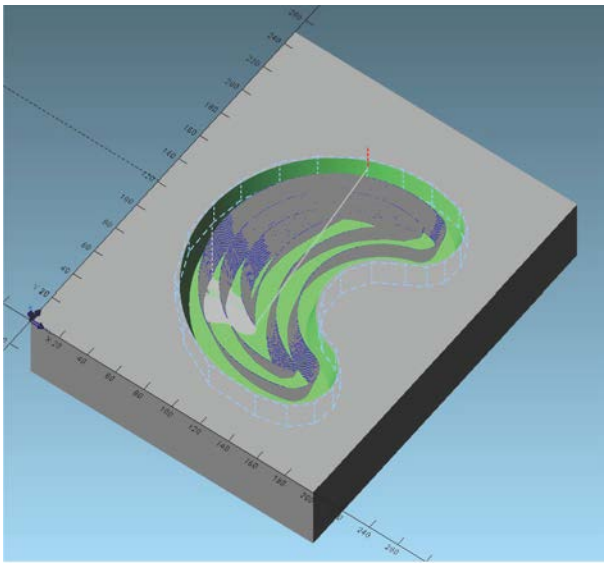

Workpiece material: AISI P20 modified (IMPAX)
Tool path created by OPUS

Figure 10. The employed test part and the tool paths required for the material removal

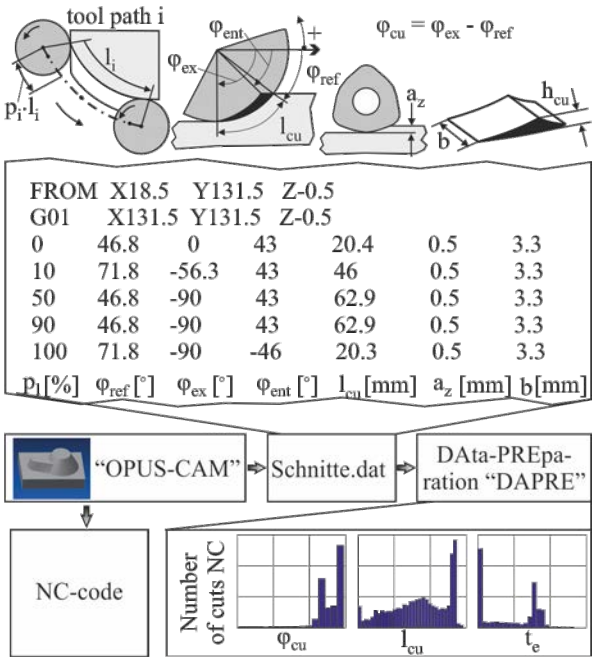

Figure 11. Determination of chip data along the tool paths by a CAD/ CAM system

The determined tool paths are presented in the lower part of Figure 10 too. The machining took place in forty z-levels. The raw material removal was accomplished using up milling and down milling as well. Both operations lead to the same final workpiece shape, but the tool wear behaviour in each case may be different.

After the tool paths have been determined, the "Schnitte.dat" file is generated by OPUS, as shown in Figure 11. This file contains geometrical data related to the chips formed in each tool path. More specifically, the parameters illustrated in Figure 10, determined at certain distances from every tool path initial point are stored into the "Schnitte.dat" file. In the first column of the file, the tool position is defined as a percentage p of the actual tool path length l_i, whereas i is the number of the tool path. At every tool position, the angle φ_{ref} of the first tool rake – workpiece contact, the corresponding entry angle φ_{ent} at the maximum cutting edge penetration into the part material and the exit angle φ_{ex} are stored. Moreover, in the following columns, the undeformed chip length l_{cu}, the axial depth of cut a_z and the chip width b are accumulated. The data of the "Schnitte.dat" file are further processed by the developed Data - PREparation (DAPRE) software.

Thus, various data, as for instance the entry impact time per chip, the undeformed chip lengths, the tool –workpiece contact angle etc. can be provided. Considering these data the coated tool wear evolution versus the number of cuts is described and in this way, the conduct of algorithms for an analytical optimization of milling process towards attaining set targets is facilitated.

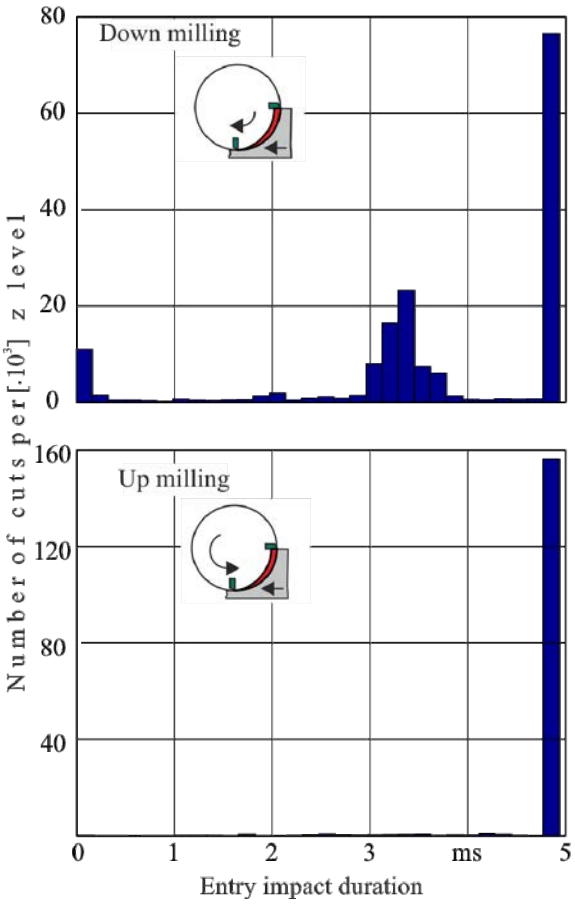

Figure 12. Histograms of the entry impact duration along the tool paths

Characteristic results of this methodology are displayed in Figure 12, where histograms of the entry impact time of the removed chips in both up and down milling kinematics are illustrated.

In up milling almost all chips were cut at impact duration of approximately 4,8 ms. In contrary, when down milling is applied almost half chips possess entry impact durations of less than 4 ms, while some of them are associated with impact durations less than 1 ms. In this way, it is expected a more intense wear evolution in down milling compared to up one.

It is has to be pointed out, that the more intense tool wear evolution in down milling of this particular test part compared to the up one, cannot stand for every milling case and depends on the workpiece and the tool edge geometry and material data.

For calculating the tool wear developed during milling of the test part, the introduced method in previous paragraph was used. The flank wear land width VB versus the number of cuts NC was calculated and experimentally detected. The measured and the calculated values of the tool wear evolution in both milling kinematics are presented in Figure 13. The experimental results converge sufficiently with the calculated ones.

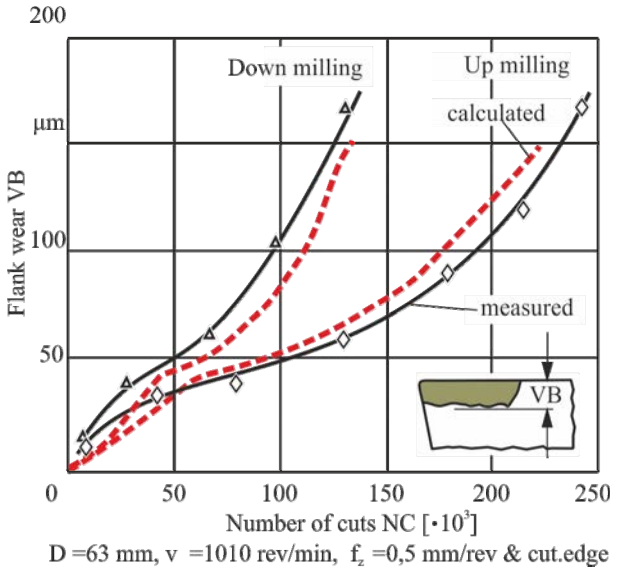

Figure 13. Calculated and measured flank wear development versus the number of cuts

8. CONCLUSIONS

The results described in this paper show the significant effect of the cutting edge entry impact duration on the coated tools wear evolution in peripheral and face milling. The effect of cutting edge entry impact duration on the coated tool fatigue failure was investigated via an impact tester with force signal modulation facilities. Moreover, based on the cutting edge impact duration, a calculation of the expected tool wear development can be carried out. In this way, the selection of optimum cutting conditions and strategies in milling with coated tools can be achieved.

REFERENCES

[1] H.-J. Jakobs, P. Winkelmann: *Aktuelle Standzeitfunktion für die Arbeitsgestaltung beim Fräsen, Fertigungstechnik und Betrieb*, Vol. 31, pp. 352–356, 1981.

[2] L.J. Dammer: *Ein Beitrag zur Prozessanalyse und Schnittwertvograbe beim Messerkopfstirnfräsen*, Dissertation, RWTH Aachen, 1982.

[3] K.-D. Bouzakis, S. Makrimallakis, G. Katirtzoglou, E. Bouzakis, G. Skordaris, G. Maliaris, S. Gerardis: *Coated tools' wear description in down and up milling based on the cutting edge entry impact duration*, CIRP Annals - Manufacturing Technology |Vol. 61, No. 1, pp.115-118, 2012.

[4] Bouzakis K.-D, Gerardis S, Katirtzoglou G, Makrimallakis S, Michailidis N, Lili E., *Increasing Tool Life by Adjusting the Milling Cutting Conditions According to PVD Films' Properties*, CIRP Annals – Manufacturing Technology, Vol. 57, No. 1, pp.105–108, 2008.

[5] K.-D. Bouzakis, G. Maliaris, S. Makrimallakis: *Strain rate effect on the fatigue failure of thin PVD coatings: An investigation by a novel impact tester with adjustable repetitive force*, International Journal of Fatigue, Vol. 44, pp. 87-97, 2012.

[6] K.-D. Bouzakis, N. Michailidis, G. Erkens: *Thin hard coatings stress-strain curves determination through a FEM supported evaluation of nanoindentation test results*, Surface and Coatings Technology, 142-144, pp. 102-109, 2001.

[7] M. Kronenberg: *Analysis of Initial Contact of Milling Cutter and Work in Relation to Tool Life*, Transactions of the ASME, pp. 217–228, 1946.

[8] K. Okushima, T. Hoshi: *The Effect of the Diameter of Carbide Face Milling Cutters on Their Failures*, Bulletin of JSME, pp. 308–316, 1963.

[9] K.-D. Bouzakis, R. Paraskevopoulou, G. Katirtzoglou, E. Bouzakis, K. Efstathiou: *Coated Tools Wear Description in Milling Facilitating Considerations towards Sustainable Manufacturing*, The 10th Global Conference on Sustainable Manufacturing, pp. 20-25, 2012.

[10] K.D. Bouzakis, R. Paraskevopoulou, G. Katirtzoglou, S. Makrimallakis, E. Bouzakis, K. Efstathiou: *Predictive model of tool wear in milling with coated tools integrated into a CAM system*, accepted for publication, CIRP Annals - Manufacturing Technology 2013.

[11] K.-D. Bouzakis, S. Makrimallakis, G. Skordaris, E. Bouzakis, S. Kombogiannis, G. Katirtzoglou, G. Malliaris: *Coated tool performance in up and down milling stainless steel, explained by film mechanical and fatigue properties*, accepted for publication Wear, 2013.

[12] L. E. Murr : *Metallurgical effects of shock and high-strain-rate loading*, In: T.Z. Blazynski (Ed.) *Materials at high strain rates*, Elsevier, Essex, England, pp.1-46, 1987.

[13] J. Harding: *The effect of high strain rates on material properties*, In: T.Z. Blazynski (Ed.) *Materials at high strain rates*, Elsevier, Essex, England, pp. 133-186, 1987.

[14] B.L. Boyce, M.F. Dilmore: *The dynamic tensile behavior of tough, ultrahigh-strength steels at strain-rates from 0.0002 s^{-1} to 200 s^{-1}*, International Journal of Impact Engineering, Vol. 36, No. 2, pp.263-271, 2009.

[15] K.D. Bouzakis: *Konzept und technologische Grundlagen zur automatisierten Erstellung optimaler Bearbeitungsdaten beim Wälzfräzen*, Habilitation, TH Aachen, 1980.

[16] K. Efstathiou: *Automatic generation of optimum technological data for numerically controlled milling based and on measurements of the workpiece solid geometry*, Ph. D. Thesis: Aristotles University, Thessaloniki, 1991.

[17] Opus-CAM, 2012, User Manual.

Serbian Tribology Society

SERBIATRIB '13

13th International Conference on Tribology

Faculty of Engineering in Kragujevac

Kragujevac, Serbia, 15 – 17 May 2013

SELECTIVE TRANSFER OF MATERIALS IN THE ASPECT OF GREEN TRIBOLOGY

Emilia Assenova[1], Gottlieb Polzer[2], Dr. Tsermaa[3], Mara Kandeva[4]

[1]Society of Bulgarian Tribologists, Sofia, Bulgaria, emiass@abv.bg

[2]Tribology Unit, 08115 Schoenfels, Germany, professor-polzer@gmx.de

[3]University of Ulan Bator, Mongolia, professor-polzer@gmx.de

[4]Technical University-Sofia, Tribology Center, Sofia, Bulgaria, kandeva@tu-sofia.bg

Abstract: *One of green tribology's principles touches the environmental implication of coatings and lubricants, development, optimization and implementation of ecology friendly manufacturing and implementation of coatings.The paper deals with green tribology in the aspect of wear reducing frictional coatings and regeneration of worn surfaces without joint dismantling. Copper frictional coatings in the case of nonabrasive treatment of steel or cast iron surfaces, their production with the assistance of selective transfer of materials between the friction surfaces are considered. In the example of frictional coating deposition, this phenomenon is supported by the rubbing of brass stick on steel cylinder surface under particular conditions of selective transfer in the presence of a special lubricant. Important is the extremely low wear of components coated under condition of selective material transfer mode with wide practical application. The interdisciplinary character of the study and application of technologies for coating formation, layer growth techniques, surface texturing, etc. involves studies by specialists of different sciences.*

Keywords: *green tribology, frictional coatings, surface design, selective transfer.*

1. INTRODUCTION

1.1 Tribology and Green Tribology

Natural resources have been cruelly consumed in the last three centuries and the earth is seriously damaged and polluted. Humanity has to survive fighting with the pollution and the deficiency of material, energy and cleanness. Generally speaking, this problem is mainly the result of the misuse of our contact with nature. So, it is contact deficiency and a way out could be sought in the science of contacts, i.e. in tribology. Radical knowledge and technologies of sustainability are needed to establish new human way of thinking.

Tribology is supposed to assist the knowledge and technologies in the purpose to meet the expectations of quality, reliability and environment sustainability. Tribology comprises the knowledge of friction, lubrication, wear, hermeticity and other process between contacting surfaces. The modern concept observes tribology problems as essentially interdisciplinary. Typical tribological studies involve the efforts of mechanical engineers, material scientists, chemists, physicists, and so forth. New areas of tribological studies have been developed at the interface of various scientific disciplines, for example, nanotribology, biotribology, geotribology, ecotribology, etc.

Recently, the new concept of '**green tribology**' has been defined as 'the science and technology of the tribological aspects of ecological balance and of environmental and biological impacts' by H. P. Jost [1,2]. The former notion was eco-tribology and stressed the interaction of contact systems with the environment [3,4]. Green Tribology means saving materials, energy, improving the environment and the quality of life. The area of Green Tribology will directly affect the economy by reducing waste and extending equipment life, improve the technological and environmental balance, and improve the sustainability and safety in the human society. Green Tribology reflects in fact the tribological aspects of ecological balance and of environmental impacts, and is expected to directly affect the reducing of waste and thermal pollution, and extending equipment quality, reliability and

life, which are some of the key challenges facing the societies today [5], [6], [7].

1.2. Wear prevention

Tribological knowledge helps to reveal and heal wear related problems. So, it is possible to improve quality significantly by measures preventing the reasons for failures related to wear of contacting surfaces. What is wear? Wear is a process of tribological interaction resulting in physico-chemical loss of material (weight, size or shape) from the surfaces in contact. Most important forms of wear are abrasion, corrosion, erosion, attrition, fretting, thermal destruction, scuffing, pitting, etching, etc. [8]

The specific field of green or environment-friendly tribology emphasizes the aspects of interacting bodies, which are of importance for material, and energy sustainability and safety, and which have huge impact upon today's environment. This includes essentially the control of friction and wear, being of importance for energy, resources and cleanness conservation [5]. One of the most important tasks of Green Tribology is ***Minimization of wear***. Wear limits the lifetime of components and creates the problem of their recycling. Wear can lead to high consumption of the natural resources. Wear creates debris and particles that contaminate the environment and can be even hazardous for humans. Moreover, the large amount of heat generated in the contact joints, also leads to its thermal distortion and failure, and to pollution of the environment with material waste and heat.

Measures for minimizing wear are related to surface processing, namely optimal material selection and surface texturing, and/or **coating the surfaces**. It leads to good health and preservation of performance quality of machines, equipment and production systems, and hence, material, energy and environment saving as a whole.

1.3. Surface coatings

There are various methods for surface coatings deposition, a diversity of approaches to study the behavior of the coatings, and numerous areas of their application.

Wear prevention coatings are applied in many areas: production industry and power industry, marine, automotive and transportation industry, aerospace techniques, agriculture, food processing, mining and metallurgy, sporting equipment industry, electronics, packaging, robotics, renewable energy sources, waste treatment and more. A great variety of parameters influences the quality of the coating, depending also on the application. Important characteristics are: thickness, porosity, microstructure, inclusions, cracks, microhardnes and adhesion and cohesion bond strength [9]. Control is realized using various standardized test methods by means of tensile test machines, scratch testers, etc.

The paper concerns the method of coating deposition during friction process. It aims and focuses on the procedures of obtaining and the study of copper frictional coatings under selective transfer mode in the case of nonabrasive treatment of steel and cast iron surfaces.

2. FRICTIONAL COATINGS UNDER CONDITIONS OF SELECTIVE TRANSFER

2.1. Background

Tribologists have the task to keep the destruction as small as possible or to stop it, in order that the system comes to the equilibrium process between destruction and regeneration. Exactly this happens in the process of selective transfer of material between friction surfaces. In the case of frictional coatings production, this phenomenon is assisted by rubbing of brass against steel under the special conditions of selective transfer.

D. N. Garkunov and G. Polzer are of the first researchers in theory and practice of selective transfer of material during friction coating deposition [10], [11], [12], [13]. Common works were carried out connecting the Tribology Center in Sofia and the Tribology Group of Prof. Polzer in Zwickau, and recently in Schoenfels, Germany. What is friction coating deposition? A steel element (e.g. a shaft) to be coated is both subjected to rotation and to the pressure of a brass stick in the presence of a special lubricant, forming a bronze-steel tribocouple (See the principle in Fig. 1).

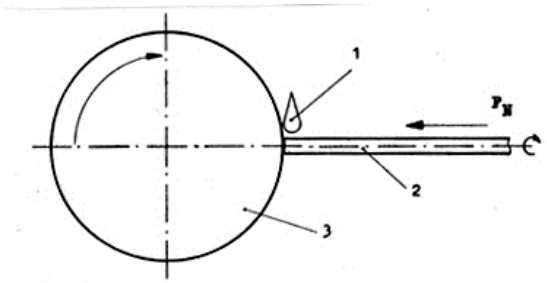

Figure 1. Principle assembly for brass deposition on shaft (1 - surface active liquid; 2 - brass rod; 3 - shaft to be coated)

The film forms on the friction surfaces in the bronze-steel tribocouple with glycerin lubrication passing firstly through dissolution of the bronze surface, where the glycerin acts as a weak acid. The atoms of the elements (tin, zinc, iron, aluminum) absorbed in bronze outgo into the lubricant, as result the bronze surface is enriched with copper.

Friction deformation of the bronze surface causes new passing of elements into the lubricant, so the bronze layer is purified and it nearly contains only copper. Its pores fill with glycerin. Glycerin is reducer for copper oxides, hence the copper film is free form oxides; it is very active with free ions and is highly adhesive for the steel surface. The steel surface is covered by thin copper layer. Self-organization and selective transfer of copper to steel take place. Before the stabilized selective transfer, the process goes on until steel and bronze are coated by 2 μm copper layers [12]. Mechanical and chemical transformations take place; e.g. formation of surface active substances on the friction surfaces; they interact chemically with the surfaces and form chemisorbed layers (see Fig. 2).

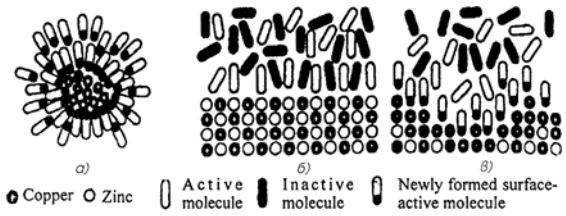

Figure 2. Formation of micelles and interaction of surface-active substances with bronze (as per [12])

Some results of the basic studies and application in the area of copper frictional coatings are presented below. Based on equation of the theoretical physics, G. Polzer [11] had formerly derived equations of self-organization at friction. Always when destruction problems are available in nature, there is either a simultaneous growth process which involves equilibrium between destruction and regeneration or destruction leads to exponential destroying of the whole system, in our case the tribological couple.

A self-organization in the system brass-glycerol-steel is observed and the obtained film – a coat with significant change of wear-resistance. Major result is the low wear of components coated under condition of selective material transfer mode. Important is also the reduction of the concentration of hydrogen at the frictional surface and, respectively, the lower hydrogen wear. It is highly important for practical applications that the inclination for welding and seizure [13] between the friction surfaces is significantly lowered under conditions of selective transfer. A considerable practical result is the possibility for dismantling-free restoration of worn units/couples.

2.2. Experimental work

The phenomenon of direct coating deposition is assisted by the rubbing/deposition of brass under the special conditions of selective transfer of material. Different processes result. In the contact zones emerges reactive coating deposition with special properties: Copper is rubbed on the steel friction surfaces with totally different electro-chemical potential, and secondly, not only the content but also the structure in the friction surfaces is being changed [13].

The compress forces at the rotation of the brass stick involve great pressure in the contact zone between stick and basic material due to the relative small contact surface, hence a positive gradient of the shear strength in depth direction of the friction surface according to I. V. Kragelsky [8].

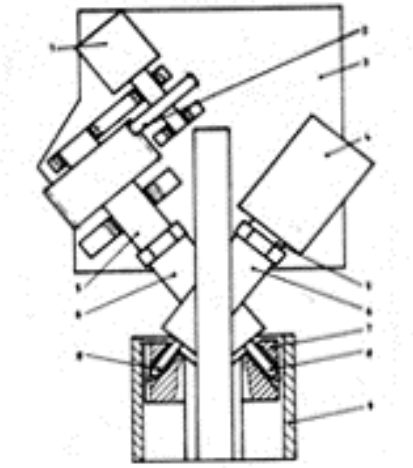

Figure 3. MBZ 3A Brass-coating device for sliding bushes (application in lathes)

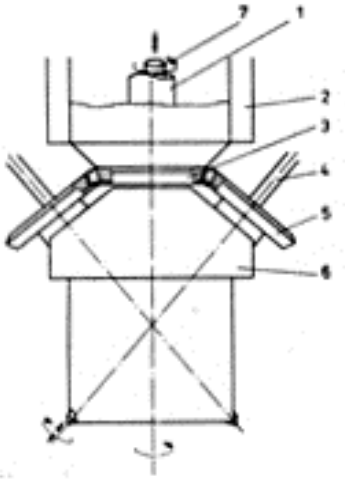

Figure 4. Brass-coating device for cylinder-bushing by boring machine

As a result, a tribological system appears which can bear higher loads at the influence of various processes. Different machines were designed and constructed at the Department Tribotechnik in Zwickau' Higher Technical School, corresponding to the principles of the frictional deposition and the ideas of the selective transfer. Many pieces of the

devices „MBZ 1" for shaft coatings and „MBZ 3 A" for application in rotating machines were manufactured (see Figs.3, 4, 5, 6), e.g. the „MBZ 3 A" for engine cylinders was produced in 30 items. Unfortunately there is not sufficient use of the advantages of the deposition of copper frictional coatings in the overall practice.

Figure 5. View of the brass-coating device MBZ 3A

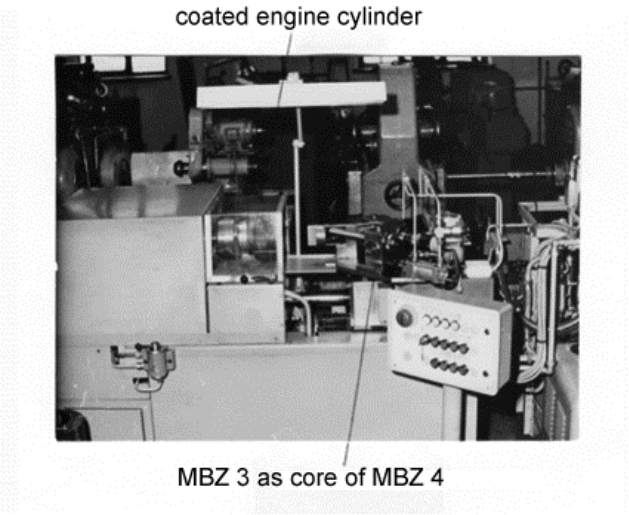

Figure 6. The brass-coating device applied in an automatic machine

Some diagrams referring to a part of the basic new results are presented below. In Fig. 7 is given the variation of hardness in depth; so the strengthening can also be obtained at different rotation speeds.

Fig. 8 shows the reduction of hydrogen concentration of the friction surface in depth. The hydrogen wear results from synergetic interaction of various surface phenomena: exoemission, adsorption, frictional destruction, which provide hydrogen extraction from the frictional surfaces. Thermal gradient is also formed, as well as electrical and magnetic fields; this leads to hydrogen diffusion in the metal, hydrogen concentration in the subsurface layer and rapid wear of this layer [12]. Metal defect formation in the friction deformed layer also increases the H_2 concentration and augments the wear. Frictional coatings, however, improve significantly the wearresistance against hydrogen wear [13].

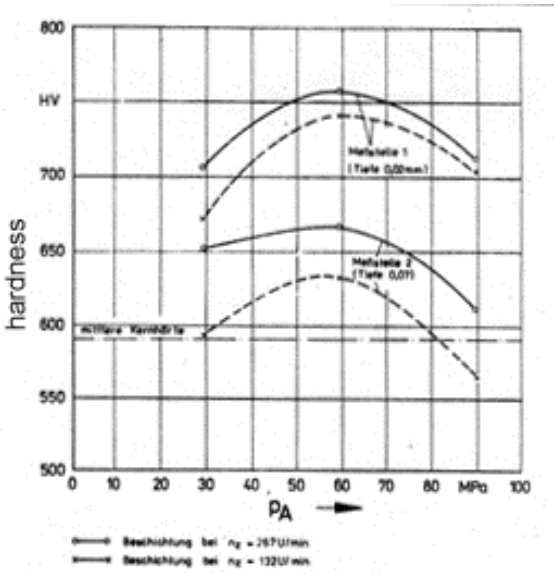

Figure 7. Hardness in different depth after frictional coating deposition on steel

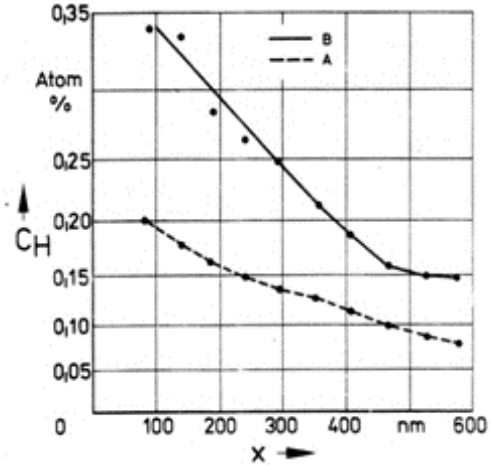

Figure. 8. Reduction of H_2 concentration at the frictional surface in depth

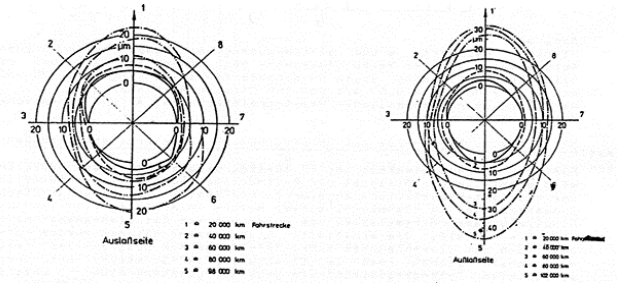

Figure 9. Wear distribution in upper dead point of engine cylinder after different sliding paths: for cylinder with frictional brass coating (left) and uncoated (right)

By means of brass frictional coating in different constructions of steel and cast iron it can be obtained not only the 10 - 20 % lowering of friction force, but also a changed wear distribution, which is to be seen, e.g., for the upper death point in

engine cylinders of 2-cylinder-twotact-Ottomotors after various completed paths (see Fig. 9). This was the reason that the brass frictional coatings were successfully applied in the practice of the company Peißig in Zwickau, especially in highly loaded race motors for more than 20 years too.

3. CONCLUSION

Green tribology should be integrated into world science and make its impact on the solutions for worldwide problems. Being a new field, green tribology has a number of challenges. A basic one of them, minimising the wear, is being discussed in above investigation of wear reduction possibilities through frictional coatings.

The study of frictional coatings and their application can be summarized in the following:

- Self-organization in the system brass-glycerol-steel under selective transfer is observed and the obtained film – a designed or controllable coat with significant change of wear-resistance – can be intentionally manipulated to influence its properties during friction.
- Important features of the coating deposited during friction under selective material transfer mode: Low wear of components at nonabrasive treatment of steel/cast iron, and lower hydrogen wear of the coated surfaces; lower inclination for welding and seizure between the friction surfaces; possibility for dismantling-free restoration of worn units/couples.

The practical implementation of brass-copper frictional coating is of extreme importance and was realized in Germany, Russia, Kazakhstan, Poland, etc.

The interdisciplinary character of the study and application of technologies for frictional coating formation, layer growth techniques, surface texturing, etc. involves intervention by specialists of different sciences. The work and collaboration between scientists of Russia, Germany, Poland, Bulgaria, Mongolia and Vietnam in this field was carried out by the International Council for Selective Transfer and Frictional coatings, established in 1990 in London.

REFERENCES

[1] H. P. Jost: *30th Anniversary and Green Tribology*. Report of a Chinese Mission to the United Kingdom, 7-14 June 2009, issued by the Tribology Network of the Institution of Engineering & Technology

[2] H. P. Jost: *The Presidential Address*, 5th WTC Kyoto, 2009.

[3] W. J. Bartz: *Ecotribology: Environmentally acceptable tribological practices*. Tribology International, Volume 39, Issue 8, August 2006, pp. 728–733.

[4] M. Kandeva, E. Assenova, M. Daneva: *Triboecology as a methodological center of modern science*. Proceedings of the 2nd European Conference on Tribology ECOTRIB 2009, Pisa, Italy, 2009.

[5] M. Nosonovski, B. Bhushan (edtrs): *Green tribology. Biomimetics, Energy Conservation and Sustainability*, Springer Verlag, 2012.

[6] R. Wood: NCats Newsletters, Univ. of Southampton, October 2011.

[7] E. Assenova, V. Majstorovic, A. Vencl, M. Kandeva: *Green tribology and quality of life*, International Convention on Quality 2012, Belgrade (Serbia), 05-07.06.2012, Proceedings, p.p. 32-38, Published in: Advanced Quality, 40, 2, p.p.26-32, 2012.

[8] I.V. Kragelsky: *Friction and Wear*, Moscow, Mashinostroienie, 1968 (in Russian; available also in English)

[9] A. Vencl, S.Arostegui, G. Favaro, F. Zivic, M. Mrdak, S. Mitrović, V. Popovic: Evaluation of adhesion/cohesion bond strength of the thick plasma spray coatings by scratch testing on coatings cross-sections, Tribology International, 44, 11, 2011, p.p. 1281-1288.

[10] D.N. Garkunov: *Triboengineering (wear and non-deterioration)*, Moscow Agricultural Academy Press, Moscow, 2000 (in Russian)

[11] G. Polzer: *Der Erfahrungsaustausch: Reibbeschichten und selective Uebertragung*, Publ. Bezirks-Neuerer-Zentrum, Gera, 1988.

[12] D.N. Garkunov: *Scientific Discoveries in Tribotechnologies. No-wear effect under friction: Hydrogen wear of metals*. MAA Publishing House, Moscow, 2007.

[13] G. Polzer, E. Assenova, Dr. Tsermaa: *Copper frictional coatings under conditions of selective transfer*, Tribological Journal BULTRIB - Sofia, Vol. 3, 2012.

Serbian Tribology Society

SERBIATRIB '13

13th International Conference on Tribology

Faculty of Engineering in Kragujevac

Kragujevac, Serbia, 15 – 17 May 2013

ABRASIVE WEAR AND WEAR-RESISTANCE OF HIGH STRENGTH CAST IRON CONTAINING Sn MICROALLOY

Mara Kandeva[1], Boryana Ivanova[2]
[1]Tribology Center, Technical University-Sofia, Bulgaria, kandeva@tu-sofia.bg
[2]Technical University-Sofia, Bulgaria, bsaykova@tu-sofia

Abstract: *A procedure for the study of wear of high strength (spheroid) cast iron under conditions of dry friction on surfaces with fixed abrasive following the kinematics scheme „pin-on-cylinder" with spiral movement has been developed. Five type specimens of high strength cast iron without and with micro alloy of various Sn contents – 0,08; 0,02; 0,06; and 0,12 mass percents were studied. The experimental results lead to graphs and diagrams of the relationships for the parameters mass and linear wear, wear rate and intensity, and wear-resistance depending on process time, sliding way and normal load.*
This study is connected with the completion of a PhD dissertation and of the tasks under the Project ДУНК-01/3 "University R&D Complex for innovation and transfer of knowledge in micro/nano-technologies and materials, energy efficiency and virtual engineering" funded by the Bulgarian Ministry of Education and Science.

Keywords: *tribology, high strength cast iron, micro alloying, abrasive wear, wear-resistance*

1. INTRODUCTION

Being a natural composite material with steel metal matrix with embedded graphite phase, the high strength (spheroid) cast iron provides a complex of properties which make it different from the conventional Fe-C alloys.

The mechanical and tribological properties are strongly dependent on the composition, structure, and on the size and distribution of the graphite inclusion, as well as on the presence of micro-alloying elements both in bulk and surface layer.

Tin (Sn) is most often used as alloying element. The usual quantities of less than 0.15 % do not influence the leaning to graphite adoption in the crystallization process.

Alloying of spheroid cast iron by Sn causes perlitization of the metal base, along with strength and hardness increase by decrease of the relative increment of collision resilience. This influences the parameters of friction and wear in the contact joints of machines [1,2,3].

The paper aims study of the parameters of wear of high strength cast iron micro-alloyed by various mass percent contents of tin (Sn) under conditions of dry friction on a surface with fixed abrasive particles.

2. MATERIALS, PROCEDURE AND PARAMETERS OF WEAR

2.1. Materials

Sample specimens of high strength cast iron with the following mass percent contents of tin (Sn): 0,018%, 0,020%, 0,032% and 0,051%. The chemical composition and the designation of the sample specimens are given in Table 1.

Wedge-shaped sample specimens were obtained through gravitational casting in the factory "Osam" in the city of Lovech.

Hardness was measured by means of Brinell hardness meter of the type 2109TB, using a steel ball of diameter 10 mm and normal load 30 kN, by 15 s hold time. [4]

Table 2 shows specimens' hardness.

Table 1: Chemical composition of sample specimens

№	Chemical element, %	Specimen's number				
		0	**1**	**2**	**3**	**4**
1	C	3,87	3,87	3,87	3,87	3,87
2	Sn	-	**0,018**	**0,020**	**0,032**	**0,051**
3	Si	1,55	1,55	1,55	1,55	1,55
4	Mn	0,34	0,34	0,34	0,34	0,34
5	P	0,029	0,068	0,063	0,075	0,077
6	S	0,012	0,051	0,059	0,047	0,060
7	Cr	0,030	0,030	0,030	0,030	0,030
8	Mo	0,018	0,019	0,020	0,017	0,018
9	Ni	0,024	0,024	0,024	0,024	0,024
10	Co	0,013	0,017	0,014	0,013	0,013
11	Cu	0,051	0,058	0,077	0,059	0,070
12	Ti	0,0013	0,0013	0,0018	0,0015	0,0013
13	W	0,126	0,126	0,135	0,123	0,126
14	Pb	0,039	0,039	0,043	0,040	0,039
15	As	0,036	0,036	0,037	0,038	0,040
16	Zr	0,003	0,003	0,003	0,003	0,003
17	B	0,0083	0,0083	0,0074	0,0091	0,0088

Table 2: Specimens' hardness

Specimen's No.	**0**	**1**	**2**	**3**	**4**
Sn, %	-	0,018	0,020	0,032	0,051
Hardness, HB	179	197	203	262	277

2.2 Procedure and device for abrasive wear study

The experimental study was realized by a procedure and device for quick tests according to the kinematical scheme „pin-on-disk". Figure 1 shows the functional scheme of the device. The procedure was elaborated in the Laboratory of Tribology at the Faculty of Industrial Technology of the Technical University – Sofia. The actually valid standards were taken into consideration [5,6].

The studied cylindrical specimen 3 (the body) was mounted fixed in an appropriate holder of the loading head 6. Its position allows that the frontal surface *K* enters in contact with the abrasive surface 2 of the horizontal disk 1 (the counter-body). The horizontal disk 1 is rotating with constant rotational speed $\omega = const$ around its vertical axis. The number of revolutions of the disk 1 is read by the revolution-counter 5.

The device allows variation of the relative sliding speed between the specimen 3 and the disk 1 using two manners: by changing the rotational speed of the disk through a control unit or by variation of the distance R between the revolution axis of the counter-body 1 and the axis of the specimen 3.

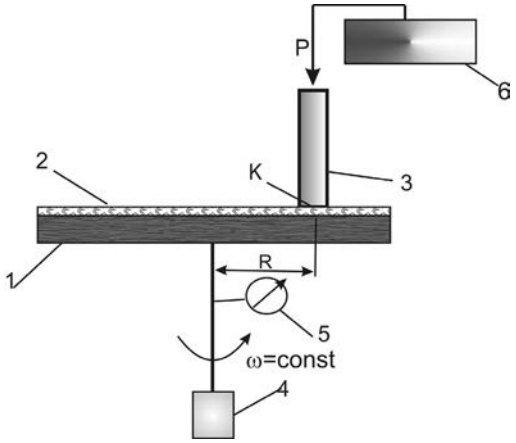

Figure 1: Functional scheme of the device "pin-on-disk"

The abrasive surface 2 of the counter-body 1 is being modeled through surfaces of impregnated carbo-corundum with hardness minimum 60% higher than the hardness of the tested coatings according to the requirements of the standard.

The procedure of the investigation comprises the following sequence:

1. The surfaces of all specimens, which are of equal cylindrical shape and size, are subjected to mechanical treatment in three stages – rough, grinding and polishing, up to obtaining the equal roughness $Ra = 0{,}4 \div 0{,}6\ \mu m$.

2. The mass of the specimen is measured before and after a given sliding path (number of cycles of interaction) by means of electronic balance of the type WPS 180/C/2 with accuracy up to 0,1 *mg*. Specimens are cleaned with a solution neutralizing the static electricity before each measurement.
3. The specimen 3 is fixed in the loading head 6 in a given position, and by means of system of leverages the normal central load *P* is being set.

2.3 Parameters of wear

Parameters of the studied mass and linear wear are given in Table 3.

Table 3. Parameters of wear

Mass wear	
mass, [mg]	m_o-m
wear rate, [mg/min]	m_o-m/t
wear intensity, [mg/m]	m_o-m/S
specific intensity, [mg/mm^{2}m]	m_o-m/A_aS,
absolute wear-resistance, [m/mg]	S/m_o-m
specific wear-resistance, [mm^{2}m/mg]	S.A_a/m_o-m
Linear wear	
wear, [µm]	h_o-h
wear rate, [µm/min]	h_o-h/t
wear intensity, [µm/m]	h_o-h/S
specific intensity [µm /mm^{2}m]	h_o-h/A_aS
absolute wear-resistance, [m/ µm]	S/h_o-h
specific wear-resistance [mm^{2}m/ µm]	S.A_a/h_o-h

The designations in the table are as follows: A_a – apparent contact area of sliding; S – sliding path.

The factor "comparative wear-resistance" ε is introduced, which is non-dimensional and gives the ratio between the absolute wear-resistance of the tested specimen and the wear-resistance of a chosen reference sample. A sample of high strength cast iron without Sn micro-alloy was accepted as reference sample by the authors.

All specimens are studied under equal conditions given in Table 3.

Table 3: Test parameters

normal load	P = 10,3 [N]
apparent contact area	$A_a = 78{,}5.10^{-6}$ [m^2]
apparent contact pressure	P_a = 13,12 [N/cm^2]
average sliding speed	V = 13,1 [cm/s]
type of the specimen	cylindrical
material density of the specimen	7,8.10^3 [kg/m^3]
initial roughness of the specimen	Ra = 0,4÷0,6 [µm]
abrasive surface	Corundum P 320

3. EXPERIMENTAL RESULTS

A part of the experimental results for the parameters of wear are given in this paper in the form of graphs, tables and diagrams.

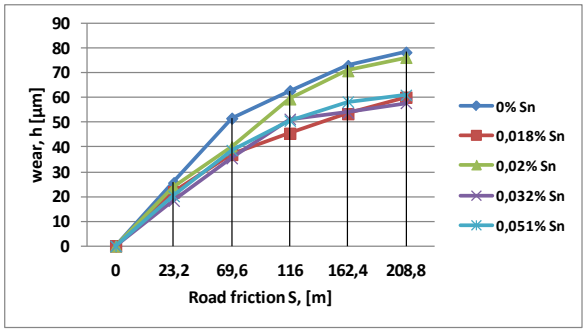

Figure 2. Variation of linear wear [µm] with the friction path [m]

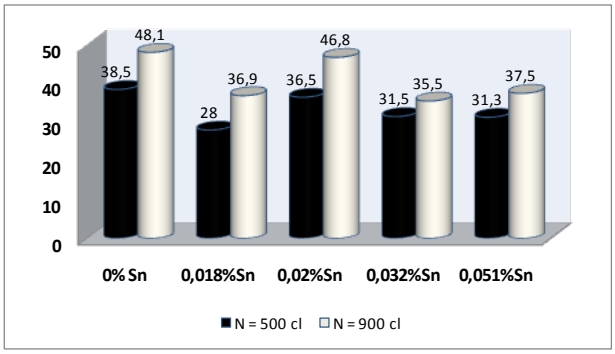

Figure 3. Diagram of mass wear [mg] of all specimens for two friction cycles

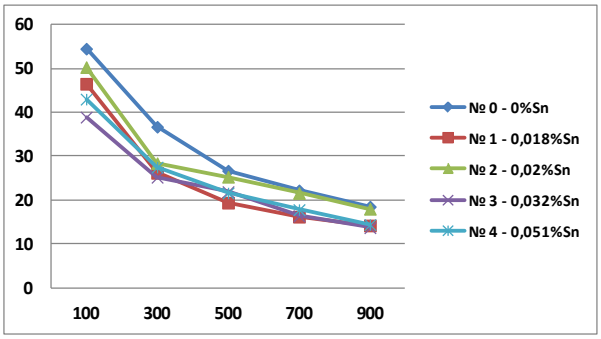

Figure 4. Variation of wear rate [µm/min] with the number of friction cycles

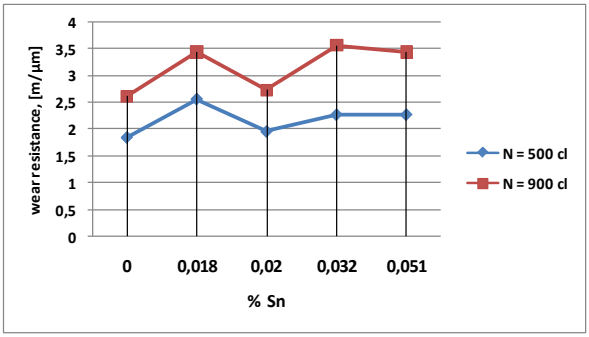

Figure 5. Variation of wear-resistance [m/µm] with the Sn % contents for two friction cycles

Table 4: Comparative wear-resistance by using as reference sample high strength cast iron without Sn micro-alloy

Number of cycles N	Comparative wear-resistance, $\varepsilon_{i,0}$			
	$\varepsilon_{1,0}$	$\varepsilon_{2,0}$	$\varepsilon_{3,0}$	$\varepsilon_{4,0}$
N = 500 cl	1,38	1,06	1,23	1,23
N = 900 cl	1,3	1,04	1,4	1,3

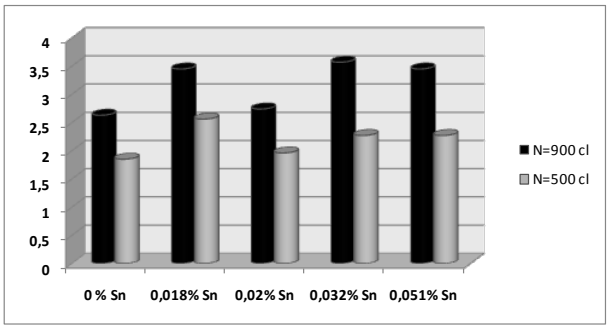

Figure 6 Wear-resistance of cast-iron [m/μm] at various Sn % contents for friction cycles number N=900 cl and N=500 cl

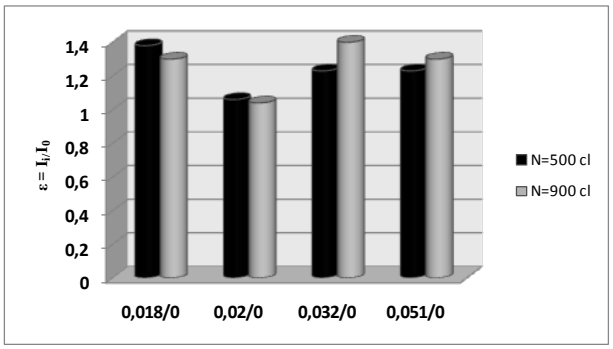

Figure 7. Diagram of the comparative wear-resistance $\varepsilon_{i,0} = I_i/I_0$ by reference sample high strength cast iron without Sn micro-alloy for two friction cycles

4. RESULTS ANALYSIS, OUTCOME AND CONCLUSIONS

The above investigations confirm the authors' outcome of earlier studies, namely that micro-alloying of high strength cast iron with Sn influences its mechanical and tribological properties [2,7].

Increasing the Sn % contents leads to increase of the hardness of the high strength cast iron.

The highest values of wear are for the specimens without Sn micro-alloy. All specimens containing Sn show higher wear-resistance compared with cast iron without Sn contents. A direct dependence exists between the % contents of Sn and hardness and wear-resistance of cast iron in the studied limits of Sn contents. Deviation of this dependence is observed for the specimen with 0,02% Sn contents. The same statement is to be seen in the earlier studies of the authors.

Maximum wear-resistance is obtained for 0,032% Sn contents. At higher contents - 0,051%, the wear-resistance decreases. The wear-resistance is equal for sliding path 500 cycles at 0,032% and 0,051% contents, however the comparative wear-resistance for the cast iron with lower Sn contents (0,032%) is higher – Table 4. Although the authors have no photos of the microstructure at this stage of the study, the last observation could be interpreted as result related to the non-homogeneous distribution of the graphite phase in the structure of the specimen.

Wear and wear-resistance are the parameters, which are most sensitive to the structure of material and the time of wear process (the friction path). It is possible that in some stages of the wearing process a structure of higher contents of the graphite phases is available in the contact zone. The relationship between wear and friction path under conditions of abrasive wear is not linear function (Figs. 2 and 4). A period of running-in is observed, which is of various duration for specimens with different contents of tin. The period of running-in will be subject of individual study.

The obtained results are sign for the authors that future systematic complex investigations on tin are needed, including also comparative study with high strength cast iron alloyed with copper.

Acknowledgement

This study is connected with the completion of a PhD dissertation and of the tasks under the Project ДУНК-01/3 "University R&D Complex for innovation and transfer of knowledge in micro/nano-technologies and materials, energy efficiency and virtual engineering" funded by the Bulgarian Ministry of Education and Science.

REFERENCES

[1] Я.Е. Гольдштейн, В.Г. Мизин, *Модифицирование и микролегирование чугуна и стали*, М., Металлургия,1986. Ya.E. Goldstein, W.G.Mizgin, Modifying and micro-alloying of cast iron and steel, Moscow, Metallurgy,1986 (in Russian)

[2] П. Добрев, Ж. Калейчева, Б. Съйкова, *Микролегиране на високояк чугун с калай*, XIII Национална конференция «Металолеене2007», Ловеч, Машини, технологии и материали; P.Dobrev, J. Kaleicheva, B. Saikova, *Micro-alloying of high-stenght cast iron with tin*, XIII Nat. Conf.

«Metal casting 2007», Machines, technologies and materials, Lovech, Bulgaria (in Bulgarian)

[3] С. Бондаренко, И. Гладкий, Повышение эксплоатационных свойств чугунов, работающих в условиях гидроабразивного износа, Вісник харнівськ. державн. техніч. Университету, Харків, 2003, вып. 14, с. 388-391. S. Bondarenko, I. Gladkij, Improvement of the operational properties of cast iron working under hydro-abrasive wear conditions, Kharkov, 2003, issue 14, pp. 388-391(in Russian)

[4] В. Анчев, В. Тошков, Л. Василева, Ж. Захаридова, Ж. Калейчева, Й. Николов, Р. Петров, В. Симеонов,Ръководство за лабораторни упражнения по материалознание, ИК „КИНГ", 2001, pp. 112-113. V. Anchev, et al., Manual for laboratory works in material science, Ed. house „KING" pp. 112-113 (in Bulgarian)

[5] БДС 14289-77, Метод за изпитване на абразивно износване при триене върху закрепени абразивни частици, Bulgarian State Standard 14289-77, Method for testing of abrasive wear at friction on fixed abrasive particles (in Bulgarian)

[6] M. Kandeva, D. Karastoyanov, A. Andonova: *Wear and tribothermal effects of nanostructured nickel chemical coatings*, Applied Mechanics and Materials. Vols. 157-158 (2012), pp. 960-963.

[7] B. Ivanova, M. Kandeva, J. Kaleicheva, R. Rangelov: *Influence of Tin on the Structure and Properties of Spherographitic Cast Iron*, 12th International Conference on Tribology, Kragujevac, Serbia, 11-13 May 2011, pp 42-45.

Serbian Tribology Society

SERBIATRIB '13

13th International Conference on Tribology

Faculty of Engineering in Kragujevac

Kragujevac, Serbia, 15 – 17 May 2013

INFLUENCE OF NANO-DIAMOND PARTICLES ON THE TRIBOLOGICAL CHARACTERISTICS OF NICKEL CHEMICAL COATINGS

Mara Kandeva[1], Dimitar Karastoianov [2], Boryana Ivanova[3], Viara Pojidaeva [4]

[1]Tribology Center, Technical University-Sofia, Bulgaria, kandeva@tu-sofia.bg

[2]Institute of Information and Communication Technologies – Bulgarian Academy of Sciences, dkarast@clmi.bas.bg

[3]Technical University-Sofia, Bulgaria, bsaykova@tu-sofia.bg

[4]University of Mining and Geology „St Ivan Rilsky" – Sofia, Bulgaria, vpojidaeva@abv.bg

Abstract: *Friction and wear of 10 types Ni chemical coatings, with and without heat treatment, containing nano-diamond particles of various size – 0;5 nm; 100 nm; 200 nm and 250 nm, are studied in the paper. Procedure and laboratory device for friction investigation in starting regime were developed. Experimental results for the influence of the particle size on the static friction force and the change of friction coefficient have been obtained. Abrasive wear has been studied by means of the procedure developed by the authors for the study of above coatings under conditions of dry friction on surfaces with fixed abrasive. The obtained results are related to the parameters linear wear, wear rate and wear-resistance. A part of this study is connected with the tasks on the 7 FP Project „Acom In (Advanced Computing Innovations)" coordinated by the Institute of Information and Communication Technologies at the Bulgarian Academy of Sciences, and the other part is carried out under the Project ДУНК-01/3 "University R&D Complex for innovation and transfer of knowledge in micro/nano-technologies and materials, energy efficiency and virtual engineering" funded by the Bulgarian Ministry of Education and Science.*

Keywords: *tribology, nano-diamond particles, coatings, friction, wear*

1. INTRODUCTION

Ni chemical coatings are obtained through the method of electro-less chemical deposition known in the literature as „Electroless Nickel".

From chemical point of view, chemical deposition is a deoxidization process which develops between positive charged metal ions M^{z+} and negative electrons *e*:

$$M_e^{z+} + ze \rightarrow Me \qquad (1)$$

where z is the valence of the metal ion.

Coatings obtained through chemical deposition differ in the methods for procurement of the electrons necessary for the deoxidization.

In the galvanic (electrolyte) methods, electric current is passed through the solution of the metal salt (electrolyte) and the metal ions are reduced to the corresponding metal atom *Me* on the cathode (the coated detail). The cathode renders, and the anode obtains electrons, which are provided by external source – the electric current.

At chemical Ni deposition an external source is not needed for providing electrons. The necessary electrons are obtained as a result of chemical reactions going between the solution and the surface of the detail to be coated. As a consequence the Ni metal ions of the solution obtain a given number of electrons depending on their valence passing thus in state of neutral atoms (*Me*). The atoms gradually build the crystal grid of the coating. In this case, the role of „supplier of electrons" is realized by different substances (chemical agents) called *reducers (deoxidizers)* from the solution [1].

Imbedding of micro- or nano-sized particles of various natures in the Ni matrix changes the physico-mechanical and the tribological characteristics of the coatings.

In connection with the improvement of the resource of tribosystems, a special interest for nanotribology represent Ni chemical coatings

containing in their structure particles of the nanosize scale [2,3]. Imbedding of nano-sized particles in the solution for the production of the Ni coating brings changes in the character of the contact interactions on three levels: interaction of nanoparticles with Ni ions into the solution with the electrons, interaction of the built atom with the surface of the detail and formation of the crystal grid of the coating [4].

The purpose of the present work is to study some characteristics of contact friction and wear for Ni chemical coatings, without and with nanodiamond particles of different size: 4 nm, 100 nm, 200 nm and 250 nm.

2. NICKEL CHEMICAL COATINGS

Ten types of coatings are studied, gathered in 5 series with number given in Table 1.

Table 1: Description of the specimens with coatings of chemical Ni containing nanodiamond particles

№ of series	Designation of the series	№	Designation of the coating	Composition of the coating	Thickness of the coating before wear, h_1, μm
I	N	1	N-	Ni	25,56
		2	N+	Ni+T°C	11,28
II	nD4	3	nD4-	Ni+Di 4 nm	23,22
		4	nD4+	Ni+Di 4 nm +T°C	8
III	nD100	5	nD100-	Ni+Di 100 nm	27,94
		6	nD100+	Ni+Di 100 nm +T°C	7,12
IV	nD200	7	nD200-	Ni+Di 200 nm	26,24
		8	nD200+	Ni+Di 200 nm +T°C	9,14
V	nD250	9	nD250-	Ni+Di 250 nm	30,5
		10	nD250+	Ni+Di 250 nm +T°C	8,7

Each series has its designation in Latin letters, correspondingly:

* N - Nickel coating without nanoparticles;
* nD - Nickel coating with diamond nanoparticles;

The number after the letter D indicates the average size of the nanoparticles – 4 nm, 100 nm, 200 nm, 250 nm. Each series includes two groups of coatings: first group - coatings without heat treatment designated by the sign (-) and second group - with heat treatment at 360°C during 6 hours designated by the sign (+).

3. ABRASIVE WEAR

3.1 Device and procedure

Experimental study of abrasive wear of Ni coatings is realized by means of the test rig TABER ABRASER according to the kinematical scheme „disk-on-disk" (Fig.1).

The specimen 1 (the body) with deposited coating 2 is in the shape of disk and is fixed appropriately on carrying horizontal disk 3 drived by electrical motor 4 with a constant rotational speed $\omega = 1[s^{-1}] = \text{const}$. The counter-body 5 is an abrasive disk (roller) of special material CS 10 mounted on horizontal axis 6 in the device 8, by means of which is set the desired normal load P in the contact zone K. Thus, the body 1 and the counter-body 5 are located on two crossed axes. Because of the constant rotational speed of the body 1 and the constant nominal contact pressure p_a, the friction in the contact zone K supports constant speed of rotation of the counter-body 5.

The procedure of the experimental study on abrasive wear is realized in the following sequence of operations:

- clean-up, cleaning of lubricants and drying of the equal specimens. The specimens represent disks of diameter 100 mm and thickness 3 mm with the deposited coatings;
- measuring of roughness of the contact surfaces of the specimens before and after wear;
- measuring of specimens mass m_o before and its mass m_i after a given friction path L by electronic balance WPS 180/C/2 of accuracy 0,1 mg. At every measurement the specimens are cleaned with appropriate solution against static electricity;

- measuring of coating thickness h_1 before wear and h_2 after wear by means of *Pocket LEPTOSKOP 2021 Fe* device in 10 points of the surface; the average value is taken for thickness of the sample;

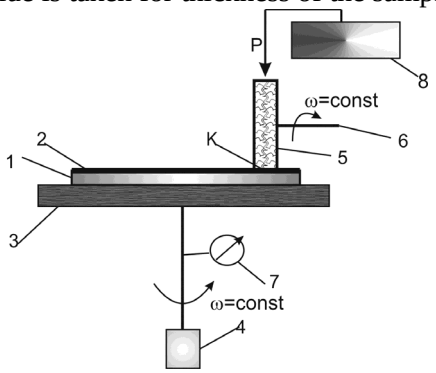

- the specimen 1 is fixed on the carrying horizontal disk 3; then the normal load *P* is set. The friction path *L* is determined by the number of cycles read by the revolution counter 8.

Figure 1. TABER ABRASER – device for study of abrasive wear

The procedure of the experimental study on abrasive wear is realized in the following sequence of operations:

- clean-up, cleaning of lubricants and drying of the equal specimens. The specimens represent disks of diameter 100 mm and thickness 3 mm with the deposited coatings;
- measuring of roughness of the contact surfaces of the specimens before and after wear;
- measuring of specimens mass m_o before and its mass m_i after a given friction path *L* by electronic balance WPS 180/C/2 of accuracy 0,1 mg. At every measurement the specimens are cleaned with appropriate solution against static electricity;
- measuring of coating thickness h_1 before wear and h_2 after wear by means of *Pocket LEPTOSKOP 2021 Fe* device in 10 points of the surface; the average value is taken for thickness of the sample;
- the specimen 1 is fixed on the carrying horizontal disk 3; then the normal load *P* is set. The friction path *L* is determined by the number of cycles read by the revolution counter 8.

Abrasive wear for all coatings is obtained by fixed equal operating conditions – nominal contact pressure given with the normal load *P*, average sliding speed *V* and parameters of the abrasive surface.

The characteristics of the experiment are given in Table 2.

Table 2. Working parameters in the experiment:

Apparent contact area	$A_a = 0,26\ \text{cm}^2$
Nominal contact pressure	$p_a = 9,42\ \text{N/cm}^2$
Average sliding speed	$V = 22,3\ \text{cm/s}$
Abrasive material	CS 10

The parameters of mass and linear wear are studied: speed, wear intensity, absolute and relative wearresistance and their change in time, respectively the friction path.

Wear intensity is determined as mass (or linear) wear for unit friction path, and absolute wearresistance - as the reciprocate value of wear intensity.

The relative wearresistance is the ratio between the absolute wearresistance of the tested coating and the absolute wearresistance of reference sample for equal friction path (number of cycles).

Two reference samples are used in the present work – Nickel coating without nanodiamond particles with heat treatment and without heat treatment.

3.2 Experimental results

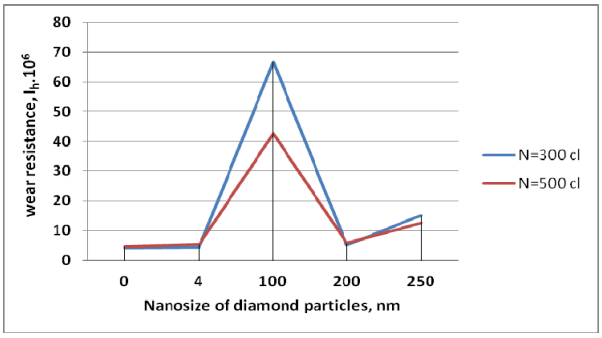

Figure 2. Dependence of wearresistance I_h on nanoparticles size for coatings without heat treatment

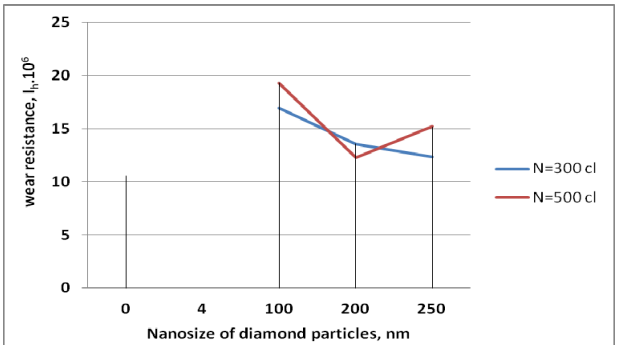

Figure 3. Dependence of wearresistance I_h on nanoparticles size for coatings with heat treatment

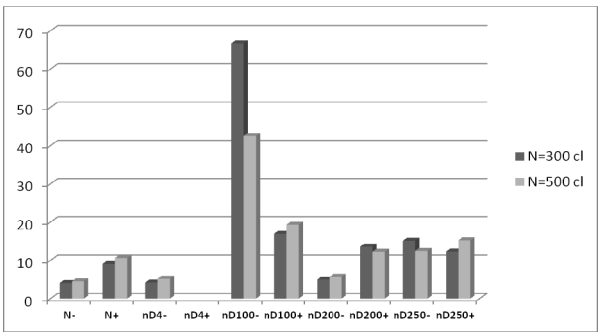

Figure 4. Wearresistance of Ni coatings without and with nanoparticles without and with heat treatment

3.3 Analysis of the experimental results

The presence of nanodiamond particles affects the value and the character of the abrasive wear. This influence becomes more complicated along with the heat treatment of the coating.

For size of nanoparticles 4 nm and 100 nm coatings with heat treatment show higher wear, and for size 200 and 250 nm the opposite effect is observed – wear is lower than that of the case without heat treatment.

The dependence of wear on nanodiamond particles size is of nonlinear character, and the various coatings show different duration of the running-in process.

The boundary number of cycles N*, where the whole coating is worn, is always bigger for coatings without heat treatment.

The highest wearresistance show Ni coatings with nanodiamond particles of the size δ = 100 nm without heat treatment.

4. STARTING CONTACT FRICTION

4.1 Theory

From the point of view of process history, or in time cross-section of the process, tribosystem undergo three friction stages: starting, kinetic and pathological friction. The starting friction, known as static friction in the classical mechanics, is done under conditions of preliminary microdisplacement in the contact zone and the tribosystem performs the transition between static state (at rest) and movement. Kinetic is the friction when the body is moving upon the counterbody.

The kinetic friction matches the stationary and the pathological regimes of contact joint operation.

The pathological friction is characterized by abrupt increase of friction with wear and seizure in contact.

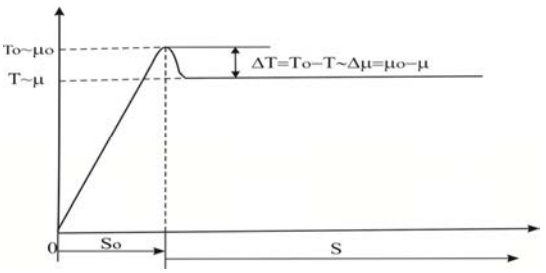

Figure 5. Variation of friction force and friction coefficient with displacement

The difference between starting friction force T_o and sliding friction force T

$$\Delta T = T_o - T \tag{1}$$

gives *the jump in the friction force* during system transition from state at rest and state of movement, and corresponds to the jump in the *friction coefficient*, i.e.

$$\Delta\mu = \mu_o - \mu \tag{2}$$

The work of the starting friction force is given by:

$$A_s\left(\vec{T}_o\right) = T_o S_o = \mu_o P S_o \tag{3}$$

And the work of the kinetic friction force is:

$$A_p\left(\vec{T}\right) = TS = \mu PS \tag{4}$$

Let present the ratio

$$\psi_s = \frac{A_s\left(\vec{T}_o\right) - A_p\left(\vec{T}\right)}{A_s\left(\vec{T}_o\right)}.100 = \frac{\mu_o PS_o - \mu PS}{\mu_o PS_o}.100$$

Then:

$$\psi_s = \frac{\Delta\mu}{\mu_o} = 100,\% \tag{5}$$

The parameter ψ_s is called relative change of the starting friction; it is the ratio between the jump of friction and the starting friction coefficient.

Similarly, for the relative change of the kinetic friction ψ_p is obtained the expression:

$$\psi_p = \frac{A_s\left(\vec{T}_o\right) - A_p\left(\vec{T}\right)}{A_p\left(\vec{T}\right)}.100 = \frac{\mu_o PS_o - \mu PS}{\mu PS}.100 = \frac{\Delta\mu}{\mu}.100$$

or

$$\psi_p = \frac{\Delta\mu}{\mu} = 100,\% \tag{6}$$

4.2 Procedure and experimental results

The parameters of starting friction have been studied using a test rig with functional scheme as shown in Figure 5.

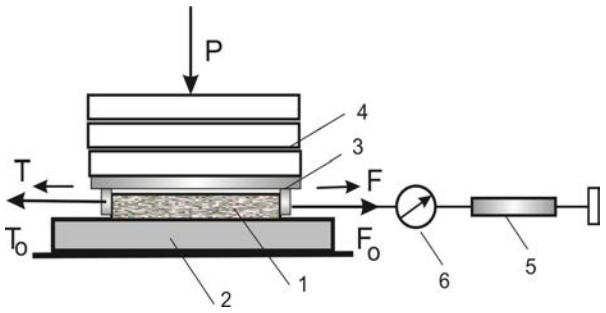

Figure 5. Functional scheme of the test rig for study of starting friction

The experimental arrangement consists of body 1 and counterbody 2, which form a contact. The body 1 is fixed in the holder 3 and is connected through the nonelastic thread with the dynamometer 6 and micrometric screw 5.

Tangential force is loaded on the body 1 near the contact surface through slow turning of the micrometric screw. The normal load P is set by means of the loading bodies 4.

The body 1 is a prismatic sample of size 30 x 50 x 8 mm made of duraluminium (*Al*), and the counterbody 2 represents a round disk of diameter ϕ 100 mm and thickness 3 mm with the deposited coating.

The procedure of measurement the friction force is of following sequence:

- The specimen 2 with coating is fixed in the bed of the base, and the body 1 is mounted in the holder 3, then they are put on the specimen 2.
- The normal load is set by the loading bodies 4.
- The elastic dynamometer 6 is put in the initial reset to zero.
- The micrometric screw 5 is turned very slowly and the pointer of the dynamometer 6 shifts with ease. In the moment of shivering of the pointer backwards, the indication of the dynamometer is read. The maximum value of the indication corresponds to the value of the starting friction force To.
- The screw keeps on turning and the indications of the dynamometer are observed; they match the kinetic friction force T after the jump of friction.
- The dial of the dynamometer is calibrated in force [N].
- During the tests the body 1 is made of the same material but for each test with different coatings a different specimen of this material is used. All specimens of the body have equal size and roughness $Ra = 0,418\ \mu m$.

Table 3 shows the results of starting and kinetic friction, and the figures give some diagrams.

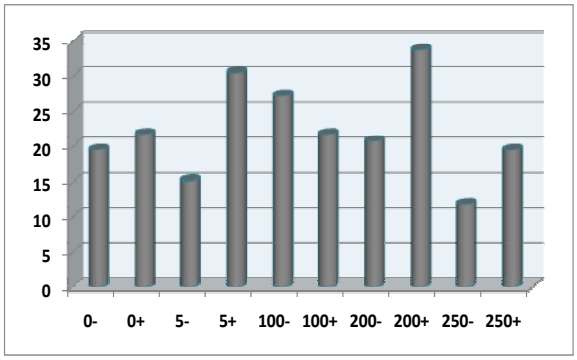

Figure 6. Diagram of starting friction force To

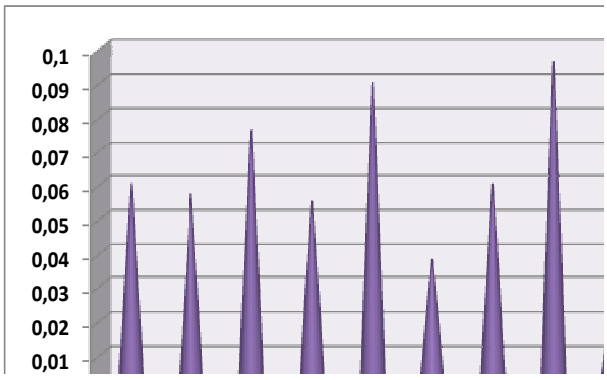

Figure 7. Diagram of the jump of friction force Δμ

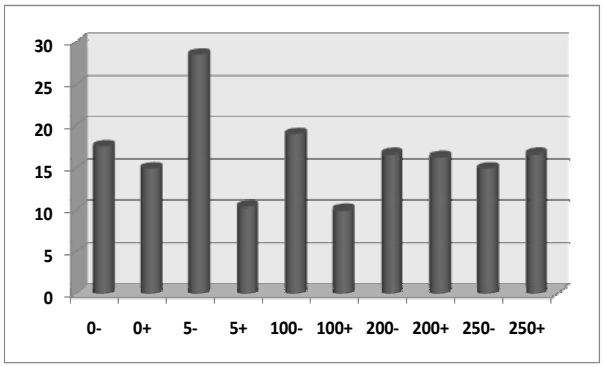

Figure 8. Diagram of the relative change of starting friction Ψs

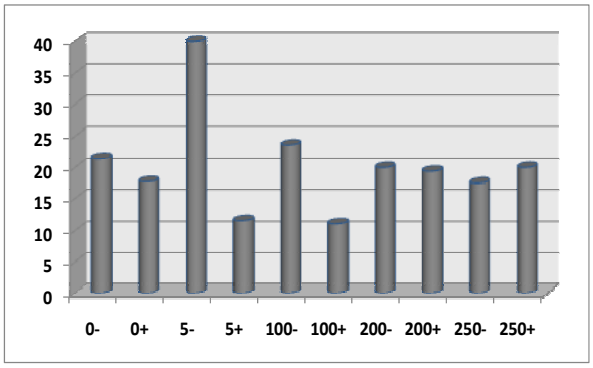

Figure 9. Diagram of the relative change of kinetic friction Ψp

Table 3. Experimental data of friction parameters

№	Series	To, [N]	T, [N]	μo	μ	Δμ	Ψs	Ψp
1	0- ($Ni^{-} - Al$)	19,62	16,35	0,34	0,28	0,06	17,6	21,4
2	0+ ($Ni^{+} - Al$)	21,8	18,53	0,38	0,32	0,057	15	17,8
3	5- ($Ni * nD5^{-} - Al$)	15,26	10,90	0,266	0,19	0,076	28,6	40
4	5+ ($Ni * nD5^{+} - Al$)	30,52	27,25	0,53	0,475	0,055	10,4	11,6
5	100- ($Ni * nD100^{-} - Al$)	27,25	21,80	0,47	0,38	0,09	19,1	23,6
6	100+ ($Ni * nD100^{+} - Al$)	21,8	19,62	0,38	0,342	0,038	10	11,1
7	200- ($Ni * nD200^{-} - Al$)	20,71	17,44	0,36	0,30	0,06	16,7	20
8	200+ ($Ni * nD200^{+} - Al$)	33,79	28,34	0,59	0,494	0,096	16,3	19,4
9	250- ($Ni * nD250^{-} - Al$)	11,99	9,81	0,20	0,17	0,03	15	17,6
10	250+ ($Ni * nD250^{+} - Al$)	19,62	16,35	0,342	0,285	0,057	16,7	20

4.3 Analysis of the experimental results

A jump in the friction force is observed for all tested tribosystems however at different values of starting friction force and kinetic friction force.

The jump is of different duration for the different coatings.

The influence of the size of nanodiamond particles upon friction parameters is not unambiguous.

The relationship between the starting friction force and the size of nanodiamond particles is strongly nonlinear. This is most clearly expressed for coatings with heat treatment. At coatings without heat treatment this relationship has clear maximum for particles size $\delta = 100\,\text{nm}$, however the value of the maximum is lower than the two maximums in the curve of the coatings without heat treatment.

Genesis and variations in the friction forces depend directly on the formation and evolution of the contact spots, the latest depending on many various factors too.

REFERENCES

[1] Gavrilov G., C. Nikolov: Electroless Nickel and Composite Coatings, Sofia, Technika, 1985.

[2] Karaguiozova Z., T. Babul, A. Ciski, S. Stavrev: *Influence of Cubic Nanostructured Additions on the Properties of Electroless Coatings*, – IJNM, Vol. **5**, No 1-2, pp. 129-138, 2010.

[3] Kralov I., P. Sinapov, K. Nedelchev, I. Ignatov, *Friction Induced Rail Vibrations*, AIP, Vol. 1497, pp. 19-25, 2012.

[4] Kandeva M., D. Karastoyanov and A. Andonova, *Wear and tribothermal effects of nanostructured nickel chemical coatings*, Applied Mechanics and Materials, Vols. 157-158, pp. 960-963, 2012

Serbian Tribology Society

SERBIATRIB '13

13th International Conference on Tribology

Faculty of Engineering in Kragujevac

Kragujevac, Serbia, 15 – 17 May 2013

WEAR BEHAVIOR OF AUSTEMPERED DUCTILE IRON WITH NANOSIZED ADDITIVES

J. Kaleicheva
Technical University of Sofia, Bulgaria, e-mail: jkaleich@tu-sofia.bg

Abstract: *The microstructure and properties of austempered ductile iron (ADI) strengthened with nanosized addtives of titanium nitride + titanium carbonitride (TiN + TiCN), titanium nitride TiN and cubic boron nitride* cBN *are investigated. The* TiN, TiCN *and* cBN, *nanosized particles are coated by electroless nickel coating EFTTOM-NICKEL prior to the edition to the melt. The spheroidal graphite iron samples are undergoing an austempering, including heating at 900°C for an hour, after that isothermal retention at 280 °C, 2 h and 380 °C, 2h. The metallographic analysis by optical metallographic microscope GX41 OLIMPUS and hardness measurements by Vickers Method are performed. The structure of the austempered ductile iron consists of lower bainite and upper bainite.Experimental investigation of the wear by fixed abrasive are also carried out. The influence of the nanosized additives on the microstructure, mechanical and tribological properties of the austempered ductile irons (ADI) is studied.*

Keywords: *nanosized particles, austempered ductile iron, hardness, wear resistance*

1. INTRODUCTION

The austempering of the iron-carbon alloys is an isothermal heat treatment, which reduces the internal stresses and deformations and increases the details' impact strength. The bainitic structure is formed at this type of heat treatment, which is widely applicable in constructional steels and ductile iron processing due to its high strength and increased toughness [1-2]. Incomplete austempering is also applied in case of heat treatment of some hypereutectoid and ledeburite steels [3]. The possibility of wider practical application of this heat treatment type requires an additional data for the bainitic transformation in iron-carbon alloys with different composition including alloys with nanomodifiers. Nanosized particles added to the iron melt in a small quantity transform the graphite morphology from laminar to vermicular one [5], increase the graphite quantity [6] and change the matrix structure, which increases the cast iron wear resistance [4-6].

The aim of the performed investigation is to study the tribological properties, the microstructure and hardness of austempered ductile iron, containing additives of nanosized particles – titanium nitride+titanium carbonitride *(TiN + TiCN)*, titanium nitride *TiN* and cubic boron nitride *cBN*.

2. MATERIAL AND INVESTIGATION METHODS

The composition of the austempered cast iron samples is: Fe-3,55C-2,67Si-0,31Mn-0,009S-0,027P-0,040Cu-0,025Cr-0,08Ni-0,06Mg wt%. The *TiN, TiCN* and *cBN*, nanosized particles are coated by electroless nickel coating EFTTOM-NICKEL [7] prior to the edition to the melt. The nickel coating improves the particles wetting into the melt and their uniformity distribution into the casting volume.

The ductile cast iron samples are undergoing austempering, including heat treatment at 900°C for an hour, after that isothermal retention at 280 °C, 2 h and 380 °C, 2h.

The austempered ductile iron samples' microstructure is observed by means of an optical metallographic microscope GX41 OLIMPUS. The samples surface is treated with 2 % HNO3 - C2H5OH solution. The hardness testing is performed by Vickers method (Table 1).

The experimental wear examination of the cast and austempered ductile iron (ADI) is performed in

friction conditions of a fixed abrasive by a cinematic scheme „pin - disc" using an accelerated testing method and device [6].

Table 1. Nanoadditives, hardness and wear resistance.

№ of sample	Micro structure	Nanosized additive	Hardness HV10	Wear resistance I
1	upper bainite	-	314	$5{,}9.10^6$
2		*TiN + TiCN*	319	$7{,}75.10^6$
3		*TiN*	317	$6{,}13.10^6$
4		*cBN*	312	7.10^6
5	lower bainite	-	388	$7{,}8.10^6$
6		*TiN + TiCN*	413	$5{,}46.10^6$
7		*TiN*	405	$7{,}34.10^6$
8		*cBN*	422	$6{,}79.10^6$

3. EXPERIMENTAL RESULTS

The cast iron structure consists of upper bainite after austempering at 380°C for 2 hours and of lower bainite after austempering at 280 °C for 2 hours (Figure 1). The bainite is an oriented needlelike grain structure of α-phase (bainitic ferrite), carbides and untransformed austenite. The α-phase is formed in the low carbon austenite area by a martensitic mechanism [1,2]. Upon cooling from the temperature of the isotherm to ambient one, a part of the untransformed austenite undergoes martensitic transformation and other its part remains as a retained austenite A in the structure.

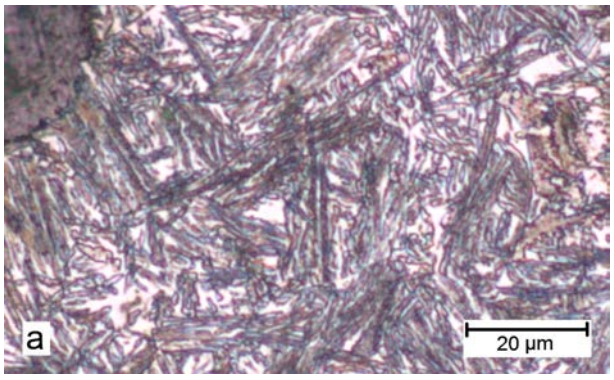

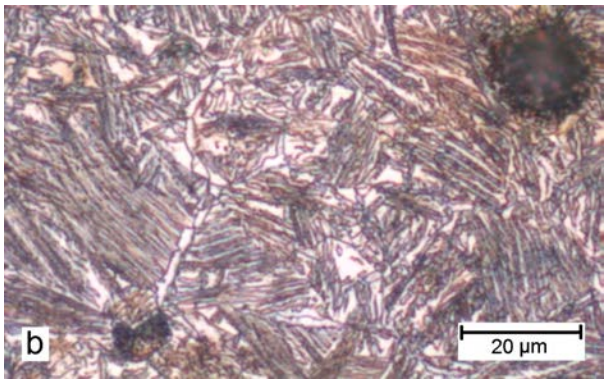

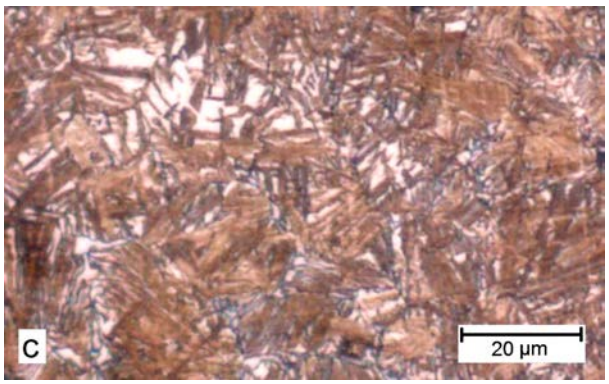

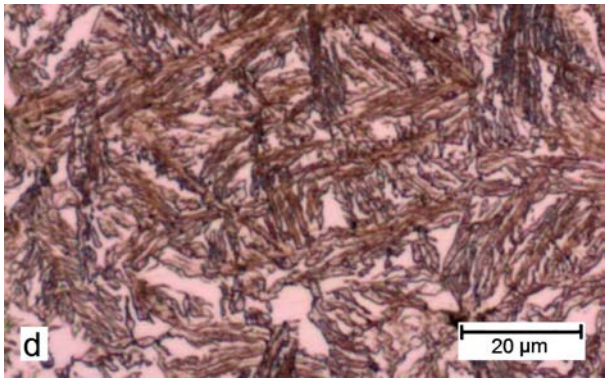

Figure 1. Lower bainitic (c) and upper bainitic (a,b,d) microstructure. *(a- sample1; b- sample 2; c, d- sample 8)*

The nanosized additives change the bainitic ferrite morphology and the austenitic conversion degree during the austempering (Figure1). The hardness of the austempered, with upper bainitic structure samples changes from 312 to 319 HV10 (Figure 2a) and this one of the samples with lower bainitic structure changes from 388 to 422 HV10 (Figure 3a). The austempered samples hardness with lower bainitic structure is higher than this one of the samples with upper bainitic structure, which is explained with the different carbon satiety of the α-phase (bainitic ferrite) and with the varying degree of austenitic transformation in the lower and upper part of the bainitic area [1,2].

The experimental data for massive wear m, the speed of wear dm/dt, absolute intensity of wear i and absolute wear resistance I of the samples and their alteration with the time of the contact interaction (Table 2, 3) are received. The massive wear m dependence on cycle's number N (friction road) and massive wear speed dm/dt dependence on the friction time *t* are presented in Figures 4 and 5. Figure 2b and 3b show the wear resistance *I* of austempered ductile cast iron samples with upper and lower bainitic structure for the same friction road $L = 700\ [m]$.

Table 2. Test results for massive wear, wear speed, intensity of wear and wear resistance *(samples 1÷4)*.

Friction road, S [m]		140	280	420	560	700
Cycles number , N		500	1000	1500	2000	2500
Time , t [min]		2,35	4,7	7,05	9,4	11,75
Massive wear, m [mg]	sample 1	22,3	32,7	38,6	42,4	46,5
	sample 2	19	24,4	28	32,8	35,3
	sample 3	20	25	32,6	38,2	44,8
	sample 4	16,3	24	27,1	33,8	39,1
Wear speed, dm/dt [mg / min]	sample 1	9,49	6,96	5,48	4,52	3,96
	sample 2	8,08	5,19	3,97	3,49	3,0
	sample 3	8,51	5,32	4,62	4,06	3,81
	sample 4	6,94	5,11	3,84	3,6	3,33
Intensity of wear, i	sample 1	$0,406.10^{-6}$	$0,298.10^{-6}$	$0,234.10^{-6}$	$0,194.10^{-6}$	$0,169.10^{-6}$
	sample 2	$0,346.10^{-6}$	$0,222.10^{-6}$	$0,17.10^{-6}$	$0,149.10^{-6}$	$0,129.10^{-6}$
	sample 3	$0,364.10^{-6}$	$0,228.10^{-6}$	$0,198.10^{-6}$	$0,174.10^{-6}$	$0,163.10^{-6}$
	sample 4	$0,297.10^{-6}$	$0,218.10^{-6}$	$0,164.10^{-6}$	$0,154.10^{-6}$	$0,142.10^{-6}$
Wear resistance, I	sample 1	$2,46.10^{6}$	$3,36.10^{6}$	$4,27.10^{6}$	$5,15.10^{6}$	$5,9.10^{6}$
	sample 2	$2,89.10^{6}$	$4,5.10^{6}$	$5,88.10^{6}$	$6,69.10^{6}$	$7,75.10^{6}$
	sample 3	$2,75.10^{6}$	$4,39.10^{6}$	$5,05.10^{6}$	$5,75.10^{6}$	$6,13.10^{6}$
	sample 4	$3,37.10^{6}$	$4,59.10^{6}$	$6,1.10^{6}$	$6,49.10^{6}$	7.10^{6}

Table 3. Test results for massive wear, wear speed, intensity of wear and wear resistance *(samples 5÷8)*.

Friction road, S [m]		140	280	420	560	700
Cycles number , N		500	1000	1500	2000	2500
Time , t [min]		2,35	4,7	7,05	9,4	11,75
Massive wear, m [mg]	sample 5	14,2	20,4	24,4	29,3	35,2
	sample 6	26,4	33,6	37,7	44,9	50,2
	sample 7	14,6	21,7	27,2	34,8	37,4
	sample 8	15,9	23,7	29,4	35	40,4
Wear speed, dm/dt [mg / min]	sample 5	6,04	4,34	3,46	3,12	2,99
	sample 6	11,2	7,15	5,35	4,78	4,27
	sample 7	6,21	4,62	3,86	3,7	3,18
	sample 8	6,76	5,04	4,17	3,72	3,44
Intensity of wear, i	sample 5	$0,259.10^{-6}$	$0,186.10^{-6}$	$0,148.10^{-6}$	$0,133.10^{-6}$	$0,128.10^{-6}$
	sample 6	$0,48.10^{-6}$	$0,306.10^{-6}$	$0,229.10^{-6}$	$0,204.10^{-6}$	$0,183.10^{-6}$
	sample 7	$0,266.10^{-6}$	$0,198.10^{-6}$	$0,165.10^{-6}$	$0,158.10^{-6}$	$0,136.10^{-6}$
	sample 8	$0,29.10^{-6}$	$0,22.10^{-6}$	$0,178.10^{-6}$	$0,159.10^{-6}$	$0,147.10^{-6}$
Wear resistance, I	sample 5	$3,86.10^{6}$	$5,38.10^{6}$	$6,75.10^{6}$	$7,5.10^{6}$	$7,8.10^{6}$
	sample 6	$2,08.10^{6}$	$3,27.10^{6}$	$4,37.10^{6}$	$4,9.10^{6}$	$5,46.10^{6}$
	sample 7	$3,76.10^{6}$	$5,05.10^{6}$	$6,06.10^{6}$	$6,31.10^{6}$	$7,34.10^{6}$
	sample 8	$3,45.10^{6}$	$4,54.10^{6}$	$5,62.10^{6}$	$6,27.10^{6}$	$6,79.10^{6}$

The wear resistance is a multifactorial parameter and to make its prognosis using the standard measured properties (hardness etc.) could be wrong, since these features are not always reliable criteria for the steels'and irons'' wear resistance evaluation. The metastable structures in the iron-carbon alloys as a martensite, bainite and retained austenite have higher resistance to abrasive wear in comparison to this one of the stable structures (ferrite, pearlite etc.). The intensive strengthening is going off during the wear process due to dynamic strain ageing of martensite and partial transformation of the metastable retained austenite in a strain-induced martensite [8].

The samples hardness with upper bainitic structure without and with nanoadditives are similar

in values (312÷319 HV10). The wear resistance *I* of these cast irons consisting nanosized additives is in the range between $6{,}13.10^6 \div 7{,}75.10^6$ and it is with 4 to 32 % higher than this one of the cast iron samples without nanoadditives ($I = 5{,}9.10^6$). Samples hardness with lower bainitic structure is 388÷422 HV10. The wear resistance of the cast iron samples with lower bainitic structure without nanoadditives ($I = 7{,}8.10^6$) is higher than this one of the cast iron samples with nanoadditives ($I = 5{,}46.10^6 \div 7{,}34.10^6$). The obtained results for the wear resistance values of the tested cast irons samples are probably related to the characteristics of structures upper bainite, lower bainite, retained austenite and martensite during abrasive wear. The different quantitative proportion between the structural components in the samples with and without nanoadditives defines the degree of strengthening and the resistance during abrasive wear due to strain ageing of the carbon sated α-solid solution (martensite and bainitic ferrite) and also to partially transformation of the retained austenite into deformation martensite.

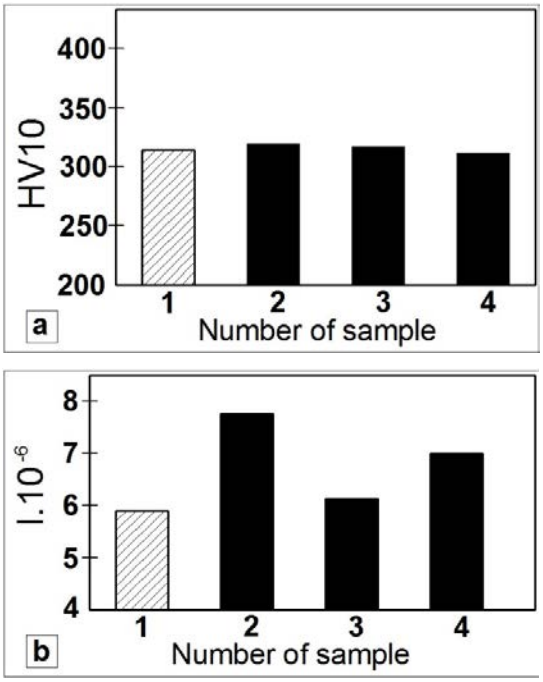

Figure 2. Hardness HV10 (a) and wear resistance *I* (b) of austempered ductile iron samples without (1) and with (2,3,4) nanoadditives.

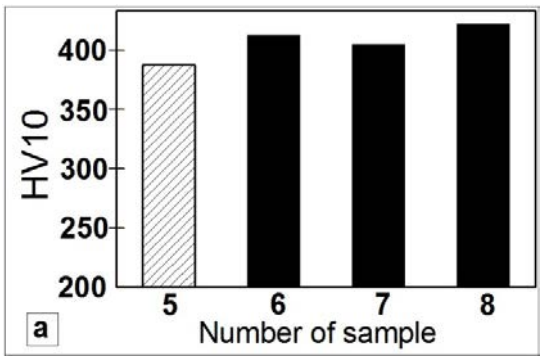

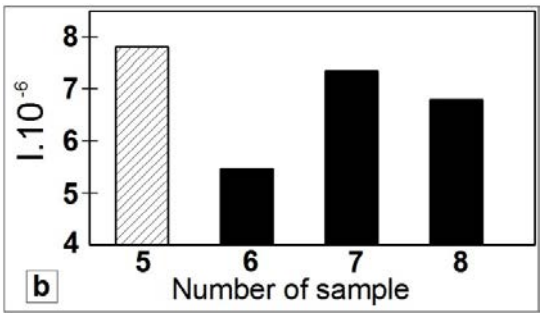

Figure 3. Hardness HV10 (a) and wear resistance *I* (b) of austempered ductile iron samples without (5) and with (6,7,8) nanoadditives.

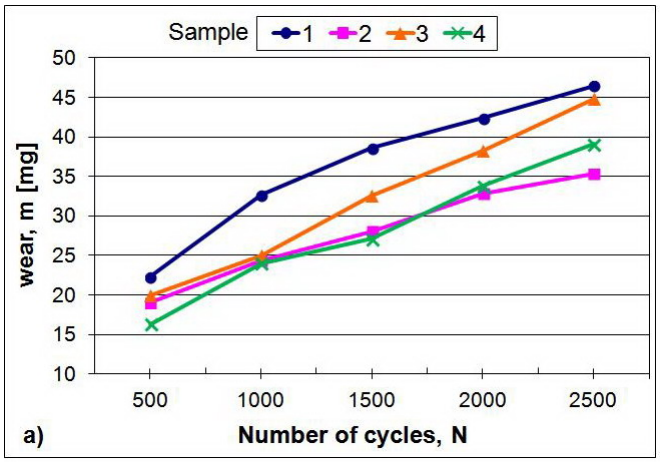

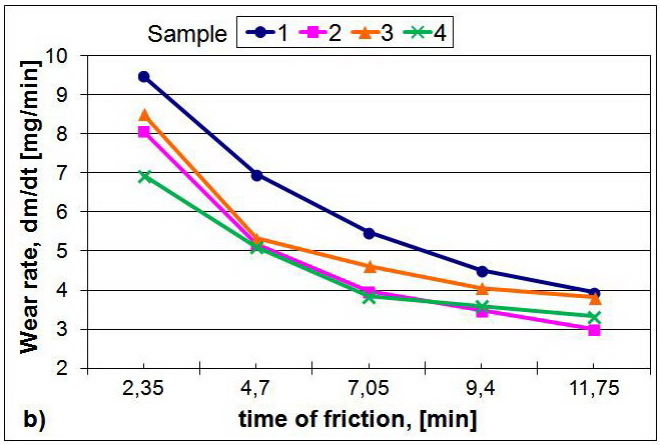

Figure 4. Dependence of the massive wear *m* on the cycles number *N* (a) and of the wear speed *dm/dt* on the friction time *t* (b) *(samples 1÷4).*

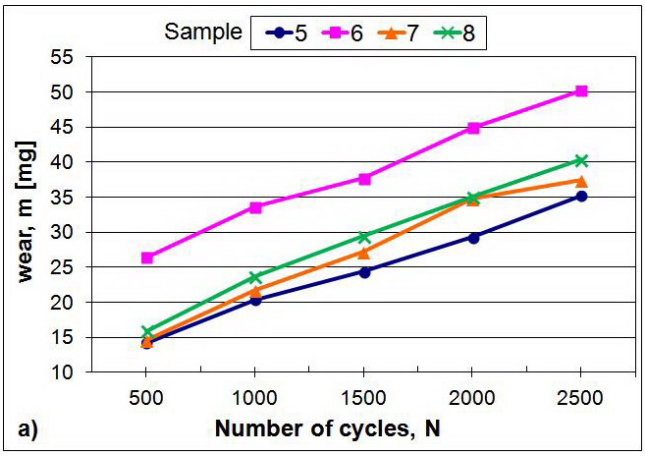

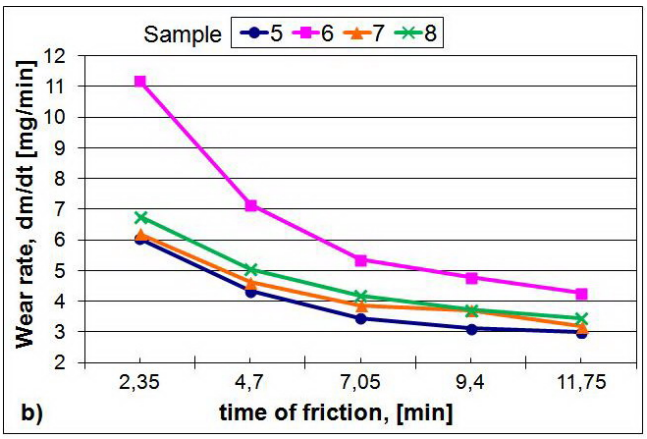

Figure 5. Dependence of the massive wear *m* on the cycles number *N* (a) and of the wear speed *dm/dt* on the friction time *t* (b) *(samples 5÷8).*

4. CONCLUSION

The microstructure, hardness HV10 and tribological properties of austempered ductile cast iron samples without and with nanosized additives of titanium nitride + titanium carbonitride (TiN + TiCN), titanium nitride TiN and cubic boron nitride *cBN* are investigated. The nanosized particles change the bainitc ferrite morphology in the austempered iron structure. In the cast iron with a upper bainitic structure the nanosized additives increase the wear resistance with 4÷32 % in comparison to this one of the irons without nanoadditives. The results for the wear resistance of the irons with lower bainitic structure show the highest value ($I = 7{,}8.10^6$) for the cast iron without nanoadditives.

ACKNOWLEDGEMENT

The presented investigations are carried out and financed under the Project "University Complex for research and development of innovations and knowledge transfer in the field of micro/nanotechnologies and materials, power effectiveness and virtual engineering", contract DUNK-01/3.

REFERENCES

[1] G.V. Kurdyumov, L.M. Utevskiy, R.I. Entin: *Transformations in Iron and Steel*, Nauka,Moscow, 1977 (In Russian).

[2] H.K.D.H.Bhadeshia: *Bainiteinsteels*, 2nd edit. London, Inst.of Materials, Cambridge, 2001.

[3] J.Kaleicheva: *Structure and Properties of High-Speed Steels after Austempering*. Int. J. Microstructure and Materials Properties 2, pp. 16-23, 2007.

[4] J. Li, M. Chen, H. Gao, Y. Zhao, *Structures and Properties of Cast Irons Reinforced by Trace Addition of Modified SiC Nanopowders*. Chinese Journal of Chemical Physics 20, pp. 625 – 631, 2007.

[5] Y. Wang, Z. Pan, Z. Wang, X. Sun, L. Wang, *Sliding wear behavior of Cr–Mo–Cu alloy cast irons with and without nanoadditives*, Wear 271, pp. 2953– 2962, 2011.

[6] J.Kaleicheva, M. Kandeva, Z. Karaguiozova, V. Mishev: Wear behavior of ductile cast irons with nanoparticle additives. *Proceedings of the 3nd Int. Conf. on Diagnosis and Prediction in Mechanical Engineering Systems DIPRE12*, May 31-June 1st 2012, Galati, Romania, Paper 38.

[7] G.Gavrilov, C. Nicolov: *Electroless Nickel and Composite Coatings*, Tehnika, Sofia, 1985 (In Bulgarian).

[8] A.Makarov: *Wear resistance increase of Iron alloys at the expense of metastable and nanocrystal structure formation*, DSc thesis, Ural Department of the Mechanical Engineering Institute of the Russian Academy of Sciences, Chelyabinsk, 2009 (In Russian).

Serbian Tribology Society

SERBIATRIB '13

13th International Conference on Tribology

Faculty of Engineering in Kragujevac

Kragujevac, Serbia, 15 – 17 May 2013

NICKEL COMPOSITE COATINGS MODIFIED BY DIAMOND NANOPARTICLES

M. Kandeva[1], N. Gidikova[2], R. Valov[2], V. Petkov[2]

[1]Technical University-Sofia, Centre of Tribology, Sofia, Bulgaria, kandeva@tu-sofia.bg

[2] Institute of Metal Science, Equipment and Technologies with Hydroaerodynamics Centre, Sofia, Bulgaria, radoslav.valov@gmail.com, vladimir2pe@yahoo.com

Abstract: *The study deals with composite Ni electro-chemical coatings on steel containing diamond nanoparticles with grain size up to 100 nm. Coatings were obtained at various concentrations of the nanoparticles in the electrolyte and at various process time.*

A procedure is developed for the study of wear parameters of the coatings under conditions of dry friction with abrasive surface. Experimental results for linear wear, wear rate, wear intensity and wear-resistance have been obtained. The study is related and financed under the Technical University - Sofia Contract DUNK-01/3 "University R&D Complex for innovation and transfer of knowledge in micro/nanotechnologies and materials, energy efficiency and virtual engineering" funded by the Bulgarian Ministry of Education and Science.

Keywords: *tribology, wear resistance, abrasive wear, Ni-coatings, diamond nanoparticles*

1. INTRODUCTION

The deposition of nickel coating on steel is applied in industry to increase the corrosion resistance and the wear resistance of the surfaces [1].

There is a lot of work done in the recent years on the application of nanoparticles of different materials and with various concentrations. This leads to improvement of the mechanical and tribological characteristics [2] [3].

The objective of the present work is to study the influence of the diamond nanoparticles concentration on the wear parameters of electrochemical nickel coatings. The wear is performed in dry friction conditions on surface with firmly embedded abrasive particles.

2. MATERIALS AND METHODS

Electrochemical nickel coatings deposited on substrate of carbon steel C45 are studied.

The electrochemical nickel depositing is performed on cylindrical samples with diameter 30 mm and height 10 mm. Standard electrolyte with composition: $NiSO_4.7H_2O$ - 240 g/l, $Na_2SO_4.10H_2O$ – 150 g/l, NaCl - 15 g/l, H_3BO_3 - 20 g/l, is used. The pH of the solution is 5.0 - 5.5. The anode is made of nickel. The temperature of galvanization is 25 - 30^0C.

The diamond nanoparticles (ND) are produced by detonation synthesis and the grain size is up to 100 nm. The nanoparticles are added in the electrolyte as water suspension. The nickel deposition is carried out with concentrations of the diamond nanoparticles 1, 5, 10 and 20 g/l at 3 A/dm^2 current density. The time of the electrochemical nickel deposition is 10 and 15 min.

The galvanization process is performed after the activation of the nanoparticles in the electrolyte and at continuous vigorous stirring during the nickel deposition. The studied parameters are the Ni yield, the thickness of the layer, the microhardness and especially the wear resistance of the coating. Their changes related to the parameters of the galvanization as current density, deposition duration and the concentration of the diamond nanoparticles (C_{NDDS}) are studied.

The data concerning the studied samples of electrochemical nickel coatings are presented in table 1. The coatings are obtained at different diamond nanoparticles concentration.

Table 1. Parameters of the electrochemical nickel coatings

Sample No	Coating	Nanoparticles concentration, g/l	Current density, A/dm^2	Process duration, min	Yield of nickel, mg/cm^2
8	Ni	-	3	10	4,87
9	Ni	-	3	15	8,06
17	Ni+nDi-1%	1%	3	10	11,18
18	Ni+nDi-1%	1%	3	15	8,89
28	Ni+nDi-5%	5%	3	15	8,31
38	Ni+nDi-10%	10%	3	15	5,66
48	Ni+nDi-20%	20%	3	15	7,05

3. DEVICE AND METHOD OF INVESTIGATION

3.1 Device for investigation of the abrasive wear at dry friction on surface with fixed particles

The experimental investigation is carried out according to the method and with the device for accelerated test by the kinematic scheme "thumb – disc". The device is presented schematically on figure 1. The method is in conformity with the existing standards [4].

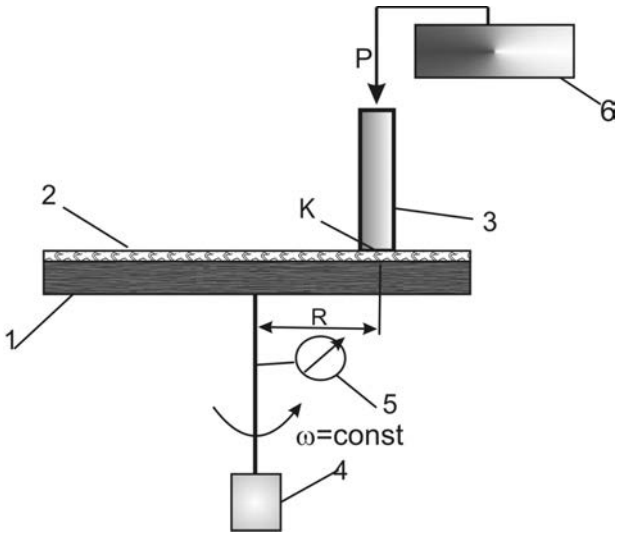

Figure 1. Functional scheme of the device "thumb – disc"

The studied cylindrical sample 3 (body) with the deposited coating K is installed immovably in suitable holder of the loading head 6. It is positioned in such a way that its front surface contacts the abrasive surface 2 of the horizontal disc 1 (counter body). The horizontal disc 1 rotates with constant angular velocity $\omega = const$ around its vertical axis. The number of cycles of disc 1 is measured with a cyclometer 5.

The device permits change in the relative sliding speed between the sample 3 and the disc 1 in two ways: by changing the angular disc velocity by control bloc and by changing the distance R between the rotation axis of the counter body 1 and the axis of the sample 3.

The abrasive surface 2 of the counter body 1 is molded by surfaces of impregnated carbo corundum with hardness at least 60 % more than that of the tested coatings which corresponds to the requirements of the standard [4].

2.2 Method for investigation of the abrasive wear

The method for investigation is performed in the following sequence of operations:

- Cleaning, degreasing and drying of cylindrical samples with equal dimensions and roughness;
- Measurement of the mass of the sample before m_0 and after m_i covering definite friction distance S (number of cycles). The measurement is done with electronic balance WPS 180/C/2 with precision 0.1 mg. The samples are dipped in special solution to prevent accumulation of static electricity. The mass wear m is determined as the difference of the two measurements;
- Measurement of the thickness of the coating before h_0 and after h_i the wear at definite friction distance S with the device Pocket LEPTOSKOP 2021 Fe at 10 points of the surface and calculating the average of the measured values;
- The normal loading P is applied along the sample axis by a lever system in the loading head and the cycle number N is read on the cyclometer which correspond to the friction distance S.

The abrasive wear of all coatings is fixed at one and the same working conditions which are presented on Table 2.

Table 2. Experimental parameters

Parameters	Values
Nominal contact pressure, p_a	1,46 [N/cm^2]
Average sliding speed, V	15,5 [cm/s]
Nominal contact area, A_a	7,065 [cm^2]
Abrasive surface	Corundum P 320

3.3 Wear parameters

The following parameters of mass and linear wear are studied:
- Absolute mass *m* (linear *h*) wear;
- Average rate of mass *dm/dt*, [mg/min] (linear *dh/dt*, [μm/min]) wear;
- Absolute intensity by mass wear i_m ,$[mg/m]$ as per the formulae:

$$i_m = m/S \qquad (1)$$

- Absolute intensity by linear wear i_h, $[\mu m/m]$, correspondingly:

$$i_h = h/S \qquad (2)$$

- The friction distance S is calculated by the corresponding number of cycles N and the distance R between the axis of rotation and the mass center of the nominal contact site by the formulae:

$$S = 2\pi RN \qquad (3)$$

- Absolute wear resistance by mass I_m, $[m/mg]$:

$$I_m = 1/i_m = S/m \qquad (4)$$

- Absolute wear resistance by linear wear I_h, $[m/\mu m]$:

$$I_h = 1/i_h = S/h \qquad (5)$$

- Comparative wear resistance $\varepsilon_{i,e}$ - dimensionless value, representing the ratio between the absolute wear resistance of the tested sample I_i and the absolute wear resistance of a standard sample I_o.

$$\varepsilon_{i,e} = I_i / I_o \qquad (6)$$

Sample with electrochemical nickel coating without diamond nanoparticles is accepted as a standard in the present study.

The index *i* indicates the percentage of the diamond nanoparticles.

3. EXPERIMENTAL RESULTS

The obtained experimental results of the mass and linear wear, the rate of wear, the absolute and the comparative wear resistance are presented in the form of graphical relations, tables and diagrams.

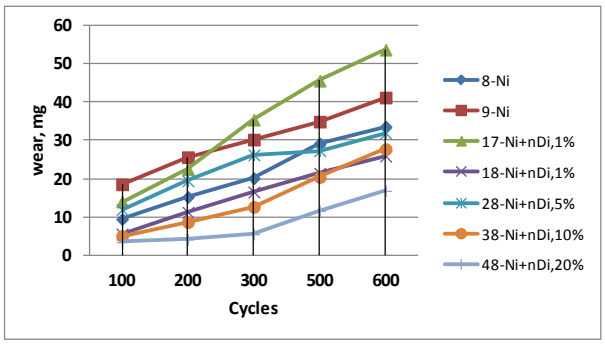

Figure 2. The relation of the mass wear m [mg] from the number N of the friction cycles

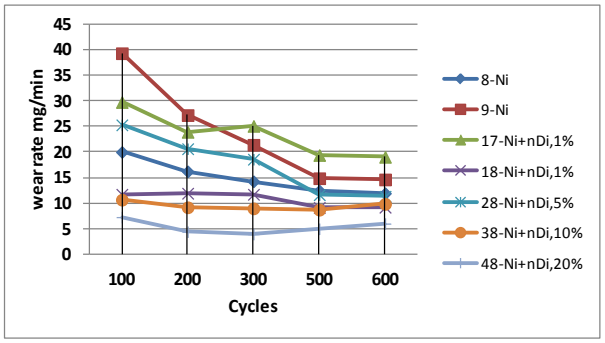

Figure 3. The relation of the rate of mass wear from the wear distance

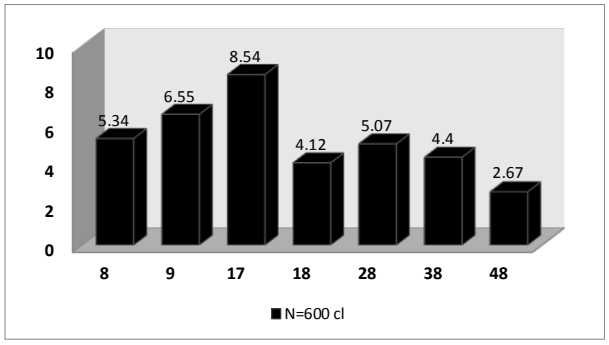

Figure 4. Linear wear in [μm] at N = 600 cl. for each sample

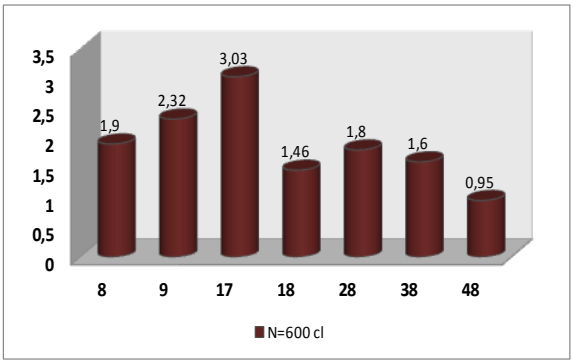

Figure 5. Rate of linear wear in [μm/min] at N = 600 cl. for each sample

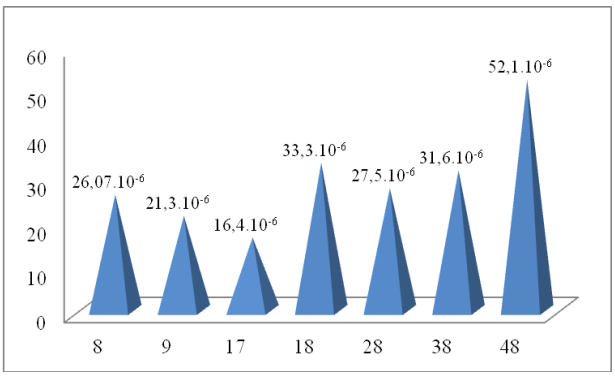

Figure 6. Wear resistance by linear wear I_h, [μm/m] at N = 600 cl. for each sample

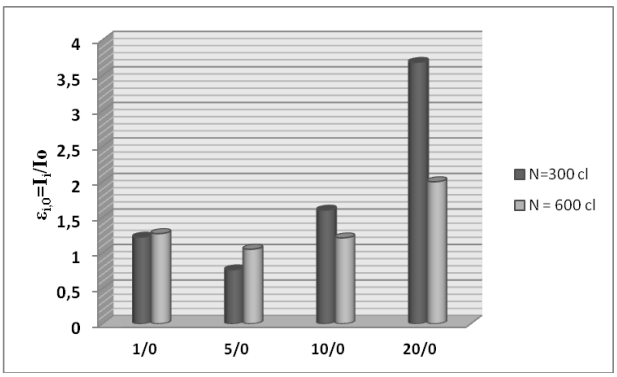

Figure 7. Diagram of the comparative wear resistance $\varepsilon_{i,0} = I_i/I_0$

Table 3. Comparative wear resistance of the samples compared to the standard – electrochemical nickel coating without diamond nanoparticles.

Number of cycles N	Comparative wear resistance, $\varepsilon_{i,e}$			
	$\varepsilon_{1,0}$	$\varepsilon_{5,0}$	$\varepsilon_{10,0}$	$\varepsilon_{20,0}$
N = 300 cl	1,22	0,76	1,60	3,68
N = 600 cl	1,27	1,05	1,21	2,00

4. ANALYSIS OF THE RESULTS

It is found that the nickel yield decreases with the increase of the diamond nanoparticles concentration in the electrolyte. The Ni yield acquires its highest values of about 12.0 mg/cm^2 at diamond nanoparticles concentration C_{NDDS} = 1g/l, current density I = 3 A/dm^2 and process duration t = 10 min.

It is found also that the microhardness of the coating at concentration of the diamond nanoparticles C_{NDDS} = 1g/l is 4800 MPa or 2.5 times more than that of pure nickel coating (1950 MPa) and 1.7 times more than that of coating at concentration of the diamond nanoparticles C_{NDDS} = 5 g/l (2800MPa).

The increase of the abrasive wear with the friction distance has nonlinear character and is different for the different coatings. This relation is linear only for coating derived from electrolyte with diamond nanoparticles concentration 5 %.

The abrasive wear rate is not constant value in time. The only exception is coating obtained from electrolyte with diamond nanoparticles concentration 10 %.

The presence of diamond nanoparticles in the electrochemical nickel coatings leads to increase of the wear resistance. The wear resistance is increased with the increase of the diamond nanoparticles content in the electrolyte and the relation is of nonlinear character.

Coating with 20 % content of diamond nanoparticles possesses the highest wear resistance – 52,1.10^{-6} at N = 600 cycles. This wear resistance is 2 times higher than the wear resistance of coating without nanoparticles.

Out of the studied coatings the coating containing 1 % nanoparticles and deposited with current density 3 A/dm^2 and process duration 10 minutes possesses the lowest wear resistance.

Comparing the wear resistance of the coatings obtained at equal diamond nanoparticles concentration 1 % and current density 3 A/dm^2, the coating obtained at process duration 15 minutes has 2 times higher wear resistance.

REFERENCES

[1] I. Petrov, P. Detkov, A. Drovosekov, M.V. Ivanov, T. Tyler, O. Shenderova, N.P.Voznekova, Y.P. Toporov, D. Schulz: *Nickel galvanic coatings co-deposited with fractions of detonation nanodiamond*, Diamond and related Materials 15, pp. 2035-2038, 2006.

[2] M. Kandeva, Il. Peichev, N. Kostova, K. Stoichkov, *Complex Study of Surface Layers and Coatings*, Journal of the Balkan Tribological Association 17, 2011.

[3] M. Kandeva, D. Karastoyanov and A. Andonova, *Wear and tribotermal effects of nanostructured nickel chemical coatings*, Applied Mechanics and Materials Vols. 157-158, pp 960-963, 2012.

[4] БДС 14289-77, Method of abrasion test by friction against embedded abragant grain

Serbian Tribology Society

SERBIATRIB '13

13th International Conference on Tribology

Faculty of Engineering in Kragujevac

Kragujevac, Serbia, 15 – 17 May 2013

TRIBOLOGICAL BEHAVIOR OF THERMAL SPRAY COATINGS, DEPOSITED BY HVOF AND APS TECHNIQUES, AND COMPOSITE ELECTRODEPOSITS NI/SIC AT BOTH ROOM TEMPERATURE AND 300°C.

A.Lanzutti[1], M. Lekka[1], E. Marin[1], L.Fedrizzi[1]

[1] Università di Udine, Dipartimento di Scienze e Tecnologie Chimiche, Via del Cotonificio 108, 33100 Udine Italy, alex.lanzutti@uniud.it

Abstract: *Both the thermal spray and the electroplating coatings are widely used because of their high wear resistance combined with good corrosion resistance. In particular the addition of both micro particles or nano-particles to the electrodeposited coatings could lead to an increase of the mechanical properties, caused by the change of the coating microsctructure.*

The thermal spray coatings were deposited following industrial standards procedures, while the Ni/SiC composite coatings were produced at laboratory scale using both micro- and nano-sized ceramic particles. All the produced coatings were characterized regarding their microstructure, mechanical properties and the wear resistance. The tribological properties were analyzed using a tribometer under ball on disk configuration at both room temperature and 300 °C.

The results showed that the cermet thermal spray coatings have a high wear resistance, while the Ni nano-composite showed good anti wear properties compared to the harder ceramic/cermet coatings deposited by thermal spray technique.

Keywords: *thermal spray coatings, nano-composite electrodeposits, Ni/SiC, micro-composite electrodeposits, HVOF, APS, dry sliding, 300°C*).

1. INTRODUCTION

The thermal spray coatings are widely used for many industrial applications [1-13] because of the possibility to deposit different type of materials, ranging from different metal alloys to ceramics, and their technological properties, in particular the high wear resistance even if they are used also as corrosion barriers at both high temperature degradation or wet corrosion.

The thermal spray coatings are mainly used for high temperature applications (oxidation resistance or fused salts resistance). Usually these types of coatings are deposited with the addition of rare earths in order to inhibit the oxidative degradation processes [1-3]. Some technological processes are used to reduce the porosity of the coating and thus increase both mechanical properties and the barrier effect to oxidative environments. Sidhu et al [2] have found that the laser remelting process increase both the mechanical properties and the oxidation resistance and leaves only a small amount of porosity to the coating (<1%). Sigh et al [3], instead, showed that the NiCr (80/20) has a good resistance to hot corrosion in molten salts at 900°C.

The literature about NiCr wear performance is scarce. Usually this kind of coating is used as bond coat for ceramic or cermet coatings in order to promote the adhesion of the deposited material to the substrate [4-6]. The NiCr 80/20 alloy is also used as metal matrix to produce composite coatings reinforced with carbides [7-9]. The WC-Co coatings, instead, were widely used and analysed by many research teams [7-12]. The interest about these types of coatings is related to their high mechanical properties that leads to high wear resistance of the coated system. Fedrizzi et al [7] performed some tribo-corrosion tests on cermet

coatings and observed their good wear resistance, related to their high hardness, but low corrosion resistance, in wet wear tests. This behaviour is related to the low toughness that promote the crack enucleations and thus the permeation of corrosion media that enhances the undermining corrosion of the coating. Toma et al [8] showed that the addition of Cr to metal matrix increased the abrasion and corrosion resistance. Fedrizzi et al [9] showed that these type of coatings can be used as an alternative to hard chromium and their performance are also increased if are used nano-sized powders. Murthy et al[11] showed that the coatings grinded have an higher wear resistance because of the production of an hard layer on surface. Other researcher [12] found out that the decrease in powder size increase the coating performance because of both reduction of the porosity and increase of the mechanical properties. This enhances both corrosion and wears protection.

The ceramic coating Cr_2O_3 was subjected to numerous studies in the area of both wear and corrosion protection. It was shown by Ahn et al that, in the reciprocating wear tests, the wear mechanism is a plastic deformation of wear debris that influence both the friction and wear behavior. This is related to a formation of CrO_2 layer under hertzian loads [4]. Bolelli et al [5] performed wear tests at room temperature on different plasma spray ceramic coatings. He found that the Cr_2O_3 coating is the hardest and most anisotropic coating with high abrasion resistance, as confirmed by Leivo et al [6], while in sliding condition the material forms a compact tribofilm. The high temperature data for this type of coatings is scarce.

The Ni based electrodeposits are widely used as both corrosion/wear barrier coatings in many applications ranging from high temperature applications to room temperature applications in both dry and wet conditions [14-21].

In this work composite coatings are also analyzed . The introduction of reinforcing particles is aimed to enhances both the wear and corrosion properties, in particular if the nano-particles are embedded to the metal matrix they produce a nano-structured microstructure.

Garcia et al [14] showed that the increase of wear properties at room temperature for micro-composite Ni/SiC coatings is a function of particle' size. In particular the decrease of particle' size leads to an increase of anti-wear properties.

The reaserch group of Zimmermann et al [15-16] observed that the addition of sub-microsized particles to the coating leads to an increase of both mechanical strength and toughness, if the reinforcing content is below the 2 wt%. Above the 2wt% they showed that some particles' coalescence is possible, during the deposition, leading to t coating embrittlement. They tried to add nano-particles to the coating and observed a notable increase of the mechanical properties.

Benea et al [17-18] in many works demonstrate that the addition of SiC nano particles, in Ni matrix, leads to an increase of the wear properties and they calculated the relation between the microstructure of the coating and the wear performance.

The wear properties of both micro composite and nano composite Ni/SiC coatings at high temperature were investigated by Lekka et al [19]. They found an increase of anti-wear properties of the composite coating at both room temperature test and 300°C compared to the pure Ni coating.

This work aimed to compare the wear performance of the most used thermal spray coatings with the anti-wear properties of the Ni composite coating, highlighting the important properties of the composite coatings produced with a simple and cheaper technique compared to the thermal spray process.

2. EXPERIMENTAL

2.1 Samples production

For all types of the deposits ASTM 387 F22 steel plates (7×10 cm) and discs (d=5 cm) have been used as substrates (chemical composition in Table 1).

Table 1: Chemical composition of steel substrate ASTM 387 F22

C	Si	Mn	P	Cr	Mo	Fe
0.11	0.31	0.5	0.025	2.2	0.9	Bal.

The thermal spray coatings have been deposited using industrial procedures. The deposited coatings were: NiCr 80/20 and NiCr 80/20 + Cr_2O_3 deposited by APS (Air Plasma Spray) technique and WC CoCr 18/4 deposited by HVOF technique.

Regarding the Ni matrix coatings, three types of deposits have been prepared: pure Ni (to be used as reference). Ni containing microparticles of SiC and Ni containing nanoparticles of SiC. The electroplating bath used was a high speed nickel sulfammate plating bath having the following composition: 500 g/l $Ni(SO\ 3NH_2)_2 \cdot 4H_2O$, 20 g/l $NiCl_2 \cdot 6H_2O$, 25 g/l H_3BO_3, 1 ml/l surfactant ($CH_3(CH)_{11}OSO_3Na$ based industrial product. The deposition was carried out using a galvanic pilot plant (12 l plating tank) under galvanostatic control at 4 A/dm^2, 50 °C, under continuous mechanical stirring. The deposition time was 2.5h in order to obtain 70–80 μm thick deposits. For the production

of the composite coatings 20g/l of micro- or nano-powders were added into the electroplating bath, dispersed using ultrasounds (200W, 24kHz) for 30min and then maintained in suspension under continuous mechanical stirring during the electrodeposition. The micro-particles have a mean dimension of 2μm and a very irregular and sharp shape, while the nano-particles have a mean diameter of 45 nm [19].

2.2 Samples characterization

The specimens characterization includes microstructure, chemical composition, microhardness, wear resistance at both room temperature and 300°C and corrosion resistance in two different environments.

The microstructure of the specimens have been analysed by SEM (Zeiss Evo-40) + EDXS (Oxford instruments INCA) in cross section. Both the SiC content and the coatings' porosity were calculated using an image analysis software [13]. For nano composite coating The SiC content was measured through the measurements of RF GDOES (HR-Profile, Horiba Jobin Yvon), calibrated using 28 CRM (Certified Reference Material) samples. The system was set up using an Ar pressure of 650Pa and a applied power of 50W. The micro-composite coating were not analysed by the GDOES because of some issues related to the plasma erosion of the reinforcing particles [21].

Micro-hardness measurements ($HV_{0,3}$) have been performed on cross section of the specimens.

Wear tests have been performed using a CETR UMT tribometer in a ball-on-disc configuration at both room temperature and at 300 °C. The testing parameters are summarized in Table 2. The volume loss has been evaluated using a stylus profilometer (DEKTAK 150 Veeco). The wear rate K [10^{-6} mm^3/Nm] has been calculated using the equation described in [22].

Table 2: Wear test parameters.

Counter material	WC sphere (d 9.5mm)
Applied load	70N
Test radius	18mm
Rotation speed	300rpm
Sliding speed	0.565 m/s
Test duration	60 min

3. EXPERIMENTAL RESULTS

3.1 Microstructural characterization

In Fig. 1 is shown the microstructure of the steel substrate.

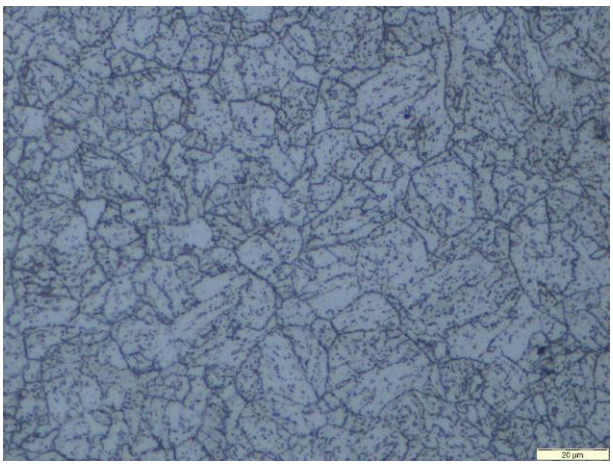

Fig.1: Microstructure of gr. 22 steel.

The Gr 22 steel presents a ferritic microstructure with some carbides precipitated in the metal matrix, that leads to the high creep strength of material. The carbides are mainly produced by Cr and Mo. The hardness of the material is about 180±20 $HV_{0,3}$ and the ferritic grain size is about 45±15 μm.

In Fig.2 are shown the SEM micrographs obtained for Thermal spray coatings and the relative data acquired by mechanical characterization and image analysis. In Tab. 3 the thermal spray coatings' properties are listed.

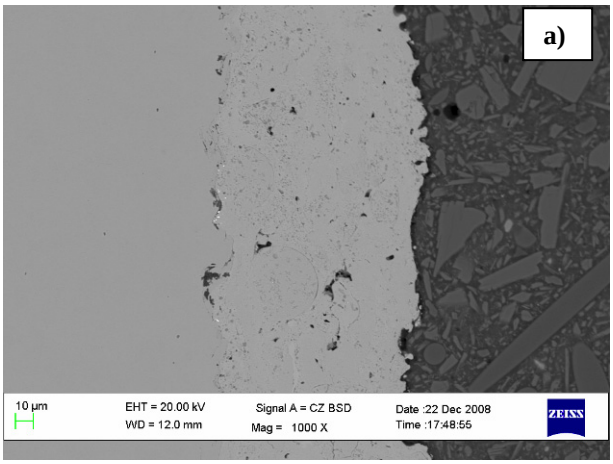

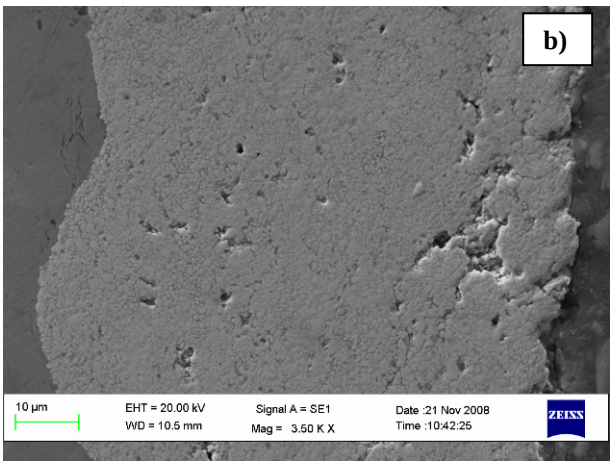

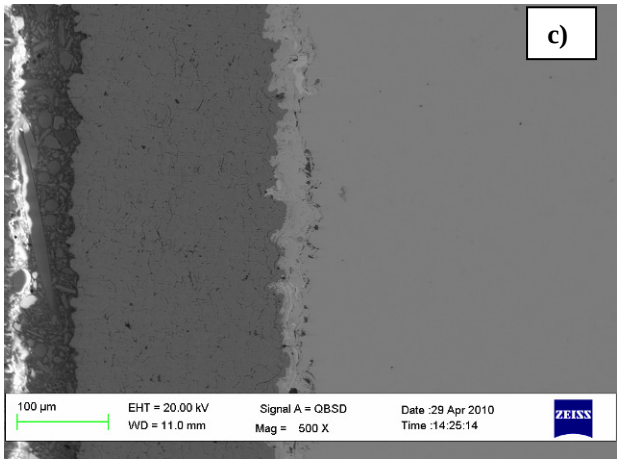

Figure 2: SEM images and microstructural characterization of thermal spray coatings: a) NiCr 80/20, b) WC CoCr 18/4 and c) NiCr 80/20+ Cr_2O_3.

Table 3: Results of thermal spray coatings' characterization.

Coating	Thickness [µm]	Porosity vol.%	Hardness $HV_{0,3}$
NiCr	98±16	6.5	359±18
WCCoCr	105±15	3.45	1027±21
NiCr+Cr_2O_3	(38+187) ± 25	5.5+10.1	(341+1118) ±24

As can be observed, the three types of thermal spray coatings present different thickness and porosity. The porosity, acquired by image analysis, is higher for the coatings deposited by APS technique compared to the HVOF deposits. This difference could be related to both powders size and impact velocity, that is lower in APS technique with respect to HVOF. Indeed, the difference in kinetic energy of the molten powders, that is higher in HVOF technique, leads to a different density on deposited coating. The hardness acquired is associated to the material deposited and the values acquired are similar to data available in scientific literature for thermal spray coatings [1-13].

The SEM micrographs obtained on cross section of Ni/SiC composite coatings previously etched (acetic acid: nitric acid 1:1) are shown in Fig.3. In Tab. 4 are listed the electrodeposited coatings' properties.

Table 4: Results of Ni/SiC electrodeposits characterization.

Coating	Thickness [µm]	SiC wt.%	Hardness $HV_{0,3}$
Ni	78±7	-	172±7
Ni/µSiC	73±8	0.8	247±8
Ni/nSiC	75 ± 5	0.15	270 ±9

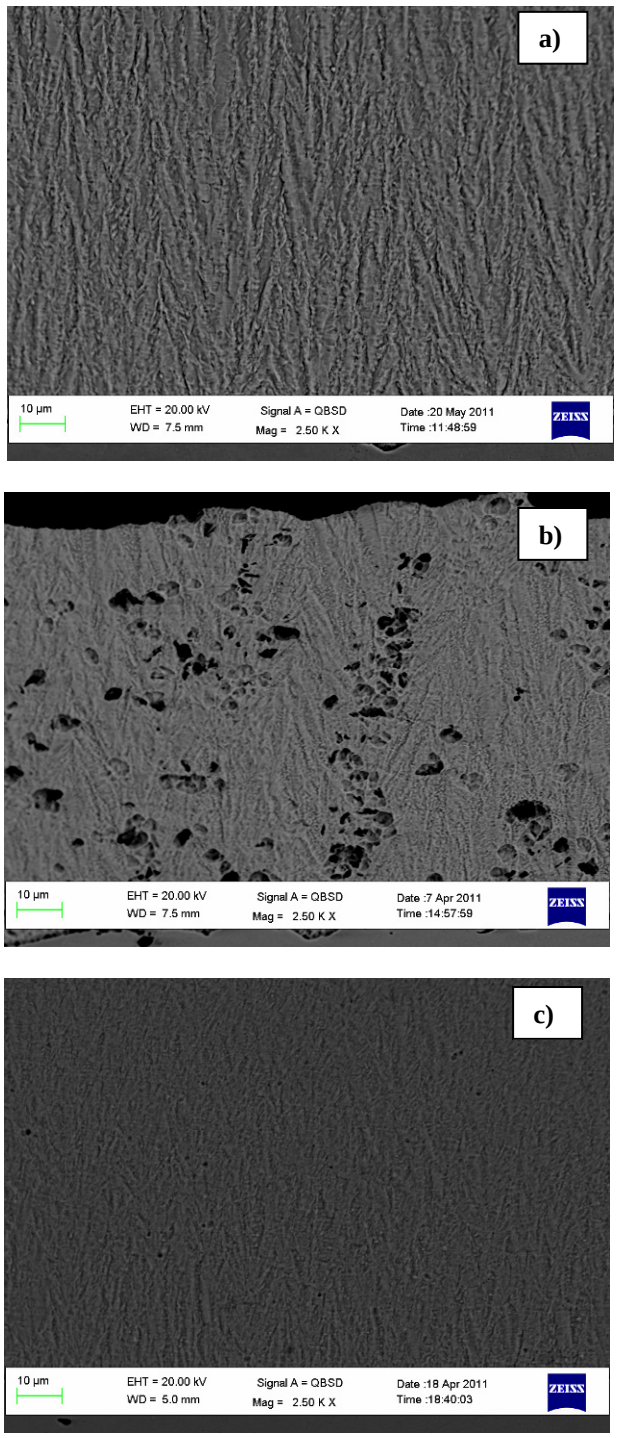

Figure 3: SEM images and microstructural characterization of electrodeposited coatings: a) pure Ni, b) Ni/µSiC and c) Ni/nSiC.

The microstructure of the electrodeposits is columnar. In the case of the pure Ni the metal columns are oriented along the direction of electrical fields. The addition of SiC micro-particles leads to a slight modification of the Ni columns orientation and size. On the other hand, the codeposition of SiC nano-particles leads to the formation of a fine grained deposit in which the Ni columns are not oriented. The addition of micro-particles leads to a microstructure columnar with a slight modification of orientation, caused probably

by the deviation of electrical field in proximity of ceramic particles that are in non-conductive material. On the contrary, the addition of nanoparticles gives a grain refinement and a multi-orientation of columns. The SiC amount is higher in the micro-composite coatings compared to the nano-composite one. The addition of particles leads to a noticeable microhardness increase due to both the presence of the particles and the grain refinement.

All the analysed samples showed a surface Roughness Ra of about 0.5µm, obtained after the surface' grinding.

3.2 Tribological characterization

All the wear tracks obtained for both bare steel, thermal spray and composite electrodeposits at both room temperature and 300°C are shown in Fig. 4-6.

In Fig. 4 the top views of the wear tracks obtained for gr.22 steel are shown, tested at both room temperature and 300°C.

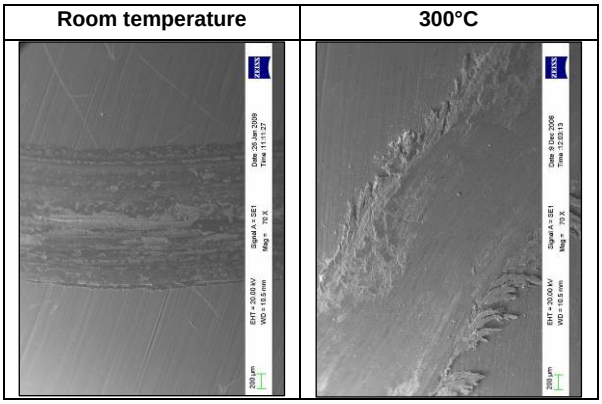

Figure 4: SEM images of the wear tracks obtained for the bare steel at both RT and 300°C.

The steel is subjected to triboxidative wear at both room temperature and 300°C. At room temperature the oxide produced is adherent to metal substrate and very homogeneus. At 300°C the oxide produced is concentrated on the wear track' sides. This phenomenon is related to the loss of mechanical properties of the substrates that permits the countermaterial to destroy the oxide layer, that is thus deposited on the sides of the wear track. At 300°C are highlighted the debris of both oxide and steel along the borders of wear track.

In Fig. 5 the top views of the wear tracks obtained for thermal spray coatings are shown, tested at both room temperature and 300°C.

For the metal matrix deposits the degradation mechanism is a triboxidation at both room temperature and 300°C, which intensity is varying in function of the coating material.

In particular the thermal spray coatings showed also other degradation mechanisms which are related to their microstructure.

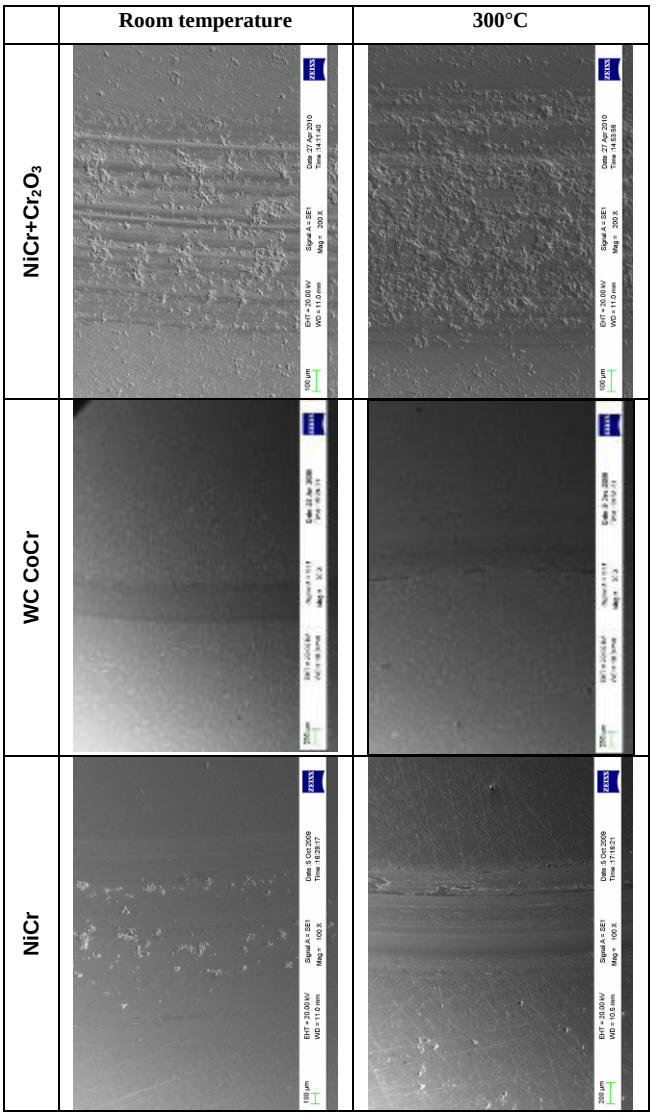

Figure 5: SEM images of the wear tracks obtained for the thermal spray coatings at both RT and 300°C.

The Ni/Cr showed a material detachment originated by contact fatigue phenomenon, aggravated by its porosity. At high temperature tests the detachment is decreased due to a possible hardness decrease of the material which allowed the sealing of porosity, thus reducing the contact fatigue failure. The cermet coatings were all subjected to triboxidation of metal matrix, more intense at high temperature. For the ceramic material (Cr_2O_3) the degradation mechanism at room temperature is similar to the NiCr coating while at high temperature test the degradation becomes more intense. This is caused by a phase change of chromium oxide which enhances the wear ratio and reduces at the same time the friction coefficient [4].

In Fig. 6 are shown the top views of the wear tracks obtained for Ni/SiC electrodeposits tested at both room temperature and 300°C.

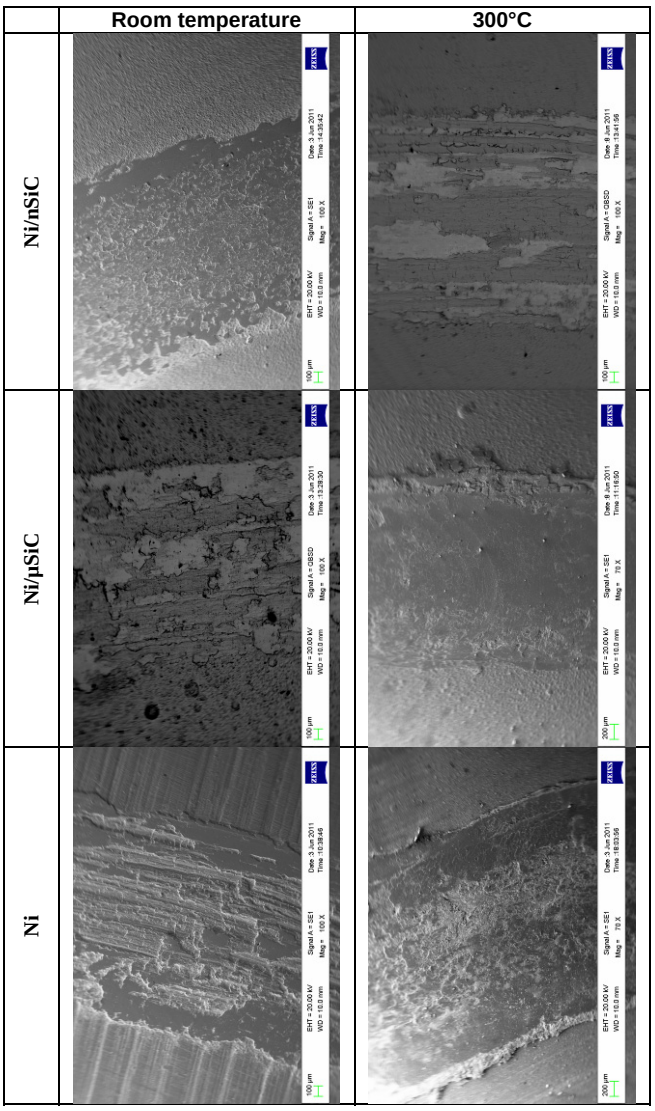

Figure 6: SEM images of the wear tracks obtained for the Ni/SiC deposits at both RT and 300°C.

The Ni electrodeposits showed, at room temperature, a triboxidation with a descaling of oxide which forms a third body between the counter material and the wear track, thus leading to the formation of secondary tracks related to abrasive wear. At high temperature the coatings showed a strong triboxidation. By EDXS analysis on pure Ni coatings, it was detected that during the wear test the steel substrate was reached. For the composite Ni/SiC coatings it seems that the oxide produced is more adherent to steel substrate at high temperature. Probably both the grain refinement and the presence of ceramic particles are linking the oxide to the metal matrix. It seems that some counter-material was transferred to the coating surface, due to a slight adhesion phenomena.

The wear rate of all tested coatings at both room temperature and 300°C are shown in Fig. 7.

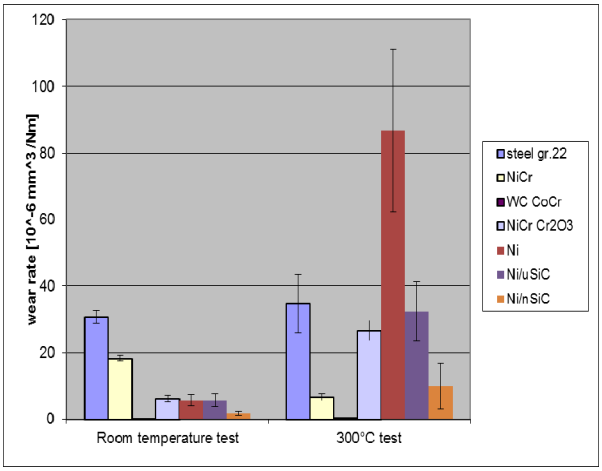

Figure 7: wear rates graph at both room temperature and 300°C for all the coatings tested.

All the coatings protect the steel substrate during the test, except for the pure Ni coating that showed, at 300°C, the highest wear rate. It is possible to observe that the cermet coating has the lowest wear rate compared to the other coatings at both test temperatures. This is related to the high amount of WC which is bonded by a metal matrix that has high oxidation resistance at the test temperatures. For this coating the wear resistance is associated to the carbide component and the particles binding is related to the metal matrix which has a high toughness. On the other hand, the NiCr coating showed a lower wear rate at high temperature tests, compared to the room temperature one, and this could be related to both high oxidation resistance of the material, that contains a high amount of Cr, and to the reduction of material detachment that consequently reduces the abrasive phenomena. The ceramic coating (Cr_2O_3) showed a high wear rate at 300°C tests due to phase change of chromium oxide under tribological contact.

The electrodeposits showed good wear resistance at room temperature, higher for the nano-composite coating. This reduction in wear rate could be related to the grain refinement of microstructure of the metal matrix, which increases also the mechanical properties of the coating. This effect is not visible in the micro-composite coatings because the reinforcement particles are usually detached from the metal matrix leading to intensive abrasive wear caused by hard particle third body contact between counter material and surface of the specimen. At high temperature the mechanical behaviour of the coating is reduced, probably because of the hardness decrease. In this case the pure Ni coating is completely removed while the micro composite coating showed a better wear resistance, compared to the pure Ni one, but the wear rate values were still higher than the thermal spray coatings wear rates. The higher wear

resistance of the nano-composite coating at 300°C is probably related to the higher mechanical properties of the metal matrix compared to the other electrodeposits.

In fig 8-9 the COF (Friction Coefficients of the tested materials) are shown.

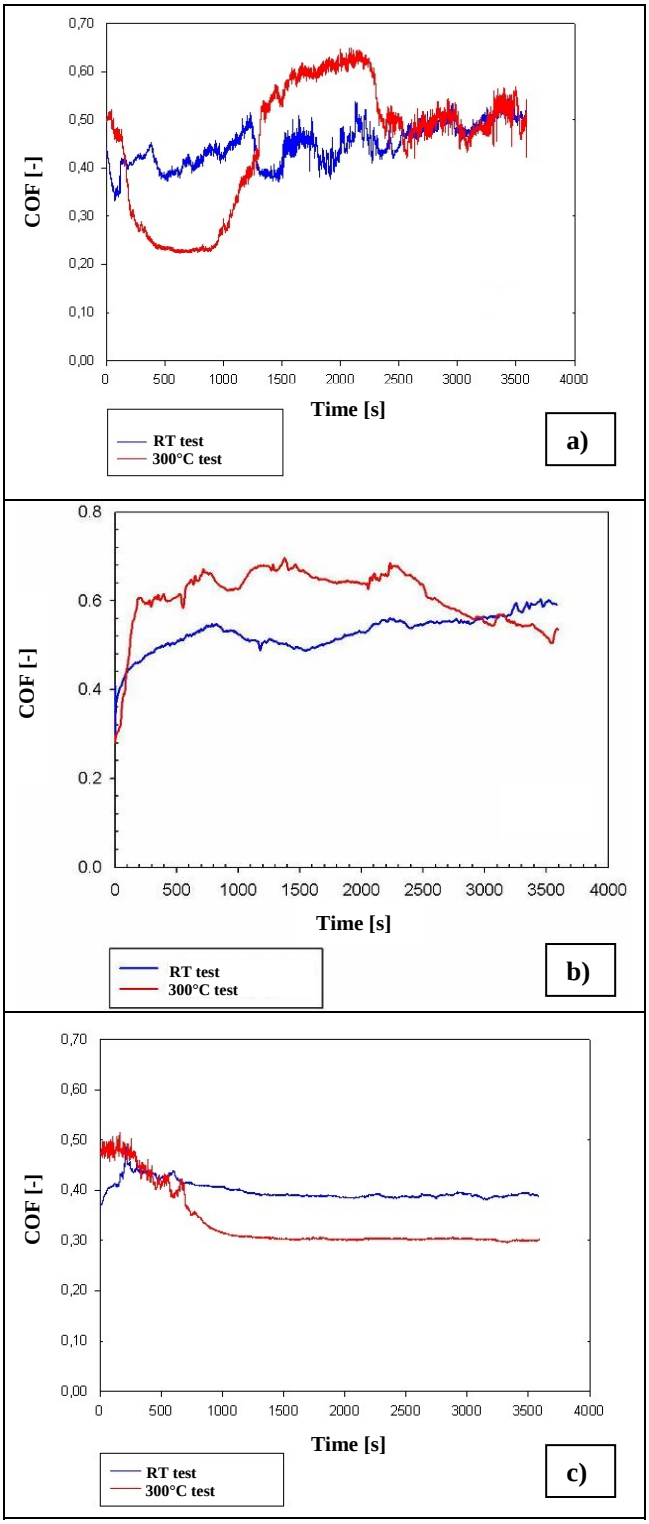

Fig.8: COF graphs at both room temperature and 300°C for the thermal spray coatings: a) NiCr 80/20, b) Wc Co Cr (18/4), c) NiCr 80/20+ Cr_2O_3.

For all the test performed on thermal spray coatings, it is possible to observe that the COF values, at the end of the test, are comparable between the tests performed at different temperature, apart the ceramic coating that showed a lower COF at high temperature due to the change phase of ceramic oxide under hertzian loads. The NiCr coatings showed a noisy COF graph because of the coating material detachment that produced abrasive particles that dissipated more energy, required to move the particles in the hertzian system. At high temperature there is a start at low COF and, at regime, it reached the same values of the test at room temperature. Probably during the start of the test the surface of the sample was covered by a oxide layer produced during the heat up of the system. The presence of oxide decreased the surface energy in proximity of the hertzian contact of the two materials, reducing the friction coefficient. When the oxide was broken the contact between the two materials was between the WC and the Ni/Cr slightly oxidized.

For the WC-CoCr coating the COF are slightly different and this is caused mainly by the number of third body particles produced during the test. Indeed is possible that at high temperature the amount of abrasive particles, that are taking part to the hertzian system, are higher due to the intense triboxidation that cause probably a high amount of descaled oxide. At the end of the test part of the particles are evacuated from the wear track reaching a COF value comparable with the room temperature test.

The COF acquired from the test performed at 300°C is lower compared to the value acquired at room temperature test. This behaviour is related to the change phase of ceramic oxide that decreased the contact energy and thus the COF. The friction coefficient values are higher at the start of the test because of possible partial fragmentation of the material caused by brittle contact between the countermaterial and the coating. This leads to have an high amount of third body particles that increase the COF value, at the beginning, that is decreasing, during the test, because of particle' evacuation form the wear track caused by the relative motion of the two materials.

The COF acquired for the Ni/SiC electrodeposits is lower compared to the pure Ni electrodeposit. This could be related to both different mechanical properties of the composite material respect to the pure Ni and possible interactions of SiC particles with countermaterial that could lower the surface energy and interaction of the 2 surfaces.

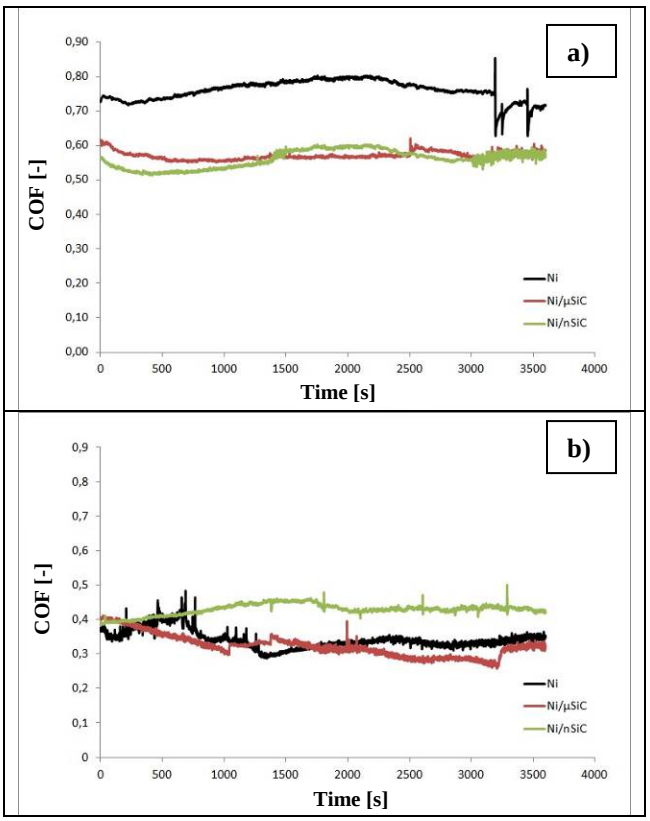

Fig.9: COF graphs at both room temperature and 300°C for the Ni/SiC composite coatings: a) Room temperature test, b) 300°C.

At high temperature the COF graphs are very similar and this behaviour could be related to the change of contact, compared with room temperature test, that is between Ni oxide and the WC sphere, instead of Ni slightly oxidized and WC.

4. CONCLUSIONS

In this work different type of coatings have been analysed deposited either by thermal spray techniques or by electrodeposition. The coatings deposited by thermal spray are: NiCr (APS), WC CoCr (HVOF) and NiCr+Cr_2O_3 (APS). The electrodeposits are Ni/SiC coatings with nano- or micro-sized particles embedded in metal matrix.

The analysed coatings showed different microstructure that depends on both deposited material and deposition technique.

Regarding the wear properties, The steel substrate showed the worst wear resistance at both room temperature and 300°C. This behaviour is related to the low mechanical properties of this steel, that are decreasing as the temperature increases.

All the tested metal matrix coatings underwent triboxidation, that was increased at high temperature test. The triboxidation behaviour depends on metal oxidation resistance. The ceramic coating was subjected to an intensive material detachment, caused mainly by the high interconnected porosity of the thermal sprayed coating. The detachment increased in function of temperature because the ceramic oxide changed phase under the hertzian loads. For all the metal matrix coatings was present a third body abrasion caused mainly by both oxide descaling and ceramic reinforcement detachment from the metal matrix.

Observing the wear rates, the WC CoCr coating showed the highest wear resistance at both room temperature and 300°C. This behaviour is related to the microstructure of the deposit: the reinforcing particles (WC) give high hardness also at high temperature and the metal matrix (CoCr) increases the toughness of the coating and acts as binder for the reinforcing particles. The electrodeposits Ni/nSiC showed a wear behaviour that is comparable with the WC CoCr one. For the nano-composite electrodeposits the synergy of both grain refinement and nano-particles embedding leads to an increase of hardness at both room temperature and 300°C. This effect probably enhances the wear resistance of the Ni metal matrix that is subjected to hertzian loads.

The COF values are strongly dependent on the material analysed but it was observed, for thermal spray coating, similar COF values between the room temperature test and the 300°C tests. The ceramic coating showed the lowest COF values at high temperature caused mainly by the production of brittle CrO_2 phase. The electrodeposits showed some differences in the COF values between the high temperature tests and the room temperature tests caused mainly by the change of hertzian contact from Ni slightly oxidized, at room temperature, to Ni strongly oxidized, at 300°C. At room temperature is visible a different in COF value between pure metal and composite coatings. This effect is related to the different mechanical properties of the coating and the possible interaction of reinforcing particles with the countermaterial in the hertzian contact/motion.

REFERENCES

[1] N.F. Ak, C. Tekmen, I. Ozdemir, H.S. Soykan, E. Celik, *NiCr coatings on stainless steel by HVOF technique*, Surface and coatings technology, Vol. 173-174, pp 1070-1073, 2003.

[2] B.S. Sidhu, D. Puri, S. Prakash, *Mechanical and metallurgical properties of plasma sprayed and laser remelted Ni-20Cr and stellite-6 coatings*, Journal of Materials Processing Technology, Vol. 159, pp 347-355, 2005.

[3] H. Singh, D. Puri, S. Prakash, *Some studies on hot corrosion performance of plasma sprayed coatings*

on Fe-based superalloy, Surface & coatings technology, vol 192, pp 27-38, 2005.

[4] H.S. Ahn, O.K. Kwon, *Tribological behaviour of plasma-sprayed chromium oxide coating*, wear, vol. 225-229, pp814-824, 1999.

[5] G. Bolelli, V. Cannillo, L. Lusvaraghi, T. Manfredini, *wear behaviour of thermally sprayed ceramic oxide coatings*, wear, vol. 261, pp 1298-1315, 2006.

[6] E.M. Leivo, M.S. Vippola, P.P.A. Sorsa, P.M.J. Vuoristo, T.A. Mantyla, *wear and corrosion properties of plasma sprayed Al2O3 and Cr2O3 coatings sealed by aluminum phosphates*, Journal of Thermal spray technology, vol. 6, pp205-210, 1997.

[7] L. Fedrizzi, L. Valentinelli, S. Rossi, S. Segna, *Tribocorrosion behaviour of HVOF cermet coatings*, Corrosion Science, Vol. 49, pp 2781-2799, 2007;

[8] D. Toma, W. Brandl, G. Maringean, *wear and corrosion behavior of thermally sprayed cermet coatings*, Surface and coatings technology, vol.138, pp 149-158, 2001.

[9] L.Fedrizzi, S. Rossi, R. Cristel, P.L. Bonora, *Corrosion and wear behaviour of HVOF cermet coatings used to replace hard chromium*, vol. 49, Electrochimica Acta, pp 2803-2814, 2004;

[10] P.L. Ko, M.F. Robertson, *wear characteristics of electrolytic hard chrome and thermal sprayed WC-10Co-4Cr coatings sliding against Al-Ni bronze in air at 21°C and at -40°C*, wear, vol 252, pp 880-893, 2002.

[11] J.K.N. Murthy, D.S. Rao, B. Venkataraman, *Effect of grinding on the erosion behavior of a WC-Co-Cr coating deposited by HVOF and detonation gun spray process*, wear, vol 249, pp592-600, 2001.

[12] C.W. Lee, J.H. Han, J. Yoon, MC Shin, S.I. Kwun, *A study on powder mixing for high fracture toughness and wear resistance of WC-CO-Cr coatings sprayed by HVOF*, Surface and coatings technology, vol. 204, pp 2223-2229, 2010.

[13] S. Deshpande, A. Kulkarni, S. Sampath, H. Herman, *Application of image analysis for characterization of porosity in thermal spray coatings and correlation with small angle neutron scattering*. Surface and coatings technology, vol. 187, pp 6-16, 2004.

[14] I. Garsia, J. Fransaer, J.P. Celis, *Role of contact frequency on the wear rate of steel in discontinuous sliding contact conditions*, Surface and Coatings technology, vol. 141, pp 171-178, 2001.

[15] A.F. Zimmermann, G. Palumbo, K.T. Aust, U. Erb, *Mechanical properties of Ni silicon carbide nanocomposites*, Material Science and Engineering, Vol A328, pp 137-146, 2002.

[16] A.F. Zimmermann, D.G. Clark, K.T. Aust, U. Erb, *pulse electroideposition of Ni-SiC nanocomposite*, Material Letters, Vol. 52, pp 85-90, 2002.

[17] L. Benea, P.L. Bonora, A. Borello, S. Martelli, F. Wenger, P. Ponthiaux, J. Galland, *Preprataion and investigation of nanostructured SiC-Ni layers by electrodeposition*, Solid State Ionics, Vol. 151 pp 89-95, 2002;

[18] L. Benea, P.L. Bonora, A. Borello, S. Martelli, *wear corrosion properties of nano-structured SiC-Ni composite coatings obtained by electroplating*, Wear, Vol. 249, pp 995-1003, 2002.

[19] M.Lekka, A. Lanzutti, A. Casagrande, C. de Leitenburg, P.L. Bonora, L. Fedrizzi, *Room and high temperature wear behaviour of Ni matrix micro. Nano-SiC composite electrodeposits*, surface and coatings technology, vol. 206, pp 3658-3665, 2012;

[20] M. Lekka, P.L. Bonora, A. Lanzutti, S. Benoni, P. Caoduro, L. Fedrizzi, *Industrialization of Ni-microSiC electrodeposition on copper moulds for steel continuos casting*, metallurgia italiana, vol 6, pp 1-7, 2012;

[21] A. Lanzutti, E. Marin, M. Lekka, P. Chapon, L. Fedrizzi, *Rf-GDOES analysis of composite metal/ceramic electroplated coatings with nano- to microceramic particles' size: issues in plasma sputtering of Ni/micro-SiC coatings.* SIA, vol. 44, pp 48-45, 2012.

[22] K. Holmberg, A. Matthews, Coatings tribology: Properties, Mechanisms, Techniques and Applications in Surface engineering, Elsevier, UK, 2009.

Serbian Tribology Society

SERBIATRIB '13

13th International Conference on Tribology

Faculty of Engineering in Kragujevac

Kragujevac, Serbia, 15 – 17 May 2013

MECHANOCHEMICAL SYNTHESIS OF NANOSIZED MIXED OXIDES

N.G. Kostova[1], M. Kandeva[2], M. Fabian[3], A. Eliyas[1], P. Balaz[3]

[1]Institute of Catalysis, Bulgarian Academy of Sciences, 1113 Sofia, Bulgaria, nkostova@ic.bas.bg

[2]Technical University of Sofia, Sofia, Bulgaria, kandeva@tu-sofia.bg

[3]Institute of Geotechnics, Slovak Academy of Sciences, 043 53 Kosice, Slovakia, balaz@saske.sk

Abstract: *Fe_2O_3-ZnO nanosized mixed oxides samples were successfully synthesized using a simple mechanochemical method. The composites were characterized by X-ray diffraction (XRD), Fourier transform infrared, and UV-visible diffuse reflectance spectroscopies The pattern of XRD shows broadening in the diffraction peaks, indicating a decrease in the particle size of the samples with milling time.*

Keywords: *nanotribology, mechanochemistry, ball-milling, X-ray diffraction*

1. INTRODUCTION

The mixed oxides find application catalysts and support for catalysts, batteries, magnetic materials and gas sensors [1, 2]. The mixed metals oxides are used in the chemical and pharmaceutical industry. The catalytic activity of mixed oxide systems is usually higher than that of the individual oxide components. The research work is aimed at achieving the maximal efficiency. In order to achieve this aim two strategies are applied in general: modification of the method of preparation and addition of dopants. The mixed oxides are usually obtained in the form of powders and these represent a substantial part of the industrial catalysts due to their low price, easiness of regeneration and their selective action. They are prepared by the sol-gel method [3], solid state reaction method [4], co-precipitation [5], citric acid method [6], solution-combustion method [7-8], thermal decomposition method [9], mechanochemical processing [10-12], gas-phase flame synthesis and aerogel method [13]. Mechanochemical processing is a method for production of nanosized materials [11]. Its main advantage is the option to synthesize nanopowders at low temperatures by a simple one-step procedure of milling. Mechanochemistry is generally performed in high-energy ball mills using powder reactant mixtures. In this work we report on Fe2O3-Zno mixed oxides formation during milling in a planetary ball mill.

2. EXPERIMENTAL

Mechanochemical synthesis of Fe_2O_3-ZnO mixed oxides was performed in a laboratory planetary mill Pulverisette 6 (Fritsch, Germany) by high-energy milling of hematite and ZnO. The following experimental conditions were applied for the mechanochemical synthesis: loading of the mill, 50 balls of 10 mm in diameter; material of milling chamber and balls was tungsten carbide; volume of milling chamber, 250 ml; room temperature; rotational speed of the mill planet carrier 400 min^{-1}; milling time, 20 min.

X-ray powder diffraction patterns (XRD) of the samples were registered at room temperature with a TUR M62 apparatus with PC management and data accumulation, using HZG-4 goniometer with CoK_α radiation. The XRD lines were identified by comparing the measured patterns to the JCPDS data cards.

Specific surface area was determined by the low temperature nitrogen adsorption method in a Gemini 2360 sorption apparatus (Micromeritics, USA).

The phase evolution during high energy ball milling was followed by Nicolet 6700 FTIR spectrometer (thermo Electron Corporation, USA).

The method of dilution of the studied sample in KBr at concentration 0.5 % was used.

The diffuse reflectance UV–vis spectra were taken with a Thermo Evolution 300 UV-Vis Spectrophotometer equipped with a Praying Mantis device with Spectralon as the reference. Spectralon is a fluoropolymer, which has the highest diffuse reflectance of any known material or coating over the ultraviolet, visible, and near-infrared regions of the spectrum.

3. RESULTS AND DISCUSSION

Textural properties of initial hematite and rutile and mechanochemically synthesized mixed oxides are presented in Table 1.

Table 1. Samples composition and textural properties

Sample code	Chemical composition [%]		Specific surface area, m^2g^{-1}	Pore volume
	Fe_2O_3	ZnO		
ZnO	0.0	100.0	5.5	0.004
ZnO-MA	0.0	100.0	3.0	0.002
0.3 FZ	0.3	99.7	5.3	0.004
4.3 FZ	4.3	95.7	5.4	0.004
14.3 FZn	14.3	85.7	5.3	0.004
66 FZ	66.0	33.0	6.6	0.005

The XRD patterns of the Fe_2O_3-ZnO mixed oxides with different iron content are presented in Fig. 1.

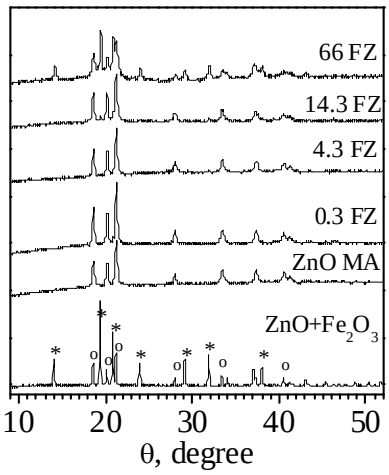

Figure 1. XRD patterns of the Fe_2O_3-ZnO sample. The mark (*) indicated the peaks corresponding to Fe_2O_3, and the marks (o) – peaks corresponding to ZnO.

The XRD diagram marks as ZnO+Fe_2O_3 corresponds to the starting mixture with molar ratio ZnO:Fe_2O_3 = 1:1 before milling. All the diffraction peaks of mechanical activated zinc oxide and 0.3 FZ sample can be well indexed to the hexagonal phase ZnO (JCPDS card no. 36-1451. A decrease in the reflection intensity was observed during milling. As milling proceeds broadening of diffraction peaks is observed due to grain size reduction.

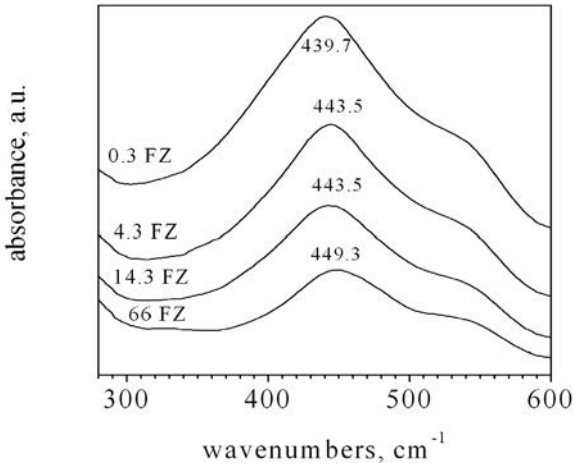

Figure 2. FTIR spectra of the Fe_2O_3-ZnO mixed oxides

Figure 2 shows the IFTR spectra the mechanically activated Fe_2O_3-ZnO mixed oxides. All the samples show prominent absorption band and shoulder at about 440 cm-1 and 550 cm^{-1}, respectively. Slight variation with increasing of iron content in the samples is due to grain size influence the band position. The band at lower frequency of 440 cm-1 corresponds to M-O stretching vibration in octahedral site. This shift can be result of higher content of oxygen vacancies present in the structure and created during mechanical activation [14].

The diffuse reflectance of the ZnO and Fe_2O_3-ZnO mixed oxides are shown in Fig. 3. The spectra of the samples in UV region exhibit an absorption peak at about 220-250 nm attributable to isolated, tetrahedral coordinated species.

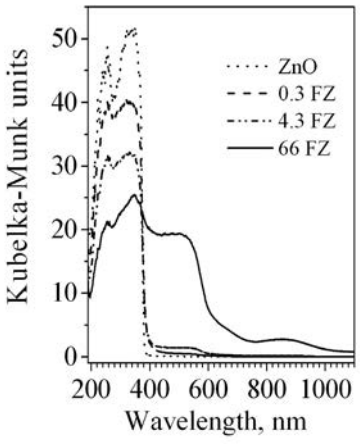

Figure 3. UV-vis diffuse reflectance spectra of ZnO and Fe_2O_3-ZnO mixed oxides

The samples with larger iron content show intense absorption in wide wavelength range from UV to visible light with absorption tail extending into infrared region. This means that Fe component was physically connected to the external surface of ZnO structure. The peak with maximum centred at

about 260 nm is related to isolated Fe^{3+} cations, while the second band at about 350 nm corresponds to small oligonuclear $(FeO)_n$ species. At higher iron content the peak around 520 nm is observed indicating the presence of iron oxide particles.

This peak can be assigned to symmetrical and spin forbidden d-d transitions of Fe^{3+} [15]. When the sample contains small iron content (sample 0.3 FZ), the band slightly shifts to the right without tail broadening. This means that the Fe component was well inserted inter the framework of the ZnO structure.

In a ball mill intense mixing takes place and reactants are brought into intimate contact with each other. Grinding reduces the particle size and increases the surface area available for reaction. New reactive surfaces are exposed during particle fracture and the introduction of dislocations increases the surface reactivity. At the point of contact between two grinding balls during a collision event, a highly localised triboplasma is formed giving energy for chemical reactions to occur.

ACKNOWLEDGEMENT

This investigation was financially supported by the National Science Fund of Bulgaria (project DNTS/Slovakia 01/3), by the Slovak Research and Development Agency (project APVV-0189-10), and through a bilateral project between Bulgarian Academy of Sciences and Slovak Academy of Sciences.

REFERENCES

[1] I.E. Wachs, K. Routray: *Catalysis science of bulk mixed oxides ACS Catalysis Vol. 2, No. 6, pp. 1235-1246, 2012.*

[2] M.V. Reddy, G.V. Subba, B.V.R. Chowdari: *Metal oxides and oxisalds as anode materials for Li ion batteries,* Chem. Rev. DOI: 10.1021/cr 3001884, 2013.

[3] B. Palanisamy, C.M. Babu, B. Sundaravel, S. Anandan, V. Murugesan: *Sol-gel synthesis of mixed Fe_2O_3/TiO_2 photocatalyst: Application for degradation of 4-chlorophenol*, J. Hazard. Mater., Vol. 252-253, pp. 233-242, 2013.

[4] S. Martha, K.H. Reddy, N. Biswal, K. Parida: *Facile synthesis of InGaZn mixed oxide nanorods for enhanced hydrogen production under visible light*, Dalton Trans. Vol. 41, pp. 14107-14116, 2012.

[5] K-T. Li, L-D. Tsai, C-H. Wu, I. Wang: *Lactic acid esterification on titania-silica binary oxides*, Ind. Eng. Chem. Res. Vol. 52, No. 13, pp. 4734-4739, 2013.

[6] H. Zhou, P. Hu, Z. Huang, F. Qin, W. Shen, H. Xu: *Preparation of NiCe mixed oxides for catalytic decomposition of N_2O*, Ind. Eng. Chem. Res. Vol. 52, No. 12, pp. 4504-4509, 2013.

[7] G.K. Pradhan, S.Martha, K.M. Parida: *Synthesis of multifunctional nanostructured zinc-iron mixed oxide photocatalysts by a simple solution-combustion technique*, Appl. Mater. Interface, Vol. 4, No. 2, pp. 707-713, 2012.

[8] G. Lauramoy, R. Carbonio, E.L. Moyano: Mixed oxides as highly selective catalysts for the *flash pyrolysis of phenacyl benzotriazole: One-pot synthesis of dibenzazepin-7-one*, ACS Catal DOI: 10.1021/cs3008335, April 3, 2013.

[9] S.M.A. Shibli, J.N. Sebeelamol: *Development of Fe_2O_3-TiO_2 mixed oxide incorporated Ni-P coating for electrocatalytic hydrogen evolution reaction*, Intern. J. Hydrogen Energy, Vol. 38, pp. 2271-2282, 2012.

[10] P. Balaz, M. Achimovicova, M. Balaz, P. Billik, Z. Cherkezova-Zheleva, J.M. Criado, F. Delogu, E. Dutkova, E. Gaffet, F.J. Gotor, R. Kumar, I. Mitov, T. Rojac, M. Senna, A. Streletskii, K. Wieczorek-Ciurowa: *Hallmarks of mechanochemistry:from nanoparticles to technology*, Chem. Soc. Rev., DOI: 10.1039/c3cs35468g, pp. 1-67, 2013.

[11] P. Balaz: *Mechanochemistry in Nanoscience and Mineral Engineering*, Springer-Verlag, Berlin Heidelberg, 2008.

[12] A.M. Al-Saie, A. Al-Shater, S. Arekat, A. Jaffar, M. Bououdina: *Effect of annealing of the structure and magnetic properties of mechanically milled TiO_2-Fe_2O_3 mixture*, Ceramics International, Vo. 39, pp. 3803-3808, 2013.

[13] K.M. Shrestha, C.M. Sorensen, K.J. Klabunde: *MgO-TiO_2 mixed oxide nanoparticles: Comparison of flame synthesis versus aerogel method; characterization and photocatalytic activitie*s, Journal of Materials Research Vol. 28, No, 3, pp. 431-439, 2013.

[14] M. Fabian, A. Eliyas, N.G. Kostova, J. Brianchn, P. Balaz: *Photocatalytic activity of nanocrystalline ghanite ($ZnAl_2O_4$) synthesized by ball milling, Micro and Nano Technology,* Proceedings of International Multidisciplinary scientific geoconference SGEM 2012, 17-23 June 2012, Albena, BulgariaBulgaria, Vol. III, pp. 391-497, ISSN: 1314-1314-2704.

[15] Y. Wang, Q. Zhang, T. Shishido, T. Takehira: *Characterization of iron-containing MCM-41 and its catalytic properties*, J. Catal. Vol. 209, pp. 186-196, 2002.

Serbian Tribology Society

SERBIATRIB '13

13th International Conference on Tribology

Faculty of Engineering in Kragujevac

Kragujevac, Serbia, 15 – 17 May 2013

WEAR OF POLISHED STEEL SURFACES IN DRY FRICTION LINEAR CONTACT ON POLIMER COMPOSITES WITH GLASS FIBRES

Dorin Rus[1] Lucian Capitanu[2]

[1] Mechanical Departament, Institute of Civil Engineering, 59 Plevnei Way, 050141, Bucharest, Romania, e-dorinrus@gmail.com

[2*] Institute of Solid Mechanics of the Romanian Academy, 15 Constantin Mille, 010141, Bucharest, Romania luciancapitanu@yahoo.com

Abstract: *It is generally known that the friction and wear between polymers and polished steel surfaces has a special character, the behaviour to friction and wear of a certain polymer might not be valid for a different polymer, moreover in dry friction conditions. In this paper, we study the reaction to wear of certain polymers with short glass fibres on different steel surfaces, considering the linear friction contact, observing the friction influence over the metallic surfaces wear. The paper includes also its analysis over the steel's wear from different points of view: the reinforcement content influence and tribological parameters (load, contact pressure, sliding speed, contact temperature, etc.). Thus, we present our findings related to the fact that the abrasive component of the friction force is more significant than the adhesive component, which generally is specific to the polymers' friction. Our detections also state that, in the case of the polyamide with 30% glass fibres, the steel surface linear wear rate order are of 10^{-4} mm/h, respectively the order of volumetric wear rate is of 10^{-6} cm^3 /h. The resulting volumetric wear coefficients are of the order (10^{-11} – 10^{-12}) cm^3/cm and respectively linear wear coefficients of 10^{-9} mm/cm.*

Keywords: *wear, composite thermoplastics, comparative wearing coefficient.*

1. INTRODUCTION

The tribological behaviour of polymers has distinctive characteristics, some of them being described by Bowden and Tabor [1]. The main concept related to the polymers' tribology is composed of three basic elements involved in friction: (i) junctions adhesion, their type and resistance; (ii) materials' shearing and fracture through friction during the contact; and (iii) the real contact area.

Friction's straining component results from the polymer's resistance to "ploughing" made by the asperities existing on the harder counter-face. The polymer's surface asperities bear elastic, plastic and viscous-elastic strains, according to the material's properties. Friction adhesion component comes out of the adhesion junctions formed on the real contact spots between the paired surfaces. Friction adhesion component in what the polymers are concerned is considered to be much greater than the straining component. Special attention should be granted to the transfer films, these transfer films being the key factors determining the tribological behaviour of polymers and polymeric composites. In what the glass fibers reinforced polymer is concerned, we also encounter a strong abrasive component [2].

Several models were developed to describe the contact adhesion. The Johnson-Kendall-Roberts (JKR) model, mentioned sometimes as the contact mechanics model [3-4] and the Derjaguin-Muller-Toporov (DMT) model [5] are the best known. The models' comparative analysis [6] shows that the JKR model is applied to bodies with micrometric dimensions and larger than that, with polymer properties, whilst the DMT model is valid for bodies with nanometer dimensions, with metal properties.

Several authors [7-17] studied the polymers' friction on hard surfaces. By using the method of

contact's conformity [18] they obtain the hardness, the deformability value (index) (which describes the coarse surfaces' deformation properties), as well as the elasticity module for organic polymers polymethylmethacrylate – PMMA; polystyrene – PS; polycarbonate – PC, ultra high molecular weight polyethylene – UHMWPE. We also describe the dependence of the imposed penetration depth, the maximum load and the straining speed, the hardness and the elastic modulus [18-22]. The typical penetrating depths are included within the approximate 10 nm to 10 μm range, whilst the applied loads are smaller than 300 mN.

We can observe the fact that almost without exception, the ploughing is accompanied by adhesion and in certain conditions it may lead to micro-cutting, which represents a supplementary adding to increase the friction force.

There are other mechanisms to dissipate the energy while straining. For instance, whenever a polymer with viscous-elastic reaction slides on a hard surface, the energy dissipation is caused by the high losses through hysteresis. This straining component is known under the name of friction due to elastic hysteresis [1]. The energy can, as well, be transported further, for instance through elastic waves generated at the interface and coming out at infinit, as, a nucleation and micro-cracks development within the material, consequence [20].

The mechanical component consists in the resistance of the softer material to harder asperities' ploughing. The adhesion component comes of the adhesion links formed between the surfaces during the friction contact. We believe that for polymers the adhesion molecular component exceeds by far the mechanical one [20], and we can explain it through the generated films' transfer on the metal counter-face. The following factors considerably affect the friction force: the contact load, sliding speed and temperature. The effects are not independent. For instance, according to the contact load and contact speed, the temperature may considerably vary, changing the friction mode [21].

2. MATERIALS AND METHODS

In order to study the metallic counter-part's wear in dry contact with glass fibres reinforced plastic materials we use Timken type friction couples (with linear contact), cylinder on plan, which allows us to attain high contact pressures, hence high contact temperatures. In this manner we notice, whether and in which conditions the plastic material transfer on the metallic surface appears, as well as the influence of the glass fibres filling during this phenomenon, and its effect on the surface's wear. As we do not follow the polymer's wear, but only the polymer's friction influence, over the samples' metallic surfaces wear, we use the unidirectional sliding movement.

We perform the tests using experimental equipment containing a Timken type linear contact friction couple, continuously controlling the normal and friction loads, and contact temperature. The unidirectional movement and the linear contact allow us to attain very high contact pressures and temperatures. We build the friction couple out of a plastic cylinder Nylonplast AVE polyamide + 30% glass fibres, which rotates at different speeds against the polished surface of a steel plan disk. The cylinder has an outer diameter of 22.5 mm and 10 mm height.

We choose as sample steel disks with 18.2 mm diameter and 3 mm thickness. We polish the disks' surfaces successively using sandpaper of different granulations (200, 400, 600 and 800) and, finally, we polish them on the felt with diamond paste. We obtain mirror polished surfaces, with roughness R_a of 0.05 μm. This metal surface's quality allows us to eliminate the influence of the metallic surface's state on the friction coefficient's evolution and visualization, to make measurements using optical microscopy and to accurately record the wear traces appeared on the metallic surfaces.

Fig.1 shows the friction couple (a) and its installation within the experimental equipment (b).

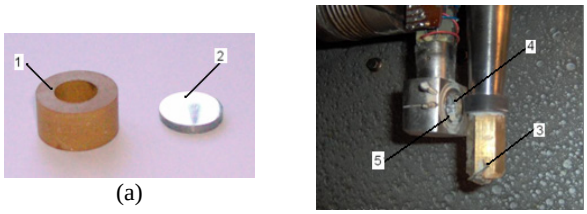

(a) (b)

Figure 1. Friction couple (a) and its installation in the experimental equipment (b), where 1 - cylindrical liner; 2 – steel disk sample; 3 – nut; 4 – hole; 5 - knife-edge.

The friction couple is build out of a cylindrical liner (1) and a plane disk type sample (2). The liner is fixed with the help of a nut (3) on the driving shaft (4), and the disk sample is placed in a special hole made within the elastic blade (5). We build the sample disk base in such a manner so that the base allows the sample to make small rotations around the edge of a knife fixed in the sample's bezel, perpendicularly on the driving arbour. In this way we ensure a uniform repartition of the load on the entire linear contact between the liner and steel sample, even if there are small building or assembling imperfections. An electric engine puts the shaft into a rotation movement using trapezoidal transmission belts.

The experimental device allows us to simultaneously measure the normal and tangential

(friction) efforts through resistive converter strain-gauges, assembled on the elastic blade (5). The use of a pair of converters strain-gauges connected within the circuits of two strain-gauges bridges, offers us the possibility to make simultaneous measurements, while separately, gives us the possibility to measure the normal and friction forces. We apply the normal load to the elastic blade, through a calibrated spring system. The installation allows us to register the friction force on an X-Y recorder. We control the tests' duration through an alarm clock and we measure the contact temperature with the help of a miniature thermocouple, connected to a millivoltmeter calibrated in ^{0}C.

I used the uni-directional testing because the purpose of investigations was the study of metallic surface wear. We perform the tests, based on Hooke's law, at normal loadings of 10; 20; 30; 40 and 50 N, loadings which are adequate to some contact pressures all calculated considering the elastic contact hypothesis, that is: 16.3; 23.5; 28.2; 32.6 and 36.4 MPa (for Nylonplast AVE polyamide with 30% glass fibres) respectively, we use sliding speeds, adequate to the diameter of the plastic composite sample, which are: 0.1856; 0.2785; 0.3713; 0.4641; 0.5570; 1.114 and 1.5357 m/s, and which resulted as a consequence of electric motor's speed and the belt pulleys' primitive diameters.

As we know [21], we may characterize a material's wearing coefficient (percentage) by wearing factor *k*. Archard's relation defines this factor:

$$V_u = kNvt \tag{1}$$

where: V_u – the wear's material volume; N - the test load; v - the sliding speed; t - the test period; k – volumetric wearing factor.
By dividing both of this relation's terms (4) by nominal contact area A, we obtain:

$$V_u / A = kNvt / A \tag{2}$$

Which means that:

$$h_u = k^* pvt \tag{3}$$

where: h_u - wear's material depth; p - the pressure on the nominal contact area and k^* is the linear wearing factor. Relation (6) expresses a general law of the wear as a function of the contact pressure p and the length of the wearing path, so that $L_f = vt$.

We could then write:

$$k = V_u / Nvt = V_u / NL_f \tag{4}$$

respectively:

$$k^* = h_u / pvt = h_u / pL_f \tag{5}$$

Considering the large area of the load (N) or pressure (p) and the relative speed values used during tests in order to evaluate the wearing reaction of the metallic counter-pieces amid the frictional couples, we use comparative wear coefficients K and K^*, defined by:

$$K = V_u / L_f = kN \ \ (\text{cm}^3 / \text{cm}) \tag{6}$$

and:

$$K^* = h_u / L_f = k^* p \ \ (\text{cm} / \text{cm}) \tag{7}$$

We consider these wearing coefficients with respect to the period in which the frictional couple functions at different sliding speeds, under certain loading conditions (contact pressure).

The main objectives of these tests are the determination of the volume of material removed by wearing, the mean depth of the wearied layers, the frictional factors and coefficients, for different loading conditions.

Coefficients k and k^* are coefficients of the wear process, while the comparative factors K and K^* are coefficients of this process's consequences, that is, the amount of resulted wear and reported to the length of the friction pathway. They can be qualitatively expressed in units of wear volume on a measure of the length of the friction pathway (cm^3 / cm), as wear's depth on a measure of the length of the friction pathway (cm / cm) or as wear's weight on a measure of the length of the sliding friction pathway (mg / cm). Coefficients K and K^* have no mathematical implication (can not simplify).

Using the procedure described in [22], at the end we obtain the mean depth (8) and the volume of worn metallic material (9):

$$h = \left(l^2 / 8r_1\right) - 0{,}527N\left(E_1 + E_2\right)LE_1E_2 \tag{8}$$

and:

$$V_u = \sum_{i=1}^{n}\left(S_i q_i\right) = 0.351\left(E_1 + E_2\right)Nl_m / E_1E_2 \tag{9}$$

where l_m is the mean width of the wear imprint.

Practically, we have to measure the width of wear imprints in three points established before, computing then the mean value of this width. With this value we can obtain the volume of worn metallic material V_u and the removed layer's mean depth h_mu.

We study the wearing of the friction couple's metallic component on linear contact Timken machinery, see Fig. 1. Almost all tests are made without lubricating the frictional surfaces, but there are also tests with micro-lubricating.

In order to calculate the metallic component's wear, we use the method described above. The equations (8) and (9) take into consideration, for the studied materials, particular forms obtained by introducing the interfering parameters numerical values, thus obtaining for a mean depth h_{mu} and a worn material volume V_u the following relations:

– Nylonplast AVE polyamide + 30% glass fibres / steel:

$$h_{mu} = l_m^2 8r_1 - 6.94 \cdot 10^{-5} N \text{ (mm)} \quad (10)$$

$$V_u = 4.55 \cdot 10^{-4} N l_m (\text{mm}^3) \quad (11)$$

The studies concerning the metallic semi-couple wear are generally based on the elastic contact hypothesis. For these plane half-couple the values for the equivalent elasticity module for Nylonplast AVE polyamide + 30% glass fibres, E = 20.25 MPa. Assuming that the plastic liner does not crush, we impose the condition $p_{max} < 0.5H$, where H stands for the Brinell hardness. The required condition allows us to establish the following values of the maximum loadings (contact pressure) of the couple:

p_1 = 16.3 MPa; p_2 = 23.5 MPa; p_3 = 28.2 MPa; p_4 = 32.6 MPa; p_5 = 36.4 Mpa.

We perform the experimental tests considering broader domains to vary the relative speed and normal loadings, or contact pressures. We use couples with liner made from thermoplastic material with linear contact on a steel surface (C120, Rp3, a.s.o.).

3. RESULTS

Table 1 is the representation of the experimental tests results, testing two friction couples, for one of the 8 different relative sliding speeds used. Table 1 represents the results of the tribological experimental tests, e.g. the mean values of the wear imprint depth h_u (10^{-4} mm), and the average values of the worn material volume V_u (10^{-6} cm^3). The average width l_m represents the arithmetical average calculated based upon 3 measured values of the wear trace's width. By dividing h_u and V_u to the duration of experimental test, we obtain the values of the wear rate in terms of depth h_{mu}(10^{-4} mm/h) and volume V_{mu}(10^{-6} cm^3/h).

Based upon the methodology described above, we process the results obtaining the variation curves of the wear with normal loading and relative speed, presented in Fig. 2 (a) and (b), for two of the tested couples, Nyloplast AVE Polyamide + 30% glass fibres / C120 steel, and respectively Nyloplast AVE Polyamide + 30% glass fibres / Rp 3 steel.

Table 1. The results of the experimental tests performed in order to determine the wear rate of metallic component. Frictional couple: Polyamide Nylonplast AVE +30% glass fibres / C120; v = 18.56 cm/s.

		Average wear rate	
N (N))	t (hour)	h_{mu} (10^{-4} mm/h)	V_{mu} (10^{-6} cm^3 /h)
10	1		
10	1	0.9649	0.1387
20	1		
20	1	2.4798	0.4404
30	1		
30	1	4.0336	0.8381
40	1		
40	1	5.4874	1.3086
50	1		
50	1	7,1635	1.8667

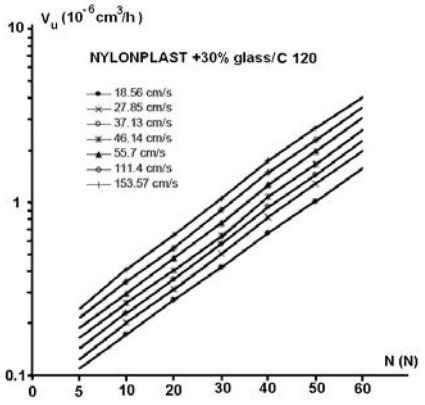

(a)

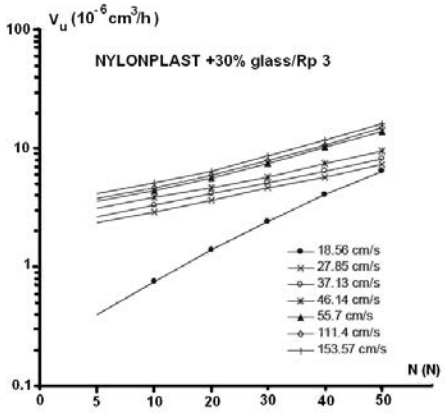

(b)

Figure 2. The results of variation curves of the wear volume with normal loading and relative speed, for tested couples (a) Nyloplast AVE Polyamide + 30% glass fibres/ C120 steel and (b) Nyloplast AVE Polyamide + 30% glass fibres/ Rp 3 steel. Measurement errors were ±1.5 %.

These curves characterize only the tested frictional couples (one combination of materials). Furthermore, we can make the comparative evaluation of different couples only qualitatively.

Thus, using relations (8) and (9) we obtain the variation curves of the "comparative wear coefficients" (as volume and depth), K (cm^3 / cm) and K^* (mm / cm). These master-curves are plotted in Fig. 3 and Fig. 4 representing the two tested and

taken into discussion couples, for different normal loading values.

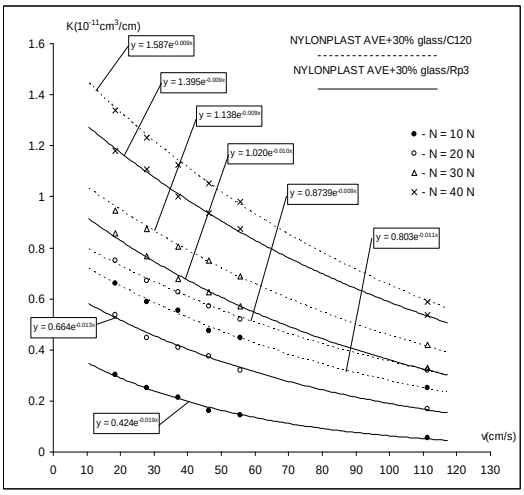

Figure 3. The variation curves of the volumetric comparative wear coefficients K (cm^3 / cm).

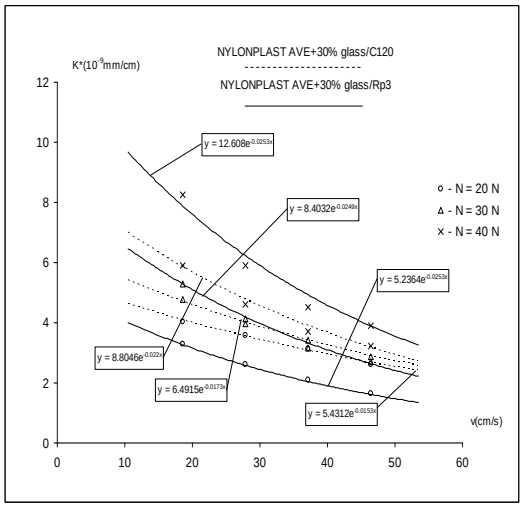

Figure 4 The variation curves of the linear comparative wear coefficients K^* (mm / cm).

In Table 2 are listed the equations for the comparative wear coefficients (the volumetric and the depth ones), for C120 and in Table 3. for Rp3 steel.

Table 2. The variation curve of compatative wear corfficient equations for Nylonplast AVE Polyamide + 30% glass fibres/C120

Load (N)	K	K^*
10	$K = 0.8030\ e^{-0,0110\ v}$	
20	$K = 0,8739\ e^{-0,0090\ v}$	$K^* = 5,4312\ e^{-0,0153\ v}$
30	$K = 1.1380\ e^{-0,0090\ v}$	$K^* = 6,4915\ e^{-0,0173\ v}$
40	$K = 1.5870\ e^{-0,0090\ v}$	$K^* = 8,8046\ e^{-0,0200\ v}$

Table 3. The variation curve of compatative wear corfficient equations for Nylonplast AVE Polyamide + 30% glass fibres / Rp3

Load (N)	K	K^*
10	$K = 0.4240\ e^{-0,0190v}$	
20	$K = 0,6640\ e^{-0,0130\ v}$	$K^* = 5,2346\ e^{-0,0253\ v}$
30	$K = 1.0200\ e^{-0,0100\ v}$	$K^* = 8,4032\ e^{-0,0249\ v}$
40	$K = 1.3950\ e^{-0,0090\ v}$	$K^* = 12,6080\ e^{-0,0253\ v}$

While measuring the wear traces widths with the help of optical microscopy, we also take microphotographs, in order to identify the plastic material's transfer and the metallic surfaces' wear mechanisms. These microphotographs prove that the wear mechanisms vary from one couple to another, due to surfaces' nature: metallic and composite plastic material, especially their hardness (59 HRC for C120 hardened steel and 62 HRC for Rp3 hardened steel), the glass fibres content, 30% and 20%, the composite plastic materials' elasto-plastic characteristics while in contact with metallic surfaces. he glass-fibres torn from the polymer matrix.

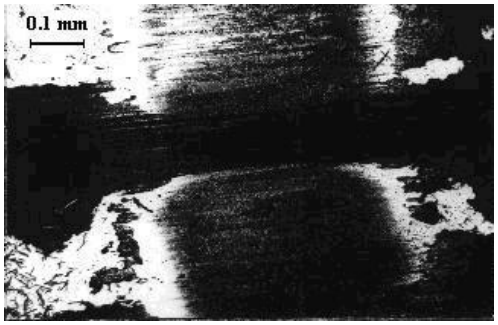

(a)

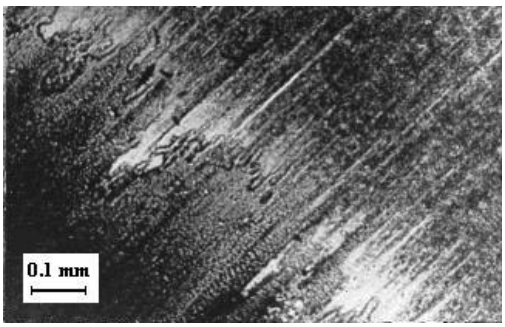

(b)

Figure 5. Wear and plastic material transfer on C120 steel surface, following the friction with Nylonplast AVE polyamide reinforced with 30% fine glass fibres (a), in experimental conditions: v = 27,85 cm/s; N =20 N; T = 150 ^{0}C; t = 60 min and (b) in experimental conditions v = 27,85 cm/s; N =30 N; T = 175 ^{0}C; t = 60 min.

Considering the same loading conditions, the two couples to which we make reference have a different behaviour. On C120 steel sample (Fig. 5), at a normal load of 20 N and a contact temperature of 150 ^{0}C, there are plastic material transfer bridges, broadways on the wear traces (Fig. 5a), as well as the glass-fibres torn from the polymer matrix. At 175 ^{0}C contact temperature, corresponding to a normal load of 30 N and a contact pressure of 2879.5 MPa, the plastic material transfer on the wear trace's edge is obvious (Fig. 5b), leaving the impression that the plastic matrix melts and drips off on the wear trace's exit edge.

Considering the same mechanical stress conditions (load and relative speed), the

microscopic inspection of the Rp3 steel samples, while in friction contact, with the same composite plastic material, reveals a less pronounced plastic material transfer through adherence onto the metallic surface, visible on the left side in Figs 6 (a) and 6 (b), and if the test duration is double (120 min), practically there is no plastic material transfer as one can see in Fig 6 (c).

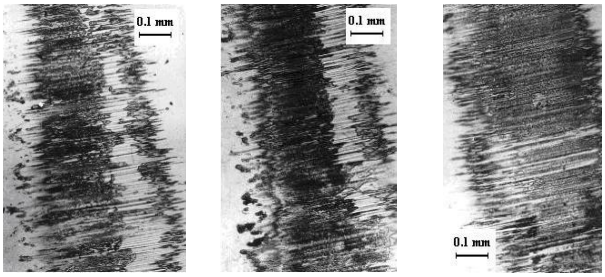

(a) v= 27,85 cm/s; N = 40 N; t = 60 min; T=217 ^{0}C

(b) v = 27,85 cm/s N = 30 N; t = 120 min; T= 175 ^{0}C

(c) v = 27,85 cm/s; N = 40 N; t = 120 min; T =237 ^{0}C

Figure 6. Wear and plastic material transfer on Rp3 steel surface, following the friction with Nylonplast AVE polyamide reinforced with 30% short glass fibres.

We consider that due to high registered contact temperature (237 ^{0}C) the transfer takes place for sure, but the transferred material is subsequently removed through friction from the contact area, under the form of wear particles following the glass fibres abrasive action. After this stage, the abrasive wear due to glass fibres becomes predominant.

It is possible that the less pronounced plastic material transfer emphasized on the Rp3 steel surfaces to be due to this steel's chemical composition and structure.

We detect the same findings in the case of Noryl polyamide +20% glass fibres in friction on the same steels, but to a lesser scale. In the case of Lexan 3412 polycarbonate reinforced with 20% glass fibres friction onto the same metallic surfaces and considering the same stress conditions, generally speaking there is no plastic material transfer. The transfer appears only if the load reaches 40 N, which corresponds to a contact pressure of 3449.7 MPa, and when the contact temperature reaches 251 ^{0}C. We do consider that probably the polycarbonate has a lesser transfer capacity than the polyamide.

4. DISCUSSION

The wear's rate values, considering the used experimental conditions, cover a large range. For greater clarity, they are presented in Table 4.

Comparing the metallic element's wear rates values at v = 46.41 cm/s and N = 40 N, it results that the polyamide reinforced with 30% glass fibres induces to the C120 steel a wear of approximately 1.110 times more higher than to the Rp3 steel. We do estimate that this phenomenon is due to Rp3 samples' higher hardness (62 HRC), in comparison to those from C120 (59 HRC).

Table 4. The variation curve of compatative wear corfficient equations for Nylonplast AVE Polyamide + 30% glass fibres/Rp3

Friction couple	Volumetric wear rate (10^{-6} cm^3/h)	Linear wear rate (10^{-4} mm/h)
v = (18.56 - 46.41) cm/s; N = 10 – 50 N		
Polyamide + 30% glass fibres/ C120	0.139 – 1.621	0.965 – 8.549
Polyamide + 30% glass fibres / Rp 3	0.214 – 1.369	2.382 – 6.004
Polycarbonate + 20% glass fibres / C120	0.244 – 1.309	3.592 – 6.366
v = (46.41 - 111.4) cm/s		
Polyamide + 20% glass fibres / C120	0.440 – 2.578	3,269 – 6,794
Polyamide + 20% glass fibres / Rp 3	0,473 – 2,549	3.792 – 6.627

Normal loads and corresponding contact pressures for the linear friction contact used during this research, lead to very high contact temperatures (180-240 ^{0}C) according to the applied normal load and relative sliding speed (see also Fig. 6a).

In several cases they exceed the polymer's melting temperature, thus being transferred on the metallic surface together with glass fibres fragments. Part of the glass fibres is smashed and still produced a predominant abrasive wear of the metallic sample's contact area, while another part is pushed out on the contact's exit edge, together with a multitude of ejected glass fibres.

We notice that only in the case of the friction couple Nyloplast AVE Polyamide + 30% glass fibres / C120 steel, there is a large plastic material transfer onto the metallic surface, which justifies the assertion that the transfer through adhesion depends on the nature and characteristics of the contact materials. From a qualitative point of view, obviously there is the fact that initially the wear process manifests itself as a wear through adherence and polymer transfer onto the metallic surface, which subsequently transforms itself into a process of abrasive wear, which leads to the plastic material removal clung onto the contact area. In what the friction couples are concerned – also see Fig. 6a.

The process' intensity depends on the fibres' content. The larger it is, the higher the intensity is. Metallic surface mechanical properties (especially the hardness), has a distinct influence over the plastic material transfer and metallic surface wear.

5. CONCLUSION

The diagrams' analysis plotted in Figs. 3 and 4 allows us to establish the variation equations for the comparative volumetric wear coefficient K and for the comparative depth wear coefficient K^*, for steel in linear contact, while in friction with glass reinforced thermoplastics.

The equations listed in Table 2 and 3, for the comparative wear coefficients (the volumetric and the depth ones), show that the variation is not a linear one, these coefficients evolving exponentially. We also notice that the decrease of the K^* coefficient with the increase of relative speed is faster than the decrease of the K coefficient.

We consider that this effect is due to the fact that the thermoplastic material deforms under load which means that for Timken type couples the increase of the wear imprint width is more effective than that of the depth of the wear imprint. From the diagrams plotted here, one can notice that the values of wear coefficients for the metallic component of the couple glass reinforced thermoplastic/steel are in the domain $(10^{-11} \div 10^{-12})$ cm^3/cm and respectively 10^{-9} mm/cm. The comparative wearing coefficients and their master-curves vs. relative speed have a special importance from the practical point of view. Based on these findings we can establish an optimal couple of materials from the design phase.

ACKNOWLEDGEMENTS

The authors would like to thank the Romanian Academy for its material and technical support offered in order to achieve these researches.

REFERENCES

[1] F.P. Bowden, D. Tabor. *The Friction and Lubrication of Solids*, part I-II, Clarendon Press, Oxford,1964.

[2] B. J. Briscoe, in: *Friction and Wear of Polymer Composites*, Ed. F. Klaus, Elsevier, Amsterdam, p. 25, 1986.

[3] K.L. Johnson, K. Kendall and A. D. Roberts, *Surface Energy and the Contact of Elastic Solids*. Proc. Roy. Soc. A324, 301 1971.

[4] K.L. Johnson, *Contacts Mechanics*, (Cambridge University Press, Cambridge, 1987.

[5] B. V. Deryagin, V. M. Muller and Yu. P. Toporov. Adhesive Contact Deformation of a Single Microelastic Sphere. *J. Colloid Interface Sci.*, 53, 314 1975.

[6] K. L. Jonson and J. A. Greenwood. An Adhesion Map for the Contact of Elastic Spheres J. Colloid Interf. Sci., 192, 326, 1997.

[7] D. Maugis, Adhesion of spheres: The JKR – DMT transition using a Dugdale model. *J. Colloid Interf. Sci.*, 150, 243 (1992).

[8] I.V. Kragelskii, *Friction and Wear* (Pergamon Press, Elmsford, 1982).

[9] N.K. Myshkin, A.V. Kovalev. Adhesion and Friction of Polymers, in *PolymerTribology*. Imperial College Press, London, 2009.

[10] V. E. Starzhynsky, A. M. Farberov, S. S. Pesetskii, S. A. Osipenko and V. A. Braginsky, *Precision Plastic Parts and Thei Production Technology*, (Nauka I Tekhnika, Minsk, 1992) (in Russian).

[11] B. J. Briscoe, Wear of polymers: an essay on fundamental aspects. *Tribology Int.*, 14, 231, 1998.

[12] G. Jintang, Tribochemical effects in formation of polymer transfer film. *Wear*, 245, 100, 2000.

[13] H. Unal, U. Sen and A. Mimaroglu, Friction and wear behavior of unfilled engineering thermoplastics. 183–187. *Tribol. Int.*, 37, 727 2004.

[14] H. Unal and A. Mimaroglu, Sliding friction and wear behaviour of polytetrafluoroethylene and its composites under dry conditions. Mater. Des., 24 (2003), 239–245*Mater. Des.*, **24**, 183 (2003).

[15] Y.K. Chen, O.P. Modi, A.S. Mhay, A. Chrysanthou, J.M. O'Sullivan, *The effect of different metallic counterface materials and different surface treatments on the wear and friction of polyamide 66 and its composite in rolling–sliding contact.* Wear 255, 714 (2003)

[16] C.J. Schwartz and S. Bahadur: *The role of filler deformability, filler–polymer bonding, and counterface material on the tribological behavior of polyphenylene sulfide (PPS).* Wear, 251, 1532 2001.

[17] Y.M. Xu, B.G. Mellor: *The effect of fillers on the wear resistance of thermoplastic polymeric coatings*. Wear, 251, 1522 2001.

[18] B.J. Briscoe, L. Fiori, E. Pelillo, *Nano-indentation of polymeric Surfaces*. J. Phys. D: Appl. Phys., 31, 2395, 1998.

[19] H. Shulga, A. Kovalev, N. Myshkin, V.V. Tsukruk, *Some aspects of AFM nanomechanical probing of surface polymer films*. European Polymer Journal, 40, 949, 2004.

[20] A. Kovalev, H. Shulga, M. Lemieux, N. Myshkin, V.V. Tsukruk, *Nano-mechanical probing of layered nanoscale polymer films with atomic force microscopy*. J. Mater. Res., 19, 716, 2004.

[21] G.M. Bartenev, V.V. Lavrentev, *Friction and Wear of Polymers*, (Elsevier, Amsterdam, 1981).

[22] L. Capitanu, A. Iarovici, J. Onisoru – *On polyamide and polycarbonate materials behaviour under dry friction*, The Annals of University "Dunarea de jos" Galati, fascicle **VIII**, Tribology, 2003, ISSN 1221-4590

Serbian Tribology Society

SERBIATRIB '13

13th International Conference on Tribology

Faculty of Engineering in Kragujevac

Kragujevac, Serbia, 15 – 17 May 2013

EXPERIMENTAL INVESTIGATION OF FRICTION COEFFICIENT AND WEAR RATE OF COMPOSITE MATERIALS SLIDING AGAINST SMOOTH AND ROUGH MILD STEEL COUNTERFACES

Mohammad Asaduzzaman Chowdhury[1]*, Dewan Muhammad Nuruzzaman[2], Biplov Kumar Roy[1], Sohel Samad[1], Rayhan Sarker[1], Abul Hasnat Mohammad Rezwan[1]

[1]Department of Mechanical Engineering, Dhaka University of Engineering and Technology, Gazipur, Bangladesh, *asadzmn2003@yahoo.com

[2]Faculty of Manufacturing Engineering, University Malaysia Pahang, Malaysia

Abstract: *In the present study, friction coefficient and wear rate of gear fiber reinforced plastic (gear fiber) and glass fiber reinforced plastic (glass fiber) sliding against mild steel are investigated experimentally. In order to do so, a pin on disc apparatus is designed and fabricated. Experiments are carried out when smooth or rough mild steel pin slides on gear fiber and glass fiber disc. Experiments are conducted at normal load 10, 15 and 20 N, sliding velocity 1, 1.5 and 2 m/s and relative humidity 70%. Variations of friction coefficient with the duration of rubbing at different normal loads and sliding velocities are investigated. Results show that friction coefficient is influenced by duration of rubbing, normal load and sliding velocity. In general, friction coefficient increases for a certain duration of rubbing and after that it remains constant for the rest of the experimental time. The obtained results reveal that friction coefficient decreases with the increase in normal load for gear fiber and glass fiber mating with smooth or rough mild steel counterface. On the other hand, it is also found that friction coefficient increases with the increase in sliding velocity for both of the tested materials. Moreover, wear rate increases with the increase in normal load and sliding velocity. The magnitudes of friction coefficient and wear rate are different depending on sliding velocity and normal load for both smooth and rough counterface pin materials.*

Keywords: *Friction coefficient, wear rate, gear fiber, glass fiber, mild steel, normal load, sliding velocity.*

1. INTRODUCTION

Numerous investigations have been carried out on friction and wear of different materials under different operating conditions. Several researchers [1-6] observed that the friction force and wear rate depend on roughness of the rubbing surfaces, relative motion, type of material, temperature, normal force, relative humidity, vibration, etc. The parameters that dictate the tribological performance of polymer and its composites include polymer molecular structure, processing and treatment, properties, viscoelastic behavior, surface texture, etc. [7-10]. There have been also a number of investigations exploring the influence of test conditions, contact geometry and environment on the friction and wear behavior of polymers and composites. [11-13] reported that the tribological behavior of polyamide, high density polyethylene and their composites is greatly affected by normal load, sliding speed and temperature. [14-15] showed that applied load and sliding speed play significant role on the wear behavior of polymer and composites. They also showed that applied load has more effect on the wear than the speed for composites. Experiments were carried out on friction and wear behavior of poly-ether-imide and its composites under different operating conditions [16-19]. Polymers and its composites are extensively used in sliding/rolling components such as gears, cams, bearings, rollers, transmission belts and grinding mills where their self-lubricating properties are exploited to avoid the need for oil or grease lubrication with its attendant problems of

contamination [20,21]. However, when the contact between sliding pairs is present, there is the problem of friction and wear. [22-24] demonstrated that the friction coefficient can, generally, be reduced and the wear resistance increased by selecting the right material combinations.

It was reported [25-27] that the influence of sliding speed on friction and wear of polymer and its composite is greater than that of applied load though some other researchers have different views. Unal et al. [28,29]reported that the applied load exerts greater influence on the sliding wear of polymer and its composites than the sliding speed. Transfer film has important effects on the tribological behavior of polymer and its' composite. If the transfer film is thin, uniform and continuous, the wear loss and the friction coefficient are low [30]. The results by [31, 32] showed that tribological performance of polymer material can be improved significantly by fibre reinforcement or fillers. The reason was that the transfer films formed and adhered close on the surface of counterface material during friction which resulted in the increase in wear resistance of the composites [31,10]. It was showed [33] that reinforcement of fibre or filler significantly improves the tribological behavior of polymeric material but this is not necessarily true for all cases. Franklin [34] reported that wear behavior of polymers under dry reciprocating sliding conditions does not always follow the generally accepted engineering rule of 'higher sliding speed, the higher wear rate'. The influence of normal load on the friction coefficient and wear rate of different polymer and composite materials was investigated [35]and it was found that the values of friction coefficient and wear rate are different for different materials. Several researchers [36-39] reported that friction coefficient of polymers and its composites rubbing against metal increases or decreases depending on the range of sliding speed and sliding pairs. Researchers [40-43] have also observed that the friction coefficient of polymers and its composites rubbing against metals decreases with the increase in load though some other researchers have different views. It was showed [45-47] that value of friction coefficient increases with the increase in load. Friction coefficient and specific wear rate values for different combinations of polymer and its composite were obtained and compared [27]. For all material combinations, it was observed that the coefficient of friction decreases linearly with the increase in applied pressure values. Unal et al. [37,29] reported that the applied load exerts greater influence on the sliding wear of polymer and its composite than the sliding velocity. Friction and wear behavior of glass fiber-reinforced polyester composite were studied and results showed that in general, friction and wear are strongly influenced by all the test parameters such as applied load, sliding speed, sliding distance and fiber orientations [48]. Moreover, it was found that applied normal load, sliding speed and fiber orientations have more pronounced effect on wear rate than sliding distance. Wang and Li [26] observed that the sliding velocity has more significant effect on the sliding wear as compared to the applied load and variations of wear rate with operating time can be distinguished by three distinct periods. These periods are running-in period, steady state period and severe wear period, respectively. The friction and the wear behavior of the polymeric material depend on the nature, thickness and stability of the transfer film that is formed and on the properties of the metallic counter face material [49]. Yang [50] studied the transfer of polytetrafluoroethylene (PTFE) on to 316 stainless steel and silicon wafers using infrared spectrophotometry and founds that it was strongly time and temperature dependent and reached a steady state after a certain period of contact. Tsukizoe and Ohmae [33] showed that reinforcement of fiber or filler significantly improve the tribological behavior of polymeric material but this is not necessarily true for all cases. Suresha et al. [38] showed that there is a strong inter-dependence on the friction coefficient and wear loss with respect to the applied loads for steel composites contact. It was found that the coefficient of friction and wear loss increase with the increase in applied normal load for all the samples evaluated.

From the aforementioned research works, it can be concluded that friction coefficient of composite materials at different normal loads and sliding velocities differs significantly. Even now a day, the effect of normal load and sliding velocity on friction coefficient and wear rate of composite materials such as gear fiber and glass fiber sliding against different counterface surface conditions is less understood. This means that more research work is needed for a better understanding of friction coefficient and wear rate of these materials under different normal loads and sliding velocities for smooth and rough mild steel counterfaces. Therefore, in order to understand more clearly, in this study experiments are carried out to investigate the influence of normal loads and sliding velocities on friction coefficient and wear rate of gear fiber and glass fiber. The effects of duration of rubbing on friction coefficient of these materials are also examined in this study.

2. EXPERIMENTAL

A schematic diagram of the experimental set-up is shown in Fig. 1 i.e. a pin which can slide on a rotating horizontal surface (disc). In this set-up a circular test sample (disc) is to be fixed on a rotating plate (table) having a long vertical shaft clamped with screw from the bottom surface of the

rotating plate. The shaft passes through two close-fit bush-bearings which are rigidly fixed with stainless steel plate and stainless steel base such that the shaft can move only axially and any radial movement of the rotating shaft is restrained by the bush. These stainless steel plate and stainless steel base are rigidly fixed with four vertical round bars to provide the rigidity to the main structure of this set-up. The main base of the set-up is constructed by 10 mm thick mild steel plate consisting of 3 mm thick rubber sheet at the upper side and 20 mm thick rubber block at the lower side. A compound V-pulley above the top stainless steel plate was fixed with the shaft to transmit rotation to the shaft from a motor. An electronic speed control unit is used to vary the speed of the motor as required. A 6 mm diameter cylindrical pin whose contacting foot is flat, made of mild steel, fitted on a holder is subsequently fitted with an arm. The arm is pivoted with a separate base in such a way that the arm with the pin holder can rotate vertically and horizontally about the pivot point with very low friction. Sliding speed can be varied by two ways (i) by changing the frictional radius and (ii) by changing the rotational speed of the shaft. In this research, sliding speed is varied by changing the rotational speed of the shaft while maintaining 25 mm constant frictional radius. To measure the frictional force acting on the pin during sliding on the rotating plate, a load cell (TML, Tokyo Sokki Kenkyujo Co. Ltd, CLS-10NA) along with its digital indicator (TML, Tokyo Sokki Kenkyujo Co. Ltd, Model no. TD-93A) was used. The coefficient of friction was obtained by dividing the frictional force by the applied normal force (load). Wear was measured by weighing the test sample with an electronic balance before and after the test, and then the difference in mass was converted to wear rate. To measure the surface roughness of the test samples, Taylor Hobson Precision Roughness Checker (Surtronic 25) was used. Each test was conducted for 30 minutes of rubbing time with new pin and test sample. Furthermore, to ensure the reliability of the test results, each test was repeated five times and the scatter in results was small, therefore the average values of these test results were taken into consideration. The detail experimental conditions are shown in Table 1.

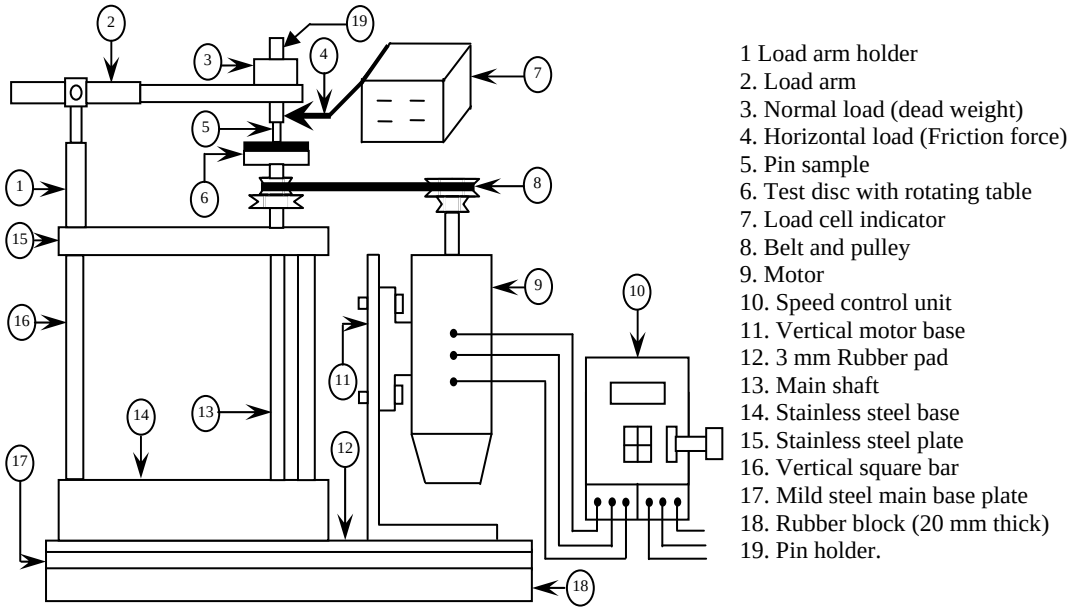

Fig. 1. Block diagram of the experimental set-up.

Table 1. Experimental Conditions.

Sl. No.	Parameters	Operating Conditions
1.	Normal Load	10, 15, 20 N
2.	Sliding Velocity	1, 1.5, 2 m/s
3.	Relative Humidity	70 (± 5)%
4.	Duration of Rubbing	30 minutes
5.	Surface Condition	Dry
6.	Disc material	(i) Gear fiber reinforced Plastic (ii) Glass fiber reinforced plastic
7.	Roughness of Gear and Glass fiber, R_a	0.70-0.80 μm
8.	Pin material	Mild steel
9.	Roughness of mild steel, R_a	(a) Smooth counterface: about 0.30 μm (b) Rough counterface: about 3.0 μm

3. RESULTS AND DISCUSSION

Figure 2 shows the variation of friction coefficient with the duration of rubbing at different normal loads for gear fiber sliding against smooth mild steel conterface. During experiment, the sliding velocity and relative humidity were 1 m/s and 70% respectively. Curves 1, 2 and 3 of this figure are drawn for normal laod 10, 15 and 20 N respectively. Curve 1 of this figure shows that during the starting, the value of friction coefficient is 0.104 and then increases very steadily up to 0.147 over a duration of 20 minutes of rubbing and after that it remains constant for the rest of the experimental time. These findings are in agreement with the findings of Chowdhury and Helali [4]. At starting of experiment, the friction force is low due to contact between superficial layer of pin and disc. As rubbing continues, the disc material becomes worn and reinforced material comes in contact with the pin, roughening of the disc surface causes the ploughing and hence friction coefficient increases with duration of rubbing. After certain duration of rubbing the increase of roughness and other parameters may reach to a certain steady value hence the values of friction coefficient remain constant for the rest of the time. Curves 2 and 3 show that for the high normal load, the friction coefficient is less and the trend in variation of friction coefficient is almost the same as for curve 1. From these curves, it is also observed that time to reach steady state values is different for different normal load. From the obtained results it is found that at normal load 10, 15 and 20 N, gear fibre takes 20, 17 and 15 minutes respectively to reach steady friction. It indicates that the higher the normal load, time to reach constant friction is less. This may be due to the fact that the higher the normal load, the surface roughness and other parameters take less time to stabilize.

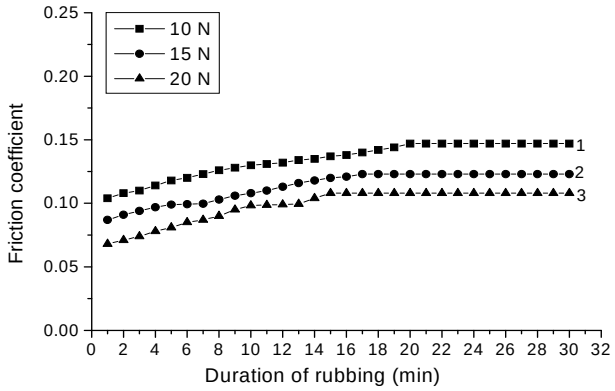

Fig. 2. Friction coefficient as a function of duration of rubbing at different normal loads (sliding velocity: 1 m/s, relative humidity: 70%, test sample: gear fiber, pin: mild steel, smooth).

Figure 3 shows the effect of the duration of rubbing on the value of friction coefficient at different normal loads for gear fiber sliding against rough mild steel counterface at sliding velocity 1 m/s and relative humidity 70%. Curve 1 of this figure drawn for normal load 10 N, shows that during starting of the experiment, the value of friction coefficient is 0.153 which rises for 22 minutes to a value of 0.195 and then it becomes steady for the rest of the experimental time. Almost similar trends of variation are observed in curves 2 and 3 which are drawn for load 15 and 20 N respectively. From these curves, it is found that time to reach steady friction is different for different normal loads. At normal load 10, 15 and 20 N, gear fiber-mild steel rough pair takes 22, 19 and 16 minutes respectively to reach steady friction That is, higher the normal load, gear fiber-mild steel rough pair takes less time to stabilize.

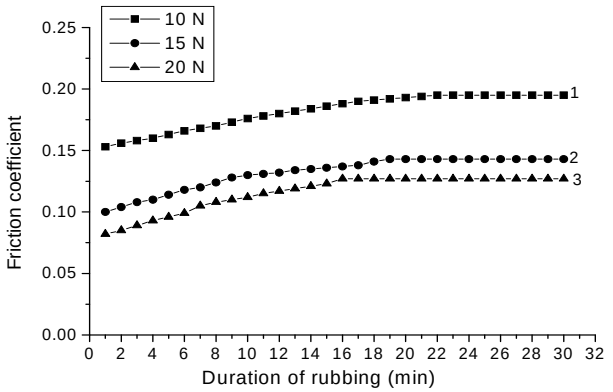

Fig. 3. Friction coefficient as a function of duration of rubbing at different normal loads (sliding velocity: 1 m/s, relative humidity: 70%, test sample: gear fiber, pin: mild steel, rough).

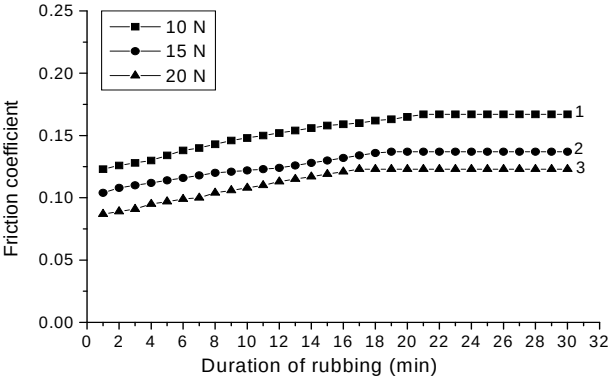

Fig. 4. Friction coefficient as a function of duration of rubbing at different normal loads (sliding velocity: 1 m/s, relative humidity: 70%, test sample: glass fiber, pin: mild steel, smooth).

Figure 4 shows the effect of the duration of rubbing on the value of friction coefficient at different normal load for glass fiber sliding against smooth mild steel counterface. Curve 1 of this figure drawn for normal load 10 N, shows that during starting of the experiment, the value of friction coefficient is 0.123 which rises for 21 minutes to a value of 0.167 and then it becomes steady for the rest of the experimental time. Almost

similar trends of variation are observed in curves 2 and 3 which are drawn for load 15 and 20 N, respectively. From the obtained results, it can also be seen that time to reach constant friction is different for different normal load and higher the normal load, glass fiber takes less time to stabilize.

Several experiments are conducted to observe the effect of duration of rubbing on friction coefficient at different sliding speeds for glass fibre sliding against rough mild steel counterface and these results are presented in Figure 5. Curve 1 of this figure drawn for normal load 10 N, shows that during starting of the experiment, the value of friction coefficient is 0.175 which rises for 22 minutes to a value of 0.225 and then it becomes steady for the rest of the experimental time. Almost similar trends of variation are observed in curves 2 and 3 which are drawn for load 15 and 20 N respectively. From these curves, it is found that time to reach steady friction is different for different normal loads. At normal load 10, 15 and 20 N, glass fiber-mild steel rough pair takes 20, 18 and 15 minutes respectively to reach steady friction That is, higher the normal load, glass fiber-mild steel rough pair takes less time to stabilize.

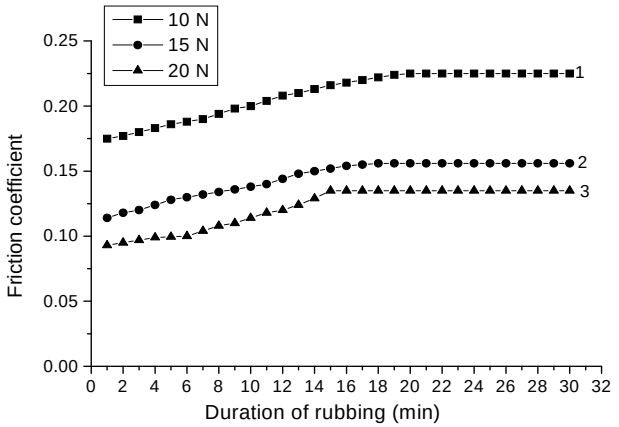

Fig. 5. Friction coefficient as a function of duration of rubbing at different normal loads (sliding velocity: 1 m/s, relative humidity: 70%, test sample: glass fiber, pin: mild steel, rough).

Figure 6 shows comparison of the variation of friction coefficient with normal load for gear fiber-mild steel smooth, gear fiber-mild steel rough, glass fiber-mild steel smooth and glass fiber-mild steel rough sliding pairs. Curves of this figure are drawn from steady values of friction coefficient shown in Figures 2-5 for gear fiber-mild steel smooth, gear fiber-mild steel rough, glass fiber-mild steel smooth and glass fiber-mild steel rough sliding pairs, respectively (to ensure the reliability of test results, each test was repeated five times and curves 1-3 of Figures 2-5 represent average value of five experiments). It is shown that the friction coefficient varies from 0.147 to 0.108, 0.195 to 0.127, 0.167 to 0.123 and 0.225 to 0.135 with the variation of normal load from 10 to 20 N for for gear fiber-mild steel smooth, gear fiber-mild steel rough, glass fiber-mild steel smooth and glass fiber-mild steel rough sliding pairs, respectively. From the obtained results, it can be seen that the coefficient of friction decreases with the increase in applied load. It is known that tribological behavior of polymers and polymer composites can be associated with their viscoelastic and temperature-related properties. Sliding contact of two materials results in heat generation at the asperities and hence increases in temperature at the frictional surfaces of the two materials which influences the viscoelastic property in the response of materials stress, adhesion and transferring behaviors [27]. From the obtained results, it can also be seen that the highest values of the friction coefficient are obtained for glass fiber-mild steel rough pair and the lowest values of friction coefficient are obtained for gear fiber-mild steel smooth pair. The values of friction coefficient of gear fiber-mild steel rough pair and glass fiber-mild steel smooth pair are found in between the highest and lowest values. It is noted that the friction coefficients of gear fiber-mild steel rough pair are higher than that of glass fiber-mild steel smooth pair. From this figure, it is also found that at identical conditions, the values of friction coefficient of gear fiber and glass fiber sliding against smooth mild steel counterface is lower than that of gear fiber and glass fiber sliding against rough mild steel counterface. It was found that after friction tests, the average roughness of gear fiber-mild steel smooth pair, glass fiber-mild steel smooth pair, gear fiber-mild steel rough pair and glass fiber-mild steel rough pair varied from 0.95-1.35, 1.25-1.65 and 1.55-1.75 and 1.67-1.91 μm respectively.

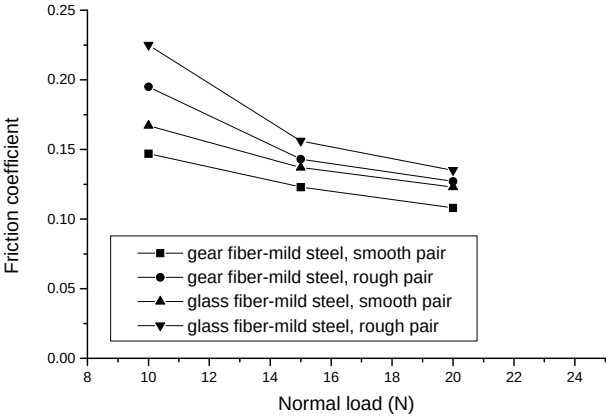

Fig. 6. Friction coefficient as a function of Normal load for gear and glass fiber for different counterface surface conditions (Sliding velocity: 1 m/s, relative humidity: 70%).

Figures 7, 8, 9 and 10 show the variation of friction coefficient with the duration of rubbing at different sliding velocities for gear fiber-mild steel smooth, gear fiber-mild steel rough, glass fiber-mild steel smooth and glass fiber-mild steel

rough sliding pairs, respectively at normal load 15 N and relative humidity 70%. Curves 1, 2 and 3 of Fig. 7 are drawn for sliding velocity 1, 1.5 and 2 m/s respectively. Curve 1 of this figure shows that at initial stage of rubbing, the value of friction coefficient is 0.087 which increases almost linearly up to 0.123 over a duration of 17 minutes of rubbing and after that it remains constant for the rest of the experimental time. At starting of experiment, the friction force is low due to contact between superficial layer of pin and disc. As rubbing continues, the disc material becomes worn and reinforced material comes in contact with the pin, roughening of the disc surface causes the ploughing and hence friction coefficient increases with duration of rubbing. After certain duration of rubbing the increase of roughness and other parameters may reach to a certain steady value hence the values of friction coefficient remain constant for the rest of the time. Curves 2 and 3 show that for the higher sliding velocity, the friction coefficient is more and the trend in variation of friction coefficient is almost the same as for curve 1. From these curves, it is also observed that time to reach steady state value is different for different sliding velocity. From the results it is found that gear fiber-mild steel smooth pair at sliding velocity 1, 1.5 and 2 m/s takes to reach constant friction 17, 14 and 11 minutes respectively. It indicates that the higher the sliding velocity, time to reach constant friction is less. This may be due to the higher the sliding velocity, the surface roughness and other parameters take less time to stabilize. From Figs. 8, 9 and 10, it can be observed that the trends in variation of friction coefficient with the duration of rubbing are very similar to that of Fig. 7 but the values of friction coefficient are different for gear fiber-mild steel rough pair, glass fiber-mild steel smooth pair and glass fiber-mild steel rough pair.

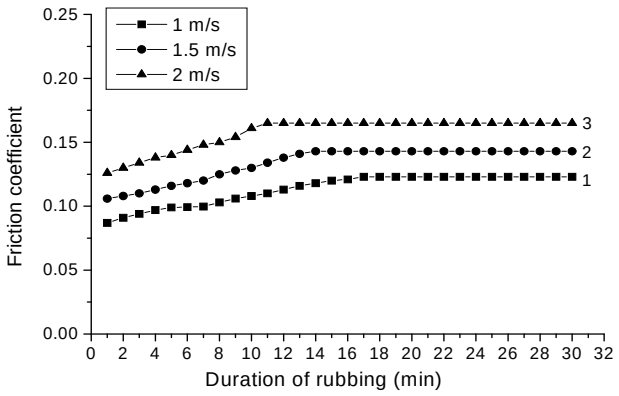

Fig. 7. Friction coefficient as a function of duration of rubbing at different sliding velocities (normal load: 15 N, relative humidity: 70%, test sample: gear fiber, pin: mild steel, smooth).

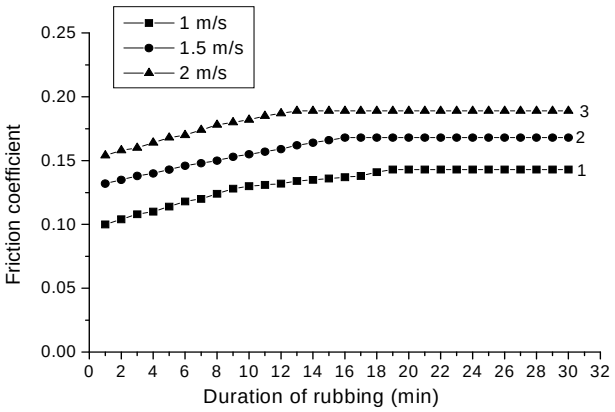

Fig. 8. Friction coefficient as a function of duration of rubbing at different sliding velocities (normal load: 15 N, relative humidity: 70%, test sample: gear fiber, pin: mild steel, rough).

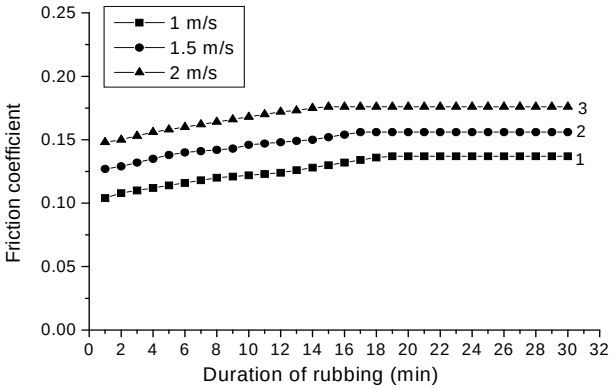

Fig. 9. Friction coefficient as a function of duration of rubbing at different sliding velocities (normal load: 15 N, relative humidity: 70%, test sample: glass fiber, pin: mild steel, smooth).

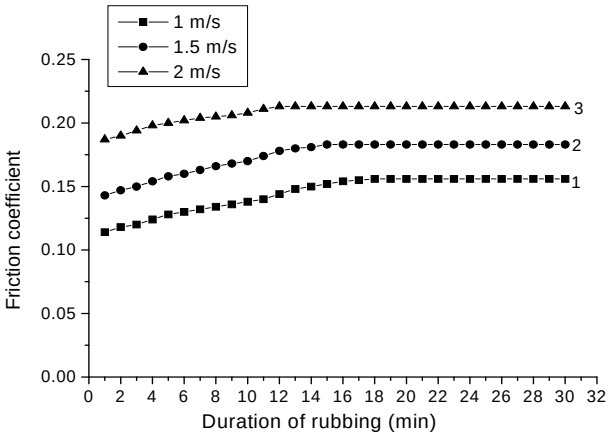

Fig. 10. Friction coefficient as a function of duration of rubbing at different sliding velocities (normal load: 15 N, relative humidity: 70%, test sample: glass fiber, pin: mild steel, rough).

Figure 11 shows the comparison of the variation of friction coefficient with sliding speed for gear fiber-mild steel smooth, gear fiber-mild steel rough, glass fiber-mild steel smooth and glass fiber-mild steel rough sliding pairs. Curves of this figure are drawn from steady values of friction coefficient shown in Figures 7–10 for gear fiber-mild steel

smooth, gear fiber-mild steel rough, glass fiber-mild steel smooth and glass fiber-mild steel rough sliding pairs. It is shown that the friction coefficient varies from 0.123 to 0.165, 0.143 to 0.189, 0.137 to 0.176 and 0.156 to 0.213 with the variation of sliding speed from 1 to 2 m/s for gear fiber-mild steel smooth, gear fiber-mild steel rough, glass fiber-mild steel smooth and glass fiber-mild steel rough sliding pairs respectively. From these results it is seen that the values of friction coefficient increase almost linearly with sliding speed. These findings are in agreement with the findings of Mimaroglu et al. and Unal et al. [27,28]. With the increase in sliding speed, the frictional heat may decrease the strength of the materials and high temperature results in stronger or increased adhesion with pin [27,51]. The increase of friction coefficient with sliding speed can be explained by the more adhesion of counterface pin material on disc. From the obtained results, it can also be seen that the highest values of the friction coefficient are obtained for glass fiber-mild steel rough pair and the lowest values of friction coefficient are obtained for gear fiber-mild steel smooth pair. The values of friction coefficient of gear fiber-mild steel rough pair and glass fiber-mild steel smooth pair are found in between the highest and lowest values. It is noted that the friction coefficients of gear fiber-mild steel rough pair are higher than that of glass fiber-mild steel smooth pair. From this figure, it is also found that at identical conditions, the values of friction coefficient of gear fiber and glass fiber sliding against smooth mild steel counterface is lower than that of gear fiber and glass fiber sliding against rough mild steel counterface. It was found that after friction tests, the average roughness of gear fiber-mild steel smooth pair, glass fiber-mild steel smooth pair, gear fiber-mild steel rough pair and glass fiber-mild steel rough pair varied from 1.05-1.45, 1.35-1.78 and 1.67-1.88 and 1.76-1.98 μm respectively.

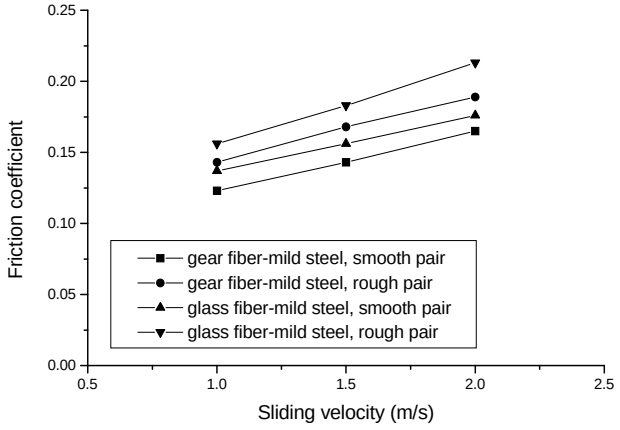

Fig. 11. Friction coefficient as a function of Normal load for gear and glass fiber for different counterface surface conditions (normal load: 15 N, relative humidity: 70%).

Variations of wear rate with normal load for gear fiber and glass fiber sliding against smooth or rough mild steel counterfaces are shown in Fig. 12. The experimental results indicate that the curves drawn showing the variation of wear rate from 0.815 to 1.453, 1.135 to 1.751, 0.929 to 1.553 and 1.638 to 2.35 mg/min with the variation of normal load from 10 to 20 N for gear fiber-mild steel smooth, gear fiber-mild steel rough, glass fiber-mild steel smooth and glass fiber-mild steel rough sliding pairs respectively. From these curves, it is observed that wear rate increases with the increase of normal load for all types of sliding pairs. When the load on the pin is increased, the actual area of contact would increase towards the nominal contact area, resulting in increased frictional force between two sliding surfaces. The increased frictional force and real surface area in contact causes higher wear. This means that the shear force and frictional thrust are increased with increase of applied load and these increased in values accelerate the wear rate. Similar trends of variation are also observed for mild steel–mild steel couples [52], i.e wear rate increases with the increase in normal load.

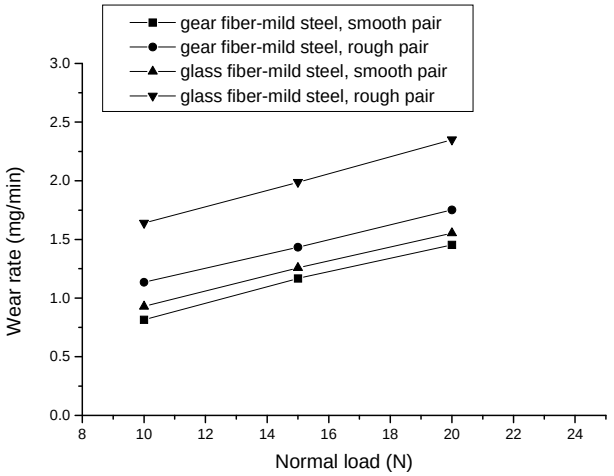

Fig. 12. Wear rate as a function of Normal load for gear and glass fiber for different counterface surface conditions (Sliding velocity: 1 m/s, relative humidity: 70%).

Figure 12 also shows the comparison of the variation of wear rate with normal load for gear fiber and glass fiber under different pin surface conditions. From the obtained results, it can also be seen that the highest values of the wear rate are obtained for glass fiber-mild steel rough pair and the lowest values of wear rate are obtained for gear fiber-mild steel smooth pair. The values of wear rate of gear fiber-mild steel rough pair and glass fiber-mild steel smooth pair are found in between the highest and lowest values. It is noted that the wear rates of gear fiber-mild steel rough pair are higher than that of glass fiber-mild steel smooth pair. From this figure, it is also found that at identical conditions, the values of wear rate of gear

fiber and glass fiber sliding against smooth mild steel counterface is lower than that of gear fiber and glass fiber sliding against rough mild steel counterface.

Variations of wear rate with sliding velocity for gear fiber and glass fibre mating with smooth or rough mild steel counterfaces are presented in Fig. 13. Curves show the variation of wear rate from 1.167 to 1.778, 1.433 to 2.25, 1.258 to 1.95 and 1.987 to 2.78 mg/min with the variation in sliding speed from 1 to 3 m/s for gear fiber-mild steel smooth, gear fiber-mild steel rough, glass fiber-mild steel smooth and glass fiber-mild steel rough sliding pairs respectively. From these curves, it is observed that wear rate increases with the increase in sliding speed for all types of material combinations. These findings are in agreement with the findings of Mimaroglu et al and Suresha et al. [27,38]. This is due to the fact that duration of rubbing is same for all sliding velocities, while the length of rubbing is more for higher sliding velocity. The reduction of shear strength of the material and increased true area of contact between contacting surfaces may have some role on the higher wear rate at higher sliding velocity [51].

Figure 13 also shows the comparison of the variation of wear rate with sliding velocity for different sliding pairs. From the obtained results, it can also be seen that the highest values of the wear rate are obtained for glass fiber-mild steel rough pair and the lowest values of wear rate are obtained for gear fiber-mild steel smooth pair. The values of wear rate of gear fiber-mild steel rough pair and glass fiber-mild steel smooth pair are found in between the highest and lowest values. It is noted that the wear rates of gear fiber-mild steel rough pair are higher than that of glass fiber-mild steel smooth pair.

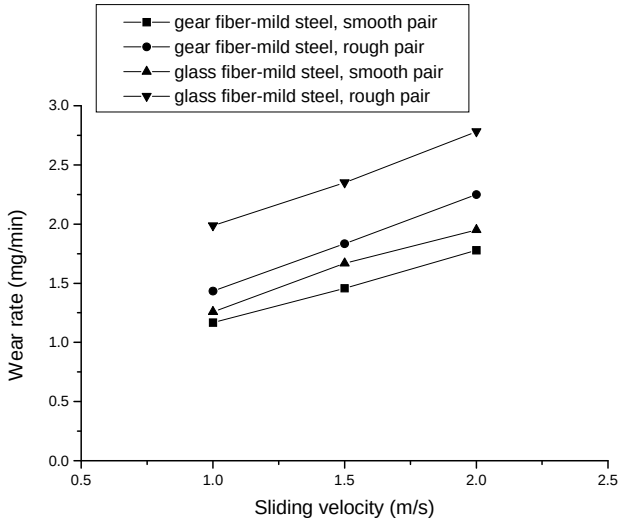

Fig. 13. Wear rate as a function of Normal load for gear and glass fiber for different counterface surface conditions (normal load: 15 N, relative humidity: 70%).

From this figure, it is also found that at identical conditions, the values of wear rate of gear fiber and glass fiber sliding against smooth mild steel counterface is lower than that of gear fiber and glass fiber sliding against rough mild steel counterface. It is due to the fact that rough surfaces generally wear more quickly and have higher friction coefficients than smooth surfaces.

4. CONCLUSION

The presence of normal load and sliding velocity indeed affects the friction force considerably. Within the observed range, the values of friction coefficient decrease with the increase in normal load while friction coefficients increase with the increase in sliding velocity for gear fiber and glass fiber sliding against smooth or rough mild steel pin. Friction coefficient varies with the duration of rubbing and after certain duration of rubbing, friction coefficient becomes steady for the observed range of normal load and sliding velocity. Wear rates of gear fiber and glass mating with smooth or rough mild steel counterface increase with the increase in normal load and sliding velocity. The highest values of the friction coefficient are obtained for glass fiber-mild steel rough pair and the lowest values of friction coefficient are obtained for gear fiber-mild steel smooth pair. The values of friction coefficient of gear fiber-mild steel rough pair and glass fiber-mild steel smooth pair are found in between the highest and lowest values. The friction coefficients of gear fiber-mild steel rough pair are higher than that of glass fiber-mild steel smooth pair. At identical conditions, the values of friction coefficient of gear fiber and glass fiber sliding against smooth mild steel counterface is lower than that of gear fiber and glass fiber sliding against rough mild steel counterface.

As (i) the friction coefficient decreases with the increase in normal load (ii) the values of friction coefficient increase with the increase in sliding velocity (iii) wear rate increases with the increase in normal load and sliding velocity and (iv) the magnitudes of friction coefficient and wear rate are different for smooth and rough counterface pins and type of materials, therefore maintaining an appropriate level of normal load, sliding velocity as well as appropriate choice of counterface surface condition and tested materials, friction and wear may be kept to some lower value to improve mechanical processes.

REFERENCES

[1] Archard, J.F.: "*Wear theory and mechanisms*", Wear Control Handbook, ASME, New York, NY, 1980.

[2] Tabor, D.: "*Friction and wear – developments over the last 50 years, keynote address*", Proceedings of the International Conference of Tribology – Friction, Lubrication and Wear, Queen Elizabeth II Conference Centre, London,Institute of Mechanical Engineering, London, pp. 157-72, 1987.

[3] Kukureka, S.N., Chen, Y.K., Hooke, C.J. and Liao, P.: "*The wear mechanisms of acetal in unlubricatedrolling-sliding contact*", Wear, Vol. 185, pp. 1-8, 1995.

[4] Chowdhury, M.A. and Helali, M.M.: "*The effect of amplitude of vibration on the coefficient of friction fordifferent materials*", Tribology International, Vol. 41, No. 4, pp. 307-14, 2008.

[5] Chowdhury, M.A. and Helali, M.M.: "*The frictional behavior of composite materials under horizontal vibration*", Industrial Lubrication and Tribology, Vol. 61, No. 5, pp. 246-53, 2009a.

[6] Chowdhury, M.A. and Helali, M.M.: "*The frictional behavior of materials under vertical vibration*", Industrial Lubrication and Tribology, Vol. 61, No. 3, pp. 154-60, 2009b.

[7] El-Tayeb, N.S.M. and Mostafa, I.M.: "*The effect of laminate orientations on friction and wear mechanisms of glass reinforced polyester composite*", Wear, Vol. 195, pp. 186-91, 1996.

[8] El-Tayeb, N.S.M. and Gadelrab, R.M.: "*Friction and wear properties of e-glass fiber reinforced epoxy compositesunder different sliding contact conditions*", Wear, Vol. 192, pp. 112-17, 1996.

[9] Bahadur, S. and Zheng, Y.: "*Mechanical and tribological behavior of polyester reinforced with short glass fibers*", Wear, Vol. 137, pp. 251-66, 1990.

[10] Bahadur, S. and Polineni, V.K.: "*Tribological studies of glass fabric-reinforced polyamide composites filled with CuO and PTFE*", Wear, Vol. 200, pp. 95-104, 1996.

[11] Watanabe, M.: "*The friction and wear properties of nylon*", Wear, Vol. 110, pp. 379-88, 1968.

[12] Tanaka, K.: "*Transfer of semi crystalline polymers sliding against smooth steel surface*", Wear, Vol. 75, pp. 183-99, 1982.

[13] Bahadur, S. and Tabor, D.: "*Role of fillers in the friction and wear behavior of high-density polyethylene*", in Lee, L.H. (Ed.), Polymer Wear and Its Control, ACS Symposium Series, Vol. 287, ACS Publications, Washington, DC, pp. 253-68, 1985.

[14] Pihtili, H. and Tosun, N.: "*Effect of load and speed on the wear behavior of woven glass fabrics and aramid fiber-reinforced composites*", Wear, Vol. 252, pp. 979-84, 2002a.

[15] Pihtili, H. and Tosun, N.: "*Investigation of the wear behavior of a glass fiber-reinforced composite and plain polyester resin*", Composites Science and Technology, Vol. 62, pp. 367-70, 2002b.

[16] Bijwe, J., Tewari, U.S., Vasudevan, P.: "*Friction and wear studies of polyetherimide composites*", Wear, Vol. 138, pp. 61-76, 1990.

[17] Bijwe, J., Indumathi, J., John Rajesh, J. and Fahim, M.: "*Friction and wear behavior of polyetherimide composites in various wear modes*", Wear, Vol. 249, pp. 715-26, 2001.

[18] Bijwe, J. and Indumathi, J.: "*Influence of fibers and solid lubricants on low amplitude oscillating wear of polyetherimide composites*", Wear, Vol. 257, No. 5/6, pp. 562-72, 2004.

[19] Bijwe, J., Indumathi, J. and Ghosh, A.K.: "*Role of fabric reinforcement on the low amplitude oscillating wear of polyetherimide composites*", Wear, Vol. 256, No. 1/2, pp. 27-37, 2004.

[20] Zhang, S.W.: '*State-of-the-art of polymer tribology*', Tribol. Int., Vol. 31, Nos. 1–3, pp.49-60, 1998.

[21] Kowandy, C., Richard, C. and Chen, Y.M.: '*Characterization of wear particles for comprehension of wear mechanisms case of PTFE against cast iron*', Wear, Vol. 265, No. 11–12, pp. 1714–1719, 2008.

[22] Yamaguchi, Y.: *Tribology of Plastic Materials: Their Characteristics and Applications to Sliding Components*, Elsevier, Amsterdam, 1990.

[23] Hooke, C.J., Kukureka, S.N., Liao, P., Rao, M. and Chen, Y.K.: "*The friction and wear of polymers innon-conformal contacts*", Wear, Vol. 200, pp. 83-94, 1996.

[24] Lawrence, C.C. and Stolarski, T.A.: "*Rolling contact wear of polymers: a preliminary study*", Wear, Vol. 132, pp. 83-91, 1989.

[25] Feyzullahoglu, E. and Saffak, Z.: '*The tribological behavior of different engineering plastics under dry friction conditions*', Mater. Design, Vol. 29, No. 1, pp. 205–211, 2008.

[26] Wang, Y.Q., Li, J.: '*Sliding wear behavior and mechanism of ultra-high molecularweight polyethylene*', Mater. Sci. Eng., Vol. 266, No. 1–2, pp. 155–160, 1999.

[27] Mimaroglu, A., Unal, H. and Arda, T.: '*Friction and wear performance of pure and glass fiber reinforced poly-ether-imide on polymer and steel counterface materials*', Wear, Vol. 262, No. 11–12, pp.1407–1413, 2007.

[28] Unal, H., Sen, U. and Mimaroglu, A.: '*Dry sliding wear characteristics of some industrial polymers against steel counterface*', Tribol. Int., Vol. 37, No. 9, pp. 727–732, 2004.

[29] Unal, H., Sen, U. and Mimaroglu, A.: '*An approach to friction and wear properties ofpolytetrafluoroethylene composite*', Mater. Design, Vol. 27, No. 8, pp. 694–699, 2006.

[30] Sirong, Y., Zhongzhen, Yu., Mai, Y-W.: *'Effects of SEBS-g-MA on tribological behavior of nylon 66/organoclay nanocomposites'*, Tribol. Int., Vol. 40, No. 5, pp. 855–862, 2007.

[31] Bahadur, S. and Kapoor, A.: '*The effect of ZnF2, ZnS and PbS fillers on the tribological behavior of nylon 11'*, Wear, Vol. 155, No. 1, pp. 49–61, 1992.

[32] Wang, J., Gu, M., Bai, S. and Ge, S.: '*Investigation of the influence of MoS2 filler on the tribological*

properties of carbon fiber reinforced nylon 1010 composites', Wear, Vol. 255, No. 1–6, pp. 774–779, 2003.

[33] Tsukizoe, T. and Ohmae, N.: '*Friction and wear of advanced composite materials*', FibreSci. Technol., Vol. 18, No. 4, pp. 265–286, 1983.

[34] Franklin, S.E.: '*Wear experiments with selected engineering polymers and polymer composites under dry reciprocating sliding conditions*', Wear, Vol. 251, No. 1–12, pp. 1591–1598, 2001.

[35] Nuruzzaman, D.M., Chowdhury, M.A. and Rahaman, M.L.: '*Effect of duration of rubbing and normal load on friction coefficient for polymer and composite materials*', Ind. Lubr. Tribol., Vol. 63, No. 5, pp. 320–326, 2011.

[36] Benabdallah, H.: '*Friction and wear of blended polyoxymethylene sliding against coated steel plates*', Wear, Vol. 254, No. 12, pp. 1239–1246, 2003.

[37] Unal, H., Mimaroglu, A., Kadioglu, U. and Ekiz, H.: '*Sliding friction and wear behavior of polytetrafluoroethylene and its composites under dry conditions*', Mater. Design, Vol. 25, No. 3, pp. 239–245, 2004.

[38] Suresha, B., Chandramohan, G., Samapthkumaran, P., Seetharamu, S. and Vynatheya, S.: *Friction and wear characteristics of carbon-epoxy and glass-epoxy woven roving fiber composites*, J. Reinf. Plast. Comp., Vol. 25, No. 7, pp.771–782, 2006.

[39] Cho, M.H., Bahadur, S. and Pogosian, A.K.: '*Friction and wear studies using Taguchi method on polyphenylene sulfide filled with a complex mixture of MoS2, Al2O3, and other compounds*', Wear, Vol. 258, No. 11–12, pp. 1825–1835, 2005.

[40] Santner, E. and Czichos, H.: "*Tribology of polymers*", Tribology International, Vol. 22, No. 2, pp. 103-9, 1989.

[41] Tevruz, T.: "*Tribological behaviours of carbon-filled polytetrafluoroethylene dry journal bearings*", Wear, Vol. 221, pp. 61-8, 1998.

[42] Tevruz, T.: "*Tribological behaviours of bronze-filled polytetrafluoroethylene dry journal bearings*", Wear, Vol. 230, pp. 61-9, 1999.

[43] Anderson, J.C.: "*The wear and friction of commercialpolymers and composites*", in Friedrich, K. (Ed.), Frictionand Wear and Polymer Composites, Composite MaterialsSeries, Vol. 1, Elsevier, Amsterdam, pp. 329-62, 1986.

[44] Stuart, B.H.: "*Tribological studies of poly (ether ether ketone) blends*", Tribology International, Vol. 31, No. 11, pp. 647-51, 1998.

[45] Unal, H., Mimaroglu, A.: "*Friction and wear behavior of unfilled engineering thermoplastics*", Material Design, Vol. 24, pp. 183-7, 2003.

[46] Unal, H. and Mimaroglu, A.: "*Influence of test conditions on the tribological properties of polymers*", Industrial Lubrication and Tribology, Vol. 55, No. 4, pp. 178-83, 2003.

[47] Suresha, B., Chandramohan, G., Prakash, J.N., Balusamy, V. and Sankaranarayanasamy, K.: "*The role of fillerson friction and slide wear characteristics in glass-epoxy composite systems*", Journal of Minerals & Materials Characterization & Engineering, Vol. 5, No. 1, pp. 87-101, 2006a.

[48] El-Tayeb, N.S.M., Yousif, B.F. and Yap, T.C.: "*Tribological studies of polyester reinforced with CSM450-R-glass fiber sliding against smooth stainless steel counterface*", Wear, Vol. 261, pp. 443-52, 2006.

[49] Clerico, M. and Patierno, V.: "*Sliding wear of polymeric composites*", Wear, Vol. 53, No. 2, pp. 279-97, 299-301, 1979.

[50] Yang, E.-L.: "*Effect of crystalline and amorphous phases on the transfer of polytetrafluoroethylene (PTFE)onto metallic substrates*", Journal of Materials Research, Vol. 7, No. 11, pp. 3139-49, 1992.

[51] B. Bhushan: *Principle and Applications of Tribology*, John Wiley & Sons, Inc., New York, 1999.

[52] M. A. Chowdhury, M. M. Helali: *The Effect of Frequency of Vibration and Humidity on the Wear rate*, Wear, Vol. 262, pp. 198-203, 2007.

Serbian Tribology Society

SERBIATRIB '13

13th International Conference on Tribology

Faculty of Engineering in Kragujevac

Kragujevac, Serbia, 15 – 17 May 2013

ABRASIVE WEAR RESISTANCE OF THE IRON- AND WC-BASED HARDFACED COATINGS EVALUATED WITH SCRATCH TEST METHOD

Aleksandar Vencl[1], Bojan Gligorijević[2], Boris Katavić[2], Bogdan Nedić[3], Dragan Džunić[3]

[1]University of Belgrade, Faculty of Mechanical Engineering, Belgrade, Serbia, avencl@mas.bg.ac.rs

[2]Institute Goša, Belgrade, Serbia, bojan.gligorijevic@institutgosa.rs, boris.katavic@institutgosa.rs

[3]Faculty of Engineering, University of Kragujevac, Kragujevac, Serbia, nedic@kg.ac.rs, dzuna@kg.ac.rs

Abstract: *Abrasive wear is one of the most common types of wear, which makes abrasive wear resistance very important in many industries. The hardfacing is considered as useful and economical way to improve the performance of components submitted to severe abrasive wear conditions, with wide range of applicable filler materials. The abrasive wear resistance of the three different hardfaced coatings (two iron-based and one WC-based), which were intended to be used for reparation of the impact plates of the ventilation mill, was investigated and compared. Abrasive wear tests were carried-out by using the scratch tester under the dry conditions. Three normal loads of 10, 50 and 100 N and the constant sliding speed of 4 mm/s were used. Scratch test was chosen as a relatively easy and quick test method. Wear mechanism analysis showed significant influence of the hardfaced coatings structure, which, along with hardness, has determined coatings abrasive wear resistance.*

Keywords: *abrasive wear, scratch test, hardfacing, iron-based and WC-based materials, SEM-EDS.*

1. INTRODUCTION

More than 50 % of all wear-related failures of industrial equipment are caused by abrasive wear [1]. The estimated costs of abrasive wear are between 1 and 4 % of the gross national product of an industrialized nation [2]. For these reasons, the abrasive wear resistance is a subject of great importance in many industries, such as agriculture, mining, mineral processing etc.

Hardfacing could be defined as "coating deposition process in which a wear resistant, usually harder, material is deposited on the surface of a component by some of the welding techniques". In most cases, hardfacing is used for controlling abrasive and erosive wear, like in mining, crushing and grinding, and agriculture industries (buckets, bucket teeth, mill hammers, ball mills, digging tools, conveyer screws, etc. [3,4]). Hardfacing is also used to control combinations of wear and corrosion, as encountered by mud seals, plows, knives in the food processing industry, pumps handling corrosive liquids, or slurries [5]. The hardfacing is considered as economical way to improve the performance of components submitted to severe wear conditions, with wide range of applicable filler materials [6,7].

The iron-based filler materials have drawn much attention due to their low cost and good resistance to abrasion in the hardfaced condition. However, their use is limited in applications where high impact loading is present, i.e. high-stress or gouging abrasion [8]. For this reason, efforts are being made towards the improvement of their impact and other properties [9]. The progress is achieved mostly by modifying the hardfaced coating's structure. Taking into account their low price and improved properties, the resistance to abrasive wear of the iron-based hardfaced coatings is normally tested against the resistance of proven, but more expensive materials, such as WC-based hardfaced coatings.

Abrasive wear has been defined as "wear by displacement of material from surfaces in relative motion caused by the presence of hard particles either between the surfaces or embedded in one of

them, or by the presence of hard protuberances on one or both of the surfaces" [10]. The second part of this definition corresponds to pure two-body abrasion, where tested material slides against harder and rougher counter face material, while the first part corresponds to the three- and two-body abrasion, respectively. Another interesting example of two-body abrasion is the abrasive erosion, which is the special case of erosive wear. Abrasive erosion has been defined as "erosive wear in which the loss of material from a solid surface is due to relative motion of solid particles which are entrained in a fluid, moving nearly parallel to a solid surface" [10]. Scratch test offers a possibility for comparison of different materials relatively easy and in short period of time, with good reproducibility [11]. In single-pass scratch test a stylus (which tip is made of hard material) slide over the test sample producing a single scratch, which seems to be appropriate simulation of the two-body abrasion.

In this study, the abrasive wear resistance of the three different hardfaced coatings (two iron-based and one WC-based) was investigated and compared.

2. EXPERIMENTAL DETAILS

2.1 Materials

The filler materials (coating materials) were manufactured by Castolin Eutectic Co. Ltd, Vienna. Their nominal chemical composition is shown in Table 1. The iron-based filler materials (basic covered electrodes) were deposited by using the shielded metal arc welding (SMAW) process. The WC-based filler material was deposited by oxy-fuel gas welding (OFW) process. The substrate material was the hot-rolled S355J2G3 steel.

Table 1. Coatings composition, process and hardness

Coating	Nominal chemical composition	Hardfacing process	Hardness HV 5
4541	Fe-Cr-C-Si	SMAW	739
5006	Fe-Cr-C-Si	SMAW	781
7888 T	WC-Ni-Cr-Si-B	OFW	677

All coatings were deposited by hardfacing in a single pass (one layer). The substrate preparation and hardfacing procedures (deposition parameters) are described elsewhere [9,12]. The measurements of near-surface hardness are performed on the cross-section of hardfaced samples by Vickers indenter (HV 5), and presented in (Table 1).

The samples for structure characterization are obtained by cutting the hardfaced materials perpendicular to coatings surface. The obtained cross-sections are ground with SiC abrasive papers down to P1200 and polished with alumina suspensions down to 1 μm. The polished surfaces are analyzed by using the scanning electron microscope (SEM) equipped with energy dispersive system (EDS). The SEM-EDS analysis was performed at University of Belgrade, Faculty of Mining and Geology by using the JEOL JSM–6610LV SEM connected with the INCA350 energy dispersion X-ray analysis unit. The electron acceleration voltage of 20 kV and the tungsten filament were used. Before SEM-EDS analysis was performed, polished surfaces were 20 nm gold coated in a vacuum chamber by use of a sputter coater device.

The Figure 1a shows the near-surface structure of the 4541 iron-based hardfaced coating. The primary austenite phase occupies more than a half of volume (50.7 vol. %) and the rest is the lamellar eutectic mixture of austenite and Cr-carbides [9]. The 5006 material during solidification achieves near-eutectic structure (Fig. 1b). A small spherical primary Cr-carbides are observed (9.1 vol. %) in the eutectic matrix. Based on Electron microprobe analysis (EMPA), both coatings 4541 and 5006 contain $(Cr,Fe)_7C_3$ primary and eutectic carbides. The Figure 1c shows a larger WC grains (60 vol. %), which are embedded in the Ni-Cr based matrix.

2.2 Scratch abrasion testing

Abrasive wear tests are carried out on the scratch tester under the dry conditions, in ambient air at room temperature (≈ 25 °C). A schematic diagram of scratch testing is presented in Figure 2. Stylus (indenter) was pressed with selected normal load

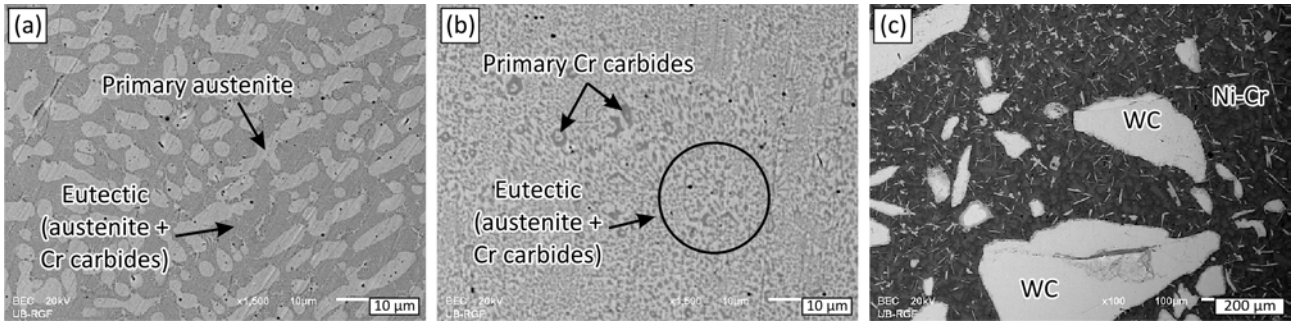

Figure 1. The structures (SEM) of: (a) 4541, (b) 5006 and (c) 7888 T hardfaced coating; back-scattered electron images

(10, 50 and 100 N) against surface of the test sample and moved with constant speed (4 mm/s), producing the scratch of certain width and length (10 mm) on the test sample. Indenter had Rockwell shape and the cone was diamond with radius of 0.2 mm.

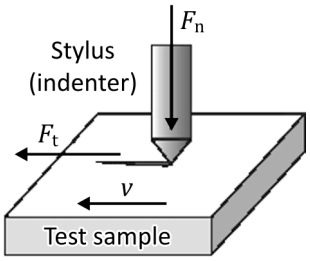

Figure 2. Schematic diagram of scratch testing

On surface of each material under investigation at least three scratches are made with a gap between scratches of at least 1 mm. Before and after testing, both the indenter and the test samples are degreased and cleaned with benzene. The wear scar widths on the surface of the test samples are measured from SEM images at the end of testing. The wear scar widths and the known indenter geometry are used to calculate the volume loss. After testing, the morphology of the test samples worn surfaces is examined with SEM.

3. RESULTS AND DISCUSSION

The results of the wear tests are presented in Figures 3, 4 and 5. Taking into account significant differences in structure homogeneity of the hardfaced coatings (Fig. 1), the repeatability of the results, in terms of standard deviations, is satisfactory (within 16 %). Wear rate of the tested materials (volume loss divided by scratch length) increases with normal loading, as expected. The highest wear exhibits coating 7888 T. Nevertheless, wear rates for all coatings are high, even for abrasive wear. The reason for this is primarily due to the experimental conditions.

The test conditions were specific, i.e. the speeds were very low (4 mm/s) and the contact stresses very high. At the end of test, the normal stresses were between 2 and 5 GPa, which depends on the material, i.e. scratch width and applied normal load. With these conditions, a high-stress or even gouging abrasion can be expected. With high-stress abrasion, the worn surface may exhibit varying degrees of scratching with plastic flow of sufficiently ductile phases or fracture of brittle phases. In gouging abrasion, the stresses are higher than those in high-stress abrasion, and they are accompanied by large particles removal from the surface, leaving deep groves and/or pits [8].

The relation between the wear rate and the hardness of tested hardfaced coatings is shown in Figure 6. The first feature is that the abrasive wear rate decreases as the hardness increases, i.e. the hardest material (coating 5006) showed the highest abrasive wear resistance.

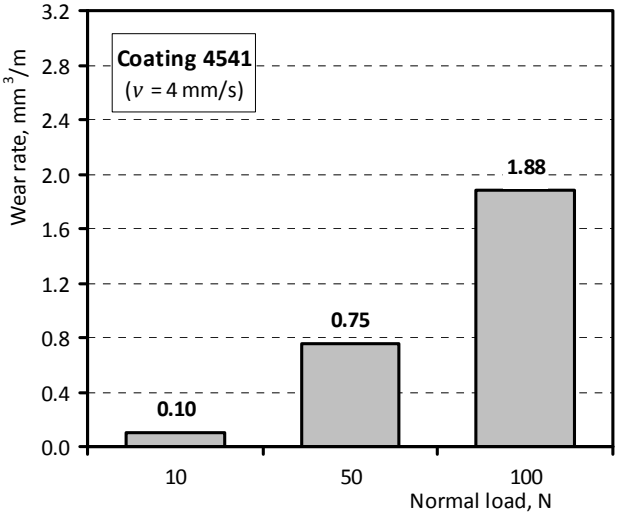

Figure 3. Wear rates of coating 4541 for different normal loads

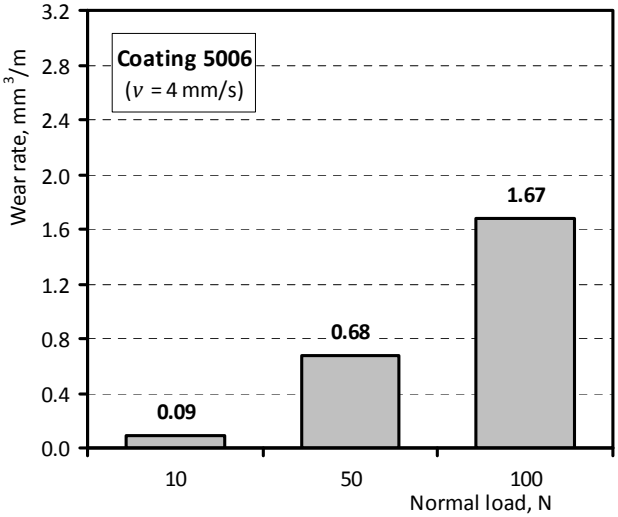

Figure 4. Wear rates of coating 5006 for different normal loads

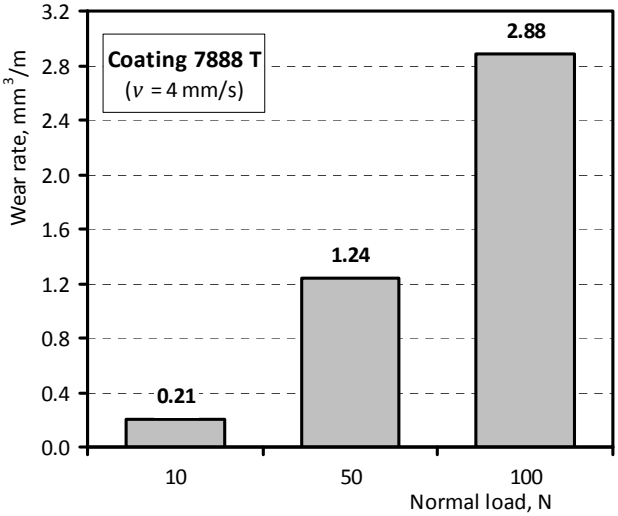

Figure 5. Wear rates of coating 7888 T for different normal loads

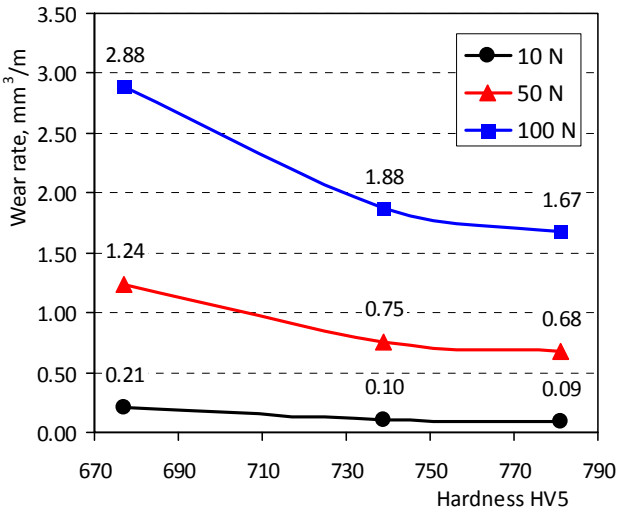

Figure 6. Wear rate vs. hardness of tested materials for different normal loads

For all applied loads, the relation between hardness and wear rate is non-linear. It is more curved for higher loads (Fig. 6). This is connected with the coatings structure and exhibited wear mechanism. Coatings 4541 and 5006 exhibit mainly ploughing abrasive wear (Fig. 7a), while coating 7888 T dominant type of abrasive wear is fracture (cracking) abrasive wear (Fig. 7b).

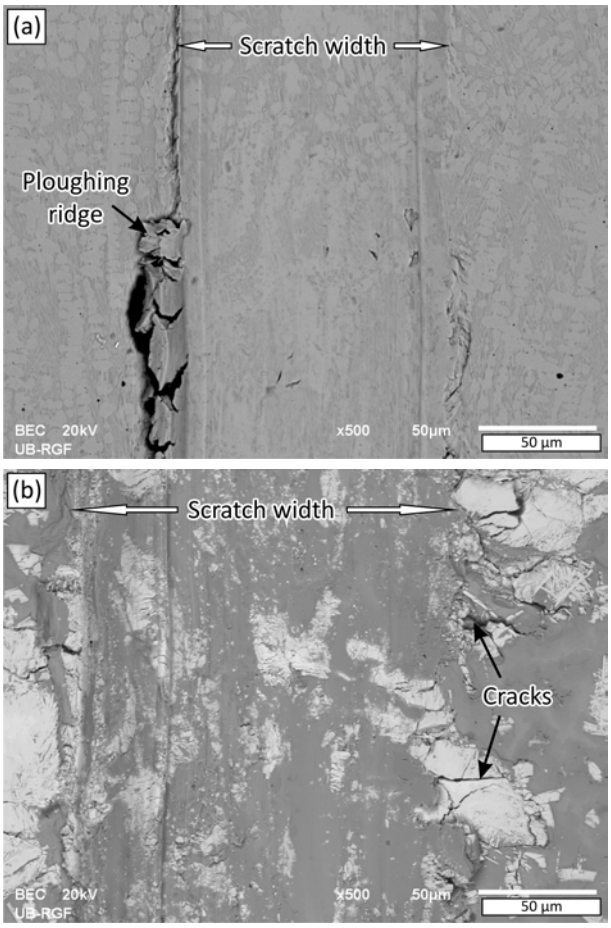

Figure 7. The wear scar appearance (SEM) of: (a) 4541 and (b) 7888 T hardfaced coating; 50 N normal load; back-scattered electron images

4. CONCLUSION

Scratch test offers relatively easy and quick comparison of different materials on abrasive wear.

Structure of tested coatings showed influence on the dominant type of abrasive wear, which together with coatings hardness determined coatings abrasive wear resistance.

Coatings with lower hardness showed lower abrasive wear resistance, but the dependence (hardness vs. wear rate) was non-linear.

In the case of iron-based coatings, dominant type of abrasive wear was ploughing and in the case of WC-based coatings, it was fracture (cracking) abrasive wear.

ACKNOWLEDGEMENT

This work has been performed as a part of activities within the projects TR 34028, TR 35021 and TR 35034. These projects are supported by the Republic of Serbia, Ministry of Education, Science and Technological Development, whose financial help is gratefully acknowledged.

REFERENCES

[1] A. Rac: *Osnovi tribologije*, Mašinski fakultet Univerziteta u Beogradu, Beograd, 1991.

[2] R.G. Bayer: *Fundamentals of wear failures*, in: *ASM Handbook Volume 11, Failure Analysis and Prevention*, ASM International, Metals Park, pp. 901-905, 2002.

[3] V. Lazić, M. Jovanović, D. Milosavljević, M. Mutavdžić, R. Čukić: *Choosing of the most suitable technology of hard facing of mixer blades used in asphalt bases*, Tribology in Industry, Vol. 30, No. 1-2, pp. 3-10, 2008.

[4] V. Lazić, M. Mutavdžić, D. Milosavljević, S. Aleksandrović, B. Nedeljković, P. Marinković, R. Čukić: *Selection of the most appropriate technology of reparatory hard facing of working parts on universal construction machinery*, Tribology in Industry, Vol. 33, No. 1, pp. 18-27, 2011.

[5] J.R. Davis, *Hardfacing, weld cladding, and dissimilar metal joining*, in: *ASM Handbook Volume 6, Welding, Brazing, and Soldering*, ASM International, Metals Park, pp. 789-829, 1993.

[6] EN 14700: *Welding consumables – Welding consumables for hard-facing*, European Committee for Standardization, Brussels, 2005.

[7] M. Šolar, M. Bregant: *Dodatni materijali i njihova upotreba kod reparaturnog navarivanja*, Zavarivanje i zavarene konstrukcije, Vol. 51, No. 2, pp. 71-76, 2006.

[8] A. Vencl, N. Manić, V. Popovic, M. Mrdak: *Possibility of the abrasive wear resistance determination with scratch tester*, Tribology Letters, Vol. 37, No. 3, pp. 591-604, 2010.

[9] B.R. Gligorijevic, A. Vencl, B.T. Katavic: *Characterization and comparison of the carbides morphologies in the near surface region of the single- and double layer iron-based hardfaced coatings*, Scientific Bulletin of the "Politehnica" University of Timişoara, Transactions on Mechanics, Vol. 57 (71), Special Issue S1, pp. 15-20, 2012.

[10] OECD, Research Group on Wear of Engineering Materials, *Glossary of Terms and Definitions in the Field of Friction, Wear and Lubrication: Ttribology*, Organisation for Economic Co-operation and Development, Paris, 1969.

[11] A. Vencl, A. Rac, B. Ivković: *Investigation of abrasive wear resistance of ferrous-based coatings with scratch tester*, Tribology in Industry, Vol. 29, No. 3-4, pp. 13-16, 2007.

[12] A. Alil, B. Katavić, M. Ristić, D. Jovanović, M. Prokolab, S. Budimir, M. Kočić: *Structural and mechanical properties of different hard welded coatings for impact plate for ventilation mill*, Welding & Material Testing, Vol. 20, No. 3, pp. 7-11, 2011.

Serbian Tribology Society

SERBIATRIB '13

13th International Conference on Tribology

Faculty of Engineering in Kragujevac

Kragujevac, Serbia, 15 – 17 May 2013

TOPOGRAPHIC AND ELECTROCHEMICAL TI6AL4V ALLOY SURFACE CHARACTERIZATION IN DRY AND WET RECIPROCATING SLIDING

Zinaida Doni[1], Mihaela Buciumeanu[2], Liviu Palaghian[3]

[1]"Dunarea de Jos" University of Galati, Romania, zinaida.doni@yahoo.com

[2]"Dunarea de Jos" University of Galati, Romania, mihaela.buciumeanu@ugal.ro

[3]"Dunarea de Jos" University of Galati, Romania, liviu.palaghian@ugal.ro

Abstract: *This present paper shows the behavior of functional integrity state of a TI6Al4V alloy under reciprocating wear sliding conditions in a comparative way for two different* counter *materials, steel and ceramic balls in dry and corrosive environment (3.5% NaCl). The surface integrity analysis of the dry reciprocating wear tests was based on the evolution of the roughness parameters with the applied load. In the case of reciprocating wear tests in corrosive environment the surface integrity analysis was based on electrochemical parameters. Comparative analysis of the evolution of the roughness parameters with the applied load shows a higher stability of the Ti6Al4V/Al_2O_3 contact pair, while from the point of view of the electrochemical parameters the tribological properties are worst than Ti6Al4V/steel ball contact pair.*

Keywords: *reciprocating wear, light alloy, roughness, surface integrity.*

1. INTRODUCTION

The required functional properties of the contact surfaces under relative motion are closely related to the surface integrity state. The modifications of the superficial layer during the machining process and subsequently during service life have an important role in defining the surface integrity state. Thus Griffiths [1] proposed to define the surface integrity state based the mechanical, chemical, metallurgical and topographical characteristics of the superficial layer and their relation to the functional performance.

Bellows and Tishler [2] stated that there are five types of modifications of the superficial layer during the machining process of a surface: mechanical, metallurgical, chemical, thermal and electrical. These characteristics are changing during the service life. Besides other functional characteristics, such as fatigue resistance, correlation between surface roughness parameters (*Ra, Rz, Rk,* etc.), and the wear rate has an important role during the friction processes of the contact surfaces under relative motion [3,4].

Thus the surface integrity state can be defined not only due to the machining processes of the surface, but also due to the operating processes. This can be called fuctional integrity state. Generally, it is intended that during the service life to maintain the same characterisics obtained from the machinig process or to have acceptable modifications.

The Ti6Al4V alloy is the most common titanium alloy due to its physical, chemical and mechanical properties, such as: high strength, low density, excellent machinability and excellent corrosive resistance. Some of the most widespread applications of these alloys include aircraft turbine engines, structural components and joints in aeronautics, structural elements in automotive and maritime constructions, medical devices (dental and orthopedic implants).

The spontaneously formation of a continue and strong adherent oxide layer in air and also water (e. g. the marine environment, body fluids) provides extensive use of these alloys.

Conventional ceramics materials such as alumina (Al_2O_3) have excellent properties, such as: high hardness and good wear resistance, excellent

dielectric properties, high resistance to chemical attack in presence of acids and alkali, high thermal conductivity, high resistance and stiffness, excellent formability and high purity. Due to these properties alumina is widely used in technical applications (e. g. automotive industry and in medical implants).

The general properties of the two types of materials (Ti6Al4V and Al_2O_3) have leaded to the use of these in applications where both wear and corrosion resistant qualities are critical. In these applications, especially under relative motion and under the action of external loads and in active chemical environments, it is mandatory to maintain the surface integrity state during the service life.

In the present paper is presented the evolution of the functional integrity state in a comparative way for two contact pairs (Ti6Al4V/Al_2O_3 and Ti6Al4V/steel ball) in dry and corrosive environment.

2. DRY WEAR AND TRIBOCORROSION FORMULATION

The analysis of the functional integrity state under dry wear conditions is based on the well known Archard's wear law [5]. It says that the amount of the material loss depends on the properties of the contact surfaces, topographical characteristics of the surfaces and test conditions. The most common form of Archard's equation is

$$\frac{V}{S} = K\frac{F_n}{H} \tag{1}$$

where V - the volumetric material loss of the body, K- the wear coefficient (it is dimensionless and always less than unity), H - the hardness of the softer body in contact, F_n - the applied normal load and S - the sliding distance.

It has been analysed the amonut of material that was removed (wear loss) in the wear process. The surface analysis of the wear tests was based on the evolution of the depth of the wear track (based on the material loss) with the applied load. Another parameter that was analyzed is the final topography of the wear track by using the 3D roughness parameters (*Sa* – Average Roughness, *Sy* - Peak-Peak Height, *Sq* - Root Mean Square Height, *Sp* - Maximum Peak Height, *Sv* - Maximum Pit Height).

In the case of reciprocating wear tests in corrosive enviroment occur the degradation processs of surfaces by tribocorrosion. This process includes the interaction between mechanical, chemical and electromechanical processes of wear that lead to loss of weight by **adding all these effects [6]:**

Wear=mechanical wear process+electrochemical (and/or chemical response) (2)

This process includes the interaction of corrosion with: solid corrosive particles (debris), particles resulted due to abrasive processes, fretting processes, processes under biological solution conditions, and triboxidation related to the mutual interaction process under relative motion conditions of the surfaces.

Generally, oxide layers are formed after the corrosive attack which protects the material from further corrosive attack. But these oxide films are susceptible to the tribological processes that will accelerate the corrosion in these areas. The galvanic activity that results between the worn and unworn surfaces under electrochemical conditions [7], leads to an anodic current I_a, [8]:

$$I_a = k_b \cdot l \cdot f \cdot \left(\frac{F_n}{H}\right)^{1/2} \cdot \int_0^{1/f} i \cdot d\tau \tag{3}$$

where: k_b – proportionality factor; l – sliding length; f– frequency of the reciprocating motion; F_n – normal load; H– surface hardness; i - corrosion current density; τ- time.

Equation (3) can be written as [9]:

$$I_p = k_b \cdot V_s \cdot \left(\frac{F_n}{H}\right)^{1/2} \cdot Q_p \tag{4}$$

where: V_s – sliding speed; Q_p - passivation charge density [5].

$$Q_p = \int_0 i_{corr} \cdot d\tau \tag{5}$$

On the other hand, electrochemical wear can be determined based on passivation current

$$V = \frac{I_p \cdot t \cdot M_{mol}}{n \cdot \rho \cdot F} \tag{6}$$

where: t – time; M – molecular weight; ρ – density; n – valence; I – Faraday's constant.

The corrosion rate [10,11] can be determined based on linear polarization and on the Stern-Geary's equation [12] as follows:

$$i_{corr} = \frac{\beta_a \cdot \beta_c}{2.3(\beta_a + \beta_c)} \cdot \frac{1}{R_p} \tag{7}$$

where: β_a şi β_c cathodic and anodic Tafel slopes (figure 1); R_r – polarisation resistance.

Thus the tribocorrosion processes can be analysed based on the evolution of the electrochemical parameters β_a, β_c, I_{corr}, E_{corr}..

If in the dry wear conditions the amount of the material loss is determined based on the ration F_n/H, in the case of wear tests in the corrosion environment conditions the wear process is influenced by the electrochemical parameters.

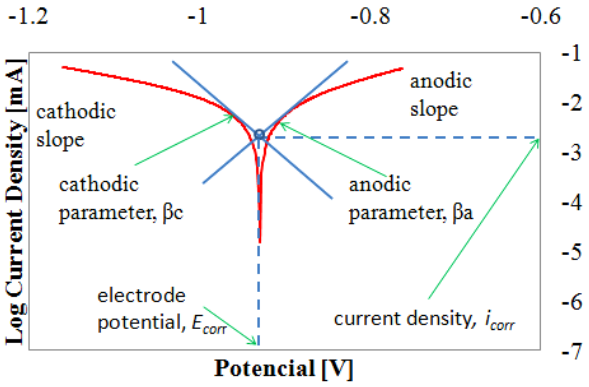

Figure 1. Typical plot derived by the Tafel extrapolation method

3. EXPERIMENTAL PROCEDURE

3.1. Materials

The material contact pairs comparatively studied in this work are: Ti6Al4V/Al_2O_3 and Ti6Al4V/steel ball.

The mechanical properties of the materials used in this study are presented in Table 1 and their chemical composition is given in Tables 2 and 3.

Table 1. Mechanical properties of Ti6Al4V alloy

Material	Mechanical properties				
	E (GPa)	$\sigma_{0.2}$ (MPa)	σ_r (MPa)	ε_r (%)	HV
Ti6Al4V	115	989	1055	16,1	360
Al2O3 (96%)	300	-	2200		1100
100Cr6	210	1034	1158	15	750

Table 2. Chemical composition (weight %) of Ti6Al4V alloy

Elements	Al	V	Fe	Sn	Ni
Ti6Al4V	6.1	4.21	0.2	0.003	0,01

Table 3. Chemical composition (weight %) of 100Cr6

Elements	C	Si	Mn	P	S	Cr	Mo
100Cr6	0.93	0,15	0.25	0.026	0.15	1.35	0.10

3.2. Experimental test set-up

Reciprocating dry wear tests were carried out on a tribometer type CETR PRO 5003D. The experiments were carried out at a frequency of 1 Hz and the total stroke length of 3 mm during 3h, using a reciprocating ball-on-plate configuration. Bearing steel and Al_2O_3 balls of 8 mm diameter were used as counterpart. The experiments were carried out at three normal loads 100, 120 and 140 N. Figure 4 presents the schematic test configuration.

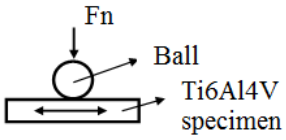

Figure 2. Schematic specimen-pad contact test configuration (F_n - normal load)

The surface roughness parameters were determined using a 3D profilometer type CETR PRO500. The roughness parameters were obtained by scanning a surface of 500x500 µm, in 200 point on each line. Multiple measurements in different areas on the wear track were carried out to obtain stable roughness values that can be representative for entire wear track. The 3D images were analyzed by using a processing image soft - Scanning Probe Imagine Processor (SPIP). The 3D roughness parameters used to describe the surface features are *Sa* – Average Surface Roughness, *Sy* - Peak-Peak Height, *Sq* - Root Mean Square Height, *Sp* - Maximum Peak Height, *Sv* - Maximum Pit Height. The initial surface roughness parameters studied were *Sa* =0.14 µm; *Sy* =3.96 µm; *Sq* =0.18 µm; *Sp* =3.34 µm; *Sv* =0.63 µm.

In corrosive conditions the reciprocating wear tests were carried out under the same conditions, with the contact pairs immersed in the electrolyte - an aqueous solution of 3.5% NaCl (figure 3). The electrochemical characteristics were obtained with a potentiostatic assembly.

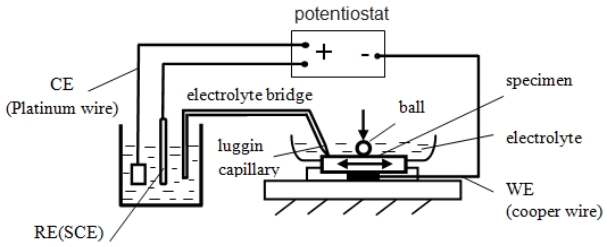

Figure 3. Schematic of the corrosion wear method

4. EXPERIMENTAL RESULTS AND DISCUSSIONS

Figure 4 shows the profiles of the wear track at the end of the test for Ti6Al4V/steel ball contact pair for the three normal loads used in this study.

Figure 5 shows the evolution of the weight loss with increasing applied normal load for both contact pairs.

Regarding the functional integrity in terms of variation with the applied load it is remarked the equivalent level of the weight loss of the steel ball at higher loads (120-140 N) (figs. 4 and 5).

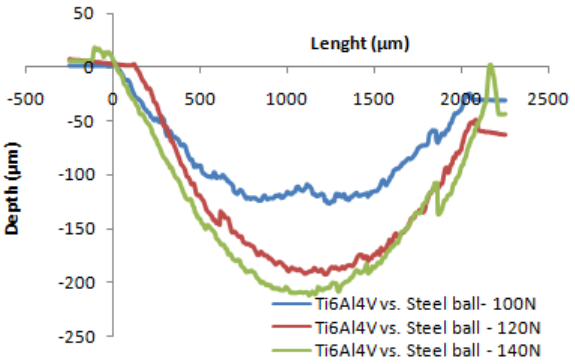

Figure 4. Evolution of the profiles with the applied normal load

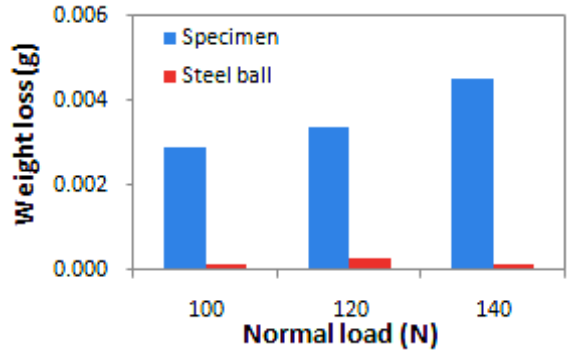

a

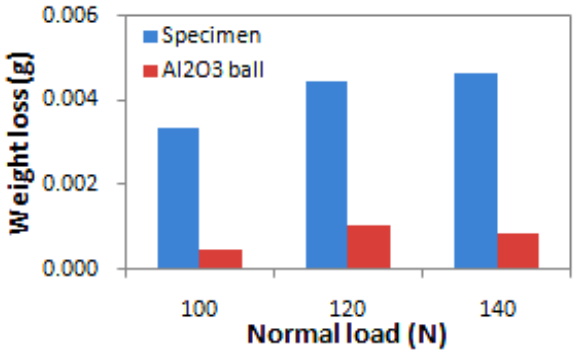

b

Figure 5. Evolution of the weight loss with increasing applied normal load: a Ti6Al4V/Al2O3 and b. Ti6Al4V/steel ball

On the other hand, in the case of Ti6Al4V/Al_2O_3 contact pair can be observed that the weight loss of the alumina ball increases with increasing applied normal load (figure 5b).

In the case of Ti6Al4V/Al_2O_3 contact pair can be observed a constant variation of the weight loss of the alumina ball counterpart (figure 5a) while in the case of Ti6Al4V/steel ball to the steel ball counterpart (figure 5b). Also, the weight loss was higher is the case of the steel ball counterpart compared to the alumina ball counterpart.

The evolution of the roughness parameters with increasing applied normal load over the functional integrity (figure 6) shows that in the case of Ti6Al4V/steel ball contact pair the roughness parameter, *Sv*, was slightly influenced by the modification of the applied normal load.

In the case of Ti6Al4V/Al_2O_3 contact pair the roughness parameters that changed with increasing applied normal load are *Sa* (figure 6a), *Sq* (figure 6b) şi *Sy* (figure 6c).

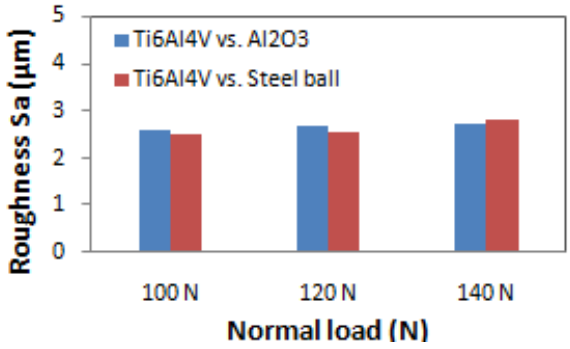

a

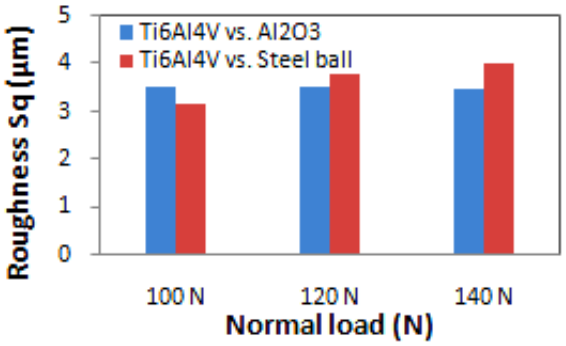

b

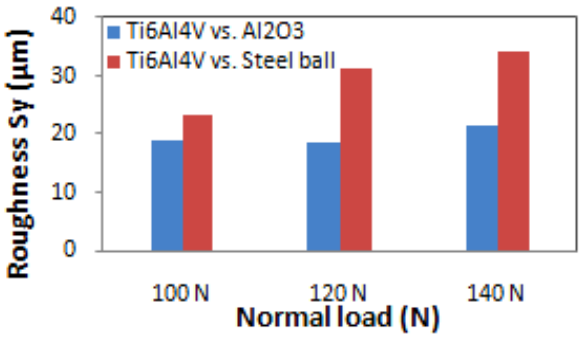

c

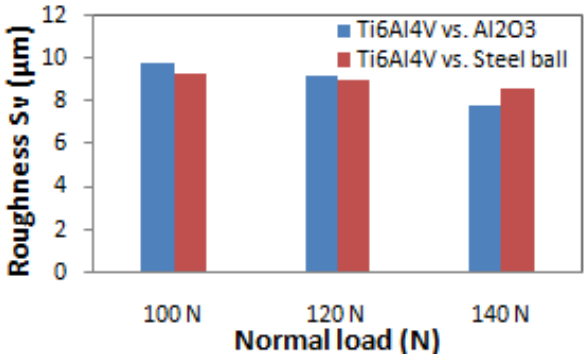

d

Figure 6. Evolution of the roughness parameters with increasing applied normal load

Although the average roughness parameter *Sa* is commonly used in the analysis of the evolution of surface topography, it does not allow to characterize the influence of roughness over the degradation process of a surface or the load level over the evolution of surface topography [13].

The roughness parameter, *Sv*, (Maximum Valley Depth) is closely related to load level. In this case (figure 6d) the constant evolution of this parameter for Ti6Al4V/steel ball contact pair indicates a low affinity of the titanium alloy to the bearing steel.

Similarly can be remarked the affinity of the titanium alloy to ceramic materials (Al_2O_3).

The evolution of the roughness parameter *Sq* (Root Mean Square) gives indications about the degree of flattening of the profile. It was observed a constant flattening level in the case of Ti6Al4V/Al_2O_3 contact pair. It gives indications about the dimensional stability of this material pairs, and consequently the possibility to use this over a long period.

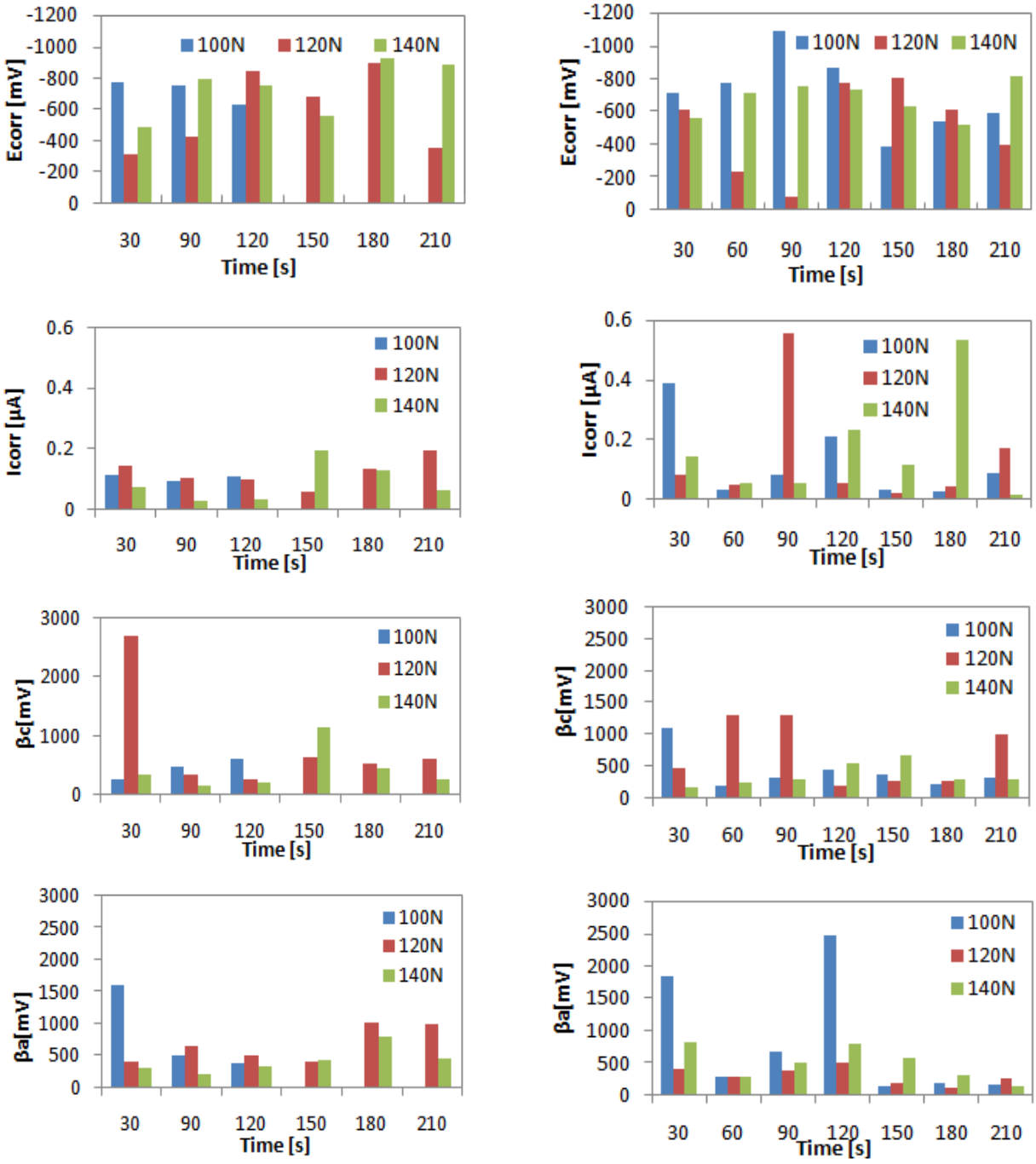

Figure 7. Evolution of the electrochemical parameters: a. Ti6Al4V/Al_2O_3 and b. Ti6Al4V/steel ball

The evolution of the roughness parameter *Sy* (Peak-Peak Height) (figure 6c) refers to the interdependence between surface roughness and its image. This is based mainly on the functional

dependence of roughness height and grey level image of surface, which means that the higher parts of the asperities correspond to higher intensity pixels. Also this parameter indicates the stability of the surface conditions with increasing normal load. This leads to a longer stability of the initial surface conditions during the service life of Ti6Al4V/Al_2O_3 contact pair. The evolution of previous mentioned roughness parameters shows that in terms of surface quality and functional maintenance the Ti6Al4V/Al_2O_3 contact pairs present a higher functional integrity level.

Figure 7a and b shows the evolution of the electrochemical parameters for both contact pairs.

The functional integrity of the tests in corrosive environment for both material pairs indicated differences in the evolution of the electrochemical parameters that characterize the electrochemical state of the contact surfaces.

Thus, in the case of Ti6Al4V/Al_2O_3 contact pair (figure 7a) at low load levels (100N) the electrochemical parameters E_{corr} and I_{corr} do not change much with time. Parameters β_a and β_c have significant variation, with an increasing tendency for β_c and a decreasing tendency for β_a. The increase of the applied load changes the evolution of those parameters with time. These will have an oscillatory tendency. In the case of Ti6Al4V/steel ball can be observed a more pronounced oscillatory evolution of all electrochemical parameters with time (figure 7b) at higher load levels than for Ti6Al4V/Al_2O_3 contact pair (except for the evolution of parameter β_c).

The analysis from the functional integrity point of view based on electrochemical criterions indicates a higher integrity level of Ti6Al4V/Al_2O_3 contact pair.

Figure 8 shows the evolution of coefficient of friction with the sliding distance in the case of dry reciprocating wear tests.

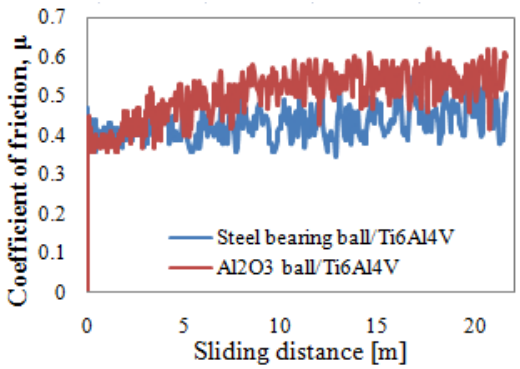

Figure 8. Evolution of the coefficient of friction with the sliding distance for dry reciprocating wear tests

Figure 9 shows the evolution of coefficient of friction with the sliding distance in the case of reciprocating wear tests in corrosive environment for both contact pairs.

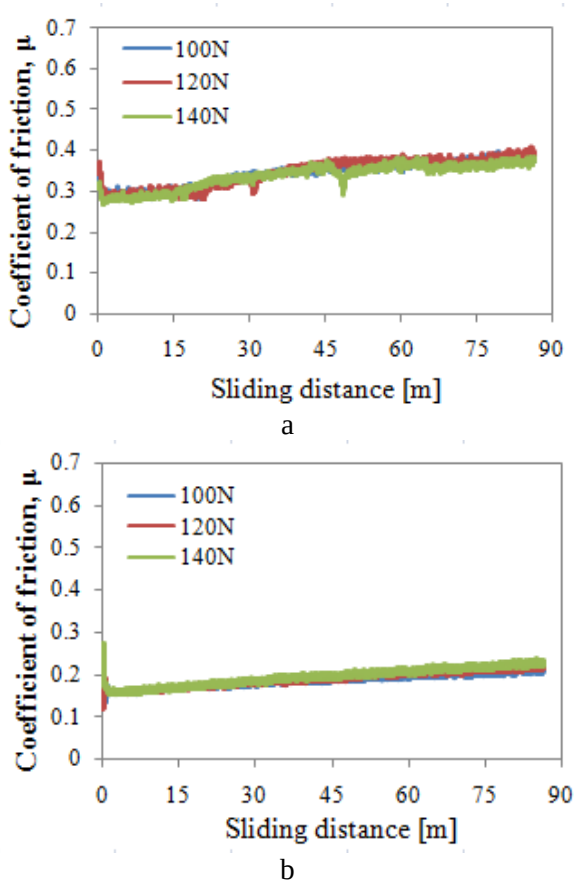

Figure 9. Evolution of the coefficient of friction with the sliding distance for reciprocating wear tests in corrosive environment: a. /Ti6Al4V/Al2O3 and b. Ti6Al4V/steel ball

The variation of COF for dry reciprocating wear conditions (figure 8) is similar for both contact pairs used in this study. The COF has a slight higher value in the case of Ti6Al4V/Al_2O_3 than Ti6Al4V/steel ball contact pairs.

Also in the case of reciprocating wear in corrosive environment the variation of COF is similar for both contact pairs. The COF was not influenced by the load level. The Ti6Al4V/steel ball (figure 9b) contact pair showed a more stable evolution of the COF at a low level than in the case of Ti6Al4V/Al_2O_3 contact pair (figure 9a).

5. CONCLUSION

This present paper showed the behavior of a TI6Al4V alloy under reciprocating wear sliding conditions in a comparative way for two different counter materials, bearing steel and ceramic balls (Al_2O_3 - 99.6%) in dry and corrosive environment (an aqueous solution of 3.5% NaCl). It aimed to highlight the tribological characteristics that shows invariability during the test and provides a high level of functional integrity of the surface.

The conclusions drawn from this work are as follows:

- in dry condition the Ti6Al4V/Al_2O_3 contact pair showed a high functional integrity degree of the surfaces in terms of surface quality, characterized by roughness parameters *Sa*, *Sq* and *Sy*, while for the Ti6Al4V/steel ball based on the roughness parameter *Sv*;

- in the case of Ti6Al4V/steel ball contact pair a better functional integrity (evaluated based on the weight loss) occurred for higher applied loads than in the case of lower loads;

- from the point of view of the electrochemical behavior a higher functional integrity occurs in the case of Ti6Al4V/Al_2O_3 contact pair at lower applied loads (assessed through parameters E_{corr} and I_{corr});

- the electrochemical parameters for Ti6Al4V/Al_2O_3 contact pair are at a lower level than those of the Ti6Al4V/steel ball contact pair;

- the evolution of the roughness parameters and the structural affinity between TI6Al4V alloy and the bearing ball conduced to a higher functional integrity level from the point of view of the evolution of COF by comparison to Ti6Al4V/Al_2O_3 contact pair.

REFERENCES

[1] B. Griffiths, *Manufacturing Surface Technology-Surface Integrity and Functional Performance*, Prenton Press, 2001.

[2] G. Bellows, D. N. Tisher, *Introduction to surface Integrity Report TM70-974*, Cincinnati: General Electric Co., 1970.

[3] N. Aris, K. Cheng, *Characterization of the surface functionality on precision machined engineering surfaces*, International Journal of Advanced Manufacturing, Vol. 38, pp. 402-409, 2008.

[4] I.S. Jawahir, E. Brinksmeier, R. M'Saoubi, D.K. Aspinwall, J.C. Outeiro, D. Meyer, D. Umbrello, A.D. Jayal, *Surface integrity in material removal processes: Recent advances*, CIRP Annals - Manufacturing Technology, Vol. 60, pp. 603–626, 2011.

[5] J.F. Archard, *Wear theory and mechanisms*. In: M.B. Peterson, W.O. Winer, Wear Control Handbook. ASME, 1980.

[6] R. J. K. Wood, *Tribo-corrosion of coatings: a review*, J. Phys. D: Appl. Phys., Vol. 40**,** pp. 5502–5521, 2007.

[7] P. Ponthiaux, F. Wenger, D. Drees, J.P. Celis, *Electrochemical techniques for studying tribocorrosion processes*, Wear, Vol. 256, pp. 459–468, 2004.

[8] S. Mischler, S. Debaud, D. Landolt, *Wear-accelerated corrosion of passive metals in tribocorrosion systems,* Journal of the Electrochemical Society, Vol. 145, pp. 750-758, 1998.

[9] J. Perret, *Modélisation de la tribocorrosion d'aciers inoxydables dans l'eau à haute pression et haute température***,** Thèse No 4727 (2010) École Polytechnique Fédérale De Lausanne.

[10] S. Feliu, J. A. Gonzalez, S. Miranda, *Possibilities and Problems of in Situ Techniques for Measuring Steel Corrosion Rates in Large Reinforced Concrete Structures*, Corrosion Science, Vol. 47, pp. 217-238, 2005.

[11] H. H. Uhlig, R. W. Revie, *Corrosion and Corrosion Control*, 3rd Edition, John Wiley and Sons, New York, 1985.

[12] M. Stern, A. L. Geary, *Electrochemical Polarization, A Theoretical Analysis of the Shape of Polarization Curves*, Journal of Electrochemical Science, Vol.104, pp. 56-63, 1957.

[13] V. Mereuta, M. Buciumeanu, L. Palaghian, *3D Roughness Parameters as Factors in Determining the Evolution of Effective Stress Concentration Factors in Fatigue Processes*, Applied Mechanics and Materials Vol. 248, pp 504-510, 2013.

Serbian Tribology Society

SERBIATRIB '13

13th International Conference on Tribology

Faculty of Engineering in Kragujevac

Kragujevac, Serbia, 15 – 17 May 2013

FRICTION COEFFICIENT OF UHMWPE DURING DRY RECIPROCATING SLIDING

Fatima Živić[1], Miroslav Babić[1], Slobodan Mitrović[1], Dragan Adamović[1], Svetlana Pelemis[2]

[1]Faculty of Engineering, University of Kragujevac, Serbia, zivic@kg.ac.rs, babic@kg.ac.rs, boban@kg.ac.rs, adam@kg.ac.rs

[2]Faculty of Technology in Zvornik, University of East Sarajevo, Bosnia and Herzegovina, alannica@gmail.com

Abstract: *This paper deals with the friction coefficient behaviour during dry reciprocating sliding of UHMWPE in contact with alumina (Al2O3), within a range of velocities typical for hip implants. Five values of normal force (100 - 1000 mN) and three values of sliding speed (4 - 12 mm/s) have been observed. Real time diagrams of the friction coefficient as a function of the sliding cycles were recorded for each test. Dynamic friction coefficient curves exhibited rather uniform behavior for all test conditions. Somewhat larger values of friction coefficient could be observed during the running-in period in case of low loads (100-250 mN) and the lowest velocity (4 mm/s). In case of high loads and speeds, friction coefficient reached steady state values shortly after the beginning of the test.*

Keywords: *UHMWPE, Dynamic friction coefficient, Reciprocating sliding.*

1. INTRODUCTION

Ultra-high molecular weight polyethylene (UHMWPE) is a unique polymer with outstanding physical and mechanical properties. Most notable are its chemical inertness, lubricity, impact resistance, and abrasion resistance. The first clinical application of UHMWPE biomaterials started in 1962 and continued with astonishing speed through the three decades of the clinical history (1962–1997), with a few clinically relevant innovations occurred beyond the removal of calcium stearate and changes in sterilization practice. Radiation crosslinked UHMWPE materials had been recently introduced to clinical practice around a year 2000. Today, second generation of radiation crosslinked materials are in clinical use, and vitamin E stabilized UHMWPE has emerged as a new, internationally standardized biomaterial.

At the November 2012 ASTM Meeting in Atlanta, GA, the UHMWPE working group considered revisions to four UHMWPE-related standards, including F648 (unfilled UHMWPE homopolymer), F2102 (FTIR analysis of oxidation), F2565 (Guide for Crosslinked UHMWPEs), and a new standard for small punch testing of medical polymers, including UHMWPE, based on F2183. The next ASTM meeting of the UHMWPE working group will be in May, 2013.

All existing data on UHMWPE indicate that for very elderly patients, artificial joints incorporating conventional UHMWPE will continue to be used. On the other hand, the more recently-introduced alternative bearing technologies, including crosslinked UHMWPE, should provide the greatest benefit to young patients (less than 60 years in age) who lead an active lifestyle and who need a total hip replacement. For patients in need of knee arthroplasty, shoulder arthroplasty, or total disc replacement, conventional UHMWPE continues to prevail as the polymeric bearing material of choice.

Polymers are large molecules synthesized from smaller molecules, called monomers. Plastics are polymers that are rigid solids at room temperature and generally contain additional additives. UHMWPE has been used as a bearing surface, in total joint prostheses, for more than 45 years.

Each year, about 2 million joint replacement procedures are performed around the world, and the majority of these joint replacements incorporate UHMWPE. Despite the success of these restorative procedures, orthopedic and spine implants have only a finite lifetime. Wear and damage of the UHMWPE components has historically been one of

the factors limiting implant longevity. In the past 10 years, highly crosslinked UHMWPE biomaterials have shown dramatic reductions in wear in clinical use around the world. The orthopedic community awaits confirmation that these reductions in wear will be associated with improved long-term survival, as expected.

UHMWPE has been used for fabricating one of the bearing components in various arthroplasties, such as acetabular cups, acetabular cup liners, tibial inserts, etc. [1, 2]. Total joints with components made of this material can function for more than twenty years if they are well designed and well implanted. Components made of UHMWPE have performed admirably in vivo. The only major concern is wear and the effect of the wear particles on the in vivo longevity of the prosthesis. Some applications of UHMWPE in biomedical area are shown in Fig. 1.

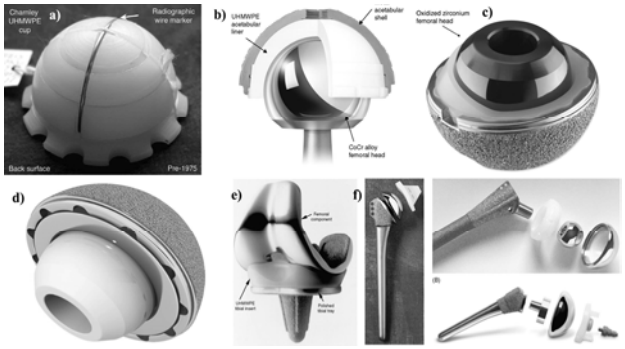

Figure 1. Application of UHMWPE [1]: a) cup; b), c), d) liners; e) total knee components; f) shoulder prosthesis system components.

Polyethylene contains the chemical elements carbon and hydrogen. Polyethylene is created through polymerization of ethene (Fig. 2), forming an extremely long, chained molecule called generally polymer. At a molecular level, the carbon backbone of polyethylene can twist, rotate, and fold into ordered crystalline regions.

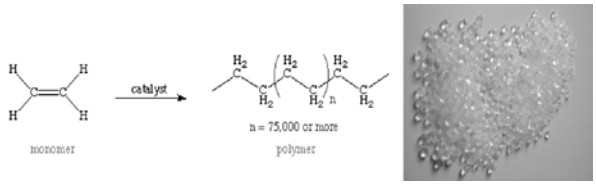

Figure 2. Left: The repeating unit of polyethylene; Right: Granulated polyethylene.

At a supermolecular level, the UHMWPE consists of powder (also known as resin or flake) that must be consolidated at elevated temperatures and pressures to form a bulk material. Further layers of complexity are introduced by chemical changes that arise in UHMWPE due to radiation sterilization and processing.

The mechanical properties of polyethylene improve slowly with rising molecular weight of the product. A dramatic change in mechanical properties, however, appears when molecular weight of the polyethylene molecule exceeds one million. This appears when more than 35000 ethylene groups are added together. Such product is called Ultra High Molecular Weight PolyEthylene. The molecular weight of the UHMWPE currently used in total joint components varies between 4 to 6 millions. Every such UHMWPE molecule is composed of 160 to 215 000 ethylene groups.

The molecular chain of UHMWPE can be visualised as a tangled string of spaghetti over a kilometer long. Because the chain is not static, but imbued with internal (thermal) energy, the molecular chain can become mobile at elevated temperatures. When cooled below the melt temperature, the molecular chain of polyethylene has the tendency to rotate about the C-C bonds and create chain folds. This chain folding, in turn, enables the molecule to form local ordered, sheetlike regions known as crystalline lamellae. These lamellae are embedded within amorphous (disordered) regions and may communicate with surrounding lamellae by tie molecules. The lamellae are on the order of 10–50 nm in thickness and 10–50 μm in length. UHMWPE has a white, opaque appearance at room temperature. At temperatures above the melt temperature of the lamellae, around 137°C, it becomes translucent. UHMWPE exhibits the composite nature due to interconnected network of amorphous and crystalline regions.

Generally speaking, many polymers undergo three major thermal transitions: the glass transition temperature (Tg), the melt temperature (Tm), and the flow temperature (Tf). The glass transition (Tg) is the temperature below which the polymer chains behave like a brittle glass. Below Tg, the polymer chains have insufficient thermal energy to slide past one another, and the only way for the material to respond to mechanical stress is by stretching (or rupture) of the bonds constituting the molecular chain. In UHMWPE, the glass transition occurs around 120°C.

UHMWPE shows two key features, the first one is the peak melting temperature (Tm), which occurs around 137°C and corresponds to the point at which the majority of the crystalline regions have melted. The melt temperature reflects the thickness of the crystals as well as their perfection. Thicker and more perfect polyethylene crystals will tend to melt at a higher temperature than smaller crystals.

As the temperature of a semicrystalline polymer is raised above the melt temperature, it may undergo a flow transition and become liquid.

Polyethylenes with a molecular weight of less than 500,000 g/mol can be observed to undergo such a flow transition (Tf). However, when the molecular weight of polyethylene increases above 500,000 g/mol, the entanglement of the immense polymer chains prevents it from flowing. UHMWPE does not exhibit a flow transition for this reason.

UHMWPE is a linear, low-pressure, polyethylene resin. It has both the highest abrasion resistance and highest impact strength of any plastic. Combined with abrasion resistance and toughness, the low coefficient of friction of UHMWPE yields a self-lubricating, non-stick surface. Static and dynamic coefficients are significantly lower than steel and most plastic materials. Elastic modulus of UHMWPE is approximately 0.69 GPa. ASTM F648-00 defines standard specification for Ultra-High-Molecular-Weight Polyethylene powder and fabricated form for surgical implants. To date it has proven to be the best polymer material for use in total joints.

Along with the extensive application of UHMWPE, the understanding of polymer tribology is becoming increasingly important. Many authors have investigated different aspects of tribological performance of UHMPWE [2-7]. The structural factors associated with surface mechanical properties (crosslinking, oxidation state, local orientation of polymer, crystallinity, etc.) can be highly variable and localized and may vary on micron spatial scales or smaller [8]. The relationship between UHMWPE mechanical properties and the in-vivo performance of a fabricated form has not been determined. While trends are apparent, specific property-polymer structure relationships are not well understood. The mechanical properties are subject to variation as the fabrication process variables (such as temperature, pressure, and time) are changed. [ASTM F-648 (2000)].

Reciprocating sliding at different test devices and from different aspects has been a subject of investigations [9-11]. Different approaches for improvement of existing UHMWPE materials have been tried. [10] investigated effects of nitrogen ion irradiation on tribological properties. [9] investigated friction and wear behavior of ultra-high molecular weight polyethylene as a function of polymer crystallinity. [2, 7, 8, 13, 14, 15] investigated crosslinking and material behavior with different approaches to crosslinking.

This paper deals with friction coefficient behaviour during dry reciprocating sliding of UHMWPE in contact with alumina (Al2O3), within a range of velocities typical for hip implants. Five values of normal force and three values of sliding speed have been observed.

2. MATERIALS AND TRIBOLOGICAL TEST

Polished rectangular flat UHMWPE samples were used for tests, supplied by the company Narcissus Ada, Serbia. Sliding tests were done at ball-on-flat configuration of CSM Nanotribometer in dry conditions. Alumina was used as a ball material (diameter, 1.5 mm), since it is extremely hard and chemically inert. Alumina is frequently used in combination with UHMWPE in artificial hip joints. Duration of each test was 3000 cycles (1 cycle, 1.6 mm), which is enough to reach stabile steady state of friction coefficient. During the test, the dynamic friction coefficients were recorded in real time, using the built-in TriboX 2.9.0 software. Five values of normal force (100 - 1000 mN) and three values of sliding speed (4 - 12 mm/s) have been tested. Maximum elastic contact stress (according to applied normal loads) were calculated by Hertz method and compared to test conditions. Characteristics of conducted tribological tests are given in Table 1.

Table 1. Tribological parameters.

Normal load values, F_n	100 mN, 250 mN, 500 mN, 750 mN, 1000 mN
Maximum elastic contact stress (according to applied normal loads)	28.5 MPa, 38.6 MPa, 48.7 MPa, 55.7 MPa, 61.3 MPa
Maximum linear speed values, v	4 mm/s; 8 mm/s; 12 mm/s

3. RESULTS AND DISCUSSION

Real time diagrams of the friction coefficient as a function of the sliding cycles (sliding distance) were recorded for each test. Friction coefficient curve is of sinusoid shape, whereat the opposite directions are marked with + and - sign, denoting coefficient of friction in two different directions of sample moving. Good agreement with reported values of friction coefficient was obtained [6, 16, 17, 18].

Dynamic friction coefficient curves exhibited rather uniform behavior for all test conditions (Fig.3). Somewhat larger values of friction coefficient could be observed during the running-in period in case of low loads (100-250 mN) and the lowest velocity (4 mm/s), as shown in Fig. 3a. In case of high loads and speeds, friction coefficient reached steady state values shortly after the beginning of the test. Maximum contact pressures in these tests were approximately from 30 - 60 MPa, representing high contact stresses exhibited in hip/knee implants. Especially extreme loading conditions are present in the knee implant system. Similar behavior (short running-in phase for the friction coefficient) was also reported by other authors [18].

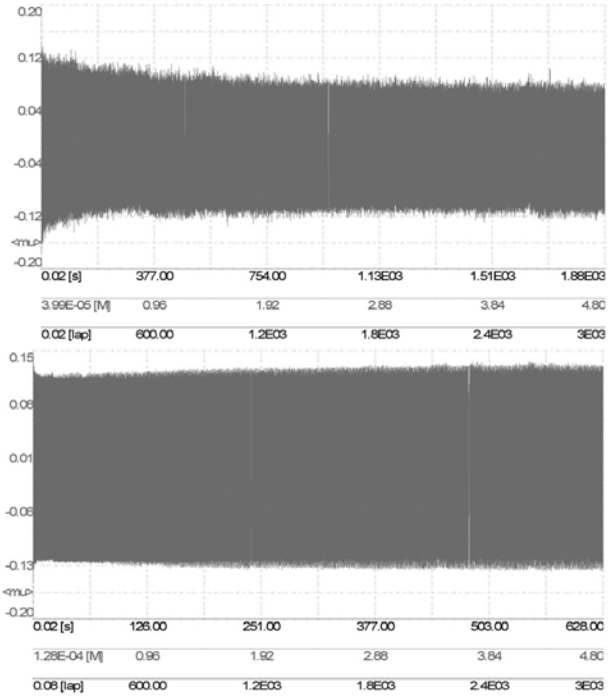

Figure 3. Dynamic friction coefficient curve during dry sliding: a) v=4 mm/s, F_N=100mN; b) v=12 mm/s, F_N=1000mN.

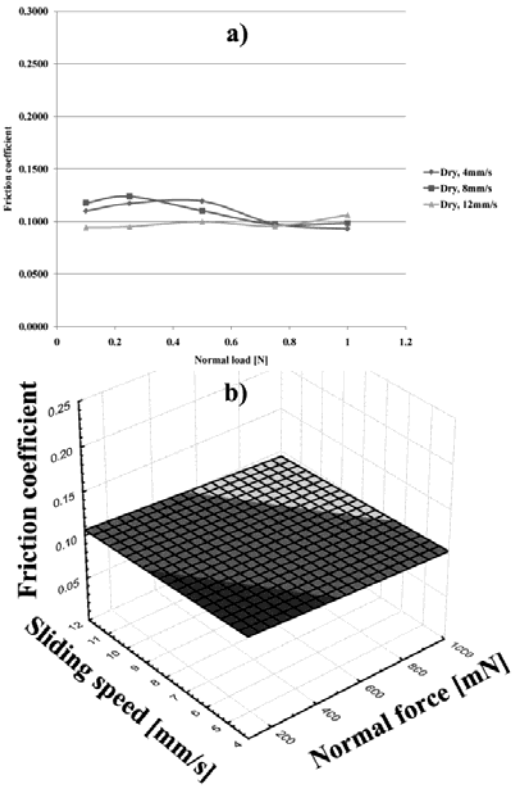

Figure 4. a) Friction coefficient as a function of the normal load; b) Friction coefficient as a function of the normal load and sliding speed.

An average value of the dynamic coefficient of friction (denoted by 'friction coefficient' further in the text) was calculated, for all test conditions, for a steady state period of friction, as the root mean square function using the raw data obtained by the nanotribometer. Comparative diagrams of variation of the average values of the dynamic friction coefficient, with load and sliding speed, are given in Fig. 4. It can be seen from presented diagrams that the sliding speed exhibited no significant influence on the friction coefficient. Load increase produced very slight decrease of the friction coefficient, for all tested conditions.

4. CONCLUSION

This research showed that UHMWPE exhibits low dynamic friction coefficient (average value around 0.1 for all tests) under dry conditions, in contact with alumina. It also showed that low loads leaded to a bit longer running-in time, but for all tests steady friction state was achieved and maintained throughout the test with very short running-in periods. Sliding speed change showed no influence on the dynamic friction coefficient.

ACKNOWLEDGMENTS

This paper is supported by TR-35021 project, financed by the Ministry of Education, Science and Technological Development of the Republic of Serbia.

REFERENCES

[1] S.M. Kurtz: *UHMWPE Biomaterials Handbook*, Elsevier, London, 2009

[2] G. Lewis: Properties of crosslinked ultra-high-molecular-weight polyethylene, Biomaterials, Vol. 22, pp. 371-401, 2001.

[3] S.W. Zhang: *State-of-the-art of polymer tribology*, Tribology International, Vol. 31, pp. 49-60, 1998.

[4] P.A. Williams, I.C. Clarke: *Understanding polyethylene wear mechanisms by modeling of debris size distributions*, Wear, Vol. 267, pp. 646-652, 2009.

[5] S. Ge, S. Wang, N. Gitis, M. Vinogradov, J. Xiao: *Wear behavior and wear debris distribution of UHMWPE against Si3N4 ball in bi-directional sliding*, Wear, Vol. 264, pp. 571-578, 2008.

[6] V. Banchet, V. Fridrici, J.C. Abry, Ph. Kapsa: *Wear and friction characterization of materials for hip prosthesis*, Wear, Vol. 263, pp. 1066-1071, 2007.

[7] A. Kilgour, A. Elfick: *Influence of crosslinked polyethylene structure on wear of joint replacements*, Tribology International, Vol. 42, No.11-12, pp. 1582-1594, 2009.

[8] J.L. Gilbert, I. Merkhan: *Rate effects on the microindentation-based mechanical properties of oxidized, crosslinked, and highly crystalline ultrahigh-molecular-weight polyethylene*, Journal of Biomedical Materials Research Part A, Vol. 71A, No.3, pp. 549–558, 2004.

[9] K.S. Kanaga Karuppiah, A.L. Bruck, S. Sundararajan, J. Wang, Z. Lin, Z.H. Xu, X. Li: *Friction and wear behavior of ultra-high molecular weight polyethylene as a function of polymer crystallinity*, Acta Biomaterialia, Vol. 4, No.5, pp. 1401-1410, 2008.

[10] L. Fasce, J. Cura, M. del Grosso, G.G. Bermúdez, P. Frontini: *Effect of nitrogen ion irradiation on the nano-tribological and surface mechanical properties of ultra-high molecular weight polyethylene*, Surface and Coatings Technology, Vol. 204, No.23, pp. 3887-3894, 2010.

[11] M. Flannery, T. McGloughlin, E. Jones, C. Birkinshaw: *Analysis of wear and friction of total knee replacements: Part I. Wear assessment on a three station wear simulator*, Wear, Vol. 265, No.7-8, pp. 999-1008, 2008.

[12] M. Flannery, E. Jones, C. Birkinshaw: *Analysis of wear and friction of total knee replacements part II: Friction and lubrication as a function of wear*, Wear, Vol. 265, No.7-8, pp. 1009-1016, 2008.

[13] J.L. Gilbert, J. Cumber, A. Butterfield: *Surface micromechanics of ultrahigh molecular weight polyethylene: Microindentation testing, crosslinking, and material behavior*, Journal of Biomedical Materials Research, Vol. 61, pp. 270–281, 2002.

[14] L.A. Pruitt: *Deformation, yielding, fracture and fatigue behavior of conventional and highly cross-linked ultra high molecular weight polyethylene*, Biomaterials, Vol. 26, No.8, pp. 905-915, 2005.

[15] C. Zhu, O. Jacobs, R. Jaskulka, W. Köller, W. Wu: *Effect of counterpart material and water lubrication on the sliding wear performance of crosslinked and non-crosslinked ultra high molecular weight polyethylene*, Polymer Testing, Vol. 23, No. 6, pp. 665-673, 2004.

[16] H.J. Cho, W.J. Wei, H.C. Kao, C.K. Cheng, *Wear behavior of UHMWPE sliding on artificial hip arthroplasty materials*, Materials Chemistry and Physics, Vol. 88, No. 1, pp.9-16, 2004.

[17] M.P. Gispert, A.P. Serro, R. Colaco, B. Saramango: *Friction and wear mechanisms in hip prosthesis: Comparison of joint materials behaviour in several lubricants*, Wear, Vol. 260, pp. 149-158, 2006.

[18] S.K. Young, M.A. Lotito, T.S. Keller: *Friction reduction in total joint arthroplasty*, Wear, Vol. 222, No. 1, pp. 29-37, 1998.

Serbian Tribology Society

SERBIATRIB '13

13th International Conference on Tribology

Faculty of Engineering in Kragujevac

Kragujevac, Serbia, 15 – 17 May 2013

THE POTENTIAL OF MAGNESIUM ALLOYS AS BIOABSORBABLE / BIODEGRADABLE IMPLANTS FOR BIOMEDICAL APPLICATIONS

Fatima Zivic[1], Nenad Grujovic[1], Geetha Manivasagam[2], Caroline Richard[3], Jessem Landoulsi[4], Vojislav Petrovic[5]

[1]Faculty of Engineering, University of Kragujevac, Serbia, zivic@kg.ac.rs, gruja@kg.ac.rs
[2]Vellore Institute of Technology, Centre for Materials Engineering, Tamil Nadu, India, geethamanivasagam@vit.ac.in
[3]François Rabelais University of Tours, Laboratory of Mechanics and Rheology, EA 2640-France, caroline.richard@univ-tours.fr
[4]Pierre & Marie Curie University of Paris, Laboratory of Surface Reactivity, UMR 7197-France, jessem.landoulsi@upmc.fr
[5]AIMME - Instituto Tecnológico Metalmecánico, Unidad de Ingeniería de Producto, Valencia, Spain, vpetrovic@aimme.es

Abstract: *The potential of magnesium alloys as bioabsorbable / biodegradable implants for biomedical applications has been extensively studied as emerging direction. This paper gives a review of current topics in this field. Research activities related to biomedical magnesium alloys have been pursued in two main directions, orthopedic and cardiovascular implants, by investigating different aspects of alloying system design, novel structures, degradation rate control, and surface modification methods. Magnesium alloys are currently considered for applications as load-bearing implant devices such as plates, screws and pins for repairing bone fracture. Highly important direction of research is degradable coronary stents. Degradable vessel stents promote stable vessel regeneration, unlike permanent stents. Different combinations of alloying elements have been investigated in order to decrease corrosion rate.Tribological issues are also important for understanding of different phenomenon related to prolongation of Mg alloys corrosion degradation time/rate, such as tribocorrosion, corrosion fatigue, and fatigue crack growth behavior.*

Keywords: *Mg alloys, Bioabsorbable / Biodegradable implants.*

1. INTRODUCTION

The beginning of the resorbable implants concepts is related to using polymers with controlled dissolution rates: polylactides and polyglycolides, back in 1970s [1]. But the problem associated with use of polymers is their mechanical properties, where metals have better characteristics and represent the promising field for advancements. The history of biodegradable magnesium (Mg) implants started shortly after the discovery of elemental magnesium by Sir Humphrey Davy in 1808 [2]. It is supposed that the pure magnesium wires were used as ligatures to stop bleeding vessels of three human patients in 1878 [2]. They elaborated corrosion induced degradation properties of pure magnesium and concluded that corrosion rate depended on the wire size. From those first attempts, many other solutions and ideas were tried, because magnesium has been recognised as the promising material for efficient degradable implants. Today, in vitro and in vivo study data exists, as well as some clinical trials data, but not so extensively present as for other biomedical metal materials, because degradable materials and Mg alloys are still having many unresolved issues if compared to the development of Ti biomedical alloys. Even today, several important drawbacks of the technology and material need to be resolved before its wide application in clinical practice.

Magnesium is the seventh most abundant element in earth's crust (2% of the total mass) and also essential and major constituent element of human body, nontoxic and biocompatible accordingly [3]. It belongs to the group of alkaline earth metals and cannot be found in elemental form in nature, but only in chemical combinations, since being highly reactive. From aspects of the Mg alloys production, important mineral forms are: magnesite MgCO3 (27% Mg), dolomite

MgCO3•CaCO3 (13% Mg), and carnallite KCl•MgCl2•6H2O (8% Mg), as well as sea water, which contains 0.13% Mg or 1.1 kg Mg per m3 (3rd most abundant among the dissolved minerals in sea water) [3]. However, Mg alloys are still lacking wide application due to several reasons, one of which is rather high price of base material and regarding degradable implants, too rapid corrosion rate when implanted, especially in solutions containing Cl^{-1}. In addition, there are certain limitations related to the processing temperatures and production protocols.

The usage of magnesium (Mg) has historically been limited by relatively high cost of production and associated energy costs. However, Mg market will steadily increase, mainly due to the low cost production in China. Magnesium is recovered by electrolysis of molten anhydrous MgCl2, by thermal reduction of dolomite, or by extraction of magnesium oxide from sea water. The global production of roughly 436,000 t (1997) is covered by melt electrolysis to 75% and by thermal reduction to 25%. Cast magnesium alloys dominate 85-90% of all magnesium alloy products, with Mg-Al-Zn system being the most widely used. Rare earth alloying additions increase cost and are of uncertain supply. US and Canada dominated magnesium production during the 1990s, however, since the late 90s, China become the main producer. Today, China dominates the world production because of the relatively low operating costs. In general, electrolytic producers in the west have been replaced by Chinese pyrometallurgical production via the Pidgeon process (Pidgeon, 1944). For example, the capital cost for Australia Magnesium (AM) Process using an electrolytic route was estimated to be $10,000/tonne Mg, while the capital cost for the Pidgeon process was estimated to be $3,000/tonne Mg in 2008.

2. MAGNESIUM ALLOYS

Magnesium alloys are standardized by ASTM norm and they are marked with letters (A, B, C, etc.), indicating main alloying elements, followed by the rounded figures of each weight in percentage terms. The alloy AZ91D, for example, is an alloy with a rated content of 9% aluminium (A) and 1% zinc (Z) [3]. The corresponding DIN specification would be MgAl9Zn1. The most common alloying elements are given in Table 1.

Different alloying elements influence the properties of the pure magnesium, depending on the wanted characteristics. The main mechanism for improving the mechanical properties is precipitation hardening and/or solid-solution hardening. One of the most important alloying elements is aluminium (Al) which increase tensile strength, by forming the intermetallic phase Mg17Al12. The use of rare earth elements (e.g. Y, Nd, Ce) has become significant, especially for designing the medical grade Mg alloy for degradable implants, since they impart a significant increase in strength through precipitation hardening. But almost all elements used so far for alloying mostly increase susceptibility to corrosion. Review of commercially produced Mg alloys today is given in Table 2 [3].

Table 1. ASTM codes for magnesium's alloying elements [3].

Abbreviation letter	Alloying element	Abbreviation letter	Alloying element
A	aluminium	N	nickel
B	bismuth	P	lead
C	copper	Q	silver
D	cadmium	R	chromium
E	rare earths	S	silicon
F	iron	T	tin
H	thorium	W	yttrium
K	zirconium	Y	antimony
L	lithium	Z	zinc
M	manganese		

Table 2. Chemical composition (in weight %; Mg is the balance; Cu, Ni in general <0.001%) of the selected Mg alloys.

Alloy	Al	Zn	Si	Fe
Mg cp/cast	0.04	<0.01	0.05	<<
AZ91/cast	10.14	1.33	0.03	<<
AZ91 Fe0.03/cast	9.56	0.86	0.04	0.03
AZ91 Fe0.05/cast	10.12	1.05	0.06	0.05
AZ91/50	9.93	0.84	0.08	<<
AZ91/5	10.09	0.87	0.11	0.01
AZ91/2.5	4.75	0.02	<<	<<
AZ91E	8.22	0.65	0.01	<0.01
AZ31	3.00	0.83	0.01	0.003
MgZa5/cast	0.04	<<	<<	<<
Mg hp				
Mg0.6Ca				
Mg1.2Ca				
Mg1.6Ca				
Mg2.0Ca				

The important innovations are expected to emerge from the materials known as metal foams, where Mg foams are investigated from aspects of obtaining even lighter components. Although Mg belongs to the lightest elements used for biomedical purposes, its porous variant is also investigated, along with possibilities to keep oxidation rate under control. Very interesting results are achieved in production of Mg foams, such as AZ91 foam with open cellular structure having a density of 50 kg/m3, whereas a cubic meter of pure solid Mg weighs 1,740 kg [1].

Energy absorption during impact or loading is inherent property of the foams. Fig. 1 shows stress–strain behavior of the foams in compression, in general [1]. From Fig. 1, it can be seen that three zones exists: I. Elastic region: deformation of the pore walls; II. A plateau of nearly constant flow stress and large strain (10–50%) and III. Densification region with steep increase of flow stress where the plastic damage occurs. Relatively wide region of constant flow stress during compressive loading explains the fact that while foams are in this interval, any increasing strain hardly entails increasing stress. If tension is observed, the stress–strain behavior of foams is approximately similar to ductile metals (curve b in Fig. 1).

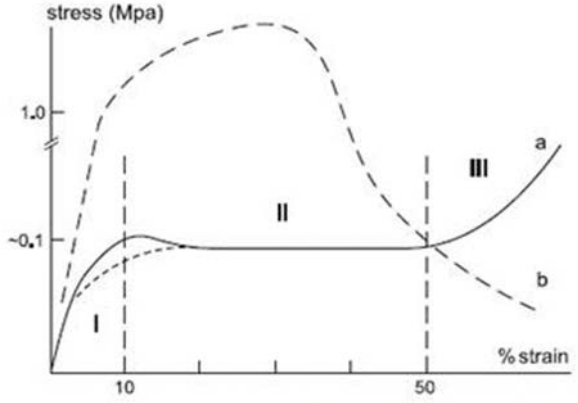

Figure 1. Stress - strain behaviour of foams.

3. MAGNESIUM ALLOYS AS DEGRADABLE IMPLANTS

The application of Mg and its alloys for degradable implants started with ligatures for blood vessels (Huse, 1878, pure magnesium) and plates, arrows, wire, sheets, rods (Payr, 1905, pure magnesium) [2]. Mg alloys have been tried in different medical areas, such as: pure Mg for band, suture from woven Mg wires, fusiform pins (in 1940); Mg–Al2%-wt. pure magnesium wires for clotting aneurysms (dog studies in 1951); Mg–Al2%-wt. for intravascular wires (rat studies in 1980) [2]. The potential of magnesium alloys as bioabsorbable / biodegradable implants for biomedical applications has been extensively studied as emerging direction. Research activities related to biomedical magnesium alloys have been pursued in two main directions, orthopedic and cardiovascular implants, by investigating different aspects of alloying system design, novel structures, degradation rate control, and surface modification methods.

Magnesium alloys are currently considered for applications as load-bearing implant devices such as plates, screws and pins for repairing bone fracture. Other metals currently used for bone implants, such as stainless steels and titanium alloys, have elastic modulus that are much higher than natural bone, leading to unwanted stress shielding. The elastic modulus of magnesium and many magnesium alloys are much closer to bone. The advantage of Mg alloys is favorable elastic response during loading (such as shown in Fig. 1). Also, the second surgery is avoided due to the degradation of the implant after its function in the body is finished. For example, compared with poly-96L/4D-lactide, the magnesium alloys AZ31 and AZ91 enhanced the osteogenesis response and increase newly formed bone [4]. Investigations showed that Mg–6Zn, Mg–Ca and Mg–Mn–Zn alloys gradually degrade within a bone and had good biocompatibility both in vitro and in vivo [4].

Highly important direction of research is degradable coronary stents. Degradable vessel stents promote stable vessel regeneration, unlike permanent stents [5, 6, 7]. However, as a vessel defect gets larger, stronger and degradable materials are paramount for stable vessel regeneration. Vessel scaffolding is necessary only for a certain, limited time, than the permanent stent has no known advantage. A stent is a miniature mesh tube, made of a biocompatible metal, biodegradable metal or polymer, placed inside of a blood vessel (cardiovascular, neurovascular and peripheral blood vessels) or a natural conduit (gastrointestinal, urinary and biliary tracts). The stent acts as a scaffold, pushing against the internal walls of the conduit/vessel to open a blocked area and thereby enables natural flow and prevents the vessel from collapsing, narrowing or closing. Stents differ greatly in their design, dimensions and material, depending on application. Coronary stents are now the most commonly implanted medical device for angioplasty, with more than 1 million implanted annually. Currently used metallic stents permanently remain in the artery and are associated with limitations such as continued mechanical stress, transfer to the tissue, and continued biological interaction with the surrounding tissue. Also, within 6 months, 30-35% patients suffer from restenosis. They are associated with late stent thrombosis and artifacts when non-invasive technologies such as MRI and MSCT are used. The stent presence is required for a period of 6 - 12 months during which arterial remodelling and healing is achieved. After this period the stent presence within the blood vessel cannot provide any beneficial effects. With the development of biodegradable implants, the concept of biomaterials has shifted from purely mechanical replacement devices towards true biological solutions. Bio-absorbable stents (Fig. 2) aim to mechanically prevent vessel recoil without the permanent presence of an artificial implant. The advantages of bioabsorbable stents are to leave no stent behind,

fully compatible with MRI/MSCT imaging, and are not associated with late stent thrombosis.

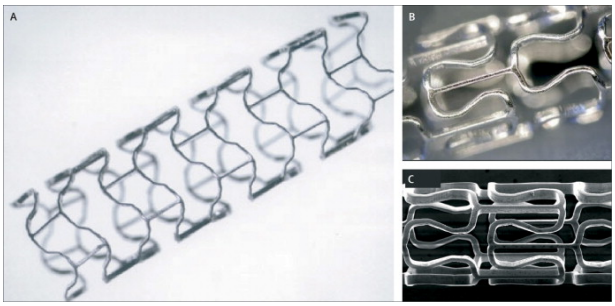

Figure 2. Bioabsorbable magnesium stent (Biotronik, Berlin, Germany) [6].

Magnesium (Mg) alloys which has been developed in the last ten years showed great potential in cardiovascular applications where temporary stent is required. Biotronik Mg Alloy Balloon expanding stent with a delivery catheter has been clinically tested to some extent [7].

Different combinations of alloying elements have been investigated in order to decrease corrosion rate. The addition of aluminium (Al) and rare earth (RE) elements has been reported to increase its strength and improve corrosion resistance. But Al could cause nerve toxicity and restraining growth to human body. Alloy containing RE is very expensive. In some alloys, the low cost Ca has been used as alloying element and Mg–Ca alloy exhibited increased corrosion resistance. The addition of Zn into Mg–Ca alloys increases the tensile strength, ductility, hardness and the kinetics of age hardening. Commercial Mg alloys such as WE43 (Mg–Y–RE–Zr), AZ91 (Mg–Al–Zn), AZ31 (Mg–Al–Zn–Mn) are under investigation. There are number of studies related to corrosion mechanisms and degradation kinetics. Published results indicate that the mechanisms affecting the corrosion behaviour of Mg-based stents in service conditions can be: internal galvanic corrosion; localized corrosion (pitting and filiform); stress corrosion cracking (SCC) and fatigue corrosion. Simultaneous effect of different corrosion mechanisms influences a stent in service, which makes the identification of correlations between in vitro and in vivo experimental results very complex and many issues has not yet been resolved. ASTM G31 (Standard Practice for Laboratory Immersion Corrosion Testing of Metals) offers general guidance for metal corrosion testing, but there are no standardized procedures for biocorrosion of biodegradable metal materials.

Low corrosion resistance of magnesium and its alloys, within the very aggressive environment in the physiological system, is the vital characteristic enabling degradability of the metal implant. On the other hand, too rapid loss of mechanical properties and/or toxic degradation products are major problems associated with Mg alloys. Also, the high corrosion rate produces rapid hydrogen gas evolution within the body. The pursued development direction is to control the speed of corrosion, along with optimization of the biological response to these implants to maximize recovery. Biologically compatible surface modifications through treatments or coating systems have been investigated as protective strategy in corrosive environments in order to optimize implant properties [8, 9]. Corrosion resistant coatings are commonly used for metals in many applications, but in area of dergadable implamnts, these coatings need to degrade along with the magnesium, or yield to the environment, leaving no harmful traces. Some of the tried solutions are: anodization, pure magnesium coating on Mg alloy, PVD coating of aluminium, but all of them have some downsides. One of the most biocompatible coating options for orthopedics is calcium phosphate coatings. Zhang et al. [9] investigated ion plating of Ti-coating on pure Mg for biomedical applications, inspired by good properties of both Ti and Mg alloys. They reported good results in improvement of the corrosion resistance of Mg and promising further potentials, but comprehensive testing of this new coating is yet to come.

Another method for increasing the corrosion resistance of a magnesium alloy is the surface structure modifications. Magnesium alloys undergo microgalvanic corrosion when multiple phases exist in an alloy, one more cathodic than another and in order to slow the corrosion rate is to modify the surface to homogenize it [8]. Amorphous surface would eliminate the formation of galvanic cells between grains and boundaries. One such a way is to make the matrix a completely amorphous bulk metallic glass to completely remove corrosion difference due to crystal structure in the metal [8]. Amorphous MgZnCa alloys have been tested in vivo to show reduced hydrogen evolution [10]. Ion implantation is another method of surface modification to increase corrosion resistance, also creating a gradual transition between the modified surface and the bulk of the material. This makes strong, adherent surfaces that do not have the problems of adhesion, thermal stresses, and crackings that separate secondary coating phases tend to have [8]. Plasma immersion ion implantation of Al, Zr, and Ti has been used to create corrosion resistance on AZ91.

4. FRICTION AND WEAR ISSUES RELATED TO MG ALLOYS

Tribocorrosion is defined as an irreversible transformation of a material from concomitant physicochemical and mechanical surface interactions occurring at tribological contacts [11]. In general, metallic implants need to be tested to tribocorrosion and wear issues, regardless of their area of application. The realised contacts between implant material and either other implant material, or organic body constituent (e.g. bone) and elements of the aggressive physiological body environment, provoke certain responses (wear debris) that need to be investigated in more depth, especially for newly developed biomaterials. It is proven that even micro contacts within small regions sometimes influence significant responses, ranging from changes in contact environment up to increasing deterioration of implant surfaces due to wear related processes. Two- or three-body contacts are frequently associated with tribocorrosion [12]. Entrapped wear debris acts as an abrasive and is defined as the third body. The main concerns related to the simultaneous action of corrosion and wear in biomedical systems are the ability of the passive layer to withstand the mechanical stresses arising from wear, the ability of the metal surface to repassivate when the passive film is removed and the resistance of the new repassivated surface to both wear and corrosion [12]. Fretting has a big influence on the corrosion behavior of orthopedic devices. The tribocorrosion and fretting corrosion mechanisms have been mainly related to in vitro laboratory investigations. However, the in vivo behavior of metallic implants under combined wear corrosion or fretting corrosion has been hardly studied [12]. Also, the corrosion fatigue of structural magnesium alloys has been studied by several authors in NaCl and borate-buffered solutions, but generally focused on applications in electronic, automotive and aerospace industries. The fatigue strength of magnesium alloys is significantly reduced in humid environments, and the fatigue limit drops drastically in NaCl solution [12]. Even though the corrosion behavior of biomedical magnesium-based alloys has been extensively studied, corrosion fatigue has received little attention and degradable material must maintain appropriate mechanical strength during the healing of the fractured bone, to provide safe orthopedic device. Also, fatigue crack propagation behavior needs to be studied for a wide variety of biodegradable Mg alloys [12]. Corrosion and wear resistances are frequently studied in synergy, because of the direct relationship between these properties and the biocompatibility of the biomedical device.

Regarding coronary stenting by using metallic implants, analysis of the fatigue crack growth behavior is of the utmost importance for its proper functioning. There are my mathematical models in the literature, but, in particular, the fatigue crack propagation approach simulating crevice corrosion conditions in physiological solutions has been hardly considered for biomedical magnesium alloys [12]. Very important aspect is tribology related phenomena during the production of magnesium biodegradable vascular stents minitubes, since magnesium alloys possess highly limited room-temperature formabilities [13]. Highly complex physical, chemical and mechanical characteristics of magnesium must be taken into consideration, in order to keep the magnesium alloy characteristics (microstructure, etc.) unchanged under the influence of e.g. severe abrasive friction and wear during cold drawing [13].

Highly important is the understanding of the Mg alloy stent behaviour at its positioning during the movement through the vasculature, at the initial interventional cardiovascular treatment. Lubricious coatings have been used for over 20 years [14] and the benefits are well established: (1) lower frictional force between the device and the vessel reduces tissue damage and prevents vasospasm; (2) improved maneuverability aids navigation of complex lesions and facilitates access to tortuous vascular sites leading to expansion of the patient population that can benefit from these treatments; and (3) reduces thrombogenicity. In addition, reduced friction between the therapy catheters and support catheters leads to improved outcomes, reduced procedure time, and, ultimately, reduced cost [14]. The stent is commonly placed at the one fixed position within a blood vessel, meaning that there are no further movement between the stent material and surrounding tissue, leading to the conclusion that wear plays no significant role. However, blood flow around the placed stent has micro influence and might provoke nano-wear debris, which is not investigated so far. Such tiny wear debris represents a form of particulate matter in the vasculature and it is well known that if large enough and in sufficient quantities, can cause occlusion of blood vessels and lead to tissue hypoxia and, ultimately, necrosis [14]. If alloying elements of Mg alloys, such as Al, Zn are considered as well, it is obvious that this area needs further studies. Since Mg alloys stents has not been widely tried in clinical practice, there are many tribology related questions to be addresses.

5. CONCLUSION

The magnesium alloys as bioabsorbable / biodegradable implants for biomedical applications are highly promising materials, but some issues need to be resolved and extensive research activities are pursued throughout the world. Different aspects of alloying system design, novel structures, degradation rate control, and surface modification methods have been tested, mainly in order to increase corrosion degradation time. Significant attention is still needed related to production processes, tribocorrosion, fatigue crack growth behaviour, wear and friction processes and other complex issues when observed within aggressive human body environment.

ACKNOWLEDGMENTS

This paper is supported by TR-35021 project, financed by the Ministry of Education, Science and Technological Development of the Republic of Serbia.

REFERENCES

[1] J.A. Helsen, Y. Missirlis: *Biomaterials, Biological and Medical Physics*, Biomedical Engineering, Springer-Verlag, Berlin Heidelberg, 2010.

[2] F. Witte: *The history of biodegradable magnesium implants: A review*, Acta Biomaterialia, Vol. 6, No. 5, pp. 1680-1692, 2010.

[3] K.U. Kainer (Ed.): *Magnesium – Alloys and Technology*, Wiley-VCH Verlag GmbH & Co. KG aA, Weinheim, 2003.

[4] S. Zhang, X. Zhang, C. Zhao, J. Li, Y. Song, C. Xie, H. Tao, Y. Zhang, Y. He, Y. Jiang, Y. Bian: *Research on an Mg–Zn alloy as a degradable biomaterial*, Acta Biomaterialia, Vol. 6, No. 2, pp. 626-640, 2010.

[5] H. Hermawan, D. Dubé, D. Mantovani: *Developments in metallic biodegradable stents*, Acta Biomaterialia, Vol. 6, No. 5, pp. 1693-1697, 2010.

[6] R. Erbel et al.: *Temporary scaffolding of coronary arteries with bioabsorbable magnesium stents: a prospective, non-randomised multicentre trial*, PROGRESS-AMS (Clinical Performance and Angiographic Results of Coronary Stenting with Absorbable Metal Stents), The Lancet, Vol. 369, No.9576, pp. 1869 - 1875, 2007.

[7] R. Waksman et al.: Early- and Long-Term Intravascular Ultrasound and Angiographic Findings After Bioabsorbable Magnesium Stent Implantation in Human Coronary Arteries, JACC: Cardiovascular Interventions, Vol. 2, No. 4, pp. 312-320, 2009.

[8] J. Waterman, M.P. Staiger: *Coating systems for magnesium-based biomaterials - state of the art*, In: W.H. Sillekens, S.R. Agnew, N.R. Neelameggham, S.N. Mathaudhu (Eds.): Proceedings of Magnesium Technology 2011, TMS, The Minerals, Metals & Materials Society, San Diego, California, USA, pp. 403-408, 2011.

[9] E. Zhang, L. Xu, K. Yang: *Formation by ion plating of Ti-coating on pure Mg for biomedical applications*, Scripta Materialia, Vol. 53, No. 5, pp. 523-527, 2005.

[10] B. Zberg, P.J. Uggowitzer, J.F. Loffler: *MgZnCa glasses without clinically observable hydrogen evolution for biodegradable implants*, Nature Materials, Vol. 8, No. 11, pp. 887-891, 2009.

[11] D. Landolt, S. Mischler, M. Stemp, S. Barril: Third body effects and material fluxes in tribocorrosion systems involving a sliding contact, Wear, Vol. 256, pp. 517-524, 2004.

[12] R.A. Antunes, M.C.L. de Oliveira: *Corrosion fatigue of biomedical metallic alloys: Mechanisms and mitigation*, Acta Biomaterialia, Vol. 8, No. 3, pp. 937-962, 2012.

[13] G. Fang, W.J. Ai, S. Leeflang, J. Duszczyk, J. Zhou: Multipass cold drawing of magnesium alloy minitubes for biodegradable vascular stents, Materials Science & Engineering C, doi: 10.1016/j.msec.2013.04.039, In Press, 2013.

[14] D.E. Babcock, R.W. Hergenrother, D.A. Craig, F.D. Kolodgie, R. Virmani: *In vivo distribution of particulate matter from coated angioplasty balloon catheters*, Biomaterials, Vol. 34, No. 13, pp. 3196-3205, 2013.

Serbian Tribology Society

SERBIATRIB '13

13th International Conference on Tribology

Faculty of Engineering in Kragujevac

Kragujevac, Serbia, 15 – 17 May 2013

ANALYSIS OF THE SURFACE LAYER FORMATION OF SINGLE CYLINDER ENGINE COMBUSTION CHAMBER WITH PHOSPHOROUS-FREE AND CONVENTIONAL ENGINE LUBRICANTS

L.YÜKSEK[1*], H.KALELİ[2], D.ÖZKAN[3], H. HACIKADİROĞLU[3]

[1]Researcher Dr., Yıldız Technical University, Faculty of Mechanical Engineering, Automotive Division
34349 Beşiktaş-İstanbul/TURKEY, lyuksek@yildiz.edu.tr

[2]Professor Dr., Yıldız Technical University, Faculty of Mechanical Engineering, Automotive Division
34349 Beşiktaş-İstanbul/TURKEY, kaleli@yildiz.edu.tr

[3]PhD. Student, Yıldız Technical University, Faculty of Mechanical Engineering, Energy Division
34349 Beşiktaş-İstanbul/TURKEY, dogus_ozkan@hotmail.com

*Corresponding author.

Abstract: *Phosphorus-free engine lubricants are gaining importance for preventing catalyst poisoning which is the major deactivation mechanism that causes three-way catalyst malfunction. The main purpose of this paper is to evaluate the mechanism of surface layer formation in combustion chamber of spark ignition engines with phosphorous-free and phosphorous containing mineral engine lubricants. An experimental endurance test was conducted for 100 hours at equal load conditions for each lubricant. Endurance tests were run with a laboratory engine test bench. Subsequently, engines dismantled and cylinder liners were cut accurately to obtain specimens for microscopic examination. Optical microscopy, scanning electron microscopy and energy dispersive X-ray spectroscopy methods were used for evaluation.*
Elemental measurements on the surface which were obtained by X-ray spectroscopy were examined statistically. Results of the experiments showed that phosphorous containing lubricant deposited more carbon and oxygen although less manganese and silica than the phosphorous containing rival. After the X-ray spectroscopy of the combustion chamber surface at top dead centre, iron element composition of the phosphorus-free lubricant was notably higher than phosphorus containing oil.

Keywords: *Phosphorous-free Oil, Combustion chamber, X-ray spectroscopy, Additive layer formation, Cylinder liner*

1. INTRODUCTION

Mechanical losses are responsible for the approximately 10-15% fuel energy loss. Half of the mechanical losses are generated by the friction between piston rings and cylinder liner. Therefore, the performance of the piston ring and cylinder liner tribological pair is the indicator of the performance and the lifespan of an internal combustion engine [1]. Particularly, wear around top dead centre is the main limiter of effective engine life. Piston rings are intended to maintain the dynamic sealing between crankcase and the combustion chamber which minimize the power losses caused by the blow-by mass transfer through the crankcase during expansion stroke [2]. Success of this sealing mainly depends on the wear rate of ring and liner pack which are primarily the function of the formed tribofilm on ring and liner surfaces. Engine lubricants are formulated to generate and sustain the protection against wear while lubrication, cooling and cleaning of the surfaces are also expected from lubricant. Modern engine lubricant can satisfy these demands with chemical compounds like anti-wear additives, anti-oxidant additives, dispersants, detergents etc. [3]. Additives also enhance the chemical composition of base lubricant [4].

Zinc dialkyldithiophosphate (ZDDP) lubricant additives are the most effective anti-wear and anti-oxidant additives in the cost and performance perspectives [5]. Therefore, it has been in use for decades. Although, ZDDP mainly contains phosphorus which is a well-known poison for three-way catalysts [6]. Environmental concerns become more dominant among authorities and individuals which result stricter emission regulations [7]. Automotive manufacturers are pressurised to produce cleaner vehicles in all terms from well to wheel. Harmful exhaust emissions are reduced through after-treatment systems like diesel oxidation catalysts, three-way catalyst and diesel particulate filters. Poisoning phenomenon related with lubricant has to be prevented, and hence, new and emerging technologies have become important. The solution is complex, namely reducing the amount of phosphorus, sulphur, zinc and magnesium without deteriorating the performance of the oil [8].

This study intended to investigate the interaction between phosphorus containing (PC) and Non-phosphorus and non-ash containing lubricant (NPNA) on the combustion chamber surface of internal combustion engines. An endurance test was conducted with two of the identical spark ignition engines. Both engines aged during 100 hours under certain load conditions which were determined according to standards. Liner surfaces are examined with electron, optical microscopy and energy dispersive X-ray spectroscopy techniques.

2. EXPERIMENTAL DETAILS

Experimental study consists of two equal endurance tests with two identical engines, specifications of which are listed in Table 1. Endurance tests were performed after a run-in period and a consecutive oil drain.

Table 1. Specifications of test engines.

Designation	Value/type
Manufacturer/Model	Honda/GX 200
Type	4-stroke air-cooled, SI
Aspiration	Naturally aspirated
Lubrication method	Splash
Number of cylinders	1
Bore x Stroke (mm)	68 x 54
Cylinder volume (cm^3)	196
Compression ratio	8.5:1
Crankcase oil capacity (l)	0.6
Speed max (rpm)	3600
Rated torque (Nm)	12.4@2500 rpm
Rated power (kW)	4.1@3600 rpm

ISO 8178 standard was selected as a reference to determine load conditions and a direct current generator was used to generate the brake load [9]. An overall scheme of the test bench is shown in Figure 1. A specially formulated NPNA lubricant and a conventional PC lubricant were used for the tests, specifications of which are listed in Table 2 under the courtesy of IDEMITSU KOSAN CO. LTD. Japanese petrochemical company.

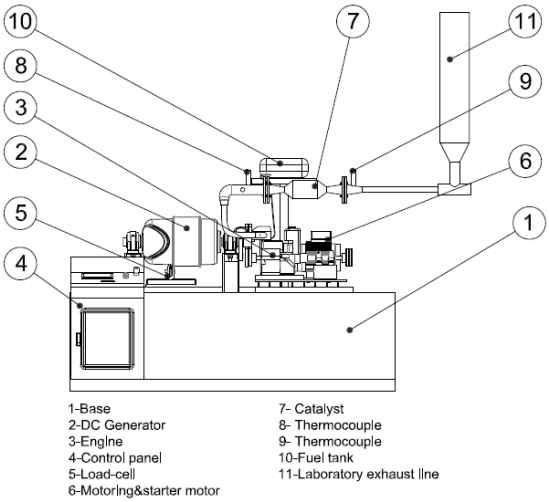

Figure 1. Schematic, CAD and real view of the test bench.

Table 2. Specifications of test oils.

Specification	PC	NPNA
SAE grade	10W30	10W30
TBN (mgKOH/g)	5.73	3.13
Viscosity 100 °C (cSt)	10.4	10.3
Viscosity index	139	142
Flash point (Celcius)	224	240
Specific gravity@15 °C	0.874	0.862
Ca content (wt %)	0.2	0
Zn content (wt %)	0.09	0
S content (wt %)	0.19	0.18
P content (wt %)	0.08	0

Operating conditions are summarized in Table 3 for both types of engine oils. PC and NPNA lubricant were aged during 100 hours under certain loading conditions, at the end of the test, cylinder liner and piston rings were machined to obtain specimens for microscopic analysis.

Table 3. Details of load conditions.

Specification	PC	NPNA
Engine speed (rpm)	2500	2500
Engine load (%)	75	75
Endurance test duration (h)	100	100
Ambient temperature (Celcius)	22±3	22±3

Typical composition of cylinder liner was required to obtain better assessment of the surface which had been provided by the engine manufacturer and these are listed in Table 4. Specimens had been ultrasonically cleaned with n-hexane.

Table 4. Typical composition of cylinder liner.

Element	Composition % mass
Fe	93.97
P	0.3
V	0.15
C	3.00
Si	2.00
Mn	0.60

3. RESULTS AND DISCUSSION

Top dead centre is the most complex surface for the tribologists where the conditions are extreme. Combustion induced pressure gradient acts upon top ring and hence contact between liner and ring surface reaches top levels and conditions become severe. Furthermore, combustion gases and soot controversially affect the lubrication in TDC area, acidic compounds, unburned hydrocarbons and soot accumulation on liner surface occurs with constant replenishment cycle. In addition to the factors explained above, high gas temperature reduces oil viscosity which also has detrimental effect on liner-ring lubrication. Base number retention capability and high temperature and high shear rate viscosity (HTHS) of engine lubricant become excessively important on TDC lubrication as well as the performance of anti-wear additive. Total base number indicates the ability of engine oil to neutralize acidic compounds which primarily originate from combustion chamber and transfer through the liner to the crankcase. The more the base number retention, the lower the oxidative wear on liner surface especially around TDC.

Downsized engines with turbochargers are on-going trend to fulfil the requirements of CO_2 emission reduction and fuel economy [10]. Low load fuel economy and torque flexibility make these types of engines favourable although increased boost levels result significantly higher contact pressures. Therefore, HTHS viscosity gains attention with rising in-cylinder pressure which is the wellness of lubricant performance under severe operation conditions.

Layer formation of anti-wear additive on TDC surface is the main factor for decreasing the liner wear. Anti-wear additive acts like buffer between ring and liner asperities and prevents adhesion. Accumulated additives on surfaces can effectively be detected through electron microscopy technique. Besides, it is possible to detect elemental distribution with X-ray spectroscopy method.

Equal tear-down processes were applied to test engines, which include dismantling of cylinder liners and piston rings. Scanning electron microscopy (SEM) and energy dispersive X-ray spectroscopy (EDS) were applied on TDC region of cylinder liner as shown in Figure 2 and Figure 3.

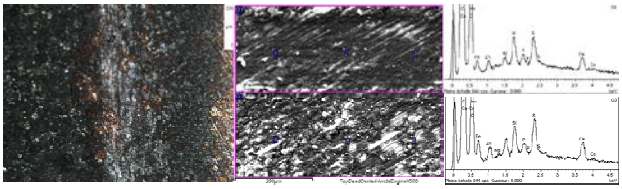

Figure 2. Optical, SEM and EDS results of PC lubricant.

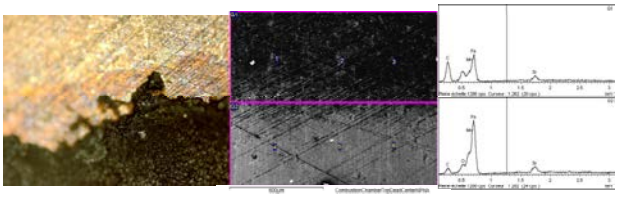

Figure 3. Optical, SEM and EDS results of NPNA lubricant.

Labels on figures indicate the location of the inspection: G1 designation borders the combustion chamber surface where the sweep motion of top ring has ended G2 designation indicates liner surface covered by piston crown. Representation of inspected surfaces are depicted in Figure 4, analyse points were determined by considering the surface layers of additive accumulation.

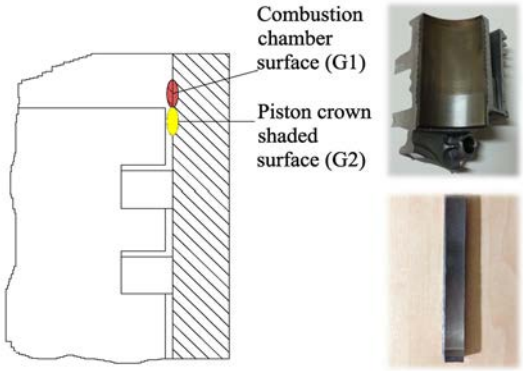

Figure 4. Schematic representation inspected surfaces.

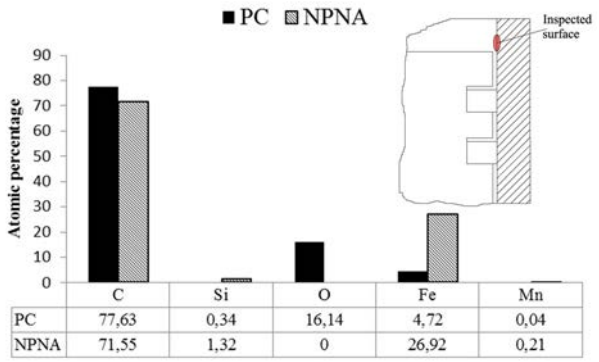

	C	Si	O	Fe	Mn
PC	77,63	0,34	16,14	4,72	0,04
NPNA	71,55	1,32	0	26,92	0,21

Figure 5. EDS result of combustion chamber surface.

EDS measurements were applied for both of the surfaces lubricated with test oils. Figure 5 shows the elemental composition of layer on the surface of combustion chamber. Higher amount of carbonaceous deposit was detected with the PC lubricant on combustion chamber surface. Similar trend observed for G2 surface as shown in Figure 6 while atomic concentration is different.

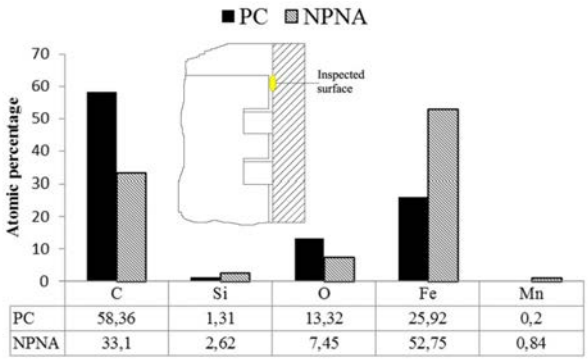

	C	Si	O	Fe	Mn
PC	58,36	1,31	13,32	25,92	0,2
NPNA	33,1	2,62	7,45	52,75	0,84

Figure 6. EDS result of TDC surface.

Carbon and oxygen levels indicate the oil film on both of the surfaces while the G1 surface environment is quite different than G2. Higher carbon concentration of PC surface of combustion chamber can be attributable to accumulation of swept portion of surface oil film.

4. CONCLUSSION

Newly developed catalyst friendly phosphorus-free engine oil and a conventional ZDDP containing engine oil were tested by applying 100 h long endurance study. Two of identical engines were aged under equal loading conditions then dismantled and analysed. The main subject of the investigation is the additive layer formation of lubricant on combustion chamber surface. Considering the measurements and observations made with optical microscope, SEM and EDS, findings can be summarized as;

A- Higher level of deposit formation was detected with PC lubricant on both combustion chamber and piston shaded surfaces.

B- PC conventional lubricant mainly differs from NPNA with oxygen content on combustion chamber surface; this discrepancy originates from the type of deposited compounds.

C- Lower deposits with NPNA on combustion surface indicate the effect of lubricant on carbonaceous deposit formation.

ACKNOWLEDGEMENT

This study was supported by Idemitsu Kosan Co. Ltd. and the authors would like to thank Dr. Hiroshi Fujita for his contributions throughout this study.

REFERENCES

[1] B.G. Rosen, R. Ohlsson, T.R. Thomas: *Wear of cylinder bore microtopography*, Wear, Vol. 198, pp. 271-279, 1996.

[2] M.F. Jensen, J. Bottiger, H.H. Reitz, M.E. Benzon: *Simulation of wear characteristics of engine cylinders*, Wear, Vol. 253, pp. 1044-1056, 2002.

[3] D. Troyer, J. Fitch: *Oil analysis basics*, Noria Corporation, Oklahoma,USA, 1999.

[4] Z. Pawlak: *Tribochemistry of Lubricating Oils*, Elsevier Science, 2003.

[5] M.A. Nicholls, T. Do, P.R. Norton, M. Kasrai, G.M. Bancroft: *Review of the lubrication of metallic surfaces by zinc dialkyl-dithlophosphates*, Tribol Int, Vol. 38, pp. 15-39, 2005.

[6] A.J.J. Wilkins, N.A. Hannington: *The Effect of Fuel and Oil Additives on Automobile Catalyst Performance*, Platinum metals review, Vol. 34, pp. 16-24, 1999.

[7] EUP, Official Journal of the European Union, (EC) No 715/2007, 2007.

[8] T. Katafuchi, N. Shimizu: *Evaluation of the antiwear and friction reduction characteristics of mercaptocarboxylate derivatives as novel phosphorous-free additives*, Tribol Int, Vol. 40, pp. 1017-1024, 2007.

[9] 8178-4:2007 *Reciprocating internal combustion engines, Exhaust emission measurement* in: Part 4: *Steady-state test cycles for different engine applications*, ISO, 2007.

[10] T.V. Johnson: *Vehicular Emissions in Review*, SAE Int. J. Engines, Vol. 5, pp. 216-234, 2012.

Serbian Tribology Society

SERBIATRIB '13

13th International Conference on Tribology

Faculty of Engineering in Kragujevac

Kragujevac, Serbia, 15 – 17 May 2013

TRIBOLOGICAL STUDY OF BIOCOMPATIBLE HYBRID ORGANIC MOLECULES FILM WITH ANTIBACTERIAL EFFECT

J.H. Horng*[1], C.C.Wei[1], S. Y. Chern[1], W.H. KAO[2], K.W. Chern[1], Y.S. Chen[1]

[1]Department of Power Mechanical Engineering, National Formosa University, Taiwan

[2]Institute of Mechatronoptic Systems, Chienkuo Technology University, Taiwan

*jhhorng@gmail.com

Abstract: *Optical glass is widely used on bioengineering and various utilities such as public touchscreen display and mobile devices. This work evaluates the feature of anti-bacterial and anti-adhesion on OTS material that mixed with biocompatibility antibacterial agent coated on the optical glass. Test samples were allocated with different bath and drying temperatures as well as reaction time. The result shows that in the contact of angle experiments, pure OTS film and mixed antibacterial films have almost the same contact angle about 105° at the condition of reaction time of 12 hours and reaction temperature of 80°C.The antibacterial test find that the order: antibacterial agent> OTS+ antibacterial agent(50%) > OTS+ antibacterial agent(10%) > OTS. At the same operation condition, OTS mixed with 50% antibacterial agent is able to increase adhesion force between OTS film and lens. It suggests that the surface treatment of optical lenses involving OTS with 50% antibacterial solution is the most to increase the antifouling and antibacterial functions and enhance the adhesion function between films and lens surfaces.*

Keywords: *self-assembled monolayer, adhesion force, friction, terminal group bonding, contact angle, anti-bacterial.*

1. INTRODUCTION

The uses of SAMs in biomedicine utilities are increasing rapidly, such as in biosensors, nonfouling surfaces, bioactive surfaces, and drug delivery [1, 2]. Octadecyltrichlorosilane (OTS) monolayer is one of the most extensively studied self-assembled monolayer [3-5]. Therefore, how to improve the adhesion and anti-bacterial performance of SAMs film becomes an attractive topic in order to enhance device application and reliability. Bierbum [6, 7] noted that the substrate surface water layers are an important factor in the formation of OTS films. Bierbum explained that OTS molecules initially spread vertically on substrate surfaces and been clustered after locating activation positions. Afterwards, other OTS molecules spread to the cluster edges and form islands. The molecules then spread outwards and cause adsorbed molecules to form connections, finally forming tightly connected monolayers. In 1998, Vaillant et al. [8] used atomic force microscopy (AFM) and a Fourier-transform infrared spectrometer (FTIR) to observe the process by which OTS molecules form films on substrate surfaces. The results showed that a larger amount of water in the solutions cause the OTS molecules to undergo a hydrolysis reaction and produce polymerization within the solution. Cloud-shaped or island-shaped molecule films form throughout the solution. In the contrast, solutions with comparatively low proportions of water exhibit point distribution and OTS molecules igrow chaotically into liquid-like form. While the surface diffusion makes OTS molecules absorbing molecules within the solution, the tightly knit, island-shaped structures are formed by messy molecule films. Resch [9] also used AFM and found that OTS molecules initially grow messily and irregularly. With the passage of time, molecules covering the surface spread horizontally and ultimately form tightly arranged molecular

films. Carraro et al. [10] examined formation of OTS SAMs under different ambient temperatures. They discovered when the ambient temperature falls below 16°C, OTS first form islands or clouds and then films. When the ambient temperature rises above 40°C, the films grow evenly instead of forming islands. In addition, films form more quickly at lower temperatures. The formation of OTS monolayer on a material surface is highly sensitive to several factors, which include the density of surface hydroxyl groups, reaction temperature, reaction environment, reaction time, solvent used to deposit OTS water content of the solvent concentration of OTS, solution age, roughness of the underlying substrate and cleaning procedures after SAM deposition [11]. Therefore, how to improve the adhesion and anti-bacterial performance of SAMs film becomes an attractive task in order to enhance device application and reliability.

2. EXPERIMENTAL

The optical lenses were ultrasonicated in acetone and then rinsed with solvent tetrahydrofuran and deionized water and immediately dipped in the OTS solution containing approximately 40 ml. For the preparation of SAMs film, OTS was dissolved in alcohol and prepared to a molar concentration of 10 mM, and then mix in different proportions of antibacterial agent (10%, 50%). The test pieces were placed in the solution at different bath temperatures and duration times and a drying time of 10 min. The test pieces were then removed and set aside for 12 hr before being ultrasonicated in acetone for 5 min to remove loosely bound material and rinsed in deionized water and blown dry with nitrogen gas. The molecular structure of OTS is shown in Table 1. It's hydrophobic properties comes from terminal group (CH_3). Main composition of biocompatibility antibacterial agent is bioflavonoid and citric acid.

For the experimental investigation of hydrophobic properties for the different surface films on the lens, FTA contact angle equipment was used to measure contact angle, as shown in Figure 1. Larger contact angle indicates better hydrophobic and anti-fouling properties of surfaces. Contact angles were measured on both sides of the water drop. Droplet profiles were captured using a video comprising of digital frames over a period of 12 seconds and transferred to a computer for angle measurement. The adhesion force between surface films and substrates were measured using atomic force microscopy (AFM) by scratch mode. AFM also was used to examine topography of samples before and after SAM deposition by non-contact mode.

Table 1. The molecular structure of OTS

SAMs	Molecular formula	Head group	Terminal group
OTS	$CH_3(CH_2)_{17}SiCl_3$	$-SiCl_3$	$-CH_3$

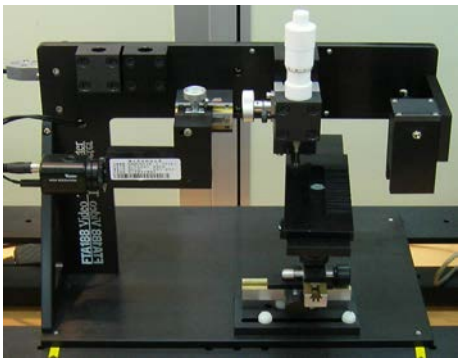

Figure 1. Contact angle equipment

3. RESULTS AND DISCUSSION

In the contact angle analysis of various operation conditions, the measurement data of each test piece was obtained from the mean of five measurements. Figure 2(a) is a photo of the contact angle for OTS material. Figure 2(b) show the contact angle changes with various reaction times and bathe temperatures.

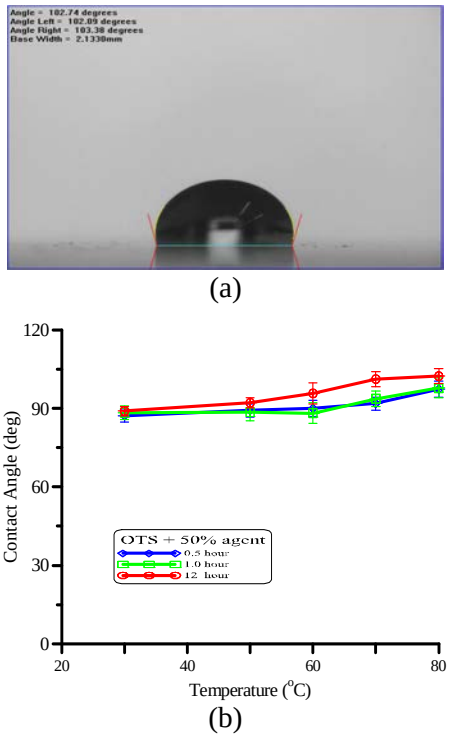

Figure 2. Contact angles (a) experimental photo (b) comparison chart for different reaction times and temperatures.

It shows that the higher the bathe temperature, the higher the contact angle. The higher the reaction time, the higher is the contact angle. However, the variation of contact angles of OTS+50% antibacterial agent films under various operation

conditions are all quite low. Bathing OTS+50% agent films at a bath temperature of 80 ℃gradually increases the contact angle to approximately 105 degree. The various reaction time and bathe temperature have extremely little influence on the contact angle. In summary, the bath temperature of $80^{\circ}C$ and duration time of 12 hours was chosen as operation condition in order to investigate the antibacterial characteristics of surface film on lenses.

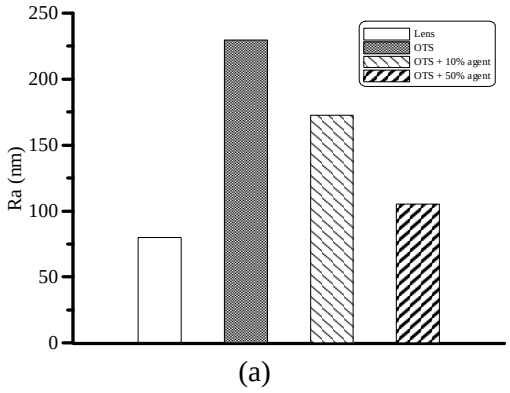

(a)

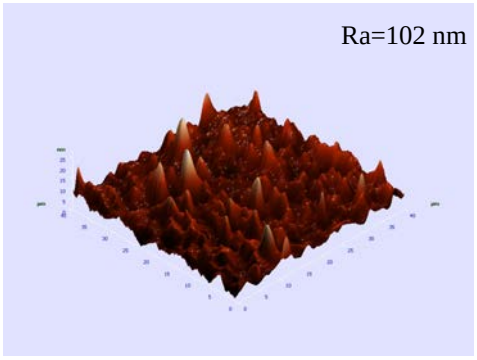

(b)

Figure 3. (a)The roughness values of the different surface films (b) 3-D topography image of the OTS + 50% agent film.

The various roughness values of different surface materials are shown in Figure. 3. Roughness test were conducted in air at a relative humidity of about 50% using AFM by non-contact mode. The scanned detection range was 40 μm × 40 μm. The various surface roughness value of different surface materials are shown in Figure 3(a). The comparison chart shows that antibacterial agent can decrease the surface roughness value of pure OTS films. The roughness value of OTS film surface adding 10% antibacterial agent is approximately 175 nm, whereas the OTS film roughness value adding 50% antibacterial agent was decreased to approximately 100 nm. The 3-D topography image for the hybrid organic molecules film (OTS + 50% agent) is shown as Figure 3(b). The island-shaped structures were formed on the surface, as mentioned in Vaillant's work [8]. It shows hybrid organic film exhibit uniform coverage the surface with regular pattern of island formation. It indicates that antibacterial agent absorbed and stored in the topographic valley of OTS film.

The reliability and beauty requirement of the display elements made from company become important in their service life. The light transmittance and film adhesion properties are one of key performances of lens. In order to explore the relation between surface film and light transmittance of lens, Figure 4 shows that transmittance of OTS film and antibacterial agent on the lens. This result indicates that the OTS surface film will decrease the light transmittance of lens. However, the antibacterial agent has extremely little influence on the transmittance of lens. The minimum value of transmittance is 93.6% under the film of OTS + 50% agent. It concludes that all transmittance of surface films is acceptable for industrial applications in our work.

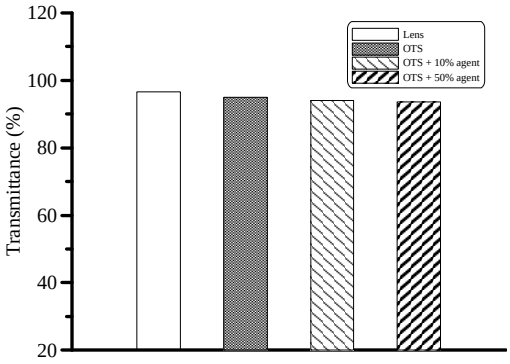

Figure 4 The light transmittance of different surface films on lens

The film adhesion is another one of key performances of lens for reliability. Figure 5 shows the effect of antibacterial agent on the critical load of surface films on the lens. It shows that antibacterial agent increases adhesion force between OTS film and lens. Mixing antibacterial agent (50%) in OTS material increases the critical load to approximately 104μN. In summary, the surface treatment of optical lenses involving OTS+ Agent (50%) is the most capable of effectively increasing anti-adhesion functions.

In the antibacterial tests, staphylococcus aureus were inoculated with different self-assembled film, and then after 24 hours to measure bacteria values (JISZ 2801:2010). Figure 6 is the comparison chart of the number of the bacteria for the different surface films. For the general lens surface, the bacteria number is about 135000 after 24 hours. The pure OTS film also has little antibacterial function. It shows that the bacteria number on OTS with 50% antibacterial agents and pure antibacterial agent surface is less than 10. It is far lower than the bacteria value, 5.3×10^4, on the OTS film.

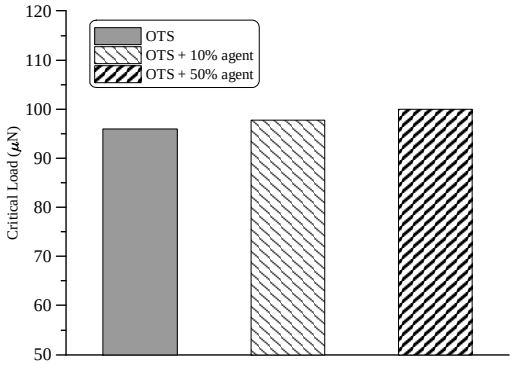

Figure 5. Critical loads between surface films and substrate

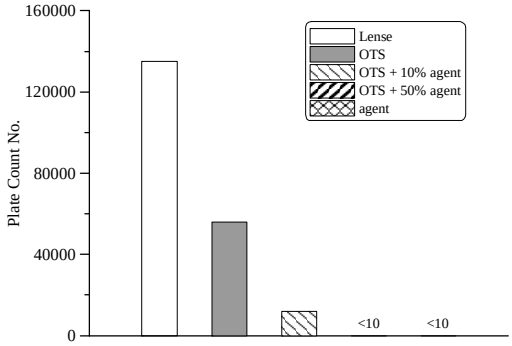

Figure 6. Effect of surface film material on antibacterial

4. CONCLUSION

This work studied the feature of anti-bacterial and anti-adhesion on OTS self-assembled monolayers which mixed with biocompatibility antibacterial agent that coated on optical lens. The results can be concluded as follows:

1. Both OTS and mixed OTS film can effectively increase the contact angle of a lens surface at various bath temperatures as well as duration time and reduces device adhesion force effectively.
2. The adding of antibacterial agent has little effect on the contact angle and light transmittance of pure OTS film.
3. The antibacterial agent can effectively reduce the surface roughness while increase the adhesion force and antibacterial abilities of pure OTS film on lens surfaces (reaction time = 12hr., reaction temperature = 80°C).

ACKNOWLEDGMENTS

The author gratefully acknowledges common Lab. for Micro-Nano Science and Technology at NFU.

REFERENCES

[1] M. Masuko, H. Miyamoto, A. Suzuki: *Tribological characteristics of self-assembled monolayer with siloxane bonding to Si surfac*, Tribology International, Vol. 40, pp. 1587-1596, 2007.

[2] G. Mani, D.M. Johnson, D. Feldman, D. Patel, A.A. Ayon, C.M. Agrawal: *Drug delivery from gold and titanium surfaces using self-assembled monolayers*, Biomaterials, Vol. 29, pp. 4561-4573, 2008**.**

[3] A.N. Parikh, D.L. Allara, I.B. Azouz, F. Rondelez: *An Intrinsic Relationship between Molecular Structure in Self-Assembled n-Alkylsiloxane Monolayers and Deposition Temperature*, Journal of Physical Chemistry, Vol. 98, pp. 7577-7590, 1994.

[4] C. Carraro, O.W. Yauw, M.M. Sung and R. Maboudian: *Observation of Three Growth Mechanisms in Self-Assembled Monolayers*, Journal of Physical Chemistry B, Vol. 102, pp. 4441-4445, 1998.

[5] R. Brambilla, F. Silveira, J. Santos: *Investigating morphological changes on octadecyl modifiedsilicas by SEM and AFM*, Modern Research and Educational Topics in Microscopy, pp. 626-633, 2007.

[6] P. Silberzan, L. leger, D. Auserre, J.J. Benatter :*Silanation of Silica Surfaces. A New Method of Constructing Pure or Mixed Monolayers*, Langmuir, Vol. 7, pp.1647-1651, 1991.

[7] K. Bierbaum, M. Grunze, A.A. Baski, L.F. Chi, W. Schrepp, H. Fuchs :*Growth of self-assembled n-alkyltrichlorosilane films on Si(100) investigated by atomic force microspcopy*, Langmuir, Vol. 11, pp.2143-2150, 1995.

[8] T.Vallant: *Formation of Self-Assembled Octadecylsiloxane Monolayers on Mica and Silicon Surfaces Studied by Atomic Force Microscopy and Infrared Spectroscopy*, Journal of Physical Chemistry B, Vol.102, pp.7190-7197,1998.

[9] R. Resch, M. Grasserbauer, G. Friedbacher, T.h. Vallant, H. Brunner, U. Mayer, H. Hoffmann: *In situ and ex situ AFM investigation of the formation of octadecylsiloxane monolayer*, Applied Surface Science, Vol. 140, pp.168-175, 1999.

[10]C. Carraro, O.W. Yauw, M.M. Sung, R. Maboudian: *Observation of Three Growth Mechanisms in Self-Assemble Monolayers*, Journal of Physical Chemistry B. Vol. 102, pp. 4441-4445, 1998.

[11] G. Mani, D.M. Feldman, O. Sunho, C.M. Agrawal: *Surface modification of cobalt-chromium-tungsten-nickel alloy using octadecyltrichlorosilanes*, Applied Surface Science, Vol. 255, pp. 5961-5970, 2009.

Serbian Tribology Society

SERBIATRIB '13

13th International Conference on Tribology

Faculty of Engineering in Kragujevac

Kragujevac, Serbia, 15 – 17 May 2013

THE INFLUENCE OF CORROSION ON THE MICROSTRUCTURE OF THERMALLY TREATED ZA27/SIC$_P$ COMPOSITES

Biljana Bobić[1], Aleksandar Vencl[2], Miroslav Babić[3], Slobodan Mitrović[3], Ilija Bobić[4]

[1]Institute ″Goša″, Belgrade, Serbia, biljanabobic@gmail.com

[2]Faculty of Mechanical Engineering, University of Belgrade, Belgrade, Serbia, avencl@mas.bg.ac.rs

[3]Faculty of Engineering, University of Kragujevac, Kragujevac, Serbia, babic@kg.ac.rs, boban@kg.ac.rs

[4]″Vinča″ Institute of Nuclear Sciences, University of Belgrade, Belgrade, Serbia, ilijab@vinca.rs

Abstract: *The influence of corrosion on the microstructure of ZA27/SiC$_p$ composites was examined. The composites were produced by compo casting technique and then subjected to the thermal treatment (T4 regime). Microstructural examinations were performed after 30-day exposure of thermally treated composites in the sodium-chloride solution. Corrosion processes have occurred in the composite matrix. Corrosion did not affect SiC particles in the composites. The local progress of corrosion in depth of the composite matrix was noticed in micro-cracks. Corrosion resistance of ZA27/SiC$_p$ composites was evaluated based on the mass loss of composite samples during the immersion test. It was found that corrosion resistance of the composites decreased with increase in content of SiC particles. The applied thermal treatment had a negative influence on the corrosion resistance of ZA27/SiC$_p$ composites.*

Keywords: *Metal-matrix composites, ZA27 alloy, Compocasting, Thermal treatment, Corrosion, Microstructure*

1. INTRODUCTION

Domestic composites with base ZA27 alloy [1, 2] have been developed with an aim to obtain composites which maintain good mechanical characteristics at elevated temperatures as well as to make composites with improved tribological properties compared to those of the matrix alloy. Particulate ZA27/SiC$_p$ composites were shown to possess significant tribological potential because of high hardness and high wear resistance [3, 4]. Within this work, domestic ZA27/SiC$_p$ composites were obtained by compo casting technique. The matrix alloy, with 27 wt. % aluminum, belongs to zinc–aluminum foundry alloys with relatively high content of aluminum (ZA alloys). The alloy is characterized by good physical, mechanical and technological properties (low density, high strength and hardness, easy machinability) [5, 6], by a substantial resistance to corrosion and high wear resistance [7–9]. This enabled commercial application of ZA27 alloy as a significant tribomaterial, especially for making bearings and bushings.

ZA27 alloy solidifies in the wide temperature range and is suitable for processing in the semi-solid state [10]. This led to the application of compo casting technique for producing domestic particulate composites with base of ZA27 alloy. Micro-particles of SiC [1], Al_2O_3 [1, 2, 11, 12], graphite [9, 13] or ZrO_2 [14] were incorporated in the semi-

solid melt of ZA27 alloy using mechanical mixing. Obtained composites were subjected to microstructural examinations [11, 12] and tribological tests [9, 13]. In addition, mechanical characteristics of the composites have been studied, at room temperature [11, 12] and moderately elevated temperatures [2]. However, corrosion behavior of domestic composites with base ZA27 alloy has not been tested so far.

Physical, mechanical and corrosion characteristics of metal-matrix composites are deeply influenced by the microstructure of metal matrices [15, 16]. It was shown that thermal treatment affected the microstructure and properties of ZA27 alloy [17–19]. A beneficial effect of T4 regime on ductility [17] and tribological characteristics of ZA27 alloy [18, 19] was noticed, although this thermal treatment resulted with minor reduction in hardness and tensile strength [18]. In addition, it was shown that T4 regime affected the microstructure and corrosion resistance of as-cast ZA27 alloy [20] and thixocast ZA27 alloy [21].

ZA27 alloy is highly corrosion resistant in atmospheric conditions and natural waters [22]. The most common form of corrosion in these environments is general corrosion, which enables calculations of the alloy corrosion rate, based on the weight loss of samples during exposure in corrosive media. Immersion tests in chloride solutions have been used frequently, because chloride ions are present in numerous corrosive environments.

Thixocast ZA27 alloy is the base of ZA27/SiC_p composites obtained by compo casting technique [23]. Accordingly, the microstructure of thixocast alloy is actually the microstructure of the composite matrix. It was shown recently that thermal treatment (T4 regime) negatively affected the corrosion behavior of thixocast ZA27 alloy [21]. However, there have been no published results until now, concerning the effect of T4 regime on the microstructure and corrosion resistance of ZA27/SiC_p composites obtained by compo casting technique.

Considering the importance of corrosion resistance for selection and application of metal-matrix composites, it was the aim of this work to study the influence of corrosion on the surface appearance and microstructure of the thermally treated ZA27/SiC_p composites. Corrosion resistance of the composites was evaluated based on the weight loss of samples during immersion in the sodium-chloride solution.

2. EXPERIMENTAL

2.1 Materials

A domestic producer of zinc-aluminum alloys (RAR Foundry® Ltd., Batajnica) has provided the master alloy for the experimental work. SiC particles (with average diameter of 40 μm) were obtained from the domestic manufacturer of abrasive products (Ginić Tocila® Ltd., Barajevo).

ZA27 alloy was conventionally melted and casted in the Department of Materials Science ″Vinča″ Institute. Chemical composition of the alloy is given in Table 1.

Table 1. Chemical composition of ZA27 alloy

Element*	Al	Cu	Mg	Zn
wt. %	26.3	1.54	0.018	balance

*Concentration of other elements (Fe, Sn, Cd, Pb) is within acceptable limits.

Compo casting technique was used for making composites with 1, 3 and 5 wt. % SiC particles. The particles were incorporated into the semi-solid melt of ZA27 alloy with use of mechanical mixing. Parameters of the applied compo casting aprocess nd description of the apparatus can be found in [23].

Composite castings were subjected to a hot pressing, in order to reduce porosity and improve the bond strength between the matrix and particulate reinforcements. Samples for microstructural examinations and corrosion testing were machine cut from the composite castings. The samples were thermally treated according to T4 regime: solutionizing at 370ºC for 3 hours, with subsequent water quenching and natural aging.

2.2 Methods

Microstructural examinations

Surface morphology and microstructure of thermally treated ZA27/SiC_p composites were examined by optical microscopy (OM) and scanning electron microscopy (SEM). Carl Zeiss optical microscope and JEOL JSM–5800 scanning electron microscope were used. Cylindrical samples (5 mm in diameter and 8 mm in height) were embedded in the polymethacrylate and then they were ground and polished. Wet grinding was performed with successively finer abrasive papers (240, 360, 600 and 800 grit SiC), while polishing was done using polishing cloth and diamond paste (particles size up to 2 μm). Aqueous solution of nitric acid (9 v/v % HNO_3) was used for etching of the samples.

The samples were rinsed with acetone and dried in the air before exposure in the test solution (3.5 wt. % NaCl). After finishing of the exposure, the samples were prepared for metallographic examination in the usual way.

Corrosion rate testing

Corrosion rates of thermally treated ZA27/SiC_p composites were calculated based on the samples mass loss during exposure in the test solution (immersion test). Preparation of the samples and testing procedure were performed in accordance with ASTM G31 [24]. The samples (18 x 28 x 3 mm), in triplicate, were suspended vertically in the stagnant sodium-chloride solution (3.5 wt. % NaCl, pH=6.7) open to the atmosphere. The test was performed at room temperature (23 ± 2°C). After 30 days of exposure, the samples were withdrawn from the test solution and rinsed with distilled water. Corrosion products were removed from the surface of the samples by chemical procedure [25]. The samples were then reweighed to determine the mass loss during exposure in the test solution.

Calculation of the average corrosion rate *CR* [mm/year] is based on the mass loss of the samples Δm [g] during the immersion test:

$$CR = \frac{8.76 \cdot \Delta m}{d \cdot A \cdot \tau} \qquad (1)$$

τ is the exposure time (720 hours), *A* is the sample surface [cm^2] and *d* [g/cm^3] is the composite density. Values of the composite density (for the composite with 1, 3 and 5 wt. % SiC particles, respectively) were calculated [23] and shown in Table 2.

Table 2. Density of ZA27/SiC_p composites

Material	ZA27/1%SiC_p	ZA27/3%SiC_p	ZA27/5%SiC_p
d [g/cm^3]	4.97	4.92	4.87

The values in Table 2 were used to calculate corrosion rates of the thermally treated ZA27/SiC_p composites.

3. RESULTS AND DISCUSSION

3.1 Microstructure of thermally treated ZA27/SiC_p composites

Surface appearance and microstructure of thermally treated ZA27/SiC_p composites were examined before exposure and after 30-day exposure in the sodium-chloride solution. Surface appearance of the composites with 3wt. % SiC particles, is shown in Figure 1a, b.

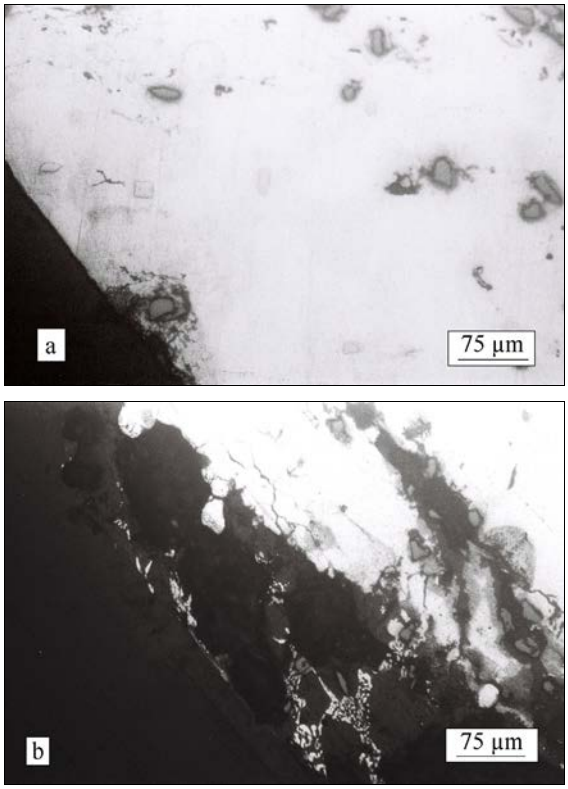

Figure 1. Surface appearance of the thermally treated composite ZA27/3wt.%SiC_p (OM, polished):
a) before exposure, b) after 30-day exposure in 3.5 wt.% NaCl.

SiC particles are uniformly distributed in the metal matrix (Fig. 1a). A few inclusions can be noticed on the surface of the composite sample and mechanical damages on the edge of the sample. Applied thermal treatment had no effect on the particles of reinforcement and their distribution in the composite matrix.

The microstructure of composites was revealed by etching (Figure 2a, b). It can be seen in Fig. 2a that SiC particles are distributed in the regions of η phase and regions of phase mixture α+η. There are no voids, due to the fallout of SiC particles from the composite base (e.g. during machining or metallographic preparation of samples). This indicates good bonding between SiC particles and the matrix alloy.

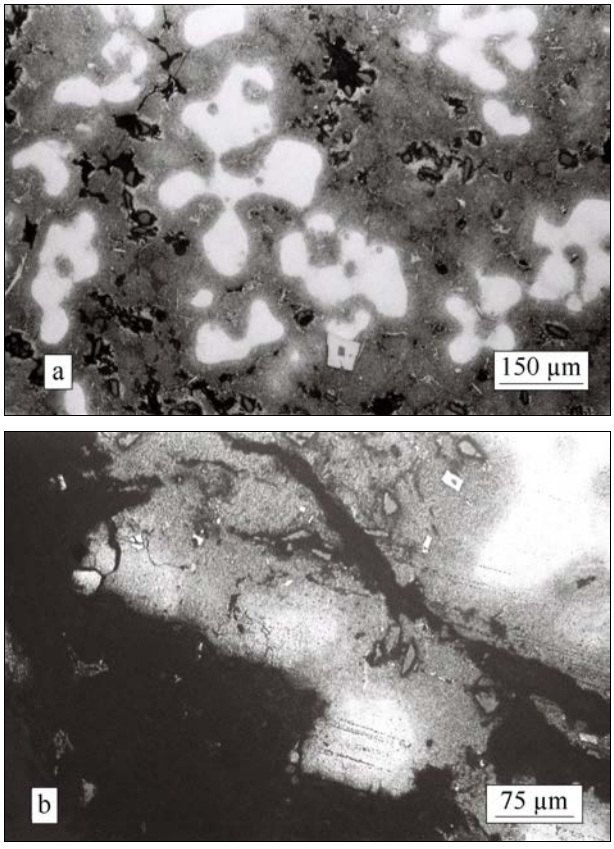

Figure 2. Microstructure of the thermally treated ZA27/3wt.%SiC_p composite (OM, etched): a) before exposure, b) after 30-day exposure in 3.5 wt.% NaCl.

Main micro-constituents in the composite matrix are also visible in Fig. 2a. The microstructure of the composite base is non-dendritic and is characterized by the presence of large primary particles [21, 23]. The primary particles are complex; they consist of a core (rich in aluminum) and a periphery (composed of the phase mixture α+η). Interdendritic η phase, rich in zinc, is located between the primary particles. The microstructure of the composite matrix and the microstructure of thixocast ZA27 alloy are morphologically very similar [23]. The applied thermal treatment (T4 regime) has caused changes in the structure of the composite matrix. The region of phase mixture α + η was expanded, while the regions of individual phases (α and η) were reduced. In addition, the size of primary particles of α phase was decreased for about 30 vol. % [21, 23]. All this resulted with finer microstructure of the composite matrix. However, the increase in number of micro-cracks on the phase boundaries η/α+η was noticed in the composite matrix after the thermal treatment [23]. Thermal stress at boundary surfaces matrix/particle, due to quenching within thermal treatment, was preceded by thermal stress during solidification of the composite mixture. The stress can cause a local deformation of the metal matrix around particles of reinforcement [26], appearance of micro-cracks or fracture of the particles. Electrolytes can be retained in the micro-cracks, causing local progress of corrosion processes into depth of the composite base.

The number of boundary surfaces matrix/particle was significantly increased in the ZA27/SiC_p composites due to the presence of SiC particles.. It can be assumed that dislocation density was also increased during cooling of the composite mixtures, due to different coefficients of linear expansion of the matrix ZA27 alloy and SiC particles.

Corrosion processes have influenced the surface appearance and microstructure of thermally treated ZA27/SiC_p composites. The surface appearance of the composites with 3 wt. % SiC_p, after 30-day exposure in the sodium-chloride solution, is shown in Fig. 1b. Large primary particles of α phase are visible in the central area of the composite sample. It can be seen that corrosion has started at places of mechanical damages, voids, inclusions. Corrosion processes occurred in the composite base, in the regions of phase mixture α+η and regions of η phase. The local progress of corrosion was noticed in the micro-cracks and pores. The micro-cracks were probably formed during solidification of the composite mixtures, in hot pressing as well as during quenching

within thermal treatment of the composites. The presence of micro-cracks negatively affected corrosion resistance of thermally treated ZA27/SiC_p composites.

SiC particles were not involved in corrosion processes because of their inherent chemical stability. However, these particles have influenced corrosion behavior of ZA27/SiC_p composites. The continuity of boundary surfaces matrix/particle is disturbed in the clusters of SiC particles. On these places micro-pores and micro-cracks can be formed. Due to the retention of sodium-chloride solution in these places, local progress of corrosion in depth of the composite matrix was noticed, as it was mentioned before.

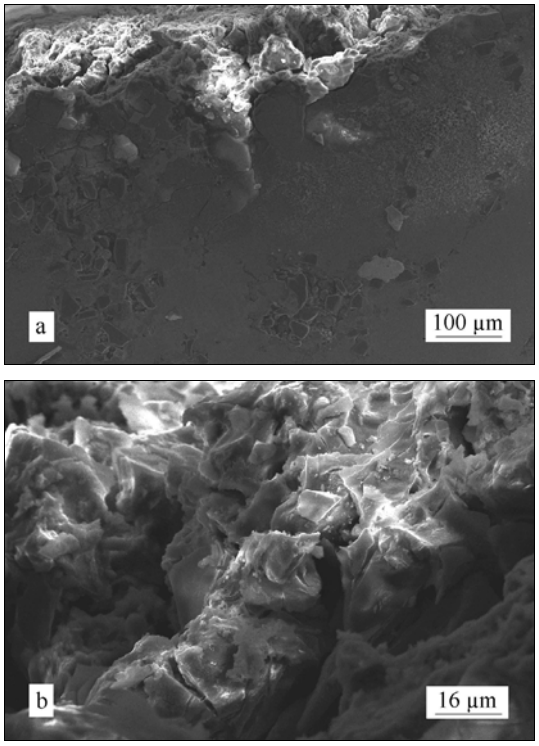

Figure 3. Corrosion products of the of thermally treated ZA27/3wt.%SiC_p composite after 30-day exposure in 3.5 wt.% NaCl (SEM): a) surface appearance, b) detail.

During exposure in the sodium-chloride solution, corrosion products were formed on the surface of the composite samples. Spongy, white deposits of the corrosion products, mostly in the form of rosettes, are shown in Figure 3a, b.

Microstructural examinations of thermally treated ZA27/SiC_p composites, after exposure in the sodium-chloride solution, made it possible to gain some insight into the influence of corrosion processes on the structure of these composite materials. It was found that corrosion started in places of mechanical damage, voids, inclusions. Corrosion processes have occurred mainly in the composite base, although in pores and micro-cracks, the local progress of corrosion in depth of the composites was noticed. Corrosion processes did not influence SiC particles.

Results of the microstructural examinations, after exposure of thermally treated ZA27/SiC_p composites in the sodium-chloride solution, are in accordance with results obtained during the immersion test.

3.2 Corrosion rate of thermally treated ZA27/SiC_p composites

After finishing of exposure in the NaCl solution, corrosion products were removed from the surface of ZA27/SiC_p composite samples by chemical procedure [25]. It was found that corrosion attack was mostly uniform, while corrosion processes took place predominantly on the composite surface. The average value of corrosion rate *CR* [mm/year] was calculated based on the mass loss of composite samples during the immersion test. The results are presented in Figure 4.

For the purpose of comparison, results of the immersion test for thermally treated ZA27 alloys (as-cast and thixocast) [21, 23] are also presented in Figure 4. It can be seen that corrosion rates of the composites are higher than those of both ZA27 alloys (as-cast and thixocast).

Corrosion resistance of the composite matrix (thermally treated thixocast ZA27 alloy) is higher than that of thermally treated composites.

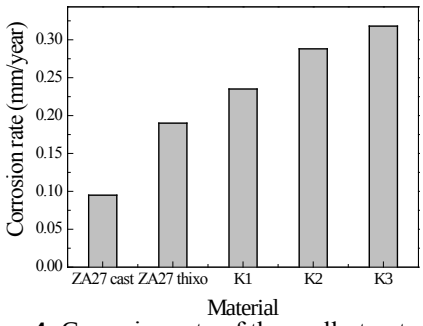

Figure 4. Corrosion rate of thermally treated ZA27 alloys and ZA27/SiC_p composites after 30-day exposure in 3.5 wt.% NaCl. K1 - ZA27/1wt.%SiC_p, K2 - ZA27/3wt.%SiC_p, K3 - ZA27/5wt.%SiC_p.

Corrosion rate of thermally treated ZA27/SiC_p composites increases with increase in content of SiC particles, because of increase

in number of micro-cracks and clusters of SiC particles. All above presented indicates lower corrosion resistance of thermally treated ZA27/SiC_p composites with higher content of particulate reinforcements.

4. CONCLUSIONS

Particulate ZA27/SiC_p composites (with 1, 3 and 5 wt.% SiC particles) were obtained by compo casting technique and subsequently subjected to the T4 thermal treatment. Thermally treated composites were exposed in the sodium-chloride solution for 30 days. The influence of corrosion on the surface appearance and microstructure of the composites was examined. Corrosion resistance of the composites was evaluated based on the mass loss of composite samples during the immersion test. According to the results presented, the following conclusions can be proposed:

1. SiC particles are uniformly distributed in the metal matrix of the particulate ZA27/3wt.%SiC_p composite that was made by compo casting technique.
2. Morphological changes and appearance of micro-cracks in the microstructure of the composite matrix were noticed after T4 thermal treatment. However, the thermal treatment had no effect on SiC particles and their distribution in the composite matrix.
3. Corrosion process has influenced the microstructure and surface appearance of thermally treated ZA27/SiC_p composites, after 30-day exposure in the sodium-chloride solution. However, corrosion did not affect SiC particles in the composites.
4. Corrosion started at places of mechanical damages, voids, inclusions. Corrosion processes ocurred mainly in the composite matrix although the local progress of corrosion was noticed in the micro-cracks.
5. Corrosion resistance of the composite matrix is higher than that of ZA27/SiC_p composites.
6. Corrosion rate of thermally treated ZA27/SiC_p composites increases with increase in content of SiC particles.
7. Applied thermal treatment (T4 regime) has shown a negative effect on the corrosion resistance of ZA27/SiC_p composites.

ACKNOWLEDGEMENTS

The Ministry of Education, Science and Technological Development of the Republic of Serbia has supported financially this work through the projects TR 35021 and OI 172005. The authors are gratefully acknowledged to the RAR® Foundry Ltd., Batajnica (Belgrade, Serbia) and Ginić Tocila® Abrasive Products Factory Ltd., Barajevo (Belgrade, Serbia), for providing the master alloy and SiC particles, to perform this research.

REFERENCES

[1] I. Bobić: *Development if Metal Forming Process in Semi-Solid State (Rheocasting and Compocasting Process) and Process Controling Effects on Quality of ZnAl25Cu3 Alloy Products,* PhD thesis, Faculty of Technology and Metallurgy, University of Belgrade, Belgrade, 2003.

[2] B. Bobić, M. Babić, S. Mitrović, N. Ilić, I. Bobić, M.T. Jovanović: *Microstructure and mechanical properties of Zn25Al3Cu based composites with large Al_2O_3 particles at room and elevated temperatures,* Int. J. Mat. Res. (formerly Z. Metallkd.), 101, pp. 1524–1531, 2010.

[3] I.A. Cornie, R. Guerriero, L. Meregalli, I. Tangerini: Microstructures and Properties of Zinc-Alloy Matrix Composite Materials, in *Proceedings of the International Symposium on Advances in Cast Reinforced Metal Composites,* 24–30.09.1988., Chicago, pp. 155–165

[4] N. Karni, G.B. Barkay, M. Bamberger: *Structure and properties of metal-matrix composite,* J. Mater. Sci. Lett., 13, pp. 541–544, 1994.

[5] E. Gervais, R.J. Barnhurst, C.A. Loong: *An analysis of selected properties of ZA alloys,* JOM, 11, pp. 43–47, 1985.

[6] E.J. Kubel Jr.: *Expanding horizons for ZA alloys,* Adv. Mater. Process., 132, pp. 51–57, 1987.

[7] R.J. Barnhurst, S. Beliste: *Corrosion Properties of Zamak and ZA Alloys,* Tech. Rep., Noranda Technology Centre, Quebec, Canada, 1992.

[8] M. Babić, R. Ninković: *Zn-Al alloys as tribomaterials,* Trib. Ind., Vol. 26, No. 1–2, pp. 3–7, 2004.

[9] S. Mitrović: *Tribological Properties of ZnAl Alloy Composites,* PhD thesis, Faculty of Mechanical Engineering, University of Kragujevac, Kragujevac, 2007.

[10] M. Flemings: *Behavior of metal alloys in the semi-solid state*, Metall. Trans. A, Vol. 22A, pp. 957–981, 1991.

[11] I. Bobić, M.T. Jovanović, N. Ilić: *Microstructure and strength of ZA-27 based composites reinforced*

with Al_2O_3 particles, Mater. Lett., 57, pp. 1683-1688, 2003.

[12] I. Bobić, R. Ninković, M. Babić: *Structural and mechanical characteristics of composites with base matrix of Rar 27 alloy reinforced with Al_2O_3 and SiC particles,* Trib. Ind., Vol. 26, No. 3–4, pp. 27–29, 2004.

[13] M. Babić, S. Mitrović, D. Džunić, B. Jeremić, I. Bobić: *Tribological behavior of composites based on ZA-27 alloy reinforced with graphite particles,* Tribol. Lett., 37, pp. 401–410, 2010.

[14] Z. Aćimović–Pavlović, K.T. Raić, I.Bobić, B. Bobić: *Synthesis of ZrO_2 Particles Reinforced ZA25 Alloy Composites by Compocasting Process,* Adv. Compos. Mater., 20, pp. 375–384, 2011.

[15] L.L. Shreir, R.A. Jarman, G.T. Burstein: *Corrosion,* Butterworth- Heinemann, Oxford, 2000.

[16] S.L. Donaldson, D.B. Miracle: *ASM Handbook Volume 21, Composites,* ASM International, 2001.

[17] I. Bobić, B. Đurić, M.T. Jovanović, S. Zec: *Improvement of Ductility of a Cast Zn–25 Alloy,* Mater. Charact., 29, pp. 277–283, 1992.

[18] M. Babić, A. Vencl, S. Mitrović, I. Bobić: *Influence of T4 heat treatment on tribological behavior of ZA27 alloy under lubricated sliding condition,* Tribol. Lett., 2, pp. 125–134, 2009.

[19] M. Babić, S. Mitrović, R. Ninković: R: *Tribological Potential of Zinc-Aluminium Alloys Improvement,* Trib. Ind., Vol. 31, No. 1–2, pp. 15–28, 2009.

[20] B. Bobić, J. Bajat, Z. Aćimović–Pavlović, M. Rakin, I. Bobić I: *The effect of T4 heat treatment on the microstructure and corrosion behaviour of Zn27Al1.5Cu0.02Mg alloy,* Corros. Sci., 53, pp. 409–417, 2011.

[21] B. Bobić, J. Bajat, Z. Aćimović–Pavlović, I. Bobić, B. Jegdić, *Corrosion behaviour of thixoformed and heat-treated ZA27 alloys in the natrium chloride solution,* Trans. Nonferr. Met. Soc. of China, to be published

[22] F.C Porter: *Corrosion Resistance of Zinc and Zinc alloys,* Marcell Dekker, New York, 1994.

[23] B. Bobić: *Examination of the Corrosion Process Impact on the Microstructure and Mechanical Properties of Zn27Al1,5Cu0,02Mg alloy Castings Reinforced with Silicon Carbide Particles,* PhD thesis, Faculty of Technology and Metallurgy, University of Belgrade, Belgrade, 2011.

[24] ASTM G31–72 (2004): *Standard Practice for Laboratory Immersion Corrosion Testing of Metals.*

[25] ASTM G1–03(2011): *Standard Practice for Preparing, Cleaning and Evaluation of Test Specimens.*

[26] R.J. Arsenault, L. Wang, C.R. Feng: *Strengthening of composites due to microstructural changes in the matrix,* Acta Metall. Mater., Vol. 39, No. 1, pp. 47–57, 1991.

Serbian Tribology Society

SERBIATRIB '13

13th International Conference on Tribology

Faculty of Engineering in Kragujevac

Kragujevac, Serbia, 15 – 17 May 2013

TRIBOLOGICAL CHARACTERISATION OF PBT + GLASS BEAD COMPOSITES WITH THE HELP OF BLOCK-ON-RING TEST

Constantin Georgescu[1], Mihai Botan[1], Lorena Deleanu[1]

[1]"Dunarea de Jos" University of Galati, Romania, constantin.georgescu@ugal.ro

Abstract: *The materials involved in this research study were produced by die moulding in order to obtain bone samples type 1A (SR EN ISO 527-2:2003). These composites have a matrix of polybutylene terephthalate (PBT) commercial grade Crastin 6130 NC010, DuPont. The values for the glass beads concentrations were established at 10% and 20% (wt). Block-on-ring tests were run in order to characterize the tribological behaviour of this friction couple (PBT and PBT composites with glass beads on steel). The block was manufactured by cutting parts from the bone samples, having the dimensions of 16.5 mm × 10 mm × 4 mm. The other triboelement was the external ring of the tapered rolling bearing KBS 30202, having dimensions of Ø35 mm × 10 mm and was made of steel grade DIN 100Cr6. There were analysed the following characteristics: friction coefficient (mean value over a test and scattering range), wear (wear rate). There are also presented particular aspects of the worn surfaces, as investigated from SEM images.*

Keywords: *PBT composite, tribological behaviour, block-on-ring test, dry sliding.*

1. INTRODUCTION

Materials based on PBT are obtained both by adding very different materials (nano and micro fibre reinforcements [1], metallic or/and ceramic powders, minerals [2], [3]), the result could be included in the class of composites, and by blending with other polymers polytetrafluoro-ethylene (PTFE) [4], polycarbonate (PC) [5], polyethylene (PE), SAN, epoxy resin, with fire resistant additives [6], both solutions directioning one or a set of the properties of PBT matrix.

The adding materials in PBT are very diverse, almost all types known for the polymeric composites (long and short fibres, particles and their mixtures), both at micro scale and nano scale. For tribological applications, the fibre nature is also diverse: glass, carbon, aramidic, titanates.

Even if the specialized literature emphasis the influence of the adding materials in PBT, upon some mechanical characteristics (traction limit and elasticity modulus) [2], [3], [7], these properties do not also reflect the tribological behaviour of these materials. This is why the testing of the polymeric composites is of high importance and, even if the results could not be extrapolated from the laboratory tests on tribotesters, to the actual friction couple, these studies are useful in materials' ranking, when the designer is interest in a particular parameter or a set of characteristics [8], [9], [10].

2. MATERIALS AND TESTING METHODOLOGY

The tested materials were produced by die moulding in order to obtain bone samples type 1A (as required by the tensile test ISO 527-2) at the Research Institute for Synthetic Fibres Savinesti, Romania, taking into account the producer specification for moulding and heat treatment [11].

These composites have a matrix of polybutylene terephthalate (PBT), commercial grade Crastin 6130 NC010, DuPont.

The recipes for the composite materials based on PBT, included in this study, were elaborated by the authors based on up-to-date documentation [1], [4], [11] and were designed in order to point out the influence of matrix and adding materials on the tribological behaviour in dry regime. Table 1 presents their compositions and the abbreviations used in this paper. The polyamide (PA) was added in low concentration in order to have a better

dispersion of the micro glass beads. The black carbon was added for both technological and tribological reasons.

Table 1. The tested materials

Material symbol	Concentration [%, wt]			
	PBT	Micro glass beads	PA	Black carbon
PBT	100	-	-	-
GB10	88	10	1.5	0.5
GB20	77.5	20	2	0.5

The tests were done using a block-on-ring tribotester, functioning on a CETR tribometer UMT-2 Multi-Specimen Test System.

The ring was the external ring of the tapered rolling bearing KBS 30202 (DIN ISO 355/720), having the dimensions of Ø35 mm × 10 mm and was made of steel grade DIN 100Cr6, having 60-62 HRC and Ra = 0.8 μm on the exterior surface.

The block was manufactured by cutting parts from the bone samples, having the dimensions of 16.5 mm × 10 mm × 4 mm.

The tests were run in dry condition, for combination (F, v), F being the normally applied load (F = 1.0 N, F = 2.5 N and F = 5.0 N) and v being the sliding speed (v = 0.25 m/s, v = 0.50 m/s and v = 0.75 m/s). The sliding distance was the same for all tests, L = 7500 m.

For evaluating the mass loss of the blocks, an analytical balance METTLER TOLEDO was used, having the measuring accuracy of 0.1 mg.

The SEM images were done with the help of the scanning electron microscope Quanta 200 3D, having a resolution of 4 nm, a magnification ×1.000.000.

3. EXPERIMENTAL RESULTS

3.1 Friction coefficient

In order to compare the three tested materials, the extreme values and the average value of the friction coefficient were graphically presented in Figure 1 as a function of the sliding speed and the normal load. These values (the lowest value, the highest value and the average one) were calculated based on the recorded values during each test (sampling rate being 10 values per second). Thus, it could be appreciated the stability of the friction coefficient by the size of the scattering interval and an average energy consumption by the average value of the friction coefficient.

For actual applications working under similar conditions of speed and load, the author would recommend the materials with a smaller scattering interval and lower values of the average friction coefficient.

The low loads and speeds produce a larger scattering interval for the friction coefficient, but the load and speed increase makes the friction coefficient diminish the average value and to narrow the scattering interval. A research report from NASA [12] had evidenced high average values of the friction coefficient of over 0.6, for three polymers sliding against steel (the tribotester: polymeric ball on steel disk).

From these research reports and the experimentally obtained data during this study, the authors point out the importance of the laboratory tests for evaluating the friction coefficient and other tribological characteristics.

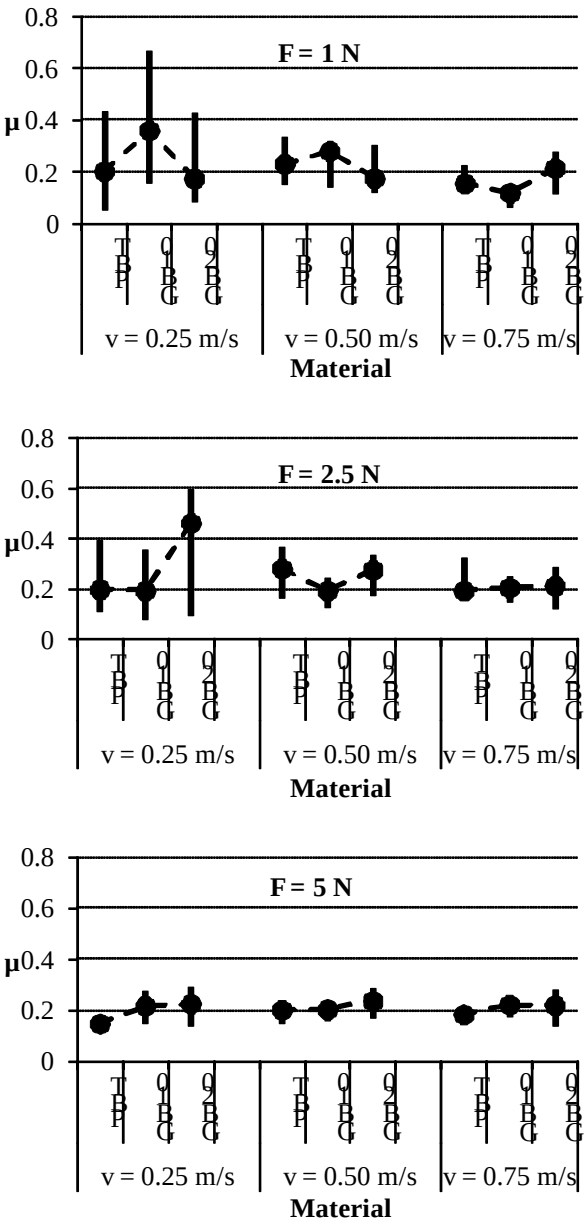

Figure 1. Variation of friction coefficient of PBT and composites with different micro glass beads content, for the sliding distance L = 7500 m

PBT has the average values of the friction coefficient, μ, in the narrowest range, around the value 0.2. The increase of this average could be explained by the elimination of the relatively big wear particles that are characteristic for this polymer (see Figure 4). The values obtained for F = 5 N are grouped under 0.2 for all the tested sliding speeds.

The composites GB10 (PBT + 10% micro glass beads) and GB20 (PBT + 20% micro glass beads) have the average value of the friction coefficient scattered on larger intervals, especially for the smaller normal loads (F = 1 N and F = 2.5 N). For F = 1 N, it is hard to establish a dependency relation of the friction coefficient on the adding material concentration and the sliding speed. It could be noticed that for blocks made of GB20, there are larger intervals.

At the sliding speed of v = 0.25 m/s, the abrasive wear is predominant, the polymer being hung (torn) and drawn from the superficial layers as micro-volumes, their size being greater at higher speeds (Figure 2). At the sliding speed of v = 0.75 m/s, the influence of the normal load on the average value of the friction coefficient is similar: μ increases from 0.12 for F = 1 N, to ~0.2 for F = 5 N.

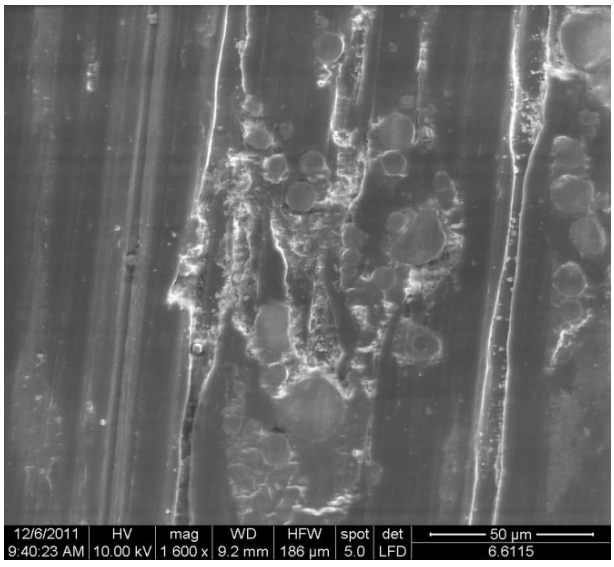

Figure 2. SEM image of the block made of GB10, for v = 0.25 m/s, F = 5 N, L = 7500 m

For the blocks made of GB20, under F = 2.5 N, the scattering of the values for the friction coefficient is the largest. The probable cause would be the micro-cutting processes that will have a more reduced intensity when the sliding speed increases. There were not noticed processes of dragging the micro glass beads on the block surfaces, meaning that the interface between the micro glass beads and the polymeric matrix is harder to damage, as compared to, for instance, the mobility of the micro glass beads in the sliding direction, but also in the depth of the superficial layer, as noticed in testing the composites with same type of micro glass beads added in a polyamide matrix [13].

The values of the friction coefficient have the tendency of being less dependent on the sliding speed for the normal load F = 5 N; this recommends these materials for an exploitation regime with different working speeds (differentiated speeds imposed by the technological process), without having very different energy consumption levels when the speed is changing.

The extreme values of the friction coefficient are caused by the generation and the detaching of the wear debris, the ring passing over a bigger micro glass beads, an agglomeration of micro glass beads or fragments of some broken ones on the surface as remained after a preferential elimination of the polymer from the superficial layer. In other studies on the polymeric composites with micro glass beads, there were no reports on fracturing the hard particles.

For the composites with PBT matrix, the authors noticed breakings of the micro glass beads, generally those of bigger diameters (20...40 μm) being broken. Figure 3 presents four broken micro glass spheres (A, B, C and D) on an area of ~ 600 μm × 600 μm in the central zone of the contact; the resulted fragments are embedded into the polymeric matrix. Such events taken place in the contact create high oscillations of the friction coefficient.

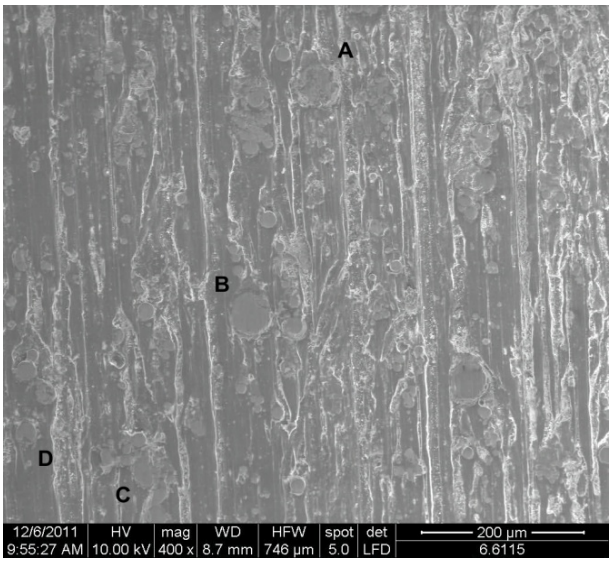

Figure 3. SEM image of a block made of GB10 – four broken micro glass beads (A, B, C and D). Test conditions: v = 0.25 m/s, F = 5 N, L = 7500 m

From SEM images (Figure 4), the wear debris were characterized as size and shape, many are made especially of polymer with only small glass debris (from fragmented micro glass beads) or small micro glass beads (but rare). During the test, the wear debris adhere one to each other and are generally big and rare (as compared to the wear debris resulted from other polymer in dry sliding against steel) and

they are volumic (Figure 4), not laminated and thin, as it is happening in the case of PTFE [14]. Generally, small micro glass beads are evacuated from the superficial layers and the polymer around the bigger ones is detached. In this scenario, one or more micro glass beads will support an individual load great enough to be broken.

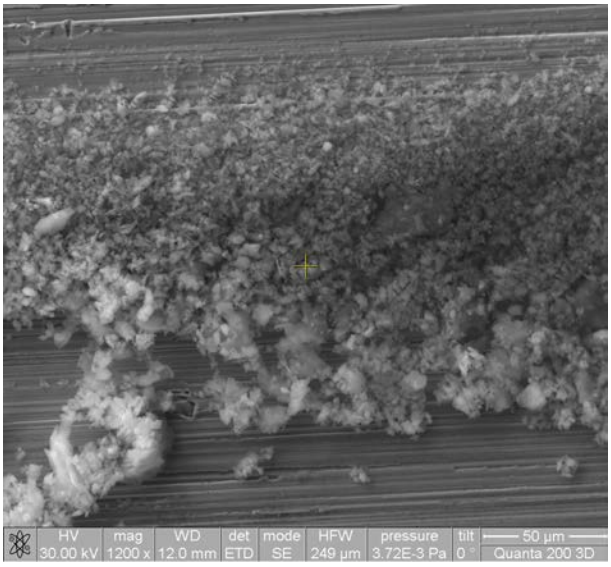

a) At the edge of the wear track from the ring

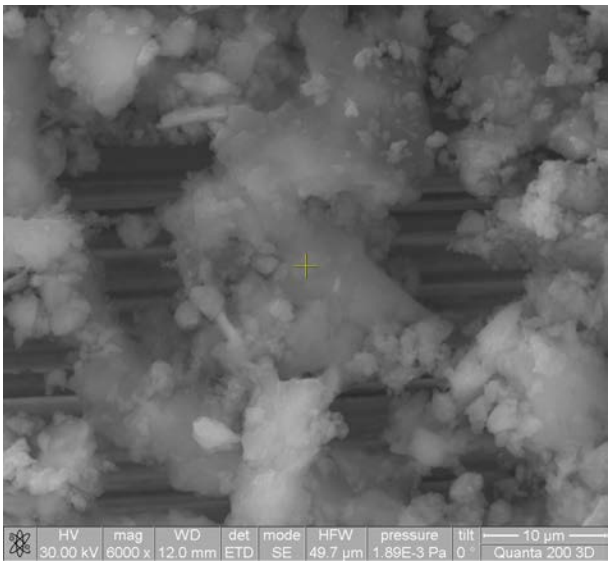

b) Wear particles made of polymer and very small fragments from the broken glass beads

Figure 4. Aspect of the wear particles generated during the test involving the sliding of the block made of GB20 on the metallic ring. Test conditions: F = 5 N, v = 0.75 m/s, L = 7500 m

At F = 1 N and v = 0.25 m/s, a larger scattering interval of the friction coefficient had resulted; there are prevailing the micro-cutting process and events implying the glass beads (overrunning of the hard asperities of the metallic ring, the breakage of the micro glass beads and rare shear of the hard asperities, the micro glass beads embedding into the polymeric matrix). A doubling of the sliding speed (v = 0.5 m/s) determines diminishing the average value of the friction coefficient characterizing these composites, from 0.15...0.28, to 0.12...0.22. At v = 0.5 m/s, both composites behave well, the friction coefficient becoming stable around the average value of 0.2. The polymer is warming and, thus, it is reducing its mechanical properties and allows for generating a very thin viscous film that is not expelled from the contact (as it happens with other polymer under high speed) and becomes a favourable factor in reducing friction also by embedding the glass beads in the soften matrix.

At F = 2.5 N, the average value of the friction coefficient has a slightly tendency of increasing when the micro glass beads concentration are increased.

At F = 5 N, the values of the analysed parameters of the friction coefficient have been reduced (figure 1), confirming the results obtained in other research [12] that the small loads generate a more intense friction for the friction couple element(s) made of polymer or polymeric composites and hard counterpart (steel). The normal force, for which the friction coefficient begins to decrease, is depending on the shape and size of the triboelements and on the working conditions [15], [16].

3.2 Wear

Taking into account the commanding parameters involved in this study (the material, by the concentration of the adding materials, the sliding speed and the load) and the recent documentation on wear parameterization [15], [16], [17], [18], [19], [20], the authors selected the wear rate (k) for analysing the experimental wear results obtained during this research.

$$k = \frac{V}{F \cdot L} = \frac{\Delta m}{\rho \cdot F \cdot L} \ [\text{mm}^3/(\text{N} \cdot \text{m})] \qquad (1)$$

where F [N] – the normal force and L [m] – the sliding distance, V [mm^3] is the material volume lost by wear, Δm [g] is the mass loss of a block, calculated as the difference of the initial mass of the block and its mass after being tested, ρ [g/mm^3] is the density of the tested block material.

The wear maps (see Figure 5) were plotted using MATLAB R2009b, the wear parameter being represented for each material as a function of the sliding speed and the normal force, with the help of a cubic interpolation.

For PBT (see Figure 5), one may notice a significant increase of the wear parameter when the normal force is decreasing - the cause could be the increase of the heightening factor for the abrasive wear under low loads and the absence of a transfer film on the hard surface due to the absence of the

mechanical pressure and thermal loading great enough for initiating and maintaining an adherence process.

For all tested sliding speeds, the tendency characterizing the wear variation as a function of load has a minimum zone around the value of 4 N.

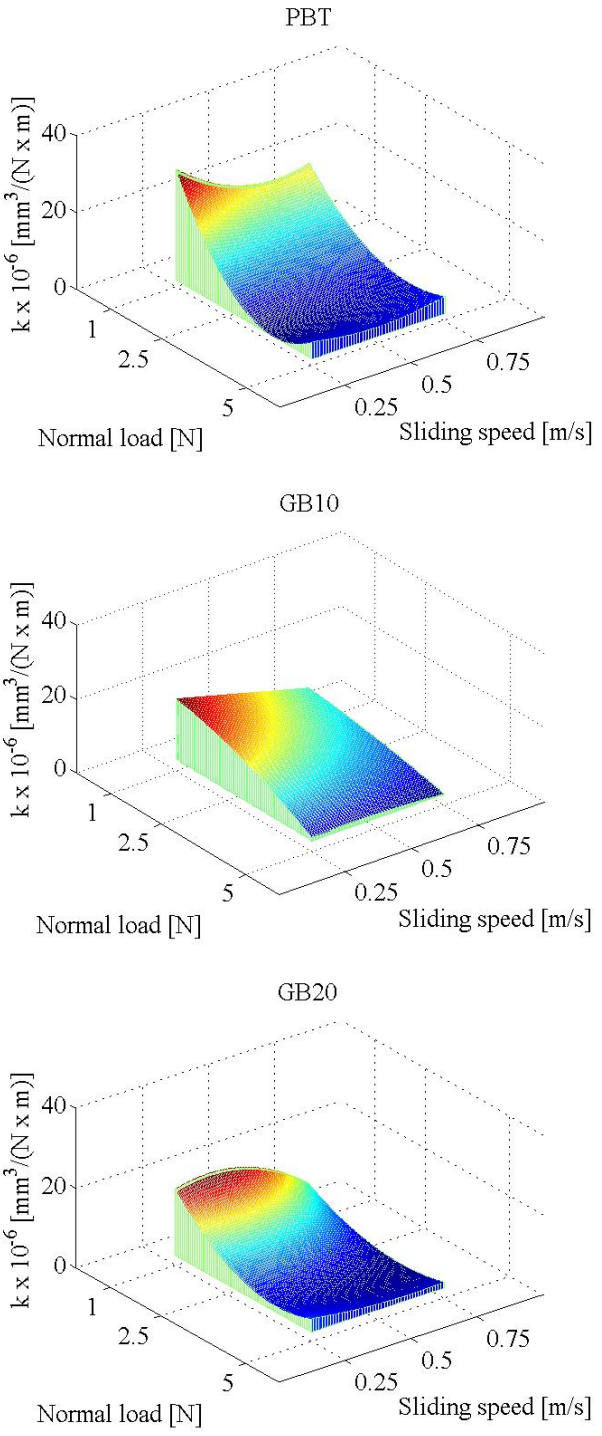

Figure 5. The wear rate for PBT and the composites PBT + micro glass beads

For the composites PBT + micro glass beads, analysing Figure 5, the following conclusions could be drawn:

- a zone with minimum values, for F = 5 N;
- an accentuated increase of the wear rate for loads smaller than 2.5 N, with higher values for the composite GB10;
- for the composite GB10, the wear rate is decreasing almost linearly when the load is increasing and it is insignificantly decreasing when the sliding speed is increasing; *k* is smaller for the two composites with micro glass beads as compared to the basic material (PBT), the lowest values being recorded for the composites, under the load F = 5 N;
- at F = 5 N, for all the tested materials, the wear rate has a very low sensitivity to the variation of the sliding speed, the smaller values being obtained for the composites.

Thus, the wear rate diminishes when introducing glass beads in PBT. The wear is diminishing due to the increase of the material resistance (see the results for the composite GB10), but when the micro glass beads concentration becomes 20%, the abrasive component of the wear process increases, too.

4. CONCLUSIONS

Adding micro glass beads in PBT makes the friction coefficient increase almost linearly with the micro glass beads massic concentration, with ~15% for each 10% of micro glass beads.

An addition of 10% micro glass beads decreases the wear rate with ~20%. When the concentration of micro glass beads is increased, the decrease of this wear parameter is smaller as compared to PBT, with ~18%.

REFERENCES

[1] C.P. Fung, P.C. Kang: *Multi-response optimization in friction properties of PBT composites using Taguchi method and principle component analysis*, Journal of Materials Processing Technology, Vol. 170, pp. 602-610, 2005.

[2] G.S. Deshmukh, D.R. Peshwe, S.U. Pathak, J.D. Ekhe: *A study on effect of mineral additions on the mechanical, thermal, and structural properties of poly(butylene terephthalate) (PBT) composites*, J Polym Res, Vol. 18, pp.1081-1090, 2011.

[3] G.S. Deshmukh, D.R. Peshwe, S.U. Pathak, J.D. Ekhe: *Evaluation of mechanical and thermal properties of Poly (butylene terephthalate) (PBT) composites reinforced with wollastonite*, Transactions of The Indian Institute of Metals, Vol. 64, No. 1 & 2, pp. 127-132, 2011.

[4] C. Georgescu, L. Deleanu: Influence of PTFE concentration on the tribological characteristics of PBT, in: *Proceedings of the 7th International Symposium KOD 2012 Machine and Industrial Design in Mechanical Engineering*, 24-26.05.2012, Balatonfured, Hungary, pp. 405-410.

[5] J. Wu, K. Wang, D. Yu: *Fracture toughness and fracture mechanisms of PBT/PC/IM blends. Part V Effect of PBT-PC interfacial strength on the fracture and tensile properties of the PBT/PC blends*, Journal of Material Science, Vol. 38, pp. 183-191, 2003.

[6] R.J. Crawford: *Plastics Engineering*, 3rd Edition, Butterworth-Heinemann, Oxford, 2002.

[7] J.A. Brydson, *Plastics Materials*, 7th Edition, Butterworth-Heinemann, Oxford, 1999.

[8] H. Czichos, T. Saito, L. Smith: *Springer Handbook of Materials Measurement Methods*, Springer Science-Business Media, 2006.

[9] A. Dasari, Z.Z. Yu, Y.W. Mai: *Fundamental aspects and recent progress on wear/scratch damage in polymer nanocomposites*, Materials Science and Engineering, Vol. 63, pp. 31-80, 2009.

[10] K. Friedrich: *Advances in Composite Tribology*, Vol. 8, Composites Materials Series, Universität Kaiseslautern, Kaiserslautern, Germany, 1993.

[11] ***: *Crastin PBT. Molding Guide*, available on-line: http://www2.dupont.com/Plastics/en_US/assets/downloads/processing/cramge.pdf

[12] W.R. Jr. Jones, W.F. Hady, R.L. Johnson: *Friction and Wear of Poly(Amide-Imide), Polyimide and Pyrone Polymers at 260°C (500°F) in Dry Air*, NASA TN D-6353, Lewis Research Center, 1971.

[13] L. Deleanu, G. Andrei, L. Maftei, C. Georgescu, A. Cantaragiu: *Wear maps for a class of composites with polyamide matrix and micro glass spheres*, Journal of the Balkan Tribological Association, Vol. 17, No 3, pp. 371-379, 2011.

[14] P. Samyn, J. Quintelier, W. Ost, P. De Baets, G. Schoukens: *Sliding behaviour of pure polyester and polyester-PTFE filled bulk composites in overload conditions*, Polymer Testing, Vol. 24, pp. 588-603, 2005.

[15] G.M. Bartenev, V.V. Lavrentev: *Friction and Wear of Polymers*, Elsevier, 1981.

[16] B.J. Briscoe, S.K. Sinha: *Wear of polymers*, Proc. Inst. Mech. Eng. Part J. Engineering Tribology, Vol. 216, pp. 401-413, 2002.

[17] H. Czikos: *Tribology – A System Approach to the Science and Technology of Friction, Lubrication and Wear*, Elsevier Scientific Publishing Company, New-York, 1978.

[18] K. Friedrich, A.K. Schlarb: *Tribology of Polymeric Nanocomposites – Friction and Wear of Bulk Materials and Coatings*, Tribology and Interface Engineering Series, 55, Elsevier, 2008.

[19] N.K. Myshkin, M.I. Petrokovets, A.V. Kovalev: *Tribology of polymers: Adhesion, friction, wear, and mass-transfer*, Tribology International, Vol. 38, pp. 910-921, 2005.

[20] K. Holmberg: Reporting Experimental Results in Tribology – Summary of the discussion on New Wear Rate Unit, in: *OECD IRG 26th Meeting*, 5-6.10.2006, Lyon, France.

Serbian Tribology Society

SERBIATRIB '13

13th International Conference on Tribology

Faculty of Engineering in Kragujevac

Kragujevac, Serbia, 15 – 17 May 2013

NORMAL FORCE INFLUENCE ON 3D TEXTURE PARAMETERS CHARACTERIZING THE FRICTION COUPLE STEEL – PBT + 10% PTFE

Constantin Georgescu[1], Lorena Deleanu[1], Catalin Pirvu[1]

[1]"Dunarea de Jos" University of Galati, Romania, constantin.georgescu@ugal.ro

Abstract: *This study presents the influence of the normal force on the surface quality of the friction couple steel – polybutylene terephthalate (PBT) + 10% polytetrafluoroethylene (PTFE). There were calculated the average values of the amplitude and functional parameters, as obtained from investigating square areas on the wear tracks, with the help of a proposed methodology, for initial and tested surfaces generated on the blocks and on counterpart ring made of rolling bearing steel, for the following test conditions: three normal forces (F = 1 N, F = 2.5 N and F =5 N), three sliding speeds (v = 0.25 m/s, v = 0.50 m/s and v = 0.75 m/s) and a sliding distance of L = 7500 m. The conclusion of the research study was that the tested normal force range has an insignificant influence on the surface quality for the tested materials. This friction couple could be recommended for variable dry regimes.*

Keywords: *PBT + PTFE material, surface texture parameters, block-on-ring test, dry sliding.*

1. INTRODUCTION

In actual application for bearings and seals in dry regime, a self-lubricating polymeric material slides on a hard surface, proved to be tribologically efficient as compared to the sliding of a polymeric material on itself [1], [2]. The adhesion and abrasion components of the friction and wear processes sinergically influence themselves. For instance, extend of the junctions depends on the elasto-plastic deformation of the asperities [3], [4], [5] and they could not be separated. For the polymer-metal contact, the deterioration of the polymer by elasto-plastic deformation is more intense and the adhesion component increases for the harder surfaces [6]. The generated transfer film characteristic for the polymer-metal friction couple, also changes the surface texture, depending of the polymer nature and the working conditions [7], [1], [2].

There are many published studies on the tribological behavior of polymeric materials [8], [7], [9], but few of them deal with the influence of the surface texture on the tribological characteristics of the polymeric materials and even fewer reported how the working conditions affect the surface texture. In 1970, Pooley and Tabor (quoted in [1]) pointed out that for PTFE, the value of the friction coefficient is only slightly affected by the surface quality when involving relatively smooth ones, but with rough surfaces the wear and the friction are intensified. Till now, the terms "smooth" and "rough" were used only in a qualitative way and there are no recommended values of the texture parameters for particular applications.

Experimental studies proved that a change of the texture parameters could significantly affect the friction and the wear. There is why the authors of this research consider the texture evaluation, before and after testing, necessary for understanding and directing the tribological processes. Many polymeric friction couples are working with frequent starts and stops and the evolution of the surface texture is of great importance for improving the reliability and the durability of these tribosystems.

For polymeric friction couples and especially for polymer – metal contacts, the wear could be related both to the amplitude and functional parameters.

As resulted from the studied documentation [12], [13], the surface quality is frequently described by parameters as Sa (arithmetic average of absolute values) and Sq (root mean squared).

The authors' estimates that for studying the worn surfaces and for obtaining correlations among the surface parameters and the testing conditions, the following parameters are more suitable: the parameters related to the maximum values of the topography (Sz – the height difference between the highest and lowest heights in the investigated area, Sv – the largest pit height, Sp – the largest peak height) and the functional parameters (Svk – reduced valley depth, Sk – core roughness depth, Spk – reduced summit height).

2. MATERIAL AND TESTING METHODOLOGY

The friction and wear behavior of PBT sliding against steel was evaluated with the help of a Universal Micro-Tribometer UMT-2 and a block-on-ring tribotester. The geometry of the frictional couple is given in figure 1.

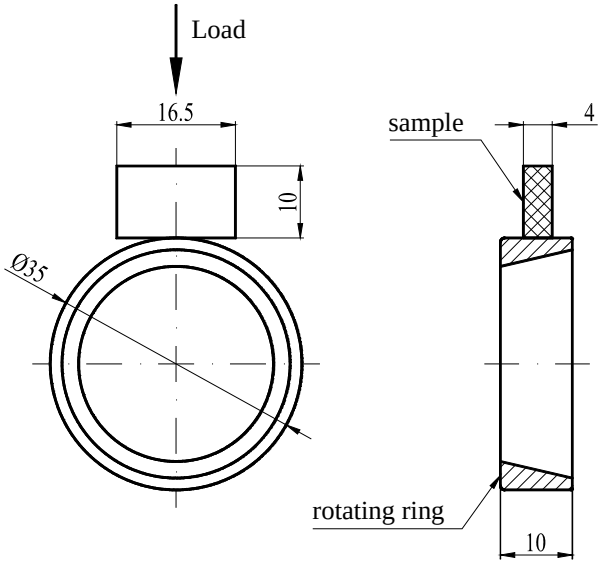

Figure 1. The shapes and dimensions of the friction couple block-on-ring

The polymeric blocks are prisms of 16.5 mm × 10 mm × 4 mm and they were obtained by injection at ICEFS Savinesti, Romania, according to the specifications of the producer from traction samples, cutting the blocks from the middle parallel zone of them.

The polymeric blend has 90% (wt) PBT, the commercial name being Crastin 6130 NC010 (as supplied in grains by DuPont) and 10% (wt) PTFE, commercial grade NFF FT-1-1T® Flontech, having the average size of the particles ~20 μm.

The other element of the friction couple was the external ring of the tapered rolling bearing KBS 30202 (DIN ISO 355/720), having the dimensions of Ø35 mm × 10 mm and they were made of steel grade DIN 100Cr6, having 60 - 62 HRC and Ra = 0.8 μm on the exterior surface.

There were selected the following test parameters: three sliding speeds (v = 0.25 m/s, v = 0.50 m/s, v = 0.75 m/s), three applied loads (F = 1.0 N, F = 2.5 N, F = 5.0 N), the sliding distance being L = 7500 m for each test done at room temperature and in a laboratory environment.

In order to do this study, the profilometer Laser NANOFOCUS μSCAN [14] was used.

For parameters' calculation it was used the software SPIP 5.1.11 [15]. Figure 2 presents a virtual (rebuilt) image of the investigated zone with the help of this software.

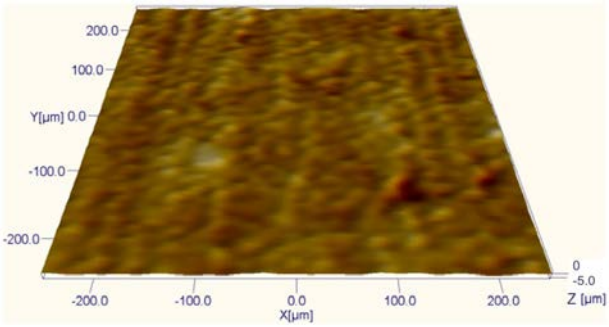

a) The initial surface

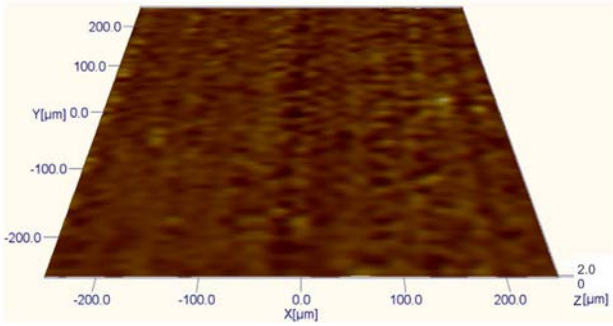

b) The worn surface (F = 5 N, v = 0.25 m/s, L = 7500 m)

Figure 2. Virtual images of the polymeric blocks made of PBT + 10% PTFE

Measurements were done for blocks made of the polymeric blend PBT + 10% PTFE and for the external rings of tapered rolling bearings, both elements being involved in block-on-ring tests, for both non-worn and worn surfaces.

For evaluating the 3D parameters involved in this study, there were selected three zones, each of 500 μm × 500 μm for the polymeric blocks and of 100 μm × 100 μm for the metallic rings, these being reduced for reason of the surface curvature. All 3D measurements were done with a step of 5 μm. The distance between lines for 3D measurements was also 5 μm. The 3D parameters are calculated for all the values z(x, y), measured on one area of 500 μm × 500 μm on the block and one area of 100 μm × 100 μm on the steel ring.

3. EXPERIMENTAL RESULTS

Taking into account that PTFE has lower mechanical properties as compared to PBT [10], it was considered necessary to study the influence of the normal force on the surface quality of this polymeric blend, before and after testing.

Figures 3, 4 and 5 present the average values of the amplitude and functional parameters, obtained with the help of the proposed methodology, for the initial and tested surfaces generated on the blocks made of PF10 (material symbol for the polymeric blend PBT + 10% PTFE), for the tested conditions: three forces and three sliding speeds and a sliding distance of L = 7500 m.

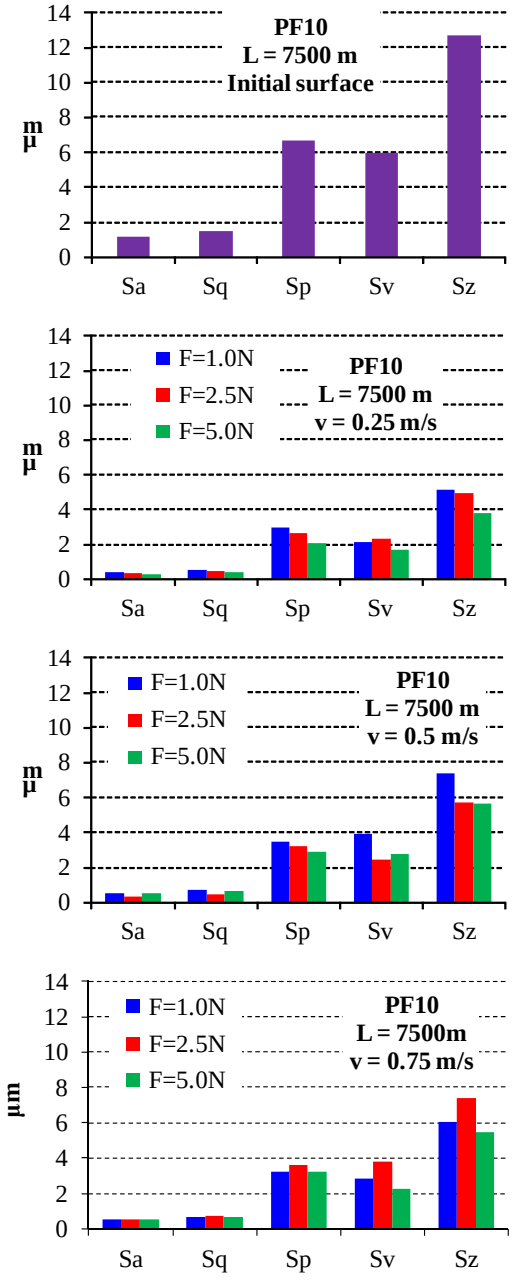

Figure 3. The influence of the normal force on the average values of the dimensional amplitude parameters for the blocks made of PF10 (PBT + 10% PTFE)

The wear track surfaces are characterized by parametric values 2...3 times lower than those of the initial surfaces as they were obtained by the moulding technology.

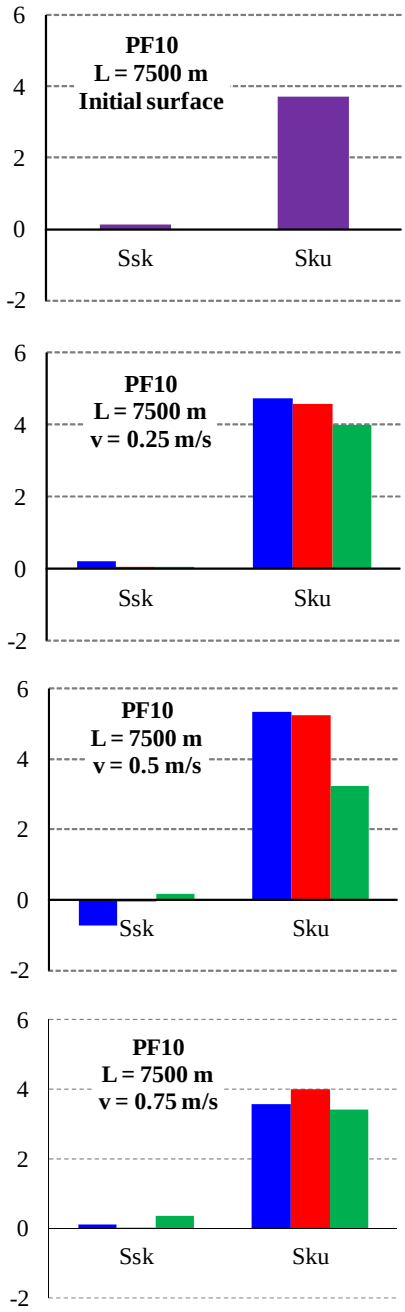

Figure 4. The influence of the normal force on the average values of the a dimensional amplitude parameters for the blocks made of PF10

The surface quality of this material is only slightly dependent on the normal force, at least for the tested values (F = 1 N, F = 2.5 N and F = 5 N).

Sa and Sq have very close values, regardless the force values, but Sp and Sz present a slight decrease when the force increases, for the test done with the sliding speeds of v = 0.25 m/s and v = 0.5 m/s.

Sku (surface Kurtosis) values greater than 3.0 indicate narrower height distribution due to the

particular ductile fracture of the polymer during adhesion – abrasion wear. Ssk (surface Skewness) has values oscillating around zero, indicating symmetric height distributions. If Ssk < 0, the bearing surface has holes and if Ssk > 0 it is a flat surface with peaks.

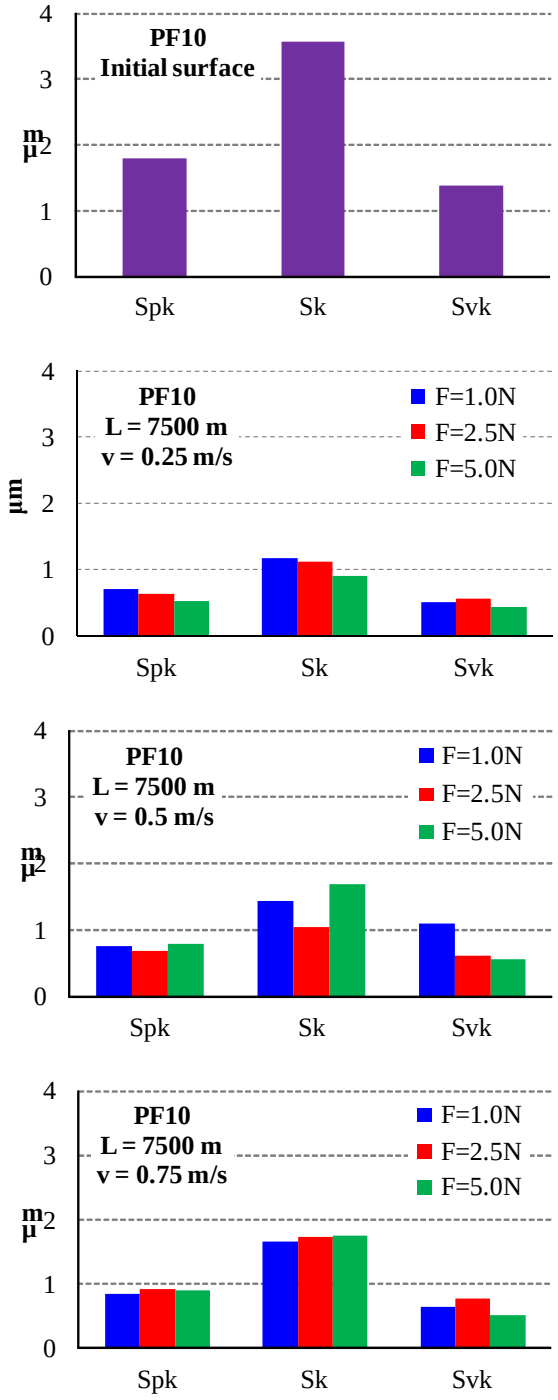

Figure 4. The influence of the normal force on the average values of the 3D functional parameters for the blocks made of PF10

It was noticed a slight decrease of the functional parameters when the load increases, for tests done with the sliding speed of v = 0.25 m/s. For the other two tested speeds (v = 0.50 m/s and v = 0.75 m/s), this poor dependence on the normal force was noticed only for Svk. The greater forces make this parameter to decrease and this tendency could be justified by the elasto-viscous behaviour of the polymeric blend; it is possible that the passing of the hard asperities laterally moves the softer material of the counterpart accompanied by an elevation of the valley bottoms between asperities, process also reported in [11], [1].

4. CONCLUSION

For the polymeric blend PBT + 10% PTFE, there was found no significant influence of the normal force on the surface quality, for the testing conditions: range of force 1 N ... 5 N, range of speed 0.25 m/s ... 0.75 m/s and the sliding distance 7500 m.

The obtained results recommend the tested material for friction couples functioning under variable conditions (speed and load) in dry sliding.

REFERENCES

[1] G.W. Stachowiak: *Wear – Materials, Mechanisms and Practice*, John Wiley & Sons, England, 2005.

[2] G.W. Stachowiak, A.W. Batchelor: *Engineering Tribology*, Butterworth-Heinemann, 2002.

[3] D. Boazu, I. Gavrilescu: *Contactul mecanic. Analiză cu elemente finite*, EUROPLUS, Galaţi, 2006.

[4] S. Creţu: *Contactul concentrat elastic-plastic*, Politehnium, Iaşi, 2009.

[5] N.B. Demkin, V.V. Izmailov: *The Relation between the Friction Contact Performance and the Microgeometry of Contacting Surfaces*, Journal of Friction and Wear, Vol. 31, No. 1, pp. 48-55, 2010.

[6] P. Samyn, J. Quintelier, W. Ost, P. De Baets, G. Schoukens: *Sliding behaviour of pure polyester and polyester-PTFE filled bulk composites in overload conditions*, Polymer Testing, Vol. 24, pp. 588-603, 2005.

[7] K. Friedrich, A.K. Schlarb: *Tribology of Polymeric Nanocomposites – Friction and Wear of Bulk Materials and Coatings*, Elsevier, pp. 17-148, 2008.

[8] B.J. Briscoe, S.K. Sinha: *Wear of polymers*, Proc. Inst. Mech. Eng. Part J. Engineering Tribology, Vol. 216, pp. 401-413, 2002.

[9] K. Friedrich, Z. Zhang, A.K. Schlarb: *Effects of various fillers on the sliding wear of polymer composites*, Composites Science and Technology, Vol. 65, pp. 2329-2343, 2005.

[10] J.A. Brydson: *Plastics Materials*, 7th Edition, Butterworth-Heinemann, 1999.

[11] K.L. Johnson: *Contacts Mechanics*, Cambridge University Press, Cambridge, 1987.

[12] L. Blunt De, X. Jiang: *Advanced Techniques for Assessment Surface Topography*, Elsevier, London, 2003.

[13] F. Blateyron: *États de surface: la norme*, Mesures, Vol. 787, pp. 44-47, 2006.

[14] ***: *NanoFocus AG µScan® – Instruction Manual.*

[15] SPIP The Scanning Probe Image Processor SPIP™, Version 5.1.11, 2012, available on-line: http://www.imagemet.com/WebHelp/spip.html.

Serbian Tribology Society

SERBIATRIB '13

13th International Conference on Tribology

Faculty of Engineering in Kragujevac

Kragujevac, Serbia, 15 – 17 May 2013

WEAR BEHAVIOUR OF COMPOSITES BASED ON ZA27 ALLOY REINFORCED WITH GRAPHITE PARTICLES

Slobodan Mitrović[1], Miroslav Babić[1], Ilija Bobić[2], Fatima Zivić[1], Dragan Dzunić[1], Marko Pantić[1]

[1] Faculty of Engineering, University of Kragujevac, Kragujevac, Serbia,
boban@kg.ac.rs, babic@kg.ac.rs, zivic@kg.ac.rs, dzuna@kg.ac.rs, pantic@kg.ac.rs

[2] INN "Vinca", Univerzitet u Beogradu, Beograd, Srbija, ilijab@vinca.rs

Abstract: *It is well known that reinforcing the matrix with graphite particles effects on friction properties, while reinforcing the matrix with hard particles (Al_2O_3, SiC, Garnet...) increases wear resistance of the matrix material, in this case ZA27 alloy.Reinforcing the matrix by adding the graphite also effects on mechanical properties of material. In this study authors made an attempt to investigate the effect of small amount of graphite reinforcement on wear behaviour of composites and in order to preserve the mechanical properties of the material. The composites with 1 and 2wt% of graphite particles were produced by compocasting procedure. Wear behaviour of unreinforced ZA27 alloy and composites were studied using, computer aided block-on-disc tribometer, under dry sliding conditions at different sliding speeds (0.25, 0.5 and 1m/s) and normal loads (10N, 30N and 50N). The obtained results revealed that composites exhibited better wear resistance in comparison to unreinforced ZA27 alloy. Better wear properties of composites in comparison to the unreinforced matrix alloy are a result of creation of graphite rich film on the contact surfaces.*

Keywords: *Composite, ZA27, Graphite, Wear.*

1. INTRODUCTION

Due to wide potential applications, composite materials have been investigated very intensively over the recent decades [1]. Metal matrix composites have emerged as an important class of engineering materials because they provide opportunity to manage the material mechanical and tribological properties [2].

Zinc-aluminium (ZA) alloys are important bearing materials, especially suitable for high-load and low-speed applications [3, 4]. ZA alloys are characterized by good tribological and mechanical properties, low weight excellent foundry castability and fluidity, good machining properties, low initial cost, and environmentally friendly technology. However, major limitations of ZA alloys are its inferior mechanical and wear properties on elevated properties. Also, this alloy exhibits dimensional instability at temperatures above 120°C [5].

Various authors have reported that the incorporation of hard particles (SiC, Al_2O_3, zircon, garnet and glass) [6-17] improves wear resistance of base alloy. Also, many researchers have reported that MMCs reinforced with graphite particles exhibits low friction and low wear rate, and suggested that such behaviour is the result of self-lubricating graphite-rich film formation on the contact surface [4, 18-20]. Mechanical properties of ZA27 alloy graphite reinforced are significantly changed by varying the amount of graphite [21]. The increase of the graphite content within the ZA27 matrix results in increase of ductility, compressive strength, corrosion resistance, but in a decrease of hardness. In spite of the significant decrease in hardness, tribological tests showed that addition of graphite particles to ZA27 alloy matrix improved wear resistance of composites [22].

Based on presented literature review small amount of graphite will not degrade mechanical properties so An attempt has been made to evaluate the drysliding wear behaviour of the ZA-27/graphite composites over a range of applied loads and slidingspeeds. The unreinforced ZA-27 alloy was tested as a referencematerial.The role of graphite in dry was discussed.

2. EXPERIMENTAL TESTING

2.1 Material

The ZA-27 alloy (27.5% Al, 2.5% Cu, 0.012% Mg, and balance Zn) was used as the base matrix alloy. The graphite particles of mean size 30 μm were used as the reinforcement. The percentage of graphite was 1 and 2 by weight. The composite specimens were obtained by the compocasting procedure, which was executed by mixing in the isothermal regime.More detailed process of the compocating procedure could be found elsewhere [4].

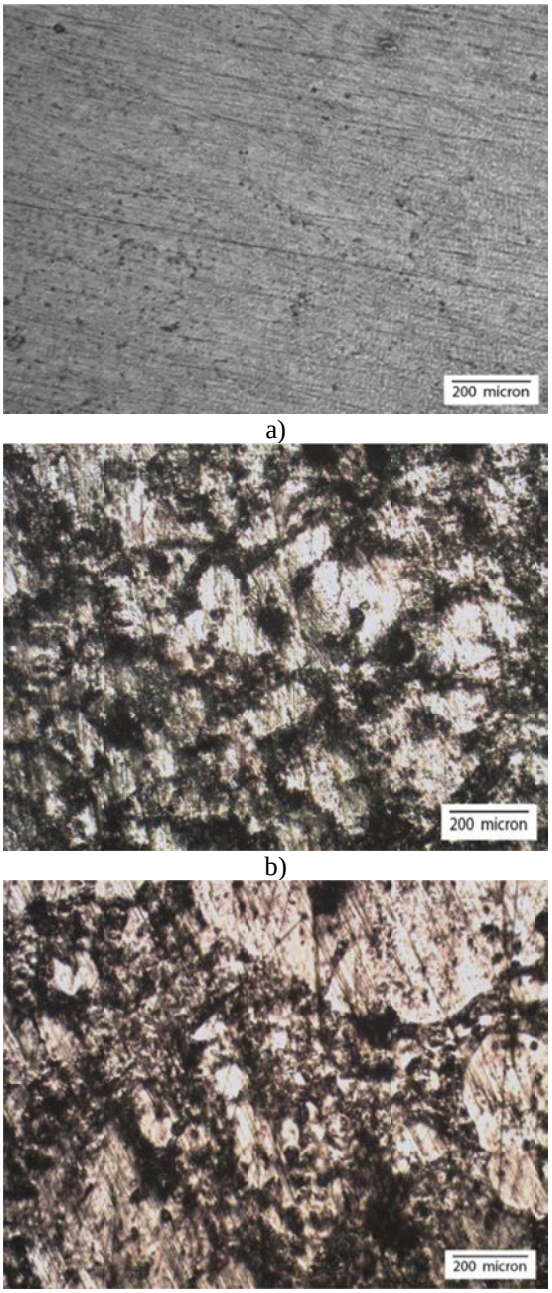

a)

b)

c)

Figure 1. Optical microscopy of tested specimens: a) unreinforced matrix alloy ZA27; b) composite with 1 wt% of graphite particles; c) composite with 2 wt% of graphite particles

After obtaining the composite materials samples, it was necessary to perform the hot pressing to reduce porosity. The samples (blocks) for the tribological investigations were then made from the ZA-27 as-cast alloy and pressed pieces.

Microstructural characterization of the alloys was carriedout using the optical microscopy on samples, similar tothose used for wear testing. The typical OM micrographs ofthe matrix alloy and composite are shown in Fig. 1.

Bulk hardness of all the samples was measured using a Brinell hardness tester with a 2.5-mm diameter steel ballindenter and at an applied load of 625 N. The load application time was 60 s. The mean values of at least fivemeasurements, conducted in different areas of each sample, show that the composite attained lower hardness (115 HB) than that of the matrix ZA-27 alloy (124 HB). Hardness of the matrix alloy was 124HB, while hardness for composites reinforced with 1 wt% and 2 wt% of graphite particles were 119 HB and 115 HB, respectively. In his investigation of mechanical properties of the cast ZA-27/ graphite particulate composites Seah found that with graphite content increase hardness monotonically decreases significantly [23]. In fact, as the graphite content is increased from 0 to 5% the hardness decreases for about 27%.

2.2 Wear tests

Samples for tribological testing were made by cutting. Cutting was realised by machine saw with intensive cooling in order to avoid changes of surface layers, due to high temperature.

Wear test were carried out in a computer aided block-on-disk sliding wear testing machine with the contact pair geometry in accordance with ASTM G 77–05. More detailed description of the tribometer is available elsewhere [4].

The test blocks (6.35x15.75x10.16 mm) were prepared from ZA27 unreinforced alloy and from composite with 1% and 2% of graphite particles. All samples prior to wear testare polished. The counter face (disc of 35 mm diameter and 6.35 mm thickness) was made of EN: HS 18-1-1-5 tool steel of 62HRC hardness. The tests were performed under dry sliding conditions at different sliding speeds (0.25 m/s, 0.5 m/s, 1 m/s) and applied loads (10 N, 30 N, 50 N). The duration of sliding was 10 min. Each experiment was repeated five times.

The tests were performed at room temperature. The wear behavior of the block was monitored in terms of the wear scar width (Figure 2). Using the wear scar width and geometry of the contact pair the wear volume (expressed in mm^3) was calculated.

Figure 2. The scheme of contact pair geometry

3. RESULTS AND DISCUSSION

Wear volume of tested ZA27/graphite composites, as well as unreinforced ZA27 alloy, as a function of sliding speed and normal load in dry sliding conditions is illustrated on figures presented down below.

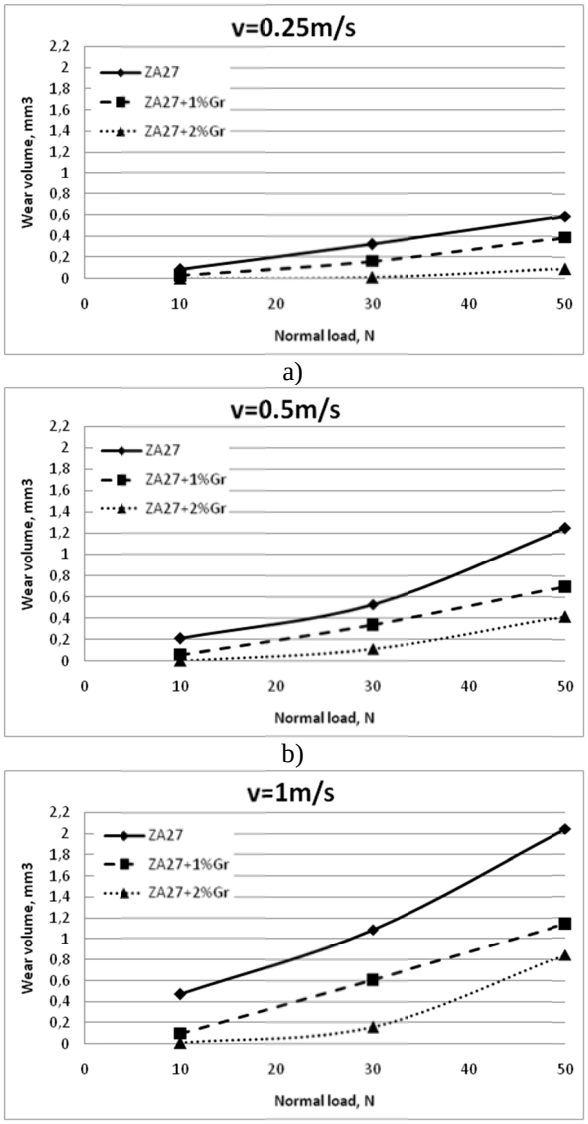

Figure 3. Wear volume of tested samples versus normal load for different sliding speeds in dry sliding conditions

The effect of normal load on wear volume of tested composites, as well as the matrix alloy specimens at different values of applied normal load is presented on Fig.3. Presented plots suggest that wear volume of all tested samples increases with normal load increase, at all values of sliding speed. Increase in wear volume with increasing of normal load is more pronounced at higher sliding speed (1 m/s), as could be clearly seen if we compare plots on Fig. 3a with plots on Fig. 3c. This phenomenon is more pronounced for unreinforced matrix alloy. According to Seah et al. [24] wear rate increases monotonically with normal load increase.

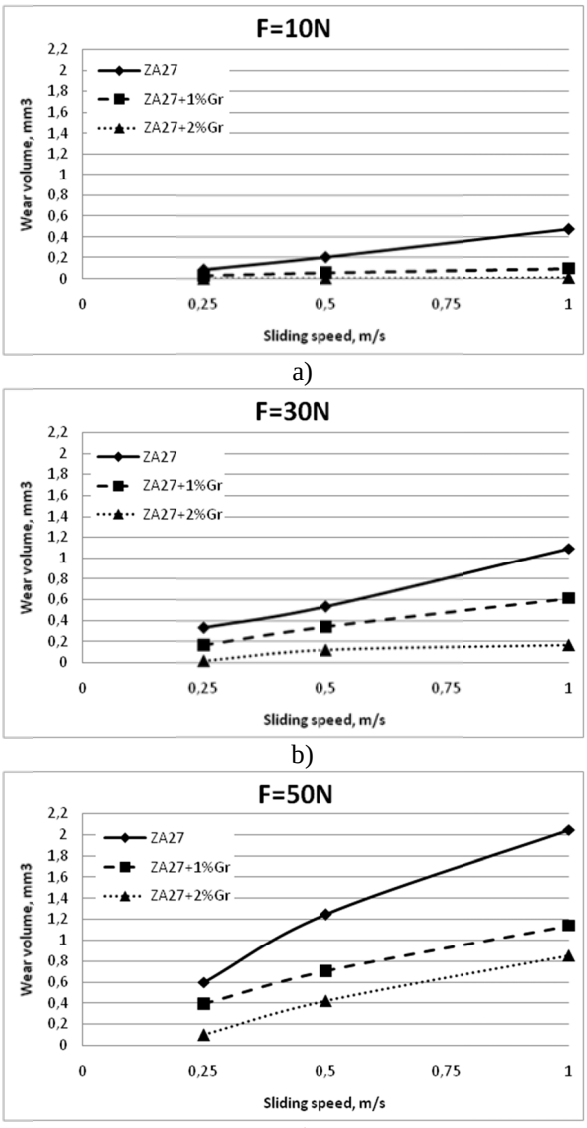

Figure 4. Wear volume of tested samples versus sliding speed under different applied normal loads in dry sliding conditions

The influence of sliding speed on wear volume of tested composites, as well as matrix alloy specimens at constant values of applied normal load is presented on Fig. 4. From presented plots it could be clearly seen that with increase of sliding speed wear volume of all tested specimens increases. Wear volume increase is more pronounced at applied load of 50N, and for unreinforced matrix alloy in comparison to the composites. Also, on the

figure 3a it could be seen that the wear of the composite with 2 wt% of graphite is almost negligible under applied load of 10N.

Seah et al. [24] have confirmed that the wear rate of as-cast ZA-27/graphite particulate decreases monotonically with an increase in sliding speed, but in our case it is inversely because of different contact geometry.

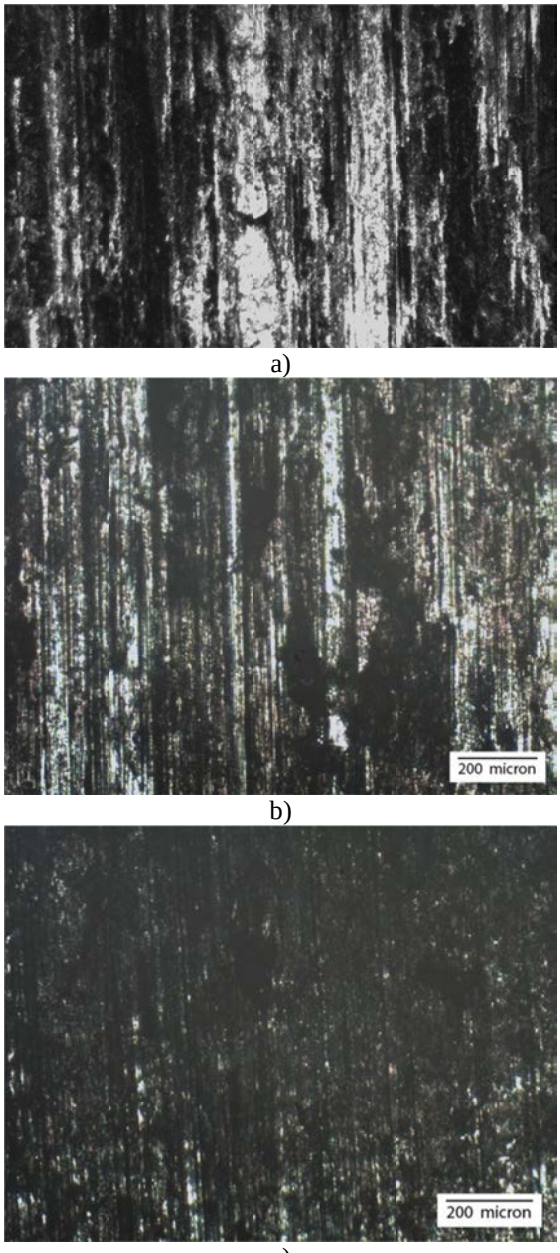

a)

b)

c)

Figure 5. Wear scars of tested specimens: a) unreinforced matrix alloy; b) and c) composites with 1 and 2 wt% of graphite particles, respectively.

Figure 5 presents wear scars of all tested specimens Based on the wear scars it could be concluded that the dominant wear mechanism was abrasive wear, because of this parallel tracks within the wear scars of all tested materials. One can clearly notice that on the worn surface the black graphite film is smeared and it covers the large portion of the contact surface. Presence of the graphite film in contact zone reduces the metal-to-metal contact between the sliding pairs.

Many researchers have reported that during dry sliding, themetal/graphite composites tribo-influenced the graphitefilm forming on the contact surface of elements [18–20], whichacts as solid lubricant that reduces metal-to-metal contactbetween the sliding surfaces. The formation of graphiterichlubricant film between the sliding surfaces has beenexplained as a result of the soft second phase (graphite)squeezing-out from the subsurface toward the mating surfacedue to extensive plastic deformation [18].

4. CONCLUSION

Based on the results presented in this paper it could be concluded:

- Generally wear volume of the composites are lesser in comparison to the unreinforced matrix alloy.
- Higher content of graphite particles within the matrix alloy results in higher wear resistance of material, composite with 2 wt% of graphite particles has lesser values of wear volumes in comparison to the composite with 1wt% of graphite particles, under the same contact conditions.
- Wear volume of all tested specimens increases with sliding speed and normal load increase.
- Higher wear resistance of ZA27/graphite composites in comparison to the unreinforced matrix alloy is a result of graphite film forming on the surface of contact elements.

ACKNOWLEDGEMENT

The study was financed by Ministry of Education, Science and Technological Development, Serbia, project No.35021.

REFERENCES

[1] Vasiliev, V.V., Morozov, E.V.: Mechanics and Analysis of Composite Materials. Elsevier, Oxford, 2001.

[2] Pruthviraj, R.D., Krupakara, P.V.: Influence of SiC additions on mechanical properties of the Zn–Al alloy (ZA-27). Int J Mater Sci 2(1), pp. 53–57, 2007.

[3] Babic, M., Ninkovic, R., Rac, A.: Sliding Wear Behavior of Zn-Al Alloys in Conditions of Boundary Lubrication. The Annals of University ''Dunarea De Jos'' of Galati Fascicle VIII. Tribology, pp. 60–64, 2005.

[4] Babic, M., Mitrovic, S., Dzunic, D., Jeremic, B., Bobic, I.: Tribological behavior of composites based

on ZA-27 alloy reinforced with graphite particles. Tribology Lett., pp. 401-410, 2010.
[5] Prasad, B.K.: Abrasive wear characteristics of a zinc-based alloy and zinc-alloy/SiC composite. Wear 252(3–4), pp. 250–263, 2002.
[6] Tjong, S.C., Chen, F.: Wear behavior of as-cast ZnAl27/SiC particulate metal-matrix composites under lubricated sliding condition. Metall Mater Trans A 28A, 1951–1955, 1997.
[7] Prasad, B.K., Das, S., Jha, A.K., Modi, O.P., Dasgupta, R., Yegneswaran, A.H.: Factors controlling the abrasive wear response of a zinc-based alloy silicon carbide particle composite. Composites A 28(4), 301–308, 1997.
[8] Prasad, B.K., Modi, O.P., Khaira, H.K.: High-stress abrasive wear behavior of a zinc-based alloy and its composite compared with a cast iron under varying track radius and load conditions. Mater SciEng A 381, 343–354, 2004.
[9] Prasad, B.K.: Abrasive wear characteristics of a zinc-based alloy and zinc-alloy/SiC composite. Wear 252(3–4), 250–263, 2002.
[10] Sharma, S.C., Girish, B.M., Kamath, R., Satish, B.M.: Effect of SiC particle reinforcement on the unlubricated sliding wear behavior of ZA-27 alloy composites. Wear 213, 33–40, 1997.
[11] Sastry, S., Krishna, M., Uchil, J.: A study on damping behavior of aluminate particulate reinforced ZA-27 alloy metal matrix composites. J Alloys Compd 346, 268–274, 2001.
[12] Sharma, S.C., Sastry, S., Krishna, M.: Effect of aging parameters on the micro structure and properties of ZA-27/aluminate metal matrix composites. J Alloys Compd 346, 292–301, 2002.
[13] Bobic, I., Jovanovic, M.T., Ilic, N.: Microstructure and strength of ZA-27 based composites reinforced with Al2O3 particles. Mater Lett 57, 1683–1688, 2003.
[14] Modi, O.P., Rathod, S., Prasad, B.K., Jha, A.K., Dixit, G.: The influence of alumina particle dispersion and test parameters on dry sliding wear behavior of zinc-based alloy. TribolInt 40, 1137–1146, 2007.
[15] Sharma, S.C., Girish, B.M., Kamath, R., Satish, B.M.: Sliding wear behavior of zircon particles reinforced ZA-27 alloy composite materials. Wear 224, 89–94. 1999.
[16] Ranganath, G., Sharma, S.C., Krishna, M.: Dry sliding wear of garnet reinforced zinc/aluminum metal matrix composites. Wear 251, 1408–1413, 2001.
[17] BabicMiroslav, Slobodan Mitrovic, Fatima Zivic, IlijaBobic: Wear Behavior of Composites Based on ZA-27 Alloy Reinforced by Al2O3 Particles Under Dry Sliding Condition, TribolLett 38, pp. 337–346, 2010.
[18] Riahi, A.R., Alpas, A.T.: The role of tribo-layers on the sliding wear behavior of graphitic aluminum matrix composites. Wear 251, 1396–1407, 2001.
[19] Yang, J.B., Lin, C.B., Wang, T.C., Chu, H.Y.: The tribological characteristics of A356.2Al alloy/Gr(p) composites. Wear 257, 941–952, 2004.
[20] Akhlaghi, F., Zare-Bidaki, A.: Influence of graphite content on the dry sliding and oil impregnated sliding wear behavior of Al 2024-graphite composites produced by in situ powder metallurgy method. Wear 266, 37–45, 2009.
[21] Seah, K.H.W., Sharma, S.C., Girish, B.M.: Mechanical properties of cast ZA-27/graphite particulate composites. Mater Des 16(5), 271–275, 1995.
[22] Sharma, S.C., Girish, B.M., Kramath, R., Satish, B.M.: Graphite particles reinforced ZA-27 alloy composite materials for journal bearing applications. Wear 219, 162–168, 1998.
[23] Seah, K.H.W., Sharma, S.C., Girish, B.M.: Effect of artificial ageing on the hardness of cast ZA-27/graphite particulate composites. Mater Des 16(6), 337–341, 1995.
[24] Seah, K.H.W., Sharma, S.C., Girish, B.M., Lim, S.C.: Wear characteristics of as-cast ZA-27/graphite particulate composites. Mater Des 17(2), 63–67, 1996.

Serbian Tribology Society

SERBIATRIB '13

13th International Conference on Tribology

Faculty of Engineering in Kragujevac

Kragujevac, Serbia, 15 – 17 May 2013

WEAR PROPERTIES OF A356/10SiC/1Gr HYBRID COMPOSITES IN LUBRICATED SLIDING CONDITIONS

Babić Miroslav[1], Stojanović Blaža[1], Mitrović Slobodan[1], Bobić Ilija[2], Miloradović Nenad[1], Pantić Marko[1], Džunić Dragan[1]

[1]Faculty of Engineering, University of Kragujevac, Kragujevac, Serbia, babic@kg.ac.rs, blaza@kg.ac.rs

[2]Institution Institute of Nuclear Sciences "Vinca", University of Belgrade, Belgrade, Serbia

Abstract: *This paper presents basic tribological properties of A356/10SiC/1Gr hybrid composites in conditions with lubrication. Hybrid composite specimen is obtained by compocasting procedure. A356 aluminium alloy is used as a base matrix alloy, reinforced with 10wt% of SiC and 1wt% of graphite. Tribological tests are done on advanced and computer supported tribometer with block-on-disc contact pair. By the experimental plan, test is conducted under three different values of sliding speed, three different values of normal load, different sliding distances, and also different lubricants. SEM and EDS are used for wear analysis. The analysis has shown the presence of MML, which means that there was transfer of material from steel disc to composite block.*

Keywords: *Hybrid composites, aluminium, SiC, graphite, wear, lubrication, MML.*

1. INTRODUCTION

Aluminium is the most attractive material in automotive, airplane, space and precise devices industry. Improvement of mechanical and tribological properties of aluminium can be achieved through aluminium reinforcement with the proper material and through creating composite material. The most effective improvement of these properties is achieved through creating hybrid composites with two or more types of reinforcements. By adding the ceramic reinforcement, mechanical properties of the matrix are changed, but in that case problem of machinability occurs. To improve machinability, the graphite is added to composite materials that are already reinforced with ceramic material. Presence of graphite reduces mechanical properties (hardness decreases), but tribological properties are improved [1-5].

Basavarajappa et al [6-8] have studied the tribological behaviour of hybrid composites with aluminum base Al2219 reinforced by SiC and graphite. They studied the tribological properties of hybrid composites with 5, 10 and 15% SiC and 3% Gr obtained with process of liquid metallurgy. The tribological tests show that wear decreases with increasing SiC content in the hybrid composite. With increasing sliding speed and normal load, wear rate of composites is growing. Mahdavi and Akhlaghi [9,10] have studied the tribological properties of Al / SiC / Gr hybrid composites obtained by In situ Powder Metallurgy process. Aluminum alloy Al 6061 is used as a base, reinforced with graphite 9% and 0 ÷ 40% SiC. The tribological tests are done on tribometer with pin on disc contact, and the composite with 20% SiC has the best properties. Further increase of SiC leads to increased wear of hybrid composites.

Suresh and Sridhara [11-14] have studied the effect of SiC content and graphite on the tribological behaviour of hybrid Al / SiC / Gr composites with aluminum base LM25 (Al-Si7Mg0.5) obtained by stircasting process.

Ames and Alpas have [15] studied the tribological testing of hybrid composites with a base of aluminum alloy A356 reinforced with 20% SiC and 3 ÷ 10% Gr. The tribological tests are done on tribometer with block on ring contact. The wear rate of hybrid composites is significantly lower than the wear rate of the base material without reinforcements, especially at low normal loads.

Vencl et al [16,17] have studied the tribological behaviour of hybrid composites with the A356

matrix reinforced with SiC, Al2O3 and graphite. The tribological tests are done on tribometer with pin on disc contact and show that the wear and friction coefficient decreases with addition of graphite.

This paper presents tribological behaviour of hybrid composites with aluminum base of A356 alloy reinforced with SiC and Gr obtained with compocasting procedure. The tests are done on computer aided block-on-disc tribometer under lubricated sliding conditions by varying the contact pairs (sliding speed and normal load).

2. EXPERIMENT

2.1 The procedure for obtaining composites

Hybrid Al / SiC / Gr composites are obtained by the modified compo-casting procedure (infiltration of particles in the semi-solidified melt A356 alloy). sub-eutectic Al-Si alloys En AlSiMg0,3 (A356 alloy) is used as a basis. Using compocasting procedure, particle reinforcements are easily infiltrated / trapped. This solves the problem of wettability on the border base and reinforcements. The cost of composite producing with that process is much lower.

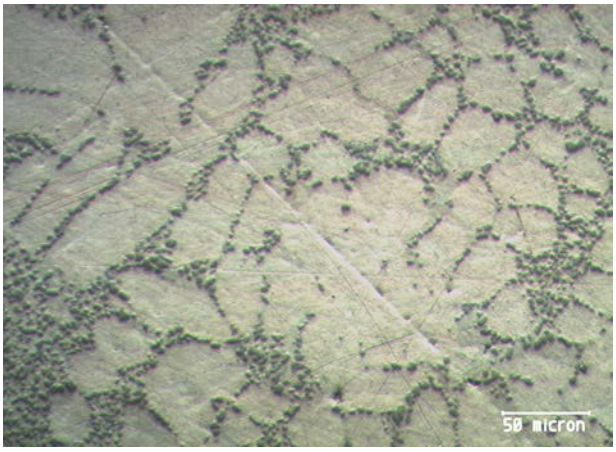

a)

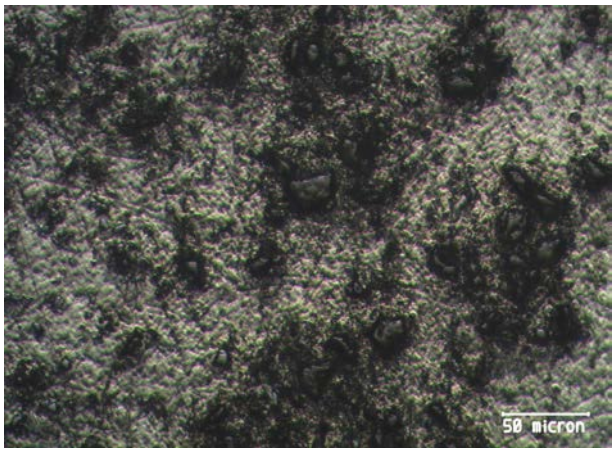

b)

Figure 1. The structure of: a) base material A356, and b) hybrid composite Al/10SiC/1Gr.

Figure 1 shows the structure of the base material A356 and the hybrid composite with 10wt%SiC and 1wt%Gr. When mixing composites, particles of graphite have become fragmented with regard to original size of 35 μm. The picture shows the distribution of SiC particulate reinforcements, the size of 39 um.

2.2 Plan of experiment and description of equipment

Tribological tests are done on advanced and computer supported tribometer with block-on-disc contact pair in accordance with ASTM G77 standard. Contact pair consists of rotating disc of diameter Dd = 35 mm and broadness bd = 6.35 mm, and a stationary block of size 6.35x15.75x10.16 mm^3. The discs are made of steel 90MnCrV8 hardness of 62-64 HRC with grinded surfaces.

The tests were performed in lubricated sliding conditions on the samples with the best structural, mechanical and anti-corrosive properties.

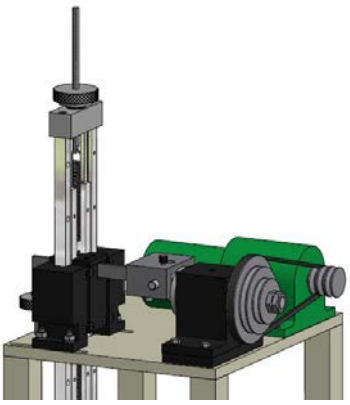

Figure 2. Tribometer.

The values of sliding speed (0.25 m / s, 0.5 m / s and 1 m / s) and the normal loads (40N, 80N and 120 N) are in accordance with the plan of experiment. The tests are performed for sliding distance of 2400 m.

Figure 3. Lubrication of the contact pair.

All tests used the same hydraulic lubricant with improved anti-wear properties, viscosity VG46 (ISO 3848). Lubricant is housed in a small tank,

and lubrication is done so that the bottom of the disc is immersed to up to depth of 3 mm into the small tank with lubricant, whose volume is 30 ml. During rotation of the disc, oil is continuously introduced into the zone of the contact and makes boundary lubrication of contact pair (Figure 3).

All experiments were repeated 5 times, and the mean values of obtained values are taken as authoritative.

3. RESULTS OF TRIBOLOGICAL TESTS

Results of tribological tests of hybrid composite Al/10SiC/1Gr and basic material A356 are shown in the following diagrams.

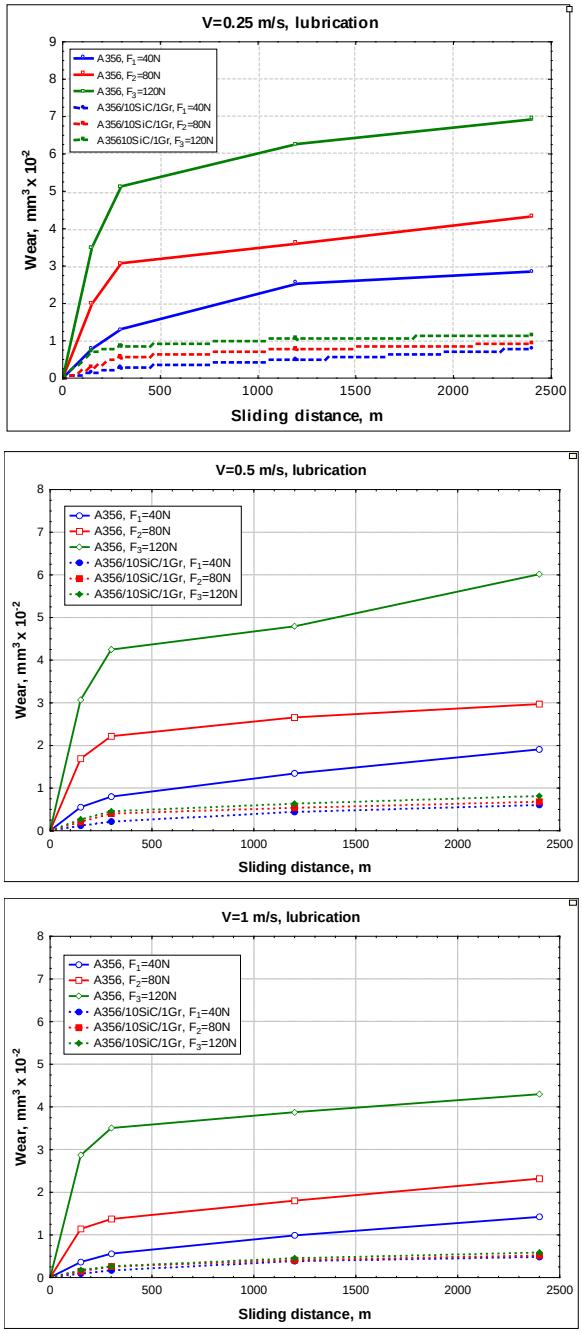

Figure 4. Wear volume for all three values of sliding speed.

Diagrams of wear volume are formed on the basis of wear scar which is obtained by measuring after 150 m, 300 m, 1200 m, 2400 m, and they are given for all three values of sliding speed (Figure 4).

It is obvious that the wear rate of the hybrid composites A356/10SiC/1Gr is several times less than the wear rate of the base material A356. With increase of sliding speed, wear rate of the hybrid composite A356/10SiC/1Gr and the base material are decreases. Wear rate dependence has almost linear dependence for all values of the normal loads (Figure 5).

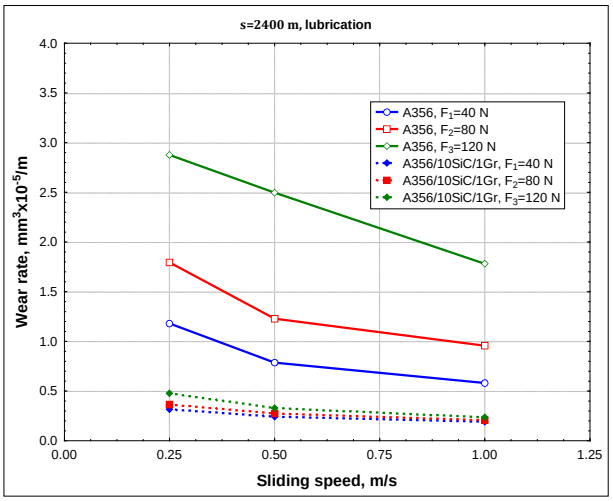

Figure 5. Wear rate dependence on sliding speed.

With increase of normal load, wear rate increases. This increase is particularly pronounced at the base material A356 (Figure 6).

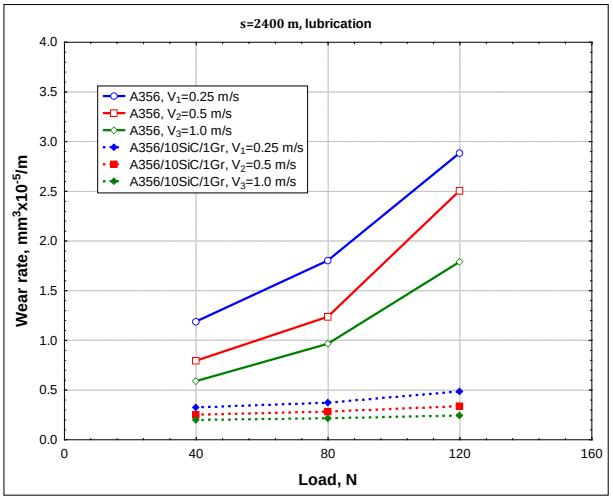

Figure 6. Wear rate dependence on normal load.

Wear rate dependence on normal load and sliding speed for sliding distance of 2400 m, is shown in Figure 7.

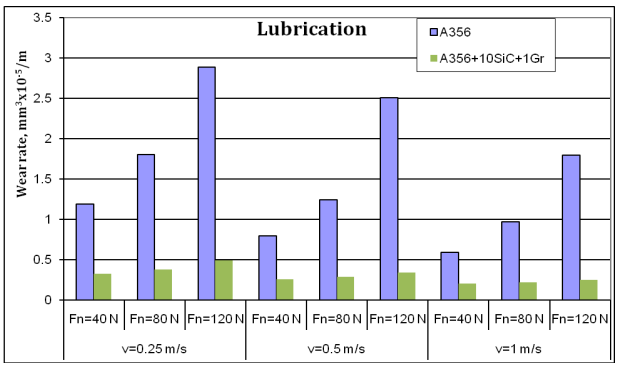

Figure 7. Wear rate dependence on normal load and sliding speed.

After the tribological tests, SEM analysis is performed for wear scar of base material A356 and hybrid A356/10SiC/1Gr composite, whose micro-photos are shown in Figure 8.

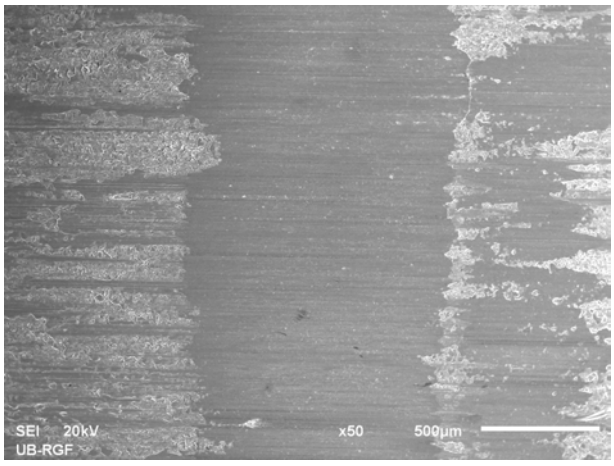

a)

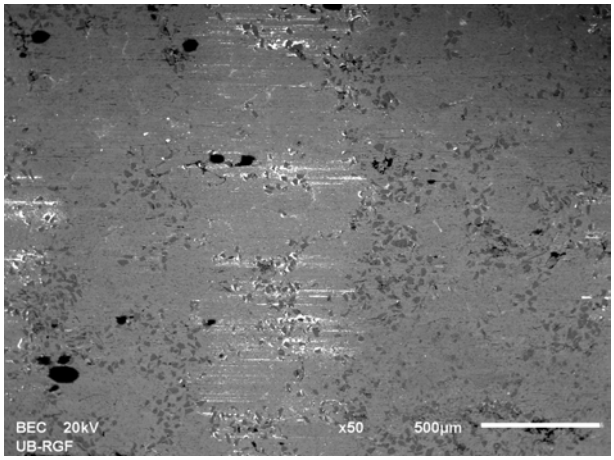

b)

Figure 8. SEM micro-photos of wear scar:
a) base material A356,
b) hybrid composite A356/10SiC/1Gr.

4. ANALYSES OF OBTAINED RESULTS

The analyses of the obtained tribological results show that the wear rate or wear volume is much lower in the hybrid composites Al/10SiC/1Gr compared to the base material. Decrease of wear rate occurs due to the effects of SiC from hybrid composite in contact with a steel disc.

Wear rate dependence on normal load and sliding speed are shown in Figures 9 and 10 as the 3D plots. Wear rate is approximated by exponential function with a high correlation coefficient.

Both tested materials show that at least wear occurs at the maximum sliding speed of 1 m / s and the minimum normal load of 40N.

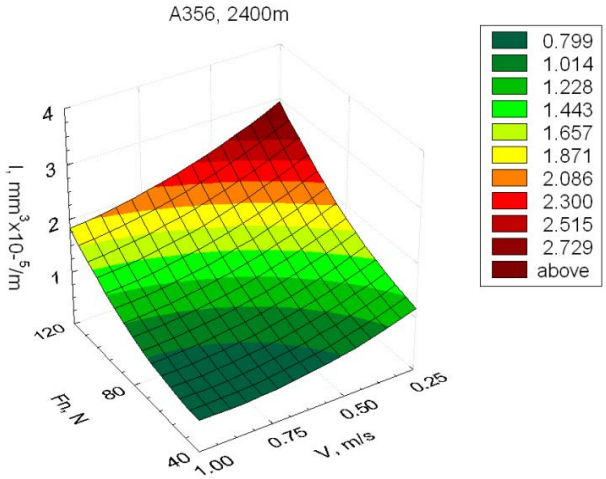

Figure 9. Wear rate dependence on the base material.

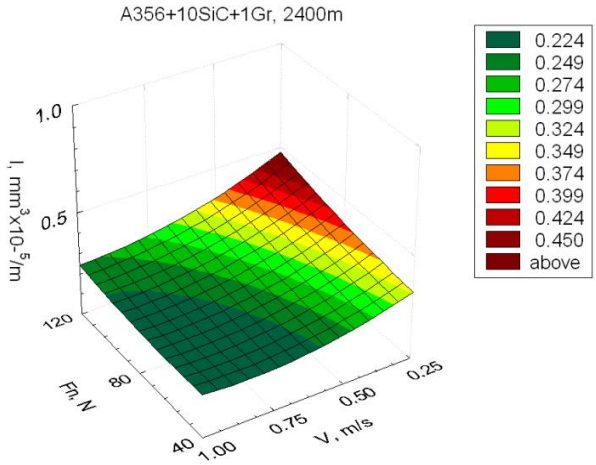

Figure 10. Wear rate dependence on the hybrid composites A356+10SiC+1Gr.

SEM microscopy shows that due to the contact of the SiC composites and Si phases from the basic A356, wear of steel disc occurs. Fe particles enter the surface layer of the composites and lead to the creation of mechanically mixed layer (MML). The formation of MML layer is characteristic of aluminum alloys reinforced with SiC [18-23]. Iron accumulates around the SiC particles taking a position of small particle of graphite. At some parts white lines appear enriched with iron oxides, which are consistent with the sliding direction (Figure 11).

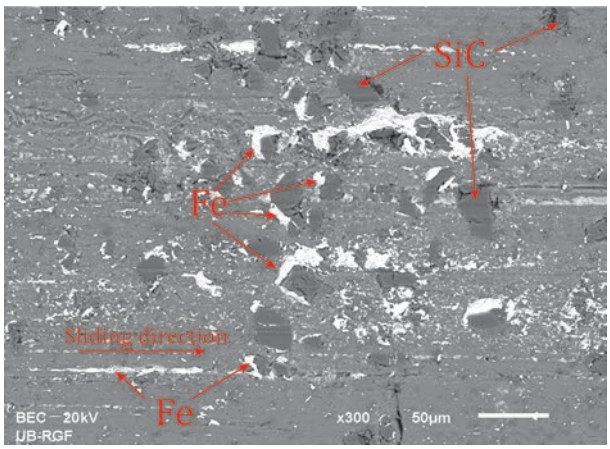

Figure 11. The accumulation of iron in the composite A356/10SiC/1Gr, 120 N, 0.25 m/s.

Figure 12 shows the SEM photograph of part of the hybrid composite A356/10SiC/1Gr. Wear scar is obtained by sliding speed of 0.25m/s and normal load of 120N in conditions of lubrication. At higher loads, the dominant wear mechanism is abrasive wear. SiC particles (darker) and iron particles (bright colours) are clearly visible on the scar. Confirmation of these assumptions is obtained by EDS analysis, as shown in the two spectrums. The first spectrum shows the presence of SiC particles, and the particles of iron and its oxides can be seen on second spectrum .

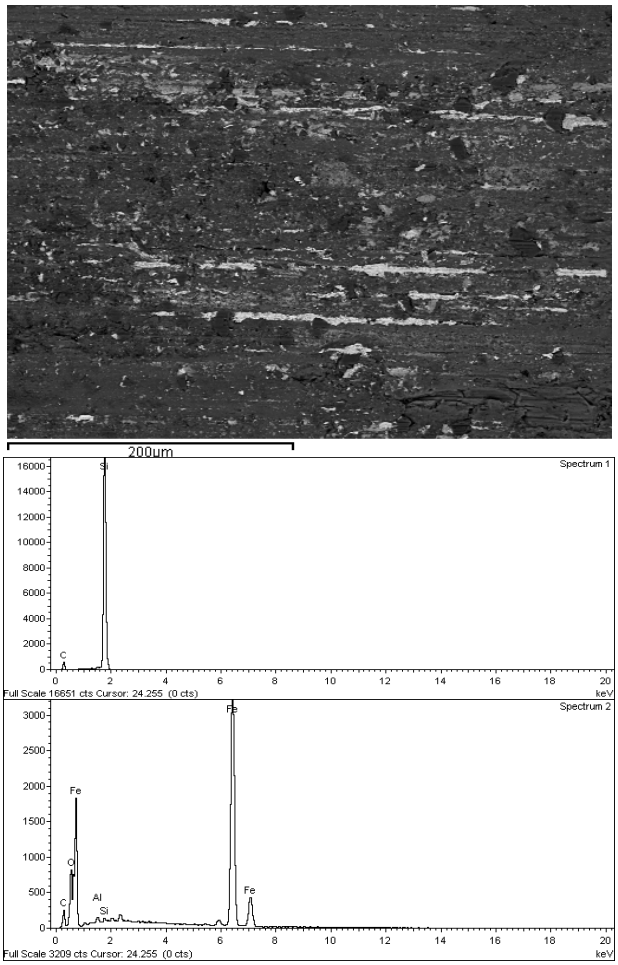

Figure 12. EDS analysis A356/10SiC/1Gr, 120N, 0.25m/s, SEM.

5. CONCLUSION

Wear tests of hybrid composites A356/10SiC/1Gr show their superior performance in relation to the base material A356. Applied compocasting modified procedure, in addition to low prices, confirms the good distribution of reinforcements in the composite.

Wear rate on A356/10SiC/1Gr hybrid composites is 3 ÷ 8 times lesser than the wear rate on the base material A356. It is especially big difference of wear rate at the lowest sliding speed of 0.25 m / s and maximum normal load of 120N. Wear rate decreases with decrease of normal load and increase of sliding speed.

SEM microscopy and EDS analysis confirm a good distribution of SiC reinforcements in the hybrid composite. Also, advent mechanically mixed layer (MML) is obvious, respectively, the appearance of iron and its oxides in the hybrid composite.

ACKNOWLEDGMENTS

This paper presents the research results obtained within the framework of the project TR–35021, financially supported by the Ministry of Education and Science of the Republic of Serbia.

REFERENCES

[1] A. Vencl: *Tribology of the Al-Si alloy based MMCs and their application in automotive industry*, u: Magagnin L. (ed.), Engineered Metal Matrix Composites: Forming Methods, Material Properties and Industrial Applications, Nova Science Publishers, Inc., New York (SAD), pp. 127-166, 2012.

[2] B. Stojanovic, M. Babic, S. Mitrovic, A. Vencl, N. Miloradovic, M. Pantic: *Tribological characteristics of aluminium hybrid composites reinforced with silicon carbide and graphite. A review*, Journal of the Balkan Tribological Association, Vol.19, No.1, pp. 83-96, 2013.

[3] N. Miloradovic, B. Stojanovic: *Tribological behaviour of ZA27/10SiC/1Gr hybrid composite*, Journal of the Balkan Tribological Association, Vol.19, No.1, pp. 97-105, 2013.

[4] S. Mitrovic, M. Babic, B. Stojanovic, N. Miloradovic, M. Pantic, D. Dzunic: *Tribological Potential of Hybrid Composites Based on Zinc and Aluminium Alloys Reinforced with SiC and Graphite Particles*, Tribology in industry, Vol. 34, No. 4, pp.177-185, 2012.

[5] P. Ravindran, K. Manisekar, R. Narayanasamy, P. Narayanasamy: *Tribological behaviour of powder metallurgy-processed aluminium hybrid composites with the addition of graphite solid lubricant*, Ceramics International, Vol. 39, No. 2, pp. 1169-1182, 2013.

[6] S. Basavarajappa, G. Chandramohan, K. Mukund, M. Ashwin, M. Prabu: *Dry sliding wear behavior of Al 2219/SiCp-Gr hybrid metal matrix composites*, Journal of Materials Engineering and Performance, Vol. 15, No. 6, pp.668-674, 2006.

[7] S. Basavarajappa, G. Chandramohan: *Dry sliding wear behavior of hybrid metal matrix composites*, Materials Science, Vol.11, No.3, pp. 253-257, 2005.

[8] S. Basavarajappa, G. Chandramohan, A. Mahadevan: *Influence of sliding speed on the dry sliding wear behaviour and the subsurface deformation on hybrid metal matrix composite*, Wear, Vol. 262, pp. 1007–1012, 2007.

[9] S. Mahdavi, F. Akhlaghi: *Effect of SiC content on the processing, compaction behavior, and properties of Al6061/SiC/Gr hybrid composites*, Journal of Materials Science, Vol. 46, No. 5, pp. 1502-1511, 2011.

[10] F. Akhlaghi, S. Mahdavi: *Effect of the SiC Content on the Tribological Properties of Hybrid Al/Gr/SiC Composites Processed by In Situ Powder Metallurgy (IPM) Method*, Advanced Materials Research, pp. 1878-1886, 2011.

[11] S. Suresha, B.K. Sridhara: *Wear characteristics* of *hybrid aluminium matrix composites reinforced* with *graphite* and *silicon carbide particulates*, Original Research Article, Composites Science and Technology, Vol. 70, No. 11, pp. 1652-1659, 2010.

[12] S. Suresha, B.K. Sridhara: *Effect of addition of graphite particulates on the wear behavior in aluminium–silicon carbide–graphite composites*, Materials & Design, Vol. 31, pp. 1804–1812, 2010.

[13] S. Suresha, B.K. Sridhara: *Effect of silicon carbide particulates on wear resistance of graphitic aluminium matrix composites*, Materials & Design, Vol. 31, No. 9, pp. 4470-4477, 2010.

[14] S. Suresha, B.K. Sridhara: *Friction characteristics of aluminium silicon carbide graphite hybrid composites*, Materials & Design, Vol.34, pp. 576-583, 2012.

[15] W. Ames, A.T. Alpas: *Wear mechanisms in hybrid composites of graphite-20% SiC in A356 aluminum alloy*, Metall.Mater.Trans. A; Vol. 26, pp. 85-98, 1995.

[16] A. Vencl, I. Bobic, S. Arostegui, B. Bobic, A. Marinkovic, M. Babic: *Structural, mechanical and tribological properties of A356 aluminium alloy reinforced with Al_2O_3, SiC and SiC + graphite particles*, Journal of Alloys and Compounds, Vol. 506, pp. 631-639, 2010.

[17] A.Vencl, I.Bobic, B.Stojanovic, *Tribological properties of A356 Al-Si alloy composites under dry sliding conditions*, Industrial Lubrication and Tribology, Vol. 66, No.3, 2014 (in print).

[18] J. Rodriguez, P. Poza, M.A. Garrido, A. Rico: *Dry sliding wear behaviour of aluminium–lithium alloys reinforced with SiC particles*, Wear, Vol. 262, pp. 292–300, 2007.

[19] L. Jung-moo, K. Suk-bong, H. Jianmin: *Dry sliding wear of MAO-coated A356/ 20 vol.% SiCp composites in the temperature range 25–180°C*, Wear, Vol. 264, pp. 75–85, 2008.

[20] R.N. Rao, S. Das, D.P. Mondal, G. Dixit: *Effect of heat treatment on the sliding wear behaviour of aluminium alloy (Al– Zn–Mg) hard particle composite*, Tribology International, Vol. 43, pp. 330–339, 2010.

[21] M. Gui, S.B. Kang: *Dry sliding wear behavior of plasma-sprayed aluminum hybrid composite coating*, Metall. Mater. Trans., A Vol. 32A, pp. 2383–2392, 2001.

[22] A.K. Mondal, S. Kumar: *Dry sliding wear behaviour of magnesium alloy based hybrid composites in the longitudinal direction*, Wear, Vol. 267, pp. 458–466, 2009.

[23] R.N. Rao, S. Das, D.P. Mondal, G. Dixit: *Dry sliding wear behaviour of cast high strength aluminium alloy (Al–Zn–Mg) and hard particle composites*, Wear, Vol. 267, pp. 1688–1695, 2009.

Serbian Tribology Society

SERBIATRIB '13

13th International Conference on Tribology

Faculty of Engineering in Kragujevac

Kragujevac, Serbia, 15 – 17 May 2013

A REVIEW OF THE TRIBOLOGICAL PROPERTIES OF PTFE COMPOSITES FILLED WITH GLASS, GRAPHITE, CARBON OR BRONZE REINFORCEMENT

Miloš Stanković[1], Aleksandar Vencl[2], Aleksandar Marinković[2]
[1]University of Belgrade, Inovation Center of Faculty of Mechanical Engineering, Belgrade, Serbia,
mstankovic@mas.bg.ac.rs
[2]University of Belgrade, Faculty of Mechanical Engineering, Belgrade, Serbia,
avencl@mas.bg.ac.rs , amarinkovic@mas.bg.ac.rs

Abstract: *Polytetrafluroethylene (PTFE) is currently finding increasing utility due to its unique properties like high chemical resistivity, low coefficient of friction and high temperature stability. However, PTFE exhibits poor wear resistance, especially abrasion. The wear resistance of PTFE can be significantly improved by addition of suitable reinforcement (filler) materials. Among the most common filler materials are glass fibers, graphite, carbon and bronze. In this paper, it is presented a review of tribological properties of composite materials with PTFE matrix and above mentioned filler materials.*

Keywords: *PTFE, composites, glass fibres, graphite, carbon fibres, bronze, friction, wear.*

1. INTRODUCTION

Nowadays, there is very intensive growth in the large scale production of the fibre reinforced polymer composites since they posses certain advantages over the metals. The advantages include lower density, less need for maintenance and lower cost [1]. Polymers and polymers reinforced with fibres are used for producing of various mechanical components, such as gears, cams, wheels, brakes, clutches, bush bearing and seals [2]. Considerable efforts are being made to extend the range of applications. Such use would provide the economical and functional benefits to both manufacturers and consumers. Many researchers have studied the tribological behaviour of polytetrafluroethylene (PTFE). Studies have been conducted with various shapes, sizes, types and compositions of fibres. In general these composites exhibit lower wear and friction when compared to pure PTFE.

The most commonly used reinforcements (fillers) for tribological applications are carbon, graphite, bronze and glass. Generally the fillers improve the wear resistance from 10 to 500 times, depending on the filler type and shape. On the other hand, coefficient of friction of various PTFE composites is strongly dependent on filler crystal structure and improvements are not so significant.

Subject of this paper are composites with PTFE matrix. Filler materials investigated in this paper are glass, graphite, carbon and bronze. Analysed tribological characteristics are coefficient of friction and wear. In most cases, friction and wear tests were carried out on pin-on-disc tribometer at ambient conditions (temperature and humidity). Counterpart material used in the experiments was always harder than composite. In most cases, counterpart material was steel. All tests were carried out at dry sliding conditions. Overall results from all analysed papers are summarized and presented in Table 1.

2. FACTORS AFFECTING POLYMER COMPOSITE WEAR AND FRICTION

There are many factors that affect material tribological properties. For polymer composites the most influential are [6]:

Normal load: In order for a polymer composite to function as a solid lubricant it must be able to support the load, as well as the tangential stresses induced by sliding. At high loads severe wear

Table 1. Overview of the results from the analysed papers (for pure PTFE and its composites at dry sliding conditions)*

Ref.	Test rig**	Type (amount and size) of the filler***	Counterpart material	Load, N (MPa)	Sliding speed, m/s	Sliding distance, m	Coefficient of friction		Specific wear rate, $mm^3/Nm \times 10^{-6}$	
							PTFE	Composites	PTFE	Composites
[7]	Ball-on-disc	1. C particles (18 %; 10 – 25 μm) + Gr flakes (7 %; 25 – 50 μm); 2. E-glass fibres (15 %; 10 × 50 – 75 μm); 3. E-glass fibres (25 %; 10 × 50 – 75 μm)	AISI 440C steel ball (d = 9 mm)	5 (point contact)	0.1	1000	0.11	0.13 – 0.16	950	90 – 700
[8]	Pin-on-disc	1. Glass fibres (17 %); 2. Bronze (25 %); 3. C (35 %)	AISI 440C steel disc	5 – 30 (0.2 – 1.1)	0.32 – 1.28	1152 – 4608	0.13 – 0.79	0.11 – 0.71	476 – 943	6 – 290
[9]	Pin-on-disc	1. Glass particles (25 %; 40 μm); 2. Bronze particles (40 %; 48 μm)	EN 32 hardened steel disc	60 (0.6)	1.5	2500	–	–	app. 567	app. 4.4 – 335
[10]	Pin-on-disc	1. Gr flake (2 %; 10 μm); 2. Gr flake (5 %; 10 μm); 3. Gr flake (10 %; 10 μm)	Stainless steel disc	25 (0.2)	1	8000	0.24	0.20 – 0.26	1650	10 – 190
[11]	Pin-on-disc	1. Bronze (25 %); 2. Bronze (40 %); 3. Bronze (60 %)	AISI 400C steel disc	5 – 200 (0.2 – 7.1)	0.32 – 2	2000	app. 0.12 – 0.22	app. 0.12 – 0.18	1000	1 – 100

* The friction and wear values in the table are approximate and can be used only as a guidance, since the authors in most cases did not presented the results in appropriate way; ** Pin – cylindrically shaped specimen (flat contact); *** C – carbon, Gr – graphite

occur, characterized by brittle fracture or severe plastic deformation. On the other hand, at low loads usually mild wear occur, characterized by the local plastic flow of the thin transfer film and surface layers (decreasing friction), together with delamination wear.

Contact area: The contact area will determine the projected contact stresses. If the load cannot be reduced, one way of reducing stress is to increase the projected contact area. However, if the area of contact becomes too large instead of the material flowing across the counterpart surface, it will have a tendency to build up, forming ridges, which can cause high localized stresses and higher adhesion, thus higher friction and wear. It is important to design a part with correct match up of load and contact area.

Sliding speed: The high sliding speeds can produce high temperatures due to friction heating. This may cause the polymer or the polymer composite additives to degrade. However in some cases higher temperature might be beneficial to the lubricating process. In order to develop a surface shear film and/or a transfer film, the molecular chain must have time to reorient. If one slides too fast over these un-oriented chains, instead of reorienting, they will fracture, leading to the production of large wear particles and high wear. Thus it is important to choose sliding speed for each particular polymer to ensure the optimum performance.

Counterpart topography: If the counterpart material is too rough it can abrade the composite and not allow a shear film or transfer film to form. Therefore, it could be generally accepted that, the smoother the counterpart the lower the wear. This has certain limits, since it is also found that over-polishing tend to remove the counterpart softer matrix material, leaving the harder phases and/or particles protruded above the surface.

Temperature: At lower temperature the friction and wear properties of most polymers are not as exceptional as they are at or above the ambient temperature. At lower temperatures polymers lose their relaxations ability, i.e. the movement of their main molecule chain do not obtains adequate degree of freedom, and thus the polymer does not obtain a great deal of plasticity. High temperatures can affect bonding between the filler material and polymer matrix. They can also affect the lubricating properties of some additives in polymer composite, since these additives might desorbs gases at certain temperature or even decompose.

3. STATE-OF-THE-ART OF PTFE COMPOSITES TRIBOLOGICAL RESEARCHES

Tribological behaviour of PTFE and its composites with filler materials such as carbon particles, graphite flakes and E glass fibres (Table 2) was investigated by Khedkar et al. [7]. Experiments were performed under the normal load of 5 N and sliding speed of 0.1 m/s. They found that the used filler additions increase wear resistance in all composites that were studied. The highest wear

resistance was found for composite containing 18 vol. % of carbon and 7 vol. % of graphite (Figure 1). The coefficient of friction values were from 0.11 to 0.16 (Figure 2). This behaviour can be attributed to the presence of hard carbon particles, which are embedded within the matrix and impart additional strength to the composite. Wear testing and SEM analysis showed that three-body abrasion was probably the dominant mode of failure for PTFE + 18 vol. % carbon + 7 vol. % graphite composite.

Table 2. Composition (vol. %) of materials

Designation	Material	Characteristic of filler material
A	Pure PTFE	99 % pure PTFE powder
B	75 % PTFE + 18 % amorphous carbon + 7 % hexagonal graphite	Carbon particles (diameter: 10 – 25 μm); graphite flakes (size: 25 – 50 μm)
C	85 % PTFE + 15 % E-glass	E-glass fibres (diameter: 10 μm; length: 50 – 75 μm)
D	75 % PTFE + 25 % E-glass	

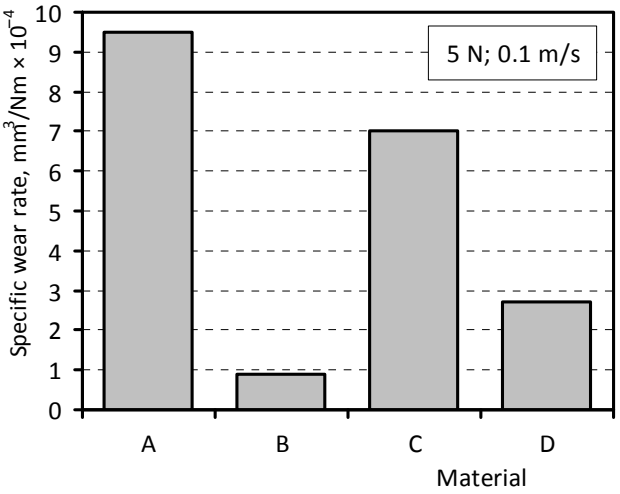

Figure 1. Average specific wear rate of PTFE and PTFE composites (adopted from [7])

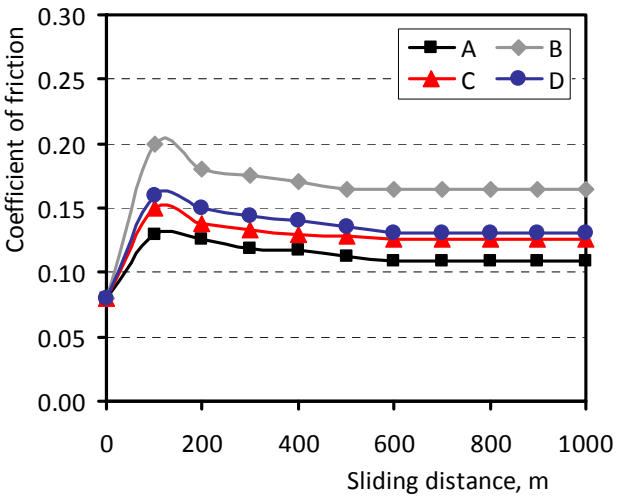

Figure 2. Frictional behaviour of PTFE and PTFE composites (adopted from [7])

Unal et al. [8] studied PTFE composites filled with glass fibres (17 %), bronze (25 %) or carbon (35 %). Experiments were performed under load range from 5 to 30 N (0.18 – 1.06 MPa) and speed range from 0.32 to 1.28 m/s. The results showed that, for pure PTFE and its composites, the coefficient of friction decrease with the increase in load. For the ranges of load and speed used in this investigation, the coefficient of friction showed very little sensitivity to the sliding speed and large sensitivity to the applied load, particularly at high load values. Figure 3 shows that sensitivity for the pure PTFE, but it is quiet similar for composites, as well. Adding glass fibres, bronze and carbon fillers to PTFE were found effective in reducing the wear rate. The maximum reductions in wear rate and coefficient of friction were obtained by PTFE reinforced with 17 % of glass fibres. The specific wear rate for PTFE + 17 % glass fibres was almost two orders of magnitude lower than for pure PTFE. By means of microscopy, it is noticed that the PTFE with glass fibre filler form a good thin and uniform transfer film which have positive influence to the wear rate.

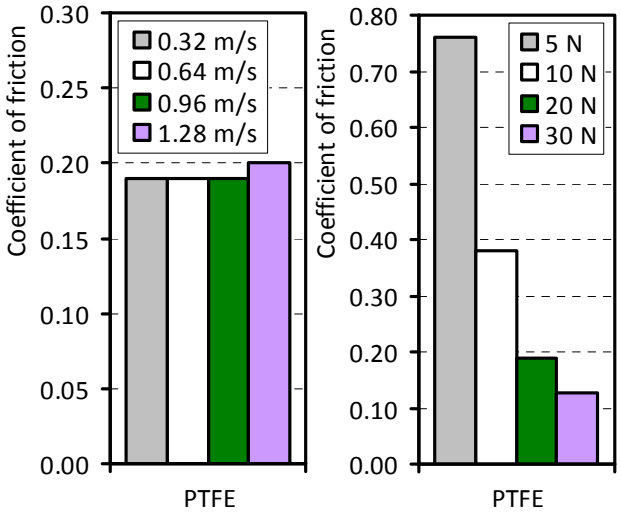

Figure 3. Sensitivity of PTFE coefficient of friction to the sliding speed (for 20 N load) and applied load (for 0.32 m/s speed) (adapted from [8])

A single influence of glass particles (25 vol. %; 40 μm) and bronze particles (40 vol. %; 48 μm) on wear behaviour of PTFE based composites was studied by Mudasar Pasha et al. [9]. The tests were done on a pin-on-disc tribometer with different normal loads (20 – 100 N, i.e. 0.2 – 1 MPa), sliding speeds (1.5 – 5.5 m/s) and distances (500 – 2500 m). The experimental results indicate that the weight loss increases with increasing load and sliding speed (Figure 4). The PTFE + 40 % bronze composite exhibits better wear resistance compare to the others (Figure 5). The transfer film formed on the counterpart surface, sliding against PTFE + 40 % bronze, is smooth, thin and uniform, which

indicates that the formation of adhesive strength between the transfer films and the counterpart surface is strong. In the case of the counterpart sliding against the pure PTFE, the transfer film is very thick.

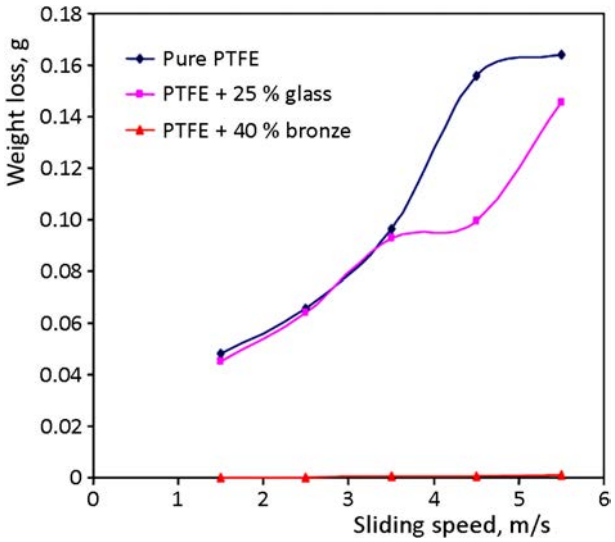

Figure 4. Weight loss vs. sliding speed at constant applied load of 60 N and sliding distance of 1500 m

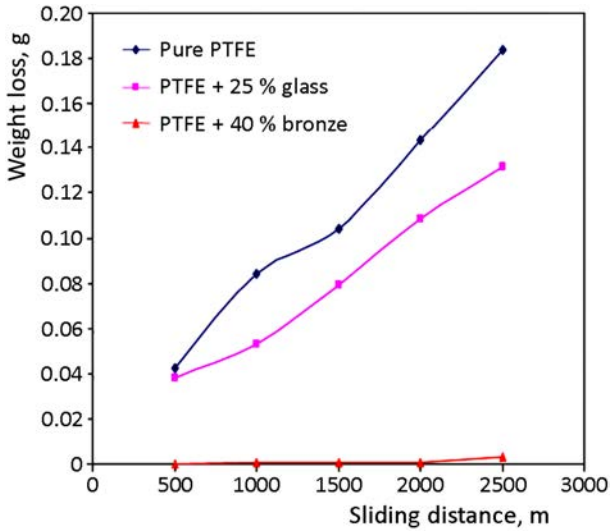

Figure 5. Wear curves of tested materials for 60 N load and speed of 1.5 m/s

Evaluation of the wear rate and coefficient of friction for graphite flake (2, 5 and 10 wt. %; 10 μm) filled PTFE composites were studied by Goyal and Yadav [10]. It was performed on a pin-on-disk tribometer under dry sliding conditions, at sliding speed of 1 m/s and 25 N load (0.19 MPa), during 8000 m. A significant decrease in wear of composites in compare to pure PTFE is noticed. The wear rates of composites with 5 and 10 wt. % of graphite were decreased 22 and 245 times, respectively (Figure 6). This decrease in wear rate is also attributed to the formation of a thin and tenacious transfer film on the counterpart surface.

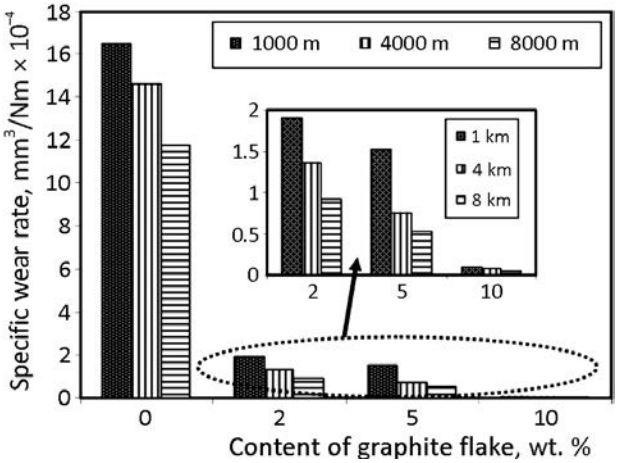

Figure 6. Specific wear rate of PTFE with various content of graphite flakes

Compared to pure PTFE, composites showed stable coefficient of friction (Figure 7). The lowest coefficient of friction was 0.20 for composites with 2 and 5 wt. % of graphite. For composite with 10 wt. % of graphite, the coefficient of friction was slightly higher and close to the value obtained with pure PTFE. Anyway, variations of the coefficient of friction are very small.

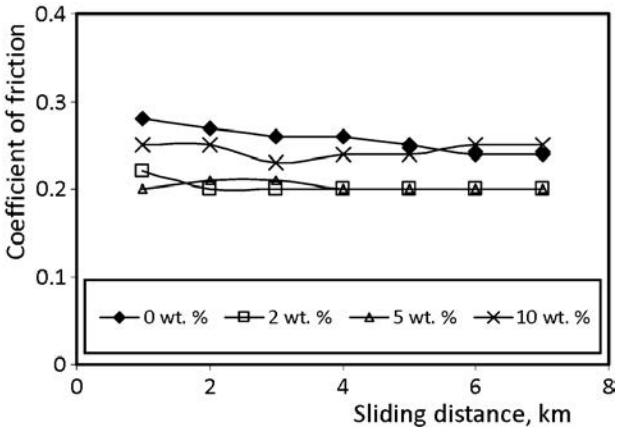

Figure 7. Coefficient of friction with various content of graphite flakes

Unal et al. [11] also studied the friction and wear behaviour of pure PTFE and bronze (25, 40 and 60 %) filled PTFE polymer composites under applied load range from 5 to 200 N (0.18 – 7.07 MPa) and sliding speed range from 0.32 to 2.0 m/s, using a pin-on-disc tribometer. The results showed that bronze filled PTFE composite exhibited lower coefficient of friction (Figure 8 and Figure 9) and higher wear resistance (Figure 10) compared to pure PTFE. The coefficient of friction of both – pure PTFE and bronze filled PTFE composites decreases when the applied load is increased from 5 to 30 N (light condition). Above 30 N the coefficient of friction remains stable.

The PTFE filled with 60 % of bronze showed higher wear resistance than pure PTFE. This behaviour can be attributed to the presence of

bronze, which is embedded within the matrix material and impart additional strength to the composite. The applied load has shown more influence on the wear behaviour of PTFE and PTFE composite than the sliding speed.

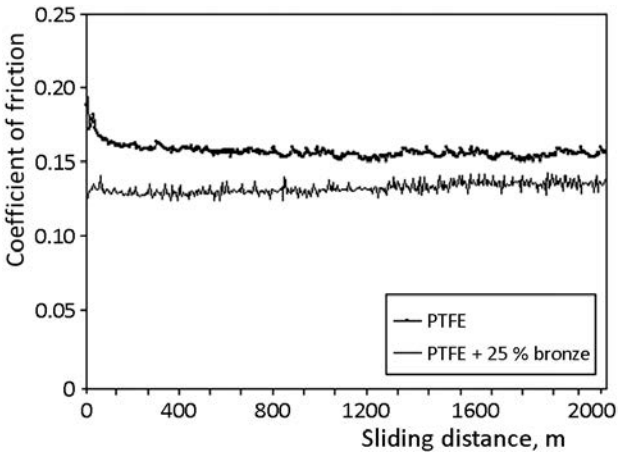

Figure 8. Variation of coefficient of friction with sliding distance (normal load: 50 N; sliding speed: 1.5 m/s)

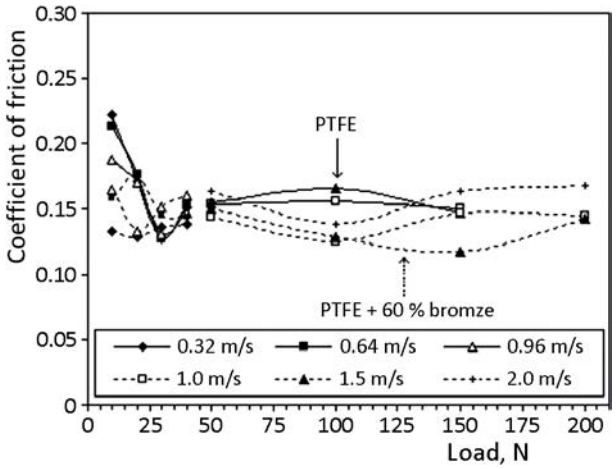

Figure 9. Variation of coefficient of friction with applied load and sliding speed for PTFE and PTFE + 60 % bronze composite

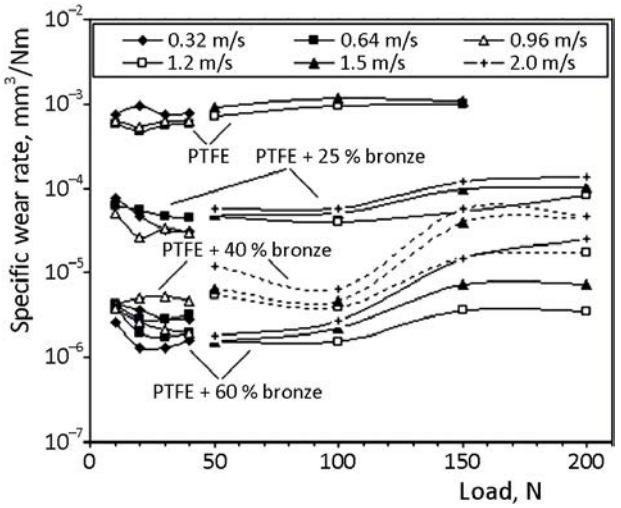

Figure 10. Variation of specific wear rate with applied load and sliding speed for PTFE and PTFE composites

In addition, it could be interested to present a diagram that shows dependence of specific wear rate on wt. % of filler materials (Figure 11) [12]. Although there are filler materials which are not subject of this paper, it might be interesting to compare specific wear rate for different polymer composites.

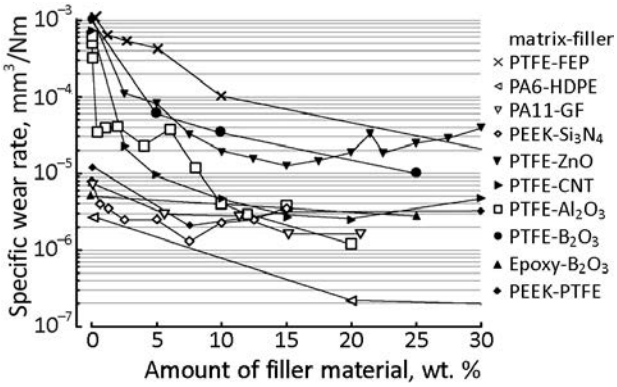

Figure 11. Specific wear rate vs. wt. % of filler material for various polymer composites
(FEP – fluorinated ethylene propylene; PA6 – polyamide 6; HDPE – high-density polyethylene; PA11 – polyamide 11; GF – glass fibre; PEEK – polyether ether ketone; CNT – carbon nanotube)

4. CONCLUSION

In this review paper, the tribological behaviour of PTFE composites, filled with glass fibres, graphite flakes, carbon, bronze or combination of mentioned filler materials has been analysed.

It is noticed that coefficient of friction usually remains in the range from 0.1 to 0.3. When pure PTFE is compared with PTFE composites, there is only slight decrease in coefficient of friction with almost all analysed composites.

On the other hand, regarding to wear of pure PTFE and its composites, influence of filler materials is quiet significant. Presence of filler material can increase wear resistance (decrease wear) up to 2 to 3 orders of magnitude. However, it can be concluded that the best results, regarding to wear resistance, were obtained by PTFE + bronze composites. Nevertheless, if we compare it to the other composites, that difference is not that significant, i.e. similar wear resistance can be obtained with appropriate amount of other mentioned filler materials.

ACKNOWLEDGEMENT

This work has been performed within the projects TR 35021, TR 34028 and TR 35011. These projects are supported by the Republic of Serbia, Ministry of Education, Science and Technological Development, whose financial help is gratefully acknowledged.

REFERENCES

[1] W. Brostow, V. Kovačević, D. Vrsaljko, J. Whitworth: *Tribology of polymers and polymer-based composites*, Journal of Materials Education 32, pp. 273-290, 2010.

[2] K. Friedrich, P. Reinicke: *Friction and wear of polymer-based composites*, Mechanics of Composite Materials 34, pp. 503-514, 1998.

[3] W.A. Glaeser: *Materials for Tribology*, Elsevier, Amsterdam, 1992.

[4] N.K. Myshkin, A.Ya. Grigoriev, V.L. Basiniuk, A.I. Mardasevich, V.G. Kudritsky, I.N. Kavaliova: *Equipments and materials for tribotesting in open space on International Space Lab*, Tribology in Industry 33, pp. 43-46, 2011.

[5] I. Zidaru, R.G. Ripeanu, I. Tudor, A.C. Drumeanu: *Research regarding the improvements of tribological behavior in three cone bits bearings*, FME Transactions 37, pp. 99-102, 2009.

[6] P.V. Kulkarni, N.K. Chapkhhane: *Development and testing of PTFE based composite bearing material for turbine pump*, International Journal of Engineering and Advanced Technology (IJEAT) 1, pp. 15-20, 2012.

[7] J. Khedkar, I. Negulescu, E.I. Meletis: *Sliding wear behavior of PTFE composites*, Wear 252, pp. 361-369, 2002.

[8] H. Unal, A. Mimaroglu, U. Kadıoglu, H. Ekiz: *Sliding friction and wear behaviour of polytetrafluoroethylene and its composites under dry conditions*, Materials & Design 25, pp. 239-245, 2004.

[9] B.A. Mudasar Pasha, D. Abdul Budan, S. Basavarajappa, S. Manjunath Yadav, B.A. Nizamuddin: *Dry sliding wear behaviour of PTFE filled with glass and bronze particles*, Tribology – Materials, Surfaces & Interfaces 5, pp. 59-64, 2011.

[10] R.K. Goyal, M. Yadav: *Study on wear and friction behavior of graphite flake-filled PTFE composites*, Journal of Applied Polymer Science 127, pp. 3186-3191, 2013.

[11] H. Unal, E. Kurtulus, A. Mimaroglu, M. Aydin: *Tribological performance of PTFE bronze filled composites under wide range of application conditions*, Journal of Reinforced Plastics and Composites 29, pp. 2184-2191, 2010.

[12] D.L. Burris, W.G. Sawyer: *A low friction and ultra low wear rate PEEK/PTFE composite*, Wear 261, pp. 410-418, 2006.

Serbian Tribology Society

SERBIATRIB '13

13th International Conference on Tribology

Faculty of Engineering in Kragujevac

Kragujevac, Serbia, 15 – 17 May 2013

WEAR CHARACTERISTICS OF HYBRID COMPOSITES BASED ON ZA27 ALLOY REINFORCED WITH SILICON CARBIDE AND GRAPHITE PARTICLES

Slobodan Mitrović [1], Miroslav Babić [1], Nenad Miloradović [1], Ilija Bobić [2], Blaža Stojanović [1], Dragan Džunić [1]

[1] Faculty of Engineering University of Kragujevac, Kragujevac, Serbia, boban@kg.ac.rs, babic@kg.ac.rs, mnenad@kg.ac.rs, blaza@kg.ac.rs, dzuna@kg.ac.rs,

[2] Institute of Nuclear Sciences "Vinča", University of Belgrade, Belgrade, Serbia, ilijab@vinca.rs

Abstract: *The paper presents the wear characteristics of a hybrid composite based on zinc-aluminium ZA27 alloy, reinforced with silicon-carbide and graphite particles. The tested sample contains 5 vol.% of SiC and 3 vol.% Gr particles. Compocasting technique has been used to prepare the samples. The experiments were performed on a "block-on-disc" tribometer under conditions of dry sliding. The wear volumes of the alloy and the composite were determined by varying the normal loads and sliding speeds. The paper contains the procedure for preparation of sample composites and microstructure of the composite material and the base ZA27 alloy. The wear surface of the composite material was examined using the scanning electronic microscope (SEM) and energy dispersive spectrometry (EDS). Conclusions were obtained based on the observed impact of the sliding speed, normal load and sliding distance on tribological behaviour of the observed composite.*

Keywords: *ZA27 alloy, hybrid composites, wear characteristics*

1. INTRODUCTION

The composite material represents the solid connection of the two or more constituents, which are joined into the unbreakable connection, for obtaining the better mechanical, tribological and other characteristics.

Metal matrix composites (MMCs) have attracted considerable attention recently because of their potential advantages over monolithic alloys [1 - 3].

Zinc–aluminium (ZA) alloys have emerged as important material for tribological applications, especially suitable for high-load and low-speed applications. Commercially available ZA alloys are characterized by good tribomechanical properties, low weight, excellent foundry castability and fluidity, good machining properties, low initial cost, and environmentally friendly technology The zinc alloy with increased content of aluminium is one of the alloys, which can be used for manufacturing the metal matrix composites. The ZA27 alloy is considered as the most prospective for obtaining the composites, since it is convenient as a substrate for several methods of composites manufacturing. Besides, it is also convenient for the heat treatment and plastic forming, thus it is possible to a posteriori influence the mechanical properties of the final products [4 - 7].

Various methods and techniques were used to substantially improve wear behaviour of Zn–Al (zinc–aluminium) alloys without lowering significantly the mechanical properties of materials [6 - 8].

Thanks to mentioned properties and good characteristics, zinc-aluminium alloys have inspired researchers to reinforce them with different dispersed reinforcement materials (SiC, Al_2O_3, graphite and garnet) in order to obtain much more enhanced mechanical and tribological properties [9 - 16].

Considering the above, ZA27/SiC/graphite composites may be a good alternative to zinc-aluminium alloys in many industrial applications.

2. EXPERIMENTAL PROCEDURE

2.1 Preparation of the composites

Hybrid ZA27/SiC/Graphite composites have been successfully prepared using the compocasting procedure.

Hybrid ZA27/SiC composite reinforced with graphite was produced at the Laboratory for materials of the Institute for nuclear sciences "Vinca". The obtained chemical structure of ZA27 alloy that was used during experimental investigations coincides with the corresponding chemical structure defined by standard. Average size of SiC particles was 26 μm, while average size of graphite particles was 15 μm.

The applied compocasting procedure consisted of two phases. During the first phase, infiltration of the particles from the secondary phases into the semisolid melt of the basic alloy was conducted with constant mechanical blending. Obtained composite casts were then subjected to hot pressing during the second phase. This was done in order to decrease porosity and get better connection between the matrix and the reinforcement particles. At the same time, better mechanical characteristic of the composite material were obtained.

2.2 Structure of the sample materials

Microstructure of ZA27 alloy and obtained composite were observed by metallurgy microscope and presented in Figure 1 and 2. Stucture of the sample of ZA27 alloy is mainly dendrite (Figure 1). Distinct uniformity of the structure was present, which indicates a favourable ratio of mechanical properties of the tested materials.

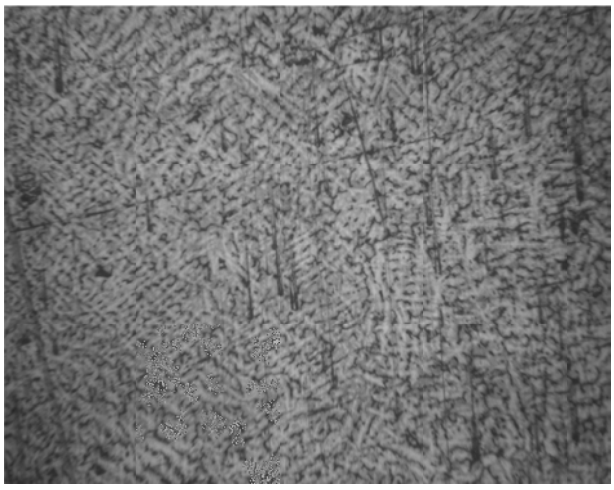

Figure 1. Microstructure of ZA27 alloy

Figure 2 shows the microstructure of the obtained composite.

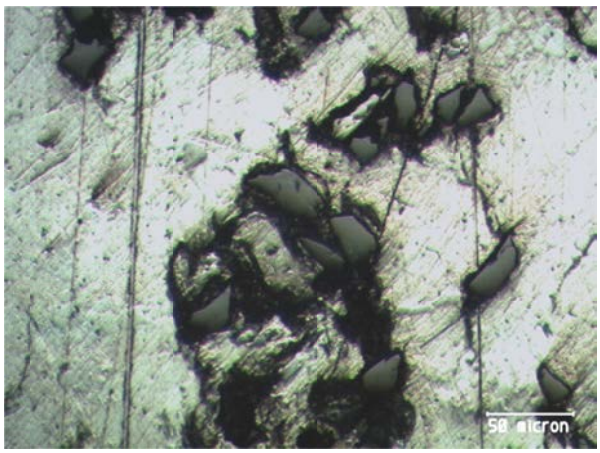

Figure 2. Microstructure of ZA27/3% SiC/3% Gr composite (magnification x 400)

A uniform distribution of SiC and graphite particles was present in tested composite materials.

2.3 Testing methods

Experimental tests were performed at the Centre for tribology of the Faculty of Engineering, University of Kragujevac.

The tests of the ZA27/SiC/Gr composite's tribological characteristics were performed on the computer supported tribometer with "block-on-disc" contact geometry (Figure 3). Tribometer provides variation of contact conditions in terms of shape, dimension and material of contact elements, normal contact load and sliding speed.

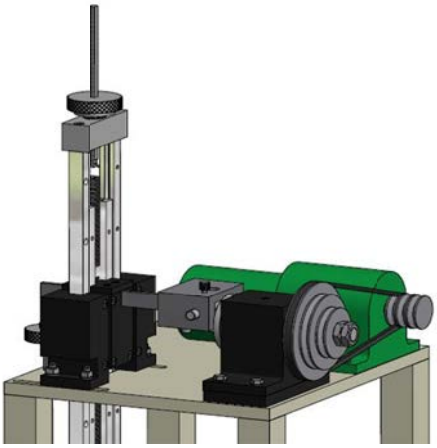

Figure 3. The "block-on-disc" tribometer

Based on the measured wear scar width on the contact surface obtained by variation of normal loads and sliding speeds, the material wear volume was calculated. The tests were performed in dry sliding conditions, with variation of sliding speed levels (0.25 m/s, 0.5 m/s and 1 m/s) and contact load levels (10 N, 20 N and 30 N). The observed sliding distances during tests were: 30 m, 60 m, 90 m, 150 m and 300 m.

The test contact pair meets the requirements of the ASTM G77-05 standard. It consists of the rotational disc with the diameter of D_d=35 mm and the width of b_d=6.35 mm and of the stationary block of the width of b_b=6.35 mm, the length of l_b=15.75 mm and the height of h_b=10.16 mm. The discs were made of 90MnV8 steel with hardness of 62 HRC and the surfaces roughness of R_a=0.40 μm. The blocks were made of the tested ZA27/5%SiC/3%Gr.

3. THE RESULTS AND DISCUSSION

The variations of dry sliding wear volume loss are presented in corresponding diagrams in the paper, depending on the sliding distance and for different values of sliding speeds and contact loads. The results of wear for given hybrid composite and for ZA27 alloy were presented in the same diagrams in order to understand the wear process evolution during tests and to make corresponding comparisons. Solid lines on the diagrams refer to the wear scar widths of the composite, while the wear scar widths of the ZA27 alloy are denoted by dashed lines.

The variation of dry sliding wear volume loss with the sliding distance for different applied loads and for a sliding speed of 0.25 m/s is presented in Figure 4. All diagrams are given for the sliding distance of 300 m.

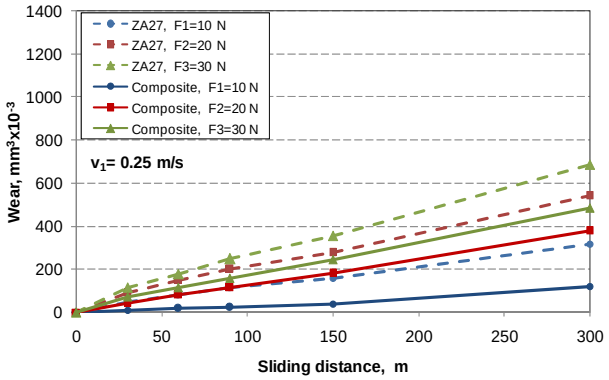

Figure 4. Variation of wear volume of ZA27 alloy and ZA27/5%SiC/3%Gr composite against sliding distance for different contact loads and for sliding speed of v=0.25 m/s.

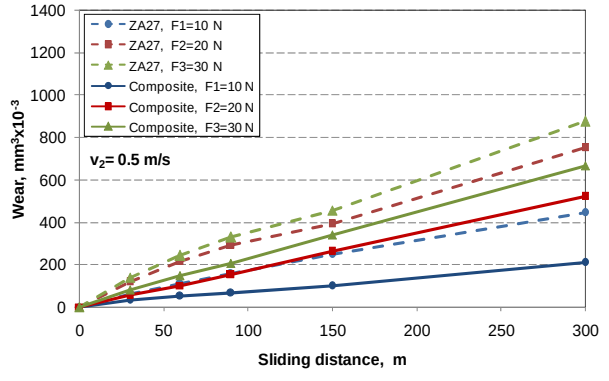

Figure 5. Variation of wear volume of ZA27 alloy and ZA27/5%SiC/3%Gr composite against sliding distance for different contact loads and for sliding speed of v=0.5 m/s.

The variation of wear volume loss of ZA27 alloy and ZA27/5%SiC/3%Gr composite depending on the sliding distance and for different applied contact loads and the sliding speed of 0.5 m/s may be seen in Figure 5.

Diagram in the Figure 6 presents the variation of wear volume loss of ZA27 alloy and ZA27/5%SiC/3%Gr composite depending on the sliding distance and for different applied contact loads and the sliding speed of 1 m/s.

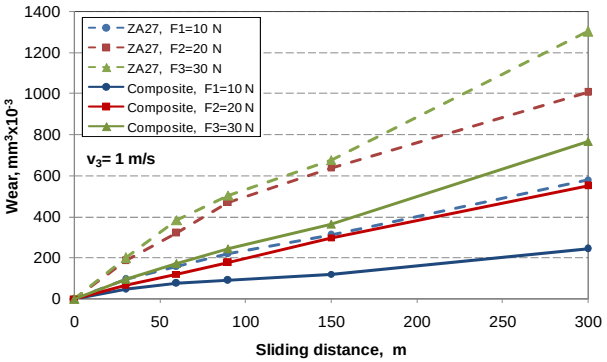

Figure 6. Variation of wear volume of ZA27 alloy and ZA27/5%SiC/3%Gr composite against sliding distance for different contact loads and for sliding speed of v=1 m/s.

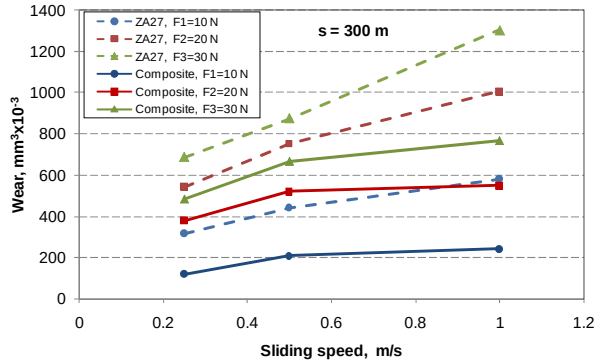

Figure 7. Wear volume of ZA27/5%SiC/3%Gr composite and ZA27 alloy depending on sliding speeds, for different contact loads and for sliding distance of 300 m.

The wear volume losses of the alloy and the composite increase with the increase of the sliding distance. The wear volume loss curves are of the same character, both for alloy and for the observed composite material. The only difference may be seen in level of wear. At the beginning, a larger slope of the curves is noticeable, so there is the intensive initial wear of the composite material. A rapid increase of wear volume loss is characteristic for sliding distance of approximately 35 m. After reaching the zone of constant wear, the wear volume loss has slight, almost linear increase.

Generally, the wear behaviour of the tested materials is characterized by very intensive wear during initial period, after which there is a period of stabilization. Wear of the composites was always significantly lower when compared to wear of the matrix ZA27 alloy.

The influence of the sliding speed on wear volume for both materials is shown in Figure 7, for different values of normal loads.

The effects of the normal load on wear volume of both composite and alloy is presented in Figure 8, for different values of sliding speeds and for sliding distance of 300 m

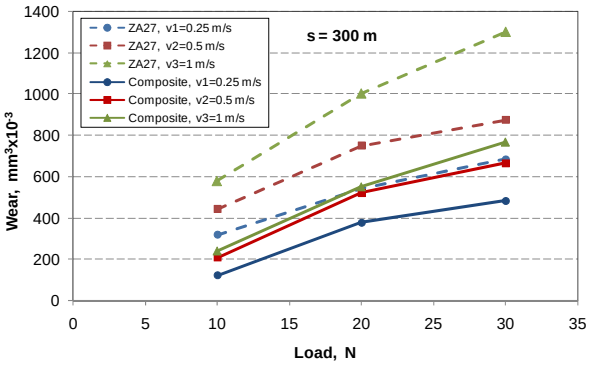

Figure 8. Wear volume of ZA27/5%SiC/3%Gr composite and ZA27 alloy depending on contact loads, for different sliding speeds and for sliding distance of 300 m.

Analytical and graphical variations in wear rate due to changes of sliding speeds and normal loads in dry sliding conditions are presented in Figures 9 and 10. Exponential regression functions were adopted. Corresponding regression functions coefficients and curvilinear correlation indices were obtained showing the good correlation between experimental data and used empirical distributions.

Wear rate of ZA27 alloy in dry sliding conditions is presented in Figure 9 and wear rate of ZA27/5%SiC/3%Gr composite in dry sliding conditions is shown in Figure 10. Variations of the wear rate as a function of the sliding speed and normal load are graphically presented for the ZA27 alloy and composite materials.

Both tested materials share basically the same nature of wear process development in all contact conditions. The observed composite material has better wear resistance, under the same test conditions.

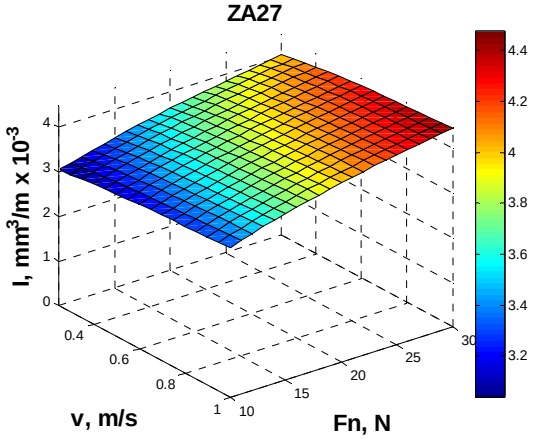

Figure 9. Wear rate of ZA27 alloy in dry sliding conditions.

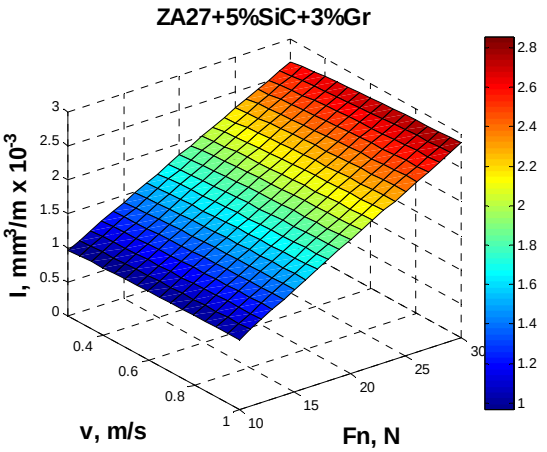

Figure 10. Wear rate of ZA27/5%SiC/3%Gr composite in dry sliding conditions.

The comparative histograms of the wear volume formed after 300 m of sliding distance, depending on the contact conditions (the sliding speed and the normal force) for the basic ZA27 alloy and ZA27/5%SiC/3%Gr composite materials are shown in Figure 11.

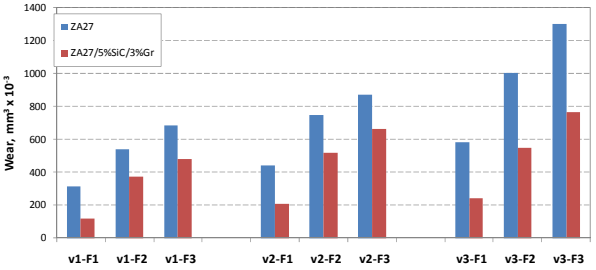

Figure 11. Comparative histograms of wear volume of ZA27 alloy and ZA27/5%SiC/3%Gr composite.

Analysis of histograms in Figure 11 shows that a trend of increase of wear with the increase of normal load may be observed. The increase of sliding speed induces also the increase of wear. This observation is valid for both tested materials. It may be noticed that the wear of the tested ZA27 alloy is always significuly higher compared to wear of the composite with addition of the SiC and graphite particles.

From the Figure 11, the influence of the normal load and sliding speed on the wear magnitude may be clearly noticed. The wear rate increases both with the increase of the normal force the increase of the sliding speed. The largest value of wear corresponds to the highest sliding speed (v_3 = 1 m/s) and to the highest value of the normal contact load (F_3 = 30 N). For the lowest sliding speed (v_1 = 0.25 m/s) and the lowest load (F_1 = 10 N), the smallest wear values were recorded.

Characterization of the microstructure of wear surface for metal matrix composites is more complex than that of the metals or alloys and an understanding of wear mechanisms is far from

complete. The SEM analysis may contribute to better understanding of this mechanism.

The SEM micrograph of the worn surface at load of 10 N and at speed of 0.25 m/s for a sliding distance of 300 m is presented in Figure 12 for the tested composite material.

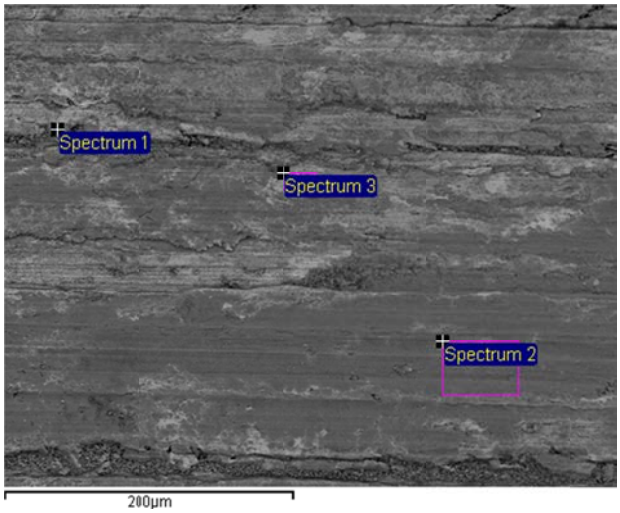

Figure 12. SEM micrographs of worn surfaces of the ZA27/5%SiC/3%Gr composite

Qualitative and quantitative chemical analyses of micro-constituents were performed using energy dispersive spectrometry (EDS), Figure 13.

Analyses confirm the presence of constituent elements like: Zn, Al, SiC, Gr (C), as well as the presence of Fe as a consequence of material transfer from the counterpart to the composite block.

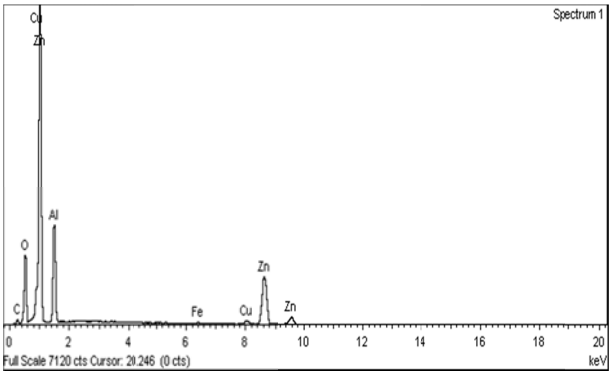

Figure 13. EDS analysis of worn surface on the ZA27/10%SIC/1%Gr composite

Microstructure of worn surface of ZA27 alloy is shown in Figure 14.

Microstructure of worn surface of ZA27/5%SiC/3%Gr composite is given in Figure 15.

Generally, the parallel grooves and scratches can be seen over all the surfaces in the direction of sliding. These grooves and scratches resulted from the contact between the worn surface of the tested material and the counter disc of significantly higher hardness.

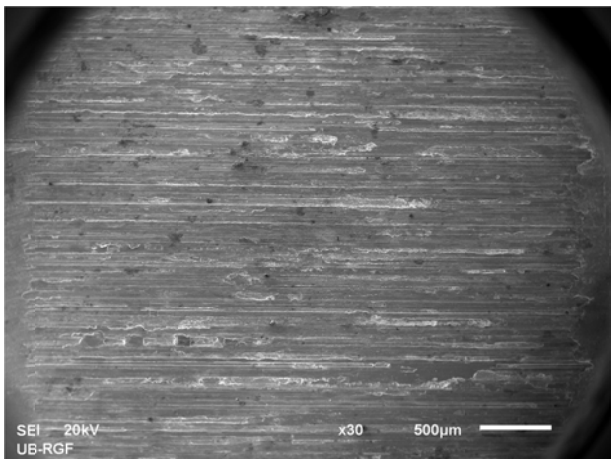

Figure 14. Appearance of the worn surface of ZA27 alloy photographed by SEM in dry sliding conditions (v_1 = 0.25 m/s, F_1 = 10 N)

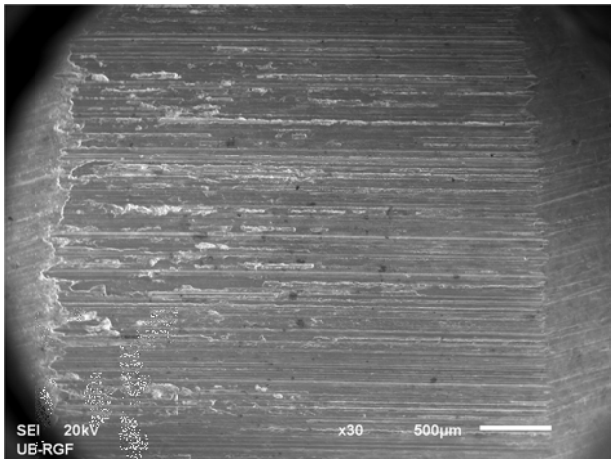

Figure 15. Appearance of the worn surface of ZA27/5%SiC/3%Gr composite photographed by SEM in dry sliding conditions (v_1 = 0.25 m/s, F_1 = 10 N)

4. CONCLUSION

This research was conducted in order to complete the tribological knowledge on developed composite materials with ZA27 alloy reinforced by the SiC and graphite particles. The goal was to confirm the further possibilities for broader application of given composites as advanced tribo-materials, in different technical systems because they have excellent wear resistance when compared with the base ZA27 alloy.

By monitoring the wear process through observation of wear volume in dry sliding conditions, the following conclusions can be made:

- Wear of the tested composite is smaller than wear of ZA27 alloy for all applied sliding speeds and normal loads.
- Wear process evolution has the same character for both tested materials (basic ZA27 alloy and ZA27/10%SiC/1%Gr composite).

- Values of the wear volume of the observed composite material increase with the increase of normal loads.
- Wear volume also increases with the increase of the sliding speed.

ACKNOWLEDGMENTS

This paper presents the research results obtained within the framework of the project TR-35021, financially supported by the Ministry of Education, Science and Technological Development of the Republic of Serbia

REFERENCES

[1] M. Babić, S. Mitrović: *Tribological characteristics of composites based on ZA alloy*, (in Serbian), Monograph, Faculty of Mechanical Engineering, Kragujevac, 2007.

[2] M. Babić, S. Mitrović, I. Bobić, *Tribological Properties of Composites with Substrate Made of the ZA-27 Alloy Reinforced by the Graphite Particles*, Tribology in industry, Vol. 29 No. 3&4, 2007.

[3] S. Mitrović, M. Babić, B. Stojanović, N. Miloradović, M. Pantić, D. Džunić: *Tribological Potential of Hybrid Composites Based on Zinc and Aluminium Alloys Reinforced with SiC and Graphite Particles*, Tribology in Industry, Vol. 34, No. 4, 177-185, 2012.

[4] M. Babić, A. Vencl, A., S. Mitrović, I. Bobić, *Influence of T4 heat treatment on tribological behavior of ZA27 alloy under lubricated sliding condition*, Tribology Letters, Vol. 36, No. 2, pp. 125-134, 2009.

[5] M. Babic, S. Mitrovic, B. Jeremic: *The Influence of Heat Treatment on the Sliding Wear Behaviour of a ZA-27 Alloy*, Tribology International, Vol. 43, No. 1-2, pp. 16-21, 2010.

[6] M. Babic, S. Mitrovic, D. Džunic, B. Jeremic, I. Bobic: *Tribological Behaviour of Composites Based on Za-27 Alloy Reinforced With Graphite Particles*, Tribology Letters, Vol. 37, No. 2, pp. 401-410, 2010.

[7] K.H.W. Seah, S.C. Sharma, B.M. Girish: *Mechanical properties of as-cast and heat-treated ZA-27/graphite particulate composites*, Composites, Part A 28A, pp. 251-256, 1997.

[8] S.C. Sharma, B.M. Girish, R. Kramath, B.M. Satish: *Graphite particles reinforced ZA-27 alloy composite materials for journal bearing applications*, Wear, Vol. 219, pp. 162-168, 1998.

[9] B.K. Prasad: *Abrasive wear characteristics of a zinc-based alloy and zinc-alloy/SiC composite*, Wear, Vol. 252, pp. 250-263, 2002.

[10] S.C. Sharma, B.M. Girish, R. Kramath, B.M. Satish: *Effect of SiC particle reinforcement on the unlubricated sliding wear behavior of ZA-27 alloy composites*, Wear, Vol. 213, pp. 33-40, 1997.

[11] B.K. Prasad: *Investigation into sliding wear performance of zinc based alloy reinforced with SiC particles in dry and lubricated conditions*, Wear, Vol. 262, pp. 262-273, 2007.

[12] S. Mitrović, M. Babić, I. Bobić: *ZA-27 alloy composites reinforced with Al_2O_3 particles*, Tribology in Industry, Vol. 29, No. 3-4, pp. 35-41, 2007.

[13] M. Babić, S. Mitrović, I. Bobić, F. Živić: *Wear behavior of composites based on ZA-27 alloy reinforced by Al2O3 particles under dry sliding condition*, Tribology Letters, Vol. 38, No. 3, pp. 337-346, 2010.

[14] A Vencl: *MMCs based on hypoeutectic Al-Si alloy: Tribological properties in dry sliding conditions*, Tribological Journal BULTRIB, Vol. 2, No. 2, pp. 17-22, 2012.

[15] N. Miloradović, B. Stojanović: *Tribological behavior of ZA-27/10SiC/1Gr Hybrid Composite*, Journal of the Balkan Tribological Association, Vol. 19, No. 1, pp. 97-105, 2013.

[16] B. Stojanović, M. Babić, S. Mitrović, A. Vencl, N. Miloradović, M. Pantić: *Tribological characteristics of aluminum hybrid composites reinforced with silicon carbide and graphite*, Journal of the Balkan Tribological Association, Vol.19, No.1, pp. 83-96, 2013.

Serbian Tribology Society

SERBIATRIB '13

13th International Conference on Tribology

Faculty of Engineering in Kragujevac

Kragujevac, Serbia, 15 – 17 May 2013

INFLUENCE OF OXIDATION LAYER GENERATED ON PREHEATED CONTACT PAIRS ON STATIC COEFFICIENT OF FRICTION

Marija Jeremić[1], Dragan Adamović[1], Slobodan Mitrović[1]
Bojan Bogdanović[1]Aleksandar Simić[1], Saša Ranđelović[1], Petar Todorović[1],
[1]Faculty of Engineering, SestreJanjić 6, Kragujevac, Serbia, mjeremic88@yahoo.com, adam@kg.ac.rs, boban@kg.ac.rs, bogdanovicboki@gmail.com, aleksandarsimickg88@gmail.com, sasarandjelovic@yahoo.com, petar@kg.ac.rs

Abstract: *The subject of the work includes theoretical considerations, conducting experimental tests which are subjected to the analysis of the test results related to the determination of the coefficient of static friction, of contact pairs which were previously heat treated. Contact pairs were, before the procedure to determine the coefficient of friction, heated to temperatures of 50°C-350°C and cooled to room temperature. Test results show that, depending on the thermal treatment of contact pairs, there is significant increase in the coefficient of friction. The authors believe that the reasons for the increase of the friction coefficient are related to the creation of oxide and changes in the surface layer of contact pairs.*

Keywords: *coefficient of static friction*, oxidation layer, pre heat treatment, normal load

1. INTRODUCTION

Precisely prediction of static friction is of the essence significance due to its application in many modern tribological systems, such as chucks, clamps, seals, micro-electromechanical systems and so on. Importance of the evaluation of the coefficient of friction is figured long time ago and that area studied some of the first scientists such as Leonardo da Vinci, Guillaume Amontons, Charles Augustin Coulomb, George Rennie and many others [1]. As the force of friction occurs when two bodies are in contacts, based on the relative speed of movement it can be divided into friction at the idle status and the friction in state of motion. Start the movement of any kind is related to the existence of static friction. The static coefficient of friction depends on many parameters, primarily from the surface of contact, normal load, atmosphere and temperature at which contact occurs, surface absorption, quality of surfaces in contact and materials of contact surfaces [2-6]. Many authors have been examining the influence of roughness parameters on the of contact surfaces for the static friction coefficient and came to the conclusion that the static coefficient of friction increases with increasing surface roughness parameters [4, 5]. Some authors have concluded that some of the roughness parameters, such as skewness and kurtosis, have more influence on the static coefficient of friction compared to other parameters [7] [8]. The friction force at idle phase increases with increasing tangential displacements up to the value that is needed to begin movement of the bodies in contact [9]. The main parameters of static friction are the maximum force of static friction, which is realized at the moment of macro displacement, and corresponding value of the micro-movement. The influence of temperature and normal load on the friction characteristics of materials is topic of numerous scientific works [10-13], especially when are concerned materials used in process of hot metal forming. Etsion and Amit [10] experimentally investigated the effect of normal load on the coefficient of static friction for a very smooth metal surface. Normal load is in the range of 10^{-3}N - 0,3N and applied to samples of small diameter made of three different aluminum

alloys in contact with nickel-plated finish. The tests were conducted in conditions of controlled humidity and air cleanliness. The dramatic increase of coefficient of static friction was noticed when the normal load reduced to the lowest level. This kind of behavior is attributed to the adhesion forces which have a significant role and which are more prominent at low normal loads and smooth surfaces. To the knowledge of authors the study of static coefficient of friction under conditions of high temperature was not the topic of more extensive theoretical and experimental works [14-17]. Behavior of the static and kinematic friction of materials coupling at different values of temperature and contact pressures investigated Chaikittiratana, Koetniyom and Lakkam [17]. Device which is used for performing of the experiment is specifically constructed for the determination of sliding friction at higher temperatures. It was established that at 100°C there isn't significant change in the coefficient of friction when the contact pressure varies. However, at a temperature of 200°C observed friction coefficient change with the change of the contact pressure. There was an increase in the coefficient of friction when the contact pressure increased from 0.147MPa - 0.252MPa. It is concluded that the increase in temperature significantly increases the coefficient of friction. One of the most important conclusions of this work is that the static coefficient of friction increases with increasing temperature, which is partly a consequence of increase the plasticity of most contact materials at higher temperatures.

The aim of this paper is to determine the influence of previously heat treated contact pairs on the value of the static coefficient of sliding friction, with contact elements made of steel. Experimental measurements were performed on instrumentation developed by the authors, in order to accurately determine the value of the static coefficient of sliding friction at higher temperatures and relatively low values of contact pressures in the variable radius of curvature of contact elements. The results could have a significant aplication in industrial applications.

2. THEORETICAL CONSIDERATIONS

Measurement of the friction coefficient at high temperature in contact pairs is associated with a number of problems of physical and technical nature. Issues related to the reliability of measurements are especially pronounced in the measurement of the friction coefficient under low contact pressure. Problems related to the fact that at high temperatures in the contact pairs must accurately measure very small values of physical quantities (normal and friction force). For measuring small values of the friction force is necessary to exist electronic components in the measuring chain (sensors of force and other electronic components). Since the force sensors, for reasons of measurement reliability, should be outside the zone of high temperatures, it becomes important ,to the signals associated with small displacement and force, that they have to be transmitted mechanically from the high temperature zone (the chamber in which the pair is heated to desired temperature) to the sensor to quantify the value of the friction and normal contact load of contact pair. Mechanical transmission chain of friction force pulls the corresponding measurement errors, especially when it comes to measure very small values of force.

The authors started from the idea that the principle of measuring the static coefficient of friction over the steep plane have to be upgraded and enable measurement in conditions of high temperatures and low values of contact pressure. The principle of measurement of coefficient of friction over the steep plane (Figure 1) is based on gravity. Static coefficient of friction, as it is known is the ratio of the friction force and the force normal to the surface of contact, where condition for equilibrium on a steep plane is given by expression $F_\mu > mg \cdot \sin\alpha$. In the limiting case of sliding friction valid equation is:

$$\mu = \frac{F_\mu}{N} = \frac{mg\sin\alpha}{mg\cos\alpha} = tg\alpha \qquad (1)$$

where are: μ – value of static friction coefficient; F_μ - friction force; m - mass of body; g - acceleration of gravity; α - steep angle of the plane.

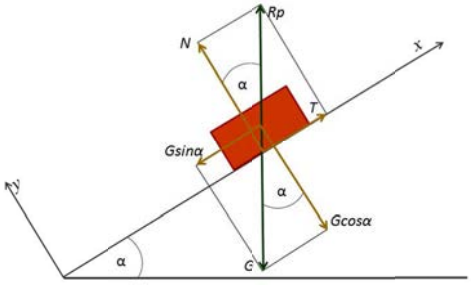

Figure 1. The balance of the body on a steep plane

Measurement error of static coefficient of friction on this principle arising from error of angle measurement in relation to an ideal horizontal position when the body which is located on a steep plane crossed from sleep in a state of motion (Figure 2), respectively:

$$\varepsilon = \frac{tg(\alpha + \Delta\alpha) - tg\alpha}{tg\alpha} \cdot 100, [\%] \qquad (2)$$

where are: ε – relative error of measurement; $\Delta\alpha$ - angular error of measurement α. If one takes into account that the friction coefficient $\mu = tg\alpha$, then the diagram given in Figure 2 can determine the relative measurement error $\varepsilon(\mu)$ which is, among other, function of coefficient of friction.

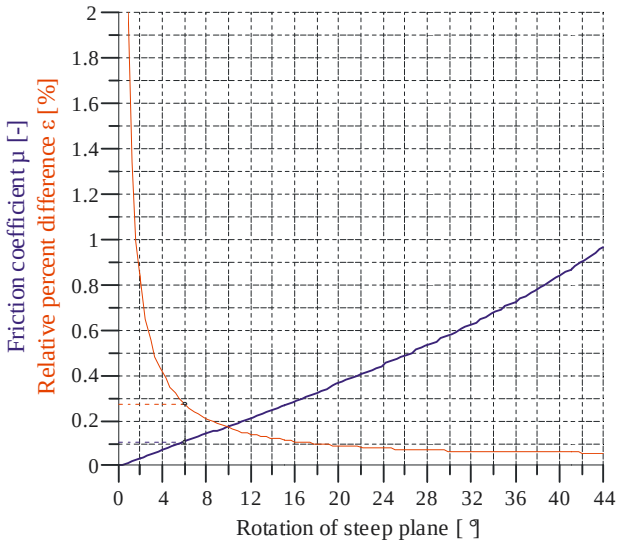

Figure 2. Graphical representation of the relative measurement error of the coefficient of friction over the steep plane

On the basis of eqquation (2) and the diagram (Figure 2) can be noted that values of the coefficient of sliding friction μ> 0.1 with $\Delta\alpha$ = 1' correspond to the measurement error which is less of 0.3%. This means that the principle of measurement can be efficiently used to determine the static friction coefficient at higher temperatures, especially if one takes into account that the sliding coefficient of static friction at elevated temperatures for most materials is greater than the above values.

3. EXPERIMENTAL RESEARCH

Experimental studies were performed on samples made of steel EN X160 CrVMo12 1 which is subjected to heat treatment hardening, with the aim to obtain the high hardness of 64 HRC and wear resistance. Tribological contact pair is realized by setting the rollers of diameters 4 *mm*, 6 *mm*, 8 *mm*, 10 *mm* and 12 *mm*, length 20 *mm*, on prism block (Figure 3). This simulates tribological contact which is, theoreticaly, realized on line. If we take into account that the mass of the rollers is small then we have small values of contact pressure. When rollers are in contact on flat surface block, in the absence of temperature, contact is achieved on tops of some asperities and in that case between most asperities there is no real physical contact. Block and the rollers are made of same material (the aforementioned). Experiments were carried out with increase of temperatures by 50°C, starting from the temperature T_1=50°C up to temperature T_2= 350°C, and after heating samples were left to cool to room temperature. Each measurement was repeated 10 times, so that a total of 350 independent experiments is performed at room temperature after heating the contact pair.

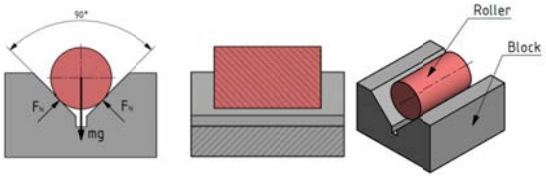

Figure 3. Schematic representation of the contact pair

The coefficient of friction was determined using specially designed devices (Figure 4). Working principle of designed Tribometer is based on rotation of steep plane, which is done on a mechanical principle to the accuracy of the readings of 1'. Namely, rotation steep plane is carried out by manually turning of nonius. Leveling of Tribometer is done using level which provides precision of reading which is less than 0,02/1000 $\mu m/m$.

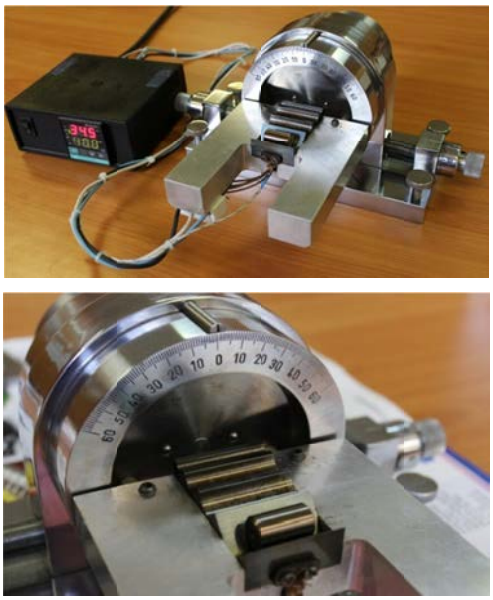

Figure 4. Measuring equipment

Contact pairs were heated to temperatures from 50°C to 350°C with the step of 50°C, after which they are cooled to room temperature. So, determining the size of the static coefficient of friction was performed with contact pairs that were heat treated at temperatures indicated. This means that contact pairs in the process of determining the static coefficient of friction were at room temperature. The results of measurement of the coefficient of friction depending on the weight of

rollers, that is, the normal contact load and temperature are shown in Table 1:

d *[mm]*	F *[N]*	T [^{0}C]	μ
12	0.174101	20	0.196581
10	0.120903	20	0.185261
8	0.077378	20	0.295619
6	0.043525	20	0.243811
4	0.019345	20	0.229694
12	0.174101	50	0.210229
10	0.120903	50	0.212484
8	0.077378	50	0.218193
6	0.043525	50	0.285514
4	0.019345	50	0.227332
12	0.174101	100	0.190895
10	0.120903	100	0.204541
8	0.077378	100	0.205629
6	0.043525	100	0.243661
4	0.019345	100	0.240049
12	0.174101	150	0.310443
10	0.120903	150	0.284418
8	0.077378	150	0.289048
6	0.043525	150	0.330971
4	0.019345	150	0.351592
12	0.174101	200	0.240052
10	0.120903	200	0.228621
8	0.077378	200	0.23437
6	0.043525	200	0.340861
4	0.019345	200	0.459168
12	0.174101	250	0.270227
10	0.120903	250	0.286718
8	0.077378	250	0.377837
6	0.043525	250	0.322573
4	0.019345	250	0.522993
12	0.174101	300	0.291725
10	0.120903	300	0.366628
8	0.077378	300	0.547985
6	0.043525	300	0.571756
4	0.019345	300	0.389194
12	0.174101	350	0.279639
10	0.120903	350	0.341781
8	0.077378	350	0.354048
6	0.043525	350	0.315233
4	0.019345	350	0.462363

According to the data from Table 1 was formed diagram of static friction coefficient which depending on the normal load and temperatures to which contact pairs are pre-treated.

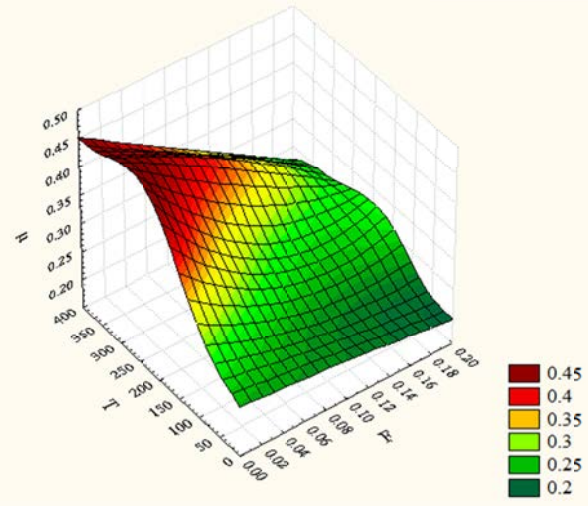

Figure 5. The static coefficient of friction which depending on the normal load and temperature

4. DISCUSSION

Based on theoretical considerations and experimental investigations it can be concluded that the physical principle of measuring the static coefficient of friction over the steep plane can be effectively applied in testing conditions at high values of temperature and low values of contact pressures. It requires a certain precision measurement instrumentation (precision measuring equipment - Tribometer), which is realized with equipment used for conducting this tests. The accuracy of the measurement was the angle of $\Delta\alpha$ = 1'. A large number of measurements and a number of repetitions of experiments under identical conditions allow statistical analysis of the results of measurements to minimize random error.

Experimental results of investigation presented in the form of 3D diagram in Figure 5 indicates that for given conditions the temperature treatment of contact pairs have substantial effect on the value of static coefficient of friction. The essential dependence of friction coefficient from temperature, which can be seen from the diagram, expressed that for temperature change from 50^0 C to 300^0 C value of the static friction coefficient increases nearly two times. Based on the foregoing, it is obvious that the changes of static friction coefficient arise from temperature effect on material in contact. It is likely that preheating of contact pairs above the temperature values close to 200^{0}C leads to physical changes in the surface layers of contact pairs.

With diagram shown in Figure 5 is possible to analyze the effect of normal load on the static coefficient of friction. Normal load in the range of 0.019 to 0, 17 N is used during experiment. From the diagram it can be seen that the minimum values of the normal load in the entire temperature range,

corresponding to the maximum value of the coefficient of friction, and reverse. This proves that the static coefficient of friction under conditions of low values of contact pressures and preheat treated contact pairs, just depends on the level of contact pressure, which is in line with tests performed in different conditions [10]. The increase in the contact pressure can lead to lower friction coefficient and reverse.

When analyzing the results, the authors of this work started from the next. Because of preheating of contact pairs it comes to decrease of hardness, which can be the reason for the increase of the friction coefficient. It is possible, and more likely, that oxidation layer is created at the surface of contact pairs with different tribological characteristics comparing to base material, steel EN X160 CrVMo12 1. Theoretically, changes in the structure changes the mechanical properties of hardened steel. With temperature increase hardness and strength decrease, while ductility and toughness increase. During the heating of the samples was three modes layoffs and low firing up to 200^0 C, the transformation of retained austenite 200^0 C - 300^0 C and removing internal stresses of 300^0 C - 400^0 C. This, with increasing tempering temperatures the hardness and strength decrease, while ductility and toughness increase. Oxidation occurs as a chemical reaction between metal and oxygen from the atmosphere. The occurrence of oxidation is possible at room temperature, however, the metals that are exposed to elevated temperatures above 200^0 C are able to create more intense oxidation layer.

The authors were not able to carry out structure analysis of surface layer with electronic microscope, so the question of large increase in the friction coefficient has two options listed. It is unlikely that changes in hardness of steel EN X160 CrVMo12 due to release 1 (Figure 6) from the value of 64 HRC to value of 60 HRC can lead to an increase in the coefficient of friction of approximately 70%. For this reason the authors believe that significant increase in the coefficient of friction is very probably due to the creation of oxides at the surface of contact pairs.

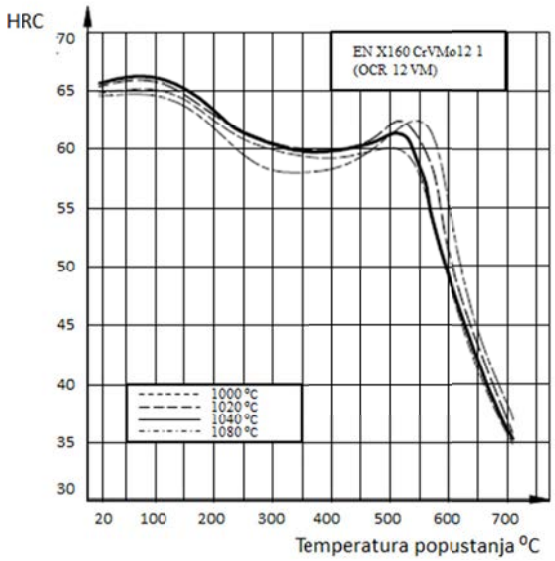

Figure 6. Releasing diagram of material

5. CONCLUSIONS

Based on these tests and analyzing the results, conclusions were made, preheated contact pairs made of steel EN X160 CrVMo12 1, at relatively low temperatures resulting leads to significant change in the value of static coefficient of friction. Results of measuring the static coefficient of sliding friction of the test material, under conditions of high temperature and small values of load contact, indicating a very significant effect of temperature and contact pressure on value. The impact of the minimum values of normal load in the entire temperature range, corresponding to the maximum value of the coefficient of friction, and vice versa. It is very unlikely that the changes of hardness of steel EN X160 CrVMo12 1 due to the release from the value 64 HRC to the value 60 HRC may lead to an increase in the coefficient of friction of approximately 70%. From this reason the authors believe that a significant increase of coefficient of friction is probably a consequence of creation of oxides at the surface of contact pairs.

REFERENCE

[1] Dowson, D., *History of Tribology*, Longman, New York, 1979

[2] K.-H. ZumGahr, K. Voelker, *Friction and wear of SiCfiberreinforced borosilicate glass mated to steel*, Wear 225–229, pp. 888–895, 1999.

[3] P. Blau, *The significance and use of the friction coefficient*, Tribol. Int. 34, pp. 585–591 2001.

[4] B. Ivkovic, M. Djurdjanovic, D. Stamenkovic: *The Influence of the Contact Surface Roughness on the Static Friction Coefficient*, Tribology in Industry, 22, pp. 41-44, 2000.

[5] U. Muller, R. Hauert: *Investigations of the coefficient of static friction diamond-like carbon films*, Surface and Coatings Technology, 174 –175, pp. 421–426, 2003.

[6] B. Polyakov, S.Vlassov, L.M. Dorogin, P. Kulis, I. Kink, R. Lohmus: *The effect of substrate roughness on the static friction of CuO nanowires*, Surface Science 606, pp. 1393–1399, 2012.

[7] N. Tayebi, A.A. Polycarpou: *Modeling the effect of skewness and kurtosis on the static friction coefficient of rough surfaces*, Tribology International 37, pp. 491–505, 2004.

[8] B. Bhushan, S. Sundararajan, W.W. Scott, S. Chilamakuri: *Stiction analysis of magnetic tapes*, IEEE Magnetics Transactions 33, pp. 3211–3213, 1997.

[9] E.L. Deladi: *Static Friction in Rubber-Metal Contacts with Application to Rubber Pad Forming Processes*, PhD thesis, University of Twente, Twente, 2006.

[10] I. Etsion, M. Amit: *The effect of small normal loads on the static friction coefficient for very smooth surfaces*, Journal of tribology, Vol.115, July 1993.

[11] O. Barrau, C. Boher, R. Gras, F. Rezai-Aria: *Wear mecahnisms and wear rate in a high temperature dry friction of AISI H11 tool steel: Influence of debris circulation*, Wear 263, pp.160–168, 2007.

[12] H. Kumar, V. Ramakrishnan, S.K. Albert, C. Meikandamurthy, B.V.R. Tata, A.K. Bhaduri: *High temperature wear and friction behaviour of 15Cr–15Ni–2Mo titanium-modified austenitic stainless steel in liquid sodium*, Wear 270, pp. 1–4, 2010.

[13] A. Chaikittiratana, S. Koetniyom, S. Lakkam: *Static/kinetic friction behaviour of a clutch facing material: effects of temperature and pressure*, World Academy of Science, Engineering and Technology 66, 2012.

[14] H. Kumar, V. Ramakrishnan, S.K. Albert, C. Meikandamurthy, B.V.R. Tata, A.K. Bhaduri: *High temperature wear and friction behaviour of 15Cr–15Ni–2Mo titanium-modified austenitic stainless steel in liquid sodium*, Wear 270, pp. 1–4, 2010.

[15] P. Mosaddegh, J. Ziegert, W. Iqbal, Y. *Tohme: Apparatus for high temperature friction measurement*, Precision Engineering 35, pp. 473–483, 2011.

[16] M. Worgull, J.F. Hetu, K.K. Kabanemi, M. Heckele, *Hot embossing of microstructures: characterization of friction during demolding*, MicrosystTechnol 14, pp. 767–773, 2008.

Serbian Tribology Society

SERBIATRIB '13

13th International Conference on Tribology

Faculty of Engineering in Kragujevac

Kragujevac, Serbia, 15 – 17 May 2013

DYNAMICS OF SAMS IN BOUNDARY LUBRICATION

Jelena Manojlović[1]

[1]The Faculty of Mechanical Engineering, University of Niš, Niš, Srbija, jmanojlo@gmail.com

Abstract: *Surfactant molecules have some properties responsible for a number of remarkable phenomena, such as oriented adsorption of surfactants at surfaces and interfaces. The capability to self-assemble into well-defined structures is often seen as being more important than their surface activity. When a surfactant solution is in contact with a solid surface, the surfactant molecules adsorb onto the surface, ideally forming an adsorbed layer of high order, termed as self-assembled monolayer (SAM). Many surface properties are influenced by such a film, and therefore, SAMs offer the capability to form ordered organic surface coatings, suitable for various applications, such as wetting or corrosion protection. Due to the flexibility in choosing the molecular architecture, organic molecules have many interesting applications, such as biosensors, in photoelectronics, in controlling water adsorption or boundary lubricant coating. This paper focuses on cationic surfactants (quaternary ammonium surfactants), with some unique properties that are not present in other surfactants.*

Keywords: *surfactants, self-assemble, boundary lubrication, nanotechnology.*

1. INTRODUCTION

A contact between two surfaces is of great importance in technology. At the interface of two materials, when they are brought together, separated or moved with respect to one another, contact formation, friction, wear or lubrication are the processes that occur [1]. Friction has long been the subject of research. All machined metal surfaces, as viewed through a microscope, have their own roughness, called asperity. Therefore, two surfaces touch at an extremely small number of points, and their true area of contact is a part of their apparent contacting area. In contact of two surfaces, the number of asperities increases due to plastic deformation of some of them. The consequence of this is the appearance of the removal of material from a surface in bearing under dynamic conditions, defined as wear [2]. In order to reduce wear, lubricants are employed between the surfaces. Friction, wear and lubrication are the center of consideration in many tribological and technological problems. Having in mind that a contact occurs in numerous asperities, the research of two contact surfaces, especially at the molecular level and the friction phenomenon at the nanometer scale, is studied by nanotribology, a branch of tribology.

In order to categorize the friction properties between two surfaces, the "Stribeck curve" was developed. Machine elements may experience several lubrication regimes, including full-film, mixed, and boundary lubrication. These regimes depend on the properties of a lubricant and operating conditions. In the case where speeds are too low and loads are too high to permit establishing a hydrodynamic film, or when the distance between contact surfaces is a few nanometers or a few molecular layers, we can define boundary lubrication (fig.1).

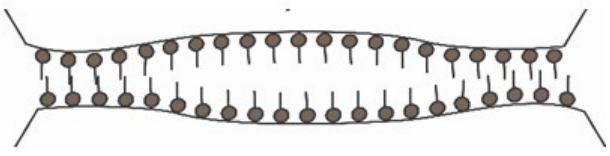

Figure 1. Boundary lubrication

The boundary films have been the subject of study for decades, since friction and wear phenomena are affected by these ultrathin films. Under friction, the dynamics of lubricants on surfaces is very important, especially the molecular behavior of lubricants in boundary lubrication. The behavior and dynamics of the boundary films,

formed during sliding, becomes more complex due to change of some experimental parameters, such as temperature [3]. The computer simulation of processes during sliding contact, when several hundreds of atoms are involved, indicates that atomic processes cannot be neglected, when we describe nanotribology experiments [1, 4]. For that purpose, several available methods can be included for research at a molecular level [5].

2. BOUNDARY LUBRICATION BY SAMS

Attractive model systems for boundary lubrication are organic self-assembled monolayers (SAMs). Preparing self-assembled monolayers is one of the most elegant ways to make ultrathin organic films of controlled thickness. The process of self-assembly is considered as a very important example of equilibrium structural organization on the molecular scale. Organic thin films are an emerging area of materials chemistry and are utilized in many application areas, such as electronic components, as well as in biomedical application [6]. There is also special interest in the possibility of manufacturing molecular layers with particular properties. Molecular self-assembly is recognized as a powerful strategy for the fabrication of nanoscale structures [7].

The interest in these systems has been further intensified in order to understand and solve friction, lubrication and related problems [8]. More recently, lubrication in a small-size system, such as the microelectromechanical system (MEMS) or nanoelectromechanical system (NEMS), is a big challenge in scientific work, especially in the study of new kind of lubricants. Different type of monolayers attached to sliding surfaces appears as a good candidate in MEMS lubrication. Therefore, the understanding of behavior between monolayers films is of great importance in tribological and nanotribological experiments.

Due to very small thickness of monolayers (range of few nanometers), new tools are required for this nanotribological studies. Widely used are the following: surface-force apparatus (SFA), the scanning tunneling miscorscope (STM), the atomic force and friction-force microscopes (AFM and FFM). Developed more than 40 years ago, the SFA is usually applied to study properties of molecularly thin films, confined between two molecularly smooth macroscopic surfaces, with surface separations at the angstrom level and forces between them. A scanning tunneling microscope (STM) is an instrument for imaging surfaces at the atomic level [1]. With the development of a number of powerful techniques in surface analysis, as mentioned above, academic interest in SAMs has regained, because of the possibilities to investigate the growth and the structure of such layers on the nanometer scale [9, 10].

3. SURFACTANTS SELF-ASSEMBLY

The word “surfactant”, does not always appear in dictionaries, because it is a contracted form of the phrase SURFace ACTive AgeNT. Surfactants are molecules essential to the chemical industry and in many products such as soaps, detergents, shampoos, softeners, pharmaceutical products, etc.

Surfactant molecules have amhiphilic properties because they consist of two distinct parts - one that has an affinity for the solvent, and the another one that does not. This dual structure is responsible for a number of remarkable phenomena, such as micelle formation in solution at a certain concentration, the so-called critical micelle concentration (cmc), and oriented adsorption of surfactants at surfaces and interfaces. Micelle formation has attracted a notable part of the surfactant research, in order to investigate the formation of micelles [11, 12], their shape [13] or their interactions [14]. Systems below the cmc have not been widely studied [15].

The self-assembled monolayers can be prepared using different types of molecules and different substrates. A very often studied SAM model system comprises thiol molecules, adsorbed onto gold, silanes on an oxide surfaces, or alkanephosphate monolayers, which was in detail reviewed by Ulman [16]. The choice of the substrates, used in the self-assembling process, is dictated by the molecules and their interactions, as well as the final application.

Self-assembled monolayers form spontaneously, when certain classes of molecules adsorb onto a solid surface from solution. When a surfactant solution is in contact with a solid surface, the surfactant molecules adsorb onto the surface, ideally forming an adsorbed layer of high order, termed as self-assembled monolayer (fig.2).

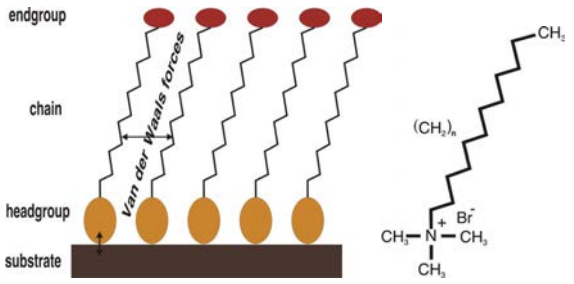

Figure 2. a) An organized monolayer on a substrate, b) CTAB chain

Many surface properties are influenced by such a film, e.g. the hydrophobicity or the wetting or

electrostatics [17]. Due to the flexibility in choosing the molecular architecture, organic molecules have many interesting applications, such as biosensors, for lubrication or in controlling water adsorption. Therefore, in recent years, much attention has been directed to the study of SAMs. However, a discrepancy still exists between the theoretical understanding and the practical importance involved in the formation of such layers.

Cationic surfactants are a small subgroup with some unique properties that are not present in other surfactants. In order to help understanding of adsorption of cationic surfactants, adsorption of quaternary ammonium surfactants onto inorganic substrates, such as mica, has been widely studied [18, 19, 20]. The process of adsorption has been investigated by different techniques [21], such as x-ray photoelectron spectroscopy (XPS), the surface forces apparatus, (SFA) [15] or contact angle (CA) measurements [22]. This paper focuses on quaternary ammonium surfactants with a cationic head group, single-tailed hexadecyltrimethylammonium bromide, CTAB, with the molecular structure $CH_3(CH_2)_{15}N^+(CH_3)_3Br^-$ (figure 2b).

4. SAMS PREPARATION AND CHARACTERIZATION

A standard protocol, which can produce a well-defined and reproducible hydrophobic CTAB film on mica, does not exist. Namely, previous studies of CTAB adsorption on various substrates, suggested that the behavior of CTAB is more complex than the behavior of other cationic surfactants [22, 23, 24], but the reason for this singularity has not been clearly determined [17].

The original goal of these experiments was to produce self-assembled monolayers and use them as model systems to study boundary lubrication. But, there was a problem concerning the results being repeated, as well as the characterization of the adsorbed CTAB layers on muscovite mica in detail. The various SAM morphologies, found on mica by the use of different adsorption protocols, demonstrate the influence of a large number of experimental parameters on the adsorption process, such as concentration, pH, temperature and humidity. They are rarely described in the literature.

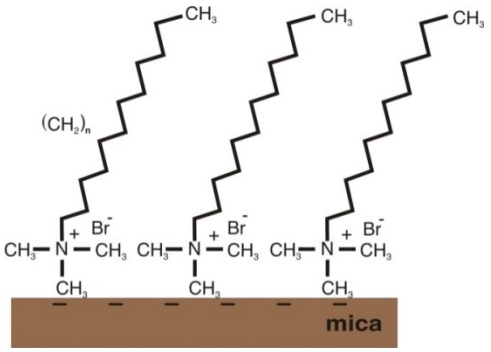

Figure 3. CTAB layer on muscovite mica

In order to characterize and determine the properties of SAMs, two techniques have been extensively used in this work, contact angle measurements and the atomic force microscopy (AFM). For example, freshly cleaved mica has contact angle less than 10° and contact angle on the SAM produced by CTAB adsorption on mica can be 140° [22]. A contact angle greater than 90° is determined on hydrophobic surfaces.

In our experiments the contact angle measurements have been used in order to define the degree of hydrophobicity of the modified mica surface and molecular order after surfactant adsorption, performed by using ultra pure water.

All contact angle measurements were averaged over several samples.

5. EXPERIMENTAL PROCEDURE

We made self-assembled monolayers of quaternary ammonium surfactants on mica. Single-tailed hexadecyltrimethylammonium bromide, CTAB, with the molecular structure $CH_3(CH_2)_{15}N^+(CH_3)_3Br^-$, was purchased from Fluka. For further purification, CTAB was recrystallized from an ethanol/acetone mixture. As a solvent, ultra pure water of resistivity 18.3MΩcm was prepared using a Barnstead EASYpure™ batch-fed water purification system. The same water quality was also used for the sample rinsing, before drying with a clean nitrogen stream.

The glassware and bottles used in the experiments were consistently cleaned by piranha solution and then rinsed with purified water to avoid any organic contamination. All the employed tools were previously cleaned in order to minimize the occurrence of molecular contamination, particularly on the high-energy mica surface.

Muscovite mica purchased from Spruce Pine Mica Company Inc. (USA) was used for the adsorption experiments. Small mica samples of 1-1.5cm^2 size, were cut by scissors. Then, they were freshly cleaved on both sides before immersion into the surfactant solution. The adsorption was

performed from the surfactant solution in a volume of 20ml.

In our first adsorption series without temperature control, a 1000ml stock solution of 10^{-2}M (~10cmc) CTAB was prepared at room temperature. Since the solubility of CTAB in water was low at room temperature, the solution was heated to 30-35°C. By dilution of this solution, prepared by adding the appropriate volume of ultra pure water, surfactant solution concentrations ranging from 10^{-3}M (~cmc) to 10^{-6}M (~cmc/1000) have been prepared. One option, called "CTAB in/CTAB out"(figure 4), involves immersion and extraction from the surfactant solution at the nominal concentration. In the water dipping step, the mica samples were dipped for 30sec into 20ml of ultra pure water to remove the excess solution and excess surfactant molecules.

After the post-rinsing step, the modified mica surface was gently blown dry with nitrogen, before the AFM imaging or contact angle measurements. This type of protocol (at different concentrations) was repeated several times to also assess the reproducibility.

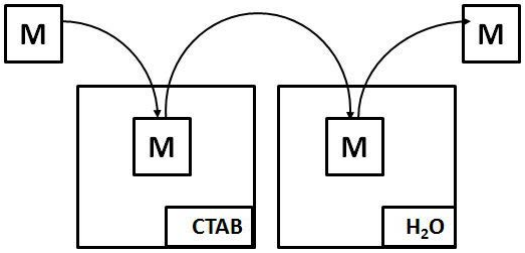

Figure 4. ″CTAB in CTAB out″ experiment

6. RESULTS OBTAINED WITHOUT TEMPERATURE CONTROL

The first two sets of experiments were realized without temperature control, in March and June 2003.

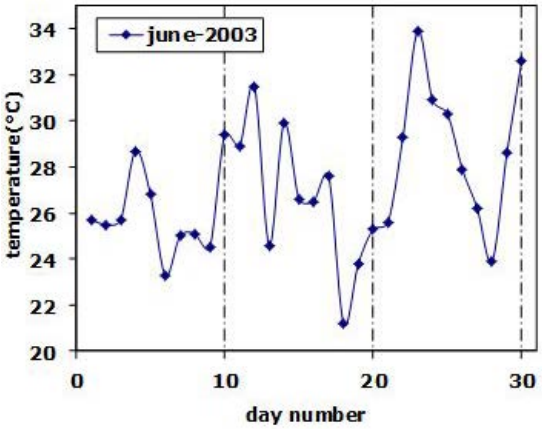

Figure 5. Local temperature recorded in June 2003 (measured at 12:40 PM in Zürich-SwissMeteo data)

During the first experiments in March, the room temperature was in the range 21±2°C, and a few months later, in June, the conditions in the laboratory were clearly different, 32±2°C. As documented by the air temperature measured outside of our building, shown in figure 5, the temperature during the summer 2003 has been much higher than in spring. In several experiments the temperature was more than 30°C.

Using the above described preparation protocols a significant number of samples have been prepared. The AFM images of two representative samples obtained by the ″CTAB in/CTAB out″ protocol at a concentration below the cmc are shown in figure 6. The AFM results observed at all solution concentrations below the cmc (from 10^{-4}M to 10^{-6}M), are very similar with the results presented in figure 6.

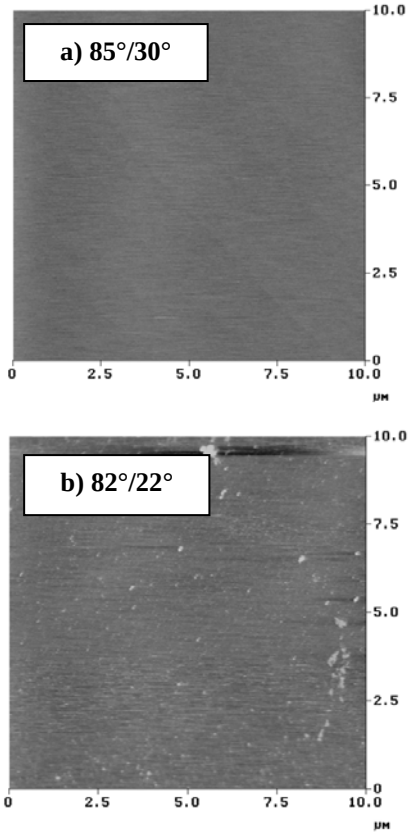

Figure 6. AFM images of CTAB on mica obtained with the "CTAB in/CTAB out" protocol at a concentration of 10^{-4}M. Advancing and receding water contact angles are also shown:
a) in March 2003 and b) in June 2003

A clear seasonal influence on SAMs adsorption has been observed in all experiments realized without temperature control, regardless of the experimental protocols. On the sample prepared in June, where the air temperature outside of the laboratory building was higher than in March (figure 5), a significant number of clusters of height between 0.5nm to 3.8nm and the size around

250nm size have been observed, according to the grey scale of the image, which represents a height range of 5nm (cf. Figure 6.b). The sample prepared in March, shown in figure 6.a, is more promising.

The advancing and receding water contact angle were measured on both samples exhibit hysteresis. Without temperature control, the reproducibility of those surfactant films was difficult to accomplish. Therefore, it was difficult to identify the most promising protocol for us.

We have performed a significant number of experiments at 10^{-2}M CTAB (i.e.10xcmc) solutions by the protocol "CTAB in/CTAB out", which nicely document the crucial role of the temperature. The results are summarized in figure 7.

Figure 7.a is representative of the sample prepared at 27°C and is qualitatively different from the samples prepared at the lower temperatures. The bright spots observed in figure 7.b represent small islands on mica with a height between 0.5-1.3nm. In figure 7.c we detect clusters of a height in order of 23nm.

7. DISCUSSION

Our adsorption results have shown that the morphology, the structure and the stability of the adsorbed films are sensitive to the experimental conditions, primarily temperature.

One very important concept of surfactant solution is the Krafft temperature, whose effect is of great importance in SAMs formation. The Krafft temperature is the minimum temperature at which surfactants form micelles. Below the Krafft temperature micelles cannot form. The Krafft temperature is a point of phase change below which the surfactant remains in crystalline form, even in aqueous solution (figure 8). Around the Krafft temperature, Tk, many physical properties of the surfactant solution reflect this transition. The transition in CTAB solution around Tk clearly occurs over a range of temperatures. Although the Krafft temperature is a well-established concept, reported values of Tk for CTAB in water vary considerably, from 20°C [17] to 25°C [14]. Krafft temperatures, close to room temperature, significantly complicate the explanation of experimental results.

According to the AFM images, the sample obtained in March 2003 (figure 6.a) revealed a homogeneous CTAB film, in contrast to the sample performed in June (figure 6.b). The reason for such a difference must be related to changes in the solution structure.

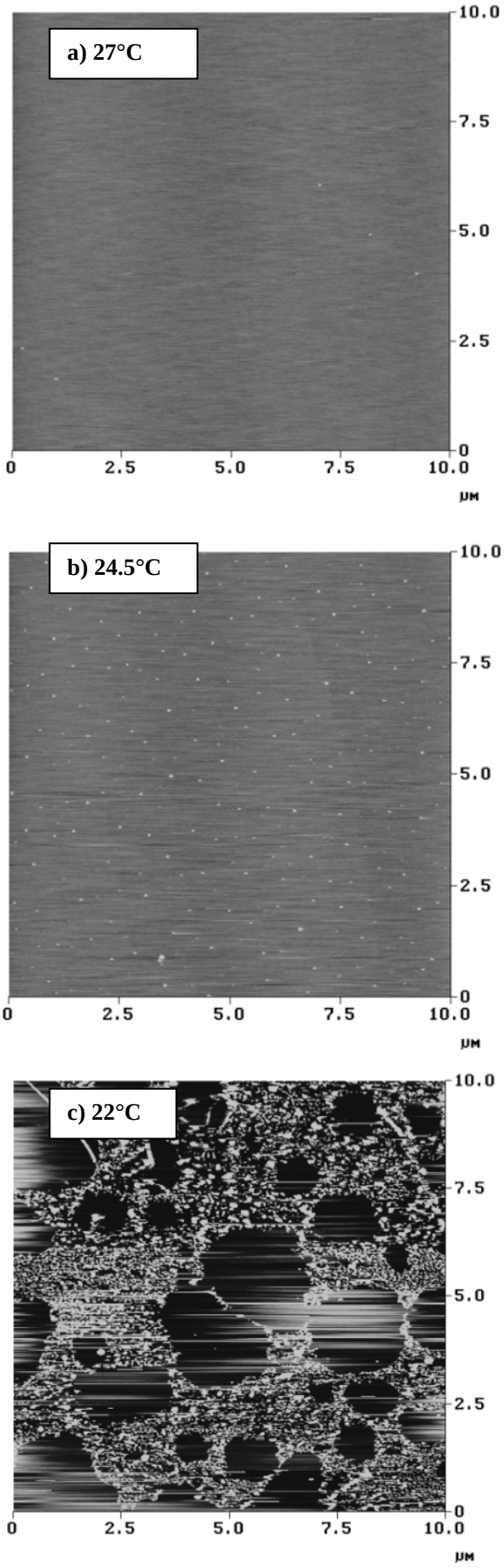

Figure 7. Series of AFM images showing the surface morphology of CTAB coated mica by the protocol "CTAB in/CTAB out" at 10^{-2}M solution at temperatures: a) 27°C, b) 24.5°C and c) 22°C.

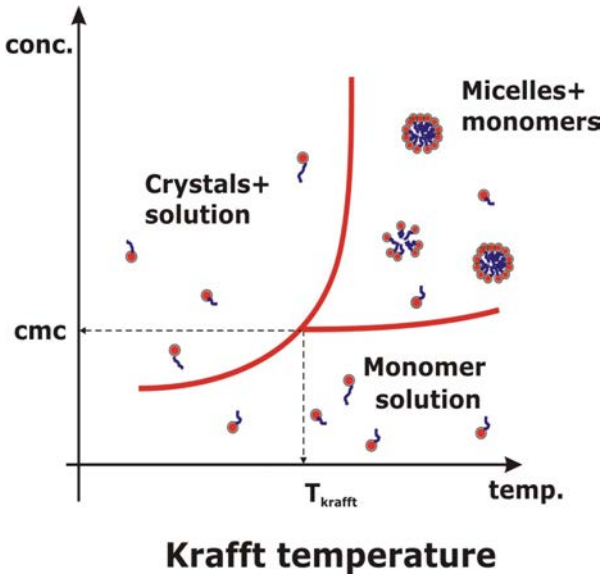

Figure 8. The structural changes in the CTAB solution in the performed experiments, such as heating/cooling cycle of solution (marked as hysteresis) and the dilution of the solution, both above the cmc

Namely, solution used in the both experiments (10^{-4}M) has been prepared by dilution of a 10^{-2}M stock solution. The room temperature in March (21±2°C) was slightly below the Krafft temperature of CTAB and we could expect that this stock solution mainly consisted of monomers. The same argument applies, of course, also to the diluted solution (10^{-4}M).

In June, however, a significant daily temperature variation, with temperatures clearly above the Krafft temperature, has been recorded, particularly in the days before the described adsorption experiment. It is to be expected that the solution structure of the stock solution is metastable and complex. The diluted solution may thus not be in thermodynamic equilibrium and consists of micelles and monomers. The clusters seen on the sample prepared under such conditions (figure 7.b) can be interpreted as micelle, adsorbed in different shapes and sizes.

The results shown in figures 6 and 7 clearly demonstrate the temperature influence on the surfactant films, morphology formed in different seasons of 2003. The variety of adsorbed film morphologies in uncontrolled conditions above the cmc can also be explained by structural changes in the stock solution. Namely, warming up the highly concentrated stock solution (10^{-2}M) to some 30°C (above the Krafft temperature) will result in the formation of micelles. Since the film shown in figure 7.b. has been adsorbed at a temperature of 24.5°C, which is near the Krafft temperature, we might expect the presence of some aggregates in the solution and also on the mica surface. Some of the micelles are expected to transform into surface-layers. The repetition of the same experiment one day later, at a room temperature of 22°C, reveals a substantially different SAM as shown in figure 7.c. Upon cooling of micellar CTAB solution from the initial value ~30°C to 22°C, the solution then consists of crystals, monomers and micelles. As a consequence of such structural changes in the solution, the complex morphology (figure 7.c) is not surprising. A distinction between monolayer or bilayer formation is not readily possible from AFM images above (figure 7). The applied test, not described here, on the samples in several experiments, suggested bilayer formation even at concentration 10^{-4}M.

8. CONCLUSION

The performed experiments describe the adsorption of quaternary ammonium surfactants onto anionic, atomically smooth, muscovite mica. The surfactant films on mica, formed according to described experimental protocols, were characterized by contact angle measurements and by AFM. We have observed that SAMs can have completely different properties, depending on the meteorological conditions, influenced by temperature. These results suggested that temperature can influence all steps in adsorption procedure, from solution preparation to the rinsing step. The fact that the Krafft temperature range of CTAB (~25°) is around room temperature, makes this system appear particularly complex.

The dynamic CA experiments and AFM measurements have shown that the exact protocol of solution and self-assembled monolayer (SAM) preparation can substantially influence the stability of the hydrophobic layer, as well as the hydrophobicity. The results indicate that the morphology and the homogeneity of SAMs depend on many parameters, and the main reason for that is probably the molecular structure of the solution, controlled by the temperature and concentration of the solution.

In this model case of quaternary ammonium surfactants, the formation of homogeneous, well-ordered and reproducible monolayers is a very challenging task. In order to assess such complex systems, systematic variation of a great number of parameters was a necessary procedure.

ACKNOWLEDGEMENTS

The author would like to gratefully acknowledge the support in obtaining and understanding the presented results provided by her mentors, Nicholas D. Spencer and Manfred Heuberger, members of the Laboratory for Surface Science and Technology (LSST), a part of the Department of Materials at the

ETH Zurich, Switzerland, where all the experiments were performed.

REFERENCES

[1] B. Bhushan, J. N. Israelachvili, and U. Landman: *Nanotribology:friction, wear and lubrication at the atomic scale*, Nature 374, pp. 607-616, 1995.

[2] NASA: *Lubrication, friction and wear*, 1971.

[3] Choa Sung-H. et al.: *A model of the dynamics of boundary film formation, Wear 177*, pp. 33-45, 1994.

[4] B. Bhushan: *Nanotribology and Nanomechanica II*, Springer, New Tork, 2011.

[5] K. Miyake, et al.: *Effects of surface chemical properties on the frictional properties of self-assembled monolayers lubricated with oleic acid*, Tribology Online 7, pp. 218-224, 2012.

[6] J. e. a. Swollen: *Molecular Monolayers and Films*, Langmuir 3, pp. 932-950, 1987.

[7] J. a. M. Mellott: *Supercritical self-assembled monolayer growth*, Journal of the American Chemical Society 126, pp. 9369-9373, 2004.

[8] M. K. Chaudhury: *Adhesion and friction of self-assembled organic monolayers*, Current opinion in colloid & interface science 2, pp. 65-69, 1997.

[9] R. o. M. S. Carpick: *Fundamental investigations of tribology with atomic force microscopy*, Chemical Reviews 97, pp. 1163-1194, 1997.

[10] D. K. Schwartz: *Mechanisms and kinetics of self-assembled monolayer formation*, Annual Review of Physical Chemistry, Vol.52, pp. 107-137, 2001.

[11] J. Oremusova et al.: *Thermodynamics of micellization of hexadecylpyridinium bromide in aqueous and alcoholic (C-1-C-4) solutions*, Collection of Czechoslovak Chemical Communications 65, pp. 1419-1437, 2000.

[12] K. K. Ghosh: *Thermodynamics of micelle formation of some cationic surfactants as a function of temperature and solvents*, Indian Journal of Chemistry, Sec. B. 37B, pp. 875-880, 1998.

[13] K.Boschkova et al.: *Lubrication in aqueous solutions using cationic surfactants - a study of static and dynamic forces*, Langmuir 18, pp. 1680-1687, 2002.

[14] PS. Goyal, VK Aswal: *Micellar structure and inter-micelle interactions in micellar solutions: Results of small angle neutron scattering studies*, Current Science 80, pp. 972-979, 2001.

[15] Y. a. J. I. N. Chen: *Effects of Ambient Conditions on Adsorbed Surfactant and Polymer Monolayers*, Journal of Physical Chemistry 96, pp. 7752-7760, 1992.

[16] A. Ulman: *An introduction to ultrathin organic films: from Langmuir-Blodgett to self assembly*, ed. Academic Press, Boston, 1991.

[17] I.Grosse, K.Estel: *Thin surfactant layers at the solid interface*, Colloid and Polymer Science 278, pp. 1000-1006, 2000.

[18] F. Zhao et al.: *Adsorption behavior of hexadecyltrimethylammonium bromida (CTAB) to mica substrates as observed by atomic force microscopy*, Science in China Ser. B Chemistry 48, pp. 101-106, 2005.

[19] S.Perkin et al.: *Stability of self-assembled hydrophobic surfactant layers in water*, Journal of Physical Chemistry B 109, pp. 3832-3837, 2005.

[20] JM Mellott et al.: *Kinetics of octadecyltrimethylammonium bromide self-assembled monolayer growth at mica from an aqueous solution*, Langmuir 20, pp. 2341-2348, 2004.

[21] B.Y. Li et al.: *Time dependent anchoring of adsorbed cationic surfactant molecules at mice/solution interface*, Journal of Colloid and Interface Science 209, pp. 25-30, 1999.

[22] Sharma,B.G. et al.: *Characterization of adsorbed ionic surfactants on a mica substrate*, Langmuir 12, pp. 6506-6512, 1996.

[23] W.A.Ducker and Erica J. Wanless: *Adsorption of hexadecyltrimethylammonium bromide to mica: Nanometer-scale study of binding-site competition effects*, Langmuir 15, pp. 160-168, 1999.

[24] S. Manne, H. Gaub: *Molecular-Organization of Surfactants at Solid-Liquid Interfaces*, Science 270, pp. 1480-1482, 1995.

Serbian Tribology Society

SERBIATRIB '13

13th International Conference on Tribology

Faculty of Engineering in Kragujevac

Kragujevac, Serbia, 15 – 17 May 2013

INFLUENCE OF RICE HUSK ASH – SILICON CARBIDE WEIGHT RATIOS ON THE MECHANICAL BEHAVIOUR OF AL-MG-SI ALLOY MATRIX HYBRID COMPOSITES

K. K. Alaneme[1], T. M. Adewale[1,2]

[1]*Department of Metallurgical and Materials Engineering Federal University of Technology, Akure, Nigeria, kkalaneme@gmail.com*

[2]*Faculty of Engineering and Physical Sciences, School of Materials, University of Manchester, Manchester, United Kingdom*

Abstract: *The influence of rice husk ash (RHA) and silicon carbide (SiC) weight ratio on the mechanical behaviour of Al-Mg-Si alloy matrix hybrid composites was investigated. RHA and SiC mixed in weight ratios 0:1, 1:3, 1:1, 3:1, and 1:0 were utilized to prepare 5, 7.5 and 10 wt% of the reinforcing phase with Al-Mg-Si alloy as matrix using two-step stir casting method. Density measurement, estimated percent porosity, tensile properties, fracture toughness, and SEM examination were used to characterize the composites produced. The results show that the composites were of good casting quality as the estimated porosity values were less than 2.5 % in all grades produced. For the three weight percent worked on, the tensile-, yield-, and specific strength decreases with increase in the weight proportion of RHA in the RHA-SiC reinforcement. However, the results show that the composites with composition of 1:3 weight ratio RHA:SiC (25% RHA: 75% SiC) offers comparable specific strength values with the single SiC reinforced Al composite grades. The strain to fractures was invariant to the weight ratio of RHA/SiC for all weight percent but the composite compositions containing RHA had improved fracture toughness compared with the single SiC reinforced Al composite grades.*

Keywords: *Aluminium matrix composites, rice husk ash, mechanical properties, scan electron microscopy, stir casting, silicon carbide.*

1. INTRODUCTION

Alternative sources of reinforcements that offer the potential of producing Aluminium matrix composites (AMCs) at reduced cost while maintaining high performance levels is attracting interests from researchers [1-2]. Compared to other engineering materials, AMCs are noted for the rare combination of properties they offer such as high specific strength and stiffness, good wear and corrosion resistance, low thermal coefficient of expansion, good high temperature mechanical properties, and excellent thermal management potentials among others [3-5]. Aluminium based matrices also have the advantage that they are the cheapest among other competing matrix materials (Copper, Titanium, Magnesium) for metal matrix composites (MMCs) development; and also are amenable to processing using techniques conventionally suited for the production of metals and alloys [6,7].

The unique properties of AMCs are derived from the material characteristics of both the matrix and the reinforcing phases [8]. The reinforcements are responsible for the improved mechanical, wear, and high temperature properties of the AMCs [9-10]. Thus the type of reinforcement and reinforcement parameters such as size, volume fraction, distribution, shape, and orientation often affect significantly the properties of AMCs [11]. The use of cheaper source of reinforcements such as industrial wastes (fly ash, red mud) [12-13] and agro wastes (rice husk ash, bamboo leaf ash, coconut shell ash) [14-15] for AMCs development is gaining popularity considering its advantage in solid waste recycling which has been a cause for major concern over the years. Additional to the advantages of low cost, availability in large quantities, and contributions to creation of a more eco-friendly environment; is lower densities which most of the agro and industrial wastes possess in

comparison with the synthetic reinforcements such as silicon carbide (SiC) and alumina (Al_2O_3) [16]. The properties achieved with the sole utilization of these cheaper source reinforcements have been reported to be lower than that of the synthetic reinforced but with promise for use in semi-structural and thermal management applications [17]. The use of hybrid reinforcements utilizing SiC/Al_2O_3 and agro waste ashes as a means of improving the properties of AMCs has attracted interest recently with very encouraging results obtained [18-19].

The present work is aimed at investigating the influence of the weight ratios of rice husk ash and silicon carbide on the mechanical behaviour Aluminium matrix hybrid composites having varied weight percent of both reinforcements. The motivation for this work is to establish optimum RHA/SiC weight ratios required to achieve optimized performance of low cost AMCs developed with the use of rice husk. Literatures on the use of synthetic/agrowaste hybrid reinforcements for AMCs development are still very limited and there is currently none that the authors are aware of that discusses the use of RHA and SiC as hybrid composites in Al-Mg-Si alloy matrix.

2. MATERIALS AND METHOD

2.1 Materials

Al-Mg-Si alloy billets with chemical composition determined using spark spectrometric analysis (Table 1) was selected as Aluminium matrix for this investigation.

Table 1. Elemental composition of Al-Mg-Si alloy.

Element	wt%
Si	0.4002
Fe	0.2201
Cu	0.008
Mn	0.0109
Mg	0.3961
Cr	0.0302
Zn	0.0202
Ti	0.0125
Ni	0.0101
Sn	0.0021
Pb	0.0011
Ca	0.0015
Cd	0.0003
Na	0.0009
V	0.0027
Al	98.88

For the hybrid reinforcing phases, silicon carbide (SiC) and rice husk ash (RHA) were selected. The silicon carbide procured was of high chemical purity with average particle size of 28µm while rice husks utilized for the processing of rice husk ash was obtained from Igbemo-Ekiti, Ekiti State (a rice producing community in south western Nigeria). Magnesium for improving wettability between the Al-Mg-Si alloy and the reinforcements was also procured.

2.2 Preparation of Rice Husk Ash

The procedure adopted is in accordance with Alaneme et al [16]. It involves the use of a simple metallic drum with perforations as burner for the rice husk. Dry rice husks placed inside the drum was ignited with the use of charcoal. The husk was allowed to burn completely and the ashes removed 24 hours later. The ash was then heat-treated at a temperature of 650^{o}C for 180 minutes to reduce its carbonaceous and volatile constituents. Sieving of the bamboo leaf ash was then performed using a sieve shaker to obtain ashes with mesh size under 50µm. The chemical composition of the rice husk ash from this process is presented in Table 2.

Table 2. Chemical Composition of the Rice Husk Ash

Compound/Element (constituent)	weight Percent
Silica (SiO_2)	91.59
Carbon, C	4.8
Calcium oxide CaO	1.58
Magnesium oxide, MgO	0.53
Potassium oxide, K_2O	0.39
Haematite, Fe_2O_3	0.21
Sodium, Na	trace
Titanium oxide, TiO_2	0.20

2.3 Composites Production

Two step stir casting process was utilized to produce the composites [20]. The process started with the determination of the quantities of rice husk ash (RHA) and silicon carbide (SiC) required to produce 5, 7.5, and 10 wt% reinforcement consisting of RHA and SiC in weight ratios 0:1, 1:3, 1:1, 3:1, and 1:0 respectively (which amounts to 0, 25, 50, 75, and 100% RHA in the reinforcement phase). The rice husk ash and silicon carbide particles were initially preheated separately at a temperature of 250^{o}C to eliminate dampness and improve wettability with the molten Al-Mg-Si alloy. The Al-Mg-Si alloy billets were charged into a gas-fired crucible furnace (fitted with a temperature probe), and heated to a temperature of 750^{o}C ± 30^{o}C (above the liquidus temperature of the alloy) to ensure the alloy melts completely. The liquid alloy was then cooled in the furnace to a semi solid state at a temperature of about 600^{o}C. The preheated rice husk ash and SiC particles along with 0.1 wt% magnesium were then charged into

the semi-solid melt at this temperature (600^{o}C) and stirring of the slurry was performed manually for 5-10 minutes. The composite slurry was then superheated to 800^{o}C± 50^{o}C and a second stirring performed using a mechanical stirrer. The stirring operation was performed at a speed of 400rpm for 10minutes before casting into prepared sand moulds inserted with chills. The designations used to represent each grade of the composites produced are presented in Table 3.

Table 3. Composite Density and Estimated Percent Porosity.

Sample Designation	Composition RHA: SiC	Theoretical density (g/cm^3)	Experimental density (g/cm^3)	% Porosity
A0	0 wt%	2.700	2.655	1.67
	5wt%			
B1	A (0:1)	2.721	2.700	0.77
B2	B (1:3)	2.691	2.650	1.52
B3	C (1:1)	2.660	2.640	0.75
B4	D (3:1)	2.630	2.590	1.52
B5	E (1:0)	2.599	2.579	0.77
	7.5 wt%			
C1	A (0:1)	2.733	2.670	2.31
C2	B (1:3)	2.689	2.640	1.82
C3	C (1:1)	2.640	2.590	1.89
C4	D (3:1)	2.595	2.570	0.96
C5	E (1:0)	2.550	2.510	1.57
	10 wt%			
D1	A (0:1)	2.743	2.690	1.9
D2	B (1:3)	2.680	2.650	1.11
D3	C (1:1)	2.620	2.610	0.3
D4	D (3:1)	2.560	2.50	2.34
D5	E (1:0)	2.500	2.497	0.12

2.4 Density Measurement

The experimental density of each grade of composite produced was determined by dividing the measured weight of a test sample by its measured volume; while the theoretical density was evaluated by using the formula:

$$\rho_{Al\text{-}Mg\text{-}Si\ /\ RHA\text{-}SiCp} = wt._{Al\text{-}Mg\text{-}Si} \times \rho_{Al\text{-}Mg\text{-}Si} + wt._{RHA} \times \rho_{RHA} + wt._{SiC} \times \rho_{SiC} \quad (2.1)$$

where, $\rho_{Al\text{-}Mg\text{-}Si\ /\ RHA\text{-}SiCp}$ = Density of Composite, $wt._{Al\text{-}Mg\text{-}Si}$ = Weight fraction of Al-Mg-Si alloy, $\rho_{Al\text{-}Mg\text{-}Si}$ = Density of Al-Mg-Si alloy, $wt._{RHA}$ = Weight fraction RHA, ρ_{RHA} = Density of RHA, $wt._{SiC}$ = Weight fraction SiC, and ρ_{SiC} = Density of SiC.

The experimental densities were compared with the theoretical densities for each composition of the RHA-SiC reinforced composites produced; and it served as basis for evaluation of the percent porosity of the composites using the relations [20]:

$$\% \text{ porosity} = \{(\rho_T - \rho_{EX}) \div \rho_T\} \times 100\% \quad (2.2)$$

Where, ρ_T = Theoretical Density (g/cm^3), ρ_{EX} = Experimental Density (g/cm^3).

2.5 Tensile Properties

The tensile properties of the composites was evaluated with the aid of tensile tests performed following the specifications of ASTM 8M-91 standards [21]. The samples for the test were machined to round specimen configuration with 6 mm diameter and 30 mm gauge length. The test was carried out at room temperature using an Instron universal testing machine operated at a strain rate of 10^{-3}/s. Three repeat tests were performed for each grade of composite produced to guarantee repeatability and reliability of the data generated. The tensile properties evaluated from the stress-strain curves developed from the tension test are - the ultimate tensile strength (σ_u), the 0.2% offset yield strength (σ_y), and the strain to fracture (ε_f).

2.6 Fracture Toughness Evaluation

The fracture toughness of the composites was evaluated using circumferential notch tensile (CNT) specimens [22]. Samples for the CNT testing were machined having gauge length, specimen diameter (D), notch diameter (d), and notch angle of 30, 6, 4.5mm, and 60^{o} respectively. The specimens were then subjected to tensile loading to fracture using an Instron universal testing machine. The fracture load (P_f) obtained from the load – extension plots generated from the CNT testing were used to evaluate the fracture toughness using the empirical relations by Dieter [23]:

$$K_{1C} = P_f/(D)^{3/2}[1.72(D/d) - 1.27] \quad (2.3)$$

where, D and d are respectively the specimen diameter and the diameter of the notched section. The validity of the fracture toughness values obtained was determined using the relations in accordance with Nath and Das [24]:

$$D \geq (K_{1C}/\sigma_y)^2 \quad (2.4)$$

Three repeat tests were performed for each composite composition and the results obtained were taken to be highly consistent if the difference between measured values for a given composite composition is not more than 2%.

2.7 Microstructural Examination

A JSM 7600F Jeol ultra-high resolution field emission gun scanning electron microscope (FEG-SEM) equipped with an EDS was used for detailed microstructural study and for determination of the elemental compositions of the composites.

3. RESULTS AND DISCUSSION

3.1 Microstructure

Figure 1 shows some representative SEM micrographs of the RHA - SiC reinforced AMCs produced. It is observed that there is a good dispersion of the RHA and SiC particulates in the Al alloy matrix and little particle clusters are observed. Thus there is no significant problem of segregation or sedimentation which often occurs during solidification of MMCs having components with different densities and wettability characteristics [25].

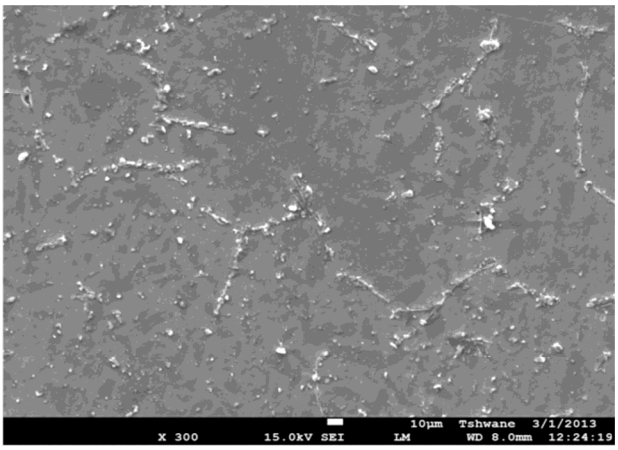

(a)

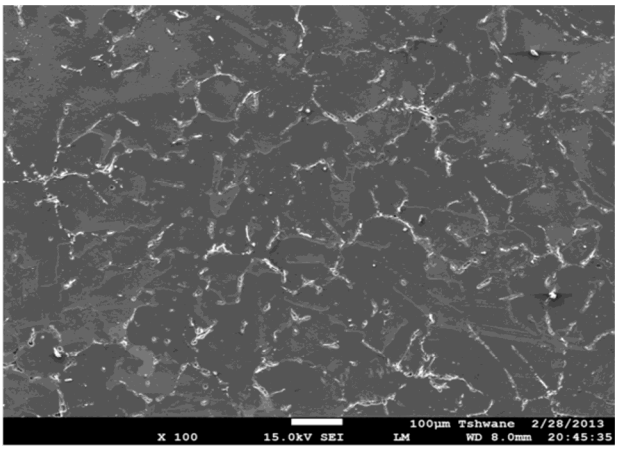

(b)

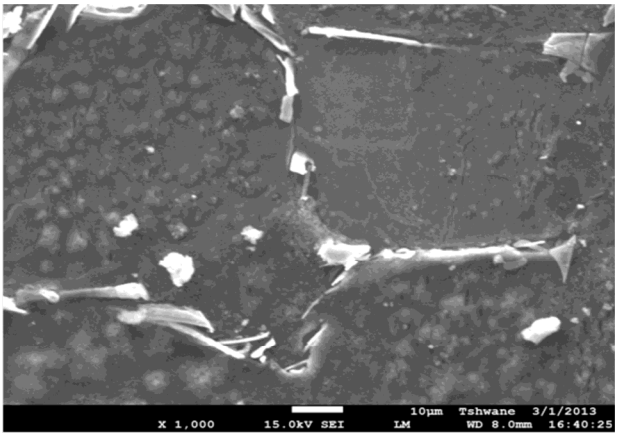

(c)

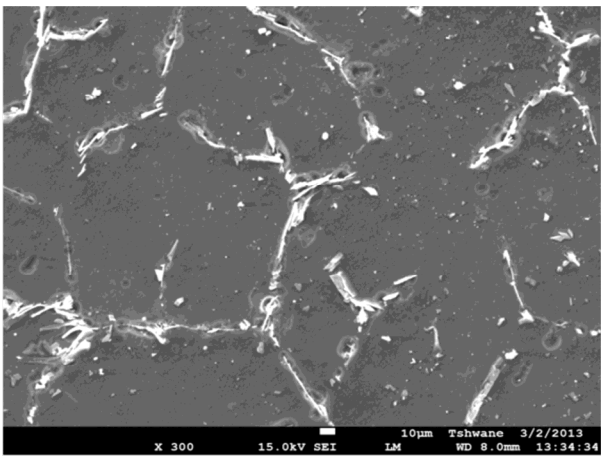

(d)

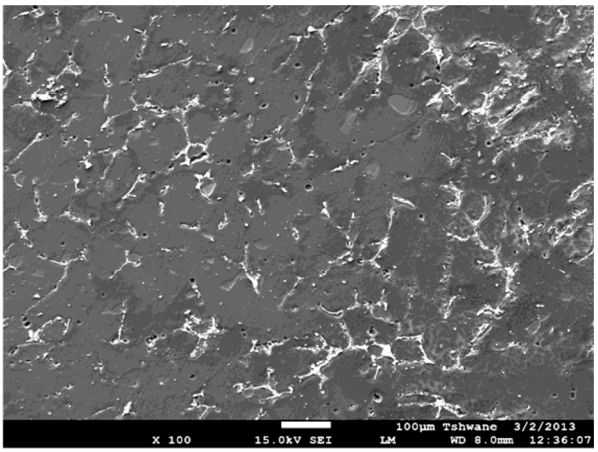

(e)

Figure 1. showing (a) SE image of the Al-Mg-Si/5 wt% SiC composite showing the SiC particles dispersed in the Al-Mg-Si matrix; (b) SE image of the 5 wt% hybrid reinforced Al-Mg-Si/RHA-SiC composite having RHA:SiC weight ratio of 1:3; (c) SE image of the 7.5 wt% hybrid reinforced Al-Mg-Si/RHA-SiC composite having RHA:SiC weight ratio of 1:3; (d) SE image of the 10 wt% hybrid reinforced Al-Mg-Si/RHA-SiC composite having RHA:SiC weight ratio of 1:3; and(e) SE image of the Al-Mg-Si/10 wt% RHA composite showing the RHA particles dispersed in the Al-Mg-Si matrix.

This shows that the two step stir casting process adopted for the production of the composites is reliable judging from the microstructures examined in Figure 1.

The EDS profiles of the particulates in the composites produced, some of which are presented in Figures 2 and 3; show peaks of aluminium (Al), oxygen (O), carbon (C), iron (Fe), silicon (Si), calcium (Ca), sodium (Na) and magnesium (Mg). The presence of these elements confirm the presence of SiC; as well as silica (SiO_2), alumina (Al_2O_3), Potassium oxide (K_2O), ferric oxide (Fe_2O_3), and Magnesium oxide (MgO) which are constituents derived from the rice husk ash (Table 2).

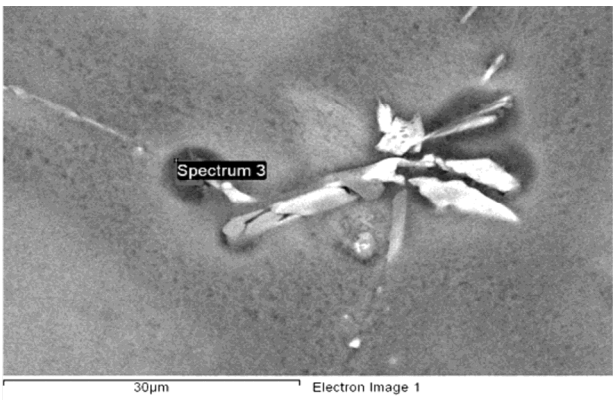

(a)

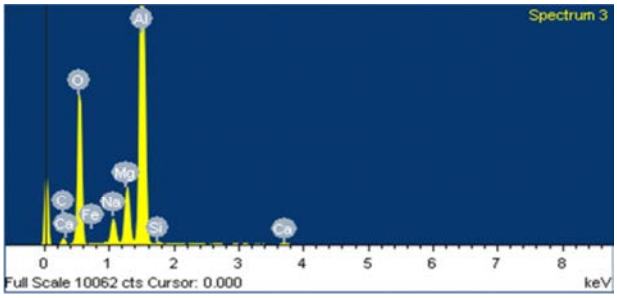

(b)

Figure 2. Showing (a) representative SE Photomicrograph showing the reinforcing particles dispersed in the Al-Mg-Si matrix; and (b) EDS profile of the particle in 2(a) confirming the presence of Al_2O_3, SiO_2, Fe_2O_3, K_2O, CaO, SiC and Na.

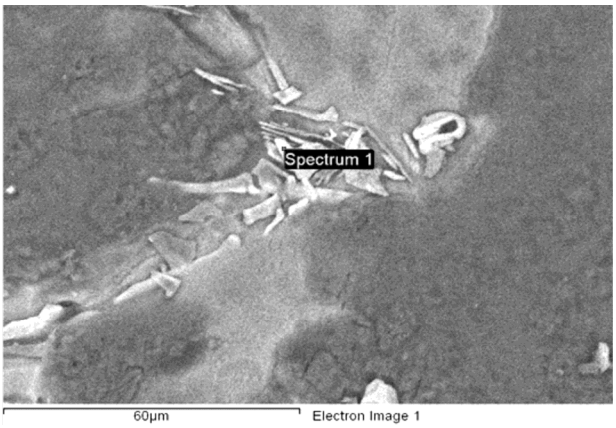

(a)

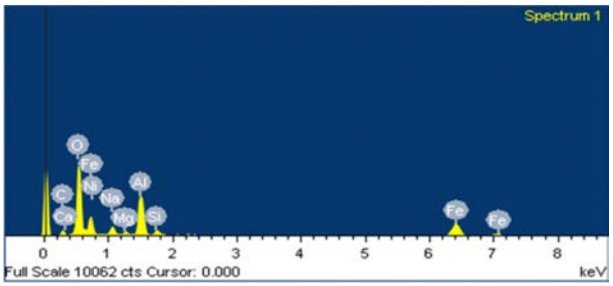

(b)

Figure 3. Showing (a) representative SE Photomicrograph of some clustered particles dispersed in the Al-Mg-Si matrix; and (b): EDS profile the particles identified in 3(a) confirming the presence of Al_2O_3, SiO_2, Fe_2O_3, SiC, Cao, and Na which are constituents from the RHA-SiC hybrid reinforcement.

3.2 Composite Density and Estimated Percent Porosity

The results of the composite densities and estimated percent porosity are presented in Table 3. It is observed from the results that the estimated porosity values are not dependent on the weight percent of the reinforcement phase or the weight ratio of RHA to SiC. It is however noted that the estimated porosity levels are less than 4 % which has been reported to be the maximum permissible in cast AMCs [26]. The low porosity levels of the composites supports our submission that the two step stir casting method adopted for producing the composites is reliable. As a result of the lower density of RHA (0.31 g/cm^3) in comparison to SiC (3.6 g/cm^3), it is expected that the density of the composites will reduce with increase in the RHA content in the composite as observed from Table 3.

3.3 Mechanical Behaviour

The variation of tensile strength and yield strength of the composites produced is presented in Figure 4. It is observed that there is a general increase in tensile strength (Figure 4a) and yield strength (Figure 4b) with increase in weight percent of the RHA-SiC hybrid reinforcement. However, for specific weight percents of the hybrid composites (that is B, C, and D series), it is noted that the tensile and yield strength decreases with increase in the weight proportion of RHA in the RHA-SiC reinforcement. For the composites containing 5 wt% of the reinforcing phase, it is observed that 4.9, 8.9, 12.5, and 15.8 % reduction in tensile strength was obtained from the composites with weight ratio RHA:SiC of 1:3, 1:1, 3:1, and 1:0 (that is containing 25, 50, 75, and 100 % RHA) in comparison to the 5 wt% SiC single reinforced Al matrix composite. For the composites containing 7.5 wt% of the reinforcing phase, reductions of 5, 9, 13.4, and 19 % were observed for the compositions of 1:3, 1:1, 3:1, 1:0 RHA:SiC weight ratios respectively (in comparison with the 7.5 wt% SiC single reinforced composite). In the case of the composites containing 10 wt% reinforcements, reductions of 4, 8.1, 13.2, and 18.3 % was observed in comparison to the 10 wt % SiC single reinforced Al matrix composite.

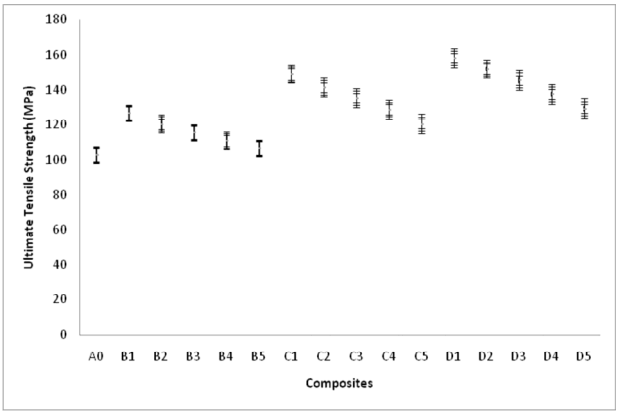

(a)

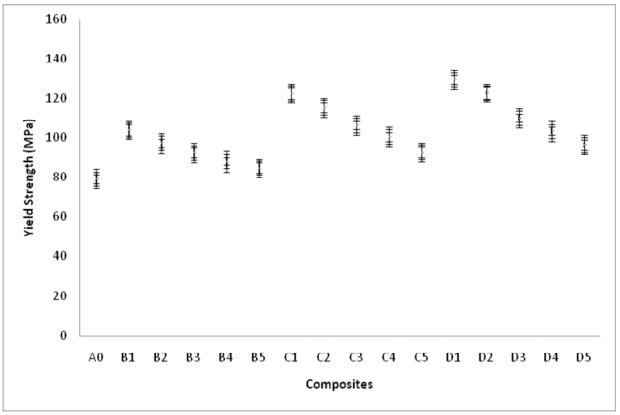

(b)

Figure 4. Showing (a) variation of tensile strength for the monolithic Al-Mg-Si alloy, single reinforced and hybrid reinforced Al-Mg-Si/RHA-SiC composites; and (b) variation of yield strength for the monolithic Al-Mg-Si alloy, single reinforced and hybrid reinforced Al-Mg-Si/RHA-SiC composites.

It has been well reported that particle reinforced AMCs achieve improved strength due to load transfer from the matrix to the particles (direct strengthening) and creation of more dislocations which serve as constraints to plastic deformation by thermal mismatch between the particles and the Aluminium matrix arising from their differences in coefficient of thermal expansion (indirect strengthening) [27-28]. Thus even in a scenario where the particles are not sufficiently strong to induce strengthening via the 'direct route' of load transfer from matrix to particles, the indirect strengthening it could offer is adequate to induce some strength improvements well and above that of the monolithic alloy. In the present case under investigation, the reduction in strength observed with increase in the RHA content of the composites is as a result of the decrease of the direct strengthening capacity of RHA which contains predominantly silica. Silica is noted to be a softer ceramic with elastic modulus of 60-70 GPa, which is within the range of Aluminium unlike SiC which has an elastic modulus of 400GPa. Thus the efficiency of load transfer from the Al matrix to the particles (load carrying capacity) of the hybrid particulates will be dependent on the amount of SiC than RHA. However, it should be noted that samples B5, C5, and D5 which contain only RHA, show a progressive increase in tensile strength and yield strength with the increased weight percent of RHA supporting our hypothesis that the indirect strengthening mechanism (which entails dislocation generation results in higher dislocation densities with increased weight percent of the particles) can result in modest improvement in strength with increase in the weight percent of the reinforcing particles.

The variation of the specific strength of the composites produced with weight ratio of RHA/SiC is presented in Figure 5. It is observed that the specific strengths of the composites generally increased with increase in the weight percent of the reinforcing phase (that is RHA-SiC weight percent). Also the specific strength values decreases with increase in the RHA content in the hybrid reinforcement. However, the % decrease in specific strength of the composites is generally lower in comparison with that of the ultimate tensile strength analyzed earlier. For the 5 wt% compositions, it is observed that 3.1, 6.8, 8.75, and 11.9 % reduction in specific strength is obtained. For the 7.5 wt % compositions (grades) 3.93, 6.2, 10 and 13.9 % reductions were obtained. In the case of the 10 wt% grade, 2.6, 5.3, 6.54, and 11.9 % reductions were obtained. The results show that the composites with composition of 1:3 weight ratio RHA:SiC (25% RHA: 75% SiC) can offer comparable specific strength values at reduced cost of production of the composite since its difference is less than 4 % for the three weight percents of reinforcement worked on.

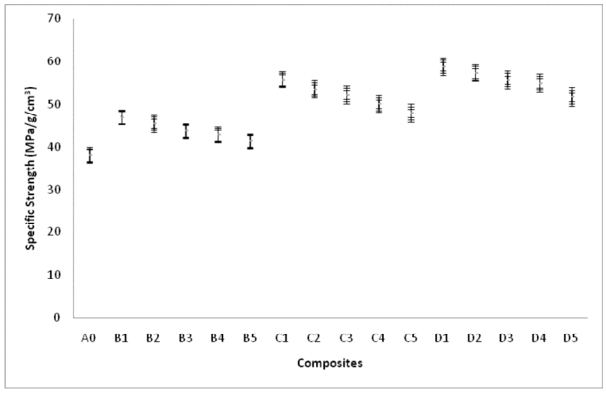

Figure 5. Variation of specific strength for the monolithic Al-Mg-Si alloy, single reinforced and hybrid reinforced Al-Mg-Si/RHA-SiC composites.

The results of the variation of strain to fracture of the composites with weight percent reinforcement and weight ratio RHA/SiC is presented in Figure 6. It is observed that there is a general decrease in ductility of the composites with increase in the weight percent of reinforcing phase

in the composites. Closer observation show that for each weight percent of hybrid composites produced, the strain to fracture was invariant to the weight ratio of RHA/SiC. It can be inferred from the results that the ductility levels of the hybrid composites is not compromised by the addition of RHA in the hybrid compositions. Thus its capacity to sustain plastic strain without fracture is not impelled by the addition of RHA.

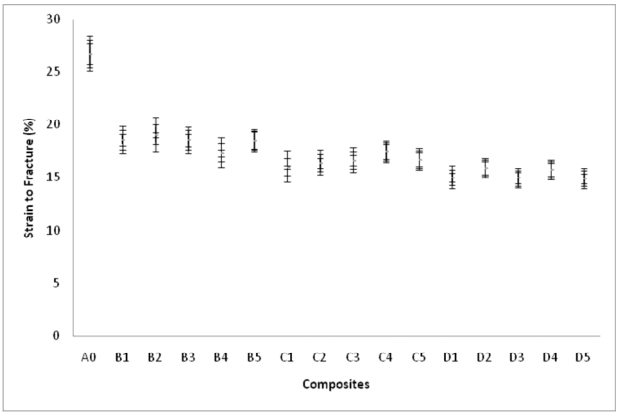

Figure 6. Variation of strain to fracture for the monolithic Al-Mg-Si alloy, single reinforced and hybrid reinforced Al-Mg-Si/RHA-SiC composites.

The fracture toughness values determined by the use of circumferential notched tensile (CNT) specimens are presented in Figure 7. The values obtained were reported as plain strain fracture toughness because the conditions for valid K_{1C} (plain strain condition) was met with the specimen diameter of 6mm when the relation $D \geq (K_{1C}/\sigma_y)^2$ [24] was utilised to validate the results obtained from the CNT testing. It is observed that the fracture toughness decreases with increase in the weight percent of the composites. But for specific weight percents of the composites (that is B, C, and D series) it is observed that the composite compositions containing RHA had improved fracture toughness results compared with the single SiC reinforced grades of the composites. Thus the addition of RHA appears to be beneficial in terms of improving the resistance to crack propagation of the composites making them slightly less susceptible to sudden crack failure in comparison with the single reinforced SiC composite grades. The mechanism of fracture in particle reinforced Al matrix composites have been reported by several authors [29-30]. The primary mechanisms of fracture have been reported to be facilitated by one or a combination of particle cracking, interfacial cracking or particle debonding [31]. In the present case, the improved fracture toughness of the composites containing RHA, is most likely due to the reduced amount of relatively harder and brittle SiC particles in the composites [19]. The SiC particles like most hard and brittle ceramic particles have a higher tendency to undergo rapid crack propagation [32].

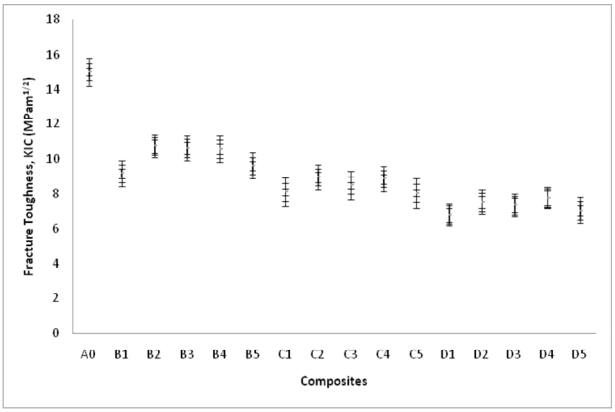

Figure 7. Variation of Fracture Toughness for the monolithic Al-Mg-Si alloy, single reinforced and hybrid reinforced Al-Mg-Si/RHA-SiC composites.

4. CONCLUSIONS

The mechanical behaviour of Al-Mg-Si alloy matrix composites containing 5, 7.5, and 10 weight percent of RHA and SiC reinforcements prepared in weight ratios 0:1, 1:3, 1:1, 3:1, and 1:0 respectively was investigated. The results show that:

1. The estimated porosity values are not dependent on the weight percent of the reinforcement phase or the weight ratio of RHA to SiC. They were however less than 2.5 % in all grades produced.
2. There is a general increase in tensile strength, and yield strength with increase in weight percent of the RHA-SiC hybrid reinforcement. However, the tensile and yield strength decreases with increase in the weight proportion of RHA in the RHA-SiC reinforcement.
3. The specific strength followed the same trend as the tensile and yield strengths; however, the % decrease in specific strength of the composites is generally lower in comparison with that of the ultimate tensile strength. The composites with composition of 1:3 weight ratio RHA to SiC (25% RHA: 75% SiC) offers comparable specific strength values with the SiC single reinforced grades of the composite.
4. There is a general decrease in ductility of the composites with increase in the weight percent of reinforcing phase in the composites. However, the strain to fracture was invariant to the weight ratio of RHA/SiC.
5. The fracture toughness decreases with increase in the weight percent of the

composites. But the composite compositions containing RHA had improved fracture toughness compared with the single SiC reinforced grades.

ACKNOWLEDGEMENT

The electron microscopy assistance rendered by Dr. P. A. Olubambi of the Department of Chemical and Metallurgical Engineering, Tshwane University of Technology, South Africa is appreciated.

REFERENCES

[1] S.D. Prasad, R.A. Krishna: *Production and Mechanical Properties of A356.2 /RHA Composites,* International Journal of Advanced Science and Technology, Vol. 33, pp. 51-58, 2011.

[2] H. Zuhailawati, P. Samayamutthirian, C.H. Mohd Haizu: *Fabrication of Low Cost Aluminium Matrix Composite Reinforced with Silica Sand*, Journal of Physical Science, Vol. 18, No. 1, pp. 47-55, 2007.

[3] T.V. Christy, N. Murugan, S. Kumar: *A comparative study on the microstructures and mechanical properties of Al 6061 alloy and the MMC Al 6061/TiB2/12p*, Journal of Minerals and Materials Characterization and Engineering, Vol. 9, No. 1, pp. 57-65, 2010.

[4] P.K. Rohatgi, B.F. Schultz, A. Daoud, W.W. Zhang: *Tribological performance of A206 aluminum alloy containing silica sand particles,* Tribol Int, Vol. 43, pp. 455–66, 2010.

[5] K.K. Alaneme, M. O. Bodunrin: *Corrosion behaviour of alumina reinforced Al (6063) metal matrix composites*, Journal of Minerals and Materials Characterisation and Engineering, Vol. 10, No. 2, pp. 1153-1165, 2011.

[6] P. Rohatgi, B. Schultz: *Light weight metal matrix composites – stretching the boundaries of metals*, Materials Matters, Vol. 2, pp. 16-19, 2007.

[7] D.B. Miracle: *Metal matrix composites - from science to technological significance*, Composites Science and Technology, Vol. 65, No. 15/16, pp. 2526-2540, 2005.

[8] K.K. Alaneme: *Influence of Thermo-mechanical Treatment on the Tensile Behaviour and CNT evaluated Fracture Toughness of Borax premixed SiCp reinforced Aluminium (6063) Composites*, International Journal of Mechanical and Materials Engineering, Vol. 7, No. 1, pp. 96-100, 2012.

[9] T. Senthilvelan, S. Gopalakannan, S. Vishnuvarthan, K. Keerthivaran: *Fabrication and Characterization of SiC, Al_2O_3 and B_4C Reinforced Al-Zn-Mg-Cu Alloy (AA 7075) Metal Matrix Composites: A Study*, Advanced Materials Research, Vol. 622-623, pp. 1295-1299, 2012.

[10] S.A. Sajjadi, H.R. Ezatpour, H. Beygi: *Microstructure and mechanical properties of Al–Al_2O_3 micro and nano composites fabricated by stir casting*. Materials Science and Engineering A, Vol. 528, pp. 8765-8771, 2011.

[11] S. Tahamtan, A. Halvaee, M. Emamy, M.S Zabihi: *Fabrication of Al/A206-Al_2O_3 nano/micro composite by combining ball milling and stir casting technology,* Materials and Design 2013, DOI: http://dx.doi.org/10.1016/j.matdes.2013.01.032.

[12] P. Naresh: *Development and characterization of metal matrix composite using red Mud an industrial waste for wear resistant applications,* PhD Thesis, Department of Mechanical Engineering, National Institute of Technology Rourkela, India, 23 – 34, 2006.

[13] J. Bienia, M. Walczak, B. Surowska B, J. Sobczaka: *Microstructure and corrosion behaviour of aluminium fly ash composites*, Journal of Optoelectronics and Advanced Materials, Vol. 5, No. 2, pp. 493-502, 2003.

[14] P.B. Madakson, D.S. Yawas, A. Apasi: *Characterization of Coconut Shell Ash for Potential Utilization in Metal Matrix Composites for Automotive Applications*, International Journal of Engineering Science and Technology (IJEST), Vol. 4, No. 3, pp. 1190-1198, 2012.

[15] S.D. Prasad, R.A. Krishna: *Tribological Properties of A356.2/RHA Composites*, Journal of Materials Science and Technology, Vol. 28, No. 4, pp. 367-372, 2012.

[16] K.K. Alaneme, I.B. Akintunde, P.A. Olubambi, T.M. Adewale: *Mechanical Behaviour of Rice Husk Ash – Alumina Hybrid Reinforced Aluminium Based Matrix Composites,* Journal of Materials Research and Technology, Vol. 2, No. 1, pp. 60-67, 2013.

[17] R. Escalera-Lozano, C. Gutierrez, M.A. Pech-Canul, M.I. Pech-Canul: *Degradation of Al/SiCp Composites produced with Rice-Hull Ash and Aluminium Cans*, Waste Management, Vol. 28, pp. 389-395, 2008.

[18] K.K. Alaneme, P.A. Olubambi: *Corrosion and Wear Behaviour of Rice Husk Ash – Alumina Reinforced Aluminium Matrix Hybrid Composites,* Journal of Materials Research and Technology, 2013 (In Press).

[19] K.K. Alaneme, E.O. Adewuyi: *Mechanical Behaviour of Bamboo Leaf Ash – Alumina Hybrid Reinforced Aluminium Based Matrix Composites,* Metallurgical and Materials Engineering, Serbia, 2013 (In Press).

[20] K.K. Alaneme, A.O. Aluko: *Production and age-hardening behaviour of borax pre-mixed SiC reinforced Al-Mg-Si alloy composites developed by double stir casting technique,* The West Indian Journal of Engineering, Vol. 34, No. 1/2, pp. 80-85, 2012.

[21] ASTM E 8M: *Standard Test Method for Tension Testing of Metallic Materials (Metric)*, Annual Book of ASTM Standards, Philadelphia; 1991.

[22] K.K. Alaneme: *Fracture toughness (K_{1C}) evaluation for dual phase low alloy steels using circumferential notched tensile (CNT) specimens,* Materials Research, Vol. 14, No. 2, pp. 155-160, 2011.

[23] G.E. Dieter: Mechanical Metallurgy, McGraw-Hill, Singapore; 1988.

[24] S.K. Nath, U.K. Das: *Effect of microstructure and notches on the fracture toughness of medium carbon steel,* Journal of Naval Architecture and Marine Engineering, Vol. 3, pp. 15-22, 2006.

[25] B.F. Schultz, J.B. Ferguson, P.K. Rohatgi: *Microstructure and hardness of Al_2O_3 nanoparticle reinforced Al–Mg composites fabricated by reactive wetting and stir mixing,* Materials Science and Engineering A, Vol. 530, pp. 87-97, 2011.

[26] M. Kok: *Production and mechanical properties of Al_2O_3 particle reinforced 2024 aluminium composites,* Journal of Materials Processing Technology, Vol. 16, pp. 381-387, 2005.

[27] K.K. Alaneme KK, A.O. Aluko: *Fracture Toughness (K1C) and Tensile Properties of As-Cast and Age-Hardened Aluminium (6063) – Silicon Carbide Particulate Composites,* Scientia Iranica, Transactions A: Civil Engineering (Elsevier), Vol. 19, No. 4, pp. 992-996, 2012.

[28] N. Chawla, Y. Shen: *Mechanical behaviour of particle reinforced metal matrix composites,* Advanced Engineering Materials, Vol. 3, No. 6, pp. 357-370, 2001.

[29] M.T. Milan, P. Bowen: *Tensile and fracture toughness properties of SiCp reinforced Al alloys: Effects of particle size, particle volume fraction and matrix strength,* Journal of Materials Engineering and Performance, Vol. 13, No. 6, pp. 775-783, 2004.

[30] M.M. Ranjbaran: *Low fracture toughness in Al 7191-20% SiCp aluminium matrix composite,* European Journal of Scientific Research, Vol. 41, No. 2, pp. 261-272, 2010.

[31] K.K. Alaneme: *Mechanical Behaviour of Cold Deformed and Solution Heat-treated Alumina Reinforced AA 6063 Composites,* The West Indian Journal of Engineering, Vol. 35, No. 2, pp. 31-35, 2013.

[32] Fracture Mechanics of Ceramics, Vol. 13 – Crack-Microstructure Interaction, R – Curve Behaviour, Editors (Bradt RC, Munz D, Sakai M, Schevchenko V Ya, White KW, Springer, First Edition, pp. 538, 2002.

Serbian Tribology Society

SERBIATRIB '13

13th International Conference on Tribology

Faculty of Engineering in Kragujevac

Kragujevac, Serbia, 15 – 17 May 2013

TRIBOLOGICAL PROPERTIES OF NANOMETRIC ATOMIC LAYER DEPOSITIONS APPLIED ON AISI 420 STAINLESS STEEL

E. Marin[1], A.Lanzutti[1],L.Fedrizzi[1]

[1] University of Udine, Department of Chemistry, Physics and Environment, Via del Cotonificio 108, 33100 Udine Italy, elia.marin@uniud.it

Abstract: *Atomic Layer Deposition (ALD) is a modern technique that allows to deposit nanometric, conformal coatings on almost any kind of substrate, from plastics to ceramic, metals or even composites. ALD coatings are not dependent on the morphology of the substrate and are only regulated by the composition of the precursors, the chamber temperature and the number of cycles.*

In this work, mono- and bi-layer nanometric, protective low-temperature ALD coatings, based on Al2O3 and TiO2, were applied on AISI 420 Stainless Steel in order to enhance its relatively low corrosion resistance in chloride containing environments. Tribological testing were also performed on the ALD coated AISI 420 in order to evaluate the wear and scratch resistance of these nanometric layers and thus evaluate their durability.

Scratch tests were performed using a standard Rockwell C indenter, under a variable load condition, in order to evaluate the critical loading condition for each coating. Wear testing were performed using a stainless steel counterpart, in ball-on-disc configuration, in order to measure the friction coefficient and to confront the wear resistance. All scratch tests scars and wear tracks were then observed by means of Scanning Electron Microscopy (SEM) in order to understand the wear mechanisms that occurred on the sample surfaces.

Corrosion testing, performed under immersion in 0.2 M NaCl solutions, clearly showed that the ALD coatings have a strong effect in protecting the Stainless Steel substrate against corrosion, reducing the corrosion current density by two orders of magnitude.

The preliminary tribological results showed that ALD depositions obtained at low temperatures have a brittle behavior caused by the amorphous nature of their structure, and thus undergo delamination phenomena during Scratch Testing at relatively low applied loads. During ball-on-disc testing, the coatings were removed from the substrate, in particular for monolayer ALD configurations, which seem to have a lower toughness when compared to bi-layer configurations..

Keywords: *Atomic Layer Deposition, Al_2O_3, TiO_2, wear, AISI 420, Stainless Steel, Scratch Test, Ball-on-disc*

1. INTRODUCTION

Martensitic stainless steels are widely used for a wide range of applications, mainly due to their balanced properties, as they couple relatively microhardness, mechanical resistance and corrosion resistance in many aggressive environments [1]. For these reasons, martensitic stainless steels are nowadays applied for: knife blades [2], oil and gas [3], offshore platforms [4], turbine blades [5], components subject to abrasive wear at relatively high temperature or aggressive environments [6].

Even so, stainless steels could show insufficient corrosion resistance in strongly aggressive media containing Cl^- and S^{2-} ions, at high temperature or very high / low pH values [7]. For these reasons, in particular circumstances Stainless Steels may need a further improvement of corrosion protection. Conventional treatments, such as painting, are

hardly applicable to Stainless Steel due to adhesion problems between paint and the metal substrate [8].

A great number of innovative treatments are nowadays under intensive study to improve Stainless Steel corrosion resistance, such as plasma detonation techniques [9], arc-ion plating [10], sol-gel deposition [11], chemical conversion layers of cerium [12] chromium [13] or other elements, Chemical Vapor Deposition [14], High-Velocity Oxy-fuel Spray (HVOF) [15], plasma-nitriding [16], and Atomic Layer Deposition [17]. All these techniques may also be applied in order to improve the tribological resistance of the substrate, as they grant higher hardness and wear abrasion when compared to stainless steel or other common metallic alloys [18-20].

The modern concept of ALD is an extension of the ALE (Atomic Layer Epitaxy), patented by Prof. Suntola [21]. Suntola's studies were mainly focused on switching effects in chalcogenide nanometric films for solid state electronic devices [22][23][24], and lately extended to a wide range of amorphous semi-conductive thin films [25]. ALD (as ALE) process involves a sequence of self-limiting surface reactions. As evidenced in 1980 by Ahonen et al. [26], the self-limiting characteristic of each reaction step differentiates ALE and ALD from other chemical vapor deposition technolnologies. In ALD each deposition cycle is clearly divided in four steps: in the first step a precursor is injected in the deposition chamber. The precursor is chosen so that its molecules will not react with each other at the deposition temperature. In ideal situations, a single monolayer is thus formed as a result of the reaction with the substrate. In the second step, the chamber is purged with nitrogen or argon gas in order to remove the excess of reactant and prevent "parasitic" CVD deposition on the substrate, which will eventually occur if two different precursors are present in the deposition chamber at the same time. In the third step, the second precursor is injected in the chamber. In the case of metal oxide layers, this is an oxidant agent, usually simple H_2O. The last step of the deposition cycle is a second purge to remove the excess of reactant with purging gas. Closed-loop repetitions of the four basic steps theoretically allow obtaining perfectly conformal deposits of any desired thickness. By avoiding the contact between the precursors throughout the whole coating process, a film growth at atomic layer control, with a thickness control within ~ 10 pm, can be obtained.

Interest in ALD has increased stepwise in the mid-1990's and 2000's, with the interest focused on silicon-based microelectronics [27]. Up to the present time, ALD processes have been used to deposit several types of nanometric films, including several chemical compounds (e.g. AsGa, CdSe,…), metal oxides (e.g. Al_2O_3, CaO, CuO, Er_2O_3, Ga_2O_3, HfO_2, La_2O_3, MgO, Nb_2O_5, Sc_2O_3, SiO2, Ta_2O_5, TiO_2, Y_2O_3, Yb_2O_3, ZnO, ZrO_2), nitrides (e.g. TiN, TaN, AlN, GaN, WN, NbN), sulfides (e.g. SrS, ZnS), carbides (e.g. TaC, TiC), fluorides (e.g. CaF2, LaF_3, MgF_2), pure metals (e.g. Ru, Ir, Ta, Pt), biomaterials (e.g. hydroxyapatite ($Ca_{10}(PO_4)_6(OH)_2$)) and even polymers (e.g. Polyimides) [28,29].

Results on the corrosion protection on stainless steel by ALD TiO_2 and Al_2O_3 layers were already obtained by Matero et al. (1999)[29], which supposed that the conformal ALD coatings could improve the corrosion resistance of different metal alloys. In 2007, Shan et al. [30] used TiO2 ALD layers to protect an undefined stainless steel, obtaining only a limited effect. In 2011, Marin et al. [31], Diaz et al. [17] and Potts et al. [32] clearly showed that the residual porosity of ALD layers decreases increasing the thickness of the layer thus improving the protection of the substrate. In most cases [31,17,32, 33] the nanometric ALD layers clearly showed a corrosion protection similar, if not superior to conventional protective technolniques and thicker coatings, even if common industrial tests (salt spray) performed on Plasma Enhanced ALD by Potts et al. [32] clearly showed a time-limited corrosion protection.

In this work, characterization of ALD coated AISI 316 L has been carried out, in order to determine the possible use of nanometric ceramic ALD coatings for the corrosion and tribological protection of stainless steel.

2. EXPERIMENTAL

2.1 Samples production

Discs of standard AISI 420 martensitic stainless steel (chemical composition wt.%: C = 0.035; P < 0.04; S < 0.03; Mn = 2.0; Si = 0.75; Cr = 16.0 – 18.0; Ni = 10.0 – 15.0; Mo = 2.0 – 3.0) were obtained by machining and cutting of bars. The discs were then grinded using SiC abrasive paper in order to obtain a surface roughness of about 100 nm Ra, which was considered to be suitable for testing, in particular in the case of Glow Discharge Optical Emission Spectrometry (GDOES) analyses and wear. Samples surface was then cleaned using ethanol in ultrasonic bath for 10 minutes and dried in a dry heat sterilizer at a temperature of 80° C for 15 minutes. Some samples were then partially masked with heat resistant laboratory tape to prevent ALD deposition on part of the substrate, thus creating a clear and sharp interface between

coated and uncoated region after adhesive tape removal.

The ALD coating was deposited using a TFS 500 reactor (Beneq Oy, Finland): Al_2O_3 layers were obtained using trimethylaluminium ($Al(CH_3)_3$) and H2O precursors and TiO_2 layers were obtained using titanium tetrachloride ($TiCl_4$) and H_2O precursors. Both depositions were performed at a temperature of 120 °C. The low temperature processes were chosen in order to obtain an amorphous structure for both layers. The number of precursor cycles for each deposition was calculated using a growth rate per cycle (GPC) of ~0.1 nm/cycle for TiO_2 and a GPC of ~0.15 nm/cycle for Al_2O_3.

The samples were coated using different ALD configurations, with an overall coating thickness of about 200 nm.

2.2 Morphology

Morphological characterization was carried out using Veeco's Digital Instrument's Nanoscope IIIa atomic force microscope (AFM) in tapping mode configuration, using a Bruker SCM-PIT tip (Antimony (n) doped Si, frequency: 60-100 kHz, elastic constant: 1-5 N/m, PtIr coated) and Carl Zeiss EVO-40 scanning electron microscope (SEM) with an operating voltage of 20 kV. Analyses were performed on the stainless steel substrate and on coated samples. In particular, SEM was used in order to scan the surface of the sample and investigate the presence of deposition defects and/or surface anomalies. AFM was mainly used to investigate the presence of surface morphological defects on the coating that were supposed to be hardly visible using SEM due to the coating transparency. AFM was also used at the interface regions between coated and uncoated substrate after adhesive tape removal in order to obtain information about the overall thickness of the deposits and confront it with the theoretical deposition rates values and the results obtained from GDOES analyses.

2.3 Composition

In-depth compositional analyses were carried out using Horiba Yobin-Yvon's RF – GD Profiler GDOES. Due to the difficulties in calibration of GDOES for the analysis of Titanium and Aluminum oxides, only qualitative compositional analyses were performed, even if a keen calibration was performed in order to obtain reliable single layer thickness values. GDOES technolnique is strongly influenced by surface roughness, which was relatively high.

2.4 Mechanical properties

In order to evaluate the resistance to delamination of the different ALD configurations, Vickers indentations were applied to the samples under different load conditions (HV0.1-0.2-0.5-1.0-2.0) and the delaminated areas have been then measured using a specific image post-processing software (Wayne Rasband, ImageJ 1.44p). As all indentation hardness tests, Vickers indentation are dependant from the mechanical characteristics of the substrate and can only be used to compare different coatings applied on the same substrate and not results from different substrates. As adhesion is strictly connected to the surface roughness [33-35], Vickers adhesion tests will give reliable results only for substrates with similar surface finishing.

2.5 Electrochemical properties

Electrochemical characterization of the different samples was performed using Potendiodynamic Polarizations. An AUTOLAB PGSTAT-20 potentiostat was used in a standard three electrodes configuration. The reference electrode was Ag/AgCl and the counter electrode was a 99.99% pure Platinum wire. All measurements have been performed in a pH 6.5, 0.2 M solution of NaCl. All polarization curves were obtained using a scan speed of 0.2 mV/s after 10 minutes of immersion of the samples, in order to stabilize the OCP. The potential has been increased from -200 mV respect to the OCP to a measured current density of about 10-3 A/cm^2.

2.6 Wear properties

Wear properties were investigated using an industrial CETR UMT tribometer in ball-on-disc configuration, using a WC counter-material. Wear testing was performed for 1, 10 and 100 cycles under dry conditions, at a relatively low rotating speed (1 rps) and at different diameters (15 mm, 18 mm, 21 mm). After testing, the wear tracks were observed using SEM and the volume losses were then estimated using a stylus profilometer.

3. EXPERIMENTAL RESULTS

3.1 Morphology

SEM resulted to be an inadequate technique for the analysis of ALD layers, since no morphological differences were found between images obtained on coated and uncoated regions and no morphological properties of the ALD layers could be correctly

resolved using this technique, even at relatively high magnifications, such as 20k or 50k.

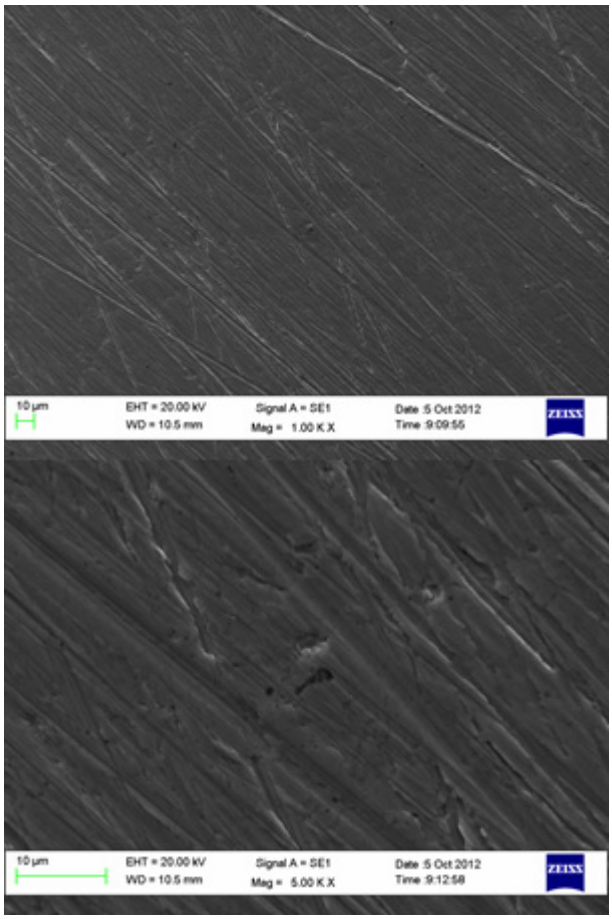

Figure 1: SEM images of Al2O3 coated sample obtained at 1000 (a) and 5000 (b) magnifications

Fig. 1 shows the SEM image obtained on the Al_2O_3 coated samples, at relatively "low" (fig. 1a) and "high" (fig. 1b) magnifications. It is only possible to discriminate the presence of scars and scratches caused by the cutting and grinding of the stainless steel substrates, while no information about the presence of the ALD layer could be obtained from these images.

Similar results were obtained in the case of the Al_2O_3/TiO_2 coated samples, at relatively "low" (fig. 2a) and "high" (fig. 2b) mangifications. It can be observed that, even for this sample, only scars and scratches caused by the mechanical cutting and grinding of the sample can be observed.

AFM observations gave similar results, with only scratches and scars clearly visible on the morphological maps obtained. In the case of the maps obtained at the interface between coating and substrate, they were successfully used in order to estimate the overall coating thickness of the different ALD layers (fig. 3).

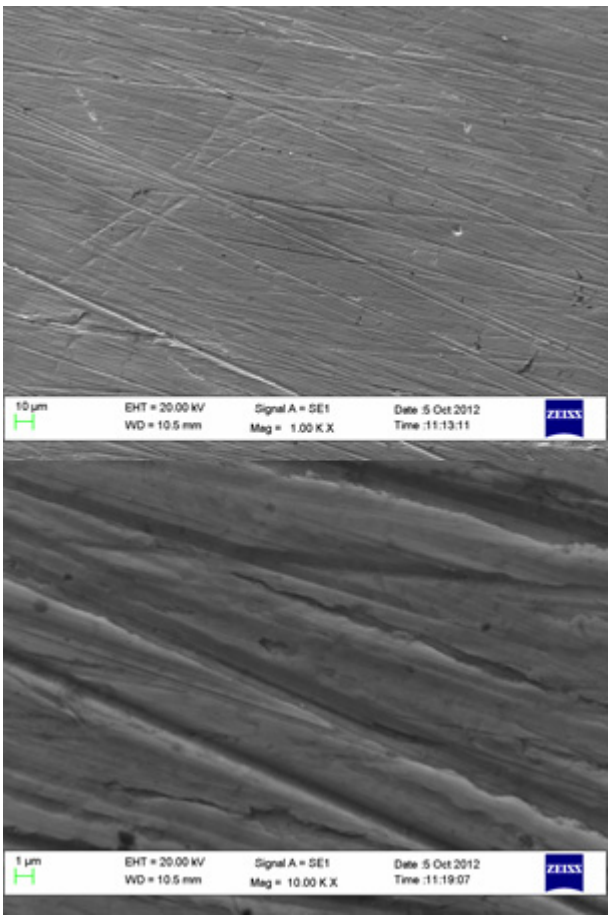

Figure 2: SEM images of Al2O3 coated sample obtained at 1000 (a) and 5000 (b) magnifications

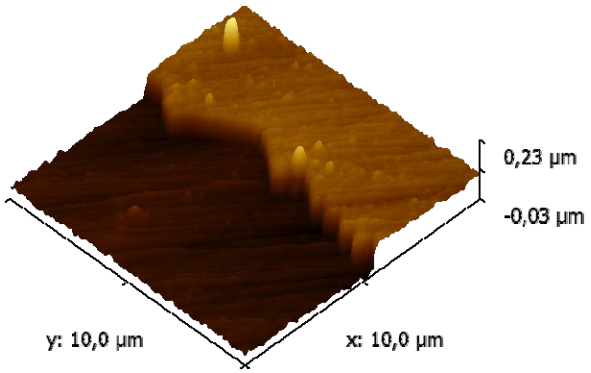

Figure 3: AFM image obtained at the interface between coated and uncoated areas of the Al_2O_3 coated sample.

The results obtained are resumed in Table 1:

Table 1: Coating thickness as obtained by AFM measurements

Coating	Thickness
	µm
Al2O3	102± 3
Al2O3/TiO2	107 ± 5

3.2 Composition

GDOES thickness measurement accuracy was strongly influenced by the sharpness of the interface region between coating and substrate. Conventionally, in this work the coating thickness

has been measured between the top surface and the intersection point between oxygen and iron signals. Since no reference materials were present for amorphous ceramics, a specific GDOES calibration was required. Sputtered crater's depth was measured using a stylus profilometer and the sputtering rate has been evaluated accordingly. Following this calibration GDOES results shall be considered semi-quantitative and for this reason the composition of the coatings and in particular of Al2O3 layers is not stoichiometric.

Fig. 4 shows the results obtained by GDOES on the Al_2O_3 coated sample.

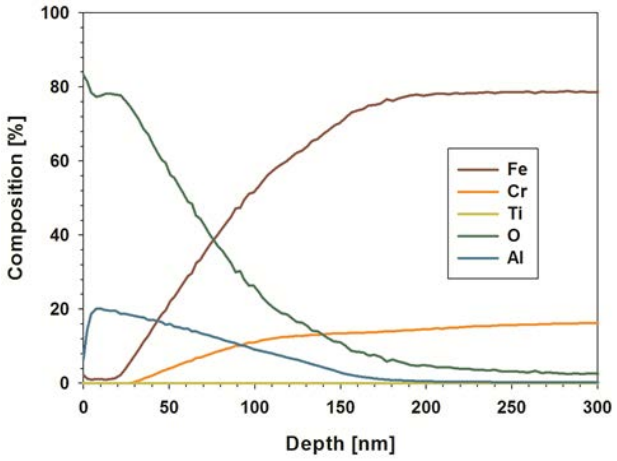

Figure 4: GDOES graph obtained for the Al2O3 coated sample. Signals of Iron, Chromium, Titanium, Oxygen and Aluminum

It can be observed that the interface between coating and substrate is not sharp. This is caused by the relatively high surface roughness obtained after the sample preparation. The iron signal, which is considered representative for the substrate, reaches a plateau at about 200 nm, which is influenced by both coating thickness and surface roughness, meaning that, after 200 nm, only substrate signals can be seen by GDOES. At about 75 nm, the two signals of Iron and Oxygen are even, while at the surface, both Oxygen and Aluminium show a peak. This behaviour is caused by the substrate roughness, which causes a strong signal overlap. For this reason, coating thickness could not be correctly estimated using GDOES, but only the thickness range could be determined. Surface peak in oxygen content can also be explained considering the well known hydrogen effect [36].

In the case of the bi-layer formed by a layer of Al2O3 followed by a second layer of TiO2, both signals of Ti and Al can be observed in the first 150-200 nm of analysis, while Oxygen can be observed for more than 300 nm. The Iron signals shows a plateau after about 170 nm. It can be observed that Titanium and Aluminium have a clear peak in the coating region. The titanium signals can be observed up to 100 nm, while the Aluminium signals can be observed up to 170 nm.

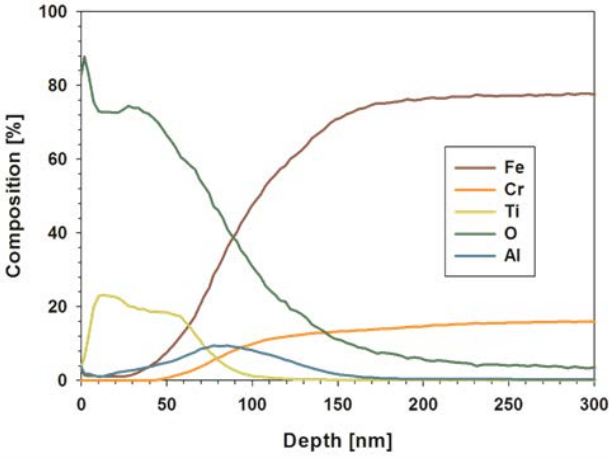

Figure 5: GDOES graph obtained for the Al2O3 coated sample. Signals of Iron, Chromium, Titanium, Oxygen and Aluminum

3.3 Mechanical properties

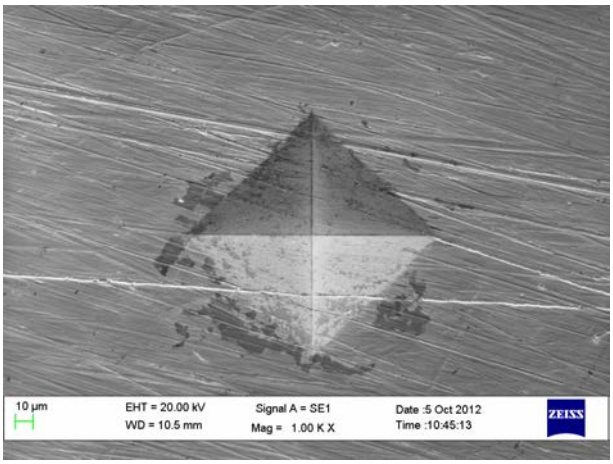

Figure 6: 3 N Vickers indentation on AISI 420 Stainless Steel coated with Al_2O_3

Vickers indentations performed on the coated sample surface were observed using SEM, as the Optical Microscope field depth resulted to be too small to sharply resolve all the delamination details on the deformed region in just one image. The dimension of the Vickers indentation is related to the applied load. Even if localized defects are hardly visible on the ALD coatings due to their transparency, larger areas with a complete coating removal resulted to be clearly visible on the SEM images. A clear example of how the delaminated areas have been evaluated is presented in Fig. 6 and Fig. 7. Fig. 6, in particular, shows a Vickers indentation as obtained using a 3 N load on the 100 nm TiO_2 coated sample, while Fig. 7 shows details of cracks and delamination obtained using a 10 N load. The results obtained for the different samples

are plotted in Fig. 8, as a function of the applied load.

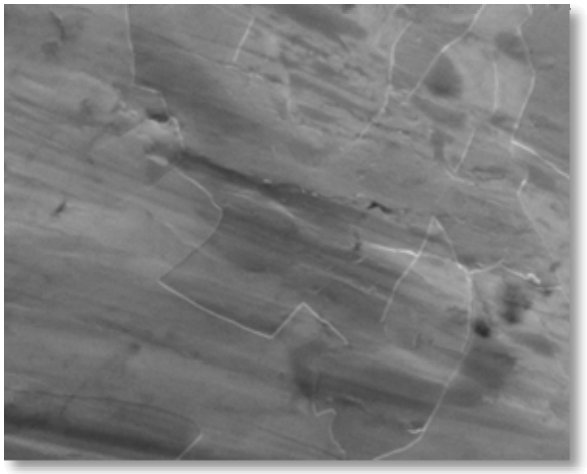

Figure 7: Cracks and delamination in proximity of a Vickers indentation (5N on Al_2O_3 coated AISI 420)

All coatings showed a clear dependence on the applied load for the delaminated Area/Load ratio, which remains almost constant only at the highest indentation loads (9.8 N = HV1 and 19.6 N = HV2).

It can be observed that the best behaviour is shown by the coating formed by two different layers, with a lower delamination, in particular at low loading conditions. At high loading conditions, and in particular at 19.6 N, the two coatings shown almost the same delamination areas.

Data dispersion was considerably high so a statistical approach was followed, with about 20 Vickers indentations per load for each sample.

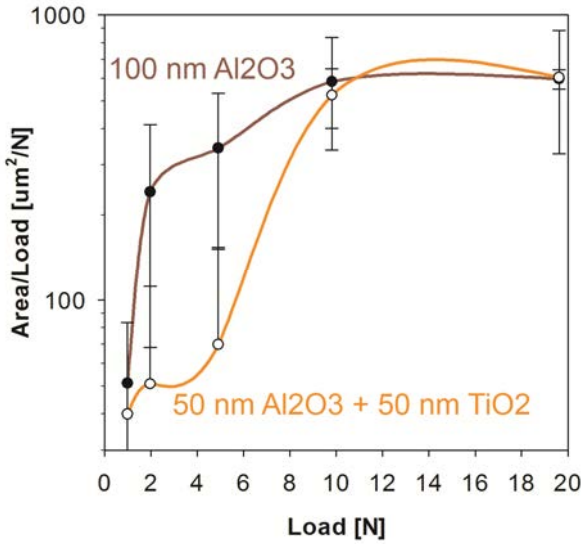

Figure 8: delamination as a function of the indentation load

3.4 Electrochemical properties

Polarization curves for the different samples with a total coating thickness of about 100 nm are shown in Fig. 9. Uncoated AISI 420 clearly shows a passive behavior in the 0.2 M NaCl solution, with a corrosion current density between 10^{-6} and 10^{-7} A/cm2 and a passive region from -0.25 to -0.1 V with respect to Ag/AgCl. The Open Circuit Potential (OCP) for uncoated AISI 316 L steel resulted to be about 0.1 V with respect to Ag/AgCl.

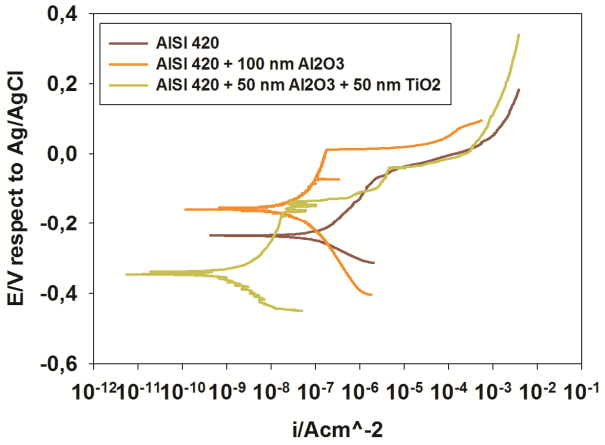

Figure 3: polarization curves obtained on both coated samples and on naked substrate

The two coatings showed two different shifts of the corrosion potential, a positive shift to about -0.15 V respect to Ag/AgCl in the case of the single layer Al_2O_3 coating and a negative shift to about -0.35 V in the case of the bi-layered structure of Al_2O_3 and TiO_2.

In the case of the single layer coating, a corrosion current density reduction of about one order of magnitude, to about $3*10^{-8}$ A/cm^2, was observed, while in the case of the bi-layered structure, the corrosion current density reduction resulted to be more intense, reaching $3*10^{-9}$ A/cm^2.

In the case of the single layer coating, the barrier effect resulted to be similar in extension to the passive range of the naked AISI 420 substrate, at lower currents, while an extended barrier effect was observed in the case of the bi-layered structure.

3.5 Wear properties

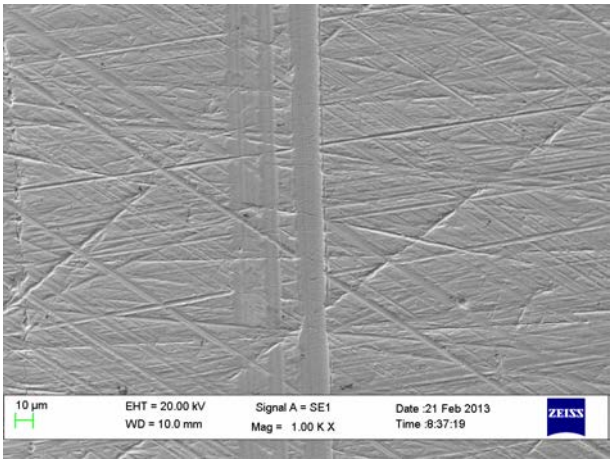

Figure 9: wear track obtained after just 10 cycles for Al_2O_3 single layer

Fig. 9 shows the wear track obtained after 10 cycles of ball-on-disc wear testing on the sample coated with a single layer of Al_2O_3. It can be observed that, even if the applied load is relatively low, a wear track is clearly visible on the surface of the sample and, in particular, third body wear scars can be observed. The pristine surface roughness of the sample has been completely removed from the surface due to the tribological contact with the WC counter-part.

EDXS localized analysis shown that the ALD layer has been completely removed from the surface due to the tribological contact.

It is possible that the clearly visible third body wear on the surface of the sample has also been caused by Al_2O_3 particles detached from the sample surface during testing.

Increasing the number of cycles, it was possible to observe the formation of a thick oxide layer inside the wear track, and strong adhesion phenomena, leading to a coarse wear track full of irregular oxide depositions.

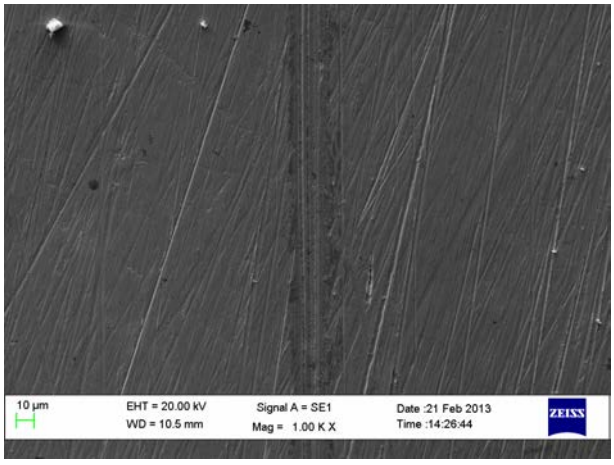

Figure 10: wear track obtained after just 10 cycles for Al_2O_3/TiO_2 bi-layer

Fig. 10 shows the wear track obtained after 10 cycles of ball-on-disc wear testing on the sample coated with a bi-layer formed by Al_2O_3 and TiO_2.

It can be observed that, as seen before for the single layer sample, the wear track is clearly visible at 1000 magnifications. Scars of third body wear are present inside the wear track, even if the track itself is smaller when compared to the track obtained from the single layer sample.

Even in this case, EDXS analyses shown that the ALD layer has been completely removed from the wear track on the sample surface, due to the tribological contact with the WC counterpart.

4. CONCLUSIONS

Nanometric ALD mono- and bi- layers, with a total thickness of about 200 nm, were successfully applied to AISI 420 martensitic stainless steel using a thermal ALD process based on H_2O, TMA and $TiCl_4$.

The applied ALD layers and the substrate where successfully characterized using SEM, AFM, GDOES, stylus profilometer, electrochemical equipment and an industrial tribometer in ball-on-disc configuration.

The morphological characterization evidenced that ALD layers are conformal and almost defect-free even at relatively high magnifications.

GDOES testing correctly discriminated the presence of the different ceramic layers on the AISI 420 substrate.

Adhesion testing showed that adhesion between AISI 420 and 200 nm ALD layers is relatively poor and cracks propagate from microhardness Vickers indentations.

Electrochemical testing clearly showed that even an ALD coating with a limited thickness of about 200 nm is sufficient to strongly improve the corrosion resistance of the martensitic stainless steel substrate, strongly reducing the corrosion current densities and widening the passive range of this material.

Wear testing results showed that ALD layers deposited at the temperature of 120 °C on martensitic stainless steel, are unable to grant tribological resistance to the substrate, due to their intrinsic brittleness and the relatively low hardness of the substrate on which they were applied.

REFERENCES

[1] H. Zhang, Y.L. Zhao, Z.D. Jiang, Materials Letters 59, 3370-3374; 2005.

[2] P.J. Hidalgo, Surcae Technology 10, 193-208; 1980.

[3] A. Turnbull, B. Nimmo, *Environment-Induced Cracking materials*, 2008, 2, 483-492;

[4] J.W. Boh, L.A. Louca, Y.S. Choo, Shreir's Corrosion 3, 1802-1878, 2010.

[5] D. Ferreno, J.A. Alvarez, E. Ruiz, D. Mendez, L. Rodriguez, D. Hernandez, Engineering FAilure Analysis, 18, 256-270, 2011.

[6] B. Fournier, M. Sauzay, C. Caes, M. Noblecourt, M. Mottot, A. Bougault, V. Rabeau, J. Man, O. Gillia, P. Lemoine, A. Pineau, International Journal of Fatigue 30 (10-11), pp. 1797-1812, 2008.

[7] C. Liu, G. Lin, D. Yang, M. Qi, Surface and Coating Technology 200, pp. 4011-4016, 2006.

[8] V.H.V. Sarmento, M.G. Schiavetto, P. Hammer, A.V. Benedetti, C.S. Fugivara, P.H. Suegama,

[9] S.H. Pulcinelli, C.V. Santilli, Surface and Coatings Technology 204, pp. 2689-2701, 2010.

[10] R. Di Maggio, L. Fedrizzi, S. Rossi, P. Scardi, Thin Solid Films 286, pp. 127-135, 1996.

[11] C. Wang, F. Jiang, F. Wang, Corrosion Science 46, 75-89, 2004.

[12] C.R. Tomachuk, C.I. Elsner, A.R. Di Sarli, O.B. Ferraz, Materials Chemistry and Physics 119, pp. 19-29, 2010.

[13] D. Pech, P. Steyer, J. P. Millet, Corrosion Science 50, 1492-1497, 2008.

[14] J. Kawakita, T. Fukushima, S. Kuroda, T. Kodama, Corrosion Science 44, 2561-2581, 2002.

[15] C.X. Li, T. Bell, Corrosion Science 48, pp. 2036-2049, 2006.

[16] C.X. Shan, X. Hou, K. L. Choy, Surface & Coatings Technology 202, pp. 2399–2402, 2008.

[17] E. Marin, L. Guzman, A. Lanzutti, W. Ensinger, L. Fedrizzi, Thin Solid Films 522, pp. 283-288; 2012.

[18] P. Corengia, F. Walther, G. Ybarra, S. Sommadossi, R. Corbari, E. Broitman, Wear, pp. 479-485, 2006.

[19] O. Choumad, X. Badiche, P. Montmitonnet, Y. Gachon, Journal of Manufacturing Processes 15, pp. 77-86, 2013.

[20] J.B. Cambon, F. Ansart, J.P. Bonino, V. Turq, Progress in Organic Coatings 75, pp. 486-493, 2012.

[21] T. Suntola, J. Antson, J. (1977) U.S. Patent 4,058,430;

[22] T. Suntola, Solid State Electron. 14 933, 1971.

[23] T. Stubb, T. Suntola, O.J.A. Tiainen, Solid State Electron., 15, 611, 1972.

[24] T. Suntola, O.J.A. Tiainen, M. Valkiainen, Thin Solid Films 227, 1972.

[25] T. Suntola, Thin Solid Films 34 9, 1976.

[26] M. Ahonen, M. Pessa, T. Suntola, Thin Solid Films 65, 301, 1980.

[27] J. Lua, J. Aarik, J. Sundqvist, K. Kukli,1, A. Harsta, J.-O. Carlsson, J. Cryst. Growth 273, 510, 2005.

[28] Bedair, S. M., The Encyclopedia of Advanced Materials, vol 1. Edited by Bloor D, Brook RS, Flemings, M.C., Mahajan, S., Oxford: Pergamon 141, 1994.

[29] R. Matero, M. Ritala, M. Leskelä, T. Salo, J. Aromaa, O. Forsén, J. Phys. IV France 09, 493, 1999.

[30] C.X. Shan, X. Hou, K. L. Choy, Surf. Coat. Technol. 202, 2147, 2008.

[31] E. Marin, A. Lanzutti, L. Guzman, L. Fedrizzi, J. Coat. Technol. Res. DOI: 10.1007/s11998-011-9327-0, 2011.

[32] S. E. Potts, L. Schmalz, M. Fenker, B. Dìaz, J. Światowska, V. Maurice, A. Seyeux,P. Marcus, G. Radnóczi, L. Tóth, M. C. M. van de Sanden, and W. M. M. Kessels, J. Electrochem. Soc. 158, 132, 2011.

[33] M. Ritala, Appl. Surf. Sci. 112, 223, 1997.

[34] J. Takadoum , H.H. Bennani, Surf. Coat. Technol. 96, 272, 1997.

[35] H.C. Barshilia, A.Ananth, J. Khan, G. Srinivas, Vac. 8, 1165, 2012.

[36] R. Payling, D.G. Jones and A. Bengtson, “Glow Discharge Optical Emission Spectrometry”, John Wiley, Chichester, 1997.

Serbian Tribology Society

SERBIATRIB '13

13th International Conference on Tribology

Faculty of Engineering in Kragujevac

Kragujevac, Serbia, 15 – 17 May 2013

PREPARATION AND CHARACTERIZATION OF QUATERNARY AMMONIUM SURFACTANTS ON MUSCOVITE MICA

Jelena MANOJLOVIĆ[1]

[1]The Faculty of Mechanical Engineering Niš, Aleksandra Medvedeva 14, 18000 Niš, Srbija

jmanojlo@gmail.com

Abstract: *In order to reduce friction, lubricants are usually employed. We describe the possibility of self-assembled monolayers (SAMs) being used as lubricants. Our aim was to produce homogeneous monolayers of surfactants on substrate. Because the surfactant behavior in the solution can be changed in contact with a substrate, we considered the adsorption mechanisms of surfactant molecules at the solid-liquid interface to be important. SAMs were prepared by using different methods, and their stability and structure was studied, but a homogeneous hydrophobic monolayer was difficult to realize. It has been shown that the factors, such as the temperature during solution preparation, frequently neglected, can be very important in the process of surfactant adsorption from solution.*

Keywords: *adsorption, SAMs, stability, muscovite mica, contact angle*

1. INTRODUCTION

The tribological research involves the study of friction, wear and lubrication. These three components between materials in contact are of fundamental importance in many areas, such as aircraft engines, automobiles, gears or bearing. Practically, in all modern mechanical machines the major problems are friction and wear. The advanced technical applications and the invention of new characterization techniques, lead to the appearance of the new field of tribology, known as micro-tribology/nano-tribology, which involves the study of friction and wear at a very small length scales. Nanotribology part of particular importance is called nanolubrication, defined as the study of ultra-thin lubricant films. The application of nanolubrication is important in a device which needs a lubricant layer of few nanometers, to reduce friction and wear. Therefore, research and testing of nano-lubricants, needed for microelectromechanical systems (MEMS) components, is a big challenge.

An attractive model system that can be used for studies in wetting, adhesion and friction of surfaces is the system of self-assembled organic monolayers (SAMs). The concept of self-assembly was invoked by Zisman, more than 50 years ago. At that time, the potential of self-assembly was not recognized, but the field of self-assembled monolayers has considerably developed in the past 30 years. Due to possibility of controlling the physical and chemical properties of these systems in a systematic way, and in order to solve many practical friction connected problems by SAMs, the interest in their study significantly increases [1,2]. The interest in the general area of self-assembly, specifically in SAMs, comes from their observed importance in science and technology.

One example of the general phenomena of self-assembly is the formation of monolayers, by self-assembly of surfactant molecules at surfaces. Self-assembled monolayers can be prepared using different types of molecules and different substrates, by very simple process, which makes SAMs manufacturable and thus technologically attractive in surface engineering [3]. Surfactant adsorption from solution can produce various SAM morphologies. It has been shown that surfactants can form monolayers, bilayers [4], or aggregates of various shapes and sizes [5]. Commonly studied factors during SAMs formation are properties of the surfactant concentration - above the cmc [6] and below the cmc [7] different chain length and head group structure [4] or types of solid surfaces (oxide

surfaces, graphite, gold, silica or mica [8]. A significant part of work has been done at a concentration above the cmc [6], in order to clarify the structure of the adsorbed layers, especially the aggregates on the surface. The properties of the adsorbed films on the solid surface seem to be dependent on experimental parameters, such as concentration, pH, temperature and humidity, rarely described in the literature.

Adsorbed surfactants have been characterized using various techniques, such as x-ray photoelectron spectroscopy (XPS) [9], contact angle measurements [10], ellipsometry [11]. The AFM was first used to image surfactant aggregates on the surface by Manne et al. [12]. This technique indeed offers a convenient method for the imaging of molecular assemblies, i.e. *in situ* [13] or rarely in *ex situ*. In order to test the stability and measure the thickness of SAMs on mica, a scratch test can be used [14]. Due to the small thickness of SAMs (~nm), the development of AFM gives a powerful tool to the visualization of the adsorbed surfactant on solid substrates and facilitates the study of the adsorption mechanism at the molecular level. It can identify defects on the sample and detect the structure of formed layers on the substrate. Over the last 20 years experiments performed with the atomic force microscope or with the other measuring techniques, have provided new insights into the physics of contact between single asperities, friction, wear and lubrication on a molecular level.

Many authors have aimed at investigating the adsorption of cationic surfactants from aqueous solution onto a variety of solid surfaces, including graphite [12], silica [15] and mica [16]. Cationic surfactants have been the most studied ones, using the technique of the direct surface forces measurements, particularly with the surfaces forces apparatus [17]. Most of the surface force work was directed towards studying the interaction between surfactant coated surfaces, for better understanding of hydrophobic forces [18]. The surface force technique has been used to probe the lubrication properties of aqueous surfactant solutions [19]. Due to the possibility to simultaneous measuring of the thickness and the intermolecular forces of surfactant films, this technique has been used as an effective tool in the study of surfactant model system.

Adsorption of cationic surfactants, especially quaternary ammonium surfactants cetyltrimethylammonium bromide-CTAB, onto relatively simple inorganic substrates, such as mica, has been studied very often, as a good model system for boundary lubrication. Depending on the conditions, it has been reported that CTAB adsorbs on mica as a compact monolayer [19] , as a stable hydrophobic surface [20], as a bilayer [6], or forms aggregates [21]. For the preparation of CTAB self-assembled films on mica, numerous adsorption protocols have been proposed in the literature. The applied procedures include the variation of many parameters, such as different temperatures in SAM preparation, the immersion time or the post-adsorption sample treatment [10]. Different conclusions about adsorption theories and the existence of numerous mechanisms, underline this broadness [22]. On the other hand, the Krafft temperature is a very important quantity for CTAB/ water solutions as previously reported [6]. Due to the important structural changes in CTAB solution, above the cmc at and above the Krafft temperature, this surfactant transition is still the area of research interest.

Our attention here will be directed toward modification of the mica surface by adsorption of quaternary ammonium surfactants, with the aim to produce hydrophobic and well-ordered homogeneous monolayers. Adsorbed layers were prepared on mica using different concentrations of surfactants in aqueous solution, below and above the critical micelle concentration, in order to check the hypothesis that the adsorption depends on the solution structure. The adsorbed layers were characterized by contact angle (CA) measurements and atomic force microscopy (AFM) imaging.

2. MATERIALS AND METHODS

The self-assembled monolayers of quaternary ammonium surfactants on mica, we made by single-tailed hexadecyltrimethylammonium bromide (CTAB), with the molecular structure $CH_3(CH_2)_{15}N^+(CH_3)_3Br^-$. CTAB was purchased from Fluka and for further purification was recrystallized from an ethanol/acetone mixture. As a solvent, ultra pure water of resistivity 18.3MΩcm was prepared, using a Barnstead EASYpure™ batch-fed water purification system. In the process of sample rinsing we used water of the same quality before drying with a clean nitrogen stream.

To avoid any contamination, the glassware and bottles used in the experiments were consistently cleaned by piranha solution and then rinsed with purified water. All the employed tools were previously cleaned in order to minimize the occurrence of a molecular contamination, particularly on the high-energy mica surface.

Mica samples preparation

For the adsorption experiments, we used muscovite mica purchased from Spruce Pine Mica Company Inc. (USA). Small mica samples of 1-1.5cm^2 size were cut by scissors and after that freshly cleaved on both sides and immersed into the surfactant solution. The adsorption was performed from the surfactant solution in a volume of 20ml.

3. EXPERIMENTAL PART

Several experiments, described in the literature, suggested that the transition through the three-phase boundary is an important step, with a significant influence on the surfactant film morphology. To distinguish effects due to adsorption at the solid-liquid interface and the deposition at the three-phase boundary (TPB), we have systematically varied the immersion/extraction protocol and defined four different experiments. All four adsorption protocols, separately described below, have been used with/without temperature control. The results observed under the temperature controlled conditions have been described.

Every experiment consists of four steps: adsorption, rinsing, drying and analysis (AFM and CA). Varying the immersion and extraction of mica sample into and out of the surfactant solution, we have defined four different adsorption protocols (figure 1).

The first option, called "CTAB in/CTAB out", involves immersion and extraction from the surfactant solution at the nominal concentration.

The second adsorption type ("CTAB in/dilute out") uses immersion into the nominal surfactant solution, a rest time and subsequent rapid (10seconds) dilution with pure water prior to extraction, in order to eliminate surfactant deposition during the transition through the TPB.

The third option ("dilute in /dilute out") prevents surfactant deposition at the TPB in both steps, immersion into solution and extraction from it. In this case, CTAB is added to the solution after the sample is submerged.

The fourth option ("dilute in/CTAB out") allows deposition at the TPB during extraction only.

In the water dipping step, the mica samples were dipped into 20ml of ultra pure water to remove the excess surfactant molecules.

The same set of adsorption experiments shown in figure 1 has been repeated at controlled temperature in the laboratory, at 18°C (below the Krafft temperature) and 30°C (above the Krafft temperature). A stock solution, 250ml of 10^{-3}M CTAB, has been prepared at controlled temperature of 18°C or 30°C. It is important to emphasize that all the used chemicals, tools and substrates were equilibrated at the defined temperature before the adsorption experiments.

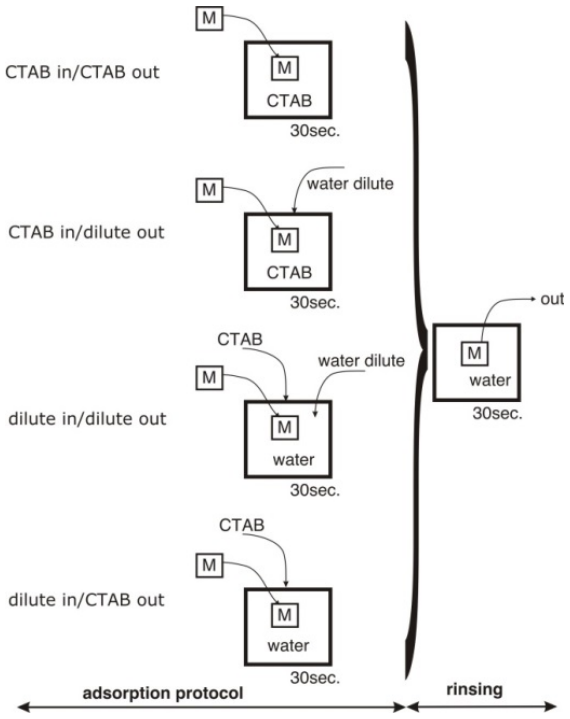

Figure 1. Schematic representation of four different adsorption protocols used to discriminate different deposition mechanisms at the three-phase boundary. All samples were dipped into ultra pure water to strip off possible excess CTAB (e.g. incomplete second layer)

After the post-rinsing step, the modified mica surface was gently blown dry with nitrogen before the AFM imaging or contact angle measurements. Each type of protocol (at different concentrations) was repeated several times to also assess the reproducibility.

The samples were imaged with an Atomic Force Microscope (Digital Instruments, Nanoscope IIIa), which was operated under ambient conditions. The images were systematically collected for different scan sizes (i.e. 10μmx10μm, 5μmx5μm and 1μmx1μm, and again 10μmx10μm) and they were repeated by scanning several different areas on a given sample. At least two samples of each preparation protocol were analyzed.

The contact angle is the angle conventionally measured through the liquid, where aliquid/vapor interface meets a solid surface. It quantifies the wettability of a solid surface by a liquid. On every sample advancing (maximal) contact angle and the receding (minimal) contact angle are measured. A water contact angle greater than 90° is determined on hydrophobic surfaces. For example, freshly cleaved mica has a contact angle less than 10°, and a contact angle on the SAM produced by CTAB adsorption on mica can be 140°.

For water contact angle measurements, after the placing the droplet on the surface, the advancing contact angle was measured, θ_a, after which the droplet was retracted, and the receding contact angle, θ_r, recorded. The times for both contact angle measurements, were similar, in the range of a few seconds duration for each.

Using hexadecane as the probing liquid, we can define a well-ordered monolayer on a substrate and the expected CA of ordered surfactant layers are around or larger than 40°. A high contact angle suggests a high degree of order and "tails-up" molecules orientation in the layer. With hexadecane only a static contact angle has been measured by placing 1μL drop on the sample. Measurements were performed at room temperature conditions and humidity. The contact angle values were detected with accuracy ±1-2°.

4. RESULTS

The influence of the temperature on the surfactant solution properties and the resulting SAM morphology, spurred us to control the temperature during the solution preparation, as well as during adsorption. Two distinct temperatures have been chosen-one below (18°C) and one above (30°C) the Krafft temperature of CTAB.

CTAB adsorption results on mica observed at low concentrations are illustrated in figure 2.a below the Krafft temperature (at 18°C), and 2.b above the Krafft temperature (at 30°C). The temperature dependence of the observed film morphology at 18°C and 30°C can be confirmed by contact angle measurements. Due to the variations determined in the different samples spots, both the results for water (advancing/receding) are given with errors.

In both groups of experiments, hydrophobic surfaces with advancing contact angles between 75° and 90° have been obtained. The significant hysteresis suggests a chemical heterogeneity or roughness in the surfactant film [24].

Considering the highest contact angles in both measurements with water and hexadecane, the most promising hydrophobic surfaces have been obtained at 18°C, using the protocol "CTAB in /CTAB out", suggesting a significant surfactant adsorption at the three-phase boundary. Therefore, this adsorption protocol has been selected for all the following measurements at 18°C.

The temperature dependence of the observed film morphology at 18°C and 30°C can be confirmed by contact angle measurements. Contact angles for various preparation protocols are summarized in the tables below. Due to the variations determined in the different samples spots, both the results for water (advancing/receding) and hexadecane are given with errors.

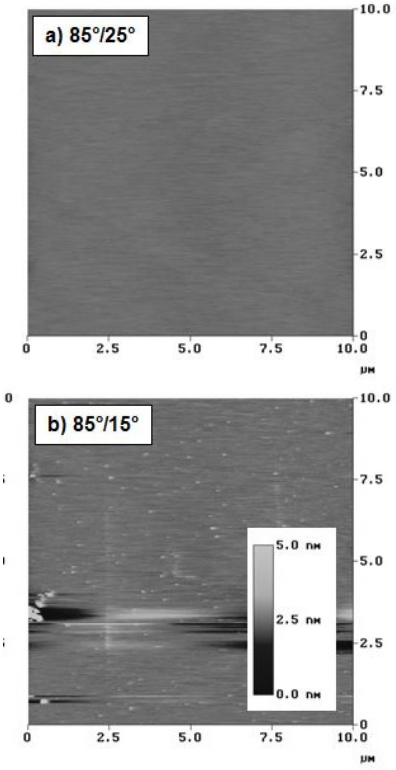

Figure 2. The comparison of AFM images of CTAB modified mica by the "CTAB in/CTAB out" protocol at controlled temperature: a) from saturated 10^{-3} M solution (at 18°C) b) from 10^{-4}M solution (at 30°C)

Table 1. Contact angle of water and hexadecane on CTAB coated mica from the saturated 10^{-3}M solution prepared at 18°C

18°C	hexadecane	water
CTAB in/CTAB out	27±2°	85°/35°
CTAB in/dilute out	19±2°	79°/25°

Table 2. Contact angle of water and hexadecane on CTAB coated mica at 30°C from 10^{-4}M solution

30°C	hexadecane	water
CTAB in/CTAB out	17±2°	85°/15°
dilute in/dilute out	14°	90°/10°
dilute in/CTAB out	12°	79°/12°
CTAB in/dilute out	7°	76°/12°

5. DISCUSSION

The structure and the stability of the adsorbed films are sensitive to the experimental conditions, primarily temperature.

According to the AFM results in figure 2.a, the adsorbed film can be the homogeneous SAM on the mica. Hysteresis in water CA indicates a hydrophobic but not homogeneous film. Similar contact angles have been reported in the literature. The decay in CA values with time shows instability of the formed layer, due to desorption of the adsorbed molecules into the water drop. A similar observation has been also made [24] and interpreted as water penetration into the monolayer, a phenomenon already known to Langmuir in 1938. The degree of water penetration can also be influenced by the local environment, e.g. relative humidity or temperature [24].

In all experiments hydrophobic surfaces with advancing contact angles between 75° and 90° have been obtained. The significant hysteresis suggests a chemical heterogeneity or roughness in the surfactant film. Measurements of hexadecane contact angle represent one of the most sensitive tools to determine the conformational order of hydrocarbon thin films. High hexadecane contact angles are observed on hydrocarbon SAMs only when the monolayers are densely packed. Using hexadecane we have observed lower values than the expected 40° for ideally ordered films.

In order to relate our SAM preparation protocols to previous work, we have compared our results with those described in the literature. Much work has been devoted to the study of the adsorption of CTAB on mica using a variety of adsorption protocols and measurement techniques. For both solution concentrations, below and above the cmc, the picture drown in the literature demonstrates a high degree of variability.

The protocol proposed by Zhao [25] was reported to produce cylinder aggregates on the mica surface at a solution concentration of 2cmc (figure 3.a). Due to the measured height of ~6nm of the features, the layer has been described as consisting of two bilayers.

At the CTAB concentration 10^{-5}M monolayers and bilayers have been observed [22], using a similar adsorption protocol at room temperature (around 25°C), as shown in figure 3.b. The AFM was operated in the surfactant solution.

We can conclude that the literature confirms that even small differences in the SAM adsorption protocol can significantly affect the surfactant film morphology on mica, especially above the cmc and the Krafft temperature. These observations are confirmed by our experimental results and there is the need to explain these variations by structural changes of the surfactant solution [26]. There are significant structural changes around the Krafft temperature. Below the bulk cmc and below the Krafft temperature, an equilibrated solution is expected to be free of micelles. At the Krafft temperature, the solubility becomes equal to the cmc and micelles will form in the solution and this temperature is very often described in the literature. But, reported values of T_k for CTAB in water vary considerably (from 20°C to 25°C), which is very close to a room temperature and complicates the explanation of experimental results.

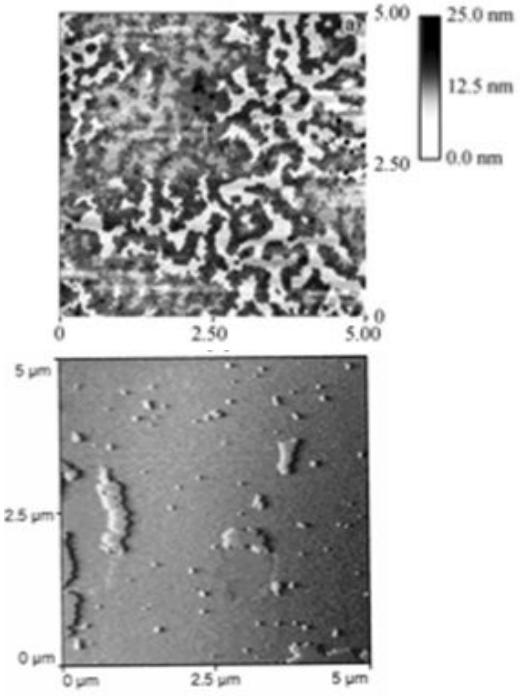

Figure 3. a) AFM topographic image of a mica surface prepared unspecified temperature conditions, using "CTAB in/CTAB out" protocol (immersion time-1min), at 2cmc, without rinsing after removal from the solution, dried with nitrogen before AFM imaging [25]; b) AFM image of a CTAB adsorbed layer on mica in a 10^{-5}M solution at 25°C for 25min immersion time, observed in the surfactant solution [22].

It is important to note that most of the experiments described in the literature do not mention the problem of temperature control, and it is not possible to reconstruct this important parameter from the information provided. We have a clear evidence that temperature is the key factor determining SAM morphology. Therefore, we have systematically studied temperature effects by rigorously controlling the temperature during all procedures.

6. CONCLUSION

The concept of self-assembly on surfaces has been treated in this research and the experiments have revisited the adsorption of CTAB onto a muscovite mica. These results demonstrate the influence of a large number of parameters on the adsorption process, as well as the morphology and

the molecular order of SAMs. The molecular structure of the solution seems to be a key element. It is chiefly controlled by the temperature and concentration of the solution. The fact that the Krafft temperature range of CTAB is around room temperature (~25°C), makes this system particularly complex.

We have systematically studied the transfer across the three-phase boundary, under different experimental conditions and different adsorption protocols. The surfactant films on mica, formed according to different experimental protocols, were characterized by contact angle measurements and by AFM. It has been observed that the transition through the three-phase boundary during sample extraction can be a step of significant influence on the SAM morphology.

A high stability of the adsorbed films is very rarely detected. The problem of reproducibility in SAMs formation can be observed by controlling the temperature during all steps, or, working below the cmc. A reproducible stability of the resulting films, however, remains an issue.

Acknowledgements: The author would like to gratefully acknowledge the support in obtaining and understanding the presented results provided by her mentors, Nicholas D. Spencer and Manfred Heuberger, members of the Laboratory for Surface Science and Technology (LSST), a part of the Department of Materials at the ETH Zurich, Switzerland, where all the experiments were performed.

REFERENCES

[1] M. K. Chaudhury: *Adhesion and friction of self-assembled organic monolayers*, Current opinion in colloid & interface science, Vol.2, pp. 65-69, 1997.

[2] S. Manne et al.: *Direct Visualization of Surfactant Hemimicelles by Force Microscopy of the Electrical Double-Layer*, Langmuir, Vol.10(12), pp. 4409-4413, 1994.

[3] A. Ulman: *Formation and Structure of Self-Assembled Monolayers*, Chem. Rev., Vol. 96, pp. 1533-1554, 1996.

[4] H. Patrick et al.: *Surface micellization patterns of quaternary ammonium surfactants on mica*, Langmuir, Vol. 15(5), pp. 1685-1692, 1999.

[5] S. Manne, H. Gaub: *Molecular-Organization of Surfactants at Solid-Liquid Interfaces*, Science, Vol. 270(5241), pp. 1480-1482, 1995.

[6] W. Ducker, E.Wanless: *Adsorption of hexadecyltrimethylammonium bromide to mica: Nanometer-scale study of binding-site competition effects*, Langmuir, Vol. 15(1), pp. 160-168, 1999.

[7] M. Fujii et al.: *Heterogeneous growth and self-repairing processes of two-dimensional molecular aggregates of adsorbed octadecyltrimethylammonium bromide at cleaved mica aqueous solution interface as observed by in situ atomic force microscopy*, Langmuir, Vol. 15(10), pp. 3689-3692, 1999.

[8] R. Atkin et al.: *Adsorption kinetics and structural arrangements of cationic surfactants on silica surfaces*, Langmuir, Vol. 16(24), pp. 9374-9380, 2000.

[9] K. Boschkova et al.: *Lubrication in aqueous solutions using cationic surfactants - a study of static and dynamic forces*, Langmuir, Vol. 18(5), pp. 1680-1687, 2002.

[10] B.Y.Li et al.: *Time dependent anchoring of adsorbed cationic surfactant molecules at mice/solution interface*, Journal of Colloid and Interface Science, Vol. 209(1), pp. 25-30, 1999.

[11] K. Eskilsson and V.V. Yaminsky: *Deposition of monolayers by retraction from solution: Ellipsometric study of cetyltrimethylammonium bromide adsorption at silica-air and silica-water interfaces*, Langmuir, Vol. 14(9), pp. 2444-2450, 1998.

[12] S. Manne et al.: *Direct Visualization of Surfactant Hemimicelles by Force Microscopy of the Electrical Double-Layer*, Langmuir, Vol. 10(12), pp. 4409-4413, 1994.

[13] J. a. M. Mellott: *Supercritical self-assembled monolayer growth*, Journal of the American Chemical Society, Vol. 126(30), pp. 9369-9373, 2004.

[14] HY Nie et al.: *Robust self-assembled octadecylphosphonic acid monolayers on a mica substrate*, Langmuir, Vol. 21(7), pp. 2773-2778, 2005.

[15] T. Horr et al.: *XPS film thickness and adsorption studies of alkyltrimethylammonium bromides and organosilanes on silica surfaces*, Colloids and Surfaces A: Physicochemical and Engineering Aspects, Vol. 102, pp. 181-190, 1995.

[16] S. Nishimura et al.: *AFM Studies of Amine Surfactant Hemimicelle Structures at the Mica-Water Interface*, Colloids and Surfaces A: Physicochemical and Engineering Aspects, Vol. 103(3), pp. 289-298, 1995.

[17] M. Rutland, J. Parker: *Surface Forces between Silica Surfaces in Cationic Surfactant Solutions - Adsorption and Bilayer Formation at Normal and High pH*, Langmuir, Vol.10(4), pp. 1110-1121, 1994.

[18] A. e. a. Rennie: *Structure of a Cationic Surfactant Layer at the Silica Water Interface*, Langmuir, Vol. 6(5), pp. 1031-1034, 1990.

[19] R. Pashley, J. Israelachvili: *A Comparison of Surface Forces and Interfacial Properties of Mica in Purified Surfactant Solutions*, Colloids and Surfaces, Vol. 2(2), pp. 169-187, 1981.

[20] M. Fujii et al.: *Two-dimensional arrangements of adsorbed alkylammonium halides on cleaved mica surface*, Langmuir, Vol. 17(4), pp. 1138-1142, 2001.

[21] B. G. Sharma et al.: *Characterization of adsorbed ionic surfactants on a mica substrate*, Langmuir, Vol. 12(26), pp. 6506-6512, 1996.

[22] G. Ceotto et al.: *Ionic surfactant films imaged by atomic force microscopy*, Journal of Molecular Catalysis A: Chemical, Vol 167(1-2), pp. 225-233, 2001.

[23] T. Davey et al.: *Krafft temperature depression in quaternary ammonium bromide surfactants*, Langmuir, Vol. 14(12), pp. 3210-3213, 1998.

[24] Y. L. Chen et al.: *Molecular Mechanisms Associated with Adhesion and Contact-Angle Hysteresis of Monolayer Surfaces*, Journal of Physical Chemistry, Vol. 95(26), pp. 10736-10747, 1991.

[25] F.Zhao et al.: *Adsorption behavior of hexadecyltrimethylammonium bromida (CTAB) to mica substrates as observed by atomic force microscopy,* Science in China Ser. B Chemistry, Vol. 48(2), pp. 101-106, 2005.

[26] Manojlovic J.: *Structure, morphology and history effects in surfactant self-assembly*, Ph.D. thesis, ETH Zurich, Switzerland , 2006.

Serbian Tribology Society

SERBIATRIB '13

13th International Conference on Tribology

Faculty of Engineering in Kragujevac

Kragujevac, Serbia, 15 – 17 May 2013

MO-C MULTILAYERED CVD COATINGS

A. Sagalovych, V. Sagalovych
Scientific technological Centre "Nanotechnologie", Kharkov, Ukraine

Abstract: *Production processes of multi-layered Mo-C coatings by the method of chemical vapor deposition (CVD) with the use of organometallic compounds were developed. Coatings are applied on technical purpose steel DIN* 1.2379 *(Х12Ф1) and DIN 1.7709 (25Х2МФ (ЭИ10) heat-treated ball with the high class of surface roughness (> 10). The average deposition rate was 50 μm/h. The optimal conditions of coatings deposition for different technological schemas were defined.*
Metallographic investigations of the obtained coatings were carried out.
Tribological studies of the friction and wear characteristics of sliding friction in conditions of boundary lubrication of Mo-C multilayered CVD *coatings shows, that coatings have low friction coefficients (0.075 - 0.095) at loads up to 2.0 kN, showed high resistance to wear and are effective in increasing the stability of the pair for precision friction pairs of hydraulical units.*

Key words: *CVD processes, multi-layered coatings, tribology.*

1. INTRODUCTION

Ever-increasing requirements to raise durability and efficiency of various newly created parts and mechanisms working in friction conditions lead to sharp increase in demands to search new materials working in the conditions of frictional contact and their tribotechnical characteristics. Complexity and integrated nature of these demands boost constant search of new materials and techniques of their production. Especially acute problem of making new highly effective wear resistant materials is for advanced industries of machine building – aircraft engineering, aggregate building, shipbuilding, rocket and space engineering.

Raise of the functional properties of parts by use of protective coatings is very widespread technological tool for today. Hardsurfacing, wear resistant, corrosion resistant, etc. functional coatings are widely applied in the industry.

Among coating deposition methods are chemical vapor deposition methods (CVD) based on the pyrolysis of gaseous metal containing compounds [1]. The relative simplicity of realization of processes, absence of high demands to vacuum (in many cases processes take place at atmospheric pressure), high coating deposition rates (up to a few millimeters per hour), and possibility of deposition of the even qualitative coatings on figurine-shaped (including internal) surfaces with great value of relationship L/d, make these methods rather perspective for deposition of the functional coatings [1-3].

Wei and Lo [4] carried out examination of deposition of Mo and Cr coatings at temperatures 170-450 °C and pressure ~ 1 torr using a mixture of carbonyl with hydrogen. Upon that, they used specially prepared carriers made of SiC and SS304. The main emphasis in the work is placed on studying of structure of obtained coatings.

In the work [5] molybdenum was deposited on a porous ceramic carrier at atmospheric pressure. Chromium was deposited from carbonyl at atmospheric pressure also, but already on the polished carriers in the work [6].

It should be pointed out that application of CVD methods to receive hardsurfacing wear- and corrosion resistant coatings was limited yet. From the point of view of practical application, development of processes of obtaining of chemical vapor deposited functional coatings on geometrically complex precision surfaces of high surface finish class (above 10 grade) is of interest. The purpose of this study is development of process of deposition of multilayered Mo-C coatings by a

chemical vapor deposition method with use organometallic compounds, studying multilayered and tribological properties of the obtained coatings and an estimate of possibility of their application in the capacity of candidate materials for precision friction pairs.

2. EQUIPMENT, TECHNIQUES, AND USED PROCEDURES

Making Mo-C coatings was carried out by a thermal decomposition of metal-containing compound – molybdenum hexacarbonyl $Mo(CO)_6$. Process development was carried out using gas-phase unit of ***Avinit*** installation intended for deposition of the multilayered functional coatings by means of complex methods (plasma-chemical CVD, vacuum-plasma PVD (vacuum-arc, magnetron), and processes of ion saturation, and treatment of surfaces by ions) united in one technological cycle), presented in [7].

Process of coating application was controlled by means of temperature of the sample, working pressure in the chamber, and a method of evaporation of molybdenum hexacarbonyl.

For heating of the sample, high-frequency heater was applied with working frequency of 3 MHz and effective power ~ 0.2 kW. Pressure was controlled by dynamical changing of velocity of a pumping-out of vacuum system within 2.6 … 13 Pa (0.02 … 0.1 torr).

Carbonyl evaporation was carried out under two process flow charts:

- The process flow chart of excessive evaporation when a considerable quantity of carbonyl was evaporated within a container volume. Then, along the heated up steam pipeline through the adjustable valve, the gas mixture immediately supplied to the sample. It allowed obtaining major streams of carbonyl and, accordingly, high concentration of molybdenum in a reaction layer. In this case the carbonyl stream depended on temperature of the carbonyl.
- Under other process flow chart (the residual atmosphere) evaporation of a small amount of carbonyl was made immediately inside chamber volume. Thus, the uniform concentration of the reaction gas consisting of carbonyl and carbonic oxide vapors was obtained. At that, molybdenum volume concentration in a chamber atmosphere decreased with the course of process.

3. PROCEDURES OF EXAMINATION

During metallographic analysis the multilayered and microlayer coatings on the basis of system Mo-C were deposited on samples.

Samples were made of structural steel DIN 1.2379 (Х12Ф1) and heat steel DIN 1.7709 (25Х2МФ (ЭИ10) which are the materials commonly used in the industry.

Samples made of steel DIN 1.7709 (25Х2МФ (ЭИ10) with a size of 20x10x5 mm were polished according to factory production method up to 8 grade surface roughness (R_a=0.32 μm). Microhardness was HB~900.

Samples made of steel DIN 1.2379 (Х12Ф1), 56... 61HRC, with a size of 10x10x10 mm were polished to surface roughness of 10 grade (Ra=0.063 μm) to demanded geometrical parameters (nonflatness ≤ 0.001мм, surface roughness – Ra 0.08 μm).

Tribological tests of antifriction and wear properties and seizure of samples with coatings were carried out with friction and wear machine 2070 SMT-1 under the "cube" - "roller" test pattern at an incremental loading (with increments of 200N) in 1-20 MPa loading range according to the procedures presented in [8, 9]. The linear slip velocities - 1.3m/s. Time of tests in each cycle – 150 seconds. Operating fluid is fuel TS-1, GOST 10227-86.

For reproducibility of results of wearing tests, mating of face surfaces by size of the contact area was controlled: not less than 90 % of a working area of each sample.

During tribological tests there were registered:

– Values of frictional force F_{tr}, normal loading N, contact pressure P, by which value mechanical losses in tribosystems were estimated;

– Temperature of devices was continuously recorded in real time during the tests in immediate proximity (1 mm) from a friction zone, with application of the sliding thermocouple. Friction coefficients were determined as $f = F_{tr}/N$.

4. RESULTS

4.1 Deposition of coatings

Technological information for process of coating deposition on steel DIN 1.7709 (25Х2МФ (ЭИ10) is presented in Tables 1.1, 1.2 and 2.

Table 1.1 Mo/Mo-C coatings obtained at puffing of carbonyl from the container.

Temperature, °C	Pressure, Pa	Exposition τ, min.	Thickness δ, μm	Deposition rate V, μm/min.	Adhesion
350	5.20	10	8	0.80	+++
	10.00	10	7	0.70	+++
	5.30	15	17	1.13	+++
	11.00	15	10	0.67	+++
	8.80	30	25	0.83	+++
	11.00	30	31	1.03	++
400	5.60	5	3	0.60	++
	5.40	10	8	0.80	+
	5.50	10	6	0.60	+
	6.10	10	8	0.80	+
	5.00	15	10	0.67	-
	5.40	15	12	0.80	-
450	7.60	5	6	1.20	+++
	5.30	15	17	1.13	+++
	7.20	15	20	1.33	+++
	5.10	30	12	0.40	+++

+++ - the coating is deleted only by pickling
++ - insignificant chipping
+ - a lot of chipping

Table 1.2 Coatings Mo/Mo-C obtained in an atmosphere of the residual gases.

Temperature, °C	Pressure, Pa	Exposition τ, min.	Thickness δ, μm	Deposition rate V, μm/min.	Adhesion
350	3.90	15	4	0.27	+++
	10.0	15	4	0.27	++
	12.0	30	10	0.33	+
	11.0	60	16	0.27	-
400	2.80	15	0.5	0.03	-
	3.20	30	1	0.03	-
	3.80	60	5	0.08	-
450	4.00	15	2	0.13	++
	30	3.70	4	0.13	+

Table 2. Parameters of CVD process of coating application.

Sample No.	Sample temperature, ° C	Exposition, min.	Microhardness H_v, kg / μm ^{2}	Thickness δ, μm
23	430	10	2500	15
25	360	10	1800	10
25	290	10	2500	10

Properties of coatings sharply differ in the set temperature interval. At 350°C and 450°C stable uniform deposition of coating with high value of microhardness is observed: HB=2200 at 350°C, HB=1700 at 450°C. The thickness of a coating depends linearly on cure time. The lower temperature, the lower adhesion to the initial sample is observed, while at 450°C the coating has the good adhesion with a carrier.

Deposition rate of the coatings obtained in an atmosphere of the residual vapors at temperature 350°C is even during long enough time intervals; however, quality of a coating deteriorates in process of magnification of coating thickness that is obviously related with accumulation of sufficient internal stresses in a film.

Parameters of CVD-process of coating application on samples made of steel DIN 1.2379 (Х12Ф1) are shown in table 2. After deposition of CVD coating samples were polished with diamond paste ASM7/3 with removal of 0.004-0.006 mm stock up to recovery of flat surface accuracy.

Change of working pressure within 0.01 … 0.1 torr affects Mo/Mo-C composition and leads to inappreciable decrease in adhesion which becomes more appreciable at magnification of a thickness of a coating.

4.2 Metallographic examination

Metallophysics measurements of the obtained samples are carried out on raster-type electronic microscope JSM T-300. Appearance of Mo-C coating on samples made of steel DIN 1.2379 (Х12Ф1) (a traversal metallographic sample) with marked zones of analysis (a) and an approximate chemical composition of analyzed zones (b) is shown in Fig. 1.

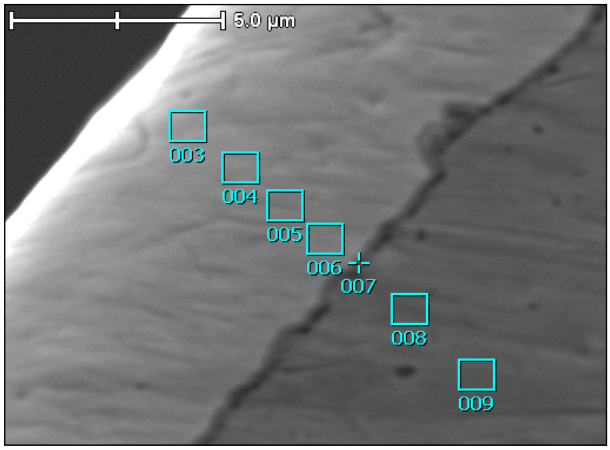

a) DIN 1.2379 (X12Ф1)

Point No.	Si	Cr	Fe	Ni	Mo	P
003					97.0	3.0
004					96.5	3.5
005			2.21		94.79	3.0
006			3.17		94.83	2.0
007		10.13	22.67	9.90	55.31	2.0
008	0.21	6.85	92.13			0.8
009	0.34	7.13	91.73			0.8

b) Chemical composition of analyzed zones.

Fig. 1. Appearance of Mo-C coating on samples made of steel DIN 1.2379 (X12Ф1) with marked zones of analysis (a), and the chemical composition of analyzed zones (b).

Appearance of Mo/Mo-C coating on the sample made of steel DIN 1.2379 (X12Ф1) in a mapping mode is shown in Fig. 2.

Appearance of Mo-C coating on samples made of steel DIN 1.7709 (25X2MФ (ЭИ10)) (a traversal metallographic sample) with marked zones of the analysis (a) and an approximate chemical composition of analyzed zones (b) is shown in Fig. 3.

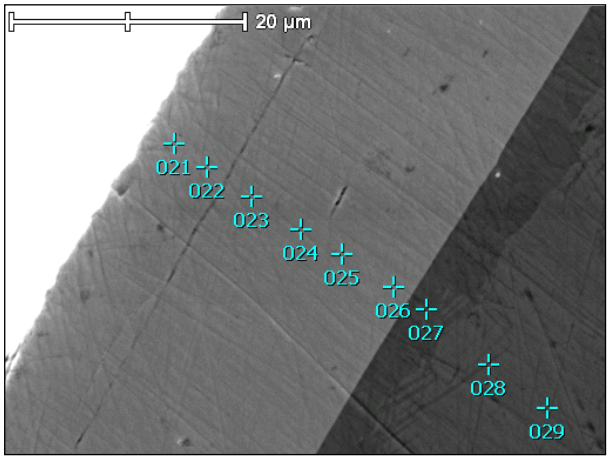

a) DIN 1.7709 (25X2 MФ (ЭИ 10)

Point No.	Si	Cr	Fe	Ni	Mo	C
021				3.40	94.12	2.48
022				3.32	94.01	2.67
023				3.05	95.61	1.34
024				3.40	94.80	1.80
025				3.18	94.64	2.18
026			2.72	1.98	93.69	1.57
027	0.17	1.93	97.69	0.22		
028	0.25	1.88	97.55	0.32		
029	0.27	1.67	97.86	0.19		

b) Chemical composition of analyzed zones.

Fig. 3. Appearance of Mo-C coating on samples made of steel DIN 1.7709 (25X2MФ (ЭИ10)) with marked zones of the analysis (a) and the chemical composition of analyzed zones (b).

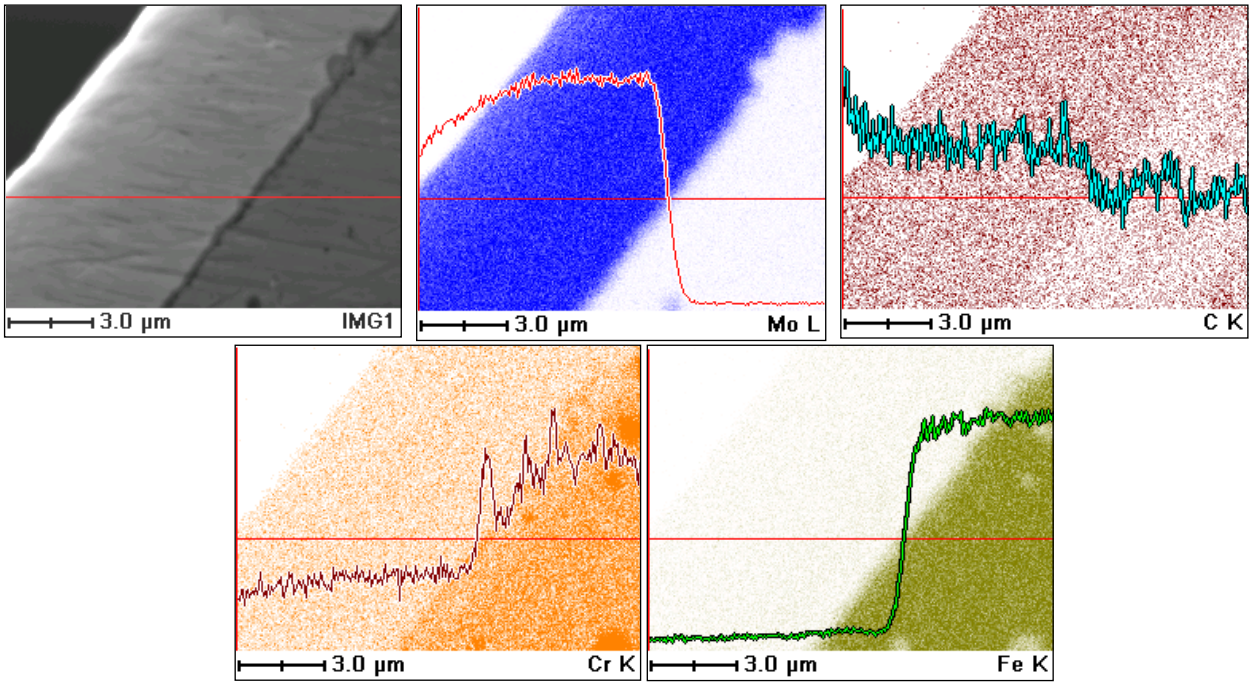

Fig. 2. Appearance of Mo/Mo-C coating on the sample made of steel DIN 1.2379 (X12Ф1) in a mapping mode. More content of the element there matches to more saturated color.

Metallophysics measurements have shown high enough extent of coincidence of phase composition of a carrier material - steels DIN 1.2379 (Х12Ф1) and DIN 1.7709 (25Х2МФ (ЭИ10)) (zones 009 and 029, accordingly).

Photos of a microrelief of coating surfaces are shown in Figs. 4 and 5.

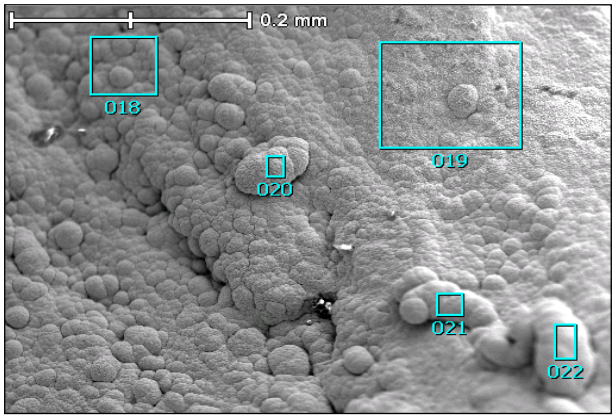

Fig. 4. A microrelief of a surface of the sample (steel DIN 1.7709 (25Х2МФ (ЭИ10)).

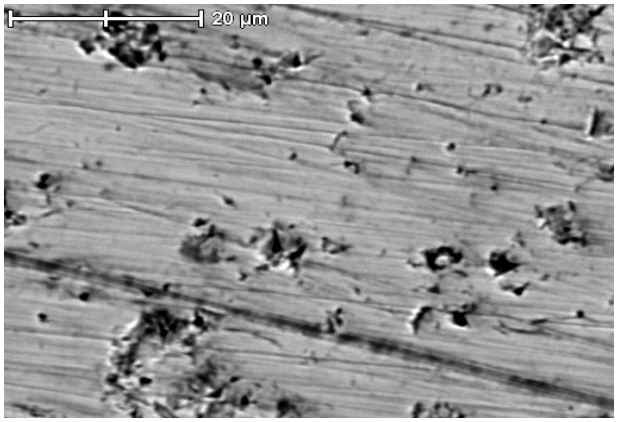

Fig. 5. A microrelief of a surface of the sample (steel DIN 1.2379 (Х12Ф1)) after its polishing.

4.3 Results of tribological tests

Multilayered and microlayer coatings on the basis of Mo-C system are deposited on basic samples - cubes made of steel DIN 1.2379 (Х12Ф1) with hardness 56 … 61HRC (HB~900) with the working planes polished by diamond paste to reach required geometrical parameters (nonflatness - ≤ 0,001mm, surface roughness - R_a 0,08 µm) for carrying out of tribological tests. Parameters of CVD-process of coating application on examined samples and properties of the obtained CVD-coatings are shown in tab. 2. After deposition of CVD coatings samples were polished by diamond paste ASM7/3 with with removal of 0.004-0.006 mm stock up to recovery of flat surface accuracy.

Results of tribological tests are presented in Figs. 6-8 and in Tab. 3.

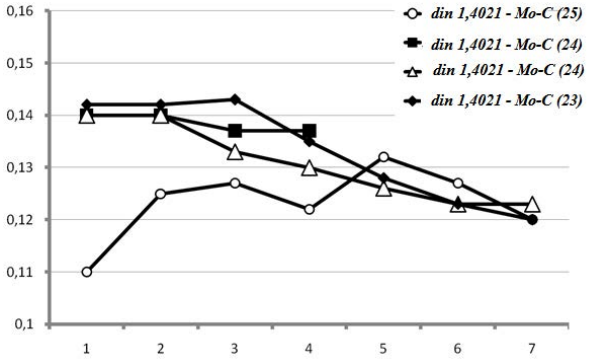

Fig. 6. Dependence of friction coefficient on loads for a friction pair Mo-C/steel DIN 1.4021 20Х3МВФ (ЭИ 415).

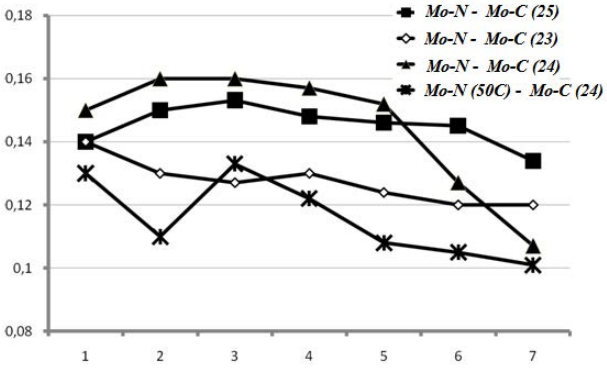

Fig. 7. Dependence of friction coefficient on a loading for a friction pair Mo-C / Avinit coating (on the basis of Mo-N).

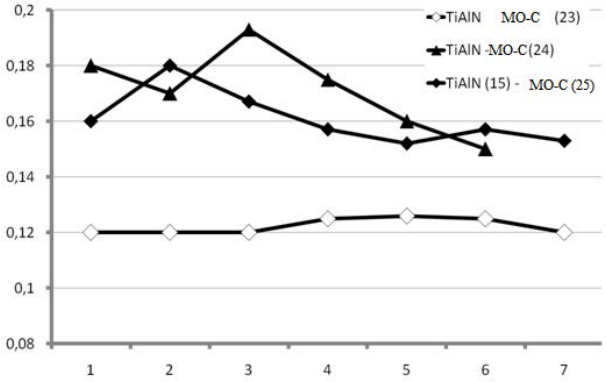

Fig. 8. Dependence of friction coefficient on a loading for a pair of a friction Mo-C / Avinit coating (on the basis of Ti-Al-N).

When carrying out tribological tests, the special priority has been given to studying of behaviour of the developed coatings in tribological matings with steels.

As is clear from the obtained data, and also by results of carried out earlier tribological studying [10, 11], the best tribological parameters in contact pair with steel are determined for Mo-C coatings.

Good tribological properties are exhibited by Mo-C coatings in case of friction in pairs with hard and extremely hard coatings which have been already used in friction pairs of precision units in aircraft aggregate building [10-12].

Table 3. Friction coefficients of samples during tribological tests.

Roller (coating)	Cube (coating)	Applied loading, kN						
		0.2	0.4	0.6	0.8	1	1.2	1.4
Avinit coating (on the basis of Mo-N) δ =1.5 μm, 2200HV	Mo-C (23)	0.14	0.13	0.127	0.13	0.124	0.12	0.12
	Mo-C (24)	0.15	0.16	0.16	0.157	0.152	0.127	0.107
	Mo-C (24)	0.13	0.11	0.133	0.122	0.108	0.105	0.101
	Mo-C (25)	0.14	0.15	0.153	0.148	0.146	0.145	0.134
Avinit coating (on the basis of Ti-Al-N) δ =1.5 μm, 3500HV	Mo-C (23)	scoring						
	Mo-C (24)	0.18	0.17	0.193	0.175	0.16	0.15	
	Mo-C (25)	scoring						
The same *Run in separately*	Mo-C (25)	0.16	0.18	0.167	0.157	0.152	0.157	0.153
The same *Run in separately*	Mo-C (23)	0.12	0.12	0.12	0.125	0.126	0.125	0.12
DIN 1.4021 20Х3МВФ (ЭИ 415), cementation, 88HRC	Mo-C (23)	0.14	0.14	0.143	0.135	0.128	0.123	0.12
	Mo-C (24)	0.14	0.14	0.137	0.137			
	Mo-C (25)	0.11	0.125	0.127	0.122	0.132	0.127	0.12
DIN 1.4021 20Х3МВФ (ЭИ 415), *run in separately*	MoC (24)	0.14	0.14	0.133	0.13	0.126	0.123	0.123

Table 4. Estimate of aging traces on samples after tribological tests.

Mo-C cube (No. 23) δ ≈ 15 μm, 2500HV; After a lapped finishing with diamond paste δ ≈ 10 μm.		
Ή	Roller (coating)	Test results
1	DIN 1.4021 20Х3МВФ (ЭИ 415), cementation, ≥88HRC	The cube has aging traces with parameters (determined using the profilogram): - depth - ≈0.4 μm; - width - 0.6 mm. The roller has a normal aging trace; signs of wear are visually absent.
2	Avinit coating (based on Mo-N) δ =1.5 μm, 2200HV	The cube has aging traces with parameters (determined using the profilogram): - depth - ≈0.5 μm; - width - 0.8 mm. The roller has a normal aging trace, signs of wear are visually absent
3	Avinit coating (based on Ti-Al-N) δ =1.5 μm, 3500HV	The cube has 2 seizure sites which are placed near to ribs of a cube, the main aging trace has following parameters (determined using the profilogram): - Depth - ≈3.4 μm; - width - 1 mm. The roller has two ring furrows which are reciprocal to the seizure sites on the cube
3 a	Avinit coating (on the basis of Ti-Al-N) δ =1.5 μm, 3500HV *Run in separately*	The cube has aging traces with parameters (determined using the profilogram): - depth - ≈1.2 μm; - width - 0.8 mm. The roller has a normal aging trace; signs of wear are visually absent.
Mo-C Cube (No. 24) δ ≈ 10мкм, 1800HV; after a lapped finishing diamond paste δ ≈ 5 μm.		
No.	Roller (coating)	Test results
4	DIN 1.4021 20Х3МВФ (ЭИ 415), cementation, ≥88HRC	The cube has large fretting in width of ≈7 mm The roller has ring traces of cube material transport
5	Avinit coating (based on Mo-N) δ =1.5 μm, 2200HV	The cube has aging traces The roller has a normal aging trace; signs of wear are visually absent.
5a		The cube has aging traces with parameters (determined using the profilogram): - depth - ≈18 μm; - width - 1.8 mm. The roller has a normal aging trace; signs of wear are visually absent.
6	Avinit coating (based on Ti-Al-N) δ =1.5 μm, 3500HV	The cube has aging traces with parameters (determined using the profilogram): - depth - ≈19μm; - width - 1.9mm. The roller has a normal aging trace; signs of wear are visually absent.
6a	DIN 1.4021 20Х3МВФ (ЭИ 415), cementation, ≥88HRC, *run in separately*	The cube has aging traces with parameters (determined using the profilogram): - depth - 0.4 μm; - width - 0.5 mm. The roller has a normal aging trace; signs of wear are visually absent.
Mo-C Cube (No. 25) δ ≈ 10μm, 2000 … 2500HV; after a lapped finishing diamond paste δ ≈ 5 μm.		
No.	Roller (coating)	Test results
7	DIN 1.4021 20Х3МВФ (ЭИ 415), cementation, ≥88HRC	The cube has aging traces with parameters (determined using the profilogram): - depth - ≈0.3 μm; - width - ≈0.5 mm. The roller has a normal aging trace; signs of wear are visually absent.

8	Avinit coating (based on Mo-N) δ =1.5 μm, 2200HV	The coating on a cube inside the trace is visually worn to the carrier. The cube has aging traces with parameters (determined using the profilogram): - depth - ≈4.4 μm; - width - 1 mm. The roller has a normal aging trace; signs of wear are visually absent.
9	Avinit coating (based on Ti-Al-N) δ =1.5 μm, 3500HV	The cube has 2 seizure sites which are placed near to ribs of a cube; flaws on a coating were formed on the same plane of a cube. The roller has two ring furrows which are reciprocal to the seizure sites on the cube.
9a	Avinit coating (based on Ti-Al-N) δ =1.5 μm, 3500HV *run in separately*	Exfoliation of the coating on the given plane of a cube, along aging traces from both its sides, is available, parameters of aging traces (determined using the profilogram): - depth - 19 μm; - width - 2 mm. The roller has a normal aging trace; signs of wear are visually absent.

When friction of cubes with Mo-C coatings over rollers with Avinit coating (on the basis of Mo-N), low enough antifrictional parameters are also observed.

Rollers with extremely hard ***Avinit*** coatings (on the basis of Ti-Al-N) exhibit higher friction coefficients, and there are cases of a scoring of Mo-C coating.

Results of an estimate of aging traces in tested friction pairs after tribological tests are shown in Table 4.

It is noted, that in case of use of already run-in rollers, minimum friction coefficients are obtained, thus cases of a scoring of Mo-C coating are not available.

Carried out tribological tests of Mo-C coatings testify to efficiency of the developed coatings for precision friction pairs («steel/coating» and «coating/coating») with the raised wear hardness and low friction coefficient.

5. CONCLUSIONS

1. Process of application of multilayered Mo-C coatings by a chemical vapor deposition method with use of organometallic compounds is developed. The multilayered composite coatings on the basis of Mo-C system are obtained. Optimization of processes of deposition of qualitative tightly interconnected coatings is carried out.
2. The kinetics of coating deposition process is studied. Coating deposition rate up to 100 μm/hour is obtained.
3. Metallographic examination confirm possibility of the low-temperature deposition of qualitative very hard Mo-C coatings in developed *CVD* process, good adhesion to carrier materials (to steels DIN 1.2379 (Х12Ф1), DIN 1.7709 (25Х2МФ (ЭИ10)) without decrease in strength properties of a steel and without a deterioration of an initial surface finish class is thus provided.
4. Multilayered and nanolayer coatings on samples for tribological tests are obtained and tribological tests of samples with coatings are carried out.
5. Possibility of postoperative machining of coatings by industrial methods without losses of the functional properties of coatings is proven.
6. Tribological tests exhibit high tribological properties of Mo-C coatings and testify to perspectivity of the developed coatings for selection of optimum constructions of coatings for raise of stability of precision friction pairs.

REFERENCES

[1] Ivanov V. E.: Crystallization of refractory metals from vapor phase / [V.E.Ivanov, E.P.Nechiporenko, V.M.Krivoruchko, V.V. Sagalovich]. //M.—Atomizdat.—1974.

[2] Sagalovich A.V. Coating the surface of the figurine-precision gas-phase method (CVD) / [A.V. Sagalovich, V.V. Sagalovich ea.]. // Physical surface engineering.—2011.— v. 9.—№ 3.— P. 229-236.

[3] Powell K.Chemical vapor deposition / [K.Powell, J. Oxley, J. Blocher Jr.]. //Translated from the English//M.—Atomizdat.—1970.

[4] Wen-Cheng J. Wei. Processing and Properties of (Mo, Cr) Oxycarbides from MOCVD / [Wen-Cheng J. Wei, Ming-Hung Lo]. //Appl. Organometallic .—1998.—v. 12.—P. 201–220.

[5] Skudin V.V. Obtaining of membranes using a method of chemical vapor deposition in a reactor with "cold" walls / [Skudin V. V, S. G. Streltsov]. //Crit. Technologies. Membrany. .—2007.—№ 2 (34).— P. 22-33.

[6] Douard A. Reactivity of Cr $(CO)_6$ in atmospheric pressure CVD processes for the growth of various metallurgical coating [Douard A, Maury F.]. //Rev. Adv. Mater. Sci.—2007.—v. 15.

[7] .Sagalovich A.V. ***Avinit*** installation for deposition of multilayered functional coatings [O.V.Sagalovich, O.V.Kononykhin, V.V. Popov ea]. // Physical surface engineering. .—2010.—v. 8.—P. 336-347.

[8] Lyubchenko A.P.. Examination of wear of vacuum-plasma coatings made of TiN at a friction on metal materials / [A.P. Lyubchenko,

A.K.Oleynik, V.M.Matsevity, ea.]. //Friction and wear.—1981.—No. 6.—P. 29-31.

[9] Dudnik S.F.. Examination of friction and wear properties of the ionic-plasma coatings o produced on an aluminium alloy / [S.F.Dudnik, A.V.Sagalovich, V.V. Sagalovich, ea.]. // Physical surface engineering.—2004.—v. 2.—P. 110-114.

[10] .Sagalovich A.V. Examination of tribological properties of multicomponent multilayered coatings of ***Avinit*** type / [A.V.Sagalovich, V.V. Sagalovich, A.V.Kononykhin, etc.]. //Bulletin of KhNARU.—2011.—v. 53.-P. 87-94.

[11] Sagalovych A. The Tribological Investigation of Multicomponent Multilayered Ion-plasma Coatings ***Avinit*** / [A. Sagalovych V. Sagalovych, A. Kononyhin ea.]. //Tribology in industry.—2011.—v. 33.—No. 2.-P. 79-86.

[12] Sagalovych A. Experimental research of multicomponent multilayer ion-plasma Avinit coatings / [A. Sagalovych V. Sagalovych, A. Kononyhin ea.]. // Physical surface engineering. .—2012.—v. 10.—P. 136-148

Tribology of Machine Elements

13th International Conference on Tribology – SERBIATRIB '13

15 – 17 May 2013, Kragujevac, Serbia

Serbian Tribology Society

SERBIATRIB '13

13th International Conference on Tribology

Faculty of Engineering in Kragujevac

Kragujevac, Serbia, 15 – 17 May 2013

EQUILIBRIUM STATE FORMATION FEATURES OF SURFACE LAYERS OF MACHINE PARTS

Vyacheslav F. Bezjazychnyj, Alexander N. Sutyagin
Federal State-Financed Educational Institution of High Professional Education "P. A. Solovyov Rybinsk State Aviation Technical University", Rybinsk, Yaroslavl region, Russian Federation,
e-mail: technology@rgata.ru

Abstract: *The article describes the problem of forming the equilibrium state of surface layer of friction units. The possibility of taking into account the parameters of the lubricant in the mathematical model of the relationship of the wear rate with the equilibrium parameters of surface layer of parts is considered. Possibility of technological support equilibrium parameters of surface layer of machine parts is discussed.*

Keywords: *friction, wear rate, surface layer, machining, quality parameters, equilibrium state.*

1. INTRODUCTION

Practice of exploitation of machines and mechanisms shows that one of the major causes of failures of various kinds of equipment is the destruction of its parts or wear. Destruction and wear usually begins with working surfaces, so the state of the last often becomes the dominant factor in determining the reliability and durability of manufactured equipment.

Study the wear of machine parts friction units indicate that the transition to the normal process of wear most of them are directed to change their initial geometry.

During the break-in such quality parameters of machine parts undergo significant changes as profile deviation, waviness, roughness of their surfaces, as well as the physical and mechanical characteristics of the surface layer. If time and the wear are large enough, the stable steady state is reached tribosystem when the geometry of parts surfaces becomes conformal.

2. THE STUDIED PHYSICAL MODEL

Research the wear can provide a theoretical justification of the possibility of existence of stable reproducing geometric shapes of surfaces and their physical and mechanical properties in wear process in the given conditions of relative motion and loading.

This rationale is based on the fundamental principles of thermodynamics of dissipative systems, which tribosystem are.

Such systems can exchange with other systems and the environment energy and mass (eg, mass worn out particles), so stationary states characterized by a constant gradient of entropy can occur

$$\Delta S = S° - S = \text{const}, \quad (1)$$

where S°– entropy of the equilibrium state of the system; S – instantaneous entropy of the system.

In the steady state, all the processes of heat and mass transfer are independent of time, as determined by the configuration of the system only in general terms and conditions on its borders.

Tribosystem exhibit properties of self-organization consist of to consistently reproduce the macroscopic space-time structures that can exist only through the exchange of flows of energy (matter).

Under self-limitation created by nature, as tribosystem located on the border of artificial devices and natural systems, and the self-organization can arise from a chaotic state, that is, the initial conditions do not matter, and the running-in period, of course, increases and decreases life of the friction units.

The equilibrium state of the surface is determined by the minimum of its free energy, which may differ from the minimum of surface,

which is responsible for one of the reasons for the deviation of the real surface of the crystal from the initially smooth and the emergence of so-called natural roughness [3]. Such modifications of surface geometry are sub roughness, which significantly exceeds the atomic scale roughness arising at vibrations of the atoms or molecules due to thermal fluctuations.

The most appropriate criterion for selecting materials for the parts of tribosystems can be taken minimum value of frictional work [4].

Friction work calculated by the formula [5]

$$W_{fr} = fFS_{fr}, \quad (2)$$

where F – normal force of friction pair elements interaction; f – a friction coefficient; S_{fr} – friction track.

Tribosystem are open thermodynamic systems that exchange energy and matter with the environment. Friction is the process of converting the external mechanical energy into internal energy in the form of vibration and wave motion of particles of tribosystem followed by thermal, thermionic, acoustic, and other phenomena. Most of this energy is converted into heat and is given to the environment, the other - is to change the physical and chemical state of the surface layers of the material. Dissipation of energy corresponds to an increase of entropy ($dS > 0$).

Energy balance of tribosystem according to the first law of thermodynamics describes by the equation.

$$W_{fr} = q + \Delta W. \quad (3)$$

where q – energy of heat exchange with the environment, ΔW – change of internal energy is the sum of the energy used to change the structure of the material and energy of heating.

At the same time, the work of the friction force is the sum of the work of plastic deformation, hysteresis loss and the elastic deformation of the dispersion, that is, the work expended in the formation of new surfaces and associated with the surface energy of solids [6, 7].

The basis of the thermodynamic approach to fracture and wear of solids is energy mechanical analogy (deformation) and thermal (melting and sublimation) of failure.

The energy spent on the deformation and fracture of solid bodies, compared with one of the thermodynamic characteristics of the material (heat of sublimation enthalpy of the solid and liquid state, latent heat of fusion). In this case, it is assumed that thermodynamic properties are independent of the structure of the material. The body is treated as a continuous, homogeneous, isotropic medium with a statistically uniformly distributed structural elements.

Plastic deformation is considered as a combination of a large number of acts of microscopic atomic-molecular rearrangements associated with the generation of sources of deformation (dislocations).

Plastic deformation of the surface temperature below the recrystallization temperature leads to work hardening of the surface layer and its strengthening. At widely differing hardness structural components of the material and repeated exposure of loading occurs initially high wear of soft base; specific pressures acting on the solid component thereby increasing, solid components are pressed into a soft base, some of them are broken up and moved further under the forces of friction. As a result of such selective wear surface enriched solid structural components and gets stitch structure that during wear of babbit, for example, according to research of M. M. Khrushchov and A. L. Kuritsyna [8].

As a result of the interaction of the interfaced parts new surfaces are formed, which is followed by the energy release, γ_{ef}, consumed for its forming [6]:

$$\gamma_{ef} = f(F, Rz, HV), \quad (4)$$

where F – the normal force of friction pair elements interaction; Rz – ten point height of irregularities [9].

Rough surface can be considered as a set of irregularities randomly located on a perfect surface and having a random size, in other words, as the realization of the random field. This approach makes it possible to represent the surface as a scalar random function [10]

$$z = z(t, \omega), \quad (5)$$

where the parameter t runs through the set of values of T, defined by the spatial arrangement of the rough surface; ω – elementary event of a probability space Ω.

To determine the surface characteristics required for calculations in tribology, often enough knowledge only first two derivatives of the function $z(t, \omega)$. Thus there is a need to calculate the density of the joint distribution of several random variables.

Quantify the contact of rough surfaces is an important step in the development of physical models of frictional interaction. It requires consideration of both the characteristics of the roughness, and the specific properties of the contacting bodies, depending on their internal structure, loading time and environmental conditions.

Most of the friction units of products used in engineering works in conditions of oiling This requires a comprehensive study of processes in the area of friction as lubricant in some way facilitates extraction of heat from the friction contact zone, the removal of the zone of wear and corrosion protection, and the protection of the friction surfaces and other structures from the effects of the environment and also seal gaps, etc.

Taking into consideration that expression, V_W / S_{fr} (V_W – the volume of the worn material, S_{fr} – the friction track) represents the value of the wear rate J_V [11], and changing of an inner energy is determined by the formula of specific energy of deformation ΔW accumulated in the material as a result of dislocation forming [12]

$$\Delta W = f\left(HV, HV_0, \alpha_0, G\right), \qquad (6)$$

where G – a displacement module of an examined material; α_0 – a parameter of interdislocation interaction; HV – a microhardness of a surface layer of an examined part at the specified depth; HV_0 – a microhardness of a undeformed material; based on energy-based approach to the problem of defining the relationship of the wear rate of work surfaces of machine parts with quality parameters of the surface layer the wear rate functional relationship with geometrical (roughness) and physico-mechanical (degree of work hardening) parameters of surface layer of machine parts during normal operation can be represented a

$$J_V = \frac{0{,}55FG(0{,}9\, f\pi S_{fr} Rz_{bal}\sigma_{0,2} + 4F)\exp(200/T)}{\pi S_{fr} Rz_{bal} N_{bal}^2 HV_0^2 \sigma_{0,2}} \qquad (7)$$

where J_V – the wear rate [m^3/m]; F – the normal force of friction pair elements interaction [N]; f – a friction coefficient; S_{fr} – the friction track [m]; Rz_{bal} – the balanced roughness of the interfaced surfaces of the components [m]; $\sigma_{0,2}$ – the yield strength conditional with the tolerance of 0,2% for the value of the plastic deformation at stressing [Pa]; T – the temperature in friction area [K]; N_{bal} – the balanced degree of hardening; HV_0 – a microhardness of a undeformed material [Pa].

3. CONCLUSION

On the basis of [13] can be defined relationship equilibrium parameters of surface layer parts with machining process parameters.

The analysis of the experimental research results of the wear rate of contacted surfaces after machining has shown that the received mathematical model of the correlation between the wear rate and the technological requirements of machining allows for calculating the wear rate of the interfaced machine components after the running-in period.

REFERENCES

[1] A. G. Suslov, A. M. Dalsky: *Nauchnye osnovy tehnologii mashinostroenija* (Scientific Basis of Mechanical Engineering), - Mashinostroenie, Moscow, 2002.

[2] A. V. Chichinadze, E. D. Brown, N. A. Boucher: *Osnovy tribologii (trenie, iznos, smazka)* (Fundamentals of tribology (friction, wear and lubrication)), - Mashinostroenie, Moscow, 2001.

[3] V. S Kombalov: *Ocenka tribotehnicheskih svojstv kontaktirujushhih poverhnostej* (Evaluation of tribological properties of contacting surfaces), - Nauka, Moscow, 1983.

[4] V. I. Butenko: *Struktura i svojstva poverhnostnogo sloja detalej tribosistem* (Structure and properties of the surface layer of parts tribosystems), - Taganrog: TTI UFU, 2012.

[5] U. N. Drozdov, V. G. Pavlov, V. N. Puchkov: *Trenie i iznos v jekstremalnyh uslovijah: Spravochnik* (Friction and wear in extreme conditions: Reference), - Mashinostroenie, Moscow, 1986.

[6] V. N. Kashcheev: *Processy v zone frikcionnogo kontakta metallov* (Processes in the area of frictional contact metals), - Mashinostroenie, Moscow, 1978.

[7] V. Weibul: *Ustalostnye ispytanija i analiz ih rezultatov* (Fatigue testing and analysis of the results), - Mashinostroenie, Moscow, 1964.

[8] I. P. Sukharev: *Prochnost sharnirnyh uzlov mashin* (The strength of hinged machine units), - Mashinostroenie, Moscow, 1977.

[9] Russian State Standard 25142-82, 1988, *Sherohovatost poverhnosti. Terminy I opredelenia*. (Surface roughness. Terms and definitions), publishing company of State Standards, Moscow.

[10] A. I. Sviridyonok, S. A. Chijik, M. I. Petrokovets: *Mehanika diskretnogo frikcionnogo kontakta* (Mechanics of discrete frictional contact), - Minsk, 1990.

[11] Russian State Standard 27674-88, *Trenie, iznashivanie i smazka. Terminy i opredelenija*, Moscow, 1988.

[12] V. F. Bezjazychnyj, A. N. Sutyagin: *Tehnologicheskoe obespechenie iznosostoikosti detalei mashin na osnove izucheniya nakoplennoi energii v poverhnostnom sloe detali pri deformacionnom uprochnenii pri obrabotke* (Machine components wear resistance technological assurance based on analysis of accumulated energy of part surface layer while strain hardening during the machining), *Uprochnyauschie tehnologii i pokrytiya*, 7, pp. 3-6.

[13] V. F. Bezjazychnyj: *Metod podobija v tehnologii mashinostroenija* (Method of Similarity in mechanical engineering), Mashinostroenie, Moscow, 2012.

Serbian Tribology Society

SERBIATRIB '13

13th International Conference on Tribology

Faculty of Engineering in Kragujevac

Kragujevac, Serbia, 15 – 17 May 2013

THE INVESTIGATION OF COATED TOOLS TRIBOLOGICAL CHARACTERISTICS INFLUENCE ON THE CUTTING PROCESS AND THE QUALITY PARAMETERS OF THE PARTS SURFACE LAYER

Fomenko Roman Nikolaevich
FSBEIHPE «Rybinsk State Aviation Technical University» named after P.A. Solovjev (RSATU), Russia,
fomenko85@mail.ru

Abstract: *The influence of cutting tools nanostructured coatings on the parameters of machined parts surface layer has been researched. The interaction between friction characteristics of coated tools and shear plane angle during machining has been determined. The results of different materials cutting with coated carbide-tipped tools have been shown.*

Keywords: *nanostructured coatings, quality parameters of the surface layer, tools friction coefficient*

1. INTRODUCTION

The most important production properties are reliability and endurance. These properties provide product safety and competitiveness. The main cause leading to breakdown of parts is fatigue cracks. Such cracks appear and propagate in thin surface layers of parts. In order to hamper crack growing, the surface layer has to exhibit certain features. They are: roughness, residual stress and strain hardening, which depend on the characteristics of cutting operation.

The cutting force, temperature of cutting, depth of wear hardening and degree of deformation are referring to the main characteristics of cutting operation. These characteristics influence on the parts quality, reliability and endurance. Technological conditions of cutting such as tools geometry, processing conditions, work material properties and tooling material properties, including tribological feathers, determine the characteristics of cutting process. Therefore there is a need to select optimal cutting conditions to provide the requirement parts quality. In order to select optimal cutting conditions, there is necessity to have a special methodic, which takes into consideration the relationship between parts quality and technological conditions.

2. TASKS OF RESEARCH

At the Rybinsk state of aviation technical university named after P. A. Solovjev (Russia) there was developed the methodic, which permit to estimate the optimal cutting conditions. On the base of this methodic underlay a functional connection between cutting rate, tools geometry and the parameters of surface layer, accuracy of machining and the rigidity of manufacturing system, including work material and tool material properties.

But all advanced tools have wear-resistant coatings that exhibit specific properties. Wear-resistant coatings have low friction coefficient in consequence of weak adhesion interaction of covering material with work material. They influence on the cutting process and quality parameters of the surface layer. Tools coverings reduce chips contact length with tools surface, cutting force, temperature of cutting and deformation of cut allowance. It causes due to increasing of a chip flow angle.

Thus the main purpose of research was the creation of the methodology for calculation of technological conditions of turning, which provides required quality and accuracy levels at the stage of machining and takes into consideration the tribological properties of coated tools.

In order to provide both high parts quality and maximum tools life one should calculate so called «optimal cutting speed» v_O. Optimal cutting rates (v_O, S_O) correspond to the optimal cutting temperature. It is constant magnitude for the define combination work – tool material [1]. When machining with this temperature, maximum tools lifetime, minimal roughness of machined surface *Ra*, minimal amount of surfaces defects have been occurred. Therefore these cutting rates should be used, when finishing work was performed for parts, which work in corrosive medium and high temperature, because the surface layer has to contain minimal amount of defects. For estimating of the optimal cutting speed the equation is obtained by prof. Silin S. S. [1]:

$$v_O = \frac{C_O \cdot a}{a_1}\left(\frac{a_1 \cdot b_1 \cdot c\rho \cdot \theta}{Pz_{\min}}\right)^n, \qquad (1)$$

where a_1, b_1 – is the thickness and the width of cut respectively [m]; a – is the coefficient of the temperature conductivity of the work material [m^2/s]; cρ – is the specific heat capacity per unit volume [$J/(m^3 \cdot s \cdot degree)$]; θ – is the temperature in the cutting area, °C; n, C_o – are coefficients, which depend on the properties of work material; $Pz_{\min}$ – is a minimal stabilized cutting force [N].

But very often there is a need to select a cutting condition, which differs from the optimal ones. Therefore the opportunity to estimate the technological conditions of turning with taking into consideration the tribological properties of coated tools, will provide the required quality and service properties of parts at the stage of machining.

The analysis of the mathematical models for estimating of the parameters of cutting process and quality of the surface level has shown, that the more important variable quantities are the shear plane angle β_1 and the adhesive component of the friction coefficient f_M. Thus the main tasks of the scientific research were:

1. To investigate the influence of tribological characteristics of coated tools on cutting process and the parameters of surface layer.
2. To define optimal cutting speed for tools with different coatings.

3. EXPERIMENTAL CONDITIONS

The wide range of cutting rates, different work materials and coated tools were selected for performing of experiments (Table 1).

In the capacity of tools were used the replaceable inserts 120412, material – VK6R (chemical composition: Co – 6%, basis – WC) and TT7K12 (chemical composition: Co – 12%, TiC – 1 %, TaC – 7%, basis – WC). The different composite nanolaminated ion-plasmous coatings were deposited on the replaceable inserts: (Ti;Si)N, (Ti,Si,Zr)CN and (Ti;Si;Al)N. Other group replaceable inserts was modified by implanting of nanoparticle TiB_2, Al_2O_3, Ta_2O_3 and ZrB_2 in work surface of tools. All selected coatings have been characterized by the minimal adhesive of the tools surfaces with work material, and also they have been provided maximum tools lifetime. The machining was performed by the regular engine lathe NH 22. The temperature was measured by means of a dynamic thermocouple of work material – tooling material. The normal component of a cutting force *Pz* was measured by using the tool dynamometer Dyna-Z, which was connected with personal computer (Figure 1). The tool dynamometer Dyna-Z is a self-sufficient measurement system, which can use without an additional power source, a tensometric station and DAQ board. And a precision measured signal can be shown and saved in a very useful for operator form [3].

Table 1. Experimental conditions

Changing parameters		Work material				
		Heat-resistant alloy (CrNi77TiAlW) EI437		Stainless steel (05Cr12Ni2Co3Mo2WV) EK26		Titanium alloy OT4
Tools geometry	Cutting angle, γ°	5		8		0
	Relief angle, α°	10		12		10
	Lead angle, φ, φ_1°	45				
	Nose radius, *r*, [mm]	1,2				
Cutting rate	Deph *t* [mm]	0,25; 0,5; 0,75; 1				
	Feed *S* [mm/rev]	0,07; 0,14; 0,2; 0,32				
	Speed *v* [m/min]	14-170		33-190		15-130
Tool material – carbide material		VK6R	TT7K12	VK6R	TT7K12	VK6R
Nanostructured coating		(Ti,Si)N	Ta_2O_3	(Ti,Si)N	Ta_2O_3	(Ti,Si)N
		(Ti,Si,Al)N	ZrB_2	(Ti,Si,Al)N	ZrB_2	(Ti,Si,Zr)CN
		TiB_2		TiB_2		ZrB_2
		Al_2O_3		Al_2O_3		Al_2O_3

Fig. 1. The dynamometer Dyna-Z

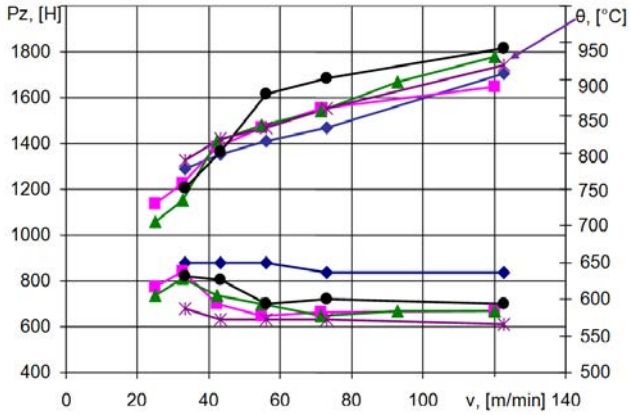

Fig. 2. The dependence of a cutting force and temperature on cutting conditions and tools cover; work material – Stainless steel EK26; Tool material – carbide material VK6R; tools geometry: $\varphi = \varphi_1 = 45°$, $\gamma = 8°$; $\alpha = 7°$, r = 1,2 mm; cutting rate: t = 1 mm; S = 0,32 mm/rev; nanostructured coatings of tool: VK6R (without cover); (Ti; Si)N; (Ti; Si; Al)N; TiB2; Al_2O_3.

4. RESULTS AND DISCUSSION

The experimental data of machinability investigation has been shown, that a cover of tool can reduce a temperature θ in a cutting area on 50-70 °C, and a cutting force *Pz* can be reduced on 10-30% (Figure 2).

Thus on the base of obtained power dependences, one can make an equation of machinability to estimate of optimal cutting speed v_O for different combination work material – coated tool. The equations of machinability for considered examples have been given on Table 2.

The optimal cutting speed of coated tool exceeds the optimal cutting speed of uncoated tool. Then fewer the coatings friction coefficient, then bigger optimal cutting speed.

In order to estimate the influence of coated tools on the parameters of surface layer, one have to determine the influence of coated tools on a shear plane angle β_1 or a criterion *B*. This criterion is one of the major parameter, which used for estimating of roughness, residual stress and strain hardening in the parts surface layer.

$B = \text{tg}\ \beta_1$ – Is the quantity, which defines the degree of allowance plastic deformation and the deformation of parts surface layer.

The quantity β_1 was estimated by means of Tim's I. A. formula using a chip reduction coefficient k_a, which was determined experimentally [1].

$$k_a = \frac{\cos(\beta_1 - \gamma)}{\sin \beta_1}, \qquad (2)$$

where γ – is a cutting angle.

Figure 3 shows the dependence of criterion *B* on the technological conditions of operation.

Table 2. The equations of machinability.

Materials	VK6R–EK26	VK6R–EK26–(Ti,Si)N	VK6R–EK26–Al_2O_3
Equation of machinability	$v_O = \frac{2{,}31 \cdot a}{a_1}\left(\frac{a_1 \cdot b_1 \cdot c\rho}{t^{0,77} \cdot S^{\frac{0,72}{t^{0,083}}}}\right)^{2,47}$	$v_O = \frac{2{,}76 \cdot a}{a_1}\left(\frac{a_1 \cdot b_1 \cdot c\rho}{t^{0,68} \cdot S^{\frac{0,766}{t^{0,106}}}}\right)^{2,48}$	$v_O = \frac{4{,}76 \cdot a}{a_1}\left(\frac{a_1 \cdot b_1 \cdot c\rho}{t^{0,737} \cdot S^{\frac{0,695}{t^{0,044}}}}\right)^{2,53}$
Friction coefficient f_M θ = 800 °C	0,44	0,35	0,16
v_O [m/min], cutting rate t = 1 [mm]; S = 0,32 [mm/rev]	56	64	102

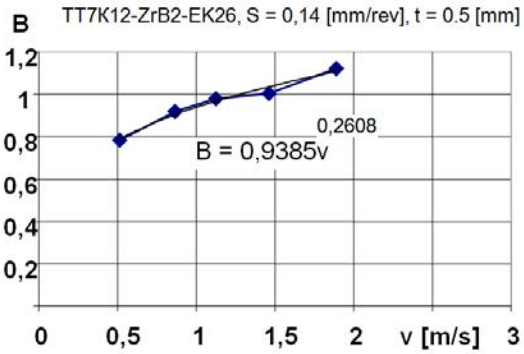

Fig. 3. The comparison the criterion B and technological conditions of operation; Work material – the stainless steel EK26, tool – TT7K12, coating – ZrB_2.

It is clearly shown, that in the time of increasing of cutting speed *v* the criterion *B* increases too. It is the reason for increasing of an angle of shear plane β_1. The angle of shear plane β_1 increases, because the materials ultimate stress σ_B reduces by reason of increasing of rate of deformation and temperature in the cutting area.

On the base of experimental research the influence of different technological conditions on the criterion *B* has been obtained. The quantity of shear plane β_1 of coated tool increases approximately on 5-10 %. But experimental equations are limited by technological conditions of experiments and couldn't be used for other conditions or other covers of tool. Therefore the methodology for estimating of a criterion B for other covers of tool has been developed. This methodology is based on the taking into consideration adhesive component of the friction coefficient f_M of coated tool.

For determination of the friction coefficient two approaches were used. According to the first approach, friction coefficient μ^F was determined as a ratio of a tangential force to a normal force of cutting:

$$\mu^F = \frac{F_{\tan}}{N} = \frac{\overline{Py} + \overline{Px}}{Pz} = \frac{Py \cdot \cos\varphi + Px \cdot \cos(90 - \varphi)}{Pz}, \quad (3)$$

where μ^F – friction coefficient; *Py*, *Px*, *Pz* – components of a cutting force, [H]; F_{tan} – tangential force to a cutter face, [H]; *N* – normal force to the cutter face, [H]; *Py* – radial component of a cutting force, [H]; *Px* – axial component of a cutting force, [H].

On the figure 4 the dependence of criterion *B* and friction coefficient μ^F on a dimensionless complex $Pe = \frac{v \cdot a_1}{a}$, which defines the technological conditions of operation, has been shown.

The comparison of curves on the figure 4 permits to create the proportion:

$$B_2 = \frac{\mu_1^F \cdot B_1}{\mu_2^F} \quad (4)$$

The magnitude of unknown criterion B_2 can be approximately estimated if the magnitudes of criterion B_1 and friction coefficients μ_1^F, μ_2^F which correspond to the tools with different coatings, are known. But the determination of the friction coefficient μ^F according to the first approach doesn't take into consideration the temperature in the cutting area.

The second approach has 'not this shortcoming. According to the second approach for determination of the friction coefficient the adhesiometer was used (figure 5). It is known, that the friction coefficient:

$$f = f_D + f_M, \quad (5)$$

where f_D – deformation component of the friction coefficient; f_M – adhesion (molecular) component of the friction coefficient:

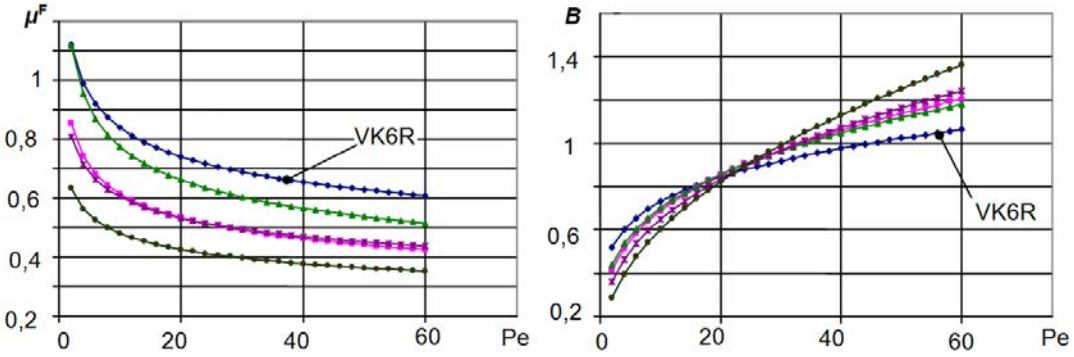

Fig. 4. The dependence of criterion *B* and friction coefficient μ^F on a dimensionless complex Pe; work material – Stainless steel EK26; tool material – carbide material VK6R; nanostructured coatings of tool: VK6R (without cover); (Ti;Si)N; (Ti;Si;Al)N; TiB_2; Al_2O_3

$$f_M = \frac{3}{4} \cdot \frac{F \cdot R}{N \cdot r}, \qquad (6)$$

where R – radius of the disc, [m]; r – radius of the impress on the sample, [m]; N – normal force, [H]; F – peripheral force on the disc, [H].

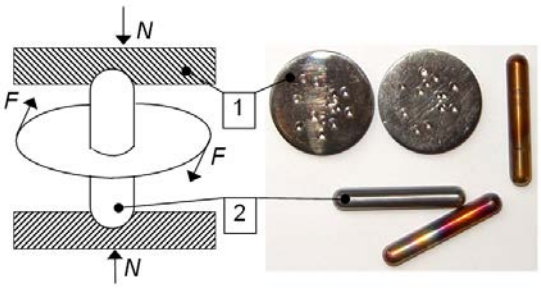

Fig. 5. The flow chart of one-ball adhesiometer; 1 – samples of the work material; 2 – indenter of the tool material; N – normal force, which impress the indenter [H]; F – peripheral force, which roll the disc, [H].

Figure 6 shows the friction coefficient, which was determined for different temperatures and combinations of work materials – coated indenter (pin).

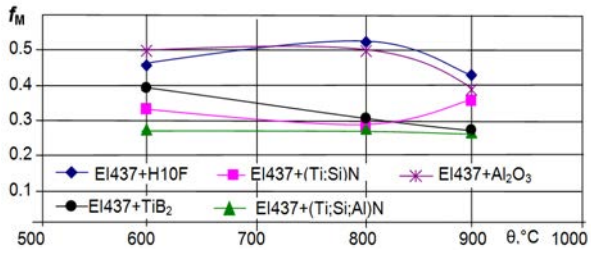

Figure 6. The influence of the temperature on a friction coefficient; work material – heat-resistant alloy EI437; tool material – carbide material H10F; nanostructured coatings of indentor: H10F (without cover); (Ti;Si)N; (Ti;Si;Al)N; TiB_2; Al_2O_3.

Thus if the magnitude of the criterion B_1 of cover 1 and the functions of friction $f_M = f(\theta)$ of cover 1 and 2 like the dependence of friction coefficient on the temperature θ are known, the magnitude of a unknown criterion B_2 of cover 2 can be approximately estimated by means of correcting coefficient:

$$k = \frac{f_M^{cover1}}{f_M^{cover2}} \qquad (7)$$

where f_M^{cover1}, f_M^{cover2} – adhesion component of the friction coefficient of work material with cover 1 and 2.

On the base of obtained results of experiments the methodology for calculation of technological conditions of turning, which provides required quality and accuracy levels at the stage of machining and takes into consideration the tribological properties of coated tools, has been developed. The methodology can estimate technological conditions of turning and solve an inverse task – it can estimate roughness, residual stress and strain hardening. The algorithm for calculation of required technological conditions of turning was implemented in the software (figure 7).

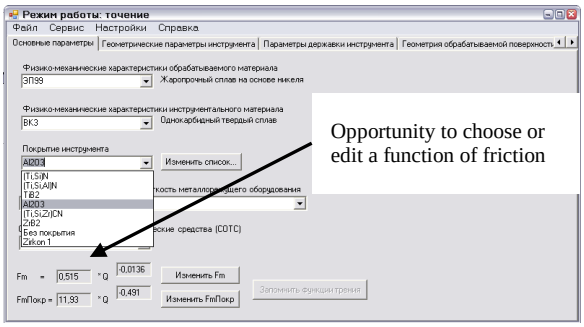

Fig. 7. The software for calculation of required technological conditions of turning.

In order to check the obtained mathematical models, the comparison of the experimental and calculated data was performed. The investigation of the parameters of surface layer has been performed on the machined parts "ring". The conditions of turning of the parts "ring": work material – stainless steel EK26; tool material – carbide material VK6R; tools geometry: $\varphi = \varphi_1 = 45°$, $\gamma = 8°$; $\alpha = 7°$, r = 1,2 mm; cutting rate: t = 0,75 mm; S = 0,2 mm/rev; nanostructured coatings of tool: (Ti;Si)N; (Ti;Si;Al)N.

The results of experiments (Table 3) have been clearly shown, that coated tool reduces the magnitude of the roughness, residual stress and strain hardening in according with the magnitude of friction coefficient. The calculation of the parameters of the surface layer was performed by means of mathematical models presented in [2] and software. The parameters of the roughness *Ra* and *Rz* reduce on the average 5 %, therefore the main cause leading to the formation of the roughness are tools geometry, feed rate, vibration and so on, but not the cover of tool. The strain hardening reduces on 20 % as compared with uncoated tool.

In order to check our obtain data we have compared the experimental and calculated distribution diagrams of tangential residual stress. The using of coated tool leads to the considerable reduces of adverse tensile residual stresses.

The distribution diagrams of the tangential residual stress are shown on a Figure 8.

Table 3. Experimental and calculated value of strain hardening h_C and parameters of the roughness *Ra* and *Rz*.

Cover	Calcul.	Exper.	Δ, %	Calcul.	Exper.	Δ, %	Calcul.	Exper.	Δ, %	Criterion B
	Ra, mkm			Rz, мкм			h_C			
VK6R	1,84	1,42	29	8,4	6,8	23	37	50	26	0,95
(Ti;Si)N	1,53	1,35	13	7	6,3	11	34	40	15	1,02
(Ti;Si;Al)N	1,64	1,34	22	7,5	5,8	29	35	40	13	1,01

The experimental distribution diagrams of the tangential residual stress were performed by means of methodology of layer-by-layer electrochemical etching. The using of coated tool leads to the considerable redaction of adverse tensile residual stress and its depth, the calculated data correlate with the experimental ones.

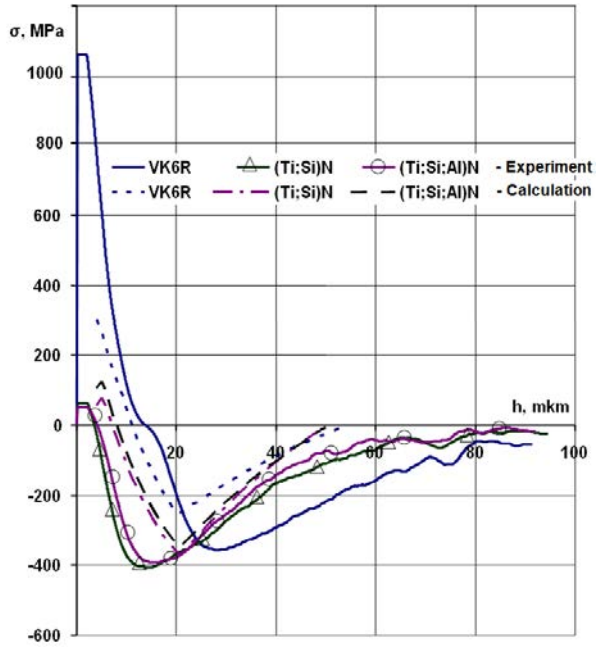

Fig. 8. The distribution diagrams of the tangential residual stress of machined part.

5. CONCLUSION (TIMES NEW ROMAN 11 PT) - ALIGN LEFT

1. The optimal cutting speed of coated tool exceeds the optimal cutting speed of uncoated tool; then less the coatings friction coefficient, then more optimal cutting speed.

2. The using of coated tool leads to the considerable redaction of adverse tensile residual stress and its depth.

REFERENCES

[1] S. S. Silin: *Similitude method of cutting*, Manufacturing, Moscow, 1979.

[2] V. F. Bezjazichnij: *The method of similarity in manufacturing engineering*, Manufacturing, Moscow, 2012.

[3] http://ooo-technolog.ru/

Serbian Tribology Society

SERBIATRIB '13

13th International Conference on Tribology

Faculty of Engineering in Kragujevac

Kragujevac, Serbia, 15 – 17 May 2013

MODELING SURFACE ROUGHNESS EFFECTS ON PISTON SKIRT EHL IN INITIAL ENGINE START UP USING HIGH AND LOW VISCOSITY GRADE OILS

Mubashir Gulzar[1], S.Adnan Qasim[1], Riaz A Mufti[1]

[1]College of Electrical and Mechanical Engineering, National University of Sciences and Technology (NUST), Pakistan, mubashir_nustian@hotmail.com

Abstract: *The absence of fully developed fluid film lubrication between Piston and Liner surfaces is responsible for high friction and wear at initial engine start-up. In this paper flow factor method is used in two dimensional Reynolds' equation to model the effects of surface roughness characteristics on Piston Skirt elastohydrodynamic lubrication. The contact of surface asperities between the two surfaces and its after effects on EHL of piston skirt is investigated. For this purpose, two different grade oils are used to show the changing effects of viscosity combined with surface roughness on different parameters including film thickness, eccentricities and hydrodynamic pressures. The results of the presented model shows considerable effects on film thickness of rough piston skirt, hydrodynamic pressures and eccentricities profiles for 720 degrees crank angle.*

Keywords: *EHL, Piston Skirt, flow factor, asperity, hydrodynamic, Vogelpohl parameter*

1. INTRODUCTION

In initial engine start-up the piston and liner surfaces are not separated by an oil film which causes maximum wear and friction between the two sliding surfaces. The effects of physical contacts between the asperities of surfaces which are in relative motion must be included in lubrication model to get a better understanding of rheology.

Hamilton, Wallowit and Allen [1] were the pioneer for taken into account the roughness effects on lubrication phenomenon and their work dates back to 1966.They developed a theory of hydrodynamic lubrication between two parallel surfaces with surface roughness on one or both of the surfaces. The classical theory of lubrication does not predict the existence of any pressure in case of sliding flat parallel surfaces. Surface roughness helps in the pressure buildup between the two interacting surfaces, so provide a load support and avoid collapse of two bodies. Early research integrated the roughness amplitude with the film thickness and developed the modified one dimensional Reynolds's equation but the presented models did not cover different regimes and asperity contacts and limited to one dimensional changes. In this prospective an exception is given in 1978 and 1979 by Patir and Cheng [2][3]. Since the contacting surfaces have an inherent roughness, so Lambda Ratio or Tallian Parameter will be used as the defining parameter between different lubrication regimes [4]. In recent research the film thickness parameter (λ) range has been investigated and redefined for different lubrication regimes [5]. The P.C. model was suitable for values of film thickness ratio $\lambda > 3$ 1.e; full film lubrication regime where asperity contacts were neglected [6][7].To minimize the wear and friction losses the elastohydrodynamic lubrication (EHL) model is presented where λ is much lesser than a value of 3 [5]. Thus the flow factor model provided by J.H. Tripp [8] is numerically modelled for hydrodynamic lubrication at initial engine start-up. Greenwood-Tripp asperity contact model is used to incorporate the asperity contact forces and asperity contact friction force in EHL between the sliding surfaces [9]. To incorporate the directional behaviour the Peklenik number [10] is defined for the rough surfaces which are generated by normal distribution using Fast Fourier Transform (FFT)[11][12]. Here isotropic surface roughness property is used.

For developing the numerical model following assumptions are taken:

1. Lubricant is incompressible and thermal effects are neglected.
2. Non-Newtonian lubricant behavior is neglected.
3. Pressure at the inlet is zero and surfaces are oil-flooded.
4. Lubricant flow is laminar and turbulence effects are neglected.
5. Leakage at the sides and edges is neglected.

2. NOMENCLATURE

C = Radial clearance between piston and liner = 10microns
C_f = Specific heat of lubricant
C_g = Distance from piston center of mass to piston pin = 0.2cm
C_p = Distance of piston-pin from axis of piston = 1 cm
F = Normal force acting on piston skirts
F_f = Friction force acting on skirts surface
F_{fh} = Friction force due to hydrodynamic lubricant film
F_G = Combustion Gas force acting on the top of piston
F_h =Normal force due to hydrodynamic pressure in film
F_{IC} = Transverse Inertia force due to piston mass
$\tilde{F}_{IC}$ = Reciprocating Inertia force due to piston mass
F_{IP} = Transverse Inertia force due to piston pin mass
$\tilde{F}_{IP}$ = Reciprocating Inertia force due to piston pin mass
F_c = Asperity Contact Force
F_{fc} = Friction force due to asperity contact
G = Shear modulus of elastic lubricant
I_{pis} = Piston inertia about its centre of mass
M = Moment acting on piston skirts
M_f = Friction moment acting on skirt surface
M_{fh} = Moment about piston pin due to hydrodynamic friction
M_h = Moment about piston pin due to hydrodynamic pressure
M_c = Asperity Contact Moment
M_{fc} = Moment due o friction force of asperity contact
R = Radius of piston
U = Piston Velocity
a = Vertical distance from skirt top to piston-pin = 0.0125m
b = Vertical distance from skirt top to piston center of gravity = 0.0015m
e_t = Piston eccentricities at skirts top surface
e_b = Piston eccentricities at skirts bottom surface
$\ddot{e}_b$ = Acceleration of piston skirts bottom eccentricities
$\ddot{e}_t$ = Acceleration of piston skirts top eccentricities
h = Film Thickness
l = Connecting rod length
m_{pis} = Mass of piston = 0.295 kg
m_{pin} = Mass of piston-pin = 0.09 kg
p = Hydrodynamic pressure
r = Crank radius = 0.0418 m
ω = Constant crankshaft speed (engine speed)
τ = Shear stress
η_A = Oil A viscosity = 0.016 Pa.s,
η_B = Oil B viscosity = 0.1891 Pa.s.
Φ = Connecting rod angle
ψ = Crank angle
ϕ_X , ϕ_y = Pressure flow factor along x and y-axis respectively
ϕ_s = Shear flow factor
σ = combined root mean square (rms)roughness
σ_1 = rms roughness of piston skirt= 1.4μm
σ_2 = rms roughness of cylinder liner = 1.5μm

3. MATHEMATICAL MODEL

3.1. Equations of Piston Motion

The forces and moments are in the form of the force and moment balance equations similar to that defined by Zhu et al [13]:

$$\begin{bmatrix} a_{11} & a_{22} \\ a_{21} & a_{22} \end{bmatrix} \begin{bmatrix} \ddot{e}_t \\ \ddot{e}_b \end{bmatrix} = \begin{bmatrix} F_h + F_c + F_s + (F_{fh} + F_{fc}) \tan \Phi \\ M_h + M_c + M_s + M_f \end{bmatrix} \quad (1)$$

$$a_{11} = m_{pin}\left(1 - \frac{a}{L}\right) + m_{pin}\left(1 - \frac{b}{L}\right) \quad (2a)$$

$$a_{12} = m_{pin}\left(\frac{a}{L}\right) + m_{pin}\left(\frac{b}{L}\right) \quad (2b)$$

$$a_{21} = \left(\frac{I_{pin}}{L}\right) + m_{pin}(a-b)\left(1 - \frac{b}{L}\right) \quad (2c)$$

$$a_{22} = m_{pin}(a-b)\left(\frac{b}{L}\right) - \left(\frac{I_{pin}}{L}\right) \quad (2d)$$

$$F_s = \tan\Phi\left(F_G + \tilde{F}_{IP} + \tilde{F}_{IC}\right) \quad (3)$$

$$M_s = F_G C_p + \tilde{F}_{IC} C_g \quad (4)$$

Using the Greenwood-Tripp's Asperity Contact Model, the values of F_c, F_{fc}, M_c and M_{fc} can be found for EHL regime [9].

3.2. Film Thickness Equation

The film thickness between the skirts and the liner given by Zhu [9]:

$$h = C + e_t(t)\cos x + \left[e_b(t) - e_t(t) \right] \frac{y}{L} \cos x \qquad (6)$$

3.3. Reynolds' Equation Modelling

Modified 2-D Reynolds equation is given as [2]:

$$\frac{\partial}{\partial x}\left(h^3 \phi_x \frac{\partial p}{\partial x} \right) + \left(\frac{R}{L} \right)^2 \frac{\partial}{\partial y}\left(h^3 \phi_y \frac{\partial p}{\partial y} \right) = 6U\eta \left(\frac{\partial h_T}{\partial x} + \sigma \frac{\partial \phi_S}{\partial x} \right) \qquad (7)$$

where ϕ_x and ϕ_y are Poiseulle or pressure flow factors and ϕ_s is Cuotte or shear flow factor [2][8].
The boundary conditions are defined as [4]:

$$\frac{\partial p}{\partial x}_{\theta=0} = \frac{\partial p}{\partial x}_{\theta=\pi} = 0 \qquad (8)$$

$p = 0$ when $x_1 \le x \le x_2$
$p(\theta, 0) = p(\theta, L) = 0$

In dimensionless form the 2-D Reynolds equation is given by [9][4]:

$$\frac{\partial}{\partial x^*}\left(h^{*3} \phi_x \frac{\partial p^*}{\partial x^*} \right) + \left(\frac{R}{L} \right)^2 \frac{\partial}{\partial y^*}\left(h^{*3} \phi_y \frac{\partial p^*}{\partial y^*} \right) = \frac{\partial h_T^*}{\partial x^*} + \sigma^* \frac{\partial \phi_S}{\partial x^*} \qquad (9)$$

Where by J. H Tripp [8]

$$\phi_X = 1 + \left[3(\gamma - 2)/(\gamma + 1) \right] \left[\sigma / h \right]^2$$

$$\phi_y = \phi_X (1/\gamma)$$

$$\phi_s = \frac{\sigma_1^{\,2}}{\sigma^2} \phi_s \left({}^{h}\!/_{\sigma}, \gamma_1 \right) - \frac{\sigma_2^{\,2}}{\sigma^2} \phi_s \left({}^{h}\!/_{\sigma}, \gamma_2 \right)$$

$$\phi_s \left({}^{h}\!/_{\sigma}, \gamma_2 \right) = \left[\frac{3}{(\gamma + 1)} (\sigma / h) \right]$$

and γ is the Peklenik number [10]

In order to read the pressure profiles conveniently, the Vogelpohl parameter M_v is introduced [4]:

$$M_v = p^* h^{*1.5}$$

The Reynolds equation in terms of the Vogelpohl parameter is given as:

$$\frac{\partial^2 M_v}{\partial .x^{*2}} + \left(\frac{R}{L} \right)^2 \frac{\partial^2 M_v}{\partial .y^{*2}} + \left(\frac{\partial .\varphi_x}{\partial .x^*} (1/\varphi) \right) \left(\frac{\partial M_v}{\partial .x^*} \right) + \left(\frac{\partial .\varphi_y}{\partial .y^*} (1/\varphi) \right) \left(\frac{R}{L} \right)^2 \left(\frac{\partial .M_v}{\partial .y^*} \right) = F M_v + G \qquad (10)$$

where

$$F = \frac{0.75\left[\left(\frac{\partial h^*}{\partial x^*} \right)^2 + \left(\frac{R}{L} \right)^2 \left(\frac{\partial h^*}{\partial y^*} \right)^2 \right]}{h^{*2}} + \frac{1.5\left[\frac{\partial^2 h^*}{\partial x^{*2}} + \left(\frac{R}{L} \right)^2 \frac{\partial^2 h^*}{\partial y^{*2}} \right]}{h^*} + \frac{1.5\left[\frac{\partial h^*}{\partial x^*} \left(\frac{\partial \varphi}{\partial x^*} \right) + \left(\frac{R}{L} \right)^2 \frac{\partial \varphi}{\partial y^*} \left(\frac{\partial h^*}{\partial y^*} \right) \right]}{h^* \times \varphi}$$

$$G = \frac{\left(\frac{\partial h^*}{\partial x^*} + \sigma^* \frac{\partial \phi_S}{\partial x^*} \right)}{(h^{*1.5} \times \phi)}$$

$$M_{v,i,j} = \frac{C_{.1}\left(M_{v,i+1,j} + M_{v,i-l,j} \right) + \left(\frac{R}{L} \right)^2 C_{.2}\left(M_{v,i,j+l} + M_{v,i,j-i} \right)}{2.C_1 + 2.C_2 + F_{i,j}} + \frac{C_{.3}\left(\frac{\partial .\varphi^*}{\partial .x^*} (1/\varphi^*) \right)\left(M_{v,i+1,j} - M_{v,i-l,j} \right)}{2.C_1 + 2.C_2 + F_{i,j}} + \frac{C_{.4}\left(\frac{\partial .\varphi^*}{\partial .y^*} (1/\varphi^*) \right)\left(M_{v,i+1,j} - M_{v,i-l,j} \right) - G_{i.j}}{2.C_1 + 2.C_2 + F_{i,j}}$$

3.4. Film Thickness in EHL Regime

EHL regime the film thickness includes film In
thickness in the rigid hydrodynamic regime and the elastic surface displacements etc. By considering the bulk elastic deformation, the lubricant film thickness

equation takes the following form [14]

$$h_{eh;} = h + f(\theta, y) + v$$

where $f(\theta, y)$ is neglected. The differential surface displacement is [14]:

$$dv = \frac{1}{\pi E'} \frac{p(x, y)\, dy dy}{\dot{r}}$$

$$\dot{r} = \sqrt{(x - x_0)^2 + \left[(y - y_0)^2 \right]}$$

$$\frac{1}{E'} = \frac{1}{2}\left[\frac{(1 - v_1^{\,2})}{E_1} + \frac{(1 - v_2^{\,2})}{E_2} \right]$$

At a specific point (x_o, y_o) the elastic deformation is [4]:

$$v(x_0, y_0) = \frac{1}{\pi E'} \iint_a \frac{p(x, y) dx dy}{\dot{r}}$$

4. RESULTS AND DISCUSSION

The hydrodynamic lubrication and EHL models of the piston skirts at 500 rpm are developed after incorporating the pressure flow and the shear flow factors. Two different oils having viscosity 0.016 Pa.s and 0.1891 Pa.s are used for a comparison and investigating the viscosity effects on different parameters which include film thickness

,eccentricities and hydrodynamic pressure profiles at 720 degree crank rotation cycle.

4.1 Piston Eccentricities

The dimensionless eccentricities of the top and the bottom surface of the piston skirts (Et and Eb) are plotted against the 720 degree crank rotation cycle. Figure 1(a) and 1(b) show eccentricity profiles for Oil A at 500 rpm. The results are plotted between a range of 1 and -1 where the physical contact between the sliding surfaces can occur. At central value '0' the motion is concentric. Figure 1(a) shows the dimensionless eccentricity profiles in the hydrodynamic lubrication regime whereas figure 1 (b) shows the similar profiles in the EHL regime. The behaviour is shown for all the four strokes where it can be seen that at the start of cycle the piston and liner axis are concentric then due to the secondary motion the profiles are highly displaced from the centre towards thrust side and non thrust side, but for Oil A the physical contact is avoided as shown in Figure 1. For Oil B , the dimensionless eccentricities profiles for hydrodynamic and EHL regime are shown in Figure 4. Figure 4 (a) shows that the contact is established at lower surface as line is meeting with -1 in rigid hydrodynamic regime. However in Figure 4 (b) the EHL regime shows the physical contact is clearly avoided. This shows that the elastic deformation of asperities help in avoiding the contact between interacting surfaces, thus help in avoiding friction related wear.

Comparison of eccentricities for both oils provides an interesting finding that the low viscosity oil can be more helpful at initial engine start-up speed of 500 rpm for rigid hydrodynamic regime as well as equally good for EHL regime.

4.2 Hydrodynamic Pressures

Three dimensional pressure fields and related pressure distribution are plotted for 720 degree crank angle. Figure 2 (a), 2(b), 2(c), 2(d) show 3- D hydrodynamic pressure profiles at 900, 4500, 6300 and 7200 crank angles at 500 rpm. The positive pressures are developed over the piston skirt and vary as shown in Figure 2. In figure 2 (a), for Oil A, at 90 degrees crank angle the pressures are biased towards bottom of piston skirt and extended to the middle of piston skirt. The peak pressure occurs at the bottom of piston skirt. In figure 2 (b), for Oil A, at 450 degrees crank angle, the pressure field shows that the hydrodynamic pressures are developed at top of piston skirt though a small ridge can be seen at bottom of piston Skirt. The peak pressures are larger than the 90 degrees angle. In figure 2 (c), at 630 degrees crank angle, the pressures are shifted towards top of piston skirt. In figure 2(d), at 720 degrees the pressure profile is more steep and developed at bottom of piston skirt showing the end of cycle. For Oil B, in figure 5(a), 5(b), 5(c), 5(d) show 3- D hydrodynamic pressure profiles at 900, 4500, 6300 and 7200 crank angles at 500 rpm speed.

For the pressure fields it can be clearly investigated that the hydrodynamic pressures are totally shifted towards top of piston skirt at 450 degrees crank angle while the case was not same in case of Oil A for similar conditions. The major change in shape of pressure filed can be observed for 630 degrees crank angle where the dimensionless pressure is biased towards bottom of piston skirt instead of top as discussed for Oil A. Thus changing the viscosity of oil is affecting the distribution of hydrodynamic pressures over piston skirt.

4.3 Hydrodynamic and EHL Film Thickness

Figure 3(a) shows the maximum and the minimum hydrodynamic film thickness for Oil A at 500 rpm and 10 micron radial clearance. The maximum film thickness is calculated before the application of load and on the other side the minimum film thickness is found after the application of load. The magnitude of minimum film thickness shows whether the film thickness is capable of avoiding the contact between sliding surfaces or not. In figure 3(a), the minimum hydrodynamic film start getting establish from start of cycle and reaches at a peak at power stroke and decrease to minimum at end of exhaust stroke and cycle continues. Similar case can be seen for Oil B in figure 6(a) , but the difference is evident at end of exhaust stroke where a second peak of film thickness can be seen. In figure 3(b) and 6(b) EHL film thickness profiles are shown. By comparing both profiles, it can be seen that in case of Oil A the EHL film thickness is greater in magnitude for different crank angles as compare to Oil B. Thus Oil A , which is low viscosity oil, will be more helpful in avoiding the contact and wear between rough piston and liner surfaces.

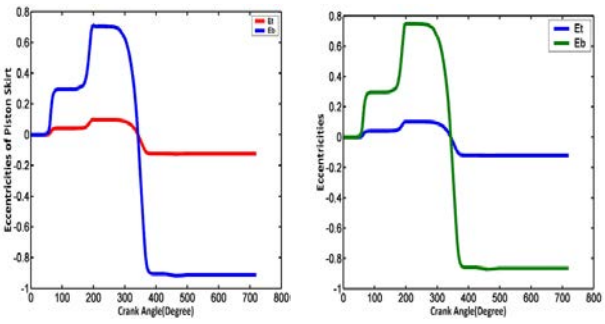

(a) (b)

Figure 1. For Oil A , Dimensionless Eccentricities at 500 rpm in (a) Hydrodynamic regime (b) EHL Regime

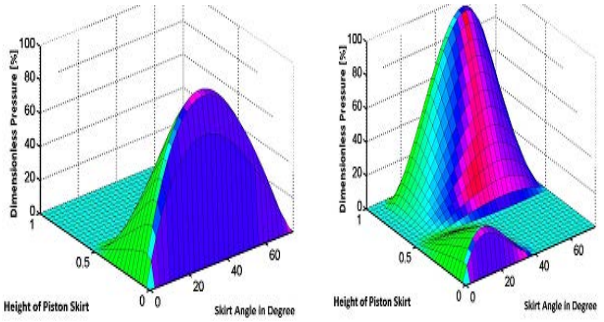

(a) (b)

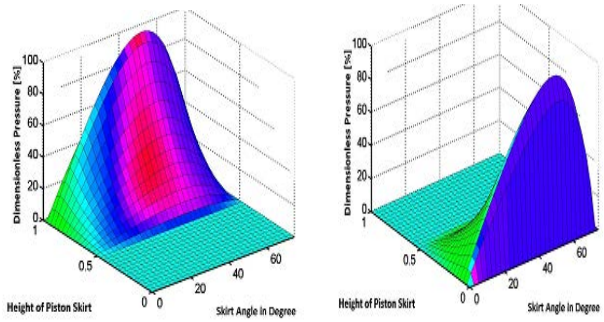

(c) (d)

Figure 2. : For Oil A, 3-D Hydrodynamic pressure fields at 500 rpm at crank angle (a) 90 degree (b) 450 degree (c) 630 degree (d) 720 degree

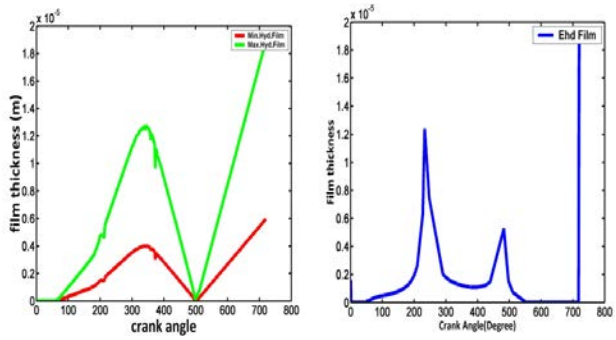

(a) (b)

Figure 3. : For Oil A, At 500 rpm (a) Film thickness profiles (b) EHL film

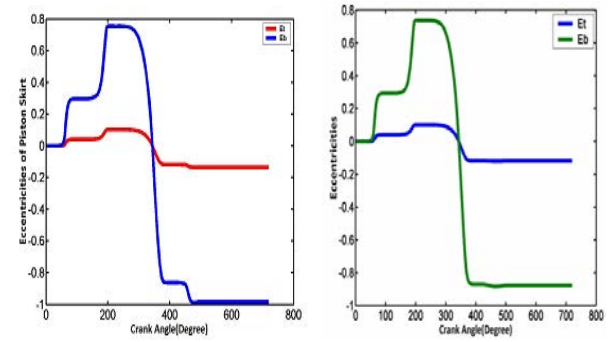

(a) (b)

Figure 4. For Oil B , Dimensionless Eccentricities at 500 rpm in (a) Hydrodynamic regime (b) EHL Regime

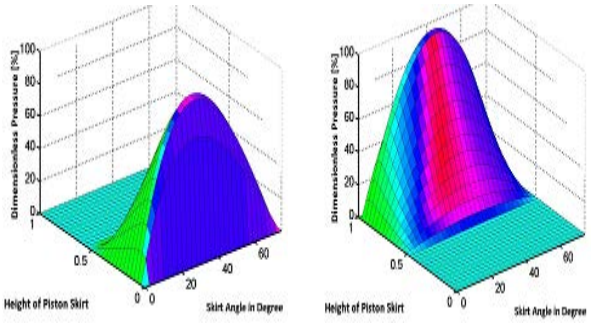

(a) (b)

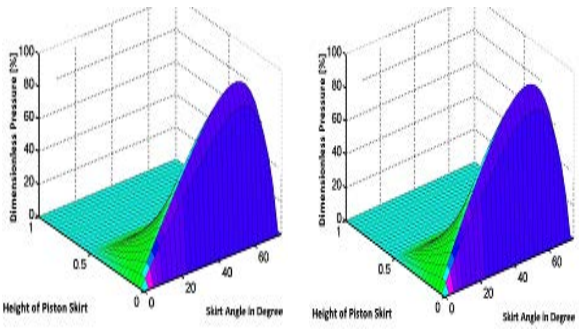

(c) (d)

Figure 5. : For Oil B, 3-D Hydrodynamic pressure fields at 500 rpm at crank angle (a) 90 degree (b) 450 degree (c) 630 degree (d) 720 degree

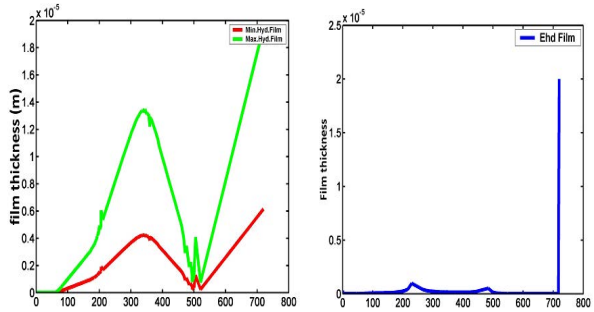

(a) (b)

Figure 6. : For Oil B, At 500 rpm (a) Film thickness profiles (b) EHL film

5. CONCLUSION

Two dimensional numerical models for hydrodynamic and EHL regimes were developed at initial engine start-up speed for isotropic rough piston skirt and cylinder. Two different grade oils were used to investigate the different parameters affecting the rough piston skirt wear phenomenon. The different rough surfaces of the interacting skirts and the liner were considered by introducing the pressure and the shear flow factors in the lubrication model. For Oil 'B' having a viscosity of 0.1891 Pa.s, the simulation results verify that a physical contact between the rough skirts and the liner surfaces cannot be avoided in the rigid

hydrodynamic regime. However, for both oils, the rough interacting surfaces deform elastically to generate a sufficiently thick film in the EHL regime. The hydrodynamic pressures shifting occur from top of piston skirt to bottom at 630 degrees crank angle by changing Oil A to Oil B at 500 rpm and 10 micron radial clearance. Comparing both oils for given conditions, Oil A is more suitable to avoid the contact and wear between interacting rough surfaces.

REFERENCES

[1] Hamilton, D. B., Walowit, J.A., & Allen, C.M. A Theory of Lubrication by Microirregularities., Journal of Basic Engineering, Trans ASME, Ser. D., March 1966, pp. 177-185.

[2] N. Patir, & H. S. Cheng, An Average Flow Model for Determining Effects of Three-Dimensional Roughness on Partial Hydrodynamic Lubrication, ASME Journal of Lubrication Technology, 100(1), pp 12-17, 1978.

[3] N. Patir, & H. S. Cheng, Application of Average Flow Model to Lubrication Between Rough Sliding Surfaces, ASME Journal of Lubrication Technology, 101 (2), pp220-230,1979.

[4] G. W. Stachowiak & A. W. Batchelor Engineering tribology, 3rd ed., Elsevier, pp. 328 2005

[5] Dong Zhu and Q Jane Wang ,On the λ ratio range of mixed lubrication, Proc IMechE Part J: Journal of Engineering Tribology pp1010–1022,226(12)

[6] Tripp JH, Hamrock BJ. Surface roughness effects in elastohydrodynamic contacts. In: Proc 1984 Leeds Lyon Symposium on Tribology 1985:30–9.

[7] H. G. Elrod, A General Theory for Laminar Lubrication with Reynolds Roughness, ASME Journal of Lubrication Technology, 101(1), pp 8-14,1979.

[8] J. H. Tripp, Surface Roughness Effects in Hydro-dynamic Lubrication: The Flow Factor Method, ASME Journal of Lubrication Technology, 105, pp 458-463,1983.

[9] J. A. Greenwood, & J. H. Tripp, The Contact of Two Nominally Flat Rough Surface, Proc. Institution of Mechanical Engineers (IMechE), UK, (185), pp 625-633,1971.

[10] Peklenik, J., New Developments in Surface Characterization and Measurement by Means of Random Process Analysis, Proc. Instn. Mech. Engrs., Volume 182, pp 108-125,1967-68.

[11] Garcia, N.; Stoll, E.: Monte Carlo Calculation of Electromagnetic-Wave Scattering from Random Rough Surfaces, Physical Review Letters, Volume 52, Issue 20, pp. 1798-1801, 1984.

[12] FFTW library - free collection of fast C routines for computing discrete Fast Fourier Transforms. Developed at MIT by Matteo Frigo and Steven G. Johnson.

[13] Zhu, D., Hu, Y., Cheng, H.S., Arai, T., and Hamai, K.:, A numerical Analysis for Piston Skirt in Mixed Lubrication, Part 2 : Deformation Consideration, ASME Journal of Tribology,pp115-125, 1992.

[14] S. A. Qasim, M. A. Malik, M. A. Khan, & R. A.Mufti, Low Viscosity Shear Heating in Piston Skirts EHL in the Low Initial Engine Start Up Speeds, *Tribology International*, *44*(10), pp. 1134-1143, 2011.

Serbian Tribology Society

SERBIATRIB '13

13th International Conference on Tribology

Faculty of Engineering in Kragujevac

Kragujevac, Serbia, 15 – 17 May 2013

STRESSES AND DEFORMATIONS ANALYSIS OF A DRY FRICTION CLUTCH SYSTEM

Oday I. Abdullah[1], Josef Schlattmann[1], Abdullah M. Al-Shabibi[2]

[1]Department of System Technology and Mechanical Design Methodology, Hamburg University of Technology, oday.abdullah@tu-harburg.de

[2]Department of Mechanical and Industrial Eng. College of Eng. / Sultan Qaboos Univeristy

Abstract: *The friction clutch is considered the essential element in the torque transmission process. In this paper, the finite element method is used to study the stresses and deformations for clutch system (pressure plate, clutch disc and flywheel) due to the contact pressure of diaphragm spring and the centrifugal force during the full engagement of clutch disc (assuming no slipping between contact surfaces). The investigation covers the effect of the contact stiffness factor FKN on the pressure distribution between contact surfaces, stresses and deformations. The penalty and Augmented Lagrangian algorithms have been used to obtain the pressure distribution between contact surfaces. ANSYS13 software has been used to perform the numerical calculation in this paper.*

Keywords: *Dry friction clutch, Stresses and deformations, pressure distribution, full engagement, 2D axisymmetric FEM.*

1. INTRODUCTION

A clutch is a very important machine element which plays a main role in the transmission of power (and eventually motion) from one component (the driving part of the machine) to another (the driven part). A common and well known application for the clutch is in automotive vehicles where it is used to connect the engine and the gearbox. Furthermore, the clutch is used also extensively in production machinery of all types. When the friction clutch begins to engage, slipping occurs between the contact surfaces (pressure plate, clutch disc and flywheel) and due to this slipping, heat energy will be generated in the interfaces friction surfaces. At high relative sliding velocity, high quantity of frictional heat is generated which lead to high temperature rise on the clutch disc surfaces and hence thermo-mechanical problems such as thermal deformations and thermo-elastic instability can occur. This in turn, can lead to thermal cracking and high rate of wear. The pressure distribution is essential factor effect on the performance of the friction clutch because of the heat generated between contact surfaces during the slipping period dependent on the pressure distribution.

Al-Shabibi and Barber [1] used the finite element method to find the transient solution of the temperature field and contact pressure distribution between two sliding disks. Two dimensional axisymmetric FE model used to explore an alternative method based on an eigenfunction expansion and a particular solution that can be used to solve the thermoelastic contact problem with frictional heating. Both constant and varying sliding speed is considered in this analysis. Results of the direct finite element simulation have been obtained using the commercial package ABAQUS. The results from the approximate solution show a good agreement with the results from the direct finite element simulation.

Lee et al. [2] used finite element method to study the effect of thermo-mechanical loads on the pressure plate and the hub plate of the friction clutch system. Three types of loads are taking into consideration the thermal load due to the slipping occurs at the beginning of engagement, the contact pressure of diaphragm spring and the centrifugal force due to the rotation. Two and three dimensional finite element models were performed

to obtain the temperature distributions and the stresses. The results show the significant effect of the thermal load on the temperatures and stresses; therefore it is desirable to increase the thickness of the pressure plate as much as possible to increase the thermal capacity of the pressure plate to reduce the thermal stresses. High stress intensity value occurs around the fillet region of the window in the hub plate.

Shahzamanian et al. [3] used numerical simulation to study the transient and contact analysis of functionally graded (FG) brake disk. The material properties vary in the radial direction from full-metal at the inner radius to that of full-ceramic at the outer radius. The coulomb contact friction is considered between the pad and the brake disk.

Two-dimensional finite element model used in the work to obtains the pressure distribution, total stresses, pad penetration, friction stresses, heat flux and temperature during the contact for different values of the contact stiffness factor. It was found, that the contact pressure and contact total stress increase when the contact stiffness factor increases and the gradation of the metal–ceramic has significant effect on the thermo-mechanical response of FG brake disks. Also, it can be concluded when the thickness of the pad increases the contact status between pad and disc changes from sticking to contact and then to near contact.

Abdullah and Schlattmann [4-8] investigated the temperature field and the energy dissipated of dry friction clutch during a single and repeated engagement under uniform pressure and uniform wear conditions. They also studied the effect of pressure between contact surface when varying with time on the temperature field and the internal energy of clutch disc using two approaches heat partition ratio approach to compute the heat generated for each part individually whereas the second applies the total heat generated for the whole model using contact model. Furthermore, they studied the effect of engagement time and sliding velocity function, thermal load and dimensionless disc radius (inner disc radius/outer disc radius) on the thermal behavior of the friction clutch in the beginning of engagement.

In this paper the finite element method used to study the contact pressure and stresses during the full engagement period of the clutches using different contact algorithms. Moreover, sensitivity study for the contact pressure is presented to indicate the importance of the contact stiffness between contact surfaces.

2. FUNDAMENTAL PRINCIPLES

The main system of the friction clutch consists of pressure plate, clutch disc and flywheel as shown in figure 1.

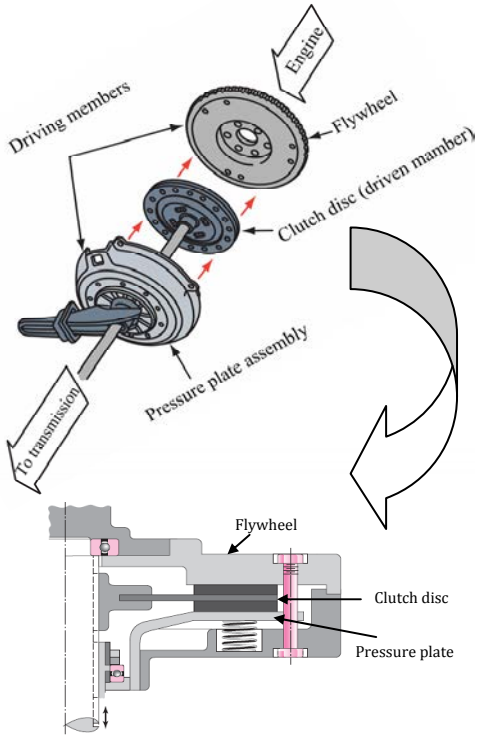

Figure 1. The main parts of clutch system

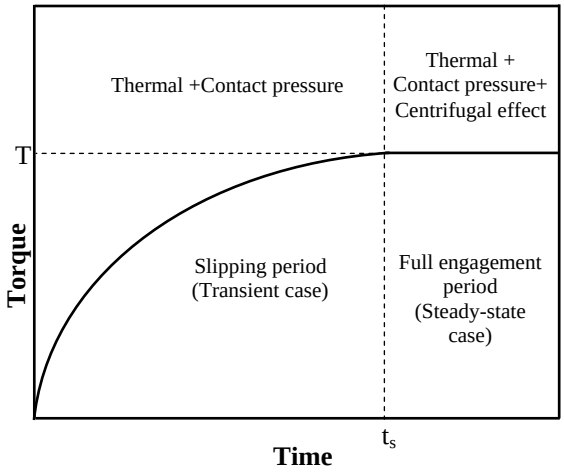

Figure 2. The load conditions during the engagement cycle of the clutch

When the clutch starts to engage the slipping will occur between contact surfaces due to the difference in the velocities between them (slipping period), after this period all contacts parts are rotating at the same velocity without slipping (full engagement period). A high amount of the kinetic energy converted into heat energy at interfaces according to the first law of thermodynamics during the slipping period and the heat generated between contact surfaces will be dissipated by conduction

between friction clutch components and by convection to environment, in addition to the thermal effect due to the slipping there is other load condition which is the pressure contact between contact surfaces. In the second period, there are three types of load conditions the temperature distribution from the last period (slipping period), the pressure between contact surfaces due to the axial force of diaphragm spring and the centrifugal force due to the rotation of the contacts parts. Figure 2 shows the load conditions during the engagement cycle of the clutch, where t_s is the slipping time and T is the transmitted torque by clutch.

3. FINITE ELEMENT FORMULATION

This section presented the steps to simulate the contact elements of friction clutch using ANSYS software. Moreover it gives more details about the types of contacts and algorithms which are used in this software.

The first step in this analysis is the modelling; due to the symmetry in the geometry (frictional lining without grooves) and boundary conditions of the friction clutch (take into the consideration the effect of the pressure and centrifugal force loads, and neglected the effect of thermal load due to the slipping), two-dimensional axisymmetric FEM can be used to represent the contact between the clutch elements during the steady-state period as shown in figure 3.

There are three basic types of contact used in Ansys software single contact, node-to-surface contact and surface-to-surface contact. Surface-to-surface contact is the most commonly type of contact used for bodies that have arbitrary shapes with relative large contact areas. This type of contact is most efficient for bodies that experience large values of relative sliding such as block sliding on plane or sphere sliding within groove [9]. Surface-to-surface contact is the type of contact assumed in this analysis because of the large areas of clutch elements in contact.

In this work, it has been assumed two types of load conditions effects on the clutch system during the steady-state period (full engagement period) the contact pressure between clutch elements due to the axial force by diaphragm spring and the centrifugal force due to the rotation.

The elements used for contact model are:

- "Plan13" used for all elements of the clutch (flywheel, clutch disc and pressure plate).
- "Conta172" used for contact surfaces that are the upper and lower surfaces of clutch disc.
- "Targe169" used for the target surfaces that are the lower surface of the flywheel and the upper surface of the pressure plate.

Figure 4 shows the details about schematic for all elements that has been used in this analysis.

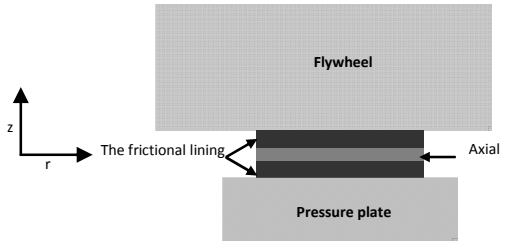

Figure 3. The Contact model for clutch system

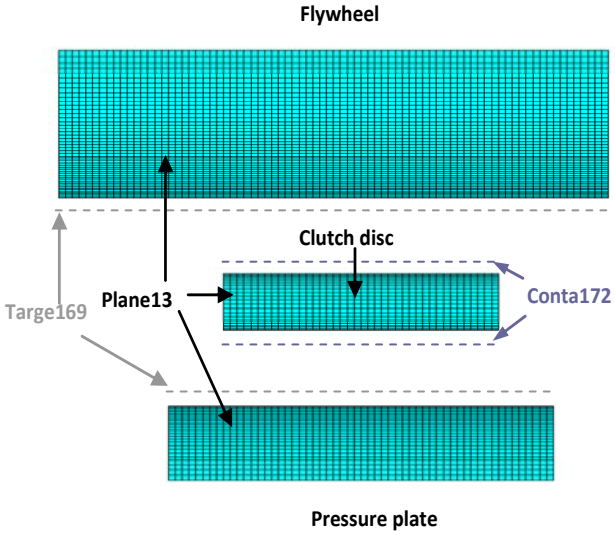

Figure 4. Schematic elements used for the friction clutch elements

The stiffness relationship between contact and target surfaces will decide the amount of the penetration. Higher values of contact stiffness will decrease the amount of penetration, but can lead to ill-conditioning of the global stiffness matrix and convergence difficulties. Lower values of contact stiffness can lead to certain amount of penetration and low enough to facilitate convergence of the solution. The contact stiffness for an element of area A is calculated using the following formula [10]:

$$F_{kn} = \int \{f_i\}(e)\{f_i\}^T \, dA \qquad (1)$$

The default value of the contact stiffness factor FKN is 1, and it is appropriate for bulk deformation. If bending deformation dominates the solution, a smaller value of KKN = 0.1 is recommended.

There are five algorithms used for surface-to-surface contact type are:

- Penalty method: this algorithm used constant "spring" to establish the relationship between the two contact surfaces (figure 5). The contact

force (pressure) between two contact bodies can be written as follows:

$$F_n = k_n x_p \quad (2)$$

Where F_n is the contact force, k_n is the contact stiffness and x_p is the distance between two existing nodes or separate contact bodies (penetration or gap).

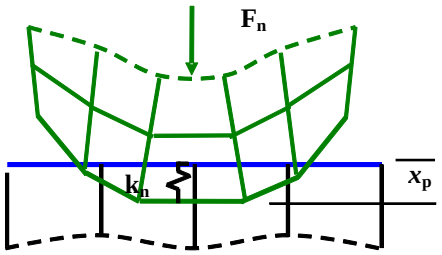

Figure 5. The contact stiffness between two contact bodies

- Augmented Lagrange (default): this algorithm is an iterative penalty method. The constant traction (pressure and frictional stresses) are augmented during equilibrium iterations so that the final penetration is small than the allowable tolerance. This method usually leads to better conditioning and is less sensitive to the magnitude of the constant stiffness. The contact force (pressure) between two contact bodies is:

$$F_n = k_n x_p + \lambda \quad (3)$$

Where λ is the Lagrange multiplier component.

- Lagrange multiplier on contact normal and penalty on tangent: this method applied on the constant normal and penalty method (tangential contact stiffness) on the frictional plane. This method enforces zero penetration and allows small amount of slip for the sticking contact condition. It requires chattering control parameters, as well as the maximum allowable elastic slip parameter.
- Pure Lagrange multiplier on contact normal and tangent: This method enforces zero penetration when contact is closed and "zero slip" when sticking contact occurs. This algorithm does not require contact stiffness. Instead it requires chattering control parameters. This method adds contact traction to the model as additional degrees of freedom and requires additional iterations to the stabilize contact conditions. It often increase the computational cost compared to the augmented lagrangian method.
- Internal multipoint constraint: this method used in conjunction with bonded contact and no separation contact to model several types of contact assemblies and kinematic constraints.

The axisymmetric finite element model of the friction clutch system with boundary conditions is shown in figure 6. A mesh sensitivity study was done to choose the optimum mesh from computational accuracy point of view. The full Newton-Raphson with unsymmetric matrices of elements is used in this analysis assuming a large-deflection effect. In all computations for the friction clutch model, it has been assumed a homogeneous and isotropic material and all parameters and materials properties are listed in Table. 1.

In this analysis also assuming there are no cracks in the contact surfaces and the actual contact area is equal to the nominal contact area.

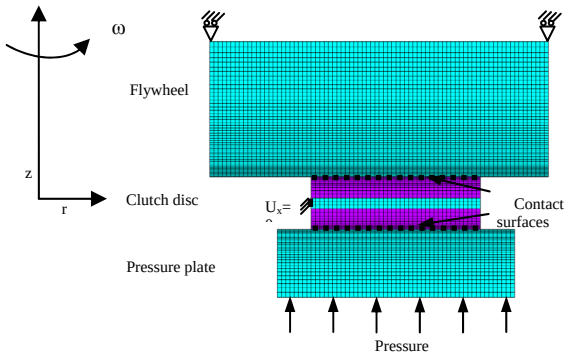

Figure 6. FE models with the boundary conditions.

Table 1. The properties of materials and operations

Parameters	Values
Inner radius of friction material & axial cushion, r_i [m]	0.06298
Outer radius of friction material & axial cushion, r_o[m]	0.08721
Thickness of friction material [m], t_l	0.003
Thickness of the axial cushion [m], $t_{axi.}$	0.0015
Inner radius of pressure plate [m], r_{ip}	0.05814
Outer radius of pressure plate [m], r_{op}	0.09205
Thickness of the pressure plate [m], t_p	0.00969
Inner radius of flywheel [m], r_{if}	0.04845
Outer radius of flywheel [m], r_{of}	0.0969
Thickness of the flywheel [m], t_f	0.01938
pressure, p [MPa]	1
Coefficient of friction, μ	0.2
Number of friction surfaces, n	2
Torque [Nm], T	432
Maximum angular slipping speed, ω_o [rad/sec]	200
Young's modulus for friction material, E_l [GPa]	0.30
Young's modulus for pressure plate, flywheel & axial cushion, (E_p, E_f, and E_{axi}), [Gpa]	125
Poisson's ratio for friction material,	0.25
Poisson's ratio for pressure plate, flywheel & axial cushion	0.25
Density for friction material, (kg/m^3), ρ_l	2000
Density for pressure plate, flywheel & axial cushion, (kg/m^3), (ρ_p, ρ_f, and ρ_{axi})	7800

4. RESULTS AND DISCUSSIONS

Series of computations have been carried out using ANSYS13 software to study the contact pressure and stresses between contact surfaces of clutch (pressure plate, clutch disc and flywheel) during a full engagement period using different algorithms and contact stiffness factor values.

The variation of the contact pressure with disc radius for both sides of clutch disc (flywheel side and pressure plate side) using penalty and augmented algorithms (FKN = 1) is shown in figures 7 and 8. From these figures, it can be seen that the identical results when using penalty and augmented (default) methods and approximately the same behaviour of contact pressure for both sides of clutch disc. The maximum contact pressure values in the flywheel side and pressure plate side are found to be 1.491 MPa and 1.524 MPa, respectively. The maximum and minimum contact pressure values occur at outer disc radius r_o and near inner radius ($1.01r_i$) for both cases, respectively.

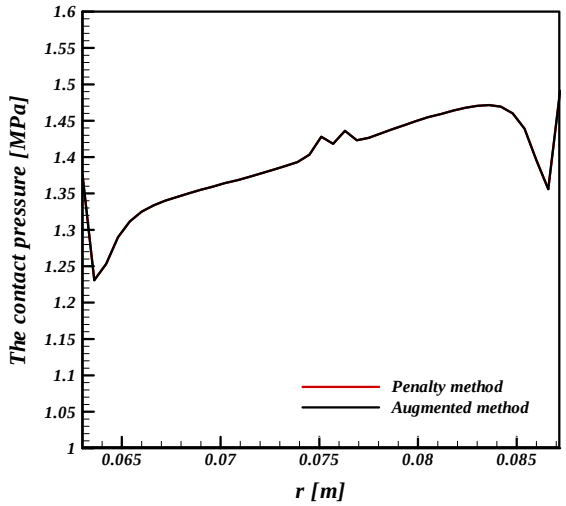

Figure 7. The variation of contact pressure with disc radius (flywheel / clutch disc)

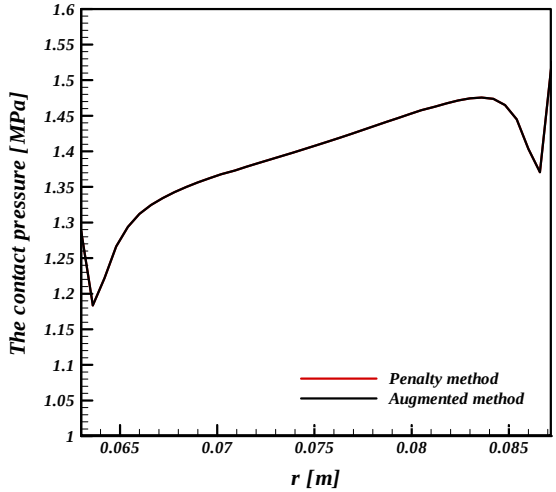

Figure 8. The variation of contact pressure with disc radius (pressure plate / clutch disc)

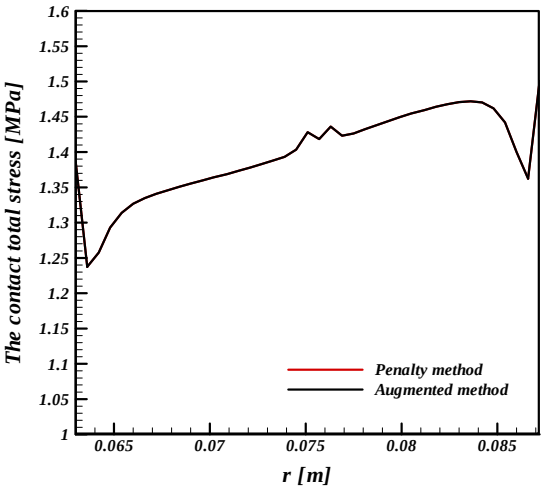

Figure 9. The variation of total contact stress with disc radius (flywheel / clutch disc)

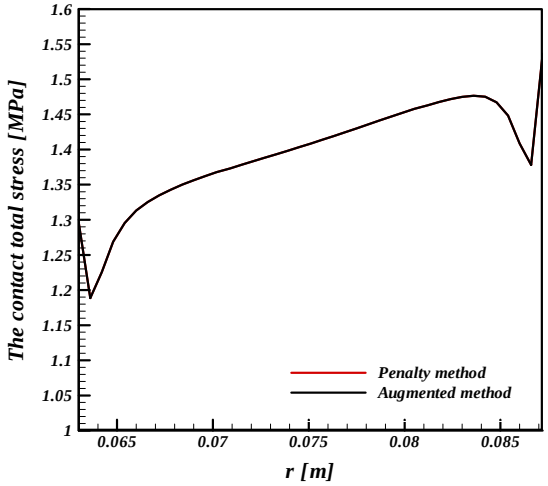

Figure 10. The variation of total contact stress with disc radius (pressure plate / clutch disc)

Figures 9 and 10 show the variation of total contact stresses with disc radius for both sides of clutch disc. It can be seen, that the total contact stresses have the same behaviour of the contact pressure.

Figures 11 and 12 demonstrate the variation of total displacement of clutch surfaces with disc radius. It's clear; the values of total deformations of clutch disc (pressure plate side) are higher than the displacements values at the flywheel side. The maximum values of total deformation in the clutch disc at flywheel and pressure plate sides are found to be $4.6529E^{-6}$ m and $2.84E^{-5}$ m, respectively.

The variation of the contact pressure for using different algorithms and different values of FKN along the radial direction at contact area of clutch disc with flywheel is shown in figures 13 and 14. It can be noted for both cases (when using penalty and augmented method), that the values of contact pressure increases when FKN increases. The percentage increasing in contact pressure when FKN change from 0.01 to 10 is found to be 19.5% and 17.9% corresponding to penalty and augmented methods, respectively.

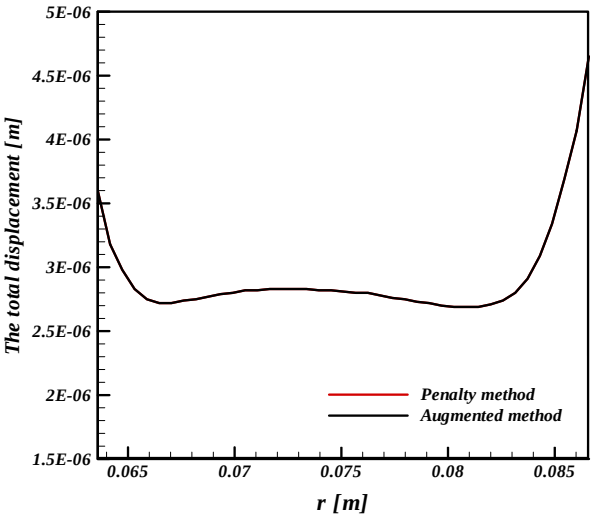

Figure 11. The variation of total displacement with disc radius (flywheel / clutch disc)

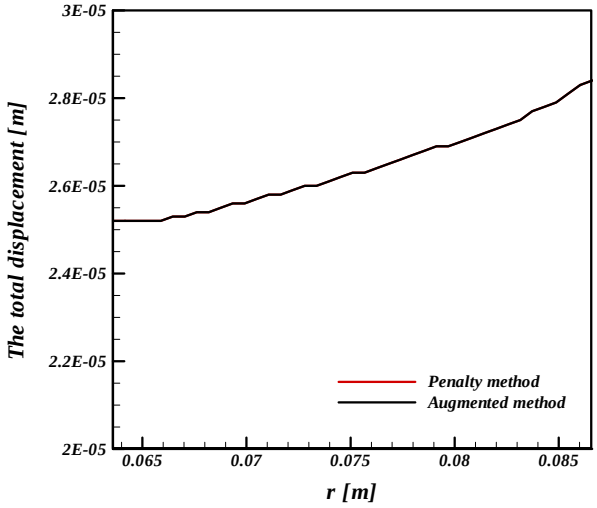

Figure 12. The variation of total displacement with disc radius (pressure plate / clutch disc)

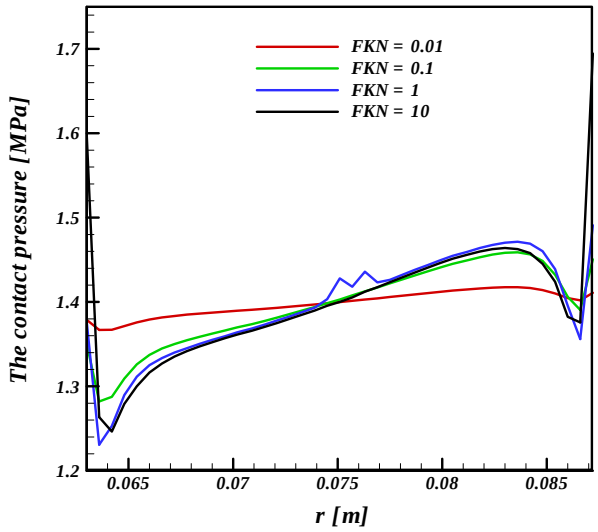

Figure 13. The variation of contact pressure with disc radius using Penalty method (flywheel / clutch disc)

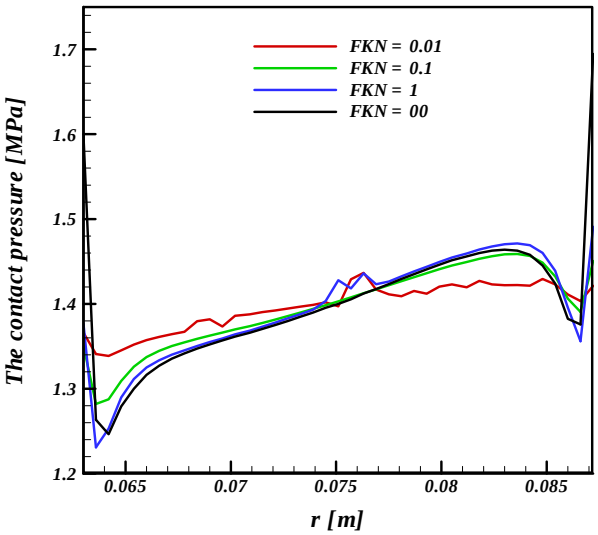

Figure 14. The variation of contact pressure with disc radius using augmented Lagrange algorithm (flywheel / clutch disc)

5. CONCLUSIONS AND REMARKS

The variations of the contact pressure, total contact stress and total displacements of the friction clutch using different contact algorithms and different values of FKN are investigated. Two-dimensional axisymmetric finite element model for the contact elements of clutch were conducted to obtain the numerical results.

The present work presents a simplified model of clutch to determine the contact pressure between contact surfaces during a full engagement period.

The conclusions obtained from the present analysis are summarized as follows:

1. The value of FKN is very important and effective on the values of contact pressure, the contact pressure is directly proportional to FKN for both contact methods (penalty and augmented).
2. The penalty method has sensitivity for FKN more than the augmented method.
3. The maximum and minimum values of contact pressure and total contact stress occur at outer disc radius and inner disc radius, respectively.

The permanent deformations and thermal cracks on the contact surfaces of clutch if taken into consideration will affect the contact pressure distribution and the actual contact area will change. These disadvantages will focus the contact pressure on small region compared with the nominal contact area.

REFERENCES

[1] Abdullah M. Al-Shabibi and James R. Barber: *Transient Solution of The Unperturbed Thermoelastic Contact Problem*, J. thermal stresses, Vol. 32, pp. 226-243, 2009.

[2] Choon Yeol Lee, Il Sup Chung, Young Suck Chai: *Finite Element Analysis of an Automobile Clutch System*, J. Key Eng. Materials, Vol 353-358, pp. 2707-2711, 2007.

[3] M.M. Shahzamanian, B.B. Sahari , M. Bayat, Z.N. Ismarrubie and F. Mustapha: *Transient and thermal contact analysis for the elastic behavior of functionally graded brake disks due to mechanical and thermal loads*, J. Materials & Design, Vol. 31, Issue 10, pp. 4655–4665, 2010.

[4] Oday I. Abdullah and Josef Schlattmann: *The Effect of Disc Radius on Heat Flux and Temperature Distribution in Friction Clutches*, J. Advanced Materials Research, Vol. 505, pp. 154-164, 2012.

[5] Oday I. Abdullah and Josef Schlattmann: *Finite Element Analysis of Dry Friction Clutch with Radial and Circumferential Grooves*, Proceeding of World Academy of Science, Engineering and Technology Conference, Paris, pp. 1279-1291, 2012.

[6] Oday I. Abdullah and Josef Schlattmann: *Effect of Band Contact on the Temperature Distribution for Dry Friction Clutch*, Proceeding of World Academy of Science, Engineering and Technology Conference, Berlin, pp. 167-177, 2012.

[7] Oday I. Abdullah and Josef Schlattmann: *The Correction Factor for Rate of Energy Generated in the Friction Clutches under Uniform Pressure Condition*, J. Adv. Theor. Appl. Mech., Vol. 5, no. 6, pp. 277 – 290, 2012.

[8] Oday I. Abdullah and Josef Schlattmann: Finite Element Analysis of Temperature Field in Automotive Dry Friction Clutch, J. Tribology in Industry, Vol. 34, No. 4, pp. 206-216, 2012.

[9] ANSYS Contact Technology Guide, ANSYS Release 11.0 Documentation, ANSYS, Inc.

[10] Mohr GA: A contact stiffness matrix for finite element problems involving external elastic restraint, Compos Struct., Vol. 12, pp. 189–91, 1979.

Serbian Tribology Society

SERBIATRIB '13

13th International Conference on Tribology

Faculty of Engineering in Kragujevac

Kragujevac, Serbia, 15 – 17 May 2013

THE WAVINESS OF AN ABRASIVE WATER JET GENERATED SURFACE

J.Baralić[1], P.Janković[2], B.Nedić[3]

[1] University of Kragujevac, Technical Faculty Čačak, Serbia, jbaralic@tfc.kg.ac.rs

[2] University of Niš, Faculty of Mechanical Engineering, Serbia, jape@masfak.ni.ac.rs

[3] University of Kragujevac Faculty of mechanical engineering, Serbia, nedic@kg.ac.rs

Abstract: *Abrasive water jet generated surface has appearance that is characteristic for all machining procedures with the beam of high-energy density. On the surface machined with these procedures, characteristic lines, which are traces resulting from the passage of beam through the workpiece, can be observed. When machining with abrasive water jet, on the generated surface occurs trace lines and waviness. The appearance of waviness is more pronounced in the lower part of the machined surface. The aim of this study is to investigate the effect of traverse speed on the waviness appearance on machined surface and the regularity at which the waviness occurs. During investigation, it was observed that in the same period of time, at all traverse speeds and the thickness of material that has been processed, there is almost the same number of waves.*

Keywords: *waviness, trverse speed, abrasive water jet*

1. INTRODUCTION

Abrasive water jet machining is one of the latest non-conventional methods, which have recently been increasingly used in industry for cutting of various materials, from those with pronounced plastic properties, to very-brittle materials. The main advantage of this machining process is that there is no occurrence of heat affected zone.

Abrasive water jet machining is based on the process of erosion as the primary mechanism for the removal of material from the workpiece. Bitter [1] has defined erosion of material as damage, which occurs as a result of single impact of abrasive particle (which is located in a fluid and is moving at high speed). Hutchings [2] has defined erosion as abrasive wear in which abrasive particles (which are also located in a fluid and moving rapidly) hitting the surface several times and thus leads to erosion of the material. The traces on the surface machined with abrasive water jet, resulting from erosion of the workpiece material, are visible under a microscope. Their direction is changing with depth of cutting, and follows the direction of the cutting beam through the workpiece. On the abrasive water jet generated surface can be observed the curved lines that are characteristic for this type of machining. Also, machined surface has a pronounced waviness in the lower part, and it increases with increasing depth of cut. These irregularities on machined surface, and the taper of cut, significantly constrain the opportunities of application of abrasive waterjet machining.

2. ABRASIVE WATER JET MACHINING

Modern installations for abrasive water jet machining work with water pressure over 400MPa, while the water jet reaches speeds of up to 1000m/s. They consist of a driver and the executive and supporting components. The driver is a unit that creates high-pressure water, while an executive componenet is a cutting head. The system components of abrasive water jet cutting machine are shown in Figure 1.

The way of working is the following: Hydraulic oil under pressure of 5÷35 MPa enters the hydraulic cylinder and intensifier. Because of large difference in the diameters of the intensifier, water pressure reaches the value of 400 MPa or more. Intensifying system is the key of equipment. Pressure value in intensifier depends on the ratio of cross sections

area of the cylinders. This ratio usually ranges between 1:10 and 1:25 and is a constant. To change the value of water pressure, it is necessary to change the oil pressure in the hydraulic system.

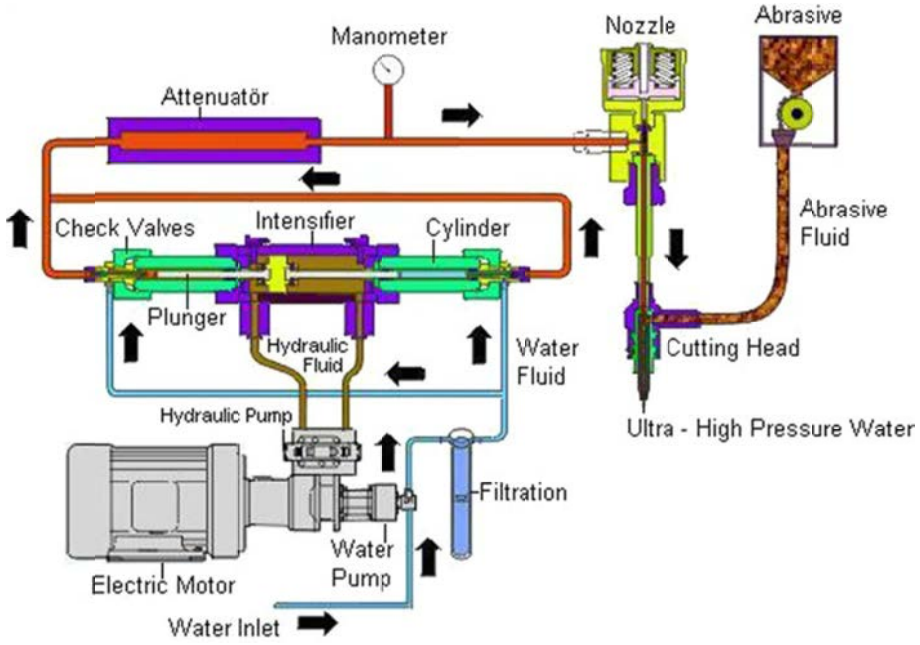

Figure 1. The system components of abrasive water jet cutting machine [3]

In order to get a jet of water, whose pressure is approximately constant, the most commonly duplex reciprocating pump- intensifier (DRP) is used. This is actually a complex cylinder which is double-acting pump, with two high pressure cylinders, joined with the back towards each other. When the first cylinder complete stroke, piston rod moves back and compresses the water in the second cylinder.

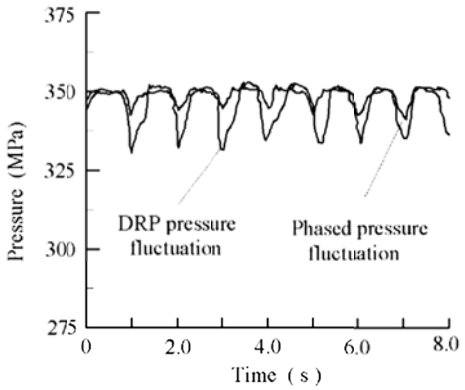

Figure 2. Fluctuations of pressure during machining with abrasive water jet [4]

These cycles are repeated successively. Because the water can be compressed 12% under the pressure of 400 MPa, the initial stage of the piston travel is used to compress the water [4]. Water is not delivered into the system until the water pressure reaches the set value. Therefore, the actions of draining water and absorbing water are discontinuous, and the pressure is fluctuant. To neutralize the pressure fluctuations, it is necessary to install an accumulator behind the intensifier.

Figure 2 is a diagram which shows the pressure fluctuations in a conventional intensifier and the phase-shifted intensifier cylinders.

3. ABRASIVE WATER JET GENERATED SURFACE

Abrasive water jet generated surface has a characteristic appearance and is shown in Figure 3. Curved lines, showing the movement of abrasive water jet through the workpiece material, can be observed in the Figure 3. The topography of the machined surface and the appearance of curved lines are the most important macroscopic properties of the surface machined with abrasive water jet. Based on the analysis of these two characteristics can result in significant information about the machining process.

Roughness of the surface machined with abrasive water jet increases with increasing depth of cut [5]. Surfaces machined with abrasive water jet are divided into two areas, fine machining zone (the upper zone) and rough zone (the lower zone). Irregularities that occur in the upper zone of the machined surface are considered as microscopic irregularities and are in the domain of roughness. Irregularities that occur in the lower zone of the machined surface have macroscopic dimensions. These irregularities are in the domain of waviness in conventional machining.

Figure 3. Appearance of the surface machined with abrasive water jet

Waviness of the machined surface is also an important phenomenon in the machining with abrasive water jet, Figure 4. It was found that there is a primary and secondary waviness on the surface machined with abrasive water jet [6]. Primary waviness is a waviness with higher step values, while the secondary waviness has less step value. For all cutting parameters, if the primary wavelength of the profile at the rough cutting zone is smaller, the surface is smoother. Guo [7] found that there is a dependence of the waviness step and focusing tube diameter, while Kovacevic [8] found a correlation between waviness step and a diameter of abrasive particles and the focusing tube diameter.

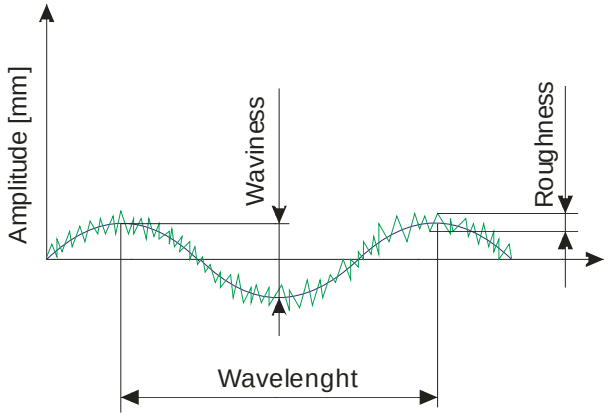

Figure 4. Waviness and surface roughness

The quality of the surface machined with abrasive water jet is influenced with system operational process parameters such as traverse speed, waterjet pressure, abrasive flow rate, standoff distance, depth of cut and angle of cutting [9].

Level of influence of certain parameters is different. The largest number of authors agrees that the most influential are traverse speed, operating pressure and the abrasive flow rate. Traverse speed of the jet has a strong influence on the surface finish of the workpiece and material removal rate [11]. Figure 5 shows the influence of traverse speed and abrasive mass flow on the waviness.

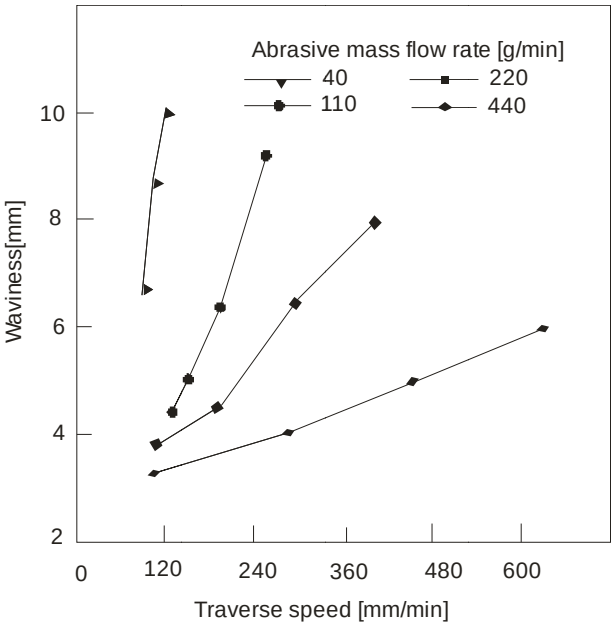

Figure 5. Parameter influence on the waviness [10]

4. EXPERIMENTAL INVESTIGATIONS

The aim of this study was to investigate influence of traverse speed on the appearance of profile waviness on machined surface. The experiments were conducted using a Byjet 4022 abrasive water jet cutting machine (Bystronic AG, Switzerland). Aluminium alloy AA-ASTM 6060 (EN: AW-6060; ISO: AlMgSi) was used as a workpiece material. Aluminum and its alloys are characterized by high reflectivity and thermal conductivity. This makes them relatively difficult to cut with lasers. Therefore, the machining with abrasive water jet is much more acceptable for aluminium alloy.

Abrasive water jet cutting involves a large number of variables that affect the cutting results (kerf width, taper and surface roughness, waviness). In the present study, the influence of the following parameters was investigated: traverse speed (the speed at which the cutting head moves along workpiece during cutting operation) and material thickness. The other process parameters were kept constant using the standard machine configuration (d_0=0.3mm; d_A=1.02mm; p=380MPa; Q=350g/min).

The samples of aluminum alloy 6 and 10mm thick were cut with different traverse speeds V=(200, 300, 400, 500, 800 i 1000 mm/min). On such machined samples, length at which the ten waves were observed, was measured, Figure 6.

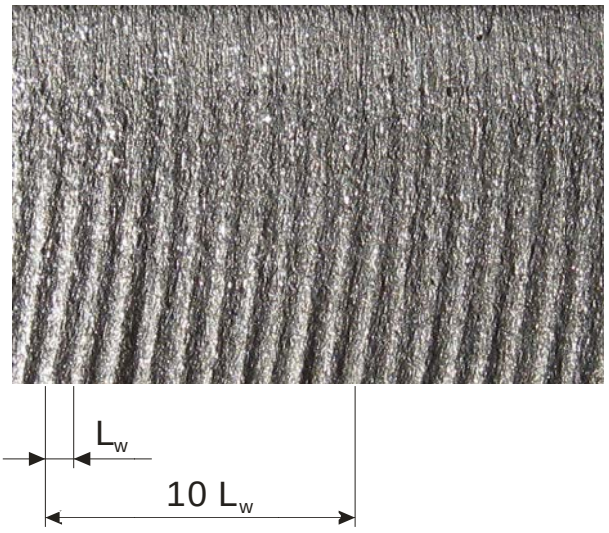

Figure 6. Measuring the length of ten waves

For this measured values ($10L_w$), based on Formula 1, the time needed to make ten waves (t_{10}) was calculated.

$$t_{10}=\frac{10L_w}{V}\cdot 60\ [s] \quad (1)$$

Based on these values, according to Formula 2, the number of waves that were made in one minute (N) was calculated.

$$t_{10}=\frac{10}{t_{10}}\cdot 60 \quad (2)$$

Table 1 shows the images of 6mm thick samples, obtained with different traverse speeds, and values for $10L_w$, t_{10} and N.

Table 1. 6mm thick samples

V [mm/min]	Images of samples	**$10L_w$ [mm]**	**t_{10} [s]**	**N [1/min]**
200		Waves are not clearly marked		
300	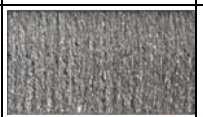	Waves are not clearly marked		
400		8.4	1.26	476.2
500	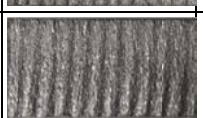	10.6	1.272	471.7
800		16.8	1.26	476.2
1000		21.1	1.266	473.9

5. CONCLUSION

By analyzing the results, it was observed that a change in traverse speed affects the wavelength and height on surface machined with abrasive water jet. As the traverse speed increases, the higher is the wavelength of profile waviness. Also, machining with higher traverse speed results in the increase of height of profile waviness. The most interesting is the fact that, regardless of the traverse speed and thickness of the workpiece, the number of waves in one minute is approximately the same. The frequency of the waves, and also the curved lines, is approximately constant and in this case ranges from 460 to 476 waves per minute. This fact can probably be explained with fluctuations in the value of the operating pressure of the abrasive water jet. In order to better explain the relationship between pressure oscillations and profile waviness frequency, more detailed examination are required.

Table 2. 10mm thick samples

V [mm/min]	Images of samples	**$10L_w$ [mm]**	**t_{10} [s]**	**N [1/min]**
200		Waves are not clearly marked		
300	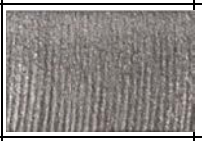	Waves are not clearly marked		
400	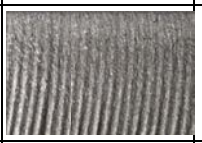	8.4	1.26	476.2
500	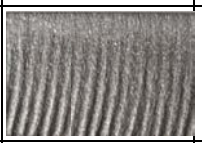	10.6	1.272	471.7
800		16.8	1.26	476.2
1000		21.1	1.266	473.9

ACKNOWLEDGMENTS

The authors would like to thank to the Ministry of Science and Technological Development of the Republic of Serbia. Paper is result of technological project TR35034: "The research of modern non-conventional technologies application in manufacturing companies with the aim of increase

efficiency of use, product quality, reduce of costs and save energy and materials" which is supported by Ministry of Education and Science of the Republic of Serbia.

REFERENCES

[1] J. Bitter: *A studu of erosion phenomena, part I,* Wear, No. 6, pp. 5-21, 1963.

[2] I.M.Hutchings, R.E.Winter, J.E.Field: Severe Solid particle erosion of metals: the removal of surface material by spherical projectils, in: *Proc.R.Sec.Lond.A.,* 348, London, pp.379-302

[3] A. Akkurt: *Cut Front Geometry Characterization in Cutting Applications of Brass with Abrasive Water Jet*, Journal of Mterials Engineering and Performance, pp. 599-606, 2010.

[4] J. Xu, B. You, X. Kong, Design and Experiment Research on Abrasive Water-jet Cutting Machine Based on Phased Intensifier, in: *Proceedings of the 17th World Congress*, Seoul, Korea, July 6-11, pp.14846-14851, 2008.

[5] J. Baralić, B. Nedić, P. Janković: The traverse speed influence on surface roughness in abrasive waterjet cutting applications, in: : *Proceedings of the 12th Int.Conf. on Tribology*, Kragujevac, Serbia, pp. 349-354, May 11 – 13, 2011.

[6] A.W.Momber, R. Kovacevic: *Principles of Abrasive Waterjet Machining,* Springer, London, 1998.

[7] N.S. Guo, H. Louis, G. Meier: Surface structure and kerf geometry in abrasive water jet cutting: formation and optimization, in: *Proc. 7-th Amer. Water Jet Conf.*, Vol. 1, Water Jet Techn. Ass.,ST.Louis, pp.1-25,1993.

[8] R. Kovacevic, R. Mohan, Y.M. Zhang: *Cutting force dynamics as a tool for surface profile monitoring in AWJ,* ASME J. Engng. For Ind. 117, pp.340-350, 1995.

[9] J.Valiček, M. Držík, M. Ohlídal, V. Mádr, L.M. Hlaváč: Optical method for surface analyses and their utilization for abrasive liquid jet automation, in: *Proc. of the 2001 WJTA American Waterjet Conference,* Minneapolis, pp. 1–11, 2001.

[10] M. Hashish: *A modeling study of jet cutting surface finish*, PED-Vol.58, pp.151-167, 1992.

[11] E. Lemma: *Maximum depth of cut and mechanics of erosion in AWJ oscillation cutting of ductile materials*, Journal of Materials Processing Technology, Vol. 160, No. 2, pp.188–197, 2005.

Serbian Tribology Society

SERBIATRIB '13

13th International Conference on Tribology

Faculty of Engineering in Kragujevac

Kragujevac, Serbia, 15 – 17 May 2013

EFFECT OF REFRACTORY ELEMENTS ON WEAR INTENSITY OF THE SURFACE LAYERS IN THE ABRASIVE SOIL MASS

J. Napiórkowski[1], P. Drożyner[1], P. Szczyglak[1]
[1]University of Warmia and Mazury in Olsztyn, Poland
napj@uwm.edu.pl, przemyslaw.drozyner@uwm.edu.pl, szczypio@uwm.edu.pl

Abstract: *The paper presents the results of researches on tthe influence of vanadium and niobium on wear intensity of the surface layers in soil mass. The investigations were conducted in the laboratory conditions on a wearing machine MZWM -1. The study adopted two types of surface layers obtained by welding with additon of niobium and vanadium. The resulting layers were tested in three kinds of soil masses: loamy sand, ligh clay and ordinary clay. Significant differences in the wear between the layers, depending on the type of soil were observed.*

Keywords: *weld overlay layer, vanadium, niobium, soil abrasive mass, the wear process.*

1. INTRODUCTION

Wear in abrasive soil mass is a natural process of destruction which intensity depends on kind of soil [2,5]. Significant here is the occurrence of various phenomena of wear, depending on the random changes in the soil, the working process parameters and material properties used in the working elements. The choice of material for elements work in soil with optimal properties for specific environmental conditions should be preceded by an analysis of the nature and type of wear on the surface and the surface layer [1,4]. The criterion for the selection of the material is chosen primarily on the basis of well-defined heterogeneous phase composition of the layer structure. It has been found that the abrasive wear resistance is the sum of the individual resistances [3].

In the case of iron alloys it is just a matter of carbide phase. Selection of carbide must take into account the specific characteristics of the interaction between Fe-Cr-C and carbide formers elements. Some of them are refractory elements such as vanadium and niobium. These elements melting at very high temperatures are quite difficult to obtain in the pure state. In chemical terms are relatively unreactive, and their reactivity decreases with increasing atomic number. Most of the niobium is used in the form of ferrosilicon, and may be used in the form of NbC carbides. Only about 6% of the total production of niobium is intended for Nb alloys production. Niobium has a relatively low solubility in iron- a (alpha), and *iron-*γ (gamma). Niobium is added to the surface layer in an amount up to 10%. The addition of niobium to the steel and heat resistance alloys gives the effect of precipitation hardening by intermetallic compounds or by NbC. Pure vanadium has good plasticity, it is easily workable and have a good welding properties under argon atmosphere. It is resistant to corrosion and influence of alkali. The vanadium in the steel forms a very hard VC carbides in combination with the resistance to tempering heat makes it is used in engineering constructions.

Aim of this study is to analyze the wear process in the soil mass in the context of the construction of the abrasive surface layers containing refractory elements V and Nb.

2. METHODS

The laboratory researches have been conducted on a wear machine "spinning mass" type. The sample was a rectangular prism with dimensions 30x25x10 mm, cut from the weld overlay padding (with additional materials) on steel

38GSA. The chemical composition, determined by methods of classical chemistry, is as follows: C - 0.38%, Mn - 1.07%, Si - 1.17%, P - 0.028%, S - 0.02%, Cr - 0 , 18% Cu - 0.16% Al - 0.022%. The microstructure of the steel: martensite with bainite and troostyt. At the same time two samples of one of each type were placed in the machine. The chemical composition of the surface layers are shown in Table 1.

Table 1. Chemical composition of layers tested

Root		Chemical composition [%]	
		Nb	V
C	Coal	5.2	5
Si	Silicon	2.2	1.5
Cr	Chrome	29	23
Nb	Niobium	6.8	-
V	Vanadium	-	10
Other	-	3.5	-
Fe	Iron	rest	rest

Each sample underwent a total of 20 000 meters with speed of about 1.7 m/s. Measurement of the mass of the sample was performed at each 2 000 meters with use of laboratory scale with accuracy of 0.0001 g, after the cleaning in an ultrasonic cleaner. At that time the mass of soil were exchanged with a new one. Samples had oscillating movement.

The study was conducted in three types of abrasive soil mass (according to USDA) in loamy sand, light clay and ordinary clay. Characteristics are shown in Table 2. Granulometric evaluation was performed using a laser particle size meter + Hydro Mastersizer 2000. Humidity of the soil was determined by measuring the weight of the dried solid at a temperature of 105 °C. The study was conducted on humid mass.

Table 2. Characteristics of soil pulp

Group grain size	Fraction [%]			Humidity weight %
	2,0-0,05 mm diameter sand	0,05-0,002 mm diameter dust	Clay below 0.002 mm in diameter	
Loamy sand	77, 48	20.83	1.69	9-11
Light clay	56.48	30.83	12.69	12-13
Ordinary clay	26.86	48.62	24.52	13-15

Microscopic examination was performed by light microscopy methods - Neophot 52 microscope coupled with a digital camera Visitron Systems. Scanning microscope JEOL JSM - 5800 LV coupled with X-ray microanalyser Oxford ISIS LINK - 300 were used for scanning electron microscopy and chemical composition microanalysis. Samples were digested with 3% HNO3 (Mi1Fe) and electro-chromic acid.

Hardness measurements of the surface layer were determined by Vickers method in accordance with DIN EN ISO 6507-1:1999. Measurements were carried out with load of 1 kg (9.807 N) acting during the 15s. To quantify the wear it was assumed unit weight wear related to 1cm2 abraded surfaces and road friction. Figure 1 presents wear machine "spinning mass" type which was used during experiment.

Figure 1. Photo of wear machine "spinning mass" type

3. RESULTS

Figures 2 and 3 shows macroscopic images of the construction of the layer containing Nb and V.

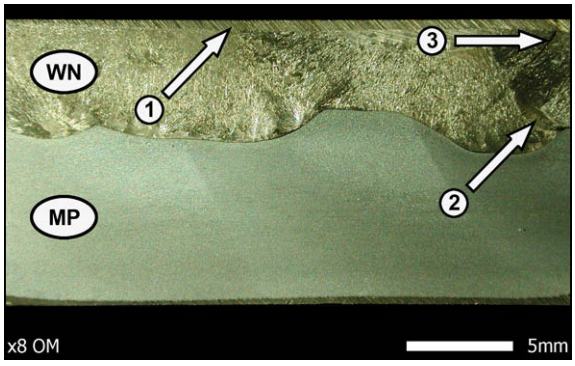

Figure 2. Macroscopic picture of the construction of the layers with Nb content. Visible traces of grinding (1). In the right part of the layer - macro cracks (2) and (3). WN – weld overlay, MP - pad material.

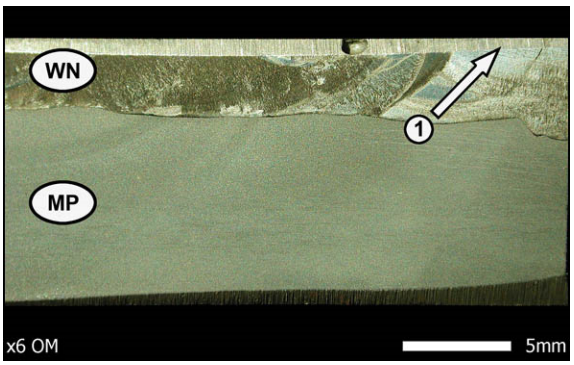

Figure 3. Macroscopic picture of the construction of the layers with V content. Visible traces of grinding (1). No evidences of macro cracks . WN – weld overlay, MP - pad material.

Figures 4 and 5 show microscopic structure of Niobium-containing layer. In addition to the narrow strip of ferritic alloy, weld overlay has homogeneous structure. Large initial separation of chromium carbides and niobium carbide are visible on background of ledeburite (Fig. 11).

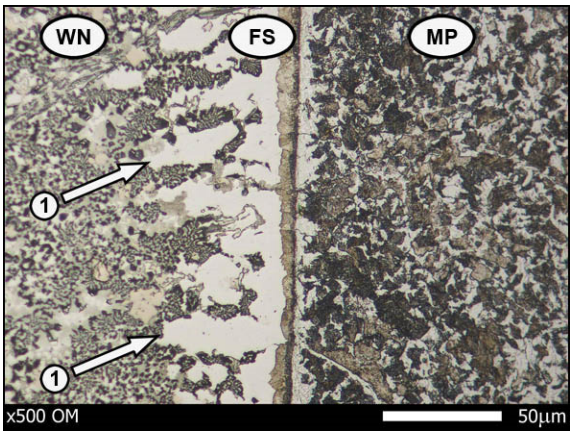

Figure 4. Microscopic image of material "Nb" fusion zone. At the junction of the weld metal pad material visible "bar" of ferrite alloy from which crystallized dendritic deposit separating the phases (1). In the material "pad" the microstructure of ferrite grains with bright dark areas of perlite. WN - layer of the deposit, FS - ferrite alloy, MP - pad material.

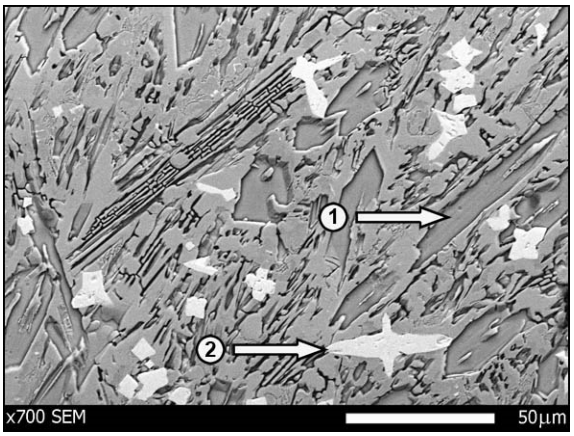

Figure 5. The microstructure of the weld layer material "Nb" of chromium carbide precipitates (1) and niobium (2).

Figures 6 and 7 show the characteristics of the surface layer containing vanadium. Outside the fusion zone, layer has a microstructure consisting of ledeburite, primary carbides of chromium and vanadium carbides.

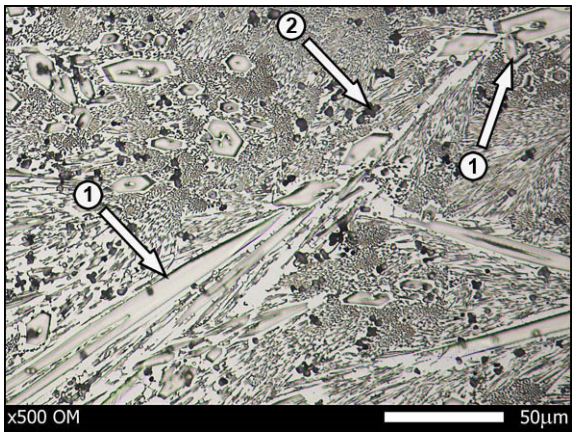

Figure 6. Microscopic images of the surface layer material "V". Ferrite tungsten alloy (mixture of construction ledeburitic) with unevenly spaced primary chromium carbide precipitates (1) and fine carbides of vanadium (2).

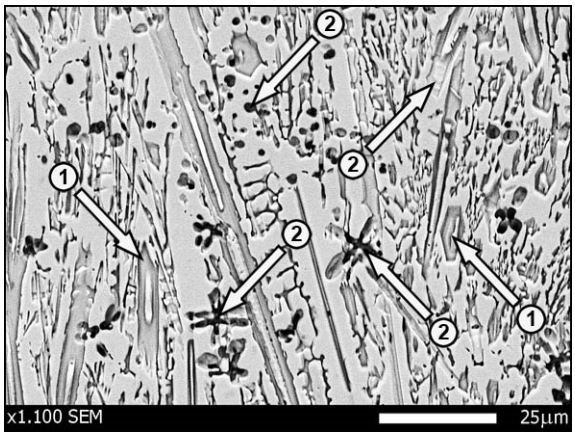

Figure 7. Microscopic image of the plastic layer "V". Ledeburitic mixture of ferrite alloy and chromium carbides M7C3 type (1) and vanadium carbides (2).

Table 2. Distribution of layers hardness

Type of layer		Material "Nb"	Material "V"
Hardness		HV 10	HV 10
The distance from the surface [mm]	0.5	694	783
	1.0	676	777
	1.5	643	733
	2.0	638	722
	2.5	612	692
	3.0	593	654
	3.5	5 of 85	639
	4.0	540	641
	4.5	541	266
	5.0	550	256
	5.5	286	-

As is clear from the measurements of hardness (table 2) test layers have diverse hardness on the cross section. The layer of vanadium content is harder for almost 90 units of the layer containing

niobium. It should be noted that for both layers gradual decrease in cross-sectional hardness was observed. Figure 8-11 presents the results of wear in different abrasive masses.

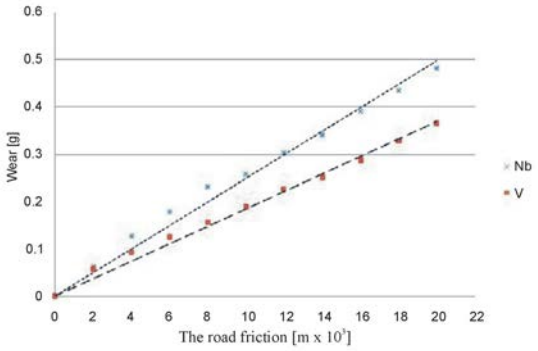

Figure 8. The course of wear layers in loamy sand.

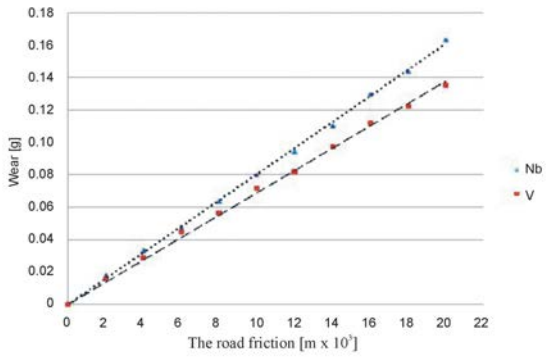

Figure 9. Mileage wear light layers in clay.

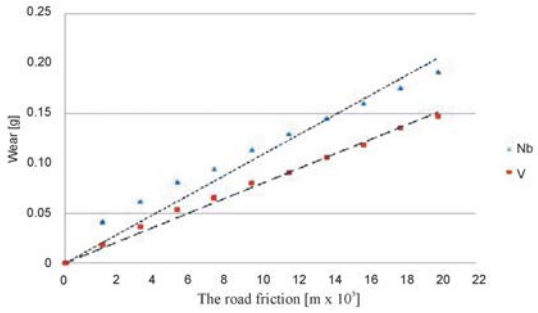

Figure 10. Light clay wear layers in the clay normal

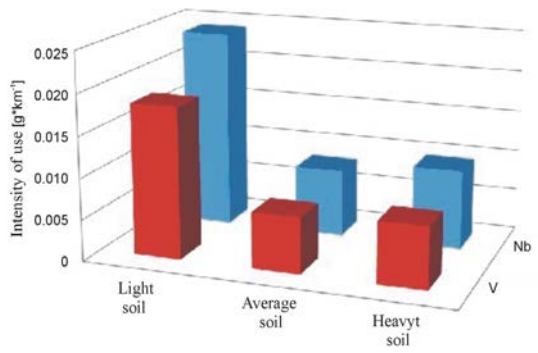

Figure 11. Comparison of intensity of layers depending on the type of mass

4. CONCLUSION

The results of the research carried out in three different soil masses showed the complexity of process of the abrasive wear in tribological discrete nodes. The highest wear was recorded in layers of sandy soil and it was higher by more than 2.5 times higher than in clay soils. Wear of layer with vanadium content was about 30% smaller than the layer containing niobium. Causes of dependence should be sought in the mechanism of wear. In the event of wear in the abrasive mass containing large amounts of silica, there was the greatest contact with the abraded area. A different analysis is required for results obtained during friction in clay soil masses. The friction in these soils had a different course than the sandy soil. Clay soil tends to form aggregates of soil, hence there are many air pores, and thus much more discontinuities friction surface than in the case of sandy soil. In addition, the impact of the clay and dust on the process of wear is negligible, but in combination with other factions can be multiplied. Greater wear in clay hard was observed due to the fact that the weight of the formed soil aggregates was greater than a light loam. The intensity of wear for layers of light and ordinary clay remained at the same level values wherein layer containing vanadium wear less intense than the layer containing niobium.

REFERENCES

[1] M.F. Buchely, J.C. Gutierrez, L.M. Le´on, A. Toro: *The effect of microstructure on abrasive wear of hardfacing alloys*, Wear, 259, pp. 52–61, 2005.

[2] J. Coronado: *Effect of Abrasive Size on Wear, Reserch Group of Fatigue and Surfaces*, Mechanical Engineering School, Universidad del Valle, Cali Colombia, 2011.

[3] J. Napiórkowski, L. Pękalska, G. Pękalski: *Structure of material and its wear resistance in the soil*, Tribologia 6, pp. 871-879, 1998.

[4] J. Napiórkowski, G. Pękalski, K. Kołakowski: *Badanie struktur i zużywania powłok napawanych w glebowej masie ściernej*, Tribologia 3/2012, pp. 111-118, 2012.

[5] J. Napiórkowski, P. Drożyner, K. Kołakowski, P. Mikołajczak: *Analysis of tribological processes of construction materials in the soil mass abrasive wear process*, International Virtual Journal for Science, Technics and Innovations for the Industry year VI, 11/2012, ISSN 1313-0226, pp. 27-29, 2012.

Serbian Tribology Society

SERBIATRIB '13

13th International Conference on Tribology

Faculty of Engineering in Kragujevac

Kragujevac, Serbia, 15 – 17 May 2013

EXPERIMENTAL ANALYSIS OF TOOTH HEIGHT CHANGING AT TIMING BELTS

Blaža Stojanović[1], Lozica Ivanović[1], Andreja Ilić, Ivan Miletić[1]

[1]Faculty of Engineering, University of Kragujevac, Serbia, blaza@kg.ac.rs, lozica@kg.ac.rs, imiletic@kg.ac.rs

Abstract: *Timing belt drives present relatively new power transmitters that transmit power by friction and form contact. Load at timing belts is under direct influence of active surface of timing belt tooth. During exploitation, the height of tooth at timing belt decrease and, by that, reduction of active surface is provoked, load increases and working life decreases. Besides of tooth height, changing of tooth width at timing belt, also presents very important factor. The tribomechanical system at pulley teeth - timing belt teeth with height changing during exploitation is analyzed in this paper. Experimental testing of tribological characteristics was done at custom design and made testing device at Center for power transmission at Faculty of Engineering in Kragujevac.*

Keywords: *timing belt, tribomechanical system, timing belt teeth, friction, testing.*

1. INTRODUCTION

Working life and reliability of timing belt transmitters are highly influenced by timing belt geometrical dimensions that means timing belt pitch, its tooth height and width. Timing belts are made of polymer materials reinforced by metallic materials and their dimensions vary during exploitation. Highest variation of geometrical dimensions occurred during running-in period of new belt. During this period, changing of timing belt pitch is highest, primarily influenced by plastic deformations of side surfaces of its tooth. After running-in period, changings of geometrical characteristics are linear with same trend for considered values [1-4].

The contacts of timing belt and pulley cause changing of geometrical properties. On the basis of kinematic analysis of pulley and belt contact in details, following three tribomechanical systems can be identificated [5, 6]:

1. belt teeth – pulley teeth
2. side surface of belt – pulley rim
3. inter teeth belt space – head of teeth pulley

Friction force in tribomechanical system belt teeth – pulley teeth is dominant factor in case of tooth height changing analyses.

2. TRIBOMECHANICAL SYSTEM BELT TEETH – PULLEY TEETH

During mashing of belt teeth with pulley teeth contact between side surfaces is done. The contact is at line, for the beginning, when belt teeth come in mash with pulley teeth. The mashing starts with impact of belt teeth and pulley teeth. The belt teeth deform, due to its elastic properties and, by that, enlargement of contact surface is done. After enlargement of contact surface, and rotations of belt and pulley, belt teeth slide on side surface of pulley, when rolling with sliding type of friction is happened.

The value of friction force decreases with length of sliding path, so its maximal value is at the base of belt teeth (Fig. 1). Simultaneously, acting point of resulting component of normal force moves from head to base of the teeth. Normal force varies with parabolic dependence:

$$N_i = -\frac{N_{\max}}{l_t^2} \cdot \left(l - l_t\right)^2 + N_{\max}, \qquad (1)$$

where is:

$N_{\max}$ - maximal value of normal force,

l - length of tooth profile and

l_t - length of sliding path.

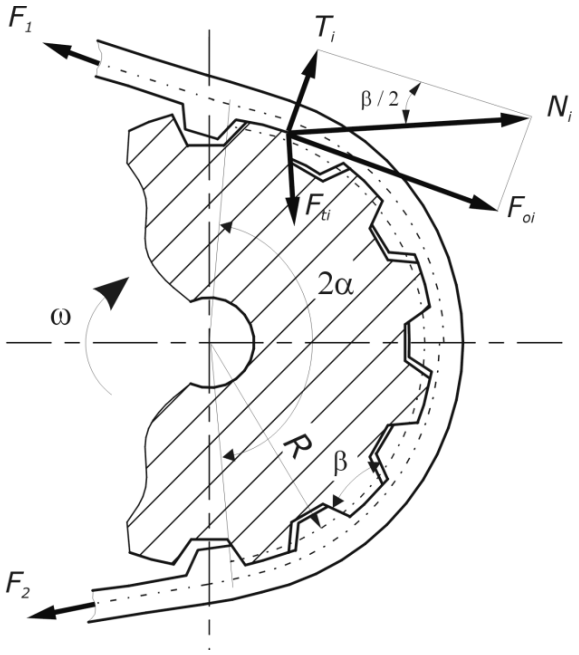

Figure 1. Friction force on side surface of belt teeth

Friction force on side surface of belt teeth can be determined by following relation:

$$F_{ti} = N_i \cdot \mu = \frac{F_{oi} \cdot \mu}{\cos(\beta/2)} \qquad (2)$$

where is:

N_i - normal force on belt teeth,

μ - friction coefficient,

F_{oi} - peripheral force that act on belt teeth and

β - belt profile angle.

3. TESTING OF TIMING BELT

Experimental testing of tribological characteristics was done at custom design and made testing device with open power loop at Center for power transmissions at Faculty of Engineering in Kragujevac [7-9]. Basic elements of testing device are (Fig. 2):

1. driving unit,
2. Cardan transmitter,
3. input shaft with measuring devices,
4. sensor for input shaft number of rotation,
5. torque sensor on input shaft,
6. considered power transmitter (timing belt-pulley),
7. output shaft,
8. mechanical brake,
9. tension mechanism and
10. signal amplifier.

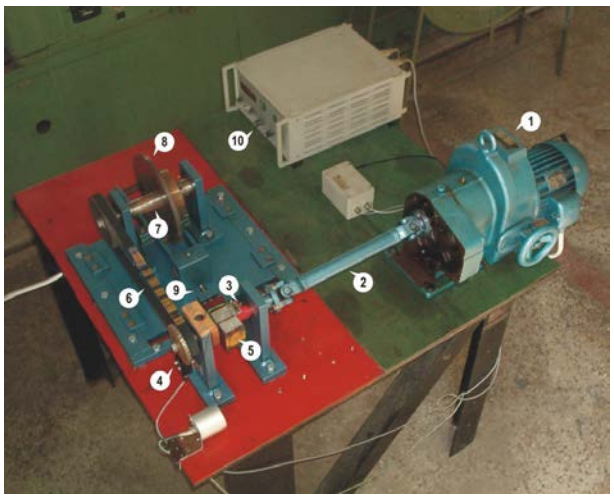

Figure 2. Device for timing belt testing.

Driving unit, type KR-11/2C (37-180 rpm^{-1}), consists of electromotor (1) type ZKT90S-4 (totally enclosed single phase asynchronous motor with cage rotor with thermal protection, size 90L, 4-pole type), friction power transmitter, and gear reductor. Design solution provides automatic regulation of pressure between friction discs and compensation of axial gap due to wear. Changing of number of rotations per minute is done manually, by rotation of wheel that by coupling of gear and bar, radially (vertically) move electromotor with conical friction disc from friction wheel. Driving unit (1) and input shaft (3) are connected by Cardan transmitter (2).

Input shaft (3) is design in the way to be elastically deformed under maximal torque load. Inductive sensor of number of rotations per minute (4), type MA1 is placed on input shaft, so as torque transducer (5) that is formed of strain gauges and signal transmitter MT2555A that is mounted by special adapter with battery compartment BK2801A.

Input and output shafts (7) are connected by considered power transmitter (6), means timing belt - pulley system. Tension of timing belt is done by the tension mechanism (9) with external threaded spindle. By spindle rotations the movements of plate with output shaft and mechanical brake are done.

Mechanical brake is specially designed for open power loop (Fig. 3). Breaking is done by acting of breaking pads on both sides of the disc. Regulation of force and torque is done manually by the means of spring and screw.

Mechanical brake obtain certain braking torque, means load torque on output shaft of timing belt – pulley power transmitter. Value of torque is presented on digital display of the signal amplifier that gets signal from measuring device on shaft by signal transmitter EV2510A. The number of rotations per minute of input shaft is also displayed on amplifier gain that gets signal from inductive sensor and impulse receiver DV2556.

Working regime of input shaft at power transmitter is measured and regulated in presented way.

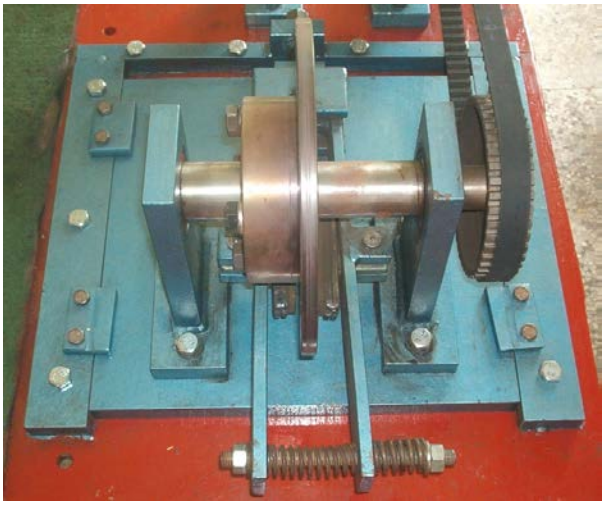

Figure 3. Mechanical Brake

By adaptations of joining elements with driving unit from one side and output shaft equipped with measuring devices testing of various types of power transmitters can be done on presented equipment with limitations in dimensions and load.

4. TESTING RESULTS

Measuring of geometrical dimensions is done at Zastava tool factory, Department of quality. In order to provide relevant analysis measuring of the following values are done at eight teeth of timing belt (Fig. 4):

- pitch (h),
- belt width (b),
- distance between belt teeth (t_1) and
- belt height (t).

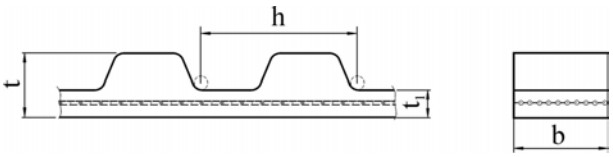

Figure 4. Basic geometrical properties of timing belt

Change of timing belt height is considered in this paper. Belt height is distance between head of belt tooth and backing surface. Measuring was done by DIGIMAR measuring device (Fig. 5). Changing of belt height (Δt) during testing can be calculated by following relation:

$$\Delta t = t_o - t,$$

where is:

t - measured value of belt height and

t_o - starting height of the belt.

Figure 5. Measuring device –DIGIMAR

Results of measuring of the belt height changing during exploitation at eight considered tooth are presented at Tab. 1 by values and at Fig. 6 by diagrams.

Table 1. Change of timing belt height $\Delta t = t_o - t$ [μm]

Exploitation period [*h*]	Δt							
	Belt teeth							
	1	2	3	4	5	6	7	8
5	52	75	34	23	17	3	32	13
10	53	77	38	30	23	15	39	15
20	62	83	46	41	36	17	42	30
50	65	96	49	52	57	26	53	51
100	65	98	50	53	57	33	53	53
150	67	101	54	53	57	35	57	53
200	68	105	58	61	57	55	74	55
250	69	109	58	65	67	63	82	63
300	76	125	63	67	67	66	84	63

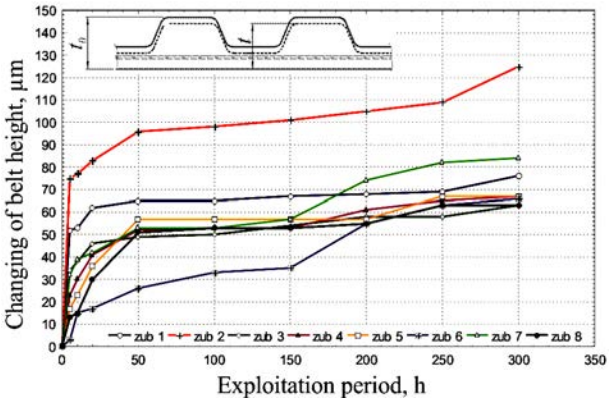

Figure 6. Changing of tooth timing belt height in exploitation

Evaluations of the obtained results implicate that belt height decreases monotonely during exploitation. During running-in period, that lasts for approximately 20 hours, this changing is very significant and it is happening on all of considered eight belt tooth. The changing during running-in period is caused by deformations of the belt, its pitch and width decrease. During period of exploitation due to normal wear belt height decreases. During period of 20 hours to 50 hours of

exploitation this changing is significant. After 50 hours of exploitation till 200 hours of exploitation, the very fast changing occurred at most of the tooth. Plastic deformation occurred during running-in period. Due to the fact that those deformations are small during period of normal wear, cylindrical wear of tooth head are not significant, so height changings are small. After 200 hours of exploitation changing of tooth heights are significant.

On the basis of the further analyses, conclusion that changings of all values are subjected to same decrease function is implicated. But, on the basis of the analysis in details it is implicated that changing of belt height is bigger than changing of inter tooth space width. This fact leads to decrease of active tooth heights that are in contact with tooth of the pulley. If the reduction of belt width after 150 hours is taken into consideration, it is implicated that value of nominal surface side of timing belt tooth also decrease. As timing belt - pulley transmitters transmit power by form contact and friction, increase of timing belt pitch and decrease of nominal active surface of tooth all together cause failures in exploitation of those transmitters.

5. CONCLUSION

The basic tribomechanical systems at timing belt – pulley transmitter are: timing belt teeth – pulley teeth, belt side – rim of the pulley, inter space of timing belt tooth – head of pulley tooth. Friction forces are highest at side surfaces of timing belt tooth and pulley tooth. Directions and values of those forces are under direct influence of meshing kinematics of timing belt transmitters.

As the consequence of friction at side and head surface of tooth, the reduction of belt height is caused. Decrease of belt width and reduction of its height cause decrease of active contact surface, that further cause increase of loads at tooth and simultaneous decrease of transmitter coefficient of efficiency. Average changing of timing belt tooth height relatively to starting value is 3.14 %.

Considered changing of geometrical properties of timing belt causes significant influence to reliability and working life of timing belt transmitters.

REFERENCES

[1] R. Perneder, I. Osborne: *Handbook Timing Belts: Princilpes, Calculations, Applications*, Springer-Verlag Berlin Heidelberg, 2012.

[2] S. Tanasijević: *Mechanical drives: chain drives, timing belt drives, cardanic drives* (in Serbian), Yugoslav tribological society, Faculty of engineering from Kragujevac, 1994.

[3] B. Stojanović, S. Tanasijević, N. Marjanović, L. Ivanović, M. Blagojević: *Wear as the Criterion of Mechanical Transmitters Working Life*, J Balk Tribol Assoc 17, pp. 215-222, 2011.

[4] B. Stojanović, M. Babić, N. Marjanović, L. Ivanović, A. Ilić: *Tribomechanical Systems in Mechanical Power Transmitters*, J Balk Tribol Assoc 18, pp. 497-506, 2012.

[5] B. Stojanović, S. Tanasijević, N. Miloradović: *Tribomechanical Systems in Timing Belt Drives*, J Balk Tribol Assoc 15, pp. 465-473, 2009.

[6] B. Stojanović, N. Miloradović, N. Marjanović, M. Blagojević, A. Marinković: *Wear of Timing Belt Drives*, J Balk Tribol Assoc 17, pp. 206-214, 2011.

[7] B. Stojanović, N. Miloradović, N. Marjanović, M. Blagojević, L. Ivanović: *Length Variation of Toothed Belt During Exploitation*, Strojniški vestnik, Vol. 57, No. 9, pp. 648-654, 2011.

[8] B. Stojanović, L. Ivanović, M. Blagojević: *Friction and Wear in Timing Belt Drives*, Tribology in Industry 32, pp. 33-40, 2010.

[9] B. Stojanović, L. Ivanović, N. Miloradović: *Testing of Timing Belt Drives*, IMK-14 37, pp. 77-80, 2010.

Serbian Tribology Society

SERBIATRIB '13

13th International Conference on Tribology

Faculty of Engineering in Kragujevac

Kragujevac, Serbia, 15 – 17 May 2013

CYCLO DRIVE EFFICIENCY

Tihomir Mačkić[1], Živko Babić[2], Nenad Kostić[3], Mirko Blagojević[4]
[1]Faculty of Mechanical Engineering Banja Luka, Bosnia and Herzegovina, tihomir.mackic@unibl.rs
[2]Faculty of Mechanical Engineering Banja Luka, Bosnia and Herzegovina, zivkobabic@unibl.rs
[3]Faculty of Engineering University of Kragujevac, Serbia, nkostic@kg.ac.rs
[4]Faculty of Engineering University of Kragujevac, Serbia, mirkob@kg.ac.rs

Abstract: *Cyclo drives have a many good characteristics: high gear ratio, compact design, two-thirds of its reduction components in contact at all times, reliability and long life in the most severe applications, minimal vibration, low noise, low backlash and extended operational life, high power density, wide variety of inputs available,… One of the most important its characteristics is high efficiency.*
Two methods for determining of cyclo drive efficiency are presented in this paper. Their complete analytical models are defined. The influence of various parameters on the cyclo drive efficiency is also analyzed (power, rotational angle of input shaft, gear ratio, …). The calculation of the cyclo drive efficiency by both methods is done for the real one-stage cyclo speed reducer. Concluding remarks and directions for future work are presented at the end of the paper.

Keywords: *cyclo drive, cycloid, gear, power losses, efficiency*

1. INTRODUCTION

Cycloidal speed reducer belong the group of planetary drives (Figure 1). Because of very wide area of application, production of cyclo drives has growing character and wide area of application: processing equipment, conveyors, presses, mixers, food industry, automotive plants, spinning machines, cranes,…

The most important working characteristics of cyclo drives are: wide range of possible gear ratios, quiet and reliable work, low level of noise and vibrations, exceptionally compact design, high efficiency rate, ... *Lehmann* gave the basic information about cycloidal gearing, [1]. The dynamic behavior of a cyclo drives is presented in Refs. [2,3]. *Kosse* investigated the hysteresis phenomenon in cyclo drives and damping properties derived from dickey curves under torsional impact load, [4]. *Liu* and other generated a new type of double-enveloping cyclo drive and calculated the torsional stiffness, [5]. The influence of friction on contact forces distribution is presented in papers [6,7]. *Sensiger* developed a new method for cycloidal gear profile, efficiency and stress optimization, [8]. *Chmurawa* and *Lokiec* presented the inside meshing and force distributions of cycloid disk with modified profile, [9]. A new concept of a two-stage cyclo drive is presented in paper [10].

Friction and wear have a greatest impact on the cyclo drive efficiency, [11, 12]. The calculation of the cyclo drive efficiency by two method (*Malhotra* and *Gorla*) for the real one-stage cyclo speed reducer is presented in this paper.

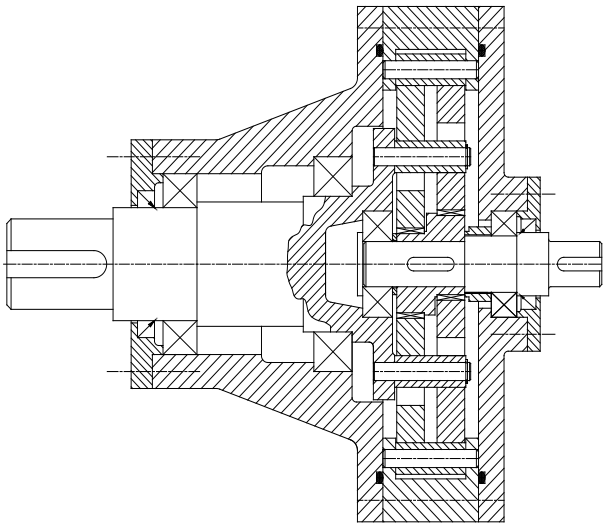

Figure 1. Cyclo drive

2. EFFICIENCY OF CYCLO DRIVE

Efficiency of cyclo drive primarily depends on the resistance due to friction between the elements of cyclo drive. Two methods for determining of cyclo drive efficiency are presented in this paper: *Malhotra* method [11] and *Gorla* method [12].

2.1 Malhotra method for calculating of cyclo drive efficiency, [11]

The various sources of power loss in a cyclo drive are:

- Rolling friction in the mounting of the cycloid disc on the input shaft,
- Rolling friction between output rollers and holes in the cycloid disc,
- Rolling friction between housing rollers and the cycloid disc,
- Sliding friction in the mounting of the output rollers,
- Sliding friction in the mounting of the housing rollers.

Design parameters are presented on Figure 2, and loads on Figure 3.

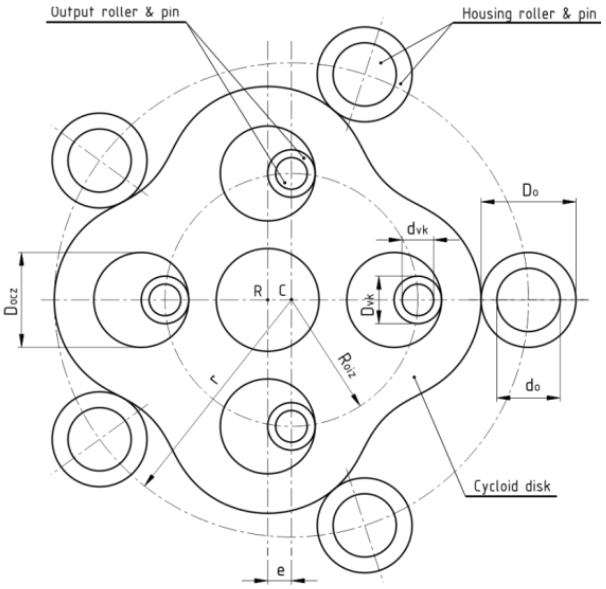

Figure 2. Geometry of cyclo drive

For the elemental rotation $d\theta$ of the cycloid disc, the rotations of the input shaft, output rollers and housing rollers are $n \cdot d\theta$, $n \cdot d\theta$ and $(n+1) \cdot d\theta$, respectively. The frictional work per rotation of the input shaft can be determined as:

$$W = \int_0^{2\pi/n} dW = \frac{f_{r1} \cdot D_m \cdot n}{D_r} \int_0^{2\pi/n} F_E(\theta) d\theta + \\ + n\left(f_{r2} + \frac{f_{s1} \cdot d_{VK}}{2}\right) \int_0^{2\pi/n} \sum_{j=1}^{q} F_{Kj}(\theta) d\theta + \\ + (u_{CR} + 1)\left(f_{r3} + \frac{f_{s2} \cdot d_O}{2}\right) \int_0^{2\pi/n} \sum_{j=1}^{q} F_{Kj}(\theta) d\theta \quad (1)$$

where: f_{r1}, f_{r2} and f_{r3} are lever arms of rolling friction, f_{s1} and f_{s2} are sliding friction coefficients, D_m is mean diameter of input shaft bearing, D_r is input shaft bearing rollers diameter, F_E is bearing reaction, d_{VK} is diameter of outpit mechanism pins, F_{Kj} is force between output roller j and cycloid disc, q is number of output rollers, u_{CR} is cyclo drive ratio and d_0 is diameter of housing pins.

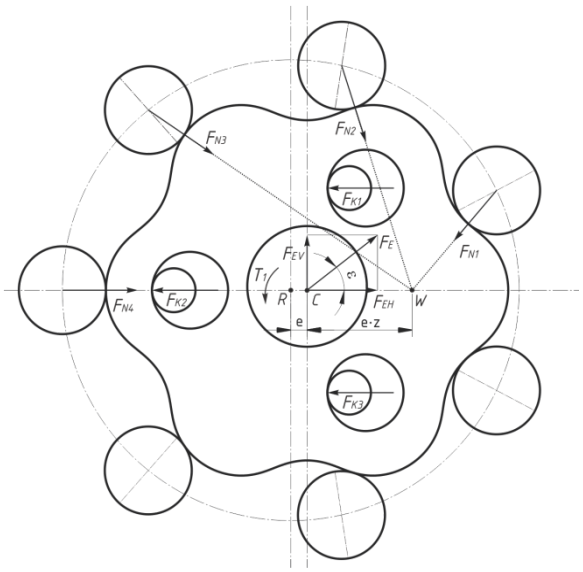

Figure 3. Loads on cycloid disc

The overall efficiency of cyclo drive is then:

$$\eta = \frac{M_a 2\pi - W}{M_a 2\pi} \quad (2)$$

where M_a is input torque.

2.2 Gorla method for calculating of cyclo drive efficiency, [12]

Power loss due to the bearing friction could be computed by means of the following equation:

$$W_{Ma} = M_a \cdot (\omega_{inner} - \omega_{outer}) \quad (3)$$

where: ω_{inner} is bearing inner race speed and ω_{outer} is bearing outer race speed.

Power loss due to the friction between the pins of the output shaft and the holes of the cycloid disc is:

$$W_K = \sum_{j=1}^{s} f_{Kj} \cdot F_{Kj} \cdot \upsilon_{Kj} \quad (4)$$

where: f_{Kj} is friction coefficient between the pins of the output shaft and the holes of the cycloid disc and υ_{Kj} is sliding speed between the pins of the output shaft and the holes of the cycloid disc.

Power loss due to friction between the cylindrical rollers, the surface of the ring gear and their housing in the planet wheel is:

$$W_N = \sum_{i=1}^{n} \rho \cdot \sin(arctg(f_{Ni})) \cdot \left|F_{Ni}\right| \cdot \left|\omega_{Ni}\right| \quad (5)$$

where: ρ is radius of cylindrical roller, f_{Ni} is friction coefficient between the cylindrical rollers and their houses and ω_{Ni} is relative rotational speed between the cylindrical rollers and the cycloid disc.

Vertical component of force F_{Ni} is calculated based on following expression:

The efficiency of cyclo drive can be calculated as:

$$\eta = \frac{P_{EM} - (W_{Ma} + W_K + W_N)}{P_{EM}} \quad (6)$$

3. CALCULATION OF CYCLO DRIVE EFFICIENCY

The efficiency of cyclo drive by two presented method is has calculated for input parameters in Table 1.

Table 1. Cyclo drive parameters

Mark	Value
P_{EM}	4,0 kW
n_{EM}	1420 min^{-1}
u_{CR}	13
f_{r1}, f_{r2}, f_{r3}	$f_{r1} = f_{r2} = f_{r3} = 0{,}003$
f_{S1}, f_{S2}	$f_{S2} = f_{S2} = 0{,}03$
d_0	8 mm
D_0	14 mm
q	8
d_{vk}	8 mm
D_{vk}	14 mm

Cyclo drive efficiency is calculated in program created in MATLAB. Values of cyclo drive efficiency are:

- η = 94,55% (*Malhotra* method),
- η = 95,03% (*Gorla* method).

Analysis of the influence of input power P_{EM}, input number of revolutions n_{EM} and gear ratio u_{CR} on cyclo drive efficiency by both method is presented in the paper, too (Figure 4, Figure 5 and Figure 6).

Dependence of cyclo drive efficiency on input power is presented on Figure 4. Input power was varied in range from 3 kW to 5 kW. Increasing the input power, cyclo drive efficiency is increasing, too (from 93% to 96%). Values of efficiency calculated by *Malhotra* [11] and *Gorla* [12] method are very similar.

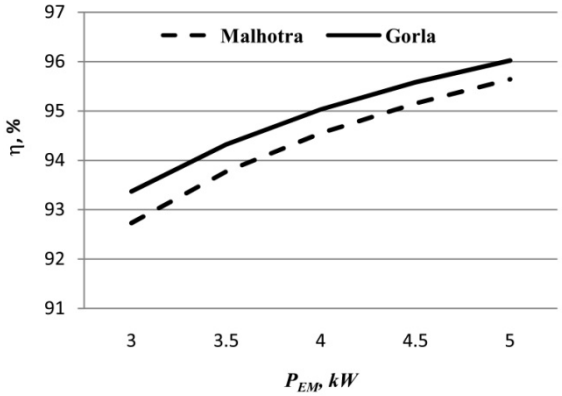

Figure 4. Dependence of cyclo drive efficiency on input power

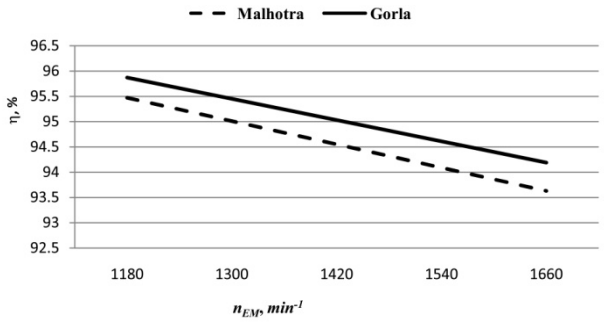

Figure 5. Dependence of cyclo drive efficiency on input number of revolutions

Dependences of cyclo drive efficiency from input number of revolutions is presented on Figure 5. Number of revolutions was varied from 1180 min^{-1} to 1660 min^{-1}. Increasing the input number of revolutions, cyclo drive efficiency decreases (for both method, Figure 5).

Dependence of cyclo drive efficiency on gear ratio is presented on Figure 6. Gear ratio was varied in range from 11 to 16. Increasing the gear ratio (*Malhotra* method), cyclo drive efficiency decreases from 95% to 94%. For *Gorla* method, cyclo drive efficiency increases from 94,8% to 95,3%.

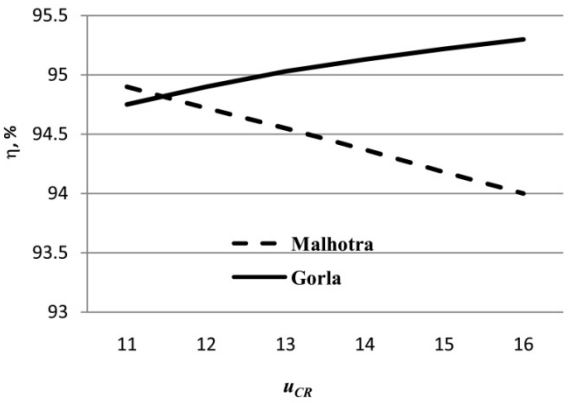

Figure 6. Dependence of cyclo drive efficiency on gear ratio

4. CONCLUSION

Two methods for calculating of cyclo drive efficiency are presented in this paper (*Malhotra* and *Gorla* method). Their complete analytical models are defined. The calculation of the cyclo drive efficiency by both methods is done for the real one-stage cyclo speed reducer.

By analyzing the results, it can be concluded the next:

- One-stage cyclo drive has very high efficiency,
- Both method (*Malhotra* and *Gorla*) have very similar values for efficiency,
- With increasing of input power, cyclo drive efficiency is increasing too,
- With increasing of input number of revolutions, cyclo drive efficiency decreases,
- With increasing of gear ratio, cyclo drive efficiency decreases (*Malhotra* method), or increases, (*Gorla* method).

REFERENCES

[1] M. Lehmann: *Calculation and measurement of forces acting on cycloidal speed reducer* (in German), PhD Thesis, Technical University Munich, Germany, 1976.

[2] S.V. Thube, T.R. Bobak: *Dynamic analysis of a cycloidal gearbox using finite element method*, AGMA Technical Paper, 2012.

[3] M. Blagojević, V. Nikolić - Stanojević, N. Marjanović, Lj. Veljović: *Analysis of cycloid drive dynamic behavior*, Scientific Technical Review, Vol. LIX, No. 1, pp. 52-56, 2009.

[4] V. Kosse: Using hysteresis loop and torsional shock loading to asses damping and efficiency of cyclo drives, *14th International Congress on Sound and Vibration*, 9-12. July, 2007, Cairns, Australia.

[5] J. Liu, S. Matsumura, B. Chen, H. Houjoh: *Torsional stiffness calculation of double-enveloping cycloid drive*, Journal of Advenced Mechanical Design, Systems and Manufacturing 6, pp. 2-14, 2012.

[6] M. Blagojević, N. Marjanović, B. Stojanović, Z. Đorđević, M. Kočić: Influence of friction on the force distribution at cycloidal speed reducer, *12th International Conference on Tribology*, 11-13.5.2011, Kragujevac, pp. 226-229.

[7] M. Blagojević, M. Kočić, N. Marjanović, B. Stojanović, Z. Đorđević, L. Ivanović, V. Marjanović: *Influence of the friction on the cycloidal speed reducer efficiency*, Journal of the Balkan Tribological Association, Vol. 18, No. 2, pp. 217-227, 2012.

[8] J. Sensiger: *Unified Approach to Cycloid Drive Profile, Stress, and Efficiency Optimization*, Journal of Mechanical Design (ASME), Vol. 132, 2010.

[9] M. Chmurawa, A. Lokiec: Distribution of loads in cycloidal planetary gear (CYCLO) including modification of equidistant, in: *16th Europian ADAMS user conference*, 2001, Berchtesgaden, Germany.

[10] M. Blagojević, N. Marjanović, Z. Đorđević, B. Stojanović, A. Dišić: *A new design of a two-stage cycloidal speed reducer*, Journal of Mechanical Design (ASME) 133, 2011.

[11] S.K. Malhotra, M.A. Parameswaran: *Analysis of a cycloidal speed reducer*, Mechanism and Machine Theory 18, pp. 491-499, 1983.

[12] C. Gorla, P. Davoli, F. Rosa, C. Longoni, F. Chiozzi, A. Samarani: *Theoretical and experimental analysis of a cycloidal speed reducer*, Journal of Mechanical Design (ASME) 130, 2008.

Serbian Tribology Society

SERBIATRIB '13

13th International Conference on Tribology

Faculty of Engineering in Kragujevac

Kragujevac, Serbia, 15 – 17 May 2013

TRIBOLOGICAL ASPECTS OF THE PROCESS OF WINDING THE STEEL ROPE AROUND THE WINCH DRUM

Miloš Matejić[1], Mirko Blagojević[1], Vesna Marjanović[1], Rodoljub Vujanac[1], Boban Simić[2]

[1]Faculty of Engineering, University of Kragujevac, Serbia,
mmatejic@kg.ac.rs, mirkob@kg.ac.rs, vmarjanovic@kg.ac.rs, vujanac@kg.ac.rs

[2]D.O.O RAPP Zastava, Serbia, bsi@rappzastava.com

Abstract: *Proper winding of the steel rope around the winch drum is great importance, mostly for: prolonging the service life of the rope, reduction of deformations of the body and the sides of the drum if the winding of the rope is multilayered, increasing of the safety factors, easier unwinding of the rope while lowering the load, even running of the drive unit, etc. The focus of this paper is on the analysis of the friction which occurs in the process of winding and unwinding the rope around the winch drum. Friction force is in its highest intensity when the rope passes from one layer to another, if the winding of the rope is multilayered. As the result of the research, certain mechanisms of winding of the rope from the aspects of the friction force were obtained, and the affect of the forces on the sides of the drum were analyzed*

Keywords: *winch, drum, rope, friction, friction force.*

1. INTRODUCTION

Modern technological achievements have enabled a great progress in the ship equipment industry. Ship winches, as one of the most important parts of the equipment, are highly developed. Their dimensions, compared to the force they use, have been reduced and the degree of efficiency has increased with the use of various kinds of compact mechanical gear and drive. The capacities for winding of the ropes have been increased for any kind of use on the vessels, from the oceanographic researches on the bottom of the ocean, to catching of the special kinds of fish.

A lot of research into vessel winches have been done: increasing of the degree of efficiency, reduction of dimensions, reduction of the mass of winches, improvement of the drive unit regarding the compactness and the power they use, improvement of the drum for rope-winding as the basic element of a winch, of the rope-winding system, development and analysis of the various types of ropes for various uses, etc.

Great attention is paid to examination and development of the ropes used for winches. Steel ropes are mostly used for vessel winches, while the synthetic ones are rarely used. Different types of cables are used for winches for oceanographic researches rather than ropes because of the transmission of information from the research devices from the bottom of the ocean to the vessel. When it comes to the development of the new types of ropes, great attention is paid both to the outer tensile and twisting forces affecting the rope, and the inner friction forces that occur between the wires of the rope, [1], [2], [3]. When examining the existing types of ropes, it is very important to examine the inner friction in the ropes, as well as the failure mechanism of the ropes, [4], [5]. In the case where the steel rope cannot be installed on a winch because of its large mass, synthetic ropes are used. Synthetic ropes are still not widely used because they are still in the development and improvement stages, [6]. Synthetic ropes can be made with the molten core for the improvement of its mechanical characteristics.

Reduction of the dimensions and the increase in the degree of efficiency of a winch is mostly achieved by installing the compact mechanical gear, gearboxes. Single-stage gearboxes with two, three or more drives are often used for increasing the compactness of the vessel winch constructions, [7]. In addition, the use of planetary gearboxes is

common for their ability to be installed within the winch drum.

Improvement of the winch drum, as the basic element of the winch, is based on the examination of the effect of the forces on the drum, experimentally and using finite element analysis, [8]. Improvement of the drum is done by reducing the thickness of the material from which the drum is made in noncritical places, while increasing it in the critical ones, and inserting the required structural stiffeners, [9], [10]. Optimization methods are also a possible approach of improvement, [11].

Improvement of the system for proper winding of the rope around the drum of the vessel winch is based on its synchronization with the number of turns of the drum. The synchronization can be done in many ways. Some of the ways are the mechanical synchronization with the power transmission or installing a special driving engine-generator for the system, which is synchronized, with the engine-generator of the winch.

In this paper, a mathematical model of winding of a steel rope around the drum is presented. The mathematical model shows the correlation between the friction and pulling forces using geometrical characteristics of winding on the winch drum and the friction coefficient. Following this, the results of the algorithm, which are also developed in this paper, mathematical model as well as comparison characteristics of friction forces for different coefficients of friction during winding, are given. Finally conclusions and guidelines for further research have been presented.

2. MATHEMATICAL MODEL OF STEEL ROPE WINDING AROUND THE WINCH-DRUM

The winding of the steel rope around the winch drum can be single-layered or multilayered. The mathematical model concerns the multilayered process of rope winding, from the first to the last layer. The model could be used for defining single-layered winding too, by excluding the upper layers from the model. The bevel of the rope due to the winding is excluded from the mathematical model, because the bevel has an insignificant effect in the majority of winding cases. Also, the assumption that during winding the rope acts as an absolute elastic body is taken, while the wound rope acts as a solid body.

2.1 General case of winding of the rope around the drum

In determining the general case of winding, an nth winding on the nth layer is observed. The winding lies upon the two windings from the previous layer (Figure 1).

The forces FWR occur as the reaction of the rope to the pulling force FW. The friction force Fμ also occurs. Further observation is done on the cross-section where the force FWR acts (Figure 2). In this cross-section, the perpendicular force FN occurs due to acting of friction force Fμ.

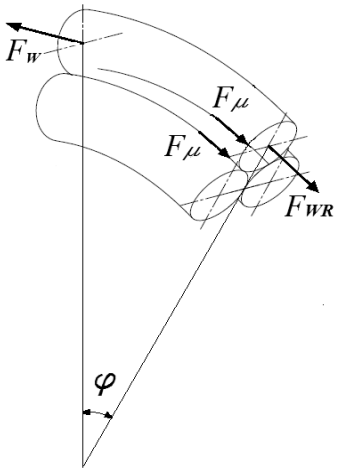

Figure 1. General spooling case

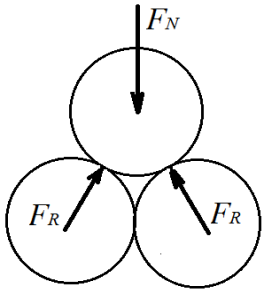

Figure 2. Cross-section of ropes in general case

Since the rope is of constant cross-section, the centers of circumferences, which make the cross-section of the rope, generally, form an equilateral triangle. Horizontal component reaction forces of the windings of the lower layer FR are annulled because of the previous claim. The connection between the perpendicular force FN and the reaction force FR is derived by setting the planar system of opposed forces, and the resulting is relation (3):

$$F_{\mathrm{R}} = \frac{F_{\mathrm{N}}\sqrt{3}}{3} \tag{1}$$

After determining the reaction, it is necessary to determine the friction force, which is caused by the tractive force. The friction force was determined by

observing the simplified tensile system of the upper layer of rope over the lower layer (Figure 3) on a small angle ±dφ/2 from the cross-section shown on the Figure 2.

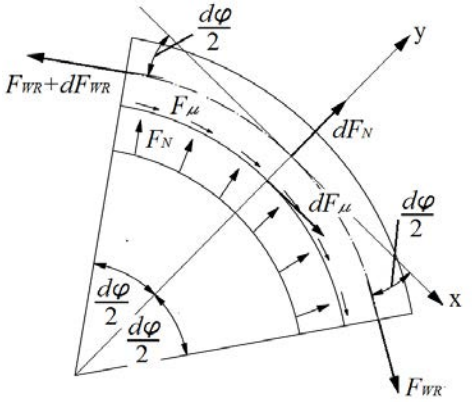

Figure 3. Basic part of the rope

For the elementary part of the rope on the angle ±*d*φ/2, the following equation system is derived:

$$x: dF\mu - \left(F_{WR} + dF_{WR}\right)\cos\frac{d\varphi}{2} + F_{WR}\cos\frac{d\varphi}{2} = 0 \quad (2)$$

$$y: dF_N - \left(F_{WR} + dF_{WR}\right)\sin\frac{d\varphi}{2} - F_{WR}\sin\frac{d\varphi}{2} = 0 \quad (3)$$

Accepting the assumptions for the basic angle ±*d*φ/2 (φ→0): cos*d*φ/2≈1, sin*d*φ/2≈*d*φ/2, $dF\mu = \mu \cdot dF_N$ i $dF_{WR}d\varphi = 0$, and by solving equations (2) and (3), the connection between the inputted pulling force F_W and the reaction force within the rope F_{WR}:

$$F_W = F_{WR} \cdot e^{\mu\varphi} \quad (4)$$

With further solving, the connection between the tractive force F_W and perpendicular force F_N is obtained, as well as the connection between the friction force $F\mu$ and the tractive force F_W:

$$F_N = \frac{F_W}{\mu}\left(1 - \frac{1}{e^{\mu\varphi}}\right) \quad (5)$$

$$F\mu = F_W\left(1 - \frac{1}{e^{\mu\varphi}}\right) \quad (6)$$

From expressions (4), (5) and (6) it can be seen that all resulting values directly depend on the tractive force F_W, coefficient of friction μ, and the angle of winding φ.

Returning the values from expression (5) to expression (1) the function of the reaction of the rope on the lower layer (7) is derived depending on the tractive force, coefficient of friction, and the angle of rope winding:

$$F_R = \frac{\sqrt{3}}{3}\frac{F_W}{\mu}\left(1 - \frac{1}{e^{\mu\varphi}}\right) \quad (7)$$

The friction force $F\mu$ in the expression (6) was calculated as the total friction force. Because of the adopted assumption about the symmetry of winding, the friction force $F\mu$ is divided into two equal parts (8) (Figure 1) in order to make a relation between the friction force appearing in the contact of the upper and lower layers.

$$F\mu_{LC} = \frac{F_W}{2}\left(1 - \frac{1}{e^{\mu\varphi}}\right) \quad (8)$$

2.2 Special case of rope winding on the drum

In the special case of rope winding on the drum (figure 4), the crossover of the rope from layer nth to the nth+1 layer is considered. The critical wind is observed in this case, during the crossover. In this case, in the beginning, the contact on the last wind of the previous lower layer and the side of the drum occurs, while in the second wind that contact is lost, and the rope changes to the general winding case.

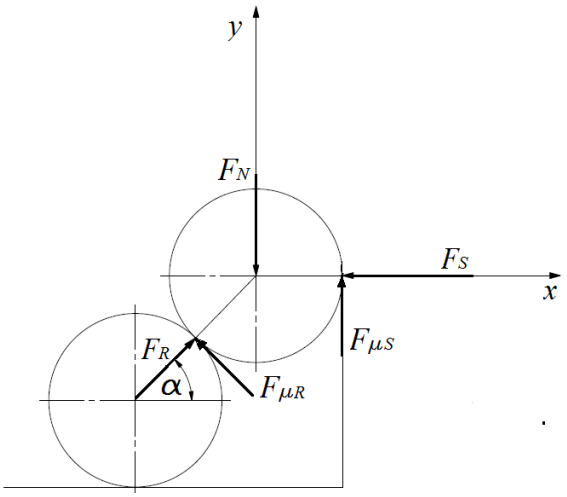

Figure 4. Special rope winding case

Establishment of the connection between the forces of reaction of the lower layer of the rope F_R, of friction between the layers of the rope $F\mu_R$ ($F\mu_R = F_R \cdot \mu_2$), forces of reaction on the side $F\mu_S$ ($F\mu_S = F_S \cdot \mu_1$) and perpendicular force F_N, in this case must be done by introducing the angle α. This changes in the interval of $0 \le \alpha \le \pi/2$, while the angle of the winding changes in the interval of $0 \le \varphi \le 2\pi$. The connection between angle α and the angle of winding φ is established according to the fact that for the angle $\varphi = 2\pi$ [rad] the rope is winding for the length of the diameter of the rope d_W, while angle α changes from 0 to π/2.

$$x: F_R\cos\alpha - \mu_2 \cdot F_R\sin\alpha - F_S = 0 \quad (9)$$

$$y: F_R\sin\alpha + \mu_2 \cdot F_R\cos\alpha - F_N + \mu_1 \cdot F_S = 0 \quad (10)$$

By solving the equations above the following expressions are obtained:

$$F_R = \frac{F_N}{(1-\mu_1\mu_2)\sin\alpha + (\mu_1+\mu_2)\cos\alpha} \quad (11)$$

$$F\mu_R = \frac{\mu_2 F_N}{(1-\mu_1\mu_2)\sin\alpha + (\mu_1+\mu_2)\cos\alpha} \quad (12)$$

$$F_S = \frac{F_N(\cos\alpha - \mu_2\sin\alpha)}{(1-\mu_1\mu_2)\sin\alpha + (\mu_1+\mu_2)\cos\alpha} \quad (13)$$

$$F\mu_S = \frac{\mu_1 F_N(\cos\alpha - \mu_2\sin\alpha)}{(1-\mu_1\mu_2)\sin\alpha + (\mu_1+\mu_2)\cos\alpha} \quad (14)$$

In the expressions (11), (12), (13) and (14) the friction coefficient μ_1 is the friction coefficient between the rope and the drum of the winch, while μ_2 is the friction coefficient between the windings of the rope.

3. FRICTION FORCES IN THE WINDING OF THE STEEL ROPE AROUND THE WINCH DRUM

For this paper a mathematical model has been developed which for given initial parameters of winding of the rope gives the friction forces diagrams, perpendicular forces, as well as the comparative friction forces diagram for different coefficients of friction. The initial parameters according to which the forces were calculated are given in Table 1.

Table 1. Initial parameters for force examination

Size description	Designation	Value
Drum length	L	100 [mm]
Wire diameter	d_W	10 [mm]
Number of winded layers	n_L	10
Load weight	m	250 [kg]
Friction coefficient	μ_1	0,25
Friction coefficient	μ_2	0,35

Mathematical model for calculating the force values has been developed in *MS Excel* software. The division of the winding angle was made with 10°, but was converted to radians for easier clarification. All of the output diagrams have the division in radians [rad] on their x - axis, and in Newtons [N] on the y – axis.

3.1 Spooling of the rope on the first layer

In the spooling of the first layer it is characteristic that the friction force occurs only on one rope inlet. Because of the relatively small friction coefficient (μ1 = 0,25) during the first layer spooling, the friction force Fμ does not have a rapid increase in the first two layers (φ ≈ 18 [rad]) regarding the greater friction coefficients (Figure 5).

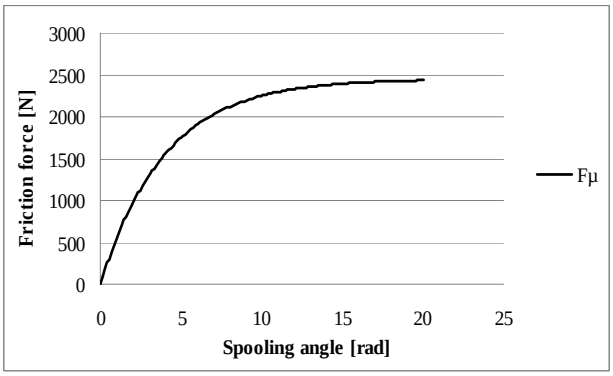

Figure 5. Friction force Fμ on the first layer dependence on the spooling angle

At the end of the third layer spool (φ ≈ 18 [rad]), the friction force is almost equal to the pulling force. It can be said with certainty that after the fourth spool, with the friction coefficient being μ1 = 0,25, the whole load of tractive force is carried by the friction force.

3.2 Rope spooling in the crossover from one layer to another

The rope spooling is most critical in the crossover from one layer to another (Figure 6). In that case, only one critical winding is observed during the crossover from layer n to layer n +1, until the rope turns to the general spooling case. In this case, it is very hard to determine the friction coefficient between the winding spool and the last spool on the previous layer because of the changing trajectory of the rope inlet. When the rope gets to this position, the friction force appears in the contact between the side of the drum and the spool that is being wound by the rope inlet, but also the friction force appears in the contact between the last spool on the previous layer and the spool being wound. In this case, the assumed coefficient of friction which occurs in the rope inlet is the same as the friction coefficient which occurs between the rope spools (μ2 = 0,35).

From the diagram on the Figure 6 which shows: the reaction force of the lower rope layer FR , friction force between the rope layers FμR , reaction force on the side FS and friction force on the side FμS , their changes during the critical spool in the crossover of the rope from one layer to another are visible. The lower rope layer reaction force FR has the steady increasing character from the beginning to the end of the critical spooling, and transcends the nominal value of the pulling force almost by two.

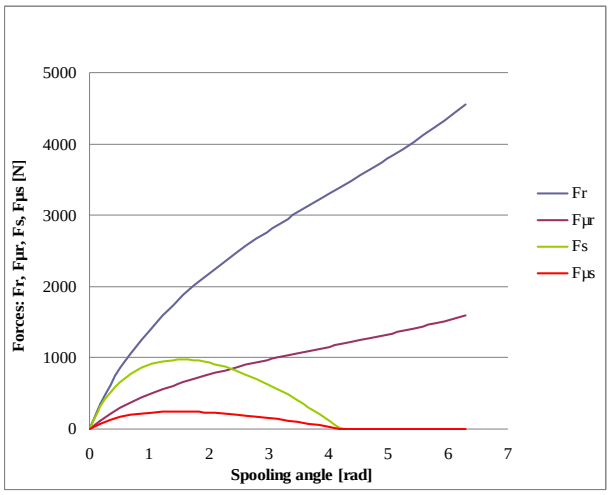

Figure 6. The reaction force of the lower rope layer FR , friction force between the rope layers FμR , reaction force on the side FS and friction force on the side FμS dependence on the spooling angle

The friction force between the layers FμR also has the increasing character from the beginning of the critical spooling and all the way to the point when the rope crosses to the general spooling case, for it is directly related to the force FR by the friction coefficient μ2, (12). The reaction force on the side of the drum FS rises up to the spooling angle of $\varphi \approx 1,5$ [rad], while after reaching the extreme value it decreases to zero. Its value equals zero at $\varphi \approx 4, 2$ [rad]. The friction force on the side FμS acts similarly, because it is related to the reaction force on the side through the friction coefficient μ1, (12). When the forces FμS and FS reach zero, the perpendicular force transfers to the last spool of the lower spooling layer exclusively by the friction force between the rope windings.

3.3 General case of rope spooling

General case of rope spooling for multilayered spooling has the greatest share in the spooling process. Generally, friction force occurs on the two rope inlets on the contact line of the winding being spooled and the two spools from the previous layer. In this case the total friction force is divided into two equal parts, (8). Friction force FμLC in line contact on the rope inlet gets close asymptotically to the half of the nominal value of the pulling force, (Figure 7). In the case of rope spooling onto the higher layers, the general case, in difference with first layer spooling, the friction force carries the total tractive force ($\varphi \approx 12 \div 15$[rad]) between the second and the third layer.

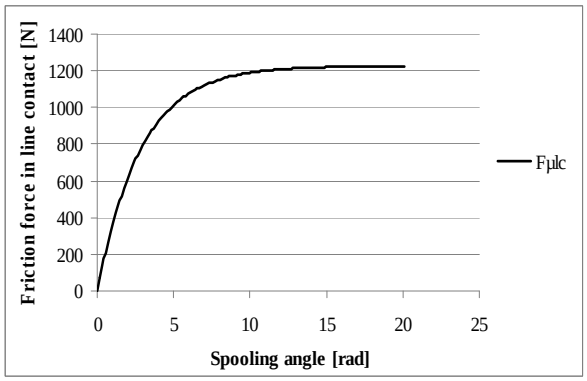

Figure 7. Friction force Fμ in general case of rope spooling dependence on the spooling angle

In this case a grater friction coefficient value is adopted from the one used for rope spooling onto the first layer (μ_2=0,35).

3.4 Comparative diagrams for different friction coefficient values

Lastly the comparative friction force diagrams (Figure 8) and perpendicular force (Figure 9) diagrams for friction coefficients $\mu = 0,2 \div 0,4$ (initial parameters are also taken from Table 1) are given. For these resulting diagrams the general rope spooling case was used.

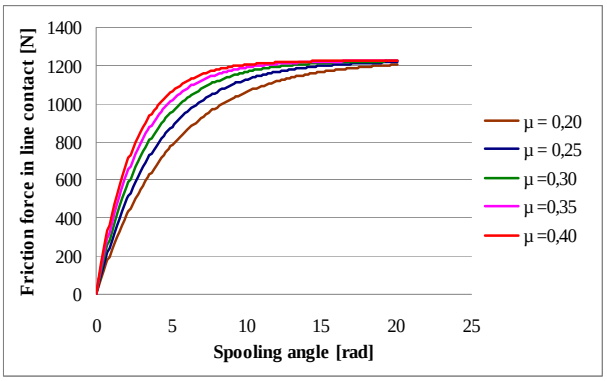

Figure 8. Friction force Fμ for different friction coefficients dependence on the spooling angle

It can be seen from Figure 8 that for all friction coefficient values the friction force has the same initial value during spooling. As expected, the highest number of spools for total transfer of puling force to friction force is necessary for the highest friction coefficient ($\varphi > 12$ [rad]), while for the lowest friction coefficient the transfer is possible only after the third spooling ($\varphi > 19$ [rad]).

With perpendicular forces the case is slightly different (Figure 9). Perpendicular forces do not exceed the nominal value of the pulling force for the value of the friction coefficient of $\mu < 0,3$. Perpendicular forces with the friction coefficient of $\mu < 0,3$ do exceed the value of nominal pulling force.

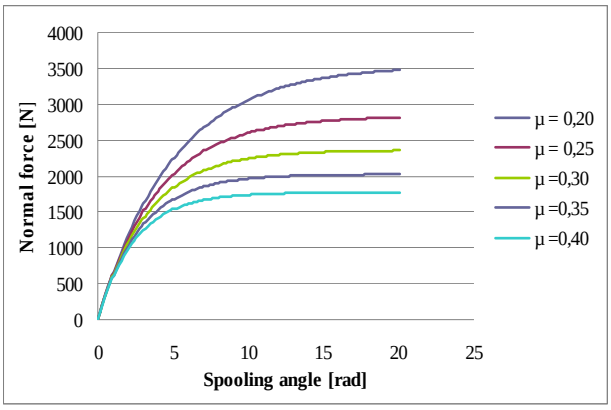

Figure 9. Perpendicular force FN for different friction coefficients dependence on spooling angle

Even though the perpendicular and friction forces are in linear correlation by the friction coefficient, the differences in their behavior occur in the general spooling case because the friction force is distributed to the two components on the rope inlets.

4. CONCLUSION

Using the mathematical model and friction force calculation, it has been shown that the friction force in the rope spooling onto the winch drum process does not depend only on the friction coefficient, but also in the position of the rope during the process. It has been shown that the greatest friction forces occur during the crossing of the rope from one layer to another. With the increase of the friction coefficient, the time needed for the pulling to friction force transfer shortens. For the transfer with a friction coefficient of 0.2 more than four spools are required ($\varphi > 24$ [rad]), while for the transfer of the same pulling force with a coefficient of 0.3 less than three spools are needed ($\varphi < 18$ [rad]). The friction coefficient value depends mostly on the rope material as well as on its characteristics, but for the first layer the material and the characteristics of the drum have an equal share. For the transfer of smaller masses, ropes with a high friction coefficient can be used, but this is not advisable for greater masses.

During the crossing of the rope from one layer to another, effect of the rope on the side of the drum in the interval when the spooling angle is $0 < \varphi < 3\pi/2$, can be seen. Decreasing this force is possible by making a special rope guide. However, this would only solve the problem for the crossing from the first to the second layer.

Further research on this topic could be focused on creating a mathematical model for spooling and an algorithm for determining forces. Experimental research could ensue on models, as well as on actual winches.

REFERENCES

[1] P. Yu-xing, Z. Zhen-cai, C. Guo-an, C. Guo-hua *Effect of Tension on Friction Coefficient Between Lining and Wire Rope with Low Speed Sliding*, Journal of China University of Mining & Technology, Vol. 17, No.3, pp 409-413, 2007.

[2] G. Rebel, M. Borellot, H.D. Chandler: *On the torsional behaviour of triangular-strand hoisting rope*, The Journal of The South African Institute of Mining and Metallurgy, Vol. 38, pp 279-287, 1996

[3] I. Argatov: *International Journal of Solids and Structures*, International Journal of Solids and Structures, Vol. 48, pp 1413–1423, 2011

[4] C.R Chaplin: *Interactive Fatigue in Wire Rope Applications*, The University of Reading, Reading RG6 6AY, UK, 2008.

[5] C. R. CHAPLIN: *Failure mechanisms in wire ropes*, Engineering Failure Analysis, Vol. 2, No. 1, pp. 45-57, 1995.

[6] S.R. Ghoreishi, P. Cartraud, P. Davies, T. Messager: *Analytical modeling of synthetic fiber ropes subjected to axial loads. Part I: A new continuum model for multilayered fibrous structures*, International Journal of Solids and Structures, Vol. 44, pp 2924–2942, 2007

[7] M. Matejić: *Calculation and design of ship winch in CAD software*, Master thesis, Faculty of engineering scince, University in Kragujevac, Kragujevac, 2012.

[8] B. Simiić: *Design and analysis of ship winch in CAD software*, Master thesis, Faculty of engineering scince, University in Kragujevac, Kragujevac, 2012.

[9] A.K. Moe: *Design consideration of winch*, Master thesis, National University of Singapore, Singapore, 2006.

[10] L.B. Teck: *Inprovment in the design of winches*, Bachelor thesis, National University of Singapore, Singapore, 2005.

[11] L. Liu, H. Liu: *Study on Optimization Design of a Hoist Roller*, Advanced Materials Research, Vols. 415-417, pp 460-463, 2012.

Serbian Tribology Society

SERBIATRIB '13

13th International Conference on Tribology

Faculty of Engineering in Kragujevac

Kragujevac, Serbia, 15 – 17 May 2013

APPLICATIVE MONITORING OF VEHICLES ENGINE OIL

Perić Sreten[1], Nedić Bogdan[2], Grkić Aleksandar[3]
[1]University of Defence in Belgrade, Military Academy, Serbia, sretenperic@yahoo.com
[2]Faculty of Engineering in Kragujevac, Serbia, nedic@kg.ac.rs
[3]University of Defence in Belgrade, Military Academy, Serbia, iralex@eunet.rs

***Apstrakt**: Confirming the basic causes of failures and their elimination, control of certain phenomena, is defining proactive maintenance, as a new method that reduces maintenance costs and prolongs the life of assets. Determination of tribomehanical systems condition has very important role in development of friction theory and practice, wear and lubrication. There are used today different physical and chemical methods and tribology methods for tribomehanical system diagnosis. Experience in technical systems exploitation shoved that the most effective failure prognosis is according to parameters, particles created as result of wear, which are reliable indicators of wear. Analysis of oil samples which contain particles, created as results of wear, enable evaluation of system tribology condition in different phases of system exploitation.*
The paper presents the physical chemical tests in the analysis of oils that are used for the assessment of his condition. Furthermore the results of experimental research of physical chemical characteristics engines oil was sampled from engines of vehicles, which were in use. The research results are originating from the research of the paper authors.

***Keywords:** Monitoring, lubrication systems, analysis oils, proactive maintenance, diagnosis.*

1. INTRODUCTION

Modern trends of diagnosis in recent years, go to the affirmation of the monitoring of oil, which has resulted in growth of interest of producers and users of oil. The reasons lie primarily in increasing the reliability, effectiveness, economy, and recently more and more present protection of the environment.

Using Oil Analysis programs for engine oils has several benefits: reduction of unscheduled vehicle downtime, improvement of vehicle reliability, help in organizing effectiveness of maintenance schedules, extension of engine life, optimization of oil change intervals and reduction of cost of vehicle maintenance.

In application, oils change their properties through [1]: contamination by combustion products and metal wear particles, consumption of additives which is chemical and bears impact on important oil functions and base oil oxidation.

The primary role of engine oil is the lubrication of moving engine parts and reducing friction and wear of metal surfaces which provides the good engine performance and its long life. In order to provide a defined quality of engine oils during production and for final products to meet the product specifications we need to know the physical chemical characteristics of engine oils.

Certain physical-chemical characteristics which are significant for the quality of engine oils are achieved by adding additives to base oils. The most frequent additives are for: improving of viscosity index-improvers, reducing pour point-depressants, maintaining engine cleanness-detergents and dispersants, preventing oxidation-antioxidants, preventing corrosion-corrosion inhibitors.

2. LUBRICANT SERVICE LIFE AND ANALYSIS

To know analytical properties of lubricants is the base to make a decision in development, production and application of lubricants. The lubricant classifications and approved system specify many performance characteristics and

analytical tests. The analytical tests are classical and instrumental. Instrumental technical have the advantages in small quantity of the sample and rapid analyze. As a part of the common proactive strategy of the hydraulic systems maintenance, concept of on-line monitoring is introduce in practice, recently [2], [3], [4], [5], [6]. It is a combination of the measurement procedures, by which sample of fluid is to be analyzed is taken directly from the system and the results of the measurements are continuously. On-line monitoring considering, first of all, control of cleanliness classes (according to ISO, NAS, SAE), control of humidity, viscosity, permittivity (acid), temperature…

The following tests are the most used in condition monitoring: Spectrometric analysis, Analytical Ferrography, Rotrode Filter Spectroscopy (RFS), Infrared Analysis (FT-IR), Viscosity, Total Acid Number (TAN), Total Base Number, Water and Particle Count.

Spectrometric analysis is a technique for detecting and quantifying metallic particulates in used oil arising from wear, contamination and additive packages. The oil sample is energized to make each element emit or absorb a quantifiable amount of energy, which indicates the element's concentration in the oil. The results represent the concentration of all dissolved metals and particles. The equipment for spectrometric analysis is the standard equipment for oil analysis laboratories today. It provides information on technical system, contamination and wears condition relatively quickly and accurately. Spectroscopy is more-or-less blind to the larger particles in an oil sample, more precisely, to particles greater than 10 μm in diameter, which are more indicative of an abnormal wear mode [7].

Analytical ferrography is a technique which separates magnetic wear particles from oil. Those particles settle on a glass slide known as a ferrogram. Microscopic examination enables to determine the wear mode and probable sources of wear in the technical system. Analytical ferrography is an exceptional indicator of abnormal ferrous wear and it is inadequate for nonferrous wear.

Rotrode Filter Spectroscopy (RFS) was first introduced in 1992. This spectrometric technique detects coarse wear metals and contaminants in a used oil sample. Diameter of those particles is up to 25 μm, but it excludes all additives. The coarse particles are especially important. They are the first indicators of abnormal wear situations.

Fourier-Transform Infra-Red Spectroscopy is a spectrometric technique for detecting organic contaminants, water and oil degradation products in a used oil sample. It monitors lubricant degradation (oxidation, nitration, sulfation, additive depletion) and liquid contaminants (water, glycol, fuel dilution).

Viscosity is the resistance of a fluid to flow and the most important lubricant physical property. The fluid is placed in a "viscometer" (a calibrated capillary tube for precise flow measurement between two pre-marked points on the tube) and pre-heated to a given temperature in a "viscosity bath" (which is usually oil-filled). After the oil reaches the desired viscosity temperature, gravity-influenced flow of the oil is initiated in the viscometer and timed between two calibrated points. This time becomes the determinant for the result.

Total Acid Number (TAN) is a neutralization number intended for measuring all acidic and acid-acting materials in the lubricant, including strong and weak acids. It is a titration method designed to indicate the relative acidity in a lubricant. The TAN is calculated from the amount of KOH consumed. The acid number is used as a guide to follow the oxidative degeneration of oil in service.

Total Base Number (TBN) is a neutralization number intended for measuring all basic (alkaline) materials in the lube (acid-neutralizing components in the lubricant additive package). The converse of the TAN, this titration is used to determine the reserve alkalinity of a lubricant. The TBN is highest when oil is new and decreases with its use. Low TBN normally indicates that the oil has reached the end of its useful life.

Water can be detected visually if gross contamination is present. Excessive water in a system destroys a lubricant's ability to separate opposing moving parts, allowing severe wear to occur with resulting high frictional heat. There are several methods used for testing the moisture contamination (crackle, FT-IR water, centrifuge, Karl Fischer) each with a different level of detection (1000 ppm or 0.1 % for first three methods and 10 ppm or 0.001 % for Karl Fischer method).

Particle Count is a method used to count and classify particulate in a fluid according to accepted size ranges, usually to ISO 4406 and NAS 1638 [8]. There are several different types of instrumentation on the market, utilizing a variety of measurement mechanisms, from optical laser counters to pore blockage monitors.

3. THE RESULTS OF OIL ANALYSIS AND DISCUSSION

In this part are presented the results of oil analysis examination during application in four-

stroke engines by physic-chemical methods in order to evaluate possibilities of engine condition monitoring by oil analysis. This part presents the results of experimental research of physic-chemical characteristics of engines oil which was sampled from engines of PUCH 300GD, Pinzgauer 710 and IKARBUS IK 104P vehicles [9], [10].

The research was carried out in two vehicles PUCH 300GD (PUCH-1, PUCH-2), two vehicles PINZGAUER 710M (PINZ-1, PINZ-2) and two vehicles IKARBUS IK 104P (IK104P-1, IK104P-2).

The research was conducted through periodic sampling oil from engine vehicles listed above.
Apart from the fresh oil ("zero" sample), samples are taken after 1.000 km, 2.000 km, 3.000 km, 4.000 km and 5.000 km for vehicles.

The physical-chemical characteristics of oil in accordance with standard methods are examined, shown in table 1.

Table 1. Implemented tests and methods for examining the physic-chemical characteristics of oil

Characteristic	Method
Kinematic viscosity, mm^2/s	SRPS B.H8.022
Viscosity Index	SRPS B.H8.024
Flash Point (°C)	ISO 2592, ASTM D 92
Pour Point (°C)	ISO 3016
Water Content, mas.%	ASTM D 95
Total Base Number (TBN), mgKOH/g	ASTM D 2896
Insoluble substances in pentane, %	ASTM D 893
Insoluble substances in benzene, %	ASTM D 4055
Fe Content, %	ASS
Cu Content, %	ASS

The analysis was done on the fresh (new) oils and oils that are used in the engines of vehicles. During the sampling of oil choice of the sampling were conducted carefully according to the actual oil usage, which enabled each sample as representative one.

The wear mechanism of a tribological lubrication system consists in the wear of contact surfaces, and lubricant consumption. If there is wear of the contact surfaces, there are wear particles present.

Regardless of the availability of numerous methods for diagnosing the physic-chemical changes of lubricants, in order to create a true picture of the condition of lubricants from the user system, it is of importance to satisfy the precondition of the possibility to obtain a representative sample. That is why it is extremely important to take the sample in a proper way.

Allowable values of deviation limits of individual characteristics of the oil are conditioned by the type of oil, working conditions and internal recommendations of the manufacturer of lubricants and users. Limited value characteristics of oils that condition the change of oil charging from engine are given in table 2. They represent the criteria for the change of oil charge. Deviation of only one source changes characteristics of oil charge, no matter of what a characteristic is about.

Table 2. Allowed values deviation of physico-chemical characteristics of new and used oil

Physical-chemical characteristics oil and products wear	Maximum allowed variation
	Motor oil
Viscosity at 40°C and 100°C, mm^2/s	20%
Viscosity Index, %	± 5 %
Total Base Number (TBN), mg KOH/gr	The fall to 50%
Flash Point, °C	20 %
Water Content, %	0,2 %
Products wear – Content Fe, ppm(μg/gr)	100 ppm
Products wear – Content Cu, ppm(μg/gr)	50 ppm

Used engine oil in examined vehicles are shown in table 3. Characteristics of zero samples of motor oil are shown in table 4, and the results used oil samples in table 5.

Table 3. Used engine oil in examined vehicles [9]

Engine oil from engine of PUCH 300 GD vehicles		
SAE classification	API classification	Manufacturer
SAE 15W-40	API SG/CE	FAM Krusevac
Engine oil from engine of PINZGAUER 710 M vehicles		
SAE classification	API classification	Manufacturer
SAE 30/S3	-	GALAX Beograd
Engine oil from engine of IKARBUS 104 P vehicles		
SAE classification	API classification	Manufacturer
SAE 15W-40	API SG/CE	FAM Krusevac

The viscosity index is an empirical number which shows how the viscosity of some oils changes by increasing or reducing the temperature. High viscosity index shows relatively small tendency of viscosity to change upon influence of certain temperature, as oppose of low viscosity index which shows greater viscosity change with temperature.

Table 4. Results of zero samples of oil from the engine [9]

Characteristic	Type of motor oil	
	FAM SAE 15W-40	Galax SAE 30/S3
Color	3,0	3,0
Density, gr/cm^3	0,881	0,902
Viscosity at 40°C, mm^2/s	104,81	104,63
Viscosity at 100°C, mm^2/s	14,12	11,67
Viscosity Index	–	–
Flash Point, °C	230	240
TBN, mg KOH/g	10,5	9,8

Table 5. The results of testing samples of used oil from engines examined vehicles [9]

Sample		PUCH –1	PUCH –2	IK104 –1	IK104 –2	PINZ –1	PINZ –2
Viscosity at 100°C, mm^2/s	0	14,1	14,1	14,1	14,1	11,6	11,6
	1	14,6	14,2	13,7	13,6	10,9	10,5
	2	15,4	15,0	12,8	13,5	10,3	10,4
	3	16,0	15,6	12,4	13,2	9,96	10,1
	4	16,6	16,1	12,3	12,9	9,3	9,6
	5	17,5	17,0	12,2	12,6	8,7	9,0
Viscosity at 40°C, mm^2/s	0	104,8	104,8	104,8	104,8	104,6	104,6
	1	111,0	110,4	96,9	104,4	100,4	100,9
	2	113,5	111,8	96,2	101,9	94,4	96,1
	3	119,4	113,8	92,3	97,1	86,3	88,6
	4	126,4	115,9	90,8	94,8	79,1	82,2
	5	132,7	127,5	90,2	93,1	75,9	76,9
Viscosity Index	0	135	135	135	135	100	100
	1	129	131	132	133	96	97
	2	122	126	130	131	93	95
	3	119	123	125	127	89	91
	4	116	120	122	124	84	87
	5	112	115	119	121	82	84
Flash Point,°C	0	230	230	230	230	240	240
	1	220	215	217	212	196	193
	2	208	210	214	210	186	177
	3	205	204	213	202	168	159
	4	197	202	210	193	154	143
	5	192	188	189	184	136	128
TBN, mgKOH/g	0	10,5	10,5	10,5	10,5	9,8	9,8
	1	9,1	9,4	8,8	8,1	9,6	9,4
	2	7,2	8,9	8,7	7,7	9,1	8,4
	3	6,5	8,7	8,4	7,2	8,3	7,8
	4	6,1	8,1	7,9	6,8	7,6	6,6
	5	5,2	7,6	7,3	6,4	7,1	6,2
Fe Content (ppm)	1	98,4	27,4	30,1	20,5	19	17,9
	2	123	59,8	32,5	46,3	19,8	40,9
	3	137,1	71,2	35,6	57,6	38,3	86,7
	4	149,4	71,4	37,5	62,8	54,3	132,8
	5	165,3	86,8	38,5	69,6	105,4	261
Cu Content (ppm)	1	4,9	2	1,5	3,2	3,5	3,3
	2	5,9	3,4	1,9	5,1	4,1	3,8
	3	6,7	3,7	3,2	6,3	5,3	6
	4	7,3	3,9	4,4	7,7	6,9	8,1
	5	7,9	5,4	4,9	9,1	8,7	9,7

During the exploitation it is desired that the viscosity changes as lesser as possible with the change of temperature. If during work temperature modes are changeable and cause major changes of viscosity that may cause disruptions in the functioning of the system, which is a manifestation of increased friction, wear and damage.

Change of engine oil Viscosity Index is shown in the figure 1. The decrease in the Viscosity Index oil is evident for all vehicles, exceeding the limit of 5 % (table 2).

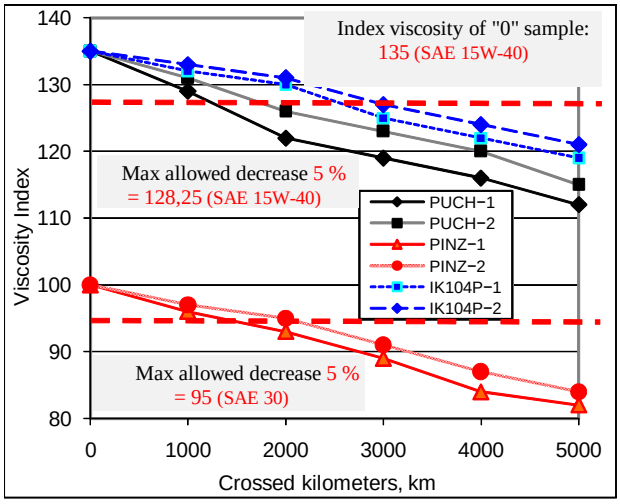

Figure 1. The change of Viscosity Index [9]

The most important engine oils characteristic is the viscosity defined as a measure of inner friction which works as a resistance to the change of molecule positions in fluid flows when they are under the impact of shear force, or in other words, it is the resistance of fluid particles to shear.

The viscosity is a changeable category and it depends on the change of temperature and pressure.

A higher temperature reduces the viscosity and makes a fluid thinner.

Multigrade engine oils among numerous additives always contain also viscosity index improvers. These additives are special types of polymers, which in small concentration significantly improve engine oils rheological properties, especially viscosity and viscosity index.

However, during engine oils utilization, degradation of viscosity index improvers i.e. Break down of polymeric molecules occurs. It results in reduction of their molecular weight what leads to viscosity loss and oil film thickness decrease, which causes undesirable phenomena of friction and wear.

Reasons for the increase of viscosity lubricants are as follows: oxidation of lubricants, cavitations due to foaming lubricants, dissolution of lubricants with water, pouring and charging system viscosity fat greater than recommended and contamination of solid particles and products wear lubricants.

The reasons for the reduction of lubricants viscosity are: lubricants contamination of fuel (for motor oil), shearing additive for reclamation viscosity, drop point of flash, grinding molecules, lubricants contamination without solubility with water, pouring and charging system viscosity less fat than recommended, and the impact of liquid

cooling. Also, the causes may be high temperature, load, uncontrolled long interval use, insufficient amount of oil in the oil system, inefficient cooling systems and the like.

As expected, kinematic viscosity usually decreases in time due to fuel penetration, or - in well maintained engines, there occurs a slight increase as a result of the increase of the oil insoluble, without fuel penetration.

Figure 2. shows the changes viscosity at 40°C engine oils during exploitation.

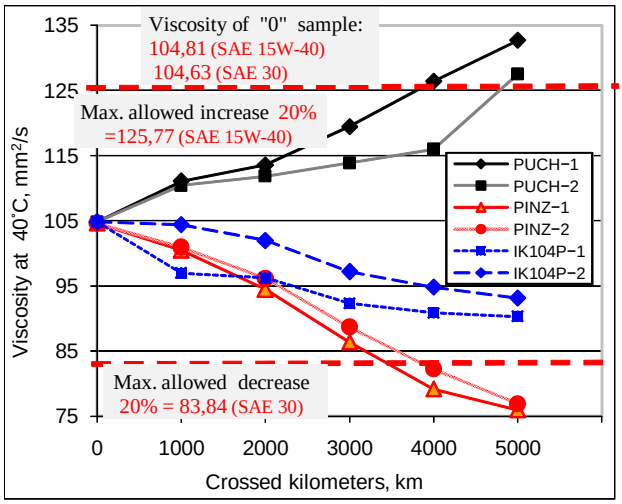

Figure 2. The change of viscosity at 40°C [9]

The increase viscosity at 40ºC engine oil is evident for PUCH-1 and PUCH-2 vehicles, exceeding the limit of 20%. The decrease viscosity at 40ºC engine oil is evident for PINZ (exceeding the limit of 20%) and IK104P vehicles.

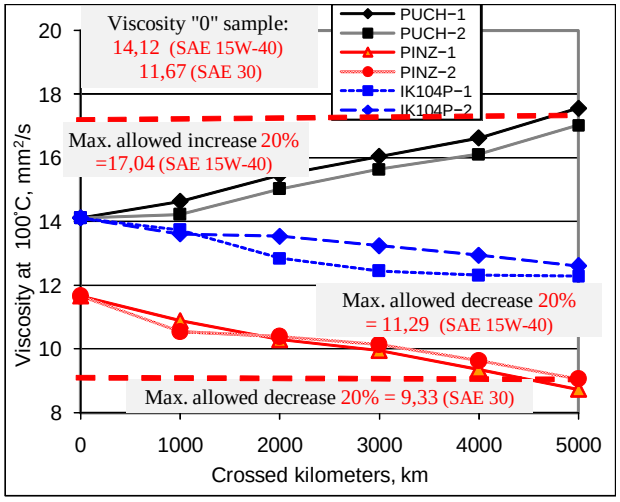

Figure 3. The change of viscosity at 100°C [9]

TBN is a neutralization number intended for measuring all basic (alkaline) materials in the lube (acid-neutralizing components in the lubricant additive package). The TBN is generally accepted as an indicator of the ability of the oil to neutralize harmful acidic byproducts of engine combustion. The TBN is highest when oil is new and decreases with its use. Low TBN normally indicates that the oil has reached the end of its useful life. TBN is a measure of the lubricant's alkaline reserve, and mostly applies to motor lubricants. If a lube contains no alkaline additives, there is little use to determine a TBN, as there will likely be none. Combustion acids attack TBN, e.g., sulfuric acid, decreasing as it consumes.

Figure 4. shows the changes of total base number (TBN) engine oils.

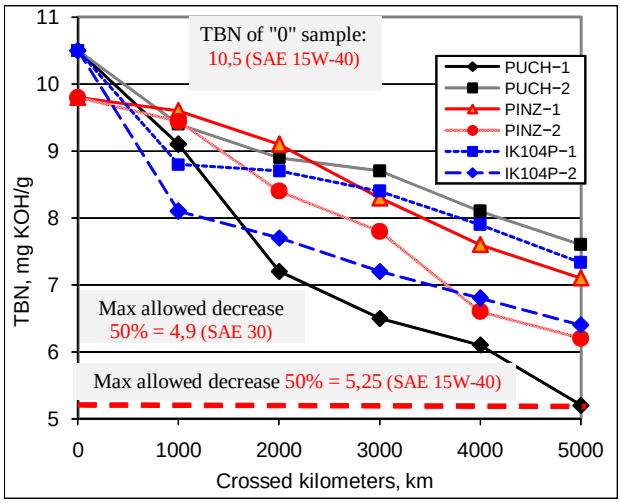

Figure 4. The change of TBN [9]

The decrease TBN engine oil is evident for all vehicles. Until 5.000 km TBN value does not exceed the allowed limit, except for PUCH-1 vehicle.

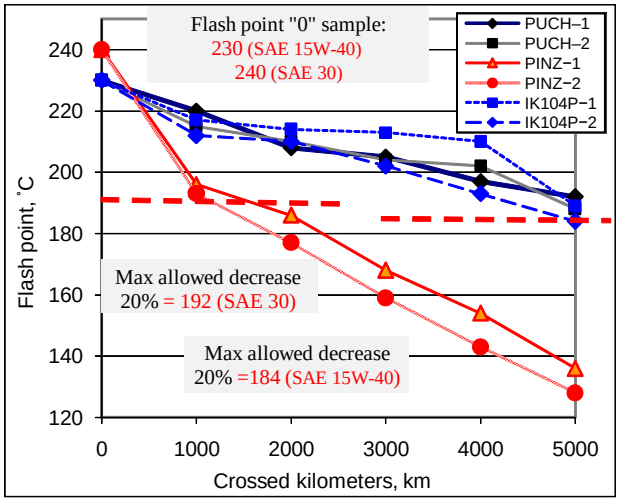

Figure 5. The change of flash point [9]

Flash point represents data that shows what temperature leads to open fire ignition by the steam created by oil heating. In engine oil analysis the flash point determines the presence of fuel oil, which is a consequence of poor motor (bad work injectors). The reduction of flash point is due to the penetration of fuel.

Figure 5 shows the change of flash point for engine oils. The decrease in the flash point is

noticeable, and by the end of exploitation testing exceeds the allowed limits (20%, table 2) for PINZ vehicles.

Analysis of the contents of different metals that are in the lubricant is very important. Metal particles are abrasive, and act as catalysts in the oxidation of oils. In motor oils, the origin of the elements may be from the additives, the wear, the fuel, air and liquid for cooling. Metals from the additives can be Zn, Ca, Ba, or Mg and that indicates the change of additives. Metals originating from wear are: Fe, Pb, Cu, Cr, Al, Mn, Ag, Sn, and they point to the increased wear in these systems. Elements originating from the liquid for cooling are Na and B, and their increased content indicates the penetration of cooling liquid in the lubricant. Increased content of Si or Ca, which originate from the air, points to a malfunction of the air filter.

Iron and copper content (figure 6 and 7), as a product of wear, in the oil charge to the end of exploitation testing has a growing trend.

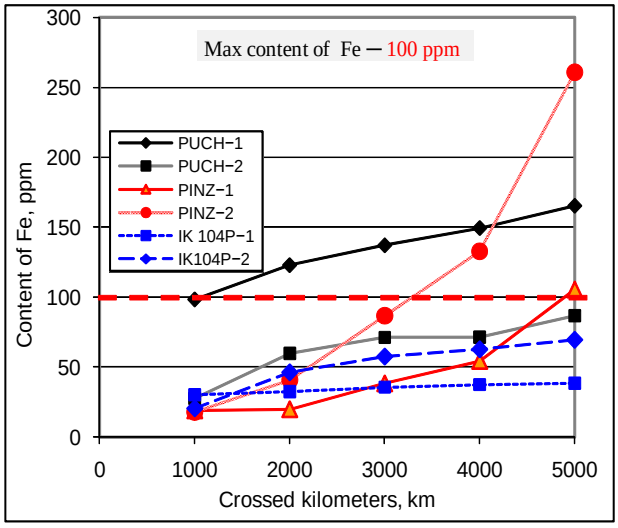

Figure 6. The change of content Fe [9]

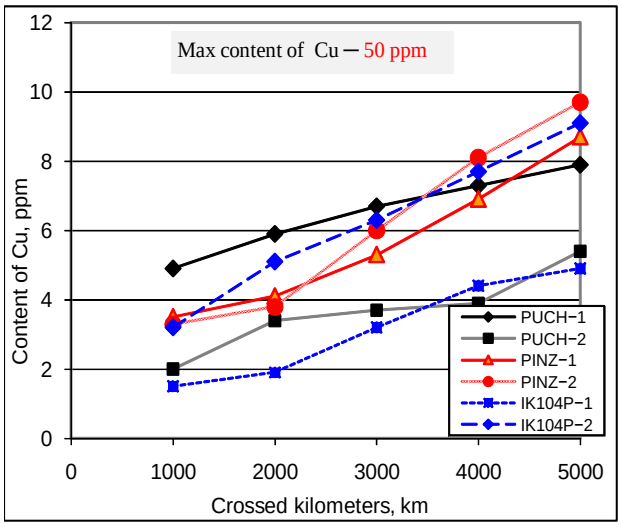

Figure 7. The change of content Cu [9]

Content of iron is significantly above the allowable limits (100 ppm, table 2) for PUCH-1 and PINZ-2 vehicles.

Content of cooper is significantly below the allowable limits (50 ppm, table 2) for all vehicles.

4. CONCLUSION

The interpretation of used oils analysis is very complex, because the individual analyses are interdependent. That is the reason why it is necessary to know the entire oil analysis, and not bring conclusions based on individual analysis results. It is also necessary to establish both normal and critical quality levels for specific oils in given engines and under specific application conditions.
The lubricant, being an inevitable factor in the tribomechanical system of engine has – apart from the usual lubricating role, also an important role in detecting the engine operation efficiency and condition. This is achieved through a systematic monitoring of oil in application and a permanent contact between the motor oil manufacturer and user.

Analyses from used oil sample should always be compared with previous samples and final conclusions should be based on “trend analysis” and has two closely related objectives: to obtain information on the lubricant drain intervals and preventive maintenance of the machine.

Investigations it was realized that there is a change of physical-chemical characteristics of oil for lubrication in the engines vehicle. These changes are in direct dependence on the state of all elements tribomechanical engines system, and depending on their functional characteristics.

REFERENCES

[1] J. Denis: *Lubricant properties analyses and testing*, Editions Tehniq, Paris, 1997.

[2] D. Grgić: On-line monitoring of oil quality and conditioning in hydraulics and lubrications systems, in: Proceedings of 10th SERBIATRIB '07, Kragujevac, Serbia, pp. 305-309.

[3] I. Mačužić, P. Todorović, A. Brković, U. Proso, M. Đapan, B. Jeremić: *Development Of Mobile Device For Oil Analysis*, Tribology in Industry 32, pp. 26-32, 2010.

[4] V. Macian, B. Tormos, P. Olmeda, L. Montoro: *Analytical approach to wear rate determination for internal combustion engine condition monitoring based on oil analysis*, Tribology International 36, pp. 771–776, 2003.

[5] L. Guan, X. L. Feng, G. Xiong, J. A. Xie: Application of dielectric spectroscopy for engine lubricating oil degradation monitoring, Sensors and Actuators A: Physical 168, pp. 22–29, 2011.

[6] V. Macian, R. Payri, B. Tormos, L. Montoro: *Applying analytical ferrography as a technique to*

detect failures in diesel engine fuel injection systems, Wear 260, pp. 562–566, 2006.
[7] R.I. Taylor, R.C. Coy: *Improved fuel efficiency by lubricant design*, 2001
[8] M. Piest and C.M. Taylor: *Automobile engine tribology*, 2000.
[9] S. Peric, *The development of a method of diagnosis the condition from the aspect of physical-chemical and tribological characteristics of lubricating oils of vehicles*, PhD thesis, Military Academy, Belgrade, 2009.
[10] S. Perić, B. Nedić: *Monitoring oil for lubrication of tribomechanical engine assemblies*, Journal of the Balkan tribological association 16, pp. 242-257, 2010.

Serbian Tribology Society

SERBIATRIB '13

13th International Conference on Tribology

Faculty of Engineering in Kragujevac

Kragujevac, Serbia, 15 – 17 May 2013

ADVANTAGES AND APPLICATIONS OF SELF-LUBRICATING PLASTIC BEARINGS

Aleksandar Marinković[1], Miloš Stanković[2]

[1]Mechanical Engineering Faculty, University of Belgrade, Serbia, amarinkovic@mas.bg.ac.rs

[2]Inovation Center of Mechanical Engineering Faculty, Serbia, mstankovic@mas.bg.ac.rs

Abstract: *Self-lubricating sliding bearings are widely used in industrial applications and we could assort them in several groups towards manufacturing or lubrication. Some of them, such are oil-retaining porous bearings have been long time studied, but plastic bearings are not enough investigated where we have just some of experimental results. Self-lubricating plastic bearings are produced on polymer basis which is optimized with fiber reinforcement and solid lubricants. They are an ideal solution for machinery that require clean and oil-free operation. Plastic bearings also perform well in dirty environments since there is no oil to attract dust and dirt. Authors of this paper describe main performances and reasons why this kind of bearings are current widely used. A few typical applications of plastic bearings are presented in the paper, taking into account advantages in lubrication, production and maintenance costs in comparison with classical rolling and sliding bearings.*

Keywords: *self-lubricating, plastic sliding bearing, polymers, dry operating.*

1. INTRODUCTION

Most of machine and equipment manufacturers are trying to eliminate or at least to reduce lubrication systems in aim to settle production costs down without sacrificing machine performances. According to significant Bearing Companies investigations, more than 50% of bearing failures are lubrication related (Figure 1). In a study by MIT, USA it was estimated approximately $240 billion is lost annually due to downtime and repairs to equipment damaged by poor lubrication [1].

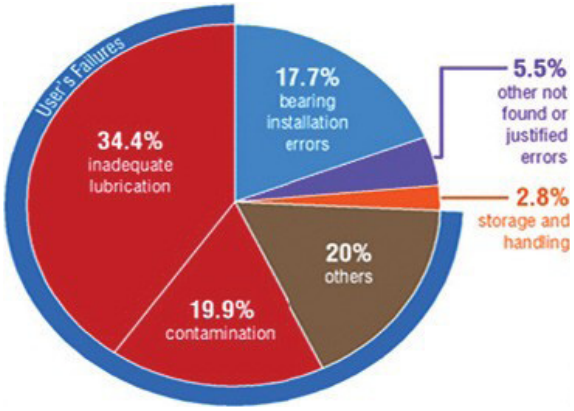

Figure 1. Types of lubricated related bearing failures

By eliminating lubrication from machinery, equipment manufacturers can minimize the costs and risks associated with maintenance for the end user. Because of lubrication problem and costs, which are dominant during the working life, a possible solution is to apply dry running plastic sliding bearing.

Plastic bearings are produced on polymer basis which is optimized with fibre reinforcement and solid lubricants. They are an ideal solution for machinery that requires clean and oil-free operation. Plastic bearings are doing well in dirty environments since there is no oil to attract dust and dirt.

2. PLASTIC BEARING MATERIALS

There are several typical groups of materials for plastic bearings, taking into account their physical-mechanical performances [2]:

- Thermoplastic materials
- Phenol and Epoxy plastic materials
- Elastomers
- Multilayer plastic materials

Thermoplastics and thermoplastic materials are polymers that turn to liquid when heated and turn solid when cooled. They can be repeatedly remelted and remolded, allowing parts and scraps to be reprocessed. In most cases they are also very recyclable. Some thermoplastics contain filler materials such as powders or fibres to provide improved strength and/or stiffness. Products in thermoplastics could also contain solid lubricant fillers such as graphite or molybdenum disulfide. Others contain metal powders or inorganic fillers with ceramics and silicates aimed to improve their mechanical and tribological performances.

Figure 2. igus® lines of plastic bearings made from high performance polymers

Polyethylene (PE), Fluoroplastics (such as PTFE), Polyamide (PA) and Polyoxymethylene (as POM) are common plastic materials from this group and in general, those are using in sliding bearing manufacturing. Detailed performances study of those materials is not aim of this paper [3], but here used to be mentioned just characteristics important for typical applications. If somebody needs plastic bearing for extreme load, than a Homopolymers or Copolymers (POM) with highest strength are recommended. In high environmental temperature conditions of the bearing exploitation Polytetrafluoroethylene (PTFE) is useful with max. working temperature around 200^{o}C. From tribology point of view, materials such PTFE is, has the lowest friction coefficient value (between 0,02 and 0,06 in dry conditions). If we need good wear resistance of the bearing, materials as Polyamide (PA) and POM plastic materials are recommended.

Other plastic materials except above explained group of Thermoplastics are not so common in use, but we could apply them in some special cases. For example, multilayer plastic materials are useful in combination with some metal as a matrix, with different coatings or solid lubricants. Because of current great plastic bearing expansion in wide range of different applications, many companies are exploring and try to on the market with their products. Most of them are sited in Europe or USA and have relatively long tradition, but last years lot of Far East companies are trying to overrun them by low cost products. Some of best known manufacturers of plastic bearings are multinational Company Igus® [4] (Figure 2) with main factories in Germany; famous bearing Company SKF has also some investigations and products in plastics; CSB Bearings [5]; Federal Mogul Germany with Glyco products; AFT Fluorotec (SW Plastics) UK; ISB Italcuscinetti Group Italia [6], etc.

3. ADVANTAGES OF PLASTIC BEARINGS

If we are taking into account proper lubrication delivery as a critical for the operation of ball bearings and most require continued maintenance for re-lubrication, this is a starting reason for thinking about their replacement with plastic bearings. There are also additional parts required to protect ball bearing from contaminants. According to several Institute research, the leading cause of bearing failure is due to contamination of the lubrication by moisture and solid particles. If as little as 0.002 percent water gets mixed into the lubrication system, it increases the probability of failure by 48 percent. Just six percent water can reduce the bearing lifetime by 83 percent.

Ball bearings require seals to keep oil in and unwanted water and liquids out, as well as wipers / scrapers to keep dust and debris out. Seals only last so long and do not perform well in dirty and dusty environments and can also increase friction in the application. In some applications where dust and debris are prevalent during operation, seals and wipers may require frequent replacement.

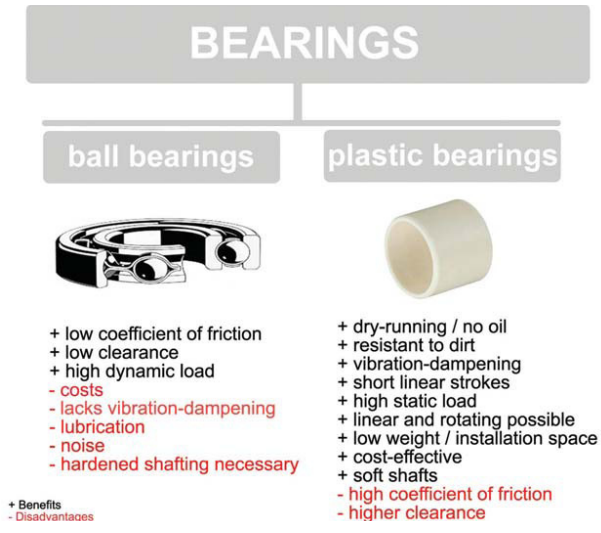

Figure 3. Comparing ball bearings to plastic bearings

4. PLASTIC BEARING APPLICATIONS

Regarding their advantages, plastic bearings are good solution for many applications in machinery that require clean and oil-free operation. They also perform well in dirty environments since there is no oil to attract dust and dirt, like the agricultural industry. Some manufactures creates individual planting row units using walking gauge wheels to deliver a consistent planting depth (Figure 4).

Figure 4. Plastic bearing application in agriculture

Oil impregnated bronze bearings with graphite plugs were used to facilitate this movement until they began causing severe problems. They were even requiring replacement two to three times a season. But the bronze bearings were experiencing high wear and premature failure due to the very abrasive conditions caused by high levels of volcanic ash in the soil, or the high salt content in the air caused corrosion and seizure. By replacing all 144 bronze bearings with iglide® selflubricating plastic bearings from igus®, the pick arms lif was increased by 5 to 6 times. The actual bearings cost 70 to 80 percent less than bronze bearings and were more reliable.

Shipbuilding and hydraulic turbine building have accumulated much experience with the use of sliding bearings made of UGET carbon plastic [7]. These include friction units of a driving rudder set of ships of different types and design (supports for rudders and rudder machines) with regard to stabilizers, interceptors, drives for actuators of Kingston valve type, and scupper screens, as well as mast elevating extending devices and mechanisms (Figure 5). Sliding bearings have been previously made of bronze, and shafts have been made of a corrosion resistant material having rather low antifriction characteristics, corrosion resistant steel or titanium alloys. Therefore, in the absence of reliable oil lubrication system there is a danger of seizure of metallic bearings, which may result in the failure of the whole mechanism. UGET carbon plastic containing poly functional epoxy resin and tissue of low module carbon fibre was developed. Bearings made of UGET carbon plastic are successfully used with shafts made of bronze and steels of different hardness and structure.

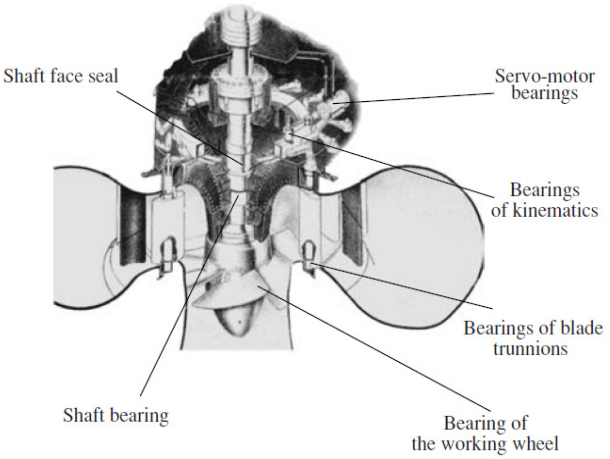

Figure 5. Sliding friction unit of a hydraulic turbine

One manufacturer specializes in vertical, form, fill and seal packaging equipment for handling a wide range of products: from green beans to candy to detergent. The machines are capable of reaching up to 160 cycles per minute and withstanding loads up to 15 pounds, while operating at speeds of 750 feet per minute (Figure 6).

The manufacturer had been using metal linear ball bearings. After the metal bearings scored the shafts and leaked grease on some of the machines, the company decided to replace them with self lubricating linear plain bearings. To date, the linear bushings have surpassed the 10 million cycle mark on some of the company's packaging machines with little to no noticeable wear.

Figure 6. Packaging machine with plastic bushings

In the quest to improve the way prostate cancer is detected and treated, a team of researchers from the Worcester Polytechnic Institute (WPI) in Massachusetts have developed a specialized magnetic resonance imaging (MRI) compatible piezoelectric actuated robot [1]. To facilitate

different types of motion, the robot uses a DryLin® linear guide system and iglide® plastic self lubricating plain bearings. The linear guides facilitate translational motion of the positioning module, which provides gross positioning for the robot's needle driver. The needle driver is a vital part of the system, as it enables the rotation and translational movement of the "needle cannula": a flexible tube inserted into the patient's body cavity for MRI-guided diagnosis and therapy (Figure 7).

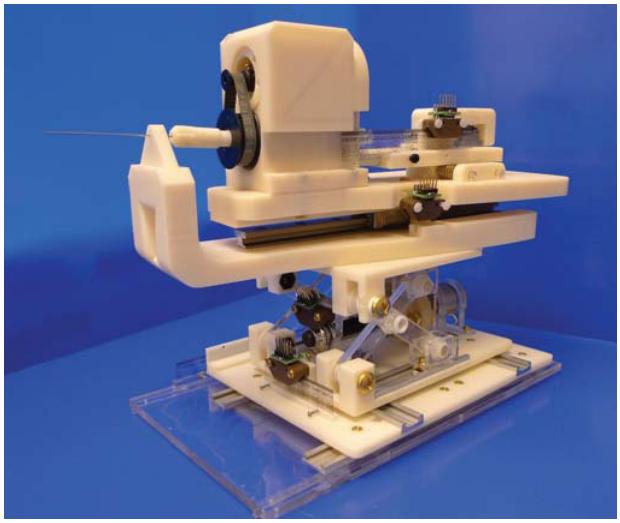

Figure 7. Plastic bearings in magnetic resonance robot

Two plastic plain bearings are used in the front and rear of the driver to constrain the needle guide. The bearings enable the robot's motor to rotate the needle using the mechanism by way of a timing belt. This rotating needle would reduce tissue damage while enhance targeting accuracy. Another 10 plain bearings were used to create a revolute joint, also known as a "pin joint" or "hinge joint", to provide single-axis rotation.

CONCLUSION

An actual scientific and practical problem could been solved concerning the development and application of high strength antifriction polymer materials in machine building. According to many researches following by experience in lot of typical applications [8], we could summarize the main benefits of plastic bearings:

- No maintenance
- Oil free, dry-running;
- Corrosion resistant;
- Cost less than ball and other bearings;
- Handle contamination well and often do not require seals or scrapers;
- High damping characteristics for vibrations, ability to reliably work under static or dynamic loads in dry conditions, such also in the presence of many lubricants (water, acids, alkali, oils, hydraulic liquids).
- This kind of bearing can be used on softer shafting, even anodized aluminium, which has excellent corrosion resistance and is usually less expensive and easier to machine than case hardened material or stainless steel.

This paper is just a part of preview and introduction in further researches of plastic bearings subjected to make simpler machine maintenance and better energy efficiency. Because of great expansion and clear explained advantages of plastic bearings application in several branches of industry, not only investigations of new polymer materials, but also deformation behaviour analysis in dry and conditions under different lubricants used to be done.

AKNOWLEDGEMENT

This work has been performed within the projects TR-35021 and TR-35011. Those projects are supported by the Republic of Serbia, Ministry of Education, Science and Technological Development, which financial help is gratefully acknowledged.

REFERENCES

[1] Mat Mowry: *The Thrue Cost of Bearing Lubrication*, igus White Paper, igus®inc.USA, 2012.

[2] Momčilo R Janković: *Exploitation Performances of Plastic Radial Sliding Bearings made in Yugoslavia*, Master Thesis, Mechanical Engineering Faculty University of Belgrade, Belgrade, 1976.

[3] S. P. Zakharychev and D. V. Otmakhov: *Using Polymer Adhesive Compositions in Design of Slider Bearings*, Polymer Science, Series D. Glues and Sealing Materials, Vol. 4, No. 4, pp. 314–316. Pleiades Publishing Ltd. 2011.

[4] Igus® Bearings Catalogue, Igus inc.USA.

[5] CSB Bi-metallic Composite Bearings, CSB France.

[6] ISB Technical Catalogue, Italcuscinetti Group, Italia.

[7] A. V. Anisimov, V. E. Bakhareva, and G. I. Nikolaev: *Antifriction Carbon Plastics in Machine Building*, Journal of Friction and Wear, Vol. 28, No. 6, pp. 541–545, Allerton Press, Inc., 2007.

[8] T.A. Osman: *Effect of lubricant non Newtonian behaviour and elastic deformation on the dynamic performance of finite journal plastic bearings*, Tribology Letters, Vol. 17, No. 1, pp. 31–40, Springer, 2004.

Serbian Tribology Society

SERBIATRIB '13

13th International Conference on Tribology

Faculty of Engineering in Kragujevac

Kragujevac, Serbia, 15 – 17 May 2013

EFFECT OF VISCOSITY ON ELASTOHYDRODYNAMIC LUBRICATION BETWEEN PARALLEL SURFACES SUBJECTED TO HIGH ACCELERATION

Usman Ali Zia[1], Aamer A. Baqai[1], Waseem Akram[1]
[1]National University of Science & Technology(NUST), Pakistan
usman_ali442@hotmail.com, aamerbaqai1@gmail.com, wasim6@gmail.com

Abstract:*Material wear due to friction is one of the most commonly experienced causes of material failure in any mechanical industry. Various studies have been conducted and as a result of these studies various lubrication solutions have been proposed. Present work is an attempt to propose an Elastohydrodynamic lubrication solutio20n for a frictional wear problem experienced in an industrial application involving the sliding contact between two parallel surfaces subjected to high acceleration. The "Numerical model for mixed lubrication" developed by Dong Zhu in 1990s has been modified to accommodate the constraints of problem at hand. The solution proposed predict the lubricant film thickness that when maintained between the contacting surfaces can avoid full metal contact, which in turn shall avoid the material wear. The present research is an attempt to comprehend the effect of change of viscosity and change of clearance between the surfaces on the value of film thickness. Different grades of nonflammable, anticorrosive Perfluoropolyether based grease (Krytox) are used. The results obtained are in the form of graphs which calculates the value of film thickness for one complete slide of one surface over the other. The results obtained by the numerical model are compared and found well-in-accordance with the experimental data available and with the analytical predictions made by scholars in the past.*

Keywords: *Tribology, Friction, Elastohydrodynamic lubrication, Krytox, Shear stress factor, hydrodynamic pressure*

1. INTRODUCTION

Wear is the major cause of material wastage and loss of mechanical performance and any reduction in wear can result in considerable savings. Friction is a principal cause of wear and energy dissipation. Considerable savings can be made by improved friction control. It is estimated that one-third of the world's energy resources in present use is needed to overcome friction in one form or another. Lubrication is an effective means of controlling wear and reducing friction. Principles studied under the field of tribology helps to analysis such problems of frictional wear. Lubrication phenomenon is being used to avoid fricational wear since the time of its discovery.

For any tribological studies the lubrication regime in which that particular machine/ application is working is very important as it steers the later research in the field. The outcome of most of these researches is a lubrication solution that if maintained between the contacting surfaces can avoid dry metal-metal contact and inturn diminishes the chances of any mechanical wear. A lubrication solution can be studied under two main types of regimes:Fluid Film Lubrication and Boundary Lubrication.

Out of these regimes, the fluid film lubrication is considered in case the required factor of safety is high so it is desired that the two contacting surfaces have minimum chances of coming in contact with each other. This requires a thick lubrication layer (exceeding a thickness of more that 1um) [1] between the surfaces so that enough hydrodynamic pressure exists to keep the surfaces apart.

Table 1: Nomenclature of Symbols.

Terms	Definition	Value	Terms	Definition	Value
F_h and M_h	Hydrodynamic Force and moment	Calculated by integrating hydrodynamic pressures	M_{MB}	Moment due to mass of primary body	Calculated by Equation (5)
F_{fh} and M_{fh}	frictional force and moment due to lubricant film	Calculated by integrating the Shear stress	$\widetilde{F_{MB}}$ and $\widetilde{F_{Fin}}$	Reciprocating inertial forces	Calculated by Equation (7)
F_{MB}	Inertial force due to primary body	Calculated by Equation (3)			Calculated by Equation (8)
F_G	Gas Force or Thrust Force	Pre-defined term	aY	Acceleration of the body	Calculated by Equation (9)
F_{Fin}	Inertial force due to Fin	Calculated by Equation (4)	I_B	Angular moment of Inertia about the body's center of mass	
x	Perpendicular distance from point of application of F_{MB} to the center of gravity of Fin		C	Constant	Obtained through experimental data
η_p	Viscosity at Pressure 'p'		p	Concerned pressure	
η_0	Viscosity at atmospheric pressure		n	Constant	Approximately 16
α	pressure viscosity co-efficient	Calculated by plotting the natural algorithm of dynamic viscosity versus pressure. The slope of this graph is α[16]			

For the case of boundary lubrication no hydrodynamic film is sustained. The coefficient of friction is very high and friction is proportional to the applied load for a certain range of sliding velocity and temperature.

Fluid film lubrication is further classified as hydrodynamic and Elastohydrodynamic lubrication, based on the fact that the surfaces under consideration show remarkable elastic deformation or not. As evident from above discussion the selection of lubrication regime is very important and is completely dependent on the circumstances under which the surfaces come in contact.

The present research is focussed on the lubrication solution for problem under the regime of elastohydrodynamic lubrication. The present research is devided into 7 sections. Section 2 focusses on the literature studied and benchmarked for the present research. The problem under consideration is explained in the section 3.

The constraints explained in the senction 3 laid down the basics for developement of a methodology for the solution, the same is explained in the section 4. Section 5 explains the results obtained on the basis of methodology of section 4. Section 6 concludes the work by drawing the conclusions based on discussions of section 5.

2. LITERATURE SURVEY:

The studies in the field of tribology initiated in 19th century with the experiment of Beauchamp Tower when he noticed that the oil film provided in between the surfaces of a journal bearing tries to pump out of a hole provided on top of the bearing. He conculded that the pumping phenomenon can be explained with the generation of hydrodynamic pressure between the bearing surfaces.

Reynolds in 1886 [2] provided the mathematical solution for the generation of above mentioned pressure. The theory presented by Reynolds provided the long waited analytical proof of the hydrodynamic pressure generated between the surfaces. This hydrodynamic pressure helps keep the surfaces apart and thus avoiding the metal-metal contact which inturn avoid the mechanical wear.

After Reynolds, many scholars tried to predict the lubricant film thickness based on his work, for problem related to different types of bearings including thrust bearing, journal bearing and slider bearing etc. The most notable work in this reagrd was done in the field of automobiles to predict the lubrication solution for piston-liner assembly.

G.M. Hamilton in 1972 [3] predicted the film thickness solution for piston-liner problem while considering the regime of hydrodynamic lubrication. Further in 1977 Hamrok and Dowson [4] formulated the empirical formulae for film thickness calculation.

For Elastohydrodynamic film thickness solution, the first realistic model was provided by Ertel and Grubin [5]. After Grubin other significant contribution in the field was made by Dowson and Higginson [6]. They described an iterative procedure that not only yielded a wide range of solutions during the next decade, but also enabled them to derive an empirical minimum-film thickness formula for line contacts.

One of the most considerable works in this regard was presented by Dong Zhu in 1991 [7, 8]. He presented a model namely "Numerical Model for Piston-Skirt assembly under mixed lubrication". He developed a new relationship for film thickness based on the eccentricities and clearance between the piston and cylinder. It was also claimed that the empirical relationship developed previously by Hamrok is not applicable for cases of high pressure and acceleration. Further in 2002 he extended his work [9-11] by considering a wider range of parameters like Load, Speed and Material properties. He also supported his theory with experimental data in a series of research papers.

The aim of the present research is to verify the applicability of Dong Zhu's model on our present assembly. However our present problem, described in detail in the next section, has different geometrical and environmental constraints, therefore it requires certain modification in the original model.

3. PROBLEM DEFINITION:

The problem at hand involves a cylindrical body sliding inside a hollow tube. The sliding action of the cylidrical body is under high accelearation and therfore involves high pressure environment. It is desirable that the body does not have any wear at its surface as it can alter the trajectory followed by it during its further operation. Based on high factor of safety required and the deforamtion of the body due to high pressure and high acceleration, elastohydrodynamic lubrication regime is considered. The assembly is shown below.

The force which forces the cylindrical body to slide is a thrust force at the base of the body. This further guides the research to be done in the field of thrust bearing. The thrust force is also responsible for the wobbling action of the cylinder inside the tube this wobbling is in itself responsible for the generation of hydrodynamic pressure in the lubricants' layers provided between the surfaces that keeps the surfaces apart and avoid mechanical wear as will be explained in more detail in later sections.

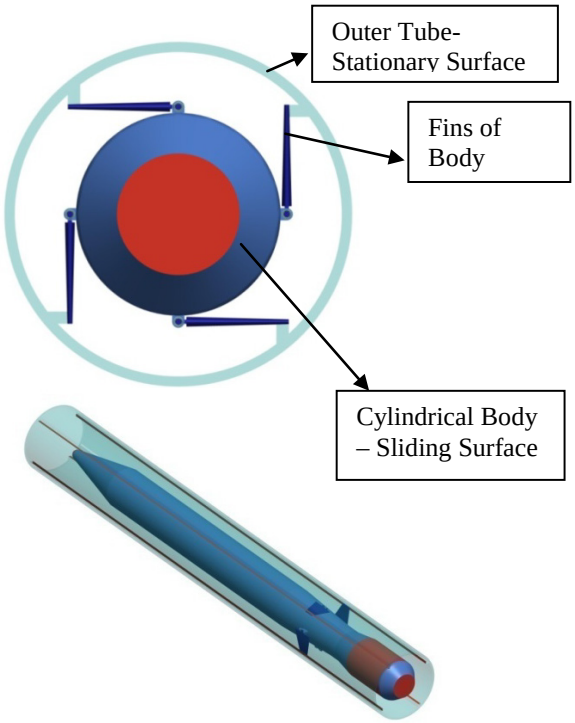

The present research tries to find a lubrication solution in term of film thickness for the assembly explained earlier. The film thickness predicted through the results of the research, if maintained in between the contacting surfaces shall be able to withstand the thrust force avoiding the surfaces to come in contact.

The model preseneted by Dong Zhu is modified based on the above mentioned constarints as shall be described in the following section.

4. MODIFIED NUMERICAL MODEL:

To model the phenomenon, following assumptions are made:

- The lubricant is an incompressible Newtonian fluid and the flow is laminar.
- Side leakage, oil starvation and surface roughness factors are neglected.
- No relative motion between the bodies under sliding motion.
- An Iso-viscous case, that is, viscosity is same in the circumferential and sliding directions.
- The fully flooded inlet and Reynolds exit conditions are applied.
- The surfaces of the ring and the liner are perfectly smooth.
- Thermal effects are neglected.

Based on the problem constraints and the assumptions made following modification are made in the Piston skirt model.

4.1. Modifying mixed lubrication model to EHL Model

As previsouly explained the lubrication regime to be considered for our present case is Elastohydrodynamic lubrcation whereas the regime of Dong Zhu's work [7] was mixed lubrcaiton. In order to incorporate this change, the terms (forces and moments) related to the contact between the two bodies are neglected.

$$F = F_h + \cancel{F_{\bar{c}}}$$
$$F_f = F_{fh} + \cancel{F_{f\bar{c}}}$$
$$M = M_h + \cancel{M_{\bar{c}}}$$
$$M_f = M_{fh} + \cancel{M_{f\bar{c}}}$$

4.2. Modification in Basic Dynamic Model

Due to different geometrical constraints the dynamic model is modified thorugh following set of equations. These equation are based on summation of forces and moments. The forces and moments acting around the Center of Gravity of the cylindrical body and fin are considered and equilibrium equations are applied at center of gravity of fin. Final equations formulated by simplifying the equilibrium equation are:

$$F_h + F_S + F_{fh} = -F_{MB} - F_{Fin} \quad (1)$$

$$M_h + M_{fh} + M_{MB} + F_{MB} * (x) = 0 \quad (2)$$

Where

$$F_{MB} = -m_{MB}\left(\ddot{e_t} + \frac{b}{L}(\ddot{e_b} - \ddot{e_t})\right) \quad (3)$$

$$F_{Fin} = -m_{Fin}\left(\ddot{e_t} + \frac{a}{L}(\ddot{e_b} - \ddot{e_t})\right) \quad (4)$$

$$M_{MB} = -I_B(\ddot{e_t} - \ddot{e_b})/L \quad (5)$$

$$F_S = F_G + \widetilde{F_{MB}} + \widetilde{F_{Fin}} \quad (6)$$

Where e_b & e_t are eccentricities at the top and bottom of the tube.

4.3. Modification in Acceleration Profile

The acceleration profile is modified based on the research by D.K. Kankane et. al. [12] while calculating the in-bore velocity of a projectile:

$$\widetilde{F_{MB}} = m_{MB} * aY \quad (7)$$

$$\widetilde{F_{Fin}} = m_{Fin} * aY \quad (8)$$

$$aY = \frac{F_G}{(m_{MB} + m_{Fin})} \quad (9)$$

4.4. Modification in Pressure-Viscosity Relationship

The numerical model for mixed lubrication uses the Barus eqution to cater for the change in viscosity due to pressure. Studies have shown that in case of high pressure problems the use of Barus equation can result in serious error in film thickness and hydrodynamic pressur calculations and therefore a new relationship developed by Chu et al. [14] in 1962 shall be used.

Barus Equation [13] $\eta_p = \eta_0 e^{\alpha p}$ (10)

Equation by Chu et. al $\eta_p = \eta_0(1 + C \times p)^n$ (11)

5. RESULTS AND CONCLUSION:

Following data is used as input for the numerical model.

Terms	Symbol Used	Value
Mass of primary body	m_{MB}	2000 Kg
Mass of fin	m_{Fin}	10 Kg
Viscosity of fluid (Krytox 215, 226, 227)	η_0	0.03204Pa.s 0.04550 Pa.s 0.07476 Pa.s
Diameter of primary body	D	0.45 m
Elastic Modulus	E	69 GPa
Thrust Force	F_G	17-32 KN

Following results have been plotted using MATLAB. The results are graphical, showing the effect of change in clearance between the contacting surfaces, viscosity and the thrust force. The graph is drawn between the film thickness and the length of the outer tube, this gives us the value of the film thickness that if maintained between the surfaces throughout the length of the tube shall avoid any metal contact between the surfaces and therefore will help diminish the mechanical wear due to it.

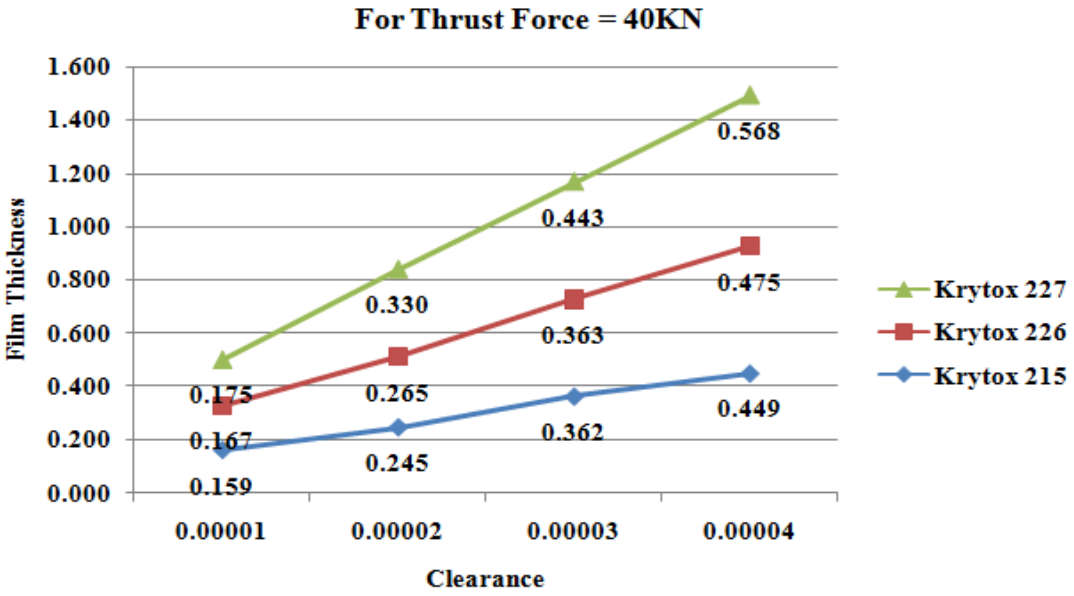

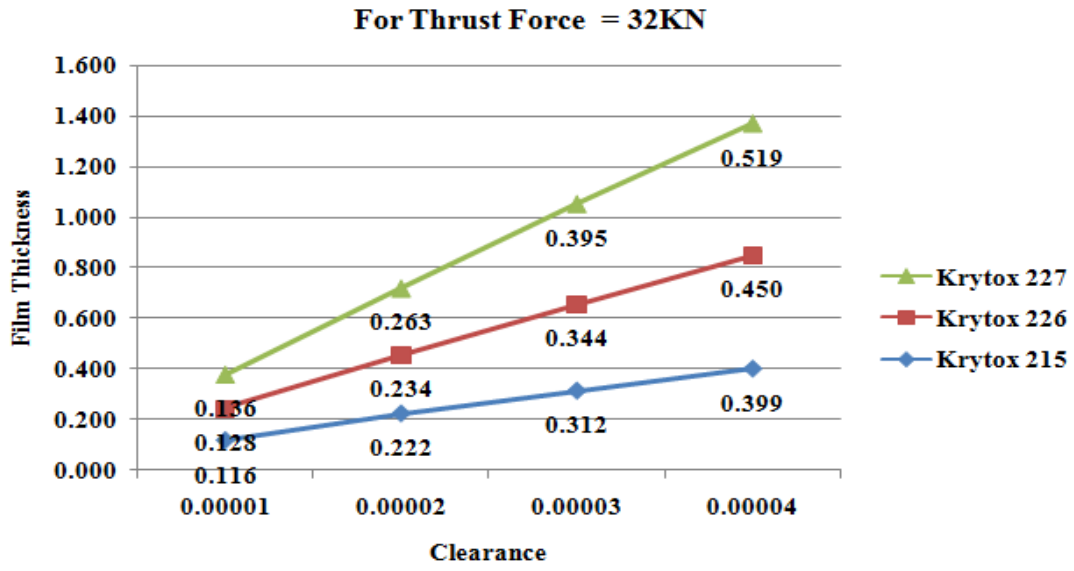

The results concluded for different grades of Krytox at different values of clearance have been attached at the end of the paper for reference purpose however a summarized graph for both case of thrust forces are plotted in MS Excel and are shown above.

Based on the graphs attached at the end of the paper and the summary graph displayed above, following is concluded:

- The film varies almost linearly throughout the length of the tube. This can be explained by the fact that during the sliding of one surface over the other the thrust force increases and this increase in the thrust force causes an increase in the hydrodynamic pressure which is directly proportional to the velocity of the sliding surface. This increase in the hydrodynamic pressure requires an increased amount of lubricant to avoid metal-metal contact.
- The small peaks in the beginning of the graph can be explained with the help of wobbling phenomenon that takes place due to the impulsive nature of the force provided.
- It is clear from the above graphs that the value of film thickness required, increases with increase in the viscosity of the liquid keeping the clearance between the surfaces constant. This conclusion is also supported by the experimental results provided in the research carried out by Crook, A. W in 1961 [15].
- It is also concluded that with increase in the clearance between the surface the value of film thickness increases this can also be

- explained with the direct relationship between the film thickness and the clearance as provided by Dong Zhu [7, 8].
- The experimental results already available for the present problem are for the case of Krytox 226 while keeping the clearance level of 0.00002 are 0.25 μm that is close in accordance with the numerically calculated value of 0.265 μm with an error of 6%.
- The summarized graph also show that the greater the value of the viscosity the greater the slope of the line which show that the effect of clearance between the contact surfaces increases with increase in the viscosity of the lubricant.

6. CONCLUSION:

Based on the above discussion it is concluded that the effect of clearance between the sliding surfaces under Elastohydrodynamic lubrication regime increases with increase in the viscosity of the lubricant and also that the increase in the thrust force requires a more thick layer of lubricant to be provided between the surfaces to avoid mechanical wear. The comparison of results with the experimental data and the analytical data of scholars from past, the applicability of the modified Dong Zhu's model for present case of sliding surfaces subjected to high acceleration is verified. The present work can be extended to incorporate the roughness of the contacting surfaces as well as to draw a comparison of Elastohydrodynamic and hydrodynamic lubrication regime's circumstances.

REFERENCES

[1] B. J. Hamrok, S. R. Schmid, B. Jacobson: *Fundamental of Fluid Film Lubrication*. Marcel Dekker Inc., 2004.

[2] O. Reynolds: *On the Theory of Lubrication and its Application to Mr. Beauchamp Tower's Experiments Including an Experimental Determination of the Viscosity of Olive Oil*, Phil. Trans., Roy. Soc. London 177, pp: 157-234, 1886.

[3] G.M. Hamilton, S.L. Moore: *The Lubrication of Piston Rings--First Paper--Measurement of the Oil-Film Thickness Between the Piston Rings and Liner of a Small Diesel Engine*, IMechE 188, pp: 253-261, 1974.

[4] B.J. Hamrock, D. Dowson: *Isothermal Elastohydrodynamic Lubrication of Point Contacts. Part III -Fully Flooded Results*, J. Lubr. Technol. 99, pp: 264-276, 1977.

[5] Morales-Espejel, E. Guillermo, A.W. Wemekamp: "*Ertel–Grubin methods in Elastohydrodynamic lubrication a review.*" Proceedings of the Institution of Mechanical Engineers, Part J: Journal of Engineering Tribology 222.1, pp: 15-34, 2008.

[6] D. Dowson, G.R. Higginson, *Elastohydrodynamic Lubrication*, Pergamon Press, Oxford, 1977.

[7] D. Zhu, H.S. Cheng, A. Takayuki, K. Hamai: *A Numerical Analysis for Piston Skirts in Mixed Lubrication-Part I: Basic Modeling* ASME Journal of Tribology, 114, pp: 553-562, 1992.

[8] D.Zhu, H.S. Cheng, A. Takayuki, K. Hamai: *A Numerical Analysis for Piston Skirts in Mixed Lubrication-Part II: Deformation Consideration* ASME Journal of Tribology, 115, pp: 125-133, 1993.

[9] D. Zhu: *Elastohydrodynamic Lubrication in Extended Parameter Ranges—Part I: Speed Effect*, Tribology transactions, 45.4, pp: 540-548, 2002.

[10] D. Zhu: *Elastohydrodynamic Lubrication in Extended Parameter Ranges—Part II: Load Effect*, Tribology transactions, 45.4, p: 549-555, 2002.

[11] D. Zhu: *Elastohydrodynamic Lubrication in Extended Parameter Ranges—Part III: Ellipticity Effect*, Tribology transactions, 46.4, pp: 585-591, 2003.

[12] D.K. Kankane, S.N. Ranade: *Computation of In-bore Velocity-time and Travel-time profiles from Breech Pressure Measurements*, Defence Science Journal, 53.4, pp: 351-356, 2003.

[13] C. Barus, *Isotherms, Isopiestics and Isometrics Relative to Viscosity*, American Journal of Science 45, pp: 87-96, 1893.

[14] P.S.Y. Chu, A. Cameron, *Pressure Viscosity Characteristics of Lubricating Oils*, Journal of the Institute of Petroleum 48, pp: 147-155, 1962.

[15] A.W. Crook, *The lubrication of rollers II. Film thickness with relation to viscosity and speed*. Phil. Transactions of the Royal Society of London. Series A, Mathematical and Physical Sciences 254.1040, pp: 223-236, 1961.

[16] G.W. Stachowiak, A.W. Batchelor, *Engineering Tribology*. Butterworth-Heinemann, 2005.

For Thrust Force of 40KN
Krytox 215 (μ = 0.03204 Pa.s)

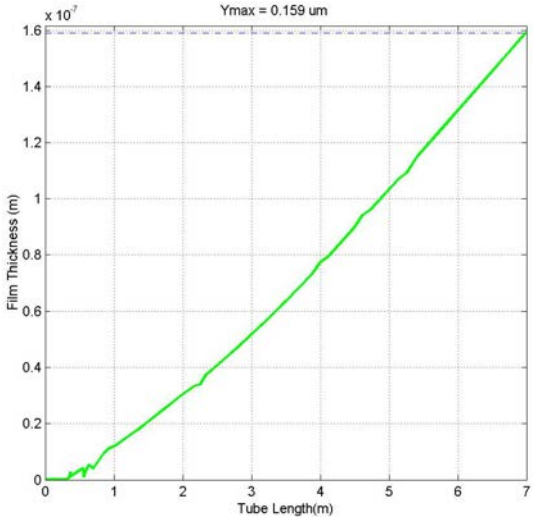

Figure 1. Clearance = 0.00001

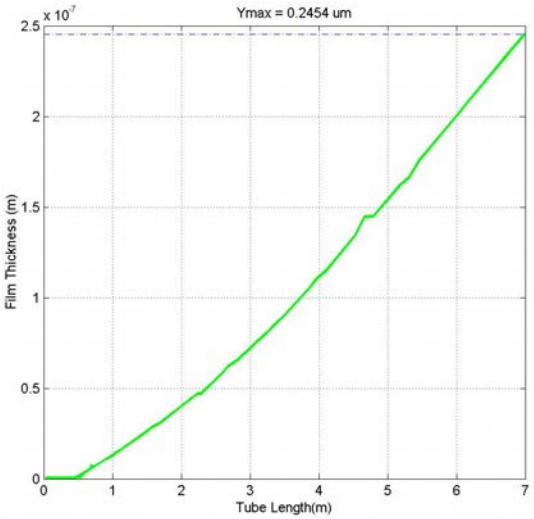

Figure 2. Clearance = 0.00002

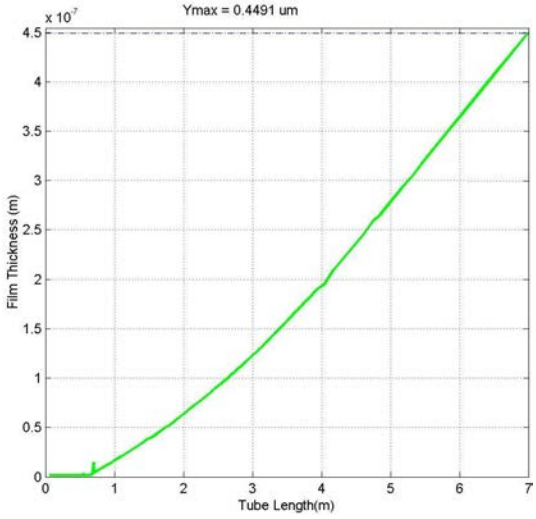

Figure 3. Clearance = 0.00003

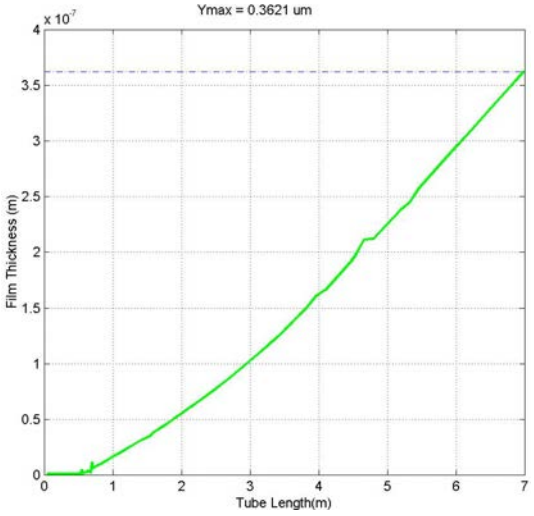

Figure 4. Clearance = 0.00004

Krytox 226 (μ = 0.0445 Pa.s)

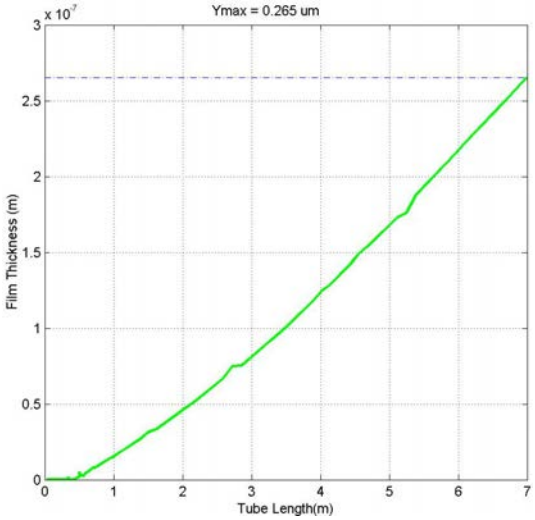

Figure 1. Clearance = 0.00001

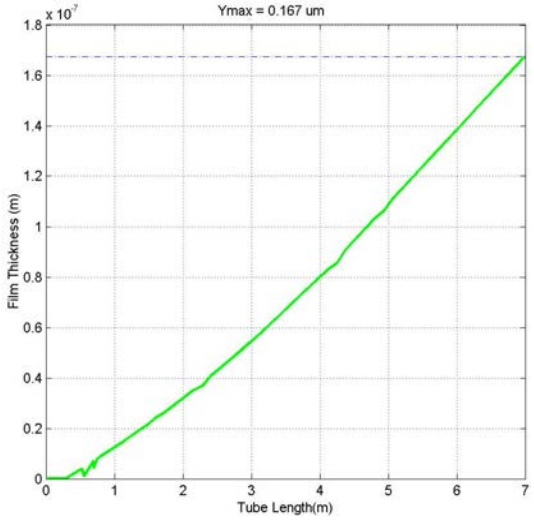

Figure 2. Clearance = 0.00002

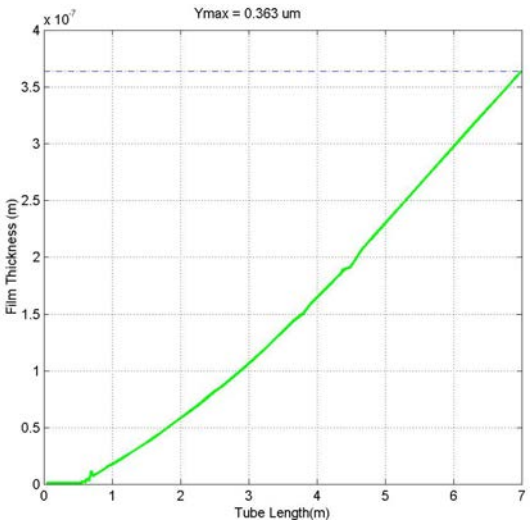

Figure 3. Clearance = 0.00003

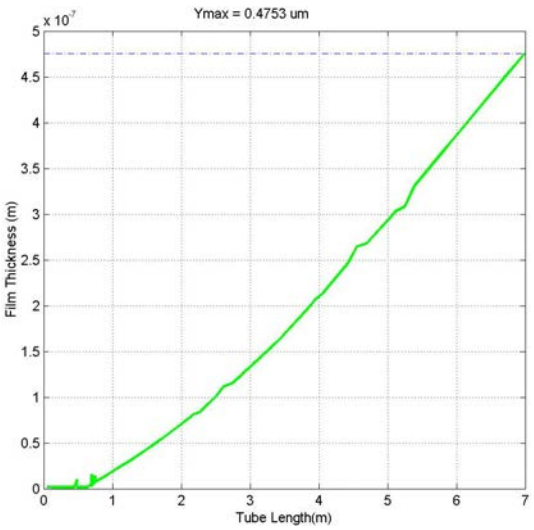

Figure 4. Clearance = 0.00004

Krytox 227 (μ = 0.07476 Pa.s)

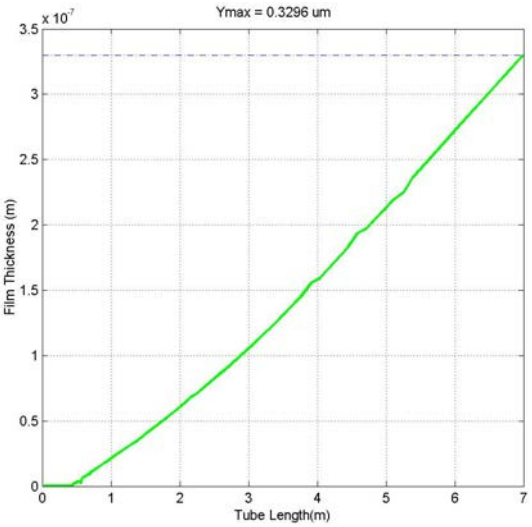

Figure 1. Clearance = 0.00001

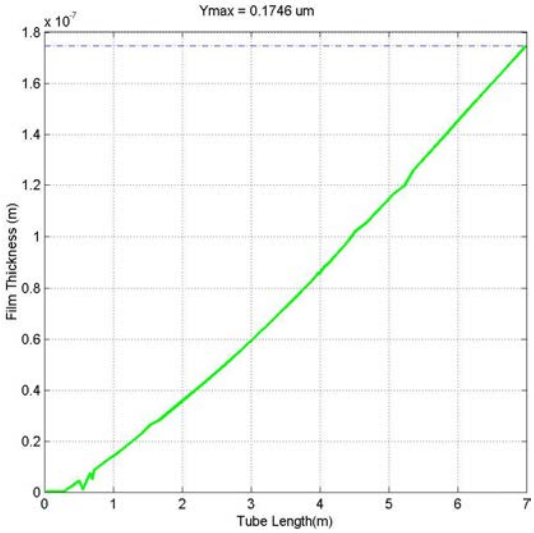

Figure 2. Clearance = 0.00002

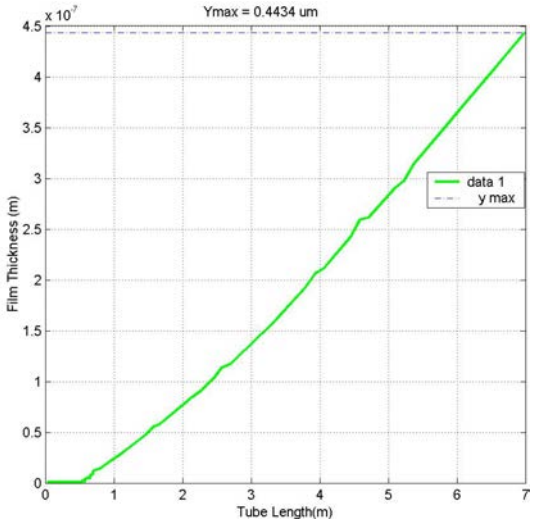

Figure 3. Clearance = 0.00003

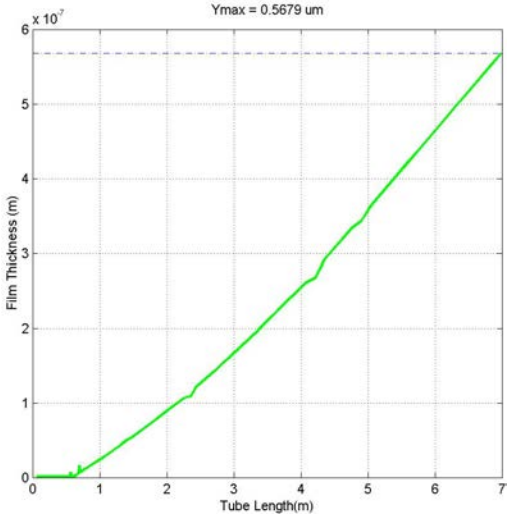

Figure 4. Clearance = 0.00004

For Thrust Force of 32KN

Krytox 215 (μ = 0.03204 Pa.s)

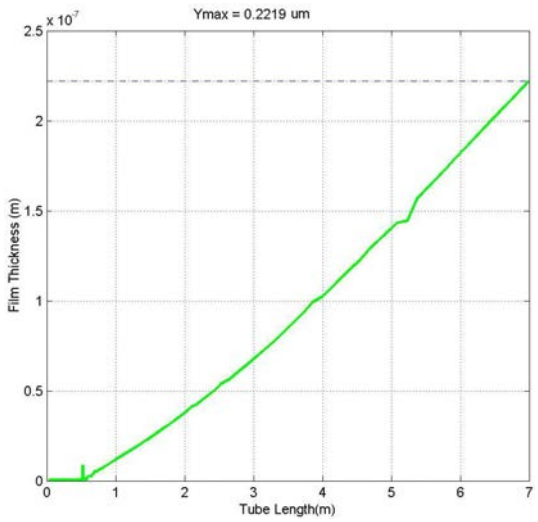

Figure 1. Clearance = 0.00001

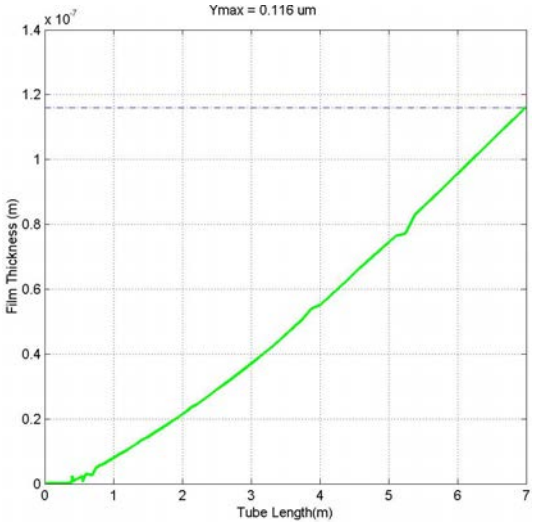

Figure 2. Clearance = 0.00002

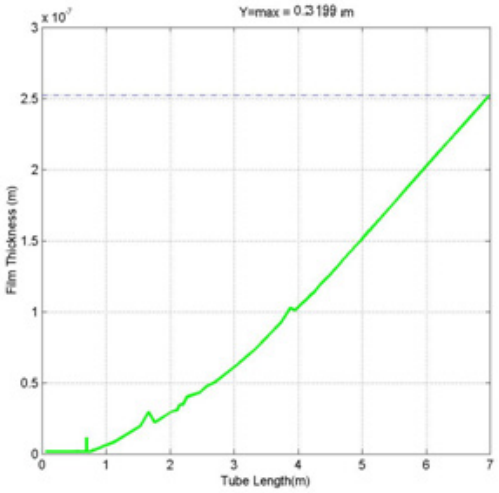

Figure 3. Clearance = 0.00003

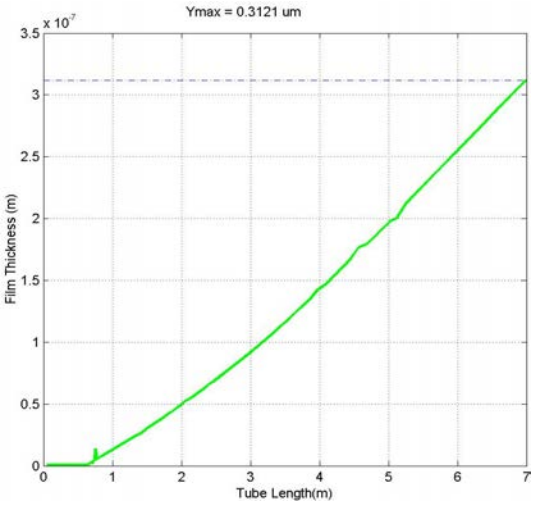

Figure 4. Clearance = 0.00004

Krytox 226 (μ = 0.0445 Pa.s)

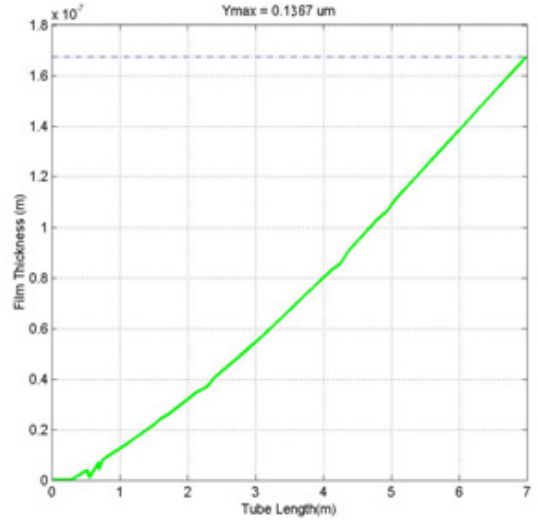

Figure 1. Clearance = 0.00001

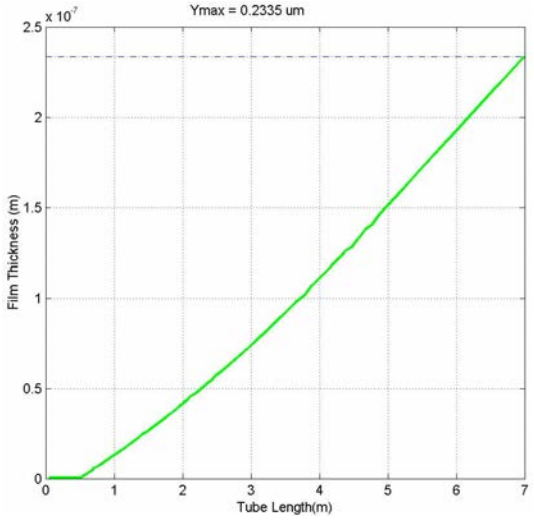

Figure 2. Clearance = 0.00002

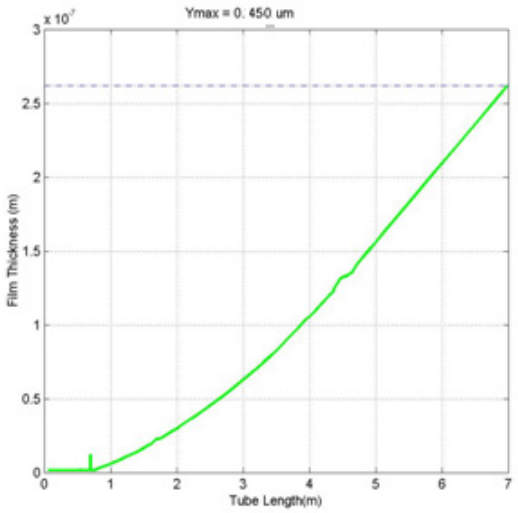

Figure 3. Clearance = 0.00003

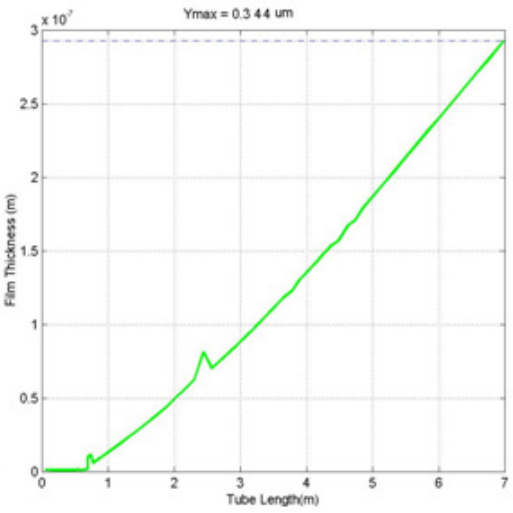

Figure 4. Clearance = 0.00004

Krytox 227 (μ = 0.07476 Pa.s)

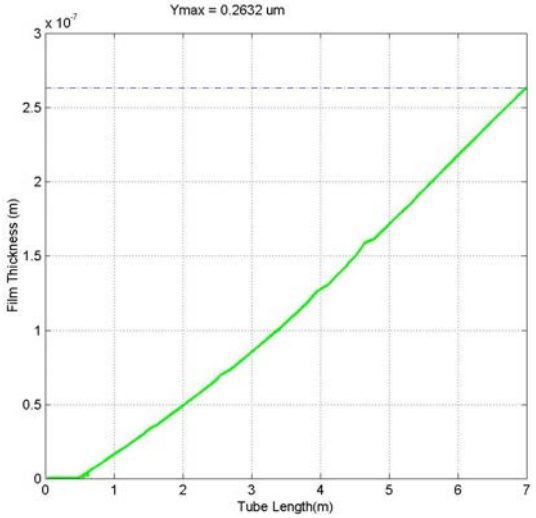

Figure 1. Clearance = 0.00001

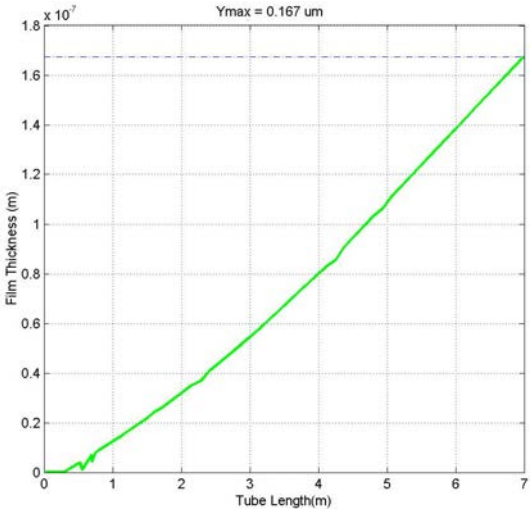

Figure 2. Clearance = 0.00002

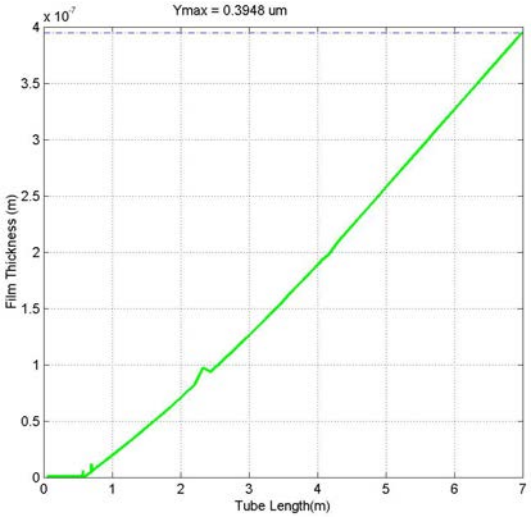

Figure 3. Clearance = 0.00003

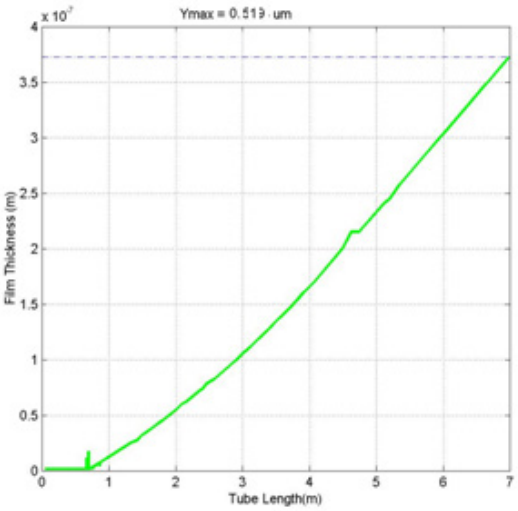

Figure 4. Clearance = 0.00004

Serbian Tribology Society

SERBIATRIB '13

13th International Conference on Tribology

Faculty of Engineering in Kragujevac

Kragujevac, Serbia, 15 – 17 May 2013

INCREASING OF TOOL LIFE FOR HOT FORGING USING SURFACE MODIFICATION

Milentije Stefanović[1], Dragan Džunić[1], Vesna Mandić[1]
Srbislav Aleksandrović[1], Dragan Adamović[1], Slobodan Mitrović[1]
[1]Faculty of Engineering University of Kragujevac, Serbia, stefan@kg.ac.rs, dzuna@kg.ac.rs, mandic@kg.ac.rs, srba@kg.ac.rs, adam@kg.ac.rs, boban@kg.ac.rs

Abstract: *Techno-economic indicators in the hot forging of steel and other materials are highly dependent on the total life of forging tools, that is, the number of forged parts requires accuracy of regeneration after etching. Key influences on the life of tools, like in every tribo-system are: the pieces of material, geometry and material tools and machines for forging and environmental conditions. Characteristics of hot forging high temperatures are in contact materials and tools, and local high working pressures, the dynamic character of the load tools etc. Tool life is usually limited to the complex mechanisms of wear and tear, as a consequence of cyclic loading, such as abrasive and adhesive wear and, thermal and mechanical fatigue, and plastic deformation. This paper presents an overview of opportunities for increasing the life of forging tools by modern techniques for modifying the working surfaces of tools, according to comparative results of different methods, and gives appropriate recommendations.*

Keywords: *Hot forging, tool life, wear, coatings*

1. INTRODUCTION

In general, forging entails the sequential deformation of the workpiece material through a number of different processes. Furthermore, each forging operation comprises all the input variables such as billet material, dies, the conditions at the die-workpiece interface, the mechanics of shape change in the workzone, and the characteristics of the processing equipment, as illustrated in Fig. 1 [1]

Thus, in designing and developing bulk metal forming processes, key technical problem areas that must be addressed include:

- workipiece material-shape and size, chemical composition and microstructure, flow properties under processing conditions (flow stress in function of strain, strain rate and temperature), thermal and physical properties
- dies or tools-geometry, surface conditions, material and hardness, surface coating, temperature, stiffness and accuracy
- interface conditions -surface finish, lubrication, friction, heat transfer
- workzone - mechanics of plastic deformation, material flow, stresses, velocities, temperatures
- equipment used -speed, production rate, force and energy capabilities, rigidity and accuracy .

The understanding of these variables allows the prediction of the characteristics of the formed product, i.e., geometry and tolerances, surface finish, microstructure and properties.

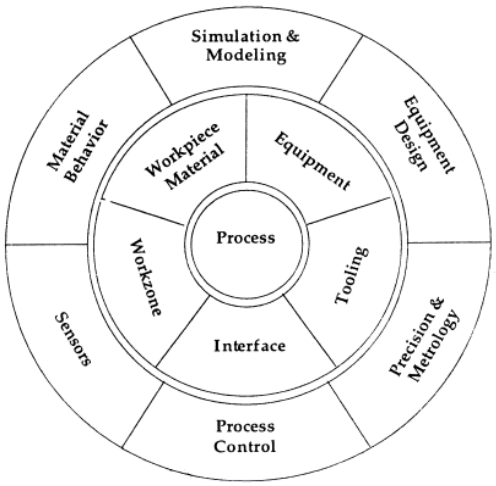

Figure 1. Variables of a bulk forming process [1]

Tools for hot forging are used in extremely difficult conditions: impact and very high mechanical load, variable partial and general thermical load, friction on the surfaces of tools and more. Each tribological system in the field of hot forging is characterized by the following elements [2]:

- contact pair, which consists of tool and workpiece-metal that is plastically deformed, with appropriate structural and mechanical properties,
- lubricant with properties relevant for hot process,
- a machine that implements processing,
- micro and macro environment

The final characteristics of the finished piece-forgings, such as size, shape, surface quality and structure depend on the values of system parameters. Figure 2. shows a global approach to the modeling of machining processes, whereas the quality of lubricants is main output.

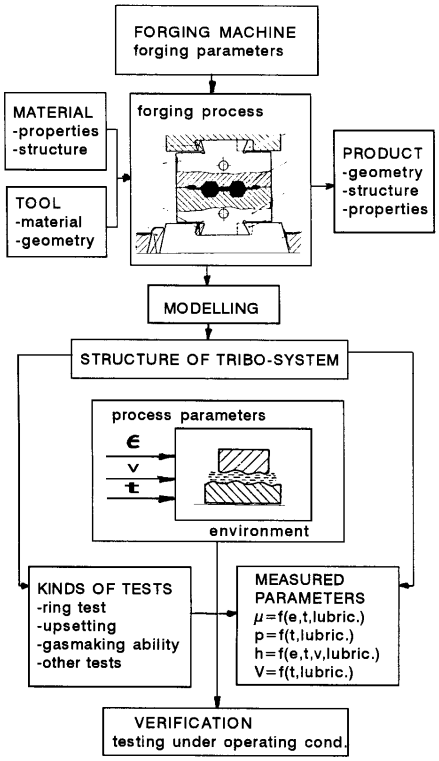

Figure 2. Tribo-modelling of hot forging process [2]

2. CAUSES OF DAMAGE TO THE TOOLS

Tools for hot forging function during cyclic mechanical and thermal loads. The complex process of tear occurs as a result of the two loads. Due to the high pressures and inadequate lubrication regime, the intensity of wear and tear due to friction is high. The main causes of damage to the tool, Figure 3:

- Wear as a result of tribological processes
- Plastic deformation,
- Thermal cracks,
- Mechanical fatigue crack growth,
- Breakdowns (die failures).

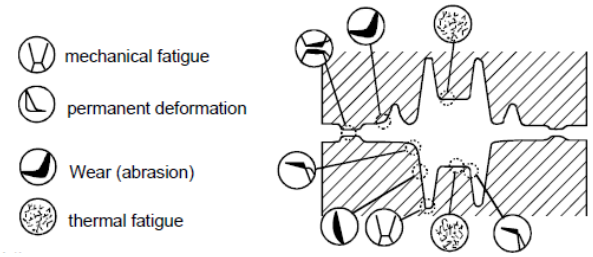

Figure 3. Failure and damaging of forging dies

Tool wear. This type of wear occurs as a result of relating the material particles from the surface of tools. Consequence of the occurrence of abrasive and adhesion processes and the formation of welded layers that are later destroyed.

Plastic deformation occurs under the influence of high pressure to the tool. As a result of resist materials, the deformation of the walls of tools and measuring tools changes.

Thermal cracks. They are caused by cyclic thermal change and show it as a grid cracks on the surface etching. Microcracks are connected and grow into large thermal cracking. They can grow on the surface and in depth.

Mechanical cracks are caused by mechanical loading tools. Consequence of fatigue, pre-treatment and initial thermal cracking. These are called large cracks.

Failure of tools is the result of hidden defects, bad thermal processing, errors in design, irregular exploitation and so on.

Generally, due to the forging temperature being well above 1000 ◦C, the temperature of the surface of the tool temporarily exceeds 500 ◦C and thus the tempering temperatures of conventional hot work tool steel. In such a case, the hardness of the tool is reduced and the mechanical impacts during forging operations can easily cause plastic deformation as well as abrasion of tool material, Figure 4 [3].

Life of forging tools is a complex function of several parameters, the most important being: structural, method design and exploitation conditions. Figure 5. demonstrates an interaction between these parameters.

Based on the analysis of tool wear, we can give the following recommendations for the design of tools [4]:

- The choice of tool material with high resistance to abrasion,
- The application of appropriate methods for improving surface properties of tools,

- Reliable exploitation tools, primarily because of the importance of lubrication,
- Use of an active role of friction,
- New design tool that allows the hydrostatic or hydrodynamic lubrication.

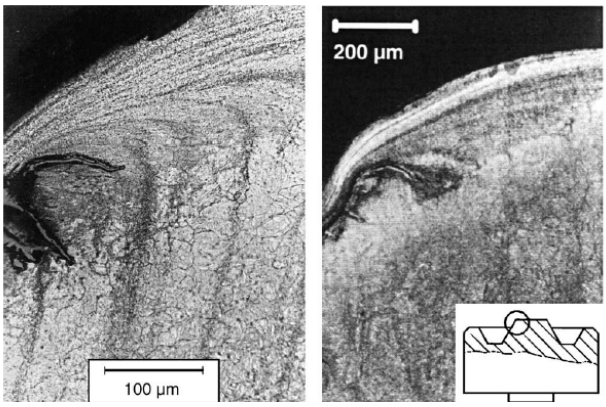

Figure 4. Microstructure of the convex radius of different hot work tool steels after 1000 forging cycles. Tool temperature, 200 ◦C; forging material, C45; forging temperature, 1100–1150 ◦C; lubricated contact; cycle time, 13 s; hardness of tools, 47 HRC.[3]

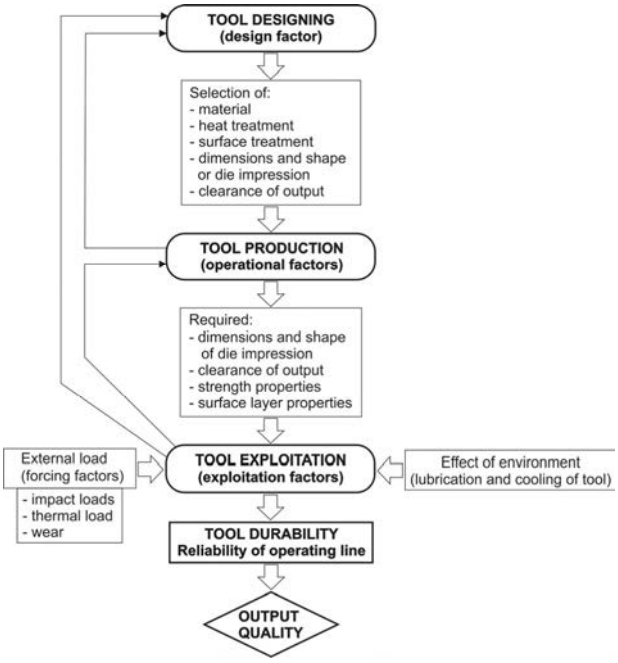

Figure 5 . The interaction of construction, technology and the industrial conditions of working tools [4]

3. METHODS OF INCREASING THE LIFE OF TOOLS

The predominant causes of damage are the result of tool wear and thermal and thermal-mechanical damage. Forging dies are exposed to high mechanical loads, which are accompanied by extreme thermal and tribological load for a very narrow surface layer. As a result of preheating steel parts at temperatures above 1000 ° C, the size of the hard oxide particles come in contact zone causing very strong abrasive wear. At elevated temperatures tribological conditions are very favorable for the processes of adhesion and a transfer of material to and from the surface of the tool. During execution of cyclic forging process heat is transferred due to contact with the heated work pieces followed by cooling lubricant tools in the form of spray, which is performed at room temperature. In this way, thermal shocks occurring within the tool material, resulting in high internal stresses initiate cracking. Further development of the cracks formed in parallel to the contact surface may lead to its peeling, when these cracks meet with cracks normal to the contact surface. In case of insufficient cooling of tools, it is possible to slightly release tool steel [5].

To increase the life of hot forging tools, different surface modification techniques are used such as welding, thermal application, electrodeposition, diffusion method and other combined methods. These special methods of surface modification increase the hardness, wear resistance and corrosion resistance of the tool at high temperatures. One possible way to satisfy all the conditions of hot forging process is a combination of thermo-chemical surface modification process (ie, carbonization and nitriding) with coating processes (ie, PVD, CVD, or PACVD), which is known in the literature as duplex modification process surface [6].

Figure 6 shows the results of testing the wear alloy tool steel to functioning in a warm envirnment (WNL-55NiCrMoV6) using various surface treatments: nitriding, sulphurizing, diffusion chroming, Cr plating, plasma spraying with metallic coatings of Cr, WFe, WC-types, burnishing [4].

Using spray-metal coatings leads to triple reduction of wear compared to conventional treatment tools. It also shows that the wear of the tool depends directly on the oxide that is generated on the surface of pieces and to a lesser extent on the oxide surface tools. Cr and WC plasma sprayed coatings should be applies to hot working tools. These coatings are characterized by considerable wear ressistance and thermal and imact fatique resistance.

According to the investigations [7] the best results for die service life were obtained for weld overlay coated dies, Table 1. Compared to received dies, the results showed an increase of 892%. The results were 206% better than TOKTEK Coatings, which held the second place.

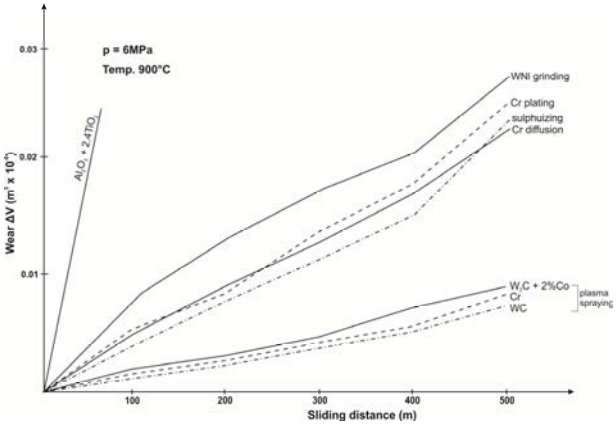

Figure 6. The influence of surface treatment and working on wear [4]

The dies can be ranged from the best to worst as weld overlay coated dies, multilayer dies TOKTEK coated, single layer AlTiN coated dies, plasma nitrided dies and dies as received. This range is also valid for the die polishing life, with the exception that it is equal for TOKTEK and AlTiN coatings.

Table 1. Number of polishing and total number of parts obtained with experimented dies [8]

Operation	Number of Forged Parts					
	As receiv.	Nitrided	AlTiN coated	TOKTEK	Weld overlay coated	
					1st forg.	2nd forg.
1st polishing	1440	3920	4810	4660	8690	8330
2nd polishing	1260	2140	1980	2030	8160	8410
3rd polishing	1320	2110	1860	1750	8240	7830
4th polishing	-	-	1720	1830		
5th polishing	-	-		1780		
Total prod.	4290	9420	12280	13210	27810	25930

4. CONCLUSION

Tools for hot forging are applied in extremely difficult conditions: impact and very high mechanical load, variable partial and general thermical load, friction on the surfaces of tools and more.

With these tools, a special kind of coating on contact surfaces is regularly applied, in order to extend their working life. There are very different methods for modifying the tool surface. The most common are different types of heat treatment, which significantly affects the hardness of the surface layers.

Shown results are related to single-layer and multilayer coatings. It's hard to make a general conclusion regarding the most influential parameters, but it is certain that the surface roughness has a significant effect on the adhesion characteristics of the coating. Also the surface hardness to which the coating is applied is very important as is the ability to carry the load in question.

Coatings based on Cr and WC, and welding procedures show the best results. From the standpoint of economy of the process of forging, welding is the best. The temperature and the percentage of nitrogen in the nitration are very important for tribological characteristics of contact layers.

The ratio of alloying components of chromium (Cr), molybdenum (Mo), and vanadium to carbon ratio (H/C) is highly significant influence on the change of tribological behavior of tool material regarding wear resistance.

ACKNOWLEDGEMENT

The authors wish to acknowledge the financial support from the Ministry of Education and Science of the Republic Serbia through the project TR 34002.

REFERENCES

[1] V. Vazquez, T. Altan: *New concepts in die design - physical and computer modeling applications*, Journal of MPT 98, pp. 212-223, 2000.

[2] M. Stefanović, R. Stanković: *Importance of Tribological Investigations in the Hot Forging*, YUTRIB 1995 Herceg Novi, pp, 181-182, 1995.

[3] Barrau, C. Boher, R. Gras, F. Rezai-Aria: *Analysis of the friction and wear behaviour of hot work tool steel for forging*, Wear, Vol. 255, pp. 1444–1454, 2003.

[4] M.Gierzynska-Dolna: *Effect of the Surface Layer in Increasing the Life of Tools for Plastic Working*: Journal of MWT 6, pp. 193-204, 1982.

[5] J. H. Beynon*: Tribology of hot metal forming*, Tribology International 31, pp. 73–77, 1998.

[6] B. Navinsek, P. Panjan, F. Gorenjak: *Improvement of hot forging manufacturing with PVD and DUPLEX coatings,* Surf. Coat. Technol. 137, pp. 255–264, 2001.

[7] M. Bayramoglua, H. Polat, N. Geren: *Cost and performance evaluation of different surface treated dies for hot forging process*, Journal of MPT 205, pp. 394–403, 2008.

Serbian Tribology Society

SERBIATRIB '13

13th International Conference on Tribology

Faculty of Engineering in Kragujevac

Kragujevac, Serbia, 15 – 17 May 2013

ANALYSIS OF TRIBOLOGICAL PROCESS DURING IRONING OF SHEET METAL MADE OF AlMg3

Dragan Adamović[1], Milentije Stefanović[1], Srbislav Aleksandrović[1], Miroslav Živković[1], Fatima Živić[1], Marko Topalović[1]

[1] Fakultet inženjerskih nauka u Kragujevcu, S. Janjić 6, 34000 Kragujevac, adam@kg.ac.rs, stefan@kg.ac.rs, srba@kg.ac.rs, zile@kg.ac.rs, zivic@kg.ac.rs,

Abstract: *The paper gives detailed analysis of tribological processes which occur in ironing, their influence on tool and formed material by means of specially developed physical model of drawing process. The typical property of such cold forming procedures is multiple repetitions of operations, i.e. several thinnings in one operation, which leads to gradual increase of thickness of glued material layer on contact surfaces of the tool. At sufficiently large thickness of glued layers, plastic forming of created glued particles occurs, i.e. their tear-off, disruption of forming process stability and increase of surface roughness of work piece. The obtained results indicate the basic influence of tribo-conditions on ironing process, tool durability and quality of obtained parts.*

Key words: *Ironing, tribo-modeling, tribological processes*

1. INTRODUCTION

Friction accompanies all physical processes that involve movement. It is also very important in metal forming, during which only external friction is considered. External friction occurs between material which is being plastically deformed and material of tool.

External friction shows significant influence on the course of plastic deformation, and thus the useful properties of the final product as well as the tool lifetime. The friction force, i.e. its contact components, show a significant influence on the stress field in a deformed metal, especially in its outer layers that came in contact with work surface of tool. Stress field has influence on the course of metal forming, and thus the movement of deformed metal surface on the acting surface of tool, and this movement have influence on the friction force. During this process, certain types of reverse elastic releases occur as well.

This type of resulted external friction between the plastically deformed metals and tool (technically dry friction with distinct adhesion effect between contact surfaces, coupled with boundary friction), significantly influences the quality of the product. If the adhesions (compounds formed by friction due to the "cold welding") are formed on surface of the tool they can be causes of scratch and allowances on the surface of the product that deteriorates its quality.

As a result of the friction notable changes in characteristic of outer layers occur, with different character of the changes that happens on the products surface layers in comparison to changes on tool surface.

The most of the work piece surface is in contact with the working surface of the tool and will have share in the friction process only once, while tool surface takes part in this process multiple times.

The characteristics of tool deformation and the work piece deformation are also different. The outer layer of the work piece (as well as the entire volume), has lower yield stress than tool, resulting in plastic deformations, while, at the same time, tool generally remains in the zone of elastic deformation. Given the fact that surface layer has the highest stress gradient, properties of outer layers, for both product and tools, will be different from properties of other parts of product and tools. As a result of the friction, tool wear occurs. Mechanism and the intensity of tool wear are functions of friction force magnitude and type of the friction [1].

Model of the phenomena that occurs in micro-zones of contact during friction is shown in Figure 1 [2]. One can distinguish three main stages of interaction between contact surfaces during friction

Stage I. At this stage contact occurs as well as mechanical action between contact surfaces which are initially covered with oxide layers, whereby the amount of oxide depends largely on the type of processes (metal forming of hot or cold), and susceptibility to oxidation of the metals that form contact pairs. The dominant phenomenon at this stage of contact is the plastic deformation, not only of the surface roughness but also, and in the considerable volume of the material.

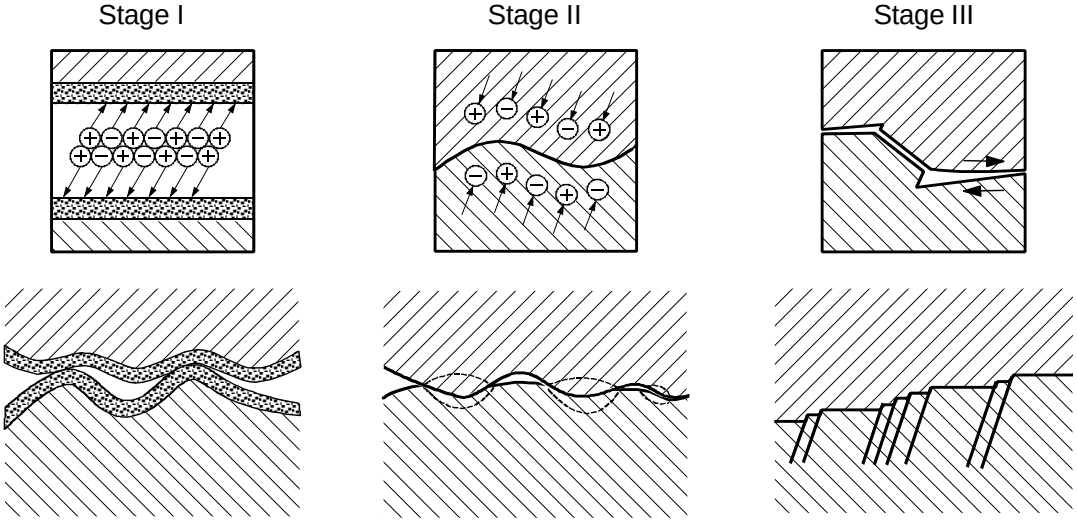

Figure 1. Model of the phenomena that occur in the micro-areas of contact during friction [1]

Stage II. As a result of molecular interaction, adhesive joints (compounds) are formed. The quantity of joints depends largely on the geometry of the contact and the specific pressure.

Stage III. This stage of the contact surface interaction includes the destruction of adhesion joints which were formed during the relative displacement of contact pair metals. Failure mechanism of contact joints can be very complex. In the first stage of joint destruction micro-slip will surely occur, and therefore the complex phenomena of movements and mutually dependent movement of dislocations. As a result of these phenomena surface defects such as micro-cracks and micro-notches can be created.

As a result of repeated displacement of deformed metals in regards to the surface of the tool, the effect of friction and the associated forming and destruction of adhesive joints, tool wear occurs.

In the case of metal forming, process is characterized by the fact that multiple repeated operations (forging or ironing) causes a gradual increase in thickness of glued layer, which means that the sum of the individual joints goes into a continuous layer.

As a result of predominance of adhesive force over resistance to plastic flow in the glued layer, in further stage glued particles suffer from plastic deformation until they are torn off and smeared.

When a sufficiently large thickness of glued layers is formed as a result of repeated process of plastic deformation (in a series of passages which leads to increasing and decreasing of mutual interaction), process begins which leads to the separation of adhesive joint from tool surface by peeling (shear) or tearing. This leads to the significant damage of the tool surface layers, and therefore to the increase in surface roughness. The occurrence of peeling or tearing depends on the type of formed joint.

In case of contact pairs with higher chemical affinity, the strength of diffusion produced joints (solid solutions) may be greater than strength of material of contact pairs, causing the destruction of joint to occur in depth of less strong and no fortified material, which means it occurs at such a depths at which there is no more squeezing.

In the case of diffusion-less joints, as well as for the occurrence of brittle inter-metallic phases, the destruction of joint will be based mainly on layered peeling of metal with less strength. Tearing off of glued particles also occurs. Further relative displacement of contact elements (the work piece is plastically deformed in relation to the tool), makes these glued particles to reappear on the surface of the friction. Afterwards they are compressed on the tool surface, which results in creation of grooving in "partner" made of material with less hardness (usually plastically deformed work piece). The type and intensity of this secondary effect depends on the hardness of the plastically deformed and strengthened adhesive joints.

In addition, as a result of cyclic loading of the tool, on its surface there might be occurrence of such defects such as intrusion and extrusion, as well as micro-cracks, which are characteristic of the metal fatigue process.

2. EXPERIMENTAL TESTS

Tests were conducted on the original tribo-model of ironing, which simulate the two-sided symmetrical zone of contact with the die and the punch [3]. This model enables the realization of high contact pressures with the respect of physical and geometric conditions of the real process (the material of the die and material of the punch, the topography of the contact surface, the angle of the die cone - α, etc.). Diagram and image of the aforementioned tribo-model is shown in Figure 2.

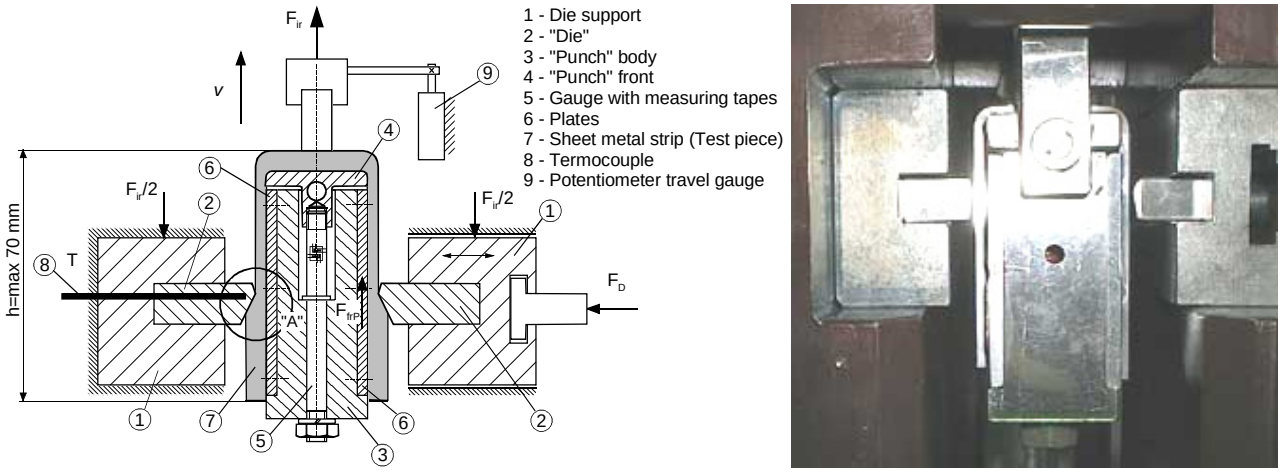

Figure 2. Diagram and image of the tribo-model used in this research

Device for testing of ironing was installed on a special machine designed for sheet metal testing ERICHSEN 142/12.

For the experiments presented in this paper, we used sheet made of aluminum alloy, AlMg3(.43) (according to EN: AlMg3 F24, and in text below only AlMg3). Mechanical properties of tested material are given in Table 1.

Table 1. Mechanical properties of tested material

Materijal	Rp, MPa	Rm, MPa	A, %	n, -	r, -
AlMg3	201.1	251.0	12.0	0.135	0.405

Contact pairs ("die" and "punch") are made of alloyed tool steel with high toughness and strength, designated as Č4750 (EN: X160CrMoV121).

3. EXPERIMENTAL RESULTS

During ironing friction coefficients of die and punch can have a wave-like (unstable) form (Fig. 3). Friction coefficients alternately rise and fall with irregular and approximately the same amplitude and frequency. At a particular time, friction coefficients can have slightly increasing, constant or slightly decreasing flow.

Very interesting explanation of this type of friction is given in the papers [4, 5]. It is considered that the wavy type friction coefficients occur when there is a micro-welding of roughness peaks in the "form of the islands".

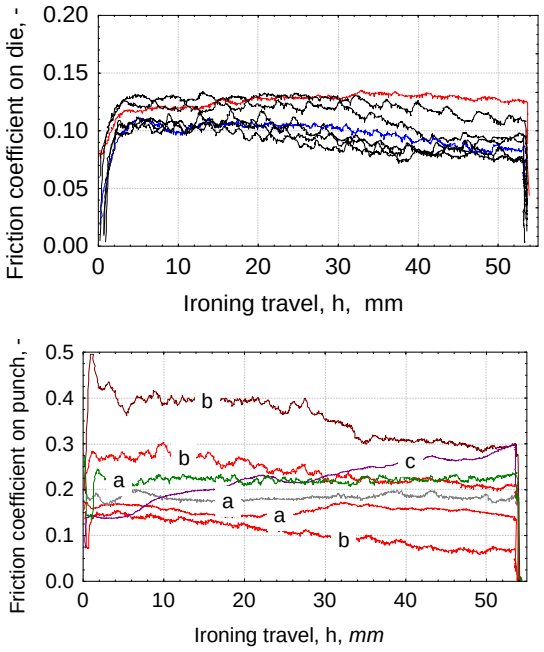

Figure 3. Examples of unstable friction coefficients on the side of the die and punch: a-constant, b-decreasing, c-growing

Subsurface layer of the contact surface on the exit part of the die, which surface is about 80% of the total contact area between the tool and the material, suffers considerable distortion due to shear stress which is result of friction forces. This stress is approximately equal to the shear stress in the weld zone. This zone is therefore called the "zone of quasi-welding". At the entrance part of the

die, where there is a layer of the lubricant which is not yet squeezed out, there is a formation of so-called "nipple slip". During this process quasi-weld zone is steadily increased and thus coefficient of friction is increased as well. When the surface of quasi-weld zone become equal to the entire friction surface, friction coefficient reaches its maximum value. In addition, due to strong friction connections, micro cracks in the subsurface layer are formed. Due to the continuous material inflow in the zone of deformation noticeable nipple is formed, which at some point, because of cracks caused by the weakening of the frictional connection, detach itself from the base material. In this way the quasi-welded zone is reduced and lubricant starts to penetrate places of broken connections, which reduces the friction coefficient. Chipped of metal fragments are trapped between the die and the surface of sheet metal and are being continuously moved towards the exit part of the die. When they came out of the zone of deformation coefficient of friction will have a minimum value. Then, the aforementioned process continuously repeats itself.

Figure 4. Aluminum glued particles on die and puncher surfaces

Some lubricants, no matter the fact that they produce satisfactory results in steel plates, in case of plates made of AlMg3 have very poor results. Their usage leads to intense gluing of aluminum onto tool, which is shown in Figure 4. Glued particles that are formed on the die during the ironing can cause severe damage to the sheet metal surface (galling) (Figure 5).

If the inadequate lubricant is used coupled with greater gripping forces, stickers are formed and contact conditions are greatly deteriorated which lead to the significant increase of drawing force for each subsequent passage (Fig. 6).

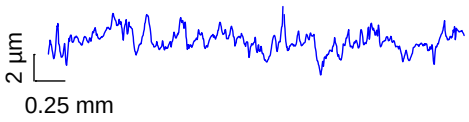

Figure 5. Grooved surface

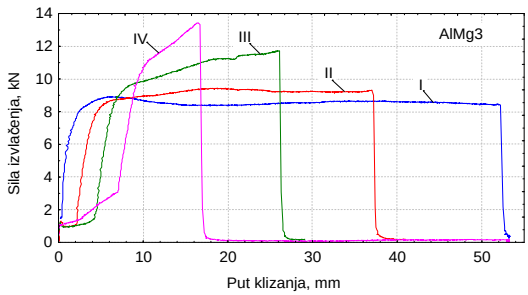

Figure 6. Change of drawing force

4. CONCLUSION

In the case of ironing one of the main characteristic of this processes is the fact that multiple repeated operations lead to a gradual increase in thickness of glued layer, which means that the sum of the individual resulting layers crosses over into the continuous layer.

As a result of predominance of the adhesion forces over resistance to plastic flow within glued layer plastic deformation of glued particles occurs followed by their tearing off and smearing.

When a sufficiently large thickness of the glued layers is achieved, as a result of the multiple repeated process of plastic deformation, process of separating glued particle from tool material begins. This separation is done by pealing (shear) or tearing off, and creates significant damage to the surface layers of tool, and therefore increases the surface roughness of the work piece. Such processes are characteristic of ironing sheet metal made of aluminum alloys, where no adequate lubricant is applied.

Acknowledgement

The part of this research is supported by Ministry of Education and Science, Republic of Serbia, Grant TR32036 and TR34002

REFERENCES

[1] Леванов А.Н, Колмогоров В.Л. и др.: *Контактное трение в процессах обработки металлов давлением*, Металлургия, 1976.

[2] Gierzynska M.: *Tarcie zużycie i smarowanie w obrobce plastycznej metali*, WNT, Warszawa, 1983.

[3] Adamović D.: *Ponašanje materijala u kontaktu pri procesima hladnog plastičnog oblikovanja sa visokim radnim pritiscima*, Doktorska disertacija, Mašinski fakultet u Kragujevcu, Kragujevac, 2002.

[4] Kawai N., Nakamura T., Seko S.: *The welding mechanism in drawing of aluminum sheet*, Journal of Engineering for Industry, Vol. 102, No. 8, pp. 229-238, 1980.

[5] Kawai N.: *Laboratory simulation for galling in metal forming, metal transfer and galling in metallic systems*, Proc. Conf. Orlando, Florida, Metal. Soc. AIME, pp.63-86, 1987.

Serbian Tribology Society

SERBIATRIB '13

13th International Conference on Tribology

Faculty of Engineering in Kragujevac

Kragujevac, Serbia, 15 – 17 May 2013

OPTIMAL DESIGN OF A CAMMECHANISM WITH TRANSLATING FLAT-FACE FOLLOWER USING GENETIC ALGORITHM

I. Tsiafis[1], S. Mitsi[1], K.D. Bouzakis[1], A. Papadimitriou[1]

[1]Aristotle University of Thessaloniki, Department of Mechanical Engineering, Greece,
tsiafis@eng.auth.gr, mitsi@eng.auth.gr,bouzakis@eng.auth.gr, thanpap22@gmail.com

Abstract: *The optimum design of a cam mechanism is a time consuming task, due to the numerous alternatives considerations. In the present work, the problem of design parameters optimization of a cam mechanism with translating flat-face follower is investigated from a multi-objective point of view. The design parameters, just like the cam base circle radius, the follower face width and the follower offset can be determined considering as optimization criteria the minimization of the cam size, of the input torque and of the contact stress. During the optimization procedure, a number of constraints regarding the pressure angle, the contact stress, etcare taken into account. The optimization approach, based on genetic algorithm, is applied to find the optimal solutions with respect to the afore-mentioned objective function and to ensure the kinematic requirements. Finally, the dynamic behaviour of the designed cam mechanism is investigated considering the frictional forces.*

Keywords: *Cam mechanism, genetic algorithms, contact stress, optimization.*

1. INTRODUCTION

The optimal design of cam mechanism is handled in many publications [1-5], where various constraints and methods are considered. Anon-linear programming technique with constraints, known as SUMT algorithm is used in [3]for optimum synthesis of a disk cam mechanism with swinging roller follower.In [4] the design parameters are determined by the minimization of the maximum compressive stress at the contact area of a cam-disk mechanism with translating roller follower, where the cam profile is described with the aid of cubic spline functions. Tsiafis et al. present in [5] a multi-objective procedure based on genetic algorithms to optimize the design parameters of a disk-cam mechanism with a roller follower.

In the present paper the problem of the design parameters optimization of a cam mechanism with a reciprocating flat-face follower is investigated, using multi-objective optimization with genetic algorithm. The design parameters for this type of mechanism are the radius of the cam base circle, the follower face width and the follower offset. The optimization is achieved by the development of programs using the high level computing language MATLAB with the GA (genetic algorithm) toolbox application. Furthermore, the dynamical analysis of the designed mechanism considering friction is investigated.

2. MATHEMATICAL FORMULATION

A cam mechanism with a translating flat-face follower is shown in figure 1. The cam is assumed to have constant angular velocity. The profile of the cam can be determined considering the kinematical and dynamical requirements of the mechanism.

The design parameters under optimization are the cam base circle R_b, the width follower face L and the follower offset e as shown in figure 1.

The optimization of the design parameters of the cam mechanism can be achieved by the minimisation of the cam size, of the torque required to drive the cam and the contact stress between the cam and the follower.

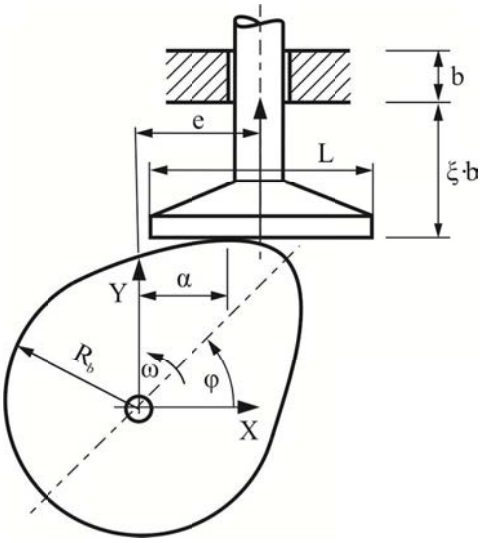

Figure 1. Cam mechanism with translating flat-face follower.

Therefore, it could be formulated as an optimization problem, where the objective function (F) takes into account the cam size (F_1), the input torque (F_2) and the maximum contact stress (F_3):

$$F = \alpha \cdot F_1 + \beta \cdot F_2 + \gamma \cdot F_3 \quad (1)$$

With

$$F_1 = R_b + L \quad (2)$$

$$F_2 = T = \frac{(P \cdot v)}{\omega} \quad (3)$$

$$F_2 = \sigma_{max} = \left[\frac{P'}{\rho \left(\frac{1-\mu_1^2}{E_1} + \frac{1-\mu_2^2}{E_2} \right)} \right]^{1/2} \quad (4)$$

where T is the input torque, P is the total normal load on the cam, v is the follower velocity, ω is the camshaft angular velocity, σ_{max} is the maximum contact stress between the follower and the cam, P' is the normal load per unit width of the contacting members, ρ is the radii of curvature of the cam, μ_1 and μ_2 are Poisson's ratio for the cam and the follower respectively and E_1, E_2 are the module of elasticity of the cam and the follower respectively. The weighting factors α, β and γ are used in order to scale the contribution of the corresponding terms in the objective function value. The minimization of the objective function determines the optimum values of the unknown parameters. During the optimization procedure the following functional constraints are imposed:

a) The maximum value of the pressure angle must be smaller than the maximum permitted: $\delta_{max} < \delta_{per}$.

The pressure angle can be calculated by [1]:

$$\delta = atan\left(\frac{v - e}{s + \sqrt{R_b^2 - e^2}} \right) \quad (5)$$

where s is the follower displacement.

b) The maximum value of the contact stress must be smaller than the material permissible strength: $\sigma_{max} < \sigma_{per}$.

c) The offset e must satisfy the constraints: $0 < e < L/2$ and $e < s$.

d) In order to avoid the follower jamming the eccentricity a must fulfil the conditions[1]:

$$a < \frac{b}{2\mu} + \frac{b \cdot \mu_0 (1 + 2\xi)}{2} \quad (6)$$

and $a < L/2$, where the dimensions a, b and the parameter ξ are explained in figure 1 and μ is the coefficient of friction between the follower stem and its guide.

The distance a is calculated with the following equation:

$$a = \left(r^2 - \left(R_b + s \right)^2 \right)^{1/2} \quad (7)$$

with $r = \left(x^2 + y^2 \right)^{1/2}$, where x and y are the cam profile coordinates.

3. PROPOSED ALGORITHM

In the present paper a multi-objective genetic algorithm (GA) method in MATLAB programming environment is used to find the optimal solution.

The input data are the cam mechanism type, the kinematic and functional requirements, the variables bounds and the algorithm parameters. In these parameters are included the initial parameters of the GA such as the population size, the crossover rate, the mutation rate, etc. and the number of the GA loops. Using the equation (1) the fitness function is defined, which is used in all steps of the algorithm.

During the genetic algorithm, starting populations are randomly generated to set variables values, which are used to calculate the fitness function value. Genetic algorithm [6] uses selection, elitism, crossover and mutation procedures to create new generations. The new generations converges towards a minimum that is not necessarily the global one. After some repetitions when the maximum generations' number is achieved, the variables values corresponding to the minimum fitness function value are selected as the optimum variables values of the genetic algorithm.

An important issue in genetic algorithms is the treatment of constraints. For each solution of the population, the objective fitness values are calculated. Furthermore, every solution is checked for constraints violation.

4. NUMERICAL APPLICATION

The introduced methodology is applied to find the design parameters of a cam mechanism with translating flat-face follower where the follower offset is set equal to zero (e=0).

Figure 2 shows the kinematic requirements per transient region of the indicated in this figure follower displacement diagram.

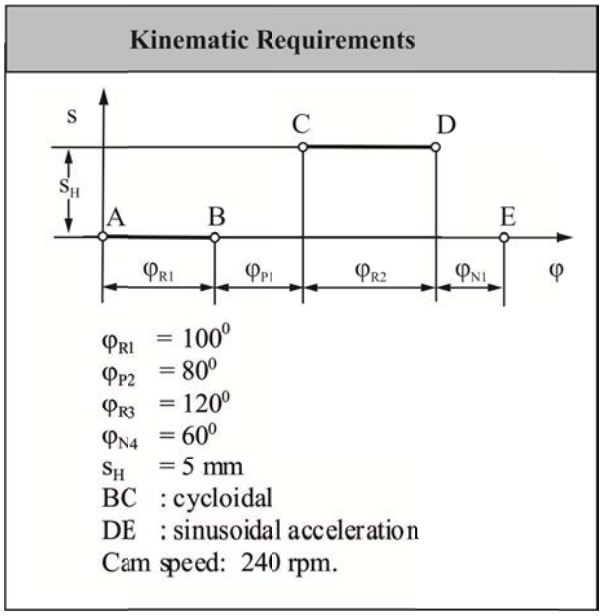

Figure 2. Kinematic requirements.

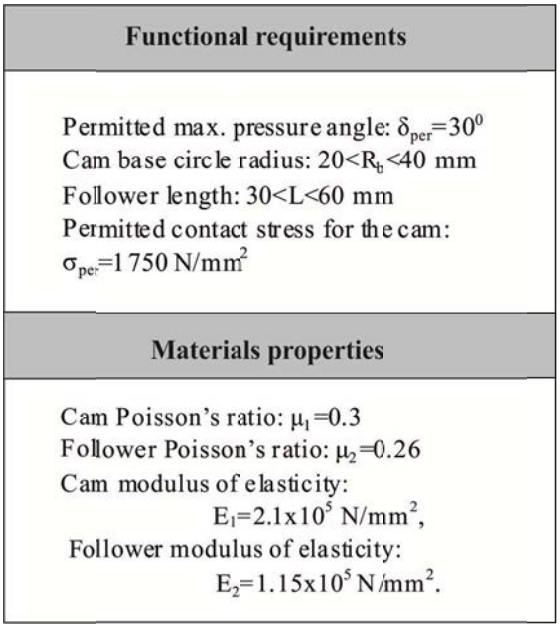

Figure 3. Materials properties and functional requirements.

The functional requirements and the material properties used in this investigation are inserted in Figure 3.

The parameters involved in all tests, mainly in GA procedure, are the same and selected as optimums through many applied tests: population of individuals=20, cross probability=80%, elite count=2 and the maximum number of generations is 100.

Considering kinematic requirements the displacement, velocity and acceleration of the follower are determined (Figure 4).

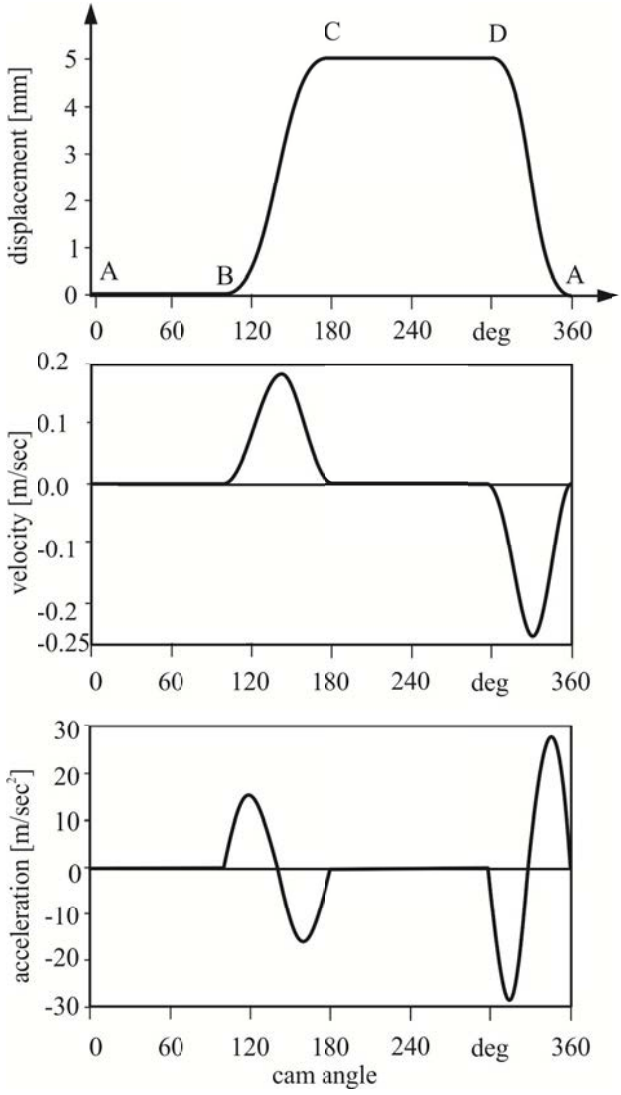

Figure 4. The follower motion diagrams.

In general the weighting factors α, β and γ of the fitness function (1) are selected considering the importance of the objectives that must be achieved by the mechanism. A high value of the weighting factor α increases the importance of first part of the objective function (F_1) that is to obtain a small cam size. After several tests the following weighting factors are chosen: α=0.1, β=0.1 and γ=0.8. Running the MATLAB codes with above mentioned parameters, the following design parameters are obtained: R_b=32.67 mm and L=53.21 mm. For constructed

mechanism these parameters are finally set: R_b=35 mm and L=50 mm.

The cam profile is shown in Figure 5. The 3D model of the designed cam mechanism is illustrated in Figure 6.

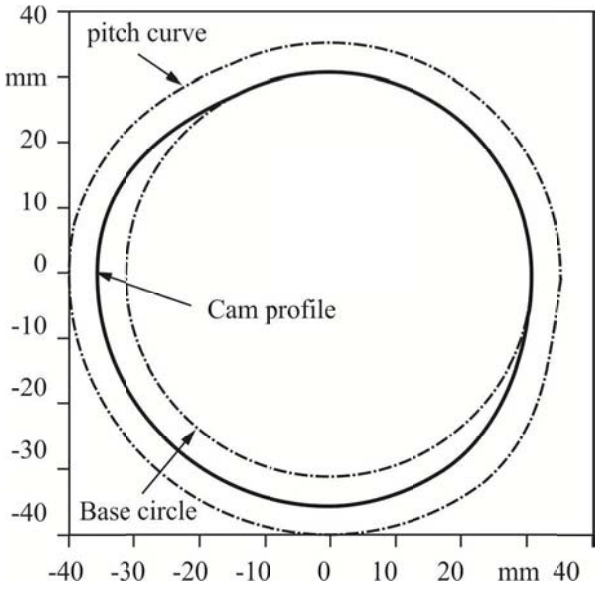

Figure 5. Cam profile.

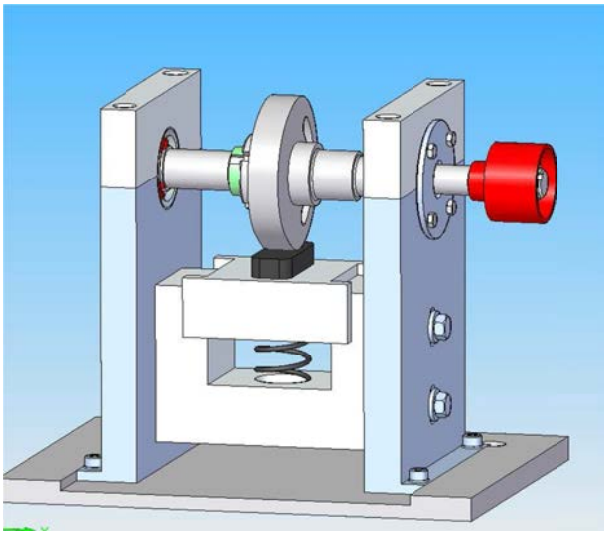

Figure 6: 3D model of the cam mechanism.

5. FORCE ANALYSIS OF CAM MECHANISM CONSIDERING FRICTION FORCES

In this section the dynamic force analysis of the designed mechanism considering the friction force between follower and its guide and the friction force between cam and flat face follower is investigated.

The force transmission of a radial cam with a reciprocating flat-faced follower is shown in figure 7, where P is the external load on the follower, μ is the coefficient of friction between the follower stem and its guide, μ_o the coefficient of friction between the cam and the flat face follower and d is the guide diameter.

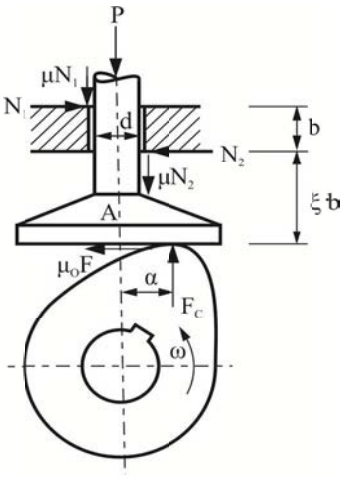

Figure 7: Force transmission of cam mechanism with translating flat-face follower.

From the equilibrium equations of horizontal and vertical forces and moments about the point A and assuming that difference the between $\mu\frac{d}{2}N_1$ and $\mu\frac{d}{2}N_2$ is negligible, the forces F_c, N_1 and N_2 are determined [1]:

$$F_C = \frac{bP}{\Gamma} \tag{8}$$

$$N_1 = \frac{\left(a-\mu_0\xi b\right)P}{\Gamma} \tag{9}$$

$$N_2 = \frac{\left[a-\mu_0 b\left(1+\xi\right)\right]P}{\Gamma} \tag{10}$$

with

$$\Gamma = b-2a\mu+\mu\mu_0 b\left(1+2\xi\right)$$

and

$$P = m\ddot{s}+c\dot{s}+k\left(s+s_0\right)+F_b$$

where m is the follower mass, s, $\dot{s}$ and $\ddot{s}$ are the displacement, velocity and acceleration of the follower respectively, c is the damping coefficient, k is the spring constant, s_0 is the initial compression of the spring and F_b is the follower weight.

Furthermore, the friction forces are written as:

$$Q_0 = \mu_0 F \tag{11}$$

$$Q_1 = \mu N_1 \tag{12}$$

$$Q_2 = \mu N_2 \tag{13}$$

and the cam shaft torque due to the friction is given by:

$$T_f = Q_0\left(R_b+s\right)+Q_1\frac{d}{2}-Q_2\frac{d}{2} \tag{14}$$

Figure 8. Constructed cam mechanism.

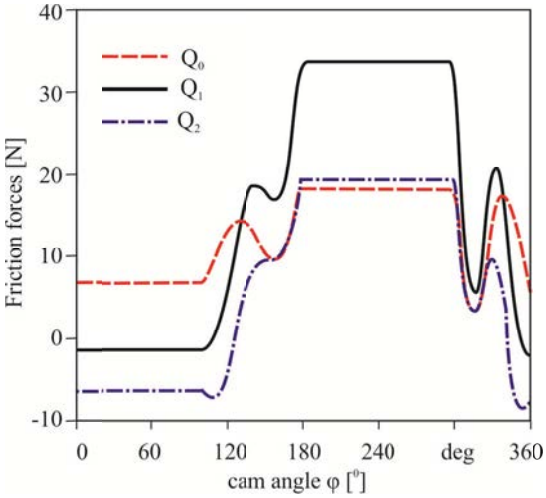

Figure 9. Friction forces of cam mechanism with translating flat-face follower

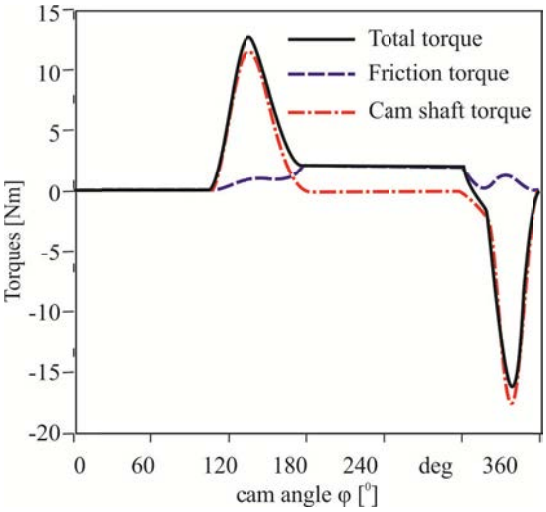

Figure 10. Input torque with and without friction.

In the designed and constructed mechanism (Figure 8) the data used in dynamic analysis are: μ=0.78, μ_0=0.15, m=1 kg, k=3004 N/m, s_0=13 mm, d= 50 mm and b=50 mm.

The damping coefficient is $c = 2\zeta \frac{\sqrt{1000\ k\ m}}{1000}$ with ζ=0.1. The spring constant k is chosen considering the spring force greater than inertia force corresponding to maximum deceleration, in order to avoid the jump phenomenon.

The parameter ξ is determined with the relation: ξ= (15-s)/b.

The diagram of friction forces versus cam angle is illustrated in Figure 9.

In Figure 10 is inserted the diagram of the input torque with and without friction.

6. CONCLUSION

In this paper the optimization of the design parameters of a cam mechanism with a flat-faced follower is approached. For this task the multi-objective optimization with genetic algorithm is applied using the high level programming language of MATLAB. The optimization satisfies constraints which are made in order to operate a cam mechanism properly. This procedure is automatic, gives results fast and it appears to be reliable. The final results provide useful information for a cam mechanism synthesis and can be used as a basis of final preference depending on the objectives that have to be succeeded.

Subsequently, after the cam mechanism synthesis, the applied friction forces are calculated. The most important conclusion is the fact that the friction forces are analogous with the action of the follower movement. This means that in the areas of dwell the friction forces are steady, whereas in the areas of rise or return the friction forces alter in an almost similar way.

REFERENCES

[1] Chen Y. F., *Mechanics and Design of Cam Mechanisms*,Pergamon Press, USA, 1982.

[2] Norton R., *Cam design and manufacturing handbook*, Industrial Press, Inc., New York, 2002

[3] Bouzakis K. D., Mitsi S., Tsiafis I., *Computer aided optimum design and NC milling of planar cam mechanisms*, International Journal of Machine Tools and Manufacture,Vol. 37, No 8, pp 1131-1142, 1997.

[4] Mitsi, S., Bouzakis, K.-D., Tsiafis, J., Mansour, G.,*Optimal synthesis of cam mechanism using cubic spline interpolation for cam NC milling*. Journal of the Balkan Tribological Association, Vol. 7, No 4, 2001, pp. 225-233.

[5] Tsiafis, I., Paraskevopoulou, R., Bouzakis, K.-D.,*Selection of optimal design parameters for a cam mechanism using multi-objective genetic algorithm*, Annals of the "Constantin Brancusi" University of TarguJiu, Engineering series, nr. 2, Romania, 2009, pp. 57- 66.

[6] Coley D., *An introduction to genetic algorithms for scientists and engineers*, World Scientific Press, 1999.

Serbian Tribology Society

SERBIATRIB '13

13th International Conference on Tribology

Faculty of Engineering in Kragujevac

Kragujevac, Serbia, 15 – 17 May 2013

INFLUENCE OF VARIOUS TYPES OF ROCK AGGREGATES ON SELECTION OF THE WORKING PARTS MATERIAL IN CIVIL ENGINEERING

V. Lazić[1], M. Mutavdžić[2], R. Nikolić[1, 3], S. Aleksandrović[1], D. Milosavljević[1], B. Krstić[1], R. Čukić[1]

[1]University of Kragujevac, Faculty of Engineering, Sestre Janjić 6, 34000 Kragujevac, Serbia

[2]Road Building Company Kragujevac, Tanaska Rajića 16, 34000 Kragujevac, Serbia

[3]University of Žilina, Faculty of Civil Engineering, Univerzitna 1, 010 26 Žilina, Slovakia

Abstract: *In this paper are presented results of theoretical and experimental investigations and mutual comparison of various types of rock aggregates from the aspect of working parts wear of different machines for preparation and deposition of the rock materials on roads. Here are considered only the most important types of building stones: limestone, dolomite marble, calcite-dolomite marble and andesite, which are exploited at four sites in Republic of Serbia. Those aggregates are convenient for manufacturing of certain layers of the driveway constructions on roads, streets, airports, as the base layer on railways and for preparation of various types of asphalt and concrete. In selection of rocks for depositing on roads, it is necessary to know both their general and specific properties. It is necessary to conduct the mineralogical-petrographic and physical-mechanical investigations and, if needed, certain special ones, as well.*

The civil engineering machines for manufacturing and building-in materials in various structural objects are exposed to different types of high loads, what is especially true for some of their working parts, which come into direct contact with the rock materials. The working life of those machines is directly dependent on the type of the building material as well as on maintenance. In exploitation, the construction mechanization is subjected to various types of corrosion and wear, and some of its parts are occasionally subjected to impact loads, as well. Certain parts are also frequently in contact with various types of stones, sands, soil, asphalt, concrete and occasionally with water.

Key words: *rock materials, aggregates, minerals, working parts, civil engineering mechanization.*

1. INTRODUCTION

Civil engineering machines for manufacturing and building in materials during construction of various building objects are subjected to different types of loads, especially some of their working elements, which are in direct contact with rock materials. Working life of construction machines' parts is directly dependent on the kind of the rock materials, properties of construction mechanization working parts and exploitation and maintenance conditions. Those machines are, during operation, exposed to different types of wear and corrosion, some working part are even exposed to occasional impact loads. Some parts of construction machines are frequently in contact with various kinds of rocks, sands, soil, asphalt, concrete, sometimes are even exposed to influence of water.

Knowing physical-mechanical properties of the rock minerals are of a special importance, both for their exploitation and for their processing and building in. Since the matter of speaking are the complex tribo-mechanical processes, in which take part different elements of construction mechanization, rocks and third objects, it is especially important to properly select material of the construction machines' working parts, as well as the technology for reparation of the damaged and worn parts of those machines.

Based on investigations of the construction rocks from four available sites, the useful data were obtained both for design and reparation of the working parts of machines for minerals' exploitation, their processing and building into roads.

2. THE MOST IMPORTANT TYPES AND PROPERTIES OF ROCK MATERIALS

Rocks mainly consist of seven groups of minerals: silicates, carbonates, oxides, sulphates,

sulphides, chlorides and hydroxides. To get a more complete picture about number of different minerals that rocks are made of, it is necessary to emphasize that only the silicate group contains about 800 minerals, categorized into various subgroups. Mineral masses in the Earth's crust can be found in forms of compounds – as solid rocks or in the unbound – dispersed form. Thus the rocks are being divided, according to strength, into weak, solid and exceptionally solid rocks, since minerals can be in the crystal, crystallite or amorphous form. Rock properties can be significantly changed due to action of water, frost or heat; thus it is highly important to know the laws of those changes. The most important properties of rocks are petrographic, physical, mechanical and technological [1-8]. All the rocks that are contained in the Earth's crust can be classified in three major groups: *magmatic*, *sediment* and *metamorphic* rocks.

In this paper are investigated properties of stones from the four near-by sites: limestone, dolomite marble, calcite-dolomite marble and andesite. The most exploited (over 70 %) is the limestone from the "Vučjak" site, thus this particular stone was taken as representative for rocks' properties experimental investigations.

3. DETERMINATION OF PETROGRAPHIC PROPERTIES

The most important petrographic properties of rocks are: *mineral composition*, *structure* and *texture*. *The structure of rocks* consists of mineral crystallite grains, whose shape and strength depend on way of coalescence during the rock formation. *The texture of rocks* consists of minerals spatial distribution and occupancy. Petrographic properties of rocks were tested according to standard SRPS.B.B8.002:1989.

The limestone site "Vučjak" mainly consists of organogenic-detritic[1] limestone. The rock's texture is massive. i.e., the mineral grains are not regularly distributed within the substrate. In Figure 1 are presented macroscopic and microscopic appearances of this rock [6].

The dolomite marble site "Samar" mainly consists of the dolomite marble. The structure of this type of rock is granoblastic. Texture is massive and noncompact. In Figure 2 are presented macroscopic and microscopic appearances of this rock [6].

The calcite-dolomite marble site "Gradac" mainly consists of this type of rocks. The rock's texture is homogeneous and compact. In Figure 3 are presented macroscopic and microscopic appearances of this rock [6].

The andesite site "Šumnik" mainly consists of this type of rock. The rock's texture is massive. In Figure 4 are presented macroscopic and microscopic appearances of this rock [6].

4. EXPERIMENTAL DETERMINATION OF SOME ROCKS PHYSICAL PROPERTIES

For construction of roads the most frequently experimentally tested are the following rocks' physical properties: specific mass, bulk mass, porosity, water absorption and compactness, since those properties directly influence changes of mechanical and technological properties of rocks and their aggregates.

4.1. Determination of specific mass (density) of rocks

In Table 1 are presented average values of specific mass of various rocks' samples [6].

4.2. Determination of rocks' porosity

Water absorption is defined by ratio of water mass and mass of solid mineral substance; for various types of rocks it ranges from 1.5 to 4.4% [6].

4.3. Determination of rock compaction possibilities

Determination of the rock bulk mass can serve as criterion for estimates of possibility of their compacting in the infilling state, what is of a great importance in construction of building objects. Complete investigation of compaction possibility of rocks requires: determination of granulometric composition, compacting possibility by the Proctor test and the Californian capacity index (cf. [1], [3-4], [7], [9 - SRPS B.B8.030: 1986]).

4.4. Influence of water, low and elevated temperatures on rock content changes

Water, low and high temperatures significantly influence some of the rocks' properties. In contact with water at low temperatures (< 0° C) and high temperatures (>100° C), the minor changes in rocks are observed, while at temperatures lower than - 25° C and higher than 500° C, the significant changes occur.

Low temperatures (frost) significantly affect rock properties, especially if the temperatures are variable. Alternating heating and cooling of rocks

[1] Detritus (latin): aggregate of small particles of crushed rocks

causes big changes of their properties. All the dry rocks endure well the low temperatures actions, while the wet rocks and rocks completely saturated with water have significantly lower resistance, since their destruction occurs due to freezing of water in cavities.

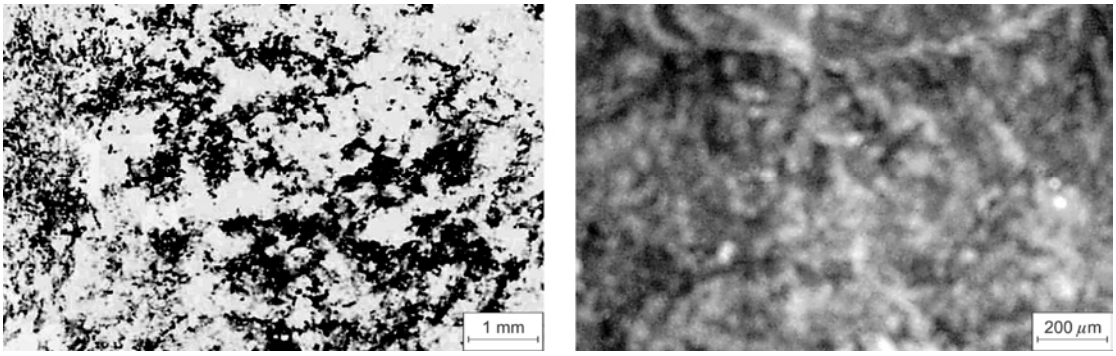

a) b)

Figure 1. Appearance of limestone structure: a) macroscopic appearance, b) microscopic appearance.

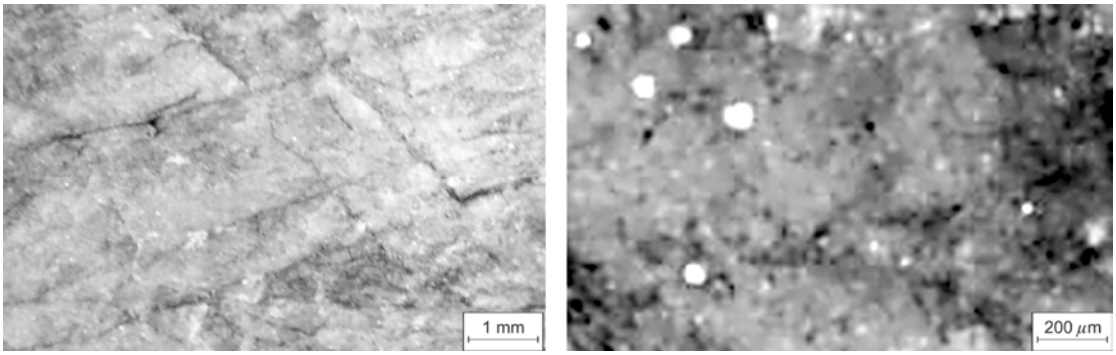

a) b)

Figure 2. Appearance of dolomite marble structure: a) macroscopic appearance, b) microscopic appearance.

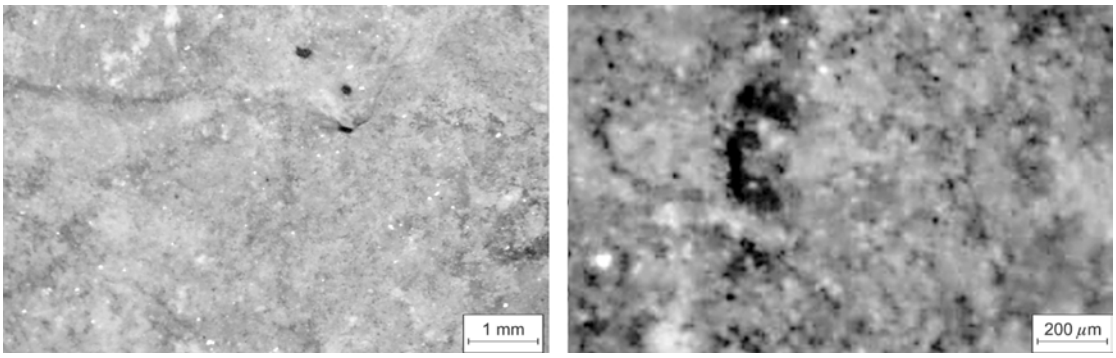

a) b)

Figure 3. Appearance of calcite-dolomite marble structure: a) macroscopic appearance, b) microscopic appearance.

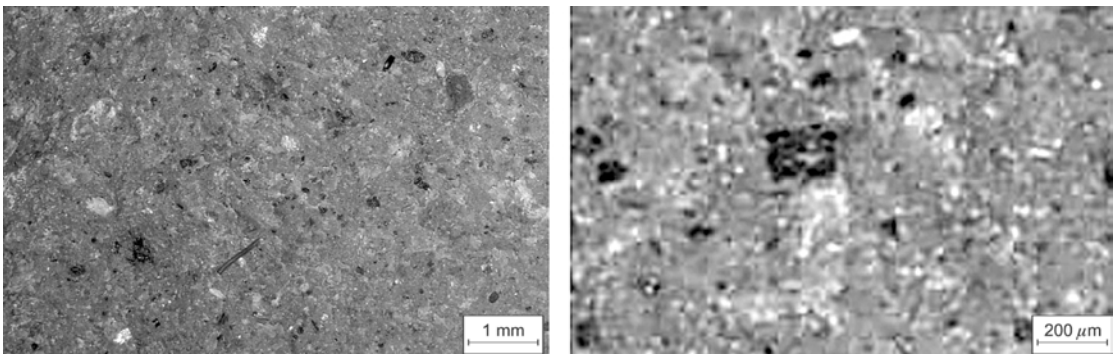

a) b)

Figure 4. Appearance of andesite rock structure: a) macroscopic appearance, b) microscopic appearance.

Table 1. Bulk masses of tested rock samples.

Tested rock property	Limestone - Vučjak	Dolomite marble - Samar	Calcite-dolomite marble - Gradac	Andesite - Šumnik
Bulk mass with pores, $\gamma_v = m_s/V$	2690	2780	2820	2630
Specific mass without pores and voids, $\rho_s = m_s/V_s$	2730	2870	2850	2750
Bulk mass coefficient, $i = \gamma_v/\rho_s$	0.985	0.969	0.989	0.956

All types of rocks well endure action of elevated temperatures up to 500° C. Further temperature increase leads to visible changes: loss of characteristic ringing sound at impact, significant decrease of strength and appearance of crumbling or total destruction if poured over with cold water. At high temperatures (over 850° C) more durable are rocks made of minerals whose heat conductivity is significantly different. More durable are firm and fine-grained rocks than the porous and coarse ones. At that temperature granites crack irregularly, while the sand rocks usually crack parallel to stratification. Limestones and marbles possess good strength up to the calcification temperature (~ 800° C), when they transform into quicklime (CaO). At high temperatures quartzites, quartz sandstones with silicon binder, clays, serpentinite, serpentinite and chromite are stable. Fireproof bricks are made of magnesite and chromite.

5. EXPERIMENTAL DETERMINATION OF MECHANICAL ROCK PROPERTIES

Of all the mechanical properties, the most frequently investigated are compressive strength, hardness, elasticity, toughness and wear resistance. The rocks' mechanical properties tests are defined by corresponding standards [9- SRPS B.B8.-012:1987 do SRPS B.B8.018:1957].

5.1. Determination of rocks hardness

The basic mineral that all the limestones are made of is calcite, thus their hardness is usually about 650 HB. Hardness of calcite-dolomite mineral depends on percentage shares of calcite and dolomite; it is usually within limits 650-850 HB, while the dolomite marble hardness is usually about 850-1150 HB. Hardness of various types of andesites is within the wide range and it depends on their type. The biotitic andesite has hardness similar to limestone, 550-700 HB, ensitite andesite 750 HB, amphibolic andesite 1000-1500 HB, while content of quartz SiO_2 (55-65%) in andesite can increase hardness up to 1800 HB. Hardness of rocks has strong influence on their processing and application, but also on damage of the working parts of the construction machinery during processing and building-in of the rock materials. This is why one must use metals that possess high hardness, with carbides in the metal substrate, or relatively soft steels, which can, under pressure or impact load, provide martensitic transformation of austenite – like the Hadfield steels [10].

5.2. Determination of rocks impact toughness

In Table 2 are presented values of impact hardness of rock materials from the four studied sites. Testing was conducted in three mutually perpendicular directions (I-I is parallel to rocks' stratification direction; II-II is perpendicular to I-I and lies in stratification plane and III-III is perpendicular to direction of the rock's stratification). This is important to emphasize, since rocks are highly anisotropic due to stratification and schistosity-inhomogeneity of rocks.

Based on these results one can conclude that those rocks have relatively low impact toughness; according to the fracture site appearance the similar conclusion can be drawn as well, since the fracture surface is rough and with sharp edges.

5.3. Determination of rocks elasticity

This property is related to solid bound rocks and it depends on type and hardness of rock minerals, structure and texture and minerals freshness, moisture, strength and direction applying of load, etc. Fine-grained rocks have higher values of elasticity modulus, than the coarse rocks of the same composition.

For the stratified and inhomogeneous rocks the elasticity modulus is higher in the direction perpendicular to than parallel to stratification and schistosity. By testing the limestone samples the following values were obtained: average Poisson's ratio $\nu = 0.36$, elasticity modulus $E = 50247$ *MPa*, shear modulus $G = 18608$ *MPa* and bulk modulus $K = 59714$ *MPa*.

Table 2. Impact toughness of some types of rocks.

Impact toughness, *MPa*	Limestone - Vučjak	Dolomite marble - Samar	Calcite-dolomite marble - Gradac	Andesite - Šumnik
Direction I-I	22.40	17.00	27.20	13.40
Direction II-II	24.20	20.60	26.10	17.20
Direction III-III	28.80	24.60	28.30	22.40
Average value	25.13	20.73	27.20	17.67

5.4. Determination of rocks' strength

Experimental determination of rocks' strength is usually done with at least three samples, most frequently with 5 samples, cut out from the rock in three mutually perpendicular directions; samples are of prismatic form; the whole is defined by adequate standards [9- srps b.b8.012:1987 to srps b.b8.018:195].

Compression strength. Determination of the compression strength was done on dry and water saturated cubic samples, cube edge is 40 ± 1 *mm*, with ground and plan parallel surfaces. The average value of the compression strength for the limestone from site Vučjak (15 samples, 5 for each direction) was R_{cm} = 131 *MPa*. Tests of samples from other sites were done in the same way. For obtaining the compression strength after 25 cycles of freezing 3 cubic samples were used; cube edge was 1000 ± 1 *mm* (Table 3).

Tensile strength. Determination of the tensile strength is conducted less frequently though it is also an important property. The tests were done on samples of the same shape and dimensions as for the compression strength; but only dry samples were tested. The average value of the tensile strength of the tested limestone samples was R_m = 6.00 *MPa*, while in large number of references reported value is about 1.5 *MPa* for the porous limestones and 6.4 *MPa* for the firm limestones. Tests of samples from other types of rocks were done in the same way and results are shown in table 4.

Bending strength. Bending tests were done on one dry sample per each type of rocks, for the direction which is perpendicular to stratification and schistosity propagation, in order to obtain the best possible results, [6].

Shear strength. Determination of shear strength was done only on limestone from the Vučjak site by the direct shear method, by the Casagrande testing device, [6].

5.5. Determination of rocks' wear resistance

Experimental investigation of the rocks' wear resistance is defined by corresponding methods: the Bome method, the Los Angeles and the Deval procedure, [9]. By the Bome method the wear resistance is checked on the cubic samples, while the other two methods are more frequently applied for the rock aggregates; results are presented in [6].

Table 3. Compression strength of some rock materials.

Rocks' type and origin	Compression strength, R_{cm}, *MPa*			Softening coefficient, K_{soft}
	Dry samples	Water saturated samples	Samples after 25 freezing cycles	
Limestone - Vučjak	131	123	117	0.94
Dolomite marble - Samar	150	136	130	0.91
Calcite dolomite marble - Gradac	161	140	138	0.87
Andesite - Šumnik	195	186	184	0.95

Table 4. Tensile strength of some rock materials.

Rocks' type and origin	Tensile strength, R_m, *MPa*			Average values
	Direction I-I	Direction II-II	Direction III-III	
Limestone - Vučjak	5.97	6.14	5.89	6.00
Dolomite marble - Samar	5.26	5.42	3.72	4.80
Calcite dolomite marble - Gradac	5.64	5.36	4.03	5.00
Andesite - Šumnik	9.48	9.82	8.90	9.40

6. SELECTION OF MATERIALS FOR THE CONSTRUCTION MECHANIZATION WORKING PARTS

Large number of parts of the construction mechanization (hoop's teeth, rippers, mixers' blades, knives for lifting and removing asphalt, knives-blades for channels digging, crushers impact beams etc.) are, during operation, in indirect or direct contact with rock materials, and, depending on the role and function of the part, they are exposed to various types of wear [10-12]. Mainly one deals with abrasive wear or a combination of several types of wear.

The main factors in selection of materials exposed to wear are their chemical composition and structure. Those materials are mainly steels and (white) cast irons. The most resistant to wear are materials of high hardness. Though that characteristic can not be the only criterion, it is mainly used for quality estimates of materials exposed to wear.

Depending on the degree of wear, machines' working parts could be replaced by the new ones, or could be subjected to reparatory hard-facing. When selecting the reparation technology, mechanism of abrasive wear is being analyzed, both theoretically and experimentally, taking into account hardness and microstructure of parts, and related wear resistance in laboratory and real operating conditions. That represents the basis for selection of the optimal procedure, technology and filler metal for working surfaces regeneration.

Investigations, until now conducted by these authors, have shown that the working life of the properly regenerated parts exceeds several times the new parts working life. Besides that, the machine down-time, assortment and quantity of the necessary spare parts are reduced. All these point to complexity of materials selection for the working parts of construction mechanization, as well as to importance of knowing the properties of the rock materials.

7. CONCLUSION

In this paper are presented investigation results of the rock materials physical and mechanical properties tests, for four types of rock materials most frequently applied in construction of driveways. The conclusion was reached that those materials are firm and homogeneous rocks, of medium to high hardness. It was determined that the compression strength values are on average 10-40 times higher than the shear, bending and tensile strengths, while the wear resistance is good in majority of studied rocks, being especially high for andesite.

Obtained results enable estimates of the individual rock material's quality and point to the complexity of the material selection for the working parts pf construction mechanization. Experimental results of rock materials properties and the complex working conditions of the tribo-system, can serve and must be taken into account in selection of the base metal and reparation technology of the damaged parts of the construction mechanization.

Acknowledgement

This research was partially financially supported through grants TR35024, TR35021, TR34002 and OI174004 of Ministry of Education and Science of Republic of Serbia.

REFERENCES

[1] M. Janjić: *Fundamentals of geology and engineering geology*, Part I, Faculty of Civil Engineering, Belgrade, 1964.

[2] M. Janjić: *Engineering geodynamics*, Faculty of Mining and geology, Belgrade, 1979.

[3] M. Janjić: *Engineering geology with geology fundamentals*, Scientific Book, Belgrade, 1982.

[4] M. Luković: *Engineering geology*, Scientific Book, Belgrade, 1950.

[5] N. Panjukov: *Engineering geology*, Civil Engineering Book, Belgrade, 1963.

[6] M. Mutavdžić: *Reparatory hard-facing of parts of machines and devices in construction mechanization*, MS thesis, Faculty of Mechanical Engineering, Kragujevac, 2007.

[7] R. Stojadinović: *Soil mechanics – I*, Faculty of Civil Engineering, Belgrade 1978.

[8] M. Muravljov: *Civil engineering materials*, Civil Engineering Book, Belgrade, 2002.

[9] Standards: JUS B.B8.001 to JUS B.B8.086.

[10] V. Lazić et al.: *The working life theoretical and experimental estimates for machine parts hard faced using austenite-manganese electrodes*, Materials end Technology, Vol. 46, No 5, pp. 547-554, 2012.

[11] M. Mutavdžić et al.: *Model investigations of the filler materials for regeneration of the damaged parts of the construction mechanization*, Tribology in Industry, Vol. 30, No. 3&4, pp. 3-9, 2008.

[12] V. Lazić et al.: *Selection of the most appropriate technology of reparatory hard facing of working parts on universal construction machinery*, Tribology in Industry, Vol. 33, No. 1, pp. 18-27, 2011.

Serbian Tribology Society

SERBIATRIB '13

13th International Conference on Tribology

Faculty of Engineering in Kragujevac

Kragujevac, Serbia, 15 – 17 May 2013

TECHNO-ECONOMIC JUSTIFICATION FOR REPARATORY HARD-FACING OF MACHINE SYSTEMS' WORKING PARTS

V. Lazić[1], R. Čukić[1], S. Aleksandrović[1], D. Milosavljević[1], R. Nikolić[1, 2], B. Krstić[1], B. Nedeljković[3]

[1]University of Kragujevac, Faculty of Engineering, Sestre Janjić 6, 34000 Kragujevac, Serbia

[2]University of Žilina, Faculty of Civil Engineering, Univerzitna 1, 010 26 Žilina, Slovakia

[3]High technical school in Kragujevac, Kosovska 8, 34000 Kragujevac, Serbia

Abstract: *Research in the field of hard-facing of various parts of mechanical systems is being done for technical and techno-economic reasons. The reasons for introducing the new reparation technologies by hard-facing are numerous: three quarters of all the mechanical parts of engineering systems could be regenerated or manufactured by hard-facing; the working life of the repaired part reaches or even exceeds the working life of a new part, while the working life of the hard-faced manufactured part surpasses several times the working life of the new part manufactured by some other technology. Large number of damaged and, frequently even broken parts causes terminations of the working process. Thus, due to difficulties in procurement of new, mainly imported parts, the alternative solution must be applied and that is regeneration by hard-facing.*

It is shown that the a proper choice of the hard-facing technology is related to the complex procedure of checking the quality of the hard-faced layer, what indicates that the reparatory operations could be performed only in specialized regeneration workshops, which are furnished with adequate equipment and corresponding expert and skilled staff. The estimated net benefit for the analysed parts is exceptionally high, regardless of the fact that the additional external and internal effects have not been quantified. After the successful application of these new manufacturing hard-facing technologies it would be possible to create the knowledge base and apply it in maintaining the parts of civil engineering machinery, forging equipment and other similar mechanical parts.

Key words: *regeneration, wear, hard-facing, costs, techno-economic analysis.*

1. INTRODUCTION

The reasons for the introduction of technology for manufacturing and reparatory hard-facing are numerous: research indicates that three-quarters of all the mechanical parts can be regenerated and manufacturing hard-faced, service life of repaired part reaches or exceeds the service life of the new part, service life of new in production hard-faced part exceeds several times that of the new part, which was not hard faced, repair costs are reduced as well as the downtime due to purchasing a new part, which increases productivity, financing costs and cost of storage are also reduced [1- 4]. A large number of damaged, and often broken, parts cause termination of the process, and the difficulties in the procurement of new, mostly imported parts, must use an alternative such as hard-facing-regeneration. In addition, the maintenance of the technical system should take in consideration manufacturing of new parts by hard-facing, what is expected to extend their service life with respect to the new working parts.

To perform the modelling of hard-facing of working parts, i.e., to prescribe general regeneration procedures, it is necessary to perform previous studies on a number of models and real working parts made of various types of steel and cast iron. While the surfacing almost every time is a unique job, because it requires the technology customized to each working part, it is possible to establish general procedure for groups of similar parts and then to apply it [2,5-6].

2. SELECTION OF THE OPTIMAL HARD-FACING TECHNOLOGY

In examining the state of the damaged parts one should first determine: whether the wear occurred during the normal exploitation or it appeared due to some mechanical damage; what is the degree of the part's wear is crucial for the decision whether it is cost-effective and

safe to use it in furter exploitation (to apply regeneration or the part) or should it be rejected. The size of expected deformation and residual stresses are also important factors in making such a decision [7-8]. After determination of the chemical composition of the base metal and working conditions, it is possible to create the basic conditions for the design of technological processes. Based on those facts and previously conducted detailed techno-economic analysis, the method of regeneration should be chosen, taking into account the local possibilities of the company. The basic requirement is to obtain the required properties of the regenerated part and, ofcourse, the reliability of the part during the estimated working life.

To achieve the above requirements it is necessary to make the proper selection of filler material for hard-facing. In some cases of reparation of working parts it is necessary to apply two or more kinds of additional material to insert an intermediate layer, the so called buffer layer, between the layer and the substrate. This reduces the large differences in the chemical composition, structure and, consequently, the thermo-physical properties, of the substrate and the deposit. Next follows the selection of the regeneration process parameters, resulting from the properties of the base and filler metal, and form demands concerning the size and shape of regenerated parts. The final stage of planning, before the experimental surfacing, is the assessment of the necessity for implementation of special measures and the previous, current and subsequent heat treatment.

For verification of the proposed technologies, the comparative tests in laboratory and in working conditions have been performed, and, in some cases, comparative test of imported parts, which were not hard-faced and the new-hardfaced parts. Laboratory tests are related to the microstructure, hardness distribution and tribological tests and working tests of comparing the working life of the new and repaired parts installed in the same machine [2-3,9].

From the point of view of techno-economic analysis, reparation welding technology is a complex set of different types of mandatory procedures, which take into account: the conditions of work, damage identification, estimation of weldability, welding process, filler material, welding and hard-facing regimes, heat treatment applied, model and real tests. Having in mind the complexity of the process, it is necessary to determine the optimal technical-technological solutions to bring the reparation process to a stage when it is possible to make a final decision, wheter to buy a new part or to repaire it.

3. EXAMPLES OF IMPLEMENTED REPAIRS

Here is considered the justification for application of the production and reparation hard-facing and it is pointed to profitabilityof repairs on examples of damaged forging hammer, forging press frame and large gear of eccentric presses. The subject matter is the reparatory welding and surfacing of the damaged or cracked forging hammers, broken and cracked frames, forging presses and large gear eccentric presses [10-11]. To determine the optimal technology of hard-facing, it was necessary to carry out tests on model and real working parts. Test hard-facing and testing of models have served to establish the initial reparation technology, and to "transfer" thus approved technologies to the working parts, which are then further checked under actual working conditions.

This paper mainly deals with the techno-economic advantages of the hard-facing technology, while the complete procedures of determining the optimal technology for each particular part were presented in papers [2-3,5,9-11].

3.1. Regeneration equipment's for forging hammer and press frame

For regeneration of responsible parts with complex geometries and large masses, made of material sutible for tempering, a detailed analysis of the working parts is required as well as the precisely proposed reparation technology.

Hammers mallets and presses frames are exposed, during the long operation, to thermal fatigue due to cyclic temperature changes and to impact loads. Due to the high costs and often to impossibility of purchasing the new working parts, it is necessary to evaluate the possibility of their repairs. Harsh working conditions sometimes lead to a complete fracture of the part and endangering the workplace safety. Figure 1 shows fracture of a forging mallet, which has originated from fatigue crack propagation.

Mallet of forging's hammer, shown in Fig. 2, and frame forging press, shown in Fig. 3, are primarily subjected to impact compression loads, and, in partially to temperature gradient, that is thermal stresses caused by uneven temperature field [2,7-8]. After a long work of these parts, i.e., large number of repeated cycles on hammer mallet and on the press frame, visible cracks were observed, and on one portion of the frame and on a single occurred the complete fracture (Fig. 1 and 3).

Taking into account that these are parts of large dimensions and complex shapes, and that components are subjected to dynamic and thermal loads, they are dimensioned on the basis of the increased safety degrees; thus the special measures are required for the manufacturing and reparatory technologies, as well. Forging press frame is made
by casting in sand, from the medium carbon cast steel. On the other hand, pneumatic forging hammer mallet, as one of the most loaded mechanical parts, is made of low alloyed steel for tempering.

Figure 1. Appearance of fractured forging hammer mallet.

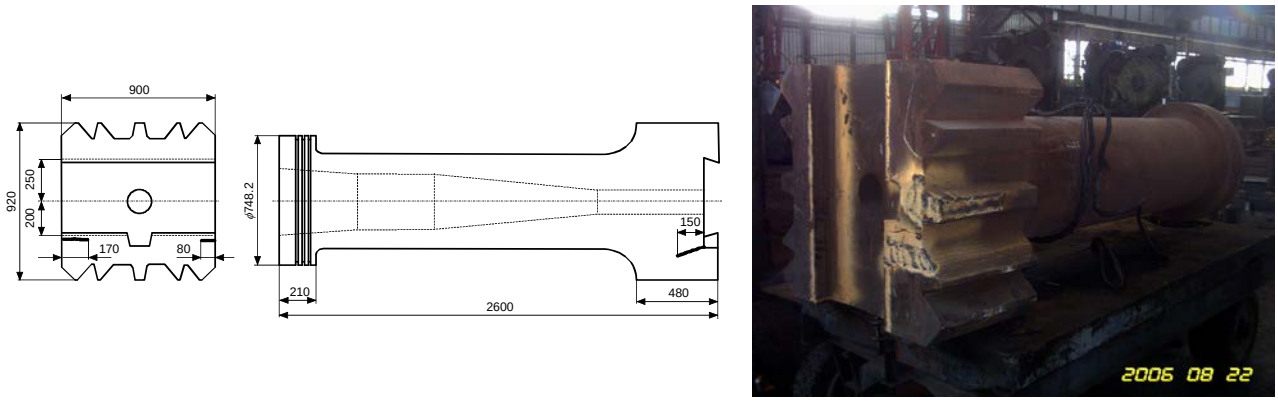

a) **b)**

Figure 2. Forging hammer mallet
a) Sketch of mallet with observed crack; b) Apperance of the regenerated mallet of mass of 6000 kg

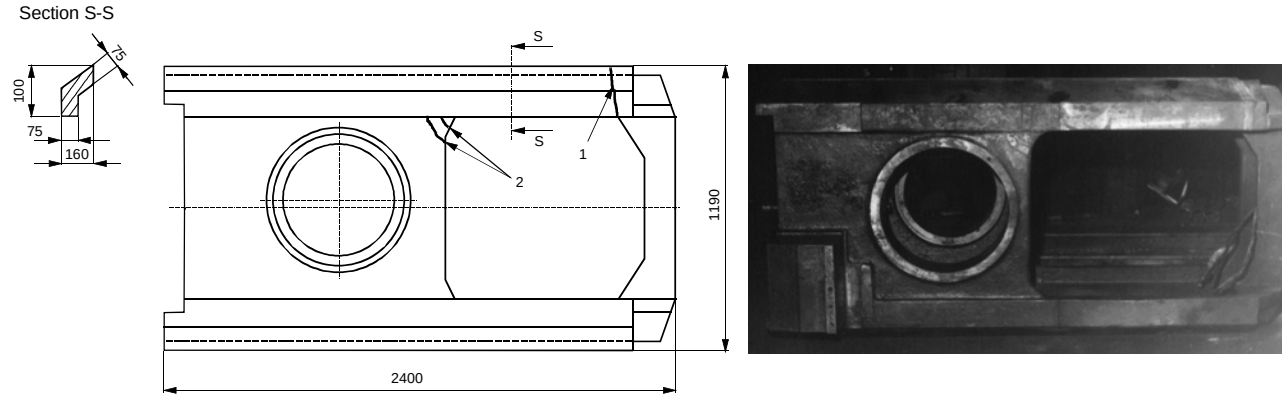

a) **b)**

Figure 3. Frame of vertical forging press.
a) sketch of the frame (1 – fracture site; 2 - observed cracks); b) regenerated, heat treated and machined part

The complete technology for regeneration of damaged forging hammers' mallets and presses' frames is shown in [6, 10-11]; here are presented only the techno-economic indicators for the mallets' regeneration.

The following data are relevant for comparison:

A. <u>The price of the new part is:</u> **<u>83987 €</u>**
(This price includes price of a new part - 67470 €, tax -12144 €, the customs 3373 € and the cost of shipping and transportation services - 1000 €);

B. <u>The total real costs of reparation of **4912 €** include</u>:

- Identification and damage detection:

3 days × 8 (nh*/day) × 10 (€/nh) = 240 €;

- Machining of damaged area:

10 days × 8 (nh/day) × 12 (€/nh) = 960 €;

- Selection of the optimal hard-facing technology:

8 days × 8 (nh/day) × 15 (€/nh) = 768 €;

- Model testing:

4 days × 8 (nh/day) × 12 (€/nh) = 384 €;

- Surfacing of real working parts:

20 days × 8 (nh/day) × 10 (€/nh) = 1600 €;

- The costs of machining operations of surfaced areas:

10 days × 8 (nh/day) × 12 (€/nh) = 960 €.

nh = norm-hour

Based on these data one can conclude that the total reparation costs are far lower than the costs of a new part (less than 6%). Therefore, the "buy" or "repaire" dilemma is apparently resolved without more detailed analysis of the positive effects that mallet regeneration allows.

3.2. Reparation of large gears - toothed hub of an eccentric press

The techno-economic analysis of reparatory welding and hard-facing of the damaged teeth of a coupling hub with mass of 500 *kg*, shown in Fig. 4, is performed after the repair has already been performed, because it is a unique part that could not be easily obtained. The coupling is exposed to harsh environmental conditions and is made of alloyed steel for tempering. Since it is a conditionally weldable steel, it was necessary to prescribe a particular reparation technology. It was established through previous model tests [5,10]. The analysis of obtained results leads to the optimal hard-facing technology which is then "transferred" to the real part.

Figure 4. Appearance a coupling hub

In economic "buy" or "repaire" analysis, an estimate of the more complete effects was not conducted, which should be performed by the *benefit-cost* (BC) analysis, or more precisely by using the *life-cycle-cost* (LCC) analysis, which would point to more precise and more clear advantages of application of this advanced technology [3]. A comparative analysis was performed after two and a half years of the hard-faced rack hub couplings operation.

As relevant for comparison the following data were taken:

A. Purchasing price of the new part: **26500 €**

(This price includes price of a new part, the cost of taxes, customs duties, freight forwarding services and transport).

B. The total real reparation costs of **3380 €** include:

- Identification and damage detection: 1 day × 8 (nh/day) × 10 (€/nh) = 80 €;
- Machining of damaged area:

2 days × 8 (nh/day) × 12 (€/nh) = 192 €;

- Selection of the optimal hard-facing technology:

1 day × 8 (nh/day) × 15 (€/nh) = 120 €;

- Model testing:

3 days × 8 (nh/day) × 12 (€/nh) = 288 €;

- Surfacing of real working parts:

10 days × 8 (nh/day) × 10 (€/nh) = 800 €;

- Costs of production services (processing hard-faced teeth and transport)

1900 €.

Based on these data one can conclude that the total cost of repairs is significantly lower than the cost of purchasing a new part (less than 13%).

4. CONCLUSION

Through the proper selection and application of the reparatory and manufacturing hard-facing technologies, it is possible to achieve a number of advantages compared to the installation of new parts. This is primarily related to the extension of the service life of the analyzed parts, increase of productivity, reduction of downtimes, reduction of inventory costs and other benefits derived by applying the welding technology.

It is shown that a proper choice of hard-facing technologies is associated with the complex procedure of checking the quality of deposits, what indicates that the repair work can be performed only in specialized workshops for regeneration, which have adequate equipment and appropriate skilled staff. The expected net benefit for the analyzed parts is very high, regardless of the fact that additional external and internal effects have not been quantified. After the successful

implementation of these new manugacturing surfacing technologies in presented areas, it is possible, by applying the similar procedure, to form a knowledge base and to use it for maintenance of equipment for forging, and other similar mechanical parts.

ACKNOWLEDGEMENT

This research was partially financially supported by Ministry of Education and Science of Republic of Serbia through grants TR35024, TR35021, TR34002 and OI174004.

REFERENCES

[1] R. Wasserman: *How to save millions by reducing inventories of spare parts*, Eutectic-Castolin Institute for the Advancement of Maintenance and Repair Welding Techniques, 1971.

[2] V. Lazić: *Optimization of the hard-facing procedures from the aspect of tribological characteristics of the hard-faced layers and residual stresses*, PhD thesis, The Faculty of Mechanical Engineering, Kragujevac, 2001. (In Serbian)

[3] R. Čukić: *Techno-economic analysis of production and reparatory hard-facing of various parts of machine systems*, PhD thesis, University of Belgrade, Serbia, 2010. (In Serbian).

[4] V. Lazić et al.: *Selection of the most appropriate technology of reparatory hard-facing of working parts on universal construction machinery*, Tribology in Industry, Vol. 33, No 1, pp. 18-27, 2011.

[5] M. Mutavdžić et al.: *Model investigations of the filler materials for regeneration of the damaged parts of the construction mechanization***,** Tribology in Industry, Vol. 30, No. 3&4, pp. 3-9, 2008.

[6] V. Lazić et al.: *Reparation of damaged mallet for hammer forging by hard-facing and weld cladding*, Technical Gazette, Vol. 16, No. 4, pp. 107-113, 2009.

[7] A. Wernoski: *Zmeczenie cieplne metali*, Wydawnictwa Naukowo - Techniczne, Warszawa, 1983. (In Polish).

[8] R. Pasierb: *Spawanie żarowytrzymalych stali chromowo-molibdenowo-wanadowych*, WNT, Warszawa, 1982. (In Polish).

[9] V. Lazić et al.: *Selection of the optimum technology of the forging dies reparation from the aspect of tribological characteristics*, TRIBOLOGIA - TEORIA I PRAKTIKA, ROK XXXVI, NR 2/2005, pp. 11-30, 2005.

[10] V. Lazić et al.: *Development and application of welding technologies for regeneration of damaged working parts of forging presses and hammers*, Welding and Joining Technologies for a Sustainable Development and Environment, 24-26. 05. 2006., Timisoara, Romania, pp. 341-346.

Serbian Tribology Society

SERBIATRIB '13

13th International Conference on Tribology

Faculty of Engineering in Kragujevac

Kragujevac, Serbia, 15 – 17 May 2013

TRIBOLOGY ASPECT OF RUBBER SHOCK ABSORBERS DEVELOPMENT

Milan Banić[1], Dušan Stamenković[2], Miloš Milošević[3], Aleksandar Miltenović[4]

[1]Faculty of Mechanical Engineering, University of Niš, Serbia, banic@masfak.ni.ac.rs

[2]Faculty of Mechanical Engineering, University of Niš, Serbia, dusans@masfak.ni.ac.rs

[3]Faculty of Mechanical Engineering, University of Niš, Serbia, mmilos@masfak.ni.ac.rs

[4]Faculty of Mechanical Engineering, University of Niš, Serbia, amiltenovic@yahoo.com

Abstract: *Rubber is a very flexible material with many desirable properties which enable its broad use in engineering practice. Rubber or rubber-metal springs are widely used as anti-vibration or anti-shock components in technical systems. Rubber-metal springs are usually realized as a bonded assembly, however especially in shock absorbers, it is possible to realize free contacts between rubber and metal parts. In previous authors research it was observed that friction between rubber and metal in such case have a significant influence on the damping characteristics of shock absorber. This paper analyzes the development process of rubber or rubber-metal shock absorbers realized with free contacts between the constitutive parts, starting from the design, construction, testing and operation, with special emphasis on the development of rubber-metal springs for the buffing and draw gear of railway vehicles.*

Keywords: *rubber friction, rubber-metal spring, shock absorber, product development.*

1. INTRODUCTION

Rubber or rubber-metal springs are widely used in industry as anti-vibration or anti-shock components giving many years of service. They have several advantages in respect to metal springs (lower price, easier installation, lower mass, reduced corrosion, no risk of fracture and no need for lubrication) [1]. However, they have one major disadvantage reflected in insufficiently reliable service life caused by rubber fatigue.

Those elements are well established to control vertical and lateral movements. Nowadays, the more demanding operating environment has made the design of such components more challenging than ever before. In addition to the design of the rubber part itself the interface between the part and the structure is also important.

The properties of the rubber-metal spring are mainly influenced by a rubber compound. Rubber compounds are generally composed of a base rubber (e.g. natural rubber), filler (e.g. carbon black) and a curing agent (e.g. sulphur). Additional components may include antioxidants, adhesion agents, flame retardant agents and special process-enhancing chemical additives. Common physical properties of rubber compounds are affected by every ingredient of a rubber recipe independently of or dependently on each other. The mixing and curing process is also critical in determining these properties. Improving one compound property always results in changing other properties, for better or for worse. Noted fact makes development of elastomeric based products a very complicated task. Up to appearance of modern computer aided tools, the development of those products relied only on previous experience of the designer and trial and error procedure. Such approach was inefficient, expensive and time consuming because it required iterative procedure combined with excessive experimental testing to achieve desired mechanical properties.

Rubber-metal springs are usually realized as a bonded assembly, however especially in shock absorbers, it is possible to realize free contacts between rubber and metal parts. In that case, connections between rubber blocks and metal plates are realized by applying pressure and resulting static friction. During the load cycle of the shock absorber, apart the energy dissipation in rubber,

additional energy is dissipated due to friction between rubber and metal parts.

In previous authors research [2] it was observed that friction between rubber and metal in such case have a significant influence on the damping characteristics of shock absorber. This paper analyzes the development process of rubber or rubber-metal shock absorbers realized with free contacts between the constitutive parts, starting from the design, construction, testing and operation, with special emphasis on the development of rubber-metal springs for the buffing and draw gear of railway vehicles.

2. DEVELOPMENT OF THE RUBBER-METAL SHOCK ABSORBER

With appearance of modern computer tools and virtual product development, the development process of shock absorbers became more efficient due to simulated experimental testing of virtual prototype. With virtual product development tools it is possible to predict the absorbing capacity and service life before the manufacturing of the product prototype which was not possible in classical development process.

The assembly of shock absorber with rubber-metal spring usually consists of a few rubber-metal elements separated with metal plates and prestressed with a central screw. A rubber-metal element represents a metal carrier in the shape of a circular plate with natural or synthetic rubber vulcanized on both sides. Therefore, the advantages of both component elements are involved: high abilities of displacement and amortization of rubber and large loads which are sustained by metal parts. These ensure the decrease of noise and amortization of impact loads. Figure 1 shows the design of buffing gear spring assembly, while Figure 2 shows the design of draw gear spring assembly.

Figure 1. Rubber-metal spring assembly of buffing gear

Figure 2. Rubber-metal spring assembly of draw gear

As already noted, these springs are used as anti-shock components, so the main properties designer must take into account are absorbing capacity and stiffness of the spring. The most important absorbing characteristic of rubber is evaluated by its hysteresis. Hysteresis is the mechanical energy loss that always occurs in an elastic material between the application and the removal of a load. If the displacement of a system with hysteresis is plotted on a graph against the applied force, the resulting curve is in the form of a loop. It depends not only on the elastomer type, but also on fillers and other compound ingredients as other mechanical properties.

The authors defined a virtual product development procedure (Figure 3) for development of rubber-metal springs used in shock absorbers. The development procedure is based on application of modern viscoplastic rubber constitutive model (Bergström-Boyce), which besides higher accuracy of prediction, enables the assessment rubber compound hysteresis and strain rate dependence which is not possible by application of hyperelastic models usual for rubber FE analysis. The parameters of rubber constitutive model (Bergström-Boyce) are determined by uniaxial compression at different strain rates and stress relaxation test on the samples of the rubber compound (∅35.7 x 17.8 mm) [3]. The samples are compressed between hardened steel plates lubricated with machine oil in order to prevent the barrelling of samples. Based on the performed experiments, the database of model parameters for the rubber compounds can be defined. Database also contains data about other significant properties of rubber compound, such as composition, common mechanical properties, etc.

The first step in procedure shown at Figure 3 is to determine the rubber compound for rubber-metal spring. From the formed database several compounds are selected based on criteria defined by widely known selection and service guide for elastomers [4] regarding the product specific requirements (creep, low-temp stiffening, heat aging,…) and the operating environment conditions (resistance to ozone, radiation, …). The selected

compounds are used for simulation of static and dynamic hysteresis of standardised specimens.

The simulation of static hysteresis test is conducted on cylindrical test samples (∅35.7 x 17.8 mm), according to the internal standard SIMF.92.006 [5]. The simulation dynamic hysteresis (Yerzley hysteresis) test is carried out on cylindrical test samples (∅19.5 x 12.5 mm) according to the standard ASTM D 945-06 [6].

The obtained results of static and dynamic hysteresis are used for final selection of rubber compound. As the main feature and an indicator of the quality of rubber-metal springs is energy absorption capacity, the compound is selected based on criterion of highest static and dynamic hysteresis obtained during simulation.

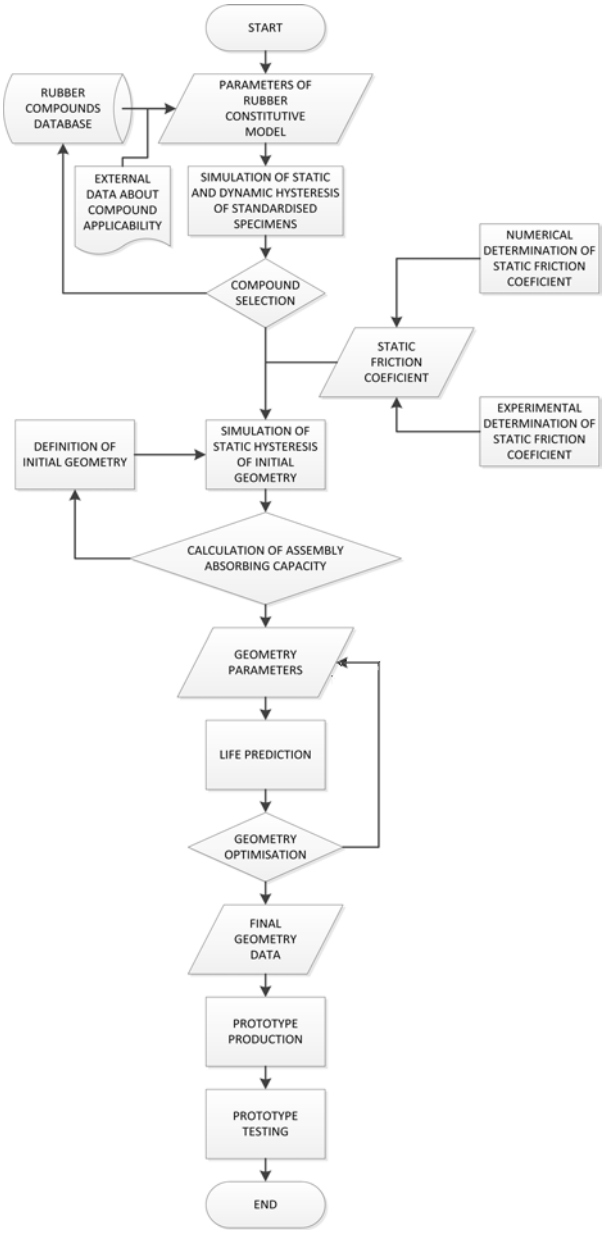

Figure 3. Procedure for development of shock absorbers with rubber-metal spring

The next step following the adoption of the rubber compound is the selection of the appropriate structural design of the basic rubber metal element and their combination into a spring package. As already noted, the main problem in developing rubber-metal springs is that a designer cannot estimate how many basic rubber metal spring elements need be combined in a serial set to achieve the required absorption capacity. The amortizing ability of a rubber-metal spring package, and therefore the constitutive number of basic rubber metal elements, should be determined by simulation using the finite element method. Based on the required operating stroke, built-in measures and assumptions about preloading of rubber-metal spring the initial design of the basic rubber metal elements is adopted. For instance, the initial geometry of the basic element of buffer rubber-metal spring is shown on Figure 4. It consisted of a metal disk with openings and vulcanized rubber parts on both sides of the plate connected through the plate's openings (Figure 4).

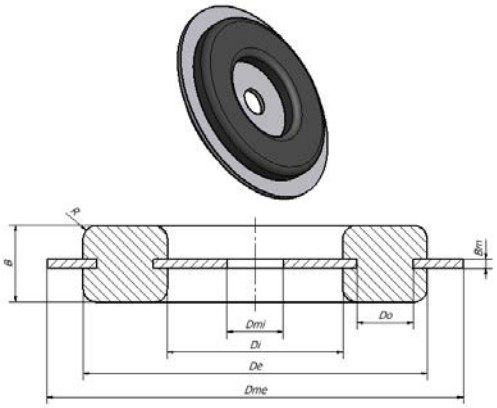

Figure 4. The basic rubber metal spring element of buffing gear

Upon the simulation of static hysteresis of basic element, the number of elements in rubber-metal assembly can be easily determined as the ratio of required spring absorption capacity and the absorption capacity of the single element. The procedure is sometimes iterative to obtain desired results with required value of normal reaction force during impact and limited number of basic elements due to installation requirements.

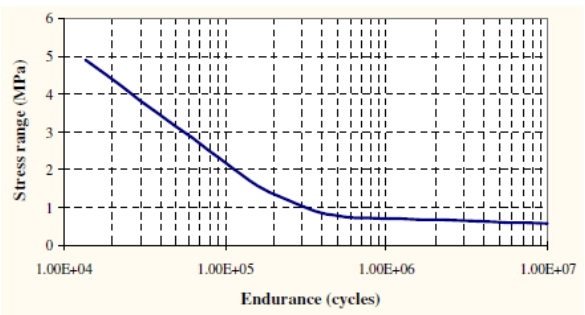

Figure 5. S-N curves of the rubber-metal element [7]

The adopted geometry parameters are further improved by optimisation. The optimization procedure is performed in order to improve the design of the spring element regarding its service life. By lowering the element stress levels values, the service life is prolonged which is obvious from Figure 5. As an example, the optimisation basic rubber metal spring element of buffing gear is performed by defining the design of experiment as a central composite design in simulation. By variation of the plate opening diameter (D_o), the number of openings (B_o) and radius on top and bottom of the rubber part of the element (R), the functional dependence of maximum equivalent stress from input parameters was obtained. Minimisation of the obtained functional dependence results in optimal geometric dimensions of the basic spring element. The functional dependence of maximal equivalent stress from input parameters is shown in Figure 6.

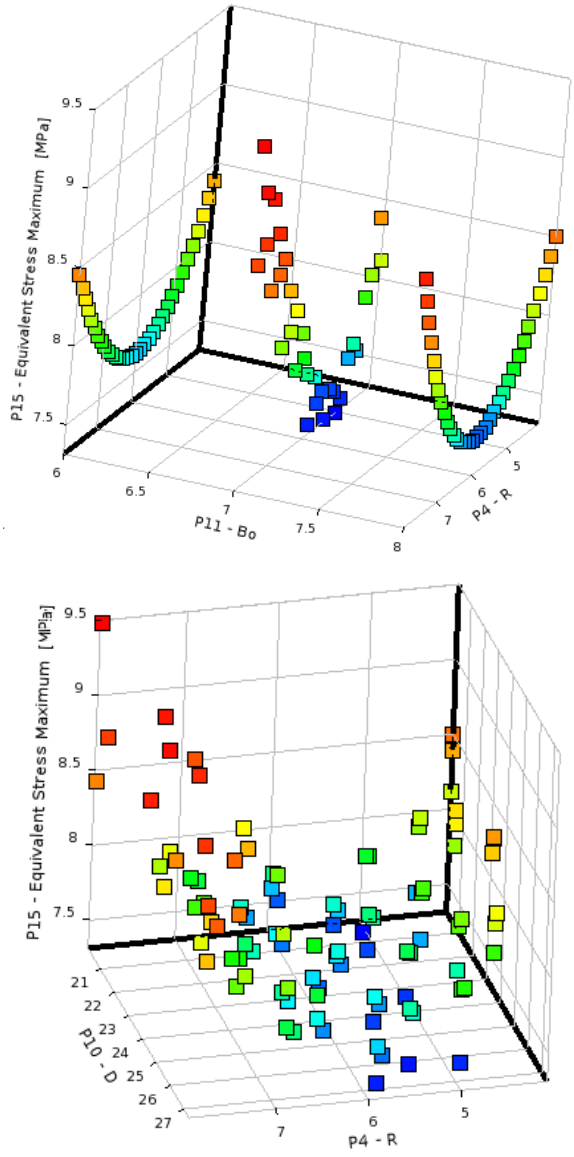

Figure 6. Functional dependence of maximal equivalent stress from the optimisation parameters

Upon the definition of final geometry of the element, the actual production and testing of prototype are performed in order to validate design and to determine the accordance with the design requirements.

3. TRIBOLOGY ASPECT OF THE SHOCK ABSORBER DEVELOPMENT

Rubber has a very high coefficient of friction which can even reach value of $\mu = 4$. High friction coefficient, and thus high grip of rubber, found its way in many engineering applications; for example, rubber is not always bonded in bushes, since its frictional grip is almost equal to a bond. During the load of unbounded rubber metal assembly in compression the friction force occurs (Figure 7). Due to high grip between the rubber and the metal the rubber is barrelling thus increasing the contact surface.

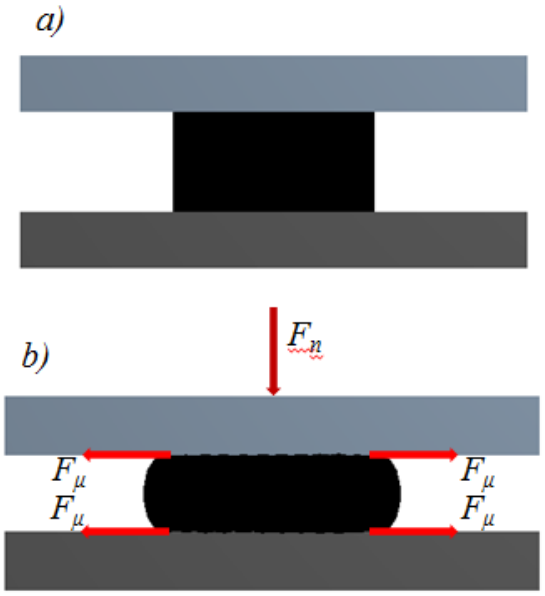

Figure 7. Compression of rubber between steel plates: a) unloaded; b) loaded

It has been noticed that the amount of the accumulated/absorbed energies of rubber-metal springs loaded in compression greatly depends on the contact between the rubber and the metal [2].

Noted findings were also confirmed by other authors. For instance, Figure 8 shows the effect of lubricating the contact between rubber and metal in compression. Provided that the steel ends are clean the grip is almost equal to that of a bonded sample.

Although bonded contact provides a higher normal reaction force during impact, the free contact such as in draw and buffer gear rubber metal spring assembly dissipates more energy as there are friction induced energy losses due to contact sliding. If the friction coefficient is sufficiently high to ensure that significant sliding

between metal and rubber will not occur shock absorber will have better absorbing properties.

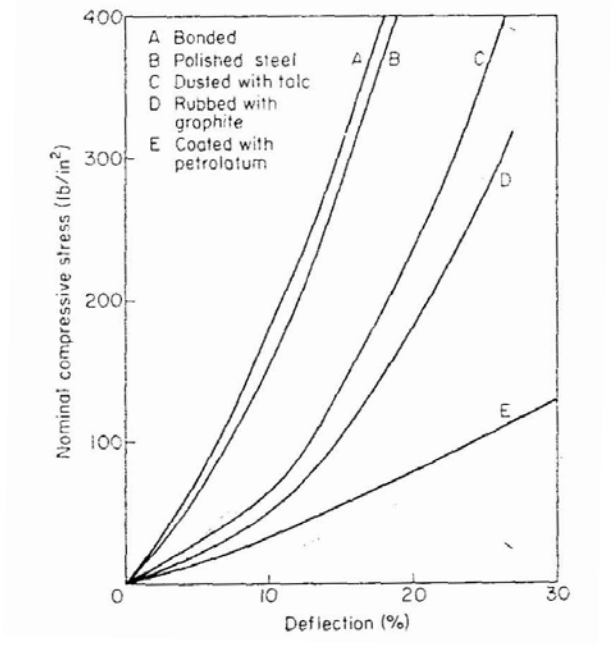

Figure 8. Effects of surface conditions on the stress/deflection curve for rubber under compression [8]

Significant sliding compromises the assembly stability and has a great effect on lowering of normal resulting force. Furthermore, the increase of the friction coefficient on the contact surfaces of the rubber element increases the shear stress and its share of the total stress also. The increasing shear stress further increases the total stress in the element and the force which resists the deformation of the element. The increase of the shear stress share of the total stress leads to the enhanced amortization capacity of rubber elements. As the high values of normal resulting force are the design requirement, it is necessary to find the balance between the sliding allowance and resulting normal force. It can be achieved by influencing the tribological contact parameters (lubrication, surface roughness of the metal part, contact pressure, …) and thus the friction coefficient value.

Based on above it can be concluded that it is not possible to actually perform the virtual development process of the shock absorber with rubber metal spring without the knowledge of the friction coefficient value in contact between the rubber and metal parts.

The coefficient of friction of rubber is highly dependent on contact pressure. As the contact pressure between the rubber and the free metal plates in shock absorbers is approximately 20 MPa, it is extremely difficult or even impossible to experimentally determine the actual value of friction coefficient at noted operating contact pressure.

The compound friction coefficient can be predicted based on experiments with rubber specimens or based on existing data on normal reaction force in similar operating conditions. By simulation of experiments on rubber specimens or previously performed experiments, the friction coefficient can be determined by goal driven optimisation procedure. The value of friction coefficient will be approximately determined when the normal reaction force obtained by simulation is equal to experimentally obtained one.

As an example, it is necessary to determine the friction coefficient in contact between rubber with trade name TG-B-712 (manufactured by company TIGAR, Pirot) and metal plate at contact pressure of 3 MPa. The rubber specimen (with dimensions (∅35.7 x 17.8 mm) was compressed between steel plates at specific tribological conditions for which it was necessary to determine the value of friction coefficient. The force-displacement data was recorded during the experiment (Figure 9).

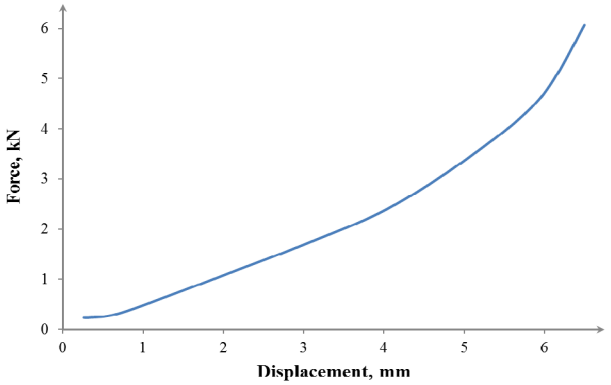

Figure 9. Experimental force – displacement data

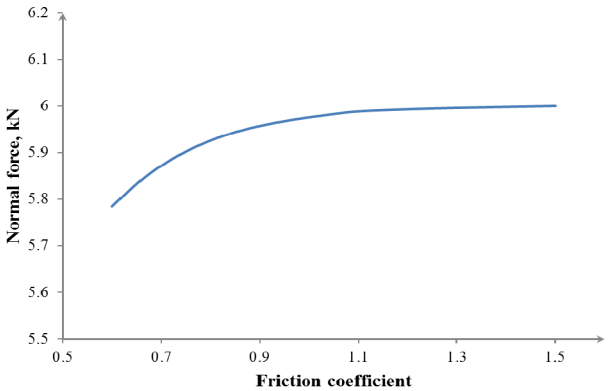

Figure 10. Functional dependence between friction coefficient and force determined by virtual experiment

The friction coefficient was determined by virtual experiment from which the functional dependence between friction coefficient and normal resulting force was obtained (Figure 10). Based on realistic experimental data (Figure 9) it is clear that the maximal resulting normal force correspond to friction coefficient value of $\mu = 1.5$.

4. CONCLUSION

Tools of virtual product development enable significant cost and time savings in the process of development of shock absorbers filled with rubber-metal springs.

But to employ the tools of virtual product development it is essential to have a value of friction coefficient in free contact between rubber and metal parts. Without the correct value of friction coefficient the proposed procedure outlined in the paper would provide incorrect data which is not suitable for shock absorber development process.

As experimental determination of friction coefficient in contact between rubber and metal at high values of contact pressure can be very problematic, the friction coefficient can be estimated by goal driven optimisation during numerical simulation of realistic experiments with existing resulting force data.

REFERENCES

[1] V. Miltenović: *Mašinski elementi-oblici, proračun, primena*, Mašinski fakultet Univerziteta u Nišu, 2009.

[2] D. Stamenković, M. Milošević: Friction at Rubber-Metal Springs, *11th International Conference on Tribology - SERBIATRIB '09*, 13-15.05.2009, Belgrade, pp. 215-219.

[3] M. Banić, *et al.: Prediction of Heat Generation in Rubber or Rubber-Metal Springs*, Thermal Science, 16 (Suppl. 2), pp. 593-606, 2012.

[4] …:Vibration & motion control catalogue, LORD Corporation, 2008.

[5] SIMF.92.006.

[6] ASTM D 945 Standard Test Methods for Rubber Properties in Compression or Shear.

[7] R. K. Luo, W. X. Wu, P. W. Cook, W.J. Mortel: *Fatigue design of rubber springs used in rail vehicle suspensions*, Proceedings of the Institution of Mechanical Engineers, Part F: Journal of Rail and Rapid Transit, 217/3, pp. 237-240, 2003.

[8] A. B. Davey, A. R. Payne: *Rubber in engineering practice*, Great Britain, 1964.

Serbian Tribology Society

SERBIATRIB '13

13th International Conference on Tribology

Faculty of Engineering in Kragujevac

Kragujevac, Serbia, 15 – 17 May 2013

EFFECTS OF USING OF MQL TECHNIQUE IN METAL CUTTING

Gordana Globočki Lakić[1], Branislav Sredanović[1], Davorin Kramar[2], Bogdan Nedić[3], Janez Kopač[2]
[1]University of Banjaluka, Faculty of Mechanical Engineering Banja Luka, Bosnia and Herzegovina
[2]University of Ljubljana, Faculty of Mechanical Engineering Ljubljana, Slovenia
[3]University of Kragujevac, Faculty of Engineering, Kragujevac, Serbia

Abstract: *In this paper an effect of using of minimal quantity lubrication (MQL) technique in turning operations is presented. Experimental research was performed on carbon steel C45E. Technological parameters: depth of cut, feed rate and cutting speed were adjusted to semi-machining and roughing. Higher values of feed and cutting speed were used, than recommended from literature, and different types of cooling and lubrication conditions in turning were applied. As a conventional procedure and technology, lubrication with flooding was applied. As special lubrication technique the MQL was used. During research, monitoring of the cutting force, chip shape, tool wear and surface roughness was performed. Relations between parameters, material machinability and economy of process were analyzed.*

Keywords: *lubrication, cutting, MQL, effects*

1. INTRODUCTION

The future of metal machining by 2020 is in the development of flexible machining systems, economical and productive processes, energy-efficient processes, production without waste, ecological production with a reduced quantity of the cooling and lubrication fluids and etc. This conclusion is based on the study National Research Council of the USA and other teams of researchers [1, 2, 3, 4].

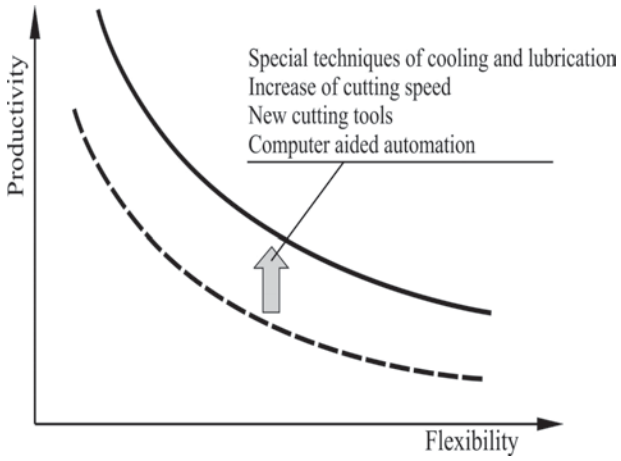

Figure 1. Possibilities to increase the productivity of manufacturing

Increasing of productivity (Fig 1.) is impossible without utilization of modern tools and machines, modern types of cooling and lubrication fluids (CLF), CLF dosing techniques, and modern equipment. Progress is not possible without knowledge of the materials machinability and expert systems for the selection of suitable machining regimes based on machinability and process modelling [3]. Phases of research, obtaining and application of knowledge in the field of cutting process are:

- study of materials machinability based on experimental research,
- modelling of the cutting process and
- integration of knowledge in expert systems and specialized databases.

The main progress in developing of high productive machining processes is realized in the area of special CLF dosing techniques. One of these techniques is minimum quantity lubrication (MQL). The analysis of previous researches have shown that this CLF dosing technique was applied for lower cutting speed (v_c = 100 -150 m/min) [5, 6, 7].

From the structure of the cost of machined part, it can be concluded that the cost of CLF participate 15%, costs of tools 10% and costs of energy consumption 4% of total costs (Fig 2).

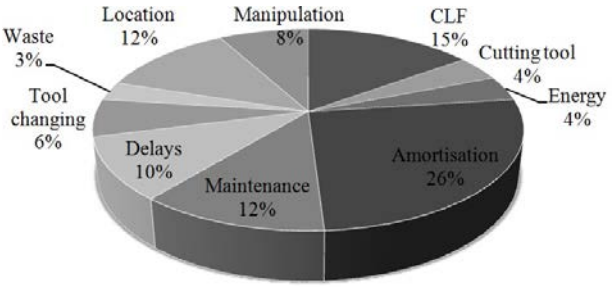

Figure 2. Structure of the machining costs

The focus of researches presented in this paper was on effects of different CFL dosing techniques in the field of higher cutting speed (v_c = 200 - 400 m/min), which contributed to the expansion of technological fields. In order to analyse the machinability when applying standard and MQL CFL dosing techniques, analysis of machining energy balance, effect of chip formation, tool life and quality of machined surface were also included [8].

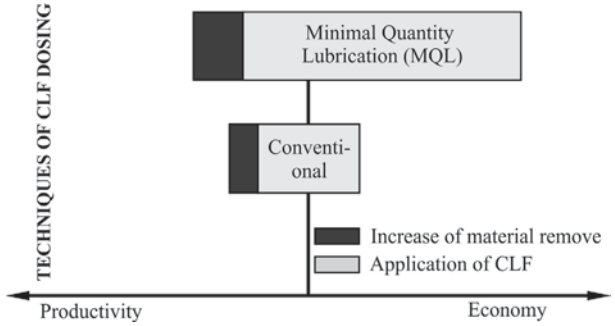

Figure 3. Influence technique of lubrication on productivity and efficiency

The studies that are presented in this paper are related to the analysis of use of modern techniques CFL dosing, with the aim of defining the directions of increasing productivity and efficiency of machining process (see Fig. 3).

2. EXPERIMENTAL SETUP

The material that was used for the experimental researches is the carbon steel C45E. This steel belongs to the group of construction steels which are used for essential parts in the machines and constructions. Workpiece is cold-rolled steel bar with a diameter of 120 mm and length of 300 mm. Research was performed on universal lathe BOEHRINGER with the following properties: 8 kW of power, maximum spindle speed of 2240 rev/min, and feed of 1.6 mm/rev. Carbide cutting tool for semi machining SNMG 1204 08 NMX was used. Tool clearance angle was 10°, rake angle 0°, and a tool tip radius was 0.8 mm without chip breakers. Tool holder was PSDN 2525 M12 with inclination angle 45° (Fig. 4).

Figure 4. Experimental setup on machine

In this research two different CLF dosing techniques were analysed:

- conventional flooding and
- special dosing technique - MQL.

In conventional flooding, CLF is dosed at the top of machining zone, from a distance of approximately 150 mm. CLF was directed on non-machined workpiece surface and rake surface of insert.

In the MQL technique, CLF was dosed using a special device which utilizes a compressed air to form an oil mist in the mixing chamber (Fig 5). During machining with MQL technique, the tool was protected from sudden changes of heat loads. The effects of rapid expansion and contraction of the tool material and the cracks appearance and coatings cracking were avoided. During the machining, due to the effect of the spray, the tool was enveloped with a thin layer of emulsion. In MQL technique spray nozzle was installed at a distance of 30 mm (L_{MQL} = 30 mm), normal to the cutting edge, with an angle of 30° (ψ_{MQL} = 30°) regarding to the rake face of tool (Fig 6.). With such recommended position of the nozzle quality lubrication of machining zone were ensured. Table 1 shows the values of the hydraulic conditions for both CLF dosing techniques.

Figure 5. MQL device

Table 1. The values of pressures and flow

Technique of CLF dosing	Pressure p [MPa]	Flow Q [l/min]
Standard flooding	0.3	2
MQL	0.3	0.0005

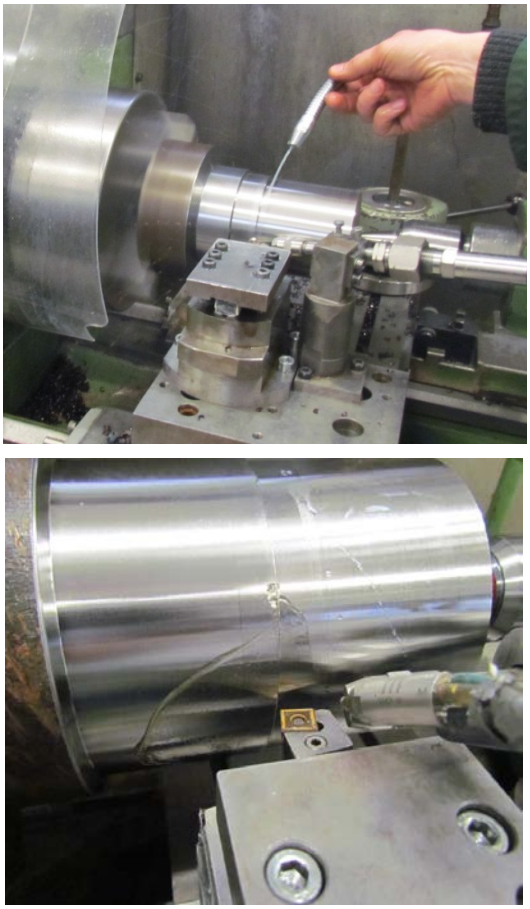

Figure 6. Position of conventional flooding (left) and MQL nozzle (right) during the experiments

Technological parameters varied in the experiments were as follows: depth of cut (a), feed (f) and cutting speed (v_c). Technological parameters were adjusted to the semi- turning, with the use of higher values (Table 2). The total numbers of experiments for both dosing techniques were 72.

Table 2. The levels of technological parameters

Parameter	The levels of variation			
	1	*2*	*3*	*4*
Cutting depth a [mm]	1.5	2.0	2.5	-
Feed s [mm/rev]	0.224	0.280	0.355	0.400
Cuuting speed v_c [m/min]	210	310	400	-

KISTLER dynamometer was used to measure three cutting force components in turning: main cutting forces (F_c), feed cutting forces (F_f) and penetration cutting force (F_p). For processing of the measured signals LabVIEW software package with specially designed program framework was used. The developed program framework enables data transmission to software package MATLAB. Monitoring and measurement of tool wear was performed using a tool microscope TM MITOTOYO 510 equipped with high-resolution camera (Fig 7). Surface roughness was measured using a mobile measuring device MITOTOYO SURFTEST SJ 301. During the experiments a chip formation process was monitored as well.

Figure 7. Measuring devices: force data acquisition (left) and tool microscope (right)

In the first phase of research cutting forces (F_c, F_f and Fp) for different combinations of input parameters were measured. At the same time the formed chips were collected, and the shape was evaluated with the purpose of technological frames definition (Fig 8).

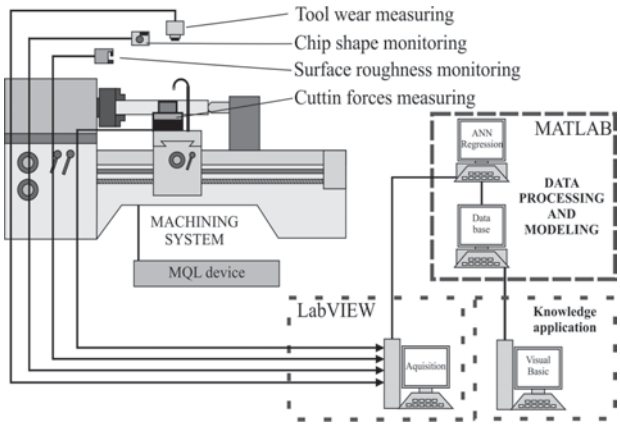

Figure 8. Data flow in measuring and monitoring

In the second phase of the experimental tests tool wear was measured, as follows: the values of concentrated wear (VB), tool wear on tool clearance face (VB') and the size of the crater on the rake face (b_w). Due to wear of tools values of surface roughness were measured, as follows: mean values of roughness (R_a) and maximum height of roughness (R_y).

3. ANALYSIS OF RESULTS

The results of experimental investigations which concerning the values of machinability parameters: cutting resistances, shape of chip, tool wear and surface roughness is shown. Modelling was performed using regression analysis and artificial neural networks (ANN).

From the analysis of the cutting forces components (Fig. 9, 10 and 11) in case of conventional CLF dosing application, it can be concluded that the value of the cutting forces components increase with increasing feed and depth of cut. When MQL technology is applied, the values of cutting forces increase with feed and depth of cut as well. The values of force components F_f and F_p were smaller than the values of F_c component for both dosing techniques, which is consistent with the theoretical assumptions. Penetration cutting forces F_p and feed cutting forces in MQL technique are greater than conventional technique of CLF dosing.

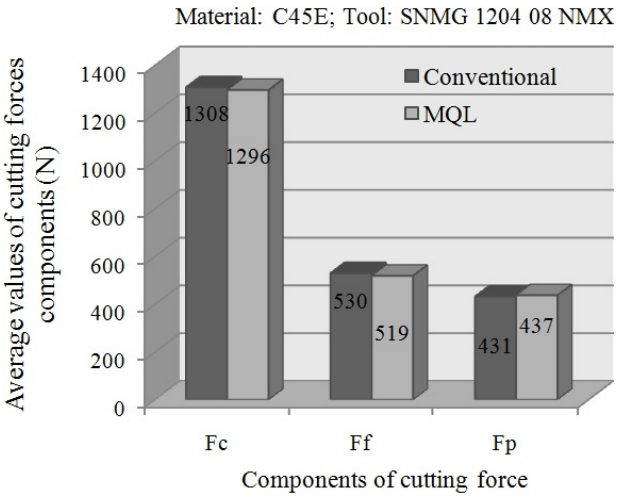

Figure 9. Comparison of the mean value of components of cutting force for both dosing techniques

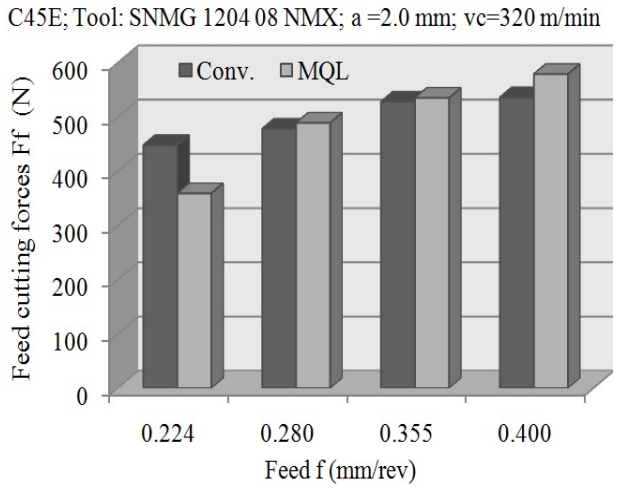

Figure 10. Values of feed cutting forces

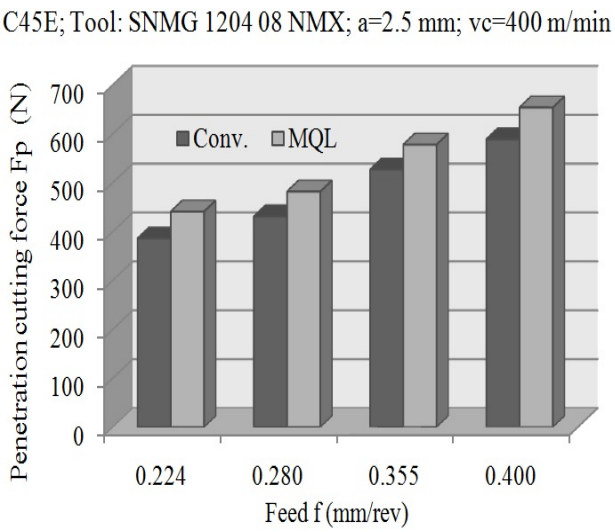

Figure 11. Values of penetration cutting force

One of the main indirect indicators of the machining process condition is chips shape. Based on chip shapes the following features can be determined: tool wear, surface roughness, the amount of generated heat and related phenomena. Conclusions based on chip shape were adopted on the basis of recommendations from the literature [1, 2, 3].

Table 3. Chip shape during machining with conventional flooding

Depth a [mm]	Cuutting speed v_c [m/min]	Feed f [mm/rev]		
		0.224	0.280	0.400
1.5	210			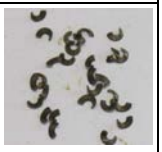
2.0				
2.5				

In table 3 forms of chips obtained when machining steel C45E while using conventional technique of CLF dosing are shown. Based on analysis of chip shapes it can be concluded that machining with lower feed rates (f = 0.224 mm/rev) and greater depths (a = 2.5 mm), creates an unfavourable chip shape. However, for the same parameters, in conditions with higher speeds, it forms more favourable chips shape.

Table 4. Chip shape during processing with MQL technique

Depth a [mm]	Cuuting speed v_c [m/min]	Feed f [mm/rev]		
		0.224	0.280	0.400
1.5	210		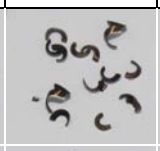	
2.0				
2.5		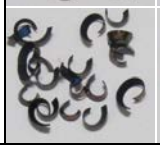	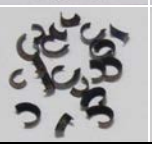	

Some chip shapes during machining of the same steel C45E, with the same tool, using MQL technique are shown in Table 4. Chips are dark, which indicates that in the machining area a larger amount of heat is generated and dissipated through the chips. It can be concluded that MQL technique provides good effects of lubrication, but the bad effects of cooling the machining zone. Based on a chip shape, it can be concluded that the use of MQL technique provide favourable shapes of chip for all analyzed machining conditions.

The technological areas for both techniques of lubrication and different depths of cut are shown in figures 12 and 13. They are based on the assessed chip suitability. From the analysis of the technological areas, it can be concluded that MQL technique offers a wider field of machining.

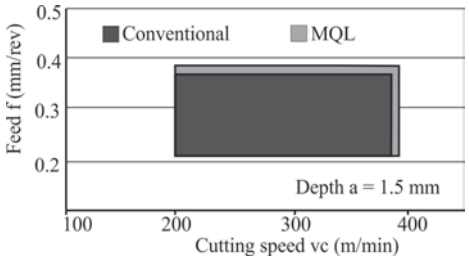

Figure 12. Technological areas for depth a = 1.5 mm

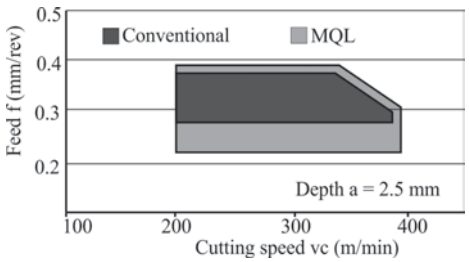

Figure 13. Technological areas for depth a = 2.5 mm

Previous studies have shown that different techniques of lubrication have a great impact on the wear of tools as well. In our study the measured parameters of tool wear were as follows: concentric wear (*VB*) and wear on the secondary surface of tool (*VB'*), and crater wear - see table 5 and 6. This parameters has direct impact on the machining process, and thus on the machinability. Criterion of tool wear was VB = 0.3 mm. Tool life in the case of MQL technique was for about 33% longer (see Fig. 14). The parameters of the surface roughness - mean height of roughness (*Ra*) and maximum roughness (*Ry*) were measured depending on the machining time. As regimes for machining the mean values of the obtained technological areas have been adopted: a = 2.0 mm and f = 0.280 mm/rev, cutting speed v_c = 320 m/min (Figure 14 and 15).

Table 5. Tool wear during machining with conventional CLF dosing

Time T [min]	Machining lenght L_c [m]	Tool wear on tool face		
		Secondary rake	Primary rake	Clerance
0.93	272			
3.75	1286		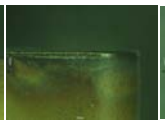	
7.23	2080		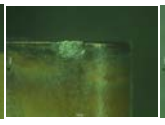	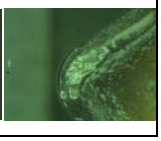

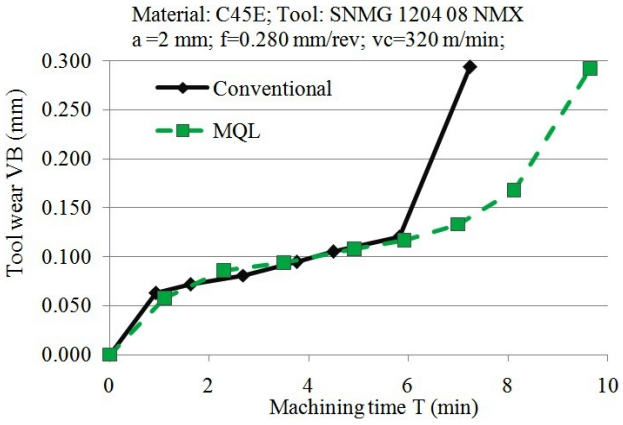

Figure 14. Comparative diagram of tool wear for different techniques of CLF dosing

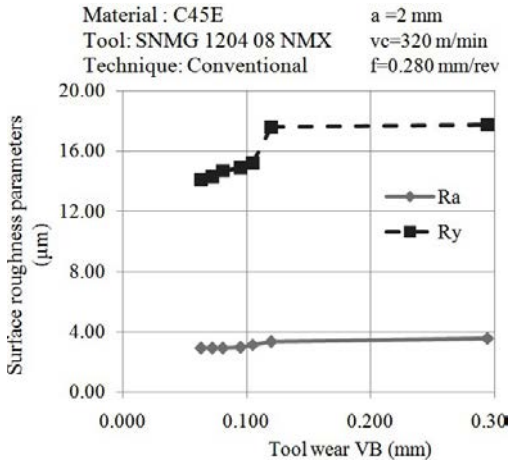

Figure 15. Surface roughness regarding the tool wear in machining with conventional CLF dosing

Figure 15 shows that tool wear take affects on the surface roughness parameters R_a and R_y. Roughness is influential parameter in assessing the machinability, and in the flooding conditions of machining, and this parameter was increased from the initial 14 µm to 18 µm at the time when tool wear achieved criterion 0.3 mm. Tool life for the given machining conditions was T = 7.23 min.

Table 6. Tool wear during machining using MQL technique

Time T [min]	Machining lenght L_c [m]	Tool wear on tool face		
		Secondary rake	Primary rake	Clerance
1.10	339		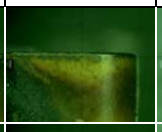	
5.92	1952			
9.65	3163			

In Table 6 the values of the tool wear parameters during machining with MQL technique of lubrication is shown. The regime a = 2.0 mm, f = 0280 mm/rev, v_c = 320 m/min was applied. In this case, it can be concluded that the tool insert enveloped with a thin layer of emulsion, which is not the case with conventional CLF dosing. Tool achieved full damage at T = 9.65 min. The higher value of tool life with MQL technique compared to conventional flooding is the result of a thin film that completely covered the tool insert surface (Figure 17).

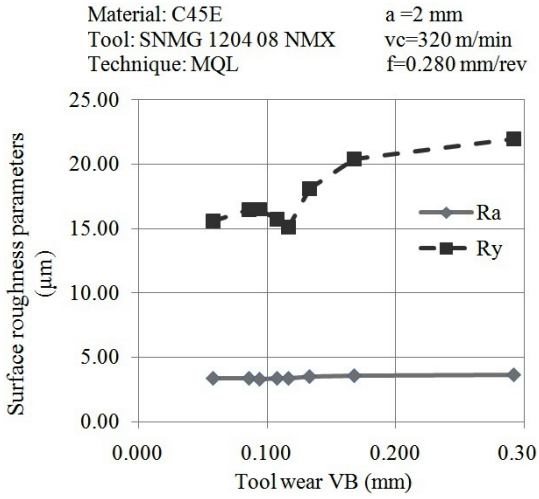

Figure 16. Changes of parameters Ra and Ry, depending on the tool wear in machining with MQL technique

The increase of R_a the parameter value during machining with MQL technique is shown in Fig. 16. It can be seen, that due to a higher percentage of heat generated during processing the value of parameter R_y is higher when machining with MQL technique than in conventional lubrication.

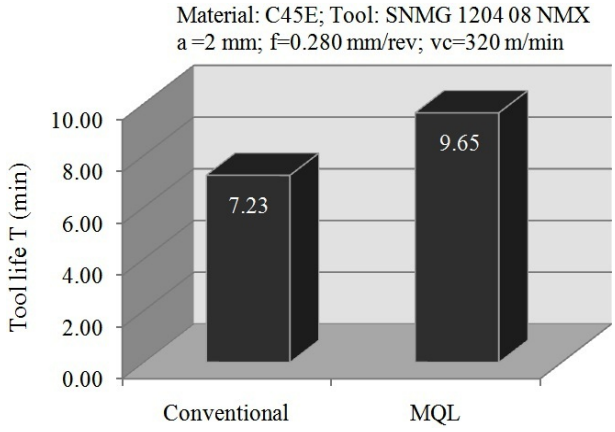

Figure 17. Values of tool life for different lubrication techniques

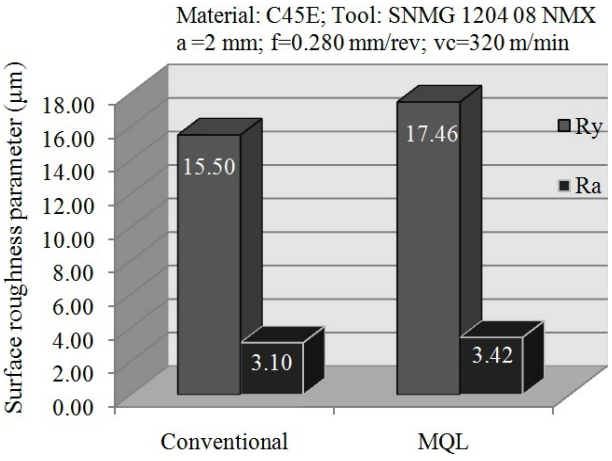

Figure 18. Values of surface roughness parameters for different lubrication techniques

Comparative analysis of results 1n the figures 17 and 18 indicates that the MQL technique provides better results in aspect of tool wear and tool life, but slightly worse results in aspect of the surface quality as consequence of thermodynamic processes in the cutting zone.

4. MODELING OF RESULTS

Examination of the experimental results was performed by multiple regression analysis. (see Fig. 19). The output values from the regression model showed a significant correlation with the experimentally measured values. The average relative error of the regression models does not exceed 5%. The models presented in the form of regression equations can be used with high accuracy of prediction. The models of main cutting force (F_c) have errors less than 2%, while the main square errors for models of forces (F_f) and (F_p) are higher. This corresponds to the theoretical assumptions of cutting parameters behaviour in the case of machining of steel C45E.

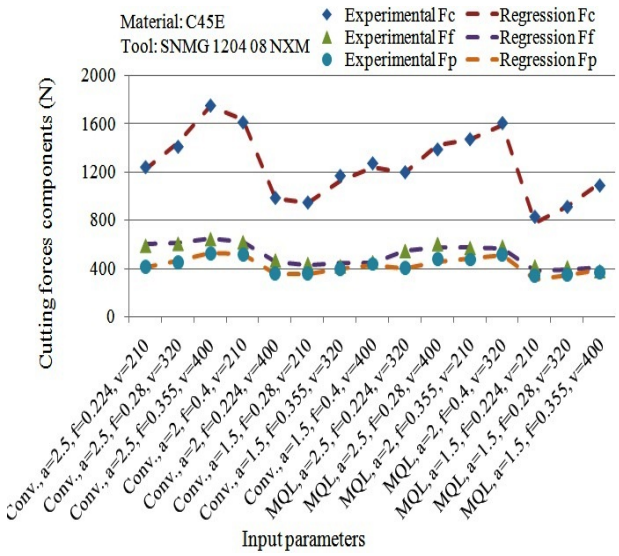

Figure 19. Comparison of outputs regression model with experimental results

The biggest errors is expected in the predictive models of forces (F_f) and (F_p) in machining with MQL technique; 4.93% and 4.44% respectively. In addition to modelling the of cutting force components, also a resultant force $F_{f,p}$, which is a resultant of (F_p) and (F_f) was modelled. These resultant forces have a higher value than the main cutting force. The resultant force ($F_{f,p}$) is a main indicator of tool wear, and with its growth usually intensive tool wear occurs.

Analyzing the models, and their corresponding exponents (Figure 19 and Table 7), it can be concluded that the depth of cut has the highest, while the cutting speed has the least influence on the main cutting force and resultant cutting force. Cutting speed and feed have a great influence on the force (F_f) and (F_p), and the resultant forces ($F_{f,p}$), especially during machining with MQL technique. It can be concluded that the increase of feed and depth of cut increases the value of the components of the cutting force. Increasing cutting speed reduces the values of cutting force because there is no negative phenomenon, such as the burrs on the tool edge.

Table 7. Models of cutting forces with coefficients of machining

Material: C45E Tool: SNMG 1204 08 NXM		Collération coefficient	Relative error (%)
$F_c = 2485 \cdot a^{0.878} \cdot f^{0.844} \cdot v^{-0.047} \cdot K_1$		0.99	1.9
$F_f = 1154 \cdot a^{0.838} \cdot f^{0.391} \cdot v^{-0.157} \cdot K_2$		0.93	3.9
$F_p = 822 \cdot a^{0.589} \cdot f^{0.644} \cdot v^{-0.052} \cdot K_3$		0.93	3.7
Techniques	K_1	K_2	$K_{,3}$
Conventional	1	1	1
MQL	0.99	0.96	1.02

Modelling of cutting force for different techniques of CLF dosing using regression analysis was done. The developed models are presented in Table 7, where the influential factors represented by the corresponding coefficient *Ki*. Developed regression models have error less than 4%, which indicates the high accuracy of the model. The applying MQL technique reduces the energy consumption compared to the conventional lubrication technique. MQL technique should be favoured in highly productive processes.

Often, multiple regression analysis is not suitable for the modelling of complex processes, which depends on a many number of factors. For modelling of such processes a large number of experimental data are needed. In our study ANN technique was applied. For this technique a special module Neural Toolbox in the software package MATLAB, is used. Modelling with ANN was conducted using a model of two-layer neural network with forward propagation.

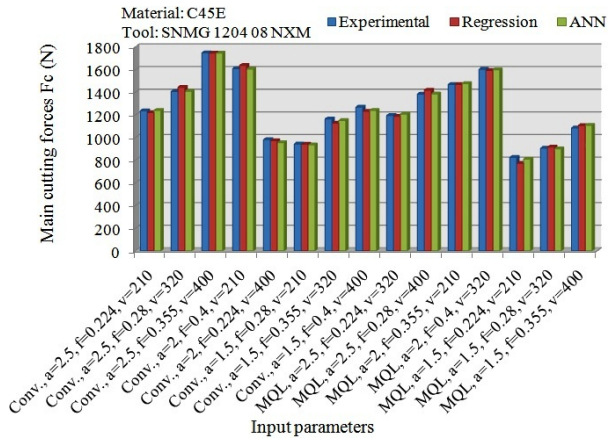

Figure 20. Output values of the main cutting force from regression model and ANN model

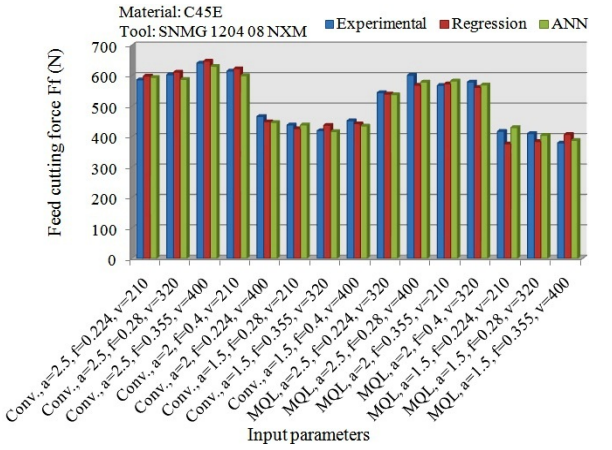

Figure 21. Output values of the feed cutting force from regression model and ANN model

Figures 20, 21 and 22 give the measured and predicted values for all cutting forces respectively. The results of predicting with the model based on ANN show that the developed models can be used for modelling the cutting force, although the set of learning, validation and testing include a relatively small number of combinations of input and output values. In order to analyse the accuracy of the multiple regression model the output values of the model are also shown on the same chart (Table 7).

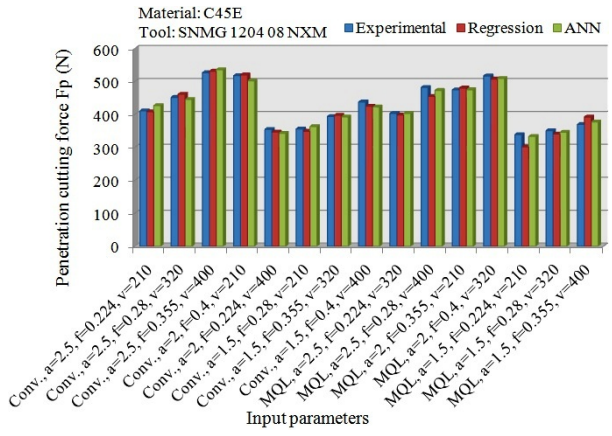

Figure 22. Output values of the penetration cutting force from regression model and ANN model

From the analysis of the diagram it can be concluded that the output values of both types of model correspond to experimental values. Mean relative error of predicted values for forces F_c, F_f and F_p in the model based on ANN is 1.01%, 2.24% and 1.71% respectively, while for regression model error is 1.85%, 3.55% and 2.92% respectively.

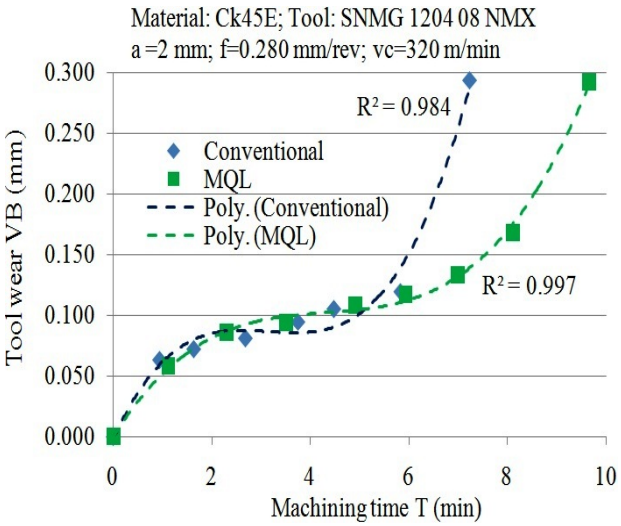

Figure 23. Modelled curves of tool wear for different lubrication technique in machining steel C45E

Modelling of tool wear was performed with a third order polynomial function. It can be concluded from Fig. 23 that matching of output values of model with the experimental values is excellent.

The parameters of the surface roughness R_a and R_y were modelled with linear function depending on the machining times and depending on the tool wear using regression analysis.

Table 8. Models of surface roughness in dependence of tool wear for different lubrication techniques

Material: C45E; a = 2.0 mm; vc = 320 m/min Tool: SNMG 1204 08 NXM	
Conv.	$R_y = 15.15 \cdot VB + 1.45 + (f^2 \cdot 10^3/(8 \cdot r))$
MQL	$R_y = 30.50 \cdot VB + 1.18 + (f^2 \cdot 10^3/(8 \cdot r))$

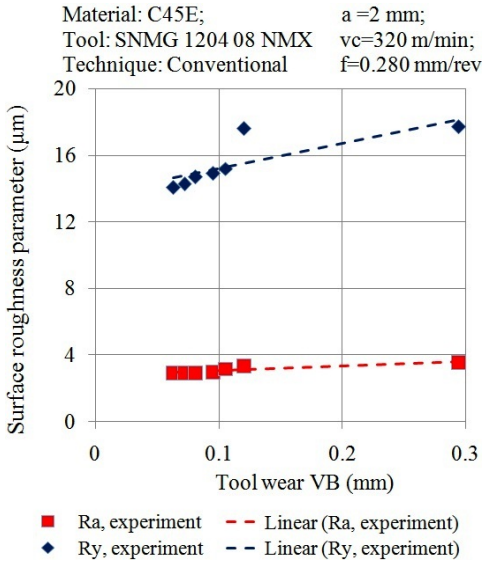

Figure 24. Models of parameters roughness for the conventional technique of CLF dosing

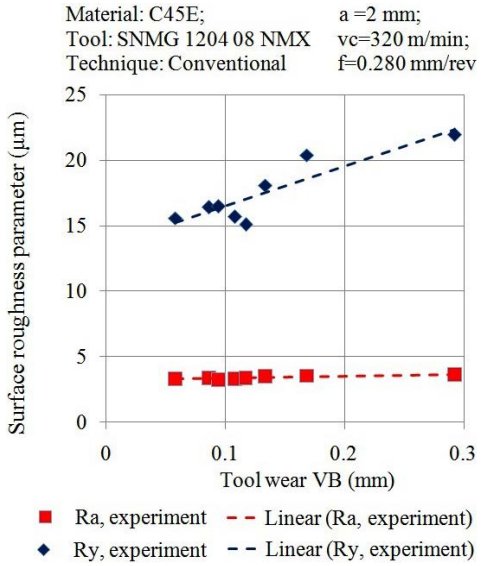

Figure 25. Models of parameters roughness for the MQL technique

If the analysis is carried out from the aspect of materials machinability, R_y is a more relevant factor than R_a, because parameter R_y indirect indicator of process condition and a direct indicator of quality as well (Fig. 24 and 25). R_y models based on regression analysis are presented in the form of the function of tool wear VB, feed f and the radius of the tool tip r for both CLF dosing techniques. The second part of this function is taken from the known empirical expression for the theoretical level of roughness.

Comparison of material machinability was made for both lubrication techniques under consideration. Machinability index of i-th material in regard to referent material is defined as:

$$I_i = \left(p_i / p_r\right)^{\pm 1} \cdot 100\% \qquad (1)$$

where is I_i machinability index of i-th material, p_i parameter value accepted for machinability evaluation of i-th material, p_r parameter value accepted for machinability evaluation of referent material.

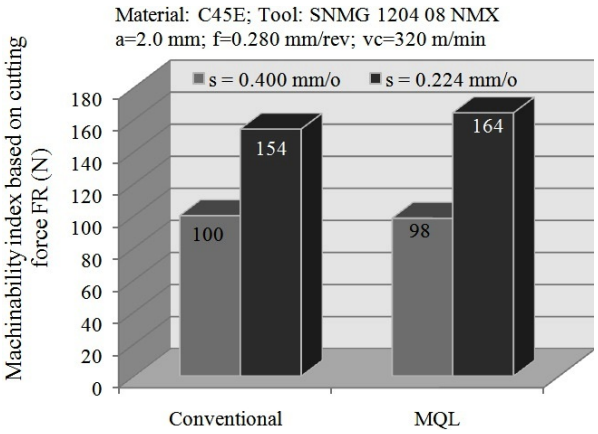

Figure 26. Values of machinability index based on energy aspect

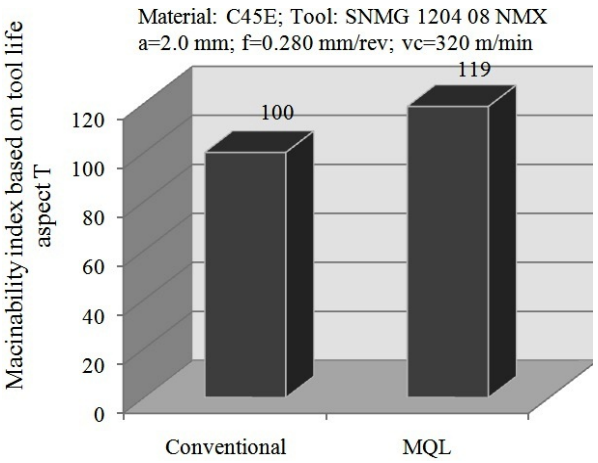

Figure 27. Values of machinability index based on the tool life aspect

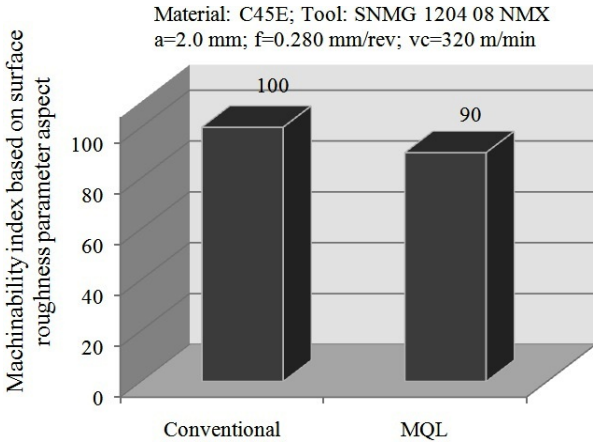

Figure 28. Values of machinability index based on surface roughness aspect

Exponent of ratio p_i/p_r has value of +1 in case that increase of chosen parameter has positive effect on machining process development; otherwise it is a -1 if effect is negative. Results of

comparison from economic, energy consumption aspect and the aspect of quality of machining are presented in figures 26, 27 and 28.

5. CONCLUSION

Machinability is very important category in the industry. Based on experimental research and using the novel model, machinability of different cooling lubrication techniques can be concluded. Cutting forces, intensity of tool wear and surface roughness were used as the machinability criteria. Analysis shows that turning with MQL is a good alternative for conventional lubrication. It is important for cost of machining and for ecology as well.

Future research will be performed in area of low cost technologies, high productive and hybrid machining processes.

REFERENCES

[1] W. Grzesik: *Advanced machining processes of metallic materials: theory, modelling and application*, Elsevier B. V., Netherland, 2008.

[2] L.G. Globočki: *Metal cutting: theory, modelling and simulation*, (in Serbian), Faculty of Mechanical Engineering , Banja Luka, BiH, 2010.

[3] J. Kopač: *Cutting forces and their influence on the economics of machining*. Journal of Mechanical Engineering, Vol. 48, No. 3, pp. 121-132, 2002

[4] F. Klocke, G. Eisenblatter: *Dry cutting – state of research*, VDI berichte, No. 1399, 1998.

[5] V.N. Gaitondea, S.R. Karnik, P. Davim: *Selection of optimal MQL and cutting conditions for enhancing machinability in turning of brass*, Journal of Materials Processing Technology, Vol. 204, pp 459–464, 2008.

[6] N.R. Dhar, M.T. Ahmed, S. Islam: *An experimental investigation on effect of minimum quantity lubrication in machining AISI 1040 steel*, Inter. Journal of Machine Tools & Manufacture, Vol. 47, pp. 748–753, 2007.

[7] K. Weinert, I. Inasaki, J.W. Sutherland, T. Wakabayashi: *Dry machining and minimum quantity lubrication*, CIRP Annals - Manufacturing Technology, Vol. 53, No. 2, pp. 511 - 537, 2004.

[8] B. Sredanović: *Developed of model for universal material machinability defining based on cutting process parameters*, MSc thesis, Faculty of Mechanical Engineering, (in Serbian), Banja Luka, BiH, 2012.

Serbian Tribology Society

SERBIATRIB '13

13th International Conference on Tribology

Faculty of Engineering in Kragujevac

Kragujevac, Serbia, 15 – 17 May 2013

TRIBOLOGICAL ASPECT OF RUBBER BASED PARTS USED IN ENGINEERING

Dušan Stamenković[1], Milan Nikolić[1], Miloš Milošević[1]
Milan Banić[1], Aleksandar Miltenović[1], Miroslav Mijajlović[1]
[1]University of Niš, Faculty of Mechanical Engineering in Niš, Serbia
dusans@masfak.ni.ac.rs, milan.nikolic.nis@gmail.com, mmilos@masfak.ni.ac.rs, milan.banic@outlook.com, amiltenovic@yahoo.com, mijajlom@masfak.ni.ac.rs

Abstract: *In most of the cases, the friction is considered as a negative side-effect concerning energy loss following every process of the power transmission. However, the friction has significant positive side effects, because it is an indispensable prerequisite for the movement of people, machines, transportation means and others. Efficiency of these movements mostly depends on the friction between rubber and different materials such as metals, concrete, earth, wood, plastic, etc. Certain standards relating to measurement and determination of the friction characteristics of rubber were established. However considering that tribology of the rubber is very complex problem, numerous studies around the world are conducted. This paper gives an overview of some of the existing standards and conducted researches in this area. The paper also provides an overview of theoretical and experimental studies of friction the rubber and the other materials, which are done at Faculty of Mechanical Engineering in Niš.*

Keywords: *coefficient of static friction, rubber, tribology, slip resistance, standards.*

1. INTRODUCTION

Movement can be realized only and merely by the friction, but during a motion, friction permanently causes different kinds of losses (energy dissipation, mass loss, movement loss). Therefore, friction is the process where positive and negative effects manifest both. In a certain situation, a large friction force is required, but in other situation small friction force is required.

Because of that, understanding the tribological interactions between the shoe and the floor materials is important in order to enhance shoe and floor design and to prevent slip and fall accidents during walking.

Since the coefficient of friction measurements were commonly adopted to evaluate slip potentials, it has been found that there were controversies in the interpretation of measurement results. The study [1] was principally focused on broadening the knowledge base and developing new ideas on which improvements in the validity and reliability of slip resistance measurements might be made. To achieve this goal, crucial problems on the current concept of slip resistance measurement were extensively analysed by a tribological point of view where principle of understanding the shoe-floor friction and wear phenomena could be made. Based on this approach, new theoretical models were suggested in paper [1].

This study discussed the limitations of present concept on slip resistance measurements and analysed the seriousness of misinterpretations on slip resistance properties that were mainly caused by over-simplified conceptions on friction phenomena between the shoe heels and floor surfaces. Based on those critical analyses, a new paradigm on friction and wear phenomena between the shoes and floors was proposed for the future researches on the slip resistance measurements.

On the basis of totality of the experimental and the simulation results as well as concepts some recommendations for dealing with the tribology of polymer-based composites – in instruction as well as industrial and research setting – are made in the paper [2].

Advantages and disadvantages of traditional and modern approaches of surface analysis based on concepts of roughness and texture are discussed in the paper [3]. Authors considered that traditional concept of rough surface based mainly on profile parameters is not fully satisfied modern trends in tribology. This paper presents a review of the problems of rough surfaces analysis in their evolution from statistical height and step parameters of profiles to dimensionless and scale invariant representation of surface texture. They concluded that texture analysis can be efficiently applied for solving practical tribological problems in micro/nanoscale.

Paper [4] presents a study on the surface quality pointing out the influence of relative sliding on the topography parameters. A comparative study of the surface topography, obtained by changing a single parameter during the tests, may reveal at least a qualitative influence of this parameter that could be useful for practicians.

The authors in paper [5] investigated the boundary friction model, which is built up by the surface topography. The model contained the effect of boundary film, adhesion, plough and lubrication. Based on the model, a coefficient for weakening plough for the lubrication was proposed. The modified model could fit for the working condition of wet friction elements.

In the paper [6] authors indicate that static friction is necessary for vehicle starting and running and show comparative information of static friction experiment of prismatic steel samples slip and tribology studies of the wheel-rail contact.

The new friction coefficient calculation procedure based on the Molecular-mechanical theory of friction is proposed in the paper [7]. This procedure considers roughness parameters and hardness of contact surfaces, as well as the relationship between the deformation component of the static friction coefficient and the total static friction coefficient determined experimentally for specific tribological conditions. Studied tribological conditions in the research are related to the press fit joints of railway vehicles drive unit components. The proposed model considers experimental research of tribomechanical pairs at which plastic deformations exist in the real area of contact.

A review of standards and methods of slip resistance measuring provided by flooring and footwear suppliers in United Kingdom is presented in paper [8]. It can be seen that a lot of suppliers didn't specify date about the slip resistance of their products.

The lack of international standards for the slip resistance of ceramic tiles is stated in the paper [9]. The paper considers recent and current potential developments in the international standardization of slip resistance. It identifies some limitations of wet barefoot ramp test, and suggests that changes should be made.

The paper [10] researches the friction between rubber and metal which can significantly influences damping characteristics of the rubber-metal springs. In the framework of the experimental research that has being conducted the coefficient of the static friction between the rubber and metal has been established in different contact conditions. Moreover, compressions of rubber-metal springs are also performed and force-deflection diagrams are recorded. In this way, the mutual influence of the static friction between the rubber and the metal pad and the accumulated/absorbed energy within a rubber-metal spring is analyzed.

Tribological approach of the contact footwear-floor is the subject of research that has started at Faculty of Mechanical Engineering in Niš. Experimental research of static friction of footwear rubber samples and different types of floor materials is presented in this paper.

2. STATIC FRICTION

In order to achieve vehicle wheel turning on the road, it is necessary to have the drive torque as well as a force of resistance in the wheel-road contact. Similarly, in order to make walking on the floor possible, a drive force delivered by the legs and a force of resistance in the footwear-floor contact are needed. This resistance is the static force of sliding friction. So, wheel rolling is achieved through the static friction force of sliding. Likewise, pedestrian can walk with the help of static friction force.

Friction represents a resisting force that opposes relative motion of bodies' surfaces that are in contact. According to the state of moving, i. e. to the resultant tangential force that induces moving there are two types of friction. The static friction or the stationary state friction that exists when the resultant tangential force is lower than the summation of all resistances that oppose moving and the kinetic friction or the moving state friction when the force that induces moving is greater than the summation of resistant forces

The diagram *F(s)* in Fig. 1 shows that the force increases from the point O to the point A, where the maximal value of the force is achieved. That is the static friction force (*Fs*). The static friction force represents a maximal tangential resistant force that acts during so called boundary relative displacement. Boundary displacement (presliding movement) can be defined as a micro moving of frictional surfaces that goes before visible or macro moving of surfaces in mutual contact (the part OA

of the graphic in Fig. 1). Futhermore, presliding movement represents a limit up to which the static friction lows between frictional surfaces are valid. After this limit the kinetic friction lows are in action. Therefore, the presliding movement is a period of relative movement characterized by an extensive increase of the reactive force and a small increase of movement. Press fit joints, screw and rivet connections, all types of friction transmitters (variators, belt transmitters, couplers), parking brakes etc. work in the mode of presliding movement.

It can be seen that the force retains the value of the static friction force (*Fs)* for a short time period and then decreases to the value of the kinetic friction force (*Fk)*. This process is followed by an intensive increase of movement.

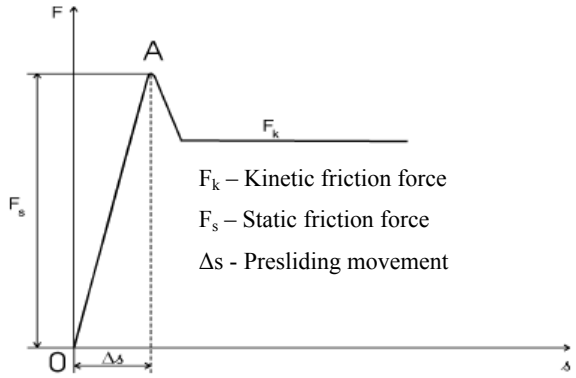

Figure 1. Static and kinetic friction

Under permanent conditions and even for the same material the coefficient of static friction value is not a constant and may vary in a certain range. The alteration of friction coefficient values is mostly stochastic, so one can only speak about the mean values of the friction coefficient.

Friction coefficient values depend on different parameters such as: nature and properties of the used materials, contact pressure value, thickness and type of surface film, contact surfaces roughness, duration of the contact, chemical interaction, presence of external bodies in the contact area, cleanness of contact surfaces, temperature of the surrounding environment, relative humidity, elasticity etc.

3. MEASUREMENT OF SLIP RESISTANCE

Nearly 11,000 workers suffered serious injury as a result of a slip in 2007 in Great Britain [8]. A key element of HSE's (Health and Safety Executive) work to reduce slips and trips is to raise awareness of how slip risks can be controlled through the use of suitable flooring and footwear. Research by the Health and Safety Laboratory has shown that a combination of factors contribute to slip accidents. There are the following influencing factors: floor, contamination, footwear, pedestrian factors, cleaning and environment.

Footwear suppliers use a variety of terms to describe their products, as like as 'slip-resistant', 'anti-slip', 'improving grip performance' etc. and these can often mislead customers. Slip-resistant industrial footwear will normally have been tested according to European standards, but many manufacturers and suppliers do not give helpful additional information, such as the degree of slip resistance and the types of work environment for which their products are most suited.

The aim of the HSE's project [8] was to collect and assess the slips safety information/literature provided by flooring and footwear suppliers in 2008 in Great Britain. A significant proportion of flooring products (55%) did not make any reference to slip resistance or provide any test data. No indication of slip resistance was given for 47% of footwear products.

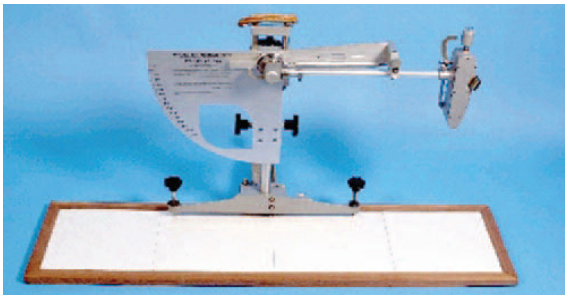

Figure 2. The pendulum friction coefficient test

A review of flooring test data showed that 54% was generated using the pendulum test (Fig. 2), 33% using the ramp test (Fig. 3), 0.2% using roughness measurements and 12.8% was generated using sled-type test methods, which in the opinion of HSE, can provide misleading results in contaminated conditions. The type of test used from footwear suppliers are: RAMP test 46 %, SATRA test 40% and HSL RAMP test 14%.

Figure 3. The ramp friction coefficient test

The information provided by footwear and flooring manufacturers was not satisfactory. Many footwear manufacturers made vague claims suggesting slip resistance and did not provide supporting data. Many flooring manufacturers avoid making reference to slip resistance altogether and information is hard to find.

Recommendation of the HSE project [8] is that it was apparent that many suppliers did not consider slip resistance to be a selling point and did not place significant emphasis on it. Currently, it is very difficult to make comparisons between products due to the number of tests used and specifications quoted. Where test data is provided, very little explanation is given and the layperson could be easily confused or misled. Footwear and flooring suppliers should be influenced to place more emphasis on the slip resistance of their products, and to use more standardized ways of assessing slip resistance; this would allow customers to make comparisons and help them to select the most appropriate product for their needs.

Slip resistance properties of flooring materials and footwear are covered by various standards in Europe. Some of the most common are:

- BS7976 – British standard that describes the specification, operation and calibration of the Pendulum test, used for assessment of floor surface slipperiness under both dry and contaminated conditions.
- DIN51130 - Laboratory based ramp test, using cleated safety boots and motor oil contamination. Results are reported as an R value, on a scale from R9 to R13, with R9 being the least slip resistant.
- DIN51097 - Laboratory based ramp test, using barefoot operators with soapy water as the contaminant. Results are reported as Class A, B or C, with A being the least slip resistant.
- EN13845 - Laboratory based ramp test specifically for resilient floor coverings with enhanced slip resistance. The test uses standardized footwear and soapy water contamination.
- EN13287 - Laboratory based mechanical slip resistance test for safety / occupational footwear. The test uses several surfaces and contaminants to assess footwear.

Because of the nature of complexity and factors involved, the measured coefficient of friction quantities show inconsistencies even as the same shoe-floor combinations are employed. This fact has been recognized as a great concern when different friction testers, sensors and/or protocols are used worldwide.

However, variations of the coefficient of friction results under the same test environments have not received much attention in this research area. Despite of this fact, most slip safety researches have reported that a particular shoe or floor surface resists the movement of a particular floor surface or one's shoe sole across its surface.

4. EXPERIMENTAL RESEARCH OF THE STATIC FRICTION

Slip accidents can happen for a number of reasons: footwear, flooring, contamination and obstacles, cleaning, human factors, environment, etc. But footwear and flooring are the most important for tribological research.

Because of the existence of many different standards and methods for assess the slip resistance, measuring of friction coefficient on tribometer in laboratory condition is very useful.

Footwear is produced most from rubber, because of its properties. The rubber is elastic, soundproof and it has low gravity density and good tribological properties.

Experimental determination of the static friction coefficient between samples of footwear soles and flooring were held on Mechanical Faculty in Niš. Static friction force can be measured only in the moment of sliding beginning for the reason that in next moment, after sliding start, this values falls on friction kinetic force value.

Experimental model for establishing static friction coefficient, projected for this investigation and which will be used for further investigation, is shown in Fig. 4.

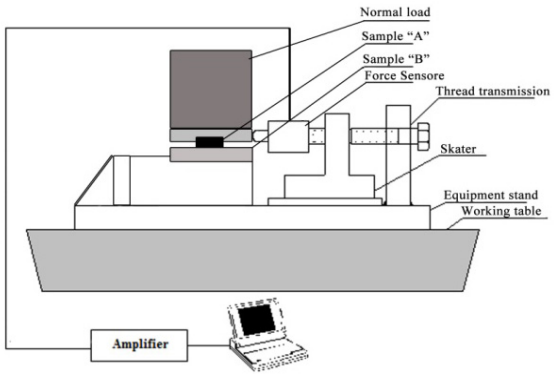

Figure 4. Schematic review of device for measuring static friction force

Measuring process was done so that by the turning the screw skater start sliding and force sensor fixed on skater pushes sample A (footwear sole sample). Sample A starts to slide on the sample B that is fixed in the base of device and pushing force is measured. Static friction force is established in the moment of sliding start.

Measuring system with experimental samples is shown in Figure 5.

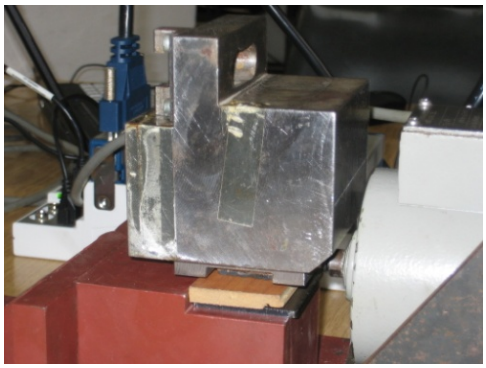

Figure 5. Measuring system

Samples used in this experimental investigation are with following characteristics:

- Footwear sole samples (sample A) are prism shaped and formed of soles cutout glued on a piece of chipboard. Nominal contact area is 30mmx30mm=900mm^2. For this investigation there are four sole samples: new rubber with relief, worn (used) rubber with texture, new flat rubber and leather.
- For floor samples (sample B) are used plates of laminate, rough ceramic tile and smooth ceramic tile. Dimensions of plates are 60mmx75mm according the measuring device.

Before testing all contact surfaces are cleaned with acetone.

Floor samples surface roughness was measured by roughness measuring device Mitutoyo Surftest SJ-301. Roughness measuring gave the following results:

1. Laminate plate: Ra=0,9µm, R_{max}=4,98µm, R_z=3,25µm,
2. Rough ceramic tile: Ra=12,85µm, R_{max}=59,04µm, R_z=43,93µm,
3. Smooth ceramic tile: Ra=0,53µm, R_{max}=3,44µm, R_z=2,24µm.

Measurements are done with weight (normal force) variations so that contact pressure was: 45kPa, 79kPa and 142kPa.

Force sensor is produced by HBM, maximum force which can be measured is 500N and sample rate is 100Hz. For each contact combination five measuring were done.

Contact surfaces are prepared in three ways: dry condition, wet condition and soap lubricated.

Tables 1, 2 and 3 show measuring results for static friction coefficient for different material combination and lubricating. Marks in the tables are: U1-new rubber with relief, U2-worn rubber with texture, U3-new flat rubber, U4-leather, P1-laminate plate, P2-rough ceramic tile and P3-smooth ceramic tile.

Table 1. Static friction coefficient of footwear sole samples and laminate floor sample (P1)

μ	U1/P1	U2/P1	U3/P1	U4/P1
dry	0,54	0,83	0,96	0,52
wet	0,39	0,66	0,67	0,65
soap	0,43	0,60	0,46	0,70

Table 2. Static friction coefficient of footwear sole samples and rough ceramic tile sample (P2)

μ	U1/P2	U2/P2	U3/P2	U4/P2
dry	0,52	0,47	0,54	0,63
wet	0,46	0,40	0,58	0,79
soap	0,38	0,54	0,39	0,77

Table 3. Static friction coefficient of footwear samples sole and smooth ceramic tile sample (P3)

μ	U1/P3	U2/P3	U3/P3	U4/P3
dry	0,25	0,69	0,44	0,47
wet	0,19	0,53	0,42	0,52
soap	0,11	0,22	0,13	0,50

Performed experiment shows that values of static friction coefficient are very unpredictable and random. Static friction coefficient of leather sample (U4) with presence of lubricants (water, soap) increases that is opposed of rubber samples with lubricants where coefficient of friction decreases. Very interesting results were in combination of rubber sample with relief (U4) and smooth ceramic tile, respectively measured static friction coefficient is very small (0,25 in dry condition until 0,11 lubricated with soap). That can be explained with small real contact area. Also, it can be conclude that for smooth ceramic tile coefficient of static friction is smallest for each sample.

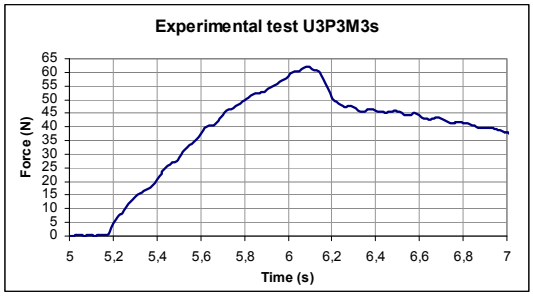

Figure 6. Friction force-time diagram for flat rubber and smooth ceramic tile (normal load 131N, dry condition)

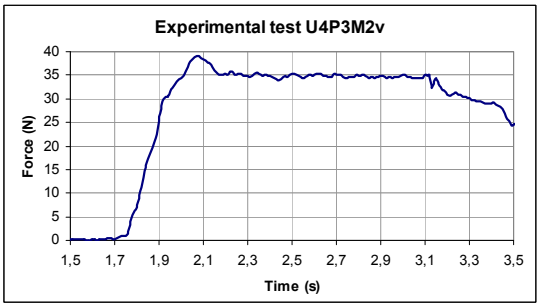

Figure 7. Friction force-time diagram for leather and smooth ceramic tile (normal load 72,28N, wet condition)

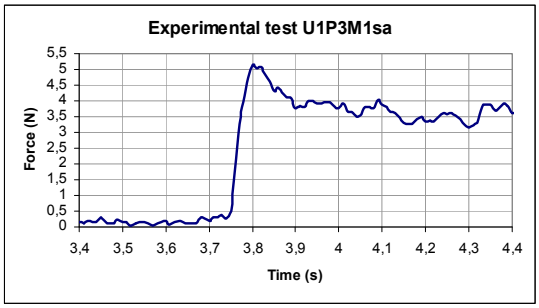

Figure 8. Friction force-time diagram for new rubber with relief and smooth ceramic tile (normal load 41,82N, soap condition)

Figures 6, 7 and 8 give the representative examples of recorded friction force in performed experimental investigation.

On the presented diagrams can be seen static and kinetic friction force when footwear sole samples slides over floor samples. Vertical axis represents force in Newtons and horizontal axis time in seconds. Diagrams show that friction force increases from zero value to the maximum value that is static friction force, and then falls to the kinetic friction force.

5. CONCLUSIONS

Due to the lack of static friction force in contact footwear-floor is often the reason for falls and injuries it is necessary to pay more attention in footwear and floor production in part of tribological properties. Certain standards about the slip resistance assessing are established in EU. Up to now in Serbia there isn't enough professional interest for this area, and it is left to the producers of footwear and floor.

Because of the existence of many different standards and methods for assess the slip resistance, measuring of friction coefficient on tribometer in laboratory condition is very useful.

According the importance of this problem and experience in earlier studies in the field of static friction, at Faculty of Mechanical Engineering in Niš is initiated research with the aim to determine tribological properties of rubber produces as footwear.

In that sense measurement of static friction coefficient between footwear sole and floor samples was performed. For that purpose it was designed measuring device for static friction estimation. Measuring results show that static friction coefficient is stochastic and unpredictable.

In further investigation it is necessary to improve measuring system and include more samples. Some samples should be industrial shoes and floors, tiles on public walkways, white stripes on pedestrian crosses the street and material other risky points where falls and accidents can happen.

REFERENCES

[1] I.J. Kim, H. Nagata: *Research on Slip Resistance Measurements — A New Challenge*, Industrial Health 46, pp.66–76, 2008.

[2] W. Brostow, V. Kovačević, D. Vrsaljko, J. Whitworth: Tribology of polymers and polymer-based composites; Journal of Materials Education 32, pp. 273 – 290, 2010.

[3] N. K. Myshkin, A.Ya. Grigoriev: *Roughness and Texture Concepts in Tribology;* Tribology in Industry Vol. 35, No. 2; p.p. 97-103; 2013.

[4] N. Diaconu, L. Deleanu, F. Potecasu, S. Ciortan: *The Influence of the Relative Sliding on the Surface Quality*; Tribology in industry, Volume 33, No. 3, p.p.110-115; 2011.

[5] W. Yanzhong , W. Bin , W. Xiangyu: *Wet Friction-Elements Boundary Friction Mechanism and Friction Coefficient Prediction*; Tribology in Industry Vol. 34, No. 4; p.p. 198-205; 2012.

[6] M. Đurđanović, D.Stamenković: *Static friction causes movement,* SERBIATRIB '07 – 10th International Conference on Tribology, p.p.. 215-218, Kragujevac 2007.

[7] D. Stamenković, M. Milošević, M. Mijajlović, M. Banić: *Estimation of the static friction coefficient for press fit joints*; Journal of the Balkan Tribological Association 17, pp. 341-355, 2011.

[8] M. Liddle: *Assessment of slips safety information/ literature provided by flooring and footwear suppliers,* RR747 Research Report, Health and Safety Executive, 2009.

[9] R. Bowman: *Slip resistance testing - Zones of uncertainty*, Bol. Soc. Esp. Ceram. 49, pp.227-238, 2010.

[10] D. Stamenković, M. Milošević: *Friction at rubber-metal spring,* SERBIATRIB '09 – 11th International Conference on Tribology, pp. 215-219, Beograd 2009.

[11] HSE: *Assessing the slip resistance of flooring,* A technical information sheet published by the Health and Safety Executive, 2012.

[12] D. Stamenković, M. Milošević: *Experimental investigation of Static Friction, International Conference* "POWER TRANSMISSIONS '03" Section III "Experimental Investigations and Applications", pp. 67-69.Varna Bulgaria, 2003.

Serbian Tribology Society

SERBIATRIB '13

13th International Conference on Tribology

Faculty of Engineering in Kragujevac

Kragujevac, Serbia, 15 – 17 May 2013

POSSIBILITY OF REPLACING THE CHORINATED PARAFFINS IN METALWORKING FLUIDS

Marica Dugić[1], Branka Kojić[1], Pero Dugić[1], Goran Dugić[1]
[1]Oil Refinery Modriča, Bosnia and Herzegovina
majad@modricaoil.com, branka@modricaoil.com, pero@modricaoil.com, gdugic@modricaoil.com

Abstract: *All components that are used for neat oil formulations for metalworking operations belong to group of chemicals that, because of its direct application, can have a big influence on the environment and especially on human health.*
With time, metalworking operations become more complex and demanding. New materials with various compositions are processed, and they demand metalworking fluids with improved antiwear properties and that provide extreme load-carrying capabilities.
Exactly these additions, known as EP additives, that had been until recently based on chlorinated paraffins, are a group of chemicals that need to be replaced as soon as possible with a components that are environmentally acceptable.
In this paper, in laboratory conditions, we investigated synthetic polymeric esters, as one of the possible substitute for chlorinated paraffins, in several neat oil formulations, which are used for various metalworking operations. From the above comparative results of analysis results it can be concluded that synthetic polymeric esters can serve like an adequate substitute for metalworking fluids which are designed for easy operations.

Keywords: *neat metalworking oil, environmentally acceptable lubricants, EP additives, chlorinated paraffins, synthetic polymeric esters.*

1. INTRODUCTION

Formulation of industrial lubricants, depending of performance that lubricants must have, requires a lot of different types of additives. Their role in the lubricants is to improve certain characterisics of lubricant or to give the lubricant brand new performance. Usual types of additives are: corrosion and oxidation inhibitor, antifoaming, viscosity index modifier, pour point depressant, antifriction and antiwear additive and additives that allow carrying heavy loads, usually called EP additives.

That large number of additives in particular lubricants formulation lead to a questions not only about the effect of additives in the lubricants, but also the influence of one additive to the another.

Complex testing of antagonism and synergism of all components on particular characteristics in different lubricant formulations are being made. It can sometimes induce a big problem, especially in recent times, when many components, due to unfavorable effect on humans and environment, are being completely banned for usage in lubricants, or their allowed dosage is greatly reduced.

Research of new environmentally acceptable components and their influence in the lubricant has started many laboratory tests and in the same time tests of their applications in service.

Analyzing the results of one survey, which the editorial of scientific magazine Tribology & Lubrication Technology made, on the question at which additive has the most influence on performance characteristics of lubricants, showed that the answer was EP additives. [1]

The subject of investigation in this paper is testing the antiwear and EP characteristics of different formulations of neat oil for metalworking operations, which in its composition have EP additives. Exactly this extras, known as EP

additives, that had been, until recently, based on chlorinated paraffins are a group of chemicals that needs to be replaced as soon as possible with components that are environmentally acceptable.

In this paper, in laboratory conditions are prepared samples of several different formulation of neat oil which are intended for different metalworking operations. Among the other standard characteristics, are also tested antiwear and EP characteristics of samples containing synthetic polymeric esters, as one of the possible replacement for chlorinated paraffines. The results of analysis are compared with the results of the samples that are formulated with chlorinated paraffins.

2. EXTREME PRESSURE (EP) ADDITIVES

Primary functions of metalworking fluids are heat control, cooling the surfaces of tools and parts processed in the cutting zone and lubrication and enduring the extreme pressures and heavy loading during processing. It is particularly important in order to achieve desired size, shape and degree of surface processing of workpiece, and longer tool lifetime. Removal of cuttings from operating zone is considered as secondary role, but it is very important and it needs to be done continually. Corrosion protection of tools, machines and workpieces is also important. Freshly processed metal have tendency to corrode faster during machine operations, than protected metal.

For metalworking it isn't enough to use only one kind of lubricant, but every applicable process requires specially formulated oil. In order to emphasize differences in characteristics of certain lubricants, in this case, of neat oils, and point out the complexity of choosing the basestocks for formulations, we start with metalworking processes, which are:

- Removal (formation of cuttings), mostly named cutting operations
- Shaping: pressing, rolling, drawing...
- Treating (surface strengthening): quenching
- Protection (corrosion protection: temporary with interprocess, during transport...)

Cutting operations can be considered as the most common in metalworking operations. Basic methods of metalworking cutting are:

- Scraping
- Planning (during operation it is identical to scraping, but the process is discontinuous
- Drilling (beveling, widely considered: drilling, widening, reaming)
- Milling (oblique and orthogonal cutting)
- Grinding (removal of thin layer of material during the finest final processing)

Operations of metal forming, such as: pressing**,** rolling, drawing (wire, profiles) are also very used and are considered as demanding.

2.1. EP additives and their role in metalworking fluids for heavy operations

Traditional additive packages that are added to neat metalworking oils in the boundary lubrication regime remain on the metal surfaces and they cannot prevent increased friction, wear and the damage to the tool. EP additives are needed to enable the application in the more difficult conditions of elevated temperatures and pressures.
The main groups of EP additives are:

1. Chlorine compounds
2. Phosphorus additives
3. Sulphur additives
4. Prebasic sulfonates (calcium and sodium)

The first three EP additives are activated in reactions with the metal surfaces in a certain temperature range. Chlorinated additives are activated at temperatures between 180 i 420 °C, phosphorus are activated at higher temperatures and sulphur at even higher temperature range which ends at 1000 °C. In the reaction with the metal surface these three types of additives produce Fe-chloride, Fe-phosphide and Fe-sulphide, which serve as a barrier to reduce friction and wear and elimination of welding.

The fourth EP additive, prebasic sulfonate, act by other mechanisms, whose process doesn't depend on temperature, and operate below 500 °C.

In each category of EP additives there are several different types. The main used chlorinated additives are chlorinated paraffin, or even called a chlorparaffine. In case of phosphorus compounds, the most common type is phosphate ester. With suphur additives those are: sulphurated fats, sulphurated esters, sulphurated hydrocarbons and polysulphide, which differ in the concentration of free (active) sulphur.

In order to select EP additive in formulations for metalworking fluids, one must be familiar with the applications itself, machining operations, state of the tools and to have defined expected performance. One of the most important information is the possibility of early cancellation of tools before the operation has reached the right temperature for EP additive to become activated. Besides the choice of EP additive, it is necessary to know the synergism with other additives included in the formulation, and also to reduce undesirable interactions which can bring to instability of product using certain combination (foaming, sludge).

The greatest influence on the formulation of neat oils for heavier operations was limiting the chlorine content. For manufacturers of these substances it was hard task to find an adequate replacement in a very short period of time.

Many studies have been done on the impact of chlorinated paraffins on the environment, and it reached its expansion in mid-nineties.

Chlorinated paraffines are divided in three classes based on the chain lenght:

- Short-chain, C_{10-13}
- Medium-chain, C_{14-17}
- Long-chain, C_{18-30}

The most commonly used chlorinated paraffins were with 35-70 % of chlorine and with the hydrocarbon base with C_{10-20}.

These studies have shown that short-chain chlorinated paraffins have the biggest potential risk of influence on the environment especially if they are not handled properly when they become waste material.[2]

In summary, therefore, the lists of undesirable chemicals in the formulations of many metalworking fluid include one of the most commonly used EP additives, chlorinated paraffin.

Chlorine in lubricants, at elevated temperatures and pressures reacts with hydrogen, and forms hydrogen chloride and dioxine, and dissolving hydrogen chloride in water forms hydrochloric acid.

A special problem brings the impossibility of rerafination of used products that contain chlorine, since chlorine acts a catalityc poison. If this products are burned, incomplete combustion also forms hydrochloric acid, which comes in environmentally round cycle and leads to increased environmental pollution. [3]

3. EXPERIMENTAL PART

Because of all findings on harmfulness of chlorparaffins, new components are being researched, which might be more ecologically acceptable, with function to serve as a replacement for chlorparaffins in all places where severe metalworking opperations are, and where it was, until recent, only EP additive.

A new generation of EP additives has been developed, that are, by their chemistry, compunds of sulphur and phosphorus, and new generation of synthetic esters is currently being tested in severe metalworking fluids. A special focus is on synergism of synthetic esters and sulphur based additives.

For research of antiwear and EP characteristics of formulations that have chlorparaffin replaced with two synthetic esters, we chose formulations for vertical broaching, drawing and final finishing operations, like fine stamping.

Characteristics of synthetic ester that were used in tested formulations are listed in Table 1. In Table 2. are listed characteristics and methods used for metalworking samples testing for all three metalworking operations. [4]

Table 1. Characteristics of syn ester 1 i 2.

Characteristic	Syn ester 1	Syn ester 2
Appearance	Hazy. Light amber	Slightly hazy. Light amber
Specific gravity @ 25 ^{0}C	1,00	1,01
Acid number, mg KOH/g	20	<5
Viscosity (cSt) at 100 ^{0}C	244	883
Viscosity index	203	267
Iodine value	<2	<5
Molecular Weight (approx.)	25 000	160 000

Table 2. Characteristics and testing methods.

Characteristic	Method	Unit
Viscosity at 40 °C	BAS ISO 3104	mm^2/s
Acid number	ISO 6618	mg KOH/g
Cu corrosion	ASTM D 130	-
Wear	ASTM D 2266-01	mm
Welding point	ASTM D 2596-98	N

Table 3. Testing results of samples for vertical broaching operations that contain chlorparaffine.

Neat oil for vertical broaching				
Sample	1	2	3	4
Chlorinated paraffine, %m/m	-	10	20	30
Additive A, m/m	4	4	4	4
Base oil, % m/m	96	86	76	66
Results				
	1	2	3	4
Wear, 40 kg, mm	0,97	0,84	0,89	**1,08**
Welding point, N	4200	3000	5500	**7000**
V at 40 ^{0}C, mm^2/s	23,14	29,58	35,12	37,22
Cu corrosion	4a	4a	4a	4a
Acid number, mg KOH/gr	0,86	0,82	0,83	0,80

As a replacement for chlorparaffin for broaching operations, syn ester 1 was chosen, that was used to prepare samples with ester concentration of 2, 6 and 10 % (Table 4). Because increased concentration of syn ester 1 didn't lead to increased welding point (Figure 3) which was a goal for this research, we gave up from further research of using this syn ester type for these kinds of broaching. Formulation of these samples contained additives based of active sulphur, but beside lower diameter of wear in wear test, welding points remained much lower than with samples that had chlorparaffin. Testing results of samples for broaching operations that contain chlorparaffin are listed in Table 3, and ones containing syn ester are in Table 4.

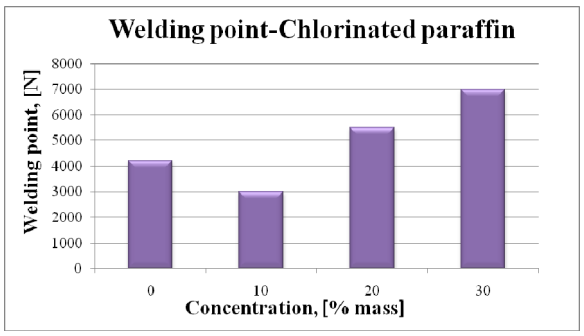

Figure 1. Test results for samples of welding points for vertical broaching operations with different concentrations of chlorparaffine.

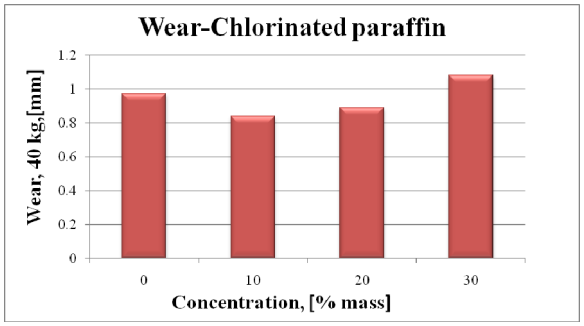

Figure 2. Test results for samples of wear scar for vertical broaching operations with different concentrations of chlorparaffine.

In Figure 1 are shown welding point values in comparison to increase of chlorparaffins content, were broaching operation require chlorparaffins content of up to 30% in order to achieve welding point of 7000 N, which will provide good processing.

In Figure 2 are shown wear diameter values compared to chlorparaffin content. Diameter wear test values in broaching opereations are not so important, welding point values.

Table 4. Test results of samples for vertical broaching operations which formulation contains Syn ester 1.

Neat oil for vertical broaching				
Sample	1	2	3	4
Syn ester 1 % m/m	-	2	6	10
Additive A,% m/m	4	4	4	4
Base oil, % m/m	96	94	90	86
Results				
	1	2	3	4
Wear, 40 kg, mm	0,96	0,76	0,61	**0,67**
Welding point, N	3800	4000	**4800**	**4800**
V at 40 ^{0}C, mm^2/s	34,47	29,85	31,58	37,83
Cu corrosion	4c	3b	3a	3b
Acid number	0,81	1,85	3,95	6,21

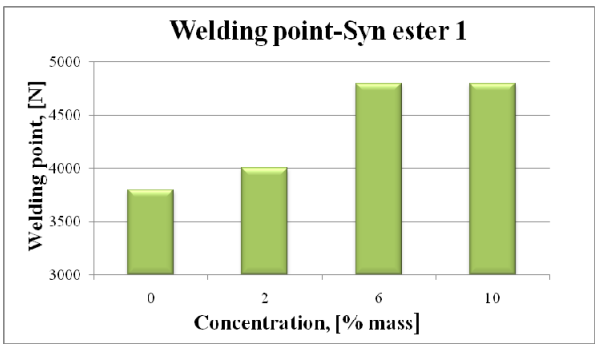

Figure 3. Test results for samples of welding points for vertical broaching operations with different concentrations of Syn ester 1.

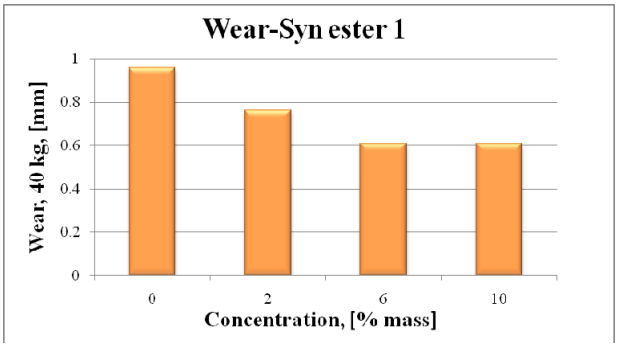

Figure 4. Test results for samples of wear scar for vertical broaching operations with different concentrations of Syn ester 1.

With Syn ester 1 are prepared samples for fine stamping operations, whose test results are compared with the classical formulations containing optimal concentration of chlorinated paraffine to meet the performance which this operation demands. Test results of welding points (Table 5. and Figure. 5.) shows that nor with the maximal concentration of Syn ester 1 do not achieve satisfactory results. Because of that, samples with Syn ester 2 are prepared where test results of welding point has shown that nor with it do not achieve the result which in practical conditions could meet all expected performance. (Table 6. and Figure 7.)

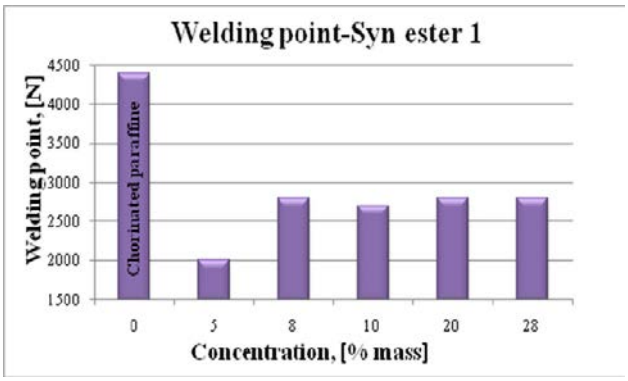

Figure 5. Test results for samples of welding points for fine stamping operations with different concentrations of Syn ester 1 and classical formulation with chlorparaffine.

Table 5. Test results of samples for fine stamping operation whose forrmulation contains chlorparaffine (Sample 1) and Syn ester 1 (2-6).

Neat oil for stamping						
Sample	1	2	3	4	5	6
Syn ester 1, % m/m	-	5	8	10	20	28
Hlorparafin	28	-	-	-	-	-
Additive package, % m/m	4	2	2	2	2	2
Base oil, % m/m	68	93	90	88	78	70
Results						
	1	2	3	4	5	6
Wear, 40 kg, mm	0,71	0,42	0,40	0,42	0,41	0,41
Welding point, N	**4400**	2000	280	2700	2800	2800
V at 40 ^{0}C	89,2	74,8	85,2	89,38	97,7	106,5
Cu corrosion	1a	1a	1a	3a	1a	3a
Acid number	1,46	5,35	6,62	7,90	13,4	18,16

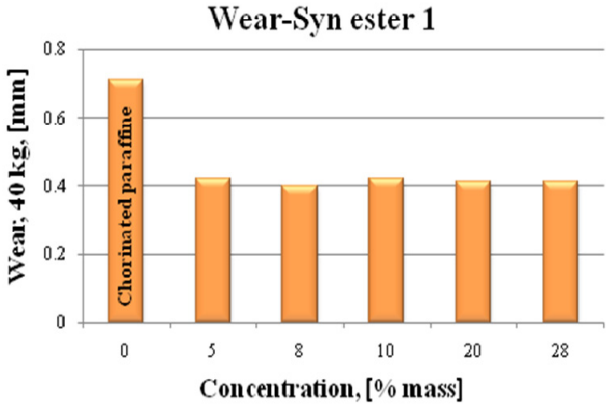

Figure 6. Test results of wear diametar with samples for stamping operations with different concentrations of Syn ester 1.

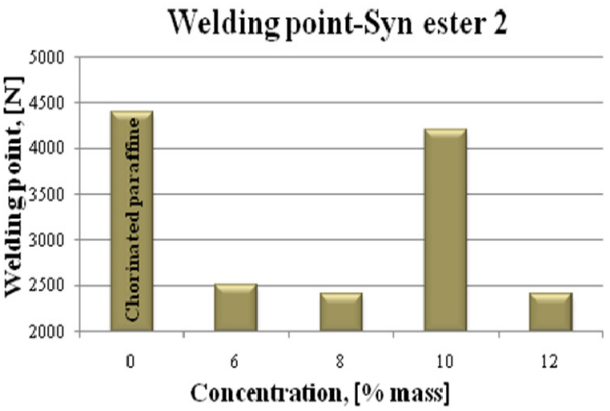

Figure 7. Test results of welding points with samples for stamping operations with different concentrations of Syn ester 2 and classical formulation with chlorparaffine.

For steel profile drawing operations there is formulation with the optimal amount of chlorparaffins and additive packages, which completly satisfies all performance demands for that operation. With Syn estrer 2 optimal quantity of additive package there is a formulation whose test welding results are close to those with chlorparaffin. (Table 7. and Figure 9.)

Table 6. Test results of samples for fine stamping operation whose forrmulation contains chlorparaffine (Sample 1) and Syn ester 2 (2-5).

Neat oil for stamping					
Sample	1	2	3	4	5
Syn ester 2, % m/m	-	6	8	10	12
Hlorparafin	28	-	-	-	-
Additive package, % m/m	4	2	2	2	2
Base oil, % m/m	68	92	90	88	86
Results					
	1	2	3	4	5
Wear, 40 kg, mm	0,71	0,45	0,47	0,5	0,45
Welding point, N	4400	2500	2400	4200	2400
V at 40 ^{0}C, mm^2/s	89,1	89,91	95,36	96,33	98,99
Cu corrosion (3 h, 100 ^{0}C)	1 a	1a	1a	1a	1a
Acid number	1,46	4,45	5,06	5,69	6,35

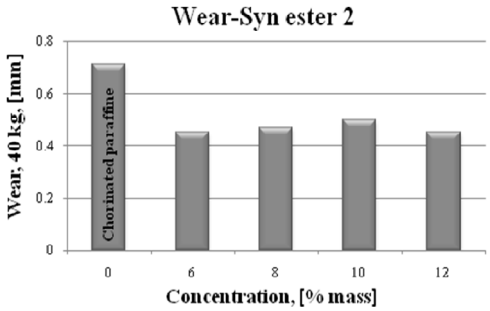

Figure 8. Test results of wear diametar with for stamping operations with different concentrations of Syn ester 2 and classical formulation with chlorparaffine.

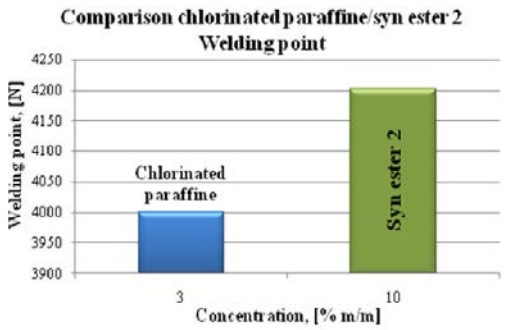

Slika 9. Test results of welding points with samples for drawing operations with classical formulation with chlorparaffine and Syn ester 2.

Table 7. Test results of oil samples for drawing operations with classical formulation with chlorinated paraffine and Syn ester 2.

Neat oil for drawing			
Sample	1	Sample	2
Chlorinated paraffine, % m/m	3	Syn ester 2, % m/m	10
Additive package, % m/m	18	Additive package, % m/m	7
Base oil, % m/m	56	Base oil, % m/m	73
Vegetable oil, % m/m	23	Vegetable oil, % m/m	10
Results			
	1		2
Wear, 40 kg, mm	0,44	Wear, 40 kg,mm	0,35
Welding point, N	4000	Welding point,N	4200
V at 40 ^{0}C, mm^2/s	44,26	Vat 40 ^{0}C, mm^2/s	40,02
Cu corrosion (3 h, 100 ^{0}C)	3a	Cu corrosion (3 h, 100 ^{0}C)	1b
Acid number, mg KOH/gr	4,67	Acid number, mg KOH/gr	7,81

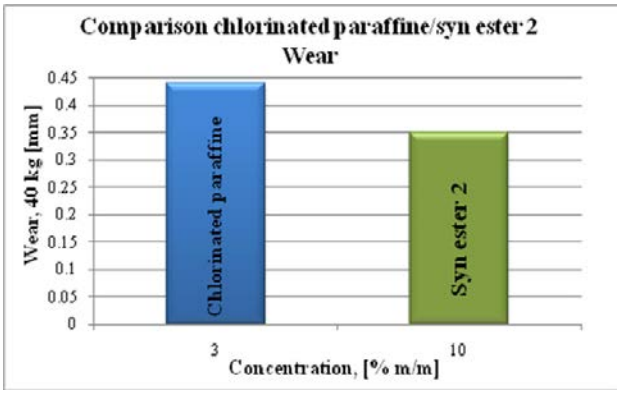

Figure 10. Test results of diameter wear with samples for drawing operations with classical formulation with chlorparaffine and Syn ester 2.

4. CONCLUSION

Test results of samples of neat oils intended for operations: broaching, fine stamping and drawing which are prepared with Syn esters, as a replacement for chlorinated paraffine, shows:

- test result of welding points has showed that at heavy operations such as a broaching with Syn ester 1 they do not achieve good results, although it is attempted to use synergistic effect of esters and additives with active sulphur.

- with stamping operations, which is also considered as heavy, welding points test showed that with two different formulated Syn estes it is impossible to achieve good results, which will also affect application conditions

- based on test results for steel profiles drawing operations, one can conclude that Syn ester 2 can be used for formulations intended for that operations, with reduced quantities of other additives.

This is the start of one comprehensive research, in laboratory and application conditions, that are being done with additive manufacturers. Test results shows that it is hard to achieve replacement for chlorparaffins in formulations of heavy metalworking operations, like broaching, deep drilling, stamping and others.

Constant arguing about usage of chlorparaffins and their allowed chain length, confuse both users and manufacturers. But it initiated many studies regarding that problematic and efforts to find adequate replacement for chlorparaffins, as soon as possible.

REFERENCES

[1] N. Canter: *Special Report: Trends in extreme pressure additives*, Tribology & Lubrication Technology, September 2007., pp.10-17

[2] T. Kelley, R. Fensterhein, A. Jaques : "Voices & Views", *Chlorinated Paraffins*, Vol.59, No.4, April 2009.

[3] *L. Rudnick, "Syntetics, Minerals oils, and Bio based Lubricants", 2006*

[4] Internal documentation of additive manufacturer

Serbian Tribology Society

SERBIATRIB '13

13th International Conference on Tribology

Faculty of Engineering in Kragujevac

Kragujevac, Serbia, 15 – 17 May 2013

QUALITY OF PLASMA CUTTING

Bogdan Nedić [1], Marko Janković[2], Miroslav Radovanović[3], Gordana Globočki Lakić[4]

[1] University of Kragujevac, Faculty of engineering, Kragujevac, nedic@kg.ac.rs

[2] Fiat automobili Srbija, Kragujevac

[3] University of Niš, Faculty of mechanical engineering, Niš

[4] Univerzitet u Banja Luci, Mašinski fakultet, Banja Luka, RS, BiH

Abstract: *The plasma arc cutting process severs metal by using a constricted arc to melt a localized area of a workpiece, removing the molten material with a high-velocity jet of ionized gas issuing from the constricting orifice. The ionized gas is a plasma, hence the name of the process. This paper analyzes quality of cut in plasma arc cutting. Quality of cut in plasma arc cutting is defined using standard EN ISO 9013. The correlation between quality of plasma cut Conclusions of other authors who investigated quality of plasma cut are also presented.In the second part of the paper, experimental investigation of plasma cut was presented. Samples of steel plate thickness of 15 mm were used for creating 17 cuts. Obtained experimental results are consistent with theoretical considerations, as well as previous experimental results.*

Keywords: Plasma arc cutting, experiment, quality of cut, process parameters

1. INTRODUCTION

The efficient manufacture of high-quality plate components is quite difficult task. One of the easiest methods of contour cutting steel is oxy-fuel cutting. With respect to oxy-fuel cutting, laser cutting, abrasive water jet cutting, and plasma cutting are new attractive advanced processes for contour cutting of plate. They have numerous advantages, namely, a narrow cut, a proper cut profile, smooth and flat edges, minimal deformation of a workpiece, the possibility of applying high feed rates, intricate profile manufacture and fast adaptation to changes in manufacturing programs [1].

Plasma cutting is an industrial process that is essentially controlled by the operator who uses recommendations given by the manufacturers of the cutting equipment. Those recommendations, however, reflect the point of view of the manufacturers' business, which includes not only selling the cutting torches but also the consumables. Yet, the manufacturers' recommendations usually lead to solutions that are technically sound in terms of cutting quality, but do not necessarily correspond to the most cost-effective solutions on the user's point of view [2].

As a result, the user attempts to optimize the cutting operations by trial-and-error every time it is needed to setup the existing equipment for a new different task.

This requires the development of full studies and apply theoretical and experimental researches among all the technological system's links, in order to establish (chose) the optimal processing variant.

2. PROCESS PARAMETERS

As in the case of other machining methods, at the plasma arc cutting (PAC), in order to obtain good results, it is very important to well know the process, this meaning to exactly know what are the parameters involved in the process and their influences (fig. 1).

Input parameters are those parameters that can be controlled, and their values are known and can be set by the operator. Output parameters related to the quality of the obtained surface. Factors which cannot be controlled coming from machines and work environment.

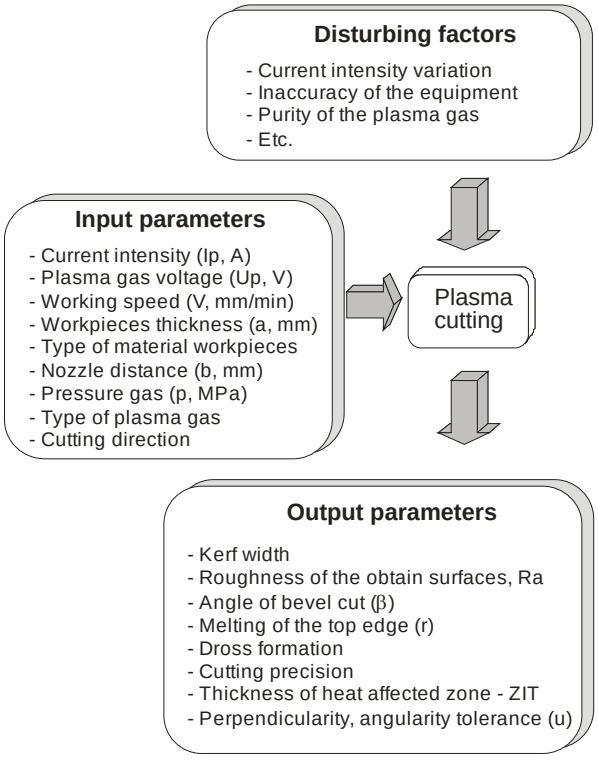

Figure 1. Parameters of plasma arc cutting [3]

3. QUALITY OF PLASMA CUTTING PROCESS

European standard "EN ISO 9013" "Thermal Cutting" defined classification of thermal cutting, contains geometrical product specification and quality. Standard applies to materials suitable for cutting with oxy-fuel (from 3 to 300 mm), plasma cutting (1 to 150 mm) and laser cutting (0.5 to 40 mm) [4], fig. 2.

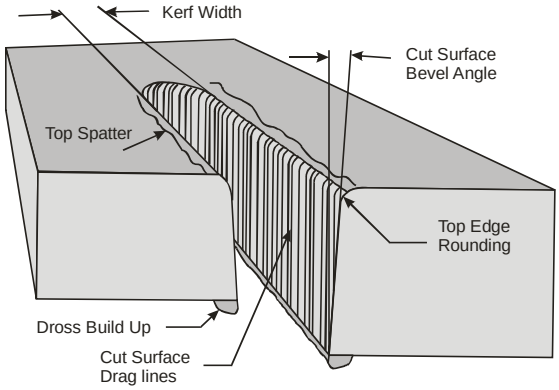

Figure 2. Quality parameters of a plasma cut *[5, 14]*

Using standard "EN ISO 9013" quality of the surface is defined by the following parameters:

- Squareness and angularity tolerance (u)
- Average peak-to-valley height (Rz5, Ra) - roughness
- Drag (n)
- Melting of the top edge (r)
- Possible formation of burrs or drops of molten metal on the bottom of the cut-edge.

This standard defines terms like: kerf width, angle of bevel cut… that can be used to define the quality of the work piece.

Squareness and angularity tolerance is defined as distance between two parallel straight lines that limit the upper and lower boundaries of the cut face profile at the teoretically correct angle, 90 degrees for square cut edges, fig. 3. Standard establishes a zone of significance for the measurement of U reduced at the the top and bottom edge by distance, Δa, related to material thickness. This measure also applies to concave and convex surfaces.

Since several works in literature highlight that the torch cutting direction and the swirling direction of the plasma gas determine a different squareness and angularity tolerance in the two sides of the cut [6], both left and right (*U*L and *U*R, respectively) were measured in order to highlight the asymmetric behaviour of the plasma beam.

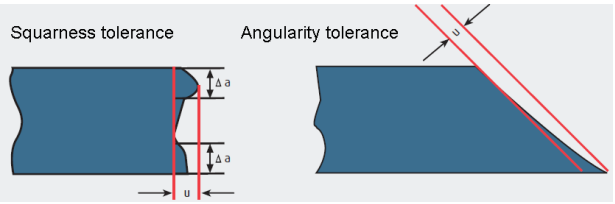

Figure 3. Squareness and angularity tolerance [5]

Surface roughness is defined cut appearance, and gives information on whether the need for further processing. Parameter surface roughness is mean height of the profile Rz5, unit is μm.

Surface roughness is influenced by more input parameters, but the most influential are: cutting speed, current and material thickness. Based on the developed mathematical model [7, 8], shows that the thickness of the material has the greatest influence on surface roughness. This is logical because current and cutting speed are functions of material thickness. Surface roughness is a function of material thickness defined by ISO 9013, based on which we can see that the thinner material have lower roughness (Fig. 4).

Roughness of the cutting edge is connected with stability of process. When the torch is too high positioning from work piece plasma arc is a long and curve. This phenomenon leads to the formation of surface waves, and lynx, and therefore to a higher Rz. When the cutting speed increases the torch moves fast and plasma arc loses stability with view to the cutting front. Therefore plasma arc can not remain perpendicular to front surface of the work piece, which is on surface cutting formed lynx. On the other side too low cutting speeds lead to excessive melting in a work zone, resulting appearance of furrows.

It is known that surface roughness of the cut is not same by depth. Experimental studies [9]

showed that diameter nozzle has a larger effect on surface roughness on upper reaches of cutting (1 mm from the top edge) than in the lower zones (5 mm from the top edge). These studies demonstrated that higher values of pressure gives lower values of Rz.

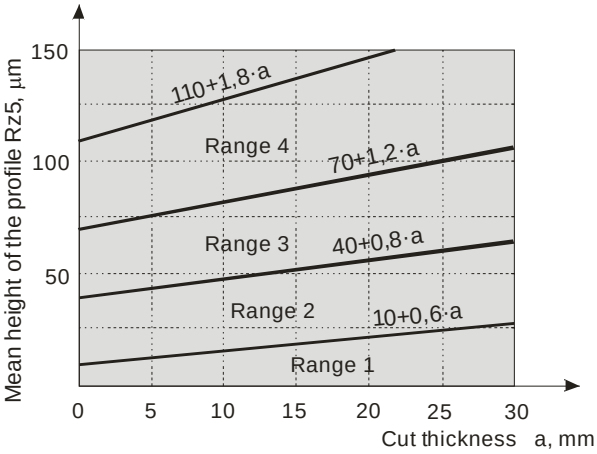

Figure 4. Influence of material thickness on Rz5 by standard "EN ISO 9013"

Surface roughness is different for the left and right sides of the cut. Surface on the right are about 25% rougher than on the left side [10].

Drag (n) is the projected distance between two edges of drag lines (lag lines) in the direction of cutting (Fig. 5.). At extremely high speeds arc becomes unstable and oscillates so the sparks and molten metal form a line in the form of a "tail" (drag lines) Fig. 5. At high speeds drag angle varies from 60 º - 80 º, while at maximum speed this angle has a value of 90 º and cut is lost. In the lower third of the cut the arc sweeps back steeply. It is probable that the hot gas, with no tendency to attach metal walls, leads the arc slightly at the bottom. Such a small amount of molten metal from the output port is not ejected.

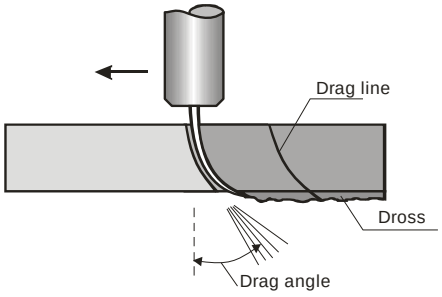

Figure 5. Dross, drag lines, drag angle [4, 11]

Melting of the top edge (r) occurs due to high cutting speeds or long distance from the nozzle to work piece. Top edge can be with overhang.

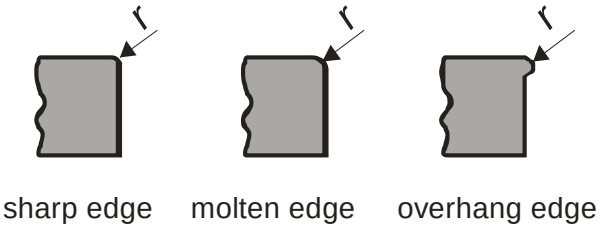

Figure 6. Melting [4]

On the top edge may appear slag spatter, accumulation of hardened metal sprayed along the edges of the cut. Basically it is easily removed. This phenomenon occurs at high speed, the large distance between the nozzle and the work piece, if the nozzle is wears. Slag spatter may also arise from the whirling motion of plasma gas. This phenomenon occurs when there is a big positive angle, because along the bevel is a difference in pressure that ejected molten metal on top.

In plasma cutting one of the biggest problems that arises is the dross (burr formation on the bottom of the kerf and spatter on the top of the kerf) Concentrations of dross will be higher in the worse side of cut. The amount of dross depends of lot parameters, but the most influential: types of materials, cutting speed and currents [7]. There are two types of molten metal on the bottom of cut-edge[12]:

- low speed dross
- high speed dross

If the cutting speed is too low plasma starts to search more material to cut. Then cut expanding to the point where more molten metal does not eject. The molten metal is accumulating along the lower edge of the large bulbous-shaped form. Thus formed molten metal are easily remove. Melted metal formed by low-speed cutting followed by the occurrence concave surface (Figure 7). It may be that the molten metal and the bottom edge forms a "bridge" over which the sectioned pieces connecting again. At extremely low speeds arc is turns off because there is not enough metal to hold arc. Increasing power or decrease distance between the nozzle and cutting objects have the same effect on appearance of molten metal. The practical counter measures for this phenomenon is removing part of the heat from the cutting zone, which is achieved by: reducing amperage or increase the distance between the nozzle and the work piece.

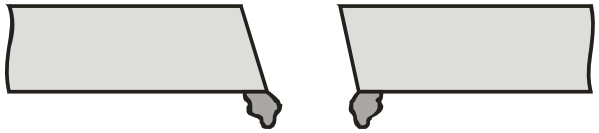

Figure 7. Low speed dross

High speed of molten metal gives a rounded tip of cut edges (Figure 8). Molten metal on the bottom

edge formed into a thin line. At these speeds arc often does not penetrate into the metal and can be shut down. Long distance between the nozzle and the work piece, and a small amperage current can lead to the same phenomenon as the speed too high. Increasing the current or reducing distance between nozzle and work piece leads to more heat in the cutting zone, which the effect of drag line is reduce, effectively reduce negative consequences of high speeds.

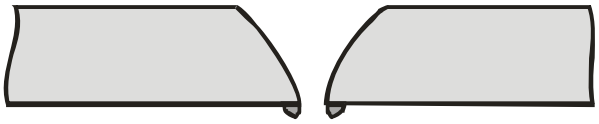

Figure 8. High speed dross

Angle of bevel cut is angle between the cut surface and the top surface of the work piece. The angle of inclination can be positive (the upper part is smaller size then the bottom) or negative (lower dimension is smaller than the upper). Plasma arc cutting will usually result in an angle on the cut surface of approximately 1 to 3° on the "good" side and 3 to 8° on the "bad" side, when using torches that swirl the plasma. With larninar-flow torches, the angle on both sides is usually about 4 to 8° [14].

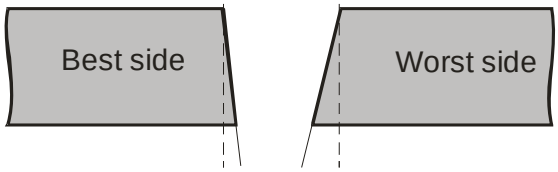

Figure 9. Positive angle of bevel cut [13]

Arc first establishes a connection with a better side of and releases heat. Cutting speed, current and distance from the work piece also have influence on angle of bevel cut.

If the cutting speed and the current have a correct value, and part have big positive angle of bevel cut, then the distance from the nozzle to work piece is too much. If the cutting speed and the current have a correct value, and distance from the nozzle and work piece is small, then angle of bevel cut will be negative. Optimal distance from the nozzle to work piece is a distance before angle of bevel cut start to appear [15].

Kerf width, the rule is that the cutting width at the plasma cutting is about 1.5-2 times bigger than the size of the nozzle exit. Cutting width is influenced by the cutting speed. If the cutting speed decreases, the cut is expanding.

4. EXPERIMENTAL EXAMINATION

In the experiment were done 17 samples. As input parameters used cutting speed V, mm/min and current intensity I, A. Steel plate material S235 JRG2 (Č0361) was 15 mm thick. Electric current of 60 A, 80 A, 100 A and 120 A was used in combination with the tablet, reduced and increased speeds value (Table 1).

Table 1. Used speeds and current intensity

samples	I, A	V , mm/min
1	60	425
2	60	530 (tablet value)
3	60	635
4	80	490
5	80	610 (tablet value)
6	80	730
7	80	870
8	80	1055
9	100	530
10	100	695
11	100	870 (tablet value)
12	100	1055
13	120	730
14	120	870
15	120	1055
16	120	1320 (tablet value)
17	120	1585

Quality of samples is defined by:

- surface roughness Ra (measured by device Talysurf 6)
- kerf width (St and Sb, defined in Fig. 10.)
- dross width (Sd) and dross higth (h), Fig. 10.
- dimension of molten metal on the bottom edge of the cut. (defined in Fig. 11.)

Ra was measured in thre points: near to upper edge (g), in the middle (s), near to lower edge (d).

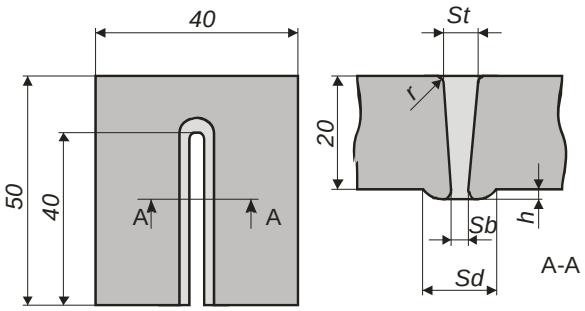

Figure 10. Measuring kerf width and molten metal on the bottom of cut

Figure 11. Measured in three points

Using a current of 60 A quality cut can be described as very poor due to large deposits of

waste material to the bottom of cut. Therefore requires additional treatment, and just cutting it very slowly (Fig. 12.).

Figure 12. Cutting with 530 mm/min and 60 A

Figure 13 shows the sample which was cutting with current intensity of 80 A and speed of 610 mm/min (tablet value). The quality of the cut can be characterized as acceptable. There are waste particles on the bottom, but not on a large extent. An additional treatment section is necessary. Using a current of 80 A and a change speed, quality is approximate when used in tablet value.

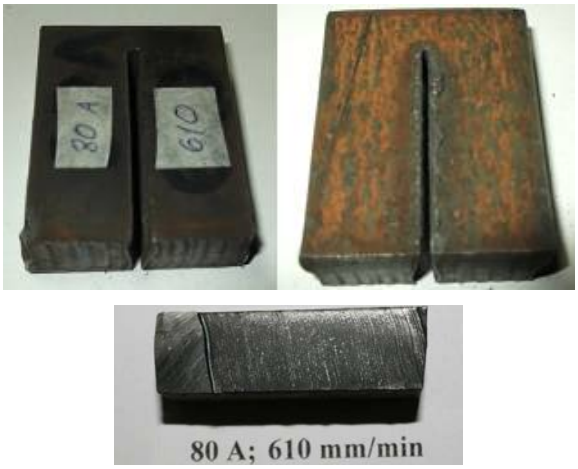

Figure 13. Cutting with 610 mm/min and 80 A

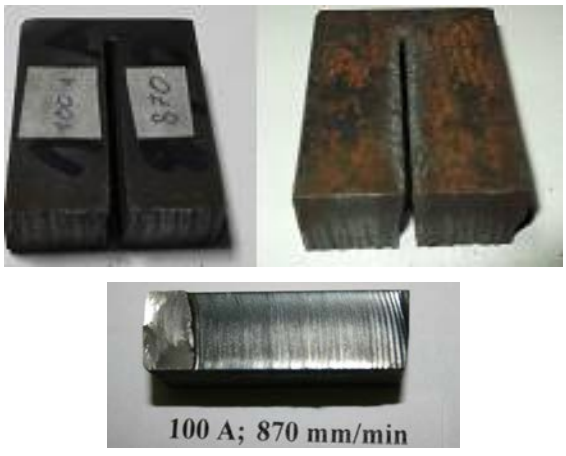

Figure 14. Cutting with 870 mm/min and 100 A

Using a current of 100 A obtained quality of the cut can be described as solid. There are waste particles on the bottom, but not on a large extent. An additional treatment section is necessary.

Using the current with intensity of 80 A the best quality is obtained by using the highest speed.

Sample of 17 is considered best combination of parameters because obtained fragment with the best quality (Fig. 15.). The best quality is obtained increasing the speed by 20% of tablet speed value.

Table 2. Measured values of Ra, kerf width and molten metal on the bottom of cut

Samples	Measur. points	Ra µm	St mm	Sb mm	h mm	Sd mm
1	g s d	10.5 17 30.7	2.14	1.2	4.78	7.12
2	g s d	12.4 21.3 40.4	2.18	1.13	5.11	7.18
3	work piece is not penetrated					
4	g s d	17.5 29.4 26.6	2.55	1.61	1.05	5.63
5	g s d	15.2 35.8 23.0	2.45	1.38	0.95	4.98
6	g s d	14.1 24.3 24.7	2.30	1.18	2.23	6.64
7	g s d	14 41 55	2,01	1,11	4,45	7,38
8	work piece is not penetrated					
9	g s d	35 19 32	2,51	1,75	3,74	10,32
10	g s d	13.0 13.0 9.8	2.54	1.54	1.16	5.21
11	g s d	12.4 8.8 13.0	2.45	1.36	0.93	7.29
12	g s d	12.0 12.4 10.1	2.36	1.23	0.93	8.40
13	g s d	16 14 18	2,68	1,82	1,15	7,58
14	g s d	17 14 20	2,46	1,67	0,80	7,83
15	g s d	10.3 11.0	2.64	1.45	0.52	3.07
16	g s d	10.8 9.9 12.9	2.55	1.29	0.66	3.24
17	g s d	8.3 10.1 9.8	2.4	1.03	not exist	-

Lower values of current are not resulted with enough heat in the cutting zone, and therefore the quality of these clips are worse. With lower currents and much higher speed than recommended may happend that clip does not penetrate, like in samples 3 and 8.

Based on of experimental results can conclude that an increase in speed reduces kerf width.

Figure 15. Cutting with 1585 mm/min and 120 A

5. CONCLUSIONS

Plasma cutting is nonconventional technology that represents the best relation between cost and quality value for money for most of the standard ports and small series production types. In addition, the processing speed is far greater than the technology of machining, and quality is comparable to the laser cutting technology.

Plasma cutting process may be used to cut any conductive material, including carbon steel, stainless steel, aluminum, copper, brass, cast metals and exotic alloys.

Obtained experimental results are consistent with theoretical considerations, as well as previous experimental results.The best quality is obtained increasing the speed by 20% of tablet speed value, which indicates that in this area have a place for further research and improvements.

ACKNOWLEDGEMENT

This paper is part of project TR35034 - The research of modern non-conventional technologies application in manufacturing companies with the aim of increase efficiency of use, product quality, reduce of costs and save energy and materials, funded by the Ministry of Education and Science of Republic of Serbia.

REFERENCES

1. M. Radovanovic, M. Madic: *Modeling the plasma arc cutting process using ANN*, Nonconventional Technologies Review – No.4/2011
2. P. Ferreira, I. Melo, A.Gonçalves-Coelho, A. Mourão: *Plasma cutting optimization by using the response surface methodology*, The annals of "DUNĂREA DE JOS" university of Galati fascicle V, technologies in machine building, ISSN 1221-4566, 2009
3. S.M. Ilii, L. Apetrei, I. Carp: *Considerations concerning plasma arc cutting machining*, International Conference on Manufacturing Engineering (ICMEN), Chalkidiki, Greece, 1-3 October 2008
4. International standard ISO 9013:2002(E)
5. Plasma working group at Linde AG, Linde Gas Department, and specialists from the company Kjellberg Finsterwalde Elektroden und Maschinen GmbH, Facts about plasma technology and plasma cutting Riverside Corporate Park10 Julius AvenueNorth Ryde, NSW 2113Australia, 2011
6. E. Gariboldi, B. Previtali: *High tolerance plasma arc cutting of commercially pure titanium*, Journal of Materials Processing Technology 160, pp. 77–89, 2005.
7. S.M. Ilii, M. CoteaŃă, A. Munteanu: *Experimental results concerning the variation of surface roughness parameter (Ra) at plasma arc cutting of a stainless steel workpiece*, International Journal of Modern Manufacturing Technologies II, ISSN 2067–3604, 2010
8. R. Bhuvenesh, M.H. Norizaman, M.S. Abdul Manan: *Surface roughness and mrr effect on manual plasma arc cutting machining*, World academy of science, engineering and technology 62, 2012
9. M. Hatala, R. Čep, Z. Pandilov: *Analysis of surface roughness and surface heat affected zone of steel EN S355J0 after plasma arc cutting*, Mechanical Engineering–Scientific Journal 29, pp. 1–6, 2010.
10. A.P. Hoult, I.R. Pashby, K. Chan: *Fine plasma cutting of advanced aerospace materials*, Journal of Materials Processing Technology 48, pp. 825-831, 1995.
11. J.A. Hogan, J.B. Lewis, A. Jordan: *Plasma processes of cutting and welding*, Naval Surface Warfare Center CD Code 2230- Design Integration Tools, Building 192, Room 138 9500 MacArthur Blvd Bethesda, MD 20817-5000, 1976.
12. D. Cook: *Plasma arc cutting-cut quality problems*, Welding design and fabrication, November 1998
13. J. Berglund: *Cut cost calculation*, Master of science programme industrial economic, Lulea university of technology, 2006.
14. B.R.Hendricks: *Simulation of plasma arc cutting*, Peninsula Technikon, faculty of Engineering, Cape Town, 1999.
15. J.V. Warren: *The Contribution of arc voltage control to quality plasma cutting*, ESAB-30213, South Carolina, USA, 2005.

Serbian Tribology Society

SERBIATRIB '13

13th International Conference on Tribology

Faculty of Engineering in Kragujevac

Kragujevac, Serbia, 15 – 17 May 2013

TRIBOLOGICAL ASPECTS OF SINTERED STEEL GEAR IN APPLICATION WORM-AND-GEAR SET

Aleksandar Miltenović[1], Milan Banić[1], Miroslav Mijajlović[1], Đorđe Miltenović[2]
[1]University of Niš, Faculty of Mechanical Engineering in Niš, Serbia,
aleksandar.miltenovic@masfak.ni.ac.rs, milan.banic@outlook.com, mijajlom@masfak.ni.ac.rs
[2]College of Textile, Leskovac, Serbia, milten2004@yahoo.com

Abstract: *Due to the low manufacturing costs, worm-and-gear set with the combination of a steel worm and a gear are used almost exclusively in automotive auxiliary drive units such as window lifters, seat adjustments and windscreen wipers. Worm-and-gear sets are a simple and compact way to achieve a high speed gear ratio. Tribological aspect of worm-and-gear set is very complex while there can occur different damage forms such as: wear, pitting or scuffing. The conditions, under which a damage form occurs, are not fully elucidated. In this paper are shown experiments that have been carried out with gear made of sintered steel Fe1.5Cr0.2Mo with different treatment methods.*

Keywords: *sintered steel, gears, worm-and-gear set, wear, pitting, scuffing*

1. INTRODUCTION

Crossed helical gears are used, for example, in automotive auxiliary drive units such as window lifters, seat adjustments, windscreen wipers, and also in home appliances. The trend towards increased comfort in motor vehicles has led to the utilization of more than a hundred servo-drives in luxury class automobiles. Important advantages of the crossed helical gears are their easy and inexpensive design, good noise performance and high ratio that can be realized in one step.

The use of gear wheels made of sintered metal can increase the load capacity of crossed helical gears. As in the case of plastic gear wheels, the large scale production of sintered metal gear wheels requires a special tool and no additional post-production costs.

Hochmann [1] determines the load capacity of material pair steel/steel with grease. The tested gears with grease have lower load capacity than tested gears with oil. Crossed helical gears have different transmission conditions, therefore, these results cannot be used.

The lubricating film thickness, pitting and scuffing load capacity correlate significantly with the base oil viscosity of grease. The addition of a special synthetic graphite as solid lubricant shows increased wear in this research. The base oil viscosity is a decisive factor for calculating the lubricating film thickness of grease, as well as for calculating the pitting load capacity according to DIN 3990 [2]. Performance data of tested lubricants is available for calculating scuffing and pitting load capacity according to DIN 3990. This data takes into account the influence of grease.

2. CHEMICAL COMPOSITION

The material combination steel/sintered metal has been investigated only in few research projects. Researchers from the company Höganäs AB, Sweden [3] investigated sintered metal Astaloy Mo (Fe0.85Mo) and Astaloy CrL (Fe1.5Cr0.2Mo).

Table 1. Chemical composition of sintered steel Fe1.5Cr0.2Mo (%)

element	measure point 1	measure point 2	measure point 3	measure point 4	measure point 5
C	0,254	0,243	0,238	0,253	0,273
Si	0,054	0,047	0,043	0,057	0,053
Mn	0,163	0,161	0,161	0,161	0,161
P	0,009	0,009	0,009	0,009	0,009
S	0,001	0,001	0,001	0,001	0,002
Cr	1,521	1,517	1,526	1,51	1,509
Ni	0,026	0,026	0,026	0,026	0,026
Mo	0,21	0,208	0,209	0,211	0,21
Cu	0,066	0,066	0,067	0,067	0,067
Al	<0,001	0,002	<0,001	<0,001	<0,001
Ti	<0,001	<0,001	<0,001	<0,001	<0,001
V	0,008	0,008	0,008	0,008	0,008
Nb	0,007	0,007	0,007	0,006	0,006
W	0,015	0,015	0,016	0,014	0,013
Co	0,007	0,007	0,007	0,007	0,007
Zr	0,002	0,002	0,002	0,002	0,001
N	0,0248	0,0235	0,0243	0,0244	0,0283
B	0,0003	0,0003	0,0003	0,0003	0,0003
Mg	0,0003	0,0003	0,0003	0,0003	0,0001
Ca	0,0055	0,0042	0,0024	0,0071	0,0063
As	0,002	0,002	0,002	0,002	0,002
Sn	<0,001	<0,001	<0,001	<0,001	<0,001
Pb	0,0021	0,0023	0,0023	0,0018	0,0018
Bi	0,002	0,002	0,003	0,002	0,002
Ce	0,002	0,002	0,002	0,002	0,002
Zn	0,003	0,003	0,002	0,003	0,003

The basic raw material for sintered steel is iron powder. The iron powder is mixed with different metal powders by using special alloy mixing techniques. A homogeneous powder mixture is important for uniform cross-sectional properties within the part. Copper increases the strength and yield strength, but decreases the elongation at break. Nickel improves the strength and relieves the weldability. Cu-Ni compound limits the volume and dimensional changes during the sintering process. Carbon (graphite) in small amounts increases the strength and hardness and improves subsequent heat treatment. Phosphorus improves the strength and elongation, but causes high sintering shrinkage.

An analysis of chemical composition of sintered material (Table 1) shows a small variation between individual samples. The chromium content is within the limits of 1.509 and 1.526%, which differs from the reference value of 0.6 to 1.7%. Molybdenum, as the second influential element, occurs in a concentration of 0.208 to 0.211% and it also differs from the reference value of 4 to 5.5%. Manganese content (0.161%) is significant and good wear resistance can be expected from such a sintered material [4]. The basis for all the tested materials is the iron-based powder Fe1.5Cr0.2Mo. The material variants are shown in Table 2. A detailed description of the additional treatment methods is given in [5].

Table 2. Material variants of the sintered steel

	Additional treatment	Density [g/cm³]	Temperature of sintering [°C]	Dimensional change A [%]
S1	without	7.50	1120	0.16
S2	case hardening	7.49	1120	0.16
S3	case hardening + shot peening	7.49	1120	0.16
S4	pyrohydrolysis	7.50	1120	0.16
S5	sinter-hardening	7.43	1120	0.16
S6	2% copper addition	7.43	1120	0.64

3. TEST CONDITIONS

The practical tests were carried out by using five test benches with a center-to-center distance of 30 mm. The transmission of the asynchronous motor was mounted on the test bench and the output torque was applied via a magnetic particle brake. On each test bench, the engine and the gearbox, as well as the gearbox and the brake, were connected with gear coupling. The measurement of the output torque was made on transmission with a torque gauge bar via a slip ring transmitter. The speeds and output torques were controlled independently for each test bench. The test bench for crossed helical gears and the position of the measuring points is shown in figure 1. The data of the test gear pair are given in table 3.

Table 3: Data of the test gear pair [6]

Parameters	Data
Centre distance	30 mm
Module	1.252 mm
Transmission ratio	40
Pressure angle	20
Wheel material	Fe1.5Cr0.2Mo
Worm material	16MnCr5
Speed	1500 – 10000 min^{-1}
Torque	12-36 Nm
Synthetic oil	Klüber GH6 1500
Mineral oil	Optigear BM 1500
Grease:	Klübersynth G34-130

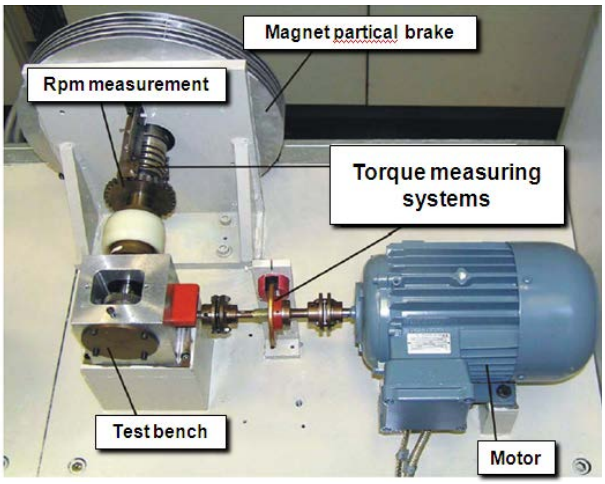

Figure 1. Test bench

4. LUBRICATION

For the sake of comparison, lubrications tests were done under same parameters and with different lubricants: synthetic oil, mineral oil and grease.

4.1. Synthethic oil

Synthetic oil made by Klüber company (Klübersynth GH6 15000) was used in tests. This oil can withstand high scuffing load capacity and has good wear protection. Furthermore, the oil reduces friction and has a flat viscosity-temperature behaviour. This oil is based on polyglycol and it is mainly used in transmissions with the material combination of steel/steel.

The additive GH6 reduces the friction coefficient and wear, especially for worm gears with the material combination steel/bronze. Very low wear intensities for worm gears can be achieved with this oil. Klübersynth GH6 oil with a viscosity of ν_{40} = 1500 mm^2/s was used for testing. Table 4 shows the characteristics of used lubricants.

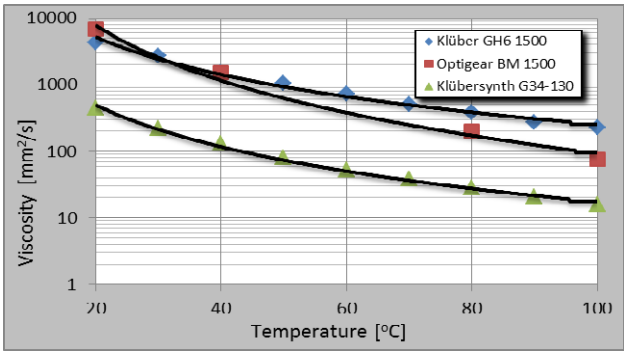

Figure 2. Viscosity-temperature behaviour for used lubricants

4.2 Mineral oil

Castrol Optigear BM 1500 was used in the experiment as the mineral oil with the same viscosity as Klübersynth GH6 1500. High performance gear oil Castrol Optigear BM contains the mineral oil-based additive package MICROFLUX Trans (MFT). This combination of load-active agents and additives adjusts to varying loads and actively prevents wear. Difficulties in the run-in phase can be reduced and problems with wear, material fatigue on surfaces (pitting) and micropitting can be avoided.

Table 4: Data of lubricants

Parameter	GH6 1500	BM 1500	G34-130
Temperature Range [°C]	-20 to 160	-10 to 90	-30 to 130
Density (20°C) [g/cm^3]	1.08	0.93	0.87
Kin. base oil viscos. DIN 51562 ν_{40} [mm^2/s]	1500	1507	150
Kin. base oil viscos. DIN 51562 ν_{100} [mm^2/s]	231	75.6	16
Consistency class DIN 51818, NLGI (grease)			0

4.3 Grease

Klübersynth G34-130 grease for small gears was used in the grease tests. Klübersynth G34-130 is grease based on synthetic hydrocarbon oil. Other ingredients are mineral oil and lithium soap as special polyureas, which serve as consistency factors. The grease has good anti-wear properties and can be used with the combination of steel and plastic.

Figure 2 presents the dependence of kinematic viscosity on temperature for the selected lubricants. The oils Klüber GH6 1500 and Castrol Optigear BM 1500 have the same viscosity at the temperature of 40°C. At higher temperatures, the viscosity of mineral oil Castrol Optigear BM 1500 is smaller than the synthetic oil Klüber GH6 1500. Lubricants dependence on the viscosity is very important at low temperatures. They should still be

flowable at high temperatures and very viscous at extremely high temperatures. The best oil in this sense is the Klüber GH6 1500 oil.

5. HERTZIAN CONTACT STRESS

The Hertzian contact stress has a significant influence on the wear rate and the width of the wear surface. The Hertzian contact stress in the crossed helical gears can be determined as the Hertzian contact stress of globoid wheel. It should be taken into consideration that the Hertzian contact stress on the crossed helical gear depends on the width of the wear surface. Therefore, a correlation between the width of the wear surface b_V and the dimensionless ratio p_m* [5] is introduced. The Hertzian contact stress by the dimensionless parameter of the average Hertzian contact stress $p_{m,V}$* is taken into account. The new Hertzian contact stress σ_{Hm} can be calculate for the average Hertzian contact stress $p_{m,V}$* according to Equation 1, depending on the output torque T_2, the E-Module E_{red} and centre distance a_s.

$$\sigma_{Hm} = \frac{4}{\pi} \cdot \sqrt{\frac{p^*_{m,V} \cdot T_2 \cdot 1000 \cdot E_{red}}{a_s^3}} \qquad (1)$$

According to the tests for sintered steel Fe1.5Cr0.2Mo with sintered-hardening (S5), the value of E-Module is $E_2 = 203759$ N/mm^2. Therefore, for the material combination of worm made of 16MnCr5 and wheel made of sintered steel Fe1.5Cr0.2Mo, the value of the reduced E-Module is $E_{red} = 227288$ N/mm^2.

The Hertzian contact stress that depends on the width of the teeth $p_{m,V}$* can be calculated using Equation 3. The ratio of the width of the globoid wheel b_{2H} to the width of wear surface b_v takes into consideration the increase of the Hertzian contact stress with decreasing width [6].

$$p_{m,V}{}^* = \left(\frac{b_{2H}}{b_v}\right)^{0,8614} \cdot p_m{}^* \qquad (2)$$

Figure 3 shows the resulting Hertzian contact stress of all tests with different lubricants and $n_1 = 1500$; 5000 und 10000 min^{-1}. In the first load step output torque is 12 Nm, each next step output torque T_2 is increased by 4 Nm, and the time duration of load level is set at 40 hours.

Higher torques leads to the increase in pressure.

There is no great difference in pressure values of Hertzian contact stress for lubrication with mineral and synthetic oil for the rotation speed $n_1 = 1500$ min^{-1} or sliding velocity $v_{gs} = 0.76$ m/s. For grease lubrication, the Hertzian contact stress is on average half the size in relation to mineral and synthetic lubricating oil.

There is great difference in pressure values of Hertzian contact stress for lubrication with mineral and synthetic oil for the rotation speed $n_1 = 5000$ min^{-1} or sliding velocity $v_{gs} = 2.53$ m/s. The values of Hertzian contact stress with synthetic oil are for about 65% higher compared to lubrication with mineral oil. Hertzian contact stresses for lubrication with synthetic oil goes up to 1400 N/mm^2.

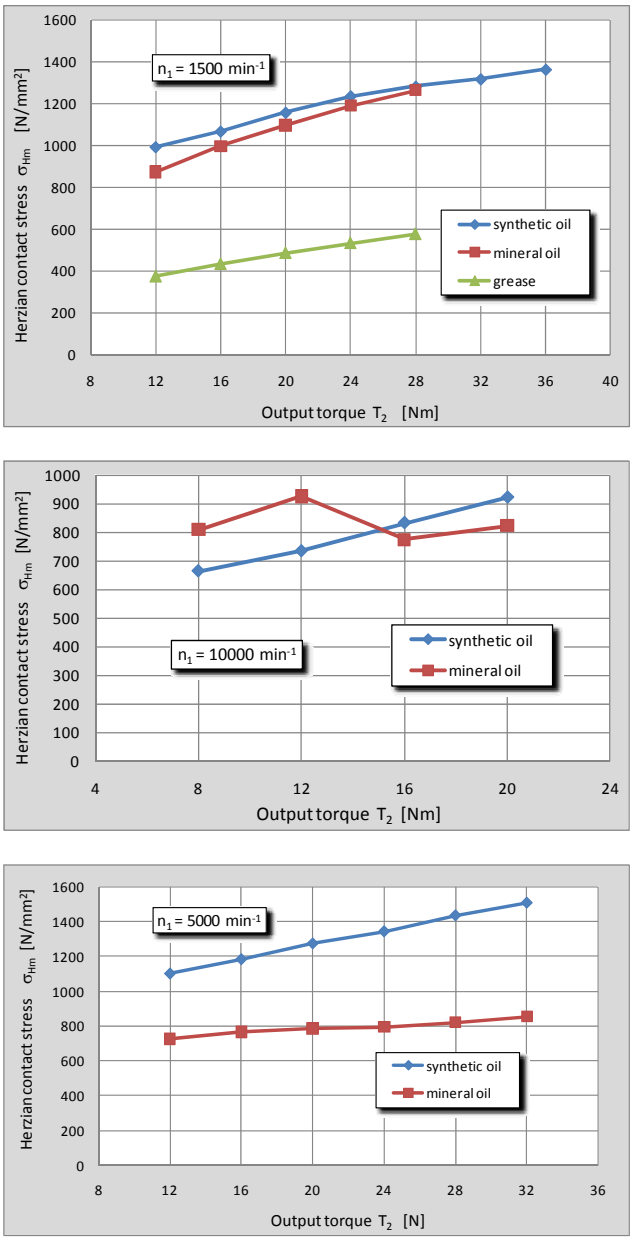

Figure 3. Hertzian contact stress σ_{Hm} for duration of the experiment with different lubrication and $n_1 = 1500$; 5000 and 10000 min^{-1}

For the rotation speed $n_1 = 10000$ min^{-1} or sliding velocity $v_{gs} = 5.05$ m/s up to the number of load changes $N_L = 0{,}9 \times 10^6$ values of Hertzian contact stress are greater for mineral oil lubrication as compared to synthetic lubricating oil. Then it

comes to the sharp increase of wear rate and to reduction of pressure. Lubrication with synthetic oil has a smaller increase of wear rate and smaller reduction of pressure.

Based on the foregoing analysis, it can be concluded that the Hertzian contact stress depends on the choice of lubricant. Synthetic lubricating oil is the most favourable from the aspect of wear, and in terms of achieving hydrodynamic lubrication. Optimal lubrication conditions were obtained for the rotation speed of $n_1 = 5000\ min^{-1}$ or sliding velocity $v_{gs} = 2.53$ m/s.

6. DAMAGE TYPES

6.1. Wear

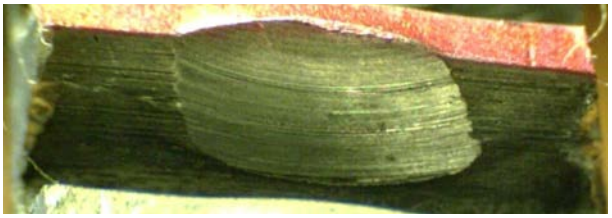

Figure 4. Wear on wheel tooth surface without additional treatment for $T_2 = 36$ Nm; $t = 260$ h; $n_1 = 5000\ min^{-1}$

tribological system are: the gear wheel (basic body), the worm (opposed body) and the lubricant (intermediate component).

Experiments with wheels with different additional treatments provide basic knowledge of sintered gears load capacity. Worm and wheel are in contact in a point. During operation, a change in the tooth flank of the wheel appears due to wear. The worm forms on the tooth flank of the wheel, a wear surface that has a shape that is identical to worm gear flank. Wear progress widens the wear surface, which leads to a lower Hertzian pressure in the tooth contact. After a certain period of operation under intensive wear progress, the steady state occurs, where a necessary oil layer exists, so that the wear progress is minimal. Figure 4 shows the form of wear damage on tooth surface of wheel made from material without additional treatment.

Figure 5 compares all experiments with wheels of different material variants after a trial of 100 h and an output torque of 20 Nm. The maximum wear, $\delta_{wn} = 115$ μm, occurred on material S2 – material with case hardening. The minimum wear, $\delta_{wn} = 7.8$ μm, occurred on S5 – sinter-hardening. Figure 4 shows the wear width of the wear surface on wheel from material S4 - "pyrohydrolysis" and S5 sinter-hardening for different speeds. The

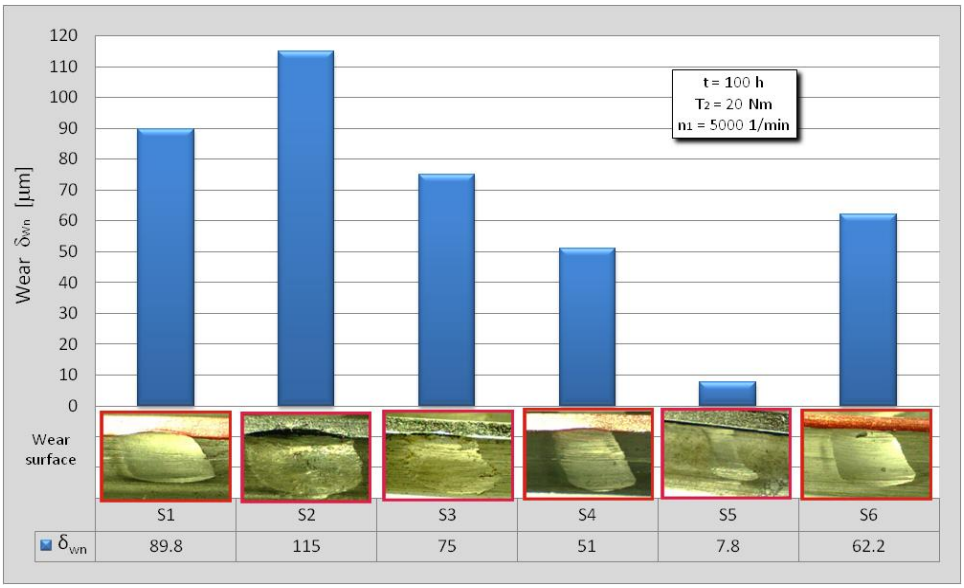

Figure 5. Wear δ_{wn} for all trials with different material variants [6]

The wear describes the continuous loss of material from the surface of the basic body which has a relative movement with respect to a solid, liquid or gaseous mating with which it is in contact [7]. Wear has exclusively mechanical causes. Different from hardness or tensile strength, wear is not a specific material property but a system property which depends on the particular tribological system. In our case, the elements of the

smallest wear width occurred at input speed $n_1 = 5000\ min^{-1}$. The reason for this is that the best experimental conditions, with regard to lubrication and wear, are at this input speed.

6.2. Wear

A large pressure on surface does not lead to a sudden failure of drive, but over the time, small

holes (pits) emerge in the shape of shell on tooth flank. Pit peak always points in the sliding direction. This damage occurs through a cyclic fatigue due to repeated elastic and plastic deformations of the surface. The holes occur only after a sufficiently large number of overrollings (from ca. $5x10^4$ load cycles). If only initial pitting is present, the situation is not dangerous. Destructive pitting destroys the flank and causes failure due to noise and fatigue. The pitting occurred on wheels made from materials S4, S5 and S6 by an output torque of 16 and 32 Nm after the trial time period of 120 h to 240 h.

Figure 6 shows initial and destructive pitting on tooth flank of wheel. In trials with material S1 – without additional treatment, initial pitting ocurred under input speed $n_1 = 5000\ min^{-1}$ and output torque of 20 Nm. In trials with material S5 – sinter-hardening, destructive pitting occurred under input speed $n_1 = 5000\ min^{-1}$ and output torque of 20 Nm and mineral oil.

Initial pitting: without additional treatment
$T_2 = 20$ Nm; $t = 120$ h; $n_1 = 5000\ min^{-1}$
Lubricant: synthetic oil

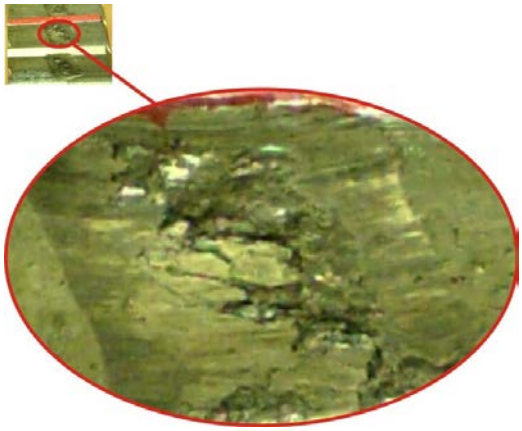

Destructive pitting: sinter-hardening variant
$T_2 = 20$ Nm; $t = 120$ h; $n_1 = 5000\ min^{-1}$
Lubricant: mineral oil

Figure 6. Pitting on wheel tooth surface [6]

6.3. Scuffing

There is a difference between cold and warm scuffing. Both damage types are caused by the lack of lubricant in contact between teeth. Cold scuffing is relatively rarely seen. It occurs mainly at low speed (< 4 m/s) and between teeth that are having relatively high hardness and rough quality of contact surfaces. Warm scuffing occurs due to great pressure and high sliding velocity between tooth flanks. Under such a load, combined effects occur which lead to the increase in temperature that disrupts the lubricant film between tooth flanks, making the contact between tooth flanks direct and dry. This can cause a short local welding of the flanks which damages both flanks. Warm scuffing is characterized by strip-shaped bands in the direction of the tooth height, and with the strongest expression in the tooth addendum and tooth root. Scuffing on high-speed gears increases the temperature and tooth forces, eventually leading to shaft fracture due to high damage on tooth flanks.

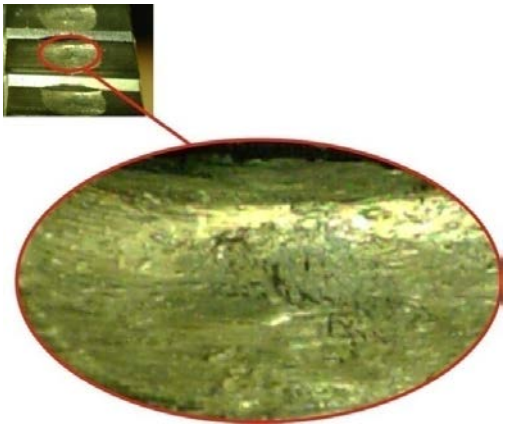

Variant with case hardening
$T_2 = 20$ Nm; $t = 160$ h; $n_1 = 5000\ min^{-1}$
Lubricant: synthetic oil

Material with 2% copper addition
$T_2 = 28$ Nm; $t = 160$ h $n_1 = 5000\ min^{-1}$
Lubricant: synthetic oil

Figure 7. Scuffing on tooth flanks of wheel for different material variants [6]

Figure 7 shows the scuffing on wheel tooth flanks for different material variants. With exception of S1, scuffing occurred on all material variants. On wheels made from materials S2 and S3, under load of $T_2 = 16$ Nm and $T_2 = 20$ Nm, the phenomenon of scuffing and significant increase of wear surface and gear forces were observed. Under output torque of $T_2 = 28$ Nm, and input speed $n_1 = 5000$ min^{-1} scuffing occurred for S4 and S6. Gear loads rose and, suddenly, the failure of worm shaft occurred. On material variant S6 "2% copper addition", scuffing occurred on tooth root in trials with input speed $n_1 = 5000$ min^{-1} and output torque of $T_2 = 28$ Nm, and a very short running time of ca. 10 minutes. Scuffing also occurred on wheel tooth flanks with speed $n_1 = 5000$ min^{-1} and output torque of $T_2 = 36$ Nm for material variant S5 sinter-hardening.

7. MAXIMUM OUTPUT TORQUE

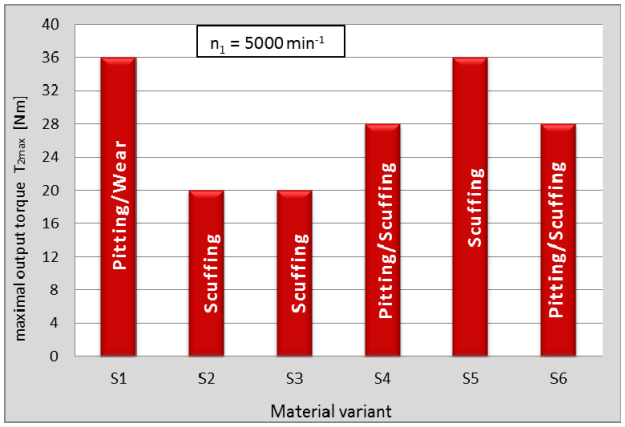

Figure 8. Comparison of maximum transmissible torque with critical damage type for different materials and input speed $n_1 = 5000$ min^{-1} [8]

Figure 8 shows maximum transmissible torque, as well as the type of critical damage, in a bar chart. With an output torque of $T_2 = 20$ Nm, materials S2 (case hardening) and S3 (case hardening and shot peening) were damaged due to scuffing. Materials S4 (pyrohydrolysis) and S6 (2 % copper addition) were damaged by pitting when output torque was $T_2 = 24$ Nm, and by scuffing at the value of $T_2 = 28$ Nm. Without an additional treatment, S1 had the most critical wear and some pitting at output torque of $T_2 = 28$ Nm. The wheels S5 (sinter-hardening) had the greatest load carrying capacity, its maximum transmissible torque being 32-36 Nm, and the scuffing being the most dangerous damage form in this case.

8. CONCLUSIONS

The research in this paper shows that tribological parameter of worm-and-gear has great influence on working characteristics in exploitation conditions. The material characteristics like microstructure, wear load capacity and damage types of molded parts can be significantly influenced by additional treatments for sintered steel.

The Hertzian contact stress of teeth in contact depends on the choice of lubricants. The smallest wear occurred in experiments with synthetic oil when Hertzian contact stresses were largest. Synthetic oil can resist the pressures of 1400 N/mm^2 at sliding velocity $v_{gs} = 2.53$ m/s.

All experiments with different material variants show that additional treatments have significant influence on wear. Under identical experimental conditions, the maximum wear δ_{wn} occurred in the trials with wheels of material variant with case hardening (115 μm) and the minimum with wheels with sinter-hardening (7.8 μm).

The pitting was observed in wheels of material variants S4, S5 and S6 by output torque from 16 to 32 Nm. The initial pitting on the tooth flank occurred on material variant without additional treatment (trials with $T_2 = 20$ Nm; $t = 120$ h; $n_1 = 5000$ min^{-1}; lubricant: synthetic oil). Destructive pitting on tooth flank occurred in material variant sinter-hardening ($T_2 = 20$Nm; $t = 120$h; $n_1 = 5000$ min^{-1}; lubricant: mineral oil).

With exception of S1, scuffing occurred on all material variants. The scuffing was the critical type of damage for wheels from material variants S2 and S3 under the output torque of $T_2 = 20$ Nm with $n_1 = 5000$ min^{-1} and by S5 under the output torque of $T_2 = 36$ Nm. For wheels of material variant S6, scuffing occurred for trials with $n_1 = 5000$ min^{-1} and output torque of $T_2 = 20$ Nm. For wheels of material variants S4 and S6, the critical type of damage was the combination of pitting and scuffing.

Lubrication with synthetic oil is the most favorable from the aspect of wear and in terms of achieving hydrodynamic lubrication. Optimal working lubrication was obtained for the rotation speed $n_1 = 5000$ min^{-1} or sliding velocity $v_{gs} = 2.53$ m/s.

REFERENCES

[1] M. Hochmann: *Tragfähigkeit von Zahnradpaarungen bei Schmierung mit Getriebefetten*, Forschungsbericht, DGMK, 2007.

[2] DIN 3990: Tragfähigkeitsberechnung von Stirnrädern, 12/2002.

[3] S. Dizdar, P. Johansson, A.B. Höganäs, 263 83 Höganäs, Sweden: P/M Materials for Gear Application; EURO PM2007, Tolouse October 16, 2007.

[4] W. Schatt, K-P. Wieters, Pulvermetallurgie-Technologien und Werkstoffe, VDI-Verlag Düsseldorf, 1994.

[5] W. Predki, A. Miltenović, *Influence of Hardening on the Microstructure and the Wear Capacity of Gears Made of Fe1.5Cr0.2Mo Sintered Steel*. International Journal "Science of Sintering" 42, pp. 183-191, (2010).

[6] Miltenović, A.: *Verschleißtragfähigkeitsberechnung von Schraubradgetrieben mit Schraubrädern aus Sintermetall*, Dissertation Ruhr-Universität Bochum, 2011.

[7] DIN 50320: Verschleiß: Begriffe – Systemanalyse von Verschleißvorgängen – Gliederung des Verschleißgebietes, 12/1979.

[8] Miltenović,A., Predki,W.: *Damage Types of Crossed Helical Gears with Wheels from Sintered Steel*. International Journal "Science of Sintering" 43, pp. 205-214, 2011.

[9] Wendt, T.: *Tragfähigkeit von Schraubradgetrieben mit Schraubrädern aus Sintermetall*, Dissertation Ruhr-Universität Bochum, 2008.

Tribometry

13th International Conference on Tribology – SERBIATRIB ’13

15 – 17 May 2013, Kragujevac, Serbia

Serbian Tribology Society

SERBIATRIB '13

13th International Conference on Tribology

Faculty of Engineering in Kragujevac

Kragujevac, Serbia, 15 – 17 May 2013

PRELIMINARY STUDY ON THE SEIZURE TREND OF A MOM-THP WITH SELF-DIRECTED BALLS

Lucian Capitanu[1], Liliana – Laura Badita[2], Virgil Florescu[2], Dumitru Catalin Bursuc[3]

[1]Institute of Solid Mechanics of the Romanian Academy, 15 Constantin Mille, 010141, Bucarest, Romania luciancapitanu@yahoo.com

[2*]National Institute for Research and Development in Mechatronics and Measurement Technique, 6-8 Sos Pantelimon, district 2, Bucharest, Romania badita_l@yahoo.com

[3]Mechanical Departament, Institute of Civil Engineering, 59 Plevnei Way, 050141, Bucharest, Romania, florescuvirgil@yahoo.com

[4]"Carol I" National Defance Academy, Bucharest, Romania, catalin258@yahoo.com

Abstract: *This work continues the approach of one of our topics relating to a MOM THP with self-directed movement balls. Experiments revealed a certain seizure in some strain conditions. Laboratory trials for balls/plane Hertzian contacts have been restarted in order to determine seizure behaviour depending on the roughness of the flat area. The trials have been carried out in BSF (body simulated fluid) lubrication conditions, much closer to the real operating conditions up against the initial tests with distilled water. Seizure burdens to different loadings and contact surfaces roughness influence over the seizure burden have been determined. Even though the minimum value of the wear must be the same with the minimum value of the surfaces roughness, given the experimental conditions, it came out from the trials results on wear that the lowest level of wear is acquired at a certain value of roughness, not at the lowest level of roughness.*

Keywords: *MOM –THP with balls, self-directed movement, seizure, optimal conditions, wear scar, friction coefficient.*

1. INTRODUCTION

Nowadays, the design solutions for Total Hip Prostheses are diverse encompassing for improving the materials used for prostheses elements and reshaping geometrically and/or tribologically the load transfer path. In such context Total Hip Prostheses with rolling balls have been found as a possible viable alternative design to current industrial products, based on low friction of rolling contact, against sliding one (now used in most industrial designs).

Different designs of Total Hip Prostheses with Different designs of Total Hip Prostheses with rolling bodies have been developed in order to improve the tribological performances of the artificial joint. We could mention here the design with ball train, proposed by Katsutoshi and Kiyoshi [1], the French "Supertête" prosthesis [2], or the design with conical rolling elements proposed by Imperial College of Science, Technology and Medicine of London [3].

The French design, obtained by "Fondation de l'Avenir" in collaboration with "Ministère de la Défense, Mission Innovation", propose the insertion of a frictional contact inside a bearing. The design suggested by Imperial College of Science, Technology and Medicine of London consists in a major modification of a elements between the femoral part stem neck and the modular hip prosthesis by introducing a rolling bearing with conical femoral artificial head.

The bearing rotation axis corresponds with the axis of femoral stem neck, the rolling elements being guided by both the external surface of stem neck and the internal surface of the ball replacing the femoral head. But changing the contact mechanism from sliding to rolling in a hip prosthesis is not an easy task due to difficulties encountered in establishing the load transfer path, a critical characteristic of tribological behavior of joint with large influence in functionality and durability of prosthesis active elements.

Basically, the sliding contact between large surfaces of femoral head and acetabular cup was replaced by a multitude of rolling contacts with a different pattern of stress distribution influenced by rolling elements position at some instant during relative movement between femoral and acetabular parts.

In the present paper, the authors focus on the original design proposed by them in [4], *i.e.* a MOM Total Hip Prosthesis with self directed rolling balls (see Fig. 1).

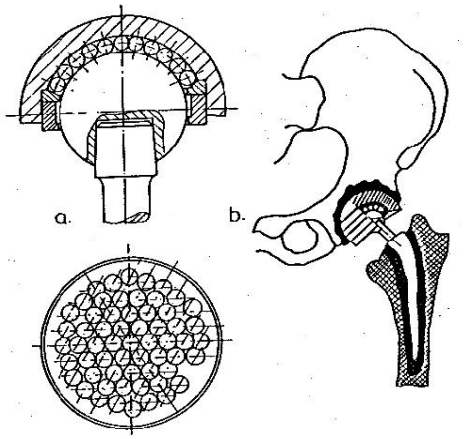

Figure 1. Total Hip Prosthesis with self directed rolling bodies.

A characteristic of this design solution is the fact that the artificial joint will work similar to a spherical bearing, having what is called a "compensation space", *i.e.* enough free space between the femoral and acetabular parts of the prosthesis to allow the movement of the balls [5].

Previous research studies performed by the authors focused on the determination of the initial position of rolling balls due to geometrical restraints of the assembly and on the estimation of the overall friction coefficients in dry and lubricated motion [5].

The geometrical studies (see [6] and [7]) have shown that generally the balls are located non-symmetrically and that the configuration for a given space and a given number of balls is not unique. Tribological studies performed by he authors (see [4], [6] and [7]) have shown very low values of overall friction coefficients (0.12 to 0.2 for dry joint and 0.006 to 0.009 in the presence of lubricants), leading to an enhanced functionality of the prosthesis itself. The present study will use the results of the previous studies in order to determine the load distribution through the balls bed and the compressions generated between the joint elements (femoral head, rolling balls, acetabular cup).

As we previously stated, a general study of the proposed design will target the following mechanical aspects:

– characterization of load transfer mechanism through the joint elements (statics of enveloping loads and/or dynamics studies of natural, physiological movements);

– evaluation of tribological behavior of all joint elements (including contact mechanics of all active interfaces – femoral head-ball, ball-ball, ball-acetabular cup);

– estimation of functional threats and damaging mechanisms for the proposed design (*i.e.* clear definition of criteria for joint locking, fatigue of prosthetic parts, wear of active elements of the joint) and determination of influencing factors for all these unwanted phenomena.

Lessons learned from previous attempts (structural overall analysis performed in [8]) lead to decoupling the statics and dynamics of the joint (FE analyses) from the tribological behavior (separate analytical evaluation) in order to save computational effort and assuming simplifications. The characteristics of the prosthesis under evaluation are as follows:

- type: Total Hip Prosthesis (THP) with self directed rolling balls;

- geometrical features: outer radius of femoral head - 14 mm*;* radius of each rolling ball 1.25 mm*;* internal radius of acetabular cup - 16.5 mm; spherical cap for balls bed (subtended angle) - 160°;

Material used for components:

- femoral head - Stellite 21;
- acetabular cup - Ti6Al4V;
- rolling balls - CoCrMo alloy.

The methodology used for computing the number of balls needed for assembling the joint and their positions inside the artificial joint is that used in [4]. The resulted configuration of artificial joint was used in order to build the numerical model for load transfer path through the balls bed.

The 3D numerical model is a large one – 58,784 elements and 73,100 nodes, with numerous surfaces in contact, requiring high computational resources and significant time for simulation. Instead of using a big model with multiple non-linearities, a simplified model was built based on the following assumed hypotheses

1. Femoral head and balls have been considered rigid (their stiffness is much higher than acetabular cup stiffness).

2. The compressive force and flexion drive moment have been maintained constant.

3. Linear elastic behavior of acetabular cup was assumed.

4. The compressive forces acting at the ball-to-ball contact surfaces are smaller than the compressive forces between balls and femoral head, respectively between balls and acetabular cup. This

assumption allows us to use, instead of spherical balls, unidimensional nonlinear elements (compression only) connecting the spots of contacts between the balls and cup, respectively between the ball and femoral head with the center of each ball.

The train of balls was not actually modeled as it is; instead of 3D representation of the balls (Fig. 5), unidimensional contact elements have been considered between the center of each ball and the active surfaces of femoral and acetabular prosthetic elements.

2. SIMULATION METHODOLOGY AND RESULTS

The 3D FE model was loaded by a compressive 1 kN force and a flexion of the joint was considered for ~37.6° (i.e. a relative maximum displacement of circumferential points located on femoral head and acetabular cup equal with 4 times the diameter of one rolling ball).

After the loads on each ball have been determined (being categorized based on balls regions rather than each ball itself) a local analysis was performed for establishing the extreme Hertzian contact parameters based on the following methodology [9]:

- maximum pressure, given by

$$p_0 = \sqrt[3]{\frac{6PE^{*2}}{\pi^3 R^2}}, \quad (1)$$

- radius of contact spot, given by

$$p_0 = \sqrt[3]{\frac{6PE^{*2}}{\pi^3 R^2}}, \quad (2)$$

- mutual approach between bodies in contact, given by

$$\delta = \sqrt[3]{\frac{9P^2}{16RE^{*2}}}, \quad (3)$$

where P is the applied compressing load, and R the relative curvature given by:

$$\frac{1}{R} = \frac{1}{R_1} + \frac{1}{R_2} \quad (4)$$

After performing the geometrical assessment, based on the methodology presented in [4], it results that the maximum number of balls needed for the spherical joint is 199, distributed on 12 consecutive rows [9] as follows:

$n_0 = 37$; $n_1 = 19$; $n_2 = 19$; $n_3 = 19$; $n_4 = 19$; $n_5 = 19$; $n_6 = 19$; $n_7 = 19$; $n_8 = 14$; $n_9 = 9$; $n_{10} = 5$; $n_{11} = 1$.

Images of the rolling balls positions for $\varphi = 0$ and $\beta = 0° \pm 15°$ (where φ and β are the azimuth and zenith angular coordinates in the spherical coordinate system associated with the femoral head). One could notice from the results of the mathematical analysis that the arrangement of the balls in the rolling space is asymmetrical and will not be uniquely determined.

After applying 1 kN compressive load onto the artificial joint having the balls train configured as resulted from the geometrical analysis [8], the loadings on each rolling ball during the 37.6° flexion were determined by FE analysis of a dynamic nonlinear model of the entire joint. Several three instances have been selected for presenting the results in both vertical a nd normal views to the flexion plane in Figs. 2.

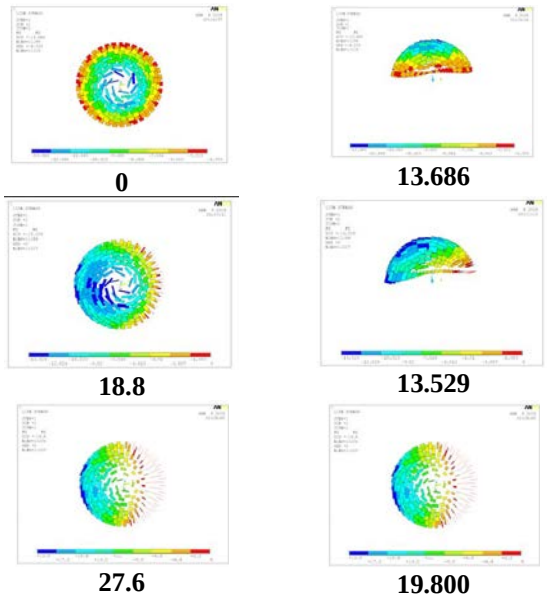

Figure 2. The compressive loadings transferred from femoral to acetabular parts of the prosthesis for different instances of flexion (between 0° and 37.6°); flexion listed in left, maximum load listed in right part of the pictures).

Its correspond to 1 - diameter, 2 - diameter, 3 - diameter and 4 - diameter relative displacements between the acetabular and femoral parts of the prosthesis.

By analyzing the plots, the following conclusions could be drawn:

a. Even for the initial condition, due to asymmetrical arrangement of the balls resulted from the geometrical analysis, there is some asymmetry of transferring the load path from the femoral head to the acetabular part [8].

b. During the flexion (especially for large angles) a part of the balls will not be loaded anymore, leading to an increase of the maximum force transmitted by intermediate of a rolling ball (from ~1.35% of the total joint compression force - as for flexion angles lower than 18.8°, to ~1.98% of the total joint compression force - as for a flexion of 37.6°) - Fig.2.

c. By analyzing the loading of each ball row, it has been determined (for the initial position, 0°

flexion) that the most loaded rows are those located close to 40°…60° from the equatorial plane (the rows located lower have small loads on each balls, and for the rows located higher each ball carries a bigger load but the number of balls is low). The distribution of rolling balls loading versus the zenith positioning angle of the rolling ball is presented in Fig. 3.

Analyzing the graph, the following conclusions could be drawn:

1. As reported before, there is a slight asymmetry of the distribution even for the initial position. This asymmetry evolves with flexion leading to unloading of some balls located peripherally outside the hemispherical area characterized by compressive loading pole.

2. The peripheral balls located closer to the compressive loading pole are generally highly loaded, but the highest loaded balls remain those positioned in intermediate rows (between 40° and 60° from the equatorial plane).

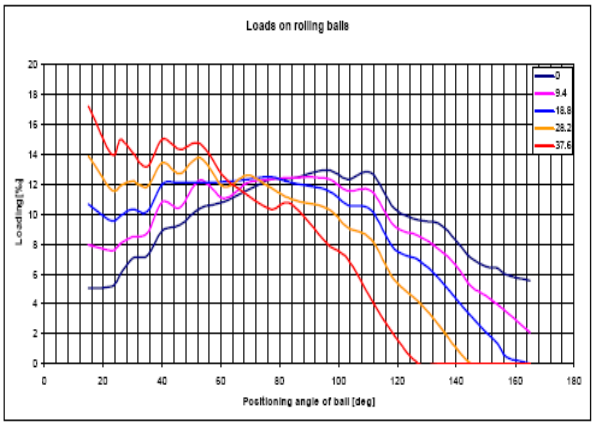

Figure 3. The rolling balls loadings versus zenith positioning angle of ball.

For the extreme maximum loadings of the balls during the analyzed flexion, a preliminary evaluation of tribological parameters of contact between femoral head and rolling balls and between rolling balls and acetabular cup has been performed by using formulae (1) - (3).

3. LABORATORY TRIALS

Experiments revealed a certain seizure in some strain conditions. Laboratory trials for balls/plane Hertzian contacts have been restarted in order to determine seizure behaviour depending on the roughness of the flat area. The trials have been carried out in BSF (body simulated fluid) lubrication conditions, much closer to the real operating conditions up against the initial tests with distilled water.

Seizure burdens to different loadings and contact surfaces roughness influence over the seizure burden have been determined.

Even though the minimum value of the wear must be the same with the minimum value of the surfaces roughness, given the experimental conditions, it came out from the trials results on wear that the lowest level of wear is acquired at a certain value of roughness, not at the lowest level of roughness.

For the tests we used the test rig presented in Fig. 4. In this test rig, the friction pair is formed from a bush with spherical profile and a flat disk shaped with a diameter of 18 mm and a thickness of 5 mm (see Fig. 5). The sphere's radius is r = 11.5 mm.

Figure 4. Experimental test rig

Figure 5. Used friction couple

In the static contact, compression stresses in contact spot, p_{max} si p_{med} (maximum pressure and mean pressure) are:

$$p_{max}^3 = 1.5\, PE^2 / \pi\, r^2\, (1-\mu^2)^2 \qquad (5)$$

$$p_{med} = \frac{P}{\pi a^2} \qquad (6)$$

and the radius of the contact surface, a, is:

$$a^3 = 1.5\left(1-\mu^2\right)P\frac{r}{E} \qquad (7)$$

where P is the load, a – radius of the contact surface, and r – radius of the sphere.

In the friction couple components (see Fig. 9) are made of steel, the quantities of equations (5), (6) and (7) become:

$$p_{max} \approx 5800 \sqrt[3]{P} \tag{8}$$

$$p_{med} \approx 1700 \sqrt[3]{P} \tag{9}$$

$$a \approx 0.09 \sqrt[3]{P} \tag{10}$$

Attention was paid to processing of working surfaces of couples. Surface state defined by topography, microstructure of surface layer and oxidation state has a major influence on the wear process.

Due to the complexity of processing by abrasion of the surface, the most reliable way to ensure a reproductible surface is stringently observance of all processing phases, which are turning of the form, finishing turning, thermal treatment, and correction of profile by polishing and superpolishing of working surface.

All the operations until smooth processing of the profile are made by current technology, noting that the intensity of the process is kept low to protect the structure of the surface layer of material.

Super-finishing operation using metallographic ground slides technique includes:

- wet polishing with sandpaper, grain size 32 μm and 17 μm;
- polishing with diamont slury, grain size 6 μm and 1 μm;
- wet polishing with slury of 2000 Å.

Finally, the surfaces are washed with distiled water, alcohol and then are dried.

The maintenance of processed couples is made in closed vessels, on silica gel. Surfaces roughness was measured with a roughness tester with parametric transducer and recording. The instrument allow recording of surface profile, and also determination of R_a and *r.m.s.*, defined as:

$$R_a = \frac{1}{l}\int_0^l |y| dx \tag{11}$$

$$r.m.s = \sqrt{\frac{1}{l}\int_0^l y^2 dx} \tag{12}$$

In Fig. 6 (A1-A8) profiles (cross-cut) of the surfaces used and of microphotographs obtained in normal lighting are presented.

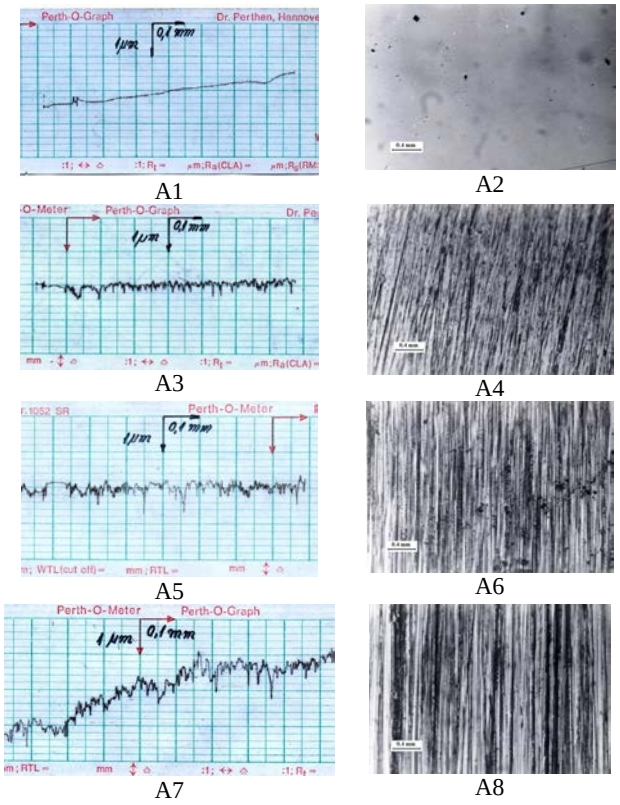

Figure 6. Profile and microfotograph of the surface with roughness R_a = 0.015 μm (A1-A2), R_a = 0.045 μm (A3-A4), R_a = 0.075 μm (A5-A6) si R_a = 0.19 μm (A7-A8).

4. RESULTS AND DISSCUSION

4.1. Evolution of the surface state in the wear process

Experimental determinations were made on these test conditions:

- Load: variabile between P = 20 ÷ 300 N for determining of seizure limit. A load of 50 N was used for wear tests.
- Sliding speed: Main speed for determining the wear rate was u = 174 cm/s. To determine the influence of speed on the wear, the device allows achieving speeds:

u = 60 cm/s; u = 18 cm/s si u = 3,2 cm/s.

- Lubricant: BSF (Body Simulated Fluid) with the density 1183 kg/m^3 and vascosity 0.84 Pa s (HyClone, SH30212.03).

Using the parameters above mentioned, the cpuple operates in elastohydrodynamic regime.

For the minimum thickness of the lubricant film, Archard [8] proposed the relationship:

$$\frac{h_0}{r} \approx 0.84\left(\frac{\alpha u \mu_0}{r}\right)^{0.741}\left(\frac{Er^2}{P}\right)^{0.074} \tag{13}$$

where: h_0-minimum thickness of lubricant film; r-radius of the sphere; α-pressure coefficient of vascosity; u-sum velocity; μ_0-dynamic viscosity at

atmospfericic pressure; *E*-reduced elasticity modulus; *P*-load.

Relation (13) reproduces satisfacatory the dependence of h_0 by the main quantities u, μ_0, r and P. The exact determination of the minimum lubricant film thickness depends on the knowledge of pressure coefficient α for lubricant used and the accuracy of the numerical coefficient of relationship (13). In working conditions, using an estimated value α, resulted a minimum lubricant film thickness $h \approx 0.06$ μm.

Spatial form of lubricant film in the loaded area results from Fig. 7 and 8, which represents two sections of lubricant film, longitudinal and cross sections (in relation to the movement) by the symetry axes.

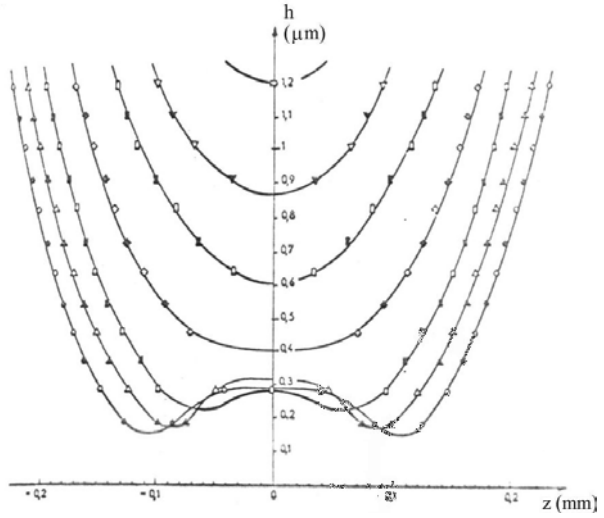

Figure 7. Variation of lubricant thickness in the $x = 0$ plane, function of load, at speed $u = 8$ cm/s.
▪ 0.7 N; ▼ 1.1 N; 1.5 N; ◊ 3 N; ▪ 4.6 N; ▲ 7.8 N; ○ 10.8 N.

Curves were obtained experimentally, under close conditions to those used by Dowson [9]. Are noticed significantly higher values for minimum thickness h_0, even at speed $u = 23$ cm/s.

To watch in good conditions the wear of fixed surface, function of couple roughness, the following solution was used: roughness of the couple was focused on one of surfaces, in particular on themobile one. Fixed surface had always the minimum roughness achievable, meaning about $R_a \approx 0.015$ μm.

As it is known, the composed roughness of the couple, expressed as standard deviations, σ, is:

$$\sigma^2 = \sigma_1^2 + \sigma_2^2 \qquad (14)$$

where σ_1, σ_2 represent the standard deviations of the two surfaces.

If one of the surfaces has small roughness, i.e. $\sigma_1 << \sigma_2$, then $\sigma \approx \sigma_1$. So it is possible to study the influence of roughness on the wear, just by changing the roughness of the of a single surface.

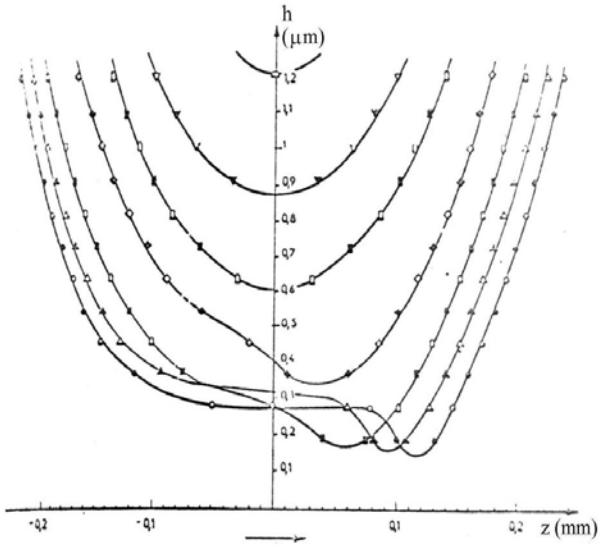

Figure 8. Variation of lubricant thickness in the $z = 0$ plane, , function of load, at speed $u = 8$ cm/s.
▪ 0.7 N; ▼ 1.1 N; 1.5 N; ◊ 3 N; ▪ 4.6 N; ▲ 7.8 N; ○ 10.8 N.

Under these conditions and at a load $P = 50$ N, speed $u = 1.74$ m/s and volume temperature of the lubricant $\theta = 50\ ^0$C, it vas determined the evolution of the surface wear function of the time, for the following roughness of the mobile surface: R_a = 0.015 μm; R_a = 0.045 μm; R_a = 0.075 μm si R_a = 0.19 μm.

In Fig. 9 are selectively presented, some wear marks obtained under some conditions mentioned above (at time $t = 5$ min.), to estimate the results reproductibility.

The worn volume for the three experimental determinations is:

E 1057; $V = 8.50 \times 10^{-5}$ mm^3;
E 1058; $V = 6.11 \times 10^{-5}$ mm^3;
E 1059; $V = 4.00 \times 10^{-5}$ mm^3;

$$\overline{V} = 6.2 \times 10^{-5} \text{ mm}^3.$$

Determinaations on several samples resulted in an average $\overline{V} = 6.2 \times 10^{-5}$ mm^3. for wear determinations, a deviations of 25% is completely satisfacatory.

Fig.10, shows the wear evolution function of time, for roughness of the bush R_a = 0.045 μm. Time of 3 sec., 1 min., and 5 min., was selected, each made with another couple. For roughness R_a = 0.015 μm, the wear evolution depending on the time was determined with same bush, the total running in time on the scar being divided into intervals of 1, 5 or 10 min. We chose this solution to monitor also the alteration of the bushis surface status. Fig. 10 shows that, except the first 5 min., wear remains at same level.

In Fig. 11 are presented the transversal profile and the image of wear imprint for sample with R_a = 0.045 μm, $t = 5$ min. (sample 703); R_a = 0.045 μm, $t = 5$ min., but with bush from the previous

determination (total running in time t = 10 min., (sample 704); R_a = 0.045 μm, t = 5 min., with the bush from the previous determination (total running time t = 20 min. (sample 705).

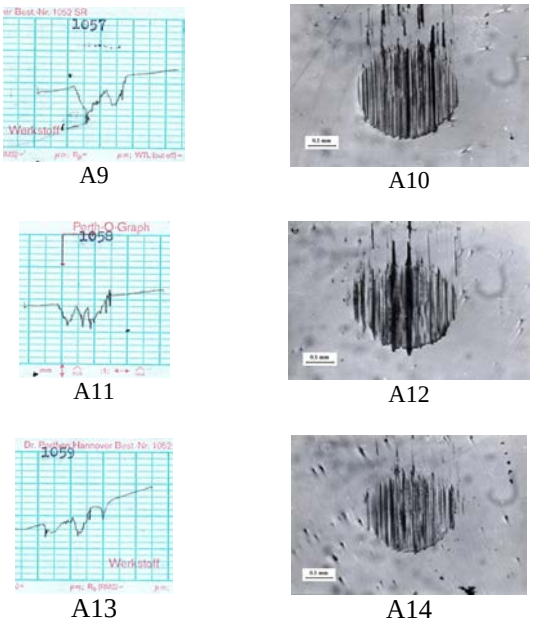

A9 A10 A11 A12 A13 A14

Figure 9. Central transversal profile and image of wear scar (magnification x 68). R_a = 0.015 μm, t = 5 min.

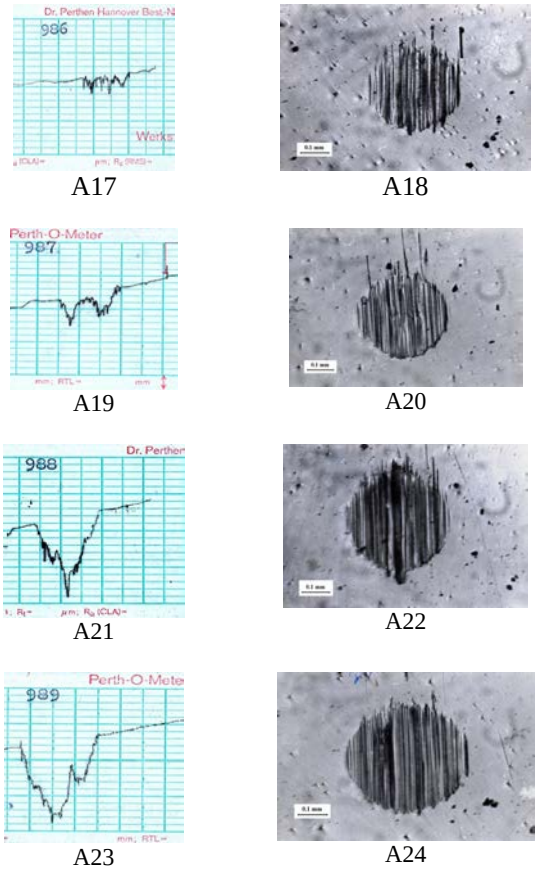

A17 A18 A19 A20 A21 A22 A23 A24

Figure 10. Central transversal profile and image of wear scar (magnification x 68). R_a = 0.045 μm, t = 5 min

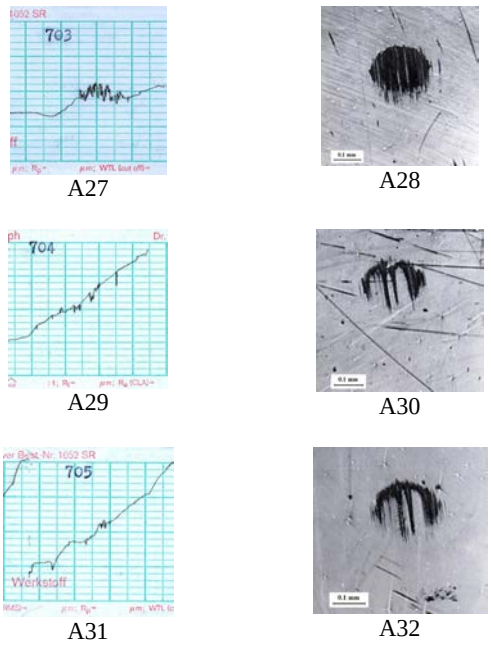

A27 A28 A29 A30 A31 A32

Figure 11. Transversal profile and image of wear imprint for samples with R_a = 0.045 μm, t = 5 min. (sample 703); R_a = 0.045 μm, t = 5 min., but the bush from the previous determination (total running in time t = 10 min. (sample 704); R_a = 0.045 μm, t = 5 min., but the bush from the previous determination ((total running time t = 20 min. (sample 705).

Wear evolution depending on the time for different roughness is shown in Fig. 12. By increasing the running time from 5 min., to 30 min., the wear does not increase only about 10%.

Is noted the rapid reduction of wear rate function of time, except the surface with roughness R_a = 0.045 μm. In the first 3 seconds it is produced between 25% and 50% of wear at 30 min. This wear evolution explained by complying surfaces, which results in changing the lubrication regime.

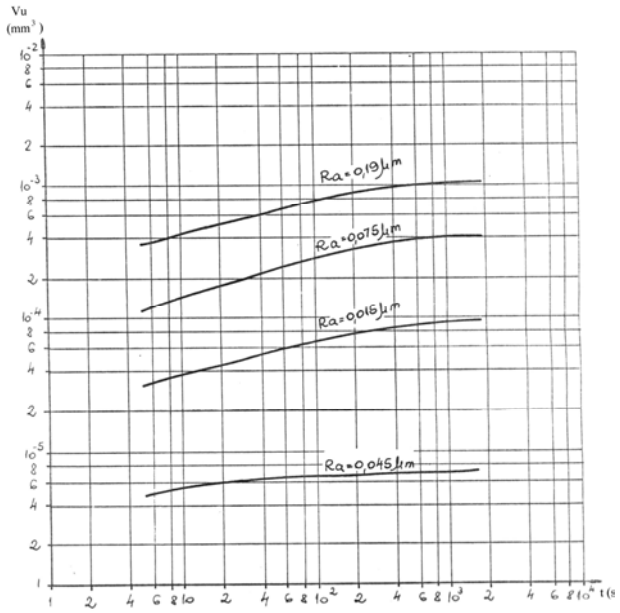

Figure 12. Wear evolution function of time, for different roughness.

Note that the amount of wear on the plateau is caused by the initial wear (during the first few seconds of operaton). This observation allows the use of wear value at t = 5 min., as representative quantity for the existing operating conditions. At this time of operation, scattering of values is lover.

In the case of surfaces with R_a = 0.045 μm, the wear is so low that during the entire period of time used, lubrication conditions remain aproximately unchanged.

Evolution of the wear function of time, for roughness R_a = 0.075 μm (samples 826, 827, 829, 830 and 832, is shown in Fig. 13.

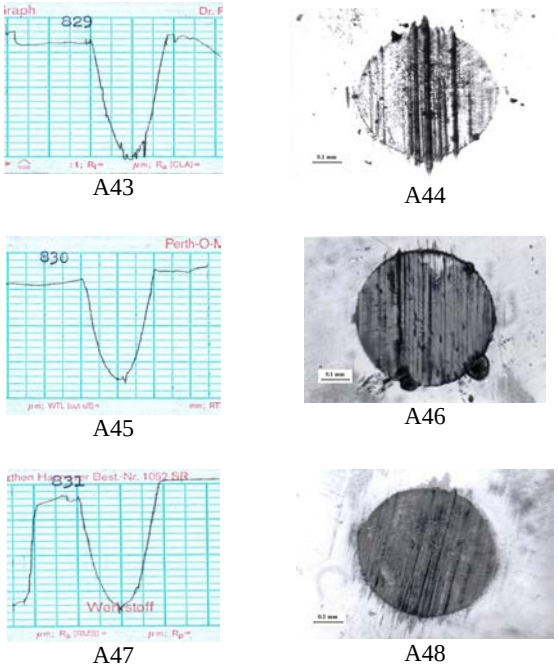

A43 A44 A45 A46 A47 A48

Figure 13. Evolution of the wear function of time, for roughness R_a = 0.075 μm (samples 826, 827, 829, 830 and 832)

Different roughness used have caused not only a diference between worn volume value, but also in the aspect of wear imprint (wear type). In the case of surfaces with R_a = 0.015 μm, R_a = 0.075 μm, (t =3 sec.) and R_a = 0.19 μm, (t =3 sec.), the wear is of adhesive type (metallic shape with prononced scratches). In the case of surfaces with R_a = 0.045 μm, oxidative wear type is prevailling. While reducing the wear rate as a result of surface compliance, surfaces with R_a = 0.075 μm and R_a = 0.19 μm, also goin in oxidative wear regime.

Evolution of the wear function of time, for roughness R_a = 0.19 μm (samples 832, 835, 849, 836, 837 si 850, is shown in Fig. 14.

For roughness R_a = 0.015 μm, R_a = 0.075 μm and R_a = 0.19 μm, the results obtained for the volume of worn material, are consistent with the strain of contact, determined by the lubricant film parameter h_{min} / σ.

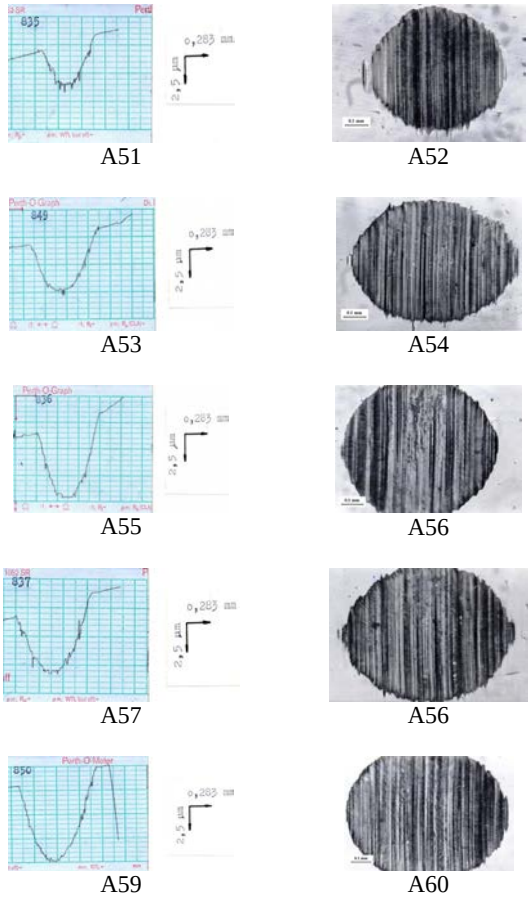

A51 A52 A53 A54 A55 A56 A57 A56 A59 A60

Figure 14. Wear evolutionear function of time, for roughness R_a = 0.19 μm (samples 835, 849, 836, 837 and 850)

For srfaces with roughness R_a = 0.045 μm, there were observed a running-in influence. After the first 5 minutes of operations, the entire contact supraface is covered with oxide. The imprint obtained after another 5 minutes, with the same bush, has a particular form, oxidative wear area restricting the half at outcome ofthe loaded area (samples A52 si A54). It follows that after running, lubrication condition improve.

Figure 15 shows the central profile and the image of wear imprinr (magnification x 68). R_a= 0.15 μm, t =30 min. Pr 997, (new bush).

A61 A62

Figure 15. Central transversal profile and image of wear imprint. R_a = 0.15 μm, t = 30 min., sample 997 (new bush).

Next, Figure 16 ilustrates the effect of running on the wear behaviour of the surface with R_a= 0.15

µm, compared with Figure 17, wich shows the effect of running on the wear behaviour of surface with R_a= 0.045 µm.

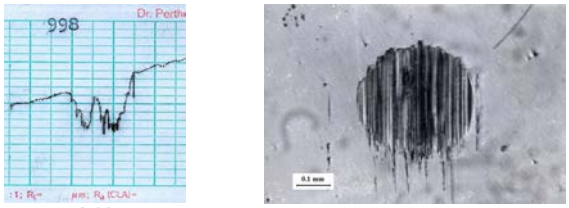

A63 A64

Figure 16. The effect of running-in on the wear behaviour of the surface with R_a= 0.015 µm, t = 5 min, Pr 998. The bush from previous determination was used.

A65 A66

A67 A68

A69 A70

Figure 17. The effect of running-in on the wear behaviour of the surface with R_a= 0.045 µm, t = 5 min, samplez 999, (new bush) 1000 and 1001 (with the bush from previous determination).

Different roughness used has caused not only a difference between worn volume values, but also in the aspect of wear imprint (wear type). In the case of surfaces with R_a = 0.015 µm, R_a = 0.075 µm, (t =3 sec.) and R_a = 0.19 µm, (t =3 sec.), the wear is of adhesive type (metallic shape with pronounced scars). In case of surfaces with R_a = 0.045 µm, oxidative wear type is prevailing. While reducing the wear rate as a result of surface compliance, surfaces with R_a = 0.075 µm and R_a = 0.19 µm also go in oxidative wear regime.

In the case of super-finished surfaces, with R_a = 0.015 µm and R_a = 0.045 µm, a favourable influence of running in is not observed.

For rouhness R_a = 0.015 µm, R_a = 0.075 µm and R_a = 0.19 µm, the results obtained for the volume of worn material, are consistent with the strain of contact, determined by the lubricant film parameter h_{min} / σ.

For surfaces with rouhness R_a = 0.045 µm, there was observed a running-in influence. After the first 5 minutes of operation, the entire contact surface is covered with oxide. The imprint obtained after another 5 minutes, with the same bush, has a particular form, oxidative wear area restricting the half at outcome of the loaded area (sample 1001). It follows that after running-in, lubrication conditions improve.

In the case of super-finished surfaces, a favourable influence of running-in is not observed.

4.2. Influence of initial roughness on the wear and friction coefficient

Surface wear, a quantity determined by the fraction of area in contact, should be a monotone function of film parameter h / σ. The minimum value of wear should coincide with the minimum value of surface roughness.

A large number of determinatons of wear, with four roughness have been made: R_a = 0.015 µm; R_a = 0.045 µm; R_a = 0.075 µm si R_a = 0.19 µm. Mean values of volume of worn material for the four roughness are:

R_a = 0.015 µm→V_u = 7.0 x10^{-5} mm^3 → μ = 0.038;
R_a = 0.045 µm→V_u = 7.0 x10^{-6} mm^3 → μ = 0.050;
R_a = 0.075 µm→V_u = 3.7 x10^{-5} mm^3 → μ = 0.038;
R_a = 0.190 µm→V_u = 1.0 x10^{-3} mm^3 → μ = 0.078.

Simultaneously with the surface wear, the friction coefficient was also measured.

In Fig. 18 reprezentative images for three of the four roughnesses are presented.

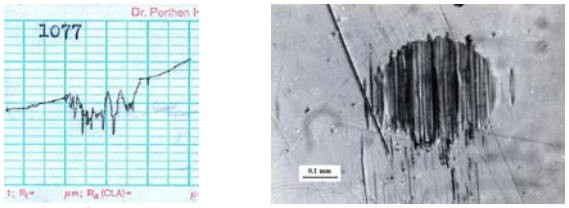

A75 A76

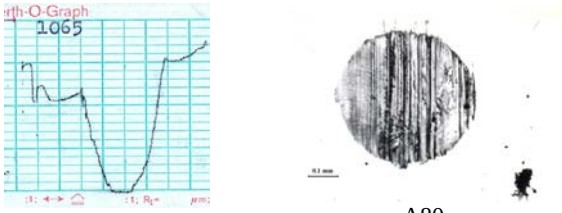

A79 A80

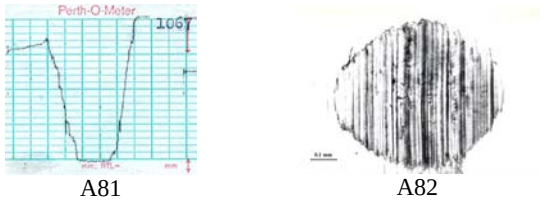

A81 A82

Figure 18. The effect of running-in on the wear behaviour of the surface with R_a= 0.015 µm, t = 5 min, Pr 998. S-a folosit bucsa de la determinarea precedenta.

Existence of an optimal roughness can be explained either by an effect on lubricant film or by a change in mecahanical properties of surface. In this case, at the optimal roughness, reduction of the ratio h / σ is compensed by increase of wear resistence of the surfaces.

5. CONCLUSIONS

From determinatios of the evolution over time of the wear, it resulted that, in the experimental conditions used, minimal wear occurs at a certain valoare of roughness and not at the minimal roughness.

Surprisingly, minimum friction coefficient does not coincide with minimal wear.

The existence of a minimum in the wear curve results for roughness R_a = 0.045 μm. At the same time the friction coefficient is minimal at roughness R_a = 0.045 μm. A mathematical relationship betveen friction coefficient and wear cannot be established.

REFERENCES

[1] B. Katsutoshi, G.E., S. Kiyoshi: US Patent 5092898 / 03.03.1992.

[2] J.P. Davant: *Chirurgie de la hance. Mieux vivre avec une prosthesis.* Fonder l'avenir, 23, pp. 53-56, 1995.

[3] M. Sadeghi-Mehr: *Investigations of Rolling Element Bearing for Hip Joint Prosthesis*, PhD Thesis, Imperial College of Science, Technology and Medicine University. London, 1997.

[4] A. Iarovici, L. Capitanu, V. Florescu, M. Baubec: "*Hip Joint Prosthesis with rolling bodies*", Proceedings of the Romanian Academy – Series A: Mathematics and Physics, Technical Sciences, Information Science, **1**, *1-2*, pp. 37-44, S. 2001.

[5] L. Capitanu, V. Florescu. *New Concepts for Improved Durability in MOM Total Hip Endoprostheses. A review.* American Journal of Materials Science. Vol.2, No. 6, December 2012.

[6] A. Iarovici, L. Capitanu, V. Florescu, M. Baubec, F. Petrescu. *Hip Joint Prosthesis with Rolling Bodies, Part I – The Balls Arrangement Analysis*. Proceedings of the Annual Symposium of the Institute of Solid Mechanics – SISOM, pp. 251-258, 2001,

[7] A. Iarovici, L. Capitanu, V. Florescu, M. Baubec, F. Petrescu. *Hip Joint Prosthesis with Rolling Bodies, Part II – Numerical and Graphical Examples*. Proceedings of the Annual Symposium of the Institute of Solid Mechanics – SISOM, pp. 259-263, 2001.

[8] A. Iarovici, L. Capitanu, J. Onisoru, V. Florescu, M. Baubec. *Stresses and deformations analysis for Hip Joint Prostheses with Rolling Bodies*. Proceeding of the Annual Symposium of the Institute of Solid Mechanics SISOM 2002, pp. 263-268.

[9] Dowson D. *Elastohydrodynamic lubrication. Interdisciplinary Approach to the lubrication of concentrated contacts*. (Ed. P.P.KU) NASA SP – 237, 1970.

Serbian Tribology Society

SERBIATRIB '13

13th International Conference on Tribology

Faculty of Engineering in Kragujevac

Kragujevac, Serbia, 15 – 17 May 2013

ANALYZING THE INFLUENCE OF THE CONSTRUCTION ELEMENT POSITION ON TORQUE TRANSMISSION BY FRICTION

Marija Jeremić[1], Bojan Bogdanović[1], Aleksandar Simić[1], Dragomir Miljanić[2]
Petar Todorović[1], Sasa Randjelovic[1], Branko Tadić[1]
[1]Faculty of Engineering, Sestre Janjić 6, Kragujevac, Serbia, mjeremic88@yahoo.com, bogdanovicboki@gmail.com, aleksandarsimickg88@gmail.com, petar@kg.ac.rs, sasarandjelovic@yahoo.com, tadic@kg.ac.rs
[2]Metalik, Nikšić, Montenegro

Abstract: *This paper is analysing the impact of the construction element position of ship winch drum on the effects of torque transmission by friction in the mechanization welding process. The driving and driven wheels (construction elements) were examined for the general case of the load distribution. Based on this examination, the construction of the device that should provide the reliable torque transmission and the movement of the drum in the process of its welding is proposed. This construction is characterized by a high level of flexibility and ability to change the friction torque based on changing drum position in regard to the driving and driven wheels (construction elements). With this new construction, problems related to the movement synchronization are avoided, unlike the all previously known constructions of this type, which lead to the positive impact on the wear intensity of friction gears.*

Keywords: *friction, wear, transfer of torque, special device, marine winch drum*

1. INTRODUCTION

Research described in the paper is related to the problems of friction torque transmission. Research is applicative and connected with design of boot device (reversal) drum ship winches during welding process. Torque transmission is performed by friction tribological contact with rubber and metal. Movement can be reached by using only the effects of friction, but friction during movement always brings different types of losses. Connected with this, knowledge of the value of coefficient of friction is very important for every engineer and designer who is involved in design and development of mechanical structures, which perform their function through interaction of surfaces which move relatively. It is well known that the process of friction follows every kind of body movement. Friction is a necessary process because only with effects of friction can be achieved starting, moving, changing speed or stopping. On the other hand, during movement, as a consequence of frictional resistance, that resistance must be overcome in order to continue movement, which is why the energy losses exist. In addition to energy loss, friction is always accompanied with wear of material on contact surfaces, which produces an additional costs and loss of functionality of elements in contact.

Friction is, therefore, such a process which, at the same time, manifests positive and negative effects. It is therefore natural that there is a tendency to eliminate its negative effects, or at least minimize, and to increase the positive [1]. A review of the knowledge of the friction force, as well as ways for measurement are presented by Peter J. Blau [2], he presented some of the most common standards-defined measuring methods for static and dynamic friction coefficient, and its potential uses. Beginning of movement of any kind is related to the existence of static friction. Static coefficient of friction depends of many parameters, especially from the surface of contact, normal load, and temperature of the atmosphere in which contact occurs, surface absorption, quality of contact surface materials [3-7]. Analyzing the rolling process [8] in the absence of any load, the conclusion is that the energy losses are result of collisions of two moving rolling mass, i.e. mass of rolling body with the body on whose surface is

rolling. Rolling resistance of radial motion of the cylinder at flat surface was investigated in the paper [9]. Tested results showed that the coefficient of rolling friction depends on the speed of cylinder movement. At low speeds of cylinder, the coefficient of rolling friction increases due to increasing of substrate rate of deformation. For higher speeds, however, the coefficient of rolling friction is reduced, thereby lowering the area of the deformed surface. The maximum force of friction at the initial moment of slip has been investigated on rubber-metal friction pairs under conditions of constant compressive deformation of the rubber during transition from the high-elastic to the glassy state questioned A. I. El'kin et al [10] in the paper. Filled butadiene-nitrile rubber compounds were studied in the temperature range from +20 to −50°C. The temperature dependence of the maximum force of friction has a sharply expressed maximum near the glass transition temperature. As the temperature falls, the force of friction at first increases, in accordance with the molecular-kinetic theory. As the temperature continues to fall, in the transition region maximum force of friction begins to rise more sharply owing to a sharp increase in the volume-mechanical friction component. The fall in the maximum force of friction below the glass transition point associated with a decrease in the deformed volume of rubber due to shrinkage and with the reduced mechanical loss factor. Persson et al [11] study the sliding friction for viscoelastic solids, e.g., rubber, on hard flat substrate surfaces. Consider first the fluctuating shear stress inside a viscoelastic solid which results from the thermal motion of the atoms or molecules in the solid. At the nanoscale the thermal fluctuations are very strong and give rise to stress fluctuations in the MPa range, which is similar to the depinning stresses which typically occur at solid-rubber interfaces, indicating the crucial importance of thermal fluctuations for rubber friction on smooth surfaces. Developed a detail model which takes into account the influence of thermal fluctuations on the depinning of small contact patches (stress domains) at the rubber-substrate interface. The experiment led to the conclusion that the amplitude of the surface roughness has a very small effect of friction sliding rubber. The effects of carbon and cellulose fibers on the tribological characteristics of rubber-based friction materials examined Akbar et al in his paper [12]. Friction tests realized with different sliding speeds and different temperatures, with the examination of the microstructure and mechanical properties of the surfaces in contact. Experimental results showed that carbon fibers had a minor effect on the coefficient friction, but that increase wear resistance. Shanahan et al [13] investigated the mechanism of adhesion that occurs in the contact pair rubber and hard metal rolling bodies. The high degree of adhesion can be apparent even at room temperature if the contact time and pressure reach sufficient values. Based on obtained results it was determined that energy, which is dissipated during rolling, refers not only to the influence that accompanies histeresis adhesive separation, but also to the losses caused by loading with large cylinder. The nature of friction between the rubber and the solid substrate is very important for many technical applications. Friction of rubber is significantly different from the friction between hard substances such as metals and ceramics. In the paper [14] it was proved that the tire has significantly favorable friction characteristics.

In order to optimize the construction were performed large number of theoretical considerations and preliminary ideas were done for a detailed review and analysis of the literature that examines this issue. Research is based on determining the transmission of torque from the special device on marine winch drum, which is done by means of friction between rubber and metal.

2. CONCEPTUAL DESING OF ROTATING EQUIPMENT FOR WELDIND

An important aspect of implementing of any automated system to the manufacturing process is its price. Because of that, design should be analyzed in detail determing which parts of the technical system are not meaningful to automate. To define the appropriate general design, project starts with the technical requirements of the product, discusses design solutions of existing products with similar functions (Figure 1). Drive of rotary positioner shown is realized by two electric motors and gears, because speed and variable speed drive is required. The principle of operation of the electric motor which drives pieces of the structure requires ensuring synchronization of movement, which is serious theoretical and practical problem.

Figure 1. Rotating positioner

Especially when the chain transfer torque transmission is based on the basis of friction. The requirement for the proper operation of structures, in the presence of synchronization, is that the motors are with the same characteristics. One of the problems of providing synchronized movement is the possible difference of phases of propulsion motors. In addition, great equalization currents can occur that can cause permanent deformation of the motor coils. In addition to these phenomena can occur torque on the wheel axle, which can cause even shaft breakage. If there is a significant phase shift of motors, engines must be harmonized, which means, must be speed up or slow down. The problem of not synchronized movement has a particularly negative impact on the frictional wear of the drive wheels.

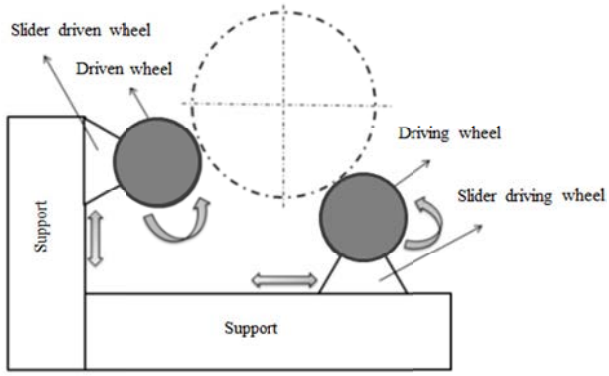

Figure 2. Conceptual design of construction

Conceptual principally solution system Apogon drum marine winch, during the drafting process is shown in Figure 2. General function of rotational structure is achieved (Figure 2) executing a series of partial functions. Rotary positioner is composed of more machine parts, sub-assemblies, subgroups and groups linked to a functional unit. A flexible shaft coupling is interconnected with the shaft and wheels so the torque and power from the engine is transmitted from one shaft to another point. Driven wheels rotating function performed under the influence of rotation of the drum. Frames construction, rely on a base that is used to keeping a distance between frames is realized, depending on the needs of the fastener.

3. ANALYSIS OF FORCES ON TRANSMISION

Dimensioning of steel structures is performed based on knowledge of layout external actions (forces and moments). Determining the ability of construction to convey given loads of force is based on the characteristics of the materials used and the allowable stress. Allowable stresses are prescribed for the steel structure and functions are determined by the choice of the material and the character of the external load. Calculation of the construction is proof load and usability of the structure under the influence of prescribed load during the life time of construction. The process of designing, calculating and dimensioning of construction is actually choice of a calculation model to credibly describe the real behavior of the structure under the prescribed load, but taking into account the optimal complexity of the model, the possibility to calculate the performance and profitability of individual parts of the structure. This work studied the loads that occur in the system. System shown in Figure 3 was examined as static system, i.e. system at rest state and the conditions that enable this state are used. External cause (external effects) on the solid body is the force that causes a change in sleep mode and the motion of the system. For the analysis of the effects of forces in the specific example of the drum with diameter D = 1000 mm and length l = 2000 mm load is the weight of the drum, which is G = 50000 N. Based on these data dimensions of construction were developed. It is necessary to determine the load distribution, especially load of friction wheel as a function of drum position (Figure 3). Rotary positioner is designed that at work most of the weight rests on the drum drive wheel. The whole system is viewed as a horizontal system which is attached to the substrate. In this case, the main task is reduced to the determination of the resistance of the supports and the force of friction.

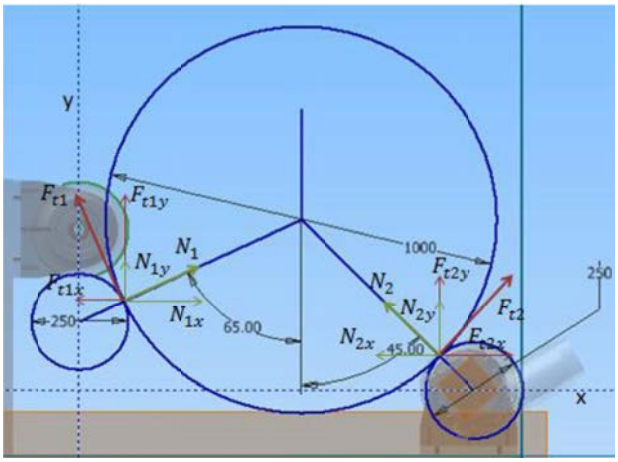

Figure 3. Schedule forces on the maximum size of the drum

In the beginning problem is solved imagining that the supports are removed and replaced by their action forces called resistance actions, as in this case the normal force wheels N_1 and N_2. It analyzes the effect of the friction forces that appear between the drum and wheel. How there are different materials in the contact zone, i.e. the interaction between the rubber and steel, the coefficients of friction μ is different. Connected with this, for the

sliding friction, apropos coefficient of friction between the drive wheel and the drum takes the value $\mu_p = 0.6$, and the value of coefficient of rolling friction between the driven wheels and drums $\mu_{kot} = 0.05$. As a starting basis for solving given problem is the determination of friction force from the equation:

$$F_{t1} = N_1 \cdot \mu_1$$
$$F_{t2} = N_2 \cdot \mu_2$$

In order that observed system was in equilibrium, the resultant of all the forces must be equal to zero. Since in the observed case of action of horizontal and vertical forces, this implies two equilibrium conditions.

$$\sum_{i=1}^{n} x_i = 0 \quad and \quad \sum_{i=1}^{n} y_i = 0$$

From the previous two conditions can be calculated unknown resistance supports N_1 and N_2. It's actually a system of two equations with two unknowns. The first condition of equilibrium is the sum of all components of the forces which act horizontally in the direction of the x axis is equal to zero:

$$\sum_{i=1}^{n} x_i = F_{t2x} - N_{2x} + N_{1x} - F_{t1x} = 0 \qquad (1)$$

where are: $F_{t1x}, F_{t2x}, N_{1x}\ i\ N_{2x}$- projection force F_t i N on the x axis.

The second condition is the sum of all forces which acting vertically on the given system is equal to zero:

$$\sum_{i=1}^{n} y_i = F_{t1y} - F_{t2y} + N_{1y} - N_{2y} - mg = 0 \quad (2)$$

where are: $F_{t1y}, F_{t2y}, N_{1y}\ and\ N_{2y}$ - projection force on the y axis.

Further analysis of the static equations depending on the angles $\varphi_1 and\ \varphi_2$ that are within the values of 65^0 to 82^0 for angle φ_1 ie. from 38^0 to 47^0 for angle φ_2 to get possible values of the forces that are shown in Table 1.

The final expressions for the calculation of reaction to friction wheels are:

$$N_2 = N_1 \frac{\mu_1 \cdot \cos\varphi_1 - \cos(90 - \varphi_1)}{\mu_2 \cdot \cos\varphi_2 - \cos(90 - \varphi_2)} \qquad (3)$$

$$\frac{\mu_1 \cdot \cos\varphi_1 - \cos(90 - \varphi_1)}{\mu_2 \cdot \cos\varphi_2 - \cos(90 - \varphi_2)} = k \qquad (4)$$

where k is a dimensionless coefficient.

Table 1. The dependence the force of angles

The dependence the friction force and the resistance supports on the angle φ_1
$F_{t1x} = -N_1 \cdot \mu_1 \cdot \cos\varphi_1$ $F_{t1y} = N_1 \cdot \mu_1 \cdot \sin\varphi_1$
$N_{1x} = N_1 \cdot \cos(90 - \varphi_1)$ $N_{1y} = N_1 \cdot \sin(90 - \varphi_1)$
The dependence the friction force and the resistance supports on the angle φ_2
$F_{t2x} = N_2 \cdot \mu_2 \cdot cos\,\varphi_2$ $F_{t2y} = N_2 \cdot \mu_2 \cdot sin\,\varphi_2$
$N_{2x} = -N_2 \cdot cos(90 - \varphi_2)$ $N_{2y} = N_2 \cdot sin(90 - \varphi_2)$

Static equilibrium conditions for the y axis is:

$$N_1 = \frac{mg}{k \cdot \mu_2 \cdot \sin\varphi_2 + k \cdot \sin(90 - \varphi_2)} + \\ + \frac{mg}{\mu_1 \cdot \sin\varphi_1 + \sin(90 - \varphi_2)} \qquad (5)$$

$$N_2 = N_1 \cdot k \qquad (6)$$

$$F_{t1} = N_1 \cdot \mu_1 \qquad (7)$$

$$F_{t2} = N_2 \cdot \mu_2 \qquad (8)$$

Showing force intensity in depending on the changes of angles, ie. depending on the position of the drum, and with the same diameter and weight of the drum, were calculated and are presented in Table 2.

Table 2. Force intensities depending on the angles

	φ_1	φ_2	N_1 [kN]	N_2 [kN]	F_{t1} [kN]	F_{t2} [kN]
1	82	38	6.03	41.41	0.30	24.85
2	80	39	6.88	41.16	0.34	24.70
3	78	40	7.75	40.88	0.39	24.53
4	76	41	8.61	40.55	0.43	24.33
5	74	42	9.48	40.19	0.47	24.11
6	72	43	10.35	39.79	0.52	23.87
7	70	44	11.22	39.35	0.56	23.61
8	68	45	12.11	38.87	0.61	23.32
9	66	46	12.99	38.35	0.65	23.01
10	65	47	13.83	38.01	0.69	22.80

Based on analysis of obtained values of the normal forces and frictional force from Table 1, it can be observed that for settings in any position, the highest intensity have a force N_2, i.e. maximum load is on the drive wheels. Based on comparative analysis calculation, as well as most of the calculation that are not shown in this paper, dependence of driving force (friction force) in the function of the drum position is established, i.e. dependance of angles $\varphi_1\ i\ \varphi_2$. This dependency of the complex form $F_{t2} = f(\varphi_1, \varphi_2)$ is shown in the diagram, which is shown in Figure 4.

It can be seen from the diagram that the function reaches a very high values of the force intensity around angles $\varphi_1\ and\ \varphi_2$ which are close to 90^0. It

is obvious that this is a so-called wedge effect, which occurs at extremely high intensity of tangential force.

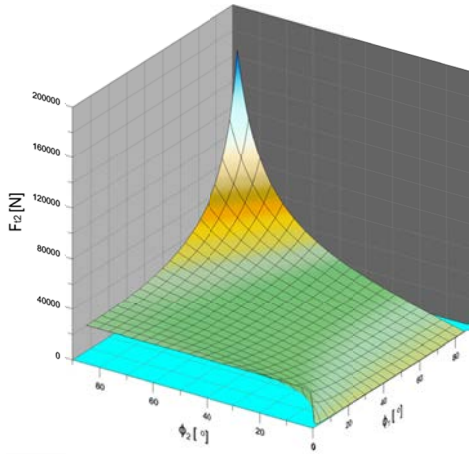

Figure 4. Diagrammatic representation of the dependence of the friction drive wheel of the angles

Ostensibly, this "extreme function" can be good solution from the driving forces aspect. However, to achieve such high values of driving force, the system must be exposed to very high values of normal load, in the order of 20 [kN]. The application of such high load is very problematic in terms of the allowable stress levels between the drum and drive wheel. For this reason, the authors find that the angles of φ_1 *i* φ_2 2 should be chosen in a range with much lower values, with which will not be intensive wear and will be ensured stability of device.

4. CONSTRUCTIVE SOLUTION OF DEVICE

Calculation of the structure derived in the previous section proves portability and usability of the structure under the influence of prescribed load during the life time of construction. Concept of special device (device for popositioning and rotation of drum during manufacturing process) presented has as main function of torque transfer (power) on the basis of friction between rubber and steel elements that are in direct contact. To ensure the power transfer, it is necessary that the force of friction is greater than torque on the wheels. In the process of development as well as design structure shown, estimate segment of profitability aspect is a key element in the design. This type of positioner is specifically designed and manufactured for the purpose of increasing productivity, reducing the intensity for the welder, because all the welding process can be performed automatically. Welding head is managed by welder, while workpiece rotates. Welding circular cylinder (drum), using a crane to set the adjustable rollers trolley. The distance of cart can adjust the size of the cylinder. In Figure 5, the different dimensions of the drum can be set on the positioner. The distance between the rollers can be, depending on needs, set by screw. Movement of rolls is possible in horizontal and vertical direction of the positioner frame. Drive for rollers are accomplished with one electric motor, which reduces the speed by worm gear. Operation of the second part of the carriage is achieved by a flexible shaft. In this way using of fluid power the synchronization of engine is avoided. Using a positioner in the production process, which gives high efficiency and cheaper process of welding, has the characteristics of light, reliability, performance and wide field of applications. Workpieces are therefore placed in the best possible way and in the most favorable position in relation to the welders, and on the basis of technical documentation.

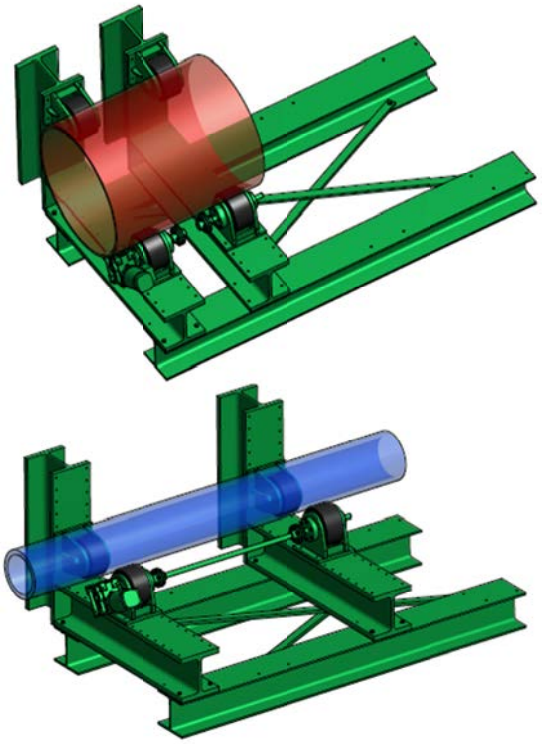

Figure 5. Different sized drum set up in the positioner

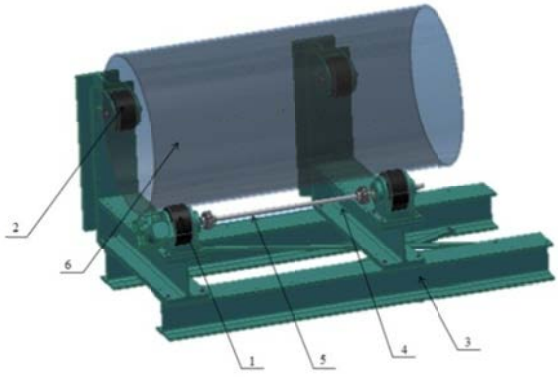

Figure 6. Rotary positioner assembly: 1- wheel drive, 2- driven wheel, 3 - base, 4- frame positioner, 5 - flexible shaft, 6 - drum

Rotary positioner (Figure 6) is composed of a number of mechanical parts, sub-assemblies, and sub-groups linked to a functional unit. Drive wheel (position 1) is one of the main structural elements and plays an important role in the performance of functions. Casing point consists of sides and base wich are welded together. Beside the basic function to combine elements and enable the proper functioning of the wheel, housing need to protect wheel from external influence. During welding of sides paralelism should be taken into account to ensure that shaft, which is fitted in the openings od sides, can smootly perform their function. Shaft allows rotating of all parts which are there, assembling at functional unit and transferring loads. Given that the direction of external loads are vertically, for reliable operation of the wheel radial bearings are fitted. Both bearing are protected against atmospheric agents' with cups. Worm gear with electric motor serves to transmit power from the engine to the working machine, and to adjust rotational speed and torque needed for shaft. Subassembly of driven wheel (position 2) is easily derived as opposed to the drive wheel subassembly. For the purpose of stiffening the case, it is necessary to construct the corresponding ribs. In this case the stationary shaft and pressed through the opening of sides, the wheel while under the influence of the load rotates around it. The wheels are made of steel coated with rubber; where rubber has a function to reduce wear process. At the ends of the shaft exist thread for nut and washner which locates bearing. The distance between the bearing housing and sides is provided with spacers. As each object, in general, can be created in several ways, analysis of possible variants is done nad optimal solution is selected. Standard steel profiles are used for base (position 3). Length of profile is chosen optimally, based on the analysis of cases in terms of parameters essential for the performance of the drafting process. The main function of the base is to ensure the proper conduct of frame structures without the possibility of drift during operation. The connection between the frame and the base is accomplished by means of threaded joints. Parallelism of the guide is provided with two rods, which are connected with bolts to linear guides. Frame positioner (position 4) is an important element of the structure. It consists of two standard steel profiles assembled by welding. The function of the frame is to connect wheels into one functional unit. Safety and reliability depends on the position of the wheels and safety and reliability of threaded fasteners. Nuts and bolts are used to connect subassembly of wheels with frame. Movement of the wheels enables frame length and the distance depends on the size of the drum being processed.

5. DISCUSSION

The introduction of new design into the production process has many advantages which are shown as follows:

- Improving the quality of welded joints is achieved thereby enabling semiautomatic welding. During rotation of the positioner, the worker can freely perform single-pass welding continuously, without interruption of the welding. The process is repeated until the drum is fully welded at the site.
- Reduced the preparatory time during welding
- Increase in profit resulting from reduced preparation time. Based on the review, with the introduction of the positioner, it is possible to produce two winches on the year, which also means, that the introduction of new design will paid in a short period of time.
- Technical features of the structure are such that it is possible to perform the procedure on the positioner gas cutting, as well as welding.

Reengineering processes need to improve organizational structure, to allow the replacement of long-term measures and measures to make quick and drastic changes to increase the quality, reduce the cost, reduce execution time of the process, improve internal and external relationships, eliminate unnecessary activities, provide a pleasant atmosphere for work and eliminate unnecessary activities.

6. CONCLUSIONS

From review of the literature sources related to the considered problem, it can be concluded that this area of research is very complex. Here is presented concept of development of special products (devices for positioning and rotation of the drum), based on knowledge of engineering science group. In order to optimize the construction, theoretical considerations made a number of conceptual designs and prepared a detailed review and analysis of the literature that examines this issue. The proposed solution does not require synchronization device for movement of two drive motors, which is a particular problem, which is discussed in the paper. The inclusion of a special device, designed for the production gets reduced value processing, minimum use of materials, better quality and more reliable weld construction

winches. The authors are inclined to think that a proper choice of frame and accessory devices for positioning, funds can be recovered at the level of the two-year. It should be noted that this positioner which is semiautomated has positive effects on welding proces in terms of safety. In particular, if one takes into account that safety in the workplace is one of the most important categories of business in modern conditions of production. On the other hand, the structure is very efficient and suitable for wide application in industrial practice. A very important advantage of this design is that the machine can be made with a lot of low cost elements. If we look at design, it is more than clear that the design does not require a particularly high accuracy and precision manufacturing. It was tended to meet function durring design of device, to be easy for manufacture, to be easy for manipulation, to have lowest cost possible and to satisfy safety requirements.

REFERENCE

[1] M. Đurđanović, D. Stamenković: *Trenje mirovanja-uslovi kretanja*, SERBIATRIB`07

[2] Peter J. Blau: *The significance and use of the friction coefficient*, Tribology International, Vol. 34, pp 585–591, 2001.

[3] K.-H. Zum Gahr, K. Voelker, *Friction and wear of SiC fiberreinforced borosilicate glass mated to steel*, Wear 225–229, pp 88–895, 1999.

[4] P. Blau, *The significance and use of the friction coefficient*, Tribol. Int. 34, pp 585–591, 2001.

[5] B. Ivkovic, M. Djurdjanovic, D. Stamenkovic: *The Influence of the Contact Surface Roughness on the Static Friction Coefficient*, Tribology in Industry, Vol. 22, No. 3&4, pp 41-44, 2000.

[6] U. Muller, R. Hauert: *Investigations of the coefficient of static friction diamond-like carbon films*, Surface and Coatings Technology 174–175, pp. 421–426, 2003.

[7] B. Polyakov, S. Vlassov, L.M. Dorogin, P. Kulis, I. Kink, R.Lohmus: *The effect of substrate roughness on the static friction of CuO nanowires*, Surface Science, Vol. 606, pp 1393–1399, 2012.

[8] D.A. Desai: *What is rolling friction*, Resonance 9, pp 52-54, 2004.

[9] T. Pöschel, T. Schwager, N.V. Brilliantov, *Rolling friction of a hard cylinder on a viscous plane*, The European Physical Journal B - Condensed Matter and Complex Systems 10, pp 169-174, 1999.

[10] A.I. El'kin, A. I. Moskovkin, E. I. Veksel'man, *Maximum force of friction in rubber-metal friction pairs under conditions of constant compressive deformation of the rubber*, Mekhanika Polimerov, Vol. 3, No. 3, pp. 533–538, 1967.

[11] B.N.J. Persson, A.I. Volokitin, *Rubber friction on smooth surfaces*, The European Physical Journal E, 21, pp 69-80, 2006.

[12] Akbar Shojaei, Mohammad Arjmand, Amir Saffar, *Studies on the friction and wear characteristics of rubber-based friction materials containing carbon and cellulose fibers*, Journal of Materials Science March 2011, Volume 46, Issue 6, pp 1890-1901

[13] M.E.R. Shanahan, N. Zaghzi, J. Schultz, A. Carré, *Hard Rubber/Metal Adhesion Assessment Using a Heavy Cylinder Rolling Test*, Adhesion 12, pp 223-238, 1988.

[14] Valentin L. Popov, *Rubber Friction and Contact Mechanics of Rubber*, Contact Mechanics and Friction, pp 255-270, 2010.

Serbian Tribology Society

SERBIATRIB '13

13th International Conference on Tribology

Faculty of Engineering in Kragujevac

Kragujevac, Serbia, 15 – 17 May 2013

USE ALGORITHM FOR CONSTRUCTION 3D VISIBILITY GRAPHS TO DESCRIBE PLASTIC AND ELASTIC DEFORMATION OF ROBOT LASER HARDENED SPECIMENS

M. Babič[1], P. Kokol[2], M. Milfelner[3], P. Panjan[4], Igor Belič[5]
[1]Emo-Orodjarna d.o.o., Slovenia, babicster@gmail.com
[2] University of Maribor, Faculty of Health Sciences, Slovenia,
[3] Tic-Lens d.o.o., Slovenia,
[4]Institute Jozef Stefan, Slovenia,
[5]Institute of Materials and Technology, Slovenia,

Abstract: *Visibility graphs have many applications. One of all applications is analyze trend line of market graph. Here we use 2D visibility graph for analyze it. Construction for 2D visibility graph is known. But in this paper, we will present algorithm for construction 3D visibility graphs. 3D Visibility computations are central in any computer graphics application. Drawing graphs as nodes connected by links in 3D space is visually compelling but computationally difficult. Construction of 3D visibility graph have big time complexity, thus require high professional computer or supercomputer. Article describe new method, algorithm for analyze 3D visibility graphs. We develop algorithm, which draws 3D visibility graphs, for analyze microstructure pictures of robot laser hardened specimens. Microstructure of robot laser hardened specimens is very complex, but we can present it with 3D visibility graphs. Algorithm for construction 3D visibility graph is very usefull in many cases, including illumination and rendering, motion planning, pattern recognition, computer graphics, computational geometry and sensor networks, military and automotive industry. This new algorithm we use to patterns recognition. In materials science, deformation is a change in the shape or size of an object due to an applied force (the deformation energy in this case is transferred through work) or a change in temperature (the deformation energy in this case is transferred through heat). With 3D visibility graphs we described elastic and plastic deformation of robot laser hardened specimens. For analysis of results, we use an intelligent system method, namely, a neural network, linear regression and support vector machine. We compare all methods.*

Keywords: *Elastic and plastic deformation, visibility graph, robot, laser, hardening,*

1. INTRODUCTION

In materials science, deformation is a change in the shape or size of an object due to an applied force (the deformation energy in this case is transferred through work) or a change in temperature (the deformation energy in this case is transferred through heat). The first case can be a result of tensile (pulling) forces, compressive (pushing) forces, shear, bending or torsion (twisting). In the second case, the most significant factor, which is determined by the temperature, is the mobility of the structural defects such as grain boundaries, point vacancies, line and screw dislocations, stacking faults and twins in both crystalline and non-crystalline solids. The movement or displacement of such mobile defects is thermally activated, and thus limited by the rate of atomic diffusion. Deformation is often described as strain.

Laser hardening is a metal surface treatment process complementary to conventional ame and induction hardening processes. A high-power laser beam is used to heat a metal surface rapidly and selectively to produce hardened case depths of up to 1,5 mm with the hardness of the martensitic microstructure providing improved properties such as wear resistance and increased strength. We will

find parameters of robot laser hardened cell, because we will reduce deformations. We observe a microstructure of robot laser hardened patterns. We find plastic and elastic deformations.

Depending on the type of material, size and geometry of the object, and the forces applied, various types of deformation may result. The image to the right shows the engineering stress vs. strain diagram for a typical ductile material such as steel. Different deformation modes may occur under different conditions, as can be depicted using a deformation mechanism map. Laser hardening is a metal surface treatment process complementary to conventional ame and induction hardening processes. A high-power laser beam is used to heat a metal surface rapidly and selectively to produce hardened case depths of up to 1,5 mm with the hardness of the martensitic microstructure providing improved properties such as wear resistance and increased strength. We will find parameters of robot laser hardened cell, because we will reduce deformations. We observe a micristructure of robot laser hardened patterns. We find plastic and elastic deformations.

2. MATERIALS AND METHOD

Our study was limited to tool steel of DIN standard 1.7225 (Fig. 1). The chemical composition of the material contained 0.38% to 0.45% C, 0.4% maximum Si, 0.6% to 0.9% Mn, 0.025% maximum P, 0.035% maximum S and 0.15% to 0.3% Mo.

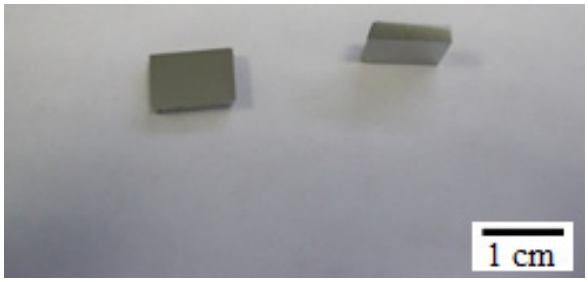

Figure 1. Transverse and longitudinal cross-section of hardened specimen

The specimen test section had a cylindrical form of dimension 25 × 10 mm (diameter × height). Specimens with porosity of about 19% to 50%, were prepared by laser technique, followed by hardening at T ∈ [1000, 1400] °C and v ∈ [2, 5] mm/s. We changed two parameters of the robot laser cell: speed v ∈ [2, 5] mm/s with steps of 1 mm/s and temperature T ∈ [1000, 1400] °C in steps of 100 °C (Fig. 2).

We develop new algorithm for construction visibility graph in 3D space. This algorithm we use to analyze mechanical properties of robot laser hardened specimens.

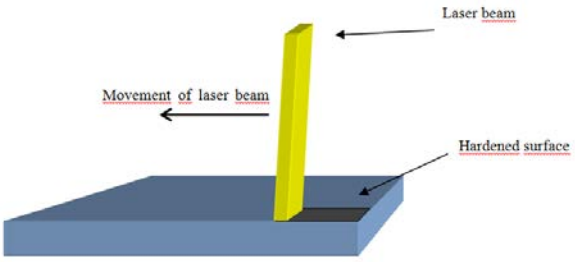

Figure 2. Robot laser hardening with different temperature and speed

Firstly, we analize profile graph of microstructure picture with visibility graph.

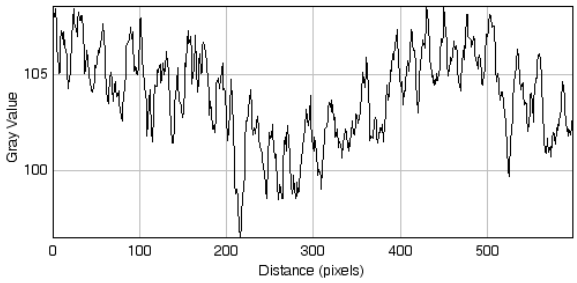

Graph 1. Profile graph of surface hardened specimen

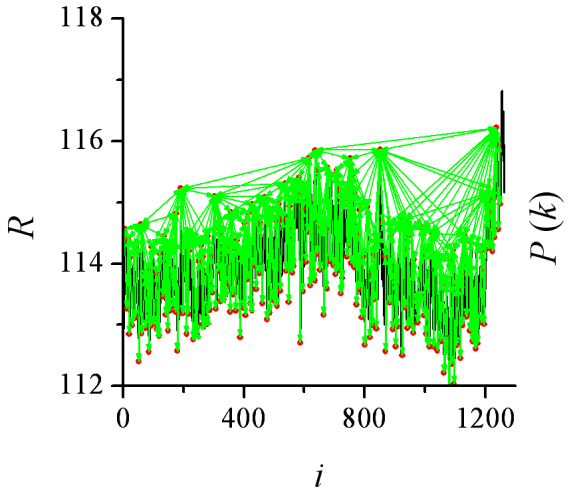

Graph 2: 2D Visibility graph for graph 1

Reason for develop constructing the visibility graph in *3D* space is analyze mechanical properties of robot laser hardening. Robot laser hardened specimens have better microstructure mechanical properties after hardening. With 3D visibility graph we describe complexity of microstructure (Fig. 2 and Fig. 3) of hardened specimens. We will know which extremes on graph of microstructure are connected.

3. RESULT

On Graph 3 is presented deformation before laser hardening. Graph 4 present deformation after laser hardening. On Graph 5 is presented relationship between hardness (HV) and depth before laser hardening. On Graph 6 is presented

relationship between hardness (HV) and depth after laser hardening.

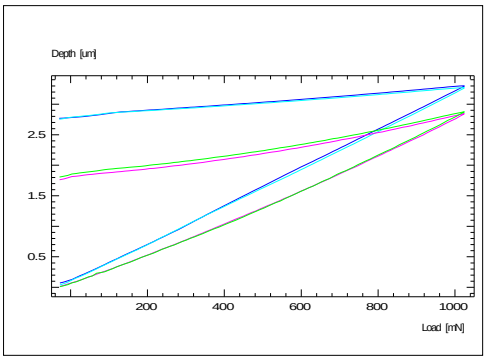

Graph 3. Deformation before laser hardening

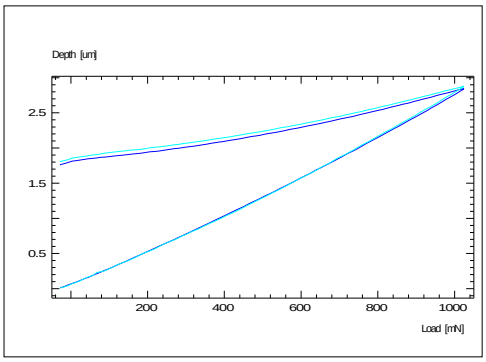

Graph 4. Deformation after laser hardening

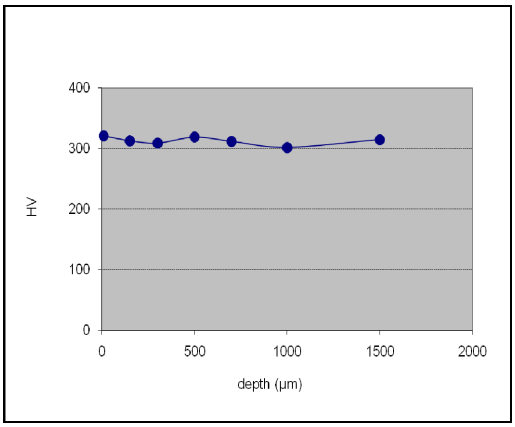

Graph 5. Hardness in depth before laser hardening

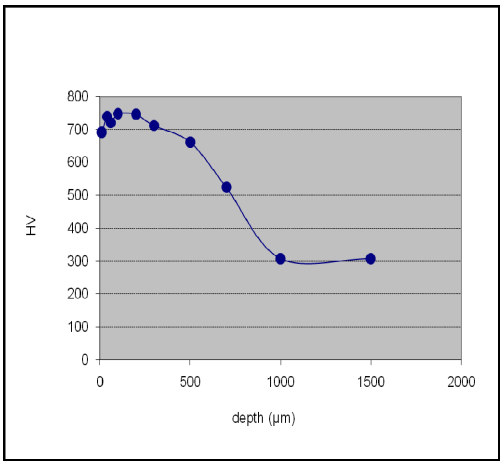

Graph 6. Hardness in depth after laser hardening

4. CONCLUSION

We made experiments hardened specimen. We present deformation on material before and after robot laser hardening. We present relationship between hardness and depth befor and after hardening. In the future we want to explore deformatiuon as a function of more parameters of a robot laser hardening. Robot laser cell parameters are strength, energy density, focusing distance, energy density in the focus, focus position, temperature and speed of hardening. We will interested to investigate deformation in the two-beam laser robot hardening (a laser beam is split into two parts).

REFERENCES

[1] B.M. Yu, P. Cheng: *A fractal permeability model for bi-dispersed porous media*, International journal of Heat Mass Transfer 45, pp. 2983–2993, 2002.

[2] Z. Q. Chen, P. Cheng, C.H. Hus: *A theoretical and experimental study on stagnant thermal conductivity of bi-dispersed porous med*ia, Int. Commun. Heat Mass Transfer 27, pp. 601–610, 2000.

[3] R. Pitchumani, B. Ramakrishnan: *A fractal geometry model for evaluating permeabilities of porous preforms used in liquid composite molding*, Int. J. Heat Mass Transfer 42, pp. 2219–2232, 1999.

[4] B.B. Mandelbrot: The fractal geometry of nature. New York: W. H. Freeman, 1982:93.

Serbian Tribology Society

SERBIATRIB '13

13th International Conference on Tribology

Faculty of Engineering in Kragujevac

Kragujevac, Serbia, 15 – 17 May 2013

USE FRACTAL GEOMETRY TO DESCRIBE FRICTION OF ROBOT LASER HARDENED SPECIMENS

M. Babič[1], P. Kokol[2], M. Milfelner[3], P. Panjan[4], Igor Belič[5]
[1]Emo-Orodjarna d.o.o., Slovenia, babicster@gmail.com
[2] University of Maribor, Faculty of Health Sciences, Slovenia,
[3] Tic-Lens d.o.o., Slovenia,
[4]Institute Jozef Stefan, Slovenia,
[5]Institute of Materials and Technology, Slovenia,

Abstract: *This paper describes some of our experience in laser surface remelting, consolidating, and hardening of steels. The process of laser hardening with remelting of the surface layer allows us to very accurately determine the depth of modified layers. In this procedure, we know the exact energy input into the material. Heating above the melting temperature and then rapidly cooling causes microstructural changes in materials, which affect the increase in hardness. Mathematics and Computer Science are very useful in many other Science. We use mathematical method, fractal geometry in engineering, exactly in laser technics. Moreover, with fractal geometry we analize complexity of robot laser hardened specimens. We analize specimens hardened with different parameters of robot laser cell. So we changed two parameters speed* $v \in [2, 5]$ *mm/s and temperature* $T \in [1000, 1400]$ *°C. In this work, we have used a scanning electronic microscope (SEM) to search and analyse the fractal structure of the robot laser hardened specimens. Friction is the force resisting the relative motion of solid surfaces, fluid layers, and material elements sliding against each other. The present study is intended to use new method, fractal geometry to describe completely friction of robot laser hardened specimens. Finally, concept of fractal geometry is applied to characterize the microstructure and derive the useful relationship between fractal dimension and microstructural features. The modeling of the relationship was obtained by the four layer neural network.*

Keywords: *Friction, fractal geometry, robot, laser, hardening,*

1. INTRODUCTION

Friction is the force resisting the relative motion of solid surfaces, fluid layers, and material elements sliding against each other.

In nature we have many geometrical objects which are irregular and cannot be described with classical Euclidian geometry. Thus we need a new method for describing the complexity and irregularity of objects. A relatively new method is fractal geometry. Recently, a concept of fractal geometry which was originally developed for the analysis of irregular features in nature has been finding increased applications in the fields of materials science for the characterization of microstructures. The key to fractal geometry is the fractal dimension, which describes the complexity of a fractal and geometrically irregular microstructure. Measuring fractal dimensions has become a common practice for describing the structural properties of roughness and hardness of heat-treated materials. We use fractal geometry in laser techniques. Laser hardening is a metal surface treatment process that is complementary to conventional aim and induction hardening processes. A high-power laser beam is used to heat a metal surface rapidly and selectively so as to produce hardened case depths of up to 1.5mm with the hardness of a martensitic micro-structure, providing improved properties such as wear resistance and increased strength.

First, we hardened tool steel standard label DIN standard 1.7225 with a robot laser cell. The chemical composition of the material contained 0.38 to 0.45% C, 0.4% maximum Si, 0.6–0.9% Mn, 0.025% maximum P, 0.035% maximum S and

0.15–0.3% Mo [18]. The specimen test section was in a cylindrical form with dimensions of 25×10mm. We changed two parameters, speed v ∈ [2, 5] mm/s in steps of 1 mm/s, and temperature T ∈ [1000, 1400] °C in steps of 100 °C. After hardening, we polished and etching all specimens. Detailed characterization of their microstructure before and after surface modifications was conducted using a field emission scanning electron microscope, JEOL JSM-7600F. We used the ImageJ program (available from the National Institute of Health, USA) to analyse these pictures. On these specimens we took measurements of roughness and hardness before and after robot laser hardening.

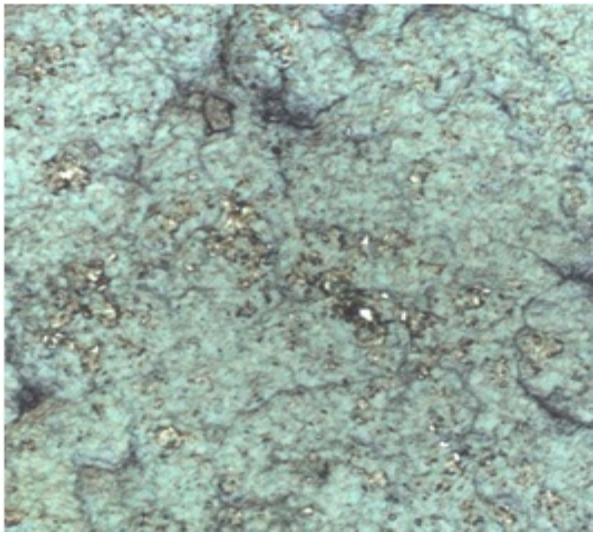

Figure 1. Microstructure before robot laser hardening

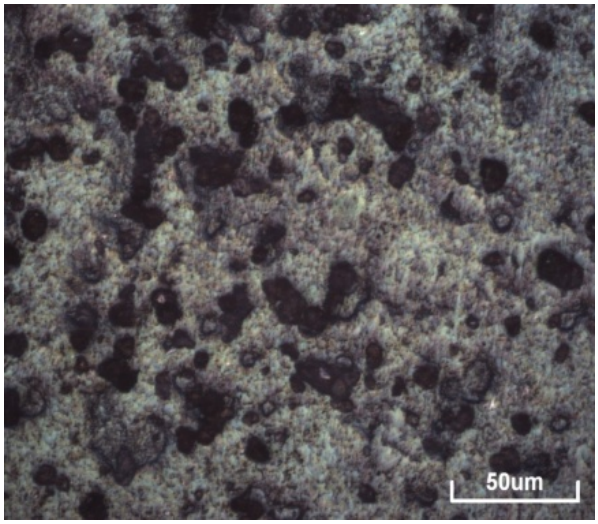

Figure 2. Microstructure of robot laser hardened specimen with 1000° C and 2 mm/s

2. MATERIALS AND METHOD

Our study was limited to tool steel of DIN standard 1.7225 (Fig. 1). The chemical composition of the material contained 0.38% to 0.45% C, 0.4% maximum Si, 0.6% to 0.9% Mn, 0.025% maximum P, 0.035% maximum S and 0.15% to 0.3% Mo.

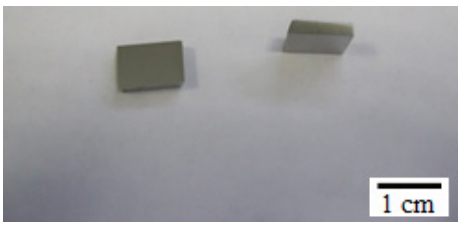

Figure 3. Transverse and longitudinal cross-section of hardened specimen

The specimen test section had a cylindrical form of dimension 25 × 10 mm (diameter × height). Specimens with porosity of about 19% to 50%, were prepared by laser technique, followed by hardening at T ∈ [1000, 1400] °C and v ∈ [2, 5] mm/s. We changed two parameters of the robot laser cell: speed v ∈ [2, 5] mm/s with steps of 1 mm/s and temperature T ∈ [1000, 1400] °C in steps of 100 °C (Fig. 2).

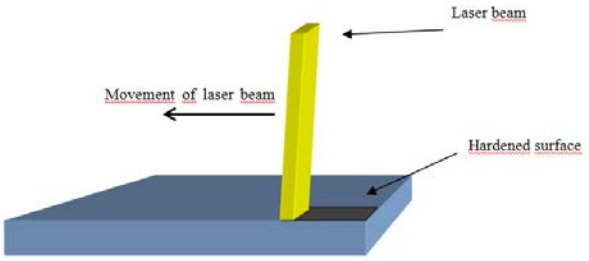

Figure 4. Robot laser hardening with different temperature and speed

A profilometer (available from the Institute Jozef Stefan, Slovenia) was used for the measurement of the surface roughness parameter R_a (arithmetic mean deviation of the roughness profile) and hardness of the robot laser hardened specimens. SEM images were converted into binary digital images (using the public domain software, ImageJ). The fractal characterization of materials properties as an applicable and potential tool has been well documented. The key parameter in fractal geometry is the fractal dimension, D, which should be determined first before we use the concept and knowledge of fractal geometry to characterize the microstructure of the robot laser hardened specimens. We calculated the fractal dimension using image processing of the SEM pictures in combination with implementation of a box-counting method (algorithm) using the ImageJ software. The measure of the fractal object, M(L), is related to the length scale, L, through a scaling in the form of Eq. (1):

$$M(L)=L^{D} \quad (1)$$

where M(L) is the surface area of a pore and D is the fractal dimension of the sample. A two-dimensional object, such as the SEM picture, can be divided into N(ε) self-similarity smaller squares,

each of which is measured by the length ε. The fractal dimension can be calculated according to Eq. (2):

$$D=\ln N(\varepsilon)/\ln \varepsilon. \quad (2)$$

Characterization of surface topography is important in applications involving friction, lubrication, and wear (Thomas, 1999). In general, it has been found that friction increases with average roughness. Roughness parameters are, therefore, important in applications such as automobile brake linings and floor surfaces. The effect of roughness on lubrication has also been studied to determine its impact on issues regarding lubrication of sliding surfaces, compliant surfaces, and roller bearing fatigue. Finally, some researchers have found a correlation between the initial roughness of sliding surfaces and their wear rate. Such correlations have been used to predict the failure time of contact surfaces. A section of standard length is sampled from the mean line on the roughness chart. The mean line is laid on a Cartesian coordinate system wherein the mean line runs in the direction of the x-axis and magnification is the y-axis. The value obtained with the formula on the right is expressed in micrometers (Om) when y=f(a).

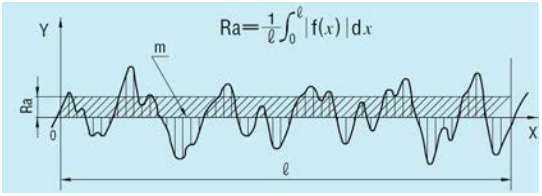

Graph 1. Arithmetical mean roughness (Ra)

3. RESULT

We studied the relationship between the fractal dimension, parameters of the robot laser cell and roughness (friction).

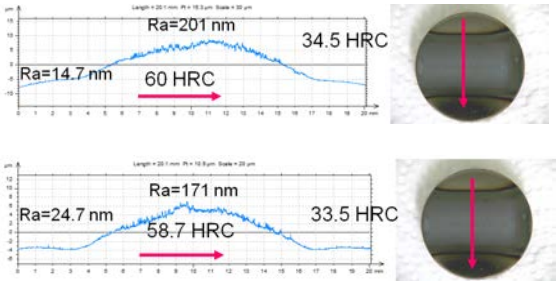

Graph 2. Roughness od robot laser hardenend specimens

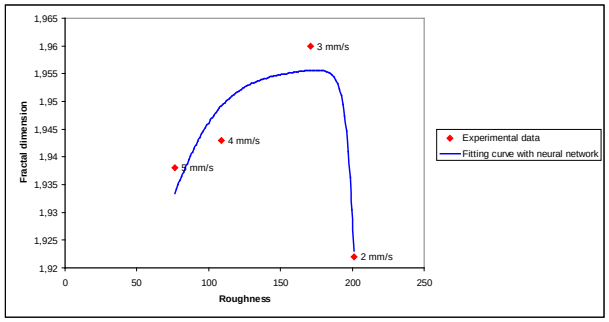

Graph 3. Relationship between fractal dimension and roughness R_a in specimens hardened at different speeds at 1000 °C

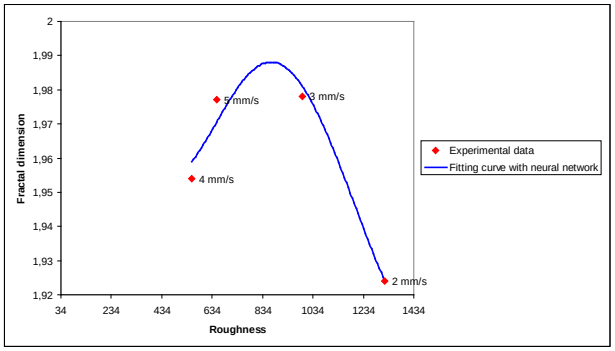

Graph 4. Relationship between fractal dimension and roughness R_a in specimens hardened at different speeds at 1400 °C

4. CONCLUSION

The paper presents the use of fractal geometry to describe the mechanical properties of robot laser hardened specimens. We use a relatively new method, fractal geometry, to describe the complexity of laser hardened specimens. The main findings can be summarized as follows:

1. A fractal structure exists in the robot laser hardened specimens.
2. We describe the complexity of the robot laser hardened specimens using fractal geometry.
3. We have identified the optimal fractal dimension of tool steel hardened with different robot laser parameters.
4. We use the box-counting method to calculate the fractal dimension for robot laser hardened specimens with different parameters.

REFERENCES

[1] B.B. Mandelbrot. *The fractal geometry of Nature*. New York: W.H. Freeman, p. 93, 1982.

[2] P.V. Yasnii, P.O. Marushchak, I.V. Konovalenko, R.T. Bishchak, *Computer analysis of surface cracks in structural elements*, Materials Science 46, pp. 833-839, 2008.

[3] P.V. Yasnii, P.O. Marushchak, I.V. Konovalenko, R.T. Bishchak, *Structural degradation and damage caused by a system of cracks to the steel of metallurgical equipment*, Materials Science 47, pp. 798-803, 2009.

[4] C.C. Barton, Fractal Analysis of Scaling and Spatial Clustering of Fractures. In: Barton, C.C. and La Pointe, P.R. (eds.), F*ractals in the Earth Sciences*. Plenum Press. New York, pp. 141-178, 1995.

[5] L.W. Fan, Y.C. Hu, T. Tian, Z.T. Yu, *The predication of effective thermal conductivities perpendicular to the fibres of wood using a fractal model and an improved transient measurement technique*, International Journal of Heat Mass Transfer 49, pp. 4116–4123, 2006.

[6] T. Ficker, *Fractal strength of cement gels and universal dimension of fracture surfaces*, Theor. Appl. Fract. Mech. 50, pp. 167–171, 2008.

[7] M.Q. Jiang, J.X. Meng, J.B. Gao, X.L. Wang, T. Rouxel, V. Keryvin, Z. Ling, L.H. Dai, *Fractal in fracture of bulk metallic glass*, Intermetallics 18, pp. 2468–2471, 2010.

[8] A. Carpinteri, S.A. Puzzi, *A fractal approach to indentation size effect*, Engineering Fract. Mech. 73, pp. 2110-2122, 2006.

Serbian Tribology Society

SERBIATRIB '13

13th International Conference on Tribology

Faculty of Engineering in Kragujevac

Kragujevac, Serbia, 15 – 17 May 2013

USE NEW PROCESS IN ROBOT LASER HARDENING TO DECREASE WEAR OF SPECIMENS

M. Babič[1], P. Kokol[2], M. Milfelner[3], P. Panjan[4], Igor Belič[5]

[1]Emo-Orodjarna d.o.o., Slovenia, babicster@gmail.com

[2] University of Maribor, Faculty of Health Sciences, Slovenia,

[3] Tic-Lens d.o.o., Slovenia,

[4]Institute Jozef Stefan, Slovenia,

[5]Institute of Materials and Technology, Slovenia,

Abstract: *The mechanism of wear is very complex and the theoretical treatment without the use of rather sweeping simplifications is not possible. The material intrinsic surface properties such as hardness, strength, ductility, work hardening etc. are very important factors for wear resistance, but other factors like surface finish, lubrication, load, speed, corrosion, temperature and properties of the opposing surface etc. are equally important. Robot laser surface-hardening heat treatment is complementary to conventional flame or inductive hardening. A high-power laser beam is used to heat a metal surface rapidly and selectively to produce hardened case depths of up to 1.5 mm with hardness values of up to 65 HRc. Laser hardening involves features, such as non-controlled energy intake, high performance constancy and accurate positioning processes. A hard martensitic microstructure provides improved surface properties such as wear resistance and high strength. We describe a new technological process of hardening, which can decrease the wear of hardened specimens. The new process uses robot laser hardening with an overlapping laser beam. First, we hardened specimens using different velocities and temperatures and then repeated the process. In addition, we present how the speed and temperature affect the wear in two different processes of robot laser hardening. Furthermore, we present the improved results after hardening with the overlap process. To analyse the results, we used one method of intelligent system, neural networks and a relationship was obtained by using a four-layer neural network. We compare both processes.*

Keywords: *Wear, robot, laser, hardening, process of overlapping,*

1. INTRODUCTION

In materials science, wear is erosion or sideways displacement of material from its "derivative" and original position on a solid surface performed by the action of another surface. Wear is related to interactions between surfaces and more specifically the removal and deformation of material on a surface as a result of mechanical action of the opposite surface. The need for relative motion between two surfaces and initial mechanical contact between asperities is an important distinction between mechanical wear compared to other processes with similar outcomes.

The definition of wear may include loss of dimension from plastic deformation if it is originated at the interface between two sliding surfaces.

However, plastic deformation such as yield stress is excluded from the wear definition if it doesn't incorporates a relative sliding motion and contact against another surface despite the possibility for material removal, because it then lacks the relative sliding action of another surface.

2. MATERIALS AND METHOD

Our study was limited to tool steel of DIN standard 1.7225 (Fig. 1). The chemical composition of the material contained 0.38% to 0.45% C, 0.4% maximum Si, 0.6% to 0.9% Mn, 0.025% maximum P, 0.035% maximum S and 0.15% to 0.3% Mo [10].

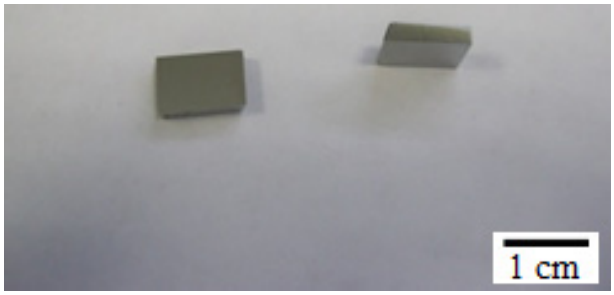

Figure 1. Transverse and longitudinal cross-section of hardened specimen

The specimen test section had a cylindrical form of dimension 25 × 10 mm (diameter × height). Specimens with porosity of about 19% to 50%, were prepared by laser technique, followed by hardening at T ∈ [1000, 1400] °C and v ∈ [2, 5] mm/s. First, we changed two parameters of the robot laser cell: speed v ∈ [2, 5] mm/s with steps of 1 mm/s and temperature T ∈ [1000, 1400] °C in steps of 100 °C (Fig. 2). Secondly, we repeated the process (Fig. 3). In addition, we hardened the specimens again with equal parameters of the robot laser cell. The microstructure of the specimens was observed with a field emission scanning electron microscope (JSM-7600F, JEOL Ltd.). An irregular surface texture was observed with a few breaks, which are represented by black islands (Fig. 4). Fig. 5 presents the boundary between the hardened and non-hardened material.

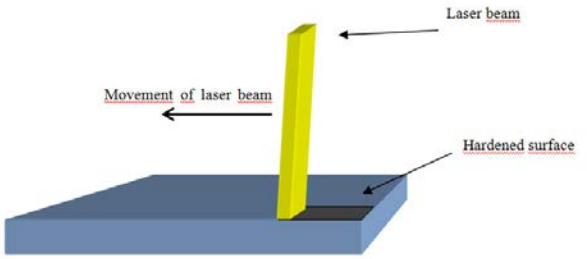

Figure 2. Robot laser hardening with different temperature and speed

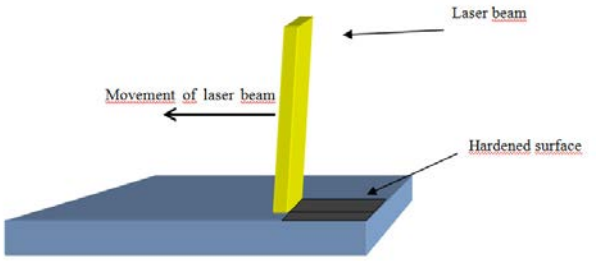

Figure 3. Repeated process of robot laser hardening

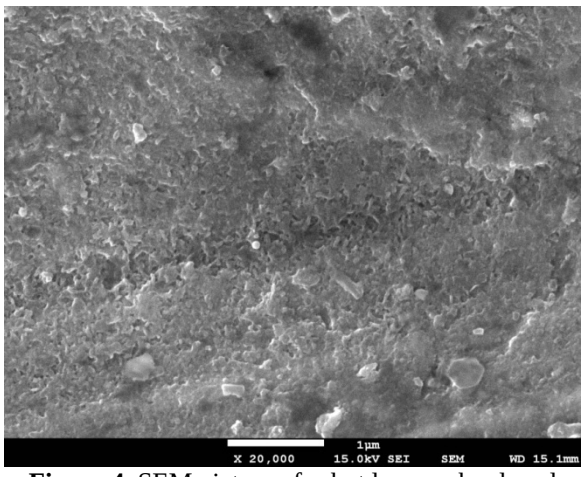

Figure 4. SEM picture of robot laser re-hardened specimen

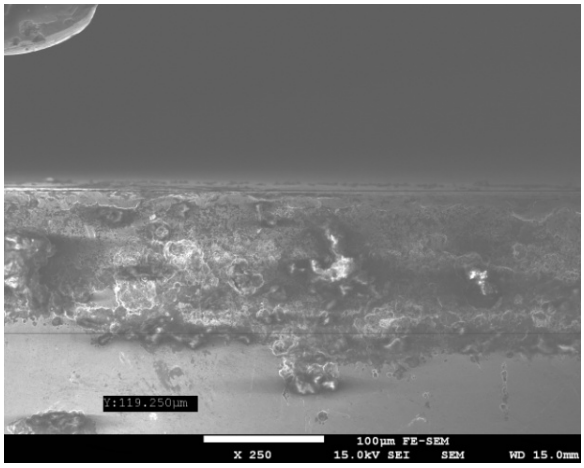

Figure 5. The boundary between work-hardened and non-hardened material

We used the method of determining the porosity from SEM images of the microstructure. It is known that in a homogenously porous material the area of pores is equal to the volume of pores in specimens. The SEM pictures were converted to binary images (Fig. 6), from which we calculated the area of pores of all pictures using the ImageJ program (ImageJ is a public domain, Java-based image processing program developed at the National Institutes of Health). The area of pores on each picture of the material was calculated and then the arithmetic mean and standard deviation of porosity were determined. To analyze he possibility of the application of fractal analysis to the heat-treated surface, we examined the relation between the surface porosity and fractal dimensions depending on various parameters of the robot laser cell. In fractal geometry, the key parameter is the fractal dimension D. The relationship between the fractal dimension D, volume V and length L, can be indicated as follows:

$$V \sim L^{D} \quad (1)$$

Fractal dimensions were determined using the box-counting method which has been proven to have higher calculation speed and more accuracy by Dougan and Shi.

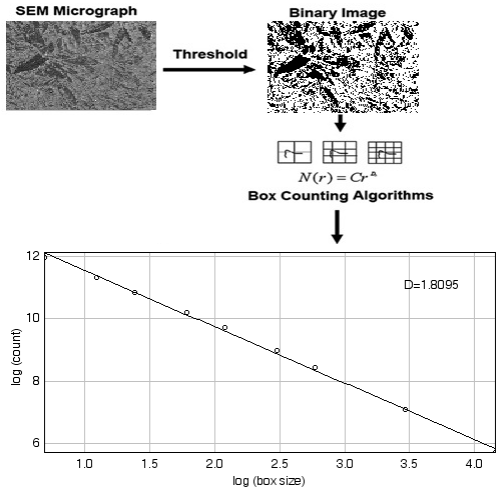

Figure 6. Calculation of fractal dimensions with box-counting method

To analyse the results we used one method of intelligent system; the neural network. Artificial neural networks (ANN) are simulations of collections of model biological neurons. A neuron operates by receiving signals from other neurons through connections called synapses. The combination of these signals, in excess of a certain threshold or activation level, will result in the neuron firing, i.e., sending a signal to another neuron to which it is connected. Some signals act as excitations and others as inhibitions to a neuron firing. What we call thinking is believed to be the collective effect of the presence or absence of firings in the patterns of synaptic connections between neurons. In this context, neural networks are not simulations of real neurons, in that they do not model the biology, chemistry, or physics of a real neuron. However, they do model several aspects of the information combination and pattern recognition behaviour of real neurons, in a simple yet meaningful way. This neural modelling has shown incredible capability for emulation, analysis, prediction and association. Neural networks can be used in a variety of powerful ways: to learn and reproduce rules or operations from given examples; to analyse and generalise sample facts and to make predictions from these; or to memorise characteristics and features of given data and to match or make associations with new data. Neural networks can be used to make strict yes-no decisions or to produce more critical, finely valued judgments. Neural network technology is combined with genetic optimisation technology to facilitate the development of optimal neural networks to solve modelling problems. Genetic optimisation uses an evolution-like process to refine and enhance the structure of a neural network until it can model the problem in the most efficient way. Neural networks are models of biological neural structures. The starting point for most neural networks is a model neuron, as shown in Fig. 7. This neuron consists of multiple inputs and a single output. Each input is modified by a weight, which multiplies with the input value.

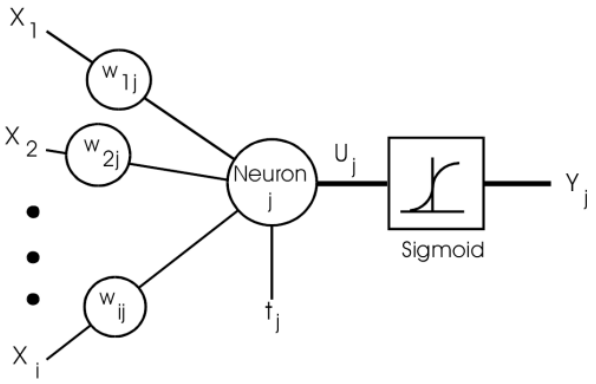

Figure 7. A neuron model

3. RESULT

Graph [1-2] present relationship between roughness R_a and hardness in specimens hardened at different speeds at 1000 °C with both process.

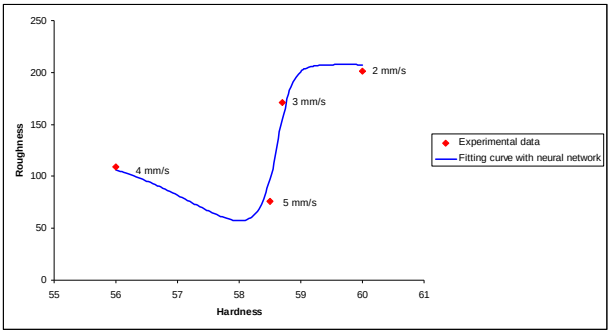

Graph 1. Relationship between roughness R_a and hardness in specimens hardened at different speeds at 1000 °C

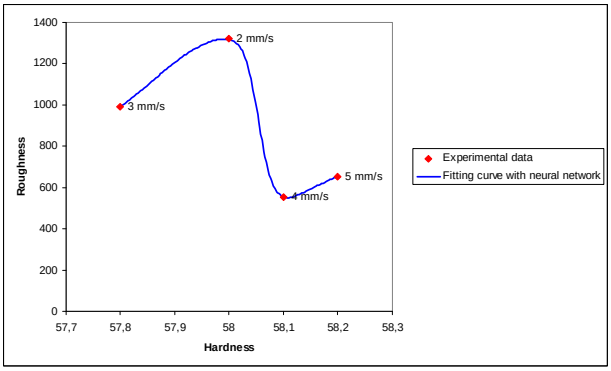

Graph 2. Relationship between roughness R_a and hardness in specimens hardened at different speeds at 1000 °C with process of overlapping

4. CONCLUSION

The paper presents using fractal geometry to describe the wear of robot laser-hardened specimens with overlap. We use the relatively new method of fractal geometry to describe the complexity of laser-hardened specimens.

REFERENCES

[1] B.B. Mandelbrot. *The fractal geometry of Nature*. New York: W.H. Freeman, 1982, p. 93.

[2] P.V. Yasnii, P.O. Marushchak, I.V. Konovalenko, R.T. Bishchak, *Computer analysis of surface cracks in structural elements,* Materials Science 46, pp. 833-839, 2008.

[3] P.V. Yasnii, P.O. Marushchak, I.V. Konovalenko, R.T. Bishchak, *Structural degradation and damage caused by a system of cracks to the steel of metallurgical equipment*, Materials Science 47, pp. 798-803, 2009.

[4] C.C. Barton, Fractal Analysis of Scaling and Spatial Clustering of Fractures. In: Barton, C.C. and La Pointe, P.R. (eds.), *Fractals in the Earth Sciences*. Plenum Press. New York, pp. 141-178, 1995.

[5] L.W. Fan, Y.C. Hu, T. Tian, Z.T. Yu, *The predication of effective thermal conductivities perpendicular to the fibres of wood using a fractal model and an improved transient measurement technique*, International Journal of Heat Mass Transfer 49, pp. 4116–4123, 2006.

[6] T. Ficker, *Fractal strength of cement gels and universal dimension of fracture surfaces*, Theor. Appl. Fract. Mech. 50, pp. 167–171, 2008.

[7] [7] M.Q. Jiang, J.X. Meng, J.B. Gao, X.L. Wang, T. Rouxel, V. Keryvin, Z. Ling, L.H. Dai, *Fractal in fracture of bulk metallic glass*, Intermetallics 18, pp. 2468–2471, 2010.

[8] A. Carpinteri, S.A. Puzzi, *A fractal approach to indentation size effect*, Engineering Fract. Mech. 73, pp. 2110-2122, 2006.

Serbian Tribology Society

SERBIATRIB '13

13th International Conference on Tribology

Faculty of Engineering in Kragujevac

Kragujevac, Serbia, 15 – 17 May 2013

DIFFERENT WAYS OF FRICTION COEFFICIENT DETERMINATION IN STRIPE IRONING TEST

S Aleksandrovic[1], M. Stefanovic[1], V. Lazic[1], D. Adamovic[1], M. Djordjevic[1], D. Arsic[1]
[1]Faculty of Engineering, University of Kragujevac, Serbia, srba@kg.ac.rs

Abstract: *The sheet metal stripe ironing laboratory test has been developed to study tribological appearances and performance of lubricants in ironing process. Most common way for friction coefficient determination in the test is use of different formulas which gives relation between active forces and reactive friction forces. In application of such formulas some difficulties occurs because of improper friction coefficient values, especially at small intensities of tensile or drawing forces. In this paper for literature approaches were analyzed and after that defining of new formula were proposed. New formula was tested numerically and experimentally. Obtained results indicated that the suggested improvements give much more acceptable values of friction coefficient. That fact is particularly significant in lubricant evaluation process.*

Keywords: *Thick sheet metal, stripe ironing test, friction coefficient*

1. INTRODUCTION

Ironing is technological process which combine characteristics of sheet metal forming and bulk forming. Thinnig strain reach over 25%, and contact pressure over 1000 MPa [1]. Most often applies in manufacture of cylindrical geometry pieces whose depth is much bigger than diameter, and bottom thickness is bigger than wall thickness.

Ironing is normally applied following deep drawing (or extrusion) when forming high, thin walled cans. Such cans are used for beverages, cartridge cases, high pressure cylinders, housings for pumps and shock absorbers etc. World annual production (especially for beverage cans) are more than billion pieces [2].

Of the sheet metal forming processes, ironing is one of the tribologically most severe, owing to the high surface expansion and normal pressure at the tool-workpiece interface. This is particularly significant in the case of forming of pour fomability materials such as stainless steel, high strength steel, etc. [3]. Because of that, use of proper performace lubricants is very significant. In order to quantify the performance of the individual lubricants, a different simulative test methods has been developed. All the tests are modelling the process conditions in ironing. It is a very convenient to use coefficient of friction at contact surfaces change as a criterion for lubricants evaluation.

For this study one of classic stripe ironing tests was chosen [4]. By analysis of acting of drawing force, side forces and friction forces well known formula was determined. This particular formula established the connection between tool geometry, forces and coefficient of friction. The formula was used in different researches, [4, 5, 6, 7, 8] in genuin or modified form.

However, by more accurate measurements of the drawing force was shown that formula gives negative friction coefficient values in range of force smaller intensities. That fact was indicated yet in article [5]. That was motive for making analysis of several approaches with goal to obtain more convenient formula appropriate for above mentioned strip reduction test.

2. DEFINING OF FRICTION COEFFICIENT

Figure 1 shows scheme of the stripe ironing test tooling which models the symmetrical contact of the sheet with the die during the ironing process. The metal strip is being placed into the holding jaw. The jaw with the sample is moving from the bottom towards the top, by the mechanical part of the device. The sample is being acted upon by the side

elements with force F_D, which simulate the industrial tool die and perform the ironing. During the ironing process the recording of the drawing force is being done at over the total length of the punch travel, by the corresponding measuring system.

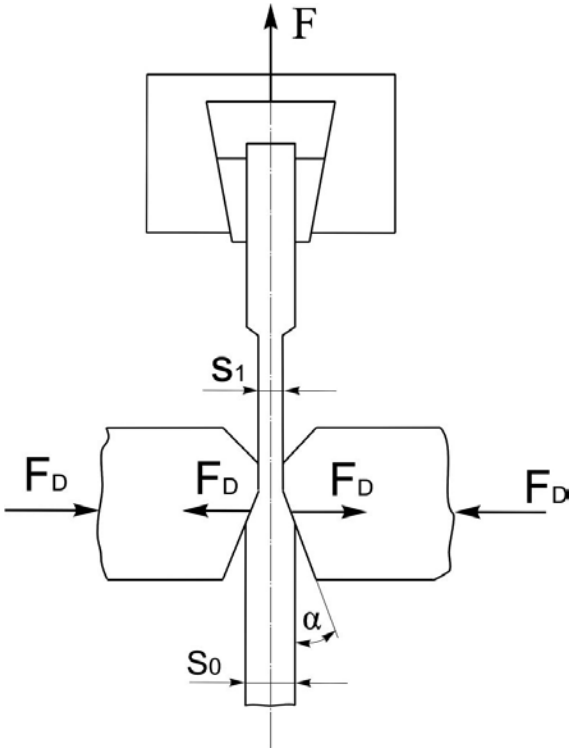

Figure 1. Stripe ironing test model

Term (1) gives friction coefficient μ dependence on drawing force (F), side force (F_D) and inclination angle α and that is well-known classic formula [4].

$$\mu = \frac{\frac{F}{2F_D} - tg\alpha}{1 + \frac{Ftg\alpha}{2F_D}} = \frac{F - 2F_D tg\alpha}{2F_D + Ftg\alpha} = \frac{F\cos\alpha - 2F_D \sin\alpha}{2F_D \cos\alpha + F\sin\alpha} \quad (1)$$

Similar term (2) was proposed in article [6]. If instead of force F is inserted F/2 term (1) was given.

$$\mu = \frac{F\cos\alpha - F_D \sin\alpha}{F_D \cos\alpha + F\sin\alpha} \quad (2)$$

Term (3) is using in article [2].

$$\mu = \frac{F\cos\alpha - 2F_D \sin\alpha}{F_D \cos\alpha + F\sin\alpha} \quad (3)$$

Previous three formulas give negative friction coefficient values for smaller intensities of drawing force in the sliding process starting phase. This notice was given yet in article [5] where was assumed that cause of such a disadvantage is negligence of the forces in narrow vertical zone between side element inclined surfaces. Scheme of forces at fig. 2 was formed according to propositions from that study [9]. After force analysis friction coefficient is given by:

$$\mu = \frac{F + 2F_D(0.25 - 2tg\alpha)}{Ftg\alpha + 4F_D} \quad (4)$$

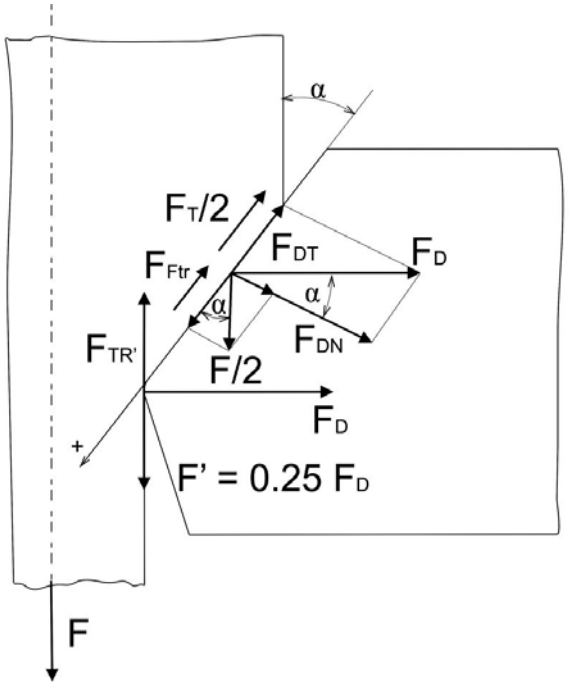

Figure 2. Force acting scheme [9]

Within a framework of the same study [9] intuitively was proposed different scheme of side forces F_D acting. It assumes that at inclined surface acting force $F_D/2$ and at narrow vertical surface also the same force $F_D/2$. In such conditions another version of previous formula was given.

$$\mu = \frac{F + 2F_D(0.25 - 2tg\alpha)}{Ftg\alpha + 2F_D} \quad (4a)$$

After analysis of the previous formulas scheme of forces in fig. 3 was formed. Based on equilibrium equation of all the forces (for contact surfaces at both sides) in vertical direction, friction coefficient is given by:

$$\mu = \frac{F}{2aF_D \cos^2\alpha + F\frac{\sin 2\alpha}{2} + 2(1-a)F_D} \quad (5)$$

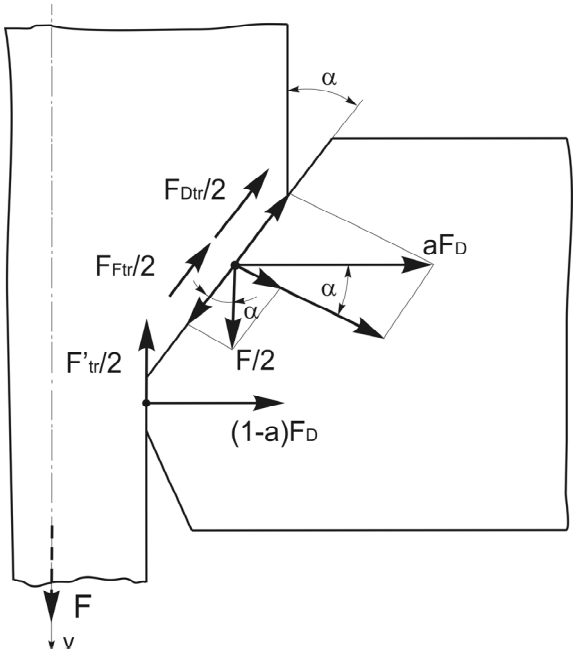

Figure 3. Modified force acting scheme

Parameter a is determining distribution of side force F_D between inclined and small vertical contact surface and his value is in the range 0 to 1. It was adopted a=0.7 in this case. Parameter a influence on friction coefficient value is very small (about 1%).

Figures 4 and 5 gives comparative overview of all the 6 formulas whereat was adopted F_D=10 kN (fig. 4) and F_D=0 kN (fig. 5). Inclination angle was 10^o. Drawing force is linearly increasing from 0 to 9500 N and lies on x axis. Clearly can be seen that formulas 1, 2 and 3 gives unreal negative friction coefficient values for smaller force F intensities. Use of 4 and 4a formulas is solving this disadvantage, but at the sliding process beginning friction coefficient have positive nonzero also unreal values. Only formula 5 gives friction coefficient values which starts from 0. That is in accordance with ironing process course. At smaller intensities of side force F_D friction coefficient values are probably higher then real.

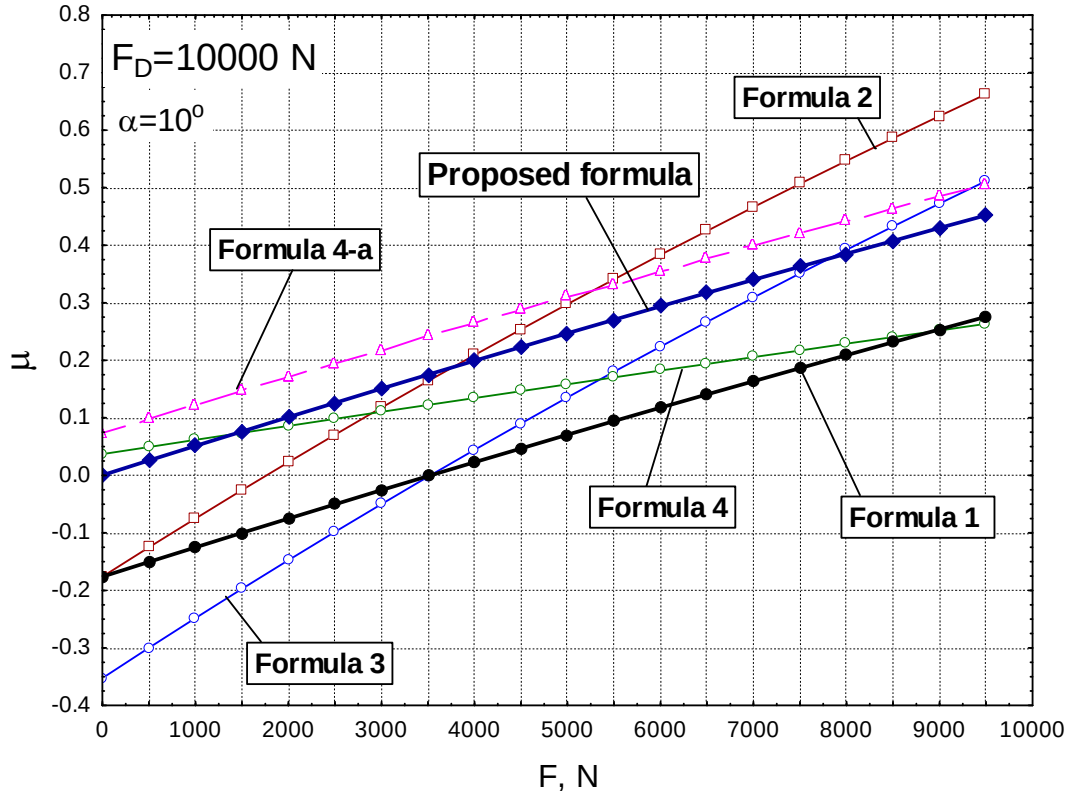

Figure 4. Friction coefficient dependencies on drawing force

As a example of formula (5) application in lubricants quality evaluation experiment giving are the figures 6 and 7. Experimental equipment is based on tribo model from fig. 1 and described with more details in [9]. Sliding process was one phase with side forces 5, 10, 15 and 20 kN. Sliding length was approximately 60 mm at speed of 100 mm/min. Stripe material is low carbon steel sheet with 2.5 mm thickness. L2 is special dry ecological lubricant based on wax and metallic soap. Lubricant layer was obtained by dipping into bath with proper solution and than drying. L3 is lithium grease with MoS_2.

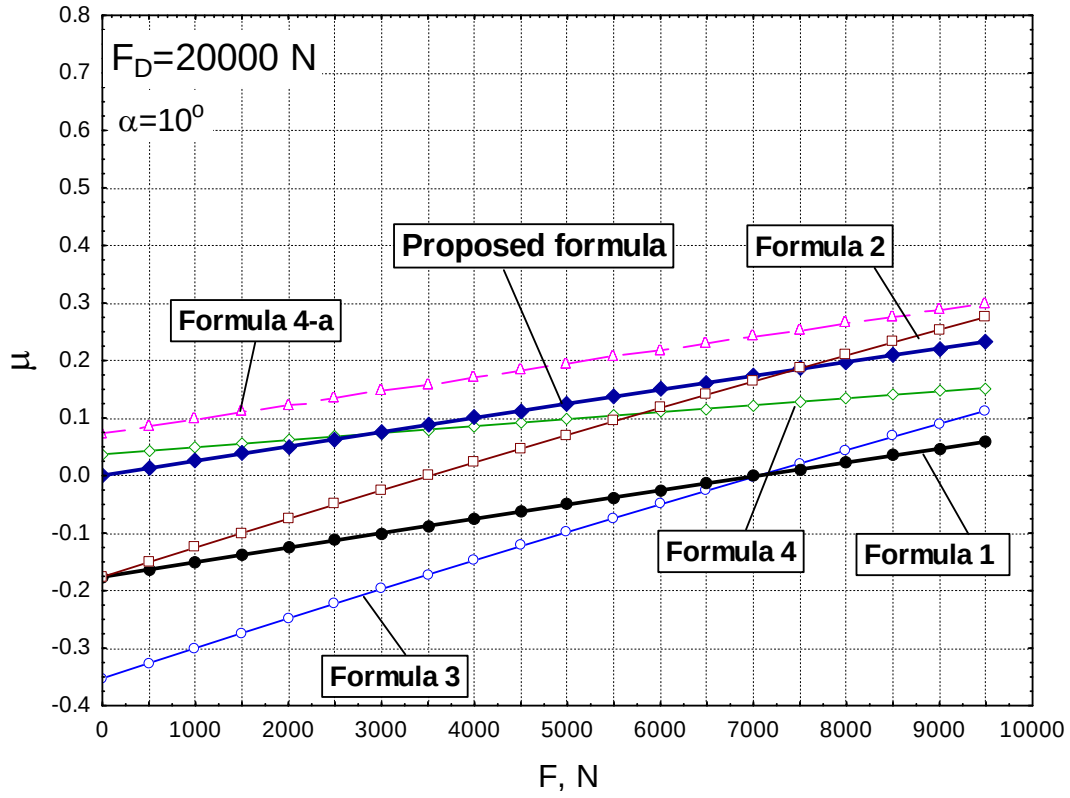

Figure 5. Friction coefficient dependencies on drawing force

By fig. 6 and fig. 7 comparison can be seen that for lubricant L3 contact pressure has no substantial influence on friction coefficient. In the case of lubricant L3 application friction coefficient is decreasing with side force decreasing.

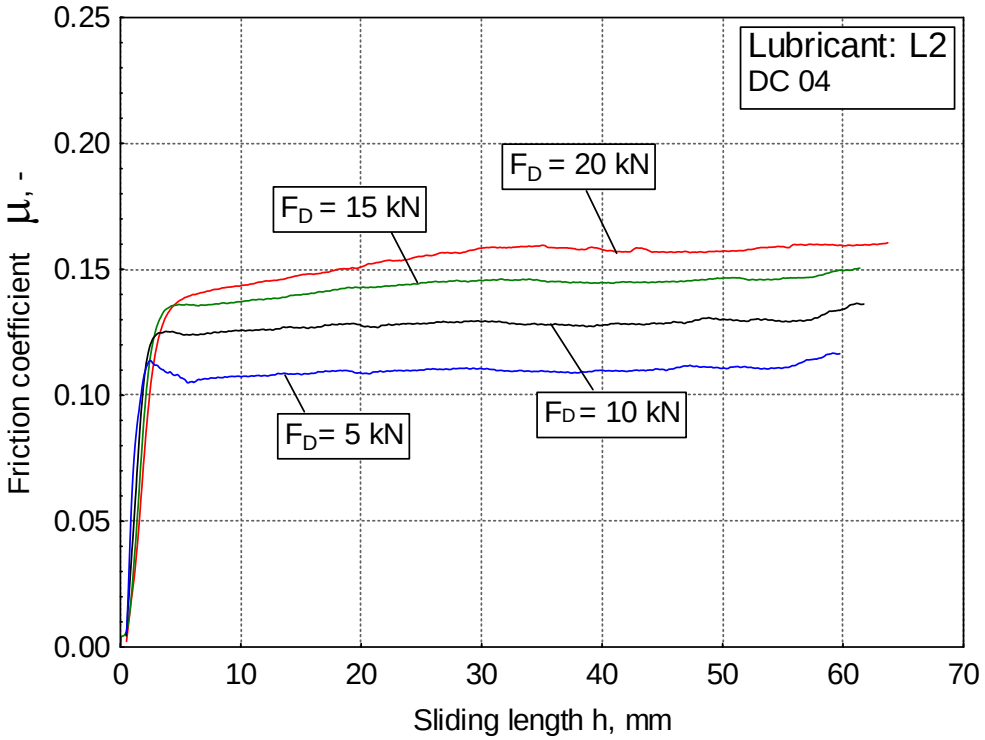

Figure 6. Friction coefficient dependencies on sliding length

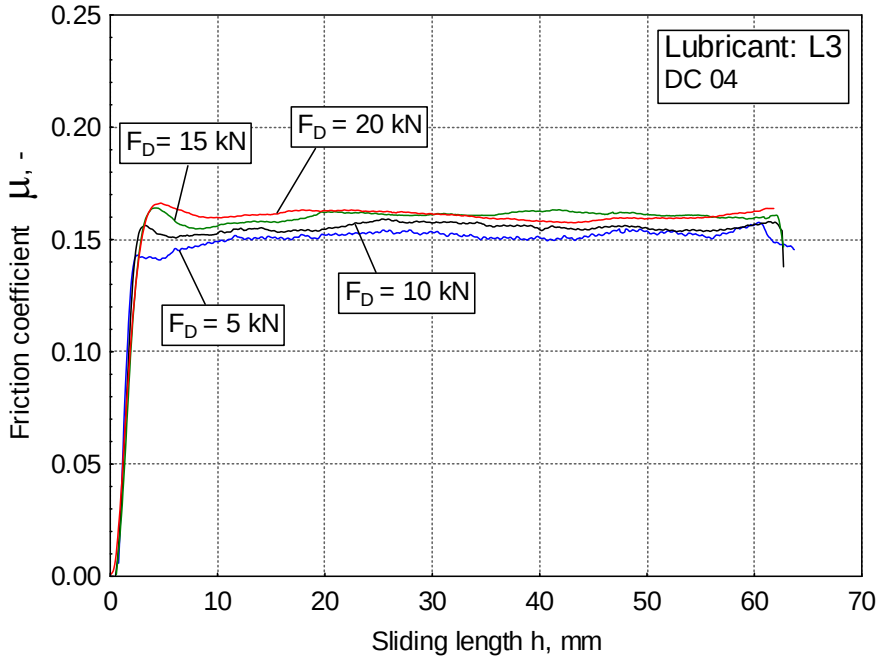

Figure 7. Friction coefficient dependencies on sliding length

3. CONCLUSION

Comparative analysis of application of the four literature formulas for the friction coefficient determining in stripe ironing test was accomplished in the first part of this study. Three formulas give negative unreal friction coefficient values for smaller intensities of drawing force in the sliding process starting phase. For one formula (in two versions) friction coefficient have positive nonzero but also unreal values at the sliding process beginning. These notices are indicating that previously mentioned formulas are inaccurate.

Different formula was suggested in the second part of this study. Proposed formula enables to determine acceptable friction coefficient values and dependencies. After performing of trial experiments the results are indicating that proposed formula can be successfully applied in the lubricant evaluation during chosen stripe ironing test process.

REFERENCES

[1] N. Bay, A. Azushima, P. Groche, I. Ishibashi, M. Merklein, M. Morishita, T. Nakamura, S. Schmid, M. Yoshida: *Environmentally benign tribo-systems for metal forming*, CIRP Annals - Manufacturing Technology 59, pp. 760 – 780, 2010.

[2] D. Adamovic, M. Stefanovic, V. Lazic, M. Zivkovic: *Estimation of Lubricants for Ironing of Steel Pieces*, Tribology in industry 26, pp. 12-20, 2004

[3] J.L. Andreasen, N. Bay, M. Andersen, E. Christensen, N. Bjerrum: *Screening the performance of lubricants for the ironing of stainless steel with a strip reduction test*, Wear 207, pp. 1-5, 1997.

[4] D. Schlosser: *Beeinflussung der Reibung beim Streifenziehen von austenitischem Blech: verschiedene Schmierstoffe und Werkzeuge aus gesinterten Hartstoffen*, Bander Bleche Rohre 7/8, pp. 302-306, 1975.

[5] P. Deneuville, R. Lecot: *The study of friction in ironing process by physical and numerical modelling*, Journal of Materials Processing Technology 45, pp. 625–630, 1994.

[6] H.C.E. van der Aa, M.A.H. van der Aa, P.J.G. Schreurs, F.P.T. Baaijens a, W.J. van Veenen: *An experimental and numerical study of the wall ironing process of polymer coated sheet metal*, Mechanics of Materials 32, pp. 423-443, 2000.

[7] S. Đačić, M. Stefanović, S. Aleksandrovic, D. Adamović: *Characteristics of Friction in Sheet Metal Sliding with Thickness Reduction*, International conference SERBIATRIB 2011, Kragujevac, Serbia, Proceedings ISBN: 978-86-86663-74-0, pp. 366-369.

[8] M. Stefanovic, S. Djacic, S. Aleksandrovic, D. Adamovic: *Importance of tribological conditions at multi-phase ironing*, 34th International conference ICPE 2011, Niš, Serbia, Proceedings ISBN: 978-86-6055-019-6, pp. 503-506.

[9] M. Djordjević, S. Aleksandrović, V. Lazić, M. Stefanović, R. Nikolić, D. Arsić: *Influence of lubricants on the multiphase ironing process*, SEMDOK 2013, Zilina-Terchova, Proceedings ISBN 978-80-554-0629-9, pp. 22-26, 2013.

Serbian Tribology Society

SERBIATRIB '13

13th International Conference on Tribology

Faculty of Engineering in Kragujevac

Kragujevac, Serbia, 15 – 17 May 2013

A NANOMECHANICAL APPROACH ON THE MEASUREMENT OF THE ELASTIC PROPERTIES OF EPOXY REINFORCED CARBON NANOTUBE NANOCOMPOSITES

G. Mansour[1], D. Tzetzis[2], K.D. Bouzakis[3]

[1]Aristotle University of Thessaloniki, Department of Mechanical Engineering, Greece, mansour@eng.auth.gr

[2]International Hellenic University, Greece, d.tzetzis@ihu.edu.gr

[3]Aristotle University of Thessaloniki, Department of Mechanical Engineering, Greece, bouzakis@eng.auth.gr

Abstract: *The mechanical behaviour of nanocomposite materials with multiwall carbon nanotube (MWCNT) reinforcements is investigated in the present paper. Epoxy nanocomposites with different weight percentages of carbon nanotubes have been characterized following tensile tests and nanoindentations. The objective of this work was to investigate the efficiency of the reinforcement provided by nanotubes and to examine the agreement between the mechanical properties of the epoxy nanocomposites obtained via a macroscale and nanoscale experimental methods. Higher increase in modulus was accomplished at weight fraction of nanotube reinforcement of 1%. The modulus as measured by the tensile tests differed an average of 18% with the results obtained from the nanoindentations, however by utilising a proper calibration method the data were corrected resulting to only a 3% difference. The modulus results obtained from the experiments were compared with the Halpin-Tsai model and with the Thostenson-Chou model accounting for the outer layer interactions of the nanotube with the hosting matrix. Arelatively good agreement was found between the models and the experiments.*

Keywords: *Nanoindentation Testing, Epoxy Nanocomposites, Multiwall Carbon Nanotubes, Elastic Properties, Microscopy*

1. INTRODUCTION

Epoxy nanocomposites using carbon nanotubes (CNTs) have been intensively investigated, following the successful synthesis of CNTs in 1991[1].CNTs have attracted considerable attention due to their unique mechanical, surface, multifunctional properties and strong interactions with the hosting matrix mainly associated to their nano-scale features. Recent experiment shave shown remarkable enhancements in elastic modulus and strength of polymer composites with an addition of small amounts of CNTs [2,3]. Among the various studies incorporating CNTs, Loos et. al [4] have investigated the matrix stiffness role on tensile and thermal properties of carbon nanotube epoxy reinforced nanocomposites. They have shown that the addition of a small amount of SWCNTs (0.25 wt.%) in soft matrices, greatly increased Young's modulus and tensile strength of such nanocomposites. The results showed that the tensile properties of soft epoxy matrices are much more influenced by the addition of carbon nanotubes than stiffer ones. Also, Kim et. al. [5] studied the effects of surface modification on rheological and mechanical properties of CNT/epoxy composites. The CNTs were modified by acid treatment, plasma oxidation, and amine treatment. The surface modified CNTs were well dispersed in the epoxy matrix and had strong interfacial bonding with the polymer matrix. The nanocomposite containing the modified CNTs exhibited higher storage and loss moduli and shear viscosity than those with the untreated CNTs, because the surface treatments provide more homogeneous dispersion of CNTs and stronger interaction between the CNT and the polymer matrix. Gojny et al. [6] have investigated the influence of different types of CNTs on the mechanical properties of epoxy based

nanocomposites. The influence of filler content, the varying dispersibility, the aspect ratio, the specific surface area and the functionalisation on the composite properties was correlated to the identified micro-mechanical mechanisms. The results showed that the produced nanocomposites have enhanced the strength and stiffness along with an increase in fracture toughness.

Despite the huge amount of experimental data available in the literature there are still debatable results concerning the elastic property and strength of such nanocomposites. This is due to the characteristic difficulties inprocessing the CNT nanofillers in polymer systems, and thereby a reliable theoretical correlation of the experimental data is still lacking. This is because the reinforcement capability of the CNTs in a polymeric matrix will depend on their amount as well as on their arrangement within the matrix which plays a fundamental role in the load transfer mechanism.

On the other hand, in context with the high prices of the CNTs, there is a requirement for procedures using small samples of nanocomposites, compared to the standard tensile test samples, in order to acquire mechanical property data on which theoretical predictions can be based. Therefore, alternative approaches have been utilised for determination of the mechanical properties of nanocomposites [7]. Nanoindentation is a simple but powerful testing technique, which can provide useful information about the mechanical properties (such as elastic modulus and hardness) of materials. It has been proven that the nanoindentation technique is the most accurate method for evaluation of the effect of carbon nanotubes on the deformation behaviour [8].

The aim of this work was to investigate the mechanical properties of MWCNTpolymer composites by nanoindentation. Elastic modulus and hardness are the properties measured by the nanoindentation technique and these were compared by results obtained by uniaxial tensile tests as well as with popular arithmetic predictions. The morphology of the nanocomposites was investigated by using a stereomicroscope and scanning electron micrographs.

2. MATERIALS

The epoxy matrix investigated was a low strength bisphenol A and epichlorohydrin epoxy resin (Epikote 816, Hexion Specialty Chemicals) containing an added proportion of Cardura E10P (glycidyl ester of neodecanoic acid) as a reactive diluent. The hardener was amine curing agent (Epikure F205, Hexion Specialty Chemicals). The nanofiller used, was multiwall carbon nanotubes (MWCNT's). The carbon nanotubes were used as-received without any further treatment.

Epoxy-based nanocomposites were prepared by mixing the nanotubes with an appropriate amount of the neat epoxy resin using an ultrasonic stirrer (Bandelin Electronic GmbH, model HD2200) for 5min followed by high mechanical mixing. This was followed by the addition of the hardener and further mechanical mixing. The mixture was degassed and then cast into release-agent-coated special formed moulds in order to form the plates for specimen fabrication. The plates were left to cure for 48hours followed by 2 hours post curing at 90ºC. As a result, a series of specimens with nanofiller contents of 0.5% and 1% by weight were obtained. Small specimens of 10x10mm were cut from the plates and polished in order to make the nanoindentation specimens.

3. EXPERIMENTAL PROCEDURES

3.1 Tensile Tests

Tensile tests were performed at room temperature (23°C) on a Zwick Z010 (Zwick, Germany) universal testing machine at a constant crosshead speed of 1 mm/min. The measurements followed the EN ISO 527 testing standard using dumbbell shaped specimens. The specimens having a 4 mm thickness were machined from the moulded plates using a Computer Numerical Control (CNC) milling machine. The overall length of dumbbell specimens was 170 mm. The length and width of narrow section were 10 and 4 mm, respectively. E-moduli were calculated within the linear part of the stress-strain curves. All presented data corresponds to the average of at least five measurements.

3.2 Nanoindentation Testing

Nanoindentation tests involve the contact of an indenter on a material surface and its penetration to a specified load or depth. Load is measured as a function of penetration depth. Fig. 1 shows the typical load and unloading process showing parameters characterizing the contact geometry. This schematic shows a generic viscoelastic-plastic material with the loading OA, and unloading AB´ segments. The plastic work done in the viscoelastic-plastic case is represented by the area W1 (OAB´). The area W2 (ABB´) corresponds to the elastic work recovered during the unloading segment. In the case of purely elastic material, the unloading curve is a straight line (AB) and $h_r=h_{max}$ (W2=0). In this case, penetration depth is the displacement into the sample starting from its surface. Numerous details on the nanoindentation

measurement process in relation to polymers can be found in references [9-11].

In the current work the nanoindentations were conducted on a Fischerscope H100 device, with a resolution of 0.1 mN. The indenter has a Berkovich diamond tip (the tip shape is a three-sided pyramid, with a triangular projected geometry and an included angle of 65.3°; tip radius 20 nm). The nanoindentations made on the surface of the specimens appeared as an equilateral triangle as shown in Fig. 2. Prior to an indentation, the indenter was driven, under computer control, toward the specimen surface. After contact, the indenter was driven into the surface, to a depth of around 0.6μm, at a constant loading rate of 0.15mN/s, until a peak load of 4.8mN was reached and subsequently the indenter was unloaded using the same rate. This peak load was then held for 5 s (in order to minimize the effect of viscoelastic deformation of the specimen, notably creep, on property measurements) and then the indenter was unloaded, to a load of zero.

The calculation method to determine the modulus and hardness of the fumed silica epoxy nanocomposites was based on the work of Oliver and Pharr [12]. According to this method, the nanoindentation hardness as a function of the final penetration depth of indent can be determined by:

$$H = \frac{P_{max}}{A} \qquad (1)$$

Where P_{max} is the maximum applied load measured at the maximum depth of penetration (h_{max}), A is the projected contact area between the indenter and the specimen. For a perfect Berkovich indenter, A can be expressed as a function of the contact indentation depth h_f as:

$$A = 3\sqrt{3}h_f^2 tan^2 65.3 = 24.5h_f^2 \qquad (2)$$

The contact indentation, h_f, can be determined from the following expression:

$$h_f = h_{max} - \varepsilon\frac{P_{max}}{S} \qquad (3)$$

where ε is a geometric constant ε=0.75 for a pyramidal indenter, S is the contact stiffness which can be determined as the slope of the unloading curve at the maximum loading point, i.e.

$$S = \left(\frac{dP}{dh}\right)_{h=h_{max}} \qquad (4)$$

The reduced elastic modulus E_r is given by:

$$E_r = \frac{S}{2\beta}\sqrt{\frac{\pi}{A}} \qquad (5)$$

Where β is a constant that depends on the geometry of the indenter. For the Berkovich indenter, β =1.034. The specimen elastic modulus (E_s) can then be calculated as:

$$\frac{1}{E_r} = \frac{1-\upsilon_s^2}{E_s} + \frac{1-\upsilon_i^2}{E_i} \qquad (6)$$

Where $E_{i,s}$, and $\nu_{i,s}$ are the elastic modulus and Poisson's ratio, respectively, for the indenter and the specimen. For a diamond indenter, E_i is 1140 GPa and ν_i is 0.07.

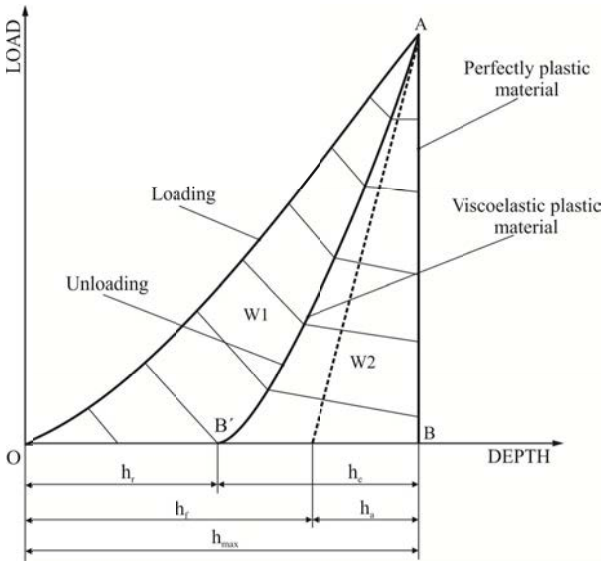

Figure 1. Schematic of indentation load-depth data of a viscoelastic-plastic where h_{max} is the maximum depth, h_e is the elastic depth rebound, h_r is the residual impression depth, h_a is the displacement of the surface at the perimeter and h_f is the contact indentation depth.

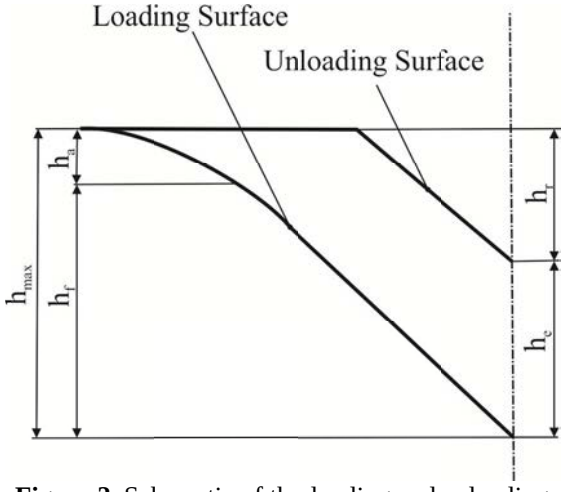

Figure 2. Schematic of the loading and unloading surfaces of an indentation (half-section) with the corresponding indentation depths.

The specimen's hardness H and elastic modulus E_s were obtained from the set of equations given above.

4. RESULTS AND DISCUSSION

4.1 Morphology

Microscope images from the of cured MWCNT epoxy nanocomposites are shown in Fig. 3.

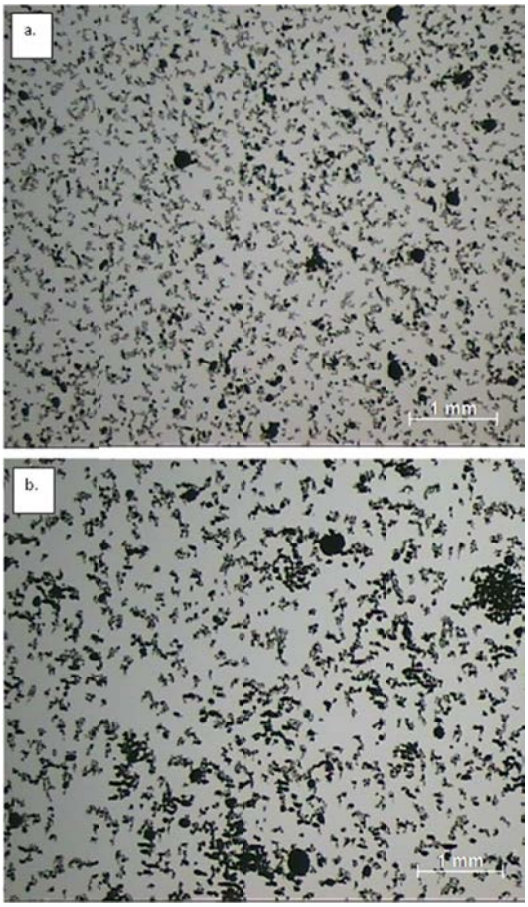

Figure 3. Stereoscope images of epoxy nanocomposites with nanotube concentrations of: a) 0.5%wt, b) 1%wt.

The nanotubes show significant agglomeration which is more pronounced in the case of 1%wt nanotube loading due to strong van der Waals interactions leading to relatively insufficient dispersion despite the ultrasonic application and the subsequent mechanical mixing. An aggregate formation could only be achieved in the epoxy matrix while these aggregates at certain areas attract each other forming greater assemblies as seen from the images. The structure of nanotube clusters observed in all specimens was very similar irrespective of the percentage loading, though slightly higher densities of particle clusters are evidently for the 1%wt nanocomposites.The processing of the epoxy nanocomposites by ultrasonic mixing produced a frothy and viscous dark solution that made the degassing procedure relatively difficult. Also, it is believed that the nanovoids could not be eliminated in total despite the degassing procedure and as during the curing period the epoxy matrix can react only with the surface of the nanotube aggregatesthe matrix itself encapsulates the nanovoids inside the agglomerated nanotubes.

4.2 Tensile Tests

The stress–strain behaviour of the nanocomposites under tension is shown in Fig. 4. The specimens revealed a characteristic plastic behaviour.

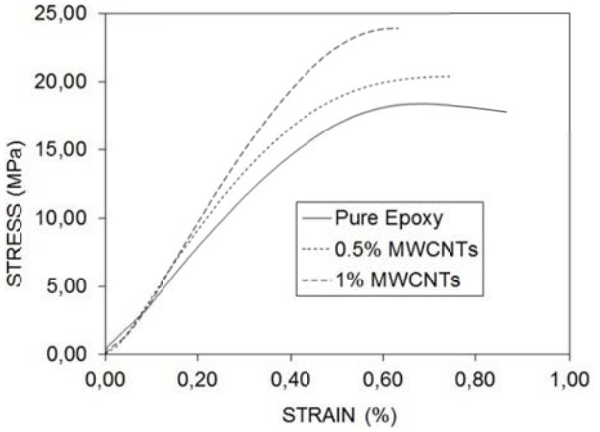

Figure 4. Typical uniaxial tensile stress-strain curves of epoxy reinforced nanocomposites.

The addition of the MWCNTs slightly increased the strength as reported in other studies [2]. The fracture surfaces of the tensile specimens were examined using a scanning electron microscope. The pure epoxy resin samples showed characteristic river lines and a smooth surface as shown in Fig. 5(a). This type of fracture behaviour is typical of brittle epoxy surfaces indicating low resistance to spontaneous crack propagation which was monitored during tensile testing of specimens.

Fig. 5(b) shows the fracture behaviour obtained from the MWCNT nanocomposites.In certain places the fracture is a mirror-like which reflects that the nanotubes were not dispersed evenly. As a result, when the external tensile force was applied, debonding may have occurred at these areas. Also, the formations of clusters produced a severely tortuous surface with certain yielding regions.

During the applied macroscopic tensile stress the local stresses around the aggregates of MWCNTs (Fig. 5c) triggered yielding of the epoxy. Additionally, before the onset of a critical crack, numerous microcracks were formed on the tensile test specimen as visually monitored during testing. The aggregates may have induced crack branching which in turn may have triggered multiple local yielding of the matrix.

The nucleation of the cracks may have developed either within network of the clusters of MWCNTs that have not infiltrated with epoxy resin or at the aggregates' interfaces.

4.3 Nanoindentation

Fig. 6 illustrates typical load–displacement curves of indentations made at a peak indentation load of 4.8mN on the pure epoxy resins and the MWCNT nanocomposites. No cracks were formed during indentation as no steps or discontinuities were found on the loading curves.

The indentation depths at the peak load range from around 0.5 to 0.6 μm. Lower indentation depths are observed for the MWCNT nanocomposites as compared with the pure epoxy samples. The hardness and elastic modulus is increased as the concentration is increased. It is well documented in the literature that the elastic modulus has an increasing trend as the percentage loading of MWCNTs is increasing [13].

There is a significant difference in elastic modulus as obtained from the nanoindentation testing compared to the one of the tensile tests as shown in Table 1.

Clearly the elastic modulus obtained from the nanoindentation testing technique was 14-18% higher than the one obtained from the tensile tests.

Table 1. Elastic moduli values as derived from experiments.

Material	$E_{tensile}$ (GPa)	$E_{nanoindentation}$ (GPa)	$E_{modified}$(GPa)
0% CNT	3,3 ± 0,12	3,9 ± 0,12	3,37
0,5%CNT	4,5 ± 0,15	5,22 ±,0,18	4,57
1%CNT	4,64 ± 0,18	5,31 ±,0,22	4,75

The process of nanoindentation measurements is a relatively complicate procedure, especially for polymeric materials as it has been reported in various studies [11, 14]. The system compliance may be too low to measure the material response property for 'soft' materials like the epoxy resin. Also, the nanoindentation technique is based on the elastic behaviour of the test material; thereby the viscoelastic behaviour may cause an error in the calculation of the elastic modulus. Moreover, there are uncertainties in tip shape calibration that directly relate to the area function (A) which is material dependent in most cases. The tip defect, which is always present due to technical limitations in the fabrication of the indenter, may greatly affect the assessment of the mechanical properties of the tested surface at the first material layers. This is exacerbated by the calibration procedure which requires a series of indentations upon the reference material at various depths and produces an intrinsic blunting effect on the calibrated tip at the deepest penetrations, which do not correspond with the tip/machine behaviour at the shallowest indentations and so the final area function extrapolated may not be exact. Therefore, the intrinsic errors may lead to results which are difficult to explain in the case of softer, viscoelastic surfaces like the solidified epoxy resin in the current case.

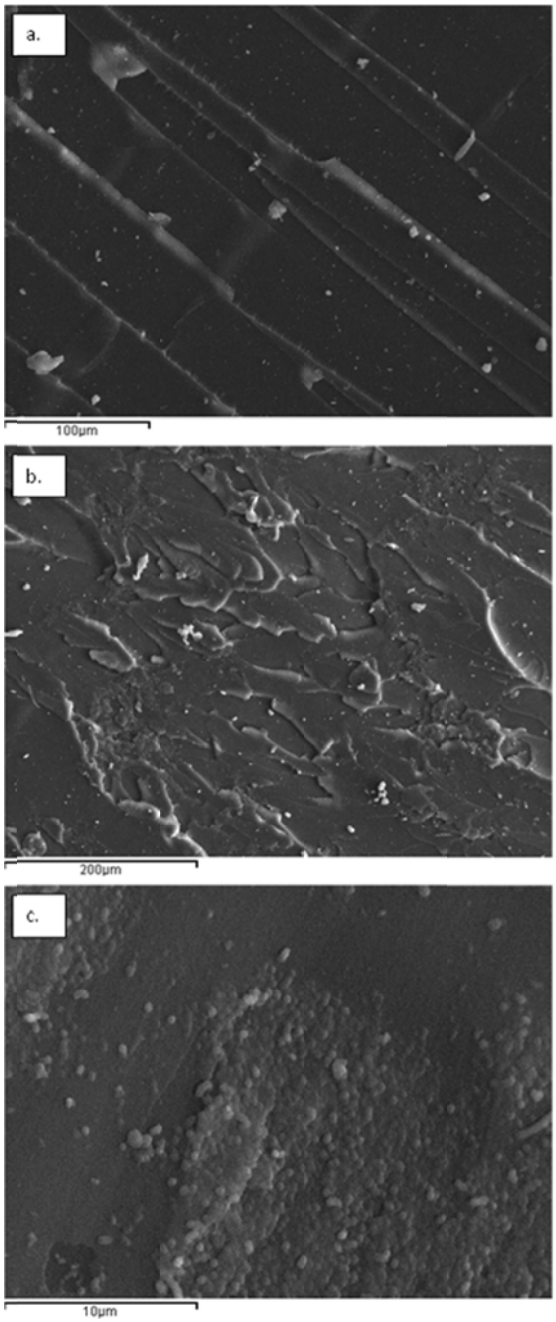

Figure 5. SEM micrographs of typical fracture surfaces of a) pure epoxy resin, b) MWCNT, c) MWCNT at higher magnification

Also, for an epoxy resin material, pile-ups and a distorted surface are usually observed around the crater of the nanoindentation. It is evident therefore that the typical calibration procedure which involves calibration on a reference material of a well-defined elastic modulus such as fused silica is not suitable for polymer materials. This is documented by the observed differences in elastic modulus between the nanoindentation results and the uniaxial tensile test measurements.

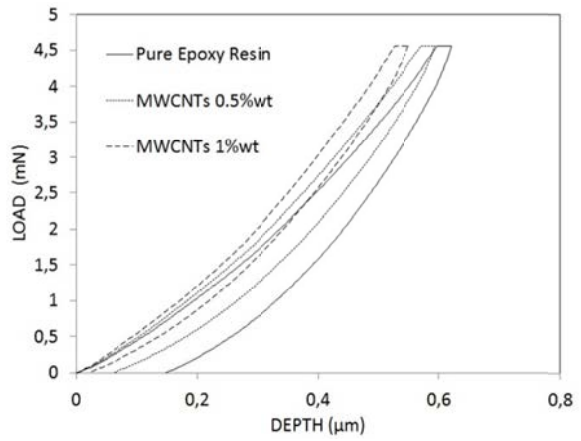

Figure 6. Loading and unloadin versus depth profiles of pure epoxy resin and MWCNT nanocomposites.

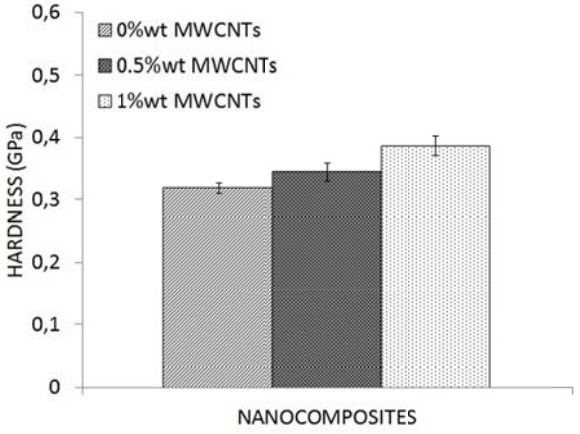

Figure 7. Hardness versus of pure epoxy resin and MWCNT nanocomposites.

Nevertheless the elastic modulus results as measured by both techniques revealed similar trends. Subsequently as suggested by other researchers [10, 11] a material depending calibration procedure has been utilized for the current measurements. Using equations (1-6) from the Oliver and Pharr [12, 15], the modified area function related to indentation depth was obtained using the elastic modulus from a tensile test of the pure epoxy resin which was 3.3 GPa. Using the new calibrated area function the elastic moduli of the nanocomposites was calculated. The result of the elastic modulus based on the modified area function is marked as modified nanoindentation. Clearly, the modified elastic modulus values shown in Table 1 are in good agreement with the elastic modulus from the uniaxial tensile tests. For MWCNTs nanocomposites the elastic modulus is increasing as measured from both the tensile tests and from the nanoindentation experiments with the proposed calibration technique.

Fig. 7 also shows the hardness of the nanocomposites as a function MWCNT concentration. In agreement with the previous outcomes the hardness follows the elastic modulus trend and increases in the case of MWCNTs as the concentration increases from 0.5%wt to 1%wt. It should be noted that when measured at small scales, the hardness is larger than at larger scales. An example of this phenomenon is the so called 'indentation size effect' which can be observed as an increase in hardness with decreasing indentation depth [16]. This effect complicates the determination of the material hardness at low indentation depths, given the small remaining impression. However, the results obtained in the current study lie within values obtained from other studies investigating MWCNT epoxy nanocomposites [17, 18].

The hardness of the carbon nanotubes themselves is higher than the one from the epoxy resin thereby this explains the small increase noticed in the presented results.

5. ELASTIC MODULUS PREDICTIONS

Despite the outstanding mechanical properties of nanotubes, the nanocomposites involving such nanofillers exhibit a very limited improvement of mechanical performances,if compared to conventional advanced composites.This opposingbehavior can beexplained by considering that the reinforcing contribution of MWCNTs is yieldednot only by their amount within the material, but also by the state of dispersion, orientation,shape and number of contacts within the matrix system. All these features play a criticalrole on the final reinforcement enhancement, and they should be taken into account if possible in order todevelop reliable models for prediction of nanocomposite effective properties.

The classical micromechanics approaches for short fibre reinforced composites were employed in this work in order todevelop predictive models for the MWCNT nanocomposites.A popular and widely adopted model to predict the stiffness of MWCNTs nanocomposites is the Halpin-Tsaimodel. The Halpin–Tsai model [19] is widely used in many literature references.It is based on a force balance model and empirical data and it isused widely for macroscopic composites.For the moduli of randomly oriented MWCNTs in the epoxy matrix, the Halpin–Tsai model may predictthe elastic modulus of the nanocomposites, E_{NC},which is governed by the following set of equations:

$$E_{NC} = E_m\left(\frac{3}{8}\frac{1+\zeta\eta_L v_{MWCNT}}{1-\eta_L v_{MWCNT}} + \frac{5}{8}\frac{1+2\eta_T v_{MWCNT}}{1-\eta_T v_{MWCNT}}\right) \quad (7)$$

$$\eta_L = \frac{\left(E_{MWCNT}/E_m\right)-1}{\left(E_{MWCNT}/E_m\right)+\zeta} \quad (8)$$

$$\eta_T = \frac{\left(E_{MWCNT}/E_m\right) - 1}{\left(E_{MWCNT}/E_m\right) + 2} \quad (9)$$

$$\zeta = 2\left(\frac{l}{d}\right) \quad (10)$$

Where E_{MWCNT} and E_m are the Young's modulus for the MWCNTs and matrix respectively while v_{MWCNT} and l/d are the volume fraction and aspect ratio of MWCNTs respectively. From Eq. 7 it can be seen that E_{NC} strongly depends on the geometry of the MWCNTs such as their aspect ratio. The length of the fibres ranges from 1-25μm while various diameterswere measured as seen in Figure 8. Taking E_{MWCNT}= 1GPa which is much greater than E_m=3.3GPa the predicted values versus the volume fraction of the nanotubes of E_{NC} based on Eq. 7 is shown in Fig. 9.It can be seen that the Halpin–Tsai formula for d=5nm gives a slight different value for E_{NC} compared to the ones measured from the nanoindentation using the calibration procedure.

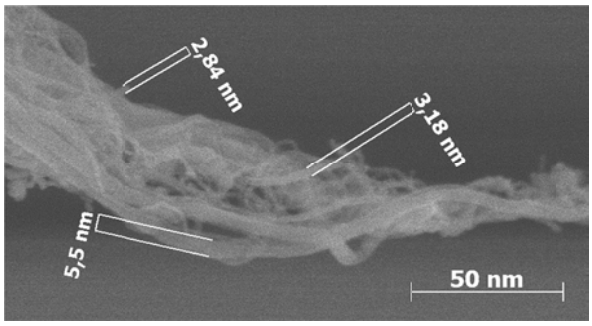

Figure 8. Measurements of the outer diameter of the MWCNTs.

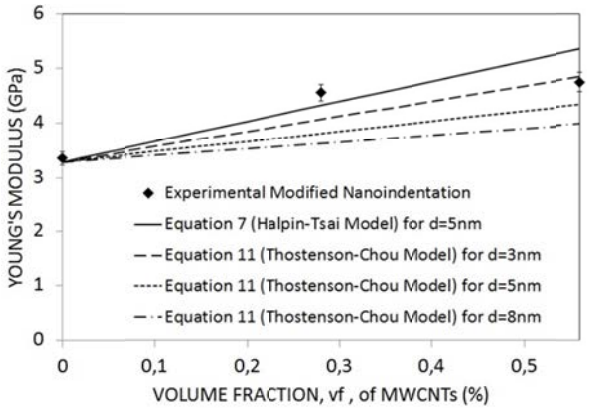

Figure 9. Comparison of the experimental modified nanoindentation results with the Halpin-Tsai and Thostenson-Chou models.

Thostenson and Chou [20]modified the Halpin Tsai theory towards its applicability tonanotube reinforced composites. Thostenson and Chou considered that, in the case ofMWCNT, only the outer shell would carry the load as logical assumption of the relativelylow bonding with inner layers. According to this assumption, the effective MWCNT elasticmodulus was evaluated by considering the application of all loads only to the outer crosssection (outer diameter and graphite layer thickness which is taken as t=0.34nm). Eq. 11 has been derived in order calculate the maximumobtainable E_{NC} for a composite with aperfect distribution of the CNTs and impregnation within the epoxy. Predictions computed by using Thostenson-Chou model show a reduced level of efficiency for large diameters while for d=3nm the prediction is compared well with the experimentally derived modulus for 1%wt (0.56%vf) MWCNTS.

This occurs despite the fact that as shown by the SEM investigations there are locally higher nanotube concentrations within the composite. Accounting for any errors associated with the experimentally derivedvaluesthe results have to be interpreted as a lower boundary of the obtainable moduli.Additionally, the presence of voids developed during mixing the hardener with the MWCNT/epoxy-suspension via ultrasonic mixing and mechanical stirring may have restrained the composites from their full mechanical performance potential. The high viscosity disabled a fully adequate degassing of the nanocomposite with voids remaining in the matrix.The initial failure had been caused by these voids and expressed itself in the reduced fracture strain in the tensile tests.

It is clear therefore that despite the fact that the models used in this work are valuable tools towards the prediction of the elastic modulus of the nanocomposites they do not totally correctly represent thevarious issues associated with the content, morphology and type of nanotubes incorporating a variety of diameters and lengths. Also, and most importantly they consider the nanotubes agglomerated-free which may be misleading when compared with experimental data.

$$E_{NC} = \frac{3}{8}\left(1 + 2\left(\frac{l}{d}\right)\left(\frac{\left(E_{MWCNT}/E_m\right) - \left(d/4t\right)}{\left(E_{MWCNT}/E_m\right) + \left(l/2t\right)}\right)v_{MWCNT}\right) \times \left(1 - \left(\frac{\left(E_{MWCNT}/E_m\right) - \left(d/4t\right)}{\left(E_{MWCNT}/E_m\right) + \left(l/2t\right)}\right)v_{MWCNT}\right)^{-1}$$

$$+\frac{5}{8}\left(1 + 2\left(\frac{\left(\mathbf{E_{MWCNT}}/\mathbf{E_m}\right) - \left(\mathbf{d}/\mathbf{4t}\right)}{\left(\mathbf{E_{MWCNT}}/\mathbf{E_m}\right) + \left(\mathbf{l}/\mathbf{2t}\right)}\right)\mathbf{v_{MWCNT}}\right) \times \left(1 - \left(\frac{\left(\mathbf{E_{MWCNT}}/\mathbf{E_m}\right) - \left(\mathbf{d}/\mathbf{4t}\right)}{\left(\mathbf{E_{MWCNT}}/\mathbf{E_m}\right) + \left(\mathbf{l}/\mathbf{2t}\right)}\right)\mathbf{v_{MWCNT}}\right)^{-1}\mathbf{E_m} \quad (11)$$

6. CONCLUSION

The nanoindentation technique has been successfully utilised in order to study the mechanical properties (i.e. hardness and elastic modulus) of MWCNT/epoxy nanocomposites. The indentation results revealed that the hardness and modulus of the nanocomposites increase with higher MWCNT concentrations. The elastic modulus data obtained by nanoindentation are comparable with those obtained by tensile testing when a suitable material calibration is applied. The results verify the capability of the nanointendation instrumented technique to characterize the mechanical properties of polymer nanocomposites using small sample amounts. Elastic modulus predictions using the Halpin-Tsai model have shown comparable results with the experimental data, while the Thorsten and Chou model provided good predictions by taking into account the outer layer of the nanotubes.

REFERENCES

[1] S. Iijima, *Helical microtubules of graphitic carbon* Nature, Vol. 354, pp. 56-58, 1991.

[2] K. Sharma, M. Shukla, Experimental study of mechanical properties of multiscale carbon fiber-*epoxy-CNT composites*, Advanced Materials Research, Vol. 383-390, pp. 2723-2727, 2012.

[3] H.U. Zaman,P.D. Hun, R.A. Khan, K.B. Yoon, *Effect of Multi-walled Carbon Nanotubes on Morphology, Mechanical and Thermal Properties of Poly(ethylene Terephthalate) Nanocomposites*, Journal of Applied Polymer Science, Vol. 128, No. 4, pp. 2433-2438, 2013.

[4] M.R. Loos, S.H. Pezzin, S.C. Amico, C.P. Bergmann, L.A.F. Coelho, *The matrix stiffness role on tensile and thermal properties of carbon nanotubes/epoxy* composites, J Mater Sci, Vol. 43, pp. 6064–6069, 2008.

[5] J.A. Kim, D.G. Seong, T.J. Kang, J.R. Youn,*Effects of Surface Modification on Rheological and Mechanical Properties of CNT/Epoxy Composites*, Carbon, Vol. 44, pp. 1898–1905, 2006.

[6] F.H. Gojny, M.H.G. Wichmann,B. Fiedler, K. Schulte, *Influence of nano-reinforcement on the mechanical and electrical properties of conventional fibre reinforced composites*, Composites Science and Technology, Vol. 65, pp. 2300–2313, 2005.

[7] P.M. Nagy, D.Aranyi, P.Horváth, P.Pötschke, S. Pegel,E.Kálmán, *Nanoindentation Investigation of Carbon Nanotube–Polymer Composites*, Internet Electron. J. Mol. Des., Vol. 5, pp. 135–143, 2006.

[8] A.K. Dutta, D. Penumadu, B. Files, *Nanoindentation testing for evaluating modulus andhardness of single-walled carbon nanotubereinforced epoxy composites*, J. Mater. Res., Vol. 19, pp. 158–64, 2004.

[9] M.R. VanLandingham,*Review of instrumented indentation*, J. Res. Natl. Inst. Stand. Technol., Vol. 108, pp. 249-265, 2003.

[10] B. J. Briscoey, L.Fiori, E.Pelillo, *Nano-indentation of polymeric surfaces*, J. Phys. D: Appl. Phys., Vol. 31, pp. 2395–2405, 1998.

[11] M.R. VanLandingham, J.S.Villarrubia, W.F. Guthrie,G.F. Meyers, *Nanoindentation of polymers: An* Overview, Macromol. Symp., Vol. 167, pp. 15-43, 2001.

[12] W.C. Oliver, G.M. Pharr, *An improved technique for determining hardness and elastic modulus using load and displacement sensing indentation experiments*, J Mater Res, Vol. 7, pp. 1564–1583, 1992.

[13] A. Montazeri,J. Javadpour, A.Khavandi, A. Tcharkhtchi,A.Mohajeri, *Mechanical properties of multi-walled carbon nanotube/epoxy composites*, Materials and Design, Vol. 31, pp. 4202–4208, 2010.

[14] M. Sánchez, J. Rams, M. Campo, A. Jiménez-Suárez, A.Ureña, *Characterization of carbon nanofiber/epoxy nanocomposites by the nanoindentation technique*, Composites: Part B, Vol. 42, pp. 638–644, 2011.

[15] W.C. Oliver, G.M. Pharr, *Measurement of Hardness and Elastic Modulus by Instrumented Indentation: Advances in Understanding and Refinements to Methodology*, J Mater Res, Vol. 19, No. 1, pp. 3–20, 2004.

[16] C.S. Han, *Influence of the molecular structure on indentation size effect in polymers*, Materials Science and Engineering A, Vol. 527, No. 3, pp. 619-624, 2010.

[17] Sajjad M., B. Feichtenschlager, S. Pabisch, J. Svehla, T. Koch, S. Seidler, H. Peterlik, G. Kickelbickd, *Study of the effect of the concentration, size and surface chemistry of zirconia and silica nanoparticle fillers within an epoxy resin on the bulk properties of the resulting nanocomposites*, PolymInt, Vol. 61, pp. 274–285, 2012.

[18] P.M. Nagy, D. Aranyi, P. Horváth, P. Pötschke, S. Pegel, E. Kálmán, *Nanoindentation Investigation of Carbon Nanotube - Polymer Composites*,Internet Electronic Journal of Molecular Design, Vol. 5, pp. 135–143, 2006.

[19] J.C. Halpin, J.L.Kardos, *The Halpin-Tsai equations: A review*,Polym. Eng. Sci., Vol. 16, pp. 344–352, 1976.

[20] E.T. Thostenson, T.W. Chou, *On the elastic properties of carbon nanotube-based composites: modeling and characterization*, J Phys D: ApplPhys, Vol. 36, pp. 573–82, 2003.

Serbian Tribology Society

SERBIATRIB '13

13th International Conference on Tribology

Faculty of Engineering in Kragujevac

Kragujevac, Serbia, 15 – 17 May 2013

SOME TRIBOLOGY STATE TESTS OF "EPDM" RUBBER BASED ON LABORATORY EXPERIMENTATIONS

Abhijit Mukhopadhyay*

*Associate Professor, Mechanical Engineering Department, Jadavpur University, Kolkata-700032, India, m_obiji@yahoo.com

Abstract: *Rubber is very useful and suitable material for a wide variety of engineering and other applications. Use of rubber as engineering material is not new. However, in the recent time, its application is gaining importance due to several other reasons. Recent and renewed researches on rubber material reveal its suitability for varied engineering applications. Several researches are also going on to enhance the property requirements of rubber for different applications.*

Rubber possesses large elasticity compared to metals, has greater damping capability, high internal friction and can accumulate energy greater than that of steel or other metals. During the deformation of rubber material, e.g., by compressive force, internal damping of the material leads to energy dissipation. This is the cause of hysteretic friction of rubber. Friction of rubber is of great practical importance at the same time it has many disadvantages too.

Amongst various rubber Ethylene Propylene Diene Monomer (EPDM) rubber emerges as a dominant elastomer for major engineering applications in automobiles, constructions, electric and electronic industries etc. The major properties of EPDM are its outstanding heat, ozone and weather resistance ability. The resistance to polar substances and steam are also good.

In automobiles EPDM rubber has a common use as seals. This includes door seals, window seals, trunk seals and sometimes hood seals. Frequently these seals are the source of noise due to the movement of the door versus the car body. This is due to friction between the EPDM rubber parts and the mating surfaces. Thus the contact iteration between the rubber sealing and the indenting object must be known to optimize the performance of rubber sealing. It I, however, need less to mention that the behavior of any viscoelastic material is very difficult to be predicted.

In the present work various tribo-characteristics of EPDM rubber of different hardness are evaluated utilizing the laboratory test facilities available in the frame work of the mechanical engineering department, production engineering department and other specialization of the Jadavpur University, Kolkata. Compression tests have been carried out using 'Instron' to determine the flow behavior of EPDM rubber of different hardness values in dry as well as in different lubricated conditions. The flow behavior like load - elongation curves, true stress - elongation curves true stress - true strain curves have been drawn from the experimental data. Abrasive wear behavior has been evaluated using a two-body abrasion tester and the pattern abrasion has been appraised through SEM/EDAX study. It has been proposed to study further the wear loss using a pin-on-plate (POP) type tribometer and conduct fretting wear test on the same material, that is, EPDM.

Experimental results revealed that the hardness values of EPDM rubber had significant effect on the flow behavior and wear characteristics. The hardness, again, depends on the carbon black (CB) concentration. Thus it can be stated that the flow behavior can be governed by controlling the CB concentration in the EPDM rubber. The results of different tests followed by comparative analysis have been furnished in the 'result and discussion' section of this paper.

Conclusion has been drawn accordingly, highlighting some of the important tribo-characteristics of EPDM rubber as well as shedding light on various possible areas of further researches those should be undertaken in the future to come.

Keywords: *EPDM, compression, flow behavior, abrasion, SEM/EDAX.*

1. INTRODUCTION

Tribological studies of rubber like materials are not new. However, in this recent time, being fuelled by several new researches and development in the field of viscoelastic materials as well as due to various property requirements of rubber for several engineering, domestic, sports and other applications, the performance evaluation of rubber is becoming very demanding and gaining renewed research interest in different parts of the globe.

Property prediction is the other driving force [2,17]. It means that the property of engineering and other materials should be predictable and there should have some useable model in that regard. It is, however, needless to be mentioned that the property of any viscoelastic material, like rubber, is very hard to be predicted. The friction and wear data base of rubbers are also not very promising due to the fact that the rubbers used in such tribotests are not characterized adequately[1].Test configurations, parameter selections, experimental conditions are all important factors which should be standardized before comparing the tribotest data generated by various agencies or researchers. All these necessitate further study and iteration of tribotest data for rubber to be used as engineering or other materials.

Ethylene Propylene Diene Monomer (EPDM) rubber is widely used as seals in automobile door, window, hood and other parts. They are subjected to wear and tear due to pressure, vibration, friction and exposure to extreme conditions of atmosphere. Though EPDM has outstanding heat, ozone, weather resistance ability and resistance to any polar substance as well as steam is also very good, still some realistic tribotest data are yet to be developed.

In the present work flow behaviors of EPDM rubber of different hardness have been evaluated. EPDM specimens have been compressed in between flat MS platens and stress-strain relationship, specific energy and loss factors have been computed subsequently for this purpose. Similarly wear characteristics have been studied in a two-body abrasion testing machine. SEM/EDAX studies have also been made to appraise the pattern abrasion, immediately after two-body abrasion testing.

2. EXPERIMENTAL

The EPDM rubber specimen for the tribo tests in this work were prepared in the laboratory of National Engineering Limited (Rubber Division), Kolkata, following the recipe code as mentioned in Table 1.

Table 1. The recipe code of different hardness of EPDM.

Ingredient	Shore Hardness				
	55Å	60Å	70Å	80Å	85Å
EPDM	100	100	100	100	100
ZnO	5	5	5	5	5
St. Acid	1	1	1	1	1
PEG 4000	1.2	1.2	1.2	1.2	1.2
FEF 550	80	130	160	170	180
P Oil(2500)	130	110	100	90	80
Sulpher	1	1	1.2	1.2	1.2
HBS	1	1	1.5	1.5	1.5
ZDBS	1	1.5	1.2	1.2	1.2
TMT	1	0.7	0.7	0.7	0.7

However it is needless to mention that the actual proportions of various ingredients are trade secret and strictly a 'not-disclosed grade'. The above table is thus only a closely indicative one.

Basic ingredients were pre-mixed in a K4/2A-MK3 (Alfred Herbert) for 6 minutes at a ram pressure of 100 psi. Curatives were then added to the pre-mixed materials on a two roll laboratory mill (330 × 150) at room temperature. Curatives are required to enhance various properties. The mixing time was approximately 10 minutes. A constant friction ratio of 1:1.25 was maintained during rolling.

Processing characteristics including optimum cure time (t_{90}) and torque difference ($\Delta m = Mh - M_l$) were determined with Oscillating Disc Rheometer equipped with computer assisted data acquisition system and supported by 'Rheosoft' software. Standard procedure as is observed in [5] and others were followed in that regard but the machine used for the purpose is Indian one and specific procedural steps for the said machine were followed accordingly. M_h and M_l are high and low Mooney (torque) respectively. The torque was monitored as a function of time and the optimum cure times were recorded from the corresponding rheographs, one such graph is shown in Figure 1.

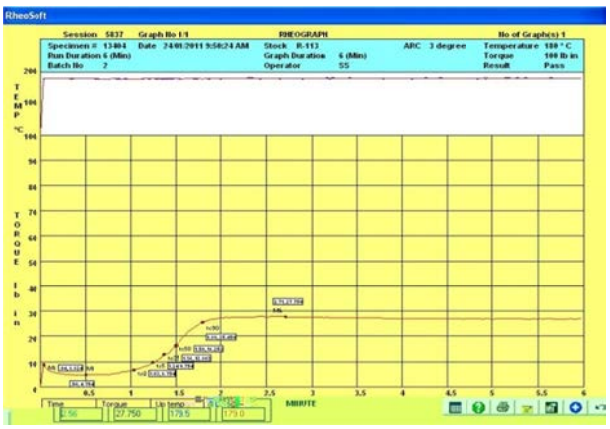

Figure 1. Torque-vs.-Time rheograph of an EPDM specimen.

The material after qualifying the rheometric analysis was ready for molding operation. Short cylindrical specimen of diameter φ (16.5±0.5) and height h (12.5±0.5) were then prepared in the steam heated hydraulic press at a pressure of 3000 psi and temperature 150^0C. The material is compressed in the press for approximately 10 minutes. The molding operation has been carried out as per IS: 3400 (part-X) - 1977 specification. The extra spew of materials have been trimmed by scissor after molding to give the specimen proper shape. The dimension, specific gravity and shore hardness values of all the samples have been measured accordingly using appropriate measuring tools and instruments for the respective parameters.

2.1 Compression test

Each test specimen was placed axysymetrically in between two flat mild steel platens. Much care had been taken in such placement to ensure an even force distribution on both the faces of the specimen. The required compressive load was provided by an Instron (model 8801; serial no. K 2342 with 'Dynacell' load cell, made in England. Maximum working pressure: 207 bar; dynamic load capacity: ± 100 KN). The machine, as shown in Figure 2, is equipped with '8800: Instron SAX V9.3' software based data acquisition system. Only one fatigue cycle had been utilized at a frequency of 0.005 Hz for the application of compressive load on the specimen. The height of each cylindrical specimen was reduced by 65%. Each test had been replicated twice to observe the repeatability of the process. The compressive load followed by load relaxation data had been recorded and later utilized to plot the loading and unloading curves.

Figure 2. 'Instron' equipped with data acquisition software.

Five different states of test had been applied during compression. One in dry condition, one under fixed contact and three with different lubricants like, talc, water and grease. Increased friction, during compression, in between the die and work piece mating surfaces leads to the development of an undesirable phenomenon known as 'barreling' or 'pan caking'. The metal spreads over the die surface to increase its diameter when it is compressed in between two die halves. Frictional force opposes the outward flow of metal near the mating zone of work piece and die halves. But the material at the mid height of the specimen is absolutely free to flow in an out ward direction. This is the basic explanation of barreling [3]. One such barreling during compression under fixed contact, using sand paper, is shown in Figure 3. This undesirable frictional force may be reduced by using some suitable lubricant. The effect of compressive load on EPDM specimen of different hardness in dry working condition, that is, without any lubricant, was appraised by the present author [4]. Similarly, the flow characteristics of EPDM rubber of different hardness under compressive load in the presence of some lubricants were studied by the present author [6]. It is not out of place to mention here that to reduce friction and wear between two mating and interacting surfaces some film of solid, liquid or gas is applied which is considered as lubricant[7]. Selection of proper lubricant(s) depends on several considerations and should be judicious [8]. In this experimental work some lubricants were selected based on the literature survey and considering the practical work environment [9-12]. The characteristics studied for this purpose includes stress-strain relationships, specific energy and loss factors.

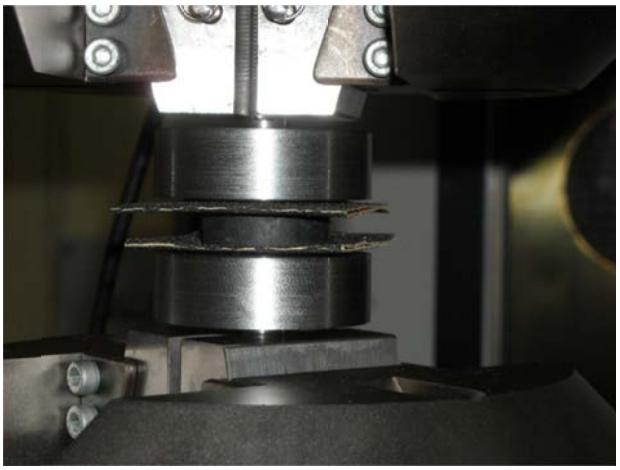

Figure 3. Compression of EPDM specimen using fixed contact.

2.2 Abrasion test

Specimen of sizes 70mm x 30mm x 2mm were cut from vulcanized rubber sheets of 150mm x 150mm x 2mm for conducting the abrasion tests. EPDM rubber of three different shore hardness values was selected for this purpose. These are 55 Å, 70 Å and 80 Å

respectively. Abrasion tests were carried out using a two body abrasion tester TR-605 (Ducom) as shown in Figure 4. The machine is designed to conduct test as per ASTM D 6037 (Test method B) and/or ISO 8251 [18]. The machine is equipped with a stepper motor drive (makes –My Com, 24 V DC, and 40 W, model no. IMS-200-220 AL) and requires an electricity of 230 V x 1 φ x 50 Hz and 100 W power. The wheel of the abrasive wear tester is made of stainless steel having a diameter of 50mm and width of 12mm. Silicon Carbide (SiC) water proof paper (Carborundam Universal) of grades ER 240, ER 220 and ER 180 were pasted on the top surface of the wheel for the purpose of abrasion. Appropriate sizes of the abrasive papers were cut and pasted on the wheel using an adhesive (Feviquick). Rubber specimens were placed in the desired position on the machine table and clamped properly. The specimens were also subjected to normal load using a dead weight. The leverage action obtained in the machine in use is 1:2, that is, a counter weight of 2N will apply 1N of normal load on the job. Then the specimens were abraded against the abrasive paper under simulated abrasive wear condition.

Figure 4. Laboratory set up of a two-body abrasion tester.

For this laboratory experimentation three different levels of four factors have been considered. The factors are hardness of EPDM rubber, abrasive grade, load on job and cycles and the levels are low, medium and high respectively. It is needless to mention that if a full factorial experimentation had been conducted with the four factors each at three levels, as mentioned, then a total of 81 experiments would have to be carried out and the number would have been multiplied accordingly for replication. In the present study, an L_9- orthogonal array has been selected based on Taguchi's experimental design technique [13] and thus only 9 experiments have been conducted. The combinations of different factors and levels as well as the specific wear rate corresponding to each combination are shown in Table 3 in Appendix-I.

3. RESULTS AND DISCUSSIONS

Table 2, in Appendix-I, indicates the flow characteristics of EPDM rubber under compressive load and in different working conditions, that is, with or without lubricants. The lubricants, as indicated in the table, are selected based primarily on the literature survey as well as from the real life experience. The compressive load imparted by Instron and corresponding height reduction data have been recorded through the data acquisition system of the machine and later on different flow characteristics like load-vs.-deflection, true stress-vs.-deflection and true stress-vs.-true stain have been calculated using the indigenously developed MATLAB code in that regard. Some flow curves are shown in Figure 5 (a), (b) and (c) as samples.

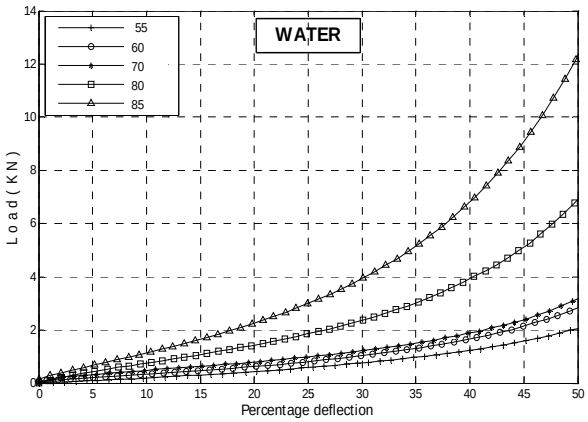

(a)

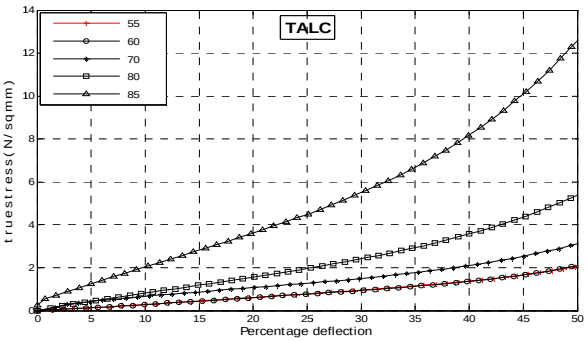

(b)

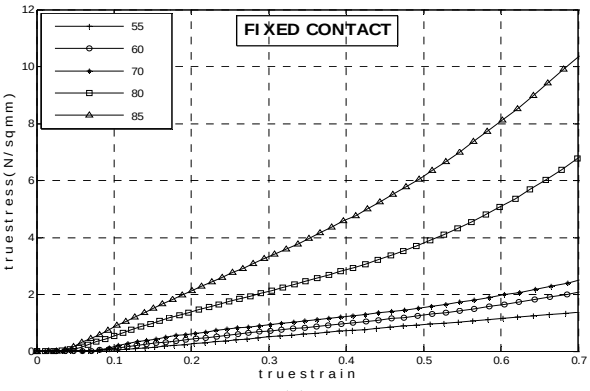

(c)

Figure 5. Flow characteristic curves are shown in (a), (b) and (c) under different conditions as indicated in the curves.

It has already been mentioned that four factors, each at three levels, have been selected to conduct the abrasion test. Table 3 indicates the said factor – level combinations and corresponding specific wear rate data which is obtained from the following formula [11]:

$$W_s = \frac{\Delta m}{\rho F L},$$

where, W_s = specific wear rate (mm^3/Nm)
Δm = mass loss recorded gravimetrically (gm)
ρ = specific gravity of EPDM (gm/cm^3)
F = the normal load on the job (N)
and, L = overall sliding distance (m)

The worn surface morphology had been studied for each sample immediately after the abrasion using a scanning electron microscope (SEM: JEOL, JSM-6360, model 75 82) to see the smallest detail of the pattern abrasion in the range of 4 – 5 nm (4 – 5 millionths of a millimeter). The test had been conducted immediately after the experiment, though it is reported by Pandey et.al. [14] that in their experiments fracture mode did not change within 72 hours of storage before conducting SEM studies and coating etc. The worn surfaces had been coated with a very thin layer of palladium (Pd) using ion sputtering machine (Auto Fine Coater: JEOL, JFC-1600) prior to SEM studies. It is not out of place to mention here that ion coating is done on non-conducting specimen (like biological specimen etc.) to be analyzed in SEM for quick and highly efficient results. This is done mainly to prevent charging of electrons at the sample [15]. For some samples energy dispersive X-ray spectroscopy (EDAX) had also been done in conjunction with SEM to find out the percentages of different elements in the sample. Elemental mapping with EDAX is helpful to get insight into the chemical changes on the surface and sub-surface of the sample[16]. As no chemical reaction is taking place in the present case hence EDAX has not done for all the specimens.

Figure 6 shows some typical pattern abrasion of EPDM as obtained from SEM studies. In figure 6(b) a chunk of rubber agglomerate has been separated leaving behind a groove (chunking and grooving). Figure 6(c) reveals the ridge formation which supports the concept of rubber wear by the process of plowing.

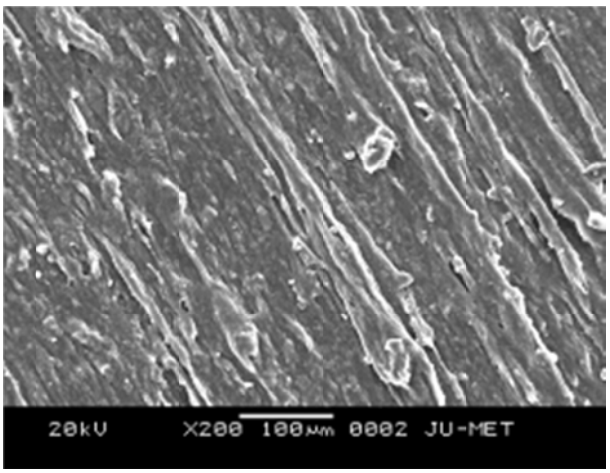

(a)

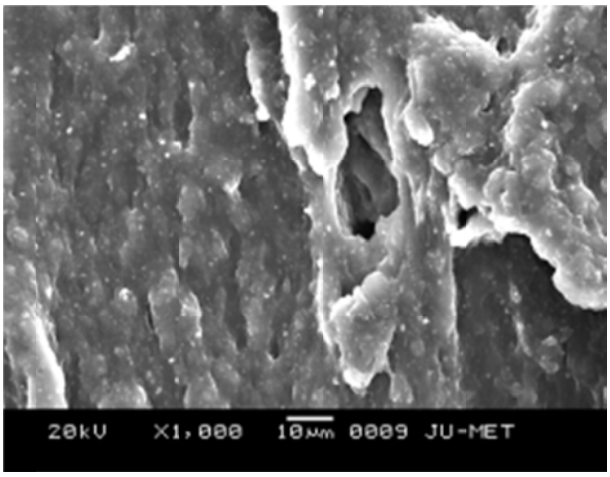

(b)

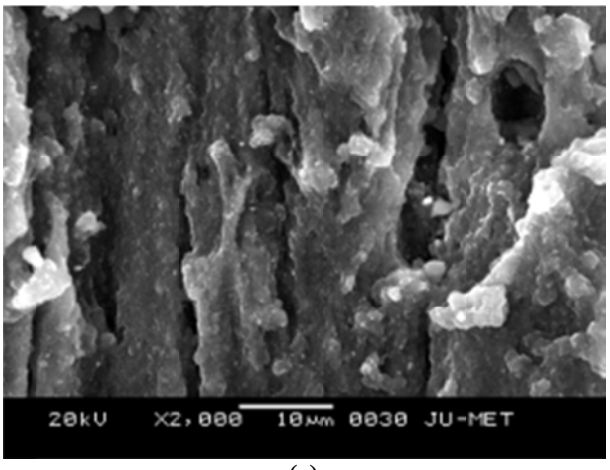

(c)

Figure 6. Worn surface morphology of EPDM corresponding to trial no.1 (×200), 2 (×1000) and 6 (×2000) as obtained from SEM studies.

The graph of the average specific wear rate is shown in Figure 7.

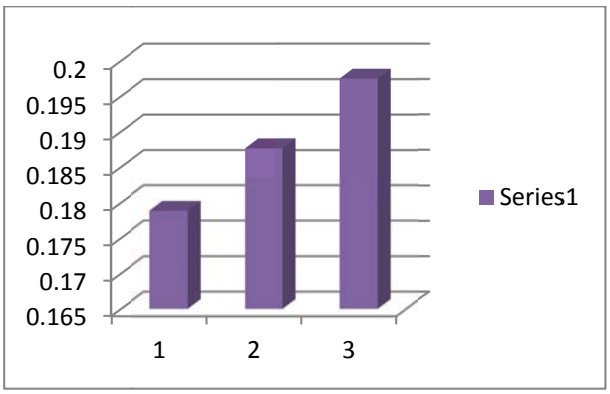

Figure 7. The specific wear rate of EPDM 55Å (1), 70Å (2) and 80Å (3).

The curves reveal that the specific wear rate is smallest for the softer rubber, that is, EPDM 55Å. The specific gravity is also smaller in case of EPDM 55Å, which depends on the hardness and hardness again depends on the carbon black (CB) content of the rubber. However, in case of flow characteristics of EPDM it is revealed that EPDM 70Å is better than others. The selection of material depends on the actual requirements in specific application area.

CONCLUSION

This experimental work is devoted for flow as well as wears characterization of EPDM rubber of different hardness in different experimental conditions. The test conditions were very difficult to be harmonized but much care was taken to obtain results as accurate as possible accepting the noise factors included in the experimentations. The results obtained are tabulated, graphed and analyzed accordingly in the previous section. Future work is proposed with different other lubricants as well as inclusion of complex operating environment, like extreme temperature and pressure conditions etc. It is also proposed to conduct fretting wear test as well as measurement of abrasion loss using pin-on-plate (POP) type of tribometer.

ACKNOWLEDGEMENT

The present work has been carried out in the frame work of Mechanical Engineering Department, Production Engineering Department and Metallurgy and Material Science Engineering Department of the Jadavpur University, Kolkata, India. The author is extremely thankful to the faculty and laboratory staff members, the students who at any point of time were involved in this work at any ways. The author is also thankful to NEL (Rubber division), Kolkata, for their very kind support in providing the work specimen for the tests, purely for academic interest.

REFERENCE

[1] Felhos D., Karger-Kocsis J.: *"Tribological Testing of Peroxide Cured EPDM Rubbers With Different Carbon Black Contents Under Dry Sliding Conditions Against Steel"*, Tribology International Vol. 41, pp. 404-415, 2008.

[2] Kalpakjian S., *Schmid Steven R.*: *"Manufacturing Processes for Engineering Materials"*, 4th. Edition, Pearson Education, 2009.

[3] Dieter George E.: *"Mechanical Metallurgy"*, McGraw-Hill, SI Metric Edition, 1988.

[4] Mukhopadhyay Abhijit: *"Flow Behavior of EPDM Rubber of Different Hardness Values Under Axysymetric Compressive Load in Dry Working Condition"*, Proceedings of the 12th. international conference on Tribology "SERBIATRIB'11", Kragujevac, Serbia, 11- 13.05.2011, pp. 56-64.

[5] Sohail Khan M.,Franke R. et.al.: *"Friction and Wear Behavior of Electron Beam Modified PTFE Filled EPDM Compounds"*, Wear, Vol. 266, pp. 175-183, 2009.

[6] Mukhopadhyay Abhijit: *"Effect of Some Lubricants on the Flow Characteristics of 'EPDM' Rubber Under Compressive Load"*, Accepted paper in the international conference on Tribology, 'BALTTRIB-2011', 17-19 Nov., 2011, Kaunas, Lithuania.

[7] Mukhopadhyay Abhijit: *"Maintenance Tribology: A New Paradigm in Maintenance"*, SURVEY (a management journal of IISWBM, Kolkata), Vol. 50 No. 3&4, pp.1-7, 2010.

[8] Lenard J.G.: *"Tribology in Metal Rolling"*, Annals of CIRP, Vol. 49, No. 2, pp. 567-590, 2000.

[9] Sofuoglu H., Rasty J.: *"Flow Behavior of Plasticine Used in Physical Modeling of Metal Forming Processes"*, Tribology International, Vol. 33, pp. 523-529, 2000.

[10] El. Tayeb N.S.M., Nasir Md.R.: *"Effect of Soft Carbon Black on Tribology of Deprotenised and polyisoprene Rubers"*, Wear, Vol. 262, pp. 350-361, 2007.

[11] Karger-Kocsis J., Mousa A., et. al.: *"Dry Friction and Sliding Wear of EPDM Rubbers Against Steel as a Function of Carbon Black Content"*, Wear, Vol. 264, pp. 359-367, 2008.

[12] Mukhopadhyay Abhijit: *"Review on the Tribological State Test in Some Metal Forming Operation in Industry"*, Mechanica Confab, Vol. 1, No. 3, pp. 29-39, 2012.

[13] Logothetis N.: *"Managing for Total Quality: From Deming to Taguchi and SPC"*, Prentice Hall of India, 2000.

[14] Pandey K.N., Setua D.K., Mathur G.N., *"Material behavior: Fracture topography of rubber surfaces: an SEM study"*, Polymer Testing, Vol. 22, No. 3, pp. 353-359, 2003.

[15] SEM/EDAX analysis, http://www.ML06\1\ANALYSISWITHSEM_EDS.PMD060317.

[16] Ginic-Markovic M., Roy Choudhury N.,et.al., *"Weatherability of coated EPDM rubber compound by controlled UV irradiation"*, Polymer

Degradation & Stability, Vol. 69, No. 2, pp. 157-168, 2000.

[17] Ludema Kenneth C.: *"Friction, Wear, Lubrication: A text book in tribology"*, CRC press, U.S., 1996.

[18] Handbook of 'Two Body Abrasion Tester: TR-605', Ducom Instruments, http://www.ducom.com.

APPENDIX – I

Table 2. Flow characteristics data of EPDM.

EPDM of different hardness	Lubricant														
	Dry			Fixed Contact			Talc			Water			Grease		
	A	B	C	A	B	C	A	B	C	A	B	C	A	B	C
55Å	2.71	2.08	2.16	1.77	1.34	9.90	2.71	2.04	2.05	1.99	1.52	1.52	1.66	1.34	1.25
60Å	3.35	2.41	2.53	2.65	2.01	6.78	2.64	2.05	2.04	2.72	2.05	2.05	2.36	1.75	1.79
70Å	4.05	3.15	3.47	3.18	2.40	2.40	3.95	3.17	3.03	3.09	2.34	2.34	2.52	2.62	1.91
80Å	9.03	5.95	6.75	8.36	6.38	2.01	7.88	6.29	5.24	6.78	5.05	4.83	6.94	3.91	5.24
85Å	16.57	10.00	12.53	13.03	9.90	1.34	16.32	12.29	12.29	11.76	9.33	8.87	-	-	-

[A: Load (KN) at 50% deflection; B: True stress (N/mm^2) at 50% deflection; C: True stress (N/mm^2 at a true strain of 0.7]

Table 3. Factor-level combinations of the experiments as per Taguchi's L_9- orthogonal array and the abrasion loss data.

Trial No.	Hardness (Shore;Å)	Abrasive grade	Load on job (N)	Cycles	Specific wear rate (mm^3/Nm)		
					1st replication	2nd replication	3rd replication
1	55	Very Fine	5	200	0.1149	0.1038	0.1094
2	55	Fine	10	400	0.2641	0.1692	0.2952
3	55	Medium	15	600	0.2279	0.1507	0.1741
4	70	Very Fine	10	600	0.1930	0.1932	0.1921
5	70	Fine	15	200	0.1991	0.2234	0.1930
6	70	Medium	5	400	0.1640	0.1963	0.1353
7	80	Very Fine	15	400	0.1775	0.2142	0.1944
8	80	Fine	5	600	0.1782	0.2685	0.1848
9	80	Medium	10	200	0.1551	0.2098	0.1951

Serbian Tribology Society

SERBIATRIB '13

13th International Conference on Tribology

Faculty of Engineering in Kragujevac

Kragujevac, Serbia, 15 – 17 May 2013

APPLICATION OF 3D SOFTWARE PACKAGES FOR DESIGNING TRIBOMETER OF MODULAR TYPE

Ivan Mačužić[1] Branislav Jeremić[1] Petar Todorović[1]
Marko Đapan[1] Milan Radenković[1] Marko Milošević[1]
[1]Faculty of Engineering Kragujevac, University of Kragujevac, Kragujevac, Serbia,
ivanm@kg.ac.rs, bane@kg.ac.rs, petar@kg.ac.rs, djapan@kg.ac.rs, radenkovic@kg.ac.rs, m.milosevic@kg.ac.rs

Abstract: *In this paper is presented advantages of modular type of tribometers using various types of softwares, especially for modelling. Designing this type of tribometer allows significant saving regarding time, space, people, raw materials as well as financial resources. Design of tribometers followed with testing and verifying, which implies simulation using various types of softwares, significantly improve the way and standards of tribometer contruction. Selection of the desired parameters which would be used in the experiments is very important and the first step in designing of the tribometer. Testing and verifying is the last step when scientists and researchers get the result of the final evaluation whether or not to proceed to construction of the tribometer.*

Keywords: *tribometer design, rapid construction, CAD software, simulation*

1. INTRODUCTION

The machines and equipment for various tribology experiments need to be maximal versatile. The versatility is reflected through possibility of providing variety of experiments. These types of equipment are specific and mostly designed, constructed and used by researchers and scientists for very complex measurements and experiments. These equipment need to be, not just versatile but very precise, providing accurate results which are used as an input for further experiments or calculations.

Tribometers are widely used for experimental research for measurement of friction characteristics under laboratory conditions. This laboratory conditions have to be pre-defined, before measurements are performed. Also, equipment and measurements are designed for conducting different types of experiments, to obtain results for further experiments. Laboratory conditions mean various parameters are constant, for example normal force, velocity, temperature and humidity [4]. Because of different types of the contact [5] versatility of equipment is the most important characteristic which is required.

There are many different types of tribometers for different use [1] [2] [3] [6]. Different use means different structure of tribometer, different processes followed with different parts of tribometer. So, rapid development of tribometers based on software for 3D modelling is required. The modular tribometer will be able to speed up process of design and construction of tribometers depending on type of experiment. Today, there are commercial universal tribometers which are not the same as modular we want to present. Universal tribometers offer the various options and different types of experiments on the same equipment. The main difference between universal and modular tribometer is that on the universal all necessary parts are already mounted on the same equipment and just small corrections in software enables working on test equipment. Also, the additional parts can be added for desired experiments [7]. On the modular tribometers researchers can choose which of the tribology parameters wish to monitor. So, after calculations and simulations of properties of equipment structure, constructors can proceed with equipment construction.

Modular tribometers are suitable for rapid construction of equipment and what is the most important, for performance evaluation and

conformance to researchers' requirements. Software for 3D modelling allows that before construction of the equipment to check, test, verify and validate successful experiment's output. This means there is a possibility of predicting success/failure of the experiments. The results of this prediction provide valuable significant data which could save, on the first place, financial resource and then time, space, people, raw materials, etc.

The aim of this paper is to propose methodology of using software for modelling tribometer which have to be designed and tested performing simulation for selected parameters. The whole process of testing, quality checking and final adjusting of modular tribometer need to be conducted before construction. Every part of tribometer is compact in size, having the best possible characteristics for selected parameters, overcome technical difficulties and the end checking is the tribometer functional.

The paper is structured as follows: Secton 2 present importance of using software for 3D modelling. Section 3 describes one example of modular tribometer and what type of experiment can be carried out. The conclusions are given in Section 4.

2. BENEFITS OF 3D TRIBOMETER MODELLING

CAD technology is ubiquitous for diverse array of fields, particularly engineering and manufacturing [9]. It is integral part of the every process where is needed to meet some goals such as reducing design to production lead time, better engineering analysis, additional flexibility and faster response for design modification [8]. All these benefits are reflected to manipulation with designing parts necessary for final construction. The greatest attention is given to:

- dimensioning of critical parts, which are necessary for conducting successful experiments resulting to relevant outputs;
- dimensioning of measurement parts;
- possibility to construct various equipment for different experiments mean that modules have been already designed for rapid design;
- simulations which are very important to see if all parts of the tribometer are properly assembled, if all system is functional or not to react in time before spending resources, before construction.
- simulations have another advantage, researches can see and conclude is there any overlapping of the work areas, some errors, mistakes and fault decisions which are made during equipment and process design;
- predicting values of the parameters which are selected for experimental research (normal load, viscosity, stress generated in the contact zone due to the given force, etc.).

All steps in design and construction depend on requirements from researches and scientists what parameters would be considered. Also, conceptual development of modules is dependant of requirements.

In our case, the most important parameters were linked with basic parameters typical for hydraulics and its components which can be found in real industrial systems. Also, we monitor processes which appear between selected pin and plate in oil environment. Based on this we could simulate and calculate if the required processes are possible to monitor and get relevant results. The most important parameters for our research were:

- liquid resistance (in our case liquid is oil) inside the container and
- stress in the contact zone due to given load.

In the next section will be presented one modular tribometer designed, tested and constructed for tribological phenomena in hydraulic components (pumps, motors, cylinders and valves).

3. EXAMPLE OF EXPERIMENTAL EQUIPMENT

The first step is defining the type and concept of the tribometer. In our case, whole concept is based on analysis of hydraulic components and characteristics of wear processes which are occur in that kind of industrial equipment. From the literature [10] [11] linear sliding movement and abrasive wear mechanism are the most common and the most important in the hydraulic components. Regarding this fact, pin-on-plate tribometer was selected to be designed and constructed because we had wear process between pin and plate in oil environment. Also, it can be able to control some of the basic tribology parameters such as load in contact, slide length, sliding speed, liquid resistance, etc.

On the figure 1 is shown model of tribometer which is divided in 3 bigger units:

- experimental unit (positions: 1, 2 3 4 and 7);
- control unit (positions: 6 and 8) and
- pneumatic drive unit (position: 5)

All units need to be well connected and functional. Potential problems with the first starting up of the constructed tribometer can be prevented

using number possibilities of 3D modelling software packages.

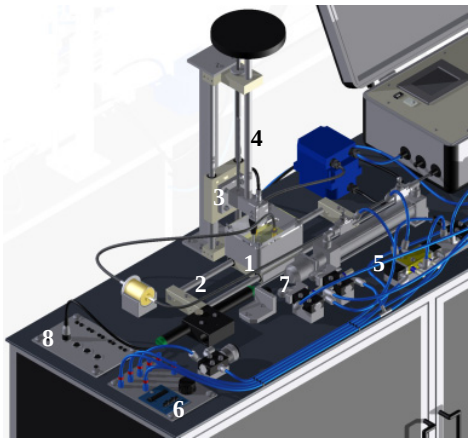

Figure 1. Sub-divided components of tribometer model

First of all, whole design of the tribometer is based on container with a plate and oil (1), placed on a horizontal linear guides (2), moving alternately, while pin is stationary. Pin bracket (3) is set to vertical linear guides (4) and given loads on the pin passed through the bar, which is also a dynamometer for measuring of friction force. Drive system for reciprocation motion is pneumatic (5) with pneumatic cycle counter (6).

On container with a plate (1) displacement transducer is fixed (7), with function to measure, in real time, container position and thus enable the accurate determination of velocity and moments when container change movement direction. On a tribometer base plate surface there is a connection panel for this transducer (8).

Now will be described the most important part of the tribometer, the contact zone where tests are performed (figure 2).

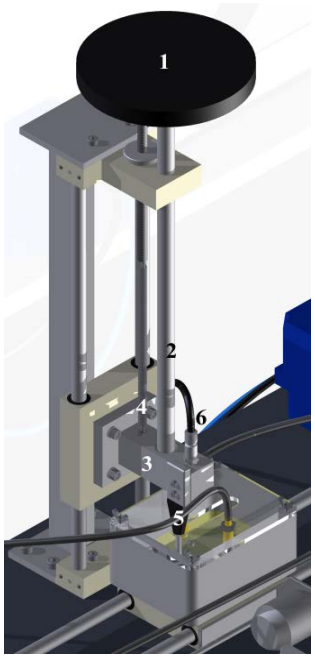

Figure 2. System for setting load and force measurement

Value of normal load in the contact zone is defined by calibrated weights (1) where the forces transferred through the shaft (2) with a spherical end are to the pin bracket (3). Compensation of own mass elements which are located on the pin bracket is performed through a spring with a threaded spindle (4). On pin bracket (3) set the single-axis piezoelectric vibration sensor (6) which measures vibrations in the tribological contact in the vertical direction.

The close-up view of the above described contact zone is shown in figure 3.

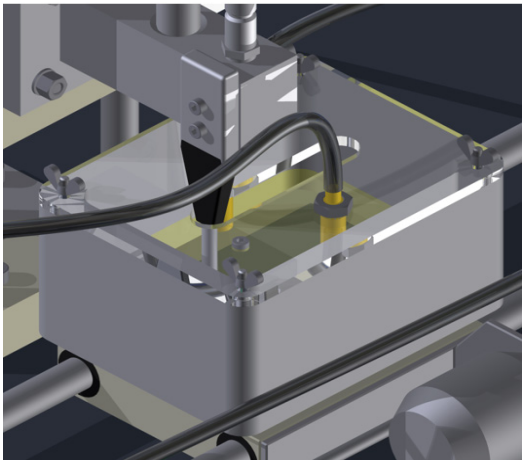

Figure 3. Close up view of contact zone

There is a plate attached at the bottom of aluminium container. Pin has cone top that fits into a spherical end of the dynamometer bar and thus carries the normal force evenly over the entire surface of contact. Container has a volume of 500 ml and is filled oil up with oil to about 1/3 of its height. Container is covered with a transparent cover on which there are connections for oil circulation - suction and return. Suction line takes oil from the bottom of container on one side and returns oil back to the surface on the other side of container. This is to ensure adequate oil mixing during circulation.

And, at the end the third part of the tribometer is pneumatic system (figure 4).

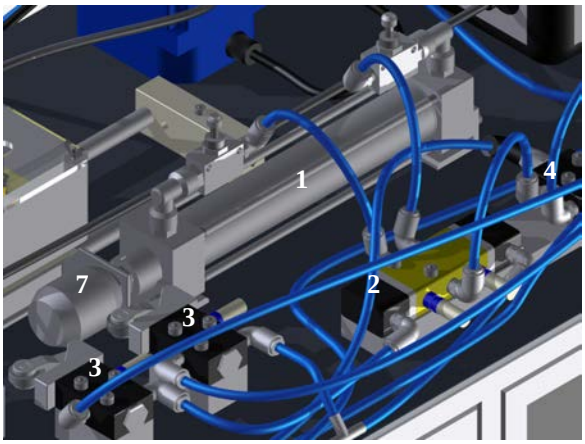

Figure 4. Pneumatic drive unit

This part is assembled of pneumatic cylinder (1), air-operated distribution valve 5/2 (2), two pneumatic limit switches (3), pneumatic logic valve 3/2 (4), pneumatic cycle counter and the reset button. Limit switches limit stroke of cylinder piston which is fixed to container. Switches are fixed and the stroke length is determined by varying the length of a cylindrical end part of cylinder (7) which activated limit switches. At both command lines, which bring compressed air to the cylinder, set of throttle valves that regulate the speed of the cylinder in both directions.

4. CONCLUSION

In the times where financial savings are more important than results, there need to be the way which will satisfy both conditions. Besides that, there is a constant need for various types of experiments which need to be precise and its results need to be accurate. Development of modular tribometers could be good solution for issues related for rapid construction of tribometer and obtaining accurate results for selected parameters. Tribometer which is designed from modules tested and verified through simulations it is very simple to proceed to the next step regarding construction. Desired and requested parameters are also important because software could obtain possible mistakes and failures in design before construction.

ACKNOWLEDGMENT

Research presented in this paper was supported by Ministry of Science and Technological Development of Republic of Serbia, Grant TR-35021, Title: Razvoj triboloških mikro/nano dvokomponentnih i hibridnih samopodmazajućih kompozita.

REFERENCES

[1] E. Sajewicz, Z. Kulesza: *A new tribometer for friction and wear studies of dental materials and hard tooth tissues*, Tribology International 40, pp. 885–895, 2007.

[2] S.K. Sinha, S.L. Thia, L.C. Lim: *A new tribometer for friction drives*, Wear, Vol 262, pp. 55–63, 2007.

[3] J.L. Dion, G. Chevallier, O.Penas, F.Renaud: A new multicontact tribometer for deterministic dynamic friction identification, Wear 300, pp. 126–135, 2013.

[4] K.D. Moerlooze, F. Al-Bender, H.V. Brussel: An experimental study of ball-on-flat wear on a newly developed rotational tribometer, Wear 271, pp. 1005– 1016, 2011.

[5] P.J. Blau: *Friction Science and Technology*, Marcel Dekker, New York, 1996.

[6] M.R. Kashani, E. Behazin, A. Fakhar: Construction and evaluation of a new tribometer for polymers, Polymer Testing 30, pp. 271–276, 2011.

[7] URL: www.microtest-sa.com/index.php?lang=en (accessed: 04.03.2013.)

[8] M.K. Malhotra, M.L. Heine, V. Grover: *An evaluation of the relationship between management practices and computer aided design technology*, Journal of Operations Management 19, pp. 307–333, 2001.

[9] W.C. Regli, V.A. Cicirello: Managing digital libraries for computer-aided design, Computer-Aided Design 32, pp. 119–132, 2000.

[10] C.B. Mohan, C. Divakar, K. Venkatesh, K. Gopalakrishna, K.S. Mahesh Lohith, T.N. Naveen: *Design and development of an advanced linear reciprocating tribometer*, Bengaluru 562112, India 2009.

[11] G.W. Stackhowiak, A.W. Batchelor, G.B. Stachowiak, *Experimental methods in tribology*, Tribology Series 44, Elsevier Science, 2004.

Serbian Tribology Society

SERBIATRIB '13

13th International Conference on Tribology

Faculty of Engineering in Kragujevac

Kragujevac, Serbia, 15 – 17 May 2013

USING OF KALMAN FILTER AS A PROGNOSTIC TOOL FOR TRIBOLOGY PROCESSES

Ivan Mačužić[1], Petar Todorović[1], Marko Đapan[1], Milan Radenković[1], Branislav Jeremić[1]
[1]Faculty of Engineering, University of Kragujevac, Kragujevac, Serbia,
ivanm@kg.ac.rs, petar@kg.ac.rs, djapan@kg.ac.rs, radenkovic@kg.ac.rs, bane@kg.ac.rs

Abstract: *The paper consider possibilities for performing of prognostic procedure for tribology processes in hydraulic equipment using advanced mathematical tool called Kalman filter. It is an algorithm that uses a series of measurements observed over time, containing noise and other inaccuracies, and produces estimates of monitored parameter that tend to be more precise than those based on a single measurement alone. Kalman filter operates recursively on streams of noisy input data to produce a statistically optimal estimate of the underlying system state.This type of procedure could be used for prognostic of state of chosen parameter of tribology system with significantly accuracy. Efficiency of Kalman filter were tested on experimental results of hydraulic oil contamination monitoring performed in laboratory conditions.*

Keywords: *Kalman filter, prognostic, tribology processes, hydraulic equipment*

1. INTRODUCTION

Prognostics is a set of activities aimed at assessing the remaining time to failure for a particular technical system or risk of presence or occurrence of one or more failure modes in the future. Prognostics efficiency can be quite satisfactory for the failure modes that have repeating time characteristics, followed by progressive degradation of key exploitation characteristics [1].

In cases of failure modes with random and unexpected events, prognostic is a very difficult task with uncertain results.

Prognostic process could be based on the model, or on the measurement results. Prognostic based on the measurement results includes the use of various mathematical tools for monitoring and predicting, such as for example Kalman filter and its simplified version known as alpha-beta-gamma filter [2].

2. KALMAN FILTER

Signal filtering, and extracting the useful signal from noise is a traditional problem in science and technology. Significant number of models and algorithms was proposed and developed for solving of this problem. In case when signal and noise spectra lies in different frequency bands, their separation can be made with appropriate band filters.

Another problem arises when the spectra of the signal and noise overlap and then statistical methods for the assessment and evaluation of the signal should be used to extract the signal. In such circumstances it is not possible to obtain an accurate absolute value of the signal, and all the methods of filtration are made only to minimize interference.

The first such analog signals filter suggested by Norbet Winer in 1940. using the method of least squares. New stage in the development of the theory of filtration began Rudolf Emil Kalman in 1960., with publication of his capital work, "A New Approach to Linear Filtering and Prediction Problems" in which it was first introduced method will become known in science as the Kalman filter [3].

The Kalman filter is a mathematical tool that can be used to assess the value of variables in different forms of real situation. Mathematically speaking Kalman filter evaluates the condition of linear systems. It is a statistical technique that combines the statistical nature of system faults with knowledge of the system dynamics, and those

matrixes describe the state of the system and their evaluation.

The significance of this method is that, on the one hand it gives excellent results in practice, while, on the other side, is theoretically attractive since it has been demonstrated that all of the filters that are applied precisely this variation achieved by minimizing the error estimates [4], which is often also called the optimal filter.

Application of Kalman filter was recently, in addition to traditional applications related to signal processing, automatic control systems and processes, and the projection of the trajectory and ballistic missiles, and a significant number of new areas such as medicine systems, global positioning satellite (GPS) navigation, computer vision, economics, and so on.

In order to use the Kalman filter to remove noise from the signal, system, or process that is considered to be such that it can be approximated as linear and present. For nonlinear systems, which can't be present or approximated as linear, the so-called. Extended Kalman filter is developed as an extension of the theory of linear Kalman filter to nonlinear systems [4].

Linear systems are those that can be represented using the following two equations. The first is the equation of state:

$$x_{k+1} = Ax_k + Bu_k + w_k \quad (1)$$

the other is the output of the system of equations:

$$y_k = Cx_k + z_k(1) \quad (2)$$

These equations are:
A - matrix that shows the relationship of current and previous step, *B* - matrix connections inputs and the current state, *C* - matrix state and do the measurements, *k* - time index, *x* - variable that indicates the state of the system, in - known input the system, *y* - the output of the system being measured, and *w* and *z* are noises where *w* is called process noise and *z* - measurement noise.

Each of these values is generally a vector that contains more than one element. Vector *x* contains all the information about the current state of the system but we are not able to measure directly. Therefore, we measure the value of the vector *y* which is a function of the vector *x* with the addition of measurement noise *z*. This means that over the measured values of the vector *y* can assess the state system described by vector *x*.

Introduced the assumption that the average value of the process noise *w* and the measurement noise *z* is zero during a time interval and that there is no correlation between them, and that the two forests have approximately a normal distribution with covariance *Sw* and *Sz*. Based on the above can be derived equations for the Kalman filter [4]:

$$K_k = AP_kC^T(CP_kC^T + S_z)^{-1} \quad (3)$$

$$\hat{x}_{k+1} = (A\hat{x}_k + Bu_k) + K_k(y_{k+1} - C\hat{x}_k) \quad (4)$$

$$P_{k+1} = AP_kA^T + S_w - AP_kC^T{S_z}^{-1}CP_kA^T \quad (5)$$

Each of the three defined equations of Kalman filter includes a series of operations with matrices where the index *T* represent matrix transposition and index *-1* represent matrix inversion. Matrix *K* is called the Kalman gain and the matrix *R* estimation of error covariance.

Obviously, the Kalman filter works recursively and takes only the value of the system state at the previous time point to generate assessment following conditions (not required the entire history of the state).

The Kalman filter can be used in different ways to handle real signals where the results are quite different nature and use. When the filter is used to estimate the previous state of the known history of the system (measured values) is obtained by eliminating the possibility of measuring noise in order to level the curve that defines the state of the system changes over time in the past. If we estimate the current state of the system is the result of filtering the measured signal [4], [5].

The filter can be used for the prediction of the system in the near future if the state of the system in estimated time is moved to next time interval in advance. This means that the estimated state and the actual state were time-shifted by an interval so in accordance with the assessment of the situation for the time moment *k+1* conducted on the basis of estimated values of *x* from time to time and measured values at the time point k + 1. This is possible because the movement of the estimated state for a time interval of pre-practice leads to temporal overlap of the estimated state *x* from *k+1* timing and the real state of *x* from *k* time. Practically on the basis of previous estimates and errors in the actual situation new value is evaluated for the next time point.

One of the great advantages of Kalman filter is its feature that it is not necessary to carry out detailed modelling of system which condition is estimated. The reason for this lies in the recursivity principle of Kalman filter and the periodic repetition of the process of assessment and correction, and built-in tendency to corrects and minimize error from step to step. This feature opens the door to a wide use in solving various technical problems since the generation of an accurate model of the real system is a very demanding and complex task [5].

3. KALMAN FILTER APPLICATION FOR PROGNOSTIC OF TRIBOLOGY PROCESSES IN HYDRAULIC

The essence of the idea for the application of Kalman filter for forecasting and prognostic of tribology processes lies in the fact that it is a tool that is least dependent on the accuracy of the model of tribology system that is considered. The procedure involves projections to prognostic in mathematical modelling of the behaviour of tribology parameters in time, which severely limits the application of other, model-based, prognostic tools, since they are directly dependent on the characteristics of the model for a specific system.

On the other hand, Kalman filter will provide very useful results even for very approximate models and also for some standard, general models of system behaviour in time (that do not even have direct link with the observed system),.

It is clear that the Kalman filter works only at discrete points in time, and its use is related to digital signal processing. Complex math, matrix transformations and calculations, represent an easy task for modern computers and processors to the stabile and to mobile devices, which also allowed the installation of Kalman filters in numerous portable monitoring devices.

As an example of application of Kalman filter for prognostic of tribology processes, trending of contamination level in hydraulic equipment will be presented.

Method of hydraulic oil contamination values prognostic (based on ISO4406 contamination level code) using Kalman filter is shown on Figure 1. From 200 measured points, that define the values of contamination level, for particles of defined size, 9 points was allocated (8 is shown from T1 to T8).

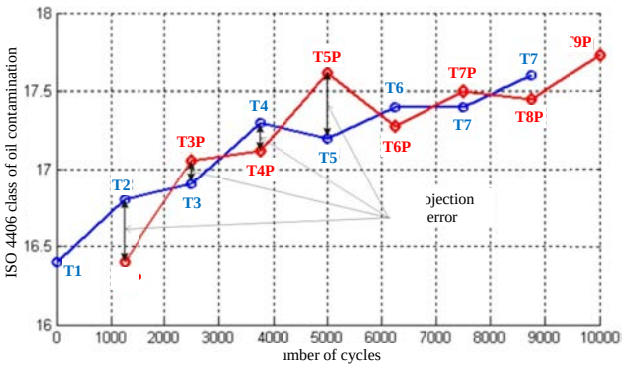

Figure 1. Kalman filter prognostic process

In this case, those are equidistant points, although, in general, do not have to be. Based on the value of the first point of T1 and set parameters of Kalman filter define the value of the first projected point in the future (T2P). Since there is no additional information other than the value of T1, Kalman filter defines point T2P so that its value is the same as the value of the point T1. This is the initial assumption that nothing will change.

At the time of obtaining the measured values of other points - T2, the projection error is calculated as the difference in point values T2 and T2P. On the basis of the projection error values and measured values point T2, Kalman filter performs the projection of the value of the third point T3P. Then a new measured value of contamination T3 is received and new projection error is calculated and the cycle is repeated.

Practically the value of each new projected point is function of the previous measured value and projection errors in the previous point.

At Figure 2, diagram obtained by the projection of contamination using a Kalman filter for the curve related to the measured contamination of hydraulic oil is shown, together with diagram of error projections. Prognostic process is conducted for 40 points, which define the value of contamination, in first attempt and 10 points in second one.

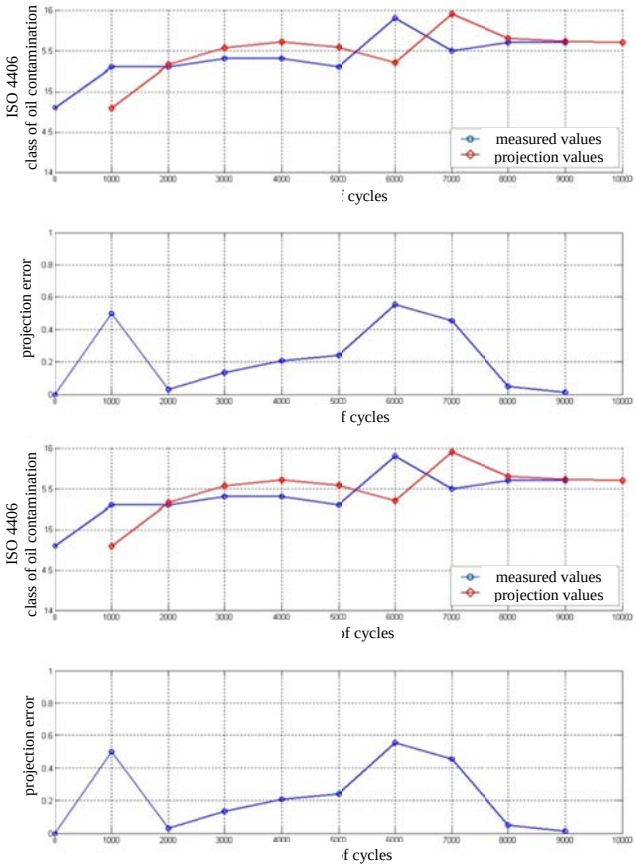

Figure 2. Kalman filter prognostic and projection error

At Figure 3. diagrams obtained by the projection of contamination using the Kalman filter for oil sample from the test with the external addition of contamination in the contact zone is shown.

Total of 3 diagrams are shown in Figure 3. refers to variants of Kalman filters with different

values influence of the measurement noise (from lower to higher)

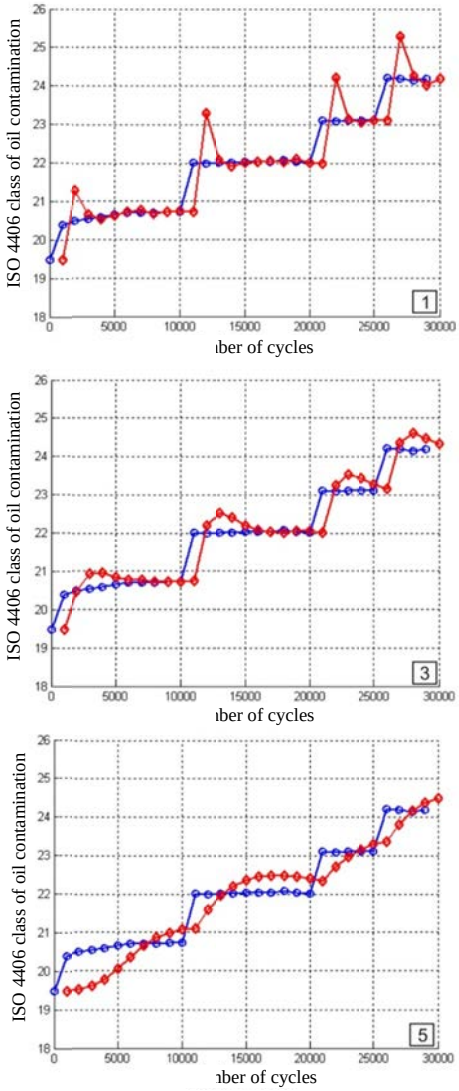

Figure 3. Kalman filter prognostic with step-change in contamination for different values of measurement noise

4. CONCLUSION

Based on shown results some general conclusions about process of prognostic using the Kalman filter could be defined:

- The examples of practical application of prognostic using Kalman filter obtained very good results in tracking of real measured values with acceptable projection error in case of measured diagrams without sudden and significant changes of contamination value.
- The biggest mistake of projection, as a rule, is right at the beginning at first projected point.
- Variations in the values of the measured signal and noise measurement have a direct impact on the accuracy of the prognostic.
- The influence of the measurement noise on the result of the projection can be adjusted using the definition of the value of the corresponding parameter in the Kalman filter equations. Increasing the value of this parameter indicates the presence of more intensive measuring noise and vice versa.
- In the case of a sharp and abrupt prognostic using a Kalman filter have visible and the expected delay in the response to change. It is clear that there is no method of forecasting, which can predict the occurrence of sudden, unexpected and abrupt changes in the values followed by the diagnostic parameter. In any case, these phenomena point to the serious irregularities and problems in the system and certainly represent an alarm signal.
- The great advantage of using Kalman filter lies in its full independence and insensitivity to the shape and characteristics of the measured contamination trend charts.

ACKNOWLEDGMENT

Research presented in this paper was supported by the Ministry of Education, Science and Technological Development of Republic of Serbia, Grant 35021

REFERENCES

[1] A. Muller, M.C. Suhner, B. Iung: *Formalisation of a new prognosis model for supporting proactive maintenance implementation on industrial system*, Reliability Engineering & System Safety 93, pp. 234-253, 2008.

[2] J. Lee, J. Ni, D. Djurdjanovic, H. Qiu, H. Liao: *Intelligent prognostic tools and e-maintenance*, Computers in Industry 57, pp. 476-489, 2006.

[3] R.E. Kalman: *A New Approach to Linear Filtering and Prediction Problems*, Journal of Basic Engineering 82 (Series D), pp. 35-45., 1960.

[4] D. Simon: *Kalman Filtering*, Embedded Systems Programming, 2001.

[5] G. Welch, G. Bishop: *An Introduction to the Kalman Filter*, Department of Computer Science University of North Carolina

Serbian Tribology Society

SERBIATRIB '13

13th International Conference on Tribology

Faculty of Engineering in Kragujevac

Kragujevac, Serbia, 15 – 17 May 2013

FRICTION COEFFICIENT ESTIMATION DURING FRICTION STIR WELDING WITH THE SINGLE SHOULDERED WELDING TOOL

Miroslav Mijajlović[1], Dušan Stamenković[1], Milan Banić[1], Aleksandar Miletnović[1], Miloš Milošević[1]
[1]University of Niš, Faculty of Mechanical Engineering in Niš, Serbia, mijajlom@masfak.ni.ac.rs, dusans@masfak.ni.ac.rs, banic@masfak.ni.ac.rs, amiltenovic@yahoo.com, mmilos@masfak.ni.ac.rs

Abstract: *Friction stir welding utilizes friction forces on the contact of the welding tool and workpieces with the goal of heating and softening workpiece material before stirring and mixing it into the weld. The process of stirring, mixing and welding is quite complex: material of workpieces in the welding zone is drastically deformed/reformed, heated, translated, rotated and softened, and finally, deposed behind the welding tool to cool, plasticize, and recrystallize as a weld. In such conditions, it is difficult to recognize friction conditions, contact surface(s), and loads on the contact. There are no fully operational analytical models for estimation of the friction coefficient during friction stir welding. This paper is giving an overview on a friction coefficient research and presents experimental results from performed friction stir welding of aluminium alloy 2024 T351. Experimental results are used as input for the modified analytical model for estimation of friction coefficient in friction stir welding.*

Keywords: *Friction Stir Welding, Friction Coefficient, Heat Generation.*

1. INTRODUCTION

Friction is one of the most important parameters for successful friction stir welding (FSW) process – this is a sentence that no researcher of FSW will try to disapprove. Such influence to the process itself has motivated the inventor of FSW to use "friction" in the name of the process.

However, friction in FSW has been never presented and explained as a parameter that can be manipulated or adjusted in some manner to improve the FSW process itself. For example, when greater friction in FSW is needed, welding tool (figure 1, b) must have threads, facets, keys etc., when less heating is needed, welding tool has to travel faster what will result in shorter contact between welding tool and some particles of workpieces what results with less friction on contact.

Nowadays experiences in FSW usage recognize technological parameters of the process (travel rate, rotation speed, duration of welding etc.) and geometry of the welding tool (shape, dimensions etc.) as best parameters for successful management of quality of FSW. Principle of "trial and error" and parameters management were successful for FSW and it has been significantly improved. It is known that better the mathematical model explaining the physical process is, the more applicable the process becomes. "Try and error" principle uses no mathematical model for improvement but always gives results and improvements. Its main disadvantage is high resource / time consumption.

In a certain way, friction is very important for almost any aspect of the FSW, but its ambiguity and complex dependencies with the other parameters of FSW make it difficult to use for management of the process. That is the main reason why friction is the least investigated physical process of FSW.

2. SINGLE SHOULDERED FSW

The first application of the FSW was with the welding tool having one probe and one shoulder (figure 1, a). Such construction requires an anvil in order to make weld creation possible. There are newer constructions of the welding tool with two shoulders and/or more than one probe.

Application and technology of FSW with a welding tool with one shoulder is in detail explained in the literature [1-3].

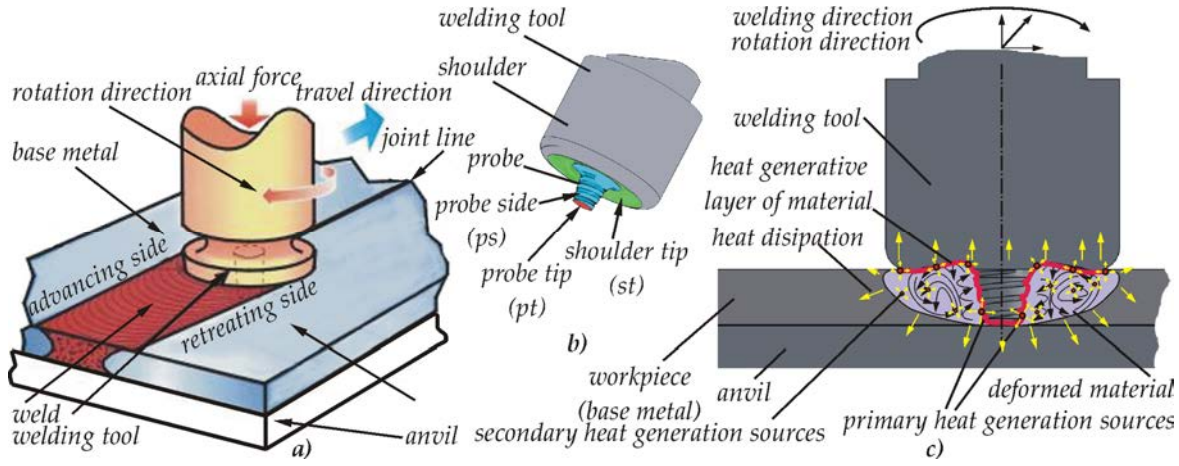

Figure 1. Friction stir welding
a – principle of FSW, b – welding tool and its active surfaces, c – heat generation and transport [1]

3. ESTIMATION OF THE FRICTION COEFICIENT DURING SINGLE SHOULDERED FSW

The newest improvement and development of the model for estimation of the friction coefficient in FSW is 4 years old Kumar's model [4] and relies on the estimation of the momentum of friction which is afterwards, with adequate mathematical model, transformed into the friction coefficient. There are several difficulties in application of such a model:

1. measuring the momentum of friction requires specific and limitedly applicable measuring/working configuration [1],
2. friction coefficient estimated during FSW by Kumar is a median value for all contacts surfaces – active surfaces of welding tool and workpieces (figure 1, b).

3.1 Specific time moments of the FSW

Mijajlovic *et al* [Ref. 5, Figure 4] gives a scheme of welding tools engagement during FSW. It is important to define specific moments of time during welding.

Probe tip is active surface that is fully engaged in the FSW process from the beginning of the plunging phase (t_0) until the end of the second dwelling phase (t_4). At the beginning of the plunging phase probe tip slides over the top surface of welding plates and there is no significant plunging into material of the welding plates. Material of the welding plates is still capable to resist influence of the contact pressure on contact between probe tip and welding plates. Plunging force is rising as the plunging phase on goes and eventually plunging force will be intensive enough to produce contact pressure that will overcome resistance of the material and welding tool will penetrate into the material (in the moment of time $t_{ps'}$). This intensive plunging will enable contact between probe side and material of welding plates and increase of engagement of the probe side – it will reach some value until the end of the plunging phase (t_1). It will be kept steady or slightly will decrease during first dwelling phase (from t_1 to t_2) and it will increase again during welding phase (after t_2). When welding tool stabilizes (in welding phase, when it reaches constant speed, at the moment of $t_{ps''}$) probe side will reach maximal engagement.

It will be kept relatively steady until the end of the second dwelling phase (t_4) and after will slightly decrease until the minimal value – when welding tool gets pulled out, at the end of the pulling out phase (t_5). Shoulder tip will involve in FSW process when firstly touches (t_{st}) the material of welding plates that was pushed upwards while plunging phase lasted. Engagement of the active surface will increase to the maximum when plunging phase ends (t_1), it will keep steady value until the end of the second dwelling phase (t_4) when it will drop to minimum [5].

3.2 Contact over the probe tip

The probe tip (*pt*) of the welding tool is rather curved than flat due to the better distribution of the contact pressure [1]. Without concern on the topology of the welding tool's probe tip, when the probe tip is pressing the workpiece while loaded with the axial force $F_z(t)$ and torque $T_{pt}(t)$, equilibrium of the force and the torque (no relative movement of the welding tool and workpieces, nor rotation of the welding tool) is reached if:

$$T_{pt}(t) \le \frac{\mu_{pt}(t) F_z(t)[d(t) - d_0(t)]}{3} = T_1(t) \qquad (1)$$

where: $\mu(t)=\mu_{pt}(t)$ – total coefficient of friction - coefficient of friction at *pt*, $d(t)$ – diameter of the

probe, $d_0(t)$ – diameter of the technological hole in the workpieces, t - time.

In such condition, the momentum of friction $M_{fr}(t)$ is:

$$M_{fr}(t) = \frac{\mu(t) F_z(t)[d(t) - d_0(t)]}{3} \quad (2)$$

and therefore, friction coefficient at *pt* is:

$$\mu(t) = \mu_{pt}(t) = \frac{3M_{fr}(t)}{F_z(t)[d(t) - d_0(t)]},\ t_0 \le t < t_{ps'} \quad (2)$$

3.3 Contact over the probe tip and the probe side

The probe side (*ps*) of the welding tool is cylindrical or coned surface with or without thread [1]. The thread is of great significance for the welding process, however, it makes great difficulties for the analysis of friction and it will be neglected in analysis.

If only the probe side is in contact with the workpieces, equilibrium between the forces, represented as the contact pressure at the probe side $p_{ps}(t)$, and the torque $T_{ps}(t)$ is:

$$T_{ps}(t) \le \frac{\mu_{ps}(t) d(t)^2 h(t) p_{ps}(t)\pi}{2} = T_2(t) \quad (3)$$

where: $\mu(t)=\mu_{ps}(t)$ – total coefficient of friction – coefficient of friction at *ps*, $h(t)$ – height of the probe (side) plunged into the workpieces.

In such condition, the momentum of friction $M_{fr}(t)$ is:

$$M_{fr}(t) = \frac{\mu(t) d(t)^2 h(t) p_{ps}(t)\pi}{2} \quad (4)$$

and therefore, friction coefficient at *pt* is:

$$\mu(t) \approx \mu_{ps}(t) = \frac{2M_{fr}(t)}{d(t)^2 h(t) p_{ps}(t)\pi},\ t_4 \le t < t_5 \quad (5)$$

When the probe tip and the probe side are simultaneously involved in the contact, equilibrium of loads and the torque at the probe tip and the probe side $T_{pt+ps}(t)$ can be expressed as:

$$T_{pt+ps}(t) \le T_1(t) + \frac{\mu(t) d(t)^2 h(t) p_{ps}(t)\pi}{2} \quad (6)$$

In such condition, the momentum of friction $M_{fr}(t)$ is:

$$M_{fr}(t) = T_1(t) + T_2(t) \quad (7)$$

Assuming that the friction coefficients at the probe side and the probe tip are the same (only as a value):

$$\mu(t) = \mu_{ps}(t) = \mu_{pt}(t),\ t_{ps'} \le t < t_{st} \quad (8)$$

transforming the equation (7), friction coefficient becomes:

$$\mu(t) \approx \frac{6M_{fr}(t)}{2F_z(t)[d(t) - d_0(t)] + 3d(t)^2 h(t) p_{ps}(t)\pi},\ t_{ps'} \le t < t_{st} \quad (9)$$

3.4 Contact over the probe tip, the probe side and the shoulder tip

The shoulder tip (*st*) of the welding tool is cylindrical or coned surface with the greatest area [1, 2]. Shoulder tip is the last active surface of the welding tool involving into the welding process.

If only the shoulder tip is in contact with the workpieces, equilibrium between the loads and the torque at the shoulder tip $T_{st}(t)$ is:

$$T_{st}(t) \le \frac{\mu_{st}(t) F_z(t)[D(t) - d_{\max}]}{3} = T_3(t) \quad (10)$$

where: $\mu(t)=\mu_{st}(t)$ – total coefficient of friction – coefficient of friction at *st*, $D(t)$ – diameter of the *st*, $d_{\max}$ – maximal diameter of the probe.

However, shoulder tip is never involved in the welding process as the only active surfaces – shoulder tip is always involved in welding simultaneously with the probe tip and the probe side and in such case, equilibrium of loads and the total torque $T_{tot}(t)$ is:

$$T_{tot}(t) \le T_1(t) + T_2(t) + T_3(t) \quad (11)$$

In such condition, the momentum of friction $M_{fr}(t)$ is:

$$M_{fr}(t) = T_1(t) + T_2(t) + T_3(t) \quad (12)$$

Assuming that the friction coefficients at the probe side, the probe tip and the shoulder tip are the same (only as a value):

$$\mu(t) = \mu_{ps}(t) = \mu_{pt}(t) = \mu_{st}(t),\ t_{st} \le t < t_4 \quad (13)$$

transforming the equation (12), friction coefficient is:

$$\mu(t) \approx \frac{6M_{fr}(t)}{2F_z(t)A + 3d(t)^2 h(t) p_{ps}(t)\pi + 2F_z(t)B},\ A = d(t) - d_0(t), B = D(t) - d_{\max},\ t_{ps'} \le t < t_{st} \quad (14)$$

3.5 Contact pressure at the probe side

Contact pressure at the probe side is mostly delivered by the welding force $F_x(t)$. Since welding force is active only during the welding phase

($t_2 \le t < t_3$), contact pressure at the probe side can be evaluated as:

$$p_{ps}(t) \begin{cases} \approx \dfrac{F_x(t)}{d \cdot h}, & t_2 < t < t_3 \\ \approx 0, & t \le t_2,\ t \ge t_3 \end{cases}, \qquad (15)$$

where: d – median diameter of the probe, h – total height of the probe.

4. EXPERIMENTAL INVESTIGATION OF THE FRICTION COEFICIENT IN FSW

Experimental researches and investigation of the friction coefficient in FSW were performed on plates made of aluminium alloy 2024 T351 [1-8]. Welding was performed with the two types of welding tool: a) "theoretical" welding tool (cylindrical welding tool with non-threaded probe) and b) welding tool with the cone, threaded probe (Figure 2).

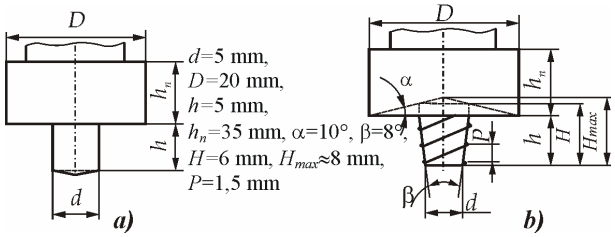

Figure 2. Welding tool

Welding was performed with the rotation speed of n=265, 600 and 910 rpm and the travel rate of v_x=1.5 to 2 mm/s. Initial plunging of the welding tool into the workpieces was performed into full material (diameter of the technological hole in workpieces d_0= 0 mm) and into technological holes with diameter of d_0= 2, 3.2 and 5 mm.

Experimental weldings were performed at the universal lathe with horizontal work axis in two measuring configurations to ensure the validity of the obtained results and consistency of the proposed measuring procedures [1].

5. THE RESULTS

First set of experiments was performed with the "theoretical" welding tool (Figure 2, a), changing the rotation speed from lower to higher and starting with the maximal dimension of the technological hole and decreasing it to the 0 – from minimal plunging force to the maximal. Measured values of torque and forces were used for calculating values of the friction coefficient (Figures 3 and 4).

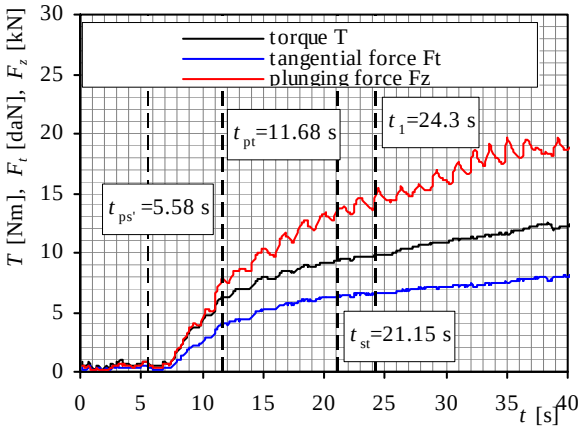

Figure 3. Diagram of measured loads: "theoretical" welding tool, n=265 rpm, d_0=5 mm

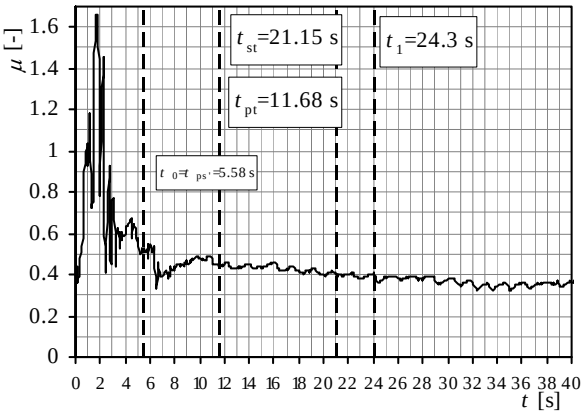

Figure 4. Friction coefficient: "theoretical" welding tool, n=265 rpm, d_0=5 mm

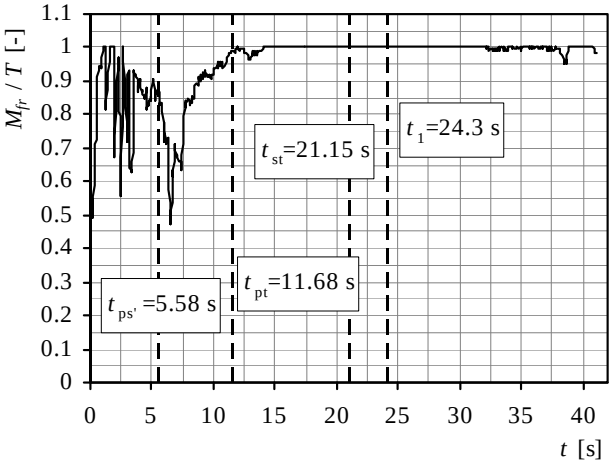

Figure 5. Ratio of the momentum of friction and the torque: "theoretical" welding tool, n=265 rpm, d_0=5 mm

Figure 5 is giving a ratio of the momentum of friction and the torque (M_{fr}/T) applied to the welding tool.

Second experiment with the "theoretical" welding tool was performed with the n=265 rpm, d_0=3.2 mm (technological hole is smaller than the diameter of the probe) and probe has cracked for 2 applied welding tools. Further experiments with the "theoretical" welding tool were cancelled.

Second set of experiments was performed with the conical welding tool - CWT (Figure 2, b), changing the rotation speed from lower to higher and starting with the maximal dimension of the technological hole and decreasing it to the 0 – from minimal plunging force to the maximal.

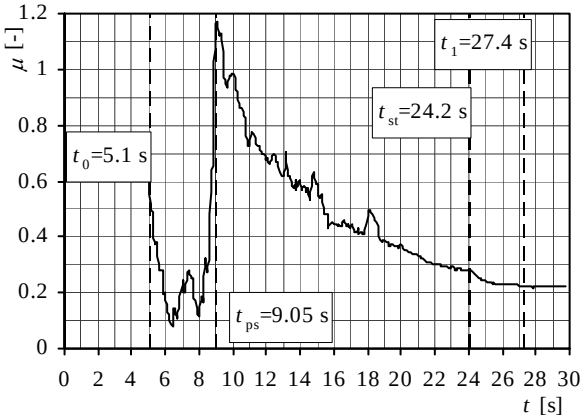

Figure 6. Friction coefficient: CWT, n=265 rpm, d_0=5 mm

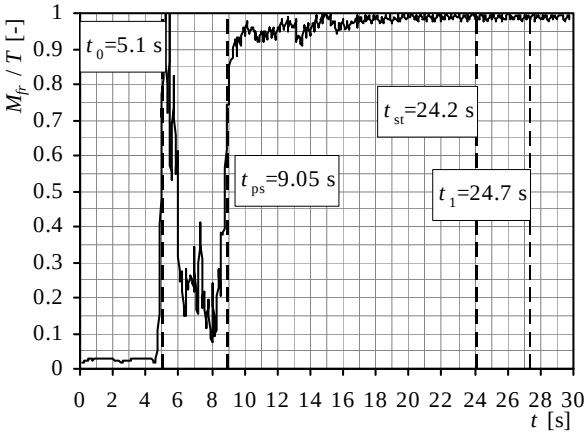

Figure 7. Ratio M_{fr}/T: CWT, n=265 rpm, d_0=5 mm

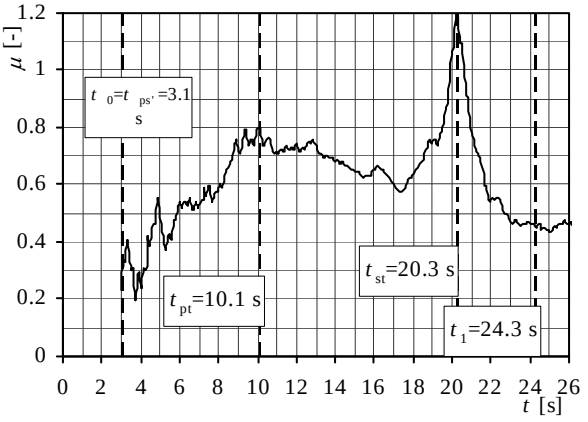

Figure 8. Friction coefficient: CWT, n=265 rpm, d_0=3.2 mm

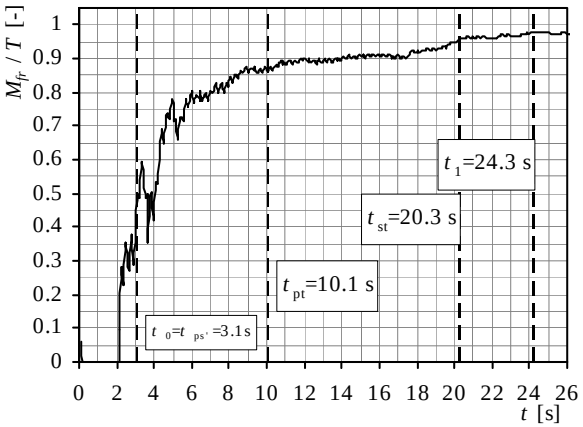

Figure 9. Ratio of the momentum of friction and the torque: CWT, n=265 rpm, d_0=3.2 mm

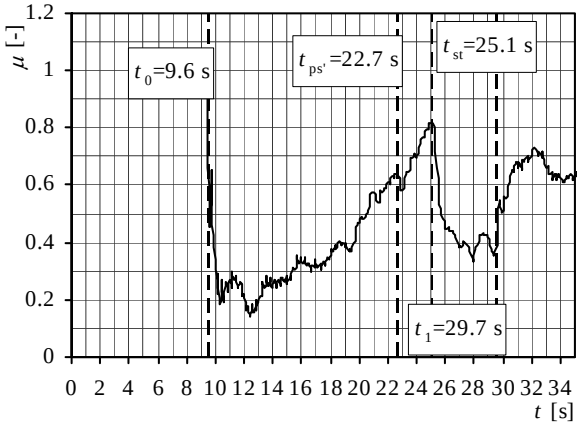

Figure 10. Friction coefficient: CWT, n=265 rpm, d_0=2 mm

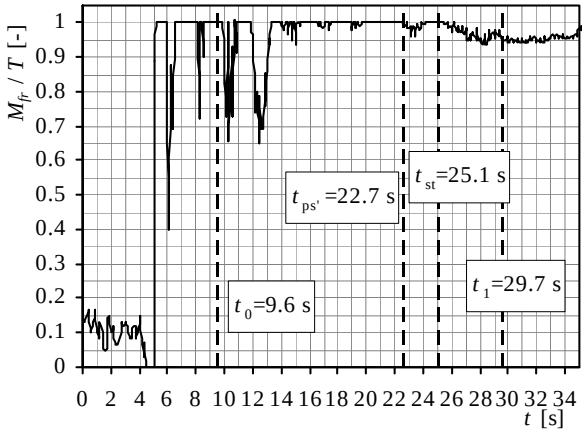

Figure 11. Ratio M_{fr}/T: CWT, n=265 rpm, d_0=2 mm

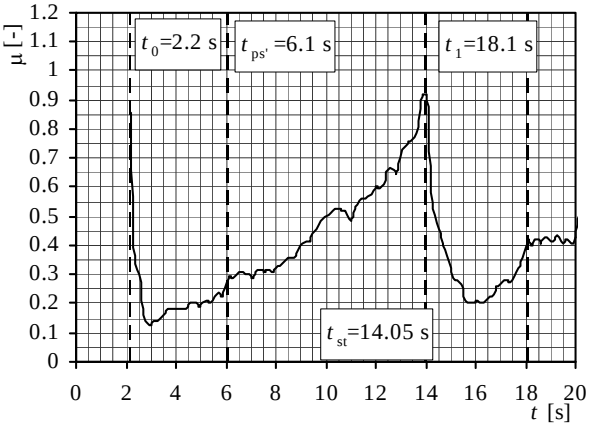

Figure 12. Friction coefficient: CWT, n=265 rpm, d_0=0 mm

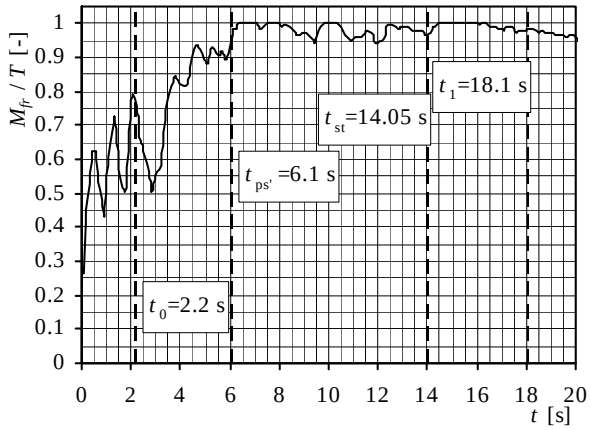

Figure 13. Ratio M_{fr}/T: CWT, n=265 rpm, d_0=0 mm

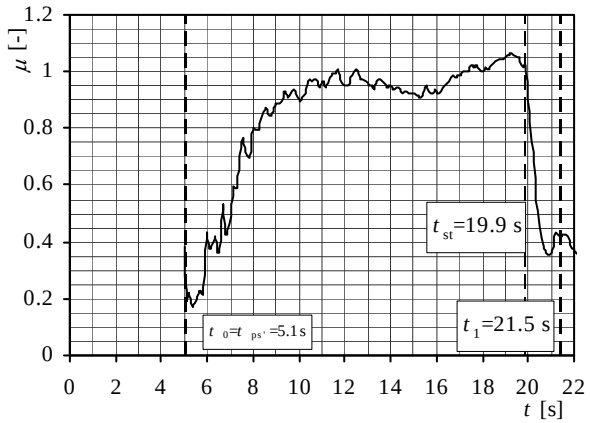

Figure 14. Friction coefficient: CWT, n=600 rpm, d_0=5 mm

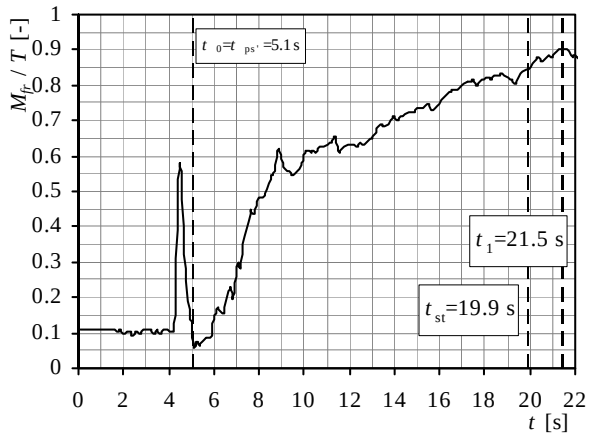

Figure 15. Ratio M_{fr}/T: CWT, n=600 rpm, d_0=5 mm

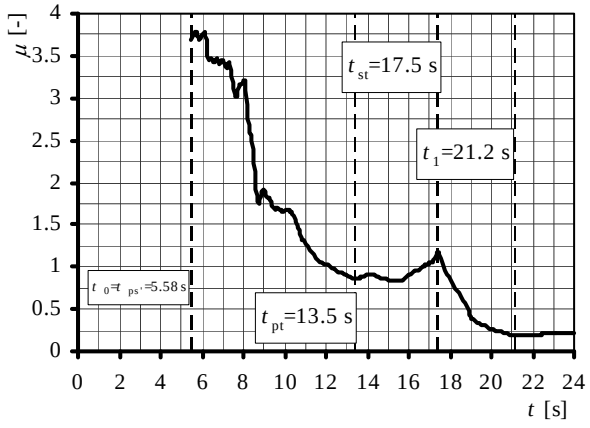

Figure 16. Friction coefficient: CWT, n=600 rpm, d_0=3.2 mm

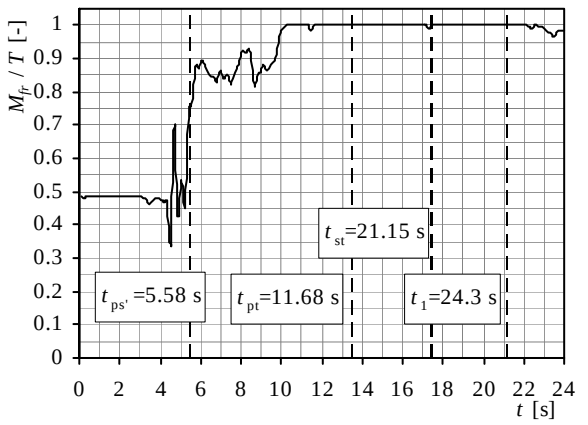

Figure 17. Ratio M_{fr}/T: CWT, n=600 rpm, d_0=3.2 mm

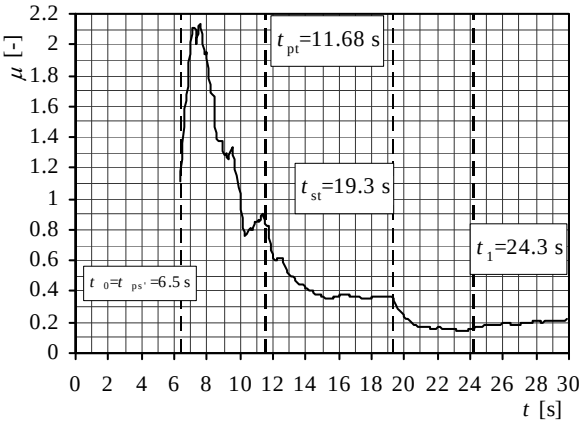

Figure 18. Friction coefficient: CWT, n=600 rpm, d_0=2 mm

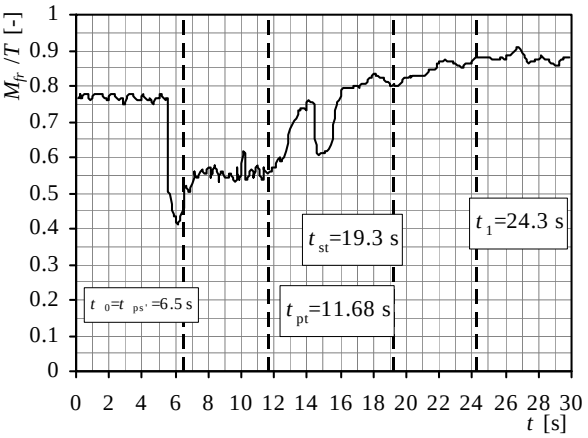

Figure 19. Ratio M_{fr}/T: CWT, n=600 rpm, d_0=2 mm

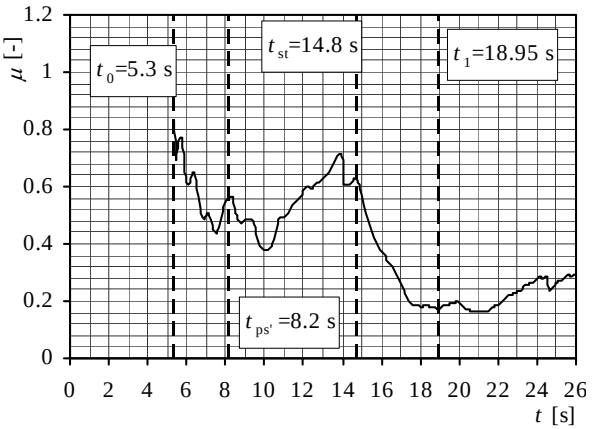

Figure 20. Friction coefficient: CWT, n=600 rpm, d_0=0 mm

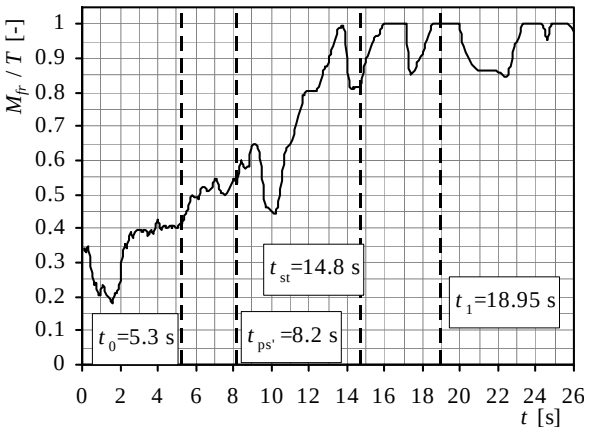

Figure 21. Ratio M_{fr}/T: CWT, n=600 rpm, d_0=0 mm

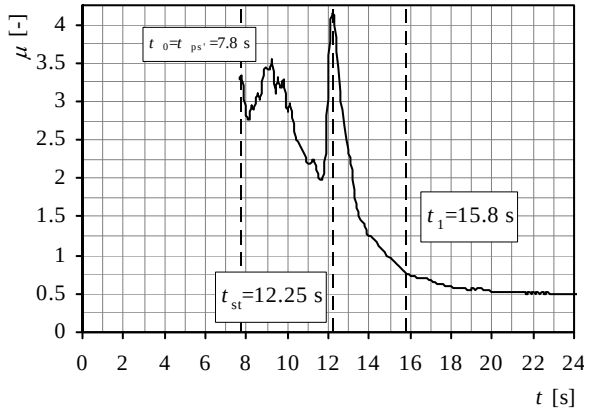

Figure 22. Friction coefficient: CWT, n=910 rpm, d_0=5 mm

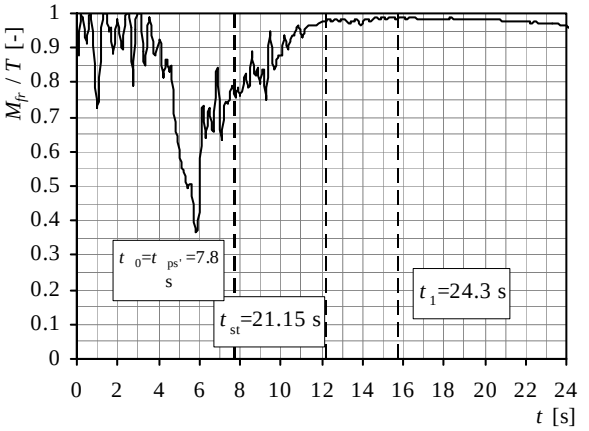

Figure 23. Ratio M_{fr}/T: CWT, n=910 rpm, d_0=5 mm

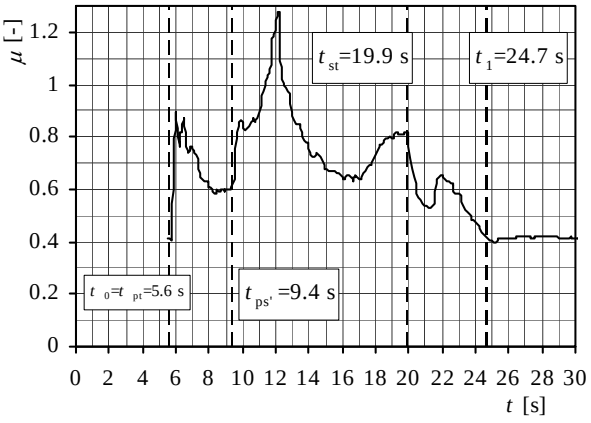

Figure 24. Friction coefficient: CWT, n=910 rpm, d_0=3.2 mm

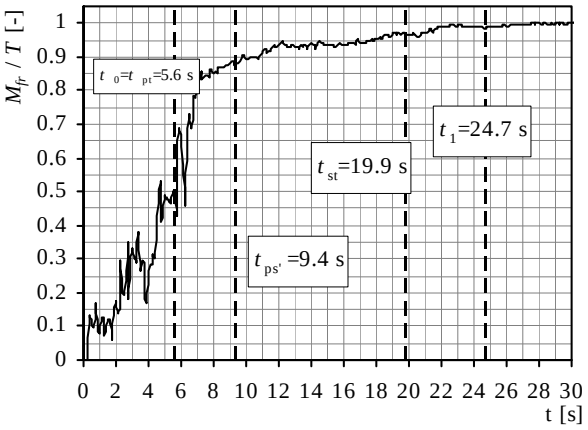

Figure 25. Ratio M_{fr}/T: CWT, n=910 rpm, d_0=3.2 mm

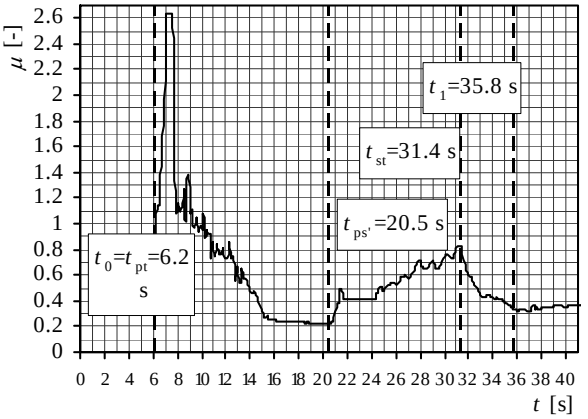

Figure 26. Friction coefficient: CWT, n=910 rpm, d_0=2 mm

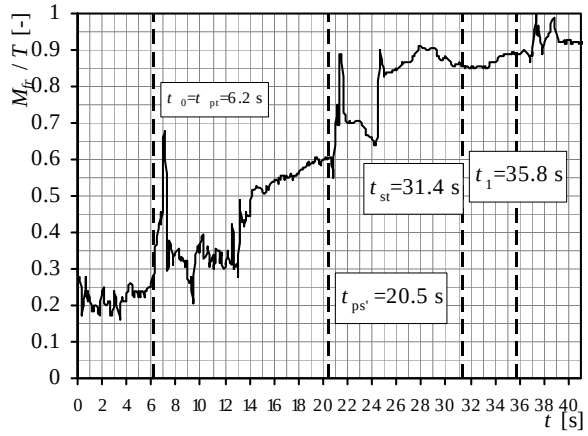

Figure 27. Ratio M_{fr}/T: CWT, n=910 rpm, d_0=2 mm

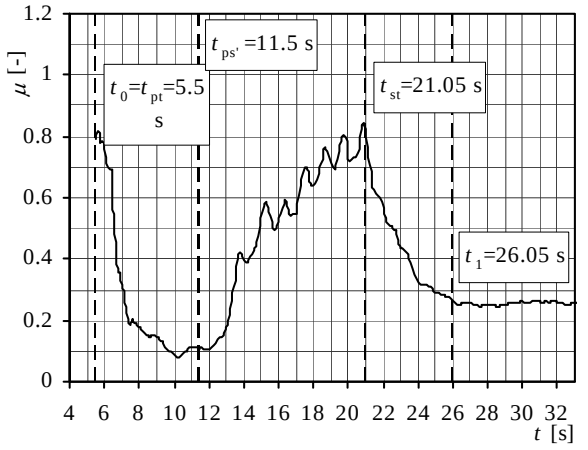

Figure 28. Friction coefficient: CWT, n=910 rpm, d_0=0 mm

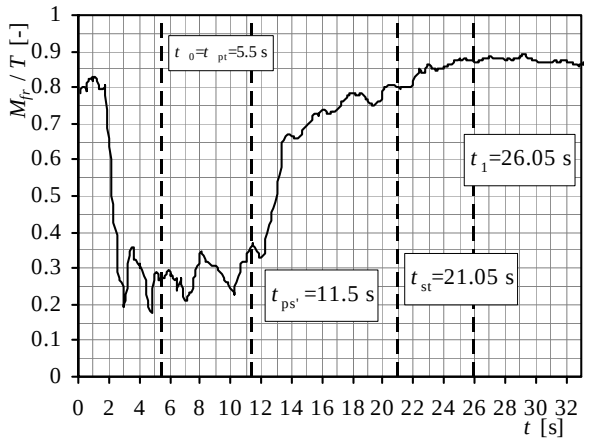

Figure 29. Ratio M_{fr}/T: CWT, n=910 rpm, d_0=0 mm

Measured values of torque and forces were used for calculating values of the friction coefficient and ratio of momentum of friction and the torque (Figure 6 to Figure 29).

6. DISCUSSION AND CONCLUSIONS

The first set of experiments with the "theoretical" welding tool has shown that welding tool without thread at the probe can not be used for welding of 2024 T351 alloy. Plunging of the welding tool into workpieces was possible only when diameter of the welding tool was the same as the diameter of the technological hole in the workpieces. During such experiment, appeared that friction coefficient, after initial stabilization, reaches almost constant value between 0.3 to 0.4 what is prescribed value for the FSW of AL 2024 T351 and the "theoretical" welding tool [1]. The ratio of momentum of friction and the applied torque has a value of 1 – there is no (or has minimal) deformation in the contact.

The conclusion was that the plunging of the "theoretical" welding tool in welding plates was impossible when small or no technological hole present what implies that welding couldn't even get started.

The second set of experiments was conducted with the coned, threaded welding tool with the prescribed technological parameters. Welding was possible, however, only welding with n=910 rpm has given the qualitative welds. During all weldings, trends and values of the friction coefficient were identical. Friction coefficient was rising from the beginning of the plunging until the moment of time when the shoulder tip involves in the welding. Common values of maximal friction coefficient reach about 1 but it is not uncommon to reach values of 2-5 (what is in correspondence with the literature-present values [1-4] but it is possible to have peak values as imperfections of the proposed method for estimation). From that moment, friction coefficient drops down and at the beginning of the first dwelling phase reaches value of about 0.2 to 0.7. However, at the end of the dwelling phase, friction coefficient in all experiments reaches the values of 0.2 to 0.5.

The ratio between the momentum of friction and the applied torque has the same trend for all experiments. It rises up to the maximal value of 1 and varies from 0.8 to 1, during every conducted experiment. The results are in agreement with the existing results [2, 3, 4].

LITERATURE

[1] Mijajlović, M., *Investigation and Development of Analytical Model for Estimation of Amount of Heat Generated During FSW (in Serbian)*, Ph. D. thesis, Faculty of Mechanical Engineering Nis, University of Nis, Nis, Serbia, 2012.

[2] V. Soundararajan, M. Valant, R. Kovačević: *An Overview of R&D Work in Friction Stir Welding at SMU*, MJoM, Metalurgija – Journal of Metallurgy, Association of Metallurgical Engineers of Serbia, 204, 12, pp. 277-295, 2006.

[3] M. Djurdjanović, M. Mijajlović, D. Milčić, D. Stamenković: *Heat Generation During Friction Stir Welding Process*, Tribology in Industry, 1-2, pp. 8-14, 2009.

[4] K. Kumar, C. Kalyan, S.V. Kailasa, T.S. Srivatsan: *An Investigation of Friction during Friction Stir Welding of Metallic Materials*, Materials and Manufacturing Processes, 24, pp. 438-445, 2009.

[5] M. Mijajlović, D. Stamenković, D. Milčić, M. Đurdanović: *Study About Friction Coefficient Estimation in Friction Stir Welding*, Balkantrib 11, The 7th International Conference on Tribology, Proceedings, Thessaloniki, Greece, pp. 323-330, 2011.

[6] M. Mijajlović, D. Milčić, B. Anđelković, M. Vukićević, M. Bjelić: *Mathematical Model for Analytical Estimation of Generated Heat During Friction Stir Welding. Part 1*, Journal of Balkan Tribological Association, 17, pp. 179-191, 2011.

[7] P. Ulysse: *Three-Dimensional Modeling of the Friction Stir-Welding Process*, Int. J. Mach. Tool. Manu. 42, pp.1549-1557, 2002.

[8] H. Schmidt, J. Hattel, J. Wert: *An Analytical Model for the Heat Generation in Friction Stir Welding*, Modeling Simul. Mater. Sci. Eng. 12, pp. 143-157, 2004.

[9] M. Mijajlović, D. Milčić, B. Anđelković, M. Vukićević, M. Bjelić: *Mathematical Model for Analytical Estimation of Generated Heat During Friction Stir Welding. Part 2*, Journal of Balkan Tribological Association, 17, pp. 361-370, 2011.

Serbian Tribology Society

SERBIATRIB '13

13th International Conference on Tribology

Faculty of Engineering in Kragujevac

Kragujevac, Serbia, 15 – 17 May 2013

MEASUREMENT INSTRUMENTATION FOR DETERMINATION OF STATIC COEFFICIENT OF ROLLING FRICTION

Petar Todorović[1], Ivan Mačužić[1], Branislav Jeremić[1], Marko Đapan[1], Branko Tadić[1]

[1]Faculty of Engineering Kragujevac, Serbia, petar@kg.ac.rs, ivanm@kg.ac.rs, bane@kg.ac.rs, djapan@kg.ac.rs, btadic@kg.ac.rs

Abstract: *This paper is considering the influence of temperature, at normal load and bend radius of contact elements on the coefficient of rolling friction. Contact pairs are made of steel DIN 17230 (100Cr6). Measurement results in a condition of high temperatures, variation of the normal load and bend radius of contact element indicate complex influence of temperature in this specific test condition. Authors' future research would be in direction of determination of static friction coefficient on the higher temperatures of contact pairs made of different materials.*

Keywords: *Measurement instrumentation, coefficient of rolling friction, high temperatures, inclined plane*

1. INTRODUCTION

For every engineer and constructor, who is engaged in design and development of mechanical constructions, knowledge of friction coefficient is very important and crucial. However, there are multiple issues, doubts and problems regarding using of friction coefficient values during experiments. These problems occur primarily because of poor applying of standard tables and under which conditions these values are measured. This is all because friction coefficient values are different from laboratory to laboratory, and depend on equipment, measuring methods and a number of other parameters that may influence on diversity of measured values. Peter J. Blau [1] has represented review of friction force and ways of its measurement. He made a list of standard measurement methods for static and dynamic friction coefficient as well as the way of its potential use.

As we know, friction occurs when two bodies are in contact and based on velocity of relative motion, friction can be static or kinetic. The static friction coefficient depends on many different parameters, primarily from surface contact, normal load, atmosphere conditions and temperature, surface absorption, quality of processing and material in contact [2-5]. There have been several studies regarding the influence of surface roughness parameters with the static friction coefficient and concluded that the coefficient of static friction will increase if surface roughness coefficient increases [3, 4]. Also, some of them concluded that some roughness parameters, like skewness and kurtosis, have a greater influence on coefficient of static friction compared to other parameters [6, 7]. Complete understanding of the coefficient of static friction is impossible without various analyses of mechanisms under which this is occurring. This issue is a goal for numerous research efforts [8-10].

As a start, some authors represented conditions under which the value of static friction is greater than the dynamic friction value, in terms of temperature influence on creep motion. Generally, at temperature above zero, static friction coefficient is higher compared to kinetic friction coefficient due to different heat activated processes. But, we cannot say that the static friction coefficient has only one value because it depends on contact and initial velocity. In order to determine static friction coefficient, Chang et al. [8] analyzed adhesion force and load in contact at rough metal surfaces. The study showed that the coefficient of static friction depends on characteristics of the material and topography of the surface in contact as well as that depends on external load versus general defined friction law. In this paper, researchers were

experimentally determined that for specific external load, coefficient of static friction will decrease if plastic characteristic of material increases and surface energy decreases. D.-H. Hwang et al [11] concluded that the coefficient of static friction is higher if contact pair is made of different material - steel/alumina, while the lower value is determined for similar materials (steel/steel). This result is consequence of "stick-slip" effect. Also, one of conclusions was that the influence of surface roughness has less influence for similar materials in contact pair, as well as the increasing value of normal load affects on increasing coefficient of static friction in contact pair of different materials, while there is no significant influence for contact pairs of the identical materials.

Etsion and Amit [12] experimentally researched the influence of normal load on coefficient of static friction with very smooth metal surfaces in a controlled laboratory conditions. Dramatically increasing coefficient of static friction was noticed when the normal load is on the lowest level. Behaviour like this is assigned to adhesion forces which have more important function regarding small normal loads and surface smoothness.

A small number of papers deal with coefficient of static friction under influence of temperature [13-16]. The most important conclusion that authors made in this papers is that the coefficient of static friction will increase if temperature is increased, which is resulted of increasing plastic characteristics of the most contact material at increased temperature. Reviewing the literature is noticed that experimental tests of coefficient of static friction were performed on experimental equipment with different design, construction and different contact geometry. Also, very interesting are measurement instruments for static coefficient of rolling friction [17-19]. Friction characteristics of rolling bearing elements depend on contact pair material, design, tolerance, topography of contact surfaces and lubricants. Authors in this paper noticed, during literature review, that there are no any papers which based their research attempts on static coefficient of rolling friction, while in conditions at higher temperature referring to issue above, there was no paper found (when this paper is written).

The aim of this paper is to determine influence of temperature on static coefficient of rolling friction on contact elements made of steel. Experimental measurements were performed on instrumentation that authors designed, developed and constructed regarding very precise determination of static coefficient of rolling friction at higher temperatures and relatively small values of contact pressure with changing radius bends of contact elements.

2. THEORETICAL CONSIDERATION

According to literature, the static coefficient of friction increases with increasing temperature. It is found that temperatures above 200°C lead to increasing of coefficient of friction which can be interpreted as a result of increasing plastic characteristics of material at increased temperature. The static coefficient of rolling friction tested in condition of increased temperature has not been subject of either theoretical or experimental research. The authors will determine the influence of temperature, normal load and radius bend of contact elements on coefficient of rolling friction by experimental methods. According to that, measure instrumentation is designed and constructed, based on inclined plane principle.

In the case of rolling friction (contiguous case – figure 1), coefficient of rolling friction is determined from formula 1 and 2:

$$M_{\mu} = N \cdot e \tag{1}$$

$$M_P = F \cdot R \tag{2}$$

where are:

M_{μ} – moment of resistance and

M_P – rolling moment.

From equations 3 and 4:

$$F = N \cdot \frac{e}{R} = f \cdot N \tag{3}$$

$$f = \frac{e}{R} = \tan\alpha \tag{4}$$

and from the body balance at inclined plate (figure 2), we get the following equation:

$$N = G \cdot \cos\alpha \tag{5}$$

$$\sin\alpha \cdot R = N \cdot e = G \cdot \cos\alpha \cdot e \Rightarrow \frac{e}{R} = \tan\alpha \tag{6}$$

where are:

f – static coefficient of rolling friction;
N – normal force;
e – coordinate that defines resultant reaction position N;
R – radius of rolling body;
G – the force of gravity;
α – angle of inclined plane.

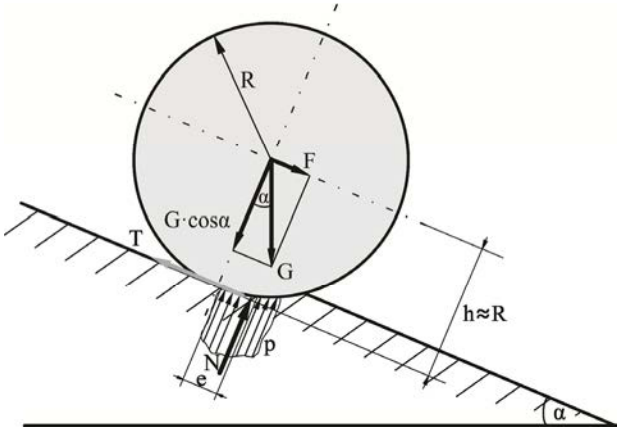

Figure 1 – The balance of rolling body at inclined plate

The authors' starting point was from theoretical assumption that the contact between ball and flat surface in laboratory conditions will be achieved on the small number of unevenness in a regard a number of unevenness at higher temperatures. Further, it is assumed that due to thermal expansion of material in the contact zone, will result as increasing of value e (figure 1). This means that as a consequence we will have an increase of rolling moment resistance and a parallel increase of the coefficient of rolling friction. The authors believe that there is some correlation between static coefficient of rolling friction and the value of thermal dilatation of contact pair. If we have in mind the stochastic nature of real contact area and nonlinear temperature field, it is hard to theoretically quantify the influence of temperature on coefficient of friction. Hence, in order to quantify the influence of various parameters on coefficient of friction, authors will provide relative extensive experimental research.

3. EXPERIMENTAL TESTS

Experimental tests were performed on a special designed and constructed tribometer. The complete measuring instrument is showed on figure 2. Also, all positions are marked with numbers and described in following text. The tribometer consists of three bigger parts, as follows:

1 – Thermoregulator. The main aim of this part is to vary a temperature (in our case is 200°C). There are two small screens; one is showing desired temperature and another current temperature.

2 – Block with thermocouple. Inside of this block, beside thermocouple, there is a system for heating and probe for temperature measurement. Also, in this part of tribometer the contact between object and block is made.

3 – Counterweight. This part enables to make rotating of the block with thermocouple with very good precision.

The tribometer operates in principle of inclined plane. Contact pair together with system for heating and probe for temperature measurement is rotated from horizontal to the desired angle α. The rotated angle of inclined plane is measured with reading precision of one minute, which for a wide interval of possible values of the coefficient of rolling friction causes the measurement error less than 3%.

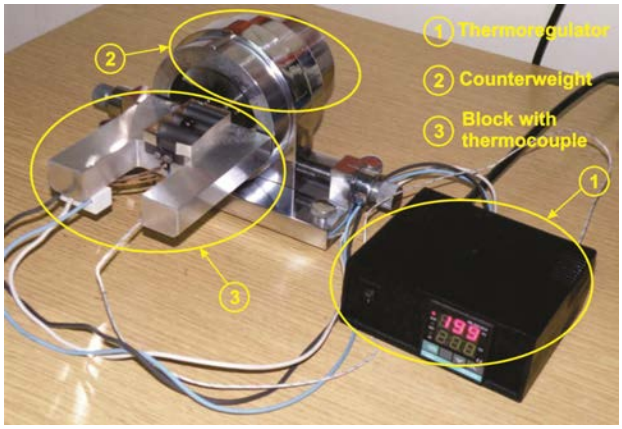

Figure 2 – Measurement instrumentation (1-Thermoregulator, 2-Counterweight, 3-Block with thermocouple)

The tests were performed with rolling balls of different diameters over channels with different radius bends. Balls weight and balls diameter were in a range from 0.04 to 0.08N and from 2.32 to 13mm respectively. Bend radius of the block covered a range from 2.5 to 8 mm. Balls and block were heated on selected temperatures, 20, 100, 150 and 200°C. Chosen material for balls and block was steel DIN 17230 (100Cr6) with hardness 62-66HRC. Hardness is achieved by quenching and tempering process. Ball roughness is Ra=0.002μm. The roughness of the block channels surface was in a range between: Ra=0.8-1μm. The figure 3 is a diagrammatic representation coefficient of rolling friction dependence regarding temperature and normal load.

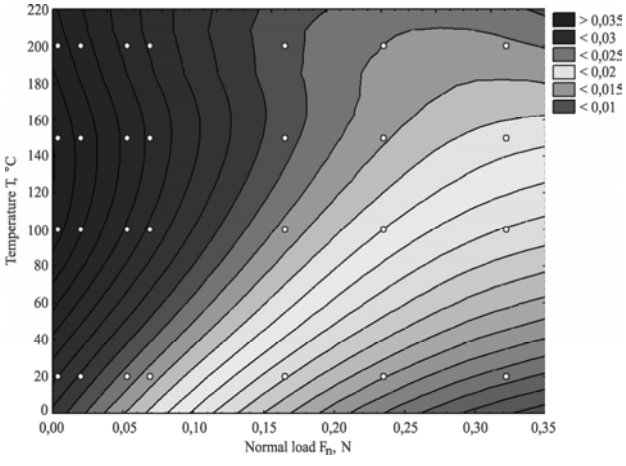

Figure 3 – Coefficient of rolling friction dependence regarding temperature and normal load

4. DISCUSSION

According to the theoretical consideration, physical principle and characteristics of inclined plane for coefficient of static friction measurement can be applicable in the conditions with higher temperatures. The measurement error is function of the angle α and value of friction coefficient, as follows:

$$\varepsilon = \frac{\tan(\alpha + \Delta\alpha) - \tan\alpha}{\tan(\alpha a} \cdot 100 \quad [\%] \qquad (7)$$

where are:
ε - measurement error and
Δα – measurement error of angle.

Measured coefficient of friction is in the range from 0.01 to 0.05 and reading precision is one minute based on computation, the measurement error is less than 3%. This result is totally acceptable. The results of experimental tests enable global overview of how larger number of parameters influence on coefficient of rolling friction. Besides variations of temperature and level of normal load, variations were made to block channel radius (the second contact element).

From diagram (figure 3) we can conclude that temperature, which is selected for contact pair heating and normal load (ball weight) has large influence on changing trend of coefficient of rolling friction. The bend radius has indirect influence on real contact surface, meaning that larger radius corresponds to 10% of lower values of friction coefficient. If we have in mind that increasing radius of block bend increases contact pressure then it can be concluded that results correspond with literature. In conjunction with above stated, it can be concluded that to lower coefficient of friction corresponds higher contact pressure.
Based on analyses of experimental results, generally it can be stated that contact temperature has significant influence on coefficient of rolling friction. However, level of temperature influence on coefficient of rolling friction is highly dependent from normal load value, especially in an area of lower values of normal load.

5. CONCLUSION

The research in the field of static friction is spread in a number of directions. The topic explored by authors aimed to draw attention that research in a field of static coefficient of rolling friction have not been carried out in order to quantify complex influence of normal load, contact surface and temperature on coefficient of rolling friction. Through theoretical consideration presented in this paper, authors hypothesized that there is necessary thermal potential in a contact zone for redistribution of contact pressure and increase of rolling moment resistance at temperatures around 200°C. The instrumentation used for static coefficient of rolling friction measurement in a condition of high temperatures functions as inclined plane and enables satisfactory determination results of static coefficient of rolling friction. In this paper the measurement error is less than 3%, for performed program of experimental research, and regarding problems of measurement of very small friction forces this is completely satisfactory. The measurement results of static coefficient of rolling friction for selected materials, in a condition of high temperatures, normal load and bend radius of contact elements variation, indicate a complex influence of temperature in the testing conditions.

Scientists' future research in this field should be directed to experimental tests of different materials in contact and optimization in order to determine minimal values of static coefficient of friction at high temperatures.

ACKNOWLEDGMENT

Research presented in this paper was supported by Ministry of Science and Technological Development of Republic of Serbia, Grant TR-35021, Title: Razvoj triboloških mikro/nano dvokomponentnih i hibridnih samopodmazajućih kompozita.

REFERENCES

[1] P. J. Blau, *The significance and use of the friction coefficient*, Tribology International, Vol. 34, No. 9, pp. 585–591, 2001.

[2] B. Ivkovic, M. Djurdjanovic, D. Stamenkovic, *The Influence of the Contact Surface Roughness on the Static Friction Coefficient*, Tribology in Industry, Vol. 22, No. 3&4, pp. 41-44, 2000.

[3] U. Muller, R. Hauert, *Investigations of the coefficient of static friction diamond-like carbon films*, Surface and Coatings Technology, Vol. 174-175, pp. 421–426, 2003.

[4] B. Polyakov, S. Vlassov, L. M. Dorogin, P. Kulis, I. Kink, R. Lohmus, *The effect of substrate roughness on the static friction of CuO nanowires*, Surface Science, Vol. 606, No. 17-18. pp. 1393-1399, 2012.

[5] N. Tayebi, A. A. Polycarpou, *Modeling the effect of skewness and kurtosis on the static friction coefficient of rough surfaces*, Tribology International, Vol. 37, No. 6, pp. 491-505, 2004.

[6] B. Bhushan, S. Sundararajan, W.W. Scott, S. Chilamakuri, *Stiction analysis of magnetic tapes*, IEEE Magnetics Transactions, Vol. 33, No. 5, pp. 3211-3213, 1997.

[7] J. S. McFarlane, D. Tabor, Relation between friction and adhesion, in: *Proceedings of the Royal Society of London. Series A,* Mathematical and Physical Science, Vol. 202, No. 1069, pp. 244-253, 1950.

[8] W.R. Chang, I. Etsion, D. B. Bogy, *Static friction coefficient model for metallic rough surfaces,* Journal of Tribology, Vol. 110, pp. 57-61, 1988.

[9] B.N.J. Persson, O. Albohr, F. Mancosu, V. Peveri, V.N. Samoilov, I.M. Sivebaek, *On the nature of the static friction, kinetic friction and creep*, Wear, Vol. 254, No. 9, pp. 835-851, 2003.

[10] J. M. Galligan, P. McCullough, *On the nature of static friction*, Wear, Vol. 105, No. 9, pp. 337-340, 1985.

[11] D.-H. Hwang, K.-H. Zum Gahr, *Transition from static to kinetic friction of unlubricated or oil lubricated steel/steel, steel/ceramic and ceramic/ceramic pairs*, Wear, Vol. 255, No. 1-6, pp. 365-375, 2003.

[12] I. Etsion, M. Amit, *The effect of small normal loads on the static friction coefficient for very smooth surfaces*, Journal of tribology, Vol.115, No. 3, 1993.

[13] H. Kumar, V. Ramakrishnan, S. K. Albert, C. Meikandamurthy, B.V.R. Tata, A.K. Bhaduri, *High temperature wear and friction behaviour of 15Cr-15Ni-2Mo titanium-modified austenitic stainless steel in liquid sodium*, Wear, Vol. 270, No. 1-2, pp. 1-4, 2010.

[14] P. Mosaddegh, J. Ziegert, W. Iqbal, Y. Tohme, *Apparatus for high temperature friction measurement*, Precision Engineering, Vol. 35, No. 3, pp. 473-483, 2011.

[15] A. Chaikittiratana, S. Koetniyom, S. Lakkam, *Static/kinetic friction behaviour of a clutch facing material: effects of temperature and pressure*, World Academy of Science, Engineering and Technology Vol. 66, 2012.

[16] M. Worgull, J. F. Hetu, K. K. Kabanemi, M. Heckele, *Hot embossing of microstructures: characterization of friction during demolding*, Microsyst Technol, Vol. 14, pp. 767-773, 2008.

[17] K. G. Budinski, *An inclined plane test for the breakaway coefficient of rolling friction of rolling element bearings*, Wear, Vol. 259, No. 7-12, pp. 1443-1447, 2005.

[18] Ta-Wei Lin, A. Modafe, B. Shapiro, R. Ghodssi, *Characterization of Dynamic Friction in MEMS-Based Microball Bearings*, IEEE Transactions on instrumentation and measurement, Vol. 53, No. 3, pp. 839-846, 2004.

[19] D. N. Olaru, C. Stamate, A. Dumitrascu, G. Prisacaru, *New micro tribometer for rolling friction*, Wear, Vol. 271, No. 5-6, pp. 842-852, 2011.

Serbian Tribology Society

SERBIATRIB '13

13th International Conference on Tribology

Faculty of Engineering in Kragujevac

Kragujevac, Serbia, 15 – 17 May 2013

IMPLEMENATION SQL REPORTING SERVICE IN THE TRIBOLOGYCAL DATA BASES

Milan Erić[1], Marko Djukić[1]

[1]University of Kragujevac, Faculty of Engineering, Serbia, ericm@kg.ac.rs, djuka84yu@gmail.com

Abstract: *In the work it will be presented one of the way how to publish the results of the scientific and research work quickly and efficiently and these results are saved in thedata bases,and this is called tribologycal researches. The developed technology in the Reporting Services enables usto avoid the writing of the application programmes or using the data in the other section of the softver,type Statistica or Excel, and it enables us directly to form th presentation part over the bases.Scientists and researchers,as the best way of scientific communication,have both the role of the creators and the users and they have started to be publishers anddistributers,and this technology enables them all of this.*

Keywords: *tribological data bases, SQL Reporting Services, processing of the reports*

1. INTRODUCTION

Today, in the world of inrormation technology, reports are the main key so that we can publish the results in the scientific researches. It can be said that the reports are the final and main step of the long and complex process of collecting, keeping, transformating and manipulating of the data. Creating of the reports is presentation of working with the data bases. All reports are not the same. The value of the report is information. Information are not just the data,but they are the data transformedinto something usefull,something that has value. This transformation is extremely important. People can read and publish the data in many different ways and that is the reason why the data are all around us,but what we need in the 21st century to to complete our job is well valued, correct, quick and appropriate information.

There are a lot of software tools for creating the reports that enable everyone to access to ana open number of the data which are all around us. However, all these who use these data are not familiar to the work technics-and that can be a huge problem. The data used to be saved and transfered orally, in the written form and today mostly in an electronic form in our computers-in the data bases but the data are not usually from the same base and they do not come from he same base. Extremely small number of reports actually has the data in the base.

Today if you want a report to be valued as good and to be in the terms of standards of using the infotmation technologies, it must be reliable, quick, to have a good presentation, to have flexible fom,connectivity and in the end that it can be used by yhe correct tool. One of the tool or technology whose develompment still is in a progress is Reporting Service (RS) which is the part of SQLServer.

All tools ana applications in RS are made using the API (Application Programming Interface). Reporting Services contains all that is necessary that researchers and well trained business users to publish a report. Completed reports are guided by a server where are they. The final users to whom these reports are mare for, have an efficient and full report.

The process of correction and analyses by using the information of Reporting Service leads to generation of knowledge of the data and it is mostly known in the IT world as Distributed intelligence (knowledge technology). In this case, Reporting Services can be seen as server-based platform with the developed tools for generating, manipulation and publishing of the reports.

Reporting Services evoluated into a sofisticated reporting platform which gives new abilities of the efficient analyses and an atractive presentation

of information which are saved on the hard discs of the server, opening complely new dimension of working with the the data and reports.

Reporting Services must be understandable, we must be able to read them and they must point to the date that we need for the analyses and verification of the results. To achieve the goal we want,we can design the report that specific data shows like a table/chart or any other form that can be understood, Figure 1.

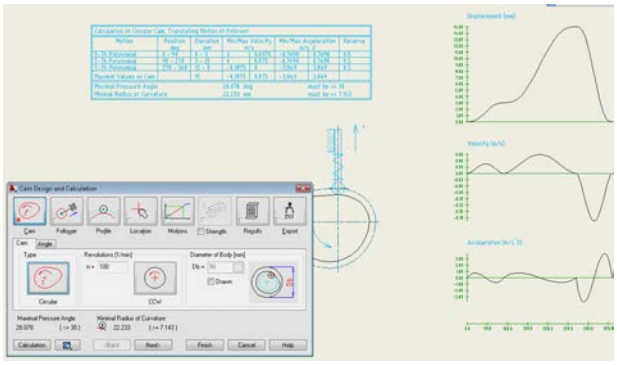

Figure 1. The picture of the standard report.

The reports can be also shown in an ad hoc form.

2. PROCESSING OF THE REPORTS USING THE REPORTING SERVICES

Reporting Services is a part of MS SQL platform which offers opportunities of processing and manipulating the data, Figure 2 [1].

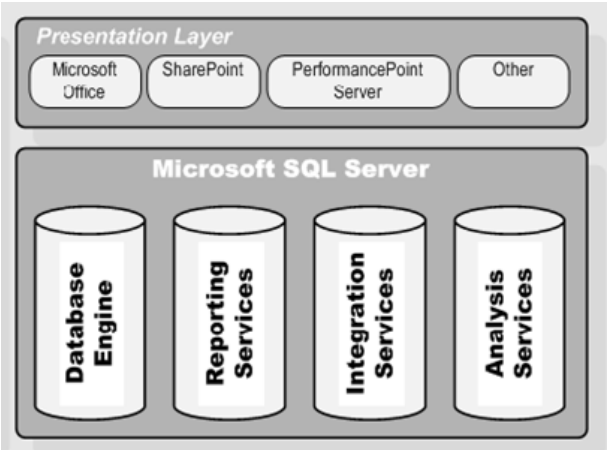

Figure 2. Architecture of the MS SQL Server platform.

Database Engine is for packing, processing and securing of the data. Integration Services supports different typrs of the data, which have the same source of the dataand technologies as well as their integration Integration Services is mainly used for transfering,transformation and reading of the data. Packets of the data of Integration Services are mainly used as sources for the reports. Analysis Services represents multi-dimension base for the quick reporting and generating of the questions and trends. The data are not for the use unless there is a way that they can be shown in a way that the users can understand them. Presentation Layer platforms enable different ways of presentation like Microsoft Office, Microsoft SharePoint, Microsoft Performance Point Server or some other comparatible applications.

Basic components and logic architecture of Reporting Services are shown in the Figure 3 [1].

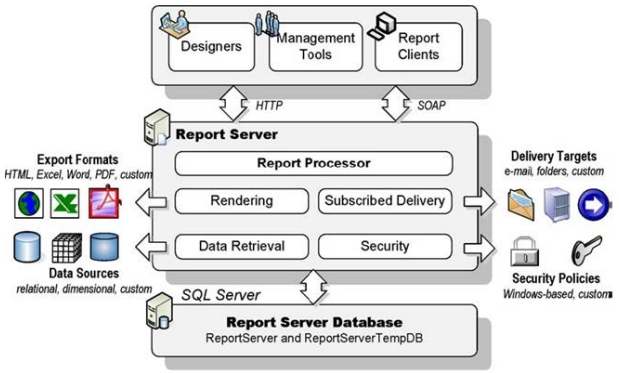

Figure 3. Reporting Services logical architecture

In the centre of Reporting Services architecture is a server , web-orientied middle part which accepts the requests,processes them and on the base of that generates the reports. An illustration shows a simple sheme of Report Server. Repot Server communicate with the the users in two ways: by url or through web service. The component Report processor is responsible for processing of the reports in so called run time. This means that the report sends the data to an user,combining the data from the base with the parametres making the final report sent in the requested form.

An important characteristic of Reporting Services is that the archecture can be enlarged through special modules which are called extensions. When the standard extensions are not enough, programmers can extend the opportunities of RS by puttingin their own extensions. Like the sources of the data,the users can export the report results in a several most popular forms like Microsoft Excel, Microsoft Word, Adobe Acrobat PDF, HTML, SCV, it can be shown in the pictures or the new extensions can be written for the sending of the report or in some other forms.

The definition of the report and its adjuctments are saved in the data base of Report Server. Report Server is implemented as two SQL Server bases (Report Server and Report Server DB) which are installed during their configuration. When we upload the report, Reporting Services saves the definition of Report Server in the data base while the other data base – Report Server DB contains and saves temporary information on the report and its thruthfullness.

2.1 The life cycle of the report

The life cycle of the report is the events or the activities of the report, start from the moment when we start creating it. In the Figure 4 we can see that the life cycle is made of Authoring, Management and Delivery phases [1].

Figure 4. Work with the report

In the Authoring phase, the author of the report uses one of the Microsoft designer reports (Report Builder). When the report is completed, the author can upload it so it can be seen by the final users. In the Management phase, the administrator configurates the generated reports and developing surrounding where it is going to be shown. The administrator can use Report Manager to organise the report in the folders as well as to set the security measures so that the access can be authorised to the users. When it is configurated, the reports can be seen to only those to whom this right is authorised. The report can be seen by the final users typing URL address in the web searcher or alternatevily using the option schedule -through some channal like an e-mail.

The designers of the report are the tools which the authors use for the definition of the data looks at the moment of creating the reports. Since the technological knowledge and the experiences of the authors can vary, it is not easy to create a designer report that can satisfy the need of the all users.In the Figure 5 allthe designer tools for the creating of the report are shown with their basic characteristics [2].

Designer	Audience	Capabilities
BIDS Report Designer	Developers, power users	Full-featured reports
Report Builder 1.0	Business users	Basic ad hoc reports
Report Builder 2.0	Power users	Full-featured reports outside Visual Studio
Visual Studio Report Designer	Developers	RDL 2005-compatible local reports

Figure 5. Tools for creating the reports and their comparison

It is important to say that all mentioned report designers support RDL standard (Report Definition Language).

2.2 Physical architecture of Reporting Service

In the Figure 6 we can see the physical architecture of the Reporting Services, which is made of three Report Server aplications: Report Manager, Report Server Web Service and Background Processor. In the physical architecture we can see an implemented network interface which includes Service Network Interfaces (SNI) which checks new requests HTTP.SYS. HTTP.SYS je HTTP driver which accepts the requests and sends them to an application that should answer to these requests. As a part of the configuration of the Reporting Services, it must be said that URL address report server i Report Manager. Reporting Services Windows service has three server applications: Report Manager, Report Server Web Service and Background Processor. Behind the scene, this service in fact creates three net applications which will host them.

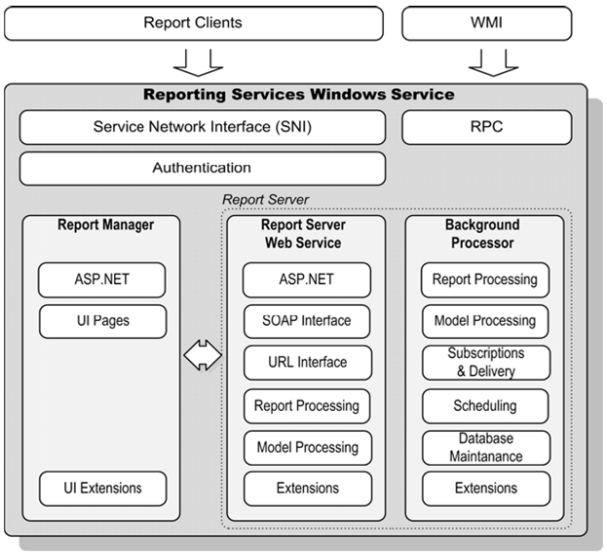

Figure 6. Reporting Services 2008 architecture

Report Manager is an ASP.NET web application which enables management and the look into the abilities of the Reporting Services instance configurated in the natural code. We can see Report Manager as a client application configurated with the report of the server. Thanks to the same hosting model, configuration adjustments of the Report Manager and Report Server Web service are kept in the same configuration file in rs report server. confingDue to this, Report Manager can add some new extensions. For example, if the user develops new extension, using C# or VB.NET we can configurate in the Report Managers a web control and later use it as we adjust the details of the report.

Report Server Web service processes the reports by using the systems on-demand. When the user clicks on the link pages where the reports are, he\she sends the requests to the Report Web, service accepts this request, processes this request and returns the report to the client. To make it easier integrations with the different types of the reports, Report Server Web service enables the use of URL and SOAP protocol and their integration options.

Background Processor is an application which job is to accept all the tasks which are in an unmarked mode. For example, when the description of the event is accepted, Background Processor interprets the description of the report and sends it to the final destination. Basically, its job is to

process the reports, not to communicate with Report Server Web service. Instead of this, both of the applications communicate with the Report Processor in the same time.

Report Processor does not save the whole report in the memory, but it is processing the report on demand, as it is shown in the Figure 7.

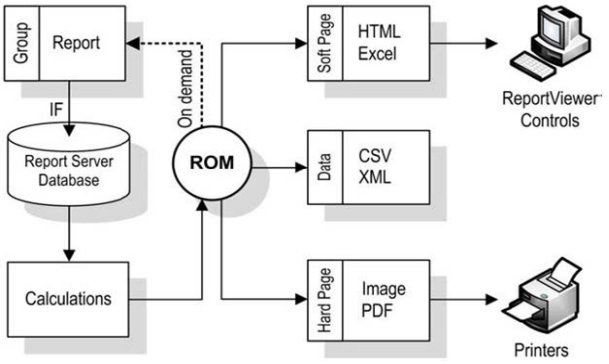

Figure 7. Grafic picture of the processing and the report

At the moment when Report Processor notes the new request, (request), it will take the data and it will match them with the report template making the middle form of the report. That report, processor saves in the Report Server Database. Point is that Report Processor takes and saves only the parts of the report, for example, grouping, sorting and etc. In the phase of the investigating of the report and saving it, Report Processor uses Render Object Model (ROM) an object which is forming the form that we can show. Textbox values and data are processing every time on-demand when we want to see the report.

2.3 The connection of the tribological bases of the data with the reports

Tribological data base, whose logic structure and content are shown in the [2], are connected to already formed template file for the creating of the report. Working surrounding is Visual Studio, where we can connect the data base to the report from the file Report.rdl created in SQL Server Business Intelligence Developer Studio. The starting point of the model form of the connection is shown in the Figure 8 [3,4].

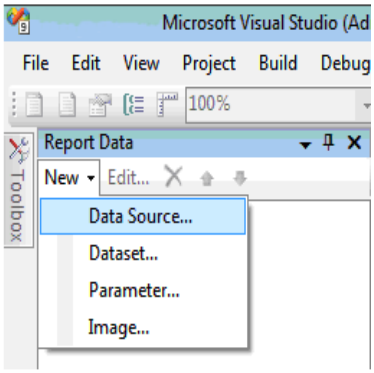

Figure 8. Adding Data Source…

After the connection is finished, it is possible to prepare the data by hand, or write SQL request, which will be use full for the report. Projection will define the columns and selection will define the lines of the data base which will be used in the report, Figure 9 [2].

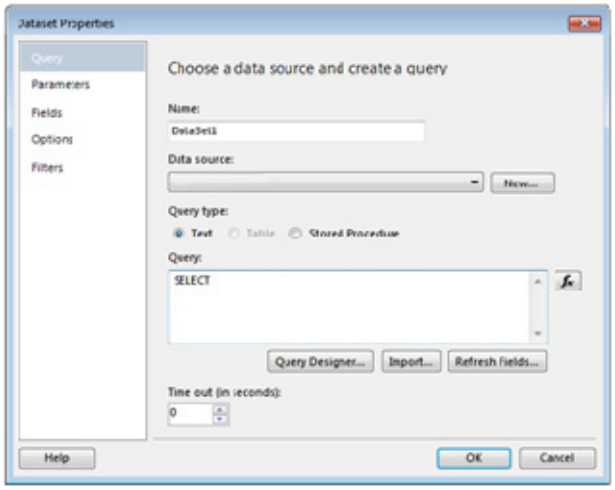

Figure 9. Defining of the requests for the data selection.

In the next step, we will select the way of the showing the data. Presentation of the data by the diagram versus the charts has more visual effects. The diagram can be added in one or two ways, moving control Chart from Toolbox or by pressing a click of the right mouse on the desktop Insert → Chart, Figure 10 [3,4].

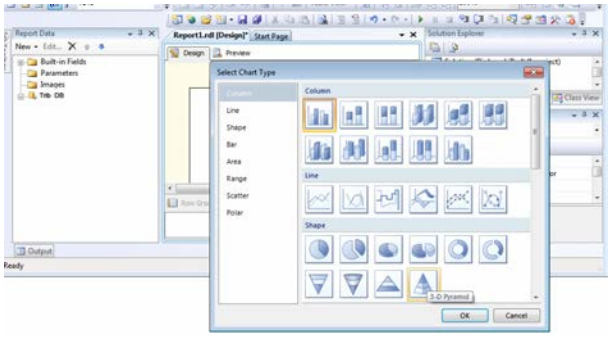

Figure 10. Selection of thr type of the diagram.

After we had sellected the diagram, we need to connect the Design Body in the dialogue window with the values which are chosen from the data base with the pararmetres of the NET control which describe the centres of the diagrams.When it is clicked on the diagram, it will show in the right,down part where we need to put the columns - results of the requestsfrom the data bases (parts in the command SELECT), Figure 11 [3,4].

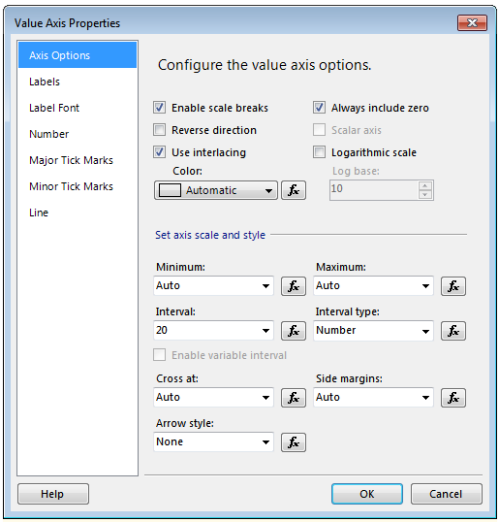

Figure 11. Adjustments of the centers of the parameters of the diagrams

After we turn off View mode, BI platform will give the Render report by processing the request and making the graphic interpretation based parameters and adjustments. In the Figure 12 we can see the final report of the base of the data, TRIBOLOGYCAL_RESULTS.

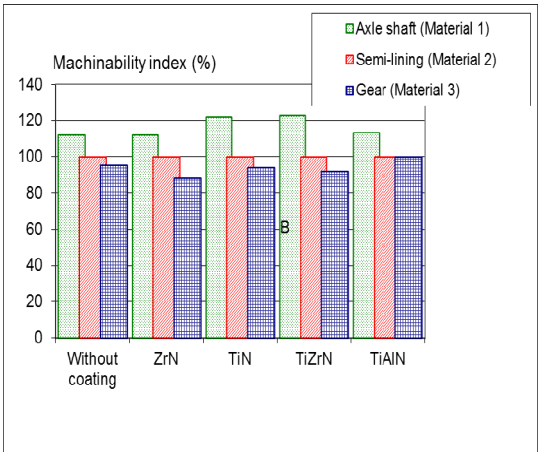

Figure 12. The final report after the adjustment of the parameters

Obviously the report is checked and the values are easily seen, can be seen and are clearly shown.

3.CONCLUSION

Reporting services is a complex and modern technology with the tendency for further adjustments and enlargement. Because of the need and implementation for these kinds of technologies, it grows the need that we must know and use them. Reporting services is a great technology which makes the job easier to the business world, and it can also be of great need to the scientists while they are publishing the results from the data base, and it facilitates the work to the IT techinicians.

REFERENCES

[1] T. Lachev: *Applied Microsoft SQL Server 2008 Reporting Services*, Prologika Press, USA, 2008.

[2] M. Erić, S. Mitrović, M. Babić, F. Živić, M. Pantić: *Application of Contemporary Information Technologies in Nanotribometry*, Tribology in Industry, Vol. 33, No. 4, pp. 159-163, 2011.

[3] B. Larson: *Delivering Business Intelligence with Microsoft SQL Server 2008*, The McGraw-Hill Companies, San Francisco, 2009.

[4] B. Larson: *Microsoft SQL Server 2008 Reporting Services*, The McGraw-Hill Professional, San Francisco, 2009.

[5] P. Turley, T. Silva, B. Smith and K. Withee: *Professional Microsoft® SQL Server® 2008 Reporting Services*, Wiley Publishing, Indianapolis, 2009.

[6] P. DeBetta, G. Low, M. Whiteborn: *Introducing Microsoft SQL Server 2008*, Microsoft Press, 2008.

[7] L. Davidson, K. Kline, S. Klein, and K. Windisch: *Pro SQL Server 2008 Relational Database Design and Implementation*, Springer-Verlag, New York, 2009.

Trenje, habanje i podmazivanje

13th International Conference on Tribology – SERBIATRIB ’13

15 – 17 May 2013, Kragujevac, Serbia

Serbian Tribology Society

SERBIATRIB '13

13th International Conference on Tribology

Faculty of Engineering in Kragujevac

Kragujevac, Serbia, 15 – 17 May 2013

VEŠTAČKO STARENJE TIKSOLIVENE ZA27 LEGURE I ČESTIČNIH ZA27/SIC KOMPOZITA

I. Bobić[1], M. Babić[2], A.Vencl[3], S. Mitrović[2], B. Bobić[4]

[1)] INN "Vinca", Univerzitet u Beogradu, Beograd, Srbija, ilijab@vinca.rs

[2)] Fakultet inženjerskih nauka, Univerzitet u Kragujevcu, Kragujevac, Srbija, babic@kg.ac.rs, boban@kg.ac.rs

[3)] Mašinski fakultet, Univerzitet u Beogradu, Beograd, Srbija, avencl@mas.bg.ac.rs

[4)] Institut "Goša", Beograd, Srbija, biljanabobic@gmail.com

Abstrakt: *ZA27 legura sa nedendritnom strukturom dobijena je tiksokasting postupkom. Čestični kompoziti sa osnovom od navedene legure dobijeni su kompokasting postupkom, odnosno infiltracijom 5 vol.% i 10 vol.% SiC čestica u poluočvrsli rastop legure. Uzorci tiksolivene ZA27 legure i kompozita bili su podvrgnuti procesu starenja na 80, 120 i 160°C (T5 režim). Strukturna ispitivanja matrične legure i kompozita i merenja promena tvrdoća tokom procesa starenja izvršena su u zavisnosti od temperature. Pokazano je da prisustvo čestica ojačivača utiče na ubrzanje procesa starenja, odnosno kompoziti dostižu maksimalne vrednosti tvrdoće za kraće vreme nego matrična legura. Sa povećanjem temperature starenja opadaju tvrdoće svih ispitivanih materijala.*

Ključne reči: *ZA27 legura, čestični kompoziti, kompokasting, veštačko starenje*

1. UVOD

Zbog dobre kombinacije fizičkih, mehaničkih i tehnoloških karakteristika ZA27 legura ima veliki komercijalni značaj. Koristi se izradu niza odlivaka različitih dimenzija. Takođe, poznata je kao legura za izradu kliznih ležajeva [1, 2]. Svojstva legure mogu se modifikovati termičkom obradom. Standardom [3] definisana je samo jedna varijanta termičke obrade ZA27 legure. Proučavanje uticaja raznih režima termičke obrade na svojstva ZA27 legure bilo je predmet rada više istraživača [4–6]. Budući da u livenom stanju legura sadrži presićene, metastabilne faze, osnovni cilj istraživanja bio je da se poboljša homogenost legure i postigne dobra kombinacija mehaničkih svojstava. Kod ZA27 legure koja sadrži Cu [2], cilj je bio da se poboljša dimenziona stabilnost proizvoda.

Zbog širokog temperaturnog intervala očvršćavanja (oko 100 ºC [1]), ZA27 legura je pogodna za preradu u poluočvrslom stanju, različitim postupcima. U zavisnosti od primenjenih procesnih parametara, moguće je dobiti leguru čiju strukturu karakteriše nedendritna morfologija [7].

Pokazano je da čestični kompoziti ZA27/SiC poseduju bolje fizičke i mehaničke karakteristike u odnosu na matričnu leguru [8, 9], kao i veću otpornost prema habanju. Posebno je proučavan uticaj procesa starenja na svojstva navedenih kompozita [10–12].

Procesi starenja imaju za cilj da omoguće stabilizaciju strukture i da poboljšaju dimenzionalnu stabilnost proizvoda pre njihove eventualne upotrebe na povišenim temperaturama. Ovo je posebno značajno kada se ima u vidu nepovoljan uticaj bakra na stabilnost dimenzija proizvoda od ZA27 legure na povišenim temperaturama [1].

Kompokasting postupak primenjen je za dobijanje čestičnih kompozita ZA27/SiC, koji su predmet ovog rada, s obzirom da je relativno jednostavan i perspektivan za dobijanje jeftinijih kompozitnih materijala.

Cilj ovog rada je da se ispita uticaj veštačkog starenja (u oblasti temperatura od 80 do 160°C) na mikrostrukturu i tvrdoću tiksolivene ZA27 legure i ZA27/SiC kompozita, koji su dobijeni kompokasting postupkom. Rezultati ispitivanja predstavljaju doprinos boljem razumevanju procesa

starenja navedenih materijala, što je od značaja za njihovu praktičnu primenu.

2. EKSPERIMENTALNI RAD

2.1 Tikso /kompokasting postupci

Tiksokasting i kompokasting izvršeni su pomoću aparature koja je ranije opisana [13].

Za potrebe eksperimentalnog rada korišćena je legura čiji hemijski sastava odgovara standardu [3]. Tiksokasting postupak sastojao se iz dve faze. U prvoj fazi dobijeni su odlivci ZA27 legure, koji su u drugoj fazi podvrgnuti toplom presovanju. Tokom prve faze vršeno je mehaničko mešanje poluočvrslog rastopa ZA27 legure na temperaturi od 460°C. Na početku je primenjena brzina mešanja od 500 o/min, u trajanju od 2,5 min, u cilju homogenizacije poluočvrslog rastopa legure. Zatim je u toku 10 min vršeno intenzivno mešanje rastopa (pri brzini mešanja od 1200 o/min), bez promene temperature. Po završetku mešanja, poluočvrsli rastop legure je izliven u čeličnu kokilu, predgrejanu na 350°C. Dobijeni su odlivci dimenzija 30x20x120 mm, od kojih su mehanički izrađeni manji uzorci (30x20x5 mm), koji su podvrgnuti toplom presovanju. Toplo presovanje je izvršeno pomoću specijalnog alata od toplootpornog čelika, na 350°C, primenom pritiska od 250 MPa. Posle toplog presovanja dobijeni su uzorci dimenzija 30x20x6 mm.

Kompokasting postupak je, takođe, izveden u dve faze; u prvoj fazi izvršeno je dobijanje odlivaka ZA27/SiC kompozita, koji su u drugoj fazi podvrgnuti toplom presovanju. U okviru prve faze izvršena je priprema poluočvrslog rastopa matrične legure, unošenje SiC čestica (prosečne veličina prečnika 24 μm) u poluočvrsli rastop i mešanje poluočvrsle kompozitne smeše. Pri dobijanju kompozita sa 5 vol.% SiC čestica (u daljem tekstu kompozit K1) vreme unošenja SiC čestica bilo je 3,5 min, pri brzini mešanja 500 o/min. Pri dobijanju kompozita sa 10 vol.% SiC čestica (u daljem tekstu kompozit K2) primenjena je ista brzina mešanja, ali je unošenje SiC čestica u poluočvrsli rastop matrične legure trajalo 7 minuta. Da bi se smanjio ukupni viskozitet poluočvrslog rastopa, povećana je radna temperatura tokom unošenja SiC čestica; od 465 do 470°C, u slučaju kompozita K1 i od 465 do 475°C u slučaju kompozita K2. Po završenom unošenju ojačavajućih čestica izvršeno je kratko, homogenizaciono mešanje (2,5 min, pri brzini od 500 o/min), a zatim intenzivno mešanje (1000 o/min) u narednih 10 min. Posle toga izvršeno je izlivanje kompozitnih masa u čeličnu kokilu, predgrejanu na 350°C.

U drugoj fazi izvršeno je toplo presovanje, pri istim parametrima koji su primenjeni kod tiksolivene ZA27 legure. Dobijeni su uzorci istih dimenzija, kao uzorci tiksolivene ZA27 legure.

2.2. Strukturna ispitivanja i merenje tvrdoće

Ispitivanje strukture vršeno je optičkom mikroskopijom (pomoću optičkog mikroskopa Carl Zeiss) i skening elektronskom mikroskopijom (pomoću skening elektronskog mikroskopa JEOL JSM – 5800).

Ispitivanja su vršena na uzorcima dimenzija 15x15x6 mm, koji su mašinski izrađeni iz otpresaka tiksolivene matrične legure i kompozita. Uzorci su brušeni pomoću brusnih papira (80, 360 i 600 grita), dok je poliranje obavljeno primenom tkanine za poliranje i paste (sa Al_2O_3 česticama). Ispitivanja pomoću SEM rađena su na poliranim uzorcima, dok su ispitivanja primenom OM vršena na poliranim i nagriženim uzorcima. Za nagrizanje je korišćen vodeni rastvor HNO_3 (9 v/v).

Merenje tvrdoće izvršeno je pre nego što su uzorci matrične legure i kompozita bili podvrgnuti procesu starenja, a zatim tokom procesa starenja, na uzorcima dimenzija 15x15x6 mm. Nezavisno od temperature starenja, najveći broj merenja tvrdoće obavljen je tokom prvog sata starenja. Merenje je zatim vršeno u određenim vremenskim intervalima. Za merenje je korišćen uređaj za merenje tvrdoće Karl Frank GMBH. Rezultati merenja izraženi su u Brinelovim jedinicama (HB). Na svakom uzorku vršeno je po pet merenja, za svaki vremenski interval tokom procesa starenja.

3 REZULTATI I DISKUSIJA

3.1 Strukturna ispitivanja

Na slici 1a prikazan je izgled mikrostrukture tiksolivene ZA27 legure. Mikrostruktura se sastoji od kompleksnih eliptičnih i globularnih polifaznih zrna. Zrna se sastoje od jezgra (svetle zone) koje čini α faza i periferije (smeša $\alpha+\eta$ faza, sive zone). Heksagonalna η faze, praktično cink, nalazi se između eliptičnih zrna (tamne zone).

Mikrostruktura prikazana na slici 1 posledica je uticaja mešanja poluočvrslog rastopa legure (tokom prve faze tiksokasting postupka) i očvršćavanja poluočvrslog rastopa ZA27 legure po završetku mešanja. Pod uticajem sila smicanja (proizvedenih mešanjem), kao i usled interakcija primarnih čestica međusobno i interakcija mešač–primarne čestice, zid lonca–primarne čestice, došlo je do usitnjavanja i transformacije primarnih čestica prema Flemingsovoj šemi [7].

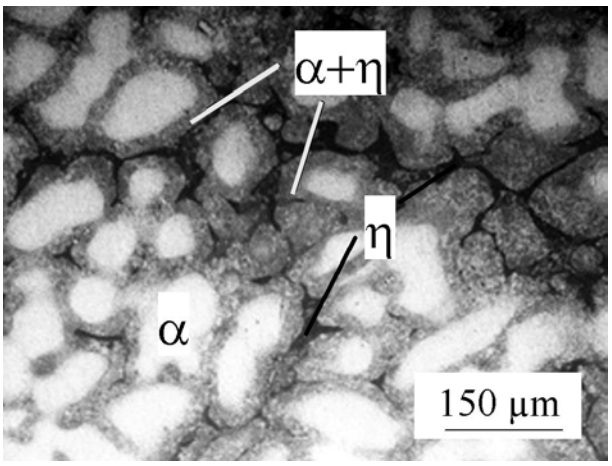

Slika 1. Mikrostruktura tiksolivene ZA27 legure (OM, nagriženo)

Rezultat toga je da su u strukturi tiksolivene ZA27 legure prisutne primarne čestice eliptičnog i kružnog oblika, što znači da je došlo promene morfologije. Međutim, osnovni elementi mikrostrukture, u pogledu faza koje nastaju tokom očvršćavanja, kvalitativno su isti kao elementi u mikrostrukturi livene ZA27 legure [1].

Na slici 2 prikazan je izgled mikrostrukture kompozita K1 i kompozita K2.

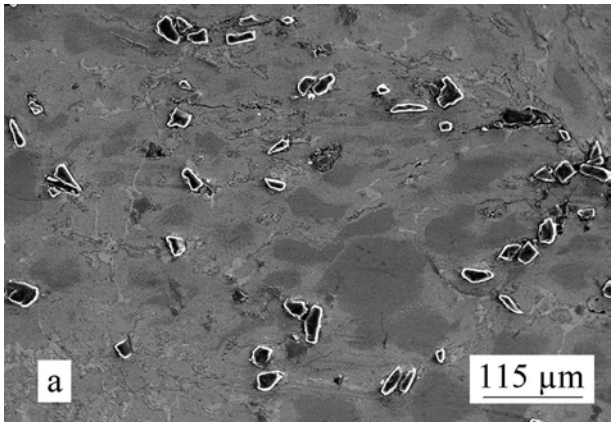

Slika 2. Mikrostrukture čestičnih kompozita ZA27/SiC (SEM, polirano).
a) K1 (ZA27+5 vol.%SiC), b) K2 (ZA27+10 vol.%SiC).

Na slici 2a prikazana je mikrostruktura kompozita K1. Postignut je relativno dobar raspored SiC čestica u metalnoj osnovi. Između čestica ojačivača vidi se struktura osnove kompozita (tiksolivena ZA27 legura), koja je ranije opisana.

Na slici 2b prikazana je struktura kompozita K2. Može se zapaziti prisustvo nakupina SiC čestica, što znači da se njihova pojava nije mogla izbeći pri dobijanju kompozita sa navedenim parametrima kompokasting postupka. Pored nakupina SiC čestica, na slici se mogu videti i SiC čestice koje nisu u međusobnom kontaktu. Čestice su smeštene u oblasti η faze i zalaze u oblast smeše faza α+η. Položaj SiC čestica je značajan zbog njihovog uticaja na osnovu kompozita, a time i na proces starenja. Mesto čestica u strukturi kompozita zavisi od procesnih parametara u prvoj fazi kompokasting postupka, kao i od načina očvršćavanja kompozitne mase posle završenog mešanja.

3.2 Tvrdoća

Promene tvrdoće sa vremenom starenja prikazane su pomoću dijagrama na slici 3 (a–c), za sve ispitivane materijala i temperature starenja: 80, 120 i 160°C. Starenje na 80 i 120°C vršeno je tokom 25 časova, dok je na 160°C starenje trajalo 5 časova.

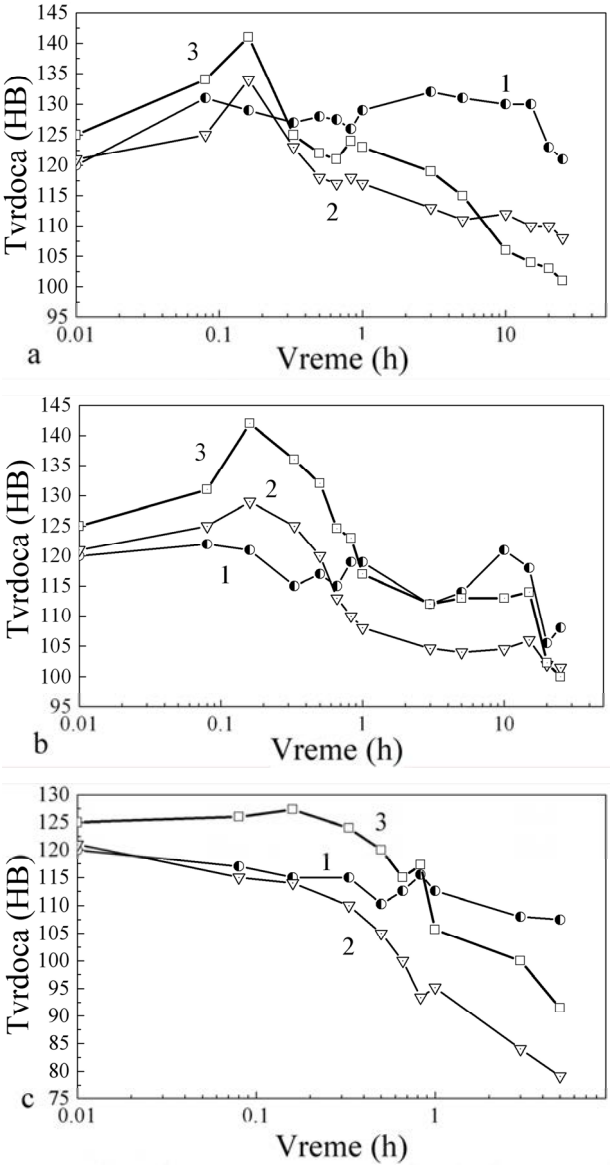

Slika 3. Promene tvrdoća tiksolivene ZA27 legure i kompozita K1 i K2 tokom starenja. Temperatura starenja: a) 80°C, b) 120°C, c) 160ºC. Krive: 1-tiksolivena ZA27 legura, 2 - K1, 3 - K2.

Na slici 3a prikazana je vremenska zavisnost tvrdoće na temperaturi starenja od 80ºC, za tiksolivenu ZA27 leguru i kompozite K1 i K2. Početna tvrdoća tiksolivene ZA27 legure (120 HB)

blago raste tokom prvih 10 min starenja. Tvrdoća zatim neprekidno opada sledećih 50 min, a posle 60 minuta starenja počinje da raste. Tiksolivena ZA27 legura postigla je maksimalnu vrednost tvrdoće posle 5 časova starenja. Od tada, pa do kraja starenja, tvrdoća neprekidno opada, tako da je najniža vrednost tvrdoće za tiksolivenu ZA27 leguru izmertena posle 25 časova starenja.

Pri starenju na 80°C tvrdoće oba kompozita (K1 i K2) u početku rastu veoma brzo, tako da su maksimalne vrednosti tvrdoće dostignute već posle 10 min starenja na ovoj temperaturi. Posle toga dolazi do brzog pada vrednosti tvrdoće, pri čemu je oko 30 min primećen zastoj, a zatim vrednosti tvrdoće pokazuju diskontinuitet u pogledu trenda, do isteka 60 min starenja. Posle ovog vremena, tvrdoće kompozita K1 i K2 kontinuirano opadaju do kraja prdviđenog vremena starenja.

Na osnovu objavljenih rezultata drugih autora [14], možemo tvrditi da se, u slučaju kompozita, dislokacije na granici čestica/matrica ponašaju kao centri kristalizacije čestica koje difunduju tokom starenja. Na taj način, povećao se broj centara kristalizacije taloga [11]), što utiče na ubrzanje procesa starenja. Usled toga, došlo je do bržeg dostizanja maksimalnih vrednost tvrdoće kod kompozita, nego kod tiksolivene osnovne legure.

Sa porastom temperature starenja, menjaju se vrednosti tvrdoće. Na slici 3b prikazana je vremenska zavisnost promene tvrdoće, pri starenju na 120°C, za tiksolivenu ZA27 leguru i kompozite K1 i K2. Tvrdoća legure blago raste tokom prvih 5 min starenja. Sa dijagrama se vidi da se na dalje tvrdoća menja diskontinuirano. Mogu se uočiti dva manja pika, jedan posle 60 min, a drugi posle 10 časova starenja. Posle toga, tvrdoća tiksolivene legure opada i najniža vrednost izmerena je posle 20 časova starenja.

ZA27 legura ima relativno nisku tačku topljenja (380°C, odnosno 653K). Zatezna ispitivanja na povišenim temperaturama [1] pokazala su da se već iznad 80°C čvrstoća pogoršava, a izduženje povećava. Takođe, rezultati ispitivanja pritisnih karakteristika livene i tiksolivene ZA27 legure [15], pokazuju da dolazi do značajnog pada vrednosti granice popuštanja $\sigma_{0,2}$, kada se dostigne temperatura od 80°C.

Pri povećanju temperature starenja od 80 na 120ºC, značajno se intenziviraju procesi starenja. Ovo se odrazilo na promene vrednost tvrdoće tokom starenja na 120°C, kako kod matrične legure, tako i kod kompozita K1 i K2. U slučaju kompozita K1, maksimalna vrednost tvrdoće dostignuta je posle 20 min starenja. Tvrdoća zatim relativno brzo opada do isteka prvih 60 min starenja. Tokom sledećih 15 časova vrednost tvrdoće se ne menja značajno. Posle 25 časova starenja izmerena je najniža tvrdoća kompozita K1. Tok promena tvrdoće kompozita K2 sličan je opisanom toku promena kod kompozita K1, ali postoji razlika u vrednostima tvrdoće. Kompozit K2 dostiže maksimalnu vrednost tvrdoće posle 20 min starenja na 120°C. Tvrdoća zatim opada do kraja trećeg sata starenja, posle čega nema znatnijih promena sve do isteka 15 sati starenja. Posle toga, tvrdoća ponovo opada i dostiže najnižu vrednost posle 25 časova starenja.

Opšte je poznato da je u uslovima starenja na nižim temperaturama brzina nukleacije taloga velika, ali je brzina rasta mala. Obrnuto, na višim temperaturama starenja brzina nukleacije taloga je manja, ali je brzina rasta velika. Prema tome, na nižoj temperaturi starenja broj centara nukleacije je veći, međučestični prostor se smanjuje, što dovodi do povećanja tvrdoće. Na osnovu ovoga, mogla se očekivati manja tvrdoća kod svih materijala koji su stareni na 120°C, u odnosu na njihovu tvrdoću pri starenju na 80°C. Ovo očekivanje ispunjeno je u slučaju tiksolivene ZA27 legure i kompozita K1, što je u saglasnosti sa [11, 14].

Analizom krivih promene tvrdoće tokom starenja kompozita, može se videti da se maksimalne vrednosti tvrdoće, u principu, povećavaju sa sniženjem temperature starenja i povećanjem količine čestica ojačivača. Međutim, u konkretnom slučaju starenja kompozita K2 na 120°C, zapažen je paradoks, koji je primećen ranije [15]. Naime, maksimalna tvrdoća kompozita K2 pri starenju na 120°C nešto je veća od maksimalne tvrdoće istog kompozita pri starenju na 80°C.

Pri starenju na 160°C (slika 3c) tvrdoće svih ispitivanih materijala opadaju u odnosu na tvrdoće postignute tokom starenja na 80 i 120°C. Na početku starenja na 160°C, tvrdoća tiksolivene ZA27 legure opada u odnosu na polaznu vrednost. Posle 1 časa od početka starenja tvrdoća malo raste. a zatim neprekidno opada do kraja starenja. Slična promena tvrdoće konstatovana je pri starenju kompozita K1. Ovo navodi na zaključak da su difuzioni procesi na ovoj temperaturi značajno ubrzani. Kod kompozita K2 dolazi do povećanja tvrdoće u odnosu na polazno stanje, tako da se posle 20 min starenja na 160°C dostiže maksimalna tvrdoća. Posle toga, tvrdoća kompozita K2 neprekidno opada do kraja ispitivanja.

Rezultati koji su dobijeni u ovom radu, ukazuju na mogućnost postizanja maksimalne tvrdoće kompozita posle relativno kratkog vremena starenja.

5. ZAKLJUČCI

Struktura tiksolivene ZA27 legure grublja je u odnosu na strukturu livene legure, što se odražava na usporavanje procesa starenja tiksolivene legure.

Prisustvo čestica ojačivača utiče na ubrzavanje procese starenja, na svim primenjenim temperaturama starenja.

Kompoziti veoma brzo dostižu maksimalne vrednost tvrdoće, što je od velikog značaja za njihovu praktičnu primenu.

ZAHVALNOST

Autori se zahvaljuju Ministarstvu za obrazovanje, nauku i tehnološki razvoj Republike Srbije koje je finansijski podržalo ovaj rad kroz projekte TR 35021 i OI 172005. Takođe se zahvaljuju Livnici RAR® doo, Batajnica (Beograd, Srbija) i Fabrici abrazivnih proizvoda Ginić Tocila® doo, Barajevo (Beograd, Srbija), koji su obezbedili master leguru i SiC čestice, za ovo istraživanje.

LITERATURA

[1] E. Gervais, R.J. Barnhurst, C.A. Loong, *An Analysis of Selected Properties of ZA Alloys*, JOM 11 (1985) 43–47.

[2] V. G. S. Mani, P. Sriram, N. Raman, S. Seshan, *AFS Transactions*, 88-100, pp.525-532, 1988.

[3] BS EN 12844:1999 *Zinc and zinc alloys*. Castings. Specifications.

[4] S. Murphy, T. Savaskan, *Metallography of Zinc-25 % Al Based Alloys in the As–Cast and Aged Conditions*, Prakt. Metallogr. 24 (1987) 204–221.

[5] I. Bobic, B. Djuric, M.T. Jovanovic, S. Zec, *Improvement of Ductility of a Cast Zn–25Al–3Cu Alloy*, Mater. Charact. 29 (1992) 277–283.

[6] P. Choudhury, K. Das, S. Das, *Evolution of as-cast and heat-treated microstructure of a commercial bearing alloy,* Mater. Sci. Eng., A 398, pp. 332–343, 2005.

[7] M. Flemings, *Behavior of* metal *alloys in the semi-solid state*, Metall. Transactions A, 22A, pp. 957-981, 1991.

[8] I. A. Cornie, R. Guerriero, L. Meregalli, I. Tangerini, *Cast Reinforced Metal Composites*, ASM International USA, pp. 155-165, 1988.

[9] N. Karni, G. B. Barkay, M. J. Bamberger, *Structure and Properties of metal-matrix composite*, J. Mater. Sci. Lett. 13, pp. 541-544, 1994.

[10] K. Seah, S. Sharma, P. R. Rao, B. Girish, *Mechanical Properties of As-Cast and Heat Treated ZA27/Silicon Carbide Particulate Composites*, Materials & Design, 16, pp. 277-281, 1995.

[11] S. C. Sharma, S. Sastry, M. Krishna, *Effect of aging parameters on the micro structure and properties of ZA27/aluminite metal matrix composites,* Journal of Alloys and Compounds 346, pp. 292-301, 2002.

[12] LI ZI-qani, ZHOU Heng-zhi, LUO Xin-yi, WANG Tao, SHEN Kai, *Aging microstructural characteristics of ZA-27 alloy and SiC_p/ZA-27 composite*, Transactions of Nomnferous Metals Society of China, 16, pp. 98-104, 2006.

[13] Z. Acimovic-Pavlovic, K. T. Raic,, I. Bobic and B. Bobic, *Synthesis of ZrO2 Particles Reinforced ZA25 Alloy Composites by Compocasting Process*, Advanced Composite Materials 20, pp. 375–384, 2011.

[14] I. Dutta, D.I. Bourell, *A Theoretical and Experimental Study of Aluminium Alloy 6061-SiC Metal Matrix Composite to Identify the Operative the Operative Mechanism for Accelerated Aging*, Materials Sience and Engineering A11, pp. 267-77, 1989.

[15] B. Bobic, M. Babic, S. Mitrovic, N. Ilic, I. Bobic, M.T. Jovanovic, *Microstructure and mechanical properties of Zn25Al3Cu based composites with large Al_2O_3 particles at room and elevated temperatures*, Int. J. Mat. Res.101 pp. 1524–1531, 2010.

[16] T. Savaskan, S. Murphy, *Decomposition of Zn-Al Alloys on qench-aging*, Materials Science and Technology, August 6, pp. 695-703, 1990.

Serbian Tribology Society

SERBIATRIB '13

13th International Conference on Tribology

Faculty of Engineering in Kragujevac

Kragujevac, Serbia, 15 – 17 May 2013

UTICAJ POVRŠINE PODLOGE NA KARAKTERISTIKE PREVLAKA CINKA

Desimir Jovanović[1], Bogdan Nedić[2], Milomir Čupović[3], Vlatko Matrušić[4]

[1]Zastava oružje AD, Kragujevac, Srbija, zo.tehnologija@open.telekom.rs

[2]Univerzitet u Kragujevcu, Fakultet inženjerskih nauka, Kragujevac, Srbija, nedic@kg.ac.rs

[3]Državni univerzitet u Novom Pazaru, Srbija, mcupovic@np.ac.rs

[4]Strojarski fakultet, Slavonski Brod, Hrvatska, vmarusic@sfsb.hr

Abstract: *Galvanske prevlake cinka se nanose da bi površina osnovnog materijala dobila odgovarajuća svojstava, kao što su: otpornost prema koroziji, hemijska postojanost, potreban estetski utisak i dr. Ispitivanja galvanskih prevlaka cinka usmerena su najčešće vezu Zn sa osnovnim materijalom, dok je veoma malo podataka o uticaju podloge na karakteristike prevlaka. Prethodna završna obrada ima veliki uticaj na formiranje fizičko-mehaničkih svojstava i strukture prevlake. U radu su prikazani rezultati istraživanja karakteristika prevlaka cinka istaloženih na podlozi dobijenoj različitom završnom obradom sa različitom tvrdoćom i topografijom.*

Keywords: *galvanske prevlake cinka, tvrdoća, topografija*

1. UVOD

Uticaj vrste postupka obrade i uslova prethodne obrade kao i pripreme površina na koje se nanose prevlake, odnosno tehnološkog nasleđa, je veoma malo istraživan. Površinski slojevi obrađenih površina dobijenih različitim postupcima obrade i režimima mogu imati različitu strukturu, što se tek u period eksploatacije može ispoljiti. Prema tome, može se reći da se karakteristike površinskih slojeva formiraju kao rezultat različitih uslova obrade u tehnološkom lancu izrade gotovog dela.

Osnovni parametri koji se nasleđuju kroz tehnološki proces izrade mogu se podeliti na dve grupe. S jedne strane to su parametri vezani za svojstva materijala: njegov sastav, strukturu, naponsko stanje i dr., dok su sa druge strane parametri vezani za makro i mikrogeometriju površina (geometrijski parametri) [1,2]. To ukazuje na kompleksnost problema i potrebu izučavanja.

Prevlake cinka se najviše koriste za zaštitu čeličnih površina od korozije. Elektrohemijske prevlake cinka mogu imati različite morfologije i teksture. Kada su ove pojave u pitanju većina istraživanja se odnosi na uticaj standardnih parametra pri taloženju prevlaka kao što su gustina struje, temperatura, sastav kupatila [6-10], dok je znatno manje pažnja posvećeno značaju pripreme površine čelične podloge. Istraživanja uticaja stanja podloge za taloženje prevlaka cinka polirane mehanički [11.12] ili elektrohemijski [10-14]. pokazuju da se morfologija i tekstura prevlake na ovim površinama znatno razlikuju.

Završna obrada površina ima veliki uticaj na formiranje fizičko - mehaničkih svojstava i strukture površinskog sloja. U radu se vrši istraživanje uticaja prethodne obrade površina i debljine prevlake na mehaničke i hemijske karakteristike prevlake cinka.

2. EKSPERIMENTALNA ISPITIVANJA

Kao osnova za nanošenje prevlaka odabran je čelik Č5730 (prema GOST-u 30HN2FA 1). Odabrani čelik se koriste za izradu cevi streljačkog oružja. Hemijski sastav osnove je prikazan u tabeli 1. Uzorci za ispitivanje su pločice dimenzija 15 x 10 x 6.3 mm (prema ASTM G 77). Nakon izrade uzoraka glodanjem, izvršena je termička obrada poboljšanjem na različite tvrdoće. Završna obrada uzoraka vršena je na više načina, brušenjem sa više režima, poliranjem, peskarenjem. Na ovaj način su

dobijene različite karakteristike površinskog sloja i različite topografije površina uzoraka.

Mikrogeometrija podloge za nanošenje prevlaka snimana je na kompjuterizovanom mernom uređaju Talysurf-6, koji omogućava kompleksno praćenje kontaktnih površina. Korišćenjem ovog mernog sistema dobijena je informacija o početnoj mikrogeometriji kontaktnih površina uzoraka.

Tabela 1. Hemijski sastav osnove Č5730

	element	***hemijski sastav %***
1	C	*0,27 -0,34*
2	Mn	*0,30 - 0,60*
3	Si	*0,17 -0,37*
4	Ni	*2,0 -2.4*
5	Cr	*0,60 - 0,90*
6	Mo	*0,20 - 0,30*
7	V	*0,10 -0,18*
8	S	*max 0,025*
9	P	*max 0,025*
10	Cu	*max 0,25*

Nanošenje galvanskih prevlaka je vršeno u pogonu za galvanizaciju fabrike "Zastava oružje" u Kragujevcu. U tabeli 2, date su karakteristike osnovnog materijala na koji je nanošena prevlaka.

Tabela 2. Karakteristike podloge uzoraka

Uzorak broj	***Vrsta obrade***	***Ra μm***	***Tvrdoća podloge, HRC***
35	*brušenje*	*0.818*	*38*
45		*0.719*	*39*
118		*0.844*	*19*
10		*0.720*	*37*
12	*šmirglanje*	*0.600*	*35*
33		*0.550*	*38*
32	*peskarenje*	*0.870*	*35*

Prevlake cinka su taložene u programiranom režimu rada jednosmernom strujom, po zadatom planu eksperimenta. U toku procesa taloženja, parametri jednosmerne struje su kontrolisani i regulisani u zadatim granicama. Korišćene anode su napravljene od olova sa 10 % kalaja.

Nanošenje prevlaka cinka je vršeno na sledeći način:

- alkalno bezcijanidno odmašćivanje sa industrijskim deterxentom,
- ispiranje u protočnoj vodi,
- dekapiranje u razređenoj hlorovodoničnoj kiselini u odnosu 1:1,
- ispiranje vodom,
- elektro-hemijsko nanošenje prevlake cinka,
  - sobna temperatura nanošenja prevlake
  - jačina struje I =3 A/dm2
  - prosvetljavanje u 2% rastvoru HNO_3 u trajanju od 50 sekundi,
- ispiranje u protočnoj vodi,
- sušenje toplim vazduhom.

Nanošenje prevlaka cinka je vršena tako što su uzorci postavljani u vertikalni položaj, usmereni na isti način. Tačkom "A" na uzorku (slika 1) je označena gornja strana uzorka. Merenje lokalne debljine prevlake cinka vršeno je na 15 tačaka prema šemi površine uzorka prikazanoj na slici 1.

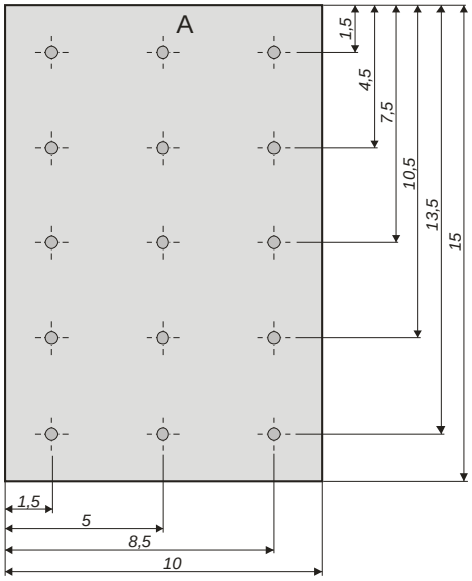

Slika 1. *Šema mesta merenja debljine prevlake*

Karakteristike (srednja vrednost debljine i hrapavost) istaloženih prevlaka date su u tabeli 3. Na slici 2, data je topografija prevlaka za uzorke 10, 12, i 32.

Tabela 3. Karakteristike prevlaka

	Uzorak broj	***Ra prevlake m***	***Debljina prevlake μm***
1	*35*	*1.070*	*8.85*
2	*45*	*1.120*	*28.90*
3	*118*	*1.130*	*23.87*
4	*10*	*1.640*	*20.16*
5	*12*	*2.360*	*36.57*
6	*33*	*2.61*	*32.26*
7	*32*	*1.180*	*10.57*

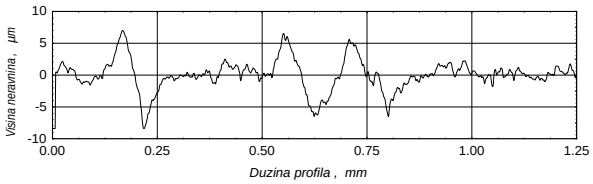

a) uzorak 10

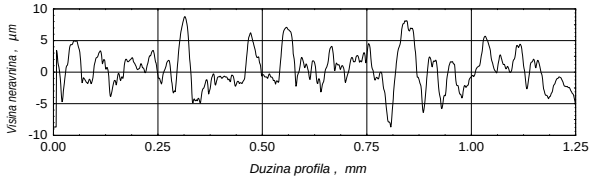

b) uzorak 12

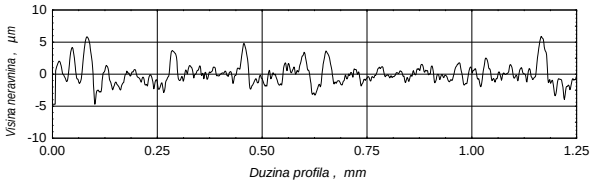

c) uzorak 32

Slika 2. Topografija nakon nanošenja prevlaka za uzorke 10, 12 i 32

Na slici 3. prikazan je izgled uzoraka pre i posle nanošenja prevlaka.

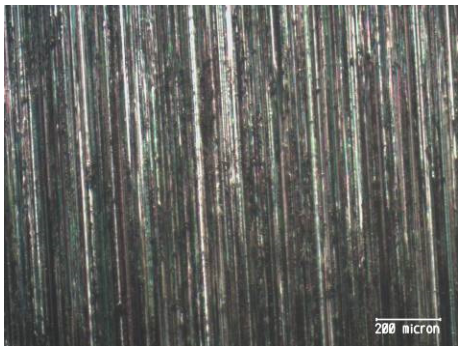

pre nanošenja prevlake

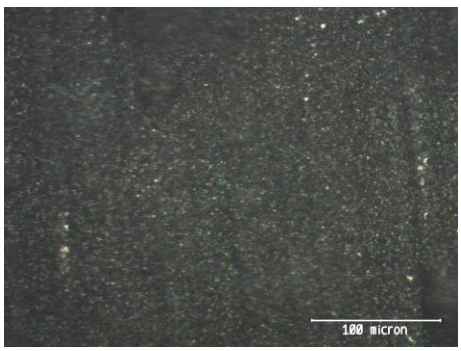

posle nanošenja prevlake

a) uzorak 10

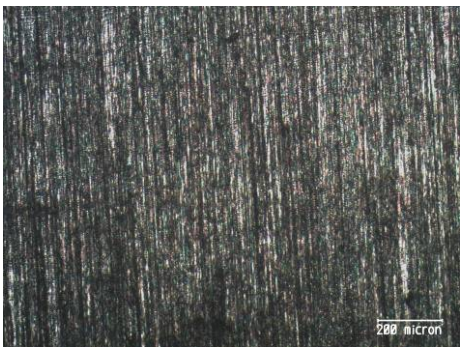

pre nanošenja prevlake

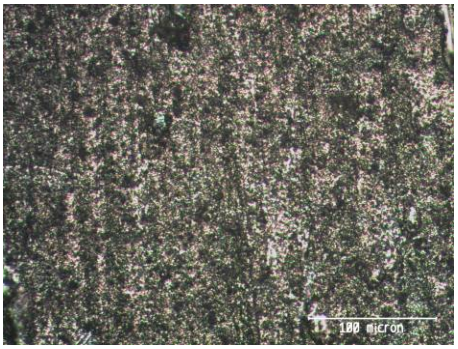

posle nanošenja prevlake

b) uzorak 12

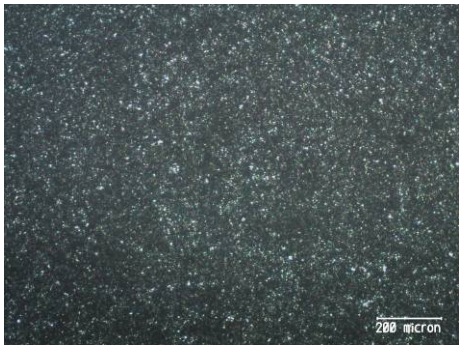

pre nanošenja prevlake

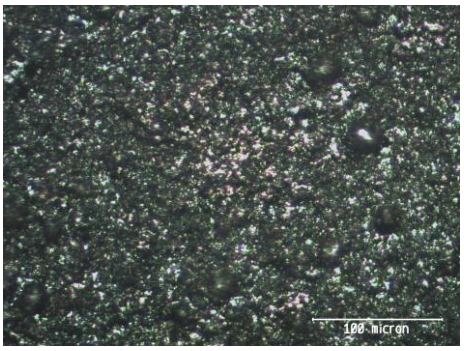

posle nanošenja prevlake

c) uzorak 32

Slika 3. Izgled uzoraka pre i posle nanošenja prevlake

3. ANALIZA REZULTATA

Na svim uzorcima prvo je izvršen pregled spoljašnjeg izgleda. Izgled prevlake praćen je

vizuelno, na dnevnoj svetlosti, pod uglom od 45º. Površina prevlake kod svih uzoraka je sjajna i glatka. Nema dendrita, pregorelih i nepokrivenih mesta.

Debljina prevlake cinka je merena na 15 mesta prema datom planu na slici 1. Na graficima, na slici 4, na osnovu rezultata merenja, prikazana je raspodela debljine prevlake po površini uzorka. Na osnovu ovih grafika se može zaključiti da debljina po širini i dužini uzorka odstupa i neravnomerna je. Najveće vrednosti za debljinu prevlake su izmerene na središnjem delu uzorka na dužini 13,5 mm od početka. Početak uzorka je označen tačkom "A". To je tačka koja označava gornju stranu uzorka pri nanošenju cinka.

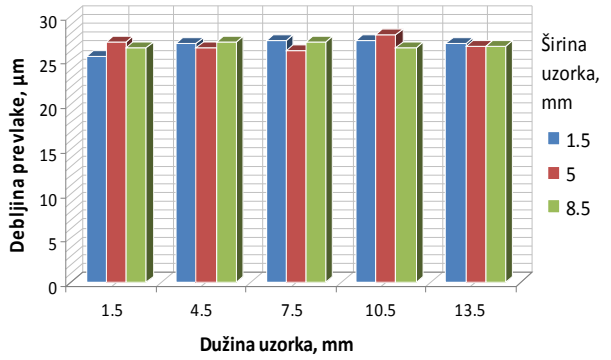

a) uzorak 45

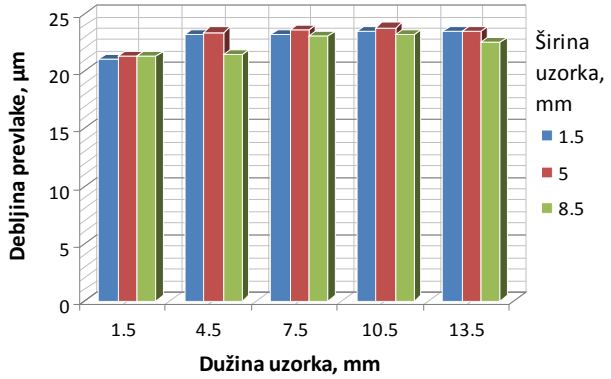

b) uzorak 118

Slika 4. Raspored debljine prevlake

Ispitivanje metodom termičkog šoka vršeno je prema standardu ISO 2819-1980. Uslovi ispitivanja:

- Temperatura zagrevanje uzoraka T=200^{0}C (prema standardu T =180^0 - 200^0 C),
- Vreme zagrevanja 1 sat.
- Kvašenje mlazom hladne vode.

Posle zagrevanja prema uslovima datim standardom uzorci se izlažu mlazu hladne vode. Prevlaka mora da ostane nepromenjena, ne sme da dođe do pojave odslojavanja prevlake sa osnovnog materijala, podloge.

Ispitivani uzorci su zadovoljili zahteve standarda. Prianjanje nanetih prevlaka cinka je dobro, nisu uočene promene na prevlaci cinka koje bi ukazale na odvajanje prevlake od osnovnog materijala, podloge.

Koroziona stabilnost prevlaka cinka određivana je praćenjem uzoraka tokom dužeg vremena izlaganja dejstvu rastvora 3% Na Cl, u skladu sa ASTM B117-64 metodom. Ispitivani su uzorci različitih karakteristika (hrapavost i tvrdoća podloge, debljina prevlake), tabela 2. Rezultati praćenja korozione stabilnosti prevlaka cinka su pokazali da nije došlo do pojave korozije, tako da se ne može uspostaviti veza između parametara prethodne obrade i korozione otpornosti.

Triboloških ispitivanjima na tribometru blok-on-disk merena širina traga habanja na bloku i na taj način određivana otpornost na habanje kao parametar habanja površini sa prevlakom cinka na ispitivanim blokovima (slika 5).

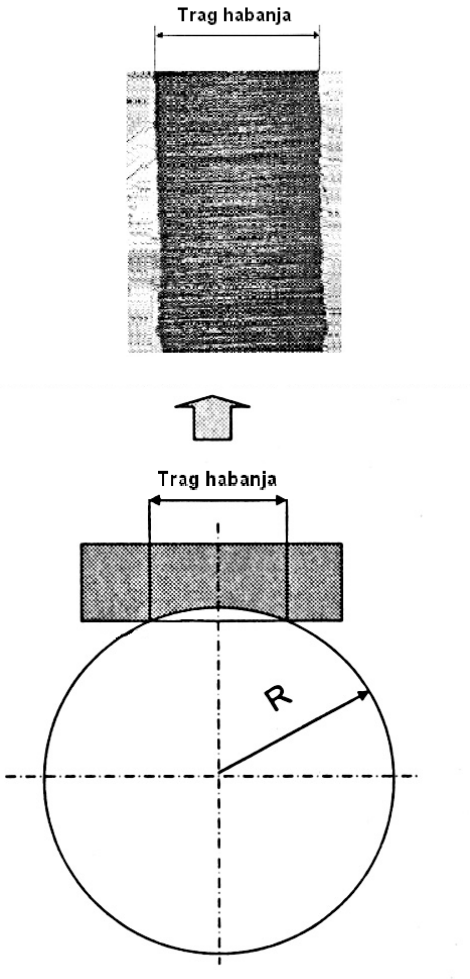

Slika 5. Trag habanja na bloku

Ispitivanje habanja prevlaka su vršena na tribometru TR-95 sa kontaktom blok-on-disk u Centru za obradu metala rezanjem i tribologiju Fakulteta inženjerskih nauka u Kragujevcu. Tribometar TR-95 omogućava variranje uslova kontakta sa aspekta oblika, dimenzija i materijala

kontaktnih elemenata, normalnog kontaktnog opterećenja i brzine klizanja. Ispitivanja se mogu vršiti u uslovima sa podmazivanjem i bez podmazivanja. Razvoj procesa habanja na bloku manifestuje se formiranjem i širenjem izraženog traga habanja. Normalno opterećenje je bilo 10 N, a brzine klizanja 0,25 m/s, 0,5 m/s i 1 m/s. Ukupan put klizanja je bio 150 m. Realizovana ispitivanja su bila sa graničnim podmazivanjem sa mineralnim hidrauličnim uljem Hidrovisk HD46 zbog velikog koeficijenta trenja u slučaju trenja bez podmazivanja i velikih vibracija u sistemu merenja sile trenja kod tribometra TR-95.

Početni nominalni linijski kontakt između diska i bloka usled razvoja procesa habanja postaje kontakt po određenoj površini, što kao posledicu ima razaranje materijala, najpre u površinskom sloju bloka (slika 6). Promena širine traga habanja ima isti karakter za sve ispitivane uzorke samo je razlika u nivou njihove pohabanosti.

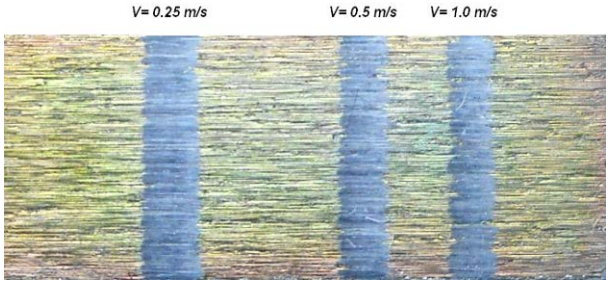

Slika 6. Širina traga habanja na bloku

Proces habanja karakteriše postizanje određenog nivoa, stabilizaciju i usporeni porast širine traga habanja tokom vremena ispitivanja. Na osnovu rezultata merenja širine traga habanja na bloku, formirani su u zavisnosti od uslova kontakt (brzina klizanja, normalna sila) pojedinačni i zbirni histogram promene širine traga habanja (slika 7). Najveće širine traga habanja odgovaraju najmanjoj brzini klizanja.

Ispitivani su uzorci različitih karakteristika (hrapavost i tvrdoća podloge, debljina prevlake). Ako se posmatra histogram, slika 7, može se zaključiti da se između hrapavosti površina uzoraka pre i posle nanošenja prevlake cinka i širine traga habanja na bloku ne može uspostaviti veza. Takođe, ne može se uspostaviti veza između tehnologija obrade uzoraka (brušenje, peskarenje i dr.) sa širinom traga habanja.

Najmanje habanje je bilo kod uzoraka 10 i 33, odnosno, kod uzoraka sa velikom tvrdoćom podloge i velikom debljinom prevlake.

Najveće habanje je bilo kod uzoraka 32, 35 i 118. Uzorak 118 ima najmanju tvrdoću a uzorci 32 i 35 najmanju debljinu prevlake cinka.

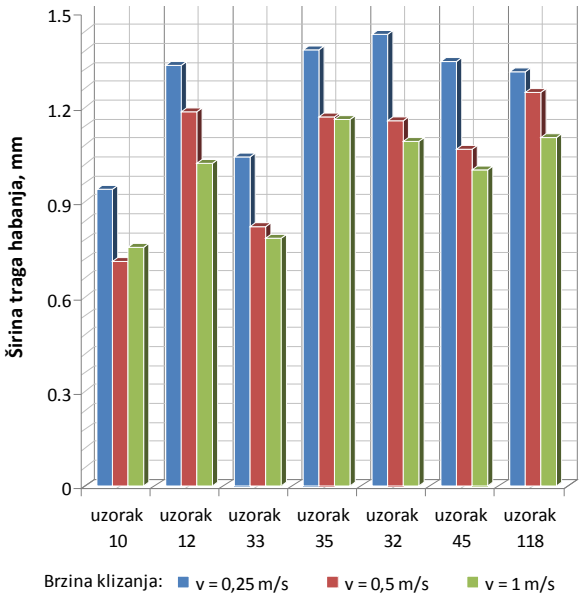

Slika 7. Širina traga habanja na bloku

4. ZAKLJUČAK

Ispitivane prevlake različitih debljina su nanete na uzorke sa različitom topografijom i tvrdoćom. Rezultati ispitivanja vizuelnim pregledom, ispitivanja korozione otpornosti i ispitivanja prianjanje prevlaka cinka za osnovni metal, podlogu, su pokazali da prevlake zadovoljavaju zahteve standarda. To znači da je valjano izabrana tehnologija priprema površina i nanošenja prevlaka.

Rezultati ispitivanja uticaja promene topografije površine na kvalitet prevlake su pokazali da nanošenjem prevlake dolazi do značajne promene topografije, odnosno povećanja hrapavosti ali da to ne utiče na ostale karakteristike prevlake cinka.

Realizovana ispitivanja i dobijenih rezultata ukazuju na postojanje zavisnosti između tvrdoće podloge, debljine prevlake i širine traga habanja pri tribološkim ispitivanjima, ali uspostavljanje korelatiuvnih veza je moguće realizacijom znatno većeg broja eksperimenata.

AKNOWLEDGEMENT

Ovaj rad je deo projekta TR35034 "Istraživanje primene savremenih nekonvencionalnih tehnologija u proizvodnim preduzećima sa ciljem povećanja efikasnosti korišćenja, kvaliteta proizvoda, smanjenja troškova i uštede energije i materijala", koga finansira Ministarstvo prosvete i nauke Republike Srbije.

LITERATURA

[1] Зинченко В. М.: *Технологическая наследственность при изготовлении деталей*, Технология металлов, № 5, 2007.

[2] П. И. Ящерицын : *Технологическое наследование эксплуатационных параметров деталей машин*. Справочник, Инженерный журнал № 9, 2004,

[3] S. Đorđević, M. Maksimović, M. G. Pavlović, K. I. Popov, *Galvanotehnika*, Tehnička knjiga, Beograd, 1998.

[4] Volker Kunz, ZINTEK–TECHSEAL-TRI-COAT Catalouge, Trebur 2001.

[5] Nedić, B., Jovanović, D., Lakić Globočki, G., I*nfluence Of Previous Machining On Characteristics Of Galvanic Coatings*, Serbiantrib - 12th International Conference on Tribology, Kragujevac, 2011.

[6] B. Nedić, D. Jovanović**, G.** Lakić-Globočki: *Scratch Testing Of Zn Coating Surfaces*, Proceedings: 34th International conference on production engineering, Niš, 2011.

[7] Raeissi, Saatchi, Golozar, Szpunar: *Effect of surface preparation on zinc electrodeposited texture*, Surface & Coating Tehnology 197, 2005,

[8] K. Deblauwe, A. Deboeck, J. Bollen, W. Timmermans, Proceeding of the 12th International Conference on Textures of Materials (ICOTOM-12), Montreal, Quebec, Canada, 9–13 August, 1999,.

[9] S. H. Hong, J. B. Kim, S. K. Lee, Mat. Sci. Forum 408–412, 2002.

[10] Kim, S. Ch. Hong, Proceeding of the 12th International Conference on Textures of Materials (ICOTOM 12), Montreal, Quebec, Canada, 9–13 August, 1999,

[11] D. Vasilakopoulos, M. Bouroushian, N. Spyrellis, Trans. IMF 79, 2001.

[12] M. Ye, J.L. Delplancke, G. Berton, L. Segers, R. Winand, Surf. Coat. Technol. 105, 1998.

[13] H. Yan, J. Downes, P.J. Boden, S.J. Harris, J. Electrochem. Soc. 143, 1996.

[14] H. Park, J.A. Szpunar, Proceeding of the 12th International Conference on Textures of Materials (ICOTOM 12), Montreal, Quebec, L Canada, 9–13 August, p. 1421, 1999.

[15] Standard ISO 2819-1980

[16] Standard ASTM B117

[17] StandardISO 4539

Serbian Tribology Society

SERBIATRIB '13

13th International Conference on Tribology

Faculty of Engineering in Kragujevac

Kragujevac, Serbia, 15 – 17 May 2013

DEFEKTACIJA REDUKTORA BKSH-335 ZA POKRETANJE TRAKASTIH TRANSPORTERA BAGERA Sch Rs 630

Svetislav Lj. Marković[1], Ljubica Milović[2], Bratislav Stojiljković[3]

[1]Visoka škola tehničkih strukovnih studija, Čačak, svetom@open.telekom.rs,

[2]Univerzitet u Beogradu, Tehnološko-metalurški fakultet, Beograd, acibulj@tmf.bg.ac.rs

[3]Muzej Nikole Tesle, Beograd, bratislav.stojiljkovic@tesla-museum.org

Apstrakt: *Remont jednog moćnog mašinskog sistema kao što je bager-glodar Sch Rs 630 je uslovljen visokim nivoom pouzdanosti, ispravnosti i funkcionalnosti svih njegovih sklopova. Iz navedenih razloga remont razmatranog reduktora mora biti praćen detaljnom defektacijom, odgovarajućom tehnologijom regeneracije, ugradnjom kvalitetnih delova (zupčanika, vratila, ležajeva) i pravilnom montažom kako elemenata u reduktor, tako i montažom reduktora na sam bager. Svi navedeni faktori od presudnog su uticaja na budući rad reduktora. Takođe, neophodno je voditi računa o ekonomskoj opravdanosti izvođenja ovakvih radova. U velikim sistemima svaki neplanirani zastoj ovakvih mašina veoma mnogo košta. Nedopustivo je da uzrok zastoja bagera bude kvar jednog ovakvog reduktora.*

Ključne reči: *bager, reduktor, defektacija, remont.*

1. UVOD

Rotorni bageri su mašine velikih gabarita, kapaciteta i težina. Jedan od takvih je i rotorni bager Sch Rs 630, nemačkog proizvođača KRUPP. Bager glodar je moćna i visoko produktivna mašina, koja se koristi na površinskim kopovima za otkopavanje ugljenih i jalovinskih masa. Spada u grupu rotornih bagera i ima teorijski kapacitet 4100 m^3/h, visina kopanja je 25 m, a dubina 6 m.

Rotorni bager se sastoji od donje i gornje gradnje sa konstrukcijom. U donju gradnju spada transportni mehanizam (šest transportnih gusenica) od kojih su dve sa hidrauličnim upravljačkim mehanizmom. Iznad transportnog mehanizma je aksijalni kuglični ležaj koji omogućuje zaokretanje gornje gradnje za 360º. Radno područje zaokretanja gornje gradnje u odnosu na donju je ±105º, a brzina okretanja gornje gradnje je 10 m/min. U donju gradnju spada još i kablovski bubanj za napajanje celog bagera visokim naponom od 6000 V. Prečnik kabla je Ø78 mm, maksimalna rezerva kabla na bubnju je 1500 m. Pogonski naponi na spravi su 500 V, komandni 220 V kao i naponi za osvetljenje, dok su naponi za ručne lampe i magnetne ventile 24 V.

Na donju gradnju, preko kugličnog aksijalnog ležaja, oslonjena je konstrukcija odložne trake, a sa gornje strane ovešena za vertikalni stub bagera. Odložna traka se zaokreće u krug nezavisno od gornje gradnje. Širina trake je 1600 mm, a brzina kojom se kreće je 4,2 m/s. Ispod odložne trake postoji i posebna traka za otpadni materijal sa sopstvenim pogonom i brzinom od 1 m/s.

U sastav gornje gradnje glodara spada utovrana traka sa radnim točkom, koja je vezana za čeličnu konstrukciju i može se podizati i spuštati preko uređaja za dizanje (čeličnih užadi). Za čeličnu konstrukciju gornje gradnje vezana je i konstrukcija protivtega, kao i montažni kran koji služi za demontažu i montažu delova pri popravci.

Radni točak je prečnika 10 m na kome je postavljeno 20 kašika zapremine 0,63 m^3. Brzina rezanja je 2,827 m/s. Broj istresa je 108-162 min^{-1}. Dozvoljeni nagibi za rad su 5%, a za transport 10%. Ukupna masa celog bagera je 1.499.641 kg, a specifični pritisak na tlo je 0,1 MPa.

Bagerom se upravlja iz dva komandna pulta: iz kabine bageriste, koja je vezana za konstrukciju prijemne trake, i iz kabine trakiste, koja se nalazi na konstrukciji odložne trake.

Slika 1. Rotorni bager - glodar VII (Sch Rs 630) snimljen noću

Reduktori pogona traka su zajedno sa elektromotorima vezani na jedno postolje. Na jednoj strani su zakačeni za rukavce pogonskog bubnja preko izlaznog zupčanika, pomoću elastičnih steznih prstenova, a sa druge strane preko pokretnog zgloba za čeličnu konstrukciju trake. Sa tako izvedenom vezom osa pogonskog bubnja i ose reduktora se uvek seku jedna u odnosu na drugu pod 90º.

Puštanje u pogon trake može se izvoditi na dva načina, sa komandnog pulta, odnosno iz kabine bageriste kada se uključuje kompletni lanac za kretanje celog sistema. Drugi način je pogon na licu mesta preko uređaja za deblokiranje (ovaj pogon se koristi prilikom popravki i proba samo tog dela uz veliku opreznost i stručni nadzor).

2. REDUKTOR BKSH–335

Reduktor BKSH-335 je dvostepeni i koristi se za pogon prijemne i odložne trake na rotornim bagerima za eksploataciju uglja u rudarskom basenu Kolubara. Njegov zadatak je da snagu sa elektromotora prenese na pogonski bubanj koji pokreće prijemnu, odnosno odložnu traku na bageru. Traka koju pokreće je beskonačna, širine 1800 mm, debljine 30 mm i ukupne dužine u oba smera ≈80 m.

Uslovi eksploatacije u kojima se reduktor koristi su prilično loši. Reduktor je pozicioniran na mestu koje je izloženo spoljašnjem uticaju vremenskih i atmosferskih neprilika, tako da radi u po kiši, snegu, prašini, mrazu, vrućini, oksidaciji... Sve pomenute nepogode utiču direktno ili indirektno na stanje reduktora i njegove prateće opreme. U sistemu EPS-a kada je u pitanju eksploatacija uglja izbegavaju se bilo kakvi neplanirani zastoji rotornih bagera. Zbog toga promene stanja reduktora, nije moguće otkloniti do sledećeg planiranog zastoja mašine. Usled toga su i česte pojave havarije ovakvih reduktora, jer otkaz jednog njegovog elementa povlači defekt drugog, pa dolazi do otkaza kompletne pogonske grupe.

Za pogon se koristi sinhroni elektromotor snage 160 kW, koji ima izlazni broj obrtaja 960 o/min. Prateći deo opreme elektromotora je i upuštač koji ima ulogu menjača. Pogonska grupa se startuje na manjem broju obrtaja, a zatim se posle kraćeg vremenskog perioda brzina povećava, da bi tek na kraju dostigla punu vrednost od 960 o/min.

Spojnica se sastoji iz kočionog točka koji je vezan za ulazno vratilo reduktora i prirubnice pričvršćene za vratilo elektromotora. Ovo je najlošiji deo pogonske grupe. Naime, ove dva nezavisna dela međusobno su povezana zavrtnjima koji jednim delom prolaze kroz gumu tvrdoće 50÷60°Sh, koja ima ulogu da amortizuje udare prilikom pokretanja pogonske grupe. Guma je često lošeg kvaliteta i vremenom dolazi do njenog deformisanja što direktno utiče na saosnost vratila na kojima se nalaze.

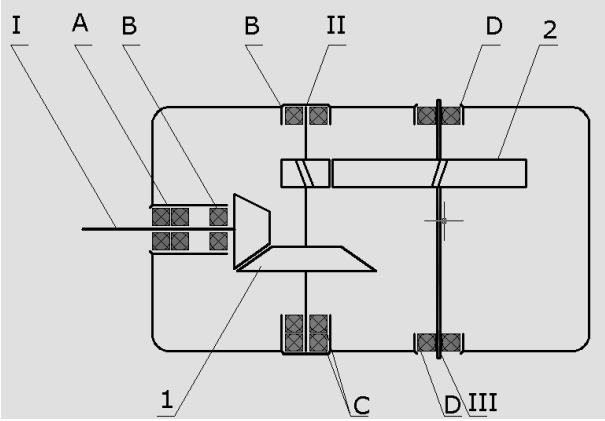

Slika 2. Šema reduktora BKSH-335
(I – ulazno vratilo, II – međuvratilo, III – šuplje vratilo,
1 – tanjirasti zupčanik, 2 – gonjeni cilindrični zupčanik,
A – par konusno-valjkastih ležajeva 31319,
B – cilindrično-valjkasti ležaj NU 2322,
C – par konusno-valjkastih ležajeva 31320,
D – dvoredi bačvasti ležaj 23044)

Kućište reduktora je dvodelno i izrađeno je od ČL0500. Ojačano je rebrima jer je dolazilo do prslina na bočnim stranama. Tokom godina rada kućište je ojačano sa po još jednim rebrom oko glavčina i sada ih ima po tri.

Slika 3. Kućište sa kočionim točkom

Slika 4. Kućište reduktora

Ulazno vratilo (označeno sa I, slika 2) je od čelika za cementaciju Č 4520 i izrađeno je zajedno sa pogonskim, konusnim zupčanikom, koji ima 13 zubaca (z_1=13), modula m_e=8 mm. Vratilo je na ulazu oslonjeno pomoću para konusno-valjkastih ležajeva 31319 (A, slika 3), a na izlazu je cilindično-valjkasti ležaj NU 2322 (B, slika 2).

Gonjeni konusni (tanjirasti) zupčanik (1, slika 2) izrađen je od čelika za cementaciju Č 4321 i spojen sa glavčinom pomoću podešenih zavrtnjeva. Ima 37 zubaca (z_2=37). Glavčina je navučena na međuvratilo (II, slika 2) i osigurana klinom, a izrađena je od čeličnog liva ČL0400.

Međuvratilo (II, slika 2) je izrađeno od čelika za cementaciju Č 4321. U jednom delu je ozubljeno, broj zuba je z_3=20, a modul m=6 mm. Oslonjeno je na jednom kraju preko para konusno-valjkastih ležajeva 31320 (C, slika 2), a na drugom pomoću cilindrično-valjkastog ležaja NU 2322 (B, slika 2).

Izlazni zupčanik (2, slika 2) je izrađen od čelika za cementaciju Č 4321. Ima 88 zubaca (z_4=88), a modul mu je m=6 mm. Navučen je na šuplje vratilo.

Šuplje vratilo (3, slika 2) je izrađeno od čelika za poboljšanje Č 4732. Oslonjeno je bačvastim dvoredim ležajevima 23044 (D, slika 2). Kroz šuplje vratilo je provučeno vratilo bubnja. Neposrednom vezom šuplje vratilo prenosi obrtni moment na vratilo bubnja, čime ga pokreće, dovodeći traku u pogon, tako da pri najvećem broju obrtaja reduktora, traka širine 1600 mm dostiže brzinu od 4 m/s.

Podmazivanje reduktora je rešeno tako što se zupčanici, vratila i ležajevi podmazuju prirodnim putem. U reduktor se pre početka rada sipa 60 l ulja tipa EP koje zadržava svoja svojstva i pri temperaturi od 70÷80°C. Ulje se sipa u za to predviđene komore do određenog nivoa i prilikom rada dolazi do prirodnog kruženja ulja bez dodatnih pumpi.

3. POSTUPAK REMONTA REDUKTORA BKSH–335

Reduktor se demontira sa pogonske grupe bagera-glodara i transportuje u radionicu na remont. Doprema se sa kočionim točkom, koji ga vezuje sa spojnicom, a bez postolja. Remontne aktivnosti su sledeće:

- obezbeđivanje adekvatnog radnog prostora za demontažu, defektaciju i montažu reduktora,
- rasklapanje i demontaža reduktora,
- defektacija delova i sklopova reduktora,
- regeneracija starih delova ili izrada novih delova (koji su defektažom utvrđeni kao neupotrebljivi u daljoj eksploataciji),
- kontrola izvršenih radova,
- kompletiranje reduktora,
- montaža podsklopova i sklopova,
- završna montaža i priprema reduktora za probni rad,
- probni rad reduktora i izrada izveštaja o ispitivanju,
- transport reduktora na bager glodar.

Radni prostor za reduktor je površine od oko 180 m^2. Ograđen je limenom ogradom visine 2 m. Snabdeven je svim potrebnim energetskim kapacitetima, kao što su:

- komprimovani vazduh,
- sistem za gasno zavarivanje,
- električna energija napona 380 V,
- iznad radnog prostora funkcioniše kran od 40 t nosivosti, koji poseduje dve kuke, jednu nosivosti do 5 t i drugu nosivosti do 40 t,
- regali postavljeni u dva nivoa duž zidova prostorije, namenjeni za odlaganje sitnih delova,
- dobro osnovno osvetljenje sa još četiri reflektora postavljena po dijagonali,
- pokretni hidraulički agregat od 2,8 l, maksimalnog pritiska 600 bar,
- radni stolovi sa stegama.

4. PRANJE I ODMAŠĆIVANJE

Reduktor se unutrašnjim transportom (viljuškarom) prenosi na pranje, gde se uklanjaju sve spolja dostupne nečistoće. Pranje se izvodi toplom vodom pod pritiskom da bi se uklonile naslage blata, uglja, masnoće od ulja...

Posle pranja reduktor se doprema u radionicu, gde se obavljaju dalje aktivnosti utvrđene tehnološkim postupkom. Defektatori pristupaju svom osnovnom zadatku, pregledu reduktora,

stvaraju sliku stanja i svoja zapažanja unose u defektacioni list.

Prvo se demontira spojnica pomoću hidrauličnog agregata, protoka 6 l/min i maksimalnog pritiska 600 bar, i hidrauločnog uređaja koji stvara silu od $5 \cdot 10^5$ N. Iz reduktora se najpre ističe staro ulje, zatim se kućište reduktora razdvaja i skidaju se svi bočni poklopci. Vade se elementi (podsklopovi) iz kućišta: ulazno vratilo, međuvratilo i izlazni zupčanik sa šupljim vratilom. Kućište reduktora se zatim ponovo sastavlja, polutke se postavljaju jedna na drugu tako da budu centrirane i ponovo stežu bez bočnih poklopaca.

Otvori za ležajeve u kućištu se odmašćuju, pripremaju za vizuelnu kontrolu stanja otvora i merenje. Podsklopovi se spremaju za defektaciju. Ozubljenja se pripremaju za vizuelnu i magnetnofluksnu kontrolu pranjem trihloretilenom. Ležajevi se odmašćuju i pripremaju za vizuelnu kontrolu i merenja zazora. Vratila se odmašćuju, a otvori u šupljem vratilu se pripremaju za defektažu.

Kao sredstva za pranje i odmašćivanje koriste se: trihloretilen, famin, za ozubljenje nitrorazređivač, naročito prilikom ispitivanja magnetnim fluksom i ultrazvukom.

Slika 5. Šuplje vratilo sa izlaznim zupčanikom i ležajevima

5. DEFEKTACIJA

Pri defektaciji kontrolišu se:

- otvori za ležajeve na kućištu,
- ukupno stanje kućišta,
- ležajevi i njihovi radijalni zazori,
- ozubljenja,
- elementi za vezu na zupčanicima (otvori, žljebovi za klinove),
- radijalna bacanja vratila,
- prečnici i pohabanost rukavaca vratila,
- pojava prslina na delovima reduktora (kontrolom magnetnim fluksom ili ultrazvukom),
- pohabanost kočionog točka.

Na kočionom točku se vrši merenje prečnika otvora u spojnici Ø75H7. Vizuelnom kontrolom radne površine kočionog točka je ustanovljen defektni sloj (risevi), koji su nastali verovatno pohabanošću obloga na paknovima (slika 6). Točak se šalje na strugarsku obradu i balansiranje.

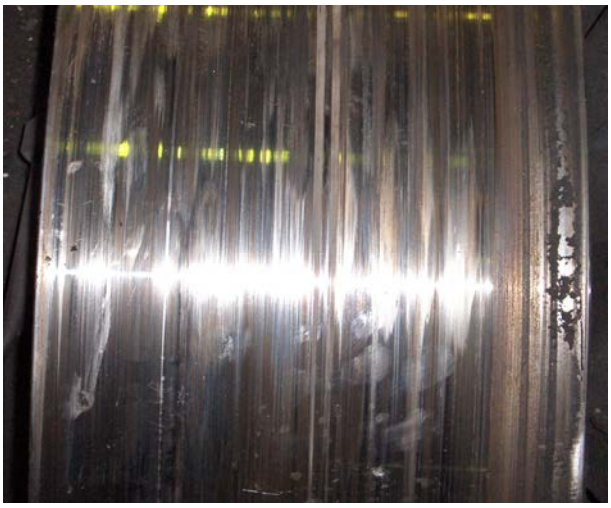

Slika 6. Prikaz oštećenog površinskog sloja kočionog točka

Na kućištu reduktora vizuelnom kontrolom proveravaju se varovi oko glavčina i svi podužni varovi, kao i promene (lom ili prsline) osnovnog materijala, zatim stanje revizionih poklopaca, kao i otvora za ležajeve (Ø275H7 – na mestu ulaznog vratila; Ø260H7 – na mestu međuvratila; Ø340H7 – na mestu izlaznog vratila), koji su ispitivani i merenjem u tri pravca (slika 7).

Slika 7. Prikaz merenja otvora za ležajeve na kućištu

Prilikom vizuelne kontrole ulaznog vratila ustanovljena su oštećenja na rukavcu na koji nailazi ležaj koji se grejao u toku rada. Skinut je cementirani sloj, tragovi su vidljivi (slika 8).

Izvršeno je magnetnofluksno ispitivanje zuba konusnog zupčanika, rukavaca i prelaznih radijusa i nisu uočene nikakve indikacije tipa spoljašnjih prslina. Istovremeno je izvršena kontrola ostalih rukavaca na ulaznom vratilu i ustanovljeno da su mere u granicama preporučenih tolerancija (Ø75k6, Ø80h8, Ø95j6 i Ø110k6). Na kraju je vršena provera radijalnog bacanja vratila. Postavljeno je na strug, pročišćena su mu središna gnezda i komparaterom su očitane mere bacanja vratila.

Slika 8. Prikaz oštećenja rukavca ulaznog vratila

Vizuelnom kontrolom tanjirastog zupčanika uočena je labavost veze između tanjirastog zupčanika i glavčine za koju je pričvršćen. Tokom rada došlo je do oštećenja otvora Ø18 mm. Otvori moraju biti razbušeni na prvu veću meru da bi se ponovo ostvarila veza podešenim zavrtnjevima. Kontrolisani su i otvor u zupčaniku i žljeb za klin, čije mere se nalaze u granicama preporučenih tolerancija.

Slika 9. Međuvratilo sa tanjirastim zupčanikom i ležajevima

Vuzuelnom kontrolom međuvratila ustanovljeno da nema oštećenja zubaca na ozubljenom delu vratila, ali su vidljiva oštećenja rukavca na koji se navlači par konusno-valjkastih ležajeva (slika 10). Merenjem je ustanovljeno da su prečnici drugih rukavaca u granicama tolerancija.

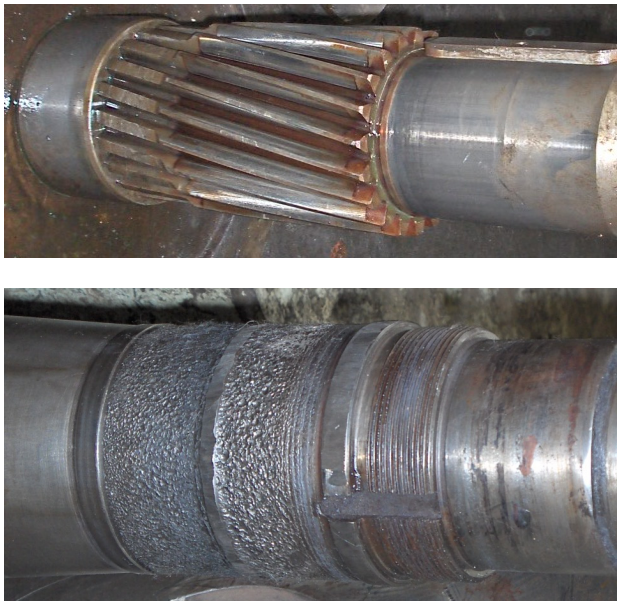

Slika 10. Međuvratilo sa oštećenim rukavcem

Vizuelnom kontrolom gonjenog cilindričnog zupčanika ustanovljeno je da nedostaje skoro polovina jednog zupca (slika 11). Zbog ovakvog oštećenja neophodna je regeneracija zupčanika.

Slika 11. Izlazni zupčanik

I šuplje vratilo je dijagnostikovano vizuelnim metodom i tehničkim merenjima. Na njemu nema vidljivih oštećena, niti tragova udara i naprsnuća. Merenjem je ustanovljeno da se sve mere nalaze u granicama tolerancija.

Defektacija ležajeva podrazumeva vizuelnu kontrolu, merenje radijalnih zazora i uparivanje paketa ležajeva. Vizuelnom kontrolom je ustanovljeno da nema oštećenja ležajeva niti

njihovih kotrljanih elemenata. Merenjem zazora na ležajevima utvrđeno je:

- paket ležajeva na ulaznom vatilu (31319) je van preporučenih tolerancija, pa je potrebna zamena,
- ležaj na ulaznom vatilu NU 2322 ima nedopušteni zazor i on se mora zameniti,
- ostali ležajevi su u granicama preporučenih tolerancija od strane proizvođača.

Slika 12. Merenje radijalnih zazora ležaja

Na osnovu rezultata merenja i ispitivanja doneta je odluka da se:

- kočioni točak na krutoj spojnici obradi struganjem na prvu veću meru radi boljeg prijanjanja paknova kočnice i izvrši dinamičko uravnoteženje(balansiranje),
- na ulaznom vratilu izvrši zamena svih ležajeva sa obaveznim uparivanjem para ležajeva 31319,
- pohabani rukavci ulaznog vratila i međuvratila regenerišu se metalizacijom sa brušenjem na nominalne mere,
- gonjeni cilindrični zupčanik regeneriše navarivanjem polomljenog zupca.

6. ZAKLJUČAK

Reduktor ulazi u redovan remont jednom godišnje, za vreme planirane investicione popravke ili remonta, ili ukoliko se desi neki neplanirani kvar ili havarija. Najčešći razlozi remonta reduktora su: zagrevanje ležajeva, curenje ulja iz reduktora, povećana bučnost reduktora, pohabanost rukavaca vratila, lom zubaca zupčanika.

LITERATURA

[1] J. Jevtić: Reduktori – proračuni i konstrukcije, Privredni pregled, Beograd, 1976.

[2] S. Marković, D. Josifović: *Regeneracija zupčanika*, monografija, Jugoslovensko tribološko društvo, Kragujevac, 1998.

[3] S. Marković: *Održavanje mašina i opreme*, Viša tehnička škola, Čačak, 2005.

[4] M. Trbojević, M. Janković, J. Vugdelija, N. Plavšić, V. Latinović: *Reduktori*, Naučna knjiga, Beograd, 1991.

[5] www.rbkolubara.co.yu.

DEFECTATION OF THE REDUCER BKSH-335 FOR THE ACTIVATION OF THE BAND TRANSPORTER OF THE DREDGER Sch Rs 630

Abstract: *The repair of a powerful mechanical system such as dredger Sch Rs 630 is based on the high level of reliability, accuracy and functioning of all its circuits. Due to the reasons listed above the rapair of the mentioned reducer must be done with thorough defectation, suitable regeneration technology, embedding of quality parts (gears, shafts, bearings) and proper installation of the parts into the reducer, and installation of the reducer onto the dredger itself. All the mentioned factors are essential and they influence the proper operation of the reducer. Also, it is necessary to pay attention to the economical adequacy of this type of work. In big systems every non-planned work failure brings enormous costs. Neither it is recommended nor acceptable that the failure in the dredger work has its cause in a malfunction of the similar reducer.*

Keywords: *dredger, reducer, defectation, repair.*

ACKNOWLEDGMENT

This work has been performed within the project TR 35011. This project is supported by the Republic of Serbia, Ministry of Science and Technological Development, which financial help is gratefully acknowledged.

Serbian Tribology Society

SERBIATRIB '13

13th International Conference on Tribology

Faculty of Engineering in Kragujevac

Kragujevac, Serbia, 15 – 17 May 2013

ISPITIVANJE MEHANIČKIH I STRUKTURNIH OSOBINA PREVLAKA OTPORNIH NA EROZIJU I VISOKE TEMPERATURE

Mihailo R. Mrdak[1]

[1]Istraživački razvojni centar, IMTEL Komunikacije a.d., Beograd, Srbija, miki@insimtel.com

Apstrakt: *Cilj ovog rada bio je da se ispitaju mehaničke i strukturne karakteristike termo-barijernih prevlaka TBC otpornih na eroziju i visoke temperature. Deponovana su tri tipa TBC sistema dvojnih prevlaka sastavljenih od metalne vezne prevlake NiCrAlCoY_2O_3 i keramičkih izolacionih prevlaka ZrO_2MgO, $ZrO_2Y_2O_3$ i $ZrO_2CeO_2Y_2O_3$. TBC sistemi prevlaka su deponovani atmosferskim plazma sprej postupkom (APS) na ohrapavljenim čeličnim substratima sa temperaturom od 160 – 180 °C. Prevlake su deponovane sa optimalnim parametrima depozicije prahova. Vezni slojevi su deponovani sa jednim prolazom plazma pištolja, a keramički slojevi sa četrnest prolaza. Procena kvaliteta slojeva je urađena ispitivanjem mikrotvrdoće metodom $HV_{0.1}$ i zatezne čvrstoće spoja ispitivanjem na zatezanje. Metalografska procena udela mikro pora (image analiza) u strukturi veznih i keramičkih slojeva je urađena tehnikom svetlosne mikroskopije. Morfologije čestica praha je urađena na SEM-u. Analize izvršenih ispitivanja su omogućile da se odaberu TBC sistemi prevlaka sa najboljim mehaničkim i strukturnim karakteristikama.*

Ključne reči: *atmosferski plazma sprej (APS), termo barijerne prevlake, mikrostruktura, interfejs, mikrotvrdoća, čvrstoća spoja.*

1. UVOD

Termo barijerne prevlake (TBC) su grupe prevlaka namenjene za posebne uslove rada zbog svojih specifičnih karakteristika. Prevlake su našle široku primenu kao zaštita delovima izloženim visokim temperaturama, visokotemperaturnoj abraziji čestica, oksidaciji i toploj koroziji. Osnovna uloga TBC je da obezbedi mogućnost rada osnovnog materijala na temperaturama koje su iznad granice njegove izdržljivosti spuštanjem stvarne temperature na donjoj površini veznog sloja TBC sistema za ΔT = 200 – 400 °C [1,2]. Keramički sloj mora da zadrži nisku toplotnu provodljivost tokom dužeg izlaganja u uslovima eksploatacije i da ima dobru otpornost na abraziju čestica, koja može da javi u različitim vidovima [3]. Keramička prevlaka se u poređenju termičkih koeficijenata razlikuje od komponente na koju se primenjuje. Ovaj sloj treba da bude usklađen sa osnovnim materijalom preko veznog sloja. Donji vezni sloj koji je tanji u odnosu na keramički sloj mora da ima dobru vezu sa substratom i keramikom, spreči difuziju na interfejsu, poveća otpornost na koroziju i smanji uticaj zaostalih napona u keramici [4-7].

Kompozitni prah NiCr-Al-Co-Y_2O_3 koji se koristi za proizvodnju veznog sloja je obložen oksidom Y_2O_3 koji je stabilizator u keramičkim prevlakama. Oksid Y_2O_3 koji je istovremeno prisutan u metalnom i keramičkom prahu poboljšava vezu između metalnih i keramičkih slojeva [8]. Za proizvodnju keramičkih slojeva koriste se prahovi kao što su Metco 210NS – ZrO_2MgO, Metco 202NS – $ZrO_2Y_2O_3$ i Metco 205NS – $ZrO_2CeO_2Y_2O_3$ i dr. [9-11]. Atmosferski plazma sprej postupak (APS) je standardni proces za deponovanje termalnih barijera. Čestice praha se ubrizgavaju u protok plazma gasa i ubrzavaju usled prenosa brzine i temperature jona na čestice praha. Pod uticajem substrata, čestice se plastično deformišu i vezuju za substrat da bi se formirala prevlaka. Proces omogućuje deponovanje širokog spektra prahova: legura, keramike, karbida, metalo-karbida, metalo-keramike, kompozitnih prahova i dr. Na kvalitet deponovanih prevlaka utiče veliki broj parametara. Opis atmosferskog plazma sprej

postupka i uticaja parametara depozicije praha na kvalitet prevlaka dat je detaljnije u radovima [12-15]. Jedan od veoma bitnih parametara koji utiče na kvalitet i trajnost TBC u eksploataciji je temperatura substrata na kojoj se deponuju slojevi. Prema ranijim istraživanjima, plazma deponovani keramički depoziti pokazuju lamelarnu strukturu sa ograničenom intelamelalnim vezivanjem [16]. Zbog toga su u depozitu prisutne mikro pore kao zapreminske greške sa velikim koncentracijama napona koji uzrokuju pojavu mikro pukotina. Ograničeno vezivanje lamela u depozitu smanjuje vrednosti tvrdoće, modul elastičnosti, žilavost loma i toplotnu provodljivost odgovarajućeg materijala [17-19].

Predgrevanje substrata se koristi za povećanje adhezije prevlake, poboljšanje mikrostrukture i mehaničkih svojstava [2, 20-22]. Svojstava TBC depozita su uglavnom pod kontrolom morfologije deponovanih čestica i interakcija/prianjanje među njima. Jedan od uzroka propadanja keramičkih prevlaka je termičko opterećenje. Nagle promene temperature mogu uzrokovati pucanje i odvajanje celog TBC sistema sa substrata zbog značajne razlike koeficijenata linearnog širenja keramike i metala. Drugi način propadanja keramičkih prevlaka nastaje od erozije čestica na visokim temperaturama. Ispitivanja otpornosti keramičkih prevlaka na eroziju čestica Al_2O_3 veličine od 15 μm do 53 μm, za isti nivo poroznosti, na 980 °C su pokazala da najveću otpornost imaju keramičke prevlake $ZrO_2CeO_2Y_2O_3$ sa zapreminskim gubitkom $1{,}72 \times 10^4$ cm^3/gm. Za prevlaku $ZrO_220Y_2O_3$ zapreminski gubitak je nešto viši $1{,}95 \times 10^4$ cm^3/gm, dok je za prevlaku ZrO_2MgO zapreminski gubitak bio najviši $3{,}03 \times 10^4$ cm^3/gm [11].

U ovom radu su ispitana tri tipa TBC sistema prevlaka $NiCrAlCoY_2O_3$ / ZrO_2MgO, $NiCrAlCoY_2O_3$ / $ZrO_2Y_2O_3$ i $NiCrAlCoY_2O_3$ / $ZrO_2CeO_2Y_2O_3$. Prahovi su deponovani na predgrejanim substratima sa temperaturom od 160 – 180 °C sa ciljem poboljšanja interlamelarne veze, mikrostrukture i mehaničkih svojstava. Izvršena su metalografska ispitivanja sadržaja mikro pora i oksida u veznim slojevima i mikro pora u keramičkim prevlakama. Za svaki sistem TBC prevlaka su ispitane mikrotvrdoće i zatezne čvrstoće spoja. Analize rezultata izvršenih ispitivanja su omogućile da se ustanovi koji sistem prevlaka ima najbolje strukturno mehaničke karakteristike.

2. EKSPERIMENTALNI DETALJI

2.1 Materijali

Materijal na kome su deponovane termalne barijere je bio od nerđajućeg čelika X15Cr13 (EN 1.4024) u termički neobrađenom stanju. Za izradu termalnih barijera su upotrebljena četiri praha firme Sulcer Metko (Sulzer Metco) sa oznakama: Metco 461 ($NiCr/Al/Co/Y_2O_3$), Metco 210NS (ZrO_2MgO), Metco 202NS ($ZrO_2Y_2O_3$) i Metco 205NS ($ZrO_2CeO_2Y_2O_3$) [8-11].

Kompozitni prah $NiCr/Al/Co/Y_2O_3$ je NiCr legura sa 17,5 tež.% Cr obložena sa 5,5 tež.% Al, 2,5 tež. % Co i 0,5 tež. % Y_2O_3. Prah koji je korišćen u eksperimentu je imao raspon granulacije čestica od 45 μm do 150 μm. Temperatura topljenja praha je 1400 °C. Na slici 1 je prikazama SEM mikrofotografija praha $NiCr/Al/Co/Y_2O_3$ na kojoj se vide čestice praha nepravilnog oblika.

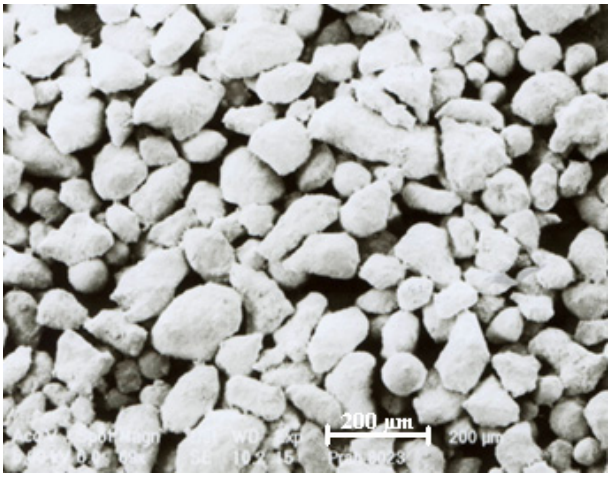

Slika 1. (SEM) morfologija čestica praha NiCr-Al-Co-Y_2O_3

Keramički prah ZrO_2MgO je proizveden topljenjem. Prednost ove metode je predlegiranost i prirodna homogenizacija čestica praha. Keramika ZrO_2MgO je predlegirana sa 25 tež.% MgO. Za eksperiment je korišćen prah uglastog oblika sa rasponom granulacije čestica od 10 μm do 53 μm. Temperatura topljenja praha je 2140 °C.

Prah $ZrO_2Y_2O_3$ je proizveden tehnološkim postupkom aglomeracije finih čestica keramike sa 80 tež.% ZrO_2 i 20 tež.% Y_2O_3 i suvim raspršivanjem. Tako proizveden prah ima sfernu morfologiju čestica. Raspon granulacije čestica je bio od 45 μm do 106 μm sa temperaturom topljenja praha 2480 °C.

Čestice praha $ZrO_2CeO_2Y_2O_3$ su proizvedene homogenizacijom u peći i procesom sferoidizacije HOSP. Keramika $ZrO_2CeO_2Y_2O_3$ je potpuno predlegirana sa 24 – 26 tež.% CeO_2 i 2 – 3 tež.% Y_2O_3. Morfologije čestica praha su prikazane na slici 2.

SEM mikrofotografija pokazuje da su čestice praha sa sfernim morfologijama koje omogućavaju odličan protok praha u mlaz plazme i uniformno topljenje. Prah koji je korišćen u eksperimentu je imao raspon čestica od 45 – 90 μm sa temperaturom topljenja 2480 °C.

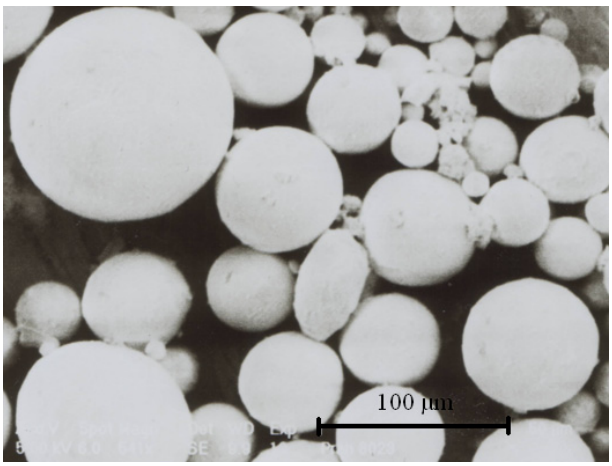

Slika 2. (SEM) morfologija čestica praha $ZrO_2CeO_2Y_2O_3$

Uzorci za merenje tvrdoće i metalografska ispitivanja su pravougaoni 70 × 20 × 1,5 mm, dok su za zateznu čvrstoću spoja korišćeni cilindrični uzorci Ø25 × 50 mm.

Merenja mikrotvrdoća su izvršena korišćenjem Vikers dijamant piramide indenter i 100 grama opterećenje ($HV_{0.1}$). Merenje je obavljeno u pravcu duž lamela, u sredini i na krajevima uzorka. Na pet mesta sprovedeno je pet očitavanja a prikazane su minimalne i maksimalne vrednosti.

Testovi zatezne čvrstoće spoja su vršeni na sobnoj temperaturi na hidrauličnoj opremi sa brzinom od 10 mm/min, za sva ispitivanja. Čvrstoća je izračunata tako što se opterećenje kidanja deli sa površinom poprečnog preseka uzorka. Geometrija uzoraka je u skladu sa ASTM C633 standardom, koji je detaljnije obrađen u radu [23]. Korišćeni su u paru dva uzoraka, od kojih je prevlaka deponovana samo na jednom od njih. Uzorci su zalepljeni lepkom i čuvani pod pritiskom jedni prema drugom u peći na temperaturi od 180 °C za 2 sata. Za svaki grupu uzoraka urađene su tri epruvete a prikazane su minimalne i maksimalne vrednosti. Mehaničke i mikrostrukturne karakterizacije dobijenih prevlaka su izvršene prema standardu Pratt & Whitney [24].

Mikrostrukturna analiza prevlaka i image analiza udela mikro pora sa oksidima u veznim prevlakama i udela mikro pora u keramičkim prevlakama urađena je na svetlosnom mikroskopu. Morfologija čestica praha i morfologija površine keramičke prevlake urađena je na SEM-u (skening elektronskom mikroskopu).

2.2 Plazma sprej parametri

Depozicija prahova je urađena sa atmosferski plazma sprej sistemom firme Plasmadyne i plazma pištoljem SG-100, sa odgovarajućim robotizovanim kontrolnim sprej uslovima. Plazma pištolj SG-100 se sastojao od katode tipa K 1083-129, anode tipa A 2084-145 i gas injektora tipa GI 2083-113. Za sve deponovane prevlake kao lučni gas korišćen je Ar u kombinaciji sa He i snaga napajanja od 40 KW. Plazma sprej parametri depozicije su prikazani u tabeli 1. Pre procesa deponovanja površine čeličnih substrata su hrapavljene sa česticama korunda veličine od 0,7 – 1,5 mm i predgrejane na temperaturu od 160 – 180 °C. Vezne prevlake VP – $NiCrAlCoY_2O_3$ su deponovane sa jednim prolazom plazma pištolja debljine 0,068 – 0,093 mm. Sve keramičke prevlake su deponovane sa 15 prolaza plazma pištolja. Prevlaka A – ZrO_2MgO je deponovana sa debljinom 0,486 – 0,50 mm, prevlaka B – $ZrO_2Y_2O_3$ sa debljinom 0,375 – 0,41 mm i prevlaka C – $ZrO_2CeO_2Y_2O_3$ sa debljinom 0,425 – 0,470 mm.

Tabela 1. Parametri depozicije prevlaka VP – $NiCrAlCoY_2O_3$, A – ZrO_2MgO, B – $ZrO_2Y_2O_3$ i C – $ZrO_2CeO_2Y_2O_3$

Parametri depozicije	VP	A	B	C
Plazma struja, I (A)	900	900	900	900
Plazma napon, U (V)	38	38	38	38
Primarni plazma gas protok Ar, l/min	47	47	47	47
Sekundarni plazma gas protok He, l/min	12	12	12	12
Noseći gas protok Ar, l/min	5	7	6	6
Protok praha, g/min	60	50	50	50
Odstojanje substrata, mm	115	100	90	90

3. REZULTATI I DISKUSIJA

3.1 Mikrotvrdoća

Vrednosti mikrotvrdoće za sve vezne prevlake $NiCrAlCoY_2O_3$ su izmerene u rasponu od min. 279 $HV_{0.1}$ do max. 322 $HV_{0.1}$. Raspodele mikrotvrdoće u veznim prevlakama su posledica različite raspodele mikro pora i oksida u deponovanim slojevima. Ove vrednosti su potvrđene image analizom pri određivanju ukupnog sadržaja mikro pora i oksida u veznim slojevima. Na slici 3 su prikazane min. i max. vrednosti mikrotvrdoće keramičkih prevlaka A – ZrO_2MgO, B – $ZrO_2Y_2O_3$ i C – $ZrO_2CeO_2Y_2O_3$.

Kao što se i očekivalo za sve tri keramičke prevlake dobile su se različite vrednosti mikrotvrdoće kao posledica uticaja različitih vrsta i sadržaja stabilizatora MgO, Y_2O_3 i kombinacije $CeO_2Y_2O_3$. Najveće vrednosti mikrotvrdoće su izmerene u keramičkim slojevima A – ZrO_2MgO sa raspodelom mikrotvrdoće od min. 611 do max. 662 $HV_{0.1}$, a najmanje vrednosti mikrotvrdoće su izmerene u slojevima C – $ZrO_2CeO_2Y_2O_3$ sa raspodelom mikrotvrdoće od min. 525 do max. 542 $HV_{0.1}$. Raspodele mikrotvrdoće u keramičkim prevlakama su, kao i u veznim prevlakama,

posledica različite raspodele mikro pora u keramičkim slojevima. Najmanja raspodela mikrotvrdoće je izmerena u keramičkim slojevima C – $ZrO_2CeO_2Y_2O_3$, a najveća u keramičkim slojevima A – ZrO_2MgO. Raspodele vrednosti mikrotvrdoće u keramičkim slojevima su bile u skladu sa sadržajem mikro pora, što su potvrdile image analize keramičkih prevlaka.

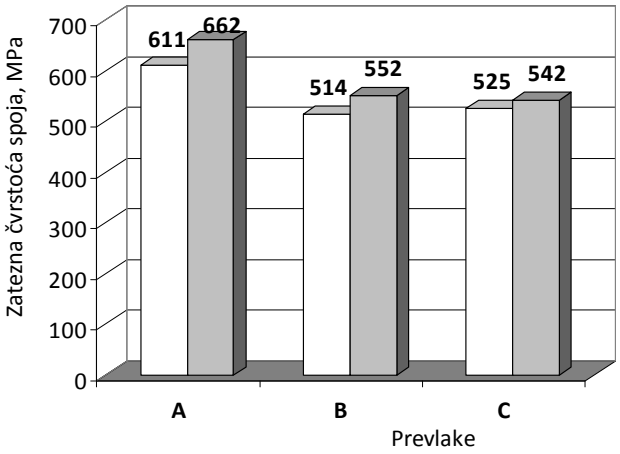

Slika 3. Mikrotvrdoća prevlaka

3.2 Zatezna čvrstoća spoja

Na slici 4 su prikazane min. i max. vrednosti zatezne čvrstoće spoja sistema prevlaka $NiCrAlCoY_2O_3$ / ZrO_2MgO, $NiCrAlCoY_2O_3$ / $ZrO_2Y_2O_3$ i $NiCrAlCoY_2O_3$ / $ZrO_2CeO_2Y_2O_3$.

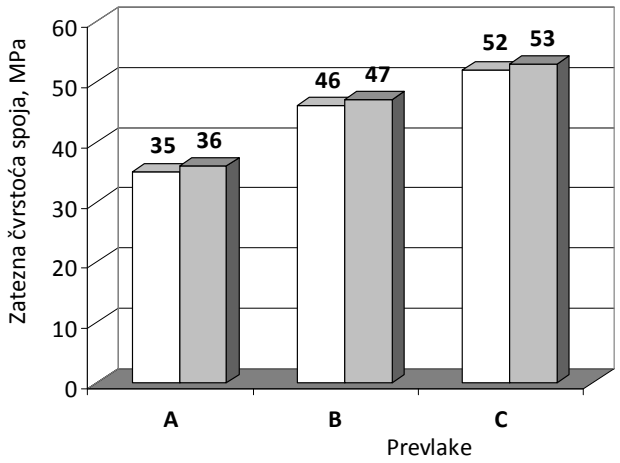

Slika 4. Zatezna čvrstoća spoja prevlaka

Za sve sisteme prevlaka su izmerene dobre vrednosti zatezne čvrstoće spoja. Predgrevanje substrata je omogućilo da se deponuju prevlake sa dobrim vezivanjem lamela vezne prevlake za supstrate i lamela vezne prevlake sa keramičkim lamelama. Veća temperatura substrata je uticala na povećanje adhezije prevlaka, mehaničkih svojstava i poboljšanje mikrostrukture, što su potvrdila metalografska ispitivanja.

Najveće vrednosti zatezne čvrstoće spoja je imao sistem prevlaka $NiCrAlCoY_2O_3$ / $ZrO_2CeO_2Y_2O_3$ sa rasponom od 52 – 53 MPa, a najniže vrednosti sistem prevlaka $NiCrAlCoY_2O_3$ / ZrO_2MgO sa rasponom od 35 – 36 MPa. Oksid Y_2O_3 koji je istovremeno bio prisutan u vezno $NiCrAlCoY_2O_3$ i keramičkoj prevlaci $ZrO_2CeO_2Y_2O_3$ je uticao na bolju inter-lamelarnu kohezivnu čvrstoću između dve prevlake. Sistem prevlaka $NiCrAlCoY_2O_3$ / $ZrO_2Y_2O_3$ je iz istog razloga imao veću vrednost zatezne čvrstoće spoja sa raspodelom od 46 – 47 MPa u odnosu na TBC sistem $NiCrAlCoY_2O_3$ / ZrO_2MgO. Izmerene vrednosti su potvrdile da temperatura substrata ima bitan uticaj na zatezne čvrstoće spoja. Za sve uzorke lom se dešavao na interfejsu između veznih slojeva i substrata.

3.3 Mikrostruktura

Image analiza veznih prevlaka $NiCrAlCoY_2O_3$ je pokazala da je ukupan sadržaj mikro pora i oksida u slojevima bio od min. 18 % do max. 22 %. Raspon ukupnog sadržaja mikro pora i oksida u veznim prevlakama su posledica različite raspodele mikro pora i oksida u deponovanim slojevima. Na slici 5 je prikazana mikrostruktura vezne prevlake $NiCrAlCoY_2O_3$ u sistemu sa keramičkom prevlakom $ZrO_2CeO_2Y_2O_3$. Vezni slojevi imaju uniformnu lamelarnu strukturu. Granice na interfejsu između podloge i prevlake se jasno mogu videti. Na interfejsu sa podlogom i keramičkim slojem nisu prisutne mikro pukotine i makro pukotine i ne postoji odvajanje slojeva prevlake i ljuštenje sa metalnih substrata.

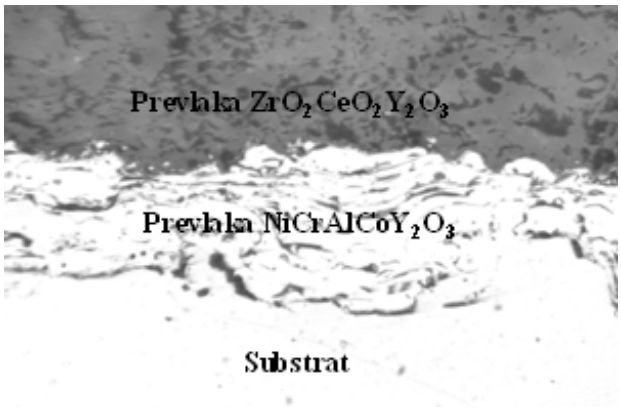

Slika 5. Mikrostruktura prevlake $NiCrAlCoY_2O_3$

Kroz slojeve $NiCrAlCoY_2O_3$ prevlake se jasno uočavaju tamni lamelarni oksidi i mikro pore. Podužne oksidne lamele oksida su formirane u tečnom stanju u plazmi [8].

SEM analiza morfologije površine keramičke prevlake $ZrO_2CeO_2Y_2O_3$ pokazuje potpuno topljenje i razlivanje keramičkih čestica na prethodno deponovani keramički sloj. Na slici 6 je prikazana SEM mikrofotografija površine keramičke prevlake $ZrO_2CeO_2Y_2O_3$.

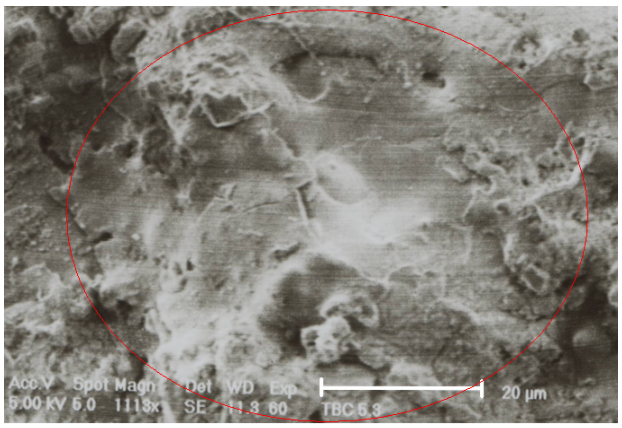

Slika 6. SEM mikrofotografija površine prevlake $ZrO_2CeO_2Y_2O_3$

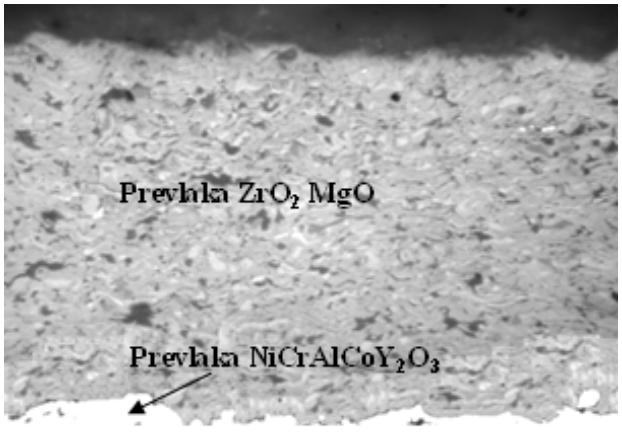

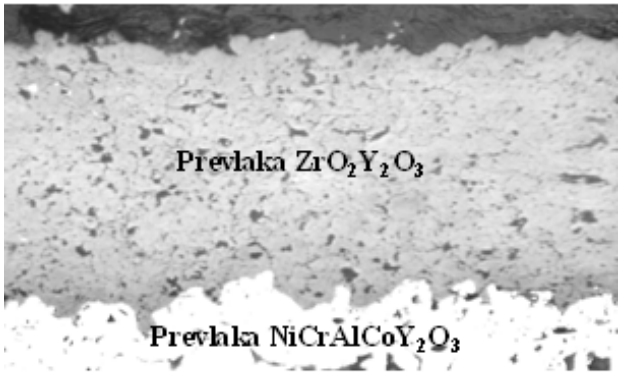

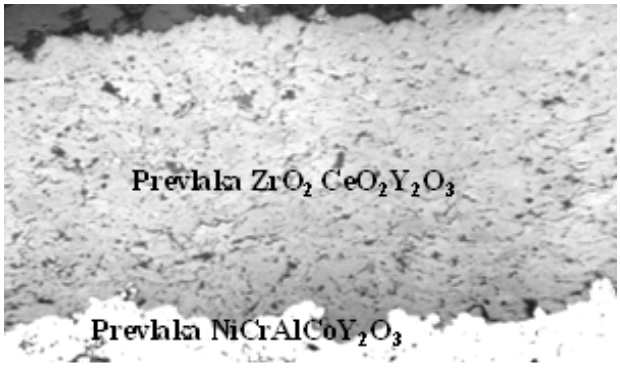

Slika 7. Mikrostrukture keramičkih prevlaka: A – ZrO_2MgO, B – $ZrO_2Y_2O_3$ i C – $ZrO_2CeO_2Y_2O_3$; uvećanje 200×

Na SEM mikrofotografiji je crvenom linijom zaokružena površina jedne istopljene i razlivene čestice praha. Potpuno istopljena čestica praha je formirala tanak disk u sudaru sa površinom prethodno deponovanog sloja. Morfologija deponovane čestice potvrđuje da su istopljene čestice u sudaru sa podlogom formirale pravilan oblik i kao takve ostvarile dobru vezu sa prethodno deponovanim česticama. U poprečnom preseku prevlake deponovane čestice imaju lamelarnu strukturu.

Image analiza ukupnog sadržaja mikro pora u keramičkim prevlakama ZrO_2MgO, $ZrO_2Y_2O_3$ i $ZrO_2CeO_2Y_2O_3$ je pokazala da slojevi imaju različiti udeo pora. Najmanji udeo mikro pora je izmeren u prevlaci $ZrO_2CeO_2Y_2O_3$ sa sadržajem od 14 %. U keramičkoj prevlaci $ZrO_2Y_2O_3$ je izmeren udeo mikro pora od 16 %, a u prevlaci ZrO_2MgO je izmeren udeo mikro pora od 17 %. Morfologija čestica praha je bitan parametar za ravnomeran tok praha u plazmi i na njegovo topljenje. Keramički prah $ZrO_2CeO_2Y_2O_3$ sa sfernom morfologijom čestica koje imaju glatku površinu su omogućile izvrsno i uniformno topljenje čestica u odnosu na klasične postupke izrade prahova [11]. Ravnomerno istopljene čestice praha se pravilnije oblikuju u sudaru sa substratom i deponuju slojeve sa manjim sadržajem pora, koji imaju veću kohezionu čvrstoću i zateznu čvrstoću spoja. Na slici 7 su prikazana mikrostrukture keramičkih prevlaka ZrO_2MgO, $ZrO_2Y_2O_3$ i $ZrO_2CeO_2Y_2O_3$.

Na interfejsu između keramičkih slojeva i veznih prevlaka nisu prisutne pukotine. Na uzorcima nije uočeno ljuštenje – piling keramičkih slojeva sa substrata. U keramičkim slojevima su prisutne tamne površine koje predstavljaju mikro pore sa različitim udelima u zavisnosti od vrste keramičke prevlake. Izmerene vrednosti sadržaja mikro pora u keramičkim slojevima su u skladu sa mikrotvrdoćama i mikrostrukturama.

4. ZAKLJUČAK

Na osnovu rezultata prikazanih u ovom radu može se zaključiti, da sistemi prevlaka $NiCrAlCoY_2O_3$ / ZrO_2MgO, $NiCrAlCoY_2O_3$ / $ZrO_2Y_2O_3$ i $NiCrAlCoY_2O_3$ / $ZrO_2CeO_2Y_2O_3$ imaju dobra svojstva. Predgrevanje substrata pre depozicije prevlaka je omogućilo da se dobiju slojevi sa dobrim mikrostrukturama i mehaničkim osobinama. Keramički prah $ZrO_2CeO_2Y_2O_3$ zbog sferne morfologije čestica praha je imao najmanji udeo mikro pora i najbolju zateznu čvrstoću spoja. Oksid Y_2O_3 koji je istovremeno bio prisutan u veznoj i keramičkoj prevlaci je uticao na bolju inter-lamelarnu kohezionu čvrstoću između dve prevlake. Sistem prevlaka $NiCrAlCoY_2O_3$ /

$ZrO_2Y_2O_3$ je takođe zbog oksida Y_2O_3 imao veću vrednost zatezne čvrstoće spoja od sistema prevlaka $NiCrAlCoY_2O_3$ / ZrO_2MgO.

Najbolje karakteristike od svih sistema prevlaka je imao TBC sistem $NiCrAlCoY_2O_3$ / $ZrO_2CeO_2Y_2O_3$.

ZAHVALNOSTI

Autor je zahvalan za finansijsku podršku Ministarstva prosvete i nauke Republike Srbije (nacionalni projekti OI 174004, TR 34016).

LITERATURA

[1] B. Basler, R. Buergel, W. Hoffelner: Proc. of 1st Int. Conf. on Plasma Surface Engineering, Germisch-Partenkirchen 1, pp. 347, 1988.

[2] M.R. Mrdak, A. Vencl, B.D. Nedeljkovic, M. Stanković: *Influence of plasma spraying parameters on properties of the thermal barrier coatings*, Materials Science and Technology, Article in Press, doi: 10.1179/1743284712Y.0000000193, 2013.

[3] A. Vencl, N. Manić, V. Popovic, M. Mrdak: *Possibility of the abrasive wear resistance determination with scratch tester*, Tribology Letters 37, pp. 591-604, 2010.

[4] E. Celik, I.H. Mutlu, E. Avci, Y.S. Hascicek: *Y_2O_3-ZrO_2 insulation coatings on AgMg sheathed Bi-2212 superconducting tapes by the sol-gel process*, IEEE Transactions on Applied Superconductivityb10, pp.1329-1332, 2000.

[5] E. Celik, I.H. Mutlu, Y.S. Hascicek: *Electrical properties of high temperature insulation coatings by the sol-gel method for magnet technology*, IEEE Transactions on Applied Superconductivity 10, pp. 1341-1344, 2000.

[6] E. Celik, E. Avci, Y.S. Hascicek: *High temperature sol-gel insulation coatings for HTS magnets and their adhesion properties*, Physica C: Superconductivity, Vol. 340, No. 2-3, pp. 193-202, 2000.

[7] A.S. Demirkiran, E. Çelik, M. Yargan, E. Avci: *Oxidation behaviour of functionally gradient coatings including different composition of cermets*, Surface and Coatings Technology 142-144, pp. 551-556, 2001.

[8] *Metco 461 Nickel Chromium-Aluminum-Cobalt-Yttria Composite Powder*, Technical Bulletin 10-315, Sulzer Metco, 2000.

[9] *Metco 210 Magnesium Zirconate Powder*, Technical Bulletin 10-108, Sulzer Metco, 2000.

[10] *Metco 202NS Zirconium Oxide Composite Powder*, Technical Bulletin 10-107, Sulzer Metco, 2000.

[11] *Metco 205NS PreAlloyed Ceria-Yttria Stabilized Zirconia Powder*, Technical Bulletin 10-338, Sulzer Metco, 2000.

[12] A. Vencl, M. Mrdak, I. Cvijović: *Microstructures and tribological properties of ferrous coatings deposited by APS (Atmospheric Plasma Spraying) on Al-alloy substrate*, FME Transactions, Vol. 34, No. 3, pp. 151-157, 2006.

[13] A. Vencl, M. Mrdak, M. Banjac: *Correlation of microstructures and tribological properties of ferrous coatings deposited by atmospheric plasma spraying on Al-Si cast alloy substrate*, Metallurgical and Materials Transactions A, Vol. 40, No. 2, pp. 398-405, 2009.

[14] M. Mrdak, A. Vencl, M. Ćosić: *Microstructure and mechanical properties of the Mo-NiCrBSi coating deposited by atmospheric plasma spraying*, FME Transactions, Vol. 37, No. 1, pp. 27-32, 2009.

[15] M. Mrdak, A. Vencl: *Uticaj parametara nanošenja NiCr prevlake plazma sprej postupkom u atmosferskim uslovima na njene mehaničke karakteristike i strukturu*, Tehnička dijagnostika 10, pp. 9-14, 2011.

[16] C.-J. Li, A. Ohmori: *Relationships between the microstructure and properties of thermally sprayed deposits*, Journal of Thermal Spray Technology 11, pp 365-374, 2002.

[17] R. McPherson, B.V. Shafer: *Interlamellar contact within plasma-sprayed coatings*, Thin Solid Films 97, pp. 201-204, 1982.

[18] S. Kuroda, T.W. Clyne: *The quenching stress in thermally sprayed coatings*, Thin Solid Films 200, pp. 49-66, 1991.

[19] C. Li, A. Ohmori, R. McPherson: *The relationship between microstructure and Young's modulus of thermally sprayed ceramic coatings*, Journal of Materials Science 32, pp. 997-1004, 1997.

[20] L. Bianchi, A.C. Leger, M. Vardelle, A. Vardelle, P. Fauchais: *Splat formation and cooling of plasma-sprayed zirconia*, Thin Solid Films 305, pp. 35-47, 1997.

[21] V. Pershin, M. Lufitha, S. Chandra, J. Mostaghimi: *Effect of substrate temperature on adhesion strength of plasma-sprayed nickel coatings*, Journal of Thermal Spray Technology 12, pp. 370-376, 2003.

[22] P. Fauchais, M. Fukumoto, A. Vardelle, M. Vardelle: *Knowledge concerning splat formation: An invited review*, Journal of Thermal Spray Technology 13, pp. 337-360, 2004.

[23] A. Vencl, S. Arostegui, G. Favaro, F. Zivic, M. Mrdak, S. Mitrović, V. Popovic: *Evaluation of adhesion/cohesion bond strength of the thick plasma spray coatings by scratch testing on coatings cross-sections*, Tribology International 44, pp. 1281-1288, 2011.

[24] *Turbojet Engine – Standard Practices Manual (PN 582005)*, Pratt & Whitney, East Hartford, USA, 2002.

TESTING THE MECHANICAL AND THE STRUCTURAL PROPERTIES OF THE COATING RESISTANT TO THE EROSION AND THE HIGH TEMPERATURE

Abstract: *The aim of this study was to investigate the mechanical and the structural characteristics of the thermo-barrier coatings (TBC) resistant to the erosion and the high temperature. The deposited are the three types TBC dual coating systems which were consisting of a metal-bonded coatings* $NiCrAlCoY_2O_3$ *and a ceramical insulating coatings* ZrO_2MgO, $ZrO_2Y_2O_3$ *and* $ZrO_2CeO_2Y_2O_3$. *TBC systems of the coatings were deposited, with process of atmospheric plasma spraying (APS), on the roughened steel substrates with a temperature of 160 – 180 °C. The coatings were deposited with the optimal parameters of deposition powders. A bonding layers were deposited with a single pass of plasma gun, and ceramical layers with a fourteen passages. Assessment of a quality layers was done by the testing microhardness with method* $HV_{0.1}$ *and bond strength by the testing on tensile. Metallographic assessment proportion of micro-pores (image analysis), in the structure of the bonding and the ceramical layers, was done with the technique of the light microscopy. The Morphology of the particles powder was done on the SEM. Analysis of the performed testings have been enabled to choose the TBC systems of the coatings with the best mechanical and structural characteristics.*

Keywords: *atmospheric plasma spraying (APS), thermo-barrier coatings (TBC), microstructure, interface, microhardness, strength bond.*

Serbian Tribology Society

SERBIATRIB '13

13th International Conference on Tribology

Faculty of Engineering in Kragujevac

Kragujevac, Serbia, 15 – 17 May 2013

IZBOR MERNE GLAVE DIFERENCIJALNOG PNEUMATSKOG KOMPARATORA ZA KONTROLU UNUTRAŠNJIH MERA MAŠINSKIH DELOVA

Dragiša Skoko[1], Cvetko Crnojević[1], Mileta Ristivojević[1]
[1]Mašinski fakultet u Beogradu, Srbija, dskoko@mas.bg.ac.rs, ccrnojevic@mas.bg.ac.rs, mristivojevic@mas.bg.ac.rs

Apstrakt: Apstrakt: *U ovom radu je analiziran uticaj promene uticajnih faktora na rad pneumatskog kommparatora.. Instalacija koja se koristi u ovu svrhu omogućava promenu pritiska napajanja, promenu izlazne mlaznice i prečnoka mlaznice merne komore komparatora. Posebna pažnja je posvećena pneumatskoj osetljivosti i dobijeno je da zavisi od pritiska napajanja i prečnika mlaznice u mernoj komori. Utvrđeno je da pneumatska osetljivost raste sa smanjenjem prečnika mlaznice u mernoj komori. Takođe je dat izbor prečnika merne glave pneumatsko komparatora za kontrolu munutrašnjih mera mašinskih delova.*

Ključne reči: *kontrola, merna glava, diferencijalni pneumatski komparator, mašinski delovi, unutrašnje mere, pneumatska osetljivost*

1. UVOD

Uporedo sa razvojem proizvodnih mašina razvija se tehnika kontrole i merenja proizvedenih komada. Prvi uređaji za kontrolu su bili mehanički. Ovi uređaji su mogli da zadovolje potrebu u pojedinačnoj i maloserijskoj proizvodnji jednostavnih komada. Razvojem savremene industrije XX-tog veka, koju karakterišu velikoserijska proizvodnja komplikovanih oblika i velika tačnost izrade, mehanički uređaji nisu mogli da zadovolje u svim segmentima proizvodnje. To naročito dolazi do izražaja u automobilskoj i avio industriji. Za merenje i kontrolu razvijeni su potpuno novi uređaji: mehanički, optički, električni, pneumatski, hidraulički i laserki uređaji. Najvažnija prednost u odnosu na mehaničke je njihova tačnost. Tačnost mehaničkih uređajaje je 1 μm, a pomoću savremenih uređaja mogu se meriti i deseti i stoti delovi mikrometra.

Pneumatski merni sistemi se intenzivno razvijaju tridesetih godina XX-tog veka, počev od najednostavnijih [1], pa sve do vrlo savremenih uređaja [2]. Zbog velike mogućnost primene, jednostavne konstrukcije, lakog održavanja, jednostavnog rukovanja a iznad svega velike tačnosti, ovi uređaji su dominantni u kontroli mašinskih delova. Prednost ovih uređaja, u odnosu na ostale, je što komprimovan vazduh koji izlazi iz mlaznica merne glave velikom brzinom, oduva mehaničke nečistoće i tanak sloj tečnosti za hlađenje komada i ostalih nečistoća. Na ovaj način se smanjuje mogućnost pojave greške pri merenju i kontroli. Druga prednost je što se može kontrolisati više mera istovremeno, bilo spoljašnjih ili unutrašnjih. Vrlo značajnu primenu ima dinamička pneumatska metoda koja se primenjuje kod obrtnih komada, znači u toku rada, bez zaustavljanja rada mašine, vrši se merenje i kontrola obratka.

Teorijske osnove ovog postupka su obrađene u literarturi [.3], [.4], [.5]. Stepen tačnosti kontrole mašinskih delova zavisi od: izbora izlazne mlaznice, pritiska napajanja p_a, prečnika prigušnice D u mernoj komori i prečnika merne glave. Uradu je prikazan postupak određivanja prečnika merne glave. Analiziran je uticaj pneumatske osetljivosti i odstupanja kontrolisanog mašinskog dela na izbor dimenzija merne glave.

2. EKSPERIMENTALNA INSTALACIJA

Za odredjivanje polja pritiska na ravnoj površini mernog komada koristi se instalacija prikazana na slici 1 i slici 2. Instacija se sastoji od pneumatskog komparatora PC, koji sadrži mernu (B1) i referentnu granu (B2), izvora vazduha pod

pritiskom CAS, koji se reguliše regulatorom pritiska PR, izlazne mlaznice N i sistema D-*r* i D-δ za fina pomeranja ravnog mernog komada. U mernoj grani se nalazi mlaznica A prečnika *D* u čijem grlu se ostvaruje kritično strujanje. U ovom radu prečnik *D* je imao vrednost 0,7 i 1 mm, koji odgovara realnim primenana, a tretitan je slučaj kada je *D*=6 mm što odgovara kada u dovodnoj grani napajanja mlaznice N nema pneumatskog prigušenja. Pritisci napajanja p_a menjani su u intervalu od 2 do 5 bar. Svi pritisci mereni su manometrima koji imaju tačnost 0,001 bar. Izlazna mlaznica N je unutrašnjeg pečnika 2 mm i spoljašnjeg 4 mm. Ostvarivanje željenih položaja *r* i δ postiže se tako što se iznad fiksnog mernog komada W pomera izlazna mlaznica N sistemima pomeranja D-*r* i D-δ

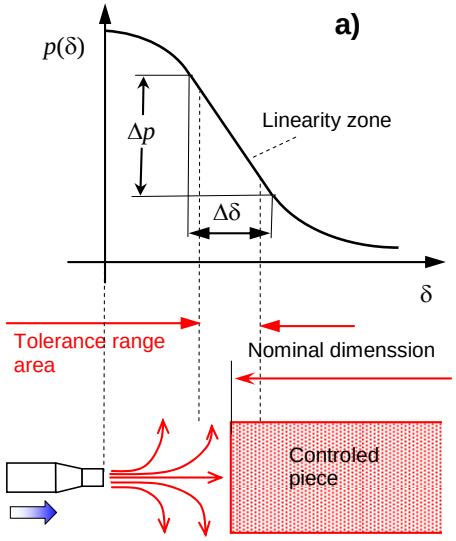

Slika 1. Shematski prikazi pritiska *p*(δ)

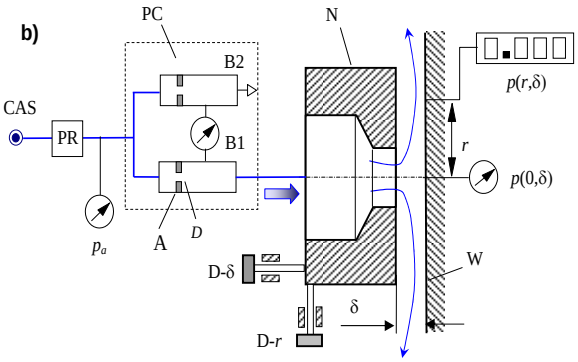

Slika 2. Shematski prikaz - merna instalacija

3.1 Mlaznice

Polje pritiska na površini mašinskog dela koji se kontroliše zavisi od geometrije izlazne mlaznice. Analizom uticajnih faktora na polje pritiska, bira se takva mlaznica da se potpuno eliminiše podpritisak na komadu koji se kontroliše ili da taj pritisak bude, ako je moguće, što manji.

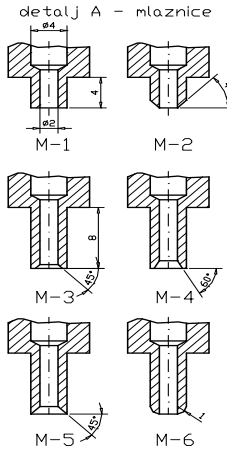

Slika 3. Geometrija izlazne mlaznice [5]

Pojava podpritiska na mernom komadu je nepoželjna zbog skupljanja nečistoća, koje remeti ispravan rad komparatora. Takođe pogodnim odabirom geometrije izlazne mlaznice teži se da polje podpritiska bude što dalje od ose mlaznice. Analiza polja pritiska na rad pneumatskog diferencijalnog komparatora je data u radu [5]. Karakteristični oblici mlaznica su dati na slici 3.

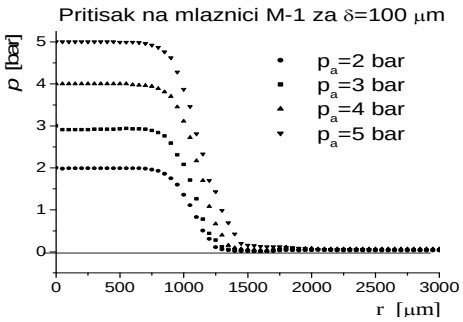

Slika 4. Dijagram p=f(r) za M-1 i p_a

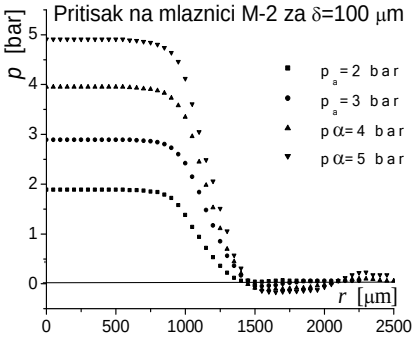

Slika 5. Dijagram p=f(r) za M-2 i p_a

Analiza uticaja pritiska napajanja i geometrije izlazne mlaznice na polje pritiska na površini mašinskog dela koji se kontroliše prikazana je na dijagramima na 4 i 5.

Analizom dijagrama, slika 4, vidi se da je polje pritiska pozitivno za mlaznicu M-1 po celoj dužini i za sve pritiske napajanja. Polje pritiska za mlaznicu M-2 je pozitivno za za p_a =2 i p_a =3 bar a za veće pritiske p_a =4 i p_a =5 bar je negativno, što nije dobro, slika 5

3.2 Pneumatska osetljivost

Oblast primene pneumatske metrologije je ograničena pravolinijskim delom dijagrama p=p(δ). Pogodnim odabirom prigušnice dobija se odgovarajuća karakteristika pneumatskog diferencijalnog uređaja - osetljivost uređaja. Pneumatska osetljivost ***S*** predstavlja odnos priraštaj pritiska Δp i rastojanja $\Delta\delta$ iz pravolinijskog dela krive zavisnosti totalnog pritiska od rastojanja mlaznice i površine mernog komada

S=. $\Delta p / \Delta\delta$ – ref [6]

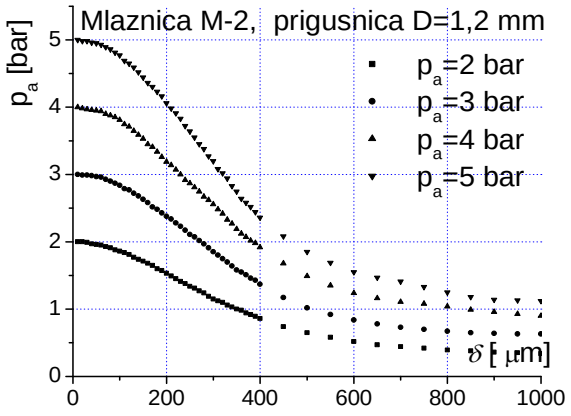

Slika 6. Dijagram p=f(δ). za M-2 i različite p_a

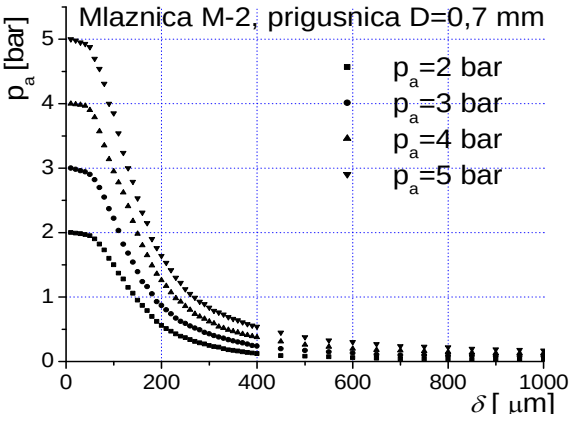

Slika 7. Dijagram p=f(δ) a M-2 i različite p_a

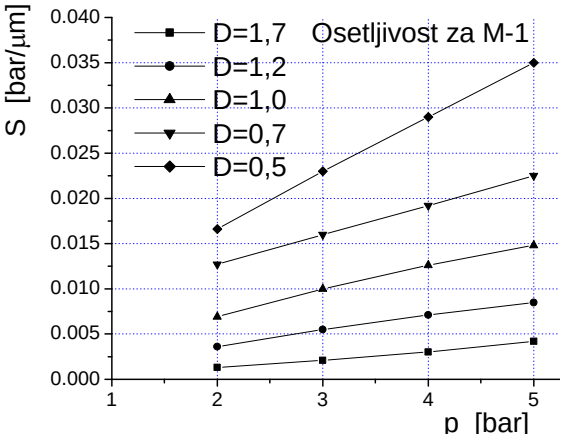

Slika 8. Osetljivost mlaznice M-1

Iz definicije pneumatske osetljivosti uređaja, proizilazi da pneumatski uređaj koji ima veće prigušenje ima veću osetljivost a pravolinijski deo krive zavisnosti pritiska i rastojanja δ ima veći ugao nagiba u odnosu na x osu tj. prava je strmija. Pneumatski diferencijalni uređaj koji ima manje prigušenje ulaznog pritiska u mernu komoru ima manju osetljivost a pravolinijski deo krive ima manji nagib u odnosu na x osu. Osetljivost uređaja je, dakle definisana nagibom krive. Osetljivost uređaja predstavlja tačnost uređaja. Opseg primene uređaja definisan je dužinom projekcije pravolinijskog dela krive na osu x. Uređaji koji imaju veću dužinu projekcije imaju veći opseg primene, tj. veću širinu tolerancijskog polja. Pneumatski diferencijalni uređaji koji su predviđeni da rade sa većim pritiskom napajanja imaju veći opseg primene.

Na dijagramima sa slike 5 vidi se da je mala osetljivost zbog malog prigušenja D=1,2 mm. Na dijagramima , slika 6 se vidi da krive imaju veliki pad tj. veliko prigušenje D=0,7 mm i veliku osetljivost.

Na slici 7, data je osetljivost mlaznica M-1 i M-2 u zavisnosti od stepena prigušenja i pritiska napajanja p_a. Veliko prigušenje daje veliku pneumatsku osetljivost i obrnuto. Isto tako se vidi da je linearno povećanje osetljivosti sa povećanjem pritiska napajanja p_a. Takođe se vidi uticaj oblika mlaznice na osetljivost. Najveća osetljivost je za mlaznicu M-5, prečnik prigušnice D=0.7 mm i p_a =5 bar i iznosi s=0,039bar/mm.

4. ODREĐIVANJE PREČNIKA MERNE GLAVE

Pneumatski uređaj za kontrolu dimenzija je specijalan manometar sa skalom, koji umesto skale pritiska ima skalu za očitavanje zazora δ (rastojanje vrha mlaznice i površine komada koji se kontroliše). Pneumatski komparator je transformisani manometar. Za zadati pritisak napajanja p_a, izabrani prečnik prigušnice D i izabranu mlaznicu M, na uređaju se očitava zazor δ za odgovarajuće vrednosti pritiska p_a. ,,Takođe u konkretnim izvođenjima pneumatskih komparatora ne meri se pritisak $p(\delta)$ na površini komada koji se kontroliše, već pritisak u komori merne grane p

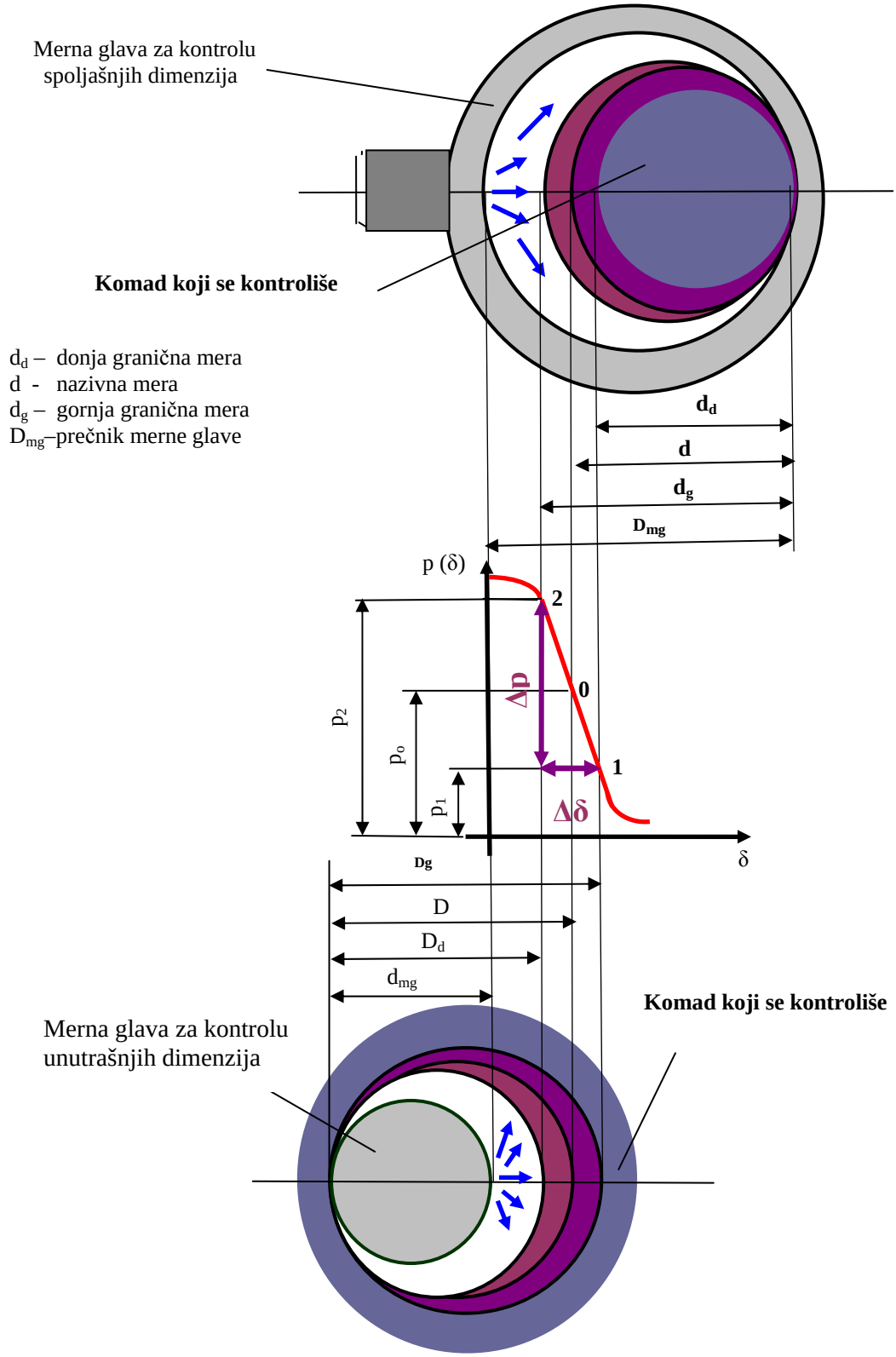

Slika 9. Šematski prikaz dijagrama p=p(δ) i merne glave za kontrolu spoljašnje i unutrašnje mere [5]

$p_{mg}(\delta)$, koji je zbog malih strujnih gubitaka približno jednak pritisku p

Zavisnost $p=p(\delta)$ prikazana dijagramom na slici 9. Na ovom dijagramu uočava se pravolinijski deo. Tačku 2 predstavlja početak pravolinijskog dela dijagrama i nju karakteriše povećan pritisak p_2 a male vrednosti δ. Na uređajima se ne koristi tačka 2 kao reperna, već tačka ispod nje ,,g"., koja ima karakteristiku manji pritisak a veće δ. Ta tačka predstavlja gornju granicu tolerancijskog polja komada koji se kontroliše. Prevedeno u kontroli spoljašnjih dimenzija to je komad sa maksimalno dozvoljenom merom i na uređaj za očitavanje tu bismo stavili reper ***es,*** što predstavlja gornje granično odstupanje. Uobičajeno je da je taj reper na merilu plave boje. Komad koji bi imao veće odstupanje od zadatog bi morao da ide na doradu. Pri kontroli unutrašnjih dimenzija ova tačka bi predstavljala minimalnu dozvoljenu meru i na uređaj za očitavanje tu bismo stavili reper koji označava minimalno odstupanje ***EI.*** U tom slučaju ova tačka predstavlja donju graničnu meru.

Povećanjem rastojanja δ smanjuje se pritisak. Naredna karakteristična tačka na pravolinijskom delu dijagrama $p=f(\delta)$ je tačka ,,0", koja uglavnom predstavlja sredinu dužine pravolinijskog dela dijagrama. Ovo je značajna tačka ovog dijagrama jer se koristi za određivanje dimenzija merne glave. Takođe njena horizontalna projekcija predstavlja nultu liniju u tolerancijama.

Treća tačka na ovom delu dijagrama je tačka ,,*d*". Karakteriše je manji pritisak i veliko δ. Ona predstavlja drugu granicu tolerancijskog polja komada koji se kontroliše. Pri kontroli spoljašnjih dimenzija to je minimalno dozvoljena mera. Na skali pneumatskog uređaja se stavi reper koji označava ***ei,*** i predstavlja donje granično odstupanje. Pri kontroli spoljašnje dimenzije komada, ako je stvarno donje odstupanje veće od zadatog, komad se odbacuje jer mu je stvarna mera manja od najmanje dozvoljene. To važi i za kontrolu unutrašnjih dimenzija. Horizontalna projekcija tačke ,,*d*" na dijagramu koristi se kao reper na skali uređaju i predstavlja ***ES,*** gornje granično odstupanje. Svaka stvarna mera koja ima veće odstupanje od zadatog je loša mera i komad se odbacuje.

4.1. Određivanje prečnika merne glave za kontrolu unutrašnjih dimenzija

Merna glava za kontrolu unutrašnjih dimenzija je valjak koji po obimu ima dve ili više identičnih mlaznica. Svaka tolerisana mera ima parametre: D - nazivnu meru, D_g – gornju graničnu meru, D_d – donju graničnu meru, ES – gornje granično odstupanje, EI – donje granično odstupanje i T - tolerancijsko polje. Pri određivanju prečnika merne glave mora se voditi računa o položaju tolerancijskog polja u odnosu na nazivnu meru. Imamo tri različita slučaja:

1. Tolerancijsko polje unutrašnje mere je simetrično u odnosu na nultu liniju, tj. kada su odstupanja ista

$ES = EI.$

$d_{mg} = D - 2\,\delta_0$ - prečnik merne glave

δ_0 – rastojanje merne glave od površine komada koji se (horizontalna koordinata tačke ,,0").

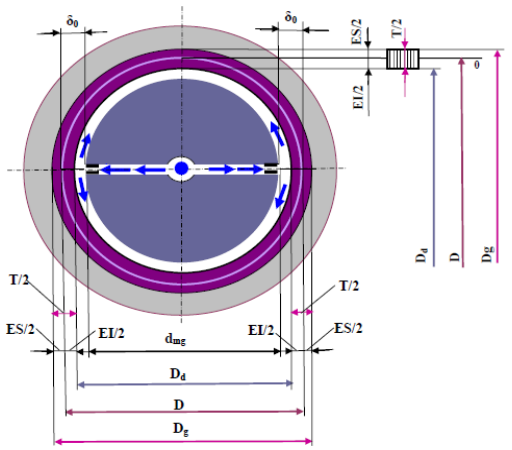

Slika 10. Prikaz simetričnog tolerancijskog polja unutrašnje mere

2. Tolerancijsko polje unutrašnje mere nalazi iznad nulte linije, radi se preslikavanje tolerancijskog polja na tolerancijsko polje ,,J_s". Ovo polje se naziva ekvivalentno tolerancijsko polje, a postiže se povećanjem prečnika merne glave za vrednost $C = EI/2 + ES/2$.

$d_{mg} = D - 2\delta_0 + (EI/2 + ES/2)$ - prečnik merne glave

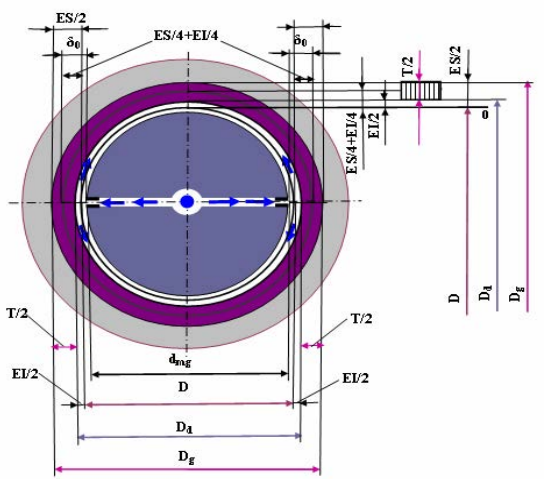

Slika 11. Prikaz nesimetričnog tolerancijskog polja unutrašnje mere - tolerancijsko polje iznad nulte linije

3. Ako se tolerancijsko polje unutrašnje mere nalazi ispod nulte linije, odstupanja su negativna.

Dato tolerancijsko polje se preslikava u tolerancijskog polja „J”. Ovo polje se naziva ekvivalentno tolerancijsko polje, a postiže se smanjenjem prečnika merne glave za vrednost $E = |EI/2 + ES/2I|$.

$d_{mg} = D - 2\,\delta_0 - |ES/2 + EI/2|$ - prečnik merne glave

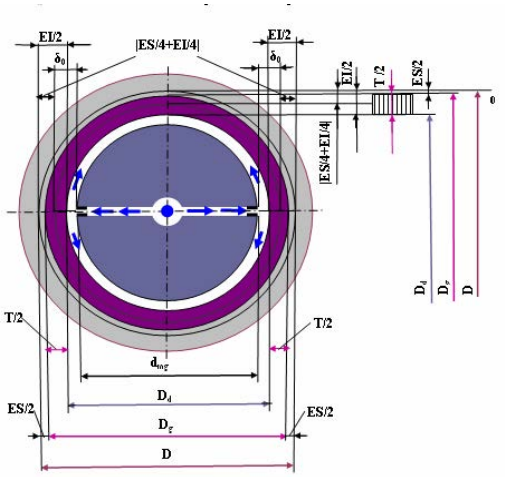

Slika 12. Prikaz nesimetričnog tolerancijskog polja unutrašnje mere - tolerancijsko polje ispod nulte linije

2. ZAKLJUČAK

Na osnovu eksperimentalnih rezultata prikazanih u ovom radu dolazi se do opštih zaključaka:

Iako se različita geometrija izlazne mlaznice prvenstveno koristi radi eliminisanja vrtložne zone izmedju mlaznice i kontrolisanog komada (ref. [2] i [5]), dati rezultati merenja pokazuju da se geometrijom izlazne mlaznice može uticati i na pneumatsku osetljivost komparatora i na promenu maksimalnog tolerancijskog polja kontrolisanog komada.

Na pneumatsku osetljivost pneumatskog komparotera se prvenstveno utiče promenom prečnika konvergentno-divergentne mlaznice merne grane. Povećanje pneumatske osetljivosti se povećava smanjenjem prečnika mlaznice merne komore, ali se i na taj način i sužava maksimalno tolerancijsko polje kontrolisane mere Za iste geometrijske parametre izlazne mlaznice i konvergentno-divergentne mlaznice merne grane pneumatska osetljivost se povećava porastom pritiska napajanja komprimovanog vazduha.

Pomoću diferencijalnog pneumatskog komparatora kontrolišu se spoljašnje i unutrašnje tolerisane mere. Za svaku tolerisanu meru mora se odrediti prečnik merne glave D_{mg} i d_{mg}. Prečnik merne glave zavisi od položaja tolerancijskog polja u odnosu na nazivnu meru, pritiska napajanja p_a i δ_0.

ZAHVALNOST

Rad je rezultat istraživanja realizovan u okviru projekta TR 35029. Rad je finansiran od Ministarstva prosvete, nauke i tehnološkog razvoja Republike Srbije na čemu sam im zahvalan.

LITERATURA

[1] Fortier, M.,: Application industrielles des écoulements gazeux à la vitesse critique, Revenu chaleur et Industrie, N°299, p.145.2. (1950)

[2] Crnojevic C., Roy G., Bettahar A. and Florent P.: Influence of regulator diameter and injection nozzle geometry on flow structure in pneumatic dimensional control systems. Transacions of ASME, Journal of Fluids Engineering, Vol. 119., pp. 609-615 (1997).

[3] Crnojević C., Skoko D.,: O nekim pojavama koje utiču na rad pneumatskog komparatora. XXXI JUPITER konferencija, Zlatibor 2005. Zbornik radova (na CD-u), str. 5.14-5.17.

[4] Roy, G., Crnojevic C., Bettahar A., Florent P.and Vo-Ngoc, D., "Influence of nozzle geometry in radial flow applications," International Conference on Fluid and Thermal Energy Conversion, Proc. Vol. 1, pp.363-368 (1994), Bali, Indonesia

[5] Skoko, D., Magistarski rad, Mašinski fakultet Beograd 2007.

[6] Skoko D., Crnojević C., : Eksperimentalno određivanje osetljivosti pneumatskog komparatora. XXXII JUPITER konferencija, Zlatibor 2007. Zbornik radova , strana -5.43.

PNEUMATIC PROBE HEAD SELECTION FOR MACHINE PARTS INTERNAL MEASURES CONTROL WITH DIFFERNTIAL PNEUMATIC CONTROLER

***Apstract**: In this paper, we analyze the influence of various parameters on the work of pneumatic controller. For that purpose, experimental installation is used, which enables the variation of the pressure of compressed air source, output nozzle and the diameter of the measuring branch nozzle of pneumatic controller. Special attention is devoted to pneumatic sensitivity and it is determined that it depends on the diameter of measuring branch nozzle and supply pressure. In addition, it is determined that pneumatic sensitivity increases with the decrease of the diameter of measuring branch nozzle. In this paper, we treated of the selection of pneumatic measuring head of diferential pneumatic controler for control internal measures of machine parts*

***Keywords:** control, pneumatic measuring head, pneumatic controller, machine parts, internal measure, pneumatic sensitivity*

Serbian Tribology Society

SERBIATRIB '13

13th International Conference on Tribology

Faculty of Engineering in Kragujevac

Kragujevac, Serbia, 15 – 17 May 2013

POVEĆANJE POUZDANOSTI PODSISTEMA KOPANJA ROTORNOG BAGERA PODEŠAVANJEM TRIBOLOŠKIH KARAKTERISTIKA REZNIH ELEMENATA

Vojin Vukotić[1], Dragan Čabrilo[1]
Rudnik i Termoelektrana Gacko, Bosna i Hercegovina, Republika Srpska

Abstrakt: *Poznato je da prilikom obrade tla, u ovom slučaju skidanja jalovone i kopanja korisne mineralne sirovine korištenjem rotornih bagera, rezni elementi mašina koji su u kontaktu sa tlom trpe opterećenje i habaju se. Rezni elementi na rotornom bageru su kofice i zubi. U ovom radu učinjen je pokušaj da se modeliranjem geometrijskih parametara zuba na kofici isti prilagode režimu i kinematici rezanja tla i smanji se nivo habanja istih. Cilj je da se poveća pouzdanost rotornog bagera preko povećanja pouzdanosti podsistema kopanja, čiji je glavni dio rotorni točak sa reznim elementima.Vršeno je snimanje vremenske slike stanja podsistema kopanja za nekoliko varijanti geometrijskog oblika zuba i proračunavana odgovarajuća pouzdanost.*
Naravno, usvojena je geometrija zuba uz koju je postignut najveći nivo pouzdanosti.

Ključne reči: *rotorni bager, pouzdanost, zubi, habanje, geometrija*

1. UVOD

Rotorni bageri su danas najrasprostranjenije osnovne mašine na površinskim kopovima. Služe za uklanjanje jalovine ili za kopanje korisne mineralne sirovine.

Po svom sastavu to je vrlo složen mašinski sistem. Sastavljen je od niza podsistema, koji svaki ponaosob obezbjeđuje određenu funkciju neophodnu za rad bagera.

Podjela na podsisteme je uglavnom sledeća:

- podsistem za kretanje bagera,
- podsistem kopanja,
- podsistem prijemnog transportera,
- podsistem odlagajućeg transportera i
- podsistem za zakretanje gornje konstrukcije.

Ukoliko samo jedan od pomenutih podsistema nije u funkciji, tada ni rotorni bager kao cjelina ne zadovoljava namjeni, odnosno ne obavlja funkciju kriterijuma u propisanim granicama.

Zapaženo je i to da je različit uticaj na raspoloživost rotornog bagera, stanje ispravnosti odnosno pouzdanost pojedinih podsistema.

Teorijskim razmatranjima i ispitivanjima kroz eksploataciju ovih mašina [2], došlo se do zaključka da je podsistem kopanja najnepouzdaniji i da njegova pouzdanost najviše snižava ukupnu pouzdanost bagera.

Na osnovu određenih istraživanja na rotornom bageru ЭR – 1250 u sklopu gatačkog ugljenog basena koje je provodio autor ovog saopštenja, [4] može se A B C dijagramom prikazati učešće otkaza po podsistemima rotornog bagera kao na sl. 1, gdje je:

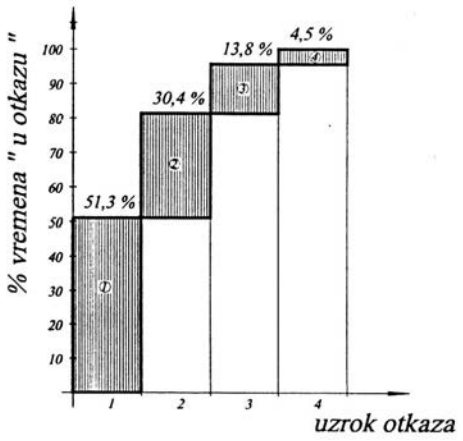

Slika 1. Analiza otkaza na bageru

1. Podsistem kopanja
2. Podsistem prijemnog transportera
3. Podsistem odlagajućeg transportera
4. Podsistem za kretanje
5. Podsistem obrtne plarforme

Očigledno je, sa pomenutog dijagrama, da podsistem kopanja u ukupnim otkazima participira sa otprilike 44%.

Podsistem kopanja sastoji se od tri glavna sklopa: pogonskog elektromotora, reduktora i radnog točka sa vedricama. Naravno svaki od ovih sklopova učestvuje u ukupnim zastojima podsistema kopanja sa svojim zastojima.

U ovom radu, predmet interesovanja i analize je sklop radnog točka sa vedricama, a sami element koji se tretira jeste zub i uticaj radne sredine na habanje istog.

2. OPŠTI PRISTUP PROBLEMU HABANJA

Habanje mašinskih dijelova je pojava koja se neminovno javlja na mašinama u toku njihova rada, odnosno eksploatacije. Posljedica je relativnog kretanja i pomjeranja dijelova u sklopu koji ostvaruju fizički kontakt.

Spada u štetne pojavne oblike u toku životnog ciklusa mašine, javlja se intenzivnije u posljednoj etapi toga ciklusa a ovim problemom se bave konstruktori mašine , rukovaoci i održavaoci iste, kako bi ovo štetno dejstvo sveli na što manju mjeru.

Naučna oblast koja se bavi ovom pojavom naziva se tribologija.

Dva su osnovna cilja koja se stavljaju pred tribologe, a to su:

- da mašina što duže traje,
- da ta mašina troši što manje energije,

a u poslednje vrijeme, javlja se i treći;

- da mašina ima što veću pouzdanost.

Zadovoljavanjem ovih ciljeva minimiziraju se i ukupni troškovi proizvodnje sa konkretnom mašinom.

2.1 Abrazivno habanje

Najveći broj mašinskih elementata radi u uslovima abrazivnog habanja. Pojava je karakteristična po tome što površina koja je u kontaktu dolazi u dodir sa tvrdim česticama – abrazivima. Abrazivi mogu biti sadržani u radnoj sredini (slučaj kod alata za obradu rezanjem, obradi tla, i sl.) ili su na drugi način dospjeli do kontaktnih površina (iz vazduha, u mazivu, prašina, pijesak, čestice blata, …).

Proces abrazivnog habanja je u uskoj vezi sa količinom i vrstom abrazivnih čestica, njihovom tvrdoćom i oblikom, kvalitetom i stanjem tarnih površina, pritiskom i temperaturom u zoni dodira, te brzinom relativnog kretanja i karakterom kretanja.

Abrazivno habanje je u dosta slučajeva bilo predmet interesovanja istraživača. Uspostavljena je zavisnost između intenziteta habanja u smislu promjene zapremine dijela na koji se habanje odnosi i normalnog opterećenja spregnutih površina i tvrdoće abrazivnih čestica.

Presudan uticaj na intenzitet abrazivnog habanja, po mišljenju mnogih autora, [1] i [3] ima opterećenje odnosno aktuelna sila na kontaktnim površinama. Intenzitet habanja je upravo proporcionalan sa veličinom opterećenja, a zavisi i od vrste i oblika tarnih površina, uglova u kontaktu, vrste trenja, režima rada te naročito od vrste obrađivanog materijala, odnosno tla koje se kopa, u slučaju rotornih bagera.

I pored svih preventivnih mjera, habanje se ne može potpuno spriječiti ali se na tu pojavu može značajno uticati ako se prethodno spozna njena suština, te mehanizam nastanka i razvoja.

2.2. Habanje zuba rotornog bagera

Problem habanja radnih elemenata na vedricama rotornih bagera prisutan je još od samog početka primjene ovih mašina, koje su se na površinskim kopovima pokazale kao vrlo produktivne i ekeonomične mašine.

U procesu kopanja dolazi do intenzivnog habanja reznih površina izazvanih suvim trenjem klizanja minerala kombinovanog sa značajnim dinamičkim udarima. To dovodi do neželjenih promjena na elementima mašine u vidu odvajanja čestica materijala sa posmatrane površine zuba.

Na proces habanja reznih elemenata, osim materijala koji se kopa utiče i niz drugih faktora, kao što su:

- materijal od koga su izrađeni rezni elementi,
- konstruktivne karakteristike zuba,
- režim rada rotornog bagera i
- specifični otpori kopanju

U procesu kopanja dolazi do klizanja materijala po reznim elementima pri čemu nastaje neželjeno habanje zuba. Proces habanja se nesumnjivo odražava na geometrijske karakteristike reznih elemenata, na njihov vijek trajanja i opštu upotrebljivost, a indirektno na kapacitet rotornog bagera, potrošnju energije i opštu spremnost bagera za normalnu eksploataciju. Očigledno je da fenomen habanja ima veliki uticaj na pogonsku spremnost i pouzdanost rotornog bagera, te ga je potrebno pažljivo proučiti kako sa aspekta uzroka i preventivnog djelovanja tako isto i u oblasti sanacije i uklanjanja eventualnih posljedica.

Kroz praksu i terenska ispitivanja odavno je poznato da povećano habanje zuba na vedricama rotornih bagera, za posljedicu, ima sledeće negativnosti:

- povećane otpore kopanju
- smanjen specifičan učinak bagera [t/h]
- povećane vibracije mašine
- povećana specifična potrošnja energije
- povećane troškove održavanja
- smanjenu pouzdanost bagera.

3. RADNA OPTEREĆENJA I VRSTE HABANJA ZUBA ROTORNOG BAGERA

Eksploatacioni uslovi za zube na rotornom bageru koji su u neposrednom kontaktu sa radnom sredinom koja se kopa, su bez sumnje, vrlo teški i složeni. Habanje zavisi prvenstveno od osobina materijala koji se kopa, otpornosti materijala zuba na habanje ili bolje reći od konstruktivne prilagođenosti zuba uslovima kopanja na konkretnom lokalitetu, odnosno kopu, kao i od režima rada bagera.

U ovom slučaju, zubi su izloženi kombinovanom dejstvu abrazije i udara, koji se manifestuju kroz nagle skokove opterećenja zuba u toku rada bagera.

Abrazivno habanje u konačnom obliku rezultira odnošenjem materijala sa radnih površina zuba i to na takav način da nakon što bude " skinut " jedan površinski sloj, dolazi pod udar procesa habanja sledeći površinski sloj, itd.

Ako uporedimo dejstvo abrazije sa brušenjem ili rezanjem kao procesima mehaničke obrade materijala, prva konstatacija je da većina abrazivnih čestica ima negativan ugao rezanja. Zbog toga one izazivaju na površinama, po kojima se taru, karakteristične ogrebotine-abrazivne brazde, praćene velikom plastičnom deformacijom i tečenjem materijala.

Istovremeno efekat rezanja, koji varira od čestice do čestice, zahvaljujući izvjesnom smicajnom dejstvu, čiji je uzrok opet negativan rezni ugao, produkuje mikro strugotinu, a to je način odnošenja materijala – abrazije.

U toku procesa habanja bagerskog zuba prisutna je situacija, što se geometrije zuba tiče, kao na slici 2.

Početna kontura vrha zuba prikazana je linijom "0". Linije "1" do "6" prikazuju konture zuba u funkciji vremena habanja u radu. Kada se zub pohaba za veličinu h_b koja je za zube postojeće konstrukcije otprilike 30÷40 mm, na odrađenih 200÷250 radnih časova geometrijski izgled vrha zuba predstavljen je linijom – "6". Tada se vrši skidanje pohabanih zuba, stavljaju se novi ili reparirani, a pohabani šalju na reparaturu.

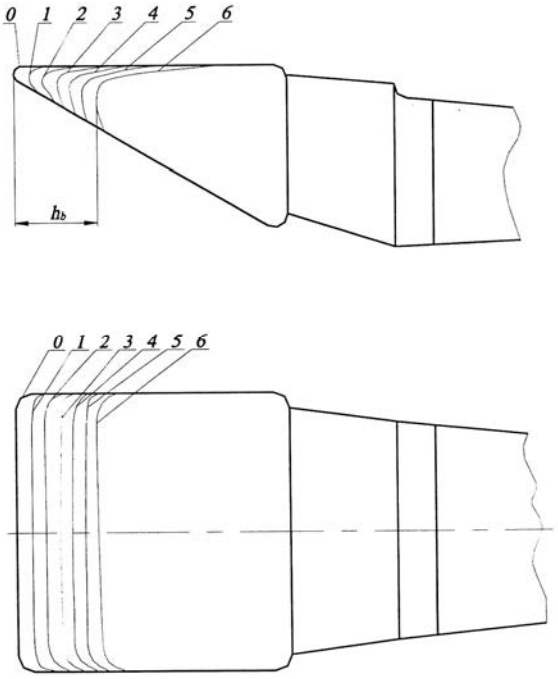

Slika 2. Faze habanja zuba

Kapacitet rotornog bagera zavisi uglavnom od rada podsistema za kopanje. Tu je veliki doprinos pravilnih i oštrih zuba kada je i kapacitet najveći. U funkciji vremena dolazi do zatupljenja zuba usljed abrazivnog habanja, odnosno do promjene njihovog geometrijskog oblika. Usljed zatupljenja zuba povećava se i otpor kopanju, a s tim u vezi dolazi do povećanog opterećenja prenosnika, pa i čitave konstrukcije podsistema kopanja.

Konačno, ovo ima za posljedicu promjenu režima rada bagera, dolazi do smanjenja njegovog kapaciteta, što se negativno odražava na ekonomske efekte proizvodnje.

4. PRILAGOĐAVANJE GEOMETRIJE OBLIKA ZUBA

Zub rotornog bagera, koji je u ovom radu predmet interesovanja, predstavlja kao pojam – mašinski element. Kada tretiramo konstrukciju bilo kog mašinskog elementa onda se tu prvenstveno misli na definisanje:

- geometrijskog oblika,
- materijala,
- kvaliteta obrade i
- termičke obrade

Ovom prilikom ćemo se ograničiti na aspekt geo-metrije zuba. Da bi na izvjestan način kvantificirali nivo po-habanosti zuba, pristupilo se mjerenju pojasa pohabanosti. Usvojen je dužinski parametar h_b prema sl.2, kao pokazatelj istrošenosti zuba. Ova veličina je mjerena u određenim vremenskim razmacima pa su na osnovu tih mjerenja konstru-isani dijagrami zavisnosti $h_b=f(t)$, sl.3.

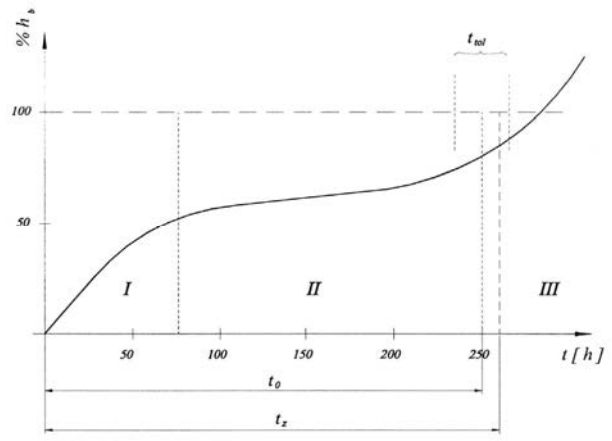

Slika 3. Kriva habanja

Na tom dijagramu uočljive su tri zone. U prvoj dolazi do početnog intenzivnog habanja zuba. Kasnije zona II , zub se ravnomjerno i umjereno haba, da bi se u zoni III počeo intenzivno habati i tada se pristupa zamjeni zuba. Opredeljujuća veličina za zamjenu zuba je veličina t_0 – teorijski vijek trajanja. Poznato je iz prakse da se zub ne mijenja striktno po isteku perioda t_0 nego posle perioda t_z , koji se nalazi u tolerantnoj zoni t_{tol} u odnosu na t_0. Veličina t_z se može iskustveno definisati relacijom:

$$t_z = (1\pm0,2)\, t_0$$

Geometriju zuba smo modelirali tako da smo za izbranu geometrijsku varijantu snimali krivu habanja zuba i upoređivali izdržljivost zuba prema tako konstruisanoj krivoj habanja uz praćenje popratnih pojava uzrokovanih habanjem zuba.

4.1. Varijanta sa originalnim zubima

Zatečeno stanje zuba na rotornom bageru je, u geometrijskom smislu, potpuno isto kao što je proizvođač bagera isporučio u originalnom obliku, sl.4.

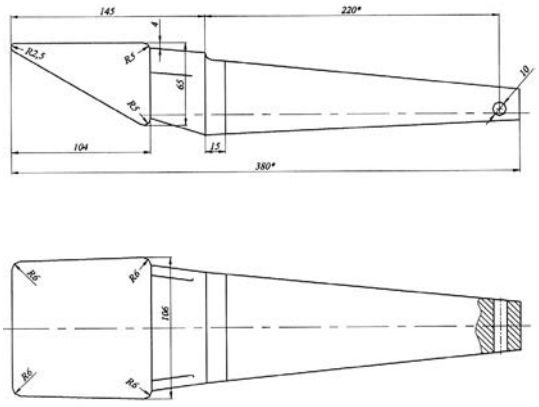

Slika 4. Originalni oblik bagerskog zuba

Geometrijski izgled zuba i vedrice sa relevantnim geometrijskim parametrima dat je na sl.5

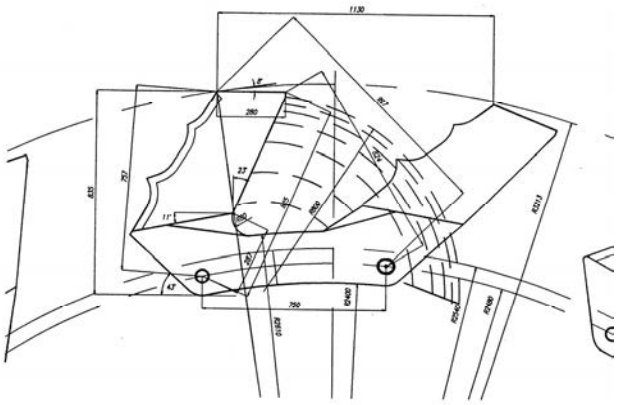

Slika 5. Geometrijski izgled vedrice sa originalnim zubima

Mjerenja parametra habanja h_b, sl.2 i konstruisanje krive habanja, sl.3 vršena su za nekoliko zuba na najopterećenijem mjestu na vedrici - čeoni zub (rezač) pa na dijagramu, sl.6 dajemo izgled krive habanja za te pozicije zuba. Konstatovano je da zub izdrži 200 ÷ 250 radnih časova dok se pohaba u nivou od $h_b \sim 40$ mm.

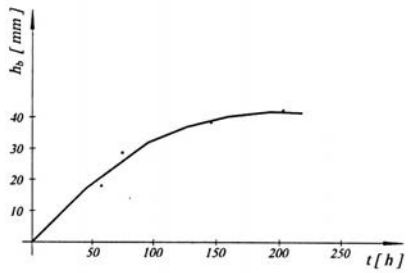

Slika 6. Kriva habanja za originalni zub

4.2. Varijanta II

Učinjena je izmjena samo u domenu geometrije zuba, a kvalitet materijala od koga je zub napravljen nije mijenjan. Predložena je geometrijska forma na osnovu savremenih stručnih saznanja, te iskustava drugih rudnika koji koriste rotorne bagere, sl.7 dok su na sl. 8 definisani osnovni geometrijski parametri zuba učvršćenog na vedrici prema radnoj sredini.

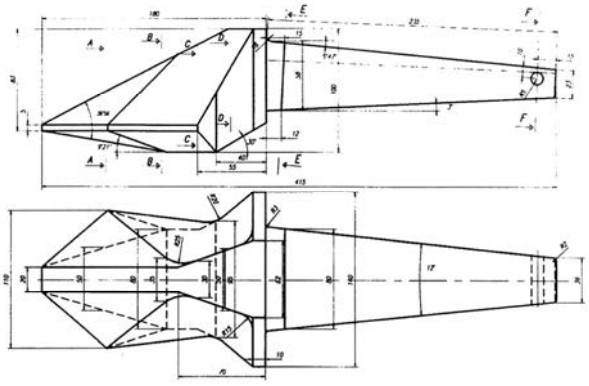

Slika 7. Oblik bagerskog zuba varijante II

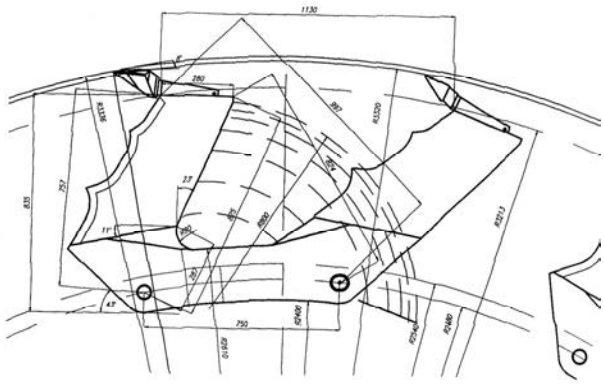

Slika 8. Geometrijski izgled vedrice sa zubima varijante II

Konstatovan je mirniji rad bagera jer je obezbjeđeno da zubi postepeno prodiru u radnu sredinu, postoji klin i u vertikalnoj i u horizontalnoj ravni, a radni dio zuba je znatno duži u odnosu na originalnu varijantu zuba. Vedrica je manje otvorena prema bloku koji se kopa, što ima za posljedicu manje "struganje" vedrice od radni blok. Prema instrumentima u kabini rukovaoca bagera zaključeno je da se otpori kopanju savlađuju uz manju angažovanu snagu mašine.

Takođe, konstatovan je značajan porast časovnog kapaciteta bagera, što se objašnjava povećanjem radne dužine zuba i manjim leđnim uglom. Prilikom ispitivanja ove konstrukcije zuba su primijećena i izvjesne negativnosti. Naime, usled ojačanog i previše isturenog leđnog dijela zuba, uočeno je da se taj leđni dio previše ukopava u radnu sredinu. Drugim rječima, taj leđni dio ne ide u otkopanu masu, koju je prethodno vrh zuba razorio, nego on svojim leđnim, isturenim dijelom "gnječi" radnu sredinu. Taj razlog, uz previše dugačak radni dio zuba (L=180 mm) dovodio je do toga da su zubi savijani, plastično deformisani i lomljeni u dijelu drške i vrata zuba. [5].

Zbog ove negativnosti nije se ni pristupalo konstrukciji krive habanja za ovu vrstu zuba.

4.3. Varijanta III

Poslije uočenih nedostataka po prethodnoj varijanti, ispitivanja su obustavljena i pristupilo se ispravkama na geometrijskom izgledu zuba:

- dužina radnog dijela skraćena je na L=165 mm,
- smanjeno je ojačanje leđnog dijela,
- zub je prema radnoj sredini otvoren na 13°14'7",
- izvršeno je bolje pasovanje drške zuba u "džep" i
- eliminisano je aksijalno pomjeranje zuba u "džepu".

Nakon tih prepravki dobili smo geometrijski izgled zuba kao na sl. 9 sa geometrijskim parametrima u zahvatu prema radnoj sredini kao na sl.10.

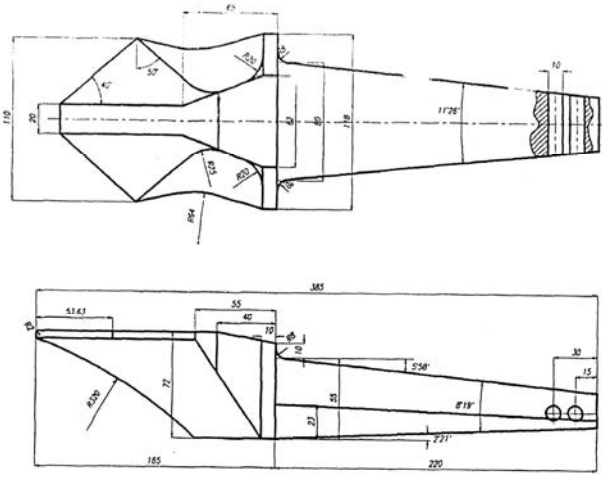

Slika 9. Geometrijski izgled zuba varijante III

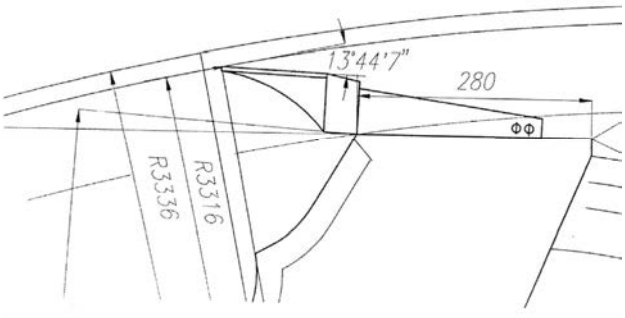

Slika 10. Geometrijski izgled vedrice sa zubima varijante III

Osnovna zapažanja u vezi rada bagera sa ovakvim zubima su:

- Bager je imao miran rad bez udara i vibracija sa izraženim amplitudama. Ovo se objašnjava time što je konstrukcija zuba samim vrhom prilagođena da postepeno ulazi u radnu sredinu i izaziva manje otpore kopanju i manje podrhtavanje bagera. Tome je doprinijela i prilagođenost leđnog ugla zuba u sprezi sa vedricom prema radnoj sredini.
- Časovni kapacitet bagera je veći za 15 do 20% u odnosu na rad sa originalnim zubima.
- Proces kopanja se odvija uz značajno manju angažovanu snagu mašine nego sa zubima originalne izvedbe.
- Manji su otpori kopanju.
- Leđni dio zuba je manje isturen pa nema neželjenog opterećenja koje je za posljedicu imalo lomljenje zuba.

- Mjereni su parametri habanja i prilikom konstrukcije krive habanja za čeone zube je konstatovano da je znatno duži vijek trajanja ove konstrukcije i da iznosi 300 ÷ 350 radnih časova, sl.11.

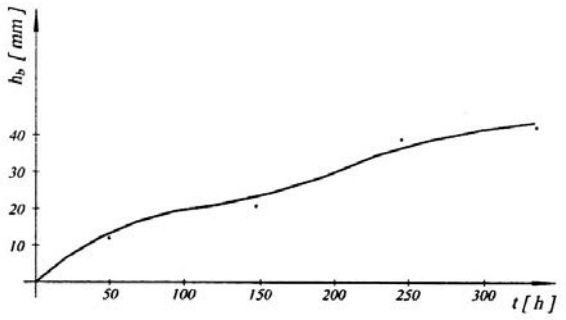

Slika 11. Kriva habanja čeonog zuba varijante III

Budući da je radna dužina ove konstrukcije zuba za 20 mm veća od odgovarajućeg dijela na originalnom zubu to se reperna dužina parametra habanja h_b od 40 mm može povećati na 50 mm, pa imajući to u vidu radni vijek zuba ove konstrukcije može iznositi i do 500 radnih časova.

Ova geometrijska varijanta usvojena je, urađena garnitura zuba za potpunu zamjenu na rotornom bageru i kroz duži period eksploatacije u dobroj mjeri potvrdila pretpostavke iz eksperimentalne faze.

ZAKLJUČAK

U sklopu provedenih istraživanja na rotorm bageru ER 1250 koji je u eksploataciji u sklopu rudnika „Gacko“ učinjen je pokušaj da se isti prilagodi uslovima radne sredine preko optimizacije geometrijskih parametara reznih elemenata – zuba.

Na osnovu polaznih teoretskih postavki iz oblasti pouzdanosti proizvodnih sistema, te karakteristika triboloških procesa na reznim elementima vršena su ispitivanja pouzdanosti podsistema kopanja rotornog bagera koristeći u početku zube originalne konstrukcije isporučioca bagera a posle u nekoliko varijanti zube predložene geometrijske izvedbe. Modeliranjem triboloških karakteristika zuba na rotornom bageru podešavanjem geometrijskih parametara istih, kao što je prikazano u radu, rezultat poboljšanja kroz predloženu geometrijsku varijantu zuba imamo:

- Manje otpore kopanju,
- Manji iznos habanja zuba,
- Veću eksploatacionu pouzdanost podsistema kopanja, a u vezi s tim i samog rotornog bagera,
- Veći radni vijek zuba,
- Manje troškove održavanja bagera,
- Mirniji rad bagera i
- Veći specifični kapacitet bagera.

Rezultati ovih istraživanja mogu se primjeniti sa velikom pouzdanošću na kopove sa sličnim radnim uslovima.

LITERATURA

[1] S. Tanasijević: *Osnovi tribologije mašinskih elemenata*, Naučna knjiga, Beograd 1989.

[2] Z. Jugović: *Uticaj abrazivnog habanja zuba rotornog bagera na njegovu pouzdanost*, Zbornik radova, Yutrib ’91 Kragujevac 1991.

[3] B. Ivković: *Osnovi tribologije u industriji prerade metala*, Građevinska knjiga, Beograd 1990.

[4] V. Vukotić: *Prilog istraživanju efektivnosti složenih energetskih sistema sa stanovišta integralne sistemske podrške (logistike) sa posebnim osvrtom na područje I BTO sistema rudnika “Gacko”*, Magistarski rad, Mašinski fakultet Mostar 1983.

[5] V. Vukotić: *Povećanje pouzdanosti podsistema kopanja rotornih bagera poboljšanjem triboloških karakteristika reznih elemenata*, Doktorska disertacija, Mašinski fakultet Kragujevac, 2002.

Serbian Tribology Society

SERBIATRIB '13

13th International Conference on Tribology

Faculty of Engineering in Kragujevac

Kragujevac, Serbia, 15 – 17 May 2013

PONAŠANJE NEHRĐAJUĆIH ČELIKA U KOMBINIRANIM UVJETIMA TROŠENJA

Goran Rozing[1], Antun Pintarić[2], Desimir Jovanović[3], Vlatko Marušić[4]
[1]Elektrotehnički fakultet Osijek, Hrvatska, goran.rozing@etfos.hr
[2]Elektrotehnički fakultet Osijek, Hrvatska, antun.pintaric@etfos.hr
[3]Zastava oružje, Srbija, j.desimir@gmail.com
[4]Strojarski fakultet Slavonski Brod, Hrvatska, vlatko.marusic@sfsb.hr

Apstrakt: *Glavna karika u proizvodnji sirovog ulja svakako je pužna preša, koja služi za isprešavanje i cijeđenje ulja iz samljevenog i zagrijanog uljnog sjemenja. U tijeku tog procesa dolazi do odnošenja čestica metala s radnih površina preše, iz čega se može zaključiti da tribosustav čine, radni dijelovi preše i suncokretovo sjemenje. Osim navedenog neizbježnog trošenja, u ovom radu analiziran je i utjecaj korozijskog trošenja dijelova pužne preše nastalog kao posljedica agresivnog djelovanja medija. Navedena trošenja ukazuju da kod pužne preše prevladavaju kombinirani uvjeti trošenja. Na ispitnim uzorcima izrađenim od austenitnih korozijskih postojanih čelika AISI 316L i AISI 304 provedeno je nitrokarburiranje u cilju povećanja tvrdoće u površinskom sloju, koja dovodi do povoljnijih tribooloških svojstava. Za potrebe eksperimentalnog rada provedena su ispitivanja korozijskog ponašanja uzoraka, ispitivanja kemijskog sastava osnovnog materijala, mehaničkih svojstava i analiza mikrostrukture. Zaključeno je da se mogući pristup produljenju vijeka dijelova sastoji ne samo u materijalu nego i u izboru postupka toplinske obrade, kojom će se postići povećanje tvrdoće odnosno povoljnija triboološka svojstva uz zadovoljavajuću korozijsku otpornost.*

Ključne reči: *trošenje, pužna preša, nehrđajući čelici, nitrokarburiranje, korozijska otpornost*

1. UVOD

Problemi trenja i trošenja u praksi su vrlo kompleksni zbog odvijanja mnogostrukih tribooloških procesa. Stoga je nužna brižljiva neposredna i posredna analiza svih komponenata i utjecaja u tribosustavu [1]. Jedan od takvih kompleksnih primjera trošenja je i pužna preša, koja služi za isprešavanje i cijeđenje ulja iz samljevenog i zagrijanog uljnog sjemenja. Proces cijeđenja jestivog ulja ovisi o mnogo parametara koji se mijenjaju u ovisnosti o vrsti uljnog sjemenja, načinu njegove pripreme i tipu preše. Nakon djelomičnog ljuštenja i kondicioniranja vodenom parom, pripremljeno sjemenje mehaničkim putem se cijedi u pužnoj preši. U tijeku tog procesa dolazi do odnošenja čestica metala s radnih površina preše, iz čega se može zaključiti da tribosustav čine, radni dijelovi preše i suncokretovo sjemenje. Uzroci trošenja radnih dijelova preše (segmenata pužnice, jarmova i noževa cjedilne korpe) su djelovanje čestica mikroabraziva SiO_2 x nH_2O u suncokretovom sjemenu [2]. Mikroabraziv sadržan u ljusci suncokreta troši radne dijelove preše a taj proces je nemoguće izbjeći. Trošenje se manifestira oštećivanjem napadnih bridova radnih dijelova preše tj. smanjenja njihovih dimenzija i promjene geometrije profila. Kao rezultat toga dolazi do smanjenja efikasnosti cijeđenja ulja [3]. Osim spomenutog neizbježnog trošenja nakon 4,5 godine (16630 sati) rada nastupilo je oštećenje izazvano djelovanjem agresivnog medija (kisele supare), a manifestiralo se pojavom tribokorozije na dosjednim dijelovima reduktora koje su u kontaktu s dosjednim površinama cjedila. Tadašnji pristup produljenju vijeka istrošenih dosjednih površina sastojao se od zamjene istrošenih površina poluprstenovima izrađenim od korozijski postojanih čelika (EN X2CrNiMo18, AISI 316L, EN) i (EN X5CrNi18-10, AISI 304) u sirovom stanju. Opisana trošenja ukazuju da kod pužne

preše prevladavaju kombinirani uvjeti trošenja koji se mogu opisati kao proces koji vodi ka degradaciji metalnih materijala, koja je rezultat mehaničkog kontakta, kombiniranog sa korozijskim djelovanjem agresivne okoline.

2. ISPITIVANJA UZORAKA/DIJELOVA U PUŽNOJ PREŠI ZA ZAVRŠNO PREŠANJE

Iz iskustva proizilazi da je trenje i trošenje materijala svojstvo sustava, jer na procese osim materijala elemenata tribosustava utječe konstrukcijska izvedba tribosustava, vrste i način opterećenja te naprezanja, način podmazivanja i drugi čimbenici. Stoga se svaki problem mora rješavati individualno, ali uzimajući u obzir temeljne parametre i utjecajne veličine u tribosustavu [1]. Nakon što su poluprsteni dvije kampanje rada pužne preše za završno prešanje kapaciteta ≈ 100t/dan bili u uporabi, prema prethodnom dogovoru, preša je rastavljena u cilju vađenja ispitnih poluprstena. Obavljena je vizualna kontrola površina na kojima su bili ugrađeni ispitni poluprsteni. S obzirom na to da su svi poluprsteni radili u istim uvjetima, odnosno da se vizualno ne uočavaju razlike u izgledu poluprstena dosjedne i zaptivne površine, ocjenjeno je da su za potrebe istraživanja u ovome radu i donošenje odgovarajućih zaključaka dovoljni poluprsteni s reduktora i s dosjedne površine cjedila. Na slici 1 prikazan je vanjski izgled poluprstena na svim površinama prije skidanja za potrebe ispitivanja.

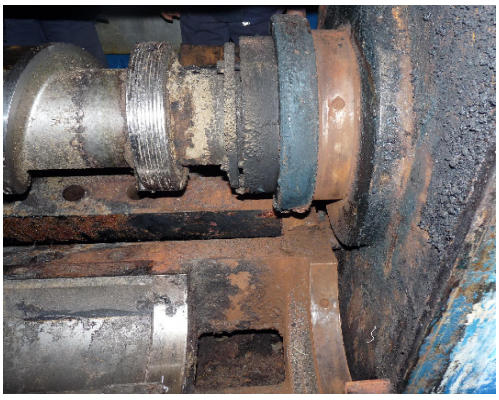

Slika 1. Vrat kućišta reduktora i površine polutke cjedila prije skidanja poluprstena

Odgovarajućim strugačima pažljivo su skinuti uzorci korozijskih produkata za potrebe kemijske analize. Utvrđeno je da u sastavu dominira korozijski produkat željezni oksid tipa FeO/Fe_2O_3, ali i da su prisutni tragovi čestica organskog porijekla iz mliva. Puno je bitniji podatak da je analizom kisele supare utvrđeno da se radi o kiselini karbonilnog tipa (zbog prisustva isparljivih masnih kiselina) i još važnije da izmjereni pH supare iznosi iznosi oko 5,2. Obavljen je vizualni pregled površina svih skinutih poluprstena. Kakateristično je uočiti da se golim okom ne uočavaju pojave korozijskih oštećenja, ali da su prisutni tanki slojevi praškastih taloga, najvjerojatnije mješavine korozijskih produkata osnovnog materijala kućišta/cjedila (GS-42CrMo4) i sitnih čestica mliva. Izgled površine poluprstena na vratu kućišta reduktora i polutke cjedila preše prikazan je na slici 2.

Slika 2. Poluprsten prije demontaže s praškastim talozima nakon ispitivanja uporabom u preši tip EP 16

Bitno je istaknuti da se na površinama osnovnog materijala kako kućišta reduktora, tako i cjedila uočava prisustvo taloga ali i da su te površine intenzivno oštećene korozijom, pri čemu se dubina oštećenja može procjeniti na 3 do 4 mm. Dimenzionalnom kontrolom pomoću pomičnog mjerila utvrđeno je da nije došlo do smanjenja debljine niti jednog poluprstena, na svima je izmjerna debljina 7 mm. Detaljnim pregledom vanjskih površina svih poluprstena, promatranjem pod SEM TOPO (skening elektronskim mikroskopom), utvrđeno je da se mogu uočiti tragovi nastali kao posljedica abrazijskog trošenja sitnim česticama mliva, zatim adhezijom uslijed kontakta poluprstena vrata reduktora s poluprstenom dosjedne površine, ali i oštećenja u formi rupica kao posljedica korozije, slika 3. Na unutarnjim površinama, koje su bile dotegnute na osnovni materijal, promatranjem pod SEM TOPO uočeno je lokalno rupičasto oštećenje, slika 4.

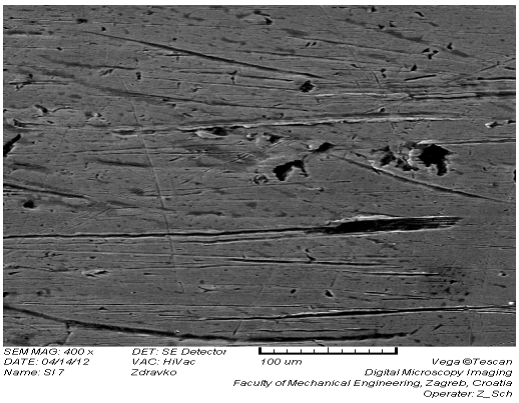

Slika 3. Karakteristični izgled vanjske površine poluprstena nakon uporabe, SEM TOPO

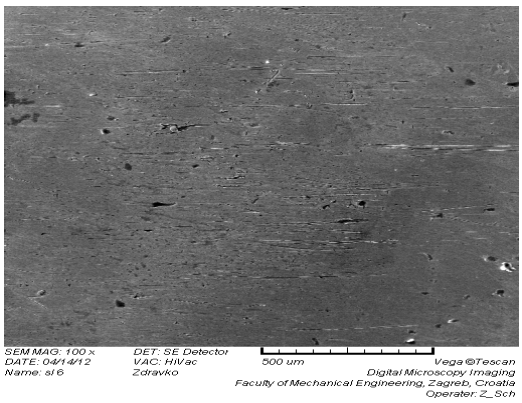

Slika 4. Karakteristični izgled unutarnje površine poluprstena nakon uporabe, SEM TOPO

To je oštećenje najvjerojatnije posljedica djelovanja kombinacije kiselina karbonilnog tipa i vodene pare koje su se nakon kondenziranja „slijevale“ preko dijelova preše i ipak prodrle u zonu kontakta poluprsten/osnovni materijal, bez obzira na to što su napravom stegnute, pri čemu je silikonska brtva trebala onemogućiti prodor supare. Izabrani nadomjesni materijali AISI 316L i AISI 304 po svom kemijskom sastavu spadaju u grupu austenitnih nehrđajućih čelika, koji imaju primjenu u prehrambenoj i procesnoj industriji. Naime, ukupno su u dva ciklusa bili u proizvodnom procesu oko 5000 sati (kroz dvije kalendarske godine). U odnosu na materijal kućišta GS-42CrMo4 znatno su se pokazali postojanijima. Na poluprstenima izrađenim iz varijantnih materijala utvrđeni su isti mehanizmi trošenja, pri čemu nisu uočene značajnije razlike u intenzitetu, kako abrazijskog i adhezijskog tako i korozijskog, bez obzira na razlike u kemijskom sastavu. Tvrdoća ugrađenog nadomjesnog materijala je iznosila oko 170÷180 HV, što se u pogonskim uvjetima pokazalo relativno dostatno, a to potvrđuju i mikroskopski snimci (slika 3 i 4) koji pokazuju tragove abrazijskog trošenja, adhezije ali i rupičaste korozije. Prva dva mehanizma trošenja su prisutnija na vanjskoj strani poluprstena cjedila, dok je treći mehanizam prisutniji na unutarnjoj strani. Razloge pojave abrazijskog trošenja treba tražiti u sastavu mliva točnije u sadržaju SiO_2 x nH_2O iz ljuske suncokreta kao glavnog nositelja abrazivnih svojstava ljuske suncokreta. Pojavu rupičaste korozije može se pojasniti zbog prisutnosti tzv. “kisele supare“.

3. EKSPERIMENTALNI DIO

Ispitivanja kemijskog sastava provedena su na uzorcima oba varijantna čelika u dostavnom stanju. Kemijskom analizom materijala određen je sastav prisutnih elemenata. Za određivanje kemijskog sastava korištena je spektrometrijska metoda, a ispitivanja su izvršena uređajem BELEC. Rezultati ispitivanja kemijskog sastava uzoraka (materijal EN X2CrNiMo18-14-3, AISI 316L i materijal EN X5CrNi18-10, AISI 304) prikazani su u tablici 1.

Tablica 1. Rezultati ispitivanja kemijskog sastava uzoraka 316L i 304

Materijal	Kemijski sastav [%]									
	C	Mn	Si	Cr	Ni	Mo	V	W	Ti,	Fe
316L	0,048	1,224	0,438	16,71	10,08	2,124	0,124	0,185	0,112	68,40
304	0,045	1,295	0,651	18,02	8,11	0,414	0,114	80,19	0,007	70,68

Tvrdoća i otpornost trošenju austenitnih nehrđajućih čelika može se bitno povećati, a da pri tome ne dolazi do značajnog gubitka otpornosti na koroziju. Jedan od pristupa kako bi se povećala površinska tvrdoća i otpornost trošenju čelika je postupak nitriranja koji nudi visokodimenzijsku stabilnost obratka [4]. Nitriranje je postupak otvrdnjavanja površine difuzijom dušika u površinske slojeve i promjena kemijskog sastava čelika [5]. Obzirom na to da na varijantnim materijalima poluprstena nisu nakon uporabe uočena korozijska oštećenja koja bi svojim intenzitetom bila uzročnik prestanka funkcionalnog rada pužne preše, zaključeno je da bi se nitrokarburiranjem varijantnih materijala moglo doprinjeti bitnom povećanju tvrdoće u površinskom sloju koja bi se odrazila na povoljnija tribološka svojstva i produljenje vijeka tribosustava pužnih preša za završno prešanje. Postupak nitrokarburiranja bio je sljedeći: uzorci su prvo predgrijani na temperaturu υ_p=380^{o}C, u trajanju od 3 sata i potom uronjeni u solnu kupku (volumena 1m^3) zagrijanu na 580^{o}C u trajanju od 5 sati. Nakon toga uzorci su hlađeni na zraku.

3.1 Ispitivanje strukture varijantnih materijala nakon nitrokarburiranja

Metalografska ispitivanja uzoraka oba varijantna materijala nakon nitrokarburiranja daju cjelovitu sliku o njihovom mikrostrukturnom stanju. Analiza mikrostrukture uzoraka obrađenih postupkom nitriranja omogućava promatranje i ruba i jezgre ispitnog uzorka. Mikrostruktura rubnog dijela nitrokarburiranih uzoraka čelika AISI 316L i AISI 304 prikazana je na slici 5.

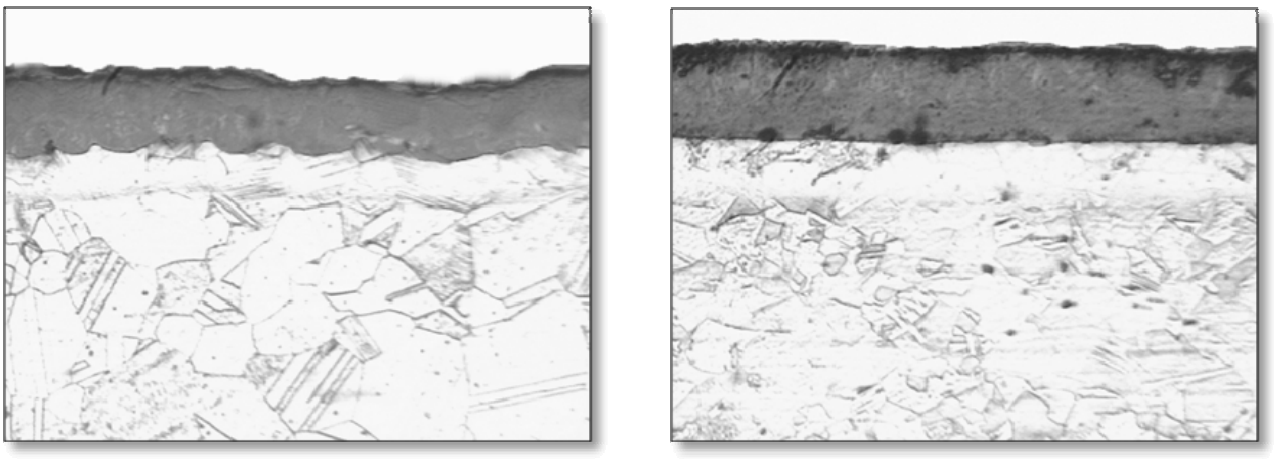

a) b)

Slika 5. Karakteristična mikrostruktura nitriranog čelika, povećanje 240x
a) uzorak 316L, b) uzorak 304

3.2 Ispitivanje mikrotvrdoća varijantnih materijala nakon nitrokarburiranja

Ispitivanje mikrotvrdoća provedena su uređajem DURIMET Leitz metodom Vickers HV 0,025 (opterećenje 0,25 N) i HV 0,5 (opterećenje 5 N), na kojemu je obavljeno i mjerenje tvrdoće osnovnih varijantnih materijala. Rezultati ispitivanja mikrotvrdoća uzoraka oba čelika metodom Vickers HV0,025 dijagramski su prikazani na slici 6

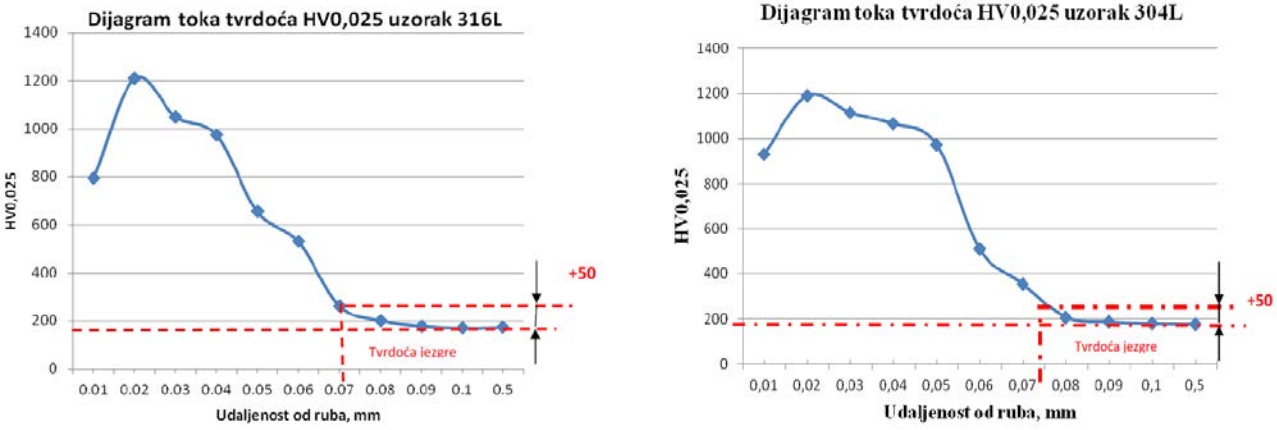

a) b)

Slika 6. Dijagramski prikaz toka mikrotvrdoća i
određivanja dubine nitriranog sloja uzorka čelika, a) 316L i b) 304

Izmjerene vrijednosti tvrdoća poboljšanog uzorka čeličnog lijeva (materijal GS-42CrMo4) kreću se od 230 do 280 HV 0,5.

3.3 Elektrokemijska korozijska ispitivanja modificiranih površina uzoraka

U eksperimentalnom dijelu ispitana su elektrokemijska svojstva nekih čelika oznaka AISI 316L, AISI 304 i GS-42CrMo4 u zasićenoj vodenoj otopini s CO_2, vrijednosti pH 4,8 do 5 pri temperaturi 50°C, kako bi se simulirali stvarni uvjeti agresivne okoline u kojima se odvija trošenje radnih dijelova preše. Uzorci za ispitivanje pripremljeni su na dimenziju Ø16x8 mm. Elektrokemijska korozijska DC ispitivanja provedena su sukladno normi ASTM G5-94 [6] na uređaju Potentiostat/Galvanostat Model 273A EG&E uz primjenu programa SoftCorr III u Laboratoriju za zaštitu materijala, Fakulteta strojarstva i brodogradnje u Zagrebu. Mjerenja su provedena u odnosu na referentnu zasićenu kalomel elektrodu (ZKE) poznatog potencijala + 0,242 V prema standardnoj vodikovoj elektrodi. Određeni su parametri opće korozije: korozijski potencijal (E_{cor}), gustoća korozijske struje (j_{cor}), brzina korozije (v_{kor}), polarizacijski otpor (R_p), piting potencijal (E_{pit}) i zaštitni piting potencijal (Ezpit). Korozijski potencijal Ecor određen je mjerenjem promjene potencijala u vremenu od 1000 s. Polarizacijski otpor materijala R_p je određen iz Tafelovog dijagrama za područje polarizacije ±20 mV u odnosu na korozijski potencijal. Rezultati elektrokemijskih ispitivanja prikazani prikazani su u tablici 2.

Tablica 2. Rezultati elektrokemijskih korozijskih ispitivanja uzoraka

Materijal/stanje	β_A [V/dek]	β_K [V/dek]	J_{cor} [$\mu A/cm^2$]	V_{cor} [mm/god]	R_p [Ωcm^2]
AISI304, nitrirano	0,078	0,103	6,62	0,067	3282
AISI316L, nitrirano	0,988	0,039	6,71	0,069	5254
GS-42CrMo4, poboljšano	0,088	0,598	86,62	1,003	250

Ciklička potenciodinamička polarizacijska mjerenja provedena su na uzorcima AISI 316L, AISI 304 i GS-42CrMo4 u zasićenoj vodenoj otopini s CO_2, vrijednosti pH 4,8 do 5 pri temperaturi 50°C. Na slici 7 prikazan je dijagram cikličke polarizacije, a na slici 8 makrostrukturalne snimke uzoraka.

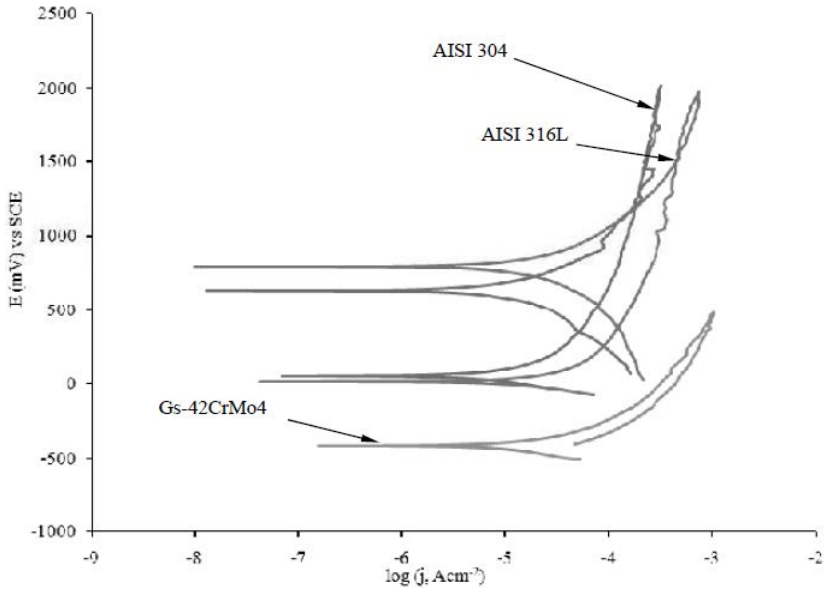

Slika 7. Dijagram cikličke polarizacije nitriranog uzorka 316L, 304 i poboljšanog uzorka GS-42CrMo4

Slika 8. Makro prikaz površine nitriranog uzorka 316L, 304 i poboljšanog uzorka GS-42CrMo4 nakon cikličke polarizacije

4. ANALIZA REZULTATA I ZAKLJUČAK

Na poluprstenima izrađenim iz varijantnih materijala različitog kemijskog sastava utvrđeni su isti mehanizmi trošenja, pri čemu nisu uočene značajnije razlike u intenzitetu, kako abrazijskog i adhezijskog tako i korozijskog trošenja. Analizom uvjeta rada pužnih preša za završno prešanje zaključeno je da se abrazivno djelovanje vrlo tvrdog SiO_2 x nH_2O (oko 1100 HV) ne može izbjeći, ali se može smanjiti povećanjem tvrdoće dijelova preše. U tome smislu zaključeno je da bi se nitriranjem varijantnih materijala moglo doprinijeti bitnom povećanju produljenja vijeka reprezentantnog tribosustava pužnih preša za završno prešanje. Na uzorcima izrađenim iz

varijantnih materijala u dostavnom stanju i u nitriranom stanju te na uzorcima osnovnog materijala provedena su ispitivanja otpornosti na elektrokemijsku koroziju, kako bi se simulirali uvjeti agresivne okoline u kojima se odvija rad dijelova preše. Rezultati elektrokemijskih ispitivanja prikazanih u tablici 2, ukazuju da materijali AISI 316L i AISI 304 imaju dvadeset puta veće vrijednosti polarizacijskog otpora R_p u odnosu na materijal GS-42CrMo4. Vrijednost brzine korozije za austenitne korozijski postojane čelike je podjednaka i četrnaest puta je manja nego za čelični lijev GS-42CrMo4. Iz dijagrama cikličkih polarizacija (slika 7) vidljivo je da nitrirani uzorci austenitnih čelika 316L i 304 ne pokazuju sklonost rupičastoj koroziji niti koroziji u procjepu, dok materijala GS-42CrMo4 pokazuje sklonost rupičastoj koroziji i koroziji u procjepu što potvrđuje makrostrukturalna snimka površine nakon ispitivanja. Analizom navedenih podataka može se potvrditi da se postupkom nitrokarburiranja u solnoj kupki znatno povećava tvrdoća površine što je bio jedan od traženih zahtjeva. Istovremeno dolazi do povećanja brzine korozije (0,067 ÷ 0,069 mm/god), ali ta brzina je znatno manja od granične vrijednosti koja iznosi 0,1 mm/god, prema kriteriju primjenjivosti metala s obzirom na prosječnu brzinu prodiranja opće korozije.

LITERATURA

[1] T. Filetin, K. Grilec: *Postupci modificiranja i prevlačenja površina*, Hrvatsko društvo za materijale i tribologiju, Zagreb, 2004.

[2] V. Ivušić, V. Marušić, K. Grilec: *Abrasion resistance of surface layers*, VTT Symposium 180& COST516 Tribology Symposium, VTT Technical Researche Centre of Finland, pp. 201-210, 1998.

[3] G. Rozing, M. Katinić, V. Marušić: *Neke specifičnosti utjecaja dominatnog mehanizma trošenja na pristup održavanju pužnih preša*, 16. Međunarodno savjetovanje ODRŽAVANJE 2010 Zagreb: HDO Hrvatsko-društvo održavatelja, pp. 120-126, 2010.

[4] B. Vasiljević, B. Nedić: *Modifikovanje površina*, Univerzitet u Kragujevcu, Mašinski fakultet u Kragujevcu, Jugoslovensko društvo za tribologiju, Kragujevac, 2003.

[5] A. Triwiyanto, P. Hussain, A. Rahman, M.C. Ismail: *The Influence of Nitriding Time of AISI 316L Stainless Steel on Microstructure and Tribological Properties*, Asian Journal of Scientific Research, Vol.6, pp .323-330, 2013.

[6] ASTM G5 – 94: Standard Reference Test Method for Making Potentiostatic and Potentiodynamic Anodic Polarization Measurements.

STAINLESS STEEL BEHAVIOR UNDER COMBINED CONDITIONS OF WEAR

Abstract: *The key element in the production of raw oil is definitely the worm press, which is used for pressing and extrusion of oil from ground and heated oil seeds. During this process, metal particles are worn from the working surfaces of the press, which indicates that the tribosystem consists of working parts of the press and sunflower seeds. Next to the aforementioned unavoidable wear, damage due to aggressive media was also observed. Wear described above indicate that at worm press overcome combined wear conditions. On the test samples made of austenitic staineless steel AISI 316L and AISI 304 nitrocarburising was conducted to increase hardness in surface layer, which leads to better tribological properties. In the experimental part of paper, there were tested corrosion behaviour of samples, chemical composition of base material, mechanical properties and microstructure analysis. It was concluded that possible extension of life time consists not only in material but also in heat treatment selection, by which increase of hardness will be achieved with reference to better tribological properties with satisfactory corrosion resistance.*

Keywords: *wear, worm press, stainless steel, nitrocarburising, corrosion resistance*

Authors Index

T

V

Z

Ž

Y

W

CIP - Каталогизација у публикацији
Народна библиотека Србије, Београд

621.89(082)
66.017:531.43(082)
539.375.6(082)

INTERNATIONAL Conference on Tribology (13 ; 2013 ; Kragujevac)
Proceedings / 13th International Conference on Tribology - SERBIATRIB '13, 15-17 May 2013., Kragujevac, Serbia ; [organized by] Serbian Tribology Society [and] Faculty of Engineering, University of Kragujevac ; editors Miroslav Babic, Slobodan Mitrovic. - Kragujevac : Serbian Tribology Society : Faculty of Engineering, 2013 (Kragujevac : Kopirnica Masinac). - [12], 455 str. : ilustr. ; 24 cm

Radovi na srp. i engl. jeziku. - Tekst stampan dvostubacno. - Tiraz 100. - Str. [5-6]: Preface / editors. - Bibliografija uz svaki rad. - Abstracts. - Registar.

ISBN 978-86-86663-98-6
1. Бабић, Мирослав [уредник] [аутор додатног текста] 2. Serbian Tribology Society (Kragujevac)
a) Трибологија - Зборници b) Машински материјали - Триболошке особине - Зборници c) Хабање - Зборници d) Мазива - Зборници
COBISS.SR-ID 198310412


SERBIATRIB '13